The Asian Monsoon

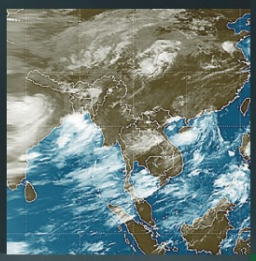

BIN WANG

Springer

PRAXIS

The Asian Monsoon

Bin Wang

The Asian Monsoon

Published in association with
Praxis Publishing
Chichester, UK

Professor Bin Wang
Department of Meteorology & International Pacific Research Center
University of Hawaii
Honolulu
Hawaii
USA

SPRINGER–PRAXIS BOOKS IN ENVIRONMENTAL SCIENCES
SUBJECT *ADVISORY EDITOR*: John Mason B.Sc., M.Sc., Ph.D.

ISBN 3-540-40610-7 Springer-Verlag Berlin Heidelberg New York

Springer is part of Springer-Science + Business Media (springeronline.com)
Bibliographic information published by Die Deutsche Bibliothek
Die Deutsche Bibliothek lists this publication in the Deutsche Nationalbibliografie; detailed bibliographic data are available from the Internet at http://dnb.ddb.de

Library of Congress Control Number: 2005931411

Cover design: Jim Wilkie
Project management: Originator Publishing Services, Gt Yarmouth, Norfolk, UK

Printed on acid-free paper

Contents

List of figures

List of tables

Preface

The Asian monsoon is a spectacular occurrence in the Earth's climate system. During summer, the monsoon engine pumps moisture transported across thousands of miles from the Indian and Pacific Oceans, producing heavy rains over south and east Asia and adjacent marginal seas; meanwhile, it dumps sinking, dry air to the north and west of Asia's monsoon area, forming the World's largest desert zone, which stretches from the Sahara and the Middle East to Mongolia. During winter, the Siberian cold wave pushes airflow across the equator, causing heavy rains over Indonesia, northern Australia, and the southern Pacific convergence zones.

What makes the Asian monsoon so powerful is the combination of thermal contrast between the World's largest landmass (Eurasian continent) and ocean basin (the Indo-Pacific Ocean) and the presence of the World's largest ridge, the Tibetan Plateau. This unique tectonic setting responds to seasonal progression of the solar radiation and Earth's rotation, producing the *monsoon climate* with its seasonal reversals in both the prevailing winds and associated precipitation, characterized by "wet" summers and "dry" winters. Positive feedback with hydrological processes amplifies the monsoon circulation. The accompanying desert and the Mediterranean climate over the subtropics are "twin" to the monsoon climate, as both are produced by the Asian monsoon system.

The giant Asian monsoon system (often called the Asian–Australian monsoon system) dominates the entire eastern hemisphere tropics and subtropics. It interacts with the El Nino/Southern Oscillation (ENSO) and extratropical circulations and has far-reaching impacts for the global climate and the environment. The Asian monsoon exemplifies the most complex interactions among Earth's surface, ocean, atmosphere, hydrosphere, and biosphere. The scientific importance of the Asian monsoon cannot be overemphasized.

The Asian monsoon is also of enormous importance to humans. About 60% of humanity inhabits the region of the Asian monsoon – a region where torrential rains,

storms, droughts, heat waves, and cold-air surges are a part of the economy, culture, and rhythms of life. The vegetation, biogeochemistry, economy, and society across the Asian monsoon regions are all critically influenced by the evolution and variability of the Asian monsoon.

The science pertaining to the monsoon has advanced enormously in the last two decades due to an increased wealth of new data from satellite observations and field experiments, and the advances in computing power and mathematical representations of coupled climate systems. My intent in compiling this book is to offer a timely summary of recent progress and also the remaining gaps in our knowledge and to provide a full and current account of scientists ever-improving, expanding understanding of the physics associated with monsoon weather and climate. Particular attention is given to the rapid progress made in monsoon predictions, some possible directions for future change, and the monsoon's impacts on economies.

In view of the topic's complexity and scientific diversity, leading scientists at the forefront of monsoon research were invited to contribute to this book. Most chapters contain an authoritative review of the subject and highlight conceptual breakthroughs as well as frontier research issues.

This volume begins with an overview of the Asian monsoon (Part One: Chapters 1–3). Chapter 1 describes the Asian monsoon as a multiscale, coupled atmosphere–ocean–land dynamic system that interacts with other components of the Earth's climate system. Chapter 2 provides a global perspective of the monsoon. Chapter 3, complementing other chapters, focuses on the most powerful boreal winter monsoon and Austral summer monsoon over the Maritime Continent and Australia; providing a comprehensive overview of the monsoon in general and the Asian–Australian monsoon in particular.

The character of the monsoon system is highly variable on many temporal and spatial scales. Part Two (Chapters 4–7) describes the monsoon variability over a broad range of timescales, from days to decades, and on various spatial scales, from the smallest mesoscale to continental and global scales. The great variety of monsoon weather is described in Chapter 4, with a detailed account of both south Asian and east Asia. Chapter 5 provides a comprehensive review of the current knowledge and issues of the monsoon's intraseasonal variations. In Chapter 6 is summarized the main features of interannual variability and possible causes. Variability on the decadal to interdecadal timescale is addressed in Chapter 7.

Understanding of the monsoon climate and its changes represents one of the most difficult challenges to climate science because of the complexity of its interactions over a wide range of atmospheric processes, as well as associated interactions between the atmosphere, ocean, and land. Part Three of this book (Chapters 8–13) is devoted to better improving the understanding of the monsoon system's physical processes and its roles associated with the Earth's climate system. This part looks at the atmospheric internal dynamical processes on a mesoscale (Chapter 8) and on large and planetary-scales (Chapter 9). Hydrological processes are also discussed (Chapter 10). Also included in this part are the interactions of the monsoon system with land surface processes (Chapter 11), and ENSO–Asian monsoon interactions (Chapter 12), and as well the roles of the Tibetan Plateau (Chapter 13). These

chapters, along with the discussions on the atmosphere–ocean interaction discussed in Chapter 1, lay out a firm basis for understanding the complex monsoon physics.

Seasonal prediction of monsoon activity is vitally important for society and remains a foremost challenge to climate prediction in the 21st century. Part Four (Chapters 14–15) deals with the numerical modeling and prediction of the monsoon activity. The governing dynamical controls and physical representations that determine the potential predictability of monsoons are explored in Chapters 14 and 15. Although the dynamical models of the coupled ocean–atmosphere–land system still have considerable difficulty in capturing the predictability, the discussions in this part of the book offer new ideas that are expected to contribute to noticeable improvements in the monsoon climate predictions in the coming decades.

Part Five of the book (Chapters 16–18) enhances the understanding of the monsoon environment and its societal influences. Evidence from paleorecord studies shows that the Asian monsoon system has undergone remarkable changes on geological timescales. Chapter 16 gives a detailed account of the past monsoon cycles according to geological, orbital, and millennial and centennial timescales. In the future, anthropogenic influences, including landuse/cover changes and atmospheric composition changes on regional and global scales, may considerably affect the future of the Asian monsoon. Possible human influences on the Asian monsoon are discussed in Chapter 17. The focus of Chapter 18 is on the monsoon's impacts on agriculture and the economy. Of note is the fact that the monsoon's influences on humanity reach far beyond agriculture – these aspects are dealt with more specifically elsewhere.

This book can be used as a comprehensive interdisciplinary text for college students, both undergraduate and graduate. It can also serve as a professional reference for research scientists and professionals in the fields of meteorology, oceanography, climate dynamics, environmental science, geography and geology, hydrology, paleoclimatology, agriculture, and the social sciences. Its informative content is such that most material in this book can also be of great value to non-specialists.

Contributors

Chapter 1 **Peter J. Webster**
School of Civil and Environmental Engineering, Georgia Institute of Technology, Atlanta, GA, 30332-0355, USA
Email: piw@eas.gatech.edu

Chapter 2 **Kevin E. Trenberth, James W. Hurrell, and David P. Stepaniak**
National Center for Atmospheric Research, PO Box 3000, Boulder, CO, 80307, USA
Email: trenbert@ucar.edu, jhurrell@ucar.edu, davestep@ucar.edu

Chapter 3 **C-P Chang[1], Zhuo Wang[1], and Harry Hendon[2]**
[1] Department of Meteorology, Naval Postgraduate School, Monterey, California, USA
[2] Bureau of Meteorology Research Centre, Melbourne 3001, Australia
Email:cpchang@nps.edu, zwang@nps.edu, hhh@bom.gov.au

Chapter 4 **Yihui Ding[1] and D. R. Sikka[2]**
[1] National Climate Center, China Meteorological Administration, No. 46 Zhongguancun Nan Da Jie, Haidian District, Beijing 100081, PR China
[2] Indian Institute of Tropical Meteorology, Pune, India
Email: dingyh@cma.gov.cn

Chapter 5 **Duane E. Waliser**
Jet Propulsion Laboratory, MS 183-505, California Institute of Technology, 4800 Oak Grove Drive, Pasadena, CA, 91109, USA
Email: duane.waliser@jpl.nasa.gov

Chapter 6 **Song Yang[1] and William K.-M. Lau[2]**
[1]NOAA's Climate Prediction Center, Camp Springs, Maryland 20746, USA
[2] NASA Goddard Space Fight Center, Laboratory for Atmospheres, Greenbelt, MD, 20771, USA
Email: song.yang@noaa.gov, lau@climate.gsfc.nasa.gov

Chapter 7 **B. N. Goswami**
Centre for Atmospheric and Oceanic Sciences, Indian Institute of Science, Bangalore, 560012, India
Email: goswamy@caos.iisc.ernet.in

Chapter 8 **Richard H. Johnson**
Colorado State University, Department of Atmospheric Science, Fort Collins, CO 80523, USA
Email: johnson@atmos.colostate.edu

Chapter 9 **Brian J. Hoskins[1] and Bin Wang[2]**
[1] Department of Meteorology, University of Reading, PO Box 243, Earley Gate, Reading, RG6 6BB, UK
[2] Department of Meteorology and International Pacific Research Center, University of Hawaii at Manoa, 2525 Correa Road, Honolulu Hawaii 96822, USA
Email: B.J.Hoskins@reading.ac.uk, wangbin@hawaii.edu

Chapter 10 **Tsing-Chang Chen**
Department of Geological and Atmospheric Sciences, 3010 Agronomy Hall, Iowa State University, Ames, IA, 50010, USA
Email: tmchen@iastate.edu

Chapter 11 **Tetsuzo Yasunari[1,2]**
[1] Hydrospheric atmospheric Research Center (HyARC), Nagoya University, Nagoya, Aichi 464-8601, Japan
[2] Frontier Research Center for Global Change (FRCGC), JAMSTEC, Yokohama, Kanagawa
Email: yasunari@atm.geo.tsukuba.ac.jp

Chapter 12 **Ngar-Cheung Lau[1] and Bin Wang[2]**
[1]Geophysical Fluid Dynamics Laboratory/NOAA, Princeton University, Princeton, New Jersey, USA
[2] Department of Meteorology and, International Pacific Research Center, University of Hawaii at Manoa, 2525 Correa Road, Honolulu, Hawaii 96822, USA
Email: gl@gfdl.gov, wangbin@hawaii.edu

Chapter 13 **Michio Yanai[1] and Guo-Xiong Wu[2]**
[1]Department of Atmospheric and Oceanic Sciences, University of California, Los Angeles, 405 Hilgard Avenue, Los Angeles, California 90095-1565, USA
[2] State Key Laboratory of Atmospheric Sciences and Geophysical Fluid Dynamics (LASG), Institute of Atmospheric Physics, Chinese Academy of Sciences, PO Box 9804, Beijing 100029, China
Email: yanai@atmos.ucla.edu, gxwu@lasg.iap.ac.cn

Chapter 14 **T. N. Krishnamurti[1], T. S. V. Vijaya Kumar[1], and A. K. Mitra[2]**
[1] Department of Meteorology, Florida State University, Tallahassee, FL 32306-4520 USA
[2] National Centre for Medium Range Weather Forecasting, New Delhi, India
Email: tnk@io.met.fsu.edu, vijay@met.fsu.edu

Chapter 15 **In-Sik Kang[1] and Jagadish Shukla[2]**
[1] Center for Climate and Environment Study, School of Earth Science, Seoul National University, Seoul 151-742, Korea
[2] Institute of Global Environment and Society, Inc., George Mason University, 4041 Powder Mill Road, Suite 302, Calverton, MD 20705-3106, USA
Email: kang@climate.snu.ac.kr, shukla@cola.iges.org

Chapter 16 **Steve C. Clemens**
Earth Systems History, Department of Geological Sciences, Brown University, 324 Brook Street, Box 1846, Providence, RI, 02912, USA
Email: steven_clemens@brown.edu

Chapter 17 **Akio Kitoh**
Climate Research Dept., Meteorological Research Institute, 1-1 Nagamine, Tsukuba, Ibaraki 305-0052, Japan
Email: kitoh@mri-jma.go.jp

Chapter 18 **Sulochana Gadgil[1] and K. Rupa Kumar[2]**
[1] Center for Atmospheric and Oceanic Sciences, Indian Institute of Science, Bangalore 560012, India
[2] Climatology and Hydrometeorology division, Indian Institute of Tropical Meteorology, Pune 411008, India
Email: sulo@caos.iisc.ernet.in, kolli@tropmet.res.in

Abbreviations

ABL	atmospheric boundary layer
AGCM	atmospheric general circulation model
AIMR	all-India monsoon rainfall
AIR	all-India rainfall
AIRI	all-Indian rainfall index
AIRS	Atmospheric Infrared Sounder
AMIP	Atmospheric Model Intercomparison Project
AMTEX	Air Mass Transformation Experiment
ANOVA	analysis of variance
AO	Arctic Oscillation
APCN	APCE Climate Network
APEC	Asia–Pacific Economic Cooperation
ARMEX	Arabian Sea Monsoon Experiment
ARPS	Advanced Regional Prediction System
ASCII	Air–sea Convective Intraseasonal Interaction
ASR	absorbed solar radiation
AUS	northern Australian region
AV	absolute vorticity
AWMI	Asian winter monsoon index
BATS	biosphere–atmosphere transfer scheme
BMRC	Bureau of Meteorology Research Centre
BOB	Bay of Bengal
BOBMEX	Bay of Bengal Monsoon Experiment
C-POL	C-Band Polarimetric Radar
CAPE	convective available potential energy
CCA	canonical correlation analysis
CCCMA	Canadian Centre for Climate Modeling and Analysis
CCM	Climate Community Model

CCSR	Center for Climate System Research
CEOF	complex empirical orthogonal function
CGCM	coupled general circulation model
CHI	southern China and East China Sea region
CI	convection index
CID	convective interaction with dynamics
CINE	convective inhibition negative energy
CISK	conditional instability of the second kind
CISO	climatological ISO
CLIVAR	Climate Variability and Predictability Programme
CMAP	Climate Prediction Center Merged Analysis of Precipitation
CMIP	Coupled Model Intercomparison Project
CNRM	Centre National de Recherches Meteorologiques
CO_2	carbon dioxide
COADS	Comprehensive Ocean–Atmosphere Data Set
COARE	Coupled Ocean–Atmosphere Response Experiment
CODAS	comprehensive ocean–atmosphere data set
COLA	Center for Ocean–Land–Atmosphere Studies
CPC	Climate Prediction Center
CRIEPI	Central Research Institute of Electric Power Industry
CRU	Climatic Research Unit
CSE	continental-scale experiment
CSIRO	Commonwealth Scientific and Industrial Research Organization
CSM	Climate System Model
CTRL	control experiment
CZ	Cane–Zebiak model
DEMETER	Development of a European Multimodel Ensemble system for
DERFs	Dynamical Extended Range Forecasts
DJF	December–January–February
DO	Dansgaard–Oeschger
DOE	Department of Energy
DTEP	deep tropical eastern/central Pacific
EAH	East African Highlands
EAM	east Asian monsoon
EASM	east Asian summer monsoon
EAWM	east Asian winter monsoon
ECMWF	European Centre for Medium-Range Weather Forecasts
ENSO	El Niño/Southern Oscillation
EOF	empirical orthogonal function
EQIO	equatorial Indian Ocean
EQUINOO	Equatorial Indian Ocean Oscillation
ERBE	Earth Radiation Budget Experiment
FCL	free convection level
FFT	fast Fourier transform
FGGE	First GARP Global Experiment

FRCGC	Frontier Research Center for Global Change
FSU	Florida State University
FSULAM	Florida State University Limited Area Model
GAME	GEWEX Asian Monsoon Experiment
GARP	Global Atmospheric Research Program
GATE	GARP Atlantic Tropical Experiment
GCM	general circulation model
GDP	Gross Domestic Product
GEWEX	Global Energy and Water Cycle Experiment
GFDL	Geophysical Fluid Dynamics Laboratory
GHG	greenhouse gas
GISP2	Greenland Ice Sheet Project 2
GISS	Goddard Institute for Space Studies
GLA	Goddard Laboratory for Atmospheres
GLACE	Global Land Atmosphere Coupling Experiment
GMS	geostationary meteorological satellite
GOALS	Global–Ocean–Atmosphere–Land–System
GOOS	Global Ocean Observing System
GP	genesis potential
GPCP	Global Precipitation Climatology Project
HadAM3	Hadley Centre Atmospheric Model version 3
HFP	Historical Forecast Project
HMR	homogeneous region monsoon rainfall
HUBEX	GAME–Huaihe Basin Experiment
HyARC	Hydrospheric Atmospheric Research Center
HYCOM	HYbrid Coordinate Ocean Model
IAP	Institute of Atmospheric Physics
IAV	interannual variability
IIOE	International Indian Ocean Expedition
IMD	India Meteorological Department
IND	India/Arabian Sea region
INDOEX	Indian Ocean Experiment
INSAT	Indian National Satellite
IO	Indian Ocean
IOD	Indian Ocean Dipole
IOP	Indian Ocean Panel; Intense Observing Period (Chapter 8)
IOZM	Indian Ocean Zonal Mode
IPCC	Intergovernmental Panel on Climate Change
IR	infrared
ISBA	interactions soil–biosphere–atmosphere
ISM	Indian summer monsoon
ISMR	Indian summer monsoon rainfall
ISO	intraseasonal oscillation
ISOV	ISO variability
ISV	intraseasonal variability

ITCZ	intertropical convergence zone
JAMSTEC	Japan Marine Science and Techonology Center
JASMINE	Joint Air–Sea Monsoon Interaction Experiment
JJA	June–July–August
JJAS	June–July–August–September
JMA	Japan Meteorological Agency
KMA	Korea Meteorological Agency
L–AI	land–atmosphere interaction
LAI	land–atmosphere interaction
LAI	leaf area index
LASG	Laboratory of Atmospheric Sciences and Geophysical Fluid Dynamics
LBC	lower boundary condition
LF	low frequency
LH	latent heat
LIM	Linear Inverse Model
LLJ	low-level jet
LPS	low-pressure systems
LPSD	low-pass standard deviation
LS	leading stratiform
LSM	land surface model
LSS	land surface schemes
LST	local solar time
LT	local time
MAM	March–April–May
MCC	mesoscale convective complex
MCS	mesoscale convective systems
MCV	mesoscale convective vortex
MEM	maximum entropy method
MH	monsoon Hadley
MIS	marine isotopic stage
MISO	monsoon ISO
MISR	multiangle imaging spectroradiometer
MJJA	May–June–July–August
MJO	Madden–Julian Oscillation
MLD	mixed layer depth
MLM	mixed layer model
MM5	Fifth-Generation NCAR/Penn State Mesoscale Model
MME	multimodel ensemble
MODIS	moderate resolution imaging Spectroradiometer
MONEX	Summer Monsoon Experiment
MONTBLEX	Monsoon Trough Boundary Layer Experiment
MPI	Max Planck Institute for Meteorology
MRF	medium-range forecast
MRG	mixed Rossby–gravity

MRI	Meteorological Research Institute
MSU	Microwave Sounding Unit
MT	monsoon trough
MTC	mid-tropospheric cyclone
NAO	North Atlantic Oscillation
NASA	National Aeronautics and Space Administration
NCAR	National Center for Atmospheric Research
NCEP	National Centers for Environmental Prediction
NCMRWF	National Centre for Medium-Range Weather Forecasting
NCSU	North Carolina State University
NDJF	November–December–January–February
NH	northern hemisphere
NHET	northern hemisphere near-equatorial trough
NIES	National Institute for Environmental Studies
NINO3.4	5°S–5°N, 170°–120°W
NMC	National Meteorological Center
NOAA	National Oceanic and Atmospheric Administration
NRC	National Research Council
NRL	Naval Research Laboratory
NWP	numerical weather prediction
OAI	ocean–atmosphere interaction
OI	optimal interpolation
OLR	outgoing long-wave radiation
OLRA	outgoing long-wave radiation anomaly
OSSE	Observing System Simulation Experiment
OSU	Oregon State University
PBL	planetary boundary layer
PC	principal component
PDF	probability distribution function
PDO	Pacific decadal oscillation
PDS	point-wise downscaling
PENR	Penninsular Indian Rainfall
PHI	Philippine Sea region
PILPS	Project for Intercomparison of Land Surface Parameterization Schemes
PMP	Possible Maximum Precipitation
POP	Principal Oscillation Pattern
PR	precipitation radar
PS	parallel stratiform
PSAC	Philippine Sea anticyclone
PSU	Penn State University
PV	potential vorticity
PWC	precipitable water content
QBM	quasibiweekly mode
QBO	quasibiennial oscillation

QuikSCAT	Quick Scatterometer
QXPMEX	Qinghai–Xizang Plateau Meteorology Experiment
RAM	Regional Atmospheric Model
RegCM	Regional Climate Model
RHC	reverse Hadley circulation
RMM	real time multivariate MJO
RWS	Rossby wave source
SACZ	South Atlantic convergence zone
SAH	south Asian High
SAM	south Asian monsoon
SAS	Simplified Arakawa–Schubert Scheme
SCS	South China Sea
SCSMEX	South China Sea Monsoon Experiment
SEAM	southeast Asian monsoon
SECHIBA	Schématisation des Echanges Hydriques à l'Interface entre la Biosphère et l'Atmosphère
SH	southern hemisphere
SHAP	sensible heat driven air-pump
SiB	simple biosphere
SLP	sea level pressure
SMH	Siberian–Mongolian High
SMIP	Seasonal Model Intercomparison Prediction
SMP	Sumatra and Malay Peninsula
SNU	Seoul National University
SOI	Southern Oscillation Index
SON	September–October–November
SPCZ	South Pacific convergence zone
SRES	Special Report on Emission Scenarios
SSA	singular spectrum analysis
SSH	sea surface height
SSiB	simplified SiB
SSM/I	Special Sensor Microwave Imager
SST	sea surface temperature
STA	seasonal transitional axis
STJ	subtropical jet stream
SVD	singular value decomposition
TAMEX	Taiwan Area Mesoscale Experiment
TAO	Tropical Atmosphere–Ocean
TBO	tropospheric biennial oscillation
TC	tropical cyclones
TCZ	tropical convergence zone
TEJ	tropical easterly jet stream
TH	Tibetan High
TKE	Turbulent Kinetic Energy
TMI	TRMM Microwave Imager

TOA	top-of-atmosphere
TOGA	Tropical Ocean–Global Atmosphere
TOPEX	Topography Eeperiment for Ocean Circulation
TRMM	Tropical Rainfall Measuring Mission
TS	trailing stratiform
TSI	total solar irradiance
U200	200-mb zonal wind
UKMO	United Kingdom Meteorological Office
UTC	universal coordinated time
VP200	velocity potential at 200 hPa
WCR	west central Indian rainfall
WCRP	World Climate Research Programme
WEB	westerlies and easterlies boundary
WGSIP	CLIVAR Working Group on Seasonal to Interannual Prediction
WISHE	wind-induced surface heat exchange
WMO	World Meteorological Organization
WMONEX	winter MONEX
WNP	western North Pacific
WNPSM	western North Pacific summer monsoon
WOCE	World Ocean Circulation Experiment
WWW	World Weather Watch

Acknowledgements

I owe a debt beyond my ability to express it to all contributors to this volume whose dedicated endeavor made this comprehensive volume possible. My acknowledgements are gratefully extended to the following reviewers for their enthusiastic support providing invaluable comments and suggestions for various chapters: Mike Alexander, Congbin Fu, Tim DelSole, Yihui Ding, Saji Hameed, Zengzhen Hu, Ryuichi Kawamura, Ben Kirtman, Akio Kitoh, R. H. Kripalani, Chongyin Li, Eric Maloney, Brian Mapes, Jun Matsumoto, Kohzoh Ninomiya, Delia Oppo, Chung-Kyu Park, Ken Sperber, Yubin Su, Hiroaki Uda, Renguang Wu, Song Yang, and Won-Tae Yun.

During the planning of the book, I benefited from constructive suggestions proffered by many colleagues. I wish to particularly acknowledge suggestions made by Kevin Trenberth, Jerry Meehl, Duzheng Ye (T.-C. Yeh), Takio Murakami, Tom Schroeder, and LinHo.

Over the past 18 years, the National Science Foundation, National Oceanic and Atmospheric Administration, and Office of Naval Research have generously and continuously supported my group in our studies of tropical meteorology and monsoons. My participation of the Asian–Australian Monsoon System studies at the International Pacific Research Center (IPRC) was in part supported by the Frontier Research System for Global Change.

Without invaluable technical assistance from my colleagues and students, this book would be much delayed. Many thanks are extended to Ping Liu who helped with webpage updating and Na Lan who compiled a single consolidated acronym list and a reference list. I appreciate Clive Horwood's encouragement and generous assistance and Larissa Leroux who edited a portion of the manuscript.

Part One

1

The coupled monsoon system

Peter J. Webster

1.1 INTRODUCTION

The monsoons have received fervent attention for nearly 350 years. Early studies (e.g., Halley, 1686; Hadley, 1735)[1] were driven by both basic scientific curiosity and commercial necessity. The Indian Ocean and south Asia were areas of intense trading activity and the success of a trading venture depended on entering and exiting the south and east Asian regions during the proper phase of the monsoon annual cycle. Later research (e.g., Blandford, 1886, 1887; Walker, 1924, 1928) revolved mainly around societal and humanitarian issues as it had been noted that the livelihood and well being of these monsoon societies depends on the variations of the monsoon and the symbiotic relationship between agricultural practices and climate. Whereas the summer rains recur each year, they do so with sufficient variability to create periods of relative drought and flood throughout the region. Figure 1.1 shows examples of the interannual variability as long-term time series of rainfall for India and north Australia. Both time series possess different means and each shows substantial interannual variability. The value of forecasting these variations well in advance has immense value and can be used to optimize agricultural practices and water resource management, and to anticipate and mitigate disasters associated with monsoon variability. Forecasting monsoon variability was a major priority when systematic forecasting efforts began over a century ago. It remains so today, as attempts are made to improve the quality of life in the monsoon regions and as society seeks avenues toward global sustainability.

Perhaps the most important achievement in the last two decades has come from the identification of the coupled ocean–atmosphere modes responsible for the El Niño–Southern Oscillation (ENSO) phenomenon (see review by Wallace *et al.*, 1998). This progress inspired the international Tropical Ocean–Global Atmosphere

[1] See Kutzbach (1987) for a thorough historical review of monsoons.

B. Wang (ed.), *The Asian Monsoon*.

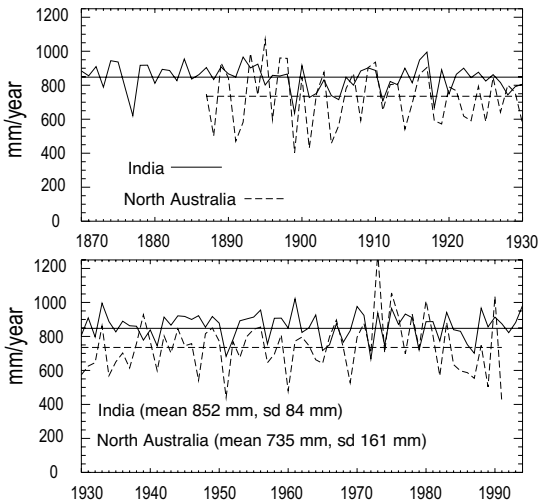

Figure 1.1. Time sequence of mean annual precipitation for India and north Australia using Indian and north Australian rainfall climatologies. Solid and dashed lines show the 'all-India' rainfall index (Parthasarathy *et al*., 1992b, 1994), and north Australian data (compiled by Lavery *et al*., 1997). In general, the Indian rainfall is less variable (mean 852 (84 mm)) compared with the north Australian rainfall (735 (161 mm)). Neither time series shows prolonged periods of multiyear drought or flood.

Programme (TOGA) which had a *de facto* emphasis on the tropical Pacific. The study of other tropical regions, including their relationship to Pacific climate variability, has become a fundamental objective of international CLIVAR (Climate Variability and Predictability Programme of the World Climate Research Programme: WCRP, 1995, 1998). These efforts aim '*... to understand and quantify ...*' fluctuations in major tropical and subtropical heat sources and sinks and thereby improve predictions of global weather and climate (NRC, 1998).

Given the scientific advances noted above, it would seem that the field is poised to advance significantly both the understanding and prediction of Asian–Australian monsoon variability. Such progress will, by necessity, be accomplished by the gathering of more data from the ocean, atmosphere, and land surface, better models, and most of all, an improved understanding of fundamental processes that conspire to produce the observed monsoon and its variability.

There are signs of improvement in obtaining sustained ocean–atmosphere observations in the Indian Ocean. Besides the International Indian Ocean Expedition (IIOE) in the mid-1960s and the WCRP World Ocean Circulation Experiment (WOCE) observations in the Indian Ocean, there have been two dedicated cruises investigating the upper ocean and interactions with the atmosphere (Hacker *et al*., 1998; Webster *et al*., 2002) as well as a number of national experiments (e.g., Bay of Bengal Monsoon Experiment, BOBMEX; Bhat *et al*., 2001). There is an increasing possibility that the ocean–atmosphere observing network in the Indian Ocean will improve to the level enjoyed in the equatorial Pacific Ocean. An international group

led by the Global Ocean Observing System (GOOS) Indian Ocean Panel (IOP) has laid out an implementation plan to which a number of nations will likely contribute (IOP, 2005). It should be noted, however, that modeling problems still persist with persistent systematic errors existing in simulations and predictions. Perhaps with a greater understanding of the monsoon system coming from the analysis of the improved observations, model errors can be reduced to the extent that useful numerically based forecasts can be made.

In the following paragraphs, we will explore what is known about the coupled ocean–atmosphere nature of the monsoon. Whereas the full coupled nature of the monsoon involves interactions with the land surface in the continental regions of Asia and Australia, we will concentrate on aspects of ocean–atmosphere interaction. Section 1.2 summarizes the state of modeling the coupled system. Section 1.3 provides an historical overview of the manner in which the field has come to develop a holistic view of the monsoon. Sections 1.4 and 1.5 discuss in detail how the annual cycle and interannual variability are controlled by negative feedbacks between the atmosphere and the ocean. Section 1.6 discusses briefly the coupled aspects of intraseasonal variability. In Section 1.7 a general theory of the regulation of the coupled atmosphere–ocean monsoon is presented.

1.2 MODELING AND PREDICTING MONSOON VARIABILITY

Early forecasting techniques were essentially empirical. However, during recent decades there has been a transition to a reliance on numerical techniques. What is the degree of fidelity of numerical simulations of the monsoon and the how accurate are forecasts of the monsoon? Unfortunately, our abilities to predict variability have not changed substantially over the last few decades. For example:

(i) For over 100 years the India Meteorological Department has used models based on empirical relationships between monsoon rainfall and worldwide climate predictors with moderate success. These efforts have been extended to different monsoon regions (see reviews by Hastenrath, 1986a,b, 1994) again with only moderate success. Many of these schemes use measures of ENSO as major predictors of monsoon variability (e.g., Shukla and Paolina, 1983; Rasmussen and Carpenter, 1983; Shukla 1987a,b). Whereas there are periods of extremely high association between ENSO and monsoon variability, there are decades where there appears to be little or no association at all (Kumar *et al.*, 1999; Torrence and Webster, 1999). This association has been particularly weak during the last 15 years.

(ii) Numerical prediction of monsoon variability on all timescales is severely handicapped by the inability of models to simulate either the mean monsoon structure or its year-to-year variability. These deficiencies have been demonstrated clearly in the Atmospheric Model Intercomparison Program (AMIP;[2]

[2] AMIP organized the integration of 39 atmospheric models using the same observed SST distributions for a 10-year period (Gates, 1992).

Sperber and Palmer, 1996) where the simulation capabilities of 39 atmospheric general circulation models, each using the same evolving sea surface temperature (SST) forcing fields, were compared. The 10-year summer rainfall for a random selection of AMIP models is shown in Figure 1.2(a) for the south Asian region (Gadgil and Sanjani, 1998). Serious discrepancies are obvious in comparison with the National Centers for Environmental Prediction/National Center for Atmospheric Research (NCEP/NCAR) reanalysis fields (upper left panel). For example, few models reproduced the climatological precipitation maximum over the Bay of Bengal but place maxima in other regions near the equator and over south Asia. Similar variability between the models is apparent in coupled ocean–atmosphere simulation comparisons (Climate Prediction Center Merged Analysis of Precipitation (CMAP2); Huffman *et al.*, 1997).

(iii) Numerical simulation and prediction of intraseasonal variability in the tropics by general circulation models is generally poor (e.g., Slingo *et al.*, 1996; Waliser *et al.*, 2003a,b). This failure is especially serious in the monsoon regions as a very large percentage of the total precipitation variance is observed in the 20–50-day period band. However, physically based Bayesian empirical schemes (e.g., Webster and Hoyos, 2004) have shown that regional precipitation characteristics are predictable with considerable accuracy 20–30 days in advance. Why models tend to show less skill than empirical techniques is not known but it is expected that it is associated with problems in convective parameterization. Krishnamurti *et al.* (1990a), for example, suggests that errors in cumulus propagation tended to erode the power in the slow intraseasonal manifold.

In summary, a combination of modeling problems and empirical non-stationarity has plagued monsoon prediction on interannual timescales. Empirical forecasts have to contend with the specter of statistical non-stationarity while numerical models currently lack simulation fidelity.

1.3 THE DEVELOPMENT OF A HOLISTIC VIEW OF THE MONSOON

During the last two decades, a holistic view of the monsoon system has started to prevail – a growing recognition that the monsoon system is strongly coupled. That is, the ocean and the atmosphere, together with the land surface, are integral components of a grander self-regulating monsoon system. We commence with a discussion of how this new view of the monsoon has emerged.

1.3.1 Impacts of remote ocean variability on the monsoon

(The success of prediction of any physical system is heightened by the degree of understanding of the phenomena. The earliest studies of the monsoon thought of the monsoon as an atmospheric phenomenon driven by gradients of solar heating of surfaces of different heat capacities. Continued research has shown that the ocean plays an active role in the atmospheric monsoon. Especially during the last decade the paradigm has shifted from the monsoon being driven by heating differences manifested as SST anomalies, to an appreciation that ocean dynamics are important and then to the realization that the monsoon is a thoroughly coupled

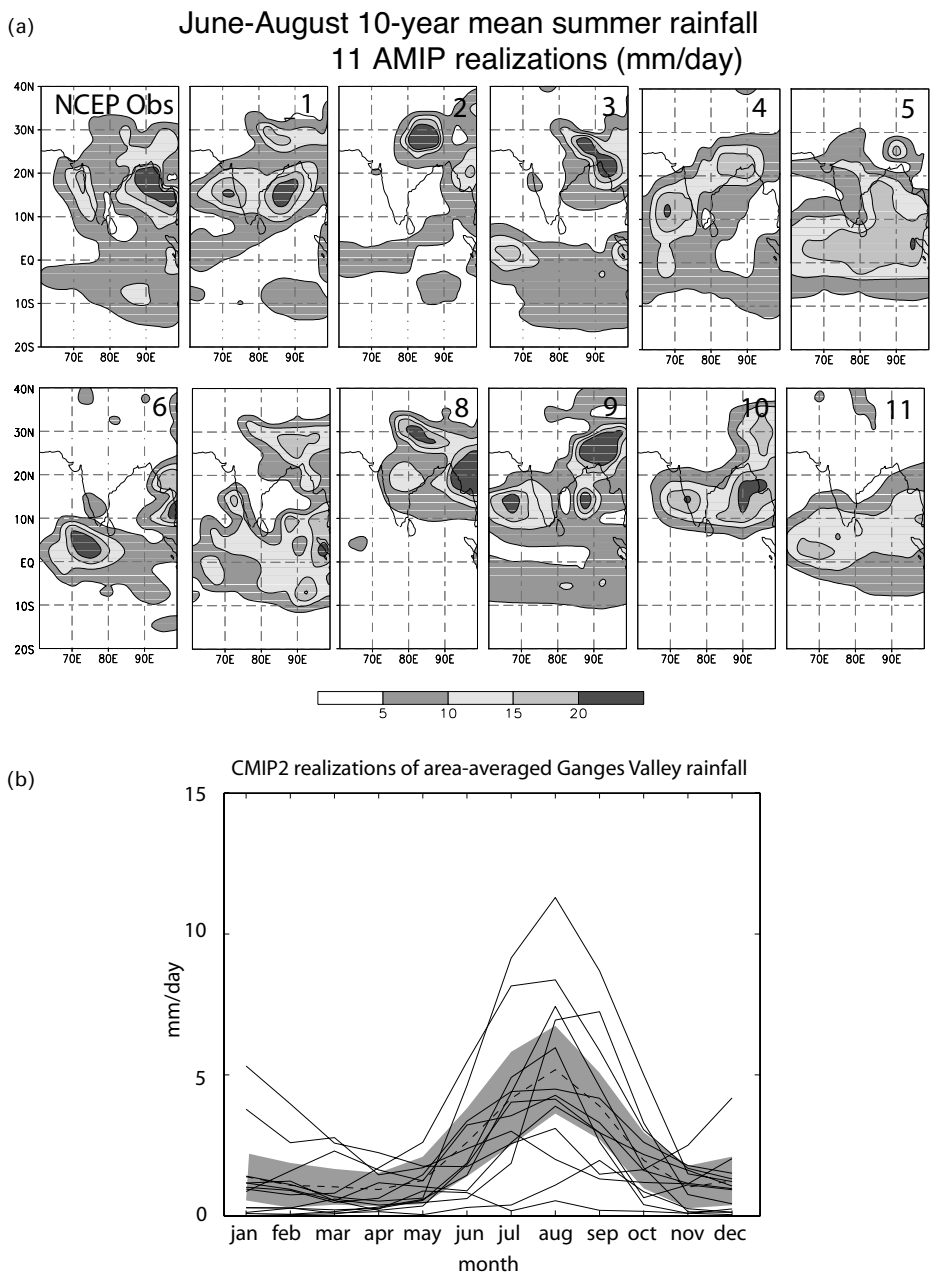

Figure 1.2. (a) Comparison of the 10-year mean summer (June through September) precipitation over the Indian Ocean–south Asian region compiled by Gadgil and Sanjani (1998) from the AMIP project (Gates, 1992). Climatologies result from 11 different models integrated using the same evolving SST fields. The upper left panel shows the NCEP/NCAR reanalysis data estimate of the mean 10-year precipitation for the same period. There is a wide spatial variability between the estimates. (b) Annual cycles of monsoon rainfall over central India from 15 different coupled climate models for the Ganges catchment from the Coupled Model Intercomparison Project (CMIP2). Heavy line shows mean of all models and shaded region encloses ± 1 standard deviation. Models with a vastly different annual cycle phase are not shown. Even so, the models show a large difference in amplitude.

atmosphere–ocean system. Furthermore, the coupled nature of the monsoon probably embraces timescales of variability ranging from intraseasonal to interannual and possibly interdecadal. The following discussion illustrates changing perceptions regarding the interaction of the atmosphere and the ocean in the monsoon system.

Walker (1924, 1928) first tied interannual variability of the monsoon to the phase of the Southern Oscillation (Southern Oscillation and its index SOI) in the early part of the 20th century. Whereas the relationship he described has waxed and waned from one decade to another (e.g., Troup, 1965; Kumar *et al*., 1999; Torrence and Webster, 1999) it accounts for about 40% of Indian monsoon rainfall variance over the last 120 years (Shukla and Paolina, 1983). For many decades, without physical underpinning, the relationship between the SOI and the monsoon was regarded as a statistical artifact. A physical linkage between the Pacific Ocean and the south Asian monsoon had to await the seminal work of Bjerknes (1966, 1969, 1971) who developed a coupled atmosphere–ocean process that described interannual oscillations in the ENSO system finding, for the first time, an integral role for the oceans. A major physical component of ENSO is the near-equatorial Walker Circulation described first by Krishnamurti *et al*. (1973a). Changes in the location of this meridional overturning cell associated with Pacific ENSO SST anomalies are thought to create a remote influence on the monsoon by varying the intensity and location of Walker Cell subsidence (e.g., Soman and Slingo, 1997; Dai and Wigley, 2000). With the exception of Lau and Wu (2001), who referred to SST responses in the Indian Ocean (driven by ENSO) as creating monsoon variability, the general opinion has been that the mode of interaction between the SST variation in the Pacific Ocean and the Indian monsoon was through alteration of Walker Circulation subsidence.

Table 1.1 provides a summary of the overall impact of ENSO variability on monsoon rains. A moderate relationship exists between ENSO and the monsoon although Troup (1965) and more recently Torrence and Webster (1999) have noted

Table 1.1. Relationship between the mean summer season rainfall in India ('All-India' rainfall from Parthasarathy *et al*., 1992b: period 1871–1994) and the north Australian summer rainfall (Lavery *et al*., 1997: period 1886–1993). A 'deficient rainfall' season is where the rainfall was at least a standard deviation below the average while a 'heavy rainfall' season has rainfall at least one standard deviation above average.

	'All-India' summer rainfall			North Australian summer rainfall		
Rainfall	Total	El Niño	La Niña	Total	El Niño	La Niña
Below average	53	24	2	49	20	4
Above average	71	4	19	58	5	17
Deficient (<1 s.d.)	22	11	2	18	9	0
Heavy (>1 s.d.)	18	0	7	17	2	5

that the relationship waxes and wanes from decade to decade. Most empirical forecast schemes have concentrated on taking advantage of an ENSO–monsoon rainfall relationship. Normand (1953) and Webster and Yang (1992) even suggest that at times the influence is reversed and there is an influence of monsoon variability on the evolution of ENSO phenomena. Webster and Yang (1992) suggest that there is a reversing of influence at different times of the annual cycle. With regard to Southern Oscillation–monsoon interactions, Normand (1953) stated:

> ... It is quite in keeping with this that the Indian monsoon rainfall has its connections with later rather than earlier events ... Unfortunately for India, the Southern Oscillation in June–August, at the height of the monsoon, has many significant correlations with later events and relatively few with earlier events ... The Indian monsoon therefore stands out as an active, not a passive feature in world weather, more efficient as a broadcasting tool than an event to be forecast ... On the whole, Walker's worldwide survey ended offering promise for the prediction of events in other regions rather than in India ...

Normand's hypothesis has been tested with mixed results in a number of model studies (e.g., Wainer and Webster, 1996; Kirtman and Shukla, 2000) leading to the suggestion that there exists a grand coupled phenomenon (Webster and Yang, 1992; Lau and Yang, 1996; Miyakoda *et al.*, 1999) of which ENSO and the monsoon are major components. Tantamount to these thoughts are that ENSO and the monsoon cannot be considered separately or that one is the slave of the other.

Figure 1.3 depicts relationships between the Niño 3 SST index (Figure 1.3(a)) and the All-India Rainfall Index (AIRI; Parthasarathy *et al.*, 1992b, 1994; Figure 1.3(b)) in the form of a wavelet analysis. Figure 1.3(c) shows the cross-wavelet modulus of the AIRI and the Niño 3 SST (Torrence and Webster, 1999). A wavelet modulus provides a history of when in the data record certain periodicities are dominant and it can be thought of as an evolving periodogram with time. Lau and Weng (1995) and Torrence and Compo (1998) provide excellent summaries of the use of wavelet analyses. The latter study is particularly useful as it provides a method of calculating significance levels of wavelet moduli shown in Figure 1.3 at the 95% level (heavy black contours). A cross-wavelet analysis shows when certain periodicities were common to both data sets. Below each wavelet analysis is a plot of the time series. The black curve represents the percentage of the total variance through the period of the analysis explained by the power at a particular time. On the right-hand side of each wavelet analysis is a fast Fourier transform (FFT), or periodogram, of the data time series and the average wavelet modulus as a function of period. The FFT and the average wavelet modulus are very similar. The FFT provides the total power in a particular frequency band averaged over the entire data record. However, there is extra information in a wavelet analysis. If, during the data record, there was just one very large amplitude event at a particular frequency, the FFT may indicate large power but not disclose that it was the result of one event. The wavelet analysis, on the other hand, localizes power in time and shows that it was not a recurring phenomenon (Lau and Weng, 1995; Torrence and Compo, 1998). With these thoughts in mind, the following conclusions can be drawn from the wavelet analysis.

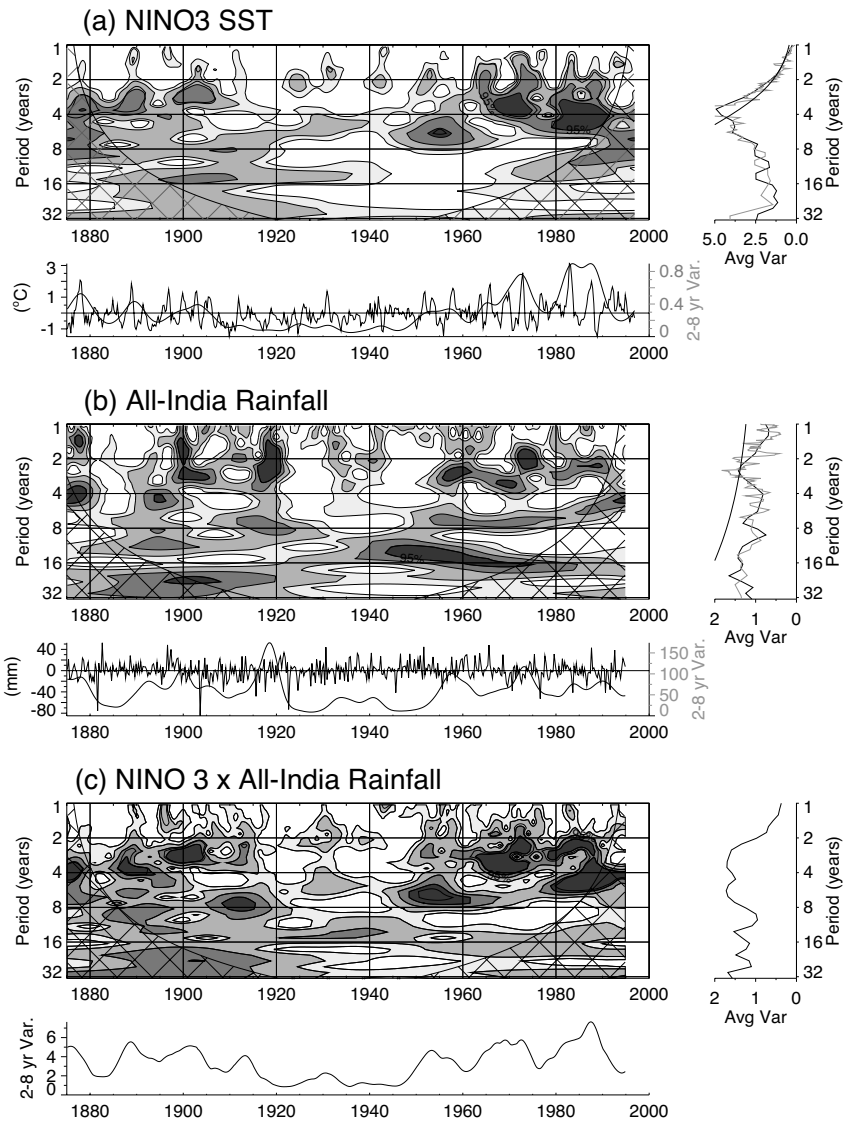

Figure 1.3. Wavelet modulus analyses of climate time series of (a) Pacific Ocean SST (1875–1992) in the Niño 3 region, (b) the all-India rainfall index (AIRI) (1875–1992), and (c) the wavelet coherency between the AIRI and the Niño 3 SST. Arrows indicate phase of the coherency relative to the legend at the bottom right of the figure. The cross-wavelet coherency modulus between the AIRI and the SST for the total period band and the 2–8-year band. Contours indicate the % of total variance at a particular frequency explained at a particular time in the data record. The dashed areas on the right and left of the moduli distributions indicate the limitations of the data to define variance of a particular period at a particular time of the data record. On the right-hand side of each modulus are periodograms the summed wavelet modulus.

After Torrence and Webster (1998) and Torrence and Compo (1998).

(i) The relationship between the Pacific Ocean SST and the AIRI are not statistically stationary. There are at least three distinct regimes in the series. Before 1920, there was considerable variance in the AIRI and the SOI, and correlations were near to -0.8 between the AIRI and the SST compared with an average over the 120-year period of -0.64. These high correlations early in the data period were the relationships that excited Walker and his colleagues. Between 1920 and 1960, there was little interannual variability in either the Pacific data or the Indian rainfall, and the correlation decreased to < -0.2. Systematic analyses of the non-stationarity of the SOI was undertaken by Treloar and Grant (1953) and Grant (1953) for the Australian region and Troup (1965) for the globe. Correlations between Darwin surface pressure (a proxy for the SOI, see Trenberth (1976)) and also surface pressures in Hawaii with southern Australian rainfall anomalies decreased from roughly -0.8 in the period 1909–1928 to about -0.2 between 1929 and 1948. Treloar and Grant (1953, p. 428) conclude that the secular reduction of correlations throws considerable doubt on the direct use of correlation relationships in forecasting. Improvement in the performance of forecast formulae cannot be expected until there is a more satisfactory method of selecting indicators, requiring in turn a better understanding of the nature of weather processes.

(ii) The decrease in the correlations that occurred in the period between 1920 and 1960 has been replaced by an extended period of high variance in the SOI and correlations that match the 1880–1920 period, and a return of much higher correlations. These earlier studies were unaware that the ENSO signal possessed a large interdecadal signal. The SST and the AIRI moduli, as well as the cross modulus, show strong signals in the 10–25-year period. Given the length of the data set, though, the conclusion should be viewed with some skepticism. However, recent coral core data from the Niño 3 region, which extents back in time to 1600, exhibits similar variability in this period band (Cobb *et al.*, 2003).

(iii) Throughout the data period (except between 1920 and 1950), there is strong biennial monsoonal variance. A number of studies (e.g., Yasunari, 1987; Rasmusson *et al.*, 1990; Barnett, 1991) have commented on a biennial periodicity in tropical circulations, especially the monsoons. The periodograms indicate that the biennial variability is particularly strong in the monsoon regions, although with less magnitude in the SST fields. However, the cross modulus indicates substantial covariance in the 2–3-year-period band.

(iv) The AIRI wavelet analysis shows substantial variance at intraseasonal timescales as well as clear interannual variability.

One of the major problems in the analysis of monsoons is finding a representative measure of their strength. Most often the total seasonal rainfall over India is used, usually in the form of the AIRI. However, compared with the scale of the Asian–Australian monsoon, India is relatively small. Consequently, researchers have sought other broader scale measures. For example, Webster and Yang (1992) used

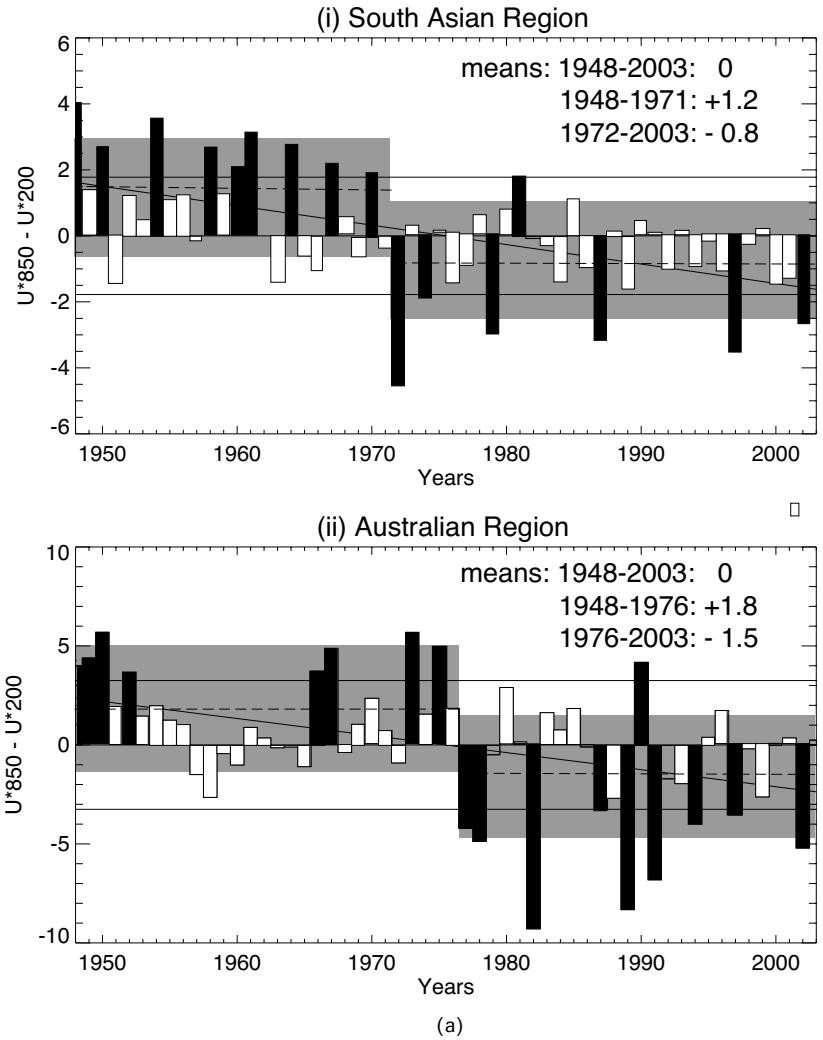

Figure 1.4. (a) Variability of the monsoon index M (equation 1.1) after Webster and Yang (1992) from 1948–2003. The index is defined in the text and is proportional to the strength of the anomalous zonal wind shear and is positive for above average monsoon rainfall and negative for a below average monsoon. Panel (i) shows the index for the south Asian region (0°–20°N, 60°–110°E) and panel (ii) for the north Australian region (0°–10°N, 120°–150°E). The diagonal line through the bars denotes the linear trend of the indices over the entire data period. Solid black bars denote deviations greater than one standard deviation. The horizontal dashed lines show two means separating before and after 1972 for the south Asian region and 1976 for north Australia. Shaded regions show the sets of standard deviations. NCEP/NCAR data has been used to compile the time series. The trend was checked in the common overlap period of the ER40 data set and the NCEP/NCAR set and similar trends were found. Shaded bars indicate rainfall exceeding ±1 standard. Similar trends are apparent in the AIRI but not in the north Australian rainfall data (Lavery *et al.*, 1997).

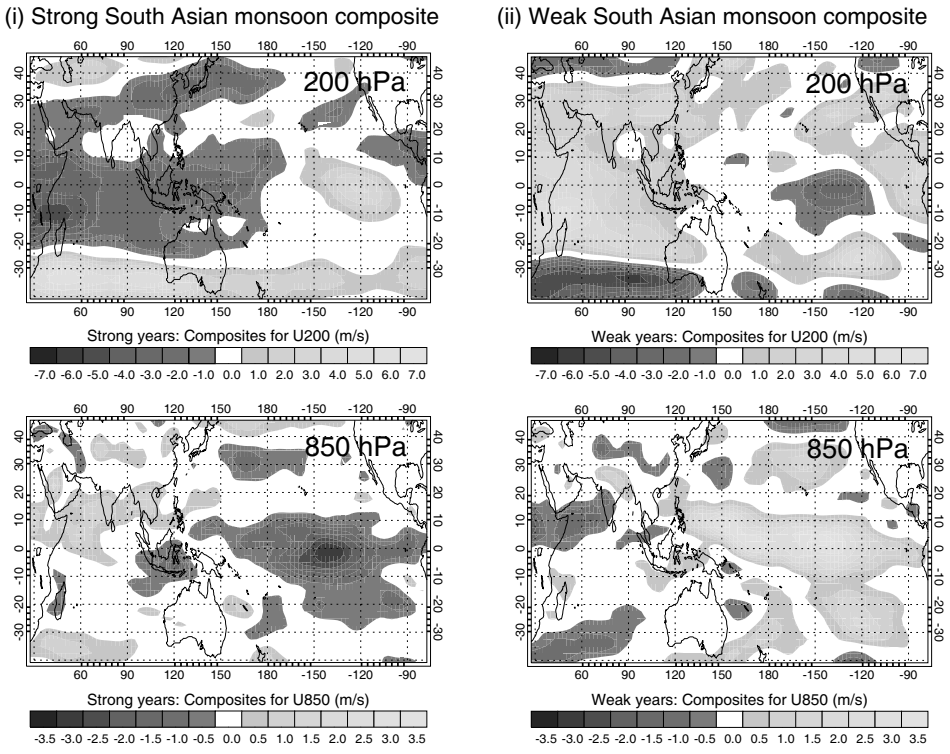

(b)

(b) Composites of 850 and 200-hPa zonal winds for strong (i) and weak (ii) monsoon seasons over South Asia as defined by the monsoon index M (equation 1.1). Large-scale changes in sign and magnitude between the extremes of the monsoon in the Indian–Pacific region. Strong monsoons are associated with enhanced low-level westerlies in the north Indian Ocean and enhanced trade winds over the Pacific Ocean. The opposite characteristics attend the weak monsoon composites. In the upper troposphere the largest changes occur in the eastern hemisphere with strong easterlies associated with the strong monsoon and anomalous westerlies with the weak monsoon. These upper level anomalies extend between $\pm 30^{\circ}$N – a much broader region than the anomalies found at 850 hPa. (*Continued overleaf*)

large-scale vertical shear over south Asia to determine the relative strength of a summer monsoon. Their index is defined as:

$$M = [U - \bar{U}]_{850\,\mathrm{hPa}} - [U - \bar{U}]_{200\,\mathrm{hPa}} \tag{1.1}$$

where U represents the mean seasonal zonal velocity component and $\bar{U}$ the long-term time mean. Other indices have also been designed (see Wang and Fan, 1999 for a review). Figure 1.4(a) shows the seasonal monsoon index M (panel i) for south Asia and seasonal composites of the 850 and 200-hPa zonal winds and the 850-mb meridional winds for weak and strong monsoons defined as being one standard deviation above or below the average. Figure 1.4(b) shows similar plots for the

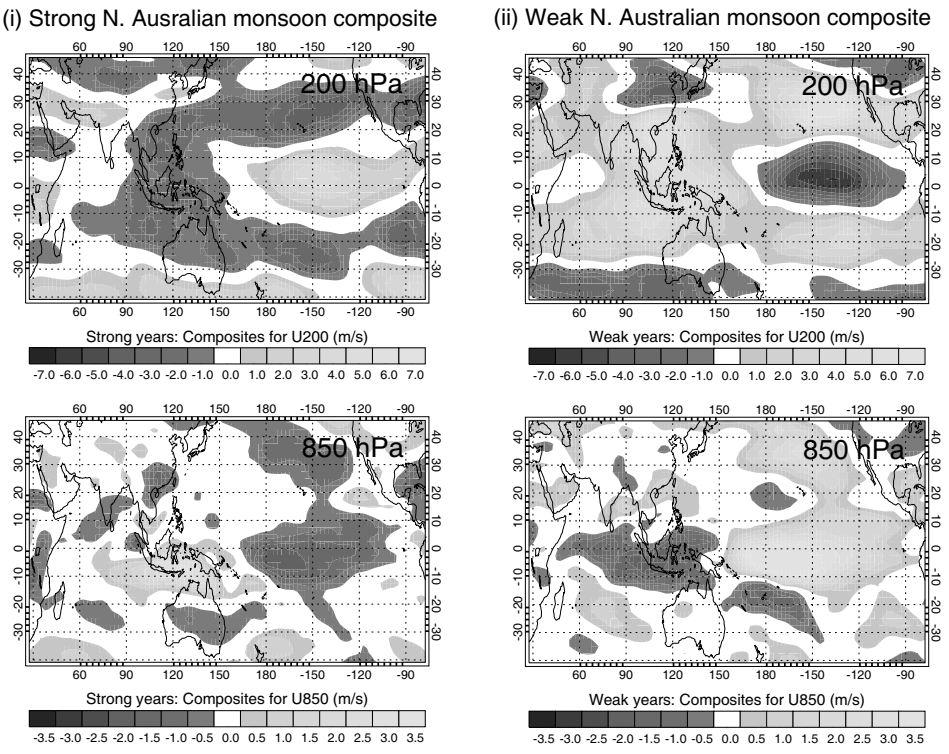

(c)

Figure 1.4. (c) Same as for (b) except for strong and weak north Australian monsoons defined in Figure 1.4(a; panel [ii]). The composites show a large response confined to the Australia–Indonesian and Pacific that appear to be associated with an enhanced Walker-type circulation for the strong monsoon and an anomalously reduced Walker-type cell for the weak monsoon.

north Australian summer monsoon. M was computed over the region 0°–20°N and 40°–110°E for the boreal summer and 0°–10°S and 120°–150°E for the austral summer. In both seasons and at both levels, the composite wind fields are substantially different with each possessing large-scale coherent variability. Of particular interest to this study is the fact that the low-level winds that form the most direct means of communication between the atmosphere and the ocean are significantly different between the two monsoon extremes. That is, one might expect that the atmospheric forcing of the ocean will be substantially different in the event of either strong or weak monsoons.

There remains a basic overriding question: whereas it is clear that there is an impact of coupled Pacific Ocean processes on the south Asian region it is unclear how these influences manifested? Is the modified atmospheric circulation associated with ENSO imposing large-scale enhanced subsidence on the monsoon regions or is the connection through modification of the Indian Ocean by ENSO-induced circula-

tion changes? In summary, we know that ENSO and the monsoon influence each other but we are not sure how this influence takes place.

1.3.2 Regional ocean variability

The IIOE, conceived in the late 1950s, is a major international effort in oceanography. The Indian Ocean was chosen because it was the most poorly documented of all ocean basins. Furthermore, it was the only ocean basin that was forced by seasonally reversing winds and there was promise that exciting and new phenomena may be discovered. Hastenrath (1994) later describes a 'monsoon ocean' driven by a wind system is unique in its annual cycle noting that '*... nowhere else on the globe is the annual reversal of the surface wind regime as spectacular as over the Indian Ocean sector ...*' (p. 57). The seasonal variability of the wind-driven circulation is vigorous and varies rapidly in magnitude and direction over a wide range of timescales.

The IIOE was conducted in 1965–1966 during which an unprecedented 36 oceanographic research ships participated. Largely from the observations taken during the IIOE, climatologies of the thermal, chemical, and dynamic properties of the Indian Ocean were computed (e.g., Swallow, 1980; Duing and Leetmaa, 1980; Duing *et al.*, 1980; Hastenrath and Greischer, 1989; Halpern *et al.*, 1988). Many studies concentrated on the vigorous Somalia Current, which connects the southern and northern hemispheres in both the boreal summer and winter (e.g., Duing *et al.*, 1980; Leetmaa, 1973). Seminal studies of wind-generated ocean waves were produced. Anderson and Rowlands (1976) and Lighthill (1969) were able to differentiate between local and remote wind forcing and wave generation in different parts of the basin. Knox (1976) found evidence of eastward propagating Kelvin waves in the equatorial central Indian Ocean and Wyrtki (1973) found strong wind-forced equatorial oceanic jets. Halpern *et al.* (1988) and Godfrey (1995) formed consensus views of the Indian Ocean. Both studies were extensive and far-reaching. Yet, these details provided little evidence of a reverse feedback: the forcing of atmospheric anomalies by an altered and wind-forced state of the ocean.

1.3.3 Impacts of regional ocean variability

Traditionally, regional oceans have been considered an important part of setting up the background forcing of the monsoon, but only in a passive thermodynamic sense. In this scheme, the ocean represents the cold pole of the heating dipole and the major supplier of moisture through evaporation. Primary moisture source regions are the Arabian Sea and the south Indian Ocean (e.g., Ghosh *et al.*, 1978; Cadet and Reverdin, 1981; Pisharoty, 1996).

Noting that there are documented SST anomalies in these ocean basins, it was a natural extension to suppose that the anomalies may influence south Asian rainfall through alterations of moisture supply. Through numerical experimentation, Shukla (1975) and Washington *et al.* (1977) found statistically significant relationships between Arabian Sea SST anomalies and Indian rainfall. Subsequent diagnostic studies (e.g., Sadhuram, 1997; Hazzallah and Sadourny, 1997; Clark *et al.*, 2000)

have found empirical evidence that these relationships exist but also found they exhibited a statistical non-stationarity. Clark *et al.* (2000), for example, found correlations as high as +0.8 occurred between equatorial Indian Ocean SSTs and Indian precipitation in the winter prior to the monsoon wet season. A combined Indian Ocean SST index generated by Clark *et al.* (2000a) has retained an overall correlation of 0.68 for the period 1945–1994, after the removal of ENSO's influence. Yet, despite the demonstrated (if spasmodic) influence of regional SSTs on the vigor of the monsoon, evidence was not found that suggested that the atmosphere and the ocean acted coherently, forming a closed feedback loop. That is, SST anomalies were found to affect winds and surface moisture fluxes (which combine to modify the overall atmospheric monsoon circulation) but there was little mention of how (or if) the anomalously forced atmospheric circulation produced the SST anomalies.

1.3.4 Intraseasonal variability and the large-scale monsoon

The summer monsoon of south Asia commences in May before petering out in September. However, during this period, the monsoon does not maintain a constant vigor but possesses a number of interspersed periods of rainfall deficit. Ramamurthy (1969) adopted the term 'break' for the periods of temporary drought. Originally, a monsoon break was thought of as cessation of the entire monsoon (Rao, 1976). However, it had also been noted that when rain ceased over central India rainfall increased over extreme northern India in the foothills of the Himalayas (e.g., Ramamurthy, 1969; Desai and Mal, 1938). This evidence led Shukla (1987a) to suggest that rather than a complete cessation of rainfall a break period is actually a '... *a spatial redistribution of the monsoon rainfall* ...' which suggested that the monsoon break was part of an active large-scale dynamical system. In fact, in any one location in south Asia, the monsoon is divided up into long periods (15–30 days) of above-average followed by periods of below-average precipitation. The pluvial period has become known as the 'active' monsoon while the intervening period of less rainfall or drought is called a 'break' monsoon. Collectively, a cycle of an active and a break monsoon is called a monsoon intraseasonal oscillation (MISO; Webster *et al.*, 1998).

Shukla (1987a) discusses four possible causes of intraseasonal variability. These are: (i) cycles in synoptic systems such as lows, depressions; (ii) variations in the position and strength of the continental monsoon trough; and (iii) quasiperiodic oscillations of the monsoon (e.g., Yasunari, 1979; Sikka and Gadgil, 1980; Webster, 1983) and the impacts of mid-latitude disturbances (e.g., Ramaswamy, 1962; Rodwell, 1997). More recent studies have suggested that the intraseasonal oscillations of the monsoon are manifestations of basin-wide processes that form along the equator before propagating northward from the eastern tropical Indian Ocean to the landmasses of south and south-eastern Asia (e.g., Webster *et al.*, 1998, 2002). These ideas support the third contention of Shukla (1987a) that intraseasonal variability is a quasiperiodic oscillation of the macroscale monsoon. Both Webster *et al.* (1998) and Webster *et al.* (2002) showed that intraseasonal variability of the monsoon impacts the thermal structure of the Indian Ocean. Finally, Han *et al.*

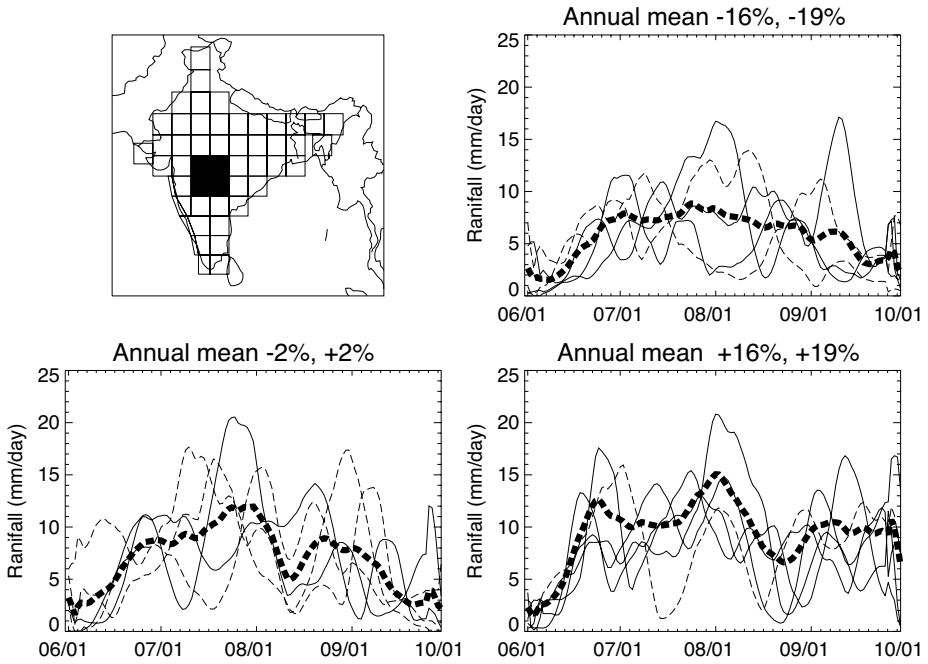

Figure 1.5. (a) Intraseasonal variability of precipitation occurs irrespective of the strength of the monsoon. 10-day running means of GPI precipitation rate central India (panel i) for the years which the summer rainfall is between 81% and 84% of the summer mean (years 1905, 1907, 1912, 1925, 1929; panel ii), between 98% and 102% (years 1937, 1957, 1966, 1967, 1976, 1980; panel iii), and between 116% and 119% (1910, 1948, 1953, 1954; panel iv). Heavy dashed curves show the mean seasonal precipitation for each category.
Data from Singh *et al.* (1992) and adapted from Webster and Hoyos (2004).
See color section for Figure 1.5(b).

(2004) has also shown clear dynamic signatures directly linked to atmospheric intraseasonal forcing. Finally, in two recent studies Stephens *et al.* (2004) and Wang *et al.* (2004b) have extended the argument to suggest that the intraseasonal variability of the monsoon is a fully coupled phenomenon. We will return to these issues later.

It is important to note that, interannual climate change is not alone in impacting monsoon society and that it may not be the most important. Intraseasonal variability occurs with far greater amplitude as the monsoon each year goes through a series of active and break periods. Figure 1.5(a) (Webster and Hoyos, 2004) shows the variability of AIRI in the location shown in panel (i). Panels (ii) to (iv) show the seasonal variability for years that are very much below average (AIRI between 81 and 84% of the long-term average), average (between 98–102%), and strongly above average (between 116–119%), respectively. The dashed line in each panel represents the long-term average of the category. There are clear differences between the mean

values in each category but, irrespective of the long-term mean, each individual year is dominated by MISOs. The active and break phases of the MISO appear to occur randomly throughout the year. From an agricultural point of view, the timing of these oscillations is critical. Even if the total rainfall proves to be above average over the entire summer, a delayed first peak or extended break could reduce the yield of a crop considerably. On the other hand, a fortuitously timed active period during a below-average year might permit a bountiful yield to be harvested later. Of course, yield could be increased whether the monsoon is average or above or below average if skillful forecasts of monsoon intraseasonal oscillations are made with sufficient lead to allow modification of agricultural practices and if, of course, the forecasts are heeded.

Figure 1.5(b; color section) illustrates another problem of using only forecasts of the annual or seasonal average monsoon rainfall. The maps show the spatial distribution of rainfall anomalies for roughly the same categories used in Figure 1.5(a). In the two extreme periods there are more above-average or below-average districts. However, there appears to be no distinct regionality that matches the annual anomaly. In the 'average' category, the situation is far more complicated with a ménage of above and below-average districts. In other words, even if an average seasonal rainfall were forecast with great accuracy, it would be difficult to downscale the forecast to provide a useful product at the regional level.

1.3.5 Emergence of the concept of the monsoon as a coupled system

During the 1980s, an accumulation of evidence from diagnostic and modeling studies suggested that there were distinct and large-scale, low-frequency changes to the heat transport and storage of the Indian Ocean. Furthermore, these changes were directly related to wind forcing and were in addition to the earlier dynamical responses described earlier (e.g., Wyrtki, 1973; Anderson and Rowlands, 1976; Leetmaa, 1976). This realization came about when it was noted that there was a substantial wind-driven meridional oceanic heat flux (e.g., Hastenrath and Lamb, 1978; Hsuing *et al.*, 1989; Hastenrath and Greischer, 1993). The results of these observational studies were corroborated with a series of modeling studies (e.g., Loschnigg and Webster, 2000). Figure 1.6 shows four estimates of oceanic zonally averaged meridional heat transfer in the Indian Ocean (Chirokova and Webster, 2005). Both data and model-based estimates show much of the same character: a strong annual cycle of oceanic heat transfer with seasonal peaks of ± 1–1.5 PW with the direction of the flux out-of-phase with solar heating. That is, during the northern hemisphere summer the heat flux is directed southwards to the winter hemisphere reversing during the boreal winter. The seasonally reversing heat flux is suggestive of a possible feedback between the ocean and the atmosphere that may regulate the strength of the monsoon (Loschnigg and Webster, 2000; Webster *et al.*, 2002; Loschnigg *et al.*, 2003).

These empirical and modeling relationships are important because they suggest that there are basin-wide relationships that may be, to some extent, independent of ENSO and, thus, inherent to the Indian Ocean–monsoon system. Some structural

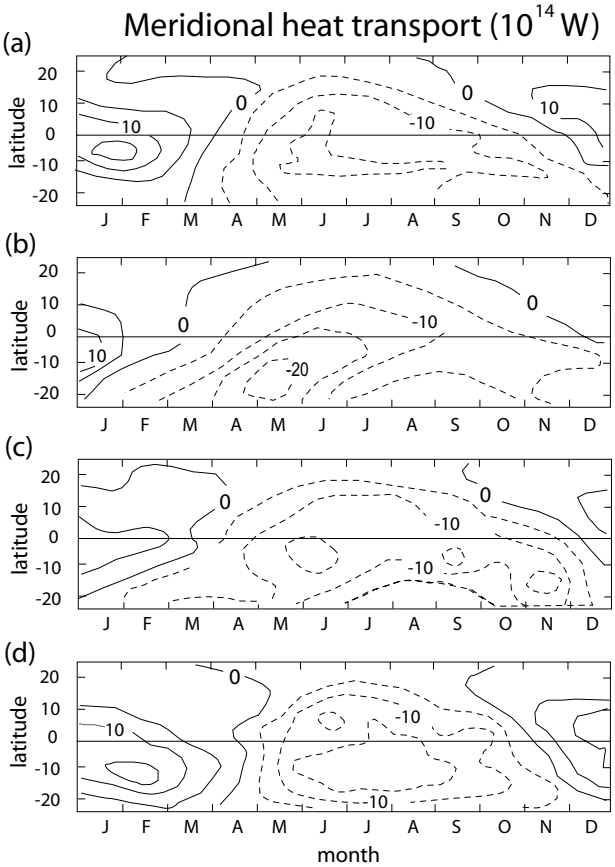

Figure 1.6. Comparison of the seasonal cycle of zonally averaged northward heat transport in the Indian Ocean: (a) Wacogne and Pacanowski (1996), (b) Hsiung *et al.* (1989), (c) Hastenrath and Greischer (1993), and (d) Chirokova and Webster (2005). Estimates (a) and (d) are made from models whereas (b) and (c) are calculated as residuals from atmospheric and surface data budgets. The four annual cycles are remarkably similar with broad northward cross-equatorial transports of heat during the autumn and southward transports during the spring and summer and early autumn.

independence of basin-wide modes is evident in Figure 1.7(a,b). These figures describe the persistence of SST in space (Figure 1.7(a)) and in time along the equator (Figure 1.7(b)). The Pacific Ocean possesses a strong persistence minimum in the boreal spring. This is the Pacific Ocean 'predictability barrier' of Webster and Yang (1992) and underscores the rapid changes that often occur in the Pacific Ocean during the boreal spring. The pattern in the Indian Ocean is quite different. Strong persistence occurs from the end of the boreal summer until the late spring of the following year. This behavior supports the contention of Meehl (1994a,b, 1997) that there is a biennial component in the Indian Ocean SST and monsoon rainfall.

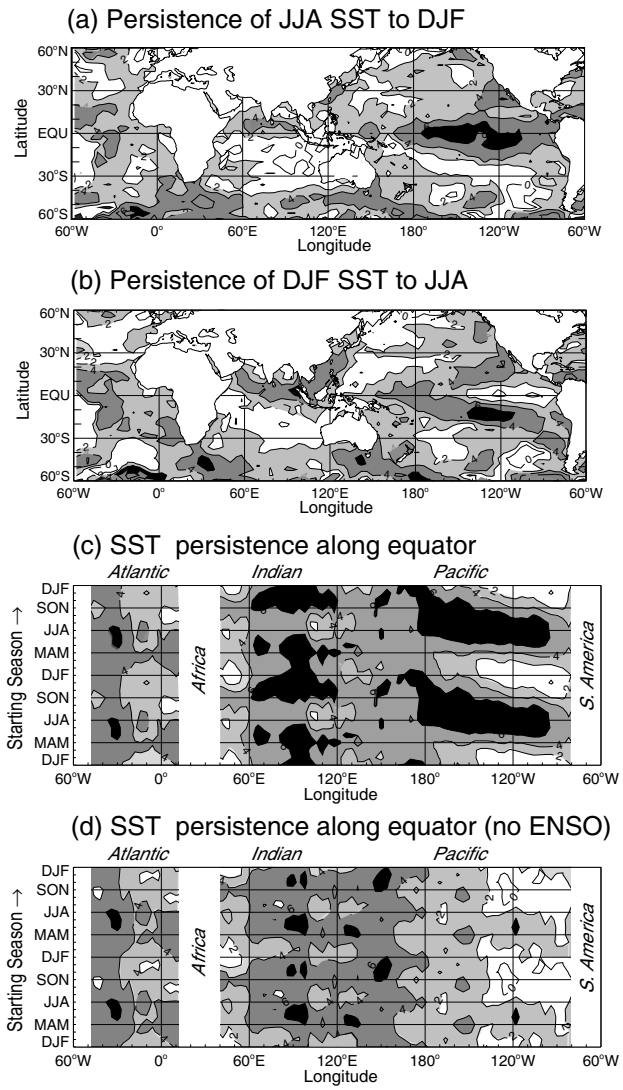

Figure 1.7. SST in the Indian and Pacific oceans possesses distinctly different annual cycles of persistence. (a) Persistence of the SST over two six-month periods: summer to winter and winter to summer. Extremely strong persistence can be seen in the eastern Pacific Ocean and the north Indian Ocean between summer and winter. However, persistence decreases substantially in the Pacific Ocean between winter and summer. It is maintained, however, in the north Indian Ocean. (b) Time sequence of the climatological persistence of SST along the equator for a two-year cycle. (c) Persistence with Niño 3 influence removed. Persistence is defined as the percentage of the seasonal signal persisting six-months later. For example, there is almost no persistence in the eastern Pacific Ocean from DJF to JJA but very large persistence from JJA to DJF. In the Indian Ocean moderate and similar persistence (40–50%) exists irrespective of season. (d) Same as (c) but with the ENSO signal removed.
From Torrence and Webster (1999).

Meehl (1994a) also noted that strong Indian monsoons were generally followed by strong north Australian summer monsoons six months later so that the entire Asian–Australian monsoon system follows a biennial pattern (Figure 1.1). The south Asian monsoon, at least as described by Indian precipitation, exhibits a smaller range of variability during its summer pluvial phase than variability exhibited by the north Australian monsoon. In fact, the south Asian monsoon has an interannual variability that is generally smaller than most heavy rainfall regions of the tropics. For example, drought or flood in south Asia rarely extend to multiple years, with rainfall oscillating biennially from slightly above-average to slightly below-average precipitation.

Evidence of further coupled ocean–atmosphere interaction was soon to follow. During the late summer and early autumn of 1997 rapid cooling developed in the eastern tropical Indian Ocean. In the weeks that followed, a warm anomaly formed in the central Indian Ocean and propagated westward (Webster *et al.*, 1999; Saji *et al.*, 1999; Yu and Reinecker, 1999, 2000). By November 1997, a distinct SST dipole had developed across the tropical Indian Ocean. Such events have been called the Indian Ocean dipole (IOD) or Indian Ocean Zonal Mode (IOZM). Figure 1.8 shows the anomalous state of the Indian Ocean in November 1997. A 6°C SST gradient is evident between the west coast of Sumatra and the east African coast (panel a). The anomalous long-wave radiation (outgoing long-wave radiation,

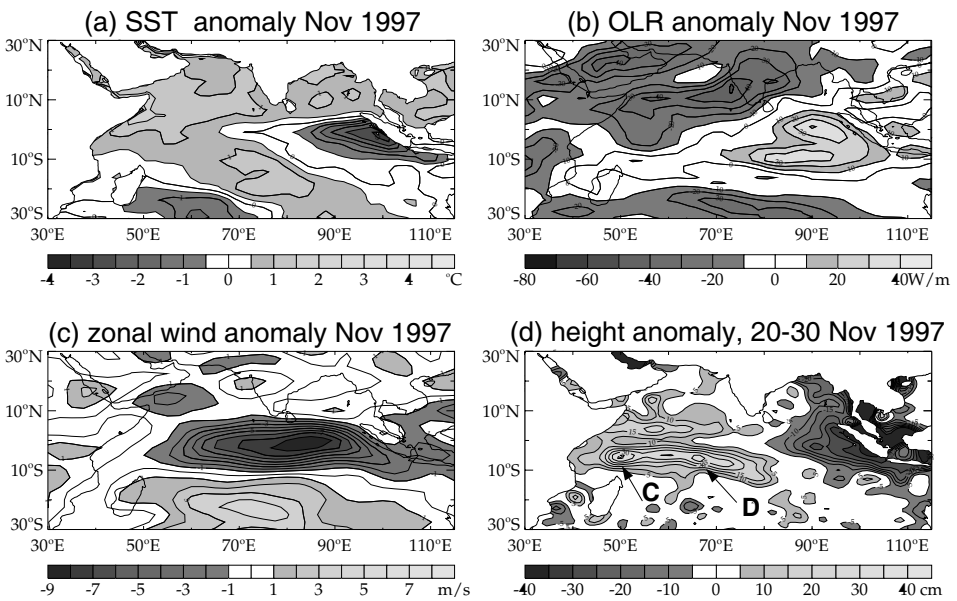

Figure 1.8. Anomalous state of the Indian Ocean, during November 1997. Panels show anomalies from the long-term November averages of: (a) SST (°K), (b) OLR ($W\,m^{-2}$), (c) zonal wind anomaly ($m\,s^{-1}$) at 925 hPa, and (d) sea level height anomaly from the TOPEX/POSEIDEN satellite (cm).

OLR) pattern suggests wetter than average conditions in the western Indian Ocean. Driven by the surface pressure gradient associated with the SST pattern, easterly anomalies of $9\,m\,s^{-1}$ dominated the central Indian Ocean (panel c). For later reference, a sea surface height (SSH) gradient of nearly 1 m existed across the Indian Ocean.

The positive phase of the IOZM appears to be highly correlated with above-average equinoctial 'short' rains of east Africa while the opposite (negative) phase is associated with seasonal drought (Clark *et al.*, 2003). Earlier studies have highlighted the impacts of the positive phase of the IOZM and had also found relationships between SST, zonal wind variations, and the African rainfall (e.g., Kapala *et al.*, 1994; Revedin *et al.*, 1986; Hastenrath and Greischer, 1993). One of the more interesting aspects of the IOZM is that it appears to be a strongly coupled mode where the eastward propagation of the warm anomaly results from cooperative interaction between the atmosphere and the ocean.

1.3.6 Emerging questions

The simulation and prediction problems alluded to earlier are, to a large degree, functions of model error associated with characterization of convection and the upscale propagation of error from parameterizations of small-scale, high-frequency phenomena. But modeling problems aside, it should be noted that the Indian Ocean region possesses, of all of the tropical oceans, the poorest network of atmospheric and oceanic observations. Deficiencies occur both in remote sensing (lack of available geosynchronous data) and *in situ* data. Currently, the Indian Ocean does not possess oceanic observations that even closely match the Tropical Atmosphere–Ocean (TAO) moored buoy array in the equatorial Pacific Ocean. Besides being a significant impairment to prediction, the lack of a moored buoy system in the Indian Ocean reduces predictability in the Pacific Ocean because intraseasonal variability usually are initiated in the Indian Ocean before propagating eastward over the Pacific warm pool. Thus, uncertainty in the state of the Indian Ocean is transmitted to uncertainty in the Pacific.

Given the problems in simulating and predicting the monsoon variability of monsoons it is well worth investigating the basic structure of monsoons from a fundamental perspective. Given further that there is increasing evidence that the monsoon is a deeply coupled ocean–atmosphere system, the investigation will probably be more fruitful if it concentrates on coupled aspects of the system. With these factors in mind, we ask a number of rather basic questions:

(i) It is clear that the monsoon is influenced by local and remote variations of SST. What is unclear is how the SST variability changes the monsoon circulation. Does the atmospheric circulation respond thermodynamically (i.e., through variations in heating and water vapor supply in surface fluxes into the atmosphere) producing feedbacks such as those suggested by Ramanathan and Collins's (1991) 'natural thermostat' hypothesis posed in an attempt to

explain why the warm pool of the western Pacific Ocean appears to be constrained to remain in the 28–30°C range?

(ii) To what degree does the ocean respond dynamically to the atmospheric response to the anomalous ocean heating and, if so, do these modes feed back to produce a further atmospheric response? Do these collective processes regulate the annual cycle and interannual variability of the monsoon?

(iii) How do the SST anomalies themselves arise? In the Pacific Ocean, SST patterns are created through the familiar ENSO coupled oceanic–atmospheric mode (Cane and Zebiak, 1985) for which there is a measurable SST response of the Indian Ocean. But how are Indian Ocean SST anomalies produced?

(iv) What factors determine the phase and the amplitude of the monsoon annual cycle? To what degree is the annual cycle influenced by the internal dynamics of the Indian Ocean as well as the thermodynamical forcing of the radiative variability?

(v) Is the phase and amplitude of the annual cycle of the monsoon controlled by factors local to the south Asian and north Australian continents or is there an appreciable influence from remote variability of the other tropical oceans?

(vi) What factors control the interannual rainfall variability of the south Asian monsoon? Are these factors regional (e.g., SST anomalies in the Indian Ocean) or are they produced by remote influences such as pacific ENSO variability? What produces the SST anomalies in the Indian Ocean?

(vii) Why are persistent multiyear anomalies of monsoon precipitation relatively rare over south Asia? Why is the year-to-year variability (as best as can be estimated from the long-term data from India) of relatively small amplitude? Is the bienniality of the monsoon rainfall an artifact of the coupled ocean–atmosphere system?

(viii) What are the relationships, if any, between the bienniality of the monsoon, the Indian Ocean dipole, and longer term interannual variability?

(ix) Is the intraseasonal variability of the monsoon a coupled ocean–atmosphere phenomena and, if so, to what degree?

A basic aim of the next section is to reframe the discussion of the monsoon to one of coupled ocean–atmosphere processes.

1.4 COUPLED ASPECTS OF THE MONSOON ANNUAL CYCLE

Figure 1.9 shows the annual cycle of the mean SST, near-surface wind vectors, and OLR for the four seasons: December to February (DJF), March to May (MAM), June to August (JJA), and September to November (SON). Some pertinent characteristics are listed briefly:

(i) In general, the warmest SSTs occur in the boreal spring where 29°C surface water covers most of the Indian Ocean north of 10°S. Except in the very far north of the basin, the SST during winter is about 28°C. With the coming of

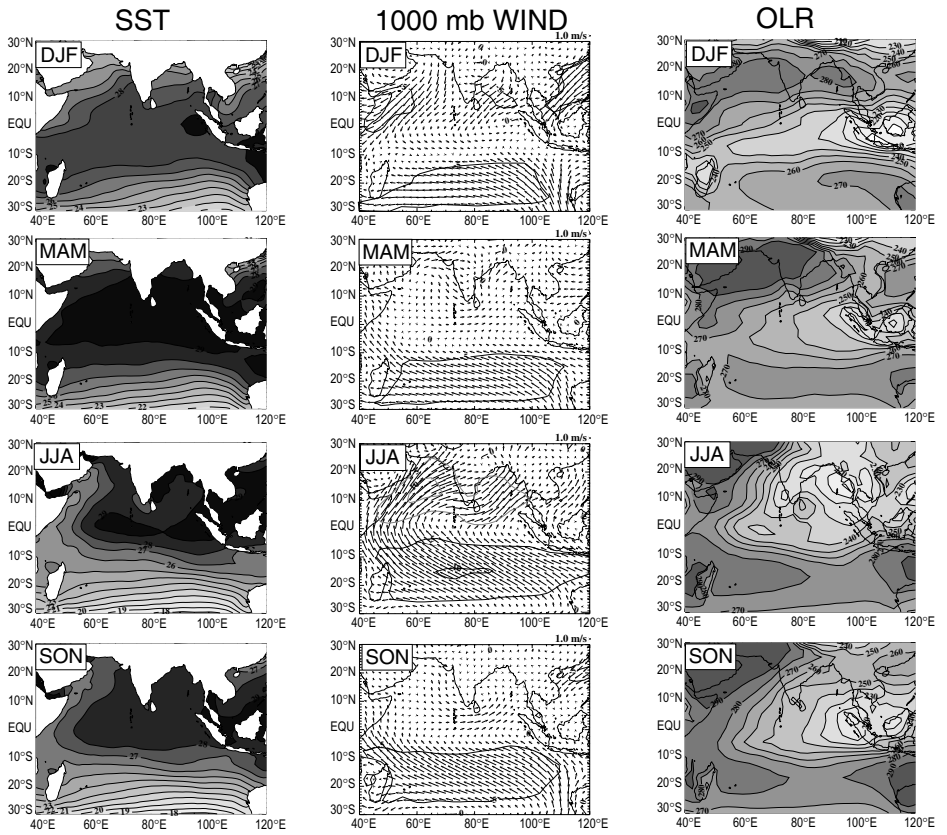

Figure 1.9. Mean annual climatology of SST (°C), near-surface wind vectors ($m\,s^{-1}$), and OLR ($W\,m^{-2}$). Data is plotted for the four seasons March, April, and May (MAM), June, July, and August (JJA), September, October, and November (SON), and December, January, and February (DJF). MAM is the warmest season in the north Indian Ocean but is depleted in convection.

summer and the quickening of the monsoon, the SST of the north Indian Ocean cools, especially in the Arabian Sea. The autumn temperatures are similar to spring but cooler in general by about a degree. In all seasons, the maximum SST gradient occurs south of the equator. Maximum SSTs exist in both hemispheres about the equator during the MAM (i.e., boreal spring and austral fall). Collectively, the combined anomalies from both hemispheres contribute to build the largest warm pool of water on the planet at that time of the year.

(ii) The lower tropospheric circulation of the Asian summer monsoon is much stronger than its wintertime counterpart and possesses a concentrated cross-equatorial flow in the western Indian Ocean compared with the broader, but weaker, reverse flow during the boreal winter. South of 10°S persistent south-easterly trade winds persist throughout the year extending northwards to the equator during the boreal summer.

(iii) During the summer, maxima in convection (low OLR) occur over south Asia with weaker extensions over equatorial North Africa and in the near-equatorial southern hemisphere. During the boreal winter, an elongated band extends across the Indian Ocean and north Australia culminating in a broad maximum over Indonesia and north Australia. Convection over Asia is located farther poleward than its southern hemisphere counterpart, and the circulations are not symmetrical between the seasons. Perhaps the most interesting aspect of these climatologies is the lack of variation of SSTs between seasons. Most notably, the SST appears to change little during the boreal spring over much of the north Indian Ocean despite weak winds and high insolation. Similarly, the winter SST in the north Indian Ocean is only a degree or so cooler than in the fall or the spring despite significant reductions in surface heating.

1.4.1 Macroscale forcing of the monsoon annual cycle

One of the critical aspects of Figure 1.9 from an oceanographic perspective is the reversing cross-equatorial, low-level atmospheric flow. This flow results from an oscillating cross-equatorial pressure gradient. Tomas and Webster (1997) and Tomas *et al.* (1999) considered the impacts of cross-equatorial pressure gradients on near-equatorial circulations. These studies were more interested in symmetric instabilities produced by the pressure gradient and their impact on the location of the Intertropical Convergence Zone (ITCZ) in different regions of the planet. However, much earlier Levitus (1987) noted that the near-surface, cross-equatorial winds in the Indian Ocean region results in a net cross-equatorial ocean heat seasonal to the south during the boreal summer and northwards during the boreal winter. Levitus's results have been born out by subsequent studies compared in Figure 1.6. Both the symmetric instability arguments of Tomas and Webster (1997) and the reversing cross-equatorial Ekman heat flux of Levitus (1987) turn out to be important.

How does the cross-equatorial pressure gradient arise? Figure 1.10 describes the annual cycle of the tropospheric thermal structure. In Figure 1.10(a) the horizontal distribution of the 200–500-mbar layer mean temperature is plotted for boreal summer (Figure 1.10(a), left) and winter (Figure 1.10(a), right). The shaded region shows a mean temperature warmer than -26°C. During summer a planetary-scale warm air mass is centered on south Asia with the maximum average layer temperature ($>-22^{\circ}$C) over the southern Tibetan Plateau, resulting in strong temperature gradients in both the north–south and east–west directions. A warm temperature ridge exists over the North American continent, and a deep temperature trough stretches from the west coast of North America to the central Pacific. A similar trough lies over the Atlantic Ocean. The upper tropospheric flow pattern during summer identifies clearly the thermal contrast between continents and oceans (e.g., Krishnamurti, 1971a,b). The boreal winter presents a very different structure. A much smaller section of the globe (north-east of Australia) is warmer than -26°C. A warm temperature ridge lies over South America, and a slightly weaker ridge covers Australia.

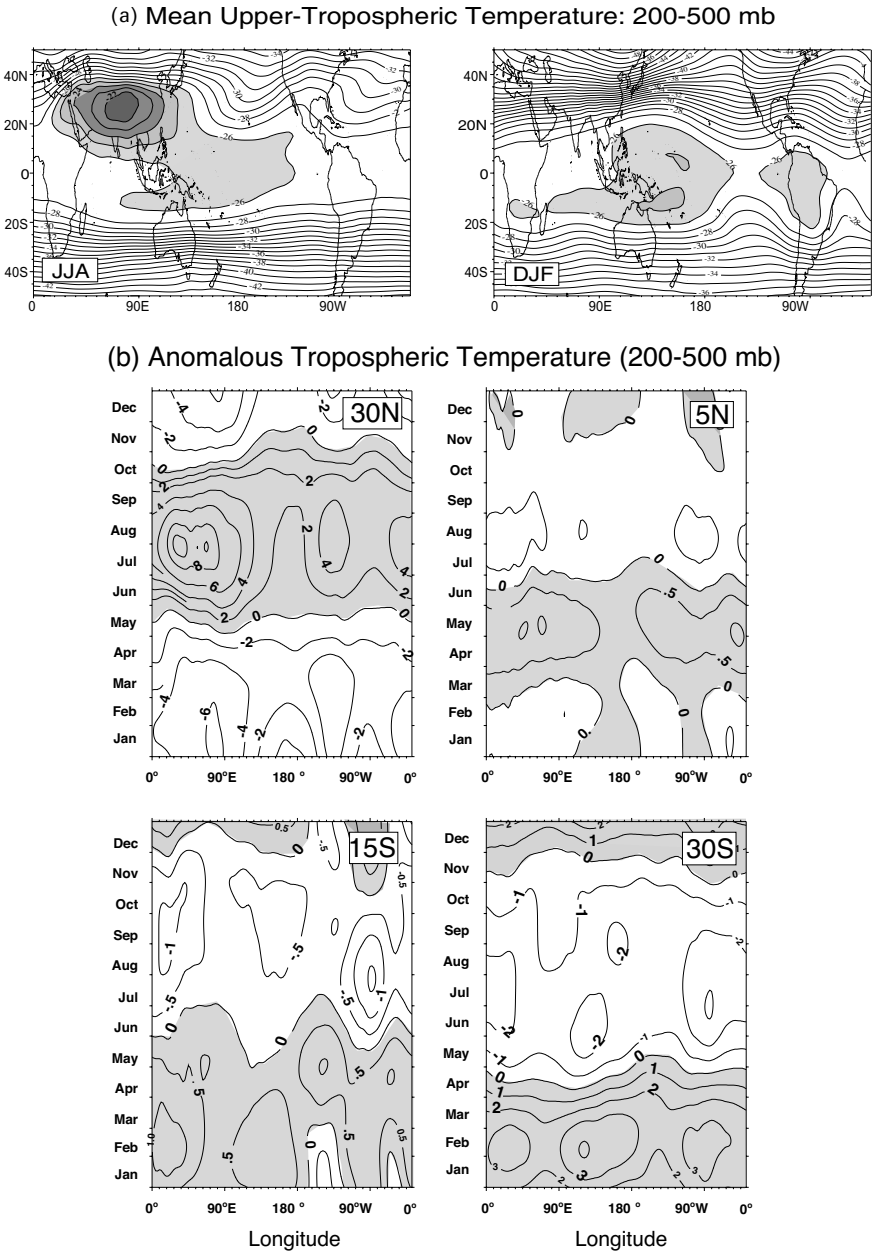

Figure 1.10. (a) Mean upper tropospheric (200–500 hPa) temperature (°C) for the boreal summer (JJA), and boreal winter (DJF), averaged between 1979 and 1992. The boreal summer plot is based on calculations first made by Li and Yanai (1996). Mean columnar temperatures warmer than −25°C are shaded. (b) Annual cycle of the mean 200–500 hPa temperatures at 90°E and 30°N, 5°N, 15°S, and 30°S. (c) Annual cycle of the mean latitudinal 200–500 hPa temperature gradients between 30°N–5°N, 30°S–5°S, and 30°N–30°S.

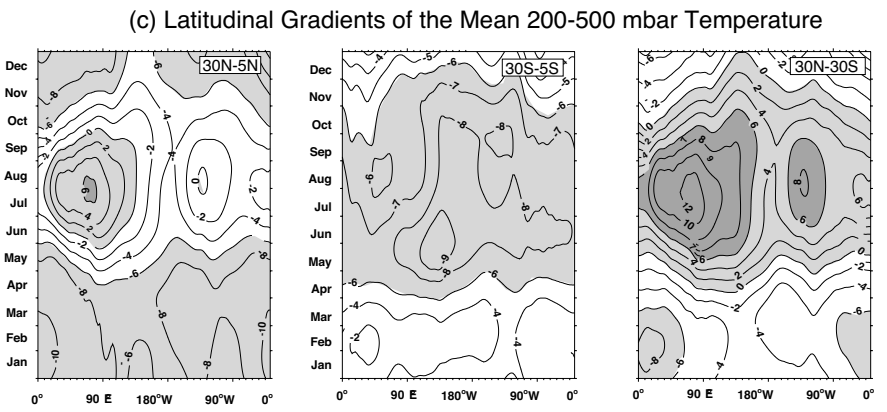

Figure 1.10. (*cont.*)

Figure 1.10(b) shows the longitudinal structure of the annual cycle of the upper tropospheric (200–500-mbar) temperature anomaly for the entire year along 30°N, 5°N, 15°S, and 30°S. The anomaly is calculated by subtracting out the mean zonally averaged annual cycle of the columnar 200–500-mbar mean temperature along the particular line of latitude. The 30°N section cuts through the temperature maximum over the Tibetan Plateau. Temperature anomalies begin to change from negative to positive in April near 90°–100°E. The temperature increases over Eurasia during summer are much larger than those over North America. The maximum temperature anomaly (9°C) occurs in the region of the Tibetan Plateau (between 60° and 105°E). Smaller maxima of mean temperature anomalies occur over North America and west Africa. In contrast, there is no appreciable change in the upper tropospheric temperature along 5°N (Figure 1.10(a), top right), which is mostly over the oceans. The southern hemisphere sections at 15° and 30°S are weak counterparts of the section along 30°N. Compared with the >9°C anomaly found over the Tibetan Plateau, anomalies have magnitudes of only 3°C at 30°S.

The longitude–time sections of the difference of the mean upper tropospheric (200–500 mbar) temperature between 30° and 5°N, (upper panel), 30° and 5°S (center panel), and between 30°N and 30°S are plotted in Figure 1.10(c). All temperature differences >6°C are shaded. The reversal of the meridional temperature gradient occurs first on the south side of the Tibetan Plateau (near 90°–100°E) and then expands over a large area extending from Africa to the western Pacific. The temperature difference reaches maximum values (>6°K) in July and becomes negative between September and October. Li and Yanai (1996) found that the onset of the Asian summer monsoon is concurrent with the reversal of meridional temperature gradient in the upper troposphere south of the Tibetan Plateau, as originally suggested by Flohn (1957). A small region of reversed temperature gradient may also be seen over North America.

The temperature gradients in the southern hemisphere never reverse. That is, at all times the mean temperature at 30°S is cooler than at 5°S because of the strongest heating occurring very close to the equator. Although Australia is a large continent,

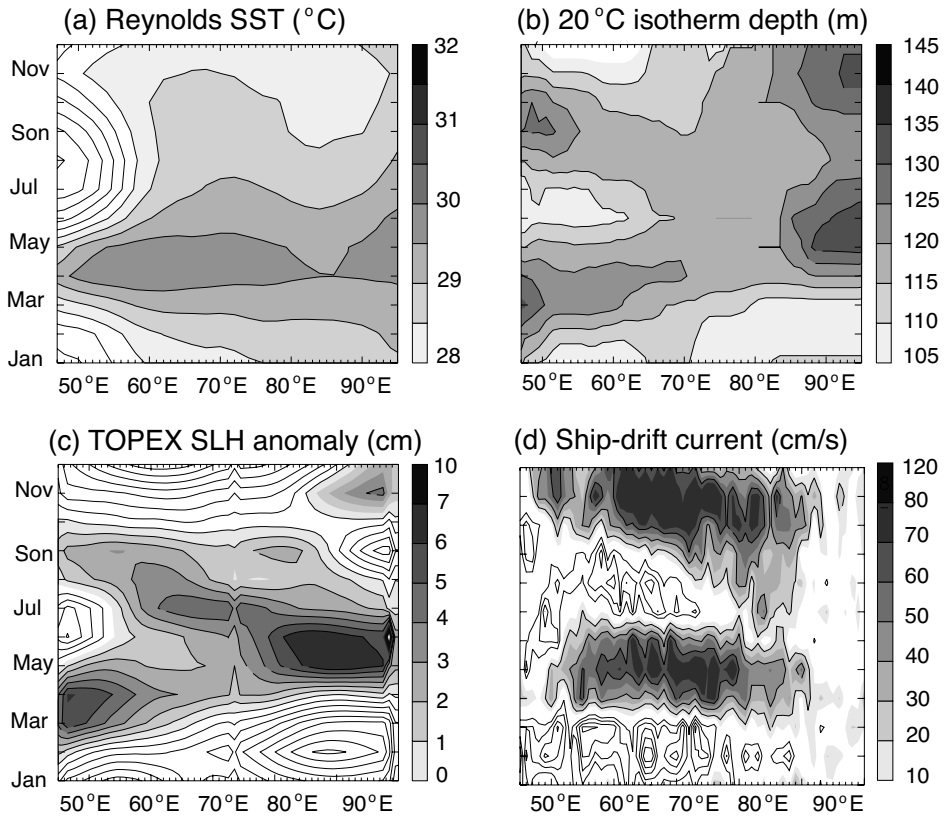

Figure 1.11. Time–latitude sections of annual cycle of (a) SST, (b) sea level height, and (c) surface currents, respectively, using Reynolds (1988) SST data, the TOPEX/POSEIDEN satellite altimeter, and (d) ship-drift.
Figures courtesy of Dr. Weiqing Han, Program in Atmospheric and Oceanic Sciences, University of Colorado.

the heating is not elevated as it is over the Himalayas. Thus, the major heating remains close to the north coast of the continent and close to the equator. Geostrophic adjustment is extremely rapid at very low latitudes, and it is difficult for a local temperature maximum to be maintained. On the other hand, geostrophic adjustment to the elevated heating over the Himalayas is sufficiently slow to allow the development of a substantial pressure field and a warm core. However, the monsoon should be viewed in a cross-equatorial context. Figure 1.10(c, right-hand panel) shows that there are still strong cross-equatorial pressure gradients that drive the boreal winter monsoon. These gradients, not as large as those occurring in the boreal summer, are the result of the intense radiational cooling over north Asia during winter.

The annual cycle of quantities that are important to ocean–atmosphere interaction, and which result from the imposition of the large-scale forcing described in the paragraphs above, are shown in Figures 1.11 and 1.12. Figure 1.11(a–c) shows the

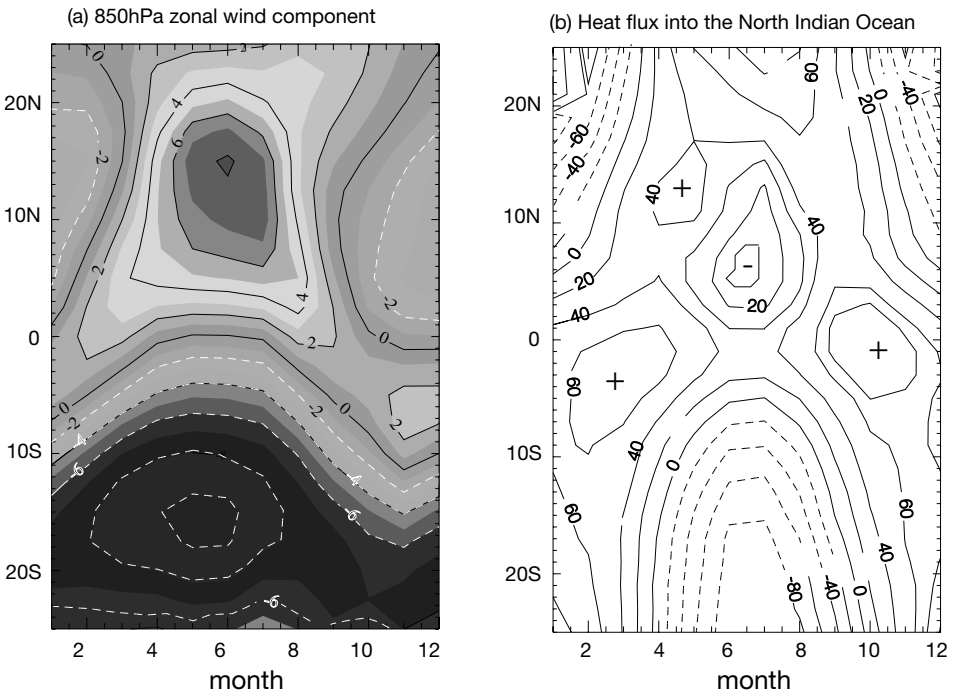

Figure 1.12. Time–latitude sections of the annual cycle of (a) 850-hPa zonal wind component (ms^{-1}) at 15°N, and (b) the heat flux (Wm^{-2}) into the north Indian Ocean averaged from the equator to 20°N.
Data from NCEP/NCAR Reanalyses (Kalnay *et al.*, 1996).

annual cycle of SST, sea level height anomaly, and surface current fields. The left-hand panels show observed values (Reynolds, TOPEX, and ship drift) and the right-hand columns show the model simulations for the HYCOM ocean model. All three fields show a strong annual cycle. Figure 1.12 shows mean climatological annual cycles of the 850-hPa zonal wind component and the heat flux into the north Indian Ocean. Of primary importance are the relatively weak winds in the boreal spring in the 0–20°N band accompanied by the very strong heat flux into the north Indian Ocean.

1.4.2 The surface heating–SST tendency paradox

One of the major outstanding problems of the climate is how the amplitude and phase of the annual cycle of the tropics, such as the cycle described above for the Indian Ocean, adopts the form observed. This problem has been the subject of intensive discussion especially with respect to the western Pacific Ocean following the introduction of the 'thermostat hypothesis' by Ramanathan and Collins (1991). Here, we are particularly interested in the regulation of SST distribution in the

Indian Ocean because of the close association between the magnitude of the SST and the vigor of the ensuing monsoon (e.g., Clark *et al.*, 2000).

Determining the surface heat balance of the tropical oceans is difficult, and large differences may occur between estimates. This should not be surprising as the surface heat balances are relatively small sums of larger terms. Furthermore, these large terms are obtained from empirical rules, some of which are not known accurately (Godfrey, 1995). Estimates of the net surface heat flux into the ocean using data from the TOGA Coupled Ocean–Atmosphere Response Experiment (TOGA COARE; Webster and Lukas, 1992; TOGA COARE, 1994), appears to be between 10 and $20\,W\,m^{-2}$ (Godfrey, 1998).

Unfortunately, the surface heat balance is less well known in the Indian Ocean. Table 1.2 provides estimates of the annual cycle of surface flux for the north Indian Ocean during the boreal spring and early summer using the Comprensive Ocean–Atmosphere Data Set (COADS; Oberhuber, 1988). Estimates are listed for the entire north Indian Ocean and for regions north of 10°N and between the equator and 10°N. The daily mean solar radiation into the north Indian Ocean is $>200\,W\,m^{-2}$ during the spring months and $181\,W\,m^{-2}$ over the entire year compared with an annual average of about $145\,W\,m^{-2}$ for the western Pacific (Webster *et al.*, 1998).

Table 1.2. The components of the surface heat balance for the north Indian Ocean (a) north of the equator, (b) from the equator to 10°N, and (c) north of 10°N. Units are $W\,m^{-2}$. The net solar radiation, net long-wave radiation, latent heat flux, sensible heat flux, and the net flux at the surface are denoted by S, LW, LH, SH, and NET, respectively. Data from COADS (Oberhuber, 1988). Heating rates of a 50-m layer for the entire north Indian Ocean are shown in the right-hand column ($K\,yr^{-1}$).

Flux ($W\,m^{-2}$)	S	LW	LH	SH	NET	dT/dt ($K\,yr^{-1}$)
(a) Entire north Indian Ocean						
DJF	125	−57	−103	−4	15	2.2
MAM	223	−49	−82	−2	90	13.4
JJA	190	−39	−117	−0	34	5.1
SON	187	−48	−88	−3	50	7.5
Annual	*181*	*−48*	*−98*	*−2*	*47*	*7.1*
(b) North Indian Ocean equator to 10°N						
DJF	181	−49	−96	−4	24	
MAM	202	−47	−88	−3	65	
JJA	178	−42	−116	−2	17	
SON	186	−46	−87	−4	50	
(c) North Indian Ocean north of 10°N						
DJF	174	−61	−105	−5	3	
MAM	232	−48	−74	−1	112	
JJA	191	−35	−113	0	44	
SON	179	−47	−88	−2	42	

The annual net surface flux averaged over the entire north Indian Ocean is about $+50\,\mathrm{W\,m^{-2}}$ or at least a factor of two or three larger than in the western Pacific warm pool (Godfrey *et al.*, 1998). Overall, it is relatively clear (taking uncertainties into account) that over the year there is a much stronger flux of heat into the north Indian Ocean than into the western Pacific Ocean (e.g., Hastenrath and Lamb, 1978; Hsiung *et al.*, 1989; Oberhuber, 1988; Hastenrath and Greischar, 1993). Furthermore, there is a far larger seasonality in this flux than in the western Pacific Ocean with maximum values occurring in spring and early summer.

It is a simple matter to estimate the changes in SST resulting just from the observed net fluxes (Table 1.2). The simplest way is to assume that the net flux is spread through an upper ocean layer of some defined depth for which the heating rate may be written as:

$$\frac{dT}{dt} = -\frac{1}{\rho C_p}\frac{dF_{net}}{dz} \tag{1.2}$$

Heating rates, assuming a 50-m surface layer, are listed in the right-hand column of Table 1.2. Alternatively, one may use a sophisticated 1-D mixed-layer model to make the same computation. Webster *et al.* (1998) used the model of Kantha and Clayson (1994) finding results quite similar to those listed in Table 1.2. Both sets of calculations suggest very different behavior in the evolution of SST than observed in nature. Figure 1.9 shows a rather gradual change in SST from one season to another whereas the calculations listed in Table 1.2 suggest that the north Indian Ocean would be continually warming at an annual rate $>7^{\circ}\mathrm{C\ yr^{-1}}$. If this were the case, the observed cyclic equilibrium noted in Figure 1.9 would not be achieved. On the other hand, using flux values for the Pacific Ocean suggests a net warming of about $1\text{–}2^{\circ}\mathrm{C\ yr^{-1}}$.

It is clear that the Ramanathan and Collins (1991) mechanism cannot regulate SST in the Indian Ocean. The warmest SSTs on the planet during spring and early summer are not associated with convection (Figure 1.9) so that there is no cloud shielding to mitigate the solar radiation flux at the surface. Furthermore, the second class of theories for regulation of the SST in the Pacific Ocean (Fu *et al.*, 1992; Stephens and Slingo, 1992; Wallace, 1992; Hartmann and Michelson, 1993) also cannot solve the problem; winds remain light during the boreal spring and early summer, and evaporation is relatively low (Figure 1.9).

It is also clear that the ocean must play an extremely important dynamic role in achieving the cyclic equilibrium of the mean annual cycle. As summarized by Godfrey (1995, p. 12):

> ... on annual average there is positive heat flux into the Indian Ocean, nearly everywhere north of 15°S. The integral of the net heat influx into the Indian Ocean over the area north of 15°S ranges between $0.5\text{–}1.0 \times 10^{15}\,\mathrm{W}$, depending on the climatology. Thus, on the annual mean, there must be a net inflow of cold water (into the north Indian Ocean), and a corresponding removal of warmed water, to carry this heat influx southward, out of the tropical Indian Ocean ...

Oceanic meridional heat transports of heat or significant thickening of the mixed layer represent the only means that allow the large net annual surface heating of the

north Indian Ocean to be removed without raising the SST substantially. It should be noted that Godfrey (1995) were referring to annually averaged ocean heat transports. In the next section we will show that the annual average is made up of seasonal swings with amplitudes that vary between ± 2 PW.

1.4.3 The role of ocean dynamics in the annual heat balance of the Indian Ocean

To understand the role of dynamical transports by the ocean, Loschnigg and Webster (2000) used the McCreary *et al.* (1993) dynamic upper ocean model, which incorporates full upper ocean dynamics and thermodynamics. Although there is little subsurface data in the Indian Ocean, the model has been shown to replicate the surface structure of the Indian Ocean, as well as its annual cycle, when the ocean model is run in stand-alone mode with prescribed atmospheric forcing (Loschnigg and Webster, 2000). The instantaneous northward heat flux between two positions along a line of constant latitude is defined as:

$$F = \rho_w C_w \iint_{xz} HvT \, dx \, dz \tag{1.3a}$$

where H, T, and v are the depth, temperature, and meridional velocity component. The heat storage in a volume is defined by

$$S = \rho_w C_w \iiint_{xyz} HT \, dx \, dy \, dz \tag{1.3b}$$

Figure 1.13(a) shows the annual cycle of meridional ocean heat transport and heat storage changes in the north Indian Ocean forced by the annual cycle of climatological winds and heating. The net surface flux into the north Indian Ocean appears to have a semiannual variation due to the combination of net solar heating and cooling by evaporation. Evaporative cooling is largest in the summer associated with the strong monsoon winds. There is also a second maximum in winter associated with the winter monsoon. Solar heating also has two minima: in summer where cloudiness has increased with the onset of the monsoon and in winter because of solar declination. Together, these two complicated heating mechanisms provide the double maximum evident in Figure 1.13(a). The major components of heat flow are between the transport and storage terms. A very strong southward flux of heat is evident during the spring and early summer, and a reverse flux is evident during the winter, when the north Indian Ocean is losing considerable amounts of heat by both evaporation, and vertical turbulence mixing which entrains colder water from below the thermocline. The net heat flux across the equator is made up of opposing flows in the upper and lower layer of the model and may be thought of as a seasonally reversing meridional ocean circulation (McCreary *et al.*, 1993). The magnitude of the net southward flux across the equator during the spring and summer months more than makes up for the excess surface flux into the north Indian Ocean, with peak summer magnitudes of meridional heat transport reaching values of 2 PW. Whereas the changes in heat storage had been anticipated by earlier studies (e.g., Vonder Haar and Oort, 1973), the strong role of advection was not anticipated.

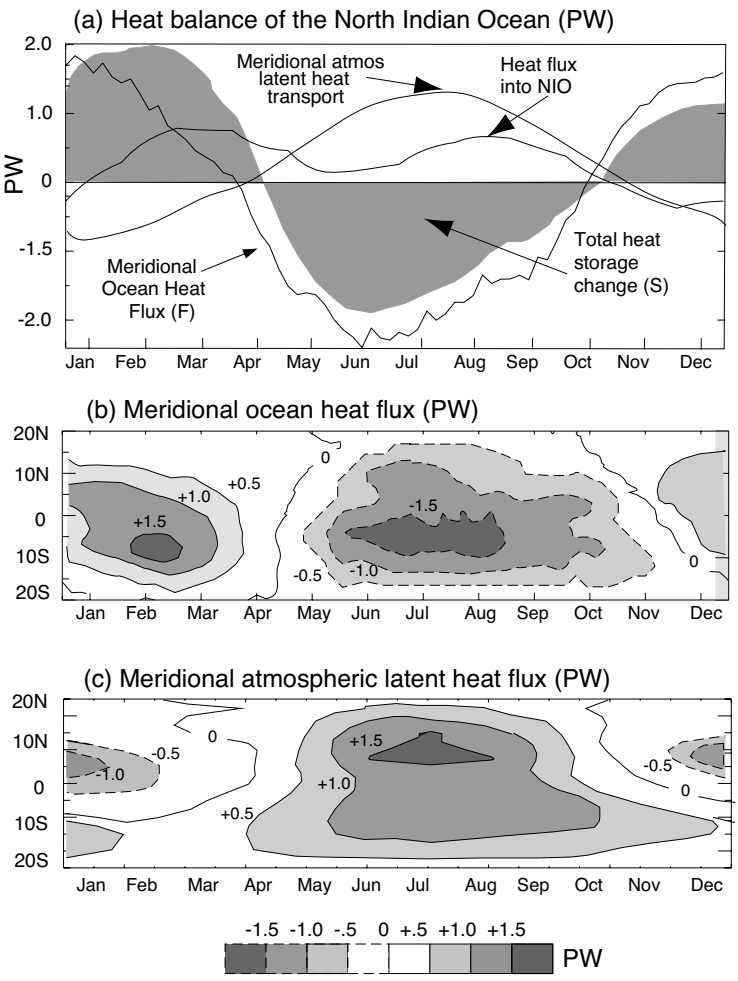

Figure 1.13. (a) Annual cycles of northward ocean heat transport across the equator (equation 1.3a), the net flux of heat into the north Indian Ocean, and the changes in heat storage (equation 1.3b) in the north Indian Ocean. (b) Latitude–time section of the annual cycle of northward ocean heat transport in the Indian Ocean. (c) Latitude–time section of the annual cycle of the northward flux of latent heat averaged throughout the troposphere. In the two lower panels, dashed lines indicate negative (southward) transport. Units in PW.

Figure 1.13(b) displays a latitude–time section of the annual cycle of the climatological meridional oceanic heat flux averaged across the basin. The year is divided into a period of northward heat flux in winter and spring, and a slightly stronger southward heat flux between late spring and early fall. Maximum transport occurs at all seasons close to 10°S near the zone of maximum SST gradient. Figure 1.13(c) shows a similar plot but for the northward flux of latent heat throughout the

troposphere. Comparing Figures 1.13(b) and (c) we find a remarkable feature – the dynamic heat transport in the ocean is equal and opposite to the direction of the atmospheric latent heat flux. That is, the oceans are transporting as much heat from the summer hemisphere to the winter hemisphere as the atmosphere is transporting from the winter to the summer hemisphere. That is, to zeroth order, the heat balance of the ocean–atmosphere system is closed.

More insight can be gained by exploring the heat storage term in the equations above. There are two components to the storage term, one relating to the change in depth of a layer of a certain temperature and one relating to the change of temperature of a layer of a fixed depth. Formally, these two components integrated in the vertical through the ocean column, may be written as:

$$S_{\Delta T}(t) = \rho_w C_w \iint H(t) \frac{\partial T(t)}{\partial t} dx\, dy \tag{1.4a}$$

and

$$S_{\Delta h}(t) = \rho_w C_w \iint T(t) \frac{\partial H(t)}{\partial t} dx\, dy \tag{1.4b}$$

Figure 1.14 (from Sahami, 2003) shows the two components of the storage terms plotted with the net surface heat flux and the northward meridional heat transport. During the winter, heat storage due to depth change is positive and almost

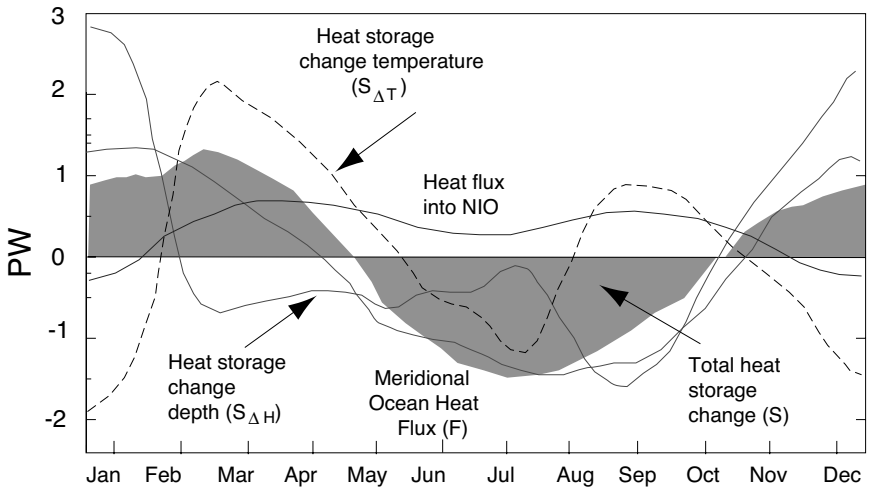

Figure 1.14. Annual cycle of the energy balance of the north Indian Ocean with the rate of heat storage broken down into storage associated with a temperature change with a constant depth of the mixed layer, and that associated with changes in depth of the mixed layer at constant temperature, as expressed in equations (1.4a) and (1.4b). The figure shows clearly that heat storage in the basin can change either through a deepening of the upper layers and/or by increasing temperature. Units in PW.
From Sahami (2003).

completely matched by storage changes due to temperature. During spring, the polarity changes but with the storage change due to depth outweighing the other component. Only during the summer are the two storage terms of the same sign. The relationship between the meridional transport of heat and the change of temperature of the north Indian Ocean (represented by $S_{\Delta T}$) is complicated. During spring and summer the two track each other very well. However, the relationship is contrary during autumn and winter when the transport and $S_{\Delta h}$ track each other. Thus, although the transport of heat in and out of the north Indian Ocean matches the total heat content of the north Indian Ocean when the surface heat flux is taken into account, the changes in heat content are not always manifested as changes in surface temperature. In a sense then, one should talk about these processes in terms of regulation of the heat content of the north Indian Ocean rather than the SST.

1.4.4 Regulation of the annual cycle: an ocean–atmosphere feedback system

From the calculations above, it is clear that without ocean transport across the equator and changes in the heat storage of the north Indian Ocean, the cross-equatorial buoyancy gradient during early summer would be very large. Yet the processes that accomplish the cross-equatorial transport of heat in the ocean are essentially wind driven (Mohanty *et al.*, 1996; McCreary *et al.*, 1993; Godfrey *et al.*, 1995). In turn, the atmospheric circulation is driven by surface fluxes and heating gradients associated with the buoyancy gradient and atmosphere–land interaction. Thus, the annual cycle in the Indian Ocean is a coupled phenomenon resulting from ocean–land–atmosphere interactions and balanced, to a large extent, by cross-equatorial oceanic transports. The form of interaction between the atmospheric monsoon flow and the ocean transport results from a coupled ocean–atmosphere feedback. A critical element of the meridional heat transport is that it is accomplished, to a large degree, by Ekman processes, a point that has been noted in previous work by Levitus (1987).

Figure 1.15 shows a schematic representing the regulation of the annual cycle in the monsoon system. The two panels represent summer and winter with relatively warm water (shaded) in the northern basin during summer and in the southern basin during winter. Surface winds, similar to those shown in Figure 1.9, are superimposed. In each season there is a strong flow from the winter to the summer hemisphere with a characteristic monsoon 'swirl'. The divergent part of the wind field (not shown: see Webster *et al.*, 1998) is also down the pressure gradient and from the winter to the summer hemisphere. The broad gray arrows represent the ocean Ekman transports associated with the surface wind forcing. Irrespective of the season, the Ekman transports are from the summer to the winter hemisphere. The total effect of the feedback is to cool the upper ocean of the summer hemisphere and warm the winter hemisphere, thus reducing the SST gradient between the summer and winter hemispheres. These transports are sufficiently large to be responsible for reducing the heating of the upper layers of the summer hemisphere to values less than those in Table 1.2. In summary, the amplitudes of the seasonal cycle of the

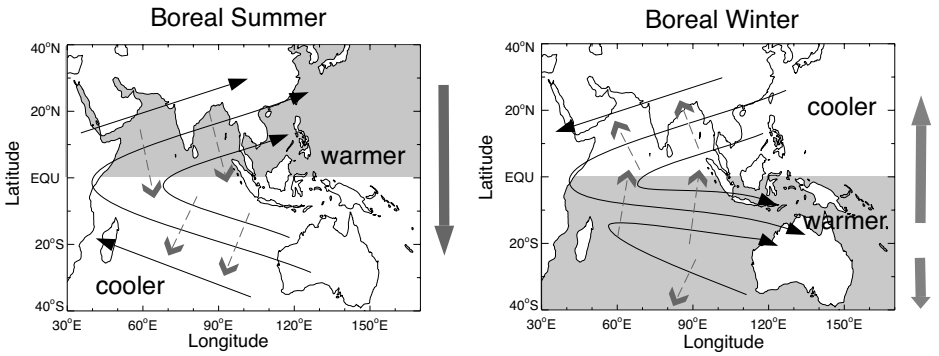

Figure 1.15. Schematic of regulation of the seasonal cycle of the Indian Ocean for (a) the boreal summer (June–September) and (b) the boreal winter (December–February). Curved solid lines indicate near-surface winds forced by the large-scale pressure gradients associated with the cross-equatorial heating gradient denoted by 'warm' and 'cool' (cf., Figure 1.10). Small gray arrows denote wind forces, Ekman drift, and the direction of the associated heat flux. The large vertical arrow denotes the sense and magnitude of the net zonally averaged heat flux reverses. Overall, the wind-driven southward flux of heat in the summer tends to cool the north Indian Ocean, while the northward flux during the winter tends to heat the north Indian Ocean, thereby reducing the SST gradient at all times of the year. The coupled ocean–atmosphere interaction described in the figure imposes a strong negative feedback on the system regulating the seasonal extrema of the monsoon.

monsoon are modulated through the negative feedbacks between the ocean and the atmosphere.

1.5 INTERANNUAL VARIABILITY OF THE COUPLED MONSOON SYSTEM

Figure 1.16 shows the difference of the near-surface wind fields between strong and weak monsoon years, defined in terms of the monsoon index shear index (M, defined in equation 1.1) and represents a more detailed version of Figure 1.4. In agreement with earlier analyses of Webster and Yang (1992) and Webster *et al.* (1998), the difference fields show a tendency for an increase in westerlies across the Indian Ocean region during strong years or, alternatively, an increase in low-level easterlies during weak years. There are important local manifestations of these difference fields. In strong monsoon years the south-westerlies toward east Africa are enhanced while, at the same time, there is an increase in onshore flow toward Sumatra. In weak monsoon years there is the reversal of the wind vectors. The form of the difference fields shown turn out to be of critical importance in understanding the manner in which the monsoon is regulated. This is because the changes in winds between the monsoon extremes occur in regions where major upwelling occurs.

An example of the impact of changing wind regimes on the Indian Ocean may be seen through the impact of an El Niño. Figure 1.17 presents a schematic

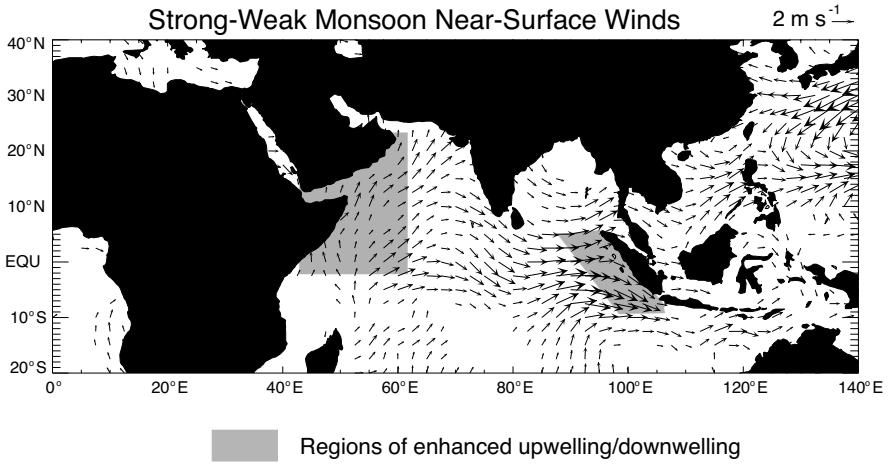

Figure 1.16. Differences in 925-hPa wind fields between strong and weak monsoons as defined in Figure 1.4. Shading denotes regions where upwelling or downwelling will be enhanced or reduced.

representation of the changes in zonal stresses between a non-El Niño and an El Niño period. Clear changes in the sea surface slope occur in both ocean basins. Also, the location of upwelling changes as well. In the case of the Indian Ocean, the upwelling regions change from the western to the eastern equatorial Indian Ocean. Such patterns are consistent with both El Niño forcing and a weak boreal summer monsoon.

1.5.1 Modes of interannual variability in the monsoon

The wavelet analysis (Figure 1.3) suggested the existence of monsoon variability with discrete periods. Here we consider major frequency bands longer than the annual cycle. These are the biennial period (first discussed by Yasunari, 1987, 1991; Rasmusson *et al.*, 1990; and Barnett, 1991), and multiyear variability that appears on ENSO timescales. Within the biennial period we include the newly discovered Indian Ocean dipole (Webster *et al.*, 1999; Saji *et al.*, 1999; Yu and Rienecker, 1999, 2000).

1.5.1.1 Biennial variability

The interannual variability of monsoon rainfall over India and Indonesia–Australia shows a biennial variability during certain periods of the data record (Figure 1.1). It is sufficiently strong and spatially pervasive during these periods to show prominent peaks in the 2–3-year period range, constituting a biennial oscillation in the rainfall of Indonesia and east Asia (Tian and Yasunari, 1992; Shen and Lau, 1995) as well as in Indian rainfall (Mooley and Parthasarathy, 1984). The 2–3-year oscillation referred to as the tropospheric biennial oscillation (TBO) in order to avoid

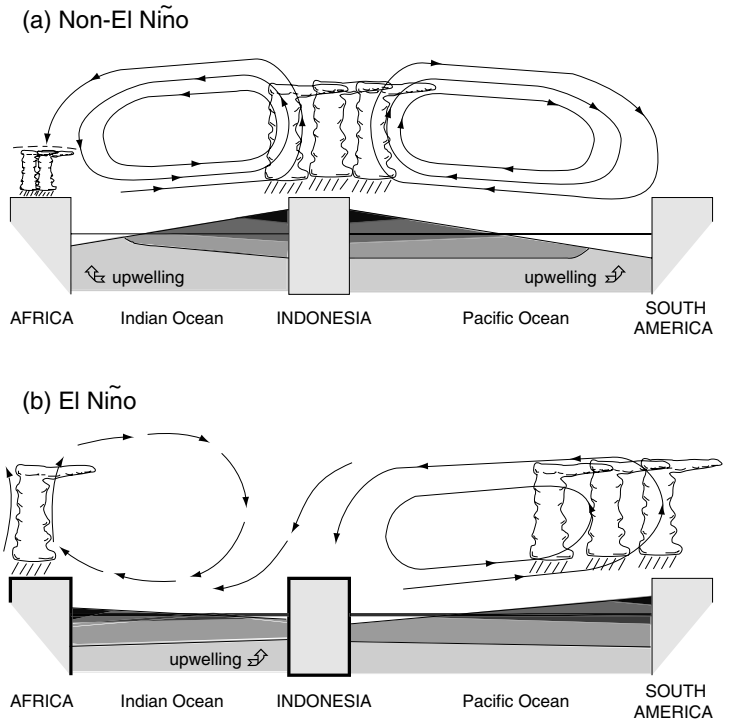

Figure 1.17. Schematic of the wind fields along the equator across the Pacific and Indian Oceans during El Niño and non-El Niño periods. With mean convection occurring over the warm pool of the western Pacific Ocean and Indonesia, the Indian and Pacific Oceans are forced by the converging winds of the surface arms of the Walker circulations. This leads to a deepening of the mixed layer in the eastern Indian Ocean and western Pacific Ocean and the promotion of upwelling on the other side of both basins. With an ENSO warm event and the eastward displacement of the Pacific/Indonesian convection, the Pacific and Indian Ocean Walker cells weaken. The wind reversal leads to a flattening or even a change in sign of the along-equator sea surface height gradient and a reversal of the locations of upwelling.

confusion with the stratospheric quasibiennial oscillation (QBO), appears to be a fundamental characteristic of Asian–Australian monsoon rainfall.

The rainfall TBO appears as part of the coupled ocean–atmosphere system of the monsoon regions, increasing rainfall in one summer and decreasing it in the next. The TBO also possesses a characteristic spatial structure and seasonality (Rasmusson *et al.*, 1990; Ropelewski *et al.*, 1992). Meehl (1994a) stratified ocean and atmospheric data relative to strong and weak Asian monsoons. Meehl (1994a) found specific spatial patterns of the TBO with a distinct seasonal sequencing. Anomalies in convection and SST migrate from south Asia toward the south-east into the western Pacific of the southern hemisphere following the seasons. Lower tropospheric wind fields associated with the TBO in the SST fields possesses an out-of-phase relation between the Indian Ocean and the Pacific Ocean basins

(Ropelewski *et al.*, 1992) with an eastward phase propagation from the Indian Ocean toward the Pacific Ocean (Yasunari, 1985; Kutsuwada, 1988; Rasmusson *et al.*, 1990; Ropelewski *et al.*, 1992; Shen and Lau, 1995) providing possible links between monsoon variability and low-frequency processes in the Pacific Ocean (Yasunari and Seki, 1992; Clarke *et al.*, 1998).

Explanations for the TBO fall into two main groups:

(i) The TBO results from feedbacks in the seasonal cycle of the atmosphere–ocean interaction in the warm water pool region, especially in the western Pacific Ocean. For example, Clarke *et al.* (1998) suggests the oscillation may be produced by an air–sea interaction instability involving the mean seasonal wind cycle and evaporation. They argue that similar instabilities are not possible in the Indian Ocean and that Indian Ocean oscillations found there are the result of Pacific instabilities.

(ii) Biennial oscillations occur as a natural variability of the monsoon coupled ocean–atmosphere–land monsoon system. As distinct from the views expressed in (i), the source of the biennial oscillation is thought to reside in the Indian Ocean. Nicholls (1983) noted a seasonal change in the feedback between the wind field and surface pressure. In the monsoon westerly (wet) season the wind speed anomaly is negatively correlated to the pressure anomaly, while in the easterly (dry) season it is positively correlated. The wind speed anomaly, on the other hand, is negatively correlated to the SST change throughout the year through physical processes such as evaporation and mixing of the surface ocean layer. Nicholls suggested that a simple combination of these two feedbacks in the course of the seasonal cycle induces an anomalous biennial oscillation. Meehl (1994a,b, 1997) substantiated Nicholls' hypothesis but focused on the memory of the oceanic mixed layer. That is, when large-scale convection over the warm water pool region, associated with seasonal migration of the ITCZ and the monsoon, is stronger (weaker), the SST will eventually become anomalously low (high) through the coupling processes listed above. The anomalous state of the SST, thus produced, would be maintained through the following dry season and even to the next wet season. In turn, the SST anomaly produces weaker (stronger) convection. In this class of hypotheses the ocean–atmosphere interaction over the warm water pool appears to be of paramount importance.

A schematic diagram of the four phases of Meehl's biennial monsoon system (Meehl, 1994a) is shown in Figure 1.18. The first panel depicts the winter season prior to the first monsoon season showing anomalously warm SSTs in the central and western Indian Ocean and cooler SSTs in the eastern Indian Ocean and the Indonesian seas. Anomalously warm SSTs in the Indian Ocean herald a stronger monsoon supposedly by a heightened surface hydrological cycle (panel 2). This is consistent with the empirical results of Clark *et al.* (2000). A stronger monsoon is accompanied by stronger wind mixing and evaporation, which leads to cooler SSTs in the central and eastern Indian Ocean. A reversal of the east–west SST gradient produces a stronger north Australian monsoon (panel 3). In turn, the colder than

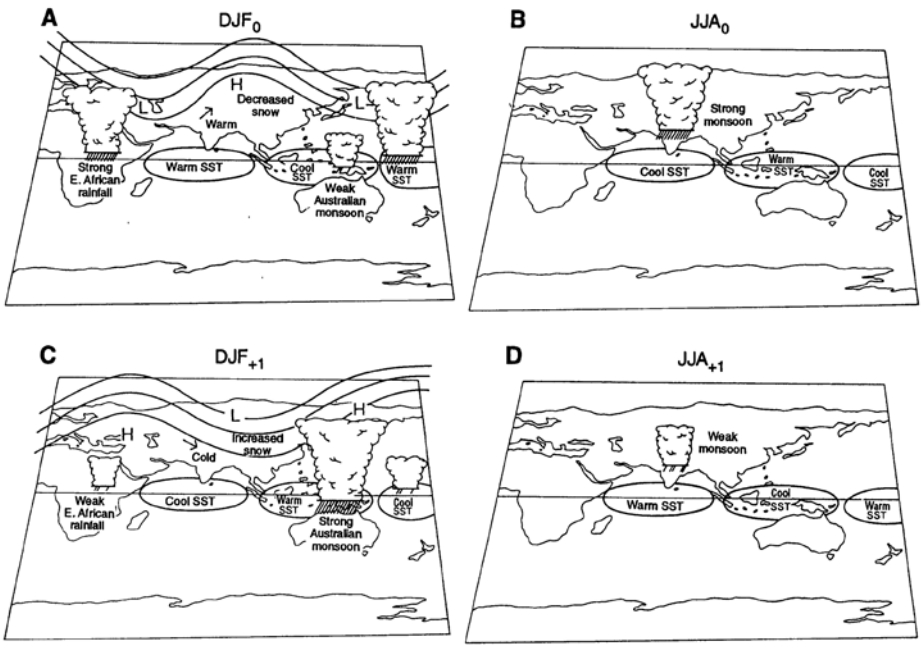

Figure 1.18. Schematic evolution of the biennial component of the monsoon circulation. (a) The winter before a strong Asian monsoon through. (b) The strong monsoon season. (c) The northern winter after the strong monsoon before a weak monsoon. (d) The following weak monsoon.
From Meehl (1994a).

normal Indian Ocean leads to a weak Indian summer monsoon (panel 4). The theory also notes that a strong south Asian monsoon is preceded by a strong east African monsoon and a weak south Asian monsoon by a weak east African monsoon. Presumably, the oscillation of the east African monsoon is associated with the change of the longitudinal SST gradient.

The sequence of SST change shown in Figure 1.18 follows observations quite closely including the oscillation of precipitation from year to year (Figure 1.1). Whereas it is very clear that the oscillation of the SST in the Indian Ocean is indelibly tied to the variability of the monsoon rains, there are two problems with the theory. First, there is no satisfactory explanation for the change in the SST gradient along the equator. That is, why does the SST change in any one location? Second, it is difficult to account for the persistence of SST anomalies for the 9 months between the end of one summer season and the start of the next. Clearly, thermodynamical processes alone cannot accomplish this. In fact, the e-folding time of a 50-m mixed layer with a 1°K anomaly at 303°K is between 40–60 days. There must be dynamical ocean processes at work in the Indian Ocean that increase the persistence of the anomalies.

Fasullo (2004) tested the hypothesis that asserts a biennial alternation exists between successive strong and weak Indian monsoon summer seasons. The basic

technique was to categorize the strongest and weakest monsoon seasons from 1871 to 2001, and compare the mean rainfall in the summer seasons that precede and follow them. He found that for the strongest monsoon seasons, statistically significant associations with the preceding summer rains exist that are consistent with the biennial hypothesis. In contrast, for years following the strongest monsoon seasons, and for years that both precede and follow the weakest monsoon seasons, significant biennial associations are largely absent. When the relationship with ENSO is considered, significant associations are found that act both in opposition to, and in support of, the biennial hypothesis. Often, weak or deficient summer rains precede strong La Niña seasons, and strong summer rains follow weak El Niño seasons. The sequences identified are associated with transitions between El Niño and La Niña conditions. However, in contradiction to the biennial hypothesis, it is also found that following strong La Niña seasons, average monsoon rainfall lies significantly above its climatological average, and the frequencies with which both deficient and weak monsoon seasons occur are significantly below their expectation values. Furthermore, during years in which ENSO conditions are near neutral, evidence of biennniality is poor. It is clear that more work needs to be done regarding biennial variability in the monsoon and the tropics in general. However, we will find the association of the biennial oscillation and ENSO, as found by Fasullo (2004), is quite consistent with the general theory of monsoon regulation presented in Section 1.7.

1.5.1.2 The Indian Ocean dipole or zonal mode

Between July 1997, and the early summer of 1998, the strongest seasonal SST anomalies ever recorded occurred in the Indian Ocean. During this period, the equatorial gradients of both SST and SSH reversed with cooler surface temperature in the eastern basin and warmer in the west. These anomalies occurred in conjunction with strong easterly wind anomalies across the equatorial Indian Ocean. The anomalies in SST and SSH persisted for almost a year and coincided with the 1997–1998 El Niño. The mean November conditions over the Indian Ocean and south Asia are shown in Figure 1.8.

Figure 1.19 (color section) shows longitude–time sections of daily values of SST (°C) and 850-hPa zonal wind ($m\,s^{-1}$) averaged between 5°N and 5°S for the period 1 January 1997 through 1 July 1998. It is clear from Figure 1.19(a) that the positive dipole pattern (warm in the west, cool in the east) is apparent as early as July 1997. The rapid decrease in eastern Indian Ocean SST occurs in September and the rapid rise in SST in the west later. Westerly wind anomalies (Figure 1.19(b)) existed as early as July (consistent with the SST gradient) before accelerating in October 1997 as the SST gradient increased.

There are two peculiar features of the SST patterns. The first is the boomerang-shaped positive SST anomaly pattern found in November 1997 (Figure 1.8(a)). The second is the lag of the formation of the warm anomaly in the west relative to the formation of the cool anomaly in the eastern Indian Ocean (Figure 1.19(a), color section). Webster *et al.* (1999) ascribed these peculiarities to the existence of strong

ocean dynamics in the transitions taking place in the Indian Ocean during the summer and fall of 1997. Hints of these processes can be seen in the sea level height longitude–time plots shown in Figure 1.20(a–c; color section). In each panel there are clear differences in propagation speed as marked by the dashed arrows. For example, along the equator (panel a), westward propagation occurs at roughly 40° of longitude in 3.5 months. At 5°S (panel b), the speed of propagation is about 40° of longitude in 4 months. At 12°S (panel c) the propagation speed has reduced to 40° in 10 months. With evidence of the dependence of phase speed variability as a function of latitude and the direction of propagation, Webster *et al.* (1999) were confident that downwelling ocean Rossby waves were responsible for the evolution of the sea height ridge in the western Indian Ocean.. The wave characteristics describe both the latitudinal and temporal lags noted in Figures 1.8(a) and 1.19(a).

Figure 1.21 (color section) shows a series of TOPEX/POSEIDON images of sea level height across the Indian Ocean for five 10-day periods from late November 1997 to early January 1998. The letters 'C' and 'D' show features of the height field identified in the mean November field (Figure 1.8(d)). Clear eastward propagations of elevated sea level height can be seen.

Another interesting feature of the equatorial latitude–height fields (Figure 1.20(a), color section) is the relatively rapid eastward propagation in mid-spring of 1997. Starting in the western Indian Ocean at the beginning of April 1997, the positive height anomaly propagated across the entire basin in two months. This is an example of an eastward propagating equatorial Kelvin wave first found by Halpern *et al.* (1988). Further analysis showed this to be an upwelling Kelvin wave. The 1997–1998 event received considerable attention (e.g., Webster *et al.*, 1999; Saji *et al.*, 1999; Yu and Rienecker, 1999, 2000). Following the summer of 1998, the SST pattern changed polarity with anomalously warm water occupying the eastern Indian Ocean with cold water in the west.

The 1997–1998 event was not an isolated event. In fact, over the last few years there has been a sequence of positive and negative dipole events in the Indian Ocean. Analysis of Indian Ocean SST data reveals that the 1997–1998 and 1961 events, the events receiving the most interest were members of a class of oscillations involving an oscillation of SST anomalies between the east and west tropical Indian Ocean. Reverdin *et al.* (1986) and Kapala *et al.* (1994) refer specifically to an event of similar magnitude in 1961. Earlier, in 1996, the SST distribution was very similar to that found in 1998. Figure 1.22(a) shows a time section of the September–November (SON) dipole index (defined by Clark *et al.*, 2000b similarly to the index defined by Saji *et al.*, 1999). The index oscillates between positive (anomalously warm west, cold east) and negative (anomalously cold west, warm east) values. It also plots the July–September Niño 3.4 SST anomaly and the October–December 'short' rains over east Africa. Strong correlations exist between all three variables although a period exists in the mid-1980s where the correlations drop to insignificant levels for nearly a decade (Figure 1.22(b)). Overall, the correlation between the dipole index and Niño 3.4 temperatures is strong ranging between 0.6 for the June–August period to 0.7 for the October–December period, exceeding in both periods the 95% confidence level (Figure 1.22(b)).

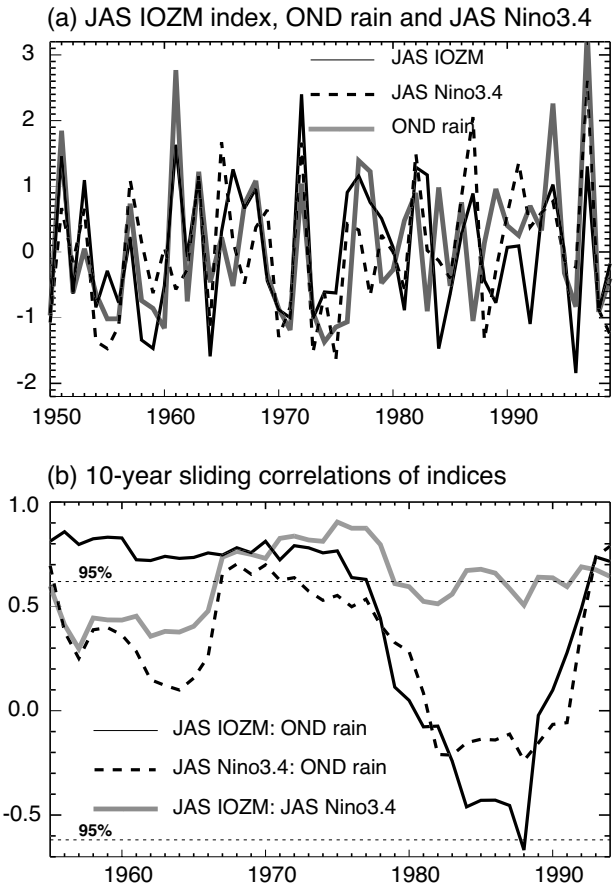

Figure 1.22. (a) Characteristics of the IOZM IOD. Normalized values of the (a) June–September IOZM Index, the October–December rain in the Kenya region, and the JAS Niño 3.4 SST index. The IOZM index is defined identically to Saji *et al.* (1999). (b) 10-year sliding correlations of the three indices listed in (a) with each other. Whereas the IOZM and the Niño 3.4 indices stay relatively constant throughout the period, correlations with the OND rainfall fall off through the 1990s.
Adapted from Clark *et al.* (2000).

Since the identification of the IOZM or (IOD), over 170 papers have appeared in major scientific journals discussing its physical nature and its impact on local and remote climates. Because of the relative abundance of data and the magnitude of the event, the 1997–1998 positive event has been studied extensively. There are a number of points that have emerged from these studies that are pertinent to subsequent discussion:

(i) The association of the Indian Ocean dipole with the El Niño of 1997–1998, or with the ENSO phenomena in general, remains unclear. Saji *et al.* (1999) for example, states that there is little or no relationship between ENSO and the

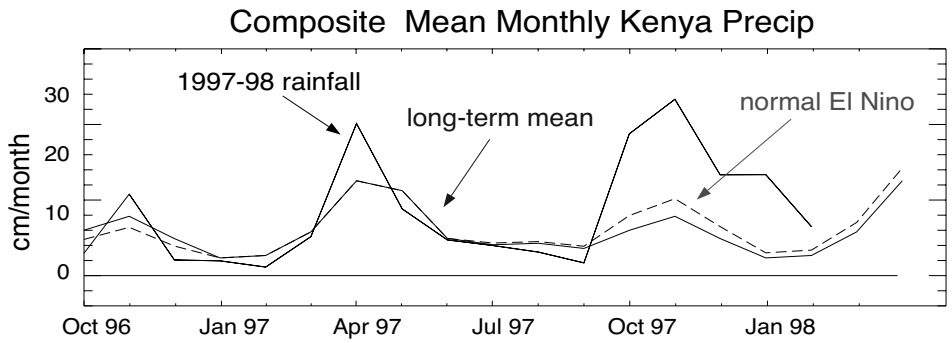

Figure 1.23. Annual cycle of the monthly Kenyan rainfall (solid thin line) vs. a composite of the Kenyan rainfall during El Niño periods (dashed line). The rainfall during the 1997–1998 period is shown as the solid heavy line. In general, during an El Niño, the 'short rains' in east Africa (October–December) are slightly above average. However, the 'long rains' (March–May) show little change. But in the 1997–1998 period, rainfall in both wet periods were the highest since 1961.

dipole. This latter claim, made using correlations with annual ENSO parameters, disappears when seasonal parameters are used as we have shown in Figure 1.22(a). Based on correlations between ENSO and the dipole, Reason *et al.* (2000) argue that the dipole is simply an extension of the ENSO influence in the Indian Ocean. Webster *et al.* (1999) state that the dipole is '*... arguably independent of ENSO ...*' based on the magnitude of the 1997–1998 event relative to normal influences of El Niño on the Indian ocean. Figure 1.23 illustrates this point. The figure shows the rainfall in the Kenyan region for the period under discussion. Whereas the associations between SST and rainfall during the 1997–1998 event are of the same sign as the normal excursions occurring during El Niño, they are orders of magnitude larger. Furthermore, during 1997–1998 the climate patterns around the Indian Ocean rim were very different from those normally associated with El Niño. Although the El Niño was the strongest in the century, monsoon rains were normal in south Asia and north Australia when drought may have been expected. Arguably, in 1997–1998, climate anomalies around the basin could be more closely associated with the anomalous conditions in the Indian Ocean than in the Pacific.

(ii) It is clear that ENSO variability may be associated with many dipole events, but it may not be involved in all. Figure 1.22(b) shows significantly reduced correlations between Niño 3.4 SST anomalies, the dipole index, and east African rainfall in the 1950s and 1960s. Instead of slightly increased rainfall in east Africa, the rainfall was the largest positive anomaly of the century, even larger than the 1961 excursion. Finally, large dipole events have occurred that are not matched by ENSO extrema, most notably the 1961 event documented by Reverdin *et al.* (1986) and Kapala *et al.* (1994).

(iii) Figures 1.24 and 1.25 (color section) show composites of SST computed for all positive and negative dipole events occurring between 1950 and 2002. Saji *et al.*

(1999) and Webster *et al.* (1999) note that the signature of the dipole commences in the early summer. This is true for both composite positive and the negative phases of the dipole. Positive events (Figure 1.24) are evident in June and both phases reach maximum amplitude in the mid to late boreal fall. The signatures of both phases have essentially disappeared by the following June.

(iv) Webster *et al.* (1999) suggest that the dipole is a coupled ocean–atmosphere instability that is essentially self-maintaining. As such, it is more properly described as a mode. Analyses suggest that the initial cooling of the eastern Indian Ocean sets up an east to west SST gradient that drives near-equatorial anomalous easterlies. In turn, these winds change the SSH to tilt upwards to the west. Relaxation of SSH anomalies, in the form of westward propagating and downwelling ocean Rossby waves, depress the thermocline in the west and enhance the warming of the western Indian Ocean. The slow propagation of these modes (1–2 m s^{-1}), and the manner in which they maintain the warm water by deepening the thermocline, assures that the dipole is a slowly evolving phenomena. Figure 1.26 (color section) provides a schematic description of the evolution of the positive phase IOZM. The figure depicts the IOZM as a distinctly coupled ocean–atmosphere phenomenon.

Later, we will argue that the IOZM or IOD is not an isolated entity but rather a component of the overall coupled ocean–atmosphere monsoon system. We will argue that the IOZM is a form of rectification of a system under the action of a strong cross-equatorial pressure gradient that occurs when the system is forced from equilibrium by external factors such as ENSO, stochastic influences, low-frequency, mid-latitude events, or land-surface processes associated perhaps with springtime anomalous snow cover over Eurasia.

1.5.1.3 Interannual variability of the monsoon and other factors

The statistical relationships shown in Table 1.1 and the wavelet analyses of Figure 1.3 indicate, to a significant degree, a common co-occurrence of monsoon variability and ENSO extremes. This relationship begs the question of when during the annual cycle does anomalously strong or weak monsoon seasons commence? To help answer this question, mean monthly circulation fields are composited for the weak and strong monsoon years defined earlier.

Figure 1.27 shows the south Asian composite annual cycle of upper and lower tropospheric zonal wind fields in the south Asian sector for strong and weak monsoons. In essence, the figure portrays the composite annual cycle of the monsoon index M defined in equation (1.1). At the time of the summer monsoon when the anomalous monsoon is defined, both the low-level westerlies and the upper level easterlies are considerably stronger during strong monsoon years than during weak years. But what is very striking is that the anomalous signal in the strength of upper level easterlies during strong years precedes the anomalous monsoon by many months. During strong years, the 200-hPa flow is 5–6 m s^{-1} less westerly than preceding weak monsoon years. In contrast, differences in the state of the lower troposphere between strong and weak years are not evident until late spring and

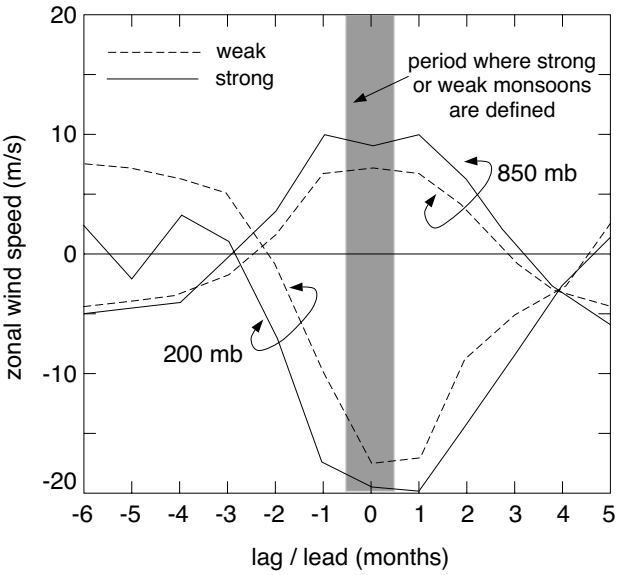

Figure 1.27. Composite of the annual variation of the 50 and 200-hPa zonal wind component in the south Asian region for years defined as strong and weak monsoon years (Figure 1.4). Note that the anomalous upper tropospheric winds are apparent some months before a strong or weak monsoon. However, such a signal is not apparent in the lower troposphere until late spring.
After Webster and Yang (1992).

summer. This surmise is supported by what is known about tropical convective regions. Noting that in monsoon regions and the tropics in general, enhanced upper tropospheric winds are usually accompanied by an enhanced lower tropospheric flow of the opposite sign. But this is clearly not the case prior to the strong monsoon, suggesting that the modulation of the upper troposphere probably results from remote influences.

1.5.2 Interannual modes in ocean heat transport

If the monsoon is indeed a coupled ocean–atmosphere system then there should be oceanic variability occurring on the same timescales as atmospheric variability. To test this hypothesis, Loschnigg and Webster (2000) forced the McCreary *et al.* (1993) dynamic ocean model with NCEP/NCAR winds for the period 1984–1990 to enclose the El Niño–La Niña doublet of 1987–1988. Chirokova and Webster (2004) extended these integrations for the period 1958–1998. In the results discussed here, 5-day average fields were used to force the model. In both cases NCEP/NCAR wind data was used and radiative forcing was obtained from Bishop and Rossow (1991).

Figure 1.28 shows components of the heat balance of the north Indian Ocean for three time periods (1969–1973, 1984–1988, and 1994–1998) of the total 40-year

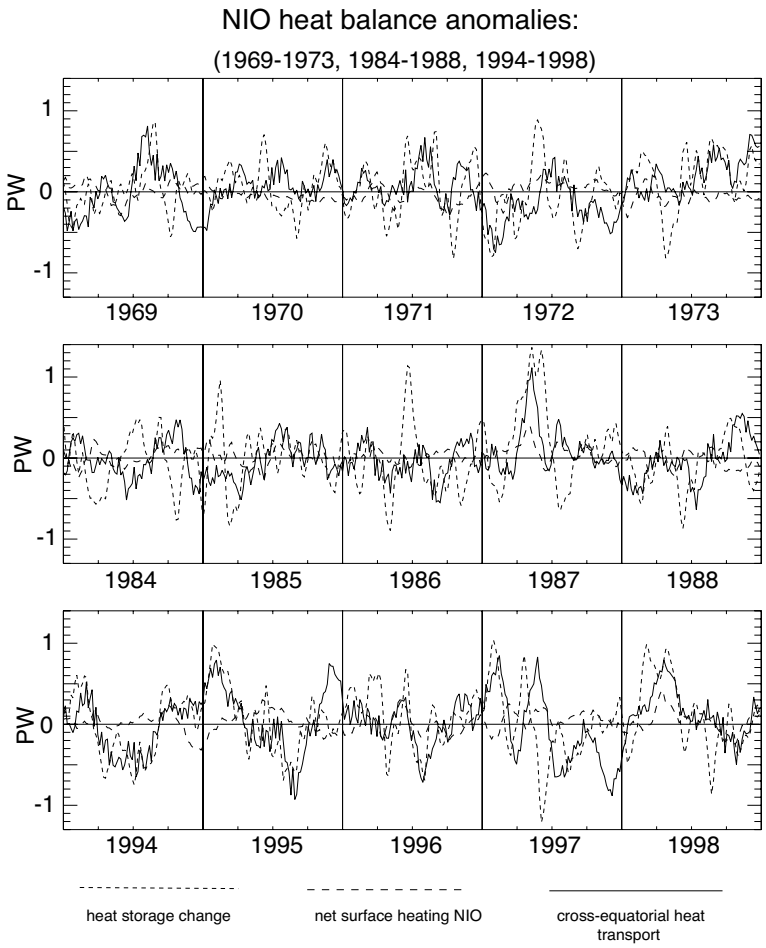

Figure 1.28. Time series of the components of the north Indian Ocean heat budget for the periods 1969–1973, 1984–1988, and 1994–1998. The seasonal cycle has been removed and a nine-point smoothing has been applied. Curves denote net heat flux (long dashed line), rate of change of heat storage (short dashed line), and meridional ocean cross-equatorial heat transport (solid line). Interannual anomalies occur at all times of the year and are of a similar magnitude to the mean annual cycle shown in Figure 1.13(a). Units in PW.
After Chirokova and Webster (2005).

integration made by Chirokova and Webster (2005). The sections show cross-equatorial heat transports, heat storage change, and net heat flux into the Indian Ocean north of the equator. For clarity, the heat flux has been shaded and a nine-point running average has been used for all three components, with the annual cycle removed. The total period contains nine El Niño and eight La Niña periods. Each component shows large interannual variability. Amplitudes of the variability are nearly as great as the climatological annual cycle (cf. Figure 1.13). Also, the variability occurs at all times throughout the year.

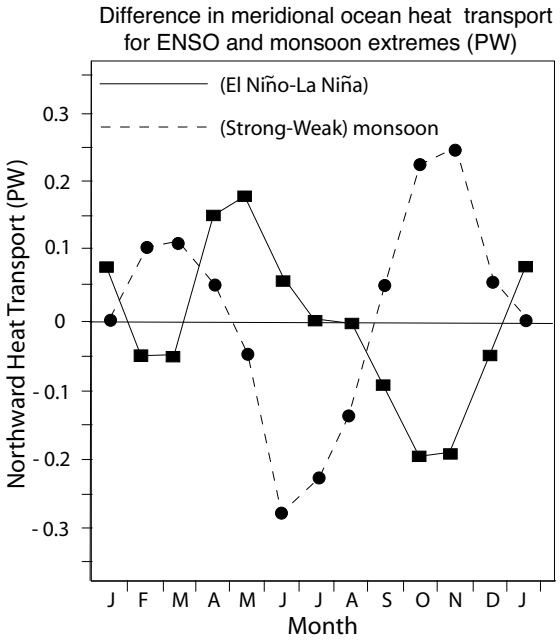

Figure 1.29. Composites of the annual cycle of differences in northward cross-equatorial ocean heat transports between El Niño and La Niña (solid curve) and strong and weak monsoons (dashed curve). Units in PW.

The time series were stratified relative to years exhibiting ENSO extrema and also relative to strong and weak monsoons as defined. Figure 1.29 shows the differences in heat fluxes between El Niño and La Niña and strong and weak monsoons as defined earlier for Figure 1.4. The differences are large and systematically correlated with the annual cycle. During a strong monsoon season, the anomalous flux is southward early in the boreal summer and negative during the boreal autumn. This enhanced southward transport during spring would seem consistent with stronger surface winds associated with the strong monsoon driving a stronger Ekman drift. The El Niño–La Niña composite is also consistent with the fact that an El Niño is normally associated with a weak monsoon, lighter surface winds, and reduced southward Ekman transport of heat across the equator. The reversed fluxes that occur in both of the cases is interesting and may be associated with a weakening (strengthening) of the monsoon induced by the changes in SST associated with the anomalous fluxes earlier in the season. Such a transport reversal may also be consistent with the biennial signal found in the region.

The long-term annual mean southward flux of heat across the equator is about 0.2 PW, matching the net annual surface heating of the Indian Ocean north of the equator (Godfrey, 1995). Given the magnitude of the anomalies shown in Figure 1.29, it would not be surprising if there were considerable interannual variability in the three components of the heat balance. In fact, this is the case. Figure 1.30

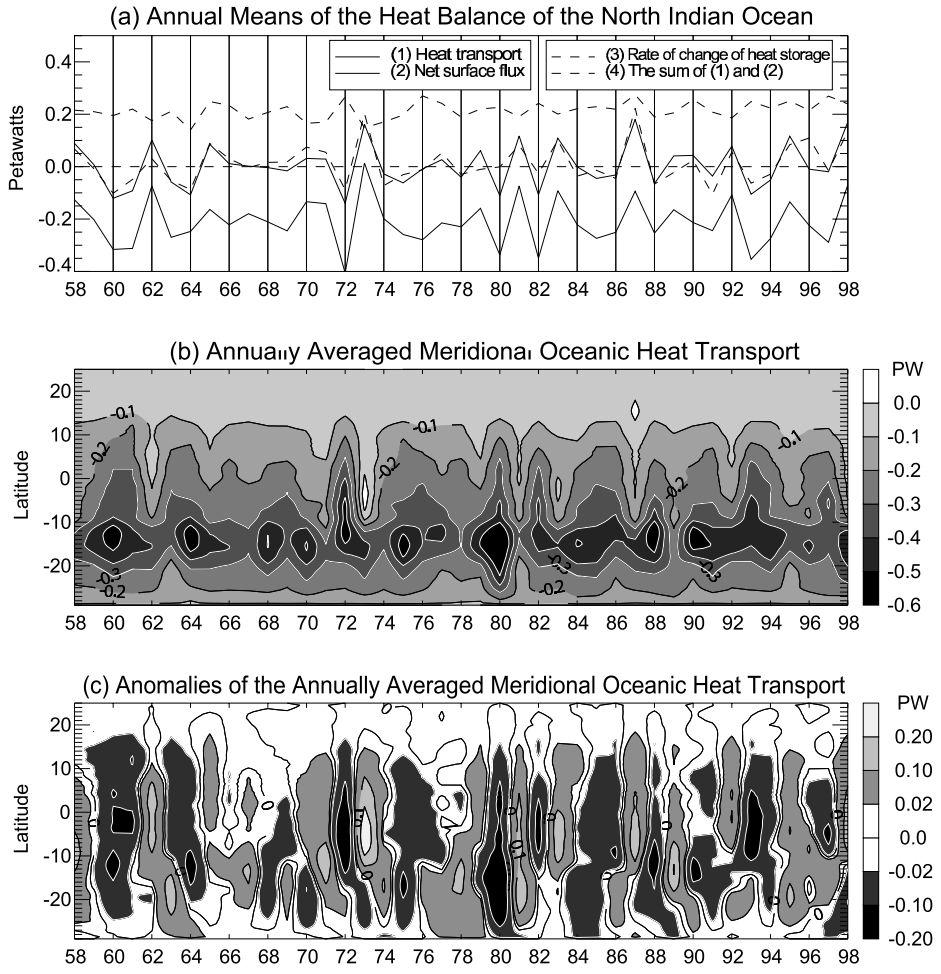

Figure 1.30. (a) Annually averaged heat budget for the north Indian Ocean. (b) Latitude–time distributions of the annually averaged meridional cross-equatorial heat transports including the long-term seasonal mean. (c) Same as (b) but with the annual average removed. Data from ocean model integrated from 1958–1998. Note the strong biennial tendency of the heat transport and that the anomalies tend to have the same sign on both sides of the equator and also extend across much of the basin. Units in PW.
After Chirokova and Webster (2005).

shows the time sections of the annual means of the components of the heat balance. Figure 1.31 shows the spectra of the cross-equatorial heat balance in the 1–10-year range.

Figure 1.30(a) plots the annual averages of the three components for the 40-year period 1958–1998. The net flux oscillates from between −0.4 PW in 1974 to a slightly positive value of +0.01 PW in the following year. Furthermore, rather than having a zero change in heat storage from year to year, the north Indian Ocean shows an

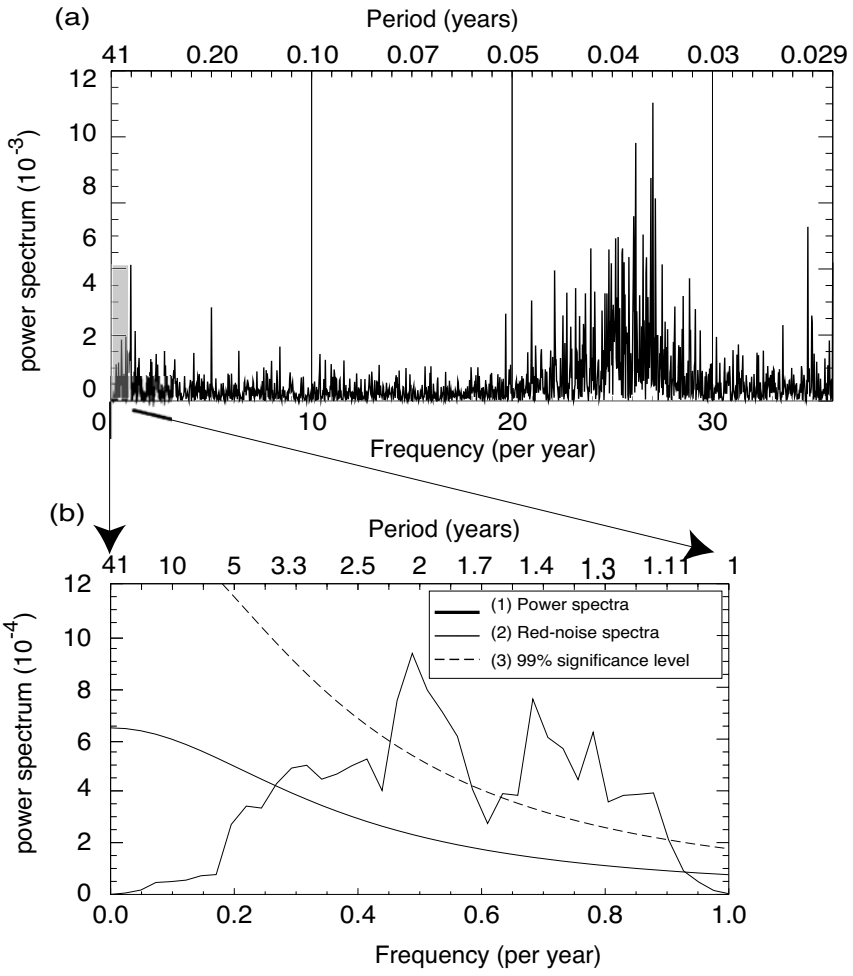

Figure 1.31. Power spectra of the cross-equatorial heat transport for periods between 1 and 10 years. The annual cycle has been removed by subtracting the first four harmonics. The 99% confidence level is calculated from the chi-square distribution, assuming a theoretical red-noise spectrum (Gilman *et al.*, 1963). The spectrum has been smoothed by a five-point running average. Each point has 10 degrees of freedom.
After Chirokova and Webster (2005).

ability to store heat in one year and lose it in another. For example, in 1965, 1973, and 1987, the net storage increased while in 1960, 1972, and 1988, the heat storage decreased. The net annual heat flux, on the other hand, is much more constant. There appears to be some evidence of considerable changes in the dynamic state of the Indian Ocean during the El Niño and La Niña years when the greatest deviations from the long-term average oceanic net meridional heat transport take place. Finally, as large changes in the heat transport and storage occur throughout

the period, while relatively small changes occur in the net heat flux into the north Indian Ocean, one can only assume that the changes are principally due to differential wind forcing of the Indian Ocean.

Figure 1.30(b) shows annual averages plotted as a function of latitude. As seen in Figure 1.13(b), the largest zonally averaged heat transports occur near 15°S. At this latitude, the heat fluxes range in values from −0.1 to −0.6 PW. An interesting observation is that if a maximum occurs at 15°S then it appears to occur at all latitudes. That is, the entire tropical Indian Ocean is anomalous in a manner consistent with changes occurring at the location of maximum flux. To check, the mean heat flux at each latitude was removed. Figure 1.30(c) shows the resulting anomalies plotted against latitude and time. In general, coherent variations with latitude appear from year to year. Furthermore, there seems to be a strong biennial component. This feature is corroborated by the spectra of variability shown in Figure 1.31. The peak at 2 years surpasses the 99% confidence level. A broader peak in the 3–5-year band surpasses the 95% level possibly indicating influences of ENSO in the annually averaged heat transports.

1.5.3 Intraseasonal ocean heat transport

It is interesting to look in detail at the differences in heat transport in the Indian Ocean for two years exhibiting considerable differences in the annual averaged characteristics. Let us choose 1997 and 1998 and plot the heat transport as a function of latitude and time in each case in Figures 1.32(a) and (b). A general annual cycle of heat transport is apparent in both years with northward transport during the winter and early spring and southward transport during summer. In that sense, both plots are broadly reminiscent of Figure 1.13(b). But two features require discussion. First, the heat transport shows very strong intraseasonal variability, suggesting a response of the ocean to high-frequency wind forcing. Second, the annual transport is −0.1 PW in 1987 and −0.25 PW in 1998 (Figure 1.30(a)). These anomalies are made up in different ways. There was considerable stronger southward transport of heat during the summer of 1988 compared with 1987. However, the northward heat transport was much stronger during the winter of 1987 than 1988.

1.5.4 Interannual regulation of the monsoon

Figure 1.15 proposes a coupled ocean–atmosphere regulatory system of the monsoon annual cycle that reduced the amplitudes of seasonal variability in both hemispheres. It is a simple matter to extend the argument to embrace interannual variability and form a model of regulation on these longer timescales. Such a system is shown schematically in Figure 1.33. Assume, for example, that the north Indian Ocean SSTs were warmer than normal in the boreal summer (left panel). The ensuing stronger monsoon flow would produce greater Ekman drifts and thus fluxes of heat to the winter hemisphere in the same manner found in Figure 1.15. If the north Indian Ocean were cooler than average for some reason (right panel), then one

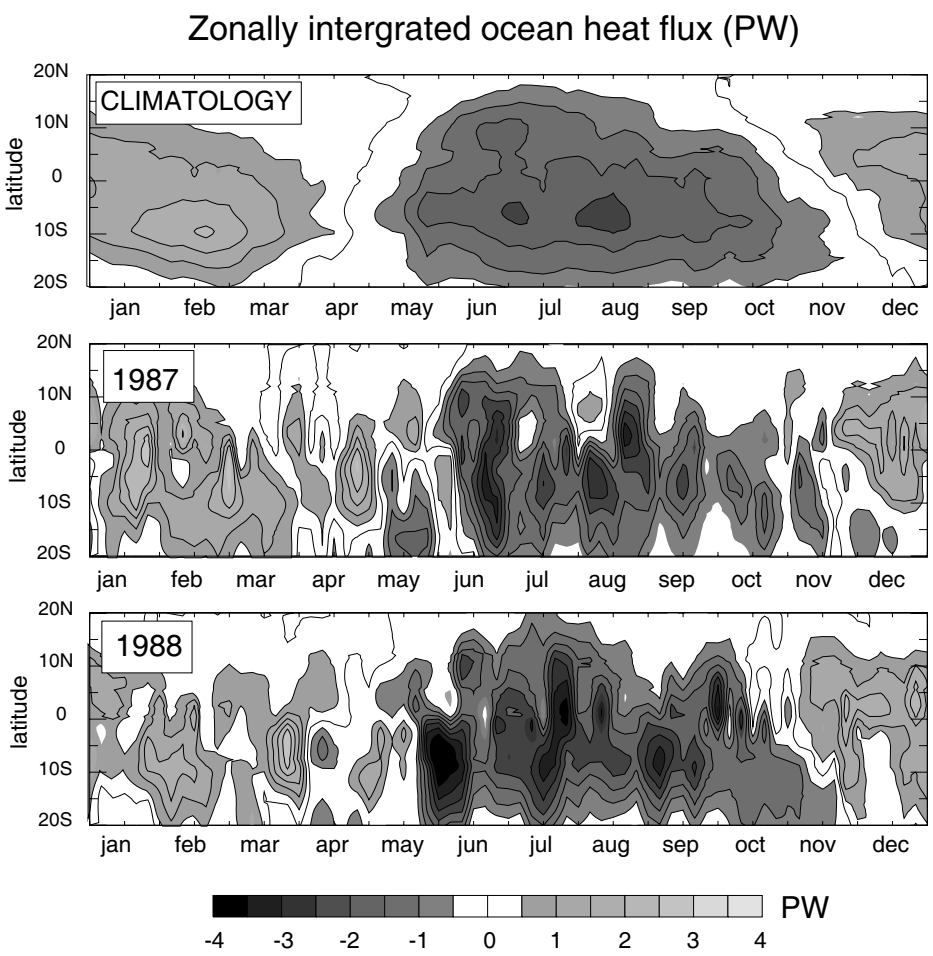

Figure 1.32. Zonally integrated heat flux averaged across the Indian Ocean for 1987 and 1988 which were weak and strong monsoon seasons, respectively. Data from the integrations of Loschnigg and Webster (2000) using the intermediate ocean model of McCreary *et al.* (1993) forced by 5-day average winds and net surface heat flux from NCEP/NCAR Reanalyses. Rather than the smooth patterns found in Figure 1.13(b), each year shows strong intraseasonal variability. Units in PW.

would expect a reversal in compensation through a reduced Ekman drift from the lighter surface winds. In a sense, the interannual regulation described here is very similar to the Meehl (1994a) theory shown in Figure 1.18. Like the Meehl theory, the natural timescale of the oscillation is biennial. In addition, because ocean heat transport is an integral part of the theory, it adds a dynamic element to Meehl's theory. In fact, the system described in Figure 1.33 is reminiscent of the situation found for 1987 and 1988 in Figure 1.32.

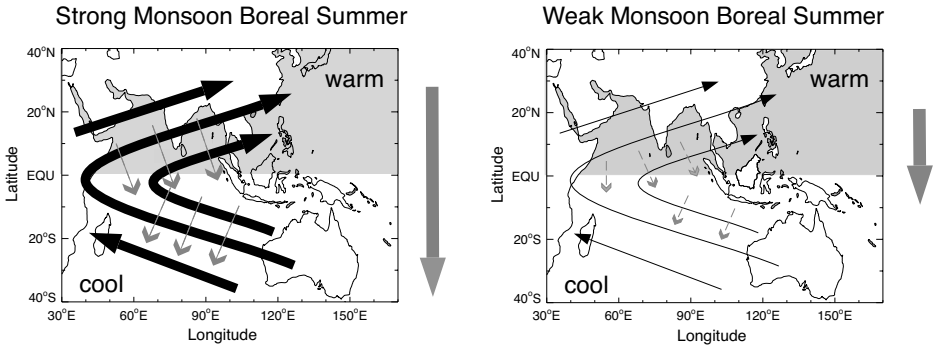

Figure 1.33. Same as Figure 1.15 except for the regulation of the interannual monsoon system and the impact of an anomalously strong and weak monsoon on the Indian Ocean. A strong monsoon which, from Figure 1.4 is related stronger than average low-level monsoon flow, drives an enhanced southward Ekman heat transport. A weak monsoon, on the other hand, is associated with a reduced Ekman heat transport. Following the reasoning of Meehl (1994; Figure 1.18), the tendency will be to produce an anomalous monsoon of the opposite sign the following year and introduce a strong biennial component into the system. The impact is to regulate the interannual variability of the monsoon.

However, the system suggested in Figure 1.33 is rather incomplete. It does not account for the influence of ENSO in the Indian Ocean but merely suggests how the coupled monsoon system will respond to an imposed SST anomaly. Nor does the theory take into account the IOZM. Later, in Section 1.7 we will attempt to include all of these features in a holistic theory of monsoon regulation.

1.6 COUPLED ASPECTS OF MONSOON INTRASEASONAL OSCILLATIONS

Intraseasonal variability of the monsoon occurs over vast spatial scales extending over the entire equatorial Indian Ocean, the Bay of Bengal, continental south Asia, and even the southern hemisphere subtropics. Figure 1.34 (color section) shows the composite precipitable water content (PWC) for the active period of the monsoon and a break period. PWC is the equivalent amount of liquid water equaling the total amount of water vapor in an atmospheric column. The active and break periods used in the composite were determined by the low-frequency precipitation variability over central India and are listed in Webster *et al.* (1998). During an active period, above-average and coherent PWC anomalies extend from the Arabian Sea to the dateline in a general north-westerly–south-easterly orientation, a distance of 10,000 km. During the composite break period a reverse configuration exists with a PWC maximum extending along the equator and a minimum over south Asia. Such large scales of low-frequency variability are apparent in multiple data sets such as precipitation, OLR, and wind fields (see Webster *et al.*, 1998), and bring periods of extended

drought and rainfall on 20–40-day timescales throughout the region, as discussed earlier in Section 3.4. The important point to be gathered from Figure 1.34 (color section) is that intraseasonal variability of the monsoon is not restricted to the littoral zones or their adjacent seas in south Asia but that it exists over the entire Indian Ocean basin.

1.6.1 The composite MISO

Figure 1.35 shows time–latitude sections of MSU precipitation for the years 1987 and 1988. Arc or boomerang shaped precipitation maxima appear to emanate slowly from the equator toward both the north and south. These features appear every 20 to 40 days (the scale of monsoon interannual variability) and propagate from the equator to 30°N in about 10 days. The southward leg tends to dissipate relatively rapidly, presumably because it propagates over colder water. Similar patterns have

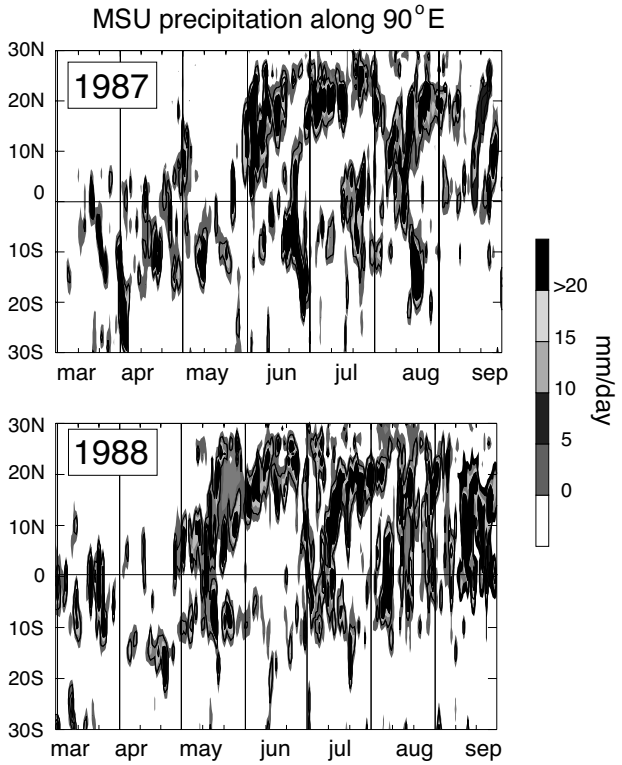

Figure 1.35. Latitude–time sections of MSU satellite precipitation product for the years 1987 and 1988 along 90°E. In general, precipitation emanates from the equator to both the northern and southern hemispheres. The northward leg becomes the active phase of the south Asian monsoon. Note that the periods of enhanced precipitation along the equator correspond to the enhanced meridional heat flux shown in Figure 1.32.

been noted by a number of earlier studies (e.g., Sikka and Gadgil, 1980; Yasunari, 1980; Webster, 1983; Hartmann and Michelson, 1993; Srivasian *et al.*, 1993). Lawrence and Webster (2001) suggest that the bifurcating cyclonic vortices or troughs represent trailing Rossby waves behind a rapidly propagating Kelvin wave, in agreement with the earlier conclusions of Wang and Rui (1990). The northward propagating convection, associated with the vortex in the eastern Indian Ocean, appears as a consistent precursor of an active phase of the south Asian monsoon.

A comparison of Figures 1.35 and 1.32 shows that there is direct connection between intraseasonal events in the atmosphere and intraseasonal variability in the ocean. In both 1987 and 1988 ocean heat transport maxima match the timing of occurrence of the atmospheric MISO events. It is clear that the atmosphere invokes a strong dynamic response in the ocean on intraseasonal timescales. However, it is less clear that the ocean, so forced, invokes changes on the atmosphere.

Lawrence and Webster (2002) extended an earlier analysis by Webster *et al.* (1998) by categorizing and compositing over 58 MISOs in the 24 summers from 1975–1999. Composites were based on the existence of a prolonged relative minimum in OLR (i.e., deep convection) in the eastern Indian Ocean (0.5°N, 85–90°E) on 20–80-day timescales (see Lawrence and Webster (2002) for details on compositing strategy). A regression technique was used similar to that developed by Kiladis and Weickmann (1992). Figure 1.36 shows composite OLR anomalies identified by this process. Lawrence and Webster (2002) found that about half of the MISOs developed *in situ* in the eastern Indian Ocean. The remainder of the events developed in the western Indian Ocean before propagating at a rate of 3–4 ms^{-1} toward the east. All of the events, irrespective of their genesis regions, showed distinctive 2 ms^{-1} northward propagation speeds as well as a southward, less extensive extension into the southern hemisphere. MISOs developing *in situ* (right-hand panels) do not appear to propagate eastward into the Pacific Ocean. The composite patterns shown in Figure 1.36 were essentially independent of the base location in the Indian Ocean or south Asian region (Lawrence and Webster, 2002) indicating that the dominant physical processes determining convection in the Indian Ocean/south Asian region were essentially the same. A recent study using satellite data (Wang *et al.*, 2004) ties together the features shown in Figure 1.36 in the context of a basin-wide, self-induction process of the coupled ocean–atmosphere system. This study poses the hypothesis that a MISO is a coupled ocean–atmosphere phenomenon. We will refer to the Wang *et al.* (2004) study later.

The reason for the poleward extension of convection into both hemispheres in the eastern Indian Ocean is not known except that the propagation occurs as a trailing Rossby wave behind the eastward convectively coupled Kelvin–Rossby packet (Wang and Rui, 1990b). It is noted, however, that because of the proximity of the heated continent to the north (e.g., Webster, 1983), and the ensuing meridional cross-equatorial pressure gradient, it is possible for low-frequency instabilities to be produced as suggested by Tomas and Webster (1997) and Tomas *et al.* (1999). In any event, the northward moving branch of the bifurcation becomes the active period of the monsoon as it moves northward through the

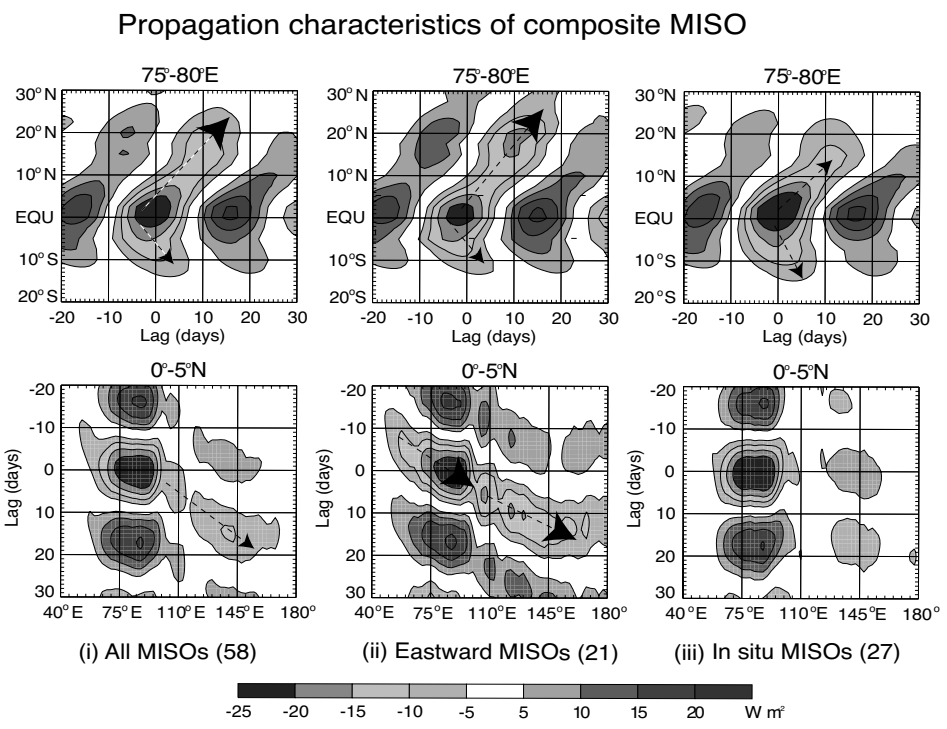

Figure 1.36. Composited satellite derived OLR ($W\,m^{-2}$) as a function of latitude (*upper row*) and longitude (*lower row*) from 58 MISOs displayed 20 days before and after maximum prolonged precipitation occurs near the equator in the 75°–85°E longitude band. The three columns represent composites for (i) for all 58 MISOs, (ii) for MISOs that formed in the eastern Indian Ocean and continued to propagate eastward, and (iii) for MISOs that formed in the eastern Indian Ocean. These locations were chosen to monitor the variation of major convection associated with a MISO as it propagates along the equator and bifurcates poleward in the eastern Indian Ocean.
Adapted from Webster and Hoyos (2004) and Lawrence and Webster (2002).

Bay of Bengal from where it extends across central India and south Asia and into the western Pacific Ocean. Prior to the bifurcation and when convection is a maximum in the east Indian Ocean along the equator (day zero of the composite) the Indian subcontinent is generally dry and in a break phase.

Figure 1.37 shows composite longitude–latitude maps of OLR, SST, and 925-hPa winds relative to day '0' of the intraseasonal mode. This base day is defined as the occurrence of strong ($>8\,mm\,day^{-1}$) precipitation lasting for more than 3 days at 80°–90°E and 5°N–5°S of the equator. The OLR composite (Figure 1.37(a)) shows organized and large-scale convection moving to the eastern Indian Ocean over a period of about eight days. Upon reaching the eastern Indian Ocean, the convective mass 'bifurcates' with the northern element moving slowly up through the Bay of Bengal and eventually over east India, Bangladesh, and South-east Asia. Convection increases along the west coast of India after day +4 coinciding with the spin up of the

active phase of the monsoon. The southern element moves southward and eastward, forming an elongated cloud band across Australia. The southern element, which is not as long-lived or intense as its northern counterpart, is still responsible for the winter hemisphere precipitation maximum just south of the equator. There is also some evidence that these southern branches are responsible for roughly 40% of the wintertime Australian rainfall. Nicholls (1989) found such associations on interannual timescales and Fasullo and Webster (1999) on shorter timescales.

The SST fields (Figure 1.37(b)) also show a coherent variation over the period of the composite MISO. Anomalous warming along the equator early in the MISO period yields to cooling as very deep convection builds up over the eastern Indian Ocean. These changes in SST are directly related to basin-scale variations in the lower tropospheric wind field (Figure 1.37(c)). The evolution of the wind field in the composite has three main periods: general anomalous counterclockwise circulation before the growth of convection along the equator, then strong convergence into the western end of the convection as the convection moves east, and finally a strengthening gyre with bifurcation of the troughs.

Figure 1.37 show that the SST has a basin-wide maximum near day -10 and a minimum at day $+5$. These extremes correspond to a minimum in the strength of the monsoon westerlies and a maximum in OLR (minimum in convection). However, the maximum in convection leads maximum monsoon winds and minimum SST by about 5 days, indicating a coupling between the atmosphere and ocean on intraseasonal timescales. The results are similar to those found by Fasullo and Webster (1999) for the tropical Indian Ocean. In addition, intraseasonal oscillations in the TOGA COARE region of the western Pacific possess similar phase relationships (Fasullo and Webster, 1999).

Although the SST variations represent coherent patterns across the entire Indian Ocean, the extrema are fairly small, ranging between $\pm 0.2\,\mathrm{C}$ through the phases of the intraseasonal oscillation. However, it is likely that the magnitudes of SST variability displayed in Figures 1.7(b) and 1.8, and computed from the Reynold's SST fields, are much smaller than those that are actually associated with the monsoon oscillation. SST variations measured during intraseasonal variations occurring in TOGA COARE showed variability between a half and an order of magnitude larger (e.g., Webster, 1994; Godfrey *et al.*, 1998). Similar variations were encountered during the Joint Air–Sea Monsoon Interaction Experiment (JASMINE; Webster *et al.*, 2001b). Furthermore, Sengupta and Ravichandran (2001) have shown, using moored buoys, that SST in the Bay of Bengal varies about $\pm 1^{\circ}\mathrm{C}$ through an intraseasonal oscillation. The reason for the underestimation may result from the fact that the Reynold's SST is a 5-day average and is computed from satellite data that is regressed to match ship observations which are perhaps more representative of subsurface temperatures than surface skin SST.

1.6.2 MISO and ocean heat transport

It is unclear from these SST changes, however, whether or not the wind variations produce a dynamic response in the ocean and whether this response is important to

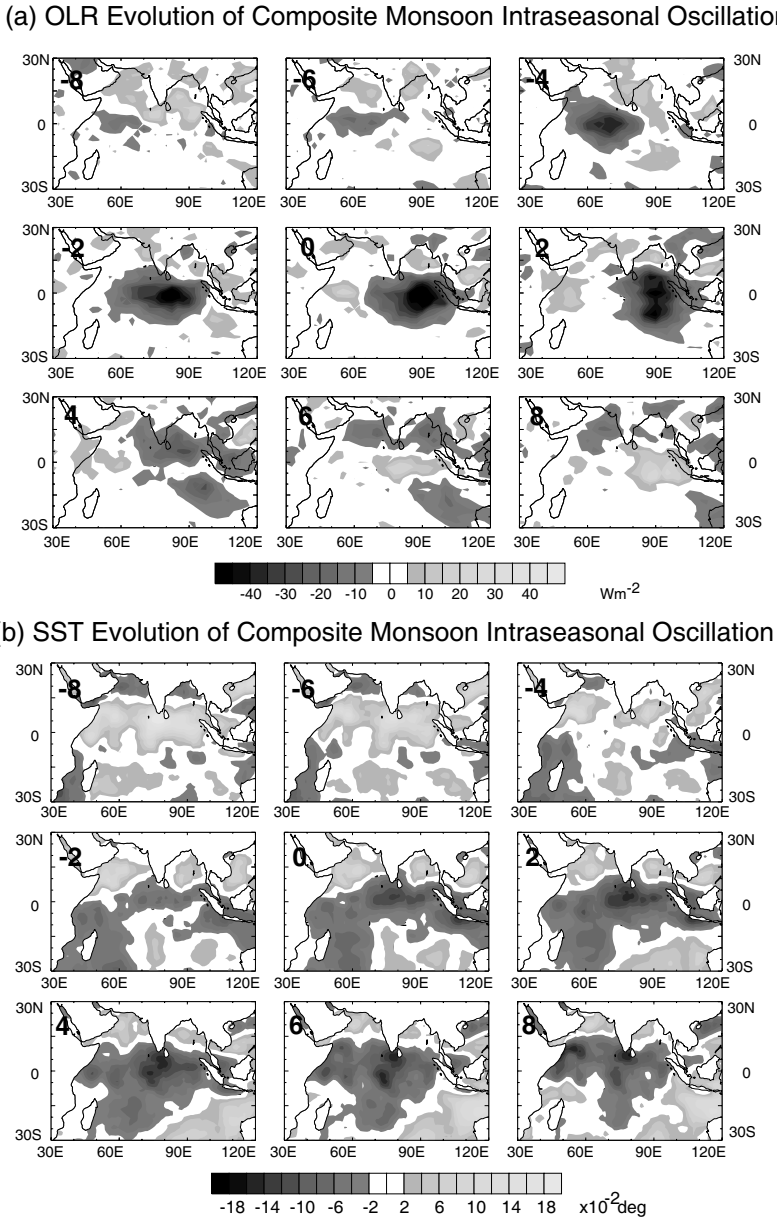

Figure 1.37. Spatial plots of the composite evolution of anomalous (a) OLR (Wm^{-2}), (b) SST (°C, Reynolds, 1988), and (c) 925-mb wind variability (with MSU precipitation rate >8 mm day^{-1} superimposed), relative to the composite monsoon intraseasonal oscillation configured from 39 events in the 1985–1995 period. Composite distributions were computed for 15 days on either side of day 0. The annual cycle was removed from all fields. Day '0' is defined as the occurrence of >10 mm day^{-1} precipitation (persisting four days) at 90°E. Panels (a)–(c) show composite OLR, SST, and NCEP/NCAR Reanalysis 925-mb wind field relative to day 0. Each member of the composites is described in detail in Webster and Tomas (1997).

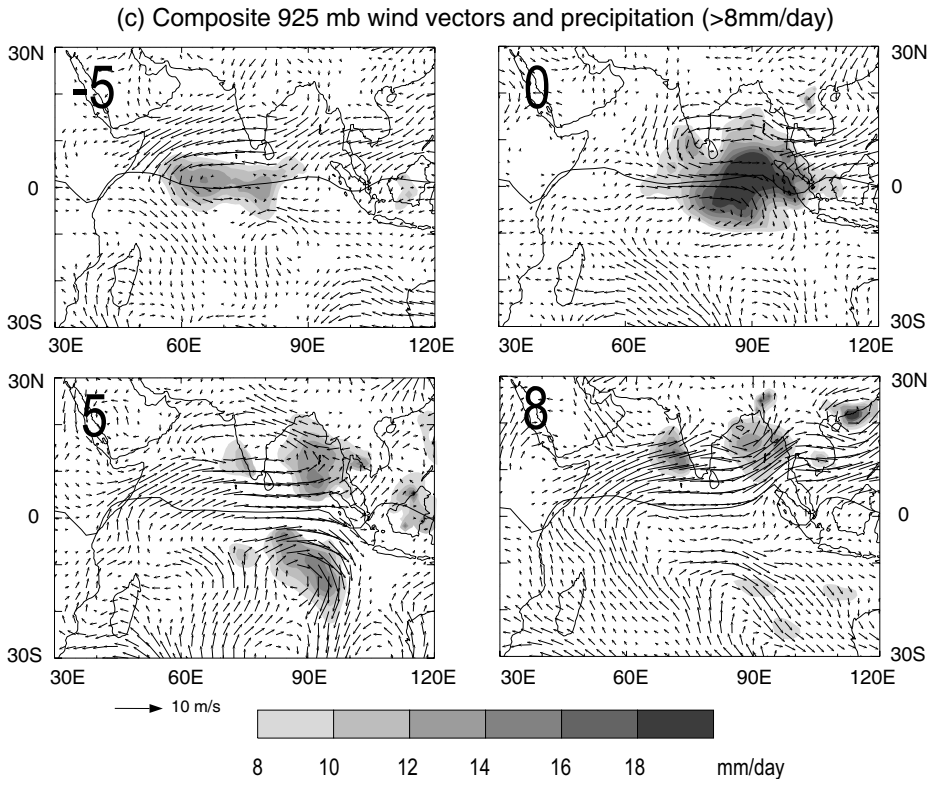

the overall heat balance of the Indian Ocean. In the absence of sufficient data to answer this question, we turn to results from the McCreary *et al.* (1993) intermediate ocean model.[3] We use the same MISO dates used for the earlier MISO compositing (Figures 1.36 and 1.37) and calculate the heat flux through the MISO period 15 days either side of Day 0. Figure 1.38(a) and (b) show the composite zonal and meridional wind stress along the equator. There is virtually no anomalous meridional wind stress associated with a MISO event (Figure 1.38(a), bottom panel). However, the zonal component contains a large signal of about 0.5 dyne cm^{-2} in the eastern Indian Ocean at day 0. Typical values of wind stress in the eastern Indian Ocean vary between 2 and 8 dyne cm^{-2}. Figure 1.39(b) shows the composite oceanic heat transport associated with a MISO. Maximum values occur near the equator with values of -0.7 PW. Integrating through the complete MISO from -15 to $+15$ days gives a net southward transport of -0.3 PW after the annual cycle and long-term mean has been removed. The heat transport to the south by one typical MISO is substantial in magnitude and similar to the net annual mean southward transport

[3] Dr. Weiqing Han of the Program in Atmospheric and Oceanic Sciences at the University of Colorado, Boulder, kindly made the calculations used in Figure 39.

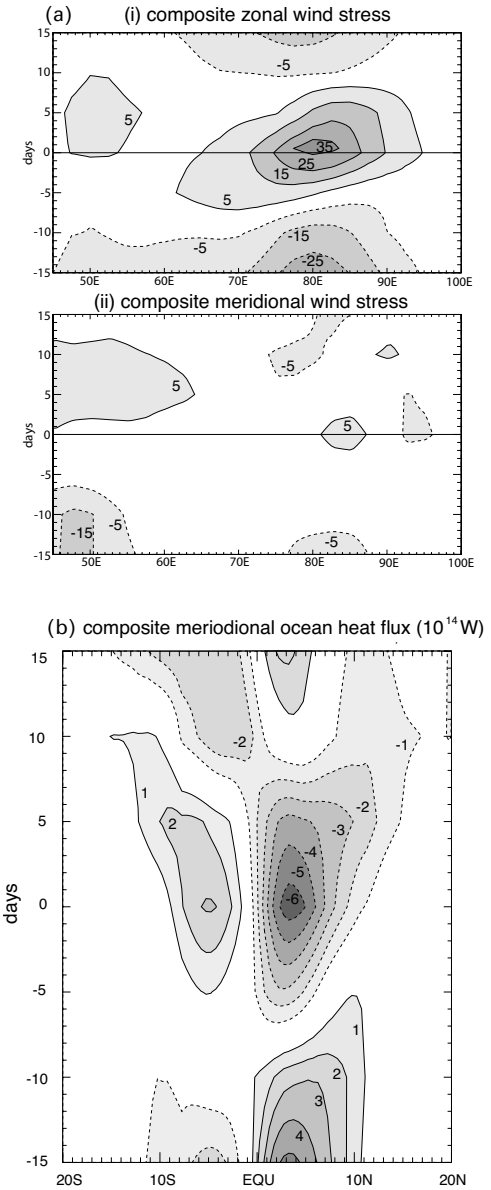

Figure 1.38. Ocean response to intraseasonal wind forcing. (a) The composite zonal (*upper panel*) and meridional (*lower panel*) wind stress relative to intraseasonal oscillations used in Figure 1.36. Day '0' refers to the maximum precipitation in the eastern Indian Ocean. There is little signal in the meridional wind stress but a strong westward zonal wind stress in the eastern Indian Ocean: (b) The composite meridional heat flux associated with a monsoon intraseasonal oscillation. Near day 0 there is an anomalous southward transport of -0.7 PW. Calculations made available by Dr. Weiqing Han, University of Colorado, using the McCreary *et al.* (1993) intermediate ocean model.

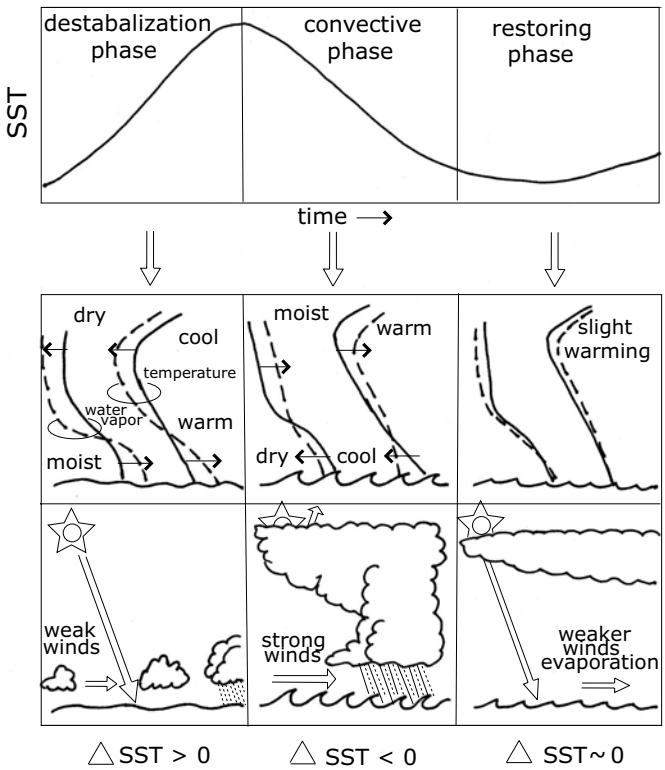

Figure 1.39. A schematic of the humidistat feedback showing its three principal phases. (*top*) The cycle of SST is a simple depiction of the SST variation as a function of time and is used as a reference for defining the three phases of the feedback. (*middle*) The schematic of how the atmospheric temperature and moisture changes during these phases defined with respect to the SST cycle. (*bottom*) Changes of cloud conditions and associated wind field and heating changes are indicated.
From Stephens *et al.* (2004).

(Figure 1.30). Thus, there is clear evidence of a role for the MISO in the heat budget of the Indian Ocean. However, whether or not the net northward heat transport would be the same with or without (e.g., forced with mean monthly fields) intraseasonal oscillations is not known. It would seem relatively simple numerical experimentation could answer this question.

1.6.3 MISO and the onset of the monsoon

The onset of the monsoon can be defined as the first major intraseasonal oscillation accompanied by a northward propagation of the precipitation maximum from the equator into the Bay of Bengal region. For example, the monsoon onset in 1987 (Figure 1.35, upper panel) follows enhanced precipitation at the equator in early

June. In 1988 (Figure 1.35, lower panel), the onset defined in this manner occurred about two weeks earlier. This definition is very different from traditional definitions (e.g., Rao, 1976), which emphasize the beginning of persistent rainfall at the southern tip of India. However, in most years precipitation occurs in the northern Bay of Bengal much earlier than precipitation in the south-east of India. Subsequent discussion will show that precipitation along the east coast of India occurs with the acceleration of the monsoon gyre after the first major monsoon intraseasonal oscillation matures and moves northward into the northern Bay of Bengal. Viewing the monsoon from a wider perspective allows the possibility of defining a monsoon within a larger geophysical context.

1.6.4 Intraseasonal variability and the self-regulation of the monsoon system

Two recent studies (Stephens *et al*., 2004; Wang *et al*., 2004) have provided evidence of tropical intraseasonal variability as a self-regulating coupled system. The first paper deals with intraseasonal variability more generically. The second paper specifically refers to the MISO and an Indian Ocean context. The earlier papers of Lau and Sui (1997) and Fasullo and Webster (1999) are also pertinent to the cycling suggested in both Stephens *et al.* (2004) and Wang *et al.* (2004).

Stephens *et al.* (2004) divide the complete intraseasonal oscillation cycle into three phases. The first phase is the destabilization phase. Here, the atmosphere becomes increasingly unstable through a combination of radiative cooling of the upper atmosphere, the gradual warming of the SST, and the development of shallow boundary layer cumulus humilis. Next, large-scale convection develops over the region, resulting in heavy precipitation, a deepening of the oceanic mixed-layer, a lowering of the SST, and a considerable moistening of the upper troposphere. This is called the 'convective phase'. Finally, there is a restoring phase where, through the combination of strong winds associated with the convection (which keeps the surface SST cool) and the enhancement of radiative heating of the upper troposphere, high clouds associated with the high humidity stabilize the atmosphere and suppress convection. Figure 1.39 shows a schematic of the three phases of the Stephens *et al.* (2004) sequence. Each phase of this the self-regulating system shown was observed in great detail during JASMINE (Webster *et al*., 2002a).

The Wang *et al.* (2004) MISO sequence involves a total of eight phases. As the study involves a description of the associated atmospheric dynamics as it responds to the heating cycles involved in the Stephens *et al.* (2004) paper, it requires a greater temporal definition. Phase 1 shows a minimum rainfall in the eastern Indian Ocean and active monsoon precipitation over India. In all of the eight phases, the complete ocean basin is considered. For example, during Phase 1 the influence of precipitation over India is related to the genesis of the next MISO over the eastern Indian Ocean. Subsequent phases describe a northward propagation of the MISO when the convective elements reach the eastern Indian Ocean and the subsequent active monsoon period over India. The Wang *et al.* (2004) paper is also unique because it uses Tropical Rainfall Measuring Mission (TRMM) data to describe the 3-D evolution of clouds and dynamics through the MISO cycle.

There have been suggestions that there is a strong connection between the MISO and the interannual variability of the monsoon. For example, Ferranti *et al.* (1997) noted that EOF patterns of interannual variations were essentially the same as those for intraseasonal variations. In accord with Hendon *et al.* (1999) for the north Australian summer monsoon, Lawrence and Webster (2001) noted that fewer MISOs occur in a strong monsoon and more with a weak monsoon and that in El Niño periods there is a tendency for there to be greater intraseasonal activity. Palmer (1994), Webster *et al.* (1998), and Goswami and Mohan (2001) came to the common conclusion that the MISO was the fundamental building block of interannual variability that might explain the common patterns shared by intraseasonal and interannual variability. Modeling studies (Ferranti *et al.*, 1997) show that principal intraseasonal and interannual components map onto each other, suggesting that interannual variability of the monsoon is closely tied to intraseasonal variations. Whether the same is true for the ocean or for the coupled ocean–atmosphere system is not known.

1.7 HOLISTIC THEORY OF MONSOON SYSTEM

In Section 1.5, we modified Meehl's theory by noting that the anomalous monsoon winds will induce ocean heat transports that will reverse the sign of the monsoon anomaly. However, there are still a number of issues that need to be considered. For example:

(i) Whereas there are dynamic elements added to the Meehl theory, one is still faced with the problem of maintaining an upper ocean temperature anomaly from one year to the next.
(ii) The regulation theories, either the Meehl theory or the modified Meehl theory, do not involve the Indian Ocean dipole. It could be possible, of course, that the dipole is an independent phenomenon. However, the similarity of the basic time period of the dipole to that of monsoon variability (essentially biennial) and the fact that the dipole emerges during the boreal summer monsoon suggests interdependence. The problem, though, is how to incorporate an essentially zonal phenomena (the dipole) and an essentially meridional phenomena (the oceanic heat transport) into a general theory of the monsoon.

A theory, shown schematically in Figure 1.40 (color section), that takes into account these two problems is now developed. The figure displays a sequence through two monsoon seasons starting (arbitrarily) in the boreal spring. There are three columns in the figure representing the anomalous meridional oceanic heat transports (column 1), the influence of the anomalous monsoon circulation on the ocean (column 2), and the evolution of the IOZM (column 3). During the two-year period, the monsoon goes through both weak and strong phases. At the same time, the IOZM progresses through a positive and negative phase. We will now argue that the morphology of the dipole and the monsoon are intimately related.

(i) The left-hand column describes essentially the regulation theory discussed in Section 4.4. The sequence starts with an anomalously cold north Indian Ocean in the boreal spring (March–May of the first year: MAM:1) that often precedes a weak monsoon (e.g., Sadhuram, 1997; Hazzallah and Sadourny, 1997; Clark *et al.*, 2000) in the summer of the first year (JJA:1). A weak monsoon is associated with a reduced southward heat transport leading to the SST distribution in the first boreal autumn (SON:2) shown in the second figure of the row. If the anomaly persists through to the second spring (MAM:2), it will lead to a strong monsoon in the second summer (JJA:2). Enhanced southward transports and reduced net heating of the Indian Ocean leads to an anomalously cold northern Indian Ocean.

(ii) Stronger and weaker summer monsoons also influence the ocean system in other ways. For example, the anomalous monsoon circulation (Figure 1.16) will influence the upwelling patterns in two major areas: Along the east Africa coast north of the equator, and along the western coast of Sumatra. Reduced south-westerly flow off Africa will decrease upwelling while offshore flow near Sumatra will enhance upwelling. Thus, during the weak monsoon of JJA:1 the changes in the monsoon circulation will create anomalously warm water in the west and colder water in the east. On the other hand, the circulation associated with the strong monsoon in JJA:2 will produce cooler water in the eastern basin (enhanced south-westerlies) and warmer water in the east (onshore winds along the Sumatra coast). In summary, changes in the monsoon winds between strong and weak monsoons can create zonal anomalies in the SST distribution.

(iii) The east–west SST gradients caused by the anomalous monsoon intensities can lead to enhancements of the zonal SST gradients by coupled ocean–atmosphere instabilities as described in detail in Webster *et al.* (1999) and summarized in Section 3.1.2. Simply, the SST gradients force zonal wind anomalies that change the distribution of low-latitude sea level height distribution. During JJA:1, the sea level height will slope upwards to the west while during JJA:2 it will slope upwards to the east. Relaxation of the sea level height takes place in the form of equatorial modes. For example, during the period JJA:1 through DJF:1 the relaxation will be in the form of downwelling Rossby waves. Besides having a slow westward propagation they are downwelling and deepen and warm the western Indian Ocean. In turn, the enhanced SST gradient will produce stronger easterly winds that will continue to maintain the east-to-west slope of the surface. Between JJA:2 and DJF:2 the onshore winds towards Sumatra will deepen the thermocline and enhance the zonal west-to-east SST gradient. In turn, responding to an increasing SST gradient, the winds themselves will be enhanced. The important aspect of the dipole is that it introduces slow dynamics into the system.

(iv) Careful inspection of Figure 1.40 (color section) shows that the impact of the dipole is to enhance the SST distributions associated with meridional heat transports shown in the first column. For example, the dipole that develops in the period JJA:1 through DJF:1 will increase the SST in the north-west

equatorial Indian Ocean. This SST enhancement can be seen by following the sequence 'a' through 'e' in Figure 1.40. On the other hand, the second dipole will cool the SST in the same location. This is the region found by Sadhuram (1997), Hazzallah and Sadourny (1997), and Clark *et al.* (2000a) to correlate most strongly in the winter with the following monsoon. Thus, the role of the dipole is to enhance and prolong the SST patterns necessary to regulate the intensity of the monsoon system.

1.8 CONCLUSIONS AND SOME REMAINING QUESTIONS

In the preceding paragraphs, we have developed a theory that regulates the monsoon on both annual and interannual timescales. The study was motivated by noting that the surface heat balances in the Indian Ocean do not match the observed evolution of the SST indicating the importance of ocean heat transports. Furthermore, it appeared curious that the year-to-year variability of the south Asian monsoon is relatively small. Thus, the theory of regulation of the monsoon rests on negative feedbacks between the ocean and the atmosphere. We are now in a position to address some of the questions raised in the introduction.

Perhaps the most important conclusion is that it is clear that the ocean involves itself in a dynamic manner in the morphology of the monsoon on all timescales at least longer than seasonal but perhaps even intraseasonal. Although the ocean is responding to forcing from the atmosphere, the response is such that a strong feedback to the atmosphere is produced. This feedback governs the amplitude and phase of the annual cycle and also modulates interannual variability. That is, the monsoon system considered holistically is self-regulating.

One of the problems that emerged in earlier theories of monsoon amplitude regulation (e.g., Meehl, 1997) is that it is difficult to understand how a SST anomaly pattern produced by an anomalous monsoon persists from one year to the next. By involving ocean dynamics in the regulation process we have managed to introduce mechanisms that allow SST anomalies to persist from one year to the next. This was accomplished by noting that the IOZM is also parented by an anomalous monsoon through the generation of zonal temperature gradients between upwelling regions. The slow dynamics of the dipole act to enhance the zonal SST gradient initiated by the anomalous monsoon irrespective of the sign of the initial perturbation. As the dipole grows, the SST anomalies so produced occur in locations that are conducive to the generation of a reverse anomaly in the monsoon. In other words, the IOZM adds the slow dynamics needed in the Meehl theory.

An immediate question is whether or not the IOZM is an independent entity or a function of forcing from the Pacific Ocean. First, there is irrefutable statistical evidence (Table 1.2) that ENSO variability in the Pacific Ocean produces a response in monsoon variability. Also, a substantial amount of the variance of the IOZM can be explained in terms of the Niño 3 SST variability. However, there are periods when the dipole and ENSO are unrelated statistically when it is difficult to

find an ENSO extrema to match the development of the dipole. There may be a way of resolving this apparent paradox. Let us assume that the dipole is a natural mode of oscillation in the Indian Ocean in much the same way as El Niño is a natural oscillation of the Pacific. Noting again that the IOZM is initiated by an anomalous monsoon, it is quite possible that a weak monsoon induced by El Niño will induce, in turn, a positive IOZM that then acts to reverse the impacts of ENSO during the following year. But, according to the hypothesis, a dipole will develop relative to an anomalous monsoon no matter how the monsoon is perturbed. Perhaps in 1961, and other such years, other factors could have perturbed the monsoon.

The results presented in this study are incomplete. They have depended on a number of empirical studies and experiments with stand-alone ocean models forced with atmospheric fields. The complete associations inferred in the conclusions above are difficult to establish from empirical studies because of the very convoluted nature of the phenomena. Further work will probably have to await experimentation with fully coupled ocean–atmosphere land models. Loschnigg *et al.* (2003) has made such a start. In their initial experiments with the NCAR coupled climate model they find considerable corroboration of the self-regulation processes and the associations between the atmosphere and the ocean described above.

It is fair to say that we are still unclear about the degree to which intraseasonal variability of the monsoon is coupled to the ocean. Lau and Sui (1997), Fasullo and Webster (1999), Stephens *et al.* (2004), and Wang *et al.* (2004) have provided convincing arguments that variations in the SST and the heat content of the mixed layer are important. Figures 1.32 and 1.38 show that there is a large variability in the heat transports associated wind variability of the MISOs. To this degree a MISO is a coupled phenomenon. What is unknown is whether the heat balance of the Indian Ocean itself would be the same with or without the existence of intraseasonal variability.

1.9 ACKNOWLEDGEMENTS

This work was made possible by grant 0328842 from the Climate Dynamics Division of the National Science Foundation. Thanks also to my research group, first at the University of Colorado and then at the Georgia Institute of Technology. Special thanks are due to Hai-Ru Chang, Galina Chirokova, Carlos Hoyos, Kamran Sahami, and Weiqing Han. In particular I would like to thanks Bin Wang for his inspiration and patience.

2

The Asian monsoon: Global perspectives

Kevin E. Trenberth, James W. Hurrell, and David P. Stepaniak

2.1 THE GLOBAL SETTING

The term 'monsoon' stems from seasonal variations in winds but it is now more generally applied to tropical and subtropical seasonal reversals in both the atmospheric circulation and associated precipitation. These changes arise from reversals in heating and temperature gradients between continental regions and the adjacent oceans with the progression of the seasons, and the extremes are often best characterized as 'wet' and 'dry' seasons rather than summer and winter. Moreover, in spite of the absence of seasonal migration of the intertropical convergence zones (ITCZs) over most of the Pacific and Atlantic Oceans between the hemispheres, it is evident that there is a global monsoon, by which we mean a global-scale persistent overturning of the atmosphere throughout the tropics and subtropics that varies with time of year (Trenberth *et al.*, 2000). The reason why the global monsoon should be emphasized is because of the coordination among regional monsoons brought about by the annual cycle of the solar heating and the apparent connections in the global divergent circulation necessitated by mass conservation. The dominant monsoon systems in the world are the Asian–Australian, African, and the American monsoons, although the latter has not been clearly identified with wind reversals (Webster *et al.*, 1998). In these sectors, the wet zone migrates from one hemisphere to the other following the sun, and the large-scale overturning atmospheric circulation reverses.

The picture of a monsoon overturning circulation is something like a thermally driven sea breeze on a larger scale, and therefore modified by the Earth's rotation, is however, highly idealized. Moreover, often only the cross-equatorial overturning comprising the local Hadley circulation has been emphasized: it is referred to as the 'lateral monsoon' in Webster *et al.* (1998). Strong rising motions in the summer hemisphere at $\sim 10^{\circ}$ latitude are, to some extent, compensated by subsidence at $\sim 20^{\circ}$ latitude in the winter hemisphere. However, in the tropics, a large component of the

B. Wang (ed.), *The Asian Monsoon*.

overturning is not meridional but is zonally oriented and is referred to as the 'Walker circulation' or the 'transverse monsoon' for overturning toward the west (Webster *et al.*, 1998). Over some parts of the tropics, including the tropical central and eastern Atlantic and Pacific Oceans, the ITCZ resides between ~5 and 10°N year round. However, it does not follow that the downward branch is similarly anchored.

The 3D character of the atmospheric circulation is dominated by the rotational (non-divergent) component, which is strongly influenced by the divergent circulation that is more physically linked to the diabatic processes that force the overall circulation. Hence, in association with the monsoon rains, an upper level anticyclone accompanies a continental heat low-pressure region at low levels while the reverse pattern is often seen over adjacent oceans. Large momentum transports occur in the meridional circulation and strongly influence the subtropical jet streams. The strongest jet of over $70\,m\,s^{-1}$ lies off the east coast of Asia in boreal winter, while off the east coast of Australia in austral winter the strongest jet is more than $50\,m\,s^{-1}$. Both are directly associated with the regions of the globe where and when the strongest overturning occurs in lower latitudes.

The existence of the direct overturning circulation implies that heat is being transported to cooler regions. Energy is generated from sources of heating in the atmosphere and, overall, there has to be transport by the atmosphere and ocean from source to sink. Heating occurs in the tropics, where it is already hot, and cooling occurs at higher latitudes. Atmospheric energy is gained in the tropics and lost at higher latitudes (Webster, 1994; Trenberth and Stepaniak, 2003a). A small amount is converted to kinetic energy and regained as friction heating. On the whole, air parcels moving polewards must have a higher moist static energy than air parcels moving equatorward. In middle latitudes the poleward heat transport is carried out by transient baroclinic eddies and stationary waves, while in the tropics the transport is dominated by large-scale overturning (Trenberth and Solomon, 1994; Trenberth and Stepaniak, 2003a). Thus the Hadley and Walker cells are thermally driven cells that transport moist static energy (Trenberth and Stepaniak, 2003b). The dominant energy outflow center, coinciding closely with the region of highest sea surface temperature (SST) in the oceans, migrates back and forth across the equator following the sun.

Another key issue is the extent to which one should think of the global monsoon as a steady circulation (Ramage, 1971), albeit made up of local small-scale disturbances (Fein and Stephens, 1987). Thus, there are active and break periods in regional monsoons, and many identified subseasonal variations, as well as pronounced interannual variability (e.g., Webster *et al.*, 1998).

Accordingly, in this chapter we set the stage for regional aspects by documenting the global scales of the atmospheric monsoon circulation, and its links to the surface, with an emphasis on the annual cycle. A series of fields is produced that relate to the development of the global monsoon circulation for the two solstitial seasons of June–July–August (JJA) and December–January–February (DJF) and their differences, although we note the astronomical definition of the seasons is more appropriate over the oceans (Trenberth, 1983). The seasonal differences highlight the seasonally varying components and they directly relate to the monsoons.

2.2 DATA

We use the Climate Prediction Center (CPC) Merged Analysis of Precipitation (CMAP) estimates from Xie and Arkin (1997), the optimal interpolation (OI) SST analysis of Reynolds *et al.* (2002), and surface air temperatures from Jones *et al.* (1999). At the top-of-atmosphere (TOA), we use the Earth Radiation Budget Experiment (ERBE) measurements of radiation for the period February 1985 to April 1989 (Trenberth, 1997; Trenberth and Stepaniak, 2003b). In the free atmosphere results are obtained using the National Centers for Environmental Prediction/National Center for Atmospheric Research (NCEP/NCAR) reanalyses (Kalnay *et al.*, 1996).

A comprehensive description of the divergent circulation of the atmosphere has been elusive owing to the difficulty of obtaining reliable fields. Errors in observations are often of the same order as the expected divergent component itself and huge observational gaps exist over the oceans. Accordingly, the only viable approach is via 4-D data assimilation (4DDA). Recent results (Trenberth *et al.*, 2000) from the two major reanalyses (NCEP/NCAR and European Centre for Medium-Range Weather Forecasts (ECMWF) (Gibson *et al.*, 1997)) agree reasonably well and therefore provide a new level of confidence. The NCEP/NCAR results from 1979 to 2001 have also been used to determine the diabatic heating and relationships to energy transports for the mean annual cycle and the interannual variability (Trenberth and Stepaniak, 2003a,b).

The series of plots that follow focus on the domain to 60° latitude in order to allow contours to be selected that reveal the character of the fields (which often are otherwise dominated by large values in polar regions).

2.3 THE MEAN SEASONAL MONSOON-RELATED VARIATIONS

2.3.1 Basic climate variables

SST is a fundamental coupled variable in climate. It results from both the external forcing of the planet governed by the orbit of the Earth around the sun and the resulting radiant fluxes, and through adjustments of the ocean surface to wind fields, surface fluxes and ocean dynamics. However, from an atmospheric viewpoint, it is often convenient and useful to think of SST as the lower boundary forcing of the atmosphere above the oceans. The seasonal mean SST fields for JJA and DJF, as well as their difference, are given in Figure 2.1 (color section). Warmest waters, exceeding 29°C, reside in the western tropical Pacific (the 'Warm Pool') and migrate back and forth across the equator with the seasons. Seasonal changes of 2 to 3°C occur in mid-latitudes but the greatest gradients of change occur within the tropics – the latter tend to become reflected in low-level atmospheric temperatures and thus sea level pressure gradients and surface winds. Nevertheless, these effects are fairly modest and tend to be overwhelmed by the rotational component of the flow.

The annual range of SST and surface air temperature (Figure 2.2, color section), measured by JJA minus DJF, highlights land–sea contrasts and relatively small annual changes over the oceans. These features reflect the very different heat capacities of ocean vs. land and the depth of the layer linked to the surface. The largest ranges occur over the continents, and except for the subtropical continents of the southern hemisphere (SH), values are smaller in the SH than in the northern hemisphere (NH) at corresponding latitudes. The largest annual ranges exceed 30°C over northern continents. The net result is that the large land masses are at least as warm as the warmest parts of the oceans in summer, but much colder in winter. The gradients between land and ocean are most pronounced in winter because radiative losses over land lead to dense air and high surface pressures that make for a stable atmosphere. In contrast, in summertime, hot land conditions lead to sea breeze effects which bring in low-level moisture and summertime rains: the monsoons, that naturally act to cool the surface. Hence the temperatures over land in summer are partly a consequence of the monsoons and not just a forcing. Of course the atmospheric circulation also plays a significant role in wintertime in moderating radiative effects.

Sea level pressure fields (Figure 2.3, color section) reflect many aspects of these changes. The main features are the subtropical anticyclones that are strongest in the winter hemisphere and extend to higher latitudes in the northern winter, most notably in the Siberian High where values exceed 1035 hPa. However, the oceanic anticyclones in northern summer over the Pacific and Atlantic are also strong persistent features directly linked to regional monsoon circulations (Hoskins, 1996; Chen *et al.*, 2001; Rodwell and Hoskins, 1996, 2001). Tropical continents are regions of low pressure, often as part of the monsoon trough. Low pressures extend over the oceans, especially in the near equatorial trough and Warm Pool region, and vary over the latter region following the SST changes. The Icelandic Low in the North Atlantic and Aleutian Low in the North Pacific are strongly evident in winter and highlight the relative warmth of the northern oceans compared with the neighboring continents. The circumpolar trough around Antarctica is a related feature but is present year round owing to the cold high Antarctic continent centered near the pole. The differences in sea level pressure between the two seasons map the land–sea contrast in the NH and temperature gradients between hemispheres well. More subtle effects arise from the tendency for the subtropical highs over the SH to shift polewards and weaken slightly in summer, away from the subtropical continents.

Average precipitation amounts (Figure 2.4, color section) better define the divergent part of the atmospheric circulation and key aspects of the monsoons. Note that plotting the JJA–DJF differences in mm day^{-1}, rather than as a percentage, emphasizes the tropical regions. The ITCZs in the near-equatorial trough stand out, as does the South Pacific convergence zone (SPCZ) with its south-eastward extension toward higher latitudes, especially in southern summer. Its extension often has frontal characteristics and has been referred to as a 'graveyard' for fronts (Trenberth, 1976). Similarly the ITCZ, located about 5–10°N over the Pacific and Atlantic oceans during the solstitial seasons, is strongest in boreal

summer. Clearly evident in the precipitation fields is the monsoonal rains over southern Asia, central Africa, and central and South America, the latter also involving the South Atlantic convergence zone (SACZ). Although the seasonal change is most striking over the land areas, it is also quite large over the oceans. The large-scale pattern of change is one of enhanced rains from 5–15°N, extending to about 35°N over Asia in northern summer and similarly over about 5°N to 30°S in the SH summer. In JJA–DJF differences, the dipole structures highlight the monsoon rains and movement of the primary zones from one hemisphere to the other.

2.3.2 The atmospheric circulations

The general circulation in the atmosphere is illustrated by flows in the lower troposphere at 850 hPa and in the upper troposphere at 200 hPa. The total vector winds for JJA, DJF, and their differences (Figures 2.5 and 2.6) are superposed on contours of geopotential height at these two levels. The lower tropospheric geopotential height resembles the sea level pressure field. The equatorial trough in DJF, the major monsoon trough over Asia in JJA, the subtropical anticyclones with strong south-east and north-east trade winds, and the higher latitude westerlies are all notable features. At 200 hPa the strong westerlies in both hemispheres dominate along with embedded subtropical jet streams that are strongest over east Asia in DJF and east Australia in JJA. At both tropospheric levels, the dominant flow is the rotational component that is largely related to the monsoon circulation. For instance, strong meridional equatorward flow on the eastern side of the subtropical anticyclones is associated with large-scale subsidence in accord with an approximate Sverdrup balance whereby $\beta v = f\partial\omega/\partial p$; where f is the Coriolis parameter, β is its meridional gradient, v is the meridional velocity, and ω is the vertical p-velocity whose vertical derivative is related to the divergence (Rodwell and Hoskins, 2001). Such a relationship, incidentally, also means that the maximum divergence is not in the center of the anticyclonic circulation. Seager *et al.* (2003) suggest that interactions of this flow at the surface with SSTs and ocean dynamics also play a role in strengthening the features of subtropical anticyclones.

Of more interest with respect to monsoons is the divergent part of the flow itself, shown with the velocity potential (Figures 2.7 and 2.8) as a very smoothed depiction of the global-scale divergence field. As low-level convergence at 850 hPa is generally manifested as upper level divergence at 200 hPa, these fields strongly indicate the large-scale monsoonal overturning circulations. The JJA–DJF differences are especially relevant for revealing the seasonally varying flow, with the enormous Asian–Australian monsoon linked to that in Africa, and the somewhat separate North and South American monsoons. However, closer examination also indicates that the upper tropospheric divergence at 200 hPa is not an exact match for the convergence at 850 hPa. Over Africa, for instance, shallower overturning is often present in the monsoon (Trenberth *et al.*, 2000) and an alternative analysis is desirable to examine the vertical structure of the overturning.

However, we first present the corresponding vertical motion fields at 500 hPa

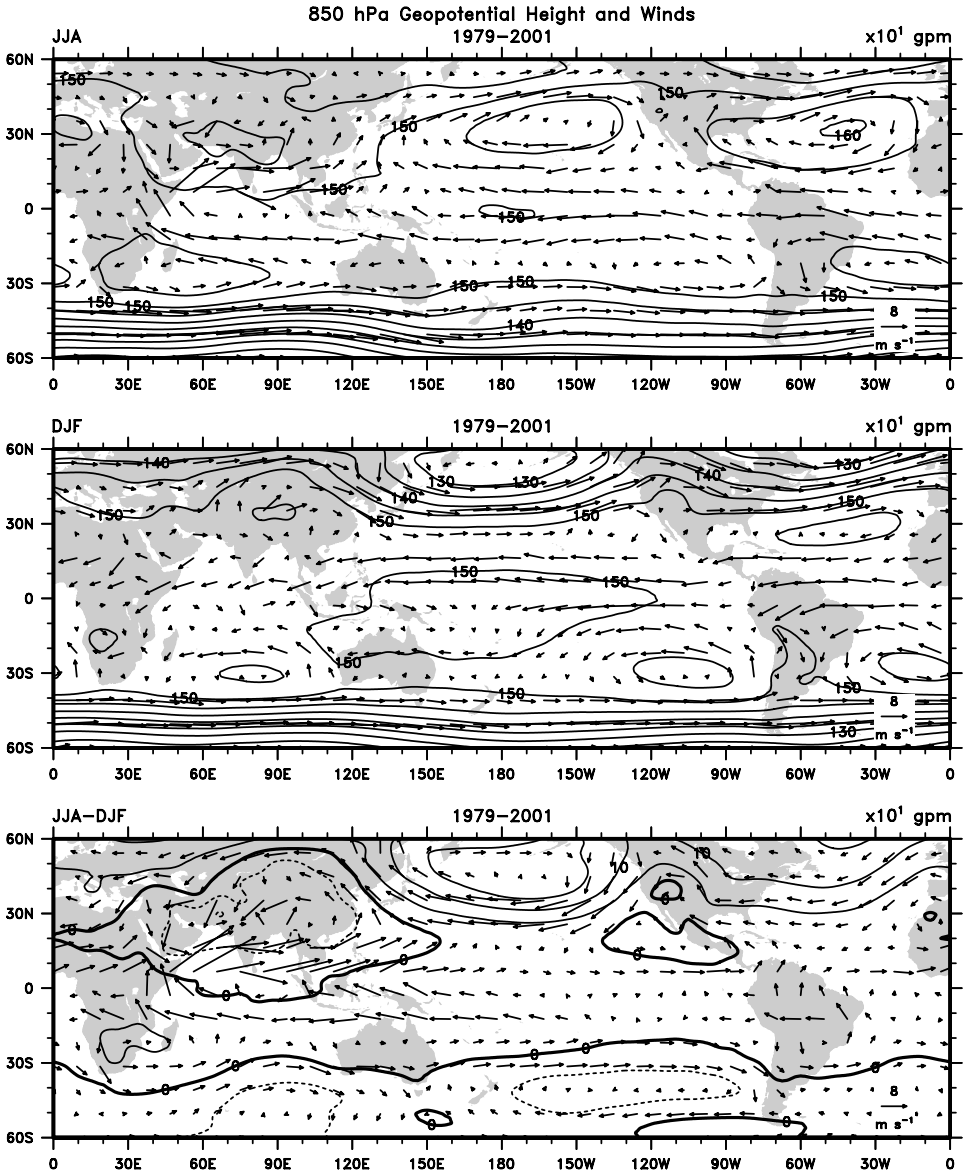

Figure 2.5. Geopotential height and vector winds at 850 hPa for 1979–2001 averaged for JJA (*top*), DJF (*middle*), and their difference JJA – DJF (*bottom*). The contour interval is 5 dam and the key vector wind is plotted at the lower right corresponding to $8\,\mathrm{m\,s^{-1}}$.

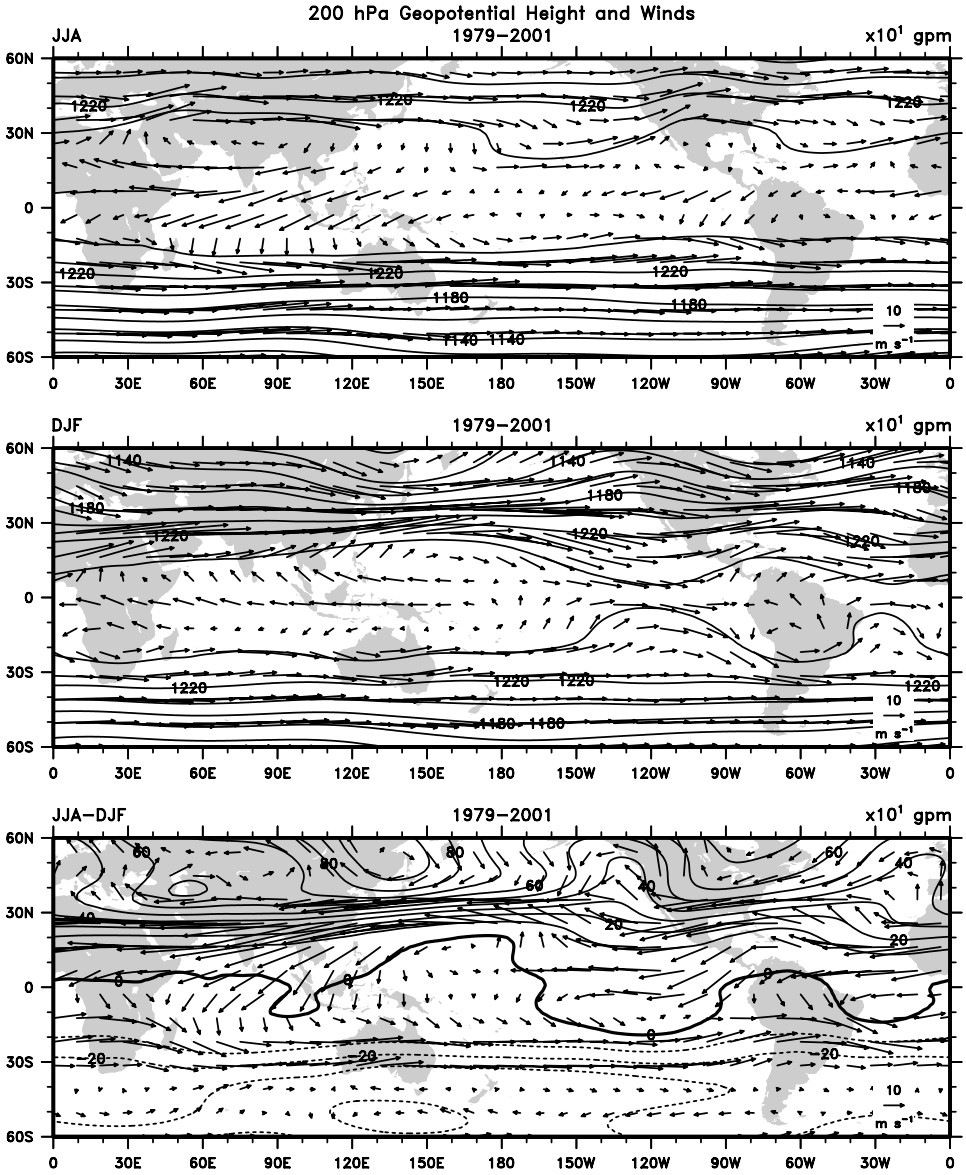

Figure 2.6. Geopotential height and vector winds at 200 hPa for 1979–2001 averaged for JJA (*top*), DJF (*middle*), and their difference JJA – DJF (*bottom*). The contour interval is 20 dam and the key vector wind is plotted at the lower right corresponding to $10\,\mathrm{m\,s^{-1}}$.

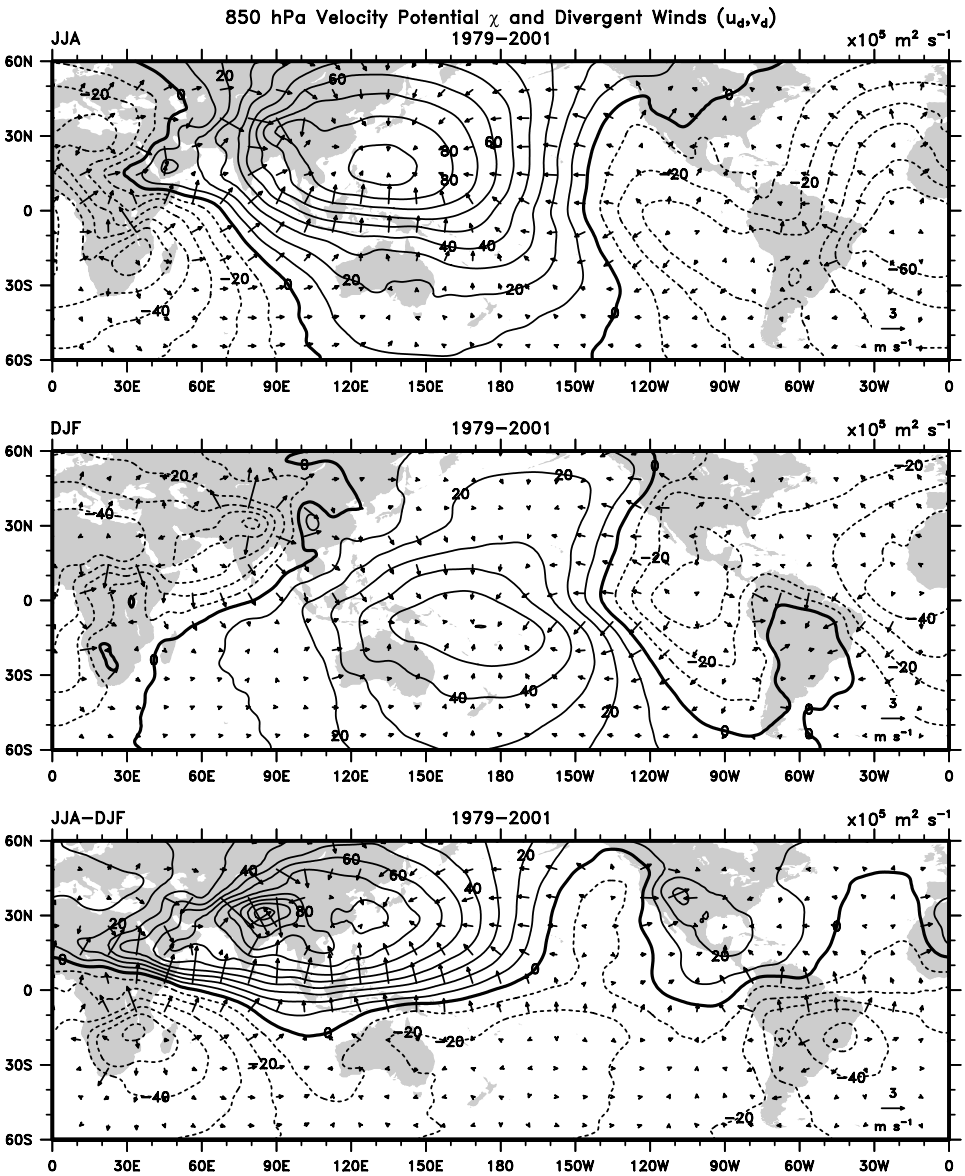

Figure 2.7. Velocity potential and divergent component of vector winds at 850 hPa for 1979–2001 averaged for JJA (*top*), DJF (*middle*), and their difference JJA – DJF (*bottom*). The contour interval is $10^6\,m^2s^{-1}$ and the key vector wind is plotted at the lower right corresponding to $3\,m\,s^{-1}$.

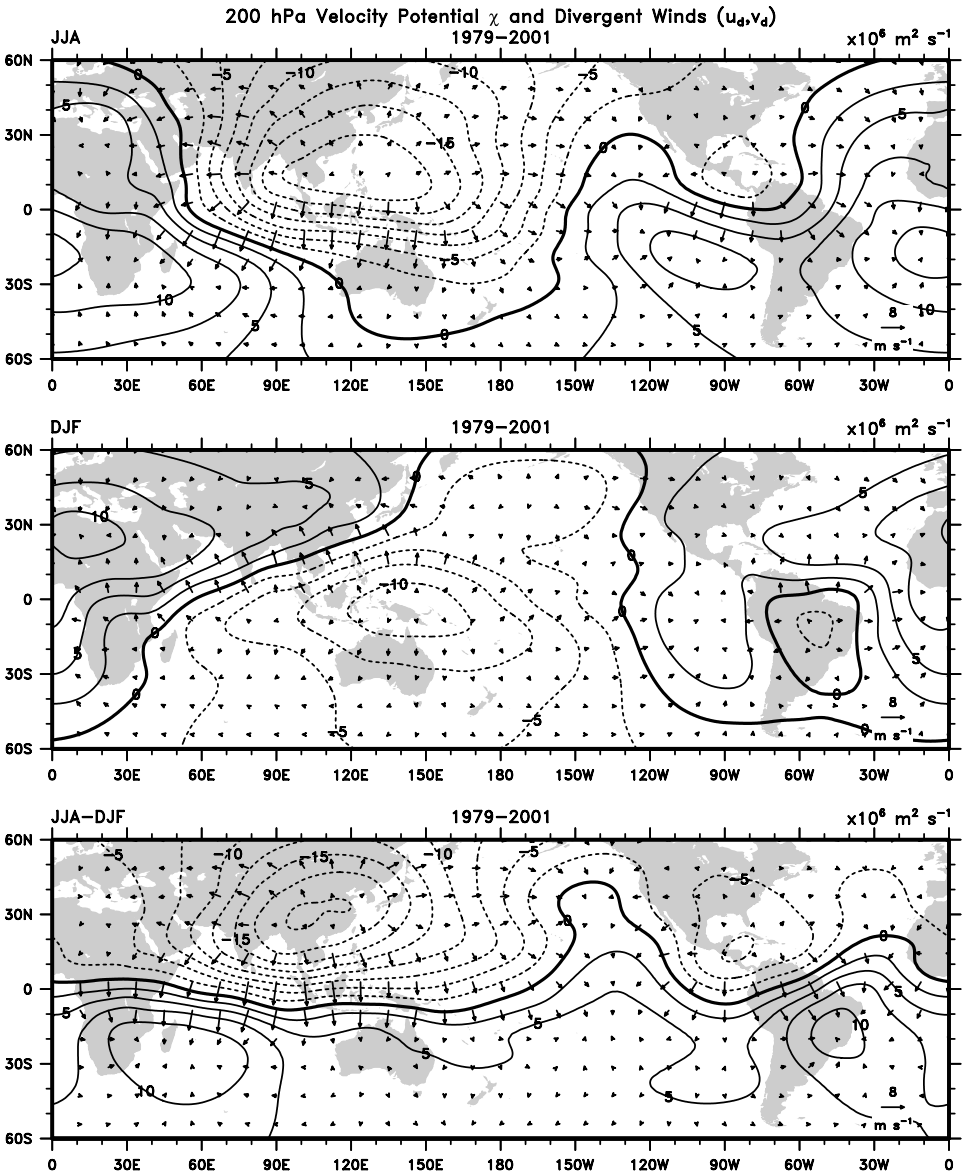

Figure 2.8. Velocity potential and divergent component of vector winds at 200 hPa for 1979–2001 averaged for JJA (*top*), DJF (*middle*), and their difference JJA – DJF (*bottom*). The contour interval is $2.5 \times 10^6\ \mathrm{m^2\ s^{-1}}$ and the key vector wind is plotted at the lower right corresponding to $8\ \mathrm{m\ s^{-1}}$.

(Figure 2.9, color section). This field is derived from the reanalyses and, while independent of the precipitation field, is strongly dependent on the assimilating model. Nevertheless, there is a marked correspondence between Figures 2.9 and 2.4 throughout the tropics and subtropics, indicating the predominance of the precipitation occurring in association with the mean flow rather than high-frequency transients. Accordingly, the monsoon rains are associated with zones of upward motion that switch from south of the equator over Africa, Australia, and South America in DJF to north of the equator over Africa, Asia, and central America in JJA. The JJA–DJF differences (Figures 2.9 and 2.4) also agree well with each other except that the central Pacific ITCZ may be weak in the NCEP reanalyses ω field and the SPCZ a bit too zonal. In other words, some of the differences may not be real. Nevertheless, these two fields do measure very different things as precipitation occurs only in upward motion, and therefore transients can lead to precipitation even if the time-mean flow is for downward motion.

To explore the global monsoon and its vertical structure in more detail, Trenberth *et al.* (2000) performed a complex empirical orthogonal function (CEOF) analysis of the mass-weighted divergent circulation that brings out two dominant modes with essentially the same vertical structures in all months of the year. The vertical structure of the first mode (Figure 2.10) is plotted as vectors, with the arrows free to rotate through 360°. All vectors tend to point either to the left or right indicating either in-phase or out-of-phase relations, respectively. The vectors are so arranged that they can be directly interpreted as showing the large-scale overturning in the upper and lower branches of, for instance, the Hadley circulation. For CEOF1 (Figure 2.10), the vertical structure is simple with a maximum in vertical motion at about 400 hPa, divergence in the upper troposphere that peaks near 150 hPa and decays to zero amplitude above 70 hPa, and convergence in the lower troposphere with a maximum at 850 hPa (NCEP) or 925 hPa (ECMWF; not shown). Spatially, this mode has a rich 3-D structure that evolves with the seasons (Figure 2.10). It accounts for 60% of the annual cycle variance of the divergent mass circulation and includes the Hadley circulation as well as three overturning transverse cells. These include the Pacific Walker circulation, an Americas–Atlantic Walker circulation, both of which comprise rising motion in the west and sinking in the east, and a transverse cell over Asia, the Middle East, north Africa, and the Indian Ocean that has rising motion in the east and sinking toward the west. These exist year round but migrate and evolve considerably with the seasons and have about a third to half of the mass flux of the peak Hadley cell. The annual cycle of the two Hadley cells reveals peak strength in early February and early August in both reanalyses (Trenberth *et al.*, 2000).

In DJF (Figure 2.10) the large-scale, low-level convergence and associated upper level divergence in CEOF1 is most apparent north and east of Australia near 10°S, and the SPCZ is clearly a part of this pattern. In the Indian Ocean the ITCZ is also evident near 10–15°S. Similarly, strong low-level convergence occurs over the Amazon while subsidence over the tropical eastern Pacific is present as the downward branch of the Walker circulation. The latter is slightly stronger relative to the Hadley circulation in the NCEP reanalyses (Trenberth *et al.*, 2000). A

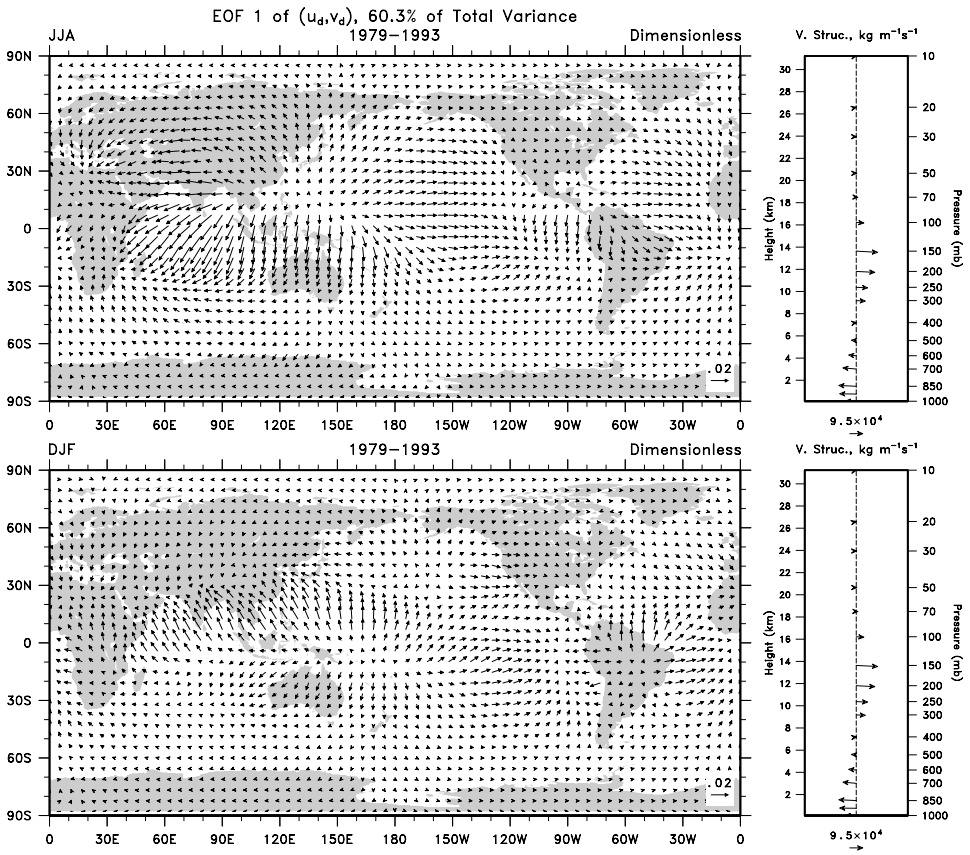

Figure 2.10. Spatial patterns of CEOF1, in which all four seasons were combined, for the divergent velocity from NCEP reanalyses for JJA (*top*) and DJF (*bottom*) corresponding to the vertical structure function of the mass weighted divergent velocity field at the right for 1979–1993 (from Trenberth *et al.* 2000). The scale vector is given below. The vertical structure vectors are referenced to that at 1,000 hPa, which is directed along the x axis; they are free to rotate through 360° but tend to be aligned, the scale factor is given below and the units are $\mathrm{kg\,m^{-1}\,s^{-1}}$. The vertical scale is in hPa with an approximate height scale given.

distinctive line of convergence in the upper troposphere occurs from 90°E to 170°W along about 30–35°N, penetrating farthest north near Japan, which bears a striking resemblance to the position of the core of the subtropical jet stream where it exceeds $50\,\mathrm{m\,s^{-1}}$ in January. A primary forcing of the rotational zonal wind component comes from the term fv_d, where v_d is the divergent meridional wind component. Since the Coriolis parameter increases with latitude, this term reaches a maximum just short of the convergence line.

The corresponding vertical motion fields (not shown) are fairly similar to those in Figure 2.9 and reveal that the pronounced subsidence in the South Pacific high is

present all year, while the subtropical high in the North Pacific is much stronger in summer. The migration across the equator of the upward motions is evident in Africa and from the Amazon region to the Mexican highlands.

While some low-level convergence is apparent in CEOF1 in the southern tropics over Africa, the main features over Africa and Australia are accounted for by the second mode (not shown), which involves relatively shallow but vigorous overturning with the maximum vertical velocities near 800 hPa, outflow from 750 to 350 hPa, and inflow peaking at 925 hPa (Trenberth *et al.*, 2000). It is especially strong over Africa, influences the Middle East, has a signature over Australia, and also is an important component of the overturning in the tropical eastern Pacific and Atlantic, and thus of the convergence zones in these regions.

2.4 DIABATIC PROCESSES: HEAT SOURCES AND SINKS

The fundamental forcing of the atmospheric circulation and climate ultimately relates to the radiation budget of the planet. To further set the stage for understanding the seasonal monsoon variations we therefore examine the diabatic forcings of the atmospheric circulation. A more complete treatment is in Trenberth and Stepaniak (2004).

The absorbed solar radiation (ASR), outgoing longwave radiation (OLR), and the net radiation are given in Figures 2.11, 2.12, and 2.13 (color section for all) for JJA, DJF, and their difference. The dominant annual cycle forcing is the change in distribution of incoming solar radiation due to the orbit of the Earth around the sun. There are important effects from albedo and clouds, but they are secondary and the pattern of ASR has a strong zonal component that is dominated by orbital effects. Figure 2.11 serves as an important reminder of just how large the seasonal variation is because JJA vs. DJF differences exceed 200 $W\,m^{-2}$. It is interesting that the zero line is not on the equator but instead lies between 0 and 10°N for the most part. There is an important cloud signature in Figure 2.11 although somewhat lost in the contours.

On the other hand, OLR (Figure 2.12, color section) is more uniform with latitude and season, and is well established to vary primarily with deep convection, owing to the high cold cloud tops. The signatures of the ITCZ, SPCZ, SACZ, and monsoon-related clouds are clear. Also, in the tropics, there is a very strong relation between the JJA–DJF differences in OLR and the patterns of change of precipitation (Figure 2.4, color section) and vertical motion (Figure 2.9, color section). In the extratropics, however, the OLR signature is much more strongly related to temperature (Figure 2.2, color section).

The cloud signature in ASR is well matched by that in the OLR signal and when the net radiation (Figure 2.13) is considered there is remarkable but well-known cancellation (Hartmann *et al.*, 2001). The net radiation seasonally is dominated by the ASR changes. Once again the zero line in the net radiation lies just north of the equator. It is this pattern of net radiation that ultimately directly drives the monsoons and their seasonal reversals.

Over land, the thermal inertia is quite small, and thus there is a tendency for land temperatures to respond to the radiative imbalance. However, over the oceans, surface heating in summer warms the upper ocean, which becomes strongly stratified (as warm water is less dense) even though some heat is mixed to lower layers by wind. In winter, surface cooling results in denser surface waters which are apt to sink, triggering convection, and bringing warmer waters to the surface from below. Surface cooling is however greatest from cold dry continental air outbreaks over western oceans where boundary currents such as the Gulf Stream lie, and turbulent surface fluxes can exceed $1{,}000\,\mathrm{W\,m^{-2}}$ for short periods of time (e.g., Neiman and Shapiro, 1993) and over $300\,\mathrm{W\,m^{-2}}$ over monthly and seasonal averages. Seasonal heat uptake by the oceans can exceed $100\,\mathrm{W\,m^{-2}}$ in the subtropics in summer which is then released to the atmosphere in winter (e.g., Trenberth and Stepaniak, 2003b, 2004), strongly mitigating the season cycle of solar radiation.

Estimates of vertically integrated diabatic heating in the atmosphere $(Q_1 - Q_f)$ are based on atmospheric heat budgets using NCEP reanalyses, computed as a residual (Trenberth and Stepaniak, 2003a,b). Note that Q_1 includes the small frictional heating (Q_f) so that their difference is the diabatic heating in the atmosphere, presented in $\mathrm{W\,m^{-2}}$ (Figure 2.14, color section). The reader will immediately recognize the strong resemblance with Figures 2.4 and 2.9 (color section). Therefore, it is also desirable to present the vertically integrated latent heating component $Q_2 = L(P - E)$, where L is the latent heat of condensation, P is precipitation rate, and E is evaporation rate. Q_2 is shown in Figure 2.15 (color section) along with the corresponding vertically integrated divergent component of the total flux of water vapor transport (Trenberth and Stepaniak, 2003a,b). The difference between these two quantities, $Q_1 - Q_f - Q_2$, is directly related to the divergence of the total atmospheric energy transports (Figure 2.16, color section) on an annual basis when changes in storage of energy in the atmosphere can be ignored. Moreover, for long-term annual means the difference between this and the net radiation (Figure 2.13, color section) should be close to zero over land and correspond to divergence of ocean heat transports over the oceans. The implied ocean heat transports have been verified by comparisons with direct measurements in ocean sections by Trenberth and Caron (2001) and have an advantage of providing a global picture.

These figures reveal that the dominant diabatic heating in the tropics comes from latent heating associated with precipitation. The heating is associated with regions of upward motion and the low-level convergence of moisture by the atmospheric circulation (Figure 2.7, and see Figure 2.15, color section) itself.

The atmospheric circulation naturally responds to these diabatic forcings and, at the same time, transports heat, energy, and moisture. The low-frequency part of the flow plays a dominant role throughout the tropics and can be depicted by monthly means, while transients, depicted by within-month variations, are prominent in the extratropics. The total energy divergence and the divergent component of the transports are given in Trenberth and Stepaniak (2004) and in Figure 2.16 (color section) for the quasistationary and transient components. The former dominates in the tropics and is more directly associated with the monsoons and the Hadley and

Walker circulations. But note how the pattern of diabatic heating associated with latent heating has largely disappeared to be replaced by moisture sources. In this depiction, the energy transport by the overturning circulations is fairly modest. In the Asian summer monsoon (top panels), the divergence of energy from the upward branch is transported mostly to 30°S in the Indian Ocean where it is further transported polewards by the transient eddies. In the Pacific and Atlantic the overturning transports energy northwards to about 30°N, where it is transported farther north in the ocean storm tracks. In these areas, there is also a component transported into the SH.

In DJF and in the interseasonal differences (JJA–DJF), the strong NH stationary waves dominate although the storm tracks over the ocean also play a major role. The difference also reveals the huge switch over the northern oceans from being a source of heat in winter to a sink in summer while the land acts in reverse.

From these figures it is clear that, from an energy budget standpoint, latent heating drives the upward branch of the monsoonal overturning circulation. There is a strong balance between adiabatic cooling associated with rising air and latent heating. However, the latent heating is also a response to the circulation itself and not a fundamental cause. The original source of the latent heating is the moisture convergence and thus ultimately evaporation from the surface, primarily over the oceans. Hence the latent heating is linked to the absorbed solar radiation. However, the latter is taken up and stored within the ocean so that maximum SSTs tend to occur at the end of the summer season in the extratropics. Moreover, some aspects of the evaporation of moisture into the atmosphere are linked to its transport and convergence into precipitation zones associated either with the ITCZ, SPCZ, SACZ, or monsoon rains. This is because the evaporation itself is also partly a result of the circulation and the turbulent fluxes into the atmosphere. In order for all this to take place, there has to be an overturning circulation in the atmosphere.

The overturning circulation in the atmosphere in low latitudes, where the Earth's rotational effects are weak, is the main way the tropical atmosphere can move energy around (in contrast to baroclinic processes at higher latitudes). Therefore, there also has to be a heat sink (cooling) in the downward branch of the circulation to balance the warming by subsidence. Conventional wisdom suggests that this cooling, usually in the subtropics, is primarily associated with OLR emitted to space. This is partly the case, but once again, the relatively clear skies are a consequence of the circulation and thus are a feedback and not a fundamental cause. Instead, on monthly and longer timescales the atmospheric energy transports are continuous between the tropics and extratropics in spite of the very different mechanisms for distributing energy, namely the overturning Hadley-type or monsoonal circulation in the tropics and the baroclinic eddies in mid-latitudes (Trenberth and Stepaniak, 2003a,b). There has to be a very tight link, therefore, between the two. Consequently it has been established that the major part of the cooling in the subtropics over the oceans comes from divergence of energy (cooling) by the baroclinic waves, which in turn are often organized into storm tracks (Figure 2.16, color section). The preferred storm tracks are slightly polewards of the main jet streams, which are a consequence of the convergence of momentum transports by both the overturning and the baroclinic

eddies. Effectively, the baroclinic eddies carry energy to higher latitudes where it is eventually radiated to space as OLR. Consequently the cooling in the downward branch of the overturning circulations is linked to OLR diabatic forcing through radiation to space at all subtropical and extratropical regions.

Normally there are two Hadley cells in the atmosphere. One is in each hemisphere. In the equinoctial seasons, both can be seen with roughly comparable strength (see Trenberth *et al.*, 2000). But in the solstitial seasons, the summer hemisphere Hadley cell is weak and the cell with subsidence into the winter subtropics becomes dominant (Figures 2.5–2.10 (for Figure 2.9, see color section)). At the top-of-atmosphere, the net radiation (Figure 2.13, color section) provides the main reason why this is so and the primary change is in ASR, not OLR. However, both the ASR and the OLR have major contributions at the Earth's surface, and to properly interpret what is happening within the atmosphere, it is necessary to also examine the surface energy budget and the key role of evaporation in providing latent energy which in turn involves the oceans and their uptake and release of stored heat (Trenberth and Stepaniak, 2003a,b, 2004).

2.5 REGIONAL MONSOONS

Six regions, from Trenberth *et al.* (2000), have been selected to illustrate and highlight meridional structures of the overturning monsoonal circulations. Here the ECMWF results are utilized because the extra 775 hPa level proves quite beneficial and the flow at 925 hPa is more distinctive. The sections, progressing eastward, include the following: (i) Africa, 10°E to 40°E, this is the land region at the equator, and so it does not include the South Atlantic; (ii) Australia–Asia, 60°E to 180°, covering the Asian–Australian monsoon; (iii) Pacific, 170°W to 90°W, containing the SPCZ and the ITCZ north of the equator; (iv) North America, 110°W to 80°W, this region is not ideal as the Central American isthmus is narrow and is not oriented strictly north–south; (v) South America, 80°W to 40°W, covering the main southern continent; and (vi) Atlantic, 30°W to 10°E, this region is a compromise as it includes some South American influences in the west.

We present the annual cycles of ω at 500 hPa and January and July cross sections of the divergent meridional circulation component. Note that because these sections are zonally limited, the circulation is not closed, and there is a third zonal dimension that conserves the mass flow. As the focus is on the direct overturning, the domain is limited to $\pm 50^\circ$ latitude.

The ITCZ migrates back and forth across the equator over Africa, as revealed by the ω field (Figure 2.17), although subtropical subsidence is most pronounced in both hemispheres in the austral winter. In addition, the African monsoon is characterized by a complex vertical structure with shallow overturning below 600 hPa. In January, shallow direct cells exist near 15°N and 25°S, and in July the southern cell moves northward and is centered near the equator. Note that the subsidence at 35°N in July is not strongly linked to the ITCZ at 10°N, but comes primarily from the transverse cell.

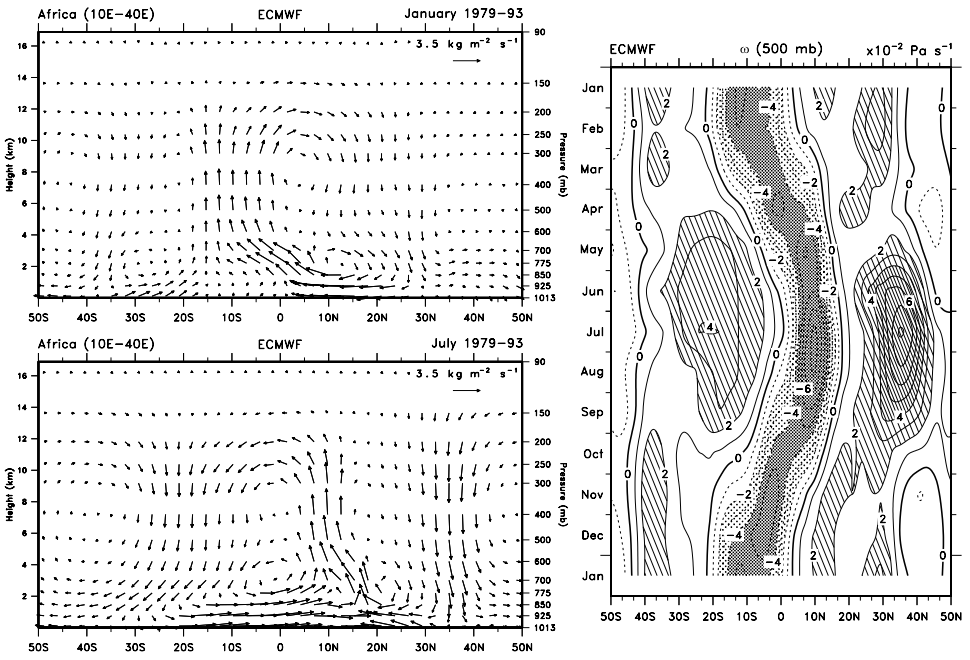

Figure 2.17. *For Africa.* Regional meridional cross sections of the divergent flow as vectors from 50°S to 50°N from ECMWF for January (*top*) and July (*bottom*). The scale vector is shown top right. To the right is shown the annual cycle of ω at 500 hPa from 50°S to 50°N in 10^{-2} Pa s^{-1}. Stippling (negative values) indicates upward motion and hatching subsidence. Adapted from Trenberth *et al.* (2000).

For the Australia–Asia sector (Figure 2.18), the ω annual cycle shows the more intense phases of the monsoons in January and July–August, with an additional upward motion branch near 30°N from April through August that reflects the elevated Tibetan plateau heat source and the Mei Yu and Baiu summer monsoon rainfalls in China and Japan, respectively (e.g., Kang *et al.*, 1999). The corresponding cross section shows the dominant deep tropospheric overturning of the Hadley circulation. For the Pacific sector (Figure 2.19), the ω annual cycle shows the ITCZ near 7°N year round but it appears weak in January when there is cancellation in the west as the SPCZ becomes more active. The latter also prevents a good view of the South Pacific high subsidence except in the northern winter. The cross sections, however, clearly show the complex vertical structure of the deep tropospheric circulation combined with the shallow overturning below 600 hPa in both hemispheres. In January, ω at 500 hPa does not indicate the main activity at all.

The North American sector (Figure 2.20) also strongly shows the shallow cell, especially south of the ITCZ. In fact, in January, there is subsidence everywhere at 500 hPa and upward motion only near 5°N below 600 hPa. In northern summer, the deeper Hadley circulation emerges more clearly although still with a shallow cell embedded.

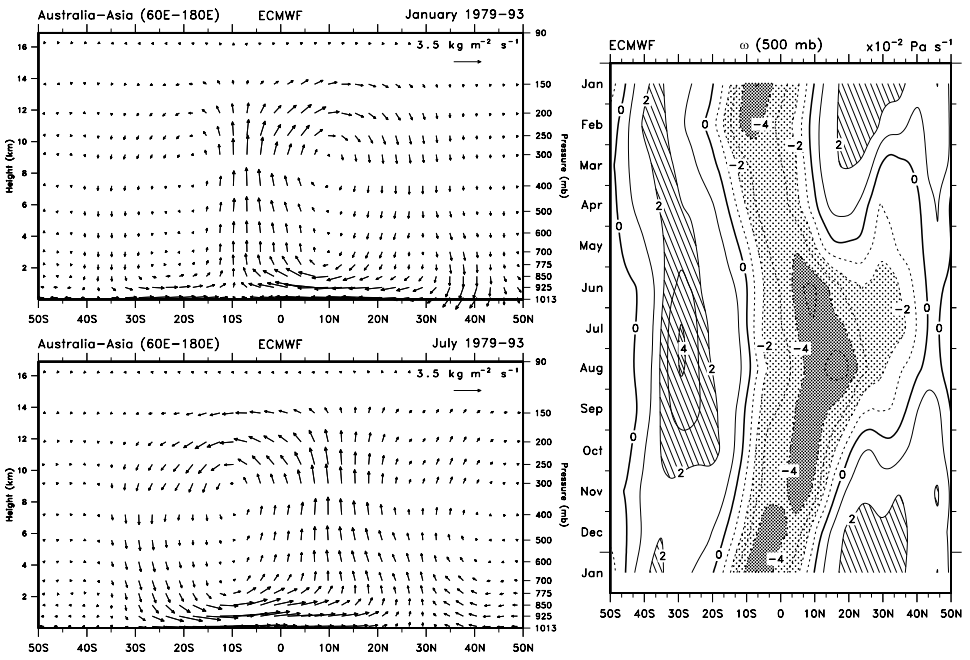

Figure 2.18. *For Australia–Asia.* Regional meridional cross sections of the divergent flow as vectors from 50°S to 50°N from ECMWF for January (*top*) and July (*bottom*). The scale vector is shown top right. To the right is shown the annual cycle of ω at 500 hPa from 50°S to 50°N in 10^{-2} Pa s^{-1}. Stippling (negative values) indicates upward motion and hatching subsidence. Adapted from Trenberth *et al.* (2000).

The South American sector (Figure 2.21) reveals the deep circulation over the Amazon in southern summer but with a large change in character in winter, where shallow overturning cells dominate north and south of the ITCZ. The ITCZ is about 7°N in southern winter and has a double structure in October as it shifts to the SH.

In the Atlantic sector (Figure 2.22), as in the Pacific, the strong ITCZ near 7°N year round is cancelled in the southern summer by migration of activity to the Amazon in the west. Again the cross sections show the importance of the shallow cells throughout the year.

The seasonal reversal in the overturning circulation implicit in the definition of the monsoon is present in Figures 2.17–2.22 in all but the central and eastern Pacific and Atlantic sectors. It is certainly true in the South American sector, where some analyses of the total flow have not noted a seasonal reversal (e.g., see Ramage, 1971; Webster *et al.*, 1998). In the narrow North American sector where the transverse overturning is a non-trivial influence, the picture is not as clear when viewed only from the standpoint of a north–south section. While the eastern ocean areas can be legitimately excluded from being called regional monsoons, they nevertheless participate in the global monsoon through the changes in large-scale overturning.

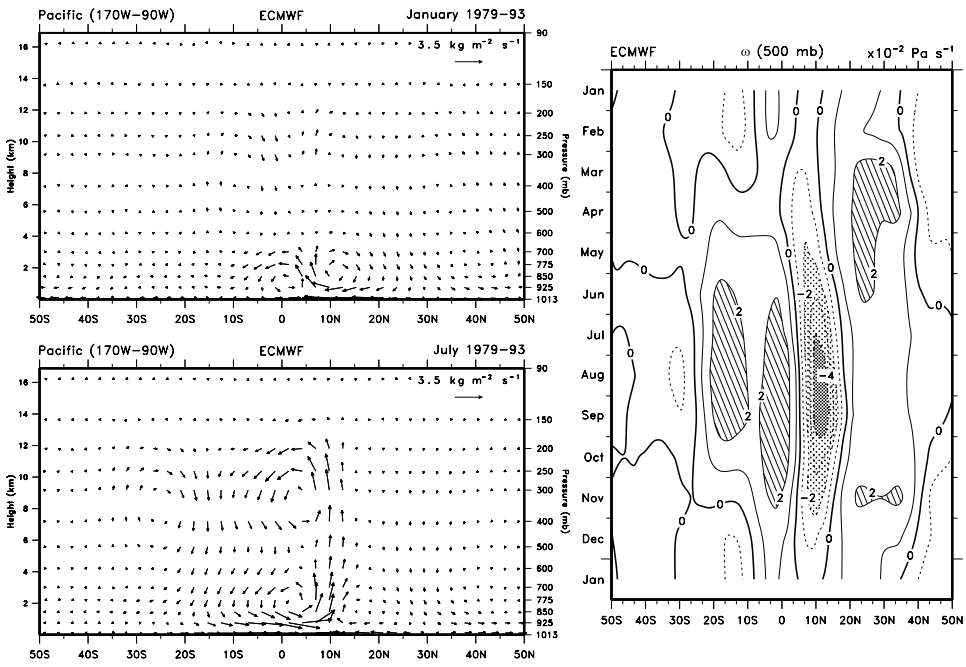

Figure 2.19. *For the Pacific*. Regional meridional cross sections of the divergent flow as vectors from 50°S to 50°N from ECMWF for January (*top*) and July (*bottom*). The scale vector is shown top right. To the right is shown the annual cycle of ω at 500 hPa from 50°S to 50°N in 10^{-2} Pa s^{-1}. Stippling (negative values) indicates upward motion and hatching subsidence. Adapted from Trenberth *et al.* (2000).

2.6 DISCUSSION AND CONCLUSIONS

There have been many and varied definitions of what constitutes a monsoon, but until recently (Trenberth *et al.*, 2000), it has not been possible to obtain a reliable perspective from the standpoint of the large-scale overturning in the atmosphere. Such persistent overturning that varies with the seasons is a key characteristic of the monsoons and has been the focus of this chapter. Nevertheless, there is also a substantial rotational component of the atmospheric circulation associated with monsoons, and this component plays a key role in transporting moisture. The migration of the sun back and forth across the equator is accompanied by the migration of the upward branch of the monsoon overturning circulation wherever continental land influences are present in the tropics and subtropics. The presence of high topography also clearly enriches and enhances the monsoon. The main exceptions are the eastern Pacific and Atlantic Oceans where the ITCZs reside north of the equator year round, although these areas have a secondary role in the global monsoon.

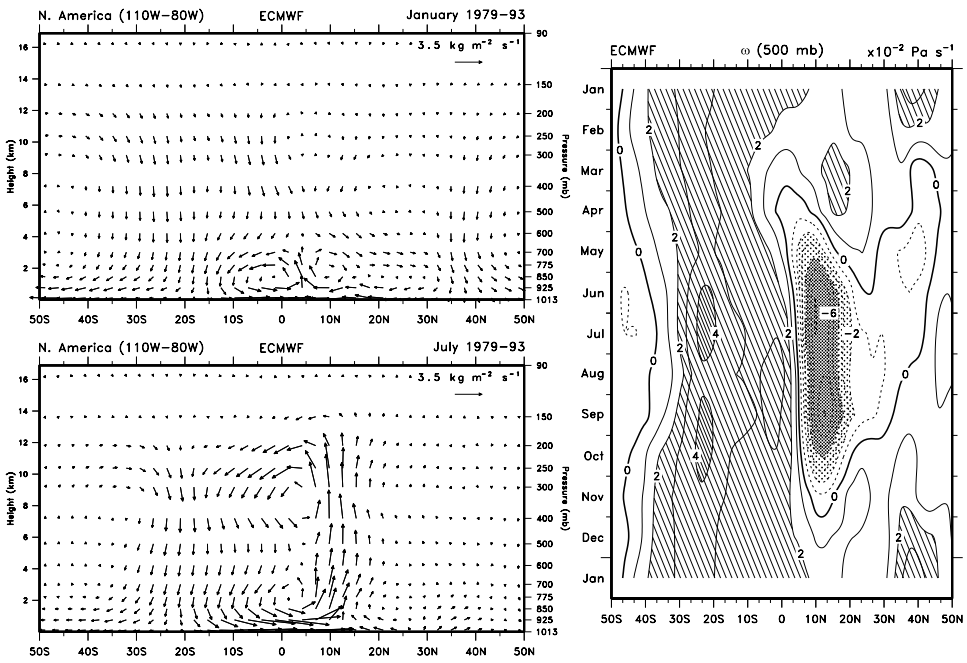

Figure 2.20. *For North America.* Regional meridional cross sections of the divergent flow as vectors from 50°S to 50°N from ECMWF for January (*top*) and July (*bottom*). The scale vector is shown top right. To the right is shown the annual cycle of ω at 500 hPa from 50°S to 50°N in 10^{-2} Pa s^{-1}. Stippling (negative values) indicates upward motion and hatching subsidence. Adapted from Trenberth *et al.* (2000).

The vertical structure of the global monsoon mass circulation remains largely unchanged throughout the year. The predominant deep overturning global mode acts throughout the troposphere and has a simple structure with a maximum in vertical motion at about 400 hPa, divergence in the upper troposphere strongest at 150 hPa and convergence in the lower troposphere. The mode decays to zero amplitude above 70 hPa. The Hadley circulation is part of the deep overturning mode, but so too are three transverse cells: the Pacific and Atlantic Walker cells, and an Asia-Africa transverse cell that overturns toward the west. While it is often useful to break down the global monsoon into these meridional and transverse components, the reality is the rich three-dimensional structure that evolves with the seasons (Figure 2.10). The vertical motion patterns and precipitation in the tropics and subtropics (both wet and dry areas) are largely accounted for by this dominant global monsoon mode.

The existence of the transverse cells has been known, at least schematically, for some time (see Krishnamurti, 1971; Krishnamurti *et al.*, 1973; Fein and Stephens, 1987). The transverse cell that has rising motion in the east and sinking toward the

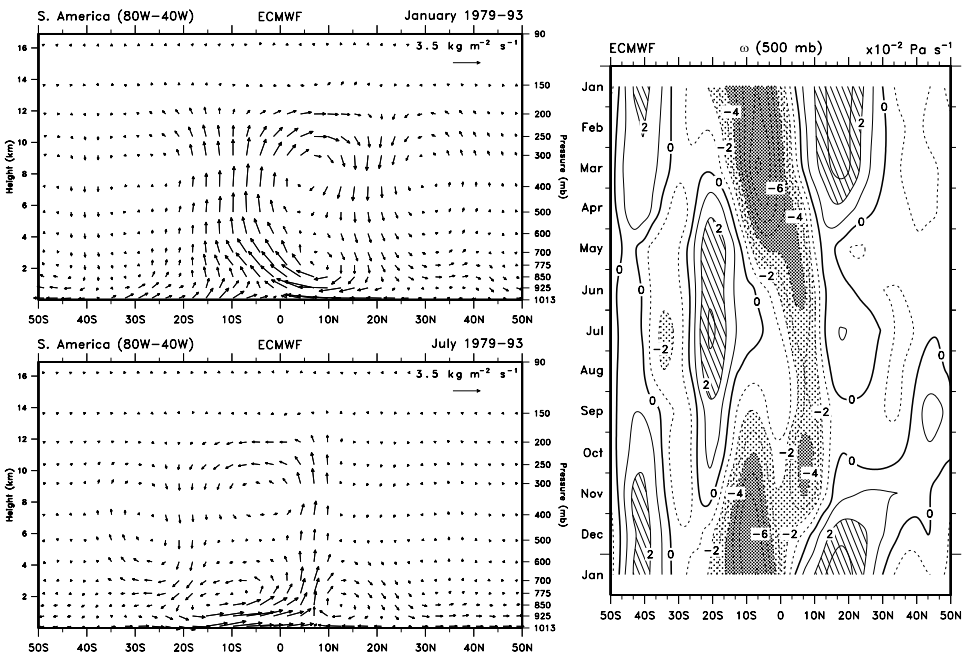

Figure 2.21. *For South America.* Regional meridional cross sections of the divergent flow as vectors from 50°S to 50°N from ECMWF for January (*top*) and July (*bottom*). The scale vector is shown top right. To the right is shown the annual cycle of ω at 500 hPa from 50°S to 50°N in 10^{-2} Pa s^{-1}. Stippling (negative values) indicates upward motion and hatching subsidence. Adapted from Trenberth *et al.* (2000).

west is strongest in January from northern Australia to the southern subtropical high in the Indian Ocean. By July the rising motion is over southeastern Asia with sinking over northern Africa and the Mediterranean, and is thus responsible for the so-called 'Mediterranean climate' of clear skies and sunny days with rains infrequent in summer.

The relationship of the global monsoon to the more regional components was illustrated by the sectoral analyses of the previous section. The meridional cross sections highlight the importance of the shallow overturning cell in low level activity and annual cycle evolution of the monsoons.

Previous definitions of monsoon areas in terms of seasonal reversals in wind and precipitation (e.g., Ramage, 1971) have not included the Americas. Webster *et al.* (1998) included the Americas on the basis of precipitation changes. Yet, from the divergent wind circulation (Figures 2.20 and 2.21), the monsoon regions should include the Americas, although the picture is complicated by the meridional sectors for North and South America being somewhat offset. Nevertheless, there is clearly a monsoonal (direct) overturning that varies seasonally.

This chapter has emphasized the slowly varying circulation and long-term averages. Many analyses have been made of precipitation during the monsoon

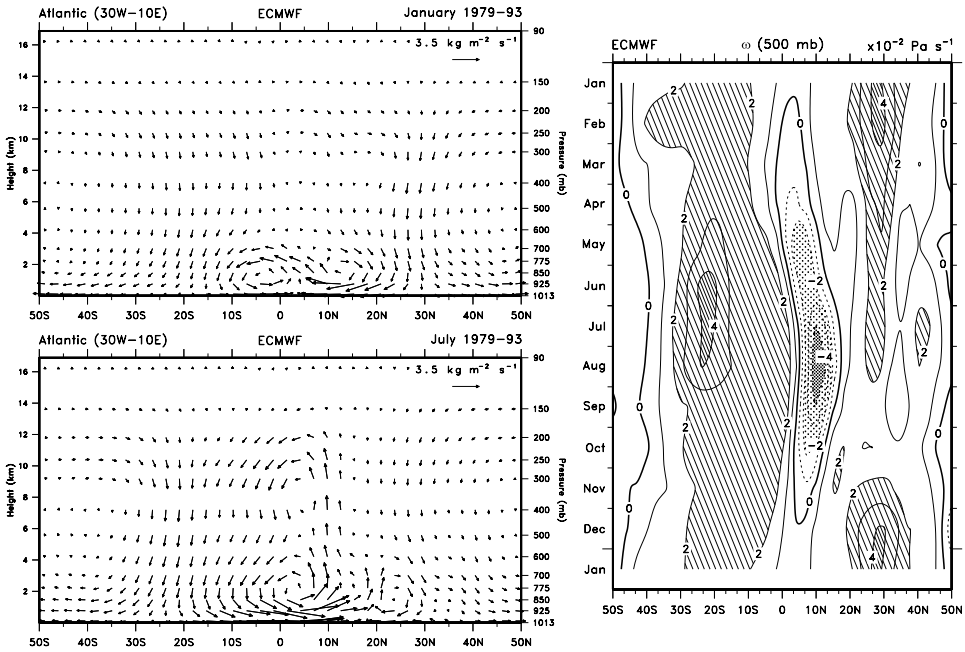

Figure 2.22. *For the Atlantic.* Regional meridional cross sections of the divergent flow as vectors from 50°S to 50°N from ECMWF for January (*top*) and July (*bottom*). The scale vector is shown top right. To the right is shown the annual cycle of ω at 500 hPa from 50°S to 50°N in 10^{-2} Pa s^{-1}. Stippling (negative values) indicates upward motion and hatching subsidence. Adapted from Trenberth *et al.* (2000).

seasons and the active and break phases of the monsoons. An analysis of the steadiness of the monsoonal circulations highlights the important roles of high frequency transients, but it also singles out the monsoon regions as those where the circulation is much more steady than in other regions, such as the extratropics (Trenberth *et al.*, 2000).

Previous analyses of interannual and interdecadal variations (e.g., see Webster *et al.*, 1998) suggest that the global system does not vary coherently, but rather the regional monsoons and ENSO are in competition with one another, although those patterns evolve in time (e.g., Kumar *et al.*, 1999). More vigorous activity in one sector is apt to create subsidence in another and help suppress activity, as the largest scales tend to be emphasized in the tropics (Webster, 1972). This is illustrated most simply by the pattern of the Southern Oscillation, which is the dominant mode of interannual variability overall (Trenberth and Stepaniak, 2003b).

2.7 ACKNOWLEDGEMENTS

This research is partly sponsored by NOAA under grants NA56GP0247 and NA17GP1376 and by a joint NOAA/NASA grant NA87GP0105.

3

The Asian winter monsoon

C.-P. Chang, Zhuo Wang, and Harry Hendon

3.1 INTRODUCTION

During most of the twentieth century the terms Asian monsoon and Indian monsoon have been used nearly interchangeably in the English literature. However, it is now increasingly realized that over vast regions of east Asia and the western North Pacific *the weather is dominated by a seasonal reversal of wind and a clearly defined period of overabundant rainfall in the annual variations*. The wet season of the subtropical and mid-latitude east Asia overlaps with that of south Asia, and both are distinct components of the Asian summer monsoon when surface south-westerly winds prevail. In this chapter, we will provide an overview of the Asian winter monsoon, in which the prevailing surface winds are north-easterly north of the equator. This chapter will focus on areas surrounding east Asia where most of the centers of activities of the Asian winter monsoon are located. For boreal winter weather systems over south Asia, the readers are referred to Chapter 4 of this book.

During boreal winter, the maximum heating moves from its boreal summer location over south Asia to the Maritime Continent–northern Australian region. North of the equator, low-level north-easterly winds prevail over a large longitudinal span, from the western Pacific to the Indian Ocean. Although differential heating and the resultant thermal direct circulation are responsible for both the Asian winter and the Asian summer monsoon circulations, the two monsoons differ in more than one way. On the one hand, the heat source region of the Asian winter monsoon is much closer to the equator (Krishnamurti, 1971), where the effect of the Earth's rotation is diminished. On the other hand, the circulation of the Asian winter monsoon encompasses a larger meridional domain such that the tropical region has a strong interaction with the extratropical region. The extratropical component of the Asian winter monsoon is characterized by prevailing low-level north-easterlies that are associated with the anticyclonic circulations of the surface Siberian–Mongolian high (SMH). This is a strong cold-core high pressure that often

B. Wang (ed.), *The Asian Monsoon*.

stays stationary near the Siberia–Mongolia region with its central sea level pressure (SLP) exceeding any other pressure system in the Earth's atmosphere (Ding, 1994). When the surface high pressure moves south-eastward toward the coastline of China and the western Pacific, intense cold air outbreaks often occur. Strong effects of these outbreaks can reach the deep tropics within a very short period (Chang *et al*., 1983), such that the term 'cold surge' is used to describe the resultant surge of the north-easterly winds by many forecasters in equatorial countries, even though a temperature signal is no longer observed. Thus, baroclinic development in middle and high latitudes usually has a stronger influence on tropical regions during the Asian winter monsoon than the Asian summer monsoon.

Downstream from the north-easterly winds, the Maritime Continent (Ramage, 1968) is an equatorial region of land and sea with its own strong monsoon characteristics. In this region, significant local variations on the seasonal reversal of winds and annual variation of rainfall exist because of the complex land–sea terrain, but near the equator the prevailing wind is generally westerly during the wet season of boreal winter and easterly during the dry season of boreal summer (e.g., Ramage, 1971; Matsumoto, 1992; McBride, 1998; Hamada *et al*., 2002; Chang *et al*., 2004a). The rainfall variation in this region is in phase with that of the Australia monsoon (McBride, 1987, 1998; Hendon and Liebmann, 1990a). Therefore, the terms Asian winter monsoon, northern winter monsoon or Australian (summer) monsoon are sometimes used to include the wet monsoon in both regions. Most of the rainfall is organized into mesoscale convective complexes that are affected by both strong land–sea breezes and larger-scale disturbances (Johnson *et al*., 2004). The latent heat release over the combined Maritime Continent–northern Australia area has long been recognized as the most important planetary scale heat source that drives the global circulation during boreal winter.

The interaction of this heat source with the strong east Asian baroclinic system and the cold air outbreaks affects the subtropical east Asian jet (Chang and Lau, 1982; Lau and Chang, 1987) and in turn may influence the weather from the western Pacific to North America (Yang *et al*., 2002; Chen and Li, 2004). Recent analysis also suggests that flare-ups of this Maritime Continent heat source may lead to downstream wave train propagation and may be related to storm development over Europe on a timescale of one to two weeks (Thorpe *et al*., 2002). During boreal winter, the western Pacific, Maritime Continent, and Australia have some of the largest errors in numerical weather prediction (Rodwell, 2005). The importance of properly representing this heat source in general circulation models was emphasized by Neale and Slingo (2003), who demonstrated that the tendency of a dry bias in the Maritime Continent region is a major source for systematic errors over both the tropical Indian and Pacific Oceans and extratropical North America and north-east Europe. They concluded that the Maritime Continent plays a critical role in the global circulation and emphasized the need for better representation of convective organization over this region of complex land–sea terrains.

In addition to the strong synoptic-scale activities associated with the anticyclones, cyclones, and cold air outbreaks in the extratropical region, the Asian winter monsoon season also coincides with the period of the highest tropical

cyclone activity of the south-western Pacific (Holland, 1984; McBride, 1995). The monsoon trough south of the equator is a favorable area of tropical cyclone development during boreal winter (Harr and Chan, 2005), particularly under the influence of the Madden–Julian Oscillation (MJO) (Madden and Julian, 1972; Hendon and Liebmann, 1990b; Hendon *et al*., 1999). Both the east Asian winter monsoon and the Australian monsoon are also affected directly by the El Niño/Southern Oscillation (ENSO) and other interannual and decadal variations in the Pacific and Indian Oceans. In order to cover the multiple-scale phenomena over the vast region of the Asian winter monsoon, this chapter will be organized in the following way. The climatological mean circulations will be described in Section 3.2, with subsection 3.2.1 covering the midlatitudes and 3.2.2 covering the tropics, respectively. The synoptic-scale weather systems and all other scales of motions that are important for a particular regime are discussed according to the three monsoon regimes, with Section 3.3 covering mid-latitude and subtropical east Asia, Section 3.4 the Maritime Continent, and Section 3.5 northern Australia. Section 3.6 will discuss interannual and longer term variations.

3.2 MEAN CIRCULATIONS

3.2.1 Mid-latitude circulations

The east Asian winter monsoon (EAWM), normally defined as between November and March (Ding, 1994), is the main mid-latitude component of the Asian winter monsoon system. The intensity of the EAWM affects the temperature and precipitation variations over eastern China, Korea, Japan, and the surrounding regions, where it has profound economic and social impact. The major components of the EAWM are shown in Figures 3.1(a–c; color section), which show the surface/sea level, 500 hPa and 300 hPa climatological mean circulations. At the surface, the EAWM is featured by the cold-core SMH, the Aleutian Low, the large meridional gradient of surface temperature over east Asia, and the predominant northerly–north-easterly flows from the Arabian Sea to western North Pacific (Figure 3.1(a)). The central pressure of the SMH often reaches 1,040 hPa and can exceed 1,080 hPa in extreme cases. Its intensity has been used as an indicator for the intensity of the EAWM in some studies (e.g., Guo, 1994; Jhun and Lee, 2004). More details of the SMH and the associated anticyclonic circulations are discussed in Chapter 4. At the surface, the northerly flow is prominent along the east Asian coast, especially over the South China Sea, where a strengthening of the winds is manifested into cold surges. These cold surges, which are characterized by sharp temperature decreases and wind speed increases, are a significant transient component of the Asian winter monsoon. The cold surges also influence the convection over the Maritime Continent and sometimes the monsoon development in the southern hemisphere. A detailed description of cold surges is given in Section 3.3.2. In the mid-troposphere (Figure 3.1(b)), the east Asian long-wave trough is located near Japan. To the south of the trough exists the subtropical jet stream, with a confluence zone

upstream of the trough. At 300 hPa (Figure 3.1(c)), the jet core located south of Japan has a maximum zonal wind exceeding 60 m s^{-1}. Overall, Figure 3.1 indicates that east Asia is a region of strong baroclinicity, marked by large vertical wind shear and cold advection throughout the troposphere.

Several investigators (e.g., Manabe and Terpstra, 1974; Murakami, 1987b) showed that topographic forcing by the Tibetan Plateau is important in maintaining the low-level flow configuration and the upper level jet of the east Asian winter circulation. Zhang *et al.* (1997) suggested that land–ocean differential heating may also provide an important driving force for the east Asian winter monsoon. Here the latent heat release associated with intense convective precipitation over the western North Pacific is the main heat source, and a strong cold dome residing to the north-east of the SMH is the heat sink. The cold dome is maintained by radiative cooling, descending motion associated with the SMH, and persistent cold advection throughout the troposphere (Ding and Krishnamurti, 1987).

3.2.2 Tropical circulations

The major heating center of the Asian monsoon shifts south-eastward from its south Asia location during the summer monsoon into the Maritime Continent and equatorial western Pacific region during the winter monsoon. The outgoing long-wave radiation (OLR) in Figure 3.1(c; color section) indicates that the maximum heating is situated south of the subtropical east Asian jet stream. This longitudinal alignment of the equatorial heat source region and the strong subtropical baroclinic zone gives rise to strong mid-latitude–tropical interactions that are a distinctive feature of the Asian winter monsoon (Chang and Lau, 1980, 1982; Compo *et al.*, 1999). Due to the vanishing Coriolis force at the equator, the upper tropospheric outflow from the Maritime Continent heat source leads to anticyclonic circulations on both sides of the equatorial heating center (Figure 3.1(c)). At the surface, the monsoon trough is situated over northern Australia, which is located to the south of the region of maximum rainfall as indicated by the distribution of the OLR in Figure 3.1(c).

The low-level, north-east monsoon winds reaching the southern South China Sea are strongly affected by the surrounding terrain. The deflection of the terrain results in northerly winds, which turn eastward after crossing the equator due to the conservation of potential vorticity (Lim and Chang, 1981). These westerlies that are situated to the north of the monsoon trough (Figure 3.1(a), color section) characterize the Indonesian wet monsoon and the Australian summer monsoon. Along about 10–15°S a line of strong cyclonic shear separates these lower latitude westerlies from southern hemisphere, higher latitude easterlies (McBride and Keenan, 1982). In addition to the low-level north-easterly winds that feed into the monsoon region across the entire northern subtropics, low-level southerly winds in the southern hemisphere subtropics also provide inflow to the Maritime Continent–Australian monsoon region. The surface wind analysis (Figure 3.1(a)) does not show a similar strong inflow into either the eastern Pacific intertropical convergence zone (ITCZ) or the South Pacific convergence zone (SPCZ) that are indicated in the OLR field (Figure 3.1(c)).

In the Australian region, lower tropospheric westerlies and associated widespread rainfall replace the dry trade easterlies that predominate during southern winter. Low-level onshore north-westerlies transport moist air inland, which allows the monsoon to expand toward the mid-latitude over arid northern Australia.

3.3 SEVERE EAST ASIAN WINTER MONSOON WEATHER

3.3.1 Explosive cyclones

Cyclones are active weather-producing systems during the Asian winter monsoon. Although most cyclones originate in eastern China, they do not deepen explosively until they move off the east Asian coast, where the cold air encounters warmer surface temperatures over the East China Sea and the Kuroshio Current (Chan and Li, 2004). The resultant baroclinicity often leads to explosive cyclogenesis, which is defined by Sanders and Gyakum (1980) as a deepening of the cyclone center pressure of at least 12 hPa in 12 hours. Figure 3.2 shows the frequency of

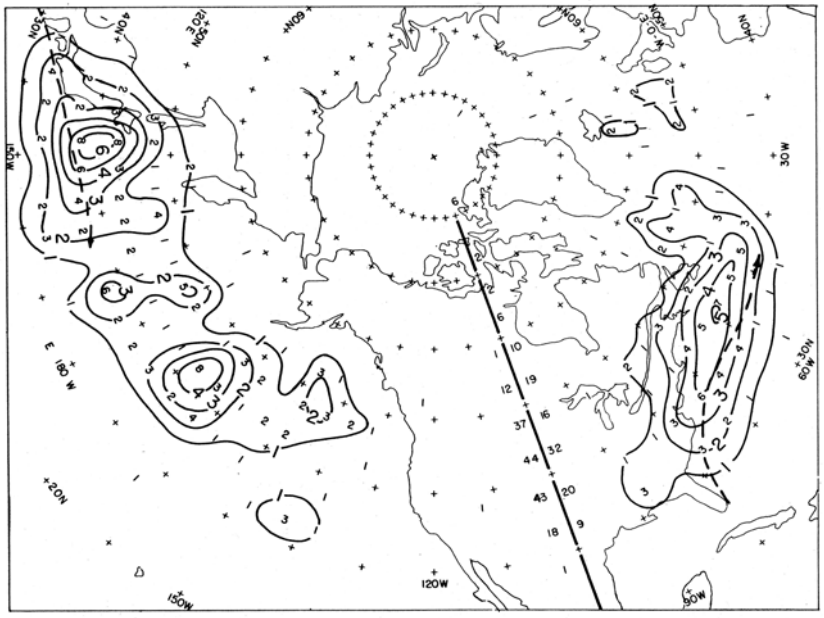

Figure 3.2. Distribution of explosive cyclogenesis during three cold seasons. Non-zero frequencies appear in each $5^\circ \times 5^\circ$ quadrilateral of latitude and longitude. Isopleths represent smoothed frequencies. The columns of numbers to the left and right of the heavy line along 100°W (i.e., 90°W → 100°W) represent, respectively, the normalized frequencies for each 5° latitude belt in the Pacific and Atlantic regions, using a normalization factor of $(\cos 42.5^\circ / \cos \phi)$. Heavy dashed lines represent the mean winter position of the Kuroshio Current and the Gulf Stream.
From Sanders and Gyakum (1980).

explosive cyclogenesis compiled by Sanders and Gyakum (1980). They found that the explosive cyclogenesis generally occurs about 700–800 km downstream from a mobile trough at 500 hPa. A maximum is found over the Kuroshio Current to the south of Japan. Gyakum *et al.* (1989) reported that more than 90% of the cyclones passing through the area of the Kuroshio Current intensify in this region. Frequent cyclogenesis is also found off the east coast of North America, within or to the north of the warm Gulf Stream. However, unlike cyclones over the North America continent where explosive cyclogenesis can occur, cyclones over the east Asian continent are less likely to develop rapidly due to their presence in the confluent region of the east Asian jet entrance. As a result, they are generally weaker than their counterparts over North America (Boyle and Chen, 1987). Sanders and Gyakum (1980) found that latent heat release has been identified as the crucial factor that determines whether a cyclone can deepen rapidly (Chen *et al.*, 1983, 1985; Chen and Dell'Osso, 1987; Li and Ding, 1989; Yi and Ding, 1992; Xu and Zhou, 1999), but the basic condition for explosive development is a zone of strong baroclinicity (e.g., Roebber, 1984). Hanson and Long (1985) suggested that the baroclinicity comes directly from the meridional gradient of sea surface temperature (SST), which they observed to have a close relationship with the frequency of explosive cyclogenesis. They postulated that the surface baroclinicity associated with the temperature gradient triggers baroclinic instability in the subtropical jet stream and leads to rapid development of a cyclone. Above the surface, Ding (1994) suggested that thermal and vorticity advection by the upper level trough is important in triggering the rising motion, and Xu and Zhou (1999) suggested that thermal and moisture advection by the low-level jet plays an important role. In addition, Ding *et al.* (2001) and Jia and Zhao (1994) suggested that a jet stream with an anticyclonic curvature enhances the baroclinic instability and upper level divergence, and thereby favors the explosive cyclogenesis.

3.3.2 Cold surges

3.3.2.1 Definition of cold surges

The cold air outbreak, which is one of the most dramatic weather events during the Asian winter monsoon, may encompass a large area from east Asia to the western Pacific. Outbreaks occur about one to three times a month (Boyle and Chen, 1987; Ding, 1994; Chen *et al.*, 2002; Chan and Li, 2004) and are typically the result of the strengthening and south-eastward movement of the SMH, which leads to an acceleration of north-easterly winds and a decrease of surface temperature to the east and south of the SMH. Outbreaks may occur with an extension of the SMH to the south-east or a split of the high-pressure area that moves toward the south-east coast of China. For a detailed discussion, the readers are referred to Section 4.5 (this book), Chan and Li (2004), and Chan (2005). When the event progresses rapidly southward and affects the tropics, particularly the vicinity of the South China Sea, it is called a 'cold surge'. This term has been used operationally as an upstream precursor for an event that may affect the equatorial region within one or two days. Because the

magnitude of the surface temperature drop diminishes over the equatorial South China Sea due to the modification by the warmer sea surface (Chang *et al.*, 1979; Johnson and Zimmerman, 1986), use of the term 'pressure surge' has also been suggested (e.g., Wu and Chan, 1995; Compo *et al.*, 1999). While various definitions of a surge exist, they usually involve a temperature drop of several degrees within a short time period, an acceleration of the north-easterly or northerly wind component, and/or a sustained period of strong winds (e.g., Lum, 1976; Chu, 1978; Boyle and Chen, 1987; Ding, 1994; Chan and Li, 2004; also see Chapter 4). Compo *et al.* (1999) showed that the relationships between variables associated with cold surges identified in a 10-year European Centre for Medium-Range Weather Forecasts (ECMWF) gridded analysis data set are robust and insensitive to the various definitions or the base points at which these definitions are applied.

Some types of wind and pressure surges affect regions other than the equatorial South China Sea. At the Hong Kong Observatory, the cold surges discussed above are also called northerly surges. Another type of surge in which the wind acceleration is primarily in the zonal direction and results in sustained surface easterly winds, is called an easterly surge (Lum, 1976; Wu and Chan, 1995, 1997; Chan, 2005). These surges are associated with an eastward movement of a low-level anticyclone to the east coast of China, and primarily affect the northern South China Sea. Their influence also tends to be short-lived due to continued eastward movement of the anticyclone away from the longitudes of the South China Sea (Chan and Li, 2004). Compo *et al.* (1999) reviewed the studies of surges that move south-eastward toward the Philippines and the tropical western Pacific. These surges have been related to the westerly wind bursts and increased convection in the equatorial western Pacific (e.g., Chu, 1988; Meehl *et al.*, 1996b).

3.3.2.2 Evolution of cold surges

The development of a cold surge typically starts with the build-up and subsequent south-eastward extension or split of the surface high-pressure area. The center of the SMH may either move south-eastward (Ding and Krishnamurti, 1987; Zhang *et al.*, 1997), or remain nearly stationary but with packets of cold air propagating eastward in conjunction with smaller high-pressure or anticyclonic centers (Wu and Chan, 1995; Chan and Li, 2004). Changes of upper tropospheric circulations over Siberia have long been recognized as precursors of cold surges. The best known change is a north-westerly flow in the vicinity of Lake Baikal that is associated with an upper level wave, which precedes a surge over the southern coast of China by 1–2 days (e.g., Ramage, 1971; Lum, 1976; Chu, 1978; Boyle and Chen, 1987). Compo *et al.* (1999) showed that upper tropospheric north-easterly anomalies associated with a developing ridge over northern Siberia may be a precursor for a surge several days later. When a short wave propagates into the quasistationary east Asian long-wave trough near Japan, the intensification of the trough strengthens the northerly wind and almost simultaneously the cold surge arrives at the southern China coast. A jet streak that is often associated with the short wave may play a key role in forcing the SMH through subsidence in the jet entrance region (Wu and Chan, 1995; Chan and

Li, 2004). Even though it originates from the mid-latitude upper levels, the surge over the South China Sea is mostly confined to a shallow layer between the surface and 850 hPa (Ramage, 1971). The strong cold advection associated with the upper level northerly wind component around Lake Baikal that precedes the cold surge must exceed the subsidence warming, so that air parcels descend the isentropic surface and reach the northern South China Sea as a cold surge.

Ramage (1971) observed a near-simultaneous development of cold surges and the intensification of the local Hadley circulation over east Asia. Chang and Lau (1980, 1982) showed that this development leads to a coherent variation of the mid-latitude and tropical planetary-scale circulations over the timescale of about one week. Prior to the surge, the mid-latitude westerly jet streak near the east Asian trough strengthens as baroclinicity over the large domain begins to increase. About one day after the surge arrives at the northern South China Sea, enhanced deep tropical convection occurs downstream from the surge and accelerates both the local Hadley and Walker circulations through increased upper level divergence. The upper tropospheric meridional return flow, which represents the southerly divergent wind component, accelerates in the entrance region of the jet streak near Japan and causes a further strengthening and eastward propagation of the jet. This process has been confirmed in many other observational studies (see Chan and Li, 2004) and general circulation model (GCM) simulations (Slingo, 1998; Neale and Slingo, 2003).

The above model describes a single cold surge event that evolves over a period of around one week. However, there are often consecutive signals of cold surges over the northern South China Sea with brief pauses of one or a few days between them such that the surges appear to be a series of sequential events. In either case, not all the individual surges are necessarily associated with the classic model of a substantial south-eastward extension or split of the SMH at the surface. However, the intensification of the upper level East Asian trough and the eastward propagation of a jet streak are always important parts of the event. An example of the evolution of a series of two surges observed at the southern coast of China at the end of 2004 is shown in Figure 3.3(a) (500-hPa geopotential height and wind speed) and 3.3(b) (sea-level pressure and surface temperature). The first case can be traced to 26 December 2004 (upper left panels in Figure 3.3(a,b)) and involved a near-stationary SMH center and an eastward-moving, upper level shortwave trough (S1) that started near Bangladesh and north-east India and had a minor jet streak to its south. Throughout the surge development, this shortwave did not interact significantly with the East Asian longwave trough to the north. The surge affected Hong Kong on 28 December 2004 with a large decrease of more than 6°C in daily-averaged surface temperature. However, the surface pressure increase was very modest and the surface moisture change was negligible. The second case can also be traced back to 26 December 2004, when a zonally oriented 500-hPa trough (Z) north of Mongolia between 45°N–50°N, 80°E–110°E began to intensify and propagate south-eastward. On 29 December 2004, another shortwave trough (S2) appeared in southern China just east of 105°E and propagated eastward. On 30 December the Z trough moved into the south-west quadrant of the East Asian longwave trough and became its south-west part. As a result, the longwave trough had a significant

extension into southern China. The East Asian trough continued to deepen the next day and sweep counterclockwise so that it was joined by S2 near Taiwan. When the second surge passed Hong Kong on 31 December, a daily-averaged surface temperature drop of slightly less than 4°C was reported. Although the temperature decrease was smaller than with the first surge, it led to the lowest temperature of the season by then. This second event, which was associated with a deeper East Asian trough and a stronger upper level jet streak, fits the classic model of a cold surge. In contrast to the first surge, the SMH center moved south-eastward toward the south-east coast of China and resulted in a sharp rise of the surface pressure and a sharp decrease in the dew-point temperature on 31 December 2004 at Hong Kong. The dryer air mass continued through the first few days of January 2005. Figure 3.3 shows that the SMH and the East Asian longwave trough continued their south-eastward and eastward movements, respectively, after the cold surge. On 31 December 2004, another shortwave trough appeared in the north-western corner of the domain and moved to the eastern boundary of Mongolia on 2 January 2005, but it did not interact with the East Asian trough which had moved to the western North Pacific. No surge resulted from this event.

While the strengthening of the East Asian longwave trough at the end of the December 2004 event followed forcing from the west, Lu (2005) showed that some of the strengthening may also have been forced from the east. On 24 December 2004, the North Pacific ridge between the Date Line and 140°W strengthened suddenly and began to expand westward over several days. This ridging from the east that resembled a blocking pattern apparently contributed to the deepening of the East Asian longwave trough, which led to the onset of cold surges when forcing by the shortwave troughs arrived from the west.

3.3.2.3 Gravity wave characteristics of cold surges

The movement of the anticyclonic circulation at the surface and the upper level troughs associated with a cold surge involves basically the advection of relative and planetary vorticity. However, the nearly spontaneous freshening of the low-level north-easterly winds over the South China Sea following the south-eastward movement of the surface high pressure (Ramage, 1971; Chang *et al.*, 1979) indicates a rapid progression of cold surges that occurs on a timescale shorter than that of the advective scale inherent in Rossby wave dynamics. Near the equator there is also often a rapid response in enhanced surface cyclonic circulations near Borneo downstream from the surge (Chang *et al.*, 1979; Meehl *et al.*, 1996b). These Borneo vortices are related to the flaring up of deep convection. The rapid developments led Lim and Chang (1981) to contemplate the possibility that the surge process may contain gravity wave characteristics. They formulated a simple linear shallow-water equation model on the equatorial beta-plane with no mean flow to study the development following an imposed pressure surge at 30°N. The solution is expressed by the summation of a series of equatorial beta-plane waves. It shows the development of inertial gravity waves, eastward-propagating Kelvin waves and mixed Rossby–gravity waves, and westward-propagating Rossby waves in the equatorial region

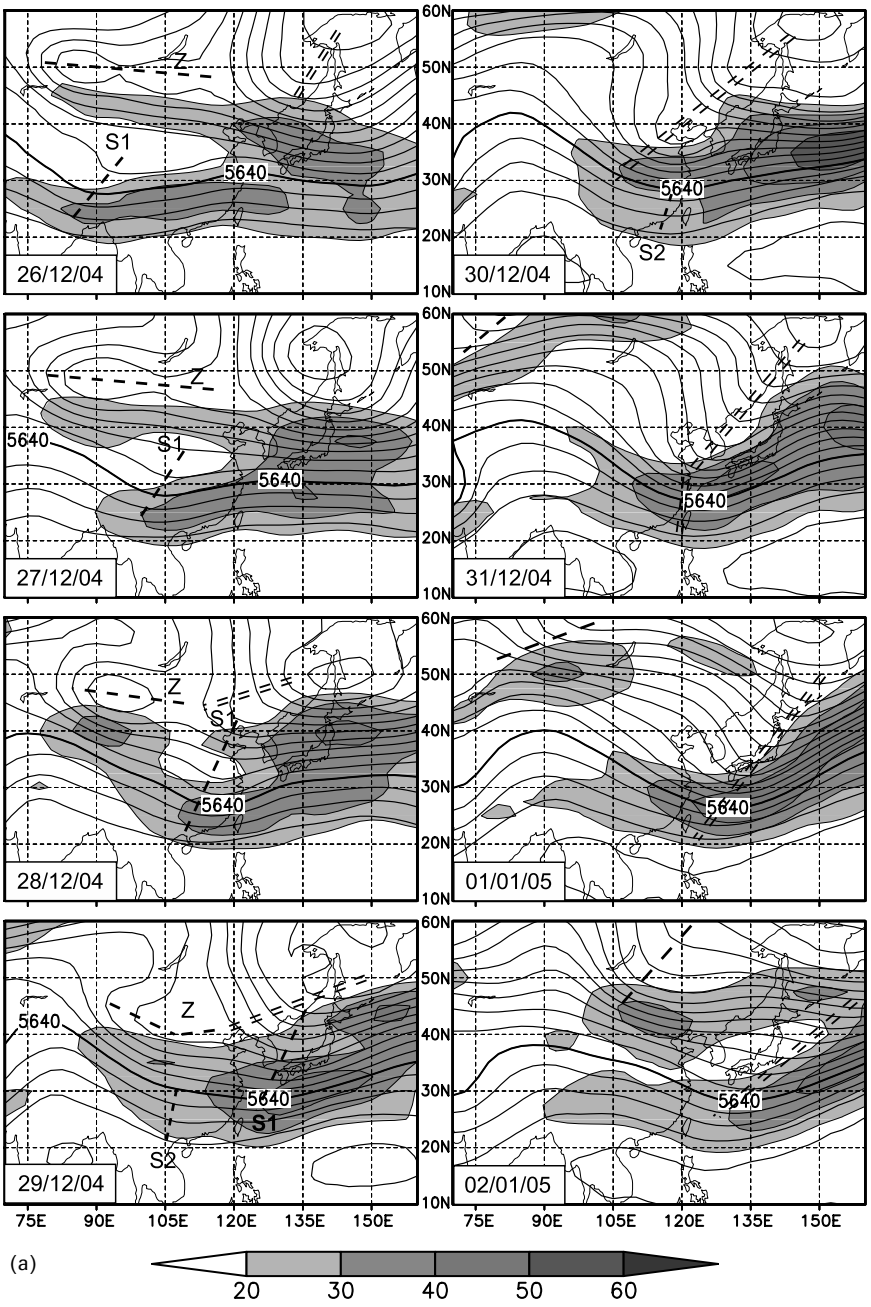

Figure 3.3. (a) Daily averaged 500-hPa geopotential height (contour intervals 60 m) and wind speed (shaded) for 26 December 2004–2 January 2005. Dashed lines indicate troughs, with Z the zonally elongated trough and S1 and S2 eastward propagating short-wave troughs. Double dashed lines indicate the east Asian trough. (b) Daily averaged sea level pressure (isobars) and surface temperature (shaded) for 26 December 2004–2 January 2005. The Hong Kong surface temperature (T) and dew point depression (DD) averaged between 00 and 12 GMT are given in the text box in each panel.

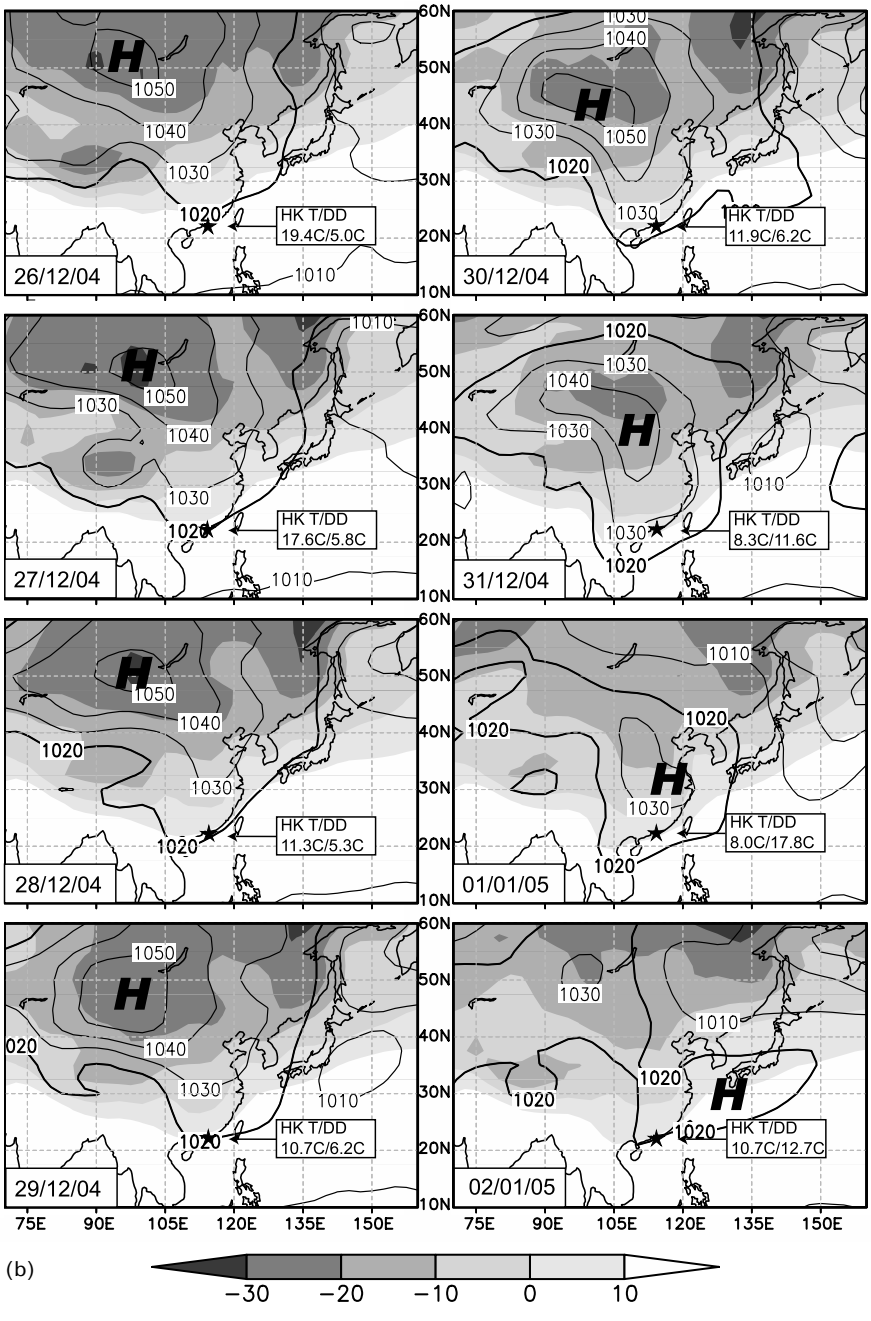
26/12/04
HK T/DD
19.4C/5.0C
30/12/04
HK T/DD
11.9C/6.2C
27/12/04
HK T/DD
17.6C/5.8C
31/12/04
HK T/DD
8.3C/11.6C
28/12/04
HK T/DD
11.3C/5.3C
01/01/05
HK T/DD
8.0C/17.8C
29/12/04
HK T/DD
10.7C/6.2C
02/01/05
HK T/DD
10.7C/12.7C
75E 90E 105E 120E 135E 150E
60N 50N 40N 30N 20N 10N
(b)
−30 −20 −10 0 10

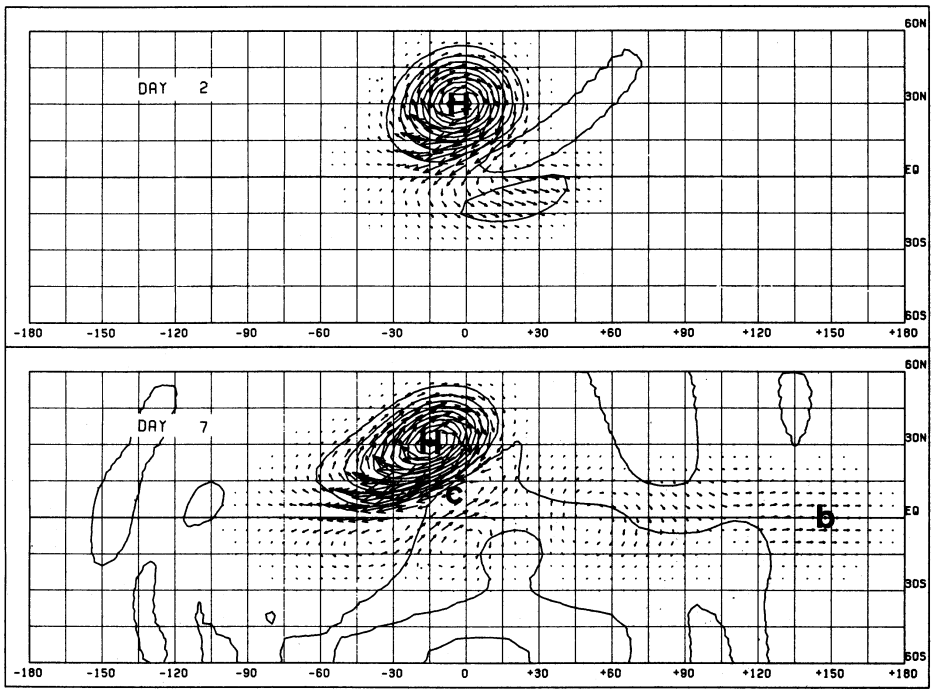

Figure 3.4. The velocity and geopotential response for days 2 and 7 after an imposed pressure forcing at 30°N in an equatorial beta-plane, shallow-water model.
Lim and Chang (1981).

(Figure 3.4). The inertial gravity waves rapidly disappear from the region and the Kelvin and mixed waves propagate away to the east. On the other hand, the Rossby wave group organizes itself into a north-east–south-west oriented pattern that resembles both the belt of north-easterly surge winds and the enhanced equatorial cyclonic circulation downstream. This pattern is the result of the Rossby wave dispersion, in which lower modes closer to the equator lead the higher modes away from the equator in the westward propagation. Lim and Chang's (1981) results suggest that the observed rapid downstream development of cold surges may be associated with the pressure-wind adjustment process, so that gravity wave characteristics, which are a natural consequence of the process, become a part of the surge dynamics.

The observational evidence to support gravity wave characteristics in cold surges was presented by Chang *et al.* (1983), who observed a two-stage process with different timescales in a cold surge in the South China Sea during the 1978–1979 Winter Monsoon Experiment. (These two stages are associated with a single cold surge. They are different from the two phases of the 26 December 2004–2 January 2005 sequence discussed in Section 3.3.2.2, in which the two phases represent two separate surges.) By analysing the surface station reports, Chang *et al.* (1983) found that at many stations the timing of the pressure rise leads that of the dew point

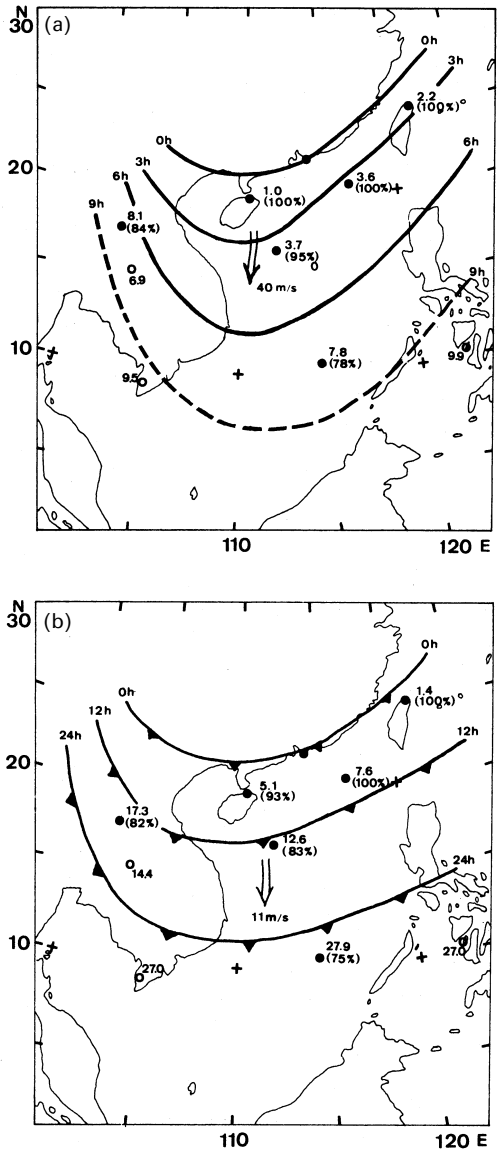

Figure 3.5. Schematic diagram for the progression of (a) an unobstructed edge and (b) an unobstructed front. The separation time (h) is relative to the passage of a system at Hong Kong (0 h). The double arrows show estimated progression speeds.
From Chang *et al.* (1983).

temperature drop, with the separation of the two stages increasing for stations farther downstream along the track of the cold surge. As a result, the cold surge extends south-westward with two propagation speeds (Figure 3.5). Chang *et al.* (1983) identified the slower system as a front by tracing the timing of the dew

point temperature drop at each station. It propagates at an advective velocity scale of around $10\,m\,s^{-1}$. Chang *et al.* (1983) called the faster system an 'edge' that is associated with the propagation of the pressure rise. The edge propagates at a velocity around $40\,m\,s^{-1}$. Based on this fast scale and the larger wind–isobar cross angle, Chang *et al.* (1983) suggested that the edge possesses the nature of a gravity wave that is fundamentally different from the advective dynamics of the front motion. This difference remains even when modifying effects of the bottom topography on planetary vorticity advection, which give rise to a length scale measured by the slope between the Tibetan Plateau and the eastern coast of China (Hsu, 1987; Compo *et al.*, 1999), are considered. The separation of these two different timescales in a cold surge was also revealed in an analysis of ship reports in the South China Sea (Chan and Li, 2004).

3.4 MARITIME CONTINENT MONSOON

The Maritime Continent is a large area of land–sea complex, consisting of Indonesia, Malaysia, and the surrounding areas between 10°S and 10°N (Ramage, 1968). The complex terrain of islands and seas in this region gives rise to strong local variations of the rainfall annual cycle (Braak, 1921–1929; Wyrtki, 1956; Ramage, 1971) and diurnal cycles. In addition, the Maritime Continent rainfall also exhibits significant interannual variations as discussed in Section 3.6.2, and is subject to strong influences of intraseasonal and synoptic-scale disturbances like the MJO, cold surges, and synoptic weather systems (Chang *et al.*, 2004a, 2005a).

3.4.1 Annual cycles and seasonal transitions

3.4.1.1 Monthly evolution

Situated between the centers of the Asian summer and the Australian summer monsoons, the Maritime Continent monsoon may be considered as a transition regime both in space and time. Lau and Chan (1983) observed that the transition from Asian summer to winter (Australian summer) is continuous and may be represented by a south-eastward progression of the large-scale maximum convection over the South-east Asian 'land bridge' (Figure 3.6). Thus, the monsoon onset over the Maritime Continent progresses orderly following the seasonal march (Tanaka, 1994). This smooth progression led many investigators (e.g., Lau and Chan, 1983; Meehl, 1987) to propose that the boreal autumn seasonal transition occurs as the maximum convection follows the sun. However, the reversed transition from Asian winter to Asian summer monsoon is not as continuous (Meehl, 1987; Yasunari, 1991; Matsumoto and Murakami, 2000, 2002; Hung and Yanai, 2004; Hung *et al.*, 2004). During the boreal spring, the maximum convection centers mostly stay near or south of the equator. As a result, the withdrawal of the Asian winter monsoon and the onset of the Asian summer monsoon are more abrupt.

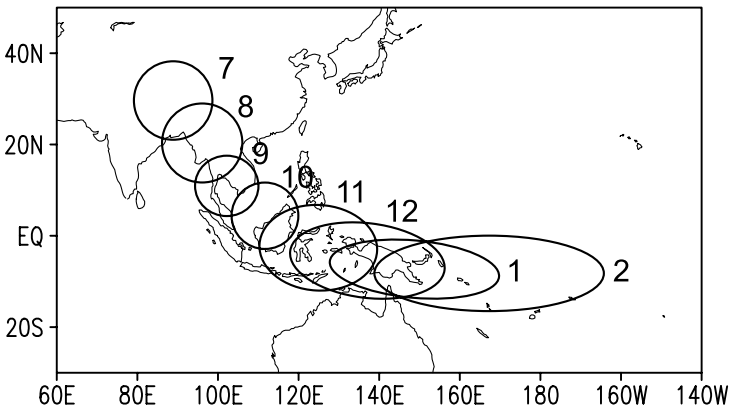

Figure 3.6. Seasonal migration of the monsoon diabatic heat sources during July–February (denoted by marching numerals). The extent of the diabatic heat sources is determined from the area with OLR $<225\,\mathrm{W\,m^{-2}}$ from monthly OLR climatology and is approximately proportional to the size and orientation of the schematic drawings.
Adapted from Lau and Chan (1983).

Figure 3.7 (color section) shows the analysed monthly mean station rainfall from October to March, overlapped with surface winds from the National Centers for Environmental Prediction/National Center for Atmospheric Research (NCEP/NCAR) reanalysis data over South-east Asia. The rainfall analysis is based on two long-term data sets: the 1990–1997 Indonesia data with 63 stations processed by Kirono *et al.* (1999) and Haylock and McBride (2001), and the ASEAN Climatic Atlas Project data over 935 stations covering Malaysia, Indonesia, Singapore, Brunei, the Philippines, and Thailand. Rainfall amounts are high throughout the region with individual monthly totals of the order of 300–500 mm. In October the higher amount of rainfall is shifted from its boreal summer location of the Indo-China Peninsula to the northern Malay Peninsula and north-western Borneo (place names are shown in Figure 3.8). In November and December the high rainfall regions continue to move southward along the eastern coast of the Malay Peninsula and western Borneo as a result of the north-easterly monsoon winds that strengthen and reach deep into the equatorial region as the season progresses. A high rainfall area also moves southward along the western coast of Sumatra, where the onshore wind is westerly. Meanwhile, heavy rainfall also occurs on the eastern coast of the Philippines, again a result of the north-easterly onshore winds. In January, rainfall over Sumatra decreases, while the maximum rainfall shifts south-eastward toward Java and other southern islands of Indonesia. This corresponds to the development and strengthening of north-westerly winds north of Java, which is the result of the strengthened north-easterly monsoon winds that cross the equator and turn eastward. The north-easterly winds weaken in February and March. As a result, rainfall over the entire region weakens, but there is no evidence of a north-westward withdrawal along the Sumatra–Malay Peninsula land bridge.

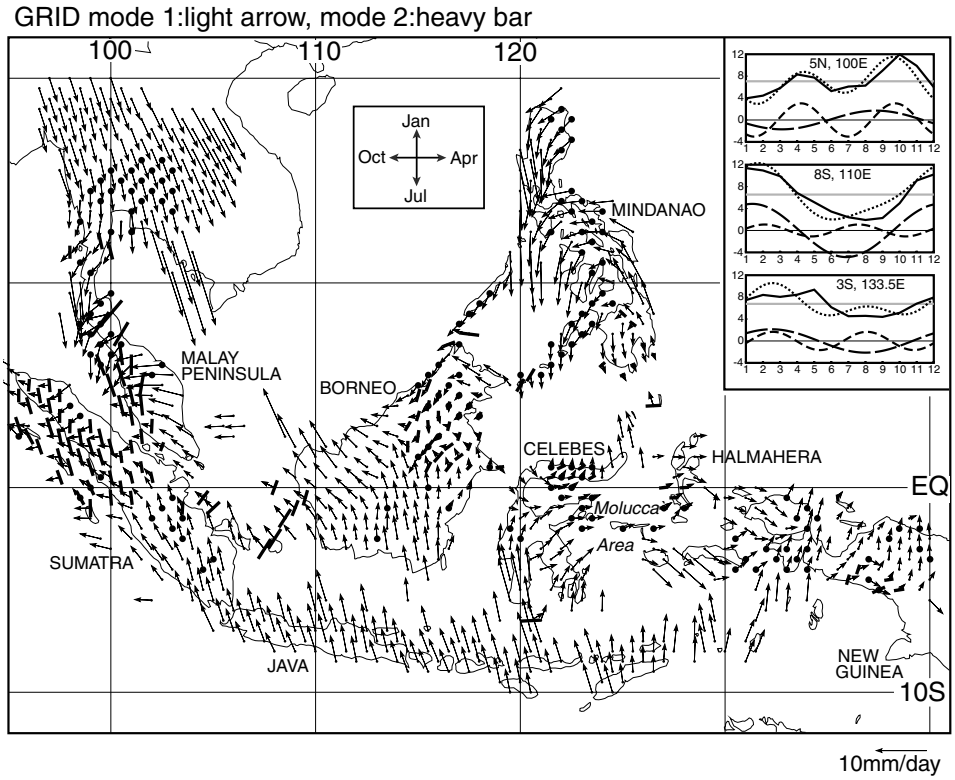

Figure 3.8. The annual cycle mode (light arrows) for analyzed station rainfall. The annual cycle phase is shown as a 12-month clock with a northward arrow indicating maximum rainfall in January. The length of the arrow defines the amplitude of the cycle. Heavy dots indicate grid points where the annual cycle mode is not important. The semiannual mode (heavy bar) is plotted if its amplitude is at least 80% of that of the annual cycle. Each bar is centered at the grid point and pointing in the two (opposite) directions of the semiannual cycle peaks. A vertical (north–south) bar indicates rainfall maximum in winter and summer and a horizontal (east–west) bar indicates rainfall maximum in spring and fall. The entire length of the bar is twice the length of an annual cycle vector with the same amplitude. Example of rainfall time series (mm day^{-1}) at grid points where the semiannual cycle is important (5°N, 100°E), the annual cycle is important (8°S, 110°E), and neither are important (3°S, 133.5°E) are shown in the upper-right insert.
Adapted from Chang *et al.* (2005b).

Chang *et al.* (2005b) pointed out that these patterns result largely from the interaction between the high topography in the region and the moisture-bearing, low-level monsoon flow. Similarly, wind–terrain interaction also dominates the rainfall distribution around Indo-China and south India during boreal summer. Therefore, while the basic annual cycle is driven by the local solar heating over the tropical monsoon region, particularly the Maritime Continent, the annual cycle of rainfall is dominated largely by interactions between the complex terrain and the annual reversal of the surface monsoonal winds.

3.4.1.2 Annual cycle and semiannual cycle of rainfall

Figure 3.8 shows the first two harmonics of the annual variation of analysed monthly station rainfall computed by Chang *et al.* (2005b). The first harmonic, which represents the annual cycle mode, is represented by a 12-month clock with length indicating the amplitude and a northward phase indicating maximum rainfall in January. The heavy dots indicate locations where the annual cycle mode is considered weak because its amplitude is no more than 40% of the maximum rainfall and the phase difference is at least two months. These locations are situated mainly in the eastern and central Philippines, north-east Borneo, southern Thailand, and parts of the north-west end of New Guinea. The reason for the weak annual cycle varies geographically. For example, in southern Thailand the wet season extends through the boreal summer; but this culminates in a period of intense rainfall at the end of the wet season around September. In contrast, in north-east Borneo the rainfall tends to be well distributed over all months of the year, so the magnitude of the annual cycle is small.

Over the western Maritime Continent the phase of the annual cycle moves in a clockwise manner, reflecting the general trend of the seasonal march that follows the sun. The annual cycle maximum occurs mostly in northern autumn in the Malay Peninsula and northern Sumatra and changes to around December in southern Sumatra. Over the rest of Indonesia, the maximum of annual cycle occurs during boreal winter in most places near and south of the equator. However, significant local variations in both amplitude and phase exist. As indicated in Figure 3.8 and discussed by Chang *et al.* (2004a, 2005b), most of these variations are due to interactions between the complex terrain and a simple annual reversal of the surface monsoonal winds. A most notable variation is over the central Celebes and the Molucca area, where the maximum in the annual cycle of rainfall tends to occur during boreal spring and early boreal summer, rather than boreal winter as is in most other places near and south of the equator. This variation has been noted by many previous investigators (e.g., Wyrtki, 1956; Ramage, 1971; Hamada *et al.*, 2002; Aldrian and Susanto, 2003; Aldrian *et al.*, 2003). Chang *et al.* (2005b) showed, by analysing QuikSCAT sea surface winds, that this is again the result of the wind–terrain interaction. An east–west oriented mountainous ridge lies along the islands in the Molucca area. The east and south sides of these islands are sheltered from the north-east monsoon winds during boreal winter, but they face the south-easterly monsoon winds against the terrain during boreal summer.

The second harmonic of the annual rainfall variation represents the semiannual cycle mode, which is plotted as short black bars in Figure 3.8 at locations where the semiannual amplitude is at least 80% of the annual cycle amplitude. The semiannual mode is comparable in magnitude to the annual cycle mode over a large area of the equatorial landmasses between 3°S–7°N, but only a very small region reflects the twice-yearly crossing of the sun. Most of the semiannual cycle appears to be due to the influence of both the summer and the winter monsoon in the western part of the Maritime Continent where the annual cycle maximum occurs in autumn.

3.4.1.3 Monsoon regimes and seasonal transitions

Chang *et al.* (2005b) used the seasonal difference fields in satellite rainfall and surface wind data to define the monsoon regimes for the four seasons. The boreal summer and winter monsoon regimes are displayed in Figure 3.9 (color section) – showing the difference in the Tropical Rainfall Measuring Mission (TRMM) precipitation radar data and QuikSCAT winds between December–January–February (DJF) and June–July–August (JJA). Here the warm colors show areas of more rainfall in JJA and the cool colors show areas of more rainfall in DJF. The general pattern reveals a structure whereby the boreal summer and winter monsoon rainfall regimes intertwine across the equator – both being strongly affected by the wind–terrain interaction. In particular the boreal winter regime extends northward to 5°N and beyond along the eastern flanks of the major island groups and landmasses, including the Philippines, Borneo, Vietnam, the Malay Peninsula, and Sumatra. In most of these areas the high boreal winter rainfall is due to the onshore north-easterly monsoon winds from the north-west Pacific and the South China Sea. Chang *et al.* (2005b) postulated that this asymmetry is due to two factors. The strong baroclinicity associated with the cold Asia continent during boreal winter gives rise to north-easterly winds that are stronger than the south-easterly winds in the southern hemisphere during boreal summer. In addition, contrary to the situation in the northern tropics, very few coastal areas between 5°S–10°S face the prevailing seasonal wind. Thus, the boreal summer monsoon regime is mostly constrained within the northern hemisphere.

The northward intrusion of the boreal winter rainfall regime north-west of Borneo is not a result of direct onshore winds, where the north-east monsoon is parallel to the coastline. This is the vicinity of the low-level, quasistationary Borneo vortices (Cheang, 1977). The north-east cold surge winds periodically enhance the low-level cyclonic shear vorticity off the north-west coast of Borneo. As a result, the Borneo vortices are often active (e.g., Johnson and Houze, 1987; Chang *et al.*, 2003, 2005a), and the deep convection and heavy rainfall frequently extend offshore by several hundred kilometers into the South China Sea.

The monsoon regimes during the transition seasons, boreal spring (March–April–May, or MAM) and boreal autumn (September–October–November, or SON), are summarized in Figure 3.10 (color section). Here the difference between a transition season rainfall and the higher of the summer or winter rainfall is plotted if the transition season rainfall is the maximum of all four seasons. The cold colors are for MAM and the warm colors are for SON. The QuikSCAT winds for both seasons are also plotted. In general, the SON monsoon rainfall dominates areas north of the equator and the western side of the domain, while the MAM monsoon rainfall dominates areas south of the equator and the eastern side of the domain. The equatorial belt of 10°S–10°N is divided near central Borneo, with the SON regime to the west and the MAM regime to the east. Away from the equator, significant northern hemisphere SON monsoon rainfall can also be found in the South China Sea and east of the Philippines. Similarly, significant monsoon rainfall does not exist in the southern hemisphere MAM regime. This is consistent

with Matsumoto and Murakami's (2000) observation that early season cold surges, that originate from the Asian continent during boreal autumn, are stronger than those that originate from Australia during boreal spring. Overall, Figure 3.10 depicts the asymmetric seasonal march noted earlier. During boreal autumn, the maximum convection moves from India south-eastward and crosses the equator, but during boreal spring the maximum rainfall remains mostly south of the equator without a north-westward progression.

Chang *et al.* (2005b) showed that this spring–autumn asymmetry may be explained by a global-scale redistribution of mass between land and ocean areas during spring and autumn whose signals can be detected over most of the Earth's atmosphere. The redistribution results from different land–ocean thermal memories and atmosphere–ocean interactions. Because of the orientation of the Asian and Australian landmasses, it produces SLP patterns that lead to asymmetric wind–terrain interactions throughout the region, and a low-level divergence asymmetry that facilitates the south-eastward march of maximum convection from the Asian summer monsoon to the Australian summer monsoon, and hinders the reverse march in boreal spring. Other hypotheses that may explain the asymmetry include seasonal varying east–west SST gradients over the equatorial Pacific and Indian Oceans (Wang, 1994; Li and Philander, 1996; Webster *et al.*, 1998), different equatorial basic flows in the western Pacific and Indian Ocean (Matsumoto and Murakami, 2002), an oceanic region of subsidence located to the west of heat sources as a Rossby wave response (Hung *et al.*, 2004), and the tendency of boundary layer convergence to occur to the east of the deep convection over the ocean (Li *et al.*, 2004).

3.4.2 Interactions of cold surges, synoptic disturbances, and MJO

The western part of the Maritime Continent that surrounds the equatorial South China Sea is influenced by large-scale disturbances that vary over a wide range of timescales: the quasibiweekly cold surges from the north, the intraseasonal MJO from the west (Chapter 5 by D. Waliser), and the synoptic-scale vortices near the west coast of Borneo. Due to the interaction between north-east monsoon winds and the terrain, these Borneo vortices have the highest frequency of occurrence of any of the other quasistationary synoptic disturbances in the entire equatorial belt (Chang *et al.*, 2004a).

Chang *et al.* (2004a, 2005a) documented the interaction of these three motion systems on the large-scale patterns of convection, low-level winds, and divergence over the equatorial South China Sea in an analysis of Geostationary Meteorological Satellite black-body temperature (T_{bb}). A convection index (CI) was used to represent the distribution of convection around the southern South China Sea, where $\mathrm{CI} = 250(^{\circ}\mathrm{K}) - T_{bb}$ for $T_{bb} < 250^{\circ}\mathrm{K}$ and $\mathrm{CI} = 0$ otherwise. They found that nearly 1/3 of boreal winter days have one or more vortex centers in the western Borneo–southern South China Sea region, and about 1/3 of these days are surge days. On the other hand, only about 1/5 of the 'no vortex' days are surge days.

The impacts of cold surges and Borneo vortices on deep convection, identified by analysing the 2–15-day filtered data, are shown in Figure 3.11 (color section). When neither surge nor vortex is present (Figure 3.11(a)), convection is reduced over the equatorial South China Sea and enhanced downstream of the mean north-easterly wind over the Malay Peninsula, Sumatra, and Java, where the monsoon wind interacts with the terrain. This pattern is almost reversed when a vortex is present without a cold surge (Figure 3.11(b)). The presence of the Borneo vortex results in a deflection of the low-level winds and convergence to the west coast of Borneo, such that the primary area of deep convection occurs more upstream near the west coast of Borneo and over the southern South China Sea. Convection over the landmasses downstream from the surge is suppressed. The presence of a cold surge basically enhances these two opposite patterns (Figures 3.11(c) and (d)). The locations of convection during surge cases with and without a vortex are similar to those in the respective no surge cases, however the magnitude is much stronger with a surge. Convection over the southern South China Sea is strongest when both surge and vortex cases are present (Figures 3.11(d)).

An extreme case of the interaction between a strong cold surge and a Borneo vortex is the rare formation of Typhoon Vamei near the equator on 26 December 2001 (Chang *et al.*, 2003). Figure 3.12 (color section) shows the sustained strong surge prior to the development of Typhoon Vamei. The surge appeared to spin up a Borneo vortex that stayed over the southern tip of the equatorial South China Sea for one week. However, such a formation is extremely rare because cold surges tend to shift the vortex center toward Borneo, where the vortex is unlikely to intensify into tropical cyclone strength over land.

The MJO over the Maritime Continent region may be represented by a singular value decomposition (SVD) on 30–60-day filtered 850-hPa winds and OLR (Chang *et al.*, 2004a, 2005a). Four phases of MJO that are defined by the two leading SVD modes are shown in Figure 3.13. During the dry phase, convection over the Maritime Continent is reduced and equatorial easterly anomalies exist between 80°–150°E. During the dry-to-wet phase, the region is in a transition from the reduced convection regime of the MJO to the active convective regime of the MJO. During the wet phase, convection is enhanced over the eastern portion of the Maritime Continent and low-level westerly anomalies exist throughout the region. During the wet-to-dry transition phase the active convection regime has moved to the equatorial western Pacific and the reduced convection regime is approaching the Maritime Continent from the west.

Chang *et al.*'s analysis showed that cold surges occur more frequently during periods of no MJO's (29%) and the wet and wet-to-dry phases (28%) of MJO periods. During the dry and dry-to-wet phases the percentage of surge days is only about 15. So the net effect of the MJO is to reduce the frequency of surges. Also, nearly twice as many vortex cases occur during periods with no MJOs than periods with MJOs. During MJO periods, the distribution of the number of vortex cases varies only modestly among the four phases.

During the MJO dry phase, the composite Borneo vortex case (Figure 3.14(a), color section) is similar to the composite of vortex cases with no surge

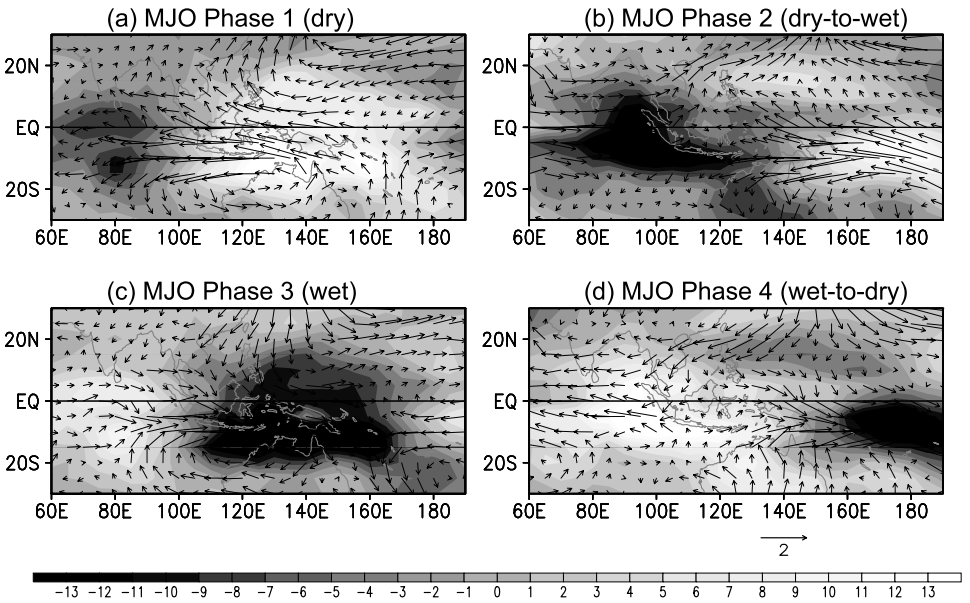

Figure 3.13. Composite 850-hPa winds ($m\,s^{-1}$) and anomalous OLR ($W\,m^{-2}$) for the four phases of the MJO based on time coefficients of an SVD analysis of the winds and OLR. The terms dry and wet refer to increased or reduced convection over the Maritime Continent. Adapted from Chang *et al.* (2005a).

(Figure 3.11(b)). This similarity indicates that the MJO dry phase may inhibit cold surges, so the Borneo vortex most likely occurs without a surge during this phase. During the dry-to-wet phase, the deep convection over the equatorial South China Sea and the low-level winds associated with the Borneo vortex (Figure 3.14(b)) become more organized. North-east winds appear over the southern South China Sea but their magnitude is much less than that in the vortex and surge composites (Figure 3.11(d)).

Although the MJO wet phase is associated with a higher cold surge frequency than the dry phase, the cyclonic circulation of the vortex seems to be more linked to cyclonic horizontal shear associated with equatorial westerly winds rather than north-easterly winds that extend through the southern South China Sea. These increased equatorial westerlies are associated with the enhanced MJO-scale convection over the eastern portion of the Maritime Continent (Figure 3.13(c)). Consequently, the center of the vortex is located over the southern South China Sea (Figure 3.14(c), color section). During the wet-to-dry phase (Figure 3.14(d)), the vortex is very weak with cyclonic shear present only over the extreme western South China Sea and Malay Peninsula. South-westerly anomalies exist over the primary region of the southern South China Sea and reduced deep convection spreads north-eastward along the west coast of Borneo.

The relationships among the MJO, cold surges, and the Borneo vortex are summarized in Figure 3.15. It is clear that the presence of the MJO is associated

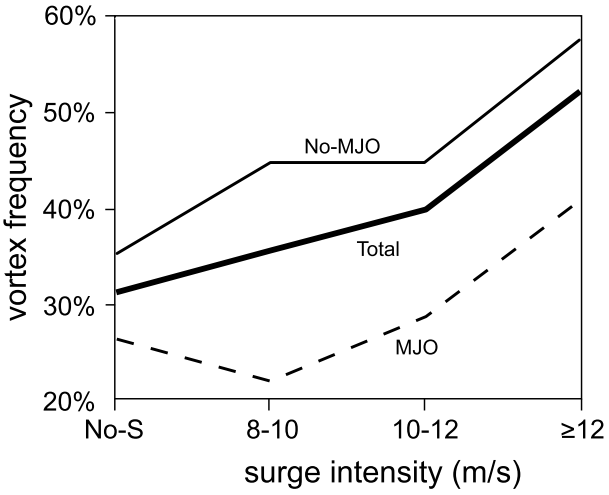

Figure 3.15. The percentage of days containing a vortex relative to the surge intensity, for all (total) days, days with no MJOs, and MJO days. The surge intensity is the average 925-hPa northerly wind along 15°N between 110°E–117.5°E.
From Chang *et al.* (2005a).

with fewer numbers of vortex cases, and the occurrence of vortex cases during periods of weak surges is most reduced during the MJO. Therefore, while the presence of a surge acts to increase the strength of the Borneo vortex, the frequency of surges is reduced when the MJO is present. Often the MJO-scale circulation pattern directly opposes the cold surge wind pattern. Therefore, weak surges may be more inhibited during periods of strong MJO. Primarily due to the impact of the MJO on cold surge intensity and frequency, 66% of the vortex cases occur during non-MJO periods. The Borneo vortex is least likely to occur when the inactive convective portion of the MJO extends to the Maritime Continent with large-scale, low-level diffluence that acts to restrict the impact of cold surges on convection in the southern South China Sea. This complex relationship among MJO, cold surges, the Borneo vortex, and the effects of the topography contribute to the variability of convection patterns over a variety of space and timescales.

3.4.3 Diurnal cycle of convection

Diurnal cycles of deep convection are a prominent feature over the Asian monsoon (Chapter 8 by R. Johnson) and the tropical western Pacific regions (Nitta and Sekine, 1994). During the Asian winter monsoon the diurnal cycle of convection over the Maritime Continent is particularly strong when the land–sea breeze is enhanced by the availability of abundant moisture. Figure 3.16 (color section) shows the diurnal cycle vectors computed from hourly CI for December 1998–2001, with the vector length indicating the amplitude and the vector direction indicating the maximum convection phase for a local 24-hour clock (same convention

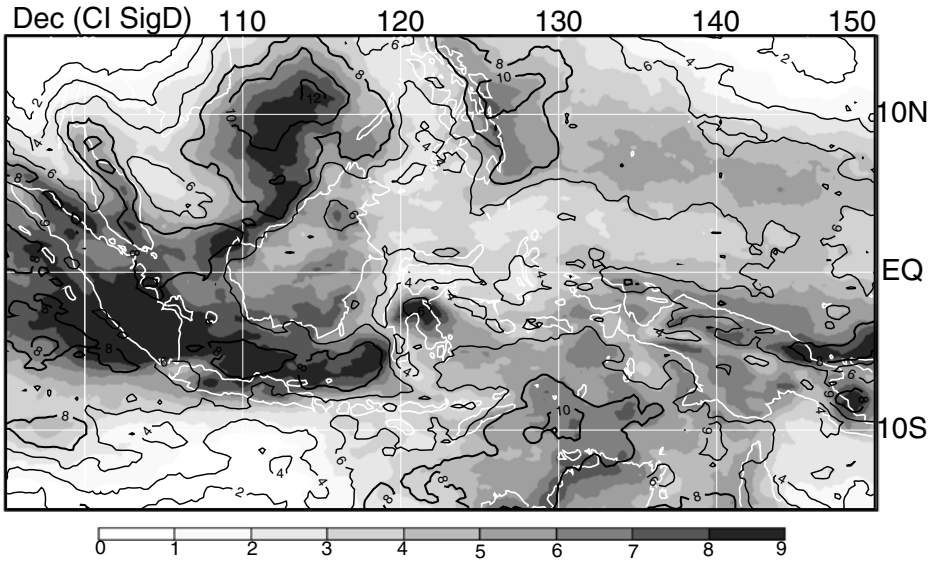

Figure 3.17. Monthly mean (scaled by shading) and standard deviation (contours) of the daily averaged CI.

as used by Murakami (1983), Ohsawa *et al.* (2001), and many others). For comparison, Figure 3.17 shows the monthly mean and standard deviation of the daily averaged CI. The ratio of the diurnal cycle amplitude over this standard deviation is a measure of the relative importance of the diurnal variability compared with the synoptic (day-to-day) variability, and is also plotted on Figure 3.16. The diurnal cycles have large amplitudes in areas around the big islands. They often overlap but do not always coincide with the most active deep convection region. Relative to the synoptic variability, the diurnal cycles are most important around the south or south-western coasts of the equatorial islands, including Borneo, Sumatra, Java, and New Guinea. This is the result of the distribution of the synoptic variability, which is large on the onshore side of the islands and the South China Sea due to the pulsation of the north-east monsoon winds, including cold surges. On the southern or south-western coasts this effect is sheltered. This pattern remains in January and February (not shown) although the difference becomes smaller because of the deeper penetration of the north-east winds southward.

The diurnal vectors over the land areas indicate maximum CI in the late afternoon and evening hours, sometimes into the late evening near midnight. However, the maximum convection usually occurs one or two hours earlier, because upper level stratiform cloud that gives the high CI values continues to expand in the outflow layer in the dissipation stage of the mesoscale cloud clusters (Houze *et al.*, 1981). On the north side of the large islands, the phase of the diurnal cycle immediately offshore occurs around early morning hours, and the diurnal signals are conspicuous over a relatively large area over the water that may be

several hundred kilometers offshore. Houze *et al.* (1981) showed that the north-east monsoon winds interact with the sea breeze and produce strong low-level convergence that enhances this offshore convection. The monsoon enhanced over-ocean diurnal cycles may occur in regions of strong oceanic convection but it may also occur in regions with only modest oceanic convection. An example of the former is over the southern South China Sea north-west of Borneo, where a region of large diurnal variability overlaps with the maximum monthly mean convection area associated with the Borneo vortices. However, north of western New Guinea the monthly mean convection is modest, but the large diurnal variability is still evident over a considerable area offshore (Liberti *et al.*, 2001).

Over most offshore regions, the diurnal cycle vectors rotate clockwise in the direction away from the coastline, indicating an outward movement of the diurnal phase with time. As a result, several hundred kilometers north-west of Borneo the diurnal maximum occurs near local noon, which is different from the early morning maximum commonly observed for deep convection over open ocean (Sui *et al.*, 1997). The outward phase movement is more extensive than can be explained by the expansion of the upper level stratiform clouds of mesoscale convective clusters. It signifies the spreading of the convective cloud clusters outward, probably through gravity wave propagation (e.g., Yang and Slingo, 2001; Mori *et al.*, 2004).

3.5 AUSTRALIAN SUMMER MONSOON

The Australian summer monsoon is traditionally referred to as the wet season in northern Australia since over three-quarters of the annual rainfall occurs during the summer monsoon. Because it is also closely related to the Maritime Continent monsoon, it is sometimes considered together with the Indonesian wet monsoon as one larger circulation system that covers the region from the equator to about 15°S and from 100°E to about 155°E.

3.5.1 Evolution and intraseasonal variability

The onset of the monsoon occurs typically in late December, and coincides with a rapid poleward contraction of the subtropical jet and ridge (Figure 3.18). After onset, the trade easterlies strengthen south of the monsoon trough and upper tropospheric easterlies develop to produce a deep tropical circulation with a baroclinic structure. The monsoon typically retreats by April.

Following the onset with an active wind burst, the monsoon is composed of bursts and breaks that typically last 1–3 weeks (Figure 3.19). The burst and breaks are often associated with a passage of the MJO, but the MJO is not the only source of intraseasonal variability, nor is it the trigger for every onset. Hendon and Liebmann (1990b) showed that over northern Australia the MJO signal shows up as a peak in the spectrum of the zonal wind and accounts for about 1/3 of the zonal wind variance in the 30–70-day period. Rainfall does not have a similar spectral peak

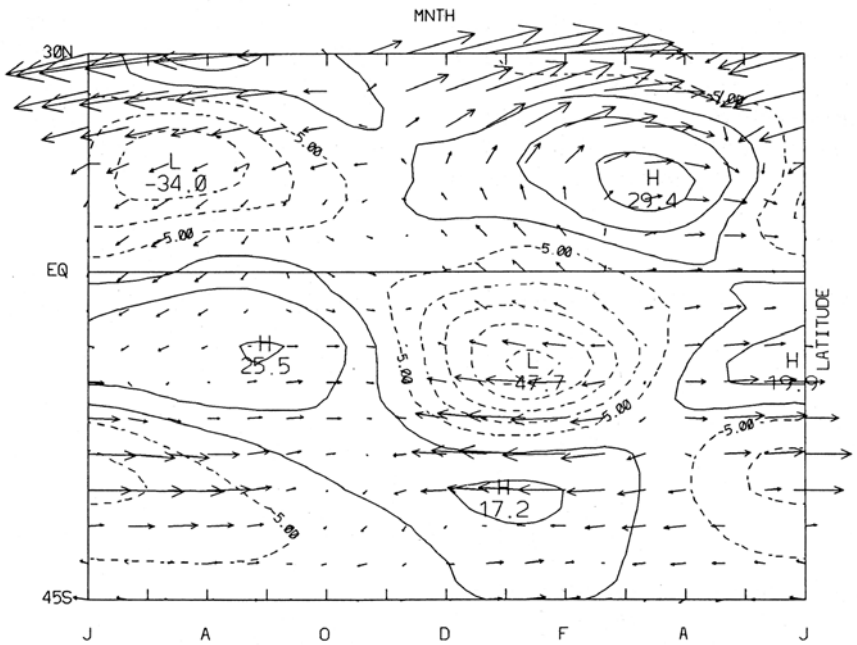

Figure 3.18. First three harmonics of the annual cycle of OLR (contours) and 200-hPa winds (vectors) averaged in the Australian sector (130°–145°E).
From Hendon and Liebmann (1990a).

within this band, although it is coherent with the zonal wind variations and leads the latter by a few days.

As will be discussed in the next section, the MJO may only play a modest role in the monsoon onset. However, a strong interannual variability exists such that during some years the MJO dominates the monsoon variability. For example, while less than 10% of the OLR convective variability can be accounted for by the MJO in the 1982/1983 monsoon, this increases to nearly 60% in the 1987/1988 monsoon. Some of this interannual variability is likely related to the interannual variation in the strength of the MJO (e.g., Hendon *et al.*, 1999).

Wheeler and Hendon (2004) used an empirical orthogonal function (EOF) analysis of the OLR and 850-hPa and 200-hPa zonal winds to separate the MJO mode into eight phases of about one week each. The structure is similar to the SVD modes in Figure 3.13 in which each of the four phases (dry, wet, and the two transitions in between) lasts about two weeks and each corresponds to two phases in Wheeler and Hendon's eight phases. They showed that suppressed conditions exist during their phases 1 and 2 (dry phase), with anomalous easterlies across and to the north of northern Australia. Active convection commences at their phase 4 (second week of the dry-to-wet transition phase), with monsoonal westerlies becoming established by their phase 5 (first week of the wet phase). An interesting tropical–extratropical teleconnection is evident during their phase 3 (first week of the dry-to-

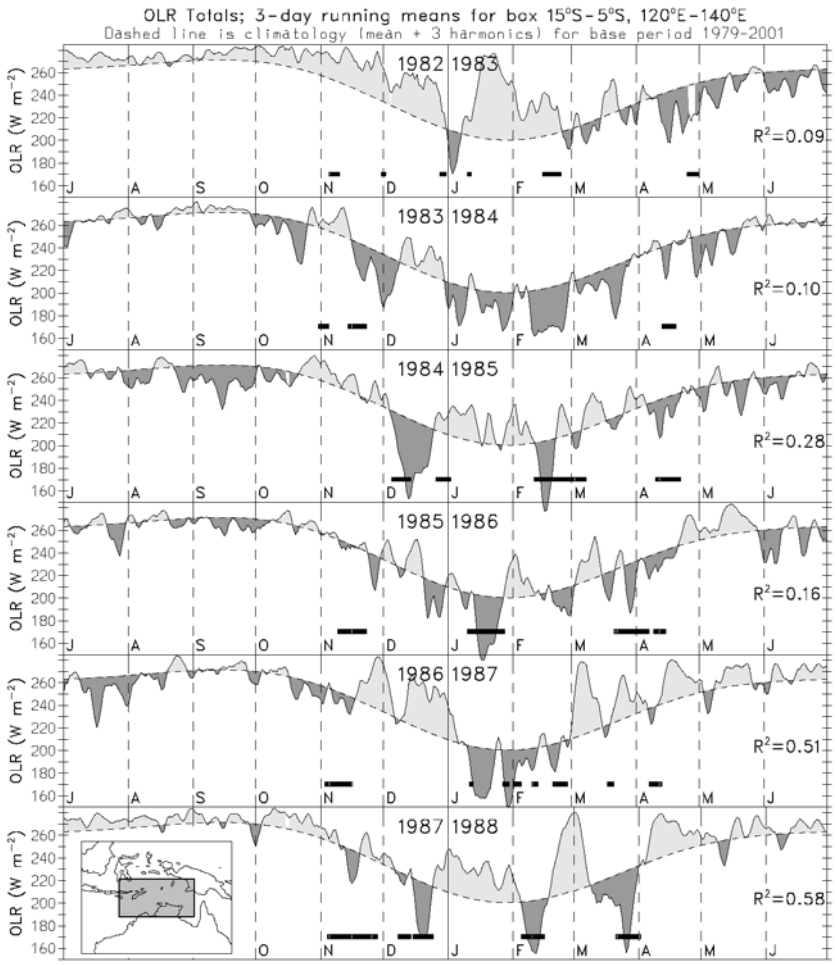

Figure 3.19. OLR averaged for the north of Australia. Dashed line is mean seasonal cycle. Heavy bars indicate periods of active convection associated with the MJO, as determined by CEOF analysis of equatorial averaged OLR and zonal wind at 850 mb and 200 mb. R^2 values represent OLR variance in the boxed region for each summer monsoon season explained by the MJO.
From Wheeler and McBride (2005).

wet transition), in which enhanced convection in south-western Australia occurs ahead of the low-level cyclone before convection becomes established to the north during their phase 4 (second week of the dry-to-wet transition). By their phase 7 (first week of the wet-to-dry transition), the active convection has moved off to the east. At their phase 8 (second week of the wet-to-dry transition), the monsoonal westerlies have decayed and suppressed conditions are re-established.

Monsoon variability is also associated with large-scale, westward propagating

disturbances (McBride and Nicholls, 1983; Davidson *et al.*, 1983; Keenan and Brody, 1988; Hendon *et al.*, 1989). Although it can be quite varied, the phase speed of the westward convective envelopes is often about the same, except in the opposite direction, as the eastward phase speed of the MJO ($\sim 5\,\mathrm{m\,s^{-1}}$). Usually the westward convection envelopes have maximum amplitude off the equator, and may be accompanied by large variations in the rotational wind as well. Such characteristics suggest that these disturbances are equatorial Rossby waves. The structure and evolution of a typical Rossby wave in the Australian region are shown in Figure 3.20 (from Wheeler *et al.*, 2000). Symmetric circulation cells are present on either side of the equator, although in individual cases such symmetry may be hard to detect. Such westward propagating waves that are detectable as far east as the Date Line have been found to lead to the development of tropical cyclones in both hemispheres (Hendon and Liebmann, 1990a; Taylor, 1998).

Another potential source of variability within the monsoon is the cross-equatorial influence of the cold surges in the South China Sea. Such influences on convection have been discussed by a number of authors (e.g., Davidson *et al.*, 1983; Love, 1985; McBride, 1987; Compo *et al.*, 1999). On the other hand, the influence at lower frequencies (MJO timescales) has been found from north-easterly flows originating in the subtropical North Pacific rather than east Asia (Sumathipala and Murakami, 1988).

3.5.2 Triggers of monsoon onset

While the monsoon onset with a switch from dry south-easterlies to wet north-westerlies is sudden, sensible heating from the ground surface, which contributes to the creation of the land–sea thermal contrast in the Australian sector, begins as early as September (Hung and Yanai, 2004). Hence, some other trigger is required to initiate the sudden onset. Possible candidates include passage of the convective phase of the MJO or other synoptic-scale tropical waves that produce moist north-westerly flow and lower tropospheric convergence (e.g., Davidson *et al.*, 1983; Hendon *et al.*, 1989), and equatorward penetration of extratropical troughs that perhaps act to destabilize the upper troposphere (e.g., Davidson *et al.*, 1983; Hung and Yanai, 2004).

Several investigators have reported that the role of the MJO on the monsoon onset is only modest (e.g., Hendon and Liebmann, 1990a; Drosdowsky, 1996). Wheeler and Hendon (2004) re-examined the relationship between monsoon onset and the state of the MJO (Figure 3.21), as defined by the eight phases described in the preceding section. When the MJO is strong, onset occurs more than 80% of the time when the MJO is in phases 4–7 (i.e., the half-cycle centered around the wet phase, when MJO low-level westerlies and broad-scale convection are in the vicinity of northern Australia) and less than 20% of the time in all the other phases (i.e., the half-cycle centered around the dry phase, when northern Australia is in the suppressed phase of the MJO). The spread of onsets from phases 4–7 covers a time window of about 20 to 30 days, which is significantly greater than the ± 4 days found by Hendon and Liebmann (1990a). Thus, it appears that the MJO limits monsoon

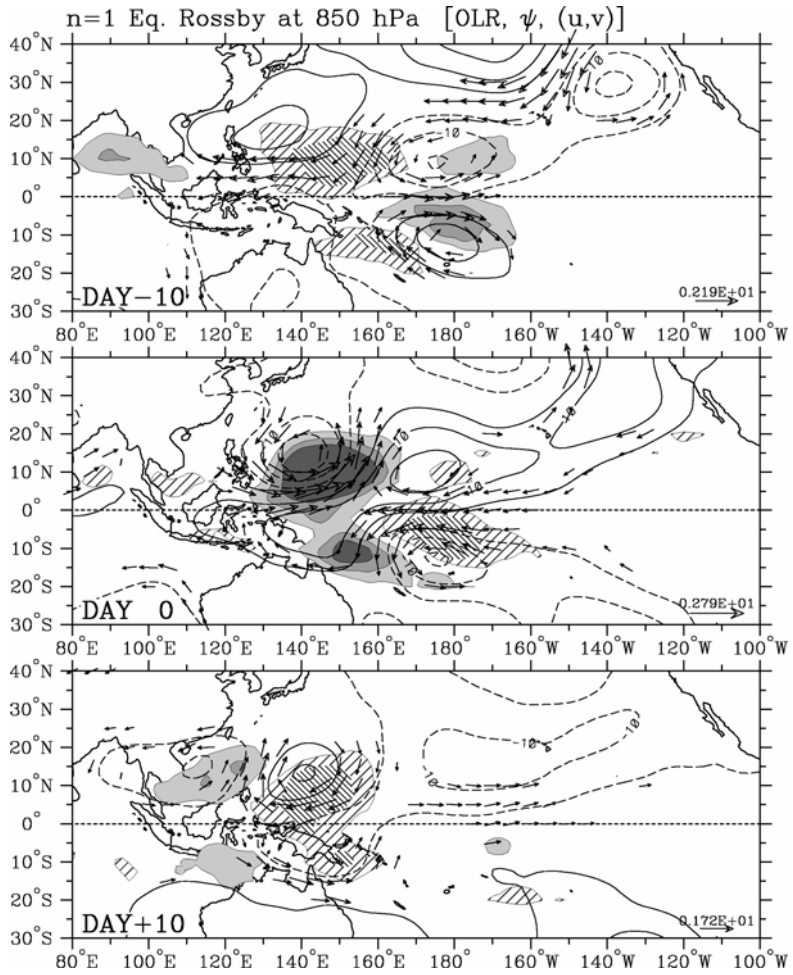

Figure 3.20. Horizontal structure of the gravest mode equatorial Rossby wave over a sequence spanning 21 days, as computed using lagged regression based on a two standard deviation anomaly in the equatorial Rossby wave filtered OLR series at 10°S, 150°E. Shading/cross-hatching shows the negative/positive OLR anomalies at the levels of −15, −10, −5, 5, and 10 W m^{-2}. Contours are streamfunctions at the 850-hPa level (interval of 5×10^5 m^2 s^{-1}), with negative contours dashed and the zero contour omitted. Vectors are the 850-hPa wind anomalies, plotted only where the local correlation of either wind component is statistically significant at the 99% level.
From Wheeler *et al.* (2000).

onset to within its active half-cycle, but the actual onset is often set by other, presumably shorter timescale phenomena.

Another possible trigger for the monsoon onset is the mid-latitude influence. Davidson *et al.* (1983) presented evidence that the onset during the Winter MONEX was heavily influenced by the synoptic-scale weather disturbances to the south and

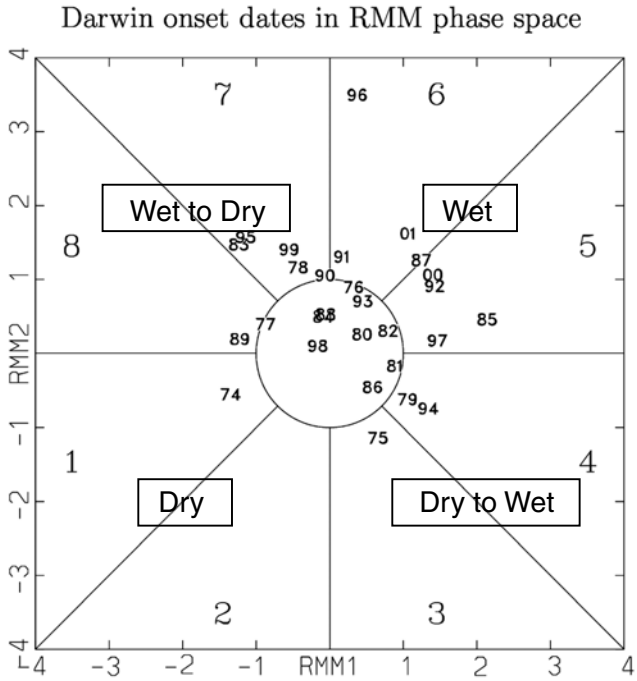

Figure 3.21. Onset date each year as a function of the eight phases of the MJO as defined by Wheeler and Hendon (2004). Onset dates are based on the daily deep-layer mean zonal wind, at Darwin, Australia as given by Drosdowsky (1996). The phase names given in small rectangular boxes correspond to those in Figure 3.13.
Adapted from Wheeler and Hendon (2004).

west of Australia. Danielsen (1993) proposed that mid-latitude cold fronts south of Australia spread cold air northward across the continent, which in turn interacts with the continental-scale sea breeze over northern Australia and triggers convection. Such a description bares much similarity to that for the South China Sea cold surges (e.g., Love, 1985).

Kawamura *et al.* (2002) proposed that onset involves an air–sea feedback, in much the same fashion as discussed by Nicholls (1981), Hendon (2003), and Wang *et al.* (2003) in the context of the SST evolution north of Australia during ENSO. They suggested that the initial sensible heating of the continent acts to drive shallow north-westerly onshore flow, which superposes the mean easterly trades to the north of Australia. Thus, the surface wind speed is reduced, which leads to reduced latent heat flux and ocean entrainment mixing, and hence increased local SST. If the low-level air is in equilibrium with higher SST, then the surface pressure will be lower, which promotes stronger north-westerly flow (i.e., akin to a Gill (1980) response to an imposed heat source). The proposed cycle would further reduce the wind speed, increase the SST, and lead to enhanced convective instability. The monsoon onset can then occur with an additional trigger, for instance the passage of the MJO.

3.5.3 Modulation of synoptic weather

Hendon and Liebmann (1990b) showed that enhanced transient kinetic energy at Darwin accompanies the wet phase of the MJO, along with enhanced rainfall variance. Although the enhanced kinetic energy occurs throughout the troposphere, the maxima are around 850 hPa and 100 hPa, which is consistent with the baroclinic structure common to many tropical systems. Liebmann *et al.* (1994) also showed a roughly 2 : 1 modulation of tropical cyclones between wet and dry MJO phases in the Indian and western Pacific sectors (see also Hall *et al.*, 2001). The hypothesis for such a modulation is that the large-scale MJO anomalies alter the climatologically favorable factors for tropical cyclone development by increasing low-level cyclonic vorticity and reducing vertical wind shear during the active MJO phase (Gray, 1979).

Interestingly, the modulation of tropical cyclone numbers by lower frequency variability is not restricted to the MJO band. Hence any form of large-scale variability with a timescale longer than that of the tropical cyclones may alter the dynamical factors favorable for cyclogenesis and influence the tropical cyclone activity.

Wheeler and Hendon (2004) also observed modulation of extreme continental rainfall by the MJO during the summer monsoon. They found a contemporaneous relationship between the highest quintile of weekly rainfall across Australia and the phase of the MJO. The normal probability of a weekly rainfall total in DJF being in the upper quintile is, by definition, 20%. Across the 'Top End' region (around Darwin), the probability varies from less than 12% in the dry phase of MJO to greater than 36% in the wet phase, which represents more than a tripling of the likelihood of extreme rainfall from the dry to wet phase of the MJO.

3.6 INTERANNUAL VARIATIONS

3.6.1 East Asian winter monsoon

The east Asian winter monsoon (EAWM) undergoes substantial variations on interannual and interdecadal timescales (Figure 3.22). A strong winter monsoon is characterized by a stronger Siberian–Mongolian High, Aleutian Low, and low-level north-easterlies along the Russian coast, a deeper mid-tropospheric trough, and an enhanced upper level jet (Jhun and Lee, 2004). The EAWM tends to be weaker in El Niño years and stronger in La Niña years (e.g., Zhang *et al.*, 1996; Tomita and Yasunari, 1996; Ji *et al.*, 1997; Wang *et al.*, 2000). Wang *et al.* (2000) suggested that warming of the equatorial eastern Pacific surface tends to induce a weak EAWM through an anomalous anticyclonic circulation over the western North Pacific. Cooling of the equatorial eastern Pacific tends to lead to opposite effects. They showed that the western North Pacific anomalous circulation is maintained by positive air–sea interaction in the presence of a north-easterly trade wind. It has a baroclinic structure but is confined in the lower troposphere. Some studies (Li, 1990; Xu and Chan, 2001; Chan and Li, 2004) also suggested that the EAWM anomalies

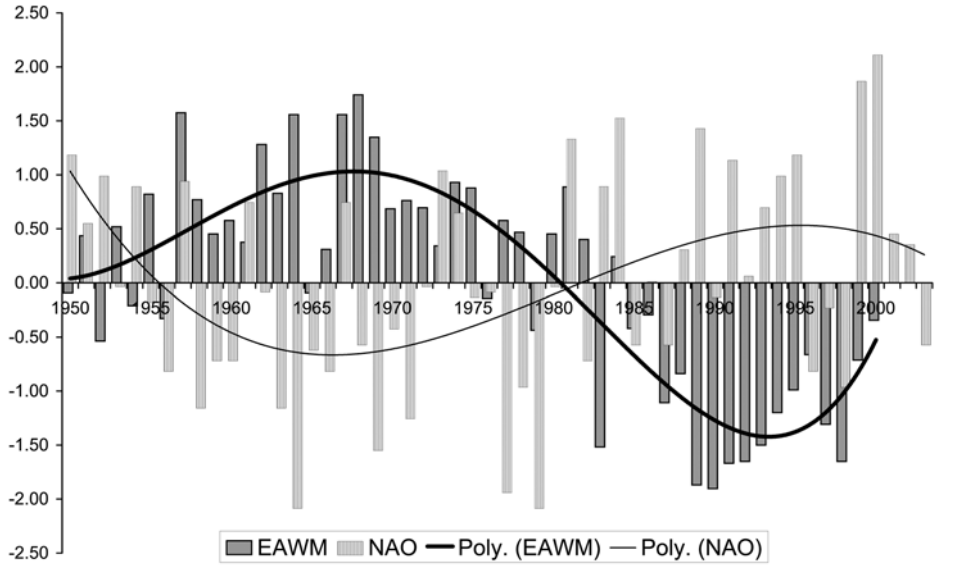

Figure 3.22. Time series of EAWM (dark shading bars) and NAO (light shading bars) indices. The thick and thin curves are the fourth order polynomial fit of the EAWM and NAO time series, which represent the decadal variations. EAWM index is defined as SLP averaged over 40°N–60°N, 70°E–120°E.
Data curtsey of Qiyuan Guo.

may trigger SST anomalies in the equatorial eastern Pacific by inducing anomalous convection and exciting anomalous westerlies in the equatorial western Pacific. Tomita and Yasunari (1996) suggested that the EAWM plays an important role in the biennial oscillation of the ENSO–monsoon system through wind evaporation feedbacks. However, Wang *et al*. (2004) pointed out that the impacts of ENSO on the EAWM are more significant while an anomalous EAWM is not a sufficient condition for ENSO occurrence.

SST in the western North Pacific and the extratropical North Pacific may also play a role in the interannual variations of the EAWM (Kitoh, 1988; Chan and Li, 2004). Yang *et al*. (2002) found that the east Asian jet steam is coupled to a teleconnection pattern spanning the Asia–Pacific–North America sector. A stronger east Asian jet steam is associated with a deeper Aleutian Low and east Asian trough and a stronger east Asian winter monsoon. They pointed out that the teleconnection associated with the east Asian jet steam differs significantly from the ENSO-related teleconnection. The former has stronger impacts on Asian and Pacific climate and is associated with extratropical North Pacific SST, instead of the tropical central-eastern Pacific SST.

Snow cover over the Eurasian continent is another factor influencing the EAWM. Several observational studies showed that positive snow cover/depth anomalies over Siberian, north-eastern China, and far-eastern Russia during the

autumn–winter season lead to a strong winter monsoon (e.g., Watanabe and Nitta, 1999; Clark and Serreze, 2000; Jhun and Lee, 2004). This is supported by general circulation model simulations, which showed that extensive snow cover induces a stronger than normal Aleutian Low and Siberian–Mongolian High, enhanced east Asian jet, and colder lower troposphere, and leads to a stronger winter monsoon (Watanabe and Nitta, 1998; Kumar and Yang, 2003; Gong *et al*., 2003). The impacts of snow cover and SST on the northern winter extratropical climate were compared in Kumar and Yang's (2003) simulation. They found that the atmosphere and the underlying snow form a positive interaction that influences the lower tropospheric temperature and circulation. The snow cover anomalies affect the atmospheric circulations through the variations of the low boundary layer properties (such as surface albedo). In contrast to the top-down influence of the tropical SST on the extratropical circulation through teleconnections, the influence of snow cover is more direct and confined to the lower troposphere.

A noteworthy interdecadal variation of the EAWM is the apparent weakening of the EAWM since the late 1980s (Figure 3.22). This weakening has been noticed by many investigators (e.g., Koide and Kodera, 1999; Watanabe and Nitta, 1999; Nakamura and Yamagata, 1999; Nakamura *et al*., 2002; Jhun and Lee, 2004) and also reported prominently in Chinese literature (Chapter 4). A remarkable signal that emerges is the possible relationship between the decadal change of the EAWM and the North Atlantic Oscillation (NAO) (Wu and Huang, 1999; Li and Li, 2000; Wu and Wang, 2002), which has a phase change in the late 1980s (Figure 3.22). The NAO is associated with changes of surface temperature and snow cover over the Eurasian continent; therefore, it may affect the EAWM through thermal advection. In addition, Watanabe (2004) suggested that the convergence anomaly over the Mediterranean Sea accompanying the NAO may induce an upper level wave train and cause surface warming over east Asia. Some studies also suggested that snow extent anomalies over Siberia may induce a phase change of NAO/AO (Arctic Oscillation) and the variations of EAWM, and cause a simultaneous correlation between the two on interdecadal timescales (Watanabe and Nitta, 1999; Cohen and Entekhabi, 2001; Gong *et al*., 2002; Jhun and Lee, 2004).

3.6.2 Relationship of the Maritime Continent/Australian monsoon with ENSO

Many investigators have noticed the considerable influence of the ENSO on the Indonesian and Australian rainfall (e.g., Braak, 1919; Nicholls, 1981, 1985; McBride and Nicholls, 1983; Hastenrath, 1987a; Ropelewski and Halpert, 1987; Allan, 1991; Nichol, 1998; Webster *et al*., 1998; McBride, 1998; Ooi, 1999; Haylock and McBride, 2001; Hamada *et al*., 2002; Hendon, 2003; McBride *et al*., 2003), but the impact is very weak during the boreal winter season (Figure 3.23 from McBride and Nicholls, 1983; see also Holland, 1986). The Australian summer monsoon rainfall is modestly correlated with ENSO (~ -0.4), but the bulk of this negative correlation comes from a strong negative correlation in the transitional season (Nicholls *et al*., 1982). Once the monsoon is active, the correlation with ENSO is very low.

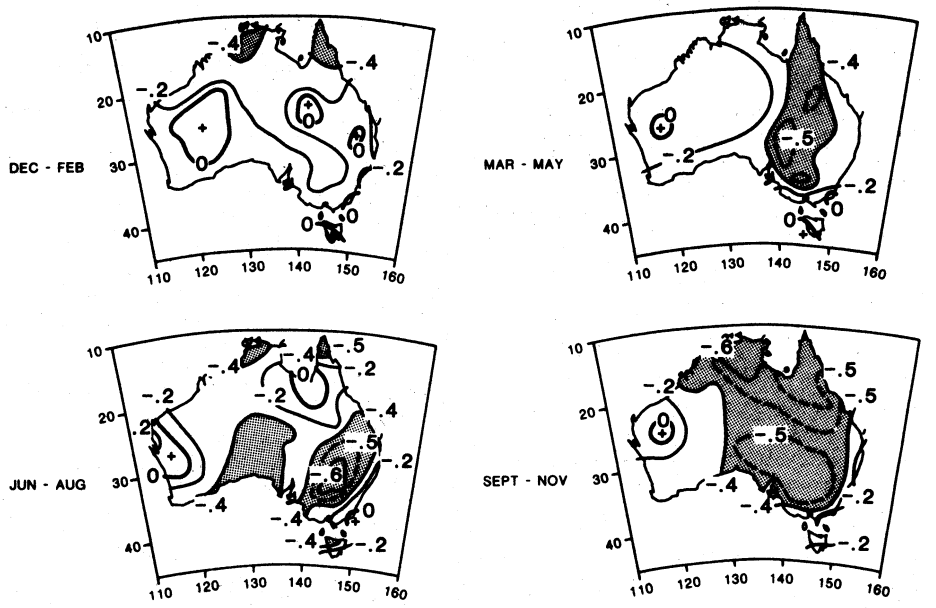

Figure 3.23. Simultaneous correlation between Darwin pressure and district rainfall for the four seasons (December–February, March–May, June–August, September–November). Data from 1932–1974.
From McBride and Nicholls (1983).

The loss of correlation is also reported between Indonesian wet monsoon season (boreal winter) rainfall and ENSO (e.g., McBride and Nicholls, 1983; Ropelewski and Halpert, 1987; Kiladis and Diaz, 1989; Haylock and McBride, 2001; Hendon, 2003; McBride *et al.*, 2003; Aldrian *et al.*, 2003; Chang *et al.*, 2004a). Haylock and McBride (2001) pointed out that the spatial coherence in the Indonesian wet season rainfall is low and therefore no single predictor is likely to explain a substantial proportion of rainfall variation over the entire region. Chang *et al.* (2004b) showed that the strong effect of the wind–terrain interactions over the Maritime Continent region may lead to local rainfall–ENSO relationships that vary among different subregions during northern winter, when the region is affected by cold surges from the north, Indian Ocean zonal wind anomalies from the west, and cross-equatorial flow from the south. They showed that during 1979–2002 the correlations between DJF rainfall and Nino 3 SST (Figure 3.24) are mostly negative over a significant part of the Maritime Continent and vicinity except near the Sumatra and Malay Peninsula (SMP, including the western sections of Java and Borneo), where the correlations range from zero to weakly positive. This area has been shown to have low correlation with ENSO in other seasons as well (Ropelewski and Halpert, 1987; Aldrian *et al.*, 2003). Thus, the low correlations between Indonesian wet monsoon rainfall and ENSO may be due in part to the averaging of rainfall in two regions with opposite characteristics. They also showed that there

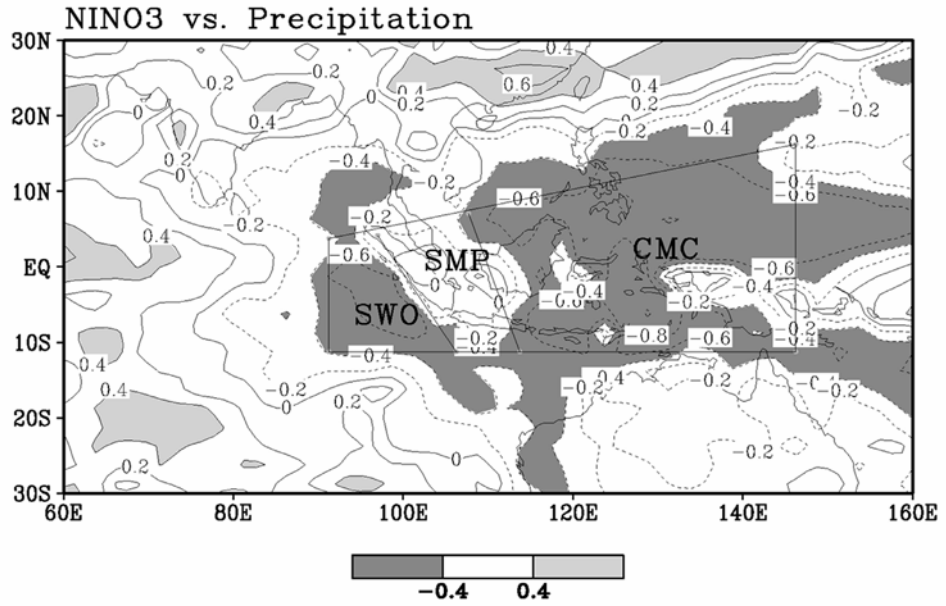

Figure 3.24. Correlations of 1979–2002 CMAP rainfall with Niño 3 SST. Areas above the 5% significance level are shaded. The following rainfall index regions are delineated: SMP (Sumatra–Malay Peninsula); SWO (south-west oceanic area south-west of Sumatra); and CMC (central Maritime Continent).
From Chang *et al.* (2004b).

was an interdecadal change around the late 1970s with an overall trend showing that the rainfall has been more negatively correlated with the ENSO in recent decades (Table 3.1). However, the correlations remain lower than those of the dry (boreal summer) and transition (boreal autumn) seasons. This is especially so for January, which has consistently insignificant correlations for all regions and decadal periods.

The onset of the Australian summer monsoon, as defined by the date of the first 250 mm of rainfall at Darwin, is negatively correlated with the ENSO (Nicholls *et al.*, 1982). Because of strong persistence of ENSO anomalies from June through November, onset of the Australian summer monsoon is predictable some months ahead. But, total wet season rainfall is not correlated with onset date (Table 3.2). Interestingly, onset date as defined by the first 250 mm of rainfall (which is about 1/4 of the wet season total) is three weeks earlier than onset as determined by the large-scale rearrangement of the tropical circulation. Thus, the strong negative correlation of El Niño with onset date and transitional season rainfall occurs before the Australian summer monsoon circulation is established (i.e., when northern Australia is still in a trade wind regime).

Probably because of persistence of ENSO anomalies from June–November, onset date of the monsoon is also related to the strength of the previous Indian monsoon. A weak Indian summer monsoon tends to occur during a developing

Table 3.1. Correlation between Niño 3 SST and area-averaged Indonesian station rainfall for western Indonesia (west of 112°E), eastern Indonesia (east of 112°E), and all Indonesia. Values above the 1% significance are in italic bold. The significance of all other values is below the 7.5% level.
From Chang *et al.* (2004b).

Winter (DJF)	1950–1978	1979–1997	1950–1997
Western Indonesia	***0.49***	0.26	0.22
Eastern Indonesia	−0.25	***−0.62***	***−0.44***
All Indonesia	0.16	−0.30	−0.17

Table 3.2. Correlation between the onset indices and Darwin wet season rainfall. The last row shows the correlation between June–August pressure and seasonal rainfall. (The 5% significance level occurs at a correlation of 0.374.)
From Nicholls *et al.* (1982).

	Darwin rainfall September–May	September–November	December–May
Date of 1st 10 mm	−0.267	−0.477	−0.084
Date of 1st 50 mm	−0.383	−0.707	−0.111
Date of 1st 100 mm	−0.289	−0.817	0.034
Date of 1st 250 mm	−0.394	−0.905	−0.040
Date of 1st 500 mm	−0.520	−0.819	−0.209
Darwin pressure: June–August	−0.335	−0.661	−0.079

El Niño, which is then followed by a late onset of the Australian summer monsoon. Joseph *et al.* (1991) pointed out that the relationship between the strength of Indian monsoon and onset date of the Australian summer monsoon seems to hold even in the absence of ENSO. They suggest that the Indian summer monsoon is capable of driving SST variations (warm in the western Indian Ocean and cold to the north of Australia), which subsequently act to delay the onset of the Australian monsoon. Chang and Li (2000) also proposed, in a tropical biennial oscillation theory, that the Indian summer monsoon affects the subsequent Australian monsoon through atmosphere–ocean interactions over the tropical western Pacific and Indian Ocean, with the tropical eastern Pacific SST acting only passively. Such possible behavior needs to be explored in coupled models with the ENSO artificially suppressed.

Hung *et al.* (2004) emphasized that the Australian summer monsoon is not related to the following Indian monsoon, which reflects both the lack of persistence of ENSO after December and lack of simultaneous relationship of the Australian summer monsoon and ENSO. They argued that the Australian summer monsoon acts to disrupt the ENSO cycle.

Hendon (2003) examined the seasonal evolution of SST anomalies through the ENSO cycle (Figure 3.25, from Hendon, 2003) to gain insight into why the ENSO's

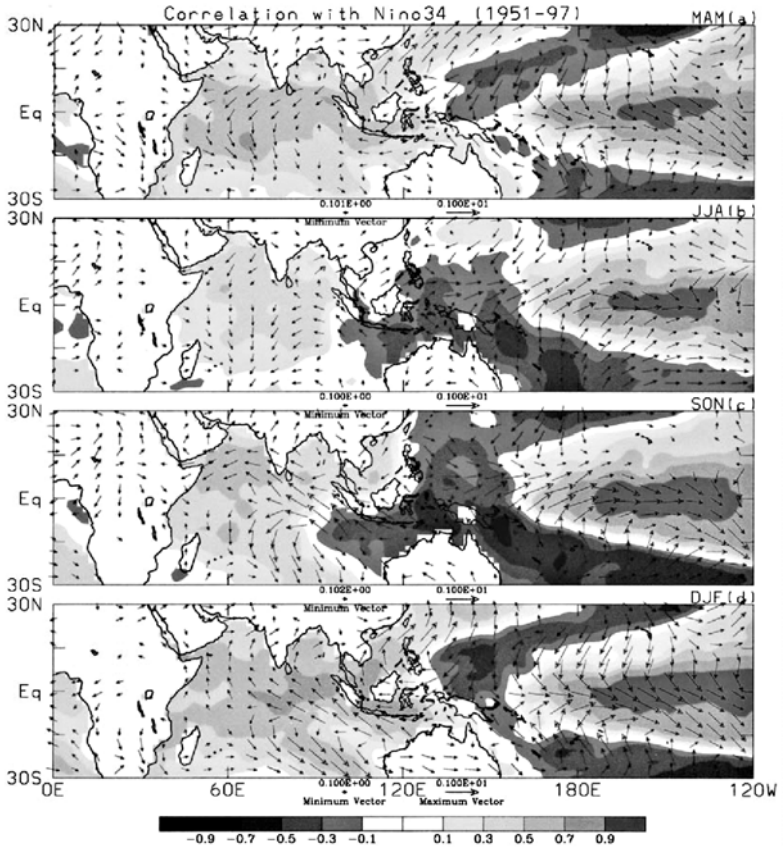

Figure 3.25. Correlation of Niño 34 SST index with SST and surface winds for the (a) MAM, (b) JJA, (c) SON, and (d) DJF seasons.
From Hendon (2003).

influence on the Australian summer monsoon wanes at the peak of the monsoon. In the southern winter (JJA) and spring (SON) of an El Niño year, SSTs are cold to the north of Australia and winds are anomalously easterly. These cold SSTs reinforce anomalous subsidence driven by the warm equatorial SSTs in the central and eastern Pacific. Hence, dry conditions in northern and eastern Australia tend to prevail in winter and spring. However, in DJF (summer), despite persistence of warm anomalies in the Pacific and the associated easterly anomalies to the north of Australia, the cold SSTs to the north of Australia disappear. The reinforcement they provide to the remotely forced subsidence thus ends.

The evolution of the SST anomalies to the north of Australia has been postulated to stem from seasonally varying air–sea feedback in the region (Nicholls, 1981; Chang and Li, 2000; Hendon, 2003; Wang *et al.*, 2003). During the winter (JJA) and spring (SON), the region experiences trade easterlies. In the mean, they act to elevate

the thermocline in the eastern equatorial Indian Ocean and to promote upwelling along the Java/Sumatra coast. In other words, the trade easterlies produce conditions favorable for air–sea coupling. Anomalous easterlies (for instance, driven remotely by El Niño in the Pacific) at this time of year, then would act to (1) increase the total wind speed (easterly anomaly acting on an easterly basic state) thereby producing surface cooling through increase latent and sensible heat flux and (2) further elevate the thermocline in the east and promote enhanced upwelling on the Java/Sumatra coast thereby producing more surface cooling in the eastern Indian Ocean. Thus, a positive feedback is produced with colder SST anomalies acting to raise surface pressure in the eastern Indian Ocean and producing stronger easterly anomalies. Once the Australian summer monsoon onsets and the mean winds become westerly, the thermocline in the east deepens and mean upwelling along the Java/Sumatra coast ceases. Anomalous easterlies now acting on a westerly basic state will decrease the total wind speed, thereby acting to warm the surface. Hence, together with the lack of communication between the subsurface anomalies and the surface (because the mean thermocline is too deep and coastal upwelling is weak), the easterly anomalies will produce a negative feedback. The positive feedback during the winter and spring and negative feedback during summer is offered as an explanation for the strong correlation between onset date and El Niño but for a weakening of the negative correlation between El Niño and northern Australia rainfall once the monsoon onsets.

Other sources of interannual variability of the summer monsoon include seasonal variations of MJO activity. Hendon *et al.* (1999) show that years of strong MJO activity tend to occur when convection over Australia is suppressed (i.e., years of strong MJO activity tend to be years with a weak summer monsoon). Seasonal MJO activity shows little relationship with ENSO (or any other SST anomalies). Hence, the seasonal rainfall variance accounted for by the level of MJO activity is independent of that accounted for by ENSO. However, as the level of MJO activity is not obviously related to SST boundary forcing (Hendon *et al.*, 1999; Slingo *et al.*, 1999), it is not clear that the MJO-induced component of seasonal monsoon variability will be predictable.

3.6.3 Long-term variability of Australian summer monsoon

Besides exhibiting strong interdecadal variability, monsoon rainfall in northern Australia has been increasing in the heart of the monsoon (north-west and north central Australia) and decreasing on the east coast (Figure 3.26, from Smith, 2004). On the broadscale, the monsoon thus can be considered to be strengthening. Wardle and Smith (2004) suggest that this upward trend of rainfall is driven by the concomitant upward trend in surface temperature across the continent, which acts to increase the land–sea temperature contrast, thereby lowering surface pressure across the continent, resulting in a stronger monsoon. However, associated with the upward trend in rainfall, surface pressure is observed to be increasing and the

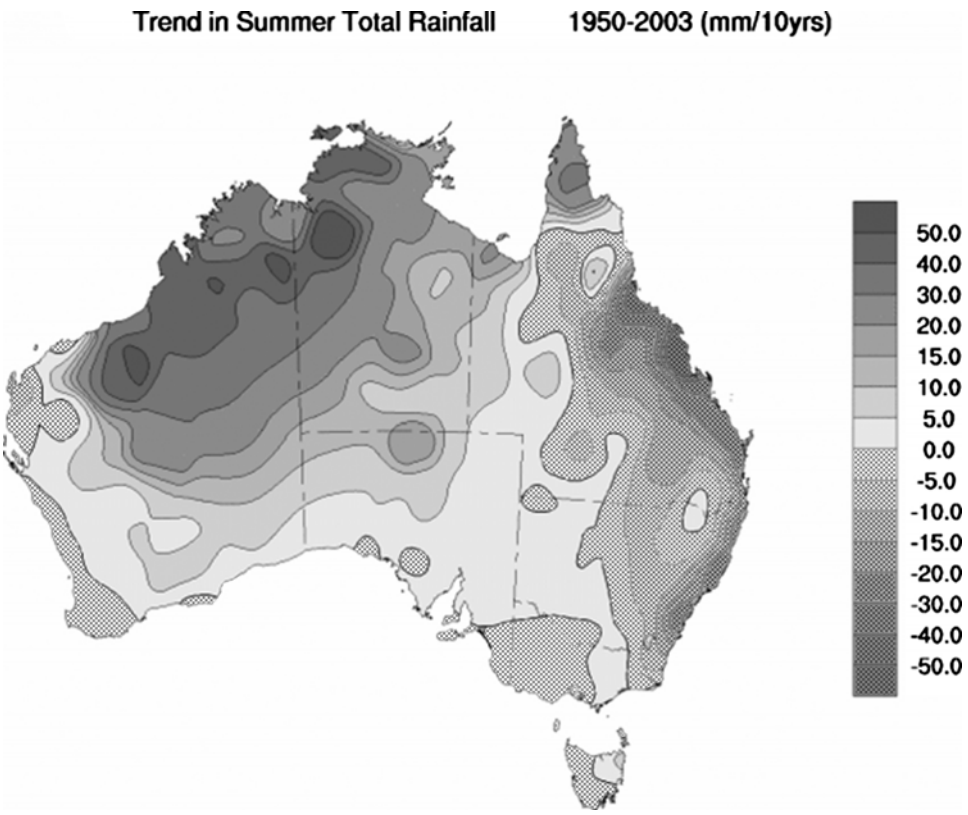

Figure 3.26. Australian summertime (DJF) rainfall trend for the period 1950–2003.

Southern Oscillation Index (standardized Tahiti minus Darwin SLP) has been decreasing (Trenberth and Hurrell, 1994). On interannual timescales, higher pressure at Darwin is associated with El Niño conditions in the Pacific, negative Southern Oscillation Index (SOI), and reduced rainfall at Australian longitudes. Thus, the positive trend in SLP together with the positive trend in rainfall is counter to the relationship anticipated from interannual behavior. The rainfall trend is negative on the east coast and does appear to be negative to the north of Australia, for instance across parts of Indonesia (Climate Change, 2001). And, when the broader scale Australian/Maritime Continent monsoon is considered (i.e., wet season rainfall over land including the Philippines and Malaysia), a decreasing trend in monsoon strength has been observed (Chase *et al*., 2003). Thus, the trend in the broadscale monsoon rainfall and surface pressure in the west Pacific is consistent with behavior associated with interannual variability. The opposite behavior across north-west and north central Australia is intriguing and warrants further investigation.

3.7 ACKNOWLEDGEMENTS

We wish to thank Mong-Ming Lu, Wing-Mo Leung, Matthew Wheeler, John McBride, and Richard Johnson for discussions; Hway-Jen Chen and Ching-Hwang Liu for help in graphics, and Robert Haney for reading the manuscript. This work was supported in part by the National Oceanic and Atmospheric Administration under grant NA01AANRG0011, the Office of Naval Research Marine Meteorology Program, and the National Science Foundation under grant ATM-010113.

Part Two

4

Synoptic systems and weather

Yihui Ding and D. R. Sikka

4.1 MAJOR RAINY SEASONS

4.1.1 Rainy seasons of the Asian monsoon region and the onset of the summer monsoon

The annual cycle of the Asian monsoon system has been customarily divided into two distinct phases: the 'wet' and 'dry' phases (Webster *et al*., 1998). The wet phase refers to the rainy season during which warm, moist, and very disturbed wind blows inland from the warm tropical oceans (the Indian and Pacific Oceans). The dry phase refers to the other half of the year when winds bring cool and dry air from the winter Asian continents. The Asian monsoon region assumes the most distinct variation of the annual cycle and the alternation of dry and wet seasons which is in concert with the seasonal reversal of the monsoon circulation features (Qian, 2000). The wet season in general begins from May and ends in October, lasting for about six months, and the dry season spans from November to April of the next year. However, for different parts of the Asian monsoon region, the durations of dry and wet seasons may be different, depending on their climate regions and the degree of effect of the Asian monsoon. For example, in south Asia, the dry and wet seasons are very well-defined while in east Asia, four seasons can be evidently perceived, although the dry and wet seasons are main modes of the annual march of the precipitation in this region. In mid-latitude regions of east Asia, such as central China along the Yangtze and Huaihe River basins and Korean Peninsula, they are not generally included in the dry and wet alternative regions because the wet period for theses regions is shorter than one month (Bao, 1987). These short rainy periods mainly occur during prevalence of the summer monsoon in these regions.

The total rainfall amount and rainfall intensity show a remarkable difference between dry and wet seasons, with a quite large annual range of precipitation that measures the amplitude of annual variation. The largest annual range exceeding

B. Wang (ed.), *The Asian Monsoon*.

17 mm day^{-1} (equivalent to a total summer precipitation greater than 1,530 mm) is found over the sea in the following areas: the central Bay of Bengal, the south-eastern Arabian Sea, the Philippine Sea, and the South China Sea (SCS; Wang and Lin, 2002). These regions with the largest annual range tend to coincide with regions of maximum summer rainfall. The ratio of summer to annual rainfall is used to delineate the relative importance of rainfalls in rainy or wet seasons with respect to annual rainfall. A large ratio implies a heavy summer rainy season vs. a dry winter. Over the Indian monsoon region and north-east continental Asia, the ratio exceeds 85%. Over the Philippine Sea, the ratio is also relatively high (over 60%). The level of 55% provides a seasonal demarcation for the equatorial perennial and monsoon rainy seasons.

Although there is a clear distinction in the characteristics of the rainy season and low-level wind variation among India, east Asia and the western North Pacific, the three components are interlinked (Tao and Chen, 1987; Wang and Lin, 2002). On the one hand, the Indian summer monsoon (ISM) and the east Asian summer monsoon (EASM) are closely related through significant exchange and transport of moisture and heat between them, and the teleconnection effect (Ding, 1994). On the other hand, the seasonal variation demonstrates a coupling between the EASM and western North Pacific summer monsoon (WNPSM) in June and July as manifested by two sudden changes. In mid-June, the monsoon rains burst simultaneously in the vicinity of the Philippines and along the Meiyu front, and in late July, when the monsoon rains start in the western North Pacific, the rainy season in north China reaches its height.

The onset of the Asian summer monsoon is a key indicator characterizing the abrupt transition from the dry season to the rainy season and subsequent seasonal march. Numerous investigators have studied this problem from the regional perspective. It is to some extent difficult to obtain a unified and consistent picture of the climatological onset dates of the Asian summer monsoon in different regions due to differences in data, monsoon indices, and definitions of monsoon onset used in these investigations. Recently, Wang and Lin (2002) have identified two phases in the evolution process of the Asian summer monsoon. The first phase or the onset phase begins with rainfall surges over the SCS in mid-May, which establishes a planetary-scale monsoon rain band extending from the south Asian marginal seas (the Arabian Sea, the Bay of Bengal, and the SCS) to the subtropical western North Pacific (WNP). At this stage, the impacts from mid-latitude and regional sea surface temperature (SST) are also important (Chang *et al.*, 1995; Chu *et al.*, 1997a; Chu *et al.*, 1997b). The second phase of the Asian monsoon onset is characterized by the synchronized initiation of the Indian rainy season and the Meyu/Baiu in early to mid-June. The peak rainy seasons tend to occur primarily in three stepwise phases: in late June over the Meiyu/Baiu regions, the northern Bay of Bengal, and the vicinity of the Philippines; in late July over India and northern China; and in mid-August over the tropical WNP (10°–22°N, 120°–160°E). The rainy season retreats southward in east Asia during August and September while the ISM and the WNPSM withdraws southward after mid-September. Ding (2004) has summarized the climatological dates of the onset of the Asian summer monsoon in different regions based

on various sources by dividing the whole onset process into four stages. (1) Stage 1 (late in April or early in May) – the earliest onset is often observed in the central Indo-China Peninsula late in April and early in May, but in some cases, the onset may first begin in the southern part or the western part of the Indo-China Peninsula. (2) Stage 2 (from mid to late May) – this stage is characterized by the areal extending of the summer monsoon northward, up to the Bay of Bengal, and eastward, down to the SCS. (3) Stage 3 (from the first 10 days to the second 10 days of June) – this stage is well known for the onset of the ISM and the arrival of the east Asian rainy season such as the Meiyu over the Yangtze River basin and the Baiu season in Japan. The onset over the Arabian Sea and the western coast of the Indian subcontinents is first observed, due mainly to the enhancement of the cross-equatorial airflow off the Somali coast and the development of the onset vortex in the central and northern Arabian Sea (Krishnamurti *et al*., 1981b; Ding, 1981). (4) Stage 4 (the first or second ten days of July) – the summer monsoon at this stage can advance up to north China, the Korean Peninsula (so-called Changma rainy season), and even north Japan. So, the onset of the east and south-east Asian summer monsoon and the south Asian summer monsoon are closely interrelated in the context of the Asian summer monsoon. However, the earliest onset of the Asian summer monsoon occurs over the Indo-China Peninsula and the SCS.

The Asian summer monsoon plays a crucial role in moisture transport and supply of precipitation in this region. In addition, the moisture transport in this region is a requirement of the moisture and water balance over the Asian monsoon region. The moisture source and sink distribution in the period of June–August indicates that most of the Asian monsoon region is a moisture sink (i.e., precipitation has a surplus over evaporation). The major regions of moisture sink are located in the Bay of Bengal, the western Indian Peninsula, the SCS, and south China, consistent with the maximum precipitation regions. The regions of moisture source are located in the Arabian Sea, the coastal area of east Africa, and the southern Indian Ocean. Therefore, much of the moisture supply available for precipitation in the Asian summer monsoon region comes from the southern hemisphere, implying the special importance of the interhemispheric moisture transport. The most remarkable moisture channel originates in the southern Indian Ocean, crossing the equator near the Somali coastal region, flowing to the Arabian Sea, the Bay of Bengal, and the SCS. From there, the moisture transport continuously flows northward into east Asia.

The secondary moisture channel comes from the southern and western periphery of the subtropical high over the West Pacific. These two moisture channels merge into a single one in the SCS and the east Asian region. The pattern of the moisture flux divergence is very similar to the patterns of precipitation and moisture source and sink. The strongest moisture convergence is located in the Bay of Bengal, most of the Indian Peninsula, the Indo-China Peninsula, the SCS, east China, and north-east Asia. Simmonds *et al*. (1999), utilizing the European Centre for Medium-Range Weather Forecasts (ECMWF) data sets, have analyzed the climatological fields of moisture transport and divergence in the Asian monsoon region. Their results are basically similar to those described here.

It is very interesting to study regional moisture budgets prior to and after the onset of the SCS summer monsoon. Before the onset of the SCS summer monsoon, the interhemispheric moisture transport is rather weak and even southward. The northward moisture transport across the northern boundaries of various regions is generally weak, except for the regions of the Indo-China Peninsula and the SCS. The moisture sinks occur in the regions of the Bay of Bengal, the Indo-China Peninsula and south China, where enhanced precipitation may be observed. After the onset the whole picture of moisture transport and budget rapidly changes and becomes well-organized (Ding and Sun, 2002). The cross-equatorial flow has its maximum moisture transport in the western part of the equatorial Indian Ocean. The second maximum moisture transport is located in the equatorial east Indian Ocean. In the south Asian and south-east Asian monsoon regions, one may see consistent eastward moisture transport, all the way to the SCS. The moisture sinks from the Indian Peninsula to the SCS are consistent with the major observed precipitation regions, with the Bay of Bengal being the largest.

The northward moisture transport through the northern boundaries has its maximum in the region of the Bay of Bengal. The SCS takes second place. However, if one combines together the moisture transport coming from the Indo-China Peninsula and the SCS, the northern moisture transport into the east Asian region will come to $22.3 \times 10^6\,\mathrm{Kg\,s^{-1}}$, which obviously exceeds the northward transport through the Bay of Bengal. This fact implies the critical role of the moisture transport from the SCS in the precipitation over east Asia.

Below, we will further illustrate the major regional characteristic features of the rainy seasons of the three subsystems of the Asian–Pacific monsoon region.

4.1.2 The south Asian monsoon region

The south Asian monsoon system, through forming a part of the vast Asian monsoon system, has several peculiarities of its own and yet interacts in many ways with the east Asian and the WNP monsoon systems. The summer monsoon season of south Asia (June to September), also known as the south-west monsoon, is the main rainy season of the region and is therefore paramount to the sustenance of its agricultural productivity.

For India as a whole, nearly 78% of the annual rainfall is produced in the summer monsoon season. However, the rainfall in the monsoon season over the homogenous southern peninsular of India contributes by only about 60% to the annual mean, and a significant amount (nearly 30% of the annual) also occurs in the postmonsoon season or the north-east monsoon rainy season. For annual as well as monsoon season rainfall, the two prominent high rainfall belts due to orographic effects are: (i) off the west coast of India and (ii) along north-east India and the foothills of the sub-Himalayan ranges. There is a general decrease of rainfall from east to west in central India and along the Gangetic plains such that the rainfall is reduced to less than one-third of its magnitude over the Gangetic west Bengal in the east to the arid regions of west Rajasthan, Saurashtraw, and Kutch in the west.

Pakistan mostly lies in an arid zone except for its northern foothills where significant rainfall occurs in the winter and premonsoon seasons. The monsoon season contributes by nearly 53% to the annual rainfall. Orographic barriers are quite important to rainfall distribution. The northern hill ranges in the western Himalayas enhance the rainfall during the monsoon, winter, and premonsoon seasons. However, the monsoon rainfall is hardly able to reach Baluchistan Province in the west as the Kirthar hills do not allow the residual moisture of the monsoon season to reach this part of Pakistan – except in some abnormal seasons when monsoon disturbances may reach too far west and cause exceptionally heavy rainfall over this area (Rahamatullah, 1952).

Bangladesh lies in the humid tropical belt and its rainy season begins in May and lasts until October. Maximum rain occurs in the period June to August. There are considerable subregional variations in the spatial distribution of rainfall over different districts. The hill districts in the south and north-east parts of the country, lying in the path of monsoon winds, receive annual rainfall of over 400 cm.

Because of the near-equatorial location of Sri Lanka, the intertropical convergence zone (ITCZ) crosses the country twice during the course of the year; firstly in May and secondly while retracing its path during December. The seasons in Sri Lanka are not precisely reckoned as per the practice followed in India. The March to April period is known as the first inter-monsoon, May to September as south-west monsoon, October to November as the second inter-monsoon and December to February as north-east monsoon (Puveswaram and Smithson, 1993; Chandrapalla, 1996). The primary rainfall maximum for Sri Lanka occurs in the period October to December and the secondary one in May–June. The hills in the center of the country exercise profound influence on rainfall distribution in both the monsoon seasons.

For Nepal the three hill ranges, viz. the southern slopes of the front range of the Chauria hills (extension of Siwalik), receive high rainfall, as the monsoon flow from the Bay of Bengal strikes the low hills at an acute angle. Rainfall first increases from the foothills to the low-altitude Chauria hills and then decreases in the low-altitude valleys and increases again in the mid-mountain valleys of Kathmandu–Pokhara, being maximum on the southern slopes of the higher Himalayas. Rainfall is much less along the great Himalayas crests since much of the moisture of the monsoon has already been rained out. Thus a complex distribution of rainfall occurs in Nepal as the orientation and elevation of the hills and valleys play a crucial role in rainfall distribution (Sikka *et al*., 2004). However, there is a general decrease of rain from east to west, the maximum rainfall occurring in central Nepal along 84–86°E. The monsoon rainy period commences early in the east and also extends in that belt even up to mid-October. The contribution of monsoon rains to the annual rainfall is over 80%.

The Maldives is a country of many islands situated in the south-east Arabian Sea and its climate is moist near-equatorial maritime. Rainfall begins to increase in the pre-monsoon season, reaches maximum in the June–September period, and then drastically falls between January–February.

The onset of the monsoon is the most anxiously awaited weather singularity in the subcontinent as it heralds the rainy season and marks the end of the hot summer. Over continental India the drama of the onset begins first across the Kerala coast, normally by 31 May (Ananthakrishnan and Soman, 1988) when heavy rains lash the coastal state after the cross-equatorial low-level jet (LLJ) (Findlatter, 1969) is established across the Somali coast into the near-equatorial Arabian Sea. This phenomenon is usually accompanied by the formation of a mid-troposphere shear zone across the central Bay of Bengal to the south-east Arabian Sea in which may be embedded a cyclonic vortex. The vortex may even intensify into a cyclonic storm either in the Bay of Bengal or south-east Arabian Sea. The cyclonic storm forming in the south-east Arabian Sea is known as the monsoon onset vortex (Krishnamurti *et al*., 1981b) after the event which occurred on 11 June 1979 during the summer MONEX year. The vortex is formed to the north of the LLJ, in the zone of maximum cyclonic shear in the lower tropospheric zonal winds. In association with the northward movement of the vortex, the large-scale monsoon current also advances northward along the west coast of India. George and Mishra (1993) made a dynamical study of the energetics of the monsoon onset vortex of June 1979 and found that combined barotropic–baroclinic instability contributes to the genesis of the vortex. On average, the onset vortex forms in nearly 50% of the years and in other years the onset is accompanied by either a mid-tropospheric shear line or formation of an offshore trough along 10°–15°N off the Kerala coast of India, with an embedded weak low-pressure area. Prior to the onset the cross-equatorial flow increases in strength, the moisture fields build up to the mid-tropospheric level 7–10 days in advance (Pearce and Mohanty, 1984), the near-equatorial cloud band in the Arabian Sea expands eastward, and the upward motion field in the troposphere near the equator enhances eventually moves northward with the advance of the monsoon. The regional onset heralds the large-scale linking of the vast south-east trade wind system and the near-equatorial westerly flow of the pre-monsoon (May) period, forming a single low-level clockwise monsoon gyre. The Arabian Sea, which is heated under the cloudless skies of the pre-monsoon, responds to the onrush of the strong LLJ, and its temperatures abruptly fall even over the south-east Arabian Sea within 2–4 days of the onslaught of strong winds and heavily clouded skies. Yin (1949) was the first to link the process of monsoon onset to the displacement of westerly troughs in the circumpolar westerlies and shift of the subtropical jet (STJ) to the north of the Himalayan periphery. Pasch (1983) examined the monsoon onset over India during 1979 from the perspective of planetary-scale circulation features and noted their gradual setting up prior to the formation of a transient disturbance off the Kerala coast. Murrakami and Ding (1982) have suggested that the onset is related to the warming of the Eurasian region by diabatic heating. Yanai *et al*. (1992) have linked the onset to the effect of the Tibetan Plateau. Thus the onset of the monsoon over India is linked to a combination of regional and planetary-scale changes over the entire Indian Ocean region. There exists a variety in the linkages of the onset process with the seasonal developments or transitions in the regional and planetary-scale features. Lack of uniqueness among them points to the initiation of chaotic dynamics with the formation of the weather system at the Kerala coast which heralds the onset process.

According to the IMD (1943), the advance of the monsoon occurs in two directions, firstly along the south-east to north-west direction in the Bay of Bengal from mid-May to early June and secondly along the west coast and adjoining peninsular of India in a south to north direction across the entire west coast of India from the end of May to mid-June. The advance is facilitated by the formation and northward movement of the synoptic system which brought the monsoon over Kerala, usually followed by an overlapping formation of another system within 3 to 5 days of the dissipation of the first system. Along the Indo-Gangetic plains the advance of the monsoon occurs from east to west and is associated with the formation of 2 or 3 monsoon depressions/lows. Each synoptic system, moving across the plains advances the monsoon by about 50 longitudes westward. The monsoon advance takes nearly 3 to 4 weeks to cover the entire Gangetic plains but there are years when the advance process is arrested as cyclogensis abruptly ceases in the monsoon trough zone. Subramanya *et al.* (1984) have examined the variability of the onset and advance process in space and time. The standard deviation of the monsoon onset date at Kerala remains about 7 days, and this period is more or less the same over almost all stations over India. Biswas *et al.* (1998) have linked the hiatus in the monsoon advance to the abnormal circulation features occurring in the Himalayan–Tibetan belt. Thus, the advance of the monsoon over the entire subcontinent is a rather slow process taking on average nearly 40 to 45 days from its start off Kerala on 31 May to its culmination by mid-July over central Pakistan. The advance process has also considerable interannual variability. It occurs in stages, each stage accompanied by a synoptic-scale disturbance pushing the boundary of the monsoon either northward or westward. Thus, a variety of planetary and regional-scale processes and synoptic-scale events are involved in the onset and advance of the monsoon over south Asia. Krishnamurti and Ramanathan (1982) have linked the sensitivity of the onset process with the building up of the heat sources over north-east India and the Indonesian region and the contribution of divergent flow to the non-divergent flow resulting in strengthening of the near-equatorial westerlies. The onset and advance phase is also linked with the low-frequency 30–40-day oscillation (Joseph and Pillai, 1988) following the mid-April one over the south-east Arabian Sea and adjoining southern Bay of Bengal. The frequency of thunderstorms over the south peninsular of India increases during mid-April when the oscillation is passing over the region. Soman and Krishnakumar (1992) and Soman and Kumar (1993) have examined in detail the monsoon onset over Kerala based on a long series of rainfall and circulation parameter data.

Figure 4.1 shows the sea level pressure and wind distribution for July over south Asia – typical of the monsoon season. The prominent regional features are the seasonal low-pressure area over Pakistan, the monsoon trough over the Gangetic plains toward the northern Bay of Bengal, and the large pressure gradients along the west coast of India. The monsoon trough bifurcates into two portions over the northern Bay of Bengal – one going to southern China across Bangladesh and north-east India, and the other into the South China Sea across Mayanmar, Cambodia, Vietnam, and Thailand. The trough is most active over India and shifts southward with a height up to the 500-hPa level. An understanding of the

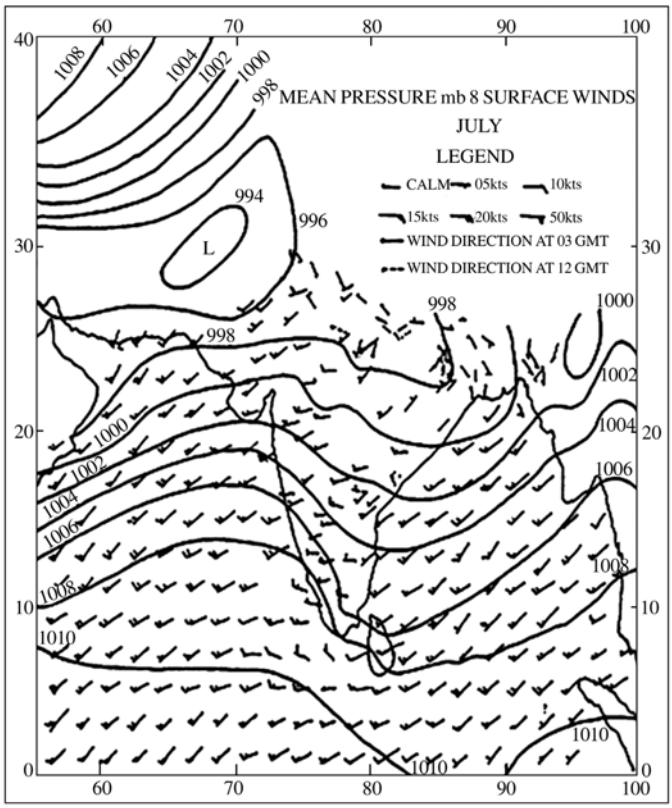

Figure 4.1. Mean sea level pressure (hPa) and surface wind distributions over south Asia for July – typical of the summer monsoon season.

atmospheric boundary layer processes within the monsoon trough along the Gangetic plains was the focus of a special observational programme known as the Monsoon Trough Boundary Layer Experiment (MONTBLEX) in 1989 and 1990 (Sikka and Narasmiha, 1995). A huge and distinct clockwise monsoon gyre in the lower troposphere is centered in the equatorial Indian Ocean connecting the south-east trades, emanating from the Mascarenes High, to the anticlockwise gyre of the monsoon trough over the Indo-Gangetic plains through the cross-equatorial LLJ off the Somali coast (Joseph and Raman, 1966; Findlatter, 1969; Krishnamurti and Bhalme, 1976). The LLJ near the top of the atmospheric boundary layer (900 hPa) is the main artery through which moisture is fed into the flow over southern parts of south Asia and is then carried across the Bay of Bengal to adjoining south-east Asia, and even into east Asia. The LLJ passes across different SST regimes over the Arabian Sea before reaching the west coast of India. At the upper troposphere the flow is reversed with an even more extensive clockwise gyre located over Tibet (the south Asian High) with divergent wind outflow becoming easterly to north-easterly toward the equator which attains maximum speeds exceeding 40–50 $m\,s^{-1}$ along

10°–15°N over southern India (Koteshwaram, 1958), known as the tropical easterly jet stream (TEJ).

The south Asian monsoon system is the most developed amongst all other regional monsoon systems in the global tropics as it develops in response to global-scale diabatic heating producing extremely large temperature gradients (between the equator to 30°N) in the entire troposphere which are enhanced by heating of the elevated Tibetan Plateau situated on its northern boundary. The plateau has the highest temperatures in the middle to upper troposphere during the monsoon season. Stout and Young (1983) have examined the low-level monsoon dynamics using satellite derived winds. Research on the south Asian summer monsoon has enormously increased in the last 50 years and has been very well reviewed, covering different periods, by Ramage (1971), Rao (1976), Das (1986), Chang and Krishnamurti (1987), Fein and Stephens (1987), Keshvamurty and Shankar Rao (1992), Asnani (1993), Pant and Rupa Kumar (1997), and Webster *et al.* (1998).

4.1.3 The east Asian monsoon region

The climatological annual rainfall pattern of China is characterized by the decrease in annual precipitation amount from south-east (>1600 mm) to north-west China (200 mm). South China is the most abundant precipitation region which is greatly affected by the summer monsoon. Over most of the Tibetan Plateau (except for its western part) the annual precipitation is relatively high. The isohyet of 400 mm is used to distinguish the arid and semiarid regions from the humid region. A salient feature of the east Asian monsoon region is its great interannual variability of precipitation. In the eastern part of China, the interannual variability (anomaly percentage) of annual precipitation changes from −22% to +25%, with north and north-east China having the maximum (Wang and Ding, 2004). In western China, the interannual variability becomes more significant – with the range −42% to +60%. If one examines the maximum interannual variability of annual precipitation, it is found that it changes from −50% to 90% in eastern China and from −80% to 200% or even greater in western China.

The rainy season in China generally begins with the onset of the summer monsoon and ends with its withdrawal (Ding, 2004). Rainfall intensity and its variation are closely related to the fluctuations of the summer monsoon. When the summer monsoon advances northward, its leading zone and the monsoon rain belt correspondingly moves from a low latitude to mid and high latitudes. In this process, as does the leading zone of the monsoonal airflow, the monsoon rain belt undergoes three standing stages and two stages of an abrupt northward jump. Based on the time–latitude cross section of 5-day rainfall amounts for eastern China (Figure 4.2) (Sun and Ding, 2002), the most conspicuous feature is the monsoon onset between 18° and 25°N as indicated by the steep rise in precipitation starting from the first 10-day period of May. This rainy episode is the so-called presummer rainy season in south China, Hong Kong, and Taiwan. This characteristic feature has been also studied by other investigators (Guo and Wang, 1981; Lau *et al.*, 1988). The first

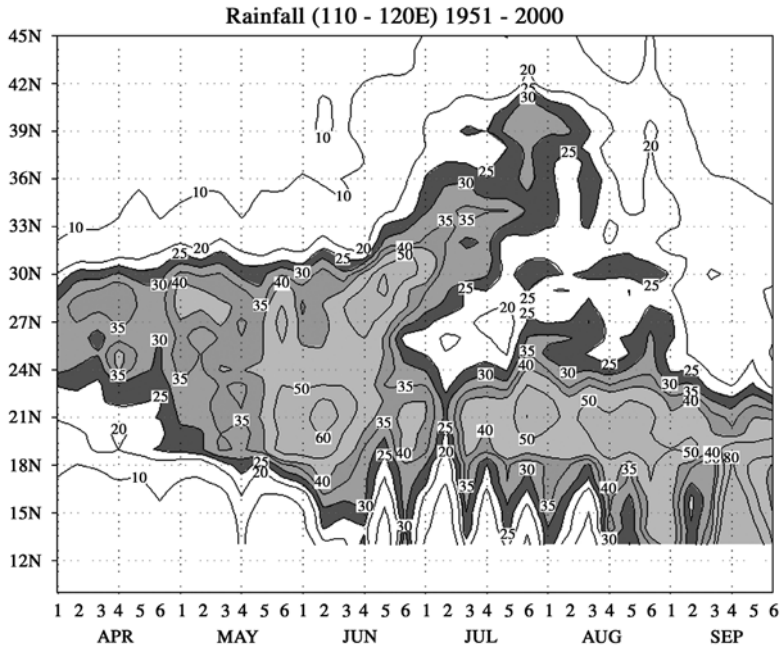

Figure 4.2. Latitude–time section of 5-day mean rainfall over eastern China (110°–120°E) from April to September averaged for 1961–1990. Regions of heavy rainfall (>50 mm) are shaded. Units are in mm.
Ding and Sun (2002).

standing stage of the major rain belt generally continues into the first 10-day period of June, and afterwards it rapidly shifts to the valley of the Yangtze River. This second stationary phase initiates the Meiyu rainy season in central China. The time span of the season on average lasts for one month (10th June–10th July). The wind and thermal fields in the Meiyu region are usually characterized by a low-pressure trough (the so-called east Asian summer monsoon trough) – a weak stationary front at the surface, significant horizontal wind shear across the front, and frequent occurrence of prolonged heavy rainfall. The Baiu in Japan and Changma in Korea also occur in similar situations, but with a regional difference in locations, timing, and duration which will be discussed later. The Meiyu rain belt is usually quasizonally oriented near 30°N over eastern China and tilts east–north-eastward toward Korea and Japan. The quasistationary front (the Meiyu front in China, Baiu front in Japan, and Changma front in Korea) often extends from a cyclonic low center west–south-westward as the center itself moves eastward or east–north-eastward. The heaviest rainfall is mostly associated with eastward moving meso to synoptic-scale disturbances along the front. Numerous investigators have studied the development mechanism of this kind of the east Asian summer monsoon (Meiyu) disturbances and their contribution to the Meiyu rainfall (Tao and Ding, 1981; Ninomiya and Akiyama, 1992; Chang *et al.*, 1998; Chang *et al.*, 2000).

From mid-July, the rain belt rapidly moves over north China and in August

farther over north-east China, the northernmost position of the summer monsoon rainfall. This standing stage of the rain belt causes the rainy season in northern China that generally lasts for one month. In the early or middle part of August the rainy season of north China comes to an end, with the major monsoon rain belt disappearing. From the end of August to early September the monsoon rain belt moves back to south China again. At this time, most of the eastern part of China is dominated by a dry spell. Note that from mid-July, the second rainy season or the revival of the rainy period (Chen *et al.*, 2003) predominates over south China, with a gap of about 20 days or one month between the presummer rainy season and this rainy season that is mainly caused by typhoons, the movement of the ITCZ, and other tropical disturbances in the monsoonal airflow. Around the beginning of October, the rainy season over eastern China more or less ends and rapidly makes way for the winter monsoon. Guo and Wang (1981), with analysis of climatological patterns of summer rainfall by use of a longer record of precipitation in China (1950–1979), similarly pointed out that the summer monsoon rain belt assumed three relatively stable periods, with the first period (the presummer rainy season in south China) having the longest persistence, the third period (the rainy season in north China) the second longest persistence, and the second period (the Meiyu season) having the shortest. Figure 4.3 shows the onset dates and durations of regional rainy seasons, which are quite consistent with the above illustrations. In south China to the south of the Yangtze River, the rainy season begins in the period from pentad 26 (6–10 May) to pentad 30 (26–30 May). It is very interesting that the earliest onset of the rainy seasons in China do not occur along the coastal areas of south China, but in its central part. In this region, the rainy season also ends earliest (pentads 36 (26–30 June)–38 (6–10 July)). In north-west China the seasonality is also quite apparent.

The Baiu season in Japan and the Changma season in Korea also occur during the seasonal northward advance of the summer monsoon. As indicated by Ninomiya and Muraki (1986), the Baiu in Japan begins in early June when rainfall in Okinawa reaches its peak. In the last ten days of June, the rainfall peak moves to the western and southern parts of Japan. Then the rainfall peak further moves northward in the first ten days of July. North of 40°N, no rainfall peaks associated with the Baiu can be observed. So, the Baiu season in Japan mainly lasts from early June to mid-July, almost concurrently with the occurrence of the Meiyu in China.

Afterwards, a break of the monsoon rainy period occurs from late July to early August in Japan (Chen *et al.*, 2003). This break of different spans is also observed in south China, central China, north-east China, Taiwan, and Korea (Figure 4.4). After the break spell, monsoon rain resumes for a period from August to September–October. Therefore, the monsoon rainfall variation during the warm season in east Asia is generally characterized by two active rainfall periods separated by a break spell. It is clearly seen from Figure 4.3 that the Meiyu rain band, forming in early May, progresses northward until the end of July, and diminishes between 40° and 45°N in north-east China and Korea, and about 40°N in Japan. The passage of the Meiyu rain band is followed by a break spell (monsoon break) which also propagates northward. Then, the monsoon rainfall revival after the break is

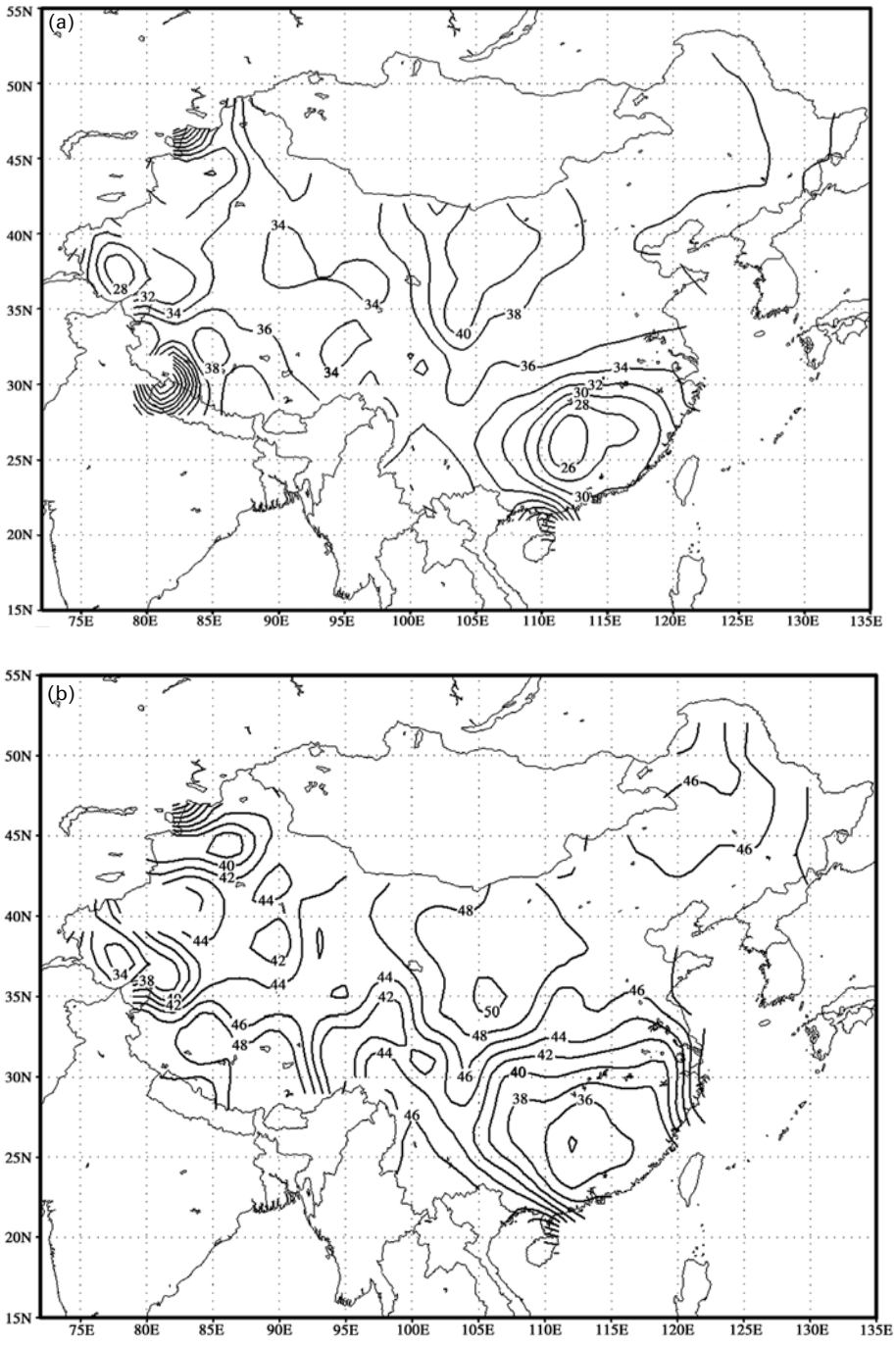

Figure 4.3. Onset (a) and ending dates (b) of regional rainy seasons in China. Units in pentad. Wang and Ding (2004).

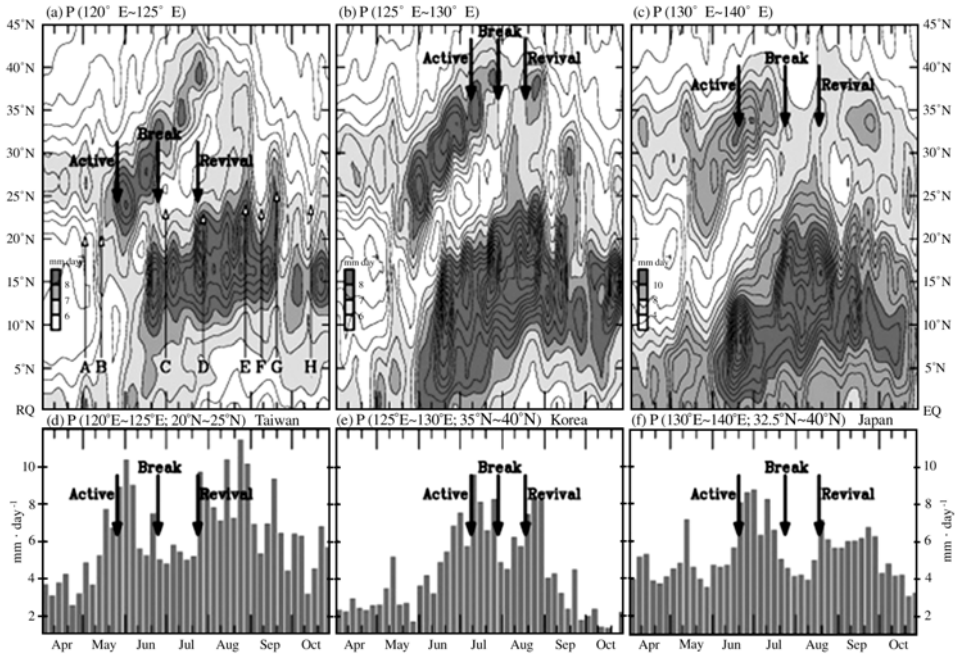

Figure 4.4. Latitudinal–time cross sections of CMAP rainfall averaged over longitudinal zones of (a) 120°–125°E, (b) 125°–130°E, and (c) 130°–140°E, and rainfall histograms of three regions: (d) Taiwan (120°–125°E, 20–25°N), (e) Korea (125°–130°E, 35°–40°N), and (f) Japan (130°–140°E, 32.5°–40°N). Different phases of summer monsoons in three regions are indicated by active, break, and revival. The contour interval of CMAP rainfall in (a)–(c) is 1 mm day^{-1}, while rainfall amounts larger than 5 mm day^{-1} are shaded.
Chen *et al.* (2003).

clearly observed. Chen *et al.* (2003) has shown that the monsoon revival in east Asia is caused by a different mechanism associated with the development of other monsoon circulation components including the ITCZ and weather systems in mid-latitudes.

The rainy season in Korea, the so-called Changma, accompanied with a belt-like peak rainfall zone, begins with the influence of the quasistationary convergence zone between the tropical maritime airmass from the south, and both continental and maritime polar air masses from the north (Oh *et al.*, 1997; Qian and Lee, 2000). Generally, during 2–7 July, the convergence zone or line of both south-westerly and north-westerly winds is located in the Huaihe River basin between the lower Yangtze River and the lower Yellow River. The major rainfall area is not observed over the Korean Peninsula. However, in the next pentad (7–11 July) when the convergence zone migrates northward, wind and intensive rainfall with 12 mm day^{-1} start to dominate the southern Korean Peninsula and Japan, which is evidently separated from the extensive area of tropical precipitation. Therefore,

based on the precipitation peak and lower tropospheric circulation features, the onset date of the north-east Asia summer monsoon or Changma rainy season can be determined as the period of the 37–39th pentad (late June–mid-July), with a significant interannual variability. Therefore, the Changma is a shorter monsoonal rainy season, with mean Changma period being 20 days to one month long. The break in late July is very short, with the duration of half a month. Starting from late August, the revival of the monsoon rainy period is also observed in Figure 4.4. The second rain spell is not long, based on the study by Chen *et al.* (2003). But Qian *et al.* (2002) pointed out that this precipitation surge can maintain until early September, forming the autumn rainy season in Korea.

4.2 SYNOPTIC SYSTEMS

A variety of synoptic weather systems including monsoon troughs/ITCZ, monsoon depressions, heat lows, mid-tropospheric cyclones, subtropical highs, mid-latitude and subtropical fronts, low-level vortices, and blocking high/polar anticyclones can considerably affect the Asian monsoon. They form during different phases of the evolution of the south Asian and east Asian monsoon systems.

4.2.1 The south Asian monsoon region

For the south Asian monsoon region, the synoptic systems are mainly of tropical nature, while they are of hybrid nature for the east Asian monsoon region due to an existence of very significant interaction between the monsoonal aircurrents and impacts from mid and high latitudes.

Figure 4.5(a) is a schematic to show the usual places of formation for the weather systems in summer in the south Asian monsoon region. They are responsible for the onset and advance phases of the monsoon during June, distribution of rainfall during the peak phase of the monsoon in July and August, and withdrawal of the monsoon from mid-September to mid-October. These transient synoptic weather systems (Alexander *et al.*, 1978; Nagar *et al.*, 1992) are influenced by the interaction of the south Asian monsoon with other regional atmospheric systems such as the following. (i) Extratropical circulation systems in the south Indian Ocean which pulsate the LLJ through the Mozambique Channel (Sikka and Gray, 1981). (ii) Extratropical systems of the northern hemisphere like western disturbances and associated troughs in the mid-latitude westerly flow across western and central Asian sectors (Pisharoty and Desai, 1956; Ramaswamy, 1962). (iii) Synoptic weather systems like the remnants of typhoon/tropical cyclones which after striking the Chinese coast near 20°N travel westward and rejuvenate into monsoon lows and depressions over the northern Bay of Bengal (Krishnamurti *et al.*, 1977; Saha *et al.*, 1981; Krishnamurti and Ardanuy, 1980). They are also influenced by the northward propagation of intraseasonal oscillations (ISOs) as well as the eastward moving Madden–Julian Oscillation (MJO) (Madden and Julian, 1972) in the near-equatorial zone. (iv) When the monsoon trough hugs the Himalayan rim, the low-level easterlies disappear entirely along the Indo-Gangetic plains and are replaced by the

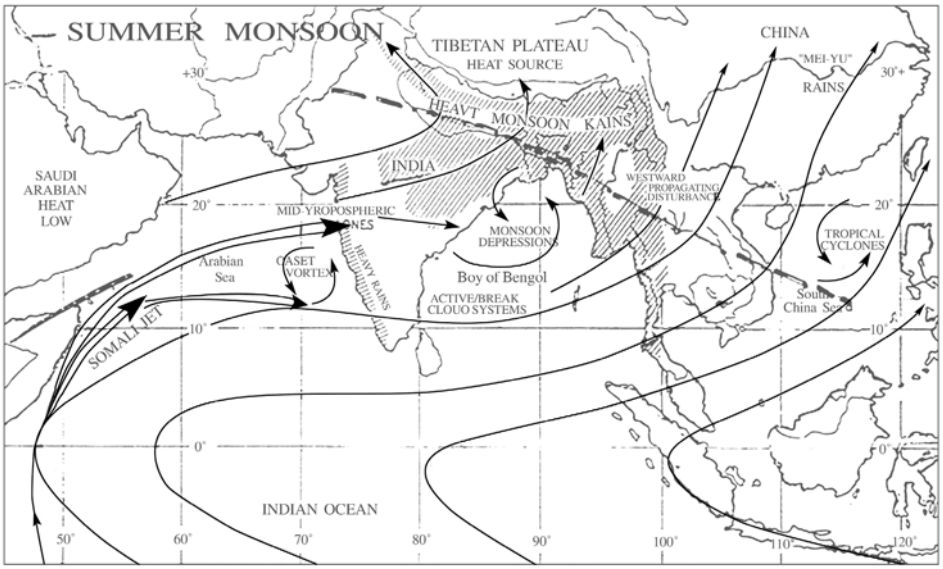

Figure 4.5. (a) Major synoptic-scale weather systems associated with summer monsoon fluctuations in south Asia.
Provided by Zhang Zuqiang.

west–north-west flow along the periphery of the Himalayas. Such a situation, if it lasts for 2 or 3 days – bringing back the monsoon trough in the Gangetic plains – is known as the temporary oscillation of the monsoon trough or temporary 'break' in the monsoon. If the submontage position of the trough sticks for more than 3–4 days, it leads to a prolonged 'break monsoon' situation. (v) The westward moving 10–20-day oscillation between 10°–15°N from the South China Sea toward India (Krishnamurti and Ardanuy, 1980) is another important ISO mode which has quite an influence on the monsoon as it interacts with the 30–40-day mode on the one hand and synoptic-scale variability on the other.

During the monsoon season, the following synoptic weather systems regulate the seasonal rains:

(i) The regional monsoon trough and its latitudinal oscillations manifested in the mid-season 'active break' cycle of the monsoon.
(ii) The low-pressure systems forming in the monsoon trough on the scale of 1,000–2,000 km and having life spans of 3–7 days, some of them having a well defined center and extending up to the mid-troposphere.
(iii) The north–south oriented offshore troughs along the west coast of India (life span of 3–7 days) with embedded mesoscale vortices of 1–2 days duration and horizontal scales of 200 km (George, 1956).
(iv) The monsoon depressions forming within the monsoon trough with a horizontal scale of 2,000–3,000 km and life spans of 3–7 days (Sikka, 1977).

(v) The mid-tropospheric cyclone forming off the north Konkan–Gujarat coast with maximum vorticity at 700–600-hPa levels, a horizontal scale of 1,000–2,000 km, and life span of 5–7 days (Miller and Keshvamurty, 1968).
(vi) The minor cyclonic circulations in the lower and middle troposphere with horizontal scale of 1,000–2,000 km and life spans of 2–5 days.
(vii) The north–south troughs from the Gangetic west Bengal to the southern peninsular of India during weak monsoon conditions with life spans of 3–7 days.
(viii) The western disturbances associated with eastward moving mid-tropospheric troughs in extratropical westerlies across Indo-Pakistan longitudes and penetrating to 30°N along 70–75°E.
(ix) The low-frequency MJO moving eastward on 30–40-day scales along near-equatorial belts which on several occasions trigger northward-moving organized convective episodes, particularly after a prolonged 'break' in the monsoon.

Monsoon trough

This is the most dominant feature of the monsoon season, situated along the Indo-Pakistan plains, and was identified even in the very early scientific studies of the monsoon by Blanford (1886). Its eastern end is locked with the warm waters of the northern Bay of Bengal with dominantly moist processes operating on a day-to-day basis showing diurnal variability also. The western end is situated in the predominantly dry convective area of western India and Pakistan and occasionally influenced by the moist processes associated with eastward moving lows/monsoon depressions/quasistationary subtropical cyclones along the Gujarat coast and southward extending western disturbances. Keshvamurty and Awade (1970) examined the dynamics of the mean monsoon trough. Anjaneylu (1969) studied the heat and moisture budget of the trough region and Mohanty *et al.* (1983) studied the moisture and heat budgets over the Arabian Sea during the monsoon. Bhide *et al.* (1997) investigated the heat sources and moisture sinks associated with the westward moving monsoon disturbances. They inferred that precursors of a monsoon 'break' lay in the alterations caused in heat sources and moisture sinks after an active monsoon disturbance moved from central India toward north-west India and adjoining Pakistan. The intraseasonal pattern of the oscillation of the monsoon trough would reveal a dominant 3–7 day synoptic-scale oscillation period (Keshvamurty, 1973; Murakami, 1976). Heavy rainfall is confined to about 1–2 degrees to the south of the monsoon trough (Raghvan, 1973). During a prolonged break monsoon episode, suppression of rainfall occurs over central India with prevalence of subsidence motion as evidenced by the appearance of stable layers and inversions in the lower/middle troposphere over north-west and central India along with prevalence of anticyclonic vorticity at 900–850 hPa between 20°–28°N (Sikka and Gadgil, 1978). In an active phase of the monsoon, the trough could have either one or two cyclonic vortices embedded in it or for a prolonged period it could remain near its normal or somewhat southward position from the

normal. The trough is located in its near-normal position or slightly south of its normal position in a good monsoon season with higher than normal cyclonic vorticity at the top of the boundary layer and north of its normal position with lower than normal cyclonic vorticity at the top of the boundary layer in a drought year (Sikka, 1999). The crux of the monsoon performance is linked with the dynamics of the monsoon trough. The standard deviation of the trough position is 1.5° in latitudes.

Monsoon lows and depressions

Eliot (1884), for the first time, recognized the existence and pre-eminent position of the monsoon lows and depressions as rain producing systems. These synoptic-scale systems form within the monsoon trough – often in the north and central Bay of Bengal and occasionally even over the north Arabian Sea and land part of the trough also. A few of the depressions (about 20%) even intensify into cyclonic storms over the northern Bay and rapidly weaken as they move over land. As most of the lows/depressions form over the northern Bay of Bengal, organized convection occurs first near the coast (south-west sector of synoptic systems) which subsequently moves inland and distributes rain along the track of the systems. This allows the land-surface processes to operate vigorously and in turn impacts on the monsoon activity.

The average life duration of these low-pressure systems is about five days for those forming over the Bay of Bengal and three days for those forming over the Indian land areas. These systems move in a west–north-west/north-west direction from the northern Bay of Bengal and weaken within the trough after traveling a distance of 500–1,000 km over land. A few even travel far westward merging with the seasonal low over western India and Pakistan. Some systems get rejuvenated while crossing 78°E by the fresh moist air incursion from the Arabian Sea while the differential thermal advection from north-west India intensifies the upward motion in the south-west sector of the system, producing abnormally heavy rainstorms with 24-hr point rainfall reaching between 30–100 cm. A few systems, while moving north-west, recurve along 75°–78°E under the influence of an approaching westerly trough and produce very heavy rains in the north-east sector of the depression/low along the foothills of western Himalayas. The formation of these systems indicate a synoptic-scale dynamic instability of the monsoon trough. The structure of monsoon depressions and associated rainfall patterns have been studied based on case studies (Koteswaram and George, 1958; Koteswaram and Bhaskar Rao, 1963; and others) and compositing of several systems (Mulki and Banerjee, 1960; Godbole, 1977; Sikka, 1977; Ding, 1981; Ding *et al.*, 1984; Sarkar and Choudhary, 1988; Prasad *et al.*, 1990; and others). Rajeevan *et al.* (2002) have examined the asymmetric thermodynamic structure of monsoon depressions using microwave satellite data composited for 10 cases. They found high liquid water content in the south-west sectors of depressions where the rainfall is known to be heaviest. Combined barotropic, baroclinic, and CISK (conditional instability of the second kind) instability theory controls the monsoon cyclogenesis (Shukla, 1978).

Structurally there is not much difference between a monsoon low and a monsoon depression except that the depression has a well-defined center and winds are stronger. Both systems have cold cores, tilting southward with height. Maximum moisture convergence occurs in the south-west sector, and the rainfall maximum is situated about 200–300 km ahead of the center (Pisharoty and Asnani, 1957; Raghavan, 1965; and others). High-intensity rainfall occurs in association with mesoscale organization within the depression area. Several studies using quasigeostrophic models and balance models have been reported in the 1970s (Rao and Rajamani, 1970; Awade and Keshvamurty, 1975; Daggupathy and Sikka, 1977; and others). It is generally believed that many of these systems form *in situ* over the warm waters of the Bay of Bengal under the upper tropospheric divergent flow of the Tibetan High and upper tropospheric easterly waves (Koteswaram and George, 1958). Their intensification into depressions or cyclonic storm stages is aided by the high moisture content and low vertical shear between the lower and upper troposphere. Ramana (1969) traced the formation of monsoon depressions with tropical storms of the South China Sea. Saha *et al.* (1981) are of the opinion that a large majority of these systems are remnants of the tropical cyclones and typhoons of the north-west Pacific and they rejuvenate over the warm waters of the Bay after passing through south-east Asia. Krishnamurti *et al.* (1977) showed that in some cases depressions form due to downstream amplification of wave energy after a tropical storm strikes the Chinese coast near 20°N. Because of the geographical location of their formation points lying close to land, they strike the coast of Bengal/Orissa/Bangladesh and hence are unable to intensify into fully mature tropical cyclones, unlike those forming in the monsoon trough over the South China Sea and the Philippine Sea. The surface winds are quite strong from the central Arabian Sea to the central Bay of Bengal during the 2–3 days prior to the formation of a depression in the Bay. The pressure gradients between 5°–20°N over the Bay at times increase to 15 hPa. Sikka and Gray (1981) linked some of the formations to the strengthening of the LLJ with a surge in southerly winds crossing the Mozambique Channel after the passage of a baroclinic system in the extratropical westerlies south of the channel. All such surges do not lead to monsoon cyclogensis, but those which occur during the eastward passage of Madden–Julian ISO are likely to influence the formation of monsoon disturbances in the Bay of Bengal. These synoptic systems also regulate the large-scale air–sea interactions over the Bay of Bengal as evidenced from the recent study (Bhat *et al.*, 2001) undertaken with the data collected by the special Bay of Bengal Monsoon Experiment (BOBMEX-1999). These monsoon lows/depressions distribute rainfall along the length and breadth of Bangladesh, submontage Nepal, India, and Pakistan as they organize the moisture convergence and rainfall on their preferred scale. The rainfall is particularly heavy when these disturbances form in an overlapping manner (sometimes three in a period of 10–20 days), possibly on the envelope of the trough position of the ISO lying over the northern Bay of Bengal. They lead to floods over the central Indian rivers, and rivers of the Gangetic plains, Bangladesh, and eastern India. Sikka (1977) discussed different aspects of monsoon depressions. The climatological distribution of low-pressure areas, depressions, and cyclonic storms of the monsoon season based on 95

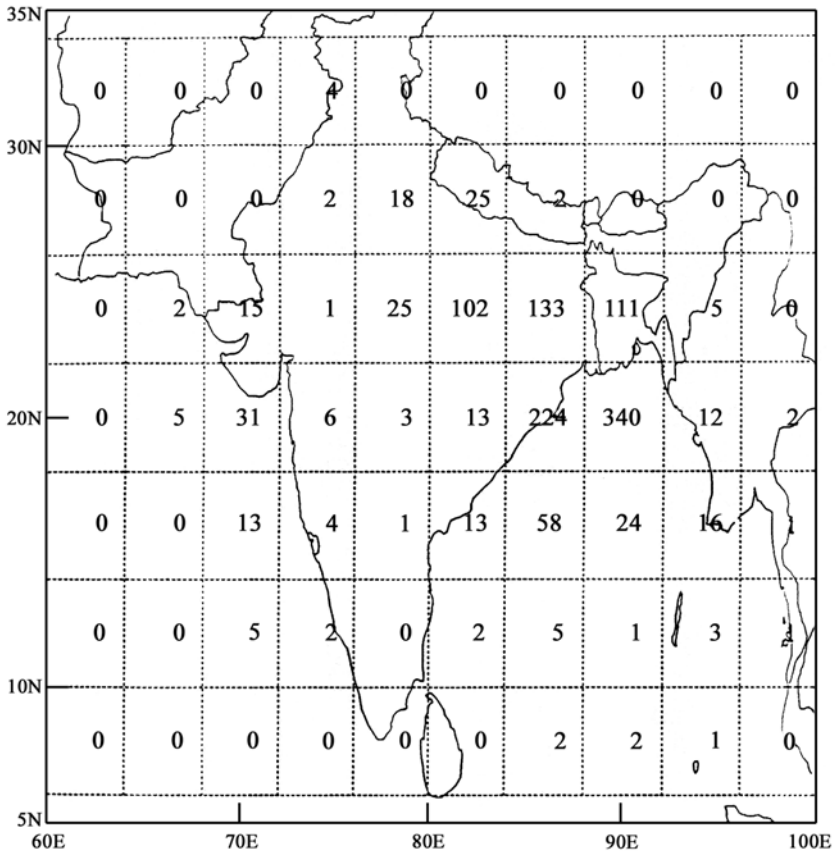

Figure 4.6. Number of low-pressure systems (lows, depressions, and cyclonic storms) which formed over 4° lat/long blocks over the south Asian region in the summer monsoon season during 1888–1983.
From Mooley and Shukla (1989).

years of data (Mooley and Shukla, 1989) shows that maximum numbers of low-pressure systems form over the northern Bay of Bengal (Figure 4.6). On a climatological basis during the monsoon season about 7 depressions and 1.5 cyclonic storms form over the Bangladesh–India–Pakistan region (mostly over the Bay of Bengal). On average about 13 low-pressure systems (lows/depressions/cyclonic storms) form during the monsoon season with a standard deviation of 2.2. There is large inter-annual variability ranging from 9–18 systems in a season (Mooley and Shukla, 1989). The drought monsoon seasons usually witness less than normal low-pressure systems. Sikka (1980) and Dhar *et al.* (1981) have suggested that the performance of the monsoon on a seasonal and monthly basis respectively depends on the total number of lows and depressions forming in the monsoon trough and the number of

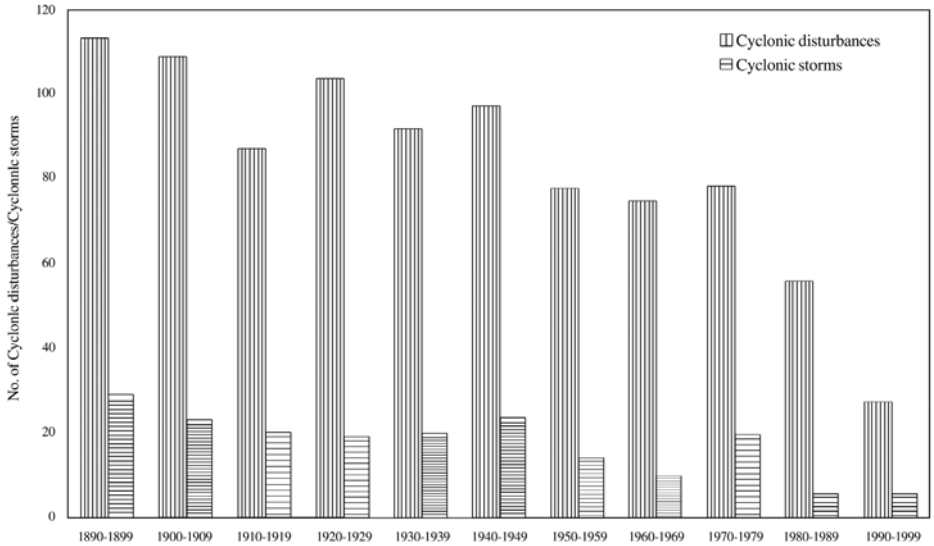

Figure 4.7. The decadal frequency of cyclonic disturbances (low and depressions) and cyclonic storms over the north Indian Ocean during the period 1899–1999.
From Singh (2001).

days with the existence of low-pressure systems. A secular decrease in the number of lows and monsoon depressions have been observed in the past two decades as shown in Figure 4.7 (Singh, 2001).

Mid-tropospheric cyclone (MTC)

An MTC is a class of monsoon disturbance, which was highlighted during the IIOE (International Indian Ocean Expedition) in the seminal paper by Miller and Keshavamurthy (1968) using research aircraft and conventional data. An MTC has a unique vertical structure as it is hardly detectable at the surface and in the upper troposphere. The largest intensity is found in the middle troposphere layer (700–500 hPa) with a cold core between the surface to 700 hPa, and warm core aloft. It is usually characterized by very intense convective and non-convective rainfall. It forms mainly over the north-eastern Arabian Sea off the north Konkan–south Gujarat coast of India and during an active phase of the monsoon from mid-June to the end of July and only occasionally over the Bay of Bengal (similarly either during the onset/advance phase or the revival phase of the monsoon after a prolonged 'break'). Often the system is generated within the monsoon cyclonic shear zone at 700 hPa which gets enhanced when a monsoon depression forming over the northern Bay of Bengal moves inland. They have a life span of about 5–7 days and produce very heavy rainfall over the north Konkan–Gujarat coast of India. Carr (1977) made a detailed observational study of MTCs using a diagnostic model

and validated all the structural characteristic features of the MTCs described above. He also found that MTCs usually occur with a frequency of one to four times per year, but more often in the period from 15 June to end of July. As the advection of warm air over western India reduces from August onward, the formation of MTCs is also perhaps reduced, but the exact cause is yet to be investigated. Mak (1975) applied a non-geostropic baroclinic model to theoretically investigate the instability related with the MTC.

Offshore troughs along the west coast of India and embedded mesoscale vortices

Another important synoptic/supersynoptic configuration in the monsoon is witnessed in the form of a south to north oriented trough near the surface along the west coast of India. The trough is particularly well marked during active monsoon conditions along the west coast as in that situation the rainfall is heaviest along the coast and decreases at the crest of the western Ghats. George (1956) was the first to suggest that mesoscale cyclonic vortices, with horizontal extents of 100–200 km and vertical extents of about 3 km, often develop in preferred zones off coastal Karnataka (10°–15°N), Konkan, Goa, and Gujarat (17°–22°N). These mesoscale vortices appear and disappear in a day or so while moving northward within the offshore trough with associated shifts in the heavy rainfall belt. Heavy rainfall exceeding $10\,\mathrm{cm\,day^{-1}}$ and even reaching over 30–$50\,\mathrm{cm\,day^{-1}}$ is often associated with the active offshore trough and is concentrated near the center of a mesoscale vortex. Organization of strong offshore convection along the west coast of India was investigated in detail by Grossman and Durran (1984) using the MONEX-1979 extensive observations. They had suggested that the upstream convergence in the monsoon boundary layer is aided by frictional convergence as the coast is approached and the orography of the western Ghats further enhances the vertical motion. Later, the latent heat released in the heavy rainfall regime tends to maintain the convection off the coast. Ogura and Yoshizaki (1988), using a theoretical model, further stressed the role of latent heat release, dynamical role of air–ocean fluxes, and orography in maintaining convection off the coast. Thus, a combination of frictional convergence along the coast, air–sea interactions, orography, and cumulus convection are responsible for the deep convection along the west coast of India in the offshore trough. The evolution and decay of these synoptic entities formed the focus of a special field experiment known as the Arabian Sea Monsoon Experiment (ARMEX) carried out by the Indian atmosphere–ocean science community during June–July of 2002 (Sikka, 2003; Francis and Gadgil, 2002).

Western disturbances, mid-season 'break' monsoon, and its revival

During the peak phase of the monsoon season over India, mid-latitude westerlies prevail to the north of 30°N only, and troughs in this extratropical regime generally pass north of the Indo-Pakistan region. The subtropical ridge along about 30°N acts as the southern limit of these troughs. However, on individual occasions these troughs penetrate southward either due to their unusual intensity or due to the

fluctuations in the intensity of the subtropical ridge. On such occasions a westerly trough in the upper–middle troposphere, and the associated western disturbance in the lower troposphere, greatly influence the activity of the monsoon trough over the Indo-Pakistan region. Mooley (1957) pointed out cases of enhanced monsoon rains over the western Himalayas and adjoining plains in association with a passing western disturbance. According to Rao (1976) western disturbances influence the monsoon trough in a complex manner, viz: (i) intensifying a lower troposphere low over western India; (ii) enhancing rainfall in a pre-existing system monsoon low over north-west India; (iii) causing recurvature of depressions and lows in the 75°–78°E belt; and (iv) shifting the monsoon trough to the foothills leading to the 'break' in the monsoon. The first three effects are opposite to the last one and relate to the organization of moisture convergence in the zone of a weather disturbance over north-west India which is enhanced by the upper tropospheric divergence ahead of a moving trough in extratropical westerlies. The last effect, which leads to the monsoon 'break', occurs in a situation when the monsoon has already remained active over central and north-western India for 10–15 days and it is time for the intraseasonal reversal of the monsoon activity in terms of rainfall as the ridge phase of the ISO is approached over the northern Bay of Bengal.

The phenomenon of 'break monsoon', already discussed to some extent, has been investigated in detail first by Ramamoorthy (1969), followed by Raghvan (1973), Pant (1983), and Rodwell (1987). More recently, there has been a renewed interest in the study of the 'break' monsoon (Krishnan *et al.*, 2000; De and Mukhopadhya, 2002; Gadgil and Joseph, 2003; Bhatla *et al.*, 2004). The frequency and total duration of 'break' monsoon episodes definitely controls the subnormal performance of the monsoon on intraseasonal and interannual scales. The 'break' monsoon phenomenon is a reverse of the 'active' monsoon spell over central and northern India and the two demonstrate the two modes of the south Asian monsoon system (Figure 4.8). Ferranti *et al.* (1997), Goswami and Mohan (2001), Krishnamurthy and Shukla (2000), and Lawrence and Webster (2001) have found similarities in the ISO and the interannual oscillation of the monsoon system. This is not surprising as it is due to the dominance of the two modes ('active' and 'break') of monsoon activity in the monsoon season. The excess and drought monsoon seasons on an interannual basis are in some way replicate 'active' and 'break' monsoon events on intraseasonal scales. Whether this dominance is precontrolled by the land surface–oceanic boundary forcing (Charney and Shukla, 1981) or results due to the internal dynamics of the monsoon and air–sea interactions remains still a moot question. The revival of the monsoon after a short 'break' (3–4 days) is due to the synoptic-scale oscillatory character of the monsoon trough. However, the revival after a prolonged 'break' is distinctly linked with the northward propagating ISO (Sikka and Gadgil, 1980; Wang and Rui, 1990; and others). Koteswaram (1950) had alluded to the westward movement of weak low-pressure systems along 10°–15°N over the Bay of Bengal as a precursor to the revival of the monsoon after a prolonged 'break'. In some years the 10–20-day westward moving ISO from the South China Sea (Krishnamurti and Bhalme, 1976; Krishnamurti and Ardanuy, 1980; Lau and Chan, 1986) is also responsible for restoring the monsoon trough at a near-normal

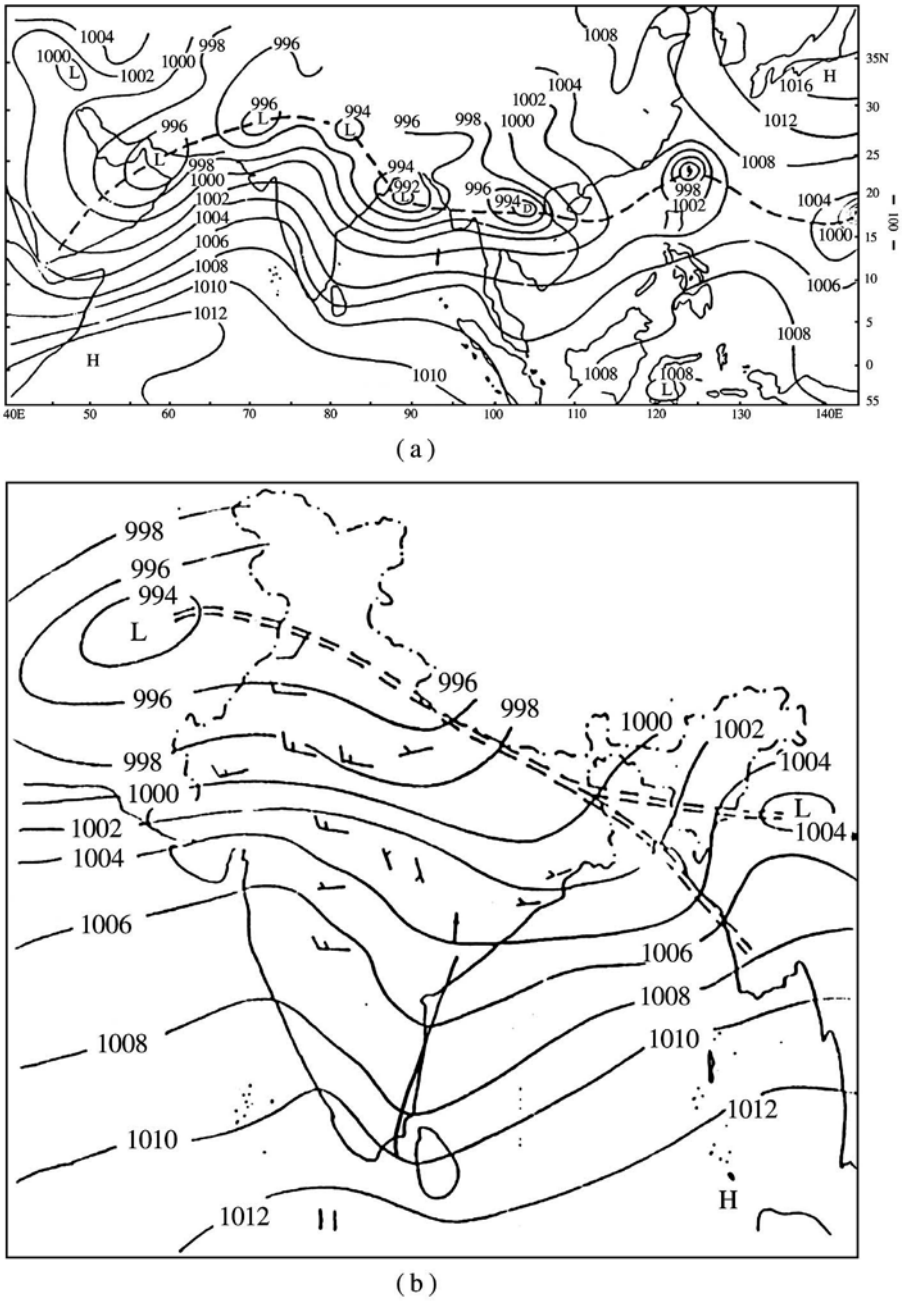

Figure 4.8. (a) A typical sea level pressure pattern in which there are five weather disturbances during the active phase of the monsoon. (b) Typical sea level isobaric pattern over south Asia during a 'break' monsoon situation with the monsoon trough lying across the foothills of the Himalayas and a north–south trough along the east coast of India.

position and hence the revival of the monsoon after a moderate duration 'break' episode.

4.2.2 The east Asian monsoon region

In the east Asian monsoon region, the major weather systems include the monsoon trough/ITCZ, tropical cyclones, the subtropical high over the western Pacific, the mid-latitude and subtropical fronts, low-level vortices, blocking highs, and polar anticyclones. Tropical cyclones will be specifically discussed in Section 4.3 and polar anticyclones will be discussed in connection with cold waves/cold surges in Section 4.5. Here, only the other five weather systems will be illustrated in more details.

The ITCZ

The ITCZ, either previously called the 'equatorial convergence zone' or the 'equatorial trough', is defined as a convergence line of airflows or a confluence zone in the air stream field (Ding, 1994). At the same time, it corresponds to the near-equatorial trough region or low-pressure region in the pressure field. On cloud images taken from weather satellites, the ITCZ is apparently identified as a single or several nearly continuous and elongated convective cloud bands. The OLR (outgoing long-wave radiation) data indicates a minimum in the ITCZ region (200–226 Wm^{-2}, in the western Pacific) (Jiang, 1988). Over the western North Pacific, the mean position of the ITCZ is 6°N. Another ITCZ is located over the south-eastern Pacific, about 5°S. Therefore, over the western North Pacific, one may observe a double ITCZ (Herqbert, 1969). In the transition season, the double ITCZ is very evident. The ITCZ in the western North Pacific is often connected to the monsoon trough in south Asia. So, some investigators (Gray, 1979) consider the ITCZ in the western North Pacific as the extension of, or one type of, the monsoon trough. The monsoon trough is characterized by the great horizontal wind shear, with the westerlies or south-westerly winds to the south and easterly trade winds to the north. Along the ITCZ/monsoon troughs, one may observe large areas of cloud systems or clusters, and even tropical cyclones or typhoons.

The position of the ITCZ monsoon troughs in the flow pattern has great seasonal variation, especially in south Asia and south-east Asia. It has a southernmost position in January, located somewhere between the equator and 5°N. In April or May, the ITCZ/monsoon trough moves northward and is situated about 5°N in south-east Asia (Matsumoto and Murakami, 2002). In July and August, the monsoon trough in the northern hemisphere shifts northward and develops. It has the northernmost position in the Indian Peninsula, reaching 20°–25°N. Over the western North Pacific and the South China Sea, the ITCZ runs from north-west to south-east, with an averaging position found at 12°–15°N (Figure 4.9). This part of the ITCZ is very active, being the birthplace of most typhoons in the north-west Pacific monsoon region. In autumn, the Asian monsoon trough retreats southward more readily than over the western Pacific (Figure 4.9(c)).

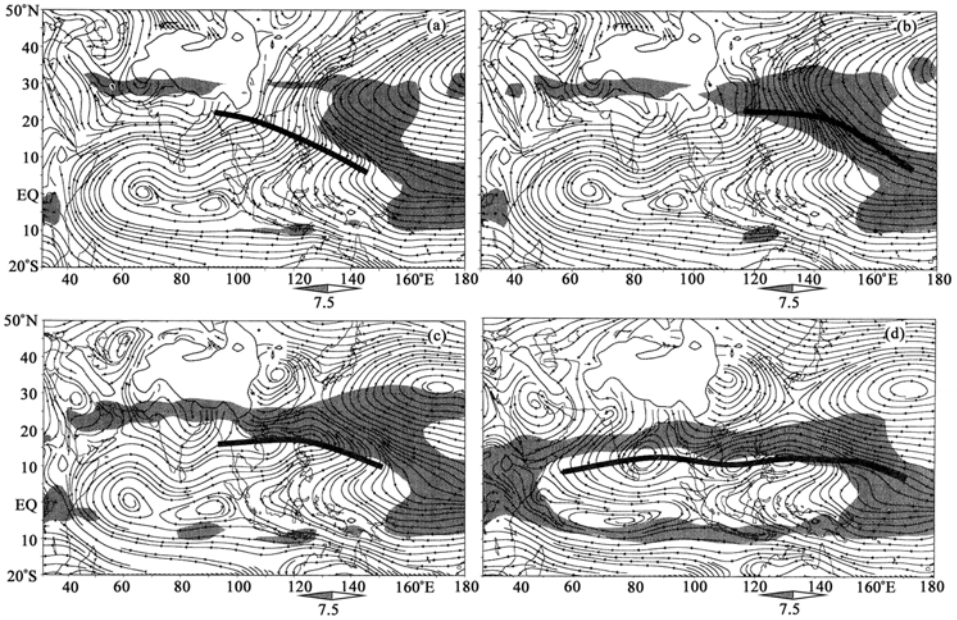

Figure 4.9. Mean 850-hpa streamline fields for July (a), August (b), September (c), and October (d), averaged for 1979–1999. The bold solid lines denote the position of the ITCZ/monsoon troughs. Shaded areas represent weak wind vertical shear, with $|V_{200} - V_{850}| > 7.5\,\mathrm{ms}^{-1}$.
From Sun and Ding (2002).

It is very interesting to note that an abrupt northward shift of the position of the ITCZ from the first 10 days of May to the middle of June occurs, which corresponds to the time period of the seasonal change in the Asian region, characterized by the onset of the summer monsoon in the South China Sea–Indo-China Peninsula and the Indian summer monsoon as well as the beginning of the Meiyu rainy season over the Yangtze River valley.

The ITCZ has significant implications for weather and climate events and circulation conditions in the western North Pacific and east Asia, especially for activity of tropical cyclones (typhoons) and precipitation. Based on 30 years of typhoon data over the western North Pacific, Ding and Reiter (1983) studied some climatological aspects of the variability of formation frequency and its relationship to the tropical general circulation in the Asian monsoon region. They found that the difference in typhoon formation between active ITCZ periods and inactive ITCZ periods is quite significant, the former frequency being 2–3 times larger than the latter. For months with many typhoons, the ITCZ is located near 20°N, and extends eastward to 160°E, whereas for months with few typhoons the ITCZ is found near 10°N and ends at about 30°E (Figure 4.10).

In the typhoon seasons of 1998 and 1999, the numbers of genesis of typhoons (TY) ($V_{\max} > 33\,\mathrm{ms}^{-1}$) and tropical storms (TS) ($V_{\max}$: 18–32 ms^{-1}) were small, with 1998 having the minimum frequency number (TS + TY: 18, normal: 28). For

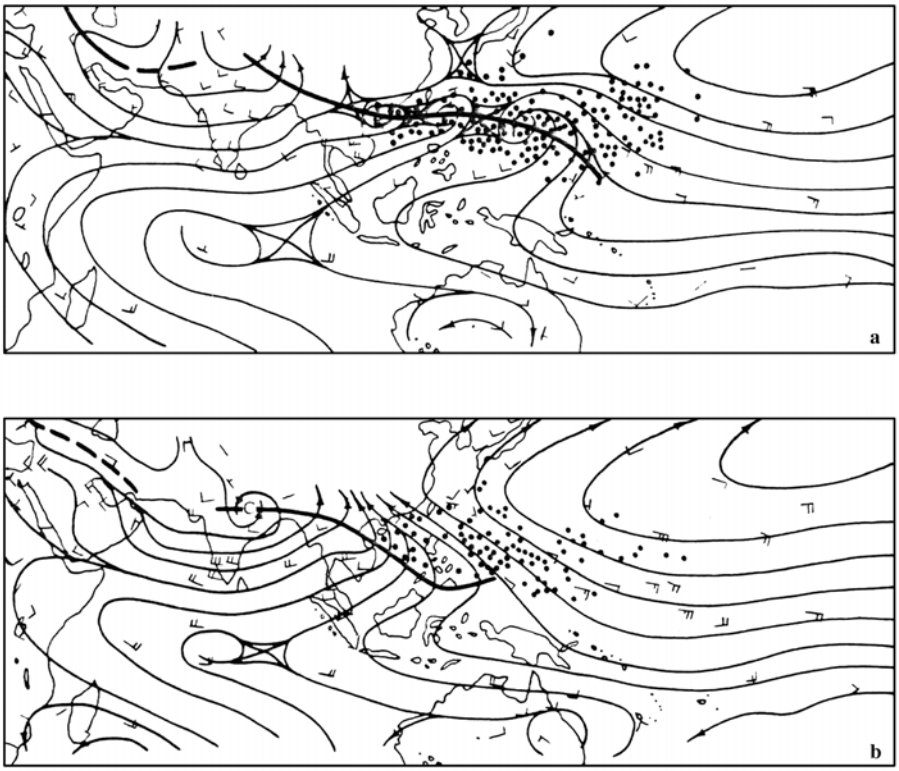

Figure 4.10. Mean streamline at 850 hpa for summer (July–September), (a) for months with many typhoons, and (b) for months with few typhoons. Black circles denote the location of first detection of typhoons.
From Ding and Reiter (1983).

the typhoon season of this year the ITCZ was very inactive. In July and August, there was no ITCZ or monsoon troughs in the tropical western North Pacific. The areas of weak wind vertical shear favorable for formation of tropical cyclones (Gray, 1967) were not significant and well-organized. The tropical western North Pacific was dominated by a low-level easterly trade wind. The circulation situation for the 1999 summer was very similar to that for 1998.

Recently, Chen *et al.* (2003) have investigated the role of the ITCZ and tropical cyclones in monsoon precipitation over the east Asian and western North Pacific regions. They pointed out that monsoon rain revival in the southern part of east Asia is caused either by tropical cyclones or the ITCZ, thus supporting the early conclusion made by Ramage (1952). Actually, the ITCZ has been rarely considered by previous studies to exert any impact on the east Asian monsoon rainfall. During the summer, the Meiyu rain band and ITCZ lie along the north-west and south-west peripheries of the western Pacific subtropical high, respectively. The sequential passage of the Meiyu rain band, the subtropical high, and the ITCZ form the

monsoon life cycle in the southern part of east Asia. In contrast, the monsoon rainfall variation in the northern part of east Asia exhibits different characteristics, but south-easterlies along the northern side of the western Pacific monsoon trough (or ITCZ) may furnish additional moisture to east China, Korea, and Japan, and initiate the monsoon revival in these regions. Some prolonged heavy rainfall events in the Yangtze River and north China were significantly affected by the ITCZ (National Climate Center, 1998). This problem will be further discussed in Sections 4.3 and 4.5.

The subtropical high over the western North Pacific Ocean

This high is one of six or seven high cells embedded in the extensive belts of high pressure nearly encircling the globe in the subtropical region to the south of the mid-latitude westerlies. It is an important component of the east Asian monsoon system. Its activity can exert an effect on the seasonal march of the east Asian summer monsoon and associated seasonal rain belts. In addition, the subtropical high can significantly affect the activity of tropical cyclones in the western North Pacific, and drought and flood events in east Asia. The subtropical high over the western Pacific assumes a marked seasonal variation in respect to its position, with an alteration between gradual shift and abrupt jump, which is closely related to the advance and retreat of major rain belts in eastern China. In general, two abrupt northward jumps may be observed (Ding, 1994; Wu *et al.*, 2002). The first jump normally occurs in the middle of June, with the ridge line of the high moving over the region of 20°–25°N. This shift indicates a northward jump of the seasonal rain belt over the Yangtze and Huaihe River valleys, heralding the end of the presummer rainy season in southern China. The second northward jump occurs in the early and middle part of July. This jump brings the ridge line of the subtropical high over the region around 30°N, thus leading to the beginning of the rainy season in northern China and the dry season in the Yangtze River valley. At this time, the tropical easterlies or south-easterlies (south-easterly monsoon) prevail over an extensive region along the southern and western flanks of the subtropical high, and the ITCZ advances northward up to its seasonal northernmost latitude, around 15°N over the western North Pacific and 15°–20°N over the South China Sea, where typhoons may frequently form.

Based on 20-year datasets of the China Meteorological Administration, NCC (1998) made a statistical study of the relationship between the activity of the Asian summer monsoon and the position of the subtropical high. Results have shown that in the case of late onset of the summer monsoon over the South China Sea, or weaker south Asian or east Asian summer monsoon, the subtropical high in summer has a position farther to the south than normal, with a probability of 0.89, 0.89, and 0.81 for June, July, and August, respectively. The opposite case is true. Recently, Tao *et al.* (2001) have also obtained a similar conclusion that for years with a stronger summer monsoon, the ridge line of the subtropical high at 500 hPa is located in the region to the north of 30°N and the Indian depression is stronger than normal.

The mid-latitude and subtropical fronts

These are one of main rain-bearing synoptic systems during the rainy season in east Asia. Actually, the major seasonal rain belt is a demonstration of the activity of this kind of planetary frontal zone. As the season progresses and the summer monsoon advances northward, the front retreats poleward. Therefore, the major seasonal rain belt moves from south China to the Yangtze River basin and Japan, and reaches north China and the Korean Peninsula. The typical frontal zone consists of the low-level baroclinic zone (the quasistationary front), synoptic-scale convergence zones (monsoon trough (Chen and Chang, 1980) or frontal low-pressure trough), and a warm and moist zone ahead of the front. During the process of the southward intrusion of cold air, a prefrontal low-level jet is usually generated (Chou *et al.*, 1990). When the frontal system and the attendant low-level jet move southward into south China, they can produce an extensive area of heavy rainfall. Often, one or several low-vortices are embedded within the frontal zone, thus greatly enhancing the intensity of heavy rains. The south-west vortex originating in the eastern periphery of the Tibetan Plateau is a prominent case of these kinds of frontal vortices (Chang *et al.*, 2000). They may continuously be created and propagate in procession eastward along the frontal zone or low-level wind shear line associated with the front. Generally, above the frontal zone, there is no major upper level trough in the westerlies. Therefore, the mid-latitude front in the east Asian summer monsoon season is a low and middle level frontal system, although the upper air synoptic systems may play an important role.

In the Yangtze River valley, Japan, and the Korean Peninsula, the rainy period from mid-June to mid-July is the noted Meiyu (Plum Rains) or Baiu season (Figure 4.11). This rainy season is characterized by the following: abundant precipitation, high relative humidity, cloudy or overcast, short daily duration of sunshine, weak surface winds, and frequent occurrence of heavy rainfall. During the Meiyu season, the Yangtze River valley is vulnerable to flooding and droughts due to the relative concentration and severity of rainfall amount which produces a great interannual variability of precipitation (-100% to $+250\%$ anomaly percentage). Figure 4.12 shows the long-term mean rainfall patterns during the Meiyu period (Liu *et al.*, 2003). The rainfall amount for the Meiyu period accounts for 30–45% of the total summer rainfall amount in this region, with the maximum precipitation found in the middle and lower reaches of the Yangtze River. Figure 4.13 (color section) illustrates the synoptic model of the Meiyu season. It can be seen that the Meiyu front, the major synoptic-scale, rain-producing system, has a unique feature in many ways different from that of the polar front from which it evolves under the conditions of the east Asian summer monsoon.

As pointed out by Chen *et al.* (2003), the monsoon rainfall and its variation in east Asia are closely related to the mid-latitude frontal activities and their evolution. The onset of the summer monsoon rainfall in each east Asian subregion and monsoon rain revivals in the northern part of east Asia is triggered by the arrival of a frontal rain band. Figure 4.14(a) clearly shows the contribution of the frontal precipitation (Chen *et al.*, 2003).

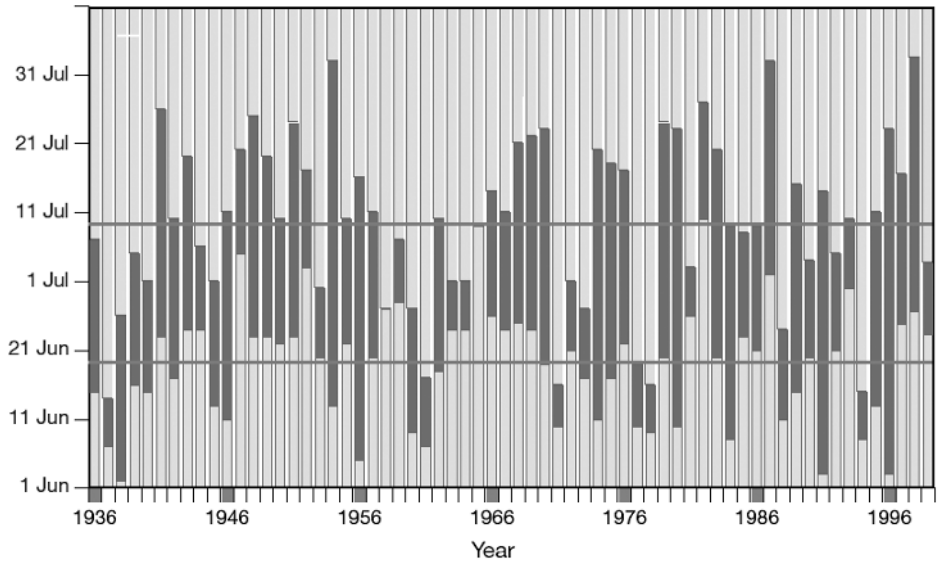

Figure 4.11. Onset and end dates of the Meiyu season over the Yangtze River basin. From WMO (2003).

Low-level vortex

The low-level vortices produced locally over the Tibetan Plateau and its sloping periphery are unique weather systems of a subsynoptic scale in the east Asian monsoon region. These topographically generated or influenced circulation systems are among the most important rain-bearing systems in east Asia during spring and summer (Ding, 1992). Low-level vortices have their geographical origin in three areas: the south-eastern part of the Plateau (called south-west (SW) vortices), the main body of the Plateau (called Plateau vortices), and the northern part of the Plateau (termed north-west (NW) vortices because of their location in the north-western part of China) (Tao and Ding, 1981; Ding, 1994). These vortices can produce excessive rainfall after they leave the Plateau if they are supplied with ample moisture and are supported by a favorable large-scale environment. The genesis and development of these vortices, especially SW vortices, are closely related to activity of monsoonal airflows. Therefore, they may be considered, to a certain extent, as the result of interaction between the Plateau and the monsoon. The Plateau vortices are obviously a weather system comprised of small-scale, shallow-depth, weak intensity, and short life cyclones. They are generated by a particular underlying surface. Once they move out of the Plateau, they generally dissipate rapidly due to the changed conditions of the underlying surface. The Plateau-produced mesoscale vortices are often generated by organized mesoscale convection. During the summer, the Plateau receives strong solar radiation, and the overlaying atmosphere often displays strong convective instability, even under the influence of a subsiding high-pressure system.

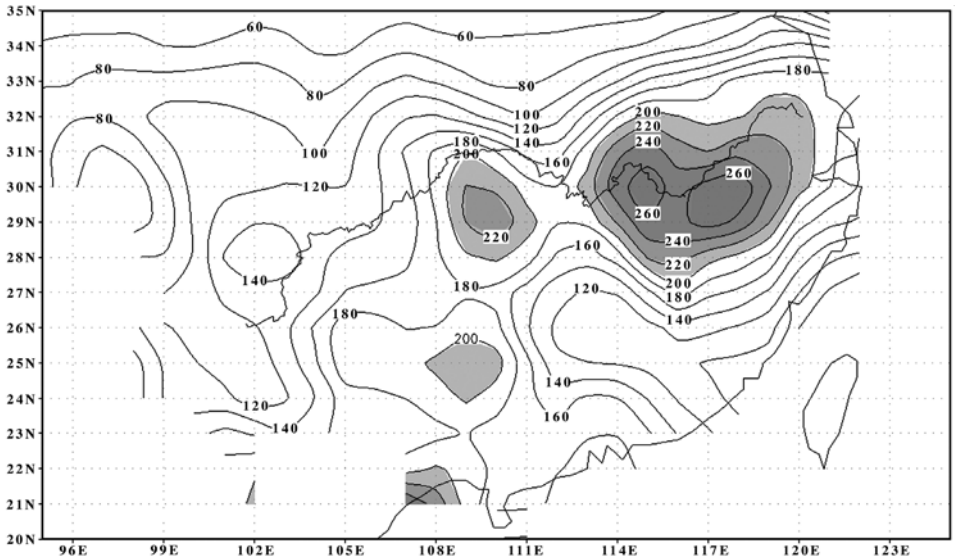

(a)

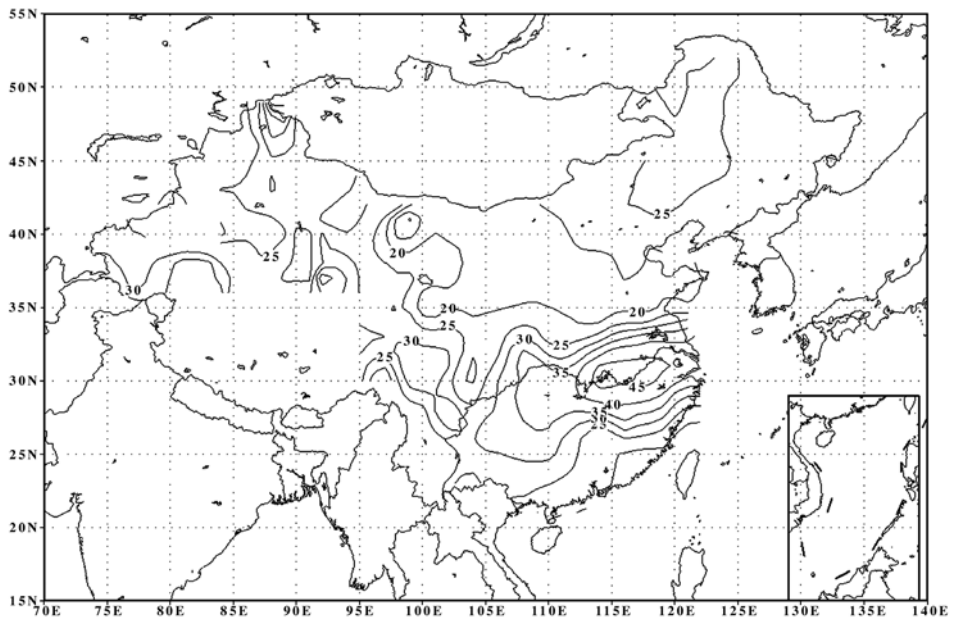

(b)

Figure 4.12. Long-term mean rainfall patterns during the Meiyu period. (a) 30-year (1971–2000) mean Meiyu rainfall pattern (units in mm) and (b) the ratio of Meiyu rainfall amount to the mean summer (June, July, and August) rainfall amount (units in %).
From Liu *et al.* (2003).

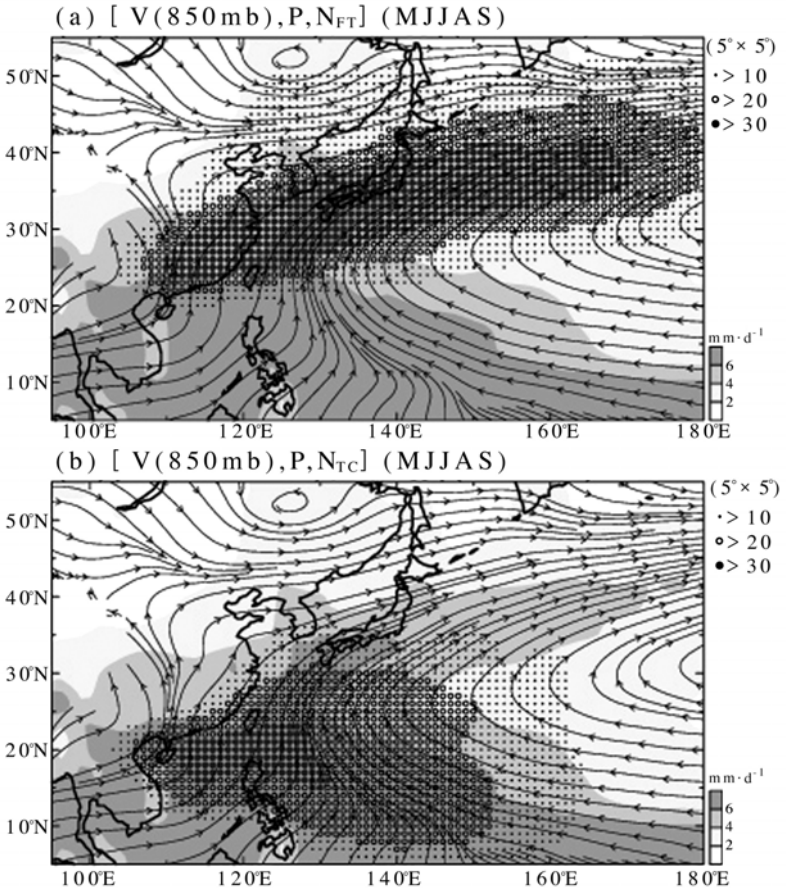

Figure 4.14. Summer (May–September) mean 850-hp streamline charts with corresponding CMAP precipitation (stippled areas), and (a) front occurrence frequency (N_{FT}: dots and open circles in the upper panel) within a square of $5^\circ \times 5^\circ$ for 1996–2002, and (b) tropical cyclone occurrence frequency (N_{TC}: dots and open circles in the lower panel) for 1979–2000.
From Chen *et al.* (2003).

With strong solar radiation, every mountain peak acts as an isolated heat island which triggers convection if moisture is available (Reiter and Tang, 1984). If the convective activity persists for long enough, a mesoscale cyclonic circulation can develop and, in turn, organize cumulus convection. In this case, the air over the Plateau is often convectively unstable ($\partial\theta e/\partial p > 0$) at low levels (Kuo *et al.,* 1986). A maximum of θ_e exists over the Plateau. The center of the Plateau vortex corresponds very well to the maxima of θ_e, suggesting a warm core structure to the Plateau vortex. The unstable air stratification may be caused by strong sensible heating from the surface, especially over the central and western parts of the Plateau.

Recent studies (Chen and Dell'Osso, 1984; Kuo *et al*., 1986) suggest that both baroclinic instability and latent heat release associated with organized convection over the Plateau might play important roles in the generation of the Plateau vortices. A vortex often develops within an existing shear line that separates the warm, moist monsoon flow to the south from the mid-latitude colder, drier air to the north. In fact, this Plateau-produced vortex is embedded within a sharp, short-wave trough. This vortex is also associated with strong convective activity throughout its life cycle. Chen and Dell'Osso (1984) also showed that the intensity of this vortex was significantly weakened when latent heat release was removed from the model.

In general, the SW vortex is defined as a 700 hPa closed cyclonic circulation over south-western China, mainly over the western part of the Sichuan Basin. It is a low-level circulation system, often only visible on 850 and 700-hPa analyses. On the surface weather map, one may often observe a negative pressure tendency during 24 hours over the low-vortex region. In this sense, the SW vortex is also called the SW low vortex. Most of the time, the vortex forms and dissipates without intense development and the severe weather associated with it, because there is usually a lack of upper level support and moisture. But if the synoptic conditions are favorable, the SW vortex may cause severe weather, especially heavy rainfall. The SW vortex may provide strong orographic lifting to trigger convection and, consequently, a large amount of rainfall on the steep topography surrounding the Sichuan Basin. Many cases may be exemplified, for example, the heavy rainfall in the Sichuan Basin on 1–14 July 1981 which has been extensively studied by numerous meteorologists (Chen and Dell'Osso, 1984; Kuo, Cheng and Anthes, 1986; Wang and Orlanski, 1987). This heavy rainfall took a large toll on human life and caused much damage to property. If the SW vortex moves eastward after its formation, it can cause heavy rainfall over the middle and lower Yangtze River valleys. If the SW vortex takes a northward track it can bring heavy rainfall to northern China. Ding *et al*. (2001) has shown a notable example of consecutive genesis, development, and eastward movement of three SW vortices in the 1999 Meiyu season.

From the synoptic viewpoint, the genesis and development of the SW vortex needs to meet two requirements: (1) the existence of a vigorous southerly airflow from the eastern slope of the Tibetan Plateau to the Sichuan Basin. It may play a dual role in the genesis of the SW vortex. Dynamically, this southerly wind produces 'differential frictional effects', a mechanism first discussed by Newton (1956) in connection with Colorado cyclone formation, thus leading to the formation of a cyclonic circulation at low levels. Thermally, the southerly wind may transport abundant warm, moist air into the eastern slope of the Plateau and the Sichuan Basin, providing the major moisture source for precipitation and the release of latent heat. (2) the necessary triggering mechanism. Most of the time, the low-pressure troughs passing over the Tibetan Plateau act as a triggering mechanism for the SW vortex. Chang *et al*. (1998) have studied the development of a low-level SW vortex which was involved by its coupling with two upper level disturbances. Both disturbances appeared later than, and upstream of, the low-level vortex. Faster eastward movements allowed them to catch up with the low-level vortex and led to a strong vertical coupling and deep tropopause folding. From the regional

viewpoint, the topography of the Tibetan Plateau is extremely important. It is suggested that the formation of the SW vortex is a consequence of the blocking effects of the mesoscale mountain range, located at the south-eastern corner of the Tibetan Plateau, on the south-westerly monsoonal flow. This is supported by the fact that the SW vortex develops mainly within the south-westerly monsoon current, that it is strongest at the lower level during both its formation and mature stages, and that low-level cyclonic vorticity is present throughout the period during which the south-westerly monsoon flows around the Plateau. In addition, researchers have argued about the importance of cold air coming from the north and north-east.

The development of the SW vortex is expected to depend greatly on the effect of latent heat release, due to the fact that this vortex is usually accompanied by a large amount of rainfall and convective activity. In order to better document the effects of strong latent heat release associated with convection, Kuo *et al.* (1986) calculated the mesoscale heat and moisture budget associated with a SW vortex which resulted in the flood catastrophe in the Sichuan Basin on 11–15 July 1981. With weak stability at the middle levels, latent heat release can induce strong, upward vertical motion, which in turn enhances low-level convergence spin-up and convective cloud development, establishing a positive feedback between the circulation of the SW vortex and cumulus. Wang *et al.* (1993) further indicate that the mesoscale vortex in the lee of the Tibetan Plateau is driven diabatically.

The blocking situation at mid and high latitudes in Eurasia

The blocking situation can exert an important effect on the onset and subsequent activity of the Asian summer monsoon. The relationship has been recognized since MONEX in 1979, as one possible precondition for the onset of the Indian summer monsoon (Sikka, 1981b; Murakami and Ding, 1982). When the Eurasian region is dominated by the blocking high during the transition season from winter to summer, the onset of the Indian summer monsoon would be delayed. In such a case, the westerlies are split into two branches, the southern one of which may flow into the region to the south of the Himalaya mountains, thus pushing surface cold highs into northern and central India. This is an unfavorable condition for the onset of the Indian summer monsoon. The late onset of the Indian summer monsoon in 1979 was a good example illustrating the effect of a blocking high. In addition, the change in tropospheric wind vertical shear induced by a mid-latitude blocking situation over Eurasia can affect the formation of a monsoon depression, especially in the Bay of Bengal (Raman *et al.*, 1981b).

In east Asia, the effect of the blocking high on the activity of the summer monsoon and monsoonal rainfalls has been studied by numerous investigators (NCC, 1998; Yang, 2001). The statistical study of blocking highs in Eurasia in summer has shown that the Oral mountains, Baikal Lake, and the Okhotsk Sea are three preferred regions of frequent occurrence (Li and Ding, 2004). Dual-blocking (Oral mountains and the Okhotsk Sea) and a dipole pattern (Okhotsk Sea) are particularly stable circulation situations which often lead to prolonged heavy rainfall over the Yangtze and Huaihe River basins. Under this circulation

situation, the planetary frontal zone in east Asia will be forced to move farther to the south than normal, thus affecting the Yangtze River basin due to a splitting of westerlies. At the same time, the seasonal northward advance of the subtropical high over the western North Pacific will be suppressed, thus resulting in an anomalously southern position. Statistics for the period of 1954–1998 have shown that the positions of subtropical highs have probabilities 0.75, 0.78, and 0.83 of being further south than normal for June, July, and August, respectively (NCC, 1998). The correlation coefficients between blocking index in the Baikal region and the precipitation amount in the Yangtze River basin in July has shown that an extensive area of positive correlation is located over the Yangtze River basin, implying that this region will have an above-normal precipitation condition if blocking situations develop over the Okhotsk or the Baikal Lake regions. The prolonged heavy rainfall events over the Yangtze River basin during the Meiyu seasons of 1954, 1991, and 1998 occurred under this circulation situation (Figure 4.15).

4.3 TROPICAL CYCLONES

The western North Pacific basin in the Asian monsoon region is a region where the tropical cyclones (with mean wind maximum $\geq 17.2\,\mathrm{ms}^{-1}$) most frequently occur from a global point of view, accounting for about 33% of a total number of approximately 80 tropical cyclones each year (Gray, 1967; Ding, 1994). In the Indian Ocean, the tropical cyclones mainly occur during premonsoon and postmonsoon seasons, with monsoon depressions dominating during the monsoon season. The annual frequency of tropical cyclones in the western North Pacific is 28.3 based on statistics for 1951–1979 by Chen and Ding (1979). Recent statistics for 50 years (1951–2000) have shown an average of 27.6 tropical cyclones, very close to the previous frequency. Based on the statistics of the Japan Meteorological Agency (JMA) (Yumoto and Matsuura, 2001), the climatological normal of tropical cyclones for 1971–2000 was 26.7, lower than the 50-year average. This may be attributed to the decrease of occurrence frequency of tropical cyclones during the 1990s. Figure 4.16 shows the annual number of tropical cyclones in the western North Pacific for the recent 50 years (Yumoto and Matsuura, 2001). Similar diagrams have been produced by Xu and Gao (2003) and Shi (2003).

It can be seen that the interannual variation is quite considerable. The year 1967 was the year with a maximum occurrence frequency of 40 tropical cyclones, while the year 1998 was the year with a minimum frequency of 14 tropical cyclones. The decadal variation is also obvious. In the 1950s, the annual number of tropical cyclones was below normal (26.0), above normal in the 1960s (31.1), nearly normal in the 1970s and 1980s (27.8 and 27.5), and much below normal in the 1990s (25.8). Especially in the period of 1995–2001, the average annual number of tropical cyclones was 5.4 less than normal. For climatological normal, the 30-year average for 1971–2000 (27.03) was nearly 2 tropical cyclones less than that for 1961–1990, reflecting a marked interdecadal variability. The typhoon season over the

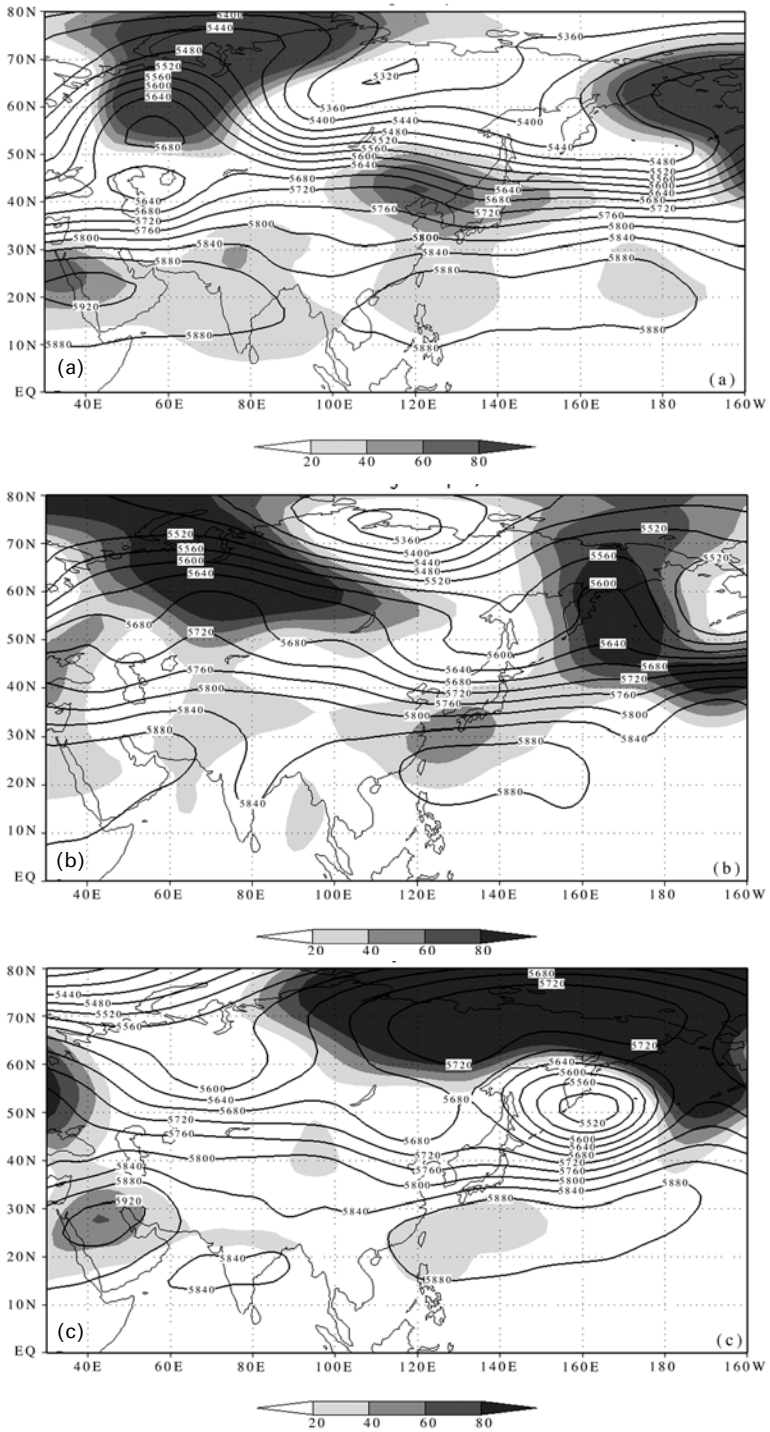

Figure 4.15. 500-hPa geopotential height fields of (a) the first stage (18–26 May), (b) the second stage (2–19 June), and (c) the third stage (30 June–13 July), of the Meiyu period. Provided by Sun Ying of National Climate Center (2003).

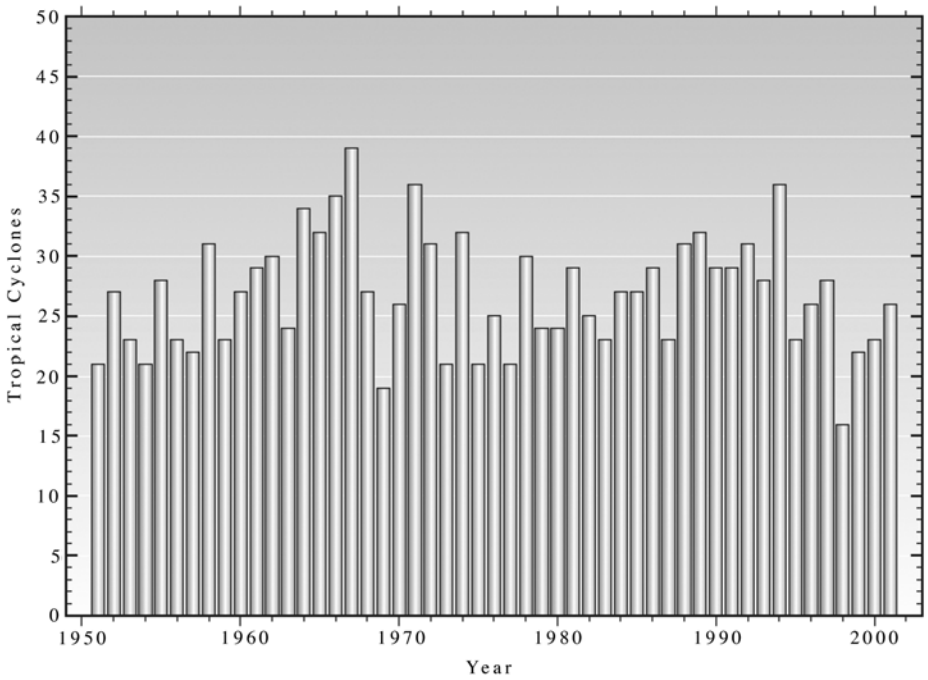

Figure 4.16. Annual number of tropical cyclones in the western north Pacific basin. From WMO (2003). Source: Yumoto and Matsuura (2001).

western North Pacific generally begins from June (1.76) and ends in November (2.58), with the culmination of occurrence observed in August (5.82), September (2.58), and October (3.98), accounting for 69% of the total annual number of tropical cyclones (Xu and Gao, 2003).

Landing tropical cyclones have very significant impacts on socioeconomic aspects and people's lives. On average, there are 7.0 tropical cyclones making landfall on China, with the maximum of 12 tropical cyclones occurring in 1971 and the minimum of 3 tropical cyclones in 1998. Although the interannual variation is large, the decadal variability is relatively small, with the minimum of 6.1 for the 1950s and maximum of 7.6 for the 1980s. The persistence duration of landing tropical cyclones has a significant interdecadal variability, with the minimum of about 4 days in the 1950s and the maximum of 6 days in the 1960s, 1970s, and 1980s. Out of the total number of 442 landfall typhoons in the most recent 50 years, 95% (421) occurred in the coastal area of south-east China, with Guangdong province having the maximum landing of tropical cyclones (33%) and Taiwan the second largest occurrence (19%). Based on the statistics of disaster areas, number of lives loss, and direct economic loss, damage in China in the most recent 20 years caused by tropical cyclones has demonstrated an increasing tendency from the mid-1980s to the mid-1990s. Afterwards, the economic losses and loss of lives have

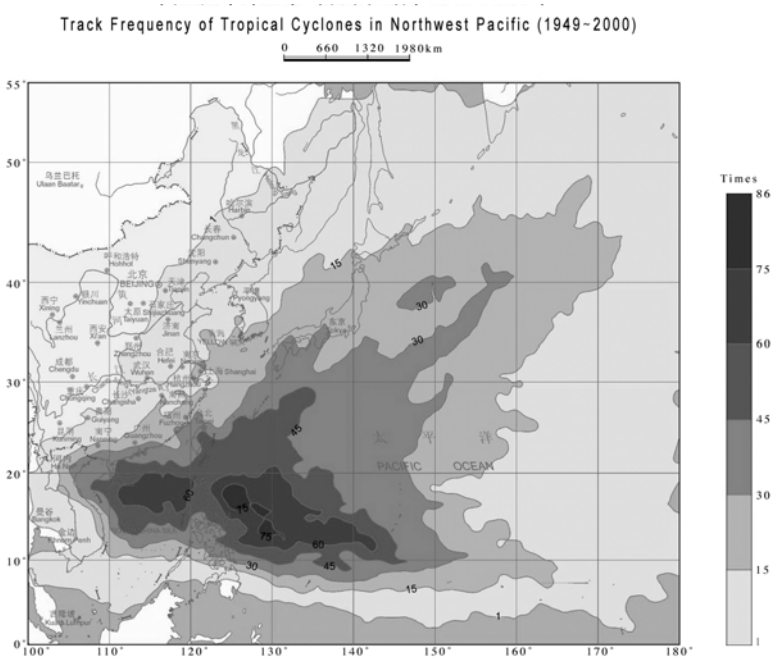

Figure 4.17. Track frequency of tropical cyclones in the north-west Pacific.
Computational method is referred to the source (Shi, 2003).

become alleviated, possibly due to a decrease in the occurrence frequency and intensity of tropical cyclones.

The tropical cyclones also significantly affect other countries and regions of east Asia and south-east Asia. The severe tropical storm Linda of 1997 was reported to be the deadliest storm to affect Vietnam since 1904 (WMO, 2003). It formed in the South China Sea and moved west–north-westward across the southern tip of Vietnam. Estimates of the dead and missing were in the thousands – mostly fishermen lost at sea. In 1999, torrential rainfall resulting from Typhoon Olga and a stationary frontal system resulted in hundreds of fatalities in the Democratic People's Republic of Korea, the Republic of Korea, and the Philippines. In 2020, Typhoon Saomai caused record-breaking rainfall over parts of Japan. In 2001, Typhoon Chebi in the Fujian province of China in June, with maximum sustained winds near 120 km h^{-1}, caused more than 150 deaths and severe tropical storm Utor killed more than 100 people when it made landfall in the Philippines in July.

As indicated in Figure 4.17 (Shi, 2003), tropical cyclones occur and move over a very broad area, although 91% of them occur between 5°N and 22.5°N over the western North Pacific (Xu and Neumann, 1984; also see Figure 4.14(b)). The most active place for tropical cyclones is found in the sea region from 110°–145°E and from 10°–30°N, with maximum in the regions to the east of the Philippines and the

south-west of Guan. Tropical cyclones can affect Japan (mainly the western part) exhibiting a high frequency of 30 tropical cyclones for 1949–2000.

The major regional origins of the initial genesis of tropical cyclones are found in the following three regions: the region to the east of the Philippines and to the south-west of Guan, the central part of the Caroline Islands and the central part of the South China Sea (Wang and Fei, 1987). Chang *et al*. (2003) showed that intense winter monsoon cold surges occurred in December 2001 near Singapore, 1.5 degrees north of the equator (see also Chapter 3.) But the regions where tropical cyclones intensify into typhoon intensity are different from their regions of origin. The major region of intensification of tropical cyclones into typhoons is located 5°–10° longitude to the east of the Philippines. In addition, the South China Sea is also a region of intensification of tropical cyclones.

Gray (1967) estimated that about 80% of all tropical cyclones originate in or just poleward of the ITCZ or monsoon trough (also see Figure 4.9(a)). On the other hand, the large-scale north-westward propagating wave patterns are also related to the genesis of western North Pacific tropical cyclones (Chang *et al*., 1996). Therefore, preferred regions of genesis vary seasonally with the annual migration of the ITCZ. Enhancement of the flow on either side of this monsoon trough increases the low-level relative vorticity and makes environmental conditions more favorable for genesis. Ding *et al*. (1977, 1994) and Gray (1979) have revealed clustering phenomenon of tropical cyclones in time and space, with multityphoons (3–5) nearly simultaneously or sequentially forming in a period of 1–3 weeks. This event mainly occurs under the conditions of an active or extended ITCZ over most of the western North Pacific in which the ITCZ may hold its easternmost position.

Numerous investigators have studied the impacts of the El Niño/Southern Oscillation (ENSO) events on the formation and movement of tropical cyclones over the western North Pacific. Although there is a general consensus that El Niño affects the location and frequency of tropical cyclones, the results are described in a qualitative and somewhat controversial way due to the differences in analysis procedures, datasets, and definitions of El Niño events used by different authors. Recently, Wang and Chan (2002) have revisited this issue using the longest possible available datasets. They studied changes in tracks, life spans, and occurrence frequency of tropical cyclones between the El Niño and La Niña years and further explained some possible mechanisms of how the ENSO events can impact tropical cyclones. They have found that the relationship between the tropical cyclone activity and ENSO events strongly depends on the intensity of ENSO episodes, with strong El Niño or La Niña events having significant impact and moderate warm (cold) events not showing definite significant impacts. They have identified two subregions where the largest variability occurs in close association with strong ENSO events: the SE (5°–17°N, 140°–180°E) and NW (17°–30°N, 120°–140°E) quadrants. During strong El Niño (La Niña) years, the tropical cyclone formation in the SE and NW quadrants exhibits a dipole anomaly pattern with enhanced (suppressed) formation in the SE (NW) quadrant (Wang and Chan, 2002). Figure 4.18 shows that in the SE quadrant the 5 warmest years had 31 tropical cyclone formations while the 6 coldest years had only 2 tropical cyclone formations. In the NW quadrant, the

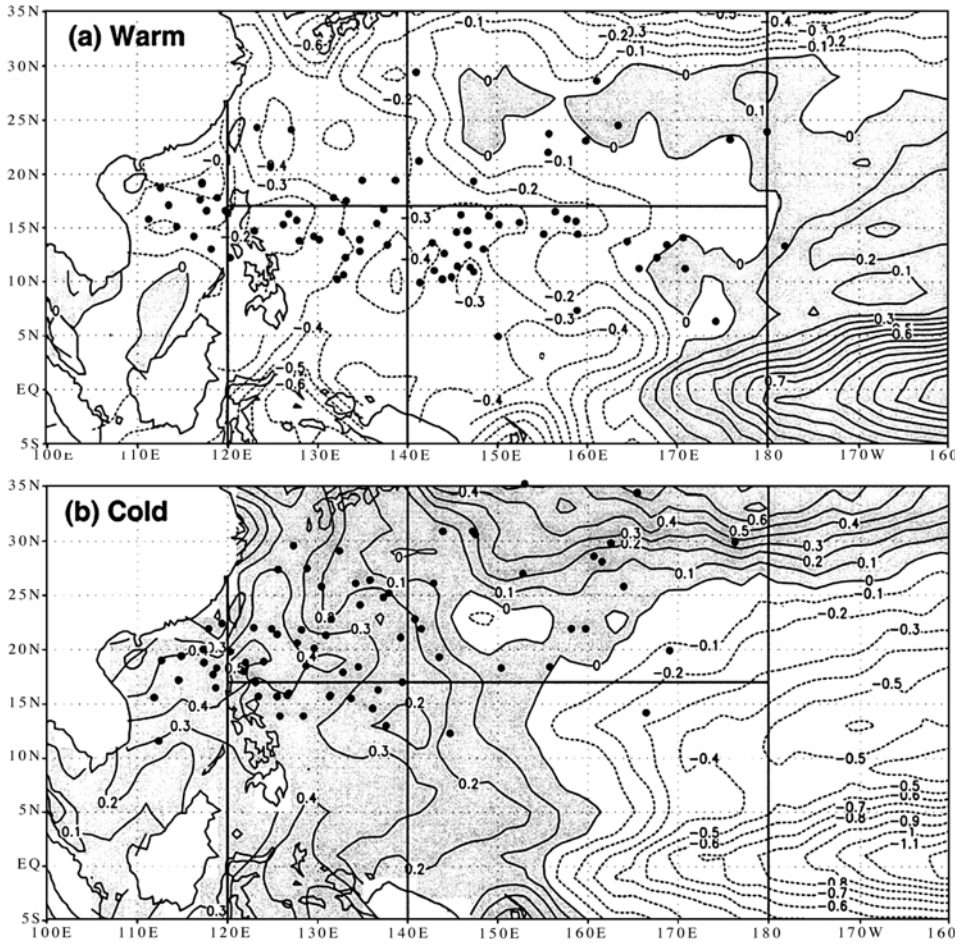

Figure 4.18. Locations of initial tropical storm formation and SST anomalies in peak season (July–September) during (a) the six strongest El Niño years (1965, 1972, 1982, 1987, 1991, 1997) and (b) the six strongest La Niña years (1970, 1973, 1975, 1988, 1998, 1999). The straight solid lines indicate boundaries of subregions of the western North Pacific.
From Wang and Chan (2002).

situation is reversed, with 28 tropical cyclones forming during the cold event years while only 7 during the warm event years. In addition, they have found that the mean life span of tropical cyclones in a strong warm event year (about 7 days) is longer than that in a strong cold event year. The tropical cyclone tracks differ substantially between the strong warm and cold event years. During El Niño autumn, the number of tropical cyclones that formed south of 15°N and recurved northward across 35°N is 2.5 times that during cold event years.

During the 1997–1998 ENSO warm event, the genesis region of tropical cyclones in 1997 shifted eastward and approximately half of the tropical cyclones formed in a region south of 20°N and east of 150°E, where storm genesis is usually less than in the west (Sun and Ding, 2002; WMO, 2003). This eastward shift is consistent with the above findings of Wang and Chan (2002). In 1999 when the La Niña persisted throughout the whole year, a record high mean genesis latitude (21.2°N), compared with normal mean genesis latitude in the NW Pacific of 16.2°N for 1951–2001, was established. In the same year, the mean lifetime of tropical cyclones was the shortest on record (3.1 days) compared with the climatological normal of 5.2 days. These results are also consistent with the above findings.

Tropical cyclones play a crucial role in the precipitation over east Asia being major rain-producing systems. As pointed out in Section 4.2 (Figure 4.14(b)), the revival of the second rainy episode in east Asia is mainly caused by tropical cyclones, in particular in south China. Therefore, abundant precipitation produced by tropical cyclones has important significance for water resource supply in this region. However, heavy rainfall or excessively heavy rainfall brought about by tropical cyclones may cause severely devastating floods over extensive areas. Typhoon Winnie in 1997 poured down torrential rainfall in Fujian, Zhejiang, and Jiangsu provinces, causing great damage, especially in Zhejiang province, with 1,282 km of sea dykes destroyed, 229 people killed, and a direct economic loss of 33.7 billion RMB (Shi, 2003). This typhoon also brought about a large amount of precipitation in north and north-east China.

Occasionally, northward or north-eastward moving typhoons suddenly change track, turn toward the west or west–north-west, and penetrate deeply inland if a blocking high to the north of the typhoon builds up rapidly, amplifies, and retrogrades. Under such conditions, the typhoon, though usually greatly weakened, drifts in an easterly current and finally becomes nearly stationary because of the blocking effect of the high-pressure ridge to the north of it. If other conditions are favorable, prolonged heavy rainfall may ensue. An unprecedented case appeared early in August 1975 when the typhoon Nina dumped torrential rainfall, with a maximum of 1,692 mm, during three days over a narrow, elongated band (120 km long and 50 km wide) the windward side of the Funiu Mountain Range. Its most prominent feature was a large blocking high located to the north of the tropical depression. Due to the blocking action of this high-pressure region, typhoon Nina showed considerably slow movement two days after landfall, and eventually changed its direction of propagation from north-eastward into westward. Finally, the depression became nearly stationary and probably made a small loop over the hilly region in the southern part of Henan province. The erratic movement lasted for more than 20 hours and was influenced by an extratropical weather system (cold front) as well as by terrain features.

On 11 September 2000, the typhoon No. 14 (Saomai) hit the Nagoya district, causing torrential rainfall. A total rainfall amount of 567 mm was recorded at Nagoya station and a precipitation intensity of 93 mm h^{-1} occurred for 19 hrs on 11 September when a cold front affected the typhoon. Floods in the Shonai River

basin exceeded the estimated high water level, with 420,000 people facing severe flooding and evacuation instructions announced.

In the south Asian monsoon region, the premonsoon and postmonsoon seasons witness the formation of tropical cyclones with different intensities such as cyclonic storms (CS), severe tropical storms (SCS), very severe cyclonic storms (VSCS-H) with cores of hurricane winds, and super cyclonic storms with maximum wind speeds in the circulation between 33–47 kt, 48–63 kt, 64–119 kt and greater than 119 kt per hour, respectively. These cyclonic storms form within the northern hemisphere near-equatorial trough (NHET) over the warm waters of the north Indian Ocean and move generally in a west–north-westerly/north-westerly direction. Some of them recurve in a north-east direction. The formation points of the cyclones shift from about 5°–7°N in March to 15°–20°N in May with the northward movement of the NHET in the premonsoon season and recede southward from 15°–18°N in October to 5°–7°N in December during the postmonsoon season. The cyclones are not only more frequent in the Bay of Bengal compared with the Arabian Sea, but the Bay cyclones are also notorious for causing large devastation to property and loss of life upon striking the coast. The storms forming in the Bay of Bengal strike the east coast belt of India. In recent years a devastating tropical cyclone of super cyclonic storm intensity (maximum wind speeds over 185 kt and a pressure drop at the center of 99 hPa) struck the Orissa coast on 29–30 October 1999, killing over 10,000 people with a storm surge of 6 m above the astronomical tide penetrating 25 km in land. There have been several other equally, or more, notorious intense storms in the past that have affected the east coast of India and Bangladesh and occasionally the Myanmar coast. Cyclones forming in November and December over the southern Bay of Bengal occasionally endanger the coast of Sri Lanka too. Cyclones forming in the Arabian Sea affect the west coast of India, the coast of Pakistan, and very occasionally even the Arabian coast. The deltaic regions of the Godavari River in Andhra Pradesh and Mahanadi River in Orissa in India and the Padma and Meghana Rivers in Bangladesh are particularly vulnerable to the destructive potential of these storms as the associated storm surges rise to 3–8 m above the astronomical tide. All loss of life is due to inundation by storm surges and floods. The destruction caused by these cyclones is nowhere of greater societal significance than over the region stretching from the east coast of India to coastal west Bengal and the coastal belts of Bangladesh.

It is important to recognise that the cyclone genesis potential (GP) is quite high in the Bay of Bengal during the two cyclone seasons (presence of NHET, high SSTs, favorable thermodynamical environment, and moderate vertical shear of tropospheric wind). Bhowmik (2003) has examined the changes in the GP during intensification of the cyclones and found that the GP attains its peak value 24–36 hours prior to cyclones reaching their highest intensity. Nearly 7% of the total number of tropical cyclones on a global and annual basis form over the North Indian Ocean (mostly over the Bay of Bengal). The average number of tropical cyclones forming over the North Indian Ocean annually is 6 with a standard deviation of 2 and a range of 1–10. The cyclone frequency may even vary between 1–3 storms in the premonsoon season and 2–5 storms in the postmonsoon season (Mandal, 1991).

Apart from the great devastation caused by these storms, they are an important source of water over the interior parts of the south peninsular of India due to the torrential rains brought by them for periods of two or three days. The structure of severe cyclonic storms/higher intensity storms is similar to those of typhoons and hurricanes in the north-west Pacific Ocean and North Atlantic Ocean. The severe cyclones have a characteristic eye (radius 20–40 km) which is surrounded by a ring of strong winds up to a distance of 100–150 km. Deep convection in the 'eye wall' region and the inflowing winds near the surface rushing slowly from a distance of 1,000 km from the center and accelerating as they approach the inner storm area are characteristic features of intense storms. Satellite pictures show characteristic features like the cumulus lines of the inflow bands, the outflow cirrus bands, the central dense overcast element, and the eye of the cyclone. Spiral rain bands, eye features, and double eye walls are also observed on radar and satellite pictures of these cyclones (Raghavan, 1990; 1997). The most prominent bands are seen in the southward quadrant coinciding with inflowing maximum winds particularly in westward moving cyclones. In recurving cyclones, cirrus cloud bands associated with the outflow appear in the north-east quadrant preferentially. Diurnal variation of cloud patterns is observed in the inner core cloudiness, being maximum at sunrise and minimum at sunset (Kelkar, 1997). The eye wall structure of the Bay of Bengal cyclones in radar and satellite pictures shows great dynamic activity as the eye forms, disappears, and reforms within several hours (Gupta and Mohanty, 1997; Kalsi, 2002).

Over the last 100 years or so research on the climatology of formation, intensification, movement, and strike points of these storms, mechanisms for their cyclogenesis and recurvature etc., have yielded much useful work. This knowledge is applied by operational forecasters in their work. Upper tropospheric flow patterns over the region of storm formation control the formation and movement of the storms. Some storms recurve under the influence of approaching westerly troughs. Anjaneylu *et al.* (1969) were among the first to study the heat, moisture, and kinetic energy budget of a Bay of Bengal cyclone in October 1963. State-of-the-art synoptic–climatological methods and high-resolution numerical prediction models are now applied for operational forecasting (Sikka, 1975; Singh, 1985; Mandal, 1991; Prasad *et al.*, 1997). However, the average vector errors in predicting the center of the cyclones remain 120, 230, and 320 km for 24, 48, and 72-hour forecasts, respectively. These are quite large errors as the tropical cyclones in the north Indian Ocean are slow-moving ones compared with the typhoons and hurricanes in the North Pacific and North Atlantic basins. Nearly 50% of the tropical depressions in the Bay of Bengal during the pre and postmonsoon seasons intensify into tropical cyclones out of which almost 80% intensify further into SCS intensity. It may take several days for a cloud cluster to develop into a tropical depression with a well defined center, but further intensification is quite rapid and a cyclone may change into VSCS-H within 48 hours or even less.

The two months of October and November in the postmonsoon season witness maximum formation of tropical cyclones with the frequency tapering off rather rapidly in December. Tropical cyclones in the premonsoon season begin to form

in April and the frequency of formation records a minor maximum in May. The Bay of Bengal cyclones most frequently strike the Andhra Pradesh coast with a second maximum in the Tamil Nadu coast. Recurving storms mostly strike Orissa and the western Bengal coasts, and some of them even strike the Bangladesh coast. On a country-wise basis, over half the number of cyclones forming in the Bay of Bengal in different categories have struck the coastal states of India. However, the frequency of SCS and VSCS-H striking the Bangladesh coast is higher. It is also noteworthy that a significant number of tropical cyclones dissipate on the Bay itself, particularly those forming in mid-November to December. This could be due to the influence of westerly troughs, advection of colder air from the north-west, and travel of the storms over cooler waters in the northern Bay of Bengal.

Mandal (1991) and Kalsi (2002) have provided good reviews of the observational forecasting/warning aspects of tropical cyclones. Ali and Chowdhury (1997) have provided risk assessment of tropical cyclones striking Bangladesh. A large number of satellite-based studies on these cyclones are available which have stressed upon the operational classification of these cyclones, and determination of their centers, their intensification potential, structures of severe cyclones with double eye walls etc. (Sikka, 1971; Kalsi and Jain, 1989; Mandal *et al.*, 1990; Kalsi, 1999) and decay of a super cyclone (Kalsi *et al.*, 2003). One of the handicaps for good prediction of the formation and movement of these storms is the lack of wind data to define the center of the cyclone for more reliable dynamical prediction. Introduction of a synthetic vortex, axisymmetric or asymmetric, and its assimilation in the dynamical prediction models, remains one of the challenging problems for reliable track prediction. Dynamical models for predicting the storm surge began to be developed in early 1970s (Das *et al.*, 1974) and a good recent review of these models is given by Dube *et al.* (1997).

4.4 FLOODS AND DROUGHTS IN THE MONSOON SEASON

Floods and droughts are important components of the Asian monsoon environment. Their occurrence is mainly attributed to the great interannual variability of monsoon rainfall as indicated in Section 4.1. From the meteorological viewpoint, droughts and floods mean an excess or deficit of rainfall relative to the normal conditions, regardless of the severity of disasters brought about by them (Ding, 1994). A number of drought and flooding indices have been designed for the climatological perspective. But, for more widespread and practical use, the departure or anomaly of rainfall from the long-term mean is used to define droughts and floods. If the precipitation departure for summer (June–August) is in the range of -25 to -50%, this period or season may be defined as the drought period/season; if the precipitation departure is less than -50%, this corresponding spell is defined as a severe drought. Contrary to this, precipitation departures of 25–50% and greater than 50% are defined as flooding and severe flooding, respectively.

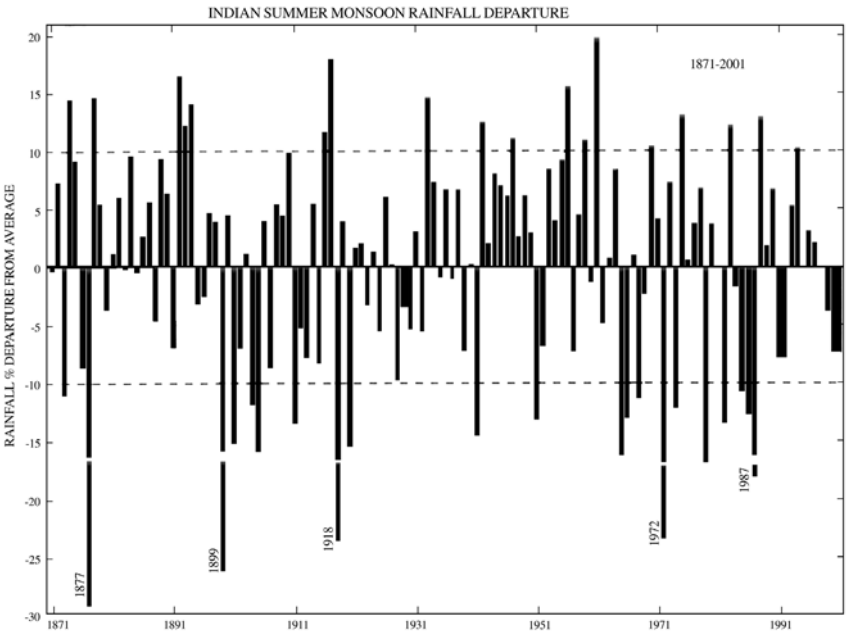

Figure 4.19. The year-to-year departure of monsoon rainfall from its norm (June– September) over India.
From IMD.

4.4.1 The south Asian monsoon region

Figure 4.19 shows the year to year departure of monsoon rainfall from its normal over India. They differ from year to year, with the great interannual variability. Significant negative departures of monsoon rainfalls occurred in 1877, 1899, 1918, 1972, and 1987, implying great deficiencies in rainfall or dry conditions. Recently, the year 2002 was a year of severe monsoon drought, whereas the year 2003 was a year of normal monsoon rainfall (figure not shown). During the monsoon season of 2002, daily rainfall remained subdued throughout the season whereas in the season of 2003, it was mostly normal or above normal except for short periods from 10–25 August and 12–22 September. Thus, the behavior of the seasonal monsoon is determined by a statistical average of independent short–medium and low-frequency modes. It is still a debatable matter whether the medium and low-frequency modulations of the monsoon are controlled by predetermined boundary forcing or by low-frequency dynamical instabilities in the region. Note that in some years the rainfall departs significantly from the seasonal normal leading to drought and excess (flood) monsoon seasons.

Floods

Floods are caused by very high rainfall spells associated with monsoon disturbances like tropical cyclones, depressions, low-pressure areas, MTCs, and western disturb-

ances. Individual flood events occur in all the major rivers of the subcontinent but those occurring in the Indus and the Ganges basins on the Indo-Pakistan flood plains, Brahmaputra basin in north-east India and Bangladesh and Mahanadi, and the Tapi and Narbada basins in central India are particularly devastating. The flood problem in the Bihar state of India is made worse by the discharge of excessive monsoon runoff from the rivers of Nepal. Individual flood events in any of the above river basins occur even in a drought monsoon year as exceptionally heavy rainfall does occur with a weather disturbance in a river basin, even though the overall performance of the monsoon may be below the normal for the season as a whole. An individual flood event in a river basin is identified by the crossing of the danger mark in the water discharge along a gauging site which results in the river water to break its embankments and cause devastation to life, property, and agricultural crops in the surrounding areas. IITM (1989, 1994) have prepared atlases for one-day Possible Maximum Precipitation (PMP) and for severe rainstorms which have affected India. Dhar and Nandargi (1995) have delineated the zones of severe rainstorms resulting in floods of Indian rivers. Dhar and Nandargi (1998) have provided an extensive review of the severe floods over India during the summer monsoon season. There are three distinct belts of one-day duration flood producing severe rainstorms oriented in east–west direction, viz. along the Indo-Gangetic plains in the eastward flowing Ganga–Yamuna basins and along central India, the eastern part of which is in the eastward flowing Mahanadi basin and the central and western parts in the westward flowing Tapi and Narbada basins. There is another devastating flooding area in north-east India and Bangladesh. The north-east Indian states are affected three or four times during a season by the heavy discharge from the Brahmaputra basin and other minor rivers in the area. Bangladesh is even more vulnerable to floods as the Brahmaputra discharge from north-east India joins the flooding waters of the Meghana and Padma Rivers due to heavy runoff from monsoon rains over the country and the discharge brought upstream from the Ganges basin across India. The flood problem of Bangladesh is further aggravated by its flat nature of its deltaic land which is hardly 10 m a.s.l. The slow discharge of the flood waters into the northern Bay of Bengal further adds to the flooding in Bangladesh when it coincides with an episode of higher elevation of the sea level in the nothern Bay on intraseasonal scales (Webster, 2003). There is yet another type of flood which occurs along the east coast of India and coastal Bangladesh during tropical cyclone seasons (pre and postmonsoon). Such floods are accompanied by heavy rainfall associated with the landfall of a cyclonic storm as well as, more importantly, the storm surge accompanying a cyclone.

Besides the individual flood events associated with heavy rainstorms, the monsoon season over India is excessively wet in some years. A monsoon season with excess rainfall of over 10% of the normal is designated as an excess or flood monsoon season. During the 1877–2000 period, there have been 10 years when the seasonal monsoon rainfall over India as a whole exceeded 13% of the normal (1874, 1878, 1892, 1894, 1917, 1933, 1956, 1961, 1975, and 1988) and in four of these years the rainfall exceeded 15% of the normal (1892, 1917, 1956, and 1961). Sikka (2000) has extensively reviewed the literature on heavy rainfall associated with individual

heavy rainstorms as well as the excess monsoon performance over all of India and on a large-scale individual meteorological subdivision basis.

Droughts

Monsoon drought is a natural disaster known to India from time immemorial as the rains in some years underperform over vast parts of south Asia. Over large parts of India the failure of rains is almost simultaneous and the two homogeneous regions affected more often simultaneously are north-west India and western central India. Usually, monsoon seasonal rainfall over north-east India and Bangladesh behave in opposite phase to the whole of India. In Pakistan, being mostly semiarid/arid, droughts are common and usually occur in the same monsoon seasons when the rains have failed over north-west India and western central India. The adverse effects of a widespread and severe drought over the Indo-Pakistan belt have been so great that the event is considered as an important marker in the collective economic and social history of the region. As the summer monsoon is the presiding deity of the agricultural economy of the region, a drought is commonly linked with a problem of agricultural productivity and for the resource-poor farm laborers it even becomes a problem of sustenance. The nexus between the drought and famine in India has been broken in the last 3 decades with the introduction of the Green Revolution technology in agriculture and extension of irrigation facilities. A vast number of monsoon–drought studies relating to the climatology of all of India, subregional and district scale droughts, and meteorological conditions on regional and global tropical scales, considered important for the incidence of droughts over India, have been reported in the literature. Keshvamurty and Awade (1974) and Sikka and Gadgil (1978) examined the dynamical abnormalities associated with the droughts over all of India in 1972. Raman and Rao (1981) linked the drought monsoon of 1979 to the presence of blocking high over Asia. Bhalme and Mooley (1980) examined the occurrence of large-scale droughts over India with anomalous monsoon circulation. Sikka (1999) has extensively reviewed the drought problem over India and discussed the morphology of several individual 'all-India' drought monsoon years. Sikka and Kulshrestha (2002) have studied the Indian droughts from a historical perspective. Monsoon droughts over India have been categorized as mild, moderate, severe, and phenomenal, if the quantum of seasonal monsoon rains has been below 1.0 of the standard deviation (SD), 1.25–1.49 of the SD, 1.50–1.99 of the SD, and equal or below 2.0 of the SD, respectively. The monsoon seasons of the years 1877, 1899, 1902, 1905 , 1918, 1920, 1965, 1972, 1979, 1987, and 2002 witnessed severe droughts, of which 1877, 1899, and 1918 were phenomenal droughts and the recent 3 years 1972, 1987, and 2002 were very close to the phenomenal category in which the deficit of seasonal rainfall was 19%. Almost all the severe droughts except those of 1920 and 1979 are associated with warm El Niño phenomenon in the central and eastern equatorial Pacific Ocean and a low Southern Oscillation Index (SOI). Walker (1924) discovered the relationship between the out-of-phase performance of monsoon over India and the Southern Oscillation (SO). Shukla and Paolino (1983) suggested that monsoon droughts occur over India in the years when the change over the SOI

difference between January and April is negative. Sikka (1980) and Rasmusson and Carpenter (1983), for the first time, noted the relationship of the monsoon droughts with El Niño warming. This was further confirmed by Mooley and Paolino (1989) who in turn suggested that monsoon droughts over India occur when the warming phase of El Niño coincides with the ongoing monsoon season. El Niño–monsoon connections have become an important aspect of monsoon interannual variability and, as expressed by Webster and Yang (1992), the two phenomena interact in a complex way. Opinions have been expressed by some researchers that the spring-predictability barrier in the El Niño prediction has its origin in the evolving Indian monsoon. Nigam (1994) sought the dynamical basis for the El Niño–monsoon connection. Kirtman and Shukla (2000), using an approach of numerical experimentation with general circulation model runs of 50 years, have attempted to link the evolution of the El Niño to the evolution of the south Asian monsoon as El Niño amplifies in October–December, following the monsoon failure. El Niño is aborted in some years when the monsoon rains perform on the excess side of normal (Sikka and Paul, 1994). Even though there is no unique one-to-one relationship between the monsoon droughts and the El Niño warming phase (only 60% of the monsoon droughts over India are associated with El Niño warming), a year has never been an excess monsoon year, if an El Niño warming is taking place in the equatorial central Pacific. Also among the 16 parameters, until recently used for the long-range forecasting of seasonal monsoon rains over India (Gowariker *et al*., 1991), there is no single parameter which is linked with monsoon failure for the 60% of the cases El Niño warming is. Thus, El Niño warming can be considered as an important precursor for the ensuing monsoon drought or at least for a very high probability of the non-incidence of an excess monsoon season. El Niño is known to have interdecadal variability. Wang (1995), Kriplani and Kulkarni (1997), Krishna Kumar *et al*. (1999), and Krishnamurthy and Goswami (2000) have expressed views that the El Niño–monsoon connection has been weakening since the 1980s. However, this could be only a temporary fluctuation on a secular basis as the most recent monsoon drought of 2002 occurred in the warming phase of an El Niño event (Sikka, 2003). Within a particular phase of the interdecadal oscillation there are several strong and weak phases of interannual variation of the monsoon. The Walker circulation over the Indo-Pacific equatorial belt, as modulated by shifts in the equatorial SSTs over the belt, interacts in a complex manner with the regional Hadley and east–west circulations over the Indian region to influence the performance of the south Asian monsoon.

South Asian monsoon rainfall is quite stable over the long term. It has the smallest interannual variability of all the major regional monsoon systems. It has no strong quasiperiodicity, except perhaps the quasibiennial oscillation (QBO). Meehl (1994, 1997) suggested a coupled land–air–sea mechanism for explaining possible QBOs in monsoon rainfall over south Asia involving the tropospheric biennial oscillation (TBO). Meehl (1994, 1997) and Wu and Kirtman (2003) have studied these links by performing sensitivity experiments using coupled GCMs in which ENSO, tropical mid-latitude interactions, and impacts of land–sea contrasts on the monsoon QBO have been examined. The incidence of droughts and floods

over India have been noted to have strong epochal behavior (Joseph, 1976; Sikka, 1980; and others), but no QBO. The epochs of 1899–1920 and 1965–1987 had 8 and 9 droughts, respectively. Whereas the epochs 1871–1898 and 1921–1964 had only 2 and 3 droughts, respectively. Thus, the 'all-India' monsoon rainfall series has performed for an extended period near to its long-term normal (1871–1898 and 1921–1964) and departed somewhat from this normal for other extended periods (1899–1920 and 1965–1987). The long-term 'all-India' monsoon rainfall series shows no significant trend. However, Rupakumar *et al.* (1992) have shown long-term decreasing trends in the rainfall series of north-east India and central north-east India homogeneous regions and an increasing trend for north-west India. Another aspect worth mentioning is that there have been only three occasions when the droughts occurred on an 'all-India' basis for two consecutive years (1904–1905, 1965–1966, 1986–1987). This again gives strength to the long-term stability of Indian monsoon rains over the scale of the country. The inter-relationship of the monsoon rainfall over India with those of Bangladesh, Nepal, Pakistan, and Sri Lanka on an individual county basis is rather weak (Pant and Rupa Kumar, 1997).

4.4.2 The east Asian monsoon region

Timing of onset and intensity of the summer monsoon have a significant effect on the occurrence of droughts and floods in east Asia. Numerous studies have been directed to statistical relationships between precipitation patterns and amount in China and activities of the east Asian summer monsoon (Ding, 1994). Table 4.1 shows this result (He and Ding, 2004), which has been obtained from different sources (Ye and Huang, 1991; Zhao, 1999). It can be seen that out of the flooding years in north China, 7 occurred during a strong or normal east Asian summer monsoon. Six flooding years were in a good correspondence to late or normal onset of the SCS

Table 4.1. Statistical relationship between droughts/floods and activities of the east Asian summer monsoon for 1961–1998.
He and Ding (2004).

			Intensity of east Asian summer monsoon			Onset timing of SCS summer monsoon		
Region			S	N	W	E	N	L
Middle and lower	F	8	3	4	1	2	2	4
valleys of Yellow River	N	16	6	7	3	4	6	6
and northern China	D	14	1	7	6	3	2	0
Yangtze and Huaihe	F	15	0	5	10	3	2	10
River basins	N	12	4	8	0	3	5	4
	D	11	6	5	0	3	3	5

Notes: S = strong, N = normal, W = weak, E = early onset, L = late onset, D = drought, F = flood, SCS = South China Sea.

summer monsoon. Among the 14 drought years, 13 years occurred during a weak or normal summer monsoon and 11 years corresponded to 9 late and 2 normal onset years of the SCS summer monsoon. For the Yangtze and Huaihe River basins, 15 flooding years unexceptionally occurred under conditions of strong (11 years) and normal summer monsoons and corresponded to 11 years of late or normal onset of the SCS summer monsoon. Among the 38 years in the Yangtze and Huaihe River basins, there were 11 drought years that fully occurred in the case of strong (6 years) or normal summer monsoons in east Asia and corresponded to 8 years of late (5 years) or normal onset.

In the 10 years with a strong summer monsoon in east Asia, there were 9 years of normal or floods in the Yellow River basin and north China, whereas these 10 years fully corresponded to normal or drought (6 years) years in the Yangtze and Huaihe River basins. In the 10 years with a weak summer monsoon, there were 9 years of normal or drought (6 years) years, whereas these 10 years fully corresponded to flooding years. Out of the 19 years with la ate onset of the SCS summer monsoon, there were 15 years for normal or drought (9 years) years in the Yellow River basin and north China, whereas there were 14 years for normal or flooding (10 years) years. From the above discussions, it can be concluded that droughts in the Yellow River basin and north China are prone to occur during the period of weak east Asian summer monsoon and early onset of the SCS summer monsoon.

The opposite case is true for floods. The floods in the Yangtze and Huaihe River basins are prone to occur during the period of the east Asian summer monsoon and late onset of the SCS summer monsoon. The droughts in this region often occur in years of strong east Asian summer monsoon.

Recently, based on an analysis of the relationship of intensity of the SCS summer monsoon with droughts and floods in China using the National Centers for Environmental Prediction (NCEP) data sets for 1951–1998, Wu *et al*. (2003) have further pointed out that in years with strong (weak) SCS summer monsoon the summer major seasonal rain belt is located in north (south) China, while summer (June and July) in the middle and lower valleys of the Yangtze River suffers from droughts (floods or pluvial) whilst the Guangdong province in south China is dominated by floods (normal and droughts) in July–September. This relationship implies that the intensity of the SCS summer monsoon has a negative correlation with precipitation in the middle and lower valleys of the Yangtze and Huaihe River basins in summer and a positive correlation with the postrainy season in the region of the Yangtze River valley and south China.

Floods

Figure 4.20 (color section) shows the geographical distribution of severe floods in China since 1931 (Shi, 2003). During the 20th century, China suffered major flood disasters in 1931, 1935, 1954, 1958, 1963, 1975, 1991, 1998, 1999, and 2003. It can be seen that the following five regions are prone to flooding: (1) southern China (an average of 1–2 times every 3 years), especially the coastal area of Guangdong province and the northern part of Guangxi province; (2) especially, the northern

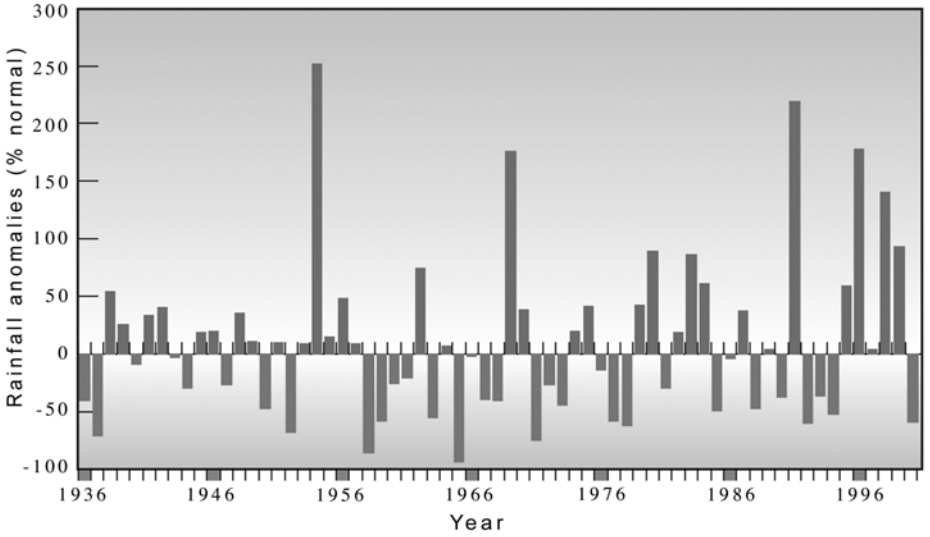

Figure 4.21. Interannual fluctuation in Meiyu rainfall along the Yangtze River basin. From WMO (2003).

part of Hunan and Jiangxi provinces (once every 2–3 years); (3) the middle and lower valleys of the Yangtze River and coastal area of eastern China (once every 2–3 years); (4) the Huaihe River valley (once every 2–3 years), the Yellow River and the Haihe River valleys (once every 3 years); and (5) the Songhuajiang and Liaohe valleys in the eastern part of north-east China. The general feature of the geographical distribution of floods for the whole of China is characterized by frequent floods in the eastern part of China, especially in the coastal areas, and the rare occurrence in the western part of China, especially in Tibetan Plateau regions. The above distribution is fully consistent with the seasonal march of the east Asian summer monsoon (Ding, 1994) and the geographical distribution of heavy rainfall (Tao and Ding, 1981).

A number of investigators have studied defficits or excesses in precipitation during the Meiyu or Baiu seasons over the middle and lower Yangtze River valley, Japan, and the Korean Peninsula and their association with droughts and floods in these regions (Ninomiya and Murakami, 1987; Ding, 1993; Oh *et al.*, 1997; Ninomiya and Kobayashi, 1999; WMO, 2003). Most of the prolonged and excessively heavy rainfall events occurred during the Meiyu and Baiu seasons. The reasons behind these events is a greater variability of interannual and intraseasonal precipitation, concentrating duration and coverage of rainfall, and a rising trend of rainfall in recent decades. Figure 4.21 shows a very significant interannual fluctuation in Meiyu rainfall along the Yangtze River (WMO, 2003). Exceptionally wet years such as 1954, 1991, and 1998 may be clearly noted. In such years, the prolonged (one or two months long) and excessive precipitation mainly led to major floods. In the history of floods in China for the most recent 100 years, the 1954 event was the

most severe flooding over the Yangtze River valley which was caused by long, persistent heavy rainfalls (June and July) in the Meiyu season, nearly one month longer than normal (Chen, 1957). During June and July 1954, not only did the rain pour down almost unceasingly over the Yangtze and Huaihe regions, but also departures from the normal rainfall as high as +300 to +600% were recorded in the middle and lower Yangtze River valley. The flooding event occurred under special large-scale circulation conditions (Ding, 1994). As pointed out by Ding and Reiter (1982), in east Asia, two significant features can be noted, one being a large negative anomaly zone stretching from central Asia to western North America, and another consisting of positive anomaly areas over the Seas of Japan and Okhotsk and over central Siberia. This anomaly pattern suggests that low-pressure disturbances were unusually active in the middle latitudes over east Asia and the Pacific Ocean. On the other hand, high-pressure ridges, or blocking highs, prevailed in higher latitudes. Such blocking situations characterize the Meiyu, together with the frequent passage of short-wave troughs and westward extensions of the subtropical high over the coastal regions south of the Yangtze River, indicated by a positive anomaly over the western Pacific north of the Philippines.

The blocking situation in high latitudes has two effects on flooding events in east Asia. It maintains the stability of large-scale circulation features over east Asia through an anchoring effect, and it forces the westerlies to flow into more southerly latitudes, thus bringing the frequent passage of short-wave troughs to the middle latitudes. A succession of such waves, coming from central Asia and moving across north-western China may advance into shear lines and vortices (low-pressure disturbances) which accompany the Meiyu front. Analyses demonstrated that about eight or nine low-pressure disturbances, mostly originating in the Plateau region and passing over the Yangtze River valley with steering troughs, were the primary cause of almost uninterrupted rainfall (Tao and Ding, 1981). Furthermore, a southward displacement of the westerlies also enables the vortices generated over the Tibetan Plateau to be steered out of that region and to grow into major rain-producing systems over the Yangtze River.

The flooding event in 1998 in the Yangtze River valley was the worst since 1954 when 30,000 people died and the rail network between Beijing and Guangzhou was paralysed for 100 days. In 1998 more than 4,000 people died, over a quarter of China's 1.2 billion people were affected by the flood waters, and more than 25 million hectares were inundated. As revealed by many recent studies (NCC, 1998; Sun and Zhao, 2003; Zhang *et al.*, 2003), this flooding event occurred under the dual-blocking situation in mid and high latitudes, continuous eastward propagation of several low-pressure disturbances, the westward extended subtropical high over the western North Pacific, and active low-frequency oscillation (mainly 20–30-day period).

Droughts

Drought is a kind of severe weather and climate disaster or extreme event that may persistently affect extensive areas of east Asia. Although droughts occur over various

regions of China, the Korean Peninsula, and Japan, the regions most vulnerable to droughts are the Huaihe, the Yellow River, and the Haihe River valleys (including most of north China). Droughts in the Korean Peninsula and Japan are mainly associated with failure or great deficit of Changma or Baiu due to their large precipitation variability. In China, drought issues are of great concern (Shi, 2003). In particular, since the 1980s prolonged droughts in north China have severely affected and threatened the agricultural growth, water supply, and river transportation. Therefore, our focus will be placed on the discussion of droughts in north China.

Almost every year, droughts occur which affect different areas in north China with varying degrees of severity. The following years may be classified as relatively severe: 1955, 1957, 1960, 1962, 1965, 1972, 1978, 1980, 1983, 1986, 1987, 1989, 1991, 1993, 1997, 1999, 2000, and 2001. As a matter of fact, relatively severe drought may occur about once every three years and an extensive severe drought once every 10 years. In north China, the frequency of occurrence of droughts is very high. As the consequences of decadal and interdecadal variability in large-scale circulation conditions and climate change, droughts in north China have shown an increasing trend since the late 1970s, which is believed to be the result of an abrupt change in climate regime, possible due to the effect of the PDO (Pacific decadal oscillation) and ENSO variability (Trenberth and Hurrelle, 1994; Wang, 1995; Li and Xian, 2003; Zhou and Huang, 2003). In the 1980s, droughts occurred very frequently – in succession for four years (1980–1983). During 1980, 1983, and 1986, droughts affected widespread regions with considerable impact (Zhang *et al.*, 2003). During this period, the annual mean precipitation amount decreased by one-third compared with that in the 1950s. Starting from the mid-1990s, droughts in north China have become more severe. In the summers of 1997–2002, the rainfall amounts decreased by 20–30% compared with normal or even 40–70% for 2001. This drought year is believed to be worst year since 1949.

Precipitation in north China mainly occurs in the summer season, accounting for almost 65–75% of the annual precipitation total. In other regions, for instance, Shanghai and Guangzhou, it only accounts for 37.3% and 43.3%, respectively, which is much lower than the percentage for north China. A high percentage of summer precipitation is associated with the active summer monsoon that may bring a large amount of moisture to the north China region. The interannual variability of annual precipitation in north China is very significant, ranging from 20–30%, and even greater than 30% for some areas. The greatest interannual variability represents the unstable or highly variable precipitation, thus a high potential possibility of the occurrence of droughts and floods (Bi, 1990). In general, if the interannual variability of precipitation exceeds 25%, agricultural crops would be affected by droughts or floods (SSTC, 1990). The droughts in north China are characterized by the following remarkable features (Ding, 1994). (1) *Prolonged duration or long persistence*. Severe droughts in north China generally occur in summer, some of which are often persistent in spring and summer or summer and autumn, or even over three seasons (spring, summer, and autumn). In 1957, 1965, 1968, 1972, and 1986, droughts lasted for between 5 and 7 months. (2) *Extensive affected areas*. For

example, in 1965, drought most severely affected about 8 provinces. Most droughts may affect considerable parts of north China, and sometimes even most of it. During the past 51 years (1950–2000) drought areas in the main agricultional regions over north China have increased (Wang *et al*., 2003). (3) *Great severity and degree of impact*. In general, the precipitation amount of severe droughts is 50–70% less than normal, even 70–80% (for instance, 1968 and 2001). 1980 was a year of severe drought. In Beijing only 35 mm of precipitation was recorded during the 40 days from the middle part of July to the last part of August, almost accounting for one-tenth of the normal precipitation amount for the same period. In 1983, only 27 mm of rainfall for July was recorded, 90% less than normal. This extreme minimum monthly rainfall amount was the lowest since 1870. (4) *The simultaneous occurrence of high temperatures, accompanying droughts*. For instance, in 1965 the mean air temperature for May–October was 1–2°C higher than normal, with the number of days of high temperatures (>35°C) being 10–35 days, 5–18 days more than normal. During the period of May–July 1971, the number of days of high temperatures for the eastern part of north China was 5–10 days, 5–10 days greater than normal, with temperatures higher than 40°C being observed a number of times. In the 1999 summer, the air temperature in the region of the Yellow River was 1–2°C higher than normal and in the 2001 summer, even 2–4°C higher. Owing to the concurrent occurrence of drought and high temperatures, evaporation is greatly augmented, so that the drought could be further enhanced or aggravated.

The cause of droughts in north China has been studied from a different perspective. As for the regional condition, three types of circulation pattern are identified that may be favorable for the occurrence of droughts in north China: (1) the subtropical continental warm high dominating the region from the Great Bend of the Yellow River to north China; (2) the westward extending subtropical high ridge over the middle and lower reaches of the Yangtze River; and (3) the north-west airflow pattern which places north China in the gap between the northern and southern frontal zones. However, drought over north China is not a regional event, but is closely linked to an anomalous general circulation in the Eurasian continent or even in the northern hemisphere. Studies have indicated that the occurrence of historically significant droughts in the USA is usually consistent with that of droughts in north China. For instance, in the 1930s, these two countries both underwent prolonged 10-year severe droughts. Also, in 1980, 1983, and 1988, the Great Plains of the USA and north China or the Yangtze River basin both had significant droughts. The year 2000 drought also had a global climate background. In addition, droughts in north China are closely correlated with the monsoon precipitation in India. Both have an almost similar trend of spatial distribution. Out of 11 drought years for the Indian region, as defined by Mooley and Parthasarathy (1984), 8 cases corresponded to droughts in north China; out of 9 flooding years for the Indian region, 5 cases corresponded to wet years. Thus, there has been an almost stable positive correlative relationship between the Indian summer precipitation and the precipitation amount in northern China. Recently, Wei *et al*. (2004) pointed out that for the 1999 and 2000 summer severe droughts in north China, there existed the stationary wave train of the EU mode that may have produced a teleconnection effect on maintenance of a deep

warm high in north China, through the intensified Rossby wave. At the same time, the feedback effect of the soil moisture from the dry surface during the drought period is also important for the development of droughts.

The second cause of occurrence of droughts in north China is the effect of ENSO events. During the onset year of the El Niño, rain pattern type II was often observed (i.e., the major seasonal rain belt is located in the area between the Yellow River and the Yangtze River which implies that North China is vulnerable to occurrence of droughts in El Niño events (Zhao *et al.*, 1989)). Liang (1990), and Liu and Ding (1995) studied the relationship between El Niño and summer rainfall in northern China. The results have shown that when the SST over the equatorial Pacific region is warmer (the onset year of El Niño), the rainfall during June–September, over the vast area of north China, is less than normal, and if the SST over the equatorial eastern Pacific region becomes colder in the following year (the following year of El Niño), the summer rainfall is greater than normal over an extensive area of north China. This result is more or less consistent with that found by NCC (1998).

The third cause for occurrence of droughts in north China is likely to be associated with global warming (IPCC, 2001). Under this condition, the hydrological cycle is possibly enhanced, thus leading to an increase in the occurrence frequency of droughts and floods. As climate extreme events, however, there have been no sufficient evidence to support this association at present. For example, in the 1998 summer when the severe flood occurred in China, an unusual global climate was observed. But the cause for this anomalous climate is not yet clear. Further evidence is needed to support the claim that this unusual climate is associated with a CO_2 induced greenhouse effect.

4.5 COLD WAVES AND COLD SURGES

Figure 4.22 shows the mean pressure and surface winds for January over south Asia. The circulation in the winter or cool season, which is sometimes less accurately termed for south Asia as the north-east monsoon, is controlled near the surface by the continental high-pressure belt over central Asia (a south-western extension of the Siberian High near 45°N,105°E) with its north-west/south-east oriented ridge passing from north Pakistan toward the south of the Gangetic plains. South of the high (ridge) pressure falls gradually into the equatorial trough zone. The ITCZ is located in the near-equatorial region of the south Indian Ocean along 8°–10°S, but due to the warm waters of the near-equatorial north Indian Ocean, a secondary convergence zone lies near 3°–5°N from the south Andaman Sea to the south-east Arabian Sea (65°–100°E). A minor cloud band with isolated organized cloud clusters appears off and on (about 10–12 days in the season) in this secondary convergence zone. The cloud clusters in the NHET, while moving westward, bring isolated rainfall over the east coast of Sri Lanka, extreme southern peninsular of India, and the Maldives. Very occasionally, even a tropical cyclone may form in the southern Bay of Bengal as happened during 4–6 February 1999. The season of 1999 was unusually wet as the NHET was quite active and cloud cluster scale

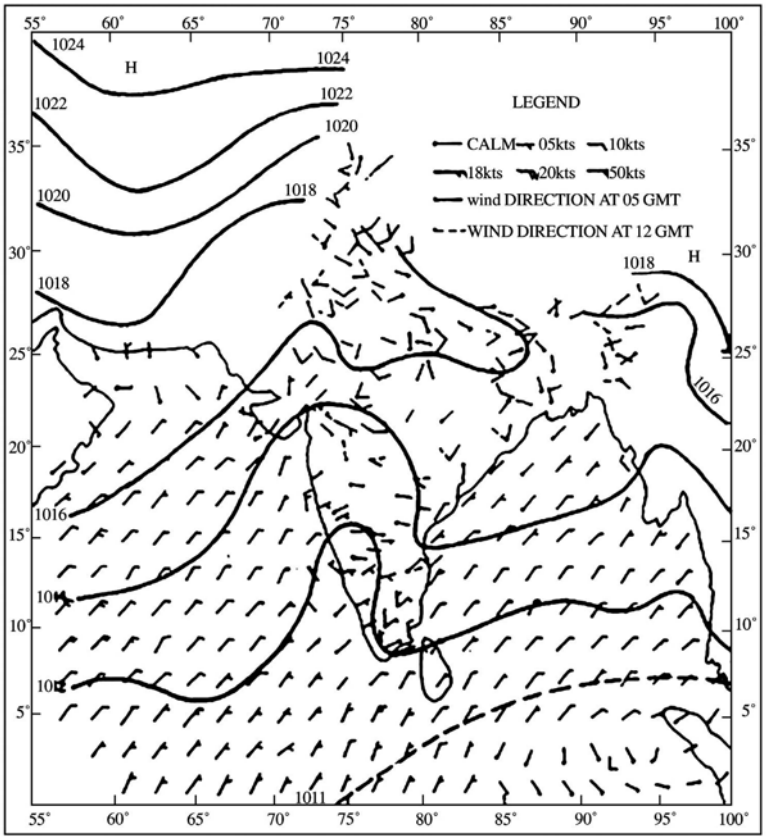

Figure 4.22. The mean sea level pressure (hPa) and surface winds over south Asia for January – typical of the winter season.

disturbances, associated with cyclonic eddies, emanating from the western Malaysian area, passed across the southern Bay of Bengal toward the Maldives (Verver *et al.*, 2001). The air flow over the region near the surface is generally light and becomes north-easterly south of 25°N. The subtropical ridge shifts southward with height. It is situated along 22°–25°N at 850 hPa and by the 200-hPa level it is shifted near 5°–8°N. Thus, subtropical westerly flow dominates over most of south Asia during winter in the middle to upper troposphere. The subtropical ridge in the northern parts of Pakistan and nearby Indian region is occasionally bifurcated by the passage of winter disturbances known as western disturbances. Western disturbances are the dominant transient systems over northern parts of south Asia in winter. They have long been regarded to originate in the Mediterranean Sea and the Caspian Sea areas and are secondary disturbances of the extratropical storm systems whose primary systems, with well-defined frontal characteristics, move in a north-easterly direction. The secondary disturbances (western disturbances) which are more important for

northern parts of south Asia, do not have any frontal characteristics and at best are occluded systems. They are linked with the troughs in the mid-latitude westerlies passing along 65°–70°E (Pisharoty and Desai 1956; Mooley, 1957). The accelerating southern branch of the upper tropospheric STJ passes along the southern rim of the Himalayas across the Gangetic plains region (75°–90°E and 25°–30°N) toward Bangladesh, finally merging with the northern branch of the STJ over southern China. The STJ in winter and premonsoon seasons fluctuates by 5–10° latitudinally with significant impact on the weather of the northern parts of south Asia, particularly in premonsoon and postmonsoon seasons (Koteswaram and Parthasarthy, 1954). The peculiar combination of large-scale features and orography induce weak cyclonic circulations, at times of depression intensity, over Pakistan and in turn induce low-pressure areas over western India. Moisture incursion takes place both from the Arabian Sea and the Bay of Bengal and upward ascent of moist air is favored by upper tropospheric divergence ahead of the westerly trough in the middle and upper troposphere. Precipitation is in the form of snowfall in the Himalayan belt of Pakistan and north-west India and rainfall in the submountain and the adjoining plains. Precipitation sometimes moves from west to east across the entire Gangetic plains along the Bihar state of India into Bangladesh. Though the contribution of the winter precipitation to the annual precipitation of south Asia is small, it is very significant for its northern parts as the snowfall feeds the perennial rivers of the Indus and upper Ganges basins in the premonsoon season. The rainfall is also agriculturally important for the winter crops in the region. Thus, western disturbances in the north and easterly waves in the form of cloud cluster scale cyclonic circulations in the NHET are the dominant transient disturbances responsible for the subregional weather. The weather during winter is mostly cool, dry, and pleasant over south Pakistan, northern and central India, and the south peninsular of India, Bangladesh, and central and southern parts of Nepal. It is occasionally disturbed by passing western disturbances which are associated with cloudiness and rainfall, followed by cold waves and fog conditions. The weather over Sri Lanka and the Maldives is also fine and only on very few occasions cloud cluster scale disturbances or easterly waves bring passing showers.

After the passage of a western disturbance over Pakistan and north-west India comes the cold winds from north to northwest. The left over moisture of a western disturbance, cold temperatures, and clear skies results in the incidence of fog along the Indo-Pakistan plains. For such fog incidences, their durations and horizontal extents appeared to have greatly increased in the last two decades over the area in winter. In some winters, the fog episodes are much prolonged (10–20 days at a stretch) and cover a distance of near 2,000 km across the plains from Pakistan up to the west Bengal state of India and at times even up to Bangladesh, as happened in January–February 1997, 1999, 2002, and 2003. The prolonged and extensive fog events have become a major disturbing factor for the smooth functioning of aviation during winter over the Indo-Pakistan region.

Cold waves are caused by the passage of western disturbances in winter (Raisircar and Datar, 1963). In the rear of a disturbance, cold air is advected over northern Pakistan and India which then spreads eastward and southward as the air

from the Himalayan region drains toward the plains. Surface temperatures fall abruptly and under clear skies minimum temperatures drop by 4–8°C below normal. Day temperatures also become reduced to 10–12°C in the northern parts of the plains, partly aggravated by persistent fog. A cold wave, which originates in the northern hills takes 1–2 days to reach the northern plains and 2–4 days to reach central and eastern India and occasionally even extends up to 15°N over south the peninsular of India within 4–6 days. Cold waves, which generally persist for 3–5 days, are responsible for a significant number of deaths due to extremely cold weather conditions during their sway in Pakistan, northern and central India, and along the Gangetic plains (particularly in the Uttar Pradesh and Bihar states of India). According to the statistics provided by De and Sinha Ray (2000), cold waves over India for the period 1978–1999 affected 18 Indian states in central and eastern India (over 70% of the geographical area of India). Their influence begins in December, peaks in January, and tapers off by March. January accounts for nearly 50% of the total cold waves which occur during the four months from December–March. Maximum numbers of deaths are caused in the two states of Bihar and Uttar Pradesh, which are situated in the central Gangetic plains just south of the Himalayan foothills. Cold waves seem to stagnate in this belt as the drainage of air is slowed down. Cold waves of India are somewhat different to the cold surges over China and adjoining regions, though their origin is due to similar meteorological situations (i.e., under the influence of cold air advection in the rear of an eastward moving extratropical disturbance and the intensification of the high pressure in the rear of the disturbance). Unlike over China, the air draining over the northern Indo-Pakistan belt, is of subtropical/mid-latitude origin and not of polar origin. Besides, the Himalayan massif on the western and central parts of the Indo-Pakistan region acts as a barrier to the full invasion of cold air. However, under the influence of an exceptionally active western disturbance, low-level air flow drains rather rapidly from Iran and its adjoining regions through the low hills of the Baluchistan province of Pakistan and the Siwalik hills of Indo-Pakistan. It also invades the northern Arabian Sea which results in a strengthening of the northerly air over the north Arabian Sea, adjoining Pakistan and western India. The pulsations of north-east winds over most of the Arabian Sea are caused in the rear of western disturbances and have similar characteristics as the cold surges in the China seas, though of less intensity.

Though the period of October to December is generally dry over major parts of South Asia, very significant amounts of rainfall are received over the south peninsular of India and Sri Lanka, especially along their eastern coasts as well as over the Maldives. In India, these rains are popularly known as the north-east monsoon and in Sri Lanka as the second intermonsoon. However, by the end of December, when the north-east monsoon blows with its full strength and has complete sway over the the northern Indian Ocean, the rainy season has practically ended. North-east monsoon rains contribute nearly 50% to the annual rains over the state of Tamil Nadu in India and over the coastal districts of the state. These rains even contribute to nearly 65% of the annual rain. So is the case for the east coast of Sri Lanka. The core region of the north-east monsoon rainfall over India consists of five

meteorological subdivisions, viz. coastal Andhra Pradesh, Rayalseema, the south interior of Karnataka, Kerala, and Tamil Nadu. The long-term weighted mean (1875–1997) rainfall for the postmonsoon season over this region is 34.9 cm with a standard deviation of 9.3 cm (coefficient of variation 27%). Range of the rainfall for the period is 45.1 cm with the highest rainfall recorded in the season being 55.2 cm and the lowest 10.1 cm observed in the years 1993 and 1876, respectively (Khole and De, 2003). North-east monsoon rains over this region have been investigated by Rao (1963), IMD (1973), Raj (1992, 2003), and others. Like the onset of the south-west monsoon over Kerala, there is also an abrupt rise in the mean daily rainfall on the date of onset of the north-east monsoon, based on superposed epocal analysis. It rises from about 2 mm to over 20 mm on the date of onset and then steadily declines in the subsequent 60–70 days. Thus, the bulk of the north-east monsoon rains over Tamil Nadu are given in a 50-day period from the onset of the rains (Raj, 1992, 2003). According to these studies the normal date of onset of the north-east monsoon rains over Tamil Nadu is 20 October with a standard deviation of 7–8 days and the earliest and latest onset have been recorded as 5 October in 1943 and 11 November in 1915, respectively. The normal duration of this rainy period is 67 days. The duration of rains show significant interannual variability with a range of 26–102 days. The total quantum of rainfall during the season also shows large interannual variability. The onset is by and large associated with a westward migratory low-pressure system from the central Bay of Bengal, which brings the first surge of north-east winds spreading from Bangladesh to Orissa and the Andhra coasts. In nearly 70% of the years the 30–40-day oscillation passing across Sri Lanka and the south Bay of Bengal excites the onset of this rainy season too as the rainfall anomalies move from south to north. The first rainy spell lasts for about 4–5 days which is followed by intervening dry and wet spells. Each rainy spell lasts for 3–4 days and occurs in association with the arrival of a migratory low-pressure system or a tropical cyclone from the Bay of Bengal. A dry spell in some years may become quite long (8–10 days at a stretch) and is broken by the arrival of an intense low-pressure system from the Bay. Intraseasonal variability of the rainfall is therefore quite marked, which is brought about by synoptic-scale disturbances.

The second intermonsoon season (October–November) rainfall for Sri Lanka has not been so extensively studied as the north-east monsoon rainy season for Tamil Nadu in India. However, good background materials are available in Suppiah and Yoshino (1984) and Suppiah (1988, 1989). It is also shown in some studies that the rainfall over Sri Lanka and Tamil Nadu in October to December is higher than normal in the years of El Niño warming, though exceptions do exist (Jayanthi and Govindachari, 1999; Khole and De, 2003).

The prevailing weather process in winter in east Asia are outbreaks of cold air which, among the most significant weather events of winter over the northern hemisphere, are marked by invasion of extremely dry and cold air over Mongolia. The associated weather includes high winds, an abrupt temperature drop, severe frost, freezing rain, heavy snowfall, and even sandstorms. The severity of this weather greatly depends upon the coldness of the air masses, pattern of synoptic systems and circulation, and the regional or local terrain features (Ding, 1994). Outbreaks of

cold air or cold waves are closely related to the activity of the east Asian winter monsoon which is the most active weather and circulation system in winter in the northern hemisphere. The winter monsoon blows out of the huge Siberian High, sweeps away the east Asian continental region, and then turns into the cold surge at lower latitudes. After crossing the equator at the longitudinal range of Singapore and Indonesia, it can further flow into the southern hemisphere to enhance the ITCZ there in summer. Therefore, the east Asian winter monsoon is a key component of the Asian–Australian monsoon system which reflects the significant interhemispheric interaction in this monsoon system. On the other hand, the east Asian winter monsoon is also a part of the winter local Hadley circulation in east Asia and western North Pacific, which is characterized by extensive downward motion (Cressman, 1981) at the left sector of the entrance region of the upper level jet steam located to the south of Japan. The winter monsoon in east Asia generally builds up between November and December and withdraws in the period from April to May. As pointed out previously, the establishment and retreat processes are rather abrupt. During the winter monsoon period, one may observe active–break cycles modulated mainly by the 10–20-day low-frequency oscillation (Ding and Krishnamurti, 1987; Ding, 1990). The active phase of the winter monsoon in general corresponds to the episode of outbreaks of cold air or cold waves. The activity of the winter monsoon may be divided in three stages in view of its evolutive process: onset, southward propagation, and interaction between low and mid-latitudes. Some investigators define the winter monsoon as affecting the mid and high-latitude regions as cold waves, with the winter monsoon invading into low latitudes as cold surges.

The east Asian winter monsoon assumes significant change and variability over different timescales that are of great concern for a number of investigators. Quasi-biennial oscillation of the intensity of the winter monsoon in east Asia is noted by Guo (1994) and Xu *et al.* (1999). More importantly, the interdecadal variability of the winter monsoon has been documented by several authors (Shi, 1996; Xu *et al.*, 1999; Yan *et al.*, 2003). They have found that since the mid-1980s the east Asian winter monsoon has shown a significant weakening in response to weakening of the intensity and eastward shift, by 4 longitudes, of the major trough anchoring off the east Asian coastal region in winter (Zeng *et al.*, 2002). From the 1950s to 1970s, the east Asian monsoon was relatively strong, especially in the 1960s and 1970s. It is believed the weakening of the east Asian winter monsoon is likely to be associated with global warming which is most significant in mid and high latitudes in the Eurasian winter. For the period of 1951–1999, the warming rate in winter (December, January, and February) in China was 0.30–0.35°C $(10a)^{-1}$, much higher than the annual mean temperature increase rate (0.06–0.07°C $(10a)^{-1}$). The long-term variations of wintertime mean temperature and precipitation in China for the most recent 50 years (1951–2000), which are derived based on 726 surface stations, have been studied (Wang *et al.*, 2004; Wang and Ding, 2004). It can be seen that the winter mean temperature has started to rapidly increase since the mid-1980s after which it maintained a continuous positive anomaly up to 2000, thus producing 17 consecutive significant warming winters in China. Warming regionality is quite obvious, with north China, north-east China, north-west China, and the

Tibetan Plateau being most significant. The long-term variation of precipitation shows a general, slight increase in most of north-west China, the Tibetan Plateau, and south-west China (Wang, 1997; Shi, 2003; Wang and Ding, 2004). It is very interesting to note that the surface wind speed has decreased significantly since the late 1970s, which is consistent with the global winter rapid warming (IPCC, 2001). Since the mid-1980s, the decrease in surface wind speed is even more obvious, which is consistent with the change in winter mean temperature.

In China, the severity of cold waves is generally classified into four grades: (1) nationwide outbreak of cold air, (2) regional outbreak of cold air, (3) severely cold air, and (4) cold air of moderate intensity (Ding, 1994). Based on the statistics of the cold air for 1951–1975 (Pan *et al.*, 1985), during each winter about 20 cold air outbreaks of different intensities affect different regions of China. On average, there are 6.3 nationwide and regional outbreaks of cold air, 4.2 severely cold air, and 8.8 cold air of moderate intensity. Of these, about three to five sweep across most of China, and bring falls in temperature of the order of 10–20°C within a 24-hour period, which are associated with strong surface winds of 15–20 ms^{-1}. Frequently, such outbreaks result in serious damage to agriculture, transportation, and other socioeconomic activities across China. However, corresponding to the long-term variation of the east Asian winter monsoon, the frequency and intensity of cold waves shows a decreasing trend. In the 1950s, cold waves were very frequent, with an averaged frequency of 5.4 nationwide outbreaks of cold air. In the 1960s there was a slight decrease in frequency. In the 1970s and 1980s, a significant decrease was observed, with the mean frequency being less than four events (Liu, 1990; Bei *et al.*, 1993; Lin and Wu, 1998; Wang and Zhou, 2000; Ding and Wang, 2001). An explanation behind this decrease in frequency of cold waves is the concurrent decrease in the east Asian winter monsoon in east Asia which is closely related to global warming as pointed out above.

Guo (1994) further pointed out that the intensity of the Siberian High associated with the winter monsoon can play a critical role in affecting the winter temperature variation in China, although the extent of southward invasion is also important. Since the 1980s, the cold high associated with the winter monsoon has decreased in intensity, but the extent of southward invasion of the winter monsoon has been enhanced. Thus, this interdecadal change may be used to explain the significant warming in north China, and slight warming or even cooling in south China.

The characteristics of cold air outbreaks are closely associated with the formation, intensification, southward excursion, transformation, and dissipation of the Siberian High (Ding and Krishnamurti, 1987). On average, a cold high passage occurs over east Asia approximately once every 4 days. The intensity of the Siberian High may reflect, to a great extent, the severity of the cold air. Based on the previous statistics of the central sea level pressure of the Siberian High for 1958–1979 (Pan *et al.*, 1985), the high has its maximum intensity in January with a mean sea level pressure (SLP) of 1,051 hPa, followed by December and February which have a mean maximum SLP of 1,051 hPa and 1,049 hPa, respectively. The highs with maximum SLP exceeding 1,080 hPa alone occur in December through February, with an extreme maximum SLP of 1,082 hPa observed in December. The number

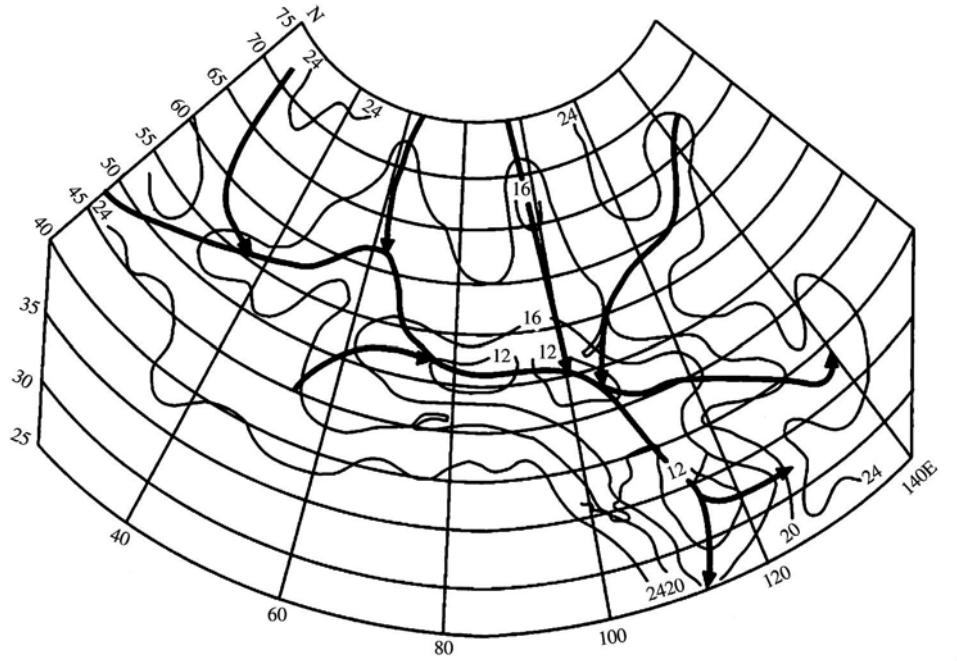

Figure 4.23. Major tracks of Siberian Highs related to outbreaks of cold air. Isopleths drawn with relative frequency (%).
From Zhang and Chen (1999).

of days with maximum SLP greater than 1,050 hPa in January accounts for 51%, in December 45%, and in October and April about 3–4%. Most of the highs' centers (70%) were observed in the region of 45°–55°N, 90–105°E. There is a close relationship between the intensity of the Siberian High and the severity of the cold air. As a rule, when the Siberian High builds up to a considerable intensity, one may anticipate an outbreak of cold air. The physical mechanism of development of the Siberian High has been studied from two perspectives: large-scale circulation adjustment (Chou, 1985) and regional conditions (Ding and Krishnamurti, 1987; Curry, 1987; Xie *et al*., 1992; Ding *et al*., 1994). For the regional mechanism, the radiative cooling produced by long-wave radiation can induce downward motion in a deep layer in the troposphere, thus leading to mass convergence at middle and upper levels and to mass divergence at low levels, and intensification of the Siberian High. This theoretical explanation is consistent with the fact that the tropospheric atmosphere where Siberian Highs are located is a deep cooling layer (heat sink). However, Xie *et al*. (1992) argued that the cooling effect is produced by adiabatic upward motion.

The tracks of the Siberian High have been studied by numerous investigators (Tao, 1955; Pan *et al*., 1985; Ding and Krishnamurti, 1987; Zhang and Chen, 1999) and they have obtained quite similar results (Figure 4.23). The early tracks of cold highs fall into five types. (1) *The north-east track*. The highs move from eastern Siberia south-westward to the region to the east of Lake Baikal and Mongolia

(the high of this track seldom occurs). (2) *The north track*. The highs originate in the Tymer Peninsula and move south-eastward down to the western part of Mongolia. (3) *The north-west track (I)*. The highs come from the Kara Sea and move south-eastwards down to the western part of Mongolia. (4) *The north-west track (II)*. The highs have their origin in northern Europe, then traverse the northern Ural region, arrive at the Siberian region, and finally merge with track (3). (5) *The west track*. The highs come from southern Europe, then move eastward and traverse the Xinjiang province of China or the western part of Mongolia. Out of the above five tracks, the latter three tracks are most frequently observed.

The Siberian High which intrudes into China has two tracks: (1) the major one extends south-eastward from the source region to west of Lake Baikal, passing the middle Yellow River valley, northern China, and the lower Yangtze River valley, and eventually extends toward the sea region to the south of Japan or down to southern China; and (2) the second track extends eastwards from Mongolia, crossing north-eastern China and moving over the Sea of Japan (Figure 4.23). Based on an examination of monthly distributions of anticyclone frequencies over east Asia and the western Pacific for the period 1957–1961, and using a $5^\circ \times 5^\circ$ latitude longitude grid, Boyle and Chen (1987) obtained a similar result. The major track of anticyclones in November extends from Mongolia to the south-west of Lake Baikal, passing south-eastward of the lower Yellow River valley, and then eastward through the Yellow Sea, southern Korea, and northern Honshu. The major track shifts southward as the winter progresses until it reaches the southern-most latitudes in February, when the anticyclones mainly pass through the low Yangtze River valley and then toward the south of Japan.

When the winter monsoon arrives in south China, the SCS and the tropical western North Pacific, it can further intensify and usually becomes the prevailing north-easterly winds at low levels. These stronger low-level northerly or north-easterly winds are so-called cold surges, and their intensity is defined by an activity index of the cold surge (Chang and Lau, 1980). In a direct sense, the term cold surge was used to describe the rapid drop in surface temperatures over south China and the freshening of the north-easterly wind over the SCS associated with the frequent wintertime outbreak of polar air mass off the coast of east and south-east Asia (Ramage, 1971). But, based on recent studies of the cold surge-related phenomena, it is customary to define a cold surge onset time by noting changes of one, or a combination, of the following indicators within a 24–48-hour period:

(1) A drop in surface temperature at Hong Kong of 5°C or more.
(2) An increase of the surface pressure gradient between coastal regions and central China of at least 5 hPa.
(3) A prevalent northerly surface flow over the SCS with a speed exceeding $5\,\mathrm{ms}^{-1}$.

In the literature, some variations of the above definition have been used. Ding (1990) has used the following criterion to define the cold surge: a northerly wind with a speed greater than $5\ \mathrm{ms}^{-1}$ in magnitude, persisting for two days. According to this definition, he studied the climatology of cold surges in east Asia and the western Pacific Ocean. The mean distribution of frequency of occurrence of northerly winds

greater than 5 ms^{-1} at 1,000 and 850 hPa clearly shows the climatological locations of the cold surge (figure not shown here). Near the surface (1,000 hPa), the maximum frequency of the cold surge (65%) occurs over the SCS. Another region of high frequency is located over the oceanic area to the east of the Philippines, but the frequency of the latter is only about half that of the former. Therefore, the strongest cold surges near the surface are observed over the SCS. This conclusion is consistent with that obtained by the study of cold surges for individual years. At 850 hPa, the frequency of occurrence of cold surges over the SCS significantly decreases, being one-half of the frequency near the surface, and the maximum of frequency shifts toward Malaysia and Indonesia. The cold surge activity over the western North Pacific almost disappears (frequency of 10%). Note that the cold surges over the SCS and the western North Pacific nearly disappear completely above 700 hPa (not shown). From the above discussion, the cold surge is a phenomenon in the shallow layer below 700 hPa. In short, it is both frequent and strongest near the surface. Both the intensity and frequency of the cold surges decrease rapidly with height, so that the phenomenon nearly vanishes at 700 hPa (Ding and Mong, 1994).

The statistics of frequency of occurrence of cold surges over the SCS in winter (November–March) for 1978–1985 (Chen and Huang, 1989) show that in winter, the frequency of occurrence of cold surges assumes a significant month-to-month variation. The maximum frequency was observed in December and January, with a mean value of 4.6 times. The secondary maxima were observed in November and January, with mean values of 4 and 4.3 times. After February, the frequency of occurrence of cold surges decreased to 3.1 times, mainly due to the weakening of cold air activity. On average, the high winds may remain for 4 days after bursts of cold surges.

During outbreaks of cold air, especially cold surges, the planetary-scale circulation over the Asian–Pacific region appears to undergo significant short-term changes on a timescale of a few days. Previously, Ramage (1971) suggested that the occurrence of a cold surge off the southern China coast is related to an intensification of the local Hadley circulation over east Asia. Later, Chang and Lau (1980) investigated the changes in the planetary-scale features, such as the Hadley-type or Walker-type circulations in relation to the cold surges during December 1964, with a special focus on the sequential changes of synoptic events associated with the cold surges. They showed that, in general, several mid-latitude and tropical circulation components vary in a coherent way during surge periods. Immediate consequence of a cold surge will intensify the local Hadley circulation in east Asia through the convection associated with pre-existing synoptic-scale disturbances in the equatorial SCS. The upper troposphere outflow from the SCS region also accelerates along the equator toward the central Pacific and the east coast of Africa, thereby strengthening the east and west Walker cells. For its detailed description see Chapter 3. Ding and Krishnamurti (1987) and Ding (1990) provided evidence to lend further support to the planetary-scale effects produced by cold surges. During the process of outbreak of cold air, a rapid eastward shift of the planetary circulation ensues with an eastward shift of the strongest divergent circulation center at 200 hPa, by about 60° longitude. This places the planetary-scale rising motions over the central

equatorial Pacific, resulting in a weakening of the normal Walker circulation. An enhancement of the convection and precipitation over the equatorial eastern Pacific is also noted.

Finally, we shall briefly discuss the issue of sandstorms in east Asia which have become an important environmental problem through the release and transport of large amounts of aerosols in the atmosphere. From the viewpoint of origin and transport of the sandstorm, it is closely related to the activity of the winter monsoon, especially clod waves that can be a triggering mechanism for sandstorms. Sandstorms occur mainly in spring and early summer, and have as their origins regions in the arid and semiarid areas in north and north-west of China such as Gansu, the central part of the Inner Mongolia provinces, and southern part of the Xingjian province. A very interesting piece of evidence is the interdecadal variability of occurrence frequency of sandstorms. In the 1950s through to the 1970s, the occurrence frequency of sandstorms was relatively high. But, since then, the occurrence frequency significantly decreased until 1996, which is fully consistent with the weakening of the east Asian winter monsoon, especially cold waves, and surface wind speed (Zhang *et al.*, 2004). The recent slight increase in frequency is believed to be the result of an extreme dry climate condition which developed in north China and the eastern part of north-west China. Due to a significant decrease of precipitation amounts, the soil layers have become quite dry and soft, thus providing another necessary prerequisite condition for the development of sandstorms (Tao *et al.*, 2003).

4.6 LOCAL SEVERE STORMS AND MESOSCALE CONVECTIVE COMPLEX EVENTS

In this section, only regional phenomena of local severe storms and mesoscale convective complex events will be illustrated. For a more general and detailed discussion of this area the reader is directed to Chapter 8.

The three months of March, April, and May represent the premonsoon season and constitute the period of transition from dry winter monsoon to wet summer monsoon over most of south Asia. The season is characterized by occasional thunderstorms which occur over different countries of the region under thermodynamical forcing while transient disturbances bring in low-level moisture from the adjacent Arabian Sea in the west and the Bay of Bengal in the east. Development of thunderstorms, which are particularly severe in the India–Pakistan–Bangladesh belt, break the monotony of hot weather on some days. Normally, strong subsidence and temperature inversions in the 700–800-hPa layer and dry winds inhibit convective activity. However, the movement of western disturbances along Indo-Pakistan belt bring occasional rains over submountain districts of the Indus–Gangetic plains and snow in the higher Himalayan ranges. Along the plains, due to intense heating and the dry environment, deep convection occurs occasionally with passing western disturbances which even take the form of hail storms. As the season advances dust storms or Andhis (Joseph *et al.*, 1980; Joseph, 1982) are generated with dark

rumbling clouds as the falling rain mostly evaporates. However, these duststorms, locally known as Andhis (occasionally having tornadic characteristics), bring great relief over Pakistan and north-west India as the accompanying downdrafts cool the environment by 8–10°C. The anvil clouds of these thunderstorms, with their downdrafts, occasionally provide the setting for an occurrence of line squalls. Climatologically, on average about 6 days both in May and June witness the duststorms in association with the passage of western disturbances over north-west India, the frequency being slightly higher in Pakistan. The thick dust raised by these storms extends occasionally up to 6–8 km and remains hanging for several days during May to mid-June over central Pakistan and the upper Gangetic plains. Strong pressure gradients in the rear of a western disturbance result in dust raising and dry winds over the Indo-Pakistan plains for days. The occasions of high dust raising winds over north-west India can vary between 8–25 in May as well as in June over the region. The thick dust layer is conspicuous up to 5 km high and allows less penetration of solar radiation during the daylight hours. It reduces outgoing infrared radiation at night, reducing diurnal temperature variation with a maximum temperature of over 42°C and minimum temperature of 32°C or higher.

Thunderstorms, mostly isolated, but sometimes widespread, occur over the west coast of Sri Lanka, the south peninsular of India, and central India and Nepal in April–May, if the upper level features such as the penetration of deep westerly trough up to 15°N over India are favorable. In-phase positioning of the waves in the mid-tropospheric tropical easterlies and subtropical westerlies over the peninsular of India are conspicuous in producing occasional widespread peninsular thunderstorms in April–May as low-level moisture is provided from the neighboring seas. The peaks of the thunderstorm activity over the south peninsular of India occur between mid-April to the end of April about 4–6 weeks prior to the onset of the monsoon. The trigger for the release of convective latent instability is provided by the daytime heating, orographic features, and sea breeze penetration. Over Sri Lanka and the Maldives, however, there is a prominent increase in rainfall which is due to the intensification of the NHET or location of the ITCZ and westward movement of cloud-cluster-scale disturbances, easterly waves, and low-pressure areas within it. Rain over Sri Lanka and the Maldives is usually accompanied by thunder and lightning. The rains during the period of March–April over Sri Lanka are also known as the first intermonsoon as the summertime ITCZ is in the process of being established.

Severe local thunderstorms known as 'norwesters' occur over eastern India and Bangladesh during the season. They are accompanied with high-speed squalls from the north-west and short-duration intense rainfall. Locally, these are known as 'Kal baisakhi' (Death in Baisakh) as they occur in the local calendar month of Baisakh (April–May) causing deaths in local communities. Norwesters are line squalls, similar to severe local storms of the midwest of USA, but less violent as they are only occasionally accompanied with tornados over the south Asian region, compared with the midwest of the USA. In local press reports, they are mistakenly described as 'cyclones'. They have been investigated substantially with the help of surface and upper air data as well as radar data and satellite photographs. The

earliest organised work was made by Sen (1931), Desai and Mal (1938), IMD (1944), Das *et al.* (1957), Raisircar (1957), and others. Subsequently, several papers have been written accounting for radar and satellite data (De, 1959; Mukherjee *et al.*, 1972; Srinivasan *et al.*, 1973; Kalsi and Bhatia, 1992; Sen Roy and Roy Bhowmik, 2003). Bhaskar Rao and Dekate (1967) examined the role of tropospheric vertical wind shear in the dynamics of these thunderstorms, while a good review about their dynamics was provided by Weston (1972). Norwesters occur over west Bengal, Orissa, and the north-east states of India and also prominently over Bangladesh. Four different types of norwesters have been classified depending upon their region of formation, time of occurrence, and direction of movement of convective cells (IMD, 1944). As both convective instability and latent instability are present almost every day over the region, its realization depends upon a synoptic-scale transient which is usually presented by the eastward passage of a remnant of a western disturbance from the west or the southward extension of a deep westerly trough across central Tibet. The synoptic-scale forcing organizes the west–east trough along the Gangetic plains with the moisture being supplied by the south-west or even south-east flow from the northern Bay of Bengal. The afternoon heating and the orographic features help to lift the low-level inversion and as this valve opens the full potential of the convective/latent instability is realized with deep moist convection sweeping either from the north-west to south-east direction (type A norwesters) or from the north-east to south-west direction over north-east India and Bangladesh (type B norwesters). Srivastava and Sinka Ray (1999), Chaudahuri and Chattopadhyay (2001), and Sen Roy and Roy Bhowmik (2003) have shown that an increase in convective available potential energy (CAPE) is less important compared with the reduction in the convective inhibition negative energy (CINE) in the thermodynamics of norwesters. The total quantum of rainfall accompanying these thunderstorms is not much (about 2–4 cm). As it occurs over a short spell its intensity is high. This is a disastrous weather phenomenon and every year hundreds of people lose their lives over the region of occurrence, particularly over Bangladesh due to boats having been capsized under the downdrafts of norwesters.

In the east Asian monsoon region, local severe storms and organized mesoscale convective systems are often observed during the premonsoon season (March–May) and sometimes during the summer monsoon season (June–September). These mesoscale convective systems may occur as isolated squall lines, hailstorms, thunderstorms, and tornadoes, but in many cases, they occur as important components embedded within convective rainstorms or persistent heavy rainfall events. The large-scale weather and circulation condition in east Asia is more favorable for occurrence of heavy rainfall, while those in North America are more favorable for the occurrence of local severe storms and mesoscale convective systems (MCSs). The warm and moist Asian monsoon under the influence of the large-scale terrain barrier of the Tibetan Plateau may flow northward in the east part of east Asia and juxtapose with cold air from mid-latitudes. The deep moist layer and concentrating (convergence) region of moisture can be established in this region due to an abundant moisture supply from the monsoonal airflow which is a necessary precondition for the occurrence of rainstorms. In contrast, in North America, 700–1,100

tonadoes are reported every year. Development of this kind of local severe storm is closely related to the topographic effect of the Rocky Mountains. The low-level warm and moist airflow coming from the Gulf of Mexico moves northward in the Great Plains to the east of the Rockies, capped by a warm and dry air layer aloft which is produced by adiabatic downward motion of the upper level westerlies going over the mountains. The strong potentially unstable situation with the existence of a warm and dry cap and temperature inversion is most favorable for outbreaks of severe local storms and MCSs.

In China, the physical conditions between heavy rain and local severe storms show significant differences (Ding *et al.*, 1980). In the case of severe storms, there is a temperature inversion or isothermal layer near the surface, whereas no inversion exists for the heavy rainfall events. Above 700 hPa, the temperature is much lower than in the case of heavy rain, with a difference of 8°C at 400 hPa. This is mainly caused by the existence of a strong upper level cold air advection along the northwesterlies behind the major troughs or cold vortices. Consequently, the lapse rate of temperature below 7 km for severe storms is 1–3°C km^{-1} greater than for heavy rain. The layer of potential instability for severe storms is deeper and the level of free convection is higher than that for heavy rains. This suggests that stronger triggering mechanisms are needed for severe storms, but once the outbreak of severe storms occurs, their development will be more vigorous and rapid than heavy rains. There are also significant differences in several physical quantities characteristic of moisture content and transport. For example, the horizontal convergence of moisture from the surface up to the 300-hPa level for heavy rains is three times as large as for severe storms. Heavy rains occur and develop under the condition of weak vertical shear, whereas severe storms develop under strong vertical shear. This large difference in vertical shear mainly results from the difference in the wind speed at upper levels. The severe storm often occurs below the axis of the upper level jet in contrast to heavy rains which occur in the region 200–500 km to the south of the jet's axis.

Based on the sounding data of 45 rainstorms in Beijing, Tian and Du (1983) have analyzed temperature, wind, and humidity conditions. It was found that during the rainstorms, the air is abnormally moist and unstable. For 850, 700, and 500 hPa, the departure of relative humidity all exceed 23%, while for 200 hPa, the departure exceeds 16%. The height of the condensational level is relatively low, so that it is very easy to reach the free convection level (FCL). For a rainstorm to occur, the warm air advection at lower and middle levels should be strong, whereas there is a cold air advection at the high level (above 400 hPa). At the same time, a considerable degree of vertical wind shear is needed. The Ri number becomes smaller during the rainstorms.

Some investigators have emphasized the importance of the so-called Ω-shaped energy systems for the occurrence of rainstorms and severe convective systems (Ma, 1980; Wu and Bei, 1982). During the 12–36 hours prior to the occurrence of rainstorms and severe convective weather, it is often observed that there is a kind of preexisting subsynoptic-scale Ω-shaped energy system (i.e., a region of high moist static energy with a region of low moist static energy at either side (to the east and the

west)). This system is mainly created by the deep layer of warm and moist upward airflow and the convergence of moisture, especially for rainstorms.

Hailstorms often occur in spring and early summer in China mainly in the following regions: the eastern part of the Tibetan Plateau and the western part of Sichuan province, the eastern and central parts of Gansu province, most of Yunan and Guizhou provinces (south-west China), the eastern part of Inner Mongolia and the northern part of north China, the eastern part of north-east China, and the middle and lower valleys of the Yangtze River. These regions, prone to occurrence of hailstorms, are mainly located in the eastern and northern peripheries of the Xizang (Tibetan)–Qinghai Plateau where topographic effects play an important role, or in regions where vigorous interaction between cold air from mid-latitudes and warm and moist air currents is usually accompanied by the development of cold fronts, extratropical cyclones, and wind shear lines. Many cases of hailstorms can be exemplified. A recent example is the hailstorm occurring on 14 May 2000 in the Hunan province. The extensive area of hail covered five counties, with a 30-mm maximum radius of hail and $26\,\mathrm{m\,s^{-1}}$ strong winds being recorded. A great deal of damage was suffered from this hailstorm. By using Doppler radar observations based on Changde, this hailstorm was found to be a convective complex consisting of 2 supercells and 1 squal line (Liao *et al.*, 2003). Tornado vortices were observed to be embedded within these supercells.

Mesoscale convective systems are a well organized, meso-α-scale (with horizontal scale of 200–2000 km) convective system which has a nearly elliptic shape and smooth edge. MCSs include the mesoscale convective complex (MCC) that has been extensively studied. Activities of the MCSs are quite frequent in China. They mainly occur in south-west China, but are often observed in connection with the major seasonal rain belts such as those during the presummer rainy season in south China, Meiyu in the Yangtze–Huaihe River basins, and the rainy period in north China. During the Baiu season in Japan MCSs are sometimes observed as an important intense rain-producing system (Ninomiya and Murakami, 1987). The preferred locations of occurrence of MCSs are the north-western periphery of the subtropical high over the western North Pacific where the warm and cold air have frequent and vigorous interactions. Sometimes, the MCSs also may be produced in east and south China due to a strong surface heating and a local unstable stratification.

The horizontal scale of the MCS over mainland China is usually similar to those observed in North America, but with ellipticity less than 0.7 and shorter durations of cold cloud tops for a considerable part of the MCSs. The MCSs usually form from merging of two or more convective cells. If there are new cells to merge continually into the MCS, it may become long-lived. The MCS cloud top has a very low temperature, sometimes less than $-80^{\circ}\mathrm{C}$ at the formative stage. As the MCS develops, the cold cloud canopy of the MCS expands in area.

Based on statistics by Miller and Fritch (1991) and the map of MCC global distribution (Laing and Fritsch, 1997), the active area for south-west vortices is the region with a high probability of occurrence of MCCs or MCSs. Figure 4.24 illustrates the distributions of cloud top temperature of a MCS generated in a south-west

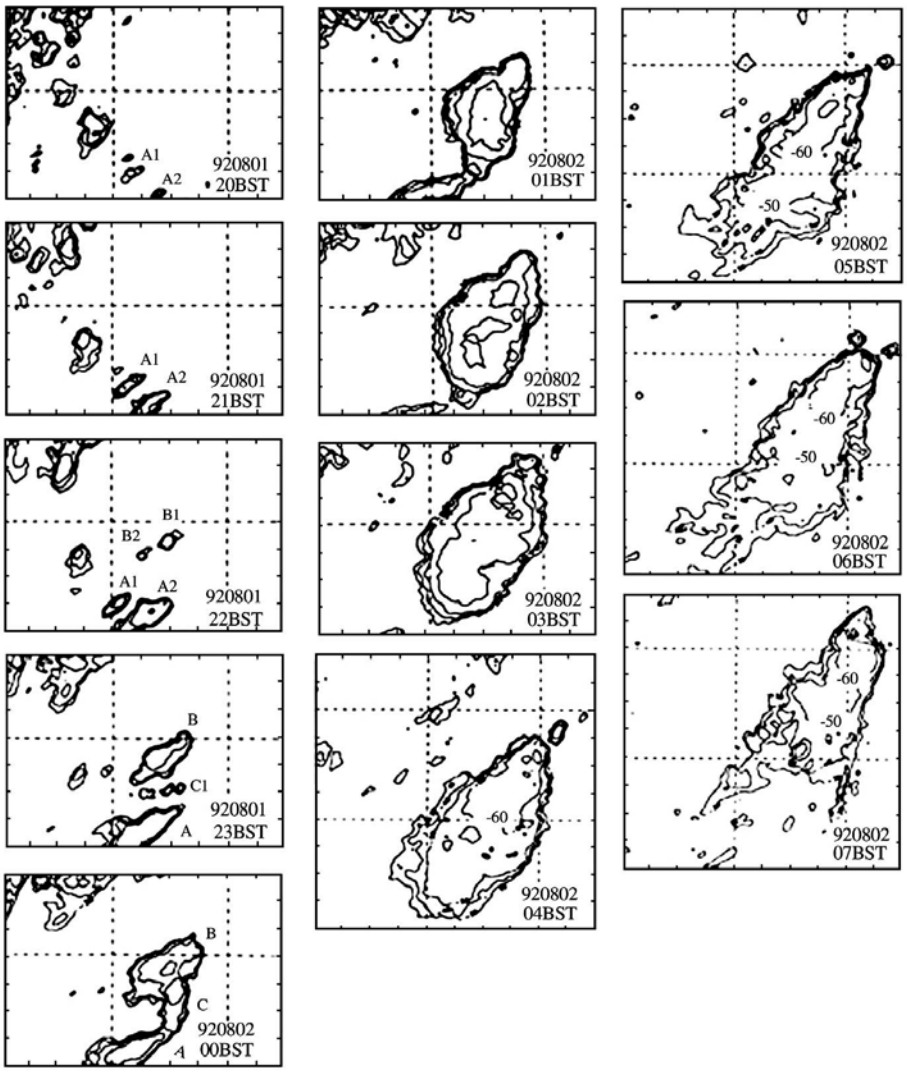

Figure 4.24. The distributions of cloud top blackbody temperature of a MCS generated in a south-west vortex for the period from 1 August (20:00 Beijing Standard Time (BST)) to 2 August (07:00 BST) 1992. Grid length in the figure is 20 km.
From Shi *et al.* (1996).

vortex (Shi *et al.*, 1996). It can be seen that this MCS evolved from the continuous growth and merging of A, B, and C convective ensembles. The cold cloud tops of $-70 \sim -80^{\circ}$C were observed when they merged together and rapidly developed. The MCSs are also generated in decaying typhoons or remnants of tropical cyclones moving inland.

For example, on 5 August 2002 when a tropical depression moved into the Shanghai region, an unprecedented torrential rainfall occurred in this region, with a daily rainfall amount of 294 mm, a 12-hour rainfall amount of 264 mm, and an hourly rainfall amount of 75.4 mm, which set a record-breaking rainfall rate for the last 50 years. This flash flood was caused by a mesoscale tropical cluster generated in a tropical depression landing on the Shanghai region. Due to an uninterrupted moisture transport into the precipitation region from the tropical ocean, this mesoscale convective cluster had a longer lifetime over land (Yang *et al.*, 2003). Feng *et al.* (2001) showed another event of the MCS related to the remnant of a decaying typhoon which brought about excessively heavy rainfall over extensive regions of north China on 3–5 August 1996, with a total rainfall amount greater than 100 mm recorded in more than 100 counties (about 8,000 km^2 in area). Around the capital of the Hebei province, the total rainfall amount exceeded 450 mm, with some observation sites reporting total rainfall amounts of 616 and 620 mm. Many reservoirs were damaged and great economic loss (of about 45.63 billion Chinese Yen) was suffered. This rainstorm was caused by two meso-α-scale convective clusters that evolved from initial meso-β-scale convective cells. The brightness temperature of cloud top reached about $-62^{\circ}C$. The MCSs associated with the Meiyu heavy rainfall are often observed and they are generally embedded within the extensive cloud and rain band of the Meiyu front, accompanied by a low-level jet to the south. A salient example is studied to illustrate the extremely strong heavy rainfall on 21–22 July 1998, with maximum hourly rainfall rate of 88.4 $mm\,h^{-1}$ (Zheng *et al.*, 2001). This event was caused by two meso-β-scale convective systems moving along a low-vortex shear line associated with the Meiyu front, with a lifetime of about 10 hours.

The MCCs were intensively studied in the 1980s and early 1990s (Ma, 1980; Miller and Fritsch, 1991). In the figures produced by Miller and Fritsch (1991) and Laing and Fritsch (1997), the MCCs in China were only observed in south-west China – associated with the south-west vortex. But, based on studies by Chinese meteorologists, the genesis regions of MCCs are not only confined to this region, they may occur over a number of other regions. In late spring and early summer, MCCs often occur over the southern part of China (Xiang and Jiang, 1995). Their mean lifetime is about 18 hours, slightly longer than that (about 10 hours) in North America. MCCs generally generate and develop in late afternoon and early evening, further grow into MCCs at night-time and dissipate in the morning of the next day. The mean area of cold cloud canopy ($\leq -52^{\circ}C$) is 1.4×10^5 km^2, slightly smaller than that in North America ($2–3 \times 10^5$ km^2). The minimum cloud top temperature is generally below $-80^{\circ}C$, with an average of $-86^{\circ}C$. The mean ellipticity of cloud areas ≥ 0.6, slightly smaller than that (≥ 0.7) in North America. Most MCCs move south-eastward, nearly parallel with the direction of mean wind in the layer of 700–500 hPa. The convective cells or ensembles that subsequently evolve into MCCs form on the leeside and then develop into MCCs under the forcing of weather systems in the tropics and mid-latitudes. Four stages may be divided for a life cycle of a MCC (i.e., genesis, development, maturity, and decay). At the genesis and development stages, the precipitation amount is relatively small, with

severe convective weather dominating. The heavy rainfalls mainly occur at the mature stage, with an intense rainfall rate of 30–50 mm hr^{-1}. Therefore, the MCCs are important rain-producing systems in the summer monsoon season in south China.

5

Intraseasonal variability

Duane E. Waliser

5.1 INTRODUCTION

While the defining variability of a monsoon system is its seasonal character, its variability about its typical seasonal evolution is often of most interest and importance. In the case of the Asian and Australian summer monsoons, their intraseasonal character is especially prominent and unique. Figure 5.1 compares annual rainfall variability along with the interannual and intraseasonal variability (ISV) for the northern and southern hemisphere summer seasons. The annual standard deviation exhibits strong variability on either side of the equator, which is a depiction of the annual meridional migration of the tropical rainfall band – a fundamental manifestation of the monsoon. The maps of interannual variability, particularly that for boreal winter, emphasize the connection to El Niño/Southern Oscillation (ENSO)-related sea surface temperature (SST) variability in the tropical Pacific Ocean. These maps of ISV illustrate two important features. First, the intraseasonal rainfall variability is as large or larger than the variability associated with the other timescales illustrated. Second, it tends to be relatively most prominent in the Asian and Australian monsoon sectors. The time series in Figure 5.2 show the annual cycle of rainfall and the anomalous evolution of unfiltered and filtered rainfall over India and northern Australia for a sample of three years. These time series emphasize the overall dominance, apart from the annual variation, of the intraseasonal timescale on these monsoon systems, including its obvious role in dictating onset and break phases. Even from these simple diagnostic figures, it is evident that ISV is a fundamental component of these monsoon systems.

The material in this chapter is devoted to describing the ISV associated with the Asian, and to some extent the Australian, summer monsoon. This includes the role it plays in the monsoons' onsets and breaks, its seasonal evolution, its interannual and decadal variability, and remote influences. In addition, the chapter will discuss what is understood regarding the important physical processes associated with monsoon

B. Wang (ed.), *The Asian Monsoon*.

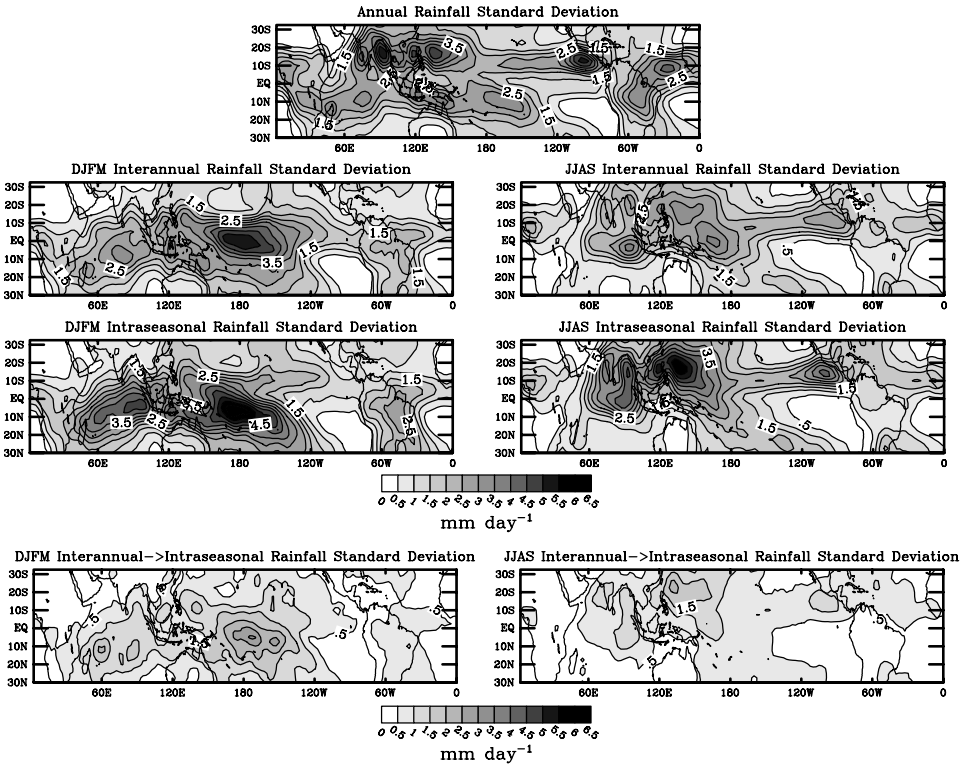

Figure 5.1. (*upper set of panels*) Rainfall variability maps for the global tropics. Rainfall data is based on pentad values of the satellite and *in situ* merged CMAP product of Xie and Arkin (1997) from 1979–1999. (*upper*) Annual cycle. In this case, the mean 73-pentad annual cycle was constructed from the data and the variance was computed about the annual mean; values shown in terms of standard deviation. (*middle*) Interannual variability. In this case, the data were low-pass filtered, retaining periods longer than 90 days. The variance of these interannual anomalies was computed for the December–March (*left*) and June–September (*right*) periods separately; values shown in terms of standard deviation. (*lower*) ISV. In this case, the data were band-pass filtered, retaining periods between 30 and 90 days. The variance of these intraseasonal anomalies was computed for the December–March (*left*) and June–September (*right*) periods separately; values shown in terms of standard deviation. (*lower set of panels*) Interannual variation of intraseasonal rainfall variability. In this case, the data were band-pass filtered, retaining periods between 30 and 90 days. The variance of these intraseasonal anomalies was computed separately for the December–March (DJFM; *left*) and June–September (JJAS; *right*) period. The variance of these values ($N = 21$ (20) for JJAS (DJFM)) was computed and is illustrated in terms of standard deviation.

ISV as well as our present capabilities and shortcomings in simulating and predicting it. While this book as a whole is devoted to the Asian monsoon, the treatment of ISV cannot be readily isolated to the boreal summer alone. The scientific developments associated with tropical ISV, including the observational and theoretical under-

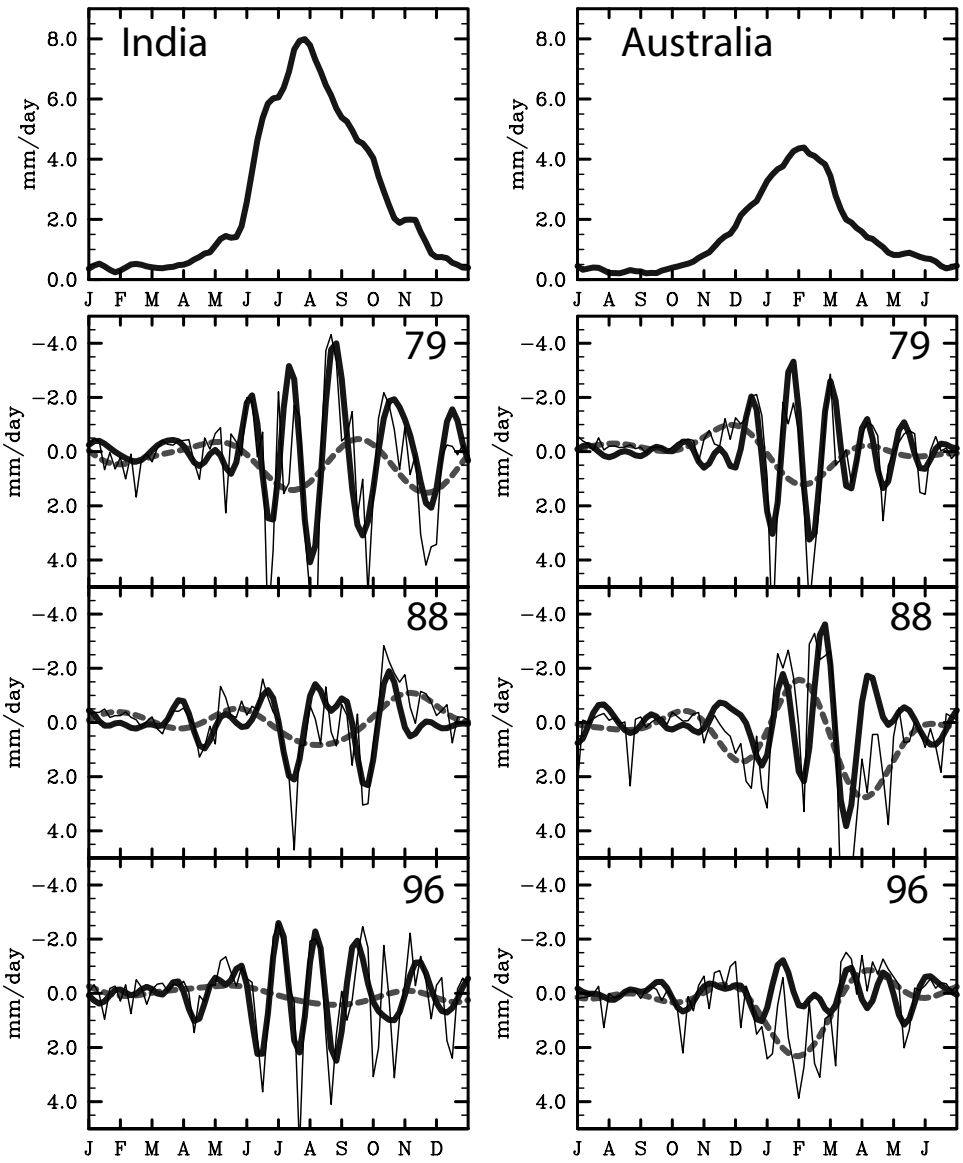

Figure 5.2. Time series of rainfall over India (*left*) and Australia (*right*). Rainfall data is based on pentad values of the satellite and *in situ* merged CMAP products of Xie and Arkin (1997) from 1979–1999. The data plotted for India (Australia) are the domain averages of the grid points lying within India (Australia, lying north of 25°S). (*top*) Mean 73-pentad annual cycle. (*lower three panels*) The thin black lines are pentad anomaly values, the thick black lines are 30–90-day band-passed values, and the thick dashed lines are 90-day low-pass values for the years 1979, 1988, and 1996.

pinnings as well as process-oriented modeling studies, have drawn from parallel, related, and/or comprehensive studies on both boreal summer and boreal winter manifestations. For this reason, much of this chapter necessarily involves review material associated with boreal summer (e.g., Asian summer monsoon) and boreal winter (e.g., Australian summer monsoon). Where possible and appropriate, the discussion is more tightly isolated to the Asian summer monsoon alone (e.g., 10–30-day variability, climatological intraseasonal oscillation (ISO), teleconnections). Note that more thorough reviews of a number of the topics discussed in this chapter can be found in Lau and Waliser (2005).

5.2 GENERAL DESCRIPTION

5.2.1 Madden–Julian Oscillation

Despite over a century of interest and study of the interannual component of the Asian monsoon (e.g., Blanford, 1884; Walker, 1923, 1924, 1928; Walker and Bliss, 1932; Walker, 1933; Banerji, 1950; Normand, 1953; Jagannathan, 1960; Banerjee *et al.*, 1978; Kung and Sharif, 1980, 1982; Shukla and Paolino, 1983; Mooley *et al.*, 1986; Hastenrath, 1987b; Shukla and Mooley, 1987; Parthasarathy *et al.*, 1988; Thapliyal and Kulshrestha, 1992; Webster and Yang, 1992; Parthasarathy *et al.*, 1994; Krishna Kumar *et al.*, 1995; Rajeevan *et al.*, 1998; Webster *et al.*, 1998; Gadgil *et al.*, 2002b; Gadgil, 2003; see also Chapter 6), the prominence of an organized intraseasonal component has only been recognized for about the last three decades. One of the first steps in this recognition came in the early 1970s with the discovery of an intraseasonal 'oscillation' in the tropics, that has since been named the Madden-Julian Oscillation (MJO; also known as the 30–60-day, 40–50-day, and tropical intraseasonal oscillation) after its discoverers (Madden and Julian, 1971). These 'oscillations' were initially detected in tropical wind and surface pressure data from available radiosonde and station data. Considering the data and computational resources available at the time, this discovery was quite remarkable. A historical perspective of this discovery can be found in Madden and Julian (2005). Subsequent to its initial detection in station data, the MJO was soon after detected in satellite observed brightness temperature/cloudiness data (Gruber, 1974; Zangvil, 1975) and has since been characterized by a number of further observational studies, a review of which can be found in Madden and Julian (1994). An additional, more recent review of the MJO as it pertains to the Australian–Indonesian monsoon can be found in Wheeler and McBride (2005).

Figure 5.3 illustrates the canonical space–time structure of an MJO event using a composite analysis of contemporary data sources. The rainfall maps illustrate its eastward propagation and equatorially trapped character. Comparison of the upper and lower tropical wind fields emphasize the baroclinic nature of its wind anomalies. In addition, it can be seen that the MJO has a global scale with wind anomalies, particularly at upper levels, being primarily characterized by wavenumber 1, and with rain and low-level winds being primarily characterized by wavenumber 2 –

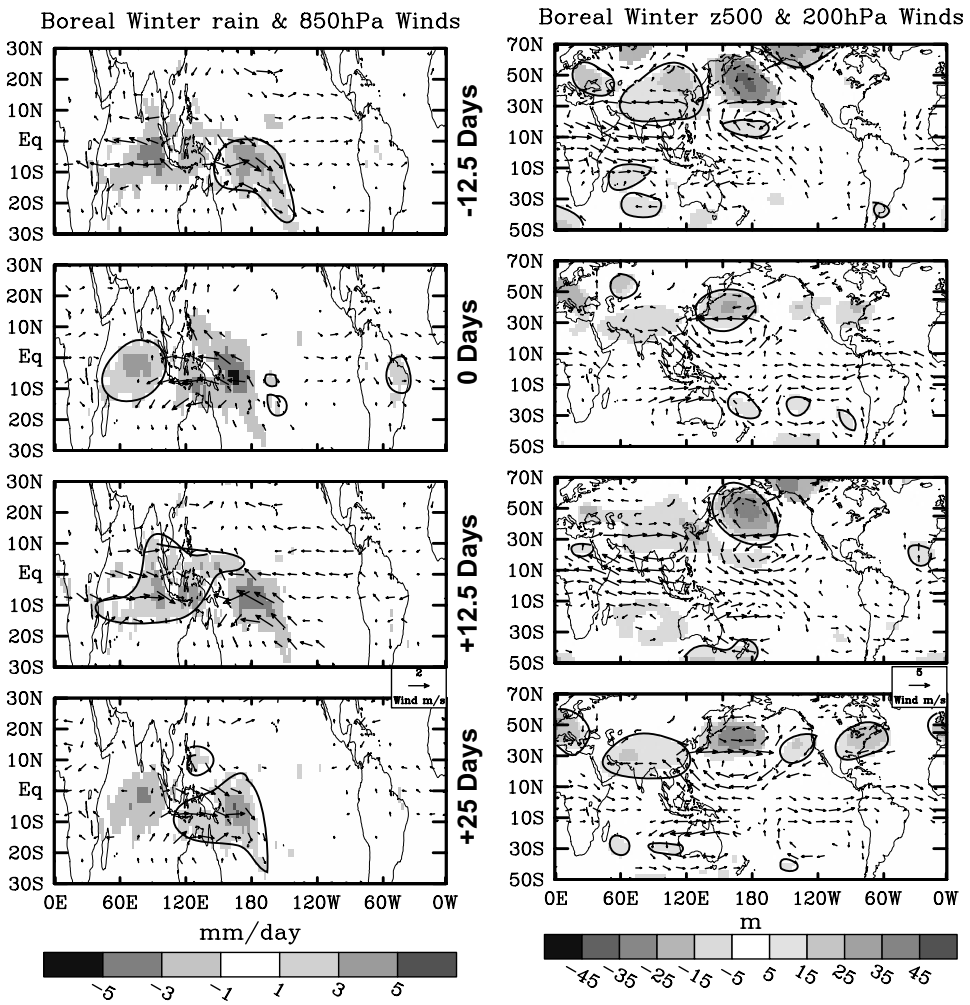

Figure 5.3. Canonical structure of an MJO event based on 5-day average (i.e., pentad) NCEP/NCAR Reanalysis (Kalnay *et al*., 1996) and CMAP rainfall data (Xie and Arkin, 1997) from 1979–2000. Data were band-pass filtered with a 30–90-day filter and then separated into boreal winter (November–April) and summer (May–October). Extended EOF (EEOF) analysis with ±5 pentad lags was performed on tropical rainfall (30°N–30°S, 30°E–180°E) to identify the dominant 'mode' for the winter and summer separately. Composite events were constructed by selecting events if the EEOF amplitude time series exceeded 1 standard deviation ($N = 43$ (49) for winter (summer)). The resulting composites have dimensions lag (−5 to +5 pentads), latitude, and longitude. In the plots above, only 4 panels of the boreal winter composite are shown, each separated by 2.5 pentads (i.e., 12.5 days). Plots on the left show composite rainfall and 850-hPa wind vectors between 30°N and 30°S. Plots on the right show 500-hPa geopotential heights and 200-hPa wind vectors between 70°N and 50°S. Only values that exceed the 90% confidence limit are shown. Positive anomalies are encircled by a single countour.

although modulated by the relatively warmer (cooler) eastern (western) hemisphere background state. For example, over the Indian and west Pacific Oceans, there is evidence of considerable interaction between the wind and rainfall anomalies. In these regions, where the coupling between the convection and warm surface waters is strong, the oscillation propagates rather slowly, about 5–10 $m\,s^{-1}$. However, once the disturbances reach the vicinity of the Date Line, and thus cooler eastern Pacific Ocean equatorial waters, the convection tends to subside and propagate south-eastward into the South Pacific convergence zone (SPCZ). Beyond the Date Line, the disturbance is primarily evident only in the wind field with characteristics similar to a dry Kelvin wave with a speed of about 15–20 $m\,s^{-1}$ or greater (e.g., Hendon and Salby, 1994).

Another important feature associated with the MJO, especially in relation to its connections to mid-latitudes and its connections to the boreal summer ISO, is its off-equatorial structure and variability. From Figure 5.3 there is evidence of off-equatorial Rossby wave gyres that straddle the near-equatorial rainfall anomalies. For example, in the composite maps at lag +12.5 days, the positive rainfall (i.e., heating) anomaly is located over the Maritime Continent. Associated with this are upper level cyclonic (anticyclonic) gyres to the north-east and south-east (north-west and south-west) centered at latitudes of about 20°. These gyres are easily identified in the maps of the MJO life cycle constructed by Hendon and Salby (1994) and are consistent with the circulation that is expected in association with a near-equatorial tropospheric heating anomaly (Matsuno, 1966; Gill, 1980). One of the important manifestations of these tropical heating and subtropical streamfunction anomalies is that they act as Rossby wave sources for mid-latitude variability (e.g., Weickmann, 1983; Liebmann and Hartmann, 1984; Weickmann *et al.*, 1985; Lau and Phillips, 1986; Sardeshmukh and Hoskins, 1988; Berbery and Noguespaegle, 1993). For example, the +12.5-day lag map of Figure 5.3 shows evidence of a wave train emanating from the tropics and extending poleward and eastward over the Pacific Ocean and North America. Such connections with the extratropics have important ramifications for mid-latitude weather variability, regime changes, and forecasting capabilities (e.g., Ferranti *et al.*, 1990; Higgins *et al.*, 2000; Jones *et al.*, 2004a).

The ISV characteristics discussed above tend to be most strongly exhibited during the boreal winter and spring when the Indo–Pacific warm pool is centered at or near the equator. From the rainfall maps in Figure 5.3, it is evident that the MJO has its greatest impact on Australian monsoon rainfall variability (e.g., right panels of Figure 5.2). However, as will become evident the principal mode of ISV that influences the Asian summer monsoon shares many of the same properties, and in large part their differences derive mainly from a consideration of the seasonal modulation of ISV. There have been a number of terminologies applied to the boreal summer ISO, ranging from simply ISO, monsoon ISO (MISO), and even just the MJO, where the latter simply takes the viewpoint that there is one inherent phenomenon modulated by the annual cycle. In this chapter, it is important to be able to distinguish the two different phenomena (or, if one prefers, the seasonal modulation of the phenomenon) and their associated research developments. Thus the form of ISV that most directly affects the Asian summer monsoon, and in this sense is

different from the MJO form of ISV that primarily affects the Australian summer monsoon, will be referred to as the boreal summer ISO or just the ISO.

5.2.2 Boreal summer ISO

Beginning around the mid to late 1970s, a number of studies began to identify intraseasonal fluctuations, with periods around 40–50 days, associated with the Asian summer monsoon. These included analysis of both cloudiness (Murakami, 1976a; Yasunari, 1979, 1980) and wind variability (Dakshinarmuti and Keshavamurty, 1976; Murakami, 1977). These initial studies set the stage, and in essence primed the community, for a very active research period on the ISO that was forthcoming in association with the First GARP (Global Atmospheric Research Program) Global Experiment (FGGE) in 1979 (NA, 1978; Fleming *et al.*, 1979). In hindsight, the FGGE year could not have turned out better in terms of providing an ideal data set for carrying out ISO-related monsoon research. For example, examination of the Indian rainfall plots such as those in Figure 5.2 for all years since 1979 illustrate that the 1979 summer had one of the most robust ISV signatures of any year since. The resulting enhanced data set from the FGGE provided the observational resources for a multitude of ISO-related studies (e.g., Lorenc, 1984; Krishnamurti and Gadgil, 1985; Murakami and Nakazawa, 1985; Cadet, 1986; Chen, 1987; Murakami, 1987a; Krishnamurti *et al.*, 1988; Krishnamurti *et al.*, 1990; Chen and Yen, 1991; Krishnamurti *et al.*, 1992a; Chen and Chen, 1993; Chen and Chen, 1995).

Figure 5.4 illustrates the canonical space–time structure of a typical boreal summer ISO event using a composite analysis of contemporary data sources (see among others, Krishnamurti and Subrahmanyam, 1982; Chen and Murakami, 1988; Goswami *et al.*, 1998; Annamalai *et al.*, 1999; Annamalai and Slingo, 2001; Hsu and Weng, 2001; Kemball-Cook and Wang, 2001; Lawrence and Webster, 2002; Hsu *et al.*, 2004). The rainfall map at lag 0 days shows that positive rainfall anomalies in the western and central Indian Ocean occur in conjunction with negative rainfall anomalies over a region extending between India and the western equatorial Pacific. This system then appears to propagate in both an eastward and northward fashion. Examination of the near-equatorial region alone gives the impression of an MJO-like phenomenon described above, although more confined in longitude. On the other hand, examination of a given longitude sector anywhere between 80°E and 130°E gives the impression of a northward-propagating phenomena (e.g., Figure 5.15, p. 239). Studies such as those by Yasunari (1979) and Lau and Chan (1986) tied these two different aspects of propagation together and pointed out the comprehensive nature of the phenomena. From these figures, it is evident now that the intraseasonal variations in rainfall depicted in Figure 5.2 are closely associated with the type of space–time variability shown in Figure 5.4 (and Figure 5.15). These variations largely account for what are often referred to as 'active' and 'break' periods of the monsoon which, as discussed above, make up a critical feature of the Asian monsoon system and its variability (Blanford, 1886; Ramaswamy, 1962; Raghavan, 1973; Ramanadh *et al.*, 1973; Krishnamurti and Bhalme, 1976;

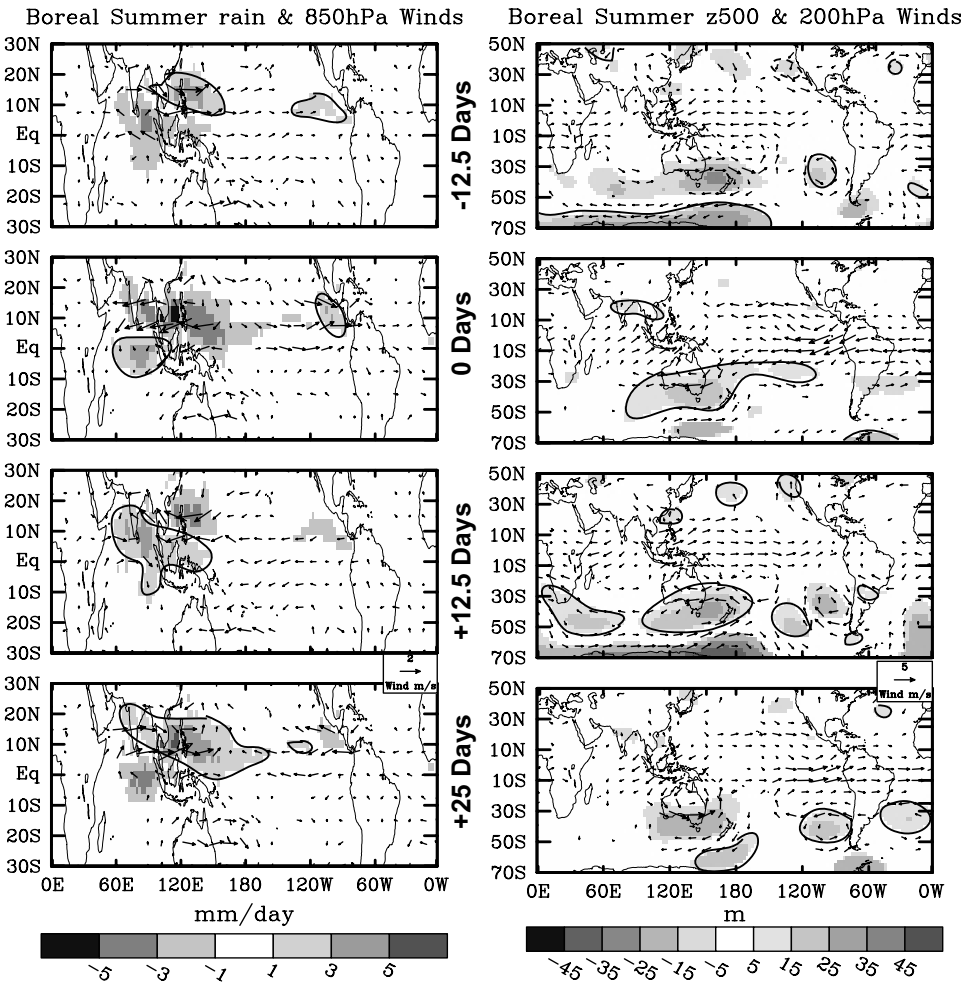

Figure 5.4. Same as Figure 5.3, except for boreal summer (May–October), and with the panels on the right extending from 50°N to 70°S.

Alexander *et al.*, 1978; Sikka, 1980; Cadet, 1983; Bhide *et al.*, 1997; Annamalai and Slingo, 2001; Gadgil, 2003; Gadgil and Joseph, 2003).

While the diagram in Figure 5.4 illustrates what might be considered a typical ISO event, it is important to recognize that these events have considerably more complexity in reality. For example, the study by Wang and Rui (1990a), and later by Jones *et al.* (2003), have further diagnosed the 'synoptic climatology' of tropical ISV events, including their seasonal modulation (see also Lawrence and Webster, 2002). Both studies used forms of convective (i.e., OLR) anomaly 'tracking', the former being more subjective and the latter an objective approach, to illustrate the typical pathways that ISV events follow. Viewed within this paradigm, each of the identified

categories of events would at some point within their eastward migration move northward into the Indian subcontinent or into south-east Asia and the western north Pacific Ocean. Apart from these types of variations, it is important to point out that there is a fair bit of variability even within the monsoon season when considering the nature of ISO events and the influence of the background state. For example, Figure 5.5 illustrates how the typical pattern of intraseasonal variance is modified over the course of the monsoon season (Kemball-Cook and Wang, 2001). During the onset month(s) of the monsoon, most of the variability occurs in the Indian sector while during the final month(s) of the monsoon, most of the variability occurs in the east Asian and western North Pacific sectors. This seasonal variation was shown to be consistent with the seasonal march of the warmest SSTs, which begin to develop in the northern Indian Ocean in the early monsoon period and eventually are found around south-east Asia and the north-western tropical Pacific in the later part of the summer.

With the above seasonal modulation in mind, Kemball-Cook and Wang (2001) produced a schematic of the synoptic evolution of an ISO event. This diagram is shown in Figure 5.6. It illustrates a mixture of the underlying wave characteristics, and their propagation features, associated with the space–time and variance structures shown in Figures 5.4 and 5.5. For both the early and late monsoon season, there is what can be considered an initiation phase in the equatorial Indian Ocean, an eastward propagating component, and a recurrent emission of Rossby waves. For the initiation phase, the main difference between early and late summer, is that during late summer there is an eastward displacement of the location of the initiation phase. For the eastward propagating component, the main difference is that in late summer, the propagation appears to be somewhat discontinuous and 'jumps' across the Maritime Continent. In addition, there is less latitudinal symmetry in late summer, as warm moist surface conditions have moved mostly to the north of the equator.

The off-equatorial disturbances shown in Figure 5.6 are associated with the emanation of Rossby waves from the near-equatorial convection anomaly. It is this feature that makes the propagating characteristics of the boreal summer ISO particularly complex. These disturbances are associated with three directions of propagation. Considered in isolation, they have an inherent westward propagation (Matsuno, 1966). This accounts for some aspects of the westward propagating variability that is found, particularly in the latter part of the summer, in the south-east Asian sector/western North Pacific Ocean and/or that is associated with higher frequency ISV that will be discussed in more detail below. On the other hand, the emanation of these Rossby waves occurs from a very large-scale, eastward-moving, near-equatorial convective anomaly (e.g., Lawrence and Webster, 2002). Finally, there are physical processes that promote northward propagation of these Rossby wave disturbances that will be discussed in Section 5.5. Considering these latter two aspects together, largely accounts for the appearance of the eastward-propagating, north-west–south-east tilted, large-scale 'rain band' evident in Figure 5.4. Note that in some constructions this 'tilted rain band' appears more like a quadrapole feature (e.g., Annamalai and Slingo, 2001). Kemball-Cook and

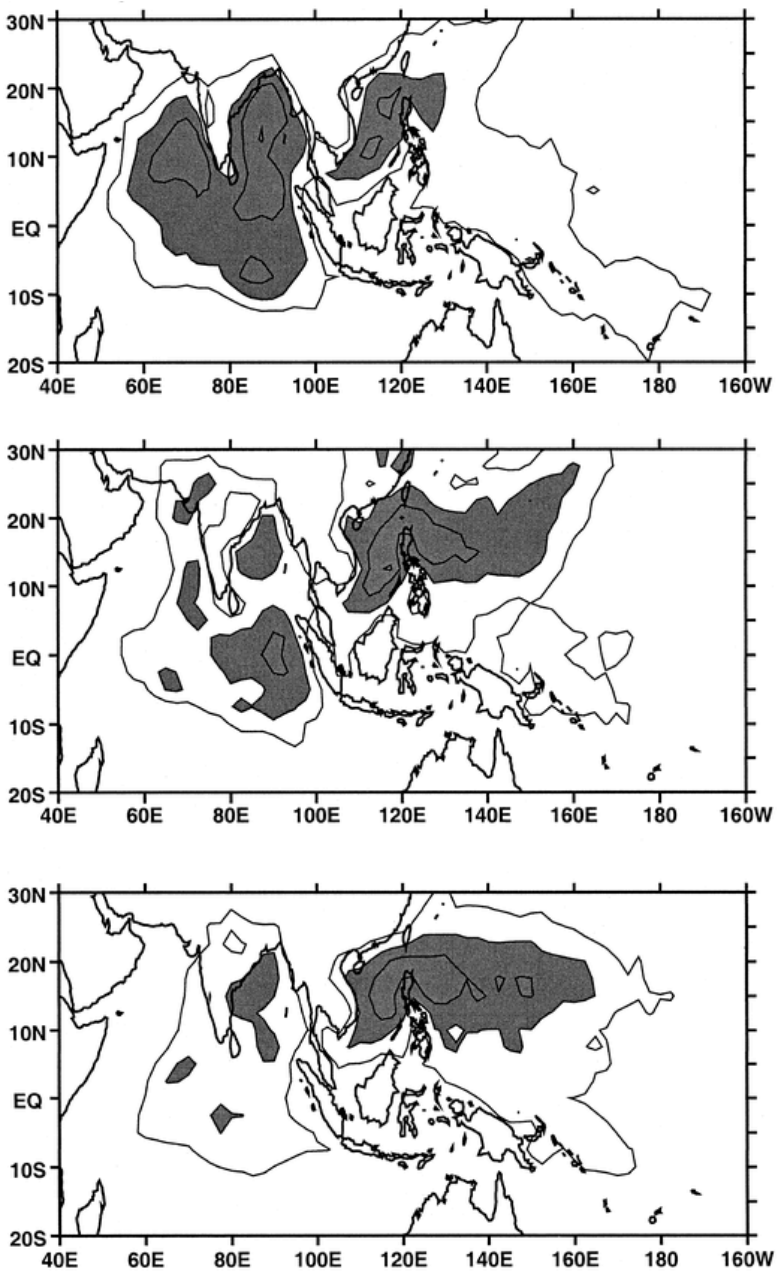

Figure 5.5. Seasonal variation of 10–100-day filtered OLR variance. (*top*) May–June average, (*middle*) July average, and (*bottom*) August–October average. Contour interval is 250 $(\mathrm{W\,m^{-2}})^2$. First contour at 500 $(\mathrm{W\,m^{-2}})^2$. Regions where the OLR variance >750 $(\mathrm{W\,m^{-2}})^2$ are shaded.
From Kemball-Cook and Wang (2001).

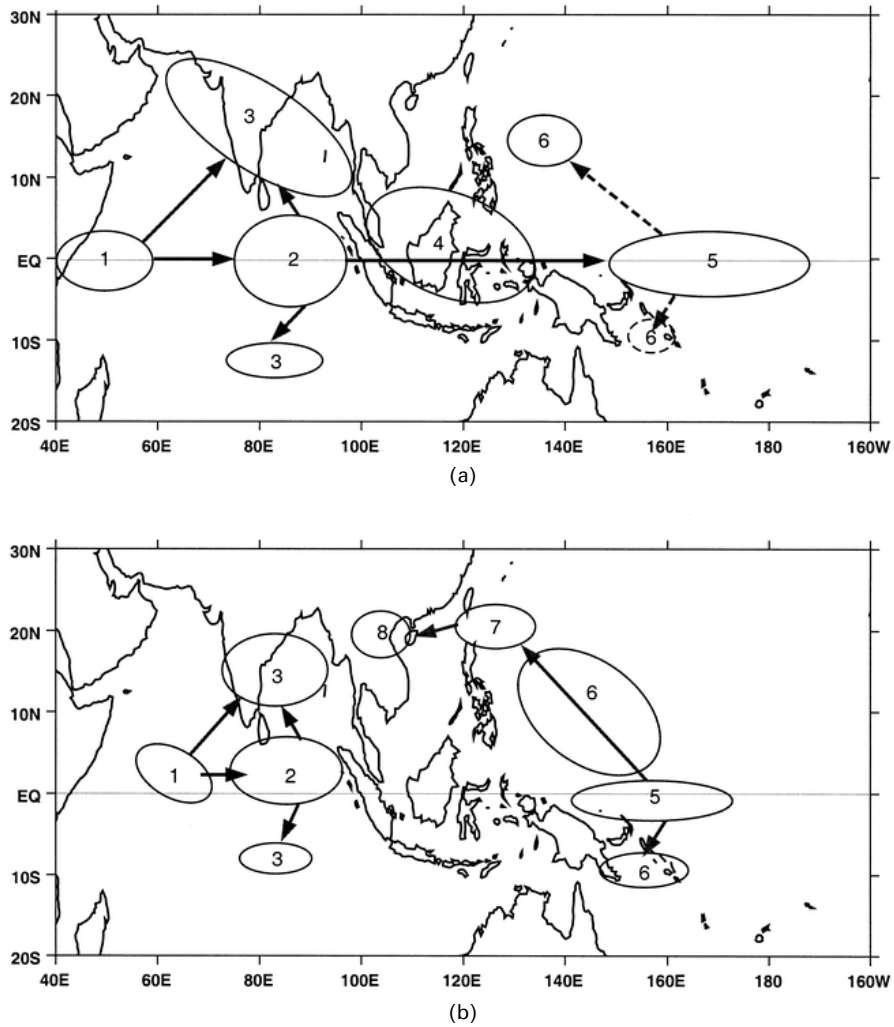

Figure 5.6. Boreal summer ISO convection life cycle for (a) May–June and (b) August–October. Ovals indicate convection, with numbers indicating the evolution of the anomaly. Horizontal arrows indicate eastward propagation of convection along or near the equator. Vertical/slanted arrows indicate poleward propagation of convection due to emanation of Rossby waves from equatorial convection. Dashed lines indicate a low-amplitude signal. From Kemball-Cook and Wang (2001).

Wang (2001) pointed out that north–south asymmetry and the enhancement of this Rossby wave component in the latter part of the monsoon season are associated with the change in the background state (e.g., SST and surface moisture) and accompanying enhancements in the large-scale easterly vertical shear (Li and Wang, 1994; Wang and Xie, 1996, 1997). For additional and more thorough reviews of the boreal summer ISO, the reader is referred to Goswami (2005) and Hsu (2005).

5.2.3 High-frequency ISV

In addition to the prevalence of ISV with a nominal timescale of 40–60 days, there is also considerable ISV at higher frequencies, at timescales of around 10–20 days. Detection of these higher frequency fluctuations came from early studies on cloudiness and conventional synoptic observations (Krishnamurti and Bhalme, 1976; Murakami, 1976b; Yasunari, 1979; Krishnamurti and Ardanuy, 1980). However, it wasn't until the 1980s and even the 1990s that enough data became available to more thoroughly document the temporal and spatial structure as well as the modulation of the variability over the course of the monsoon season (Lau *et al.*, 1988a; Tanaka, 1992; Chen and Chen, 1993; Fukutomi and Yasunari, 1999; Chen *et al.*, 2000; Annamalai and Slingo, 2001; Hsu and Weng, 2001). For example, Figure 5.7 shows Annamalai and Slingo's depiction of the 10–20-day mode calculated from 10–20-day band-passed OLR data using Principal Oscillation Pattern (POP; Hasselmann, 1988) analysis. This mode accounted for about 1/4 of the subseasonal monsoon variability while the 30–60-day (i.e., ISO) accounted for about 2/3. In contrast to the lower frequency ISO, this mode's variability is focused almost entirely over east Asia and the north-west tropical Pacific region. Moreover, their analysis indicates that in contrast to the 30–60-day mode, whose large-scale structure appears to originate in the equatorial Indian Ocean and propagate northward/north-eastward, the 10–20-day mode originates in the equatorial western Pacific and propagates westward/north-westward in the form of Rossby waves at about $5\,\mathrm{m\,s^{-1}}$.

Based on the studies noted above, another noteworthy feature of the 10–20-day mode is that it has a relatively strong seasonal variation. In particular, during the early summer monsoon period (e.g., May–July), there is considerable 30–60-day variability exhibited at and near the equator and in particular in the Indian sector, with relatively little 10–20-day variability evident. However, as the monsoon season progresses, the focal point of the 30–60-day variability moves north-eastward (Figure 5.5) with strong 10–20-day variability developing in the east Asian and north-western tropical Pacific Ocean. The concurrence of high amounts of 30–60 and 10–20-day variability in this region during the latter half of the monsoon makes this period and region of the monsoon particularly challenging to diagnose, understand, and model. More generally, the role of the 10–20-day variability in determining or modulating monsoon onset breaks, either separately or in conjunction with 30–60-day variability, is still an outstanding question.

As there have been less observational studies of the 10–20-day variability compared with the 30–60-day ISO mode, there have also been fewer hypotheses as to its origin. Krishnamurti and Bhalme (1976) suggested the 10–20-day mode could arise from a cloud–radiation–convective feedback. While plausible, there was no quantitative support provided for a selection of the given timescale and none for the overall spatial structure – which was probably not that well defined at the time. Goswami and Mathew (1994) invoked an evaporation–wind feedback (see Section 5.5) to describe the instability but their most unstable mode had a zonal wavelength of about $9–12 \times 10^3$ km which is significantly larger than the $5–6 \times 10^3$ km wavelength evident in Figure 5.7. Recently, Chatterjee and Goswami (2004) used a

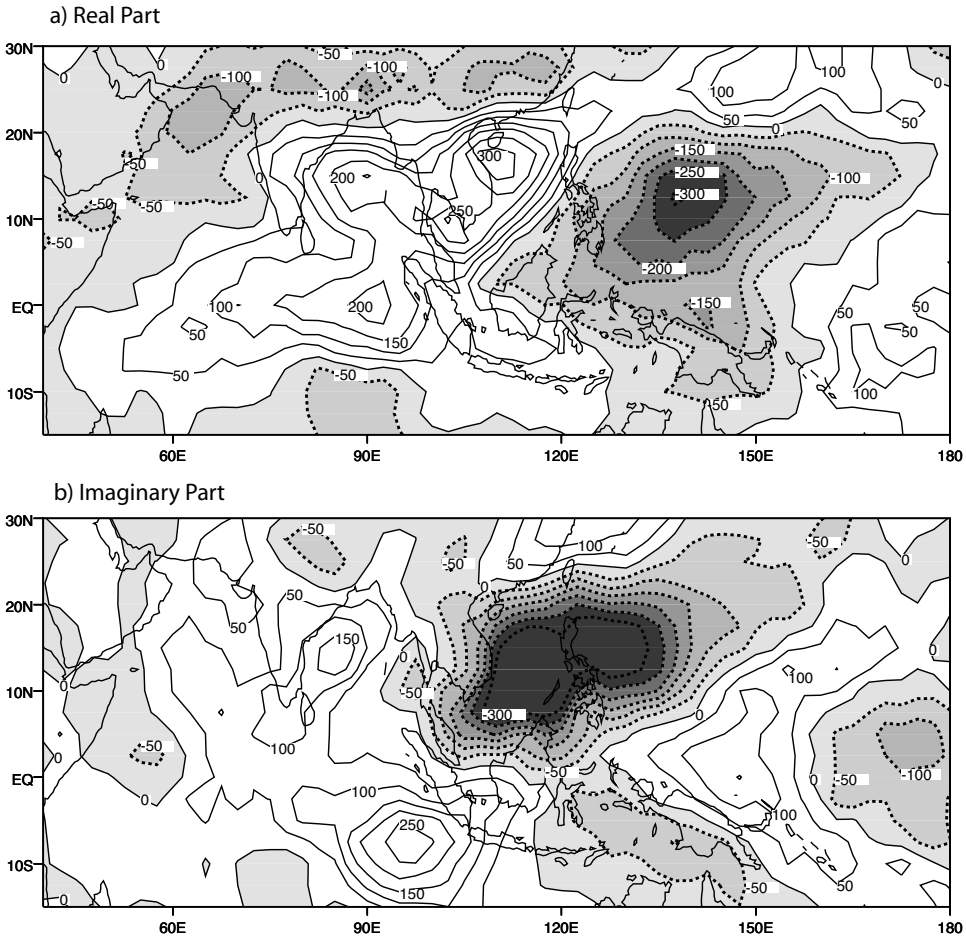

Figure 5.7. Real and imaginary POPs for an analysis of 10–20-day band-pass filtered OLR data. The rotation period of the POP is 17 days and the decay time is 20 days. The contour interval is 50 and the shading denotes negative values. Taken together, these two patterns depict an westward/north-westward propagating oscillation.
From Annamali and Slingo (2001).

simplified 2-layer atmospheric model coupled to a steady Ekman boundary layer to examine the nature of the 10–20-day mode (referred to as the quasibiweekly mode; QBM). Their model results suggest that the QBM is an $n = 1$ Rossby wave which is modified by the mean background state. The latter provides for the 'dynamic equator', and thus the Rossby wave itself, to be displaced northward giving the modal structure of the pattern more consistency with the observations. The source of instability comes from the interaction between convective heating and frictional moisture convergence within the (off-equatorial) region of low-level vorticity.

5.2.4 Climatological ISO

While Figure 5.2 suggests a fair amount of year-to-year variability in the character of the monsoon's ISO variability (discussed in more detail in Section 5.4), there is actually enough year-to-year similarity to make up what has been termed the 'climatological ISO' (CISO; after Wang and Xu, 1997). This feature has been detected and examined by a number of studies (Lau *et al.*, 1988a; Kang *et al.*, 1989; Nakazawa, 1992; Wang and Xu, 1997; Kang *et al.*, 1999) and is illustrated in the time–latitude diagrams constructed by Kang *et al.* (1999) that are shown in Figure 5.8. In each case, long-term average (~5 summers) values of pentad cloud fraction is shown. These diagrams illustrate that the mean evolution of the monsoon

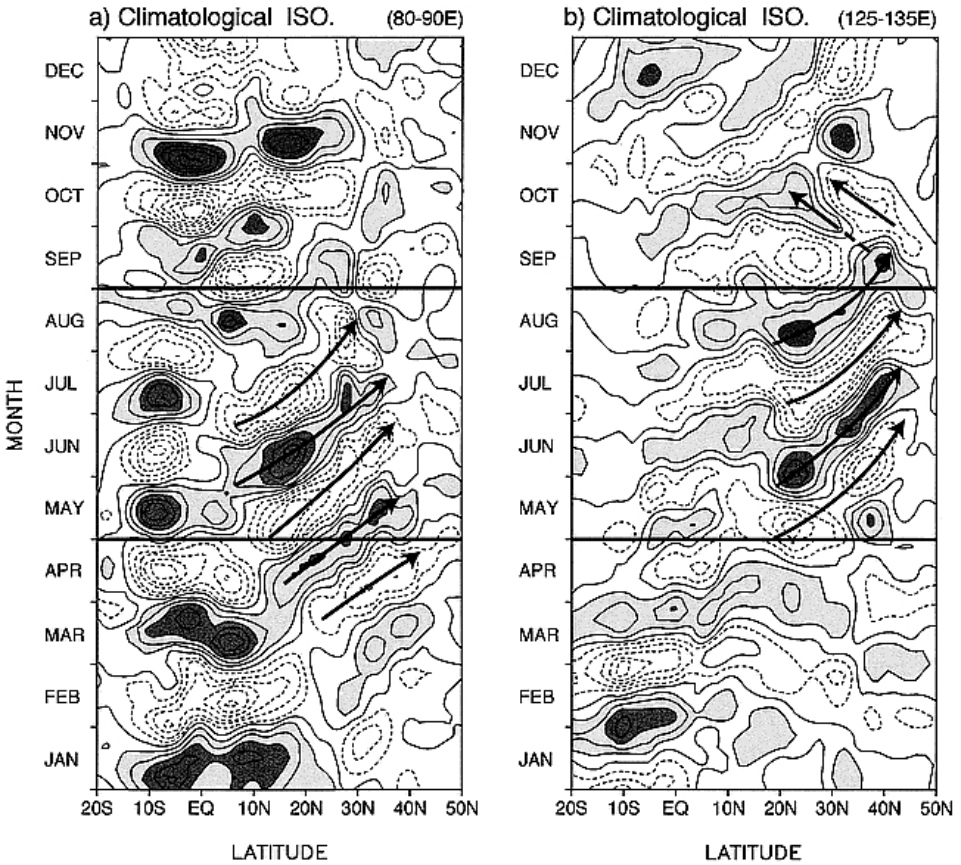

Figure 5.8. Hovmoeller diagrams of climatological intraseasonal component of cloud fraction along longitudinal bands of (a) 80°–90°E and (b) 125°–135°E. Contour interval is 0.02. Light and dark shading indicates the cloud fractions between 0.02 and 0.06 and those greater than 0.06, respectively.
From Kang *et al.* (1999).

exhibits structured (northward) propagation characteristics similar to the 'synoptic' ISO events described above. While the number of years used in their analysis is relatively few to ensure statistical significance, the analysis of Wang and Xu (1997) uses 17 years of OLR to illustrate that the subseasonal variability (i.e., CISOs) exhibited in the mean climatology is distinct from its smooth seasonal evolution.

The above line of research has helped support, and dovetailed with, a parallel line of research that has over the years discussed the multistage onset of the Asian summer monsoon, particularly in the south-east Asian region (e.g., Ding, 1992; Matsumoto, 1992; Tanaka, 1992; Ueda *et al.*, 1995; Wu and Wang, 2001; Wang and LinHo, 2002). For example, the northward propagation of the climatological convection that begins in mid-May (Figure 5.8) is associated with the monsoon onset in the South China Sea region and then subsequently in mid June the onset of the Meiyu in Central China and the Baiu in Japan. By this time, the South China Sea region is undergoing a climatological withdrawal, which subsequently happens in central China and Japan as the convective signal moves further north ($\sim 40^{\circ}$). By around early August, there is a return of active conditions around 20°N and another northward propagating climatological feature. While the CISO provides a framework for understanding, and even predicting, regional monsoon onset characteristics, it should be emphasized that just as the ISO might be considered a fundamental building block of the climatological onset, it can also produce a fair amount of variability to the onset and even be responsible for delaying or producing false onsets (Flatau *et al.*, 2001; Flatau *et al.*, 2003).

5.3 SYNOPTIC ORGANIZATION AND REMOTE INFLUENCES

The subseasonal time and planetary spatial scales of the boreal summer ISO give it the means to modulate synoptic activity at considerably smaller time and space scales as well as the circulation in regions remote from the main convective disturbances. This section briefly examines a number of interactions of this sort, including both local and remote organization of tropical storm activity. While a number of studies have noted a modulation of synoptic activity such as tropical storms by ISV in the Indian sector (Yasunari, 1981; Murakami *et al.*, 1986; Liebmann *et al.*, 1994), Goswami *et al.* (2003) have performed a recent analysis for the period 1954–1993 with very clear demonstrable results pertaining to the Indian monsoon. Their analysis focused on the development and subsequent tracks of low-pressure systems (i.e., lows and depressions; LPS). They first developed an ISO index based on filtered 850-hPa relative vorticity. Then they plotted the genesis and track information for the LPS that occurred within what they referred to as the 'active' and 'break' phases of the ISO (analogous to the 4th and 2nd panels of Figure 5.4, respectively); their results are shown in Figure 5.9. In the active phase, there is a strong preference for the development of LPS to occur in what amounts to the seasonal mean position of the monsoon trough and region of maximum relative vorticity (Chapters 2, 4, and 9), both of which are accentuated during the 'active' phase of the ISO. In the break phase, there is a clear diminution of LPS

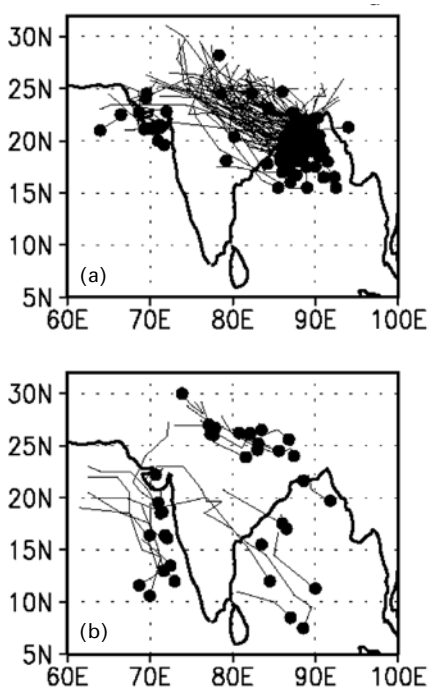

Figure 5.9. Tracks of LPS for the period 1954–1983 during extreme phases of the boreal summer ISO. (a) 'Active' ISO phase (analogous to the 4th panel of Figure 5.4) and (b) 'break' ISO phase (analogous to the 2nd panel of Figure 5.4). Dark dots represent the genesis point of the LPS and their lines show the tracks.
From Goswami *et al.* (2003).

development, with the few that do develop occurring on the northward and southward edges of the seasonal mean trough – regions where the ISO in the 'break' phase (as referred to here) is enhancing convective activity and low-level vorticity. They noted a 3.5 times increase in LPS development during the active vs. the break phase. Also noteworthy in their study was that they determined that this so-called 'clustering' of LPS activity was separately modulated by both 30–60-day and 10–20-day frequency bands in approximately equal amounts, and that the clustering was particularly strong when the enhancement effect from both bands acted on concert.

Along with the Indian sector, there is also significant evidence for synoptic modulation by ISV in the east Asian and north-western tropical Pacific Ocean. Many of the studies on this topic have been concerned with the modulation of tropical cyclones. As with the LPS results above, a number of studies have found that typhoons tend to develop in active monsoon trough regions (Harr and Elsberry, 1995; McBride, 1995). Since the location and spatial extent of the monsoon trough is strongly modulated by ISO activity, it is expected that modulations of typhoon activity occur in conjunction with the ISO. For example, Nakazawa (1986) found that during the FGGE year, tropical cyclones tended to occur in the convective

phases of the ISO, including both the 15–25 and 30–60-day variations. Curiously, prior to this, Gray (1978) found that tropical cyclone formation tended to cluster in 1–2 week periods with these periods being separated by 2–3 weeks. Clearly, Gray was seeing the effect of the ISO but had too little data to work with and as yet the ISO was just beginning to be detected and defined. Maloney and Dickinson (2003) performed a detailed analysis of the energetics of this relationship and found that when 850-hPa wind anomalies are westerly (i.e., the 4th panel of Figure 5.4), small-scale eddies tend to grow through barotropic eddy kinetic energy conversion from the mean flow. The development of these eddies, together with strong surface convergence and 850-mb cyclonic shear that occur in conjunction with this phase of the ISO (i.e., the 4th panel of Figure 5.4 between about 120°–150°E and about 5°–20°N), and the high mean sea surface temperatures during the late boreal summer, create the favorable environment for tropical cyclone formation. Along with the evidence for ISO modulation of tropical cyclones, there is also considerable evidence for the modulation of more generalized synoptic disturbances and wave activity in the east Asian and tropical west Pacific Ocean region (Nakazawa, 1986; Lau and Chan, 1988; Sui and Lau, 1992; Salby and Hendon, 1994; Hartmann and Maloney, 2001; Straub and Kiladis, 2003).

Just as noteworthy as the local modulation of tropical convective activity by ISO is evidence from a number of studies that such modulation can extend to a near global extent (Higgins *et al.*, 2000; Maloney and Hartmann, 2000a,b; Mo, 2000). These studies have each examined the downstream influence of the boreal summer ISO on tropical storm and/or hurricane development. For example, Maloney and Hartmann (2000a,b) found evidence that the ISO, through its effects on low-level winds in the eastern Pacific (see the 2nd and 4th panels of Figure 5.4) has a strong modulating effect on hurricane development in the eastern Pacific and Gulf of Mexico. Mo (2000) found that this influence extends to the tropical storm activity in the Atlantic. The study by Higgins *et al.* (2000) demonstrated the global nature of these influences by compositing the 200-hPa velocity potential anomalies for 21 strong ISO events between 1979 and 1997. Then as shown in Figure 5.10, they posted the point of origin of all tropical storms that developed into hurricanes/typhoons and that occurred during those 21 ISO events. Clearly evident is a robust, global-scale modulation by the ISO wavenumber one circulation anomaly that leads to an enhancement (suppression) of hurricane/typhoon formation in the rising (subsiding) branch of the anomalous circulation. The results described in this section, coupled with the potential predictability of the ISO itself, discussed in Section 5.7, provide a valuable means to possibly predict, on a regional scale, the occurrence of regimes when extreme tropical events are more or less likely to occur.

5.4 LOW-FREQUENCY VARIABILITY

It is evident from Figure 5.2 that the amount and character of the ISV associated with the Asian and Australian monsoon systems varies considerably from year to year. For example, as mentioned above, the 1979 FGGE year was characterized by

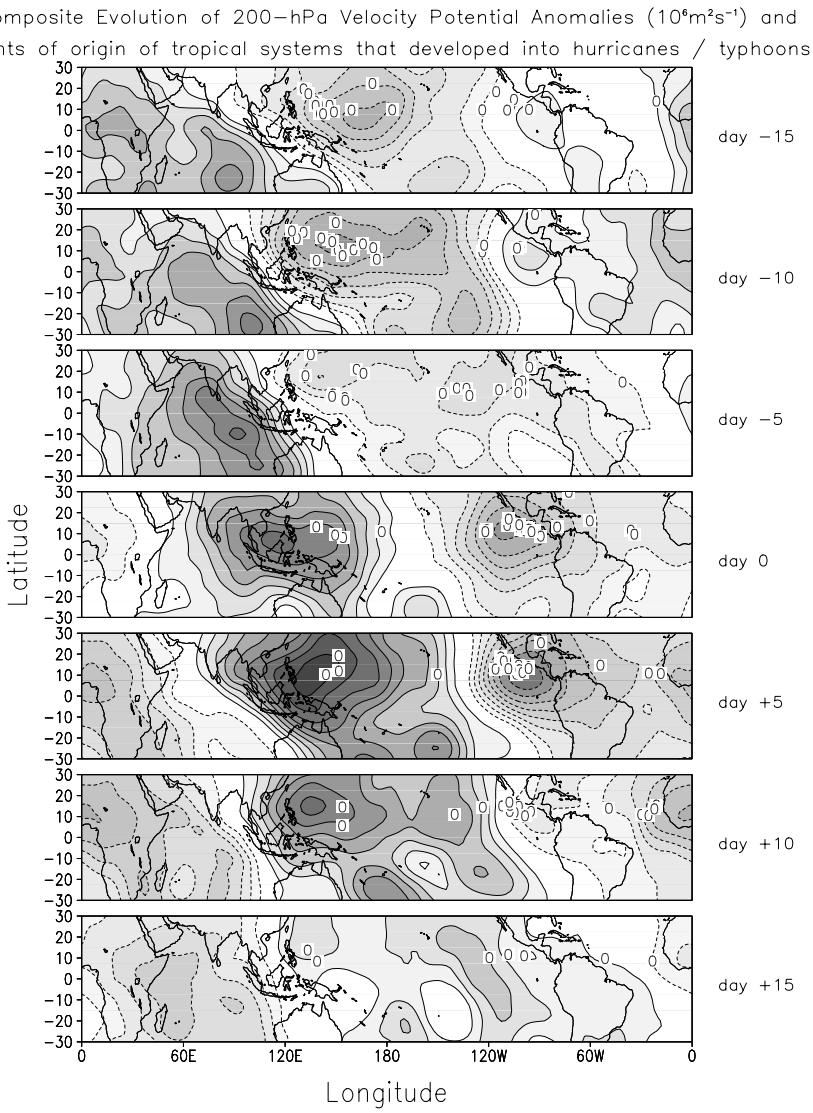

Figure 5.10. Composite evolution of 200-hPa velocity potential anomalies associated with the boreal summer ISO and points of origin of tropical systems that developed into hurricanes/typhoons. Note that panels 1–4 in Figure 5.4 roughly correspond to lags −5, +5, +15, and −15 days, respectively. The light (dark) shading roughly corresponds to regions where convection is favored (suppressed) as represented by 200-hPa velocity potential anomalies Composites are based on 21 ISO events, each considered over a 35-day period. Hurricane track data is for the period July–September for 1979–1997. Points of origin in each panel are for different storms – only those that occurred during the 21 selected ISO events. Contour interval is $0.5 \times 10^6\ \mathrm{m^2\ s^{-1}}$, negative contours are dashed, and the zero contour is omitted for clarity.
From Higgins *et al.* (2000).

very large and regular intraseasonal fluctuations in both the Indian and Australian summer monsoon sectors. On the other hand, 1988 exhibited rather weak ISV over India and rather typical variability over Australia, vice versa for 1996. The lower set of maps in Figure 5.1 quantify this variability by illustrating the amount of year-to-year variability associated with the intraseasonal variance presented in the upper set of panels. Specifically, the two intraseasonal maps in the upper set of plots in Figure 5.1 show the typical amount of intraseasonal rainfall variability in any given season, and the two lower maps show the interannual variability associated with this quantity. When considering these quantities in terms of variance (as opposed to standard deviation which is what is illustrated; see caption for details), the typical change from year to year is of the order of 30%. Thus, the variations are considerable and these have a profound impact on the year-to-year character of the summer monsoons. This section reviews the low-frequency variations of the ISV, namely the interannual variations (see Chapter 7 for decadal and interdecadal variations) as well as considerations of whether and how the ISV itself may produce a rectified signal onto the seasonal and/or interannual mean state.

5.4.1 Interannual variability

A number of observational studies have noted interannual variations of ISV in the observational record. Most of this research was initiated in association with the MJO (e.g., Lau and Chan, 1988; Salby and Hendon, 1994) although there have since been a substantial number of investigations involving the boreal summer ISO. These investigations have tended to fall into one of three categories: (1) determining what mechanisms are responsible for producing the observed interannual variability of ISV, (2) determining how the interannual variability in ISV might modulate the interannual character of the monsoon, and (3) understanding the degree that the interannual variations in ISV, primarily the MJO in this case, influence the development and evolution of interannual SST variability (e.g., ENSO). The first two of these are addressed in more detail below. The latter of the three lies beyond the scope of this chapter. However, recent summary and review discussions of this issue can be found in Zhang *et al.* (2001), Lau (2005), and Kessler (2005).

Figure 5.11 shows Hendon *et al.*'s (1999) illustration of the interannual variability of the MJO. These calculations are based on a number of different MJO indices. It shows for example that the winter/spring periods of 1984, 1989, and 1996 exhibited particularly pronounced MJO activity while the winter/spring periods 1975, 1982, and 1994 exhibited very weak MJO activity. Apart from the impact that this interannual variability may have on ENSO evolution, most of the research performed in conjunction with interannual MJO variability seeks to understand the underlying cause of this behavior. One of the first attempts at this came from Fink and Speth (1997) who endeavored to test three (although not completely distinct) possibilities for interannual MJO variability: tropical SST, phase of ENSO, and atmospheric precipitable water. Apart from finding that the MJO propagated further east during El Niño years (see also, Gutzler, 1991; Gualdi *et al.*, 1999a; Hendon *et al.*, 1999; Kessler, 2001; Waliser *et al.*, 2001), they found no strong

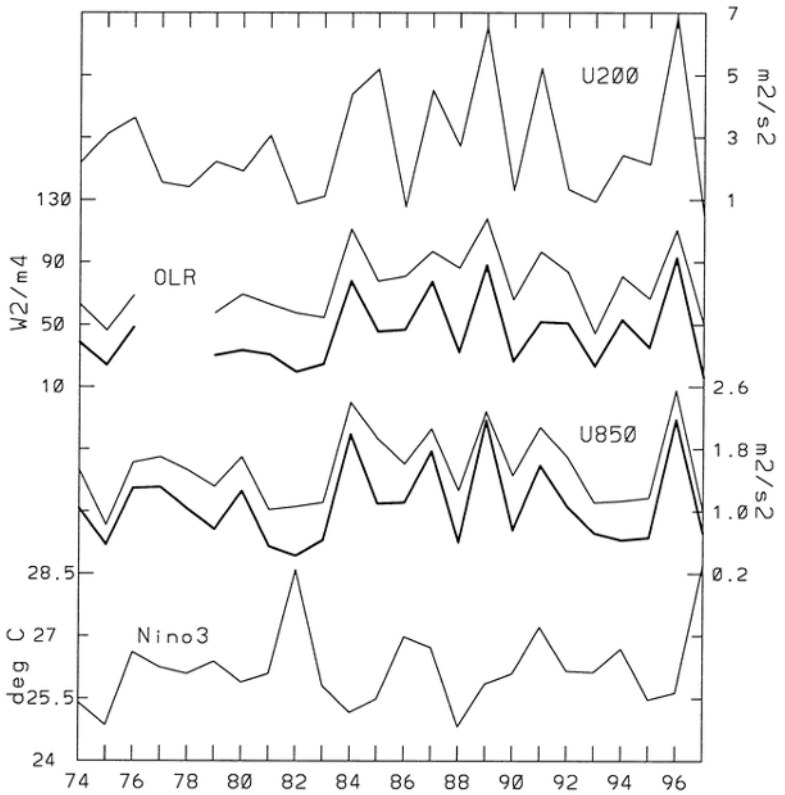

Figure 5.11. Interannual variations of MJO activity based on a number of different indices (*upper plots*) and Niño 3 SST variability (*lower plot*).
See Hendon *et al.* (1999) for details.

indicator among these three factors that could account for interannual variability of the MJO. Keep in mind that as with studies addressing the impact of the MJO on ENSO evolution, such interpretations have to be cautious about how the MJO activity is defined (e.g., Kessler, 2001; Lau, 2005). The studies by Slingo *et al.* (1999) and Hendon *et al.* (1999) each examined in some detail the observed relation between tropical interannual SST variability and MJO activity, where the latter was determined in a number of ways (e.g., OLR, low-level winds, upper level winds, principal components; Figure 5.11). The results showed that the relation was very weak, and correlations of only about -0.3 were evident between seasonal mean SST anomalies in the tropical eastern Pacific and various indices of MJO activity. Hendon *et al.*'s results indicated that most of this negative relation was associated with diminished MJO activity during the 1982–1983 and 1997–1998 El Niños. If these two periods are removed then there is virtually no correlation between the two quantities.

Given the limited observational record length and the unknowns associated with what part of the SST field is important in this regard, a number of authors have

addressed this same question via model predictability studies. The question being, given a reasonable representation of the MJO and a specification of observed SSTs, does the model's MJO exhibit any interannual predictability that could be traced to the interannual SST anomalies? Using a 4-member 45-year integration of the UK Meteorological Office (UKMO) atmospheric general circulation model (GCM; HADAM2a), Slingo *et al.* (1999) found virtually no reproducibility of the interannual variability of the MJO (i.e., only about 10% could be ascribed to external forcing). Gualdi *et al.* (1999a) used a 15-member with the ECHAM4 atmospheric GCM (AGCM) and found that with enough members (~8 or more), some evidence of year-to-year reproducibility was found (~20%). Similar results for the MJO were also found by Waliser *et al.* (2001) who used a 10-member 10-year integration with the NASA/GLA AGCM. Considering all the results above, it would appear that in general MJO activity is, at best, only weakly related to interannual SST variability, albeit the study by Chen *et al.* (2001) suggests that there might be decadal modulations to this relationship.

The above study by Waliser *et al.* (2001) also includes an examination of the same question for the boreal summer ISO. Overall, the results were analogous to those above (i.e., on average, only a very weak relation between interannual SST and ISV was found). However, the ensemble did demonstrate significantly enhanced predictability during the spring of 1982/1983. This same characteristic was found during the spring of 1997/1998 in a second 10-member ensemble that was conducted for the period September 1996–August 1998. In each of these cases, the ensemble means exhibited a decrease in ISV activity, a feature that is also echoed in the observations. Such behavior was also found in the modeling study of Krishnan and Kasture (1996). In an observational assessment, Lawrence and Webster (2001) found there to be very little relationship between ENSO and boreal summer ISO activity. While these results are suggestive of at most intermittent predictability of boreal summer ISO activity, the results of the observational analysis by Teng and Wang (2003) illustrated in Figure 5.12 indicate a much more robust relationship. These two panels illustrate the interannual variability in ISV associated with boreal summer ISV activity, distinguishing between the early summer, near-equatorial eastward propagating variability (upper) and the later summer, northern tropics, westward propagating variability (lower). In each case, there is a significant positive relationship with interannual eastern Pacific SST variability (~0.7 and ~0.6, respectively).

The contrast between the Teng and Wang (2003) results and those described above raises two questions. First, why is there such a strong seasonal dependence in the interannual connection to SST for the eastward-propagating component of ISV? Based on the various methods of analysis, and considering the discussion of Teng and Wang, the difference may lie in the degree to which the activity over the Indian Ocean is weighted into the analysis. For example, the global and empirical orthogonal function (EOF)-based measures used by the model and MJO-based studies discussed above (i.e., not the Teng and Wang study) may not be sensitive to subtle increases in ISV activity in the Indian Ocean during El Niño. Also, most AGCMs, including the NASA/GLA model used by Waliser *et al.* (1999a) exhibit

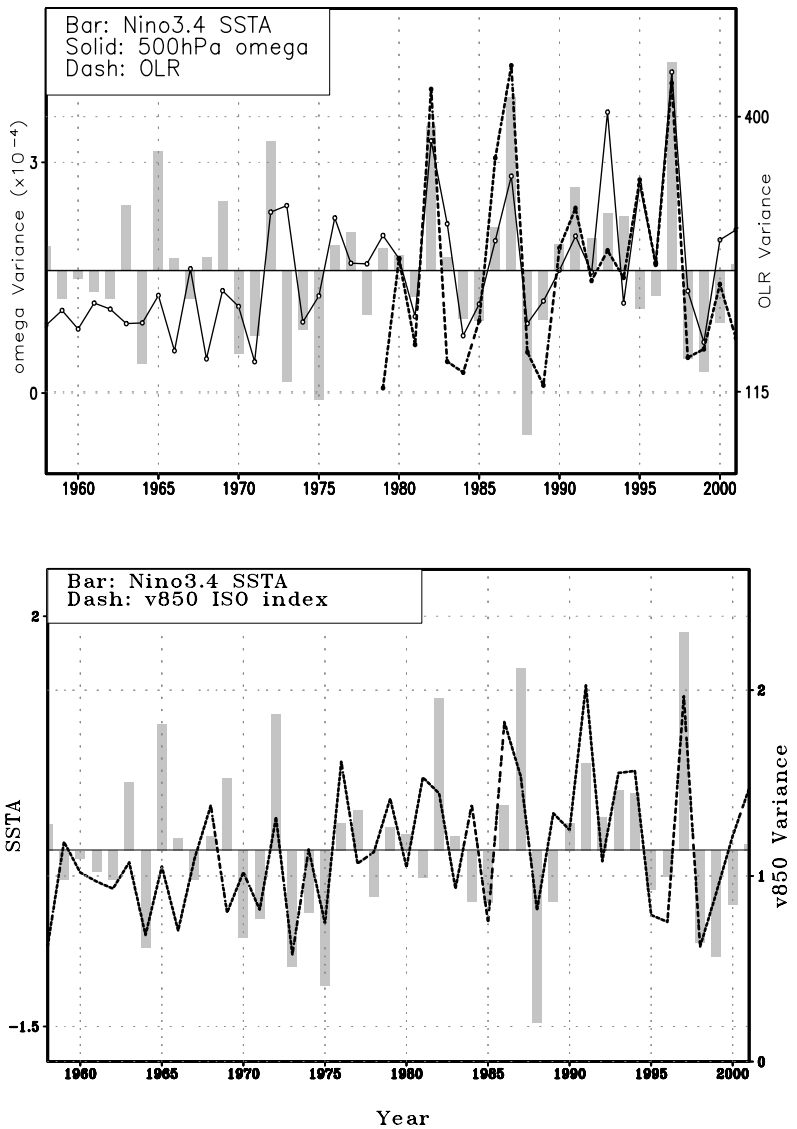

Figure 5.12. (*upper*) May–July 500-hPa vertical velocity MJO index (solid) during 1958–2001, the OLR MJO index (dash) during 1979–2001, and May–July mean Niño 3.4 SST anomaly (bar; see scale on lower plot) during 1958–2001. Vertical velocity and OLR data taken from the NCEP/NCAR Reanalysis (Kalnay *et al.*, 1996) and the OLR construction of Liebmann and Smith (1996), respectively. The MJO index is defined as the mean spectrum density for 20–50-day eastward-propagating wavenumber 1 (at 40°E–180°) anomalies averaged at 2.5°S–5°N for the vertical velocity and at 5°S–10°N for OLR. (*lower*) Similar to upper diagram, except for July–October mean Niño 3.4 SST anomaly (bar) and mean spectrum density of 10–50-day wavenumber 1–3 (at 100°E–180°) westward-propagating 850-hPa meridional wind anomaly (dash) at 5°–20°N. From Teng and Wang (2003).

relatively weak ISV activity in the Indian Ocean (Waliser *et al.*, 2003e) and thus may be incapable of reproducing the correct relationship for this part of the tropical ocean. Some evidence for the above reasoning comes from the modeling study of Krishnan and Kasture (1996). Beyond this degree of understanding, it is still yet to be fully determined how the eastward component of boreal summer ISV activity is connected to ENSO-related interannual SST variability. The second question is why does the westward propagating component exhibit a positive relation? Teng and Wang argue that this enhancement is based on the increased easterly vertical shear in association with developing El Niños. This enhanced easterly shear facilitates the emanation of the westward propagating Rossby waves which form the dynamical basis of the westward propagating variability (Wang and Xie, 1996; Xie and Wang, 1996). As yet, no model-based study has been undertaken to determine the degree to which this latter relationship can be represented in GCMs and exploited in predictions.

The second category of studies mentioned above involves understanding how the interannual variability of the monsoon may be influenced by the interannual variability of ISV, which for the most part have been directed towards boreal summer conditions (for boreal winter, see Hendon *et al.*, 1999 and Wheeler and McBride, 2005). For example, the study by Yasunari (1980) found that intraseasonal 'cloudiness fluctuations' exhibited longer periods during El Niño years. While the sample for this study was very limited, the modeling results of Krishnan and Kasture (1996) support this finding. The results of their study also suggested that El Niño conditions could influence the timescale of ISO-like oscillations in the monsoon region through the interaction with the reverse Hadley circulation (RHC) set up by the large-scale monsoon flow. The study by Teng and Wang (2003) discussed above would suggest that the character of the monsoon should be influenced via the ENSO-related sensitivity of the north-westward propagating component of the ISO. Another form of interannual modulation of the character of the monsoon arises from variations in onset dates, some of which may actually arise from the influence of the boreal summer ISO (Wu and Wang, 2000; Flatau *et al.*, 2001; Flatau *et al.*, 2003).

Another line of research in this second category of studies follows from the study of Ferranti *et al.* (1997). They studied the relationship between interannual and intraseasonal variability in a 10-member ensemble of 10-year ECMWF (European Centre for Medium-Range Weather Forecasts) climate simulations and found that the interannual and intraseasonal fluctuations share a common mode of spatial variability. That is to say that 'wet' ('dry') monsoon years would tend to have an anomalous structure along the lines of the 4th (2nd) panel of Figure 5.4. Similar results concerning the spatial structure of the dominant interannual and intraseasonal modes were found in an observational analyses of Annamalai *et al.* (1999) and Sperber *et al.* (2000). In the latter study, they showed that the probability distribution function (PDF) of the principal component time series of the dominant mode of subseasonal variability undergoes a shift in its mean, not its (Gaussian) form, between weak and strong monsoon years. Additional analysis indicated that these shifts were primarily due to changes in the basic state. For example,

Annamalai *et al.* (1999) found that El Niño tended to predispose the PDFs of the principal components of the leading intraseasonal modes toward more break conditions (see, e.g., the 2nd panel of Figure 5.4). Along similar lines, Molteni *et al.* (2003) examined an ensemble of seasonal hindcasts and found that the 2-D PDF of the principal components of the two leading intraseasonal modes changed from a unimodal distribution during El Niño to a bimodal distribution during La Niña. Lawrence and Webster (2001) examined the relation between interannual monsoon variability (i.e., seasonal mean OLR anomalies) and the amount of intraseasonal variability within the season and found that ISO activity exhibits a strong inverse relationship with the seasonal mean Indian summer monsoon strength. In an analysis of both long-record reanalysis and OLR data, Goswami and Mohan (2001) also found the common mode of interannual variability and argued that wet (dry) monsoon years were simply associated with a greater frequency of occurrence of the active (break) phase of the ISO.

While there are a number of common links in the studies above which suggest that monsoon ISO variability might undergo regime changes related to ENSO, there is still a need to sort out more clearly the effects from ENSO, how this may change over the course of the monsoon season, and if there is a decadal modulation of this influence? In addition, there still seems to be a debate regarding whether or not the level and type of boreal summer ISO activity influences the seasonal mean monsoon? If it does, and it turns out that the ISO activity is largely insensitive to interannual SST variability (e.g., ENSO), then this makes the problem of seasonal prediction of the monsoon particularly difficult.

5.4.2 Rectification onto low-frequency variability

The material at the end of the previous subsection highlights the fact that the nature of the intraseasonal variability over a given period (e.g., season) can produce variability on a longer timescale. For example, the results of Lawrence and Webster (2001) discussed above indicates that more (less) ISO activity is associated with a weaker (stronger) seasonal monsoon rainfall. While it is far from clear what aspect of the variability presupposes what, it is clear that ISV involves significant and important timescale interactions. A similar line of research considers this question more directly (i.e., how does the presence of ISV alter the basic state of the atmosphere and/or ocean systems?). The first explicit study along these lines was by Kessler and Kleeman (2000) who considered the questions of how the MJO might modulate the mean state of the ocean, as well as how it may influence the development and evolution of El Niño? As indicated above, the latter of these lies outside the scope of this chapter and is best addressed by the other reviews cited. Briefly, the former part of their examination involved comparing the differences in the response of a tropical Pacific ocean with annual cycle forcing and annual cycle forcing plus an analytical representation of idealized MJO forcing. Their results showed that the low-frequency (e.g., seasonal mean timescale) ocean response to the MJO in the equatorial western Pacific consisted of a cooling ($\sim 0.4^{\circ}$C) and eastward current anomaly ($\sim 0.2\,\mathrm{m\,s^{-1}}$). Such values are considerable in the context of coupled

climate modeling and climate change scenarios, particularly given that at least in some cases there seems to be an influence of SST on the MJO itself (see discussion above and in Section 5.5).

The study by Waliser *et al.* (2003b) examined the same rectification issue with the same model and considered the Indian Ocean as well. In addition, in their study the MJO forcing was based on a composite construction from observations. For the boreal winter analysis, and thus the MJO, the low-frequency ocean response consisted of a much weaker cooling ($\sim$0.1°C) in the equatorial western Pacific (and Indian) Ocean region, a relatively larger warming in the Maritime Continent region ($\sim$0.3°C), a fair amount of mixed layer depth (MLD) shallowing ($\sim$5 m) in most of the above regions, and a westward equatorial Pacific Ocean current anomaly ($\sim$0.1 m s^{-1}). The reasons for the differences between these results and those of Kessler and Kleeman (2000) are too numerous to elaborate on here but include the differences in MJO forcing, model vertical resolution, and the manner in which wind 'gustiness' was handled. The main points to emphasize here are that there is evidence for a low-frequency effect onto the ocean from ISV but yet too few studies to make any sort of robust determination – even in the sign of the effect.

For their boreal summer study, Waliser *et al.* (2004) showed that the imposed ISO forcing and associated ocean response exhibit a low-frequency rectification, namely a mean SST warming ($\sim$0.1°C) and MLD shoaling ($\sim$7 m) over much of the northern Indian and north-western tropical Pacific Oceans. The rectified SST signal was found to be mostly associated with a rectified signal in the short-wave forcing, although the MLD shoaling resulted mostly from non-linear mixed layer processes. The rectified signal in the short-wave forcing comes about through the large-scale organization of the ISO/MJO, namely that the convective/cloudiness anomaly organizes itself over smaller spatial scales than the corresponding subsidence region – a feature common to convection at all scales. The net effect is that over the life cycle of the MJO/ISO there is slightly more positive surface solar heating than surface cooling. This feature was also discussed in the context of rainfall and water vapor in the study of Myers and Waliser (2003). A related examination by Shinoda and Hendon (2002) regarding the rectified enhancement of wind speed and latent heat flux by the MJO found both quantities enhanced ($\sim$1 m s^{-1} and 20 W m^{-2}) over the western Pacific when averaged over the life cycle of a typical MJO. The most recent study involving rectification is that of Han *et al.* (2004) who used a model framework to show that imposed intraseasonal wind variability acts to weaken the equatorial seasonal surface currents, in part due to the asymmetric response of the ocean mixed layer to wind direction and vertical processes. Taken together, the above studies indicate that the potential for rectifying ISV onto longer timescales exists. While more research is needed in this area, there is presently enough evidence to suggest that these issues be taken into account when considering a (coupled) model's representation of climate in conjunction with its ability to properly represent the ISV.

While the discussion in this section has only been able to provide a brief review of the low-frequency variability associated with ISV (see Chapter 7 for discussion of decadal variability), it illustrates the very complex interplay between

the intraseasonal and longer timescales that contain both upscale and downscale interactions. Moreover, the discussion makes it painfully obvious that very few firm hypotheses or answers exist regarding mechanisms, and in some cases there is still not a confident determination of the basic nature of the relationships – even in a statistical sense. This all serves to illustrate that this area of ISV research on one hand is largely in its infancy and at this point is probably most hindered by a lack of quality, long-term data and/or models with which to further address the problem rather than a lack of interest or merit in the problem.

5.5 THEORY AND PHYSICAL PROCESSES

While the theory for many tropical wave motions (Matsuno, 1966) tended to precede their observation and characterization, the opposite is the case for the MJO/ISO (Madden and Julian, 2005). Since the discovery of this phenomenon, there has been ample opportunity and data sets to characterize many of its basic features. However, the articulation of a succinct and somewhat well agreed upon theory has remained a challenge. Most notably this has been due to the fact that on the one hand the MJO/ISO is a planetary-scale phenomenon yet it is apparent that cumulus convection, and its organization on a wide range of time and space scales (Nakazawa, 1988; Lau *et al.*, 1991), is an inherent and vital component. In addition, there appears to be non-trivial interactions with the mean state circulation, the surface conditions – including coupling to the ocean, clouds, radiation, and possibly even mid-latitude variability. Distilling these processes and features into something simple enough to be coined a 'theory', yet retaining enough complexity to provide for adequate realism when judged against observations, makes this task particularly difficult. This section reviews the physical processes that are thought to play a key role in producing the MJO/ISO and the theories that have been put forward to try and succinctly capture the physical essence of the phenomenon. As with much of the material above, the theoretical developments pertaining to the boreal summertime ISO have largely followed from research initially put forth to describe the MJO. Thus, this section first discusses these topics with regard to the MJO, with an effort to limit the discussion to only the most essential aspects. Then, the final subsection discusses the same set of issues as they pertain to the boreal summer ISO. For a more thorough review of this subject, the reader is referred to Wang (2005).

5.5.1 Atmospheric dynamics

As the MJO was most readily observed in the atmosphere in terms of wind and cloud fluctuations, the early theories focused on instability mechanisms dealing primarily with the atmosphere alone. The first notable inroad for providing some theoretical basis for the MJO involved a form of conditional instability of the second kind (CISK). The concept of CISK was developed to explain the intensification of tropical depressions into hurricanes as well as the maintenance of the latter (Charney and Eliassen, 1964; Ooyama, 1964). The concept was developed further to examine possible interactions between cumulus convection and the large-scale

divergence field of tropical waves (Yamasaki, 1969; Hayashi, 1970; Lindzen, 1974a,b). In these studies, low-level convergent (divergent) areas of equatorial wave motions were tied to atmospheric heating (cooling) to examine the influence on instability growth and propagation speed. The most notable shortcomings of the earliest contributions in this area involved a tendency to amplify short rather than planetary-scale waves and to have phase speeds for the excited waves propagating too fast.

There have been a significant number of variations on the wave–CISK theme to remedy these shortcomings. For example, changing from a linear heating formulation to a non-linear one (e.g., positive heating for upward motion but no cooling for downward motion) does allow for planetary-scale descending regions but at the cost of having the convective region reduced to the smallest scale, either grid-scale in a numeric framework (Lim *et al.*, 1990) or infinitesimal in an analytic framework (Dunkerton and Crum, 1991; Wang and Xue, 1992). One line of research to reduce the phase speed of conventional wave–CISK modes involves varying the specification of the vertical heating profile or the inclusion of the first two gravest vertical modes (Lau and Peng, 1987; Chang and Lim, 1988; Mapes, 2000). There has yet to be resolution on this issue as Takahashi (1987) and Sui and Lau (1989) found that heating maximized in the lower troposphere tended to favor MJO-like modes while Cho and Pendlebury (1997) found that heating, maximized in the upper troposphere, was better. Additional work in this area has shown sensitivity to the parameterization of the convective heating (Neelin and Yu, 1994) and the inclusion of non-linear advection (Hendon, 1988).

Another significant variation on the wave–CISK theme provides for coupling the free atmosphere to a frictional boundary layer (Wang, 1988a; Salby *et al.*, 1994). Inclusion of boundary layer friction results in an apparent 'coupling' between moist Kelvin and Rossby modes (Wang and Rui, 1990b). One of the fundamental features of this paradigm, often referred to as 'frictional wave–CISK', is that to the east of the convective heating the low-level winds associated with the Kelvin wave component turn equatorward in response to the friction and produce a region of low-level moisture convergence. This process favors both eastward propagation of the convective system and thus the entire planetary structure but also acts as an important source of energy for growth/maintenance. The inclusion of the Rossby mode under this framework also favors the development of the planetary scale, slows down the eastward propagation to values more consistent with observations, and plays an important role in dissipating energy that would otherwise cause the pure wave–CISK Kelvin wave instability to grow unrealistically fast. It should be noted that Moskowitz and Bretherton (2000) showed that the qualitative wave destabilization effects from friction appear to be insensitive to the convective parameterization employed which suggests that the theoretical basis for frictional wave–CISK is not necessarily tied to subjective choices in its implementation. On the other hand, they also argue that the values of surface drag used in the earlier study by Wang and Rui (1990b) are unrealistically large which overemphasizes the contribution of frictional wave–CISK to the mechanism of MJO instability (see counter argument in Wang, 2005).

As illustrated in the MJO life cycle maps constructed by Hendon and Salby (1994), there is strong observational evidence that the dynamical structure of the MJO does exhibit both Kelvin and Rossby wave components. An analogous figure from their study for the low-level wind structure indicates easterly zonal wind anomalies to the east of the convection, consistent with Kelvin wave dynamics, but which have a convergent meridional component consistent with the impacts of friction. A number of additional studies have shown evidence that supports the notion of low-level frictional moisture convergence to the east of the convection which appears at least consistent with frictional wave–CISK (e.g., Jones and Weare, 1996; Maloney and Hartmann, 1998; Matthews, 2000). In addition, there have been a number of diagnostic studies of model simulations of the MJO that have illustrated the frictional wave–CISK mechanism at work within the model generated MJOs (e.g., Lau and Lau, 1986; Lau *et al.*, 1988b; Sperber *et al.*, 1997; Waliser *et al.*, 1999a; Lee *et al.*, 2003).

In contrast to the wave–CISK mechanism(s), which operates on the principal that latent heat release from convection is an important source of energy for the instability, the 'evaporation–wind feedback' theory ((Emanuel, 1987; Neelin *et al.*, 1987), often later referred to as wind-induced surface heat exchange (WISHE; Yano and Emanuel, 1991)) claims that diabatic heating due to cumulus convection is nearly compensated by adiabatic cooling. Further, it is assumed that a region of anomalous convection forces low-level easterly winds to the east and low-level westerly winds to the west of the convective region. If large-scale convection is present in a region of mean easterly winds, the strength of the wind speed anomalies (and likely the evaporation anomalies) is increased to the east and decreased to the west of the convective region. The positive anomalies of surface latent heat flux to the east of the convection increase the low-level moist static energy, which leads the wave vertical velocity and induces unstable eastward propagating modes that exhibit some resemblance to the MJO.

The evaporation–wind feedback theory has been criticized based on the fact that over a large portion of the eastern hemisphere where the MJO is most prevalent, the climatological winds are extremely weak or even westerly (Wang, 1988). Neelin (1988) and Emanuel (1988) argued that given the large zonal scale of the MJO, the requirement for mean easterlies to the east of the convection typically holds in most cases of convection occurring in the eastern Indian Ocean and western Pacific. While the MJO does have a planetary scale at upper levels, particularly in regards to wind, the wind's interaction with convection in the eastern hemisphere significantly reduces its zonal length scales of variability, especially near the surface. Thus, while it is understood that the above mechanism doesn't fit with observations in the western/central Indian Ocean, it may not be very plausible to cite in regards to the eastern Indian and western Pacific either. A related difficulty facing the evaporation–wind feedback theory comes from a number of studies that document the observed relation between deep convection and evaporation associated with the MJO. These studies have shown that evaporation anomalies are typically higher to the west, rather than to the east, of the convection anomaly (Jones and Weare, 1996; Lin and Johnson, 1996b; Lau and Sui, 1997; Jones *et al.*, 1998; Shinoda *et al.*, 1999;

Woolnough *et al.*, 2000), which is at odds with one of the central premises of the evaporation–wind feedback theory. This behavior has also been observed in some of the more successful modeling simulations of the MJO (Sperber *et al.*, 1997; Waliser *et al.*, 1999a).

A couple of additional points that have relevance to the evaporation–wind feedback theory and the discussion above can be drawn from the following modeling studies. First, it is worth noting that recent analysis suggests that in order for a GCM to exhibit a robust eastward propagating MJO, it is necessary that the model produces a good simulation of the equatorial westerlies that extend from the Indian Ocean well into the western Pacific (Waliser *et al.*, 2003a; Sperber, 2004). Second, Kirtman and Vernekar (1993) examined a simplified model that contains both the wave–CISK and evaporation–wind feedback mechanisms and found that the model wave speeds were found to better match the observed speeds over a wider range of parameter values for the combined mechanism than for evaporation–wind feedback acting alone. Lin *et al.* (2000) examined the relative roles of evaporation–wind feedback and mid-latitude forcing of the MJO in an idealized GCM and found that evaporation–wind feedback alone was not a sufficient mechanism to produce MJO variability of adequate amplitude and that the forcing from mid-latitudes was, at least in that model, an important source of MJO forcing (see also Hsu *et al.*, 1990; Slingo, 1998). Finally, based on sensitivity experiments from an AGCM coupled to a slab mixed layer with different depths (e.g., 2–50 m), Maloney and Sobel (2004) showed that the model exhibits realistic amplitudes of intraseasonal convection only when SST variations, and thus in turn its effects on evaporation–wind feedback, are properly phased relative to the intraseasonal convection anomalies.

Apart from the MJO instability/maintenance mechanisms discussed above, a number of studies have suggested mechanisms that are driven by local feedbacks. For example, both Hu and Randall (1994, 1995) and Raymond (2001) argue for the role of radiative–convective feedbacks. In the latter case, clouds associated with the convective event trap long-wave radiant energy and lead to additional tropospheric heating that helps to destabilize the event. While past studies in this area have generally been based on GCM work and have not lead to any conclusive/comprehensive results (Slingo and Madden, 1991; Mehta and Smith, 1997; Lee *et al.*, 2003), the recent diagnostic study by Lin and Mapes (2004) has estimated that atmospheric integrated radiative heating may augment the condensational heating by as much as 10–15%. In another variation, Blade and Hartman (1993) argued that the timescale associated with the MJO derives from the time for the large-scale convection event to evolve through its life cycle (and thus 'discharge' the excess moist static energy) plus the time it takes the atmosphere to moisten again (and thus 'recharge'). They referred to this theory as the 'discharge–recharge' hypothesis. A number of additional studies have also suggested the importance of water vapor feedback in the regards to the MJO (Goswami and Mathew, 1994; Woolnough *et al.*, 2000; Kemball-Cook and Wang, 2001). The relevance of the above types of mechanisms cannot be ruled out at this stage. Even though the MJO/ISO is not consistent with a stationary oscillation (Zhang and Hendon, 1997) that might ensue when considering only local feedbacks,

it is quite possible that the above sorts of mechanisms play complimentary roles to those that are based on a wave-like infrastructure (Sobel and Gildor, 2003). For example, it could be that these local feedback mechanisms do play a role in establishing the instability and in some sense setting the timescale, and the wave activity simply propagates the signal, and in some cases these two processes can constructively (destructively) interact (e.g., via circumnavigation) to produce very robust or very weak MJO/ISO seasons.

Within the recent review of MJO theory by Wang (2005) is an attempt to provide a comprehensive or universal view of MJO/ISO theory (see his Figure 10.1) taking into account the most essential processes and feedbacks. Embedded within this discussion is a distillation of a simplified theoretical model of the MJO as well as the ISO. The fundamental mode of instability for the MJO is referred to as the 'frictional CID'. In regards to terminology, this is a combination of 'frictional wave–CISK' and 'convective interaction with dynamics' (after Neelin and Yu, 1994). The basics of the instability derive from low-frequency equatorial waves, convective latent heating, boundary layer dynamics (i.e., friction), and some accounting for the spatial distribution of atmospheric moisture. Generally speaking, this instability and the equations it derives from are the same as those associated with 'frictional wave–CISK' discussed above. However, given the instability occurs in a dynamic regime stable to wave–CISK, that the overall processes involved are consistent with CID, and that the frictional boundary layer component is so essential, the author deemed 'frictional CID' as the most appropriate terminology. For a more complete description of the equations and a quantitative analysis of the instability, the reader is referred to Wang (2005).

5.5.2 Air–sea interaction

Most of the early observational research regarding the MJO/ISO focused on upper level winds and satellite data such as the OLR. This is due at least in part to a dearth of near-surface observations with adequate time and spatial resolution to sample the MJO/ISO. However, as it became clear that the MJO was a recurrent and pronounced signature in the tropical climate, attention started to turn toward near-surface conditions and the interaction of the MJO with the ocean. This began with the study by Krishnamurti *et al.* (1988) who detected sizable intraseasonal variations in a number of near-surface meteorological quantities that directly influence the turbulent heat exchange as well as in SST. Little more was done in this area until the advent of a number of new data sources that included TOGA/TAO, TOGA COARE, atmospheric reanalysis products, and remotely sensed (near-) surface measurements via satellite. From this point, a wealth of studies documented the relationships between the MJO, air–sea heat, momentum and mass fluxes, and SST (e.g., Krishnamurti *et al.*, 1988; Jones and Weare, 1996; Lin and Johnson, 1996b; Waliser, 1996; Weller and Anderson, 1996; Zhang, 1996; Hendon and Glick, 1997; Lau and Sui, 1997; Jones *et al.*, 1998; Shinoda *et al.*, 1998; Woolnough *et al.*, 2000; Shinoda and Hendon, 2001; Waliser *et al.*, 2003b).

From the studies listed above, it has become abundantly clear that, at a

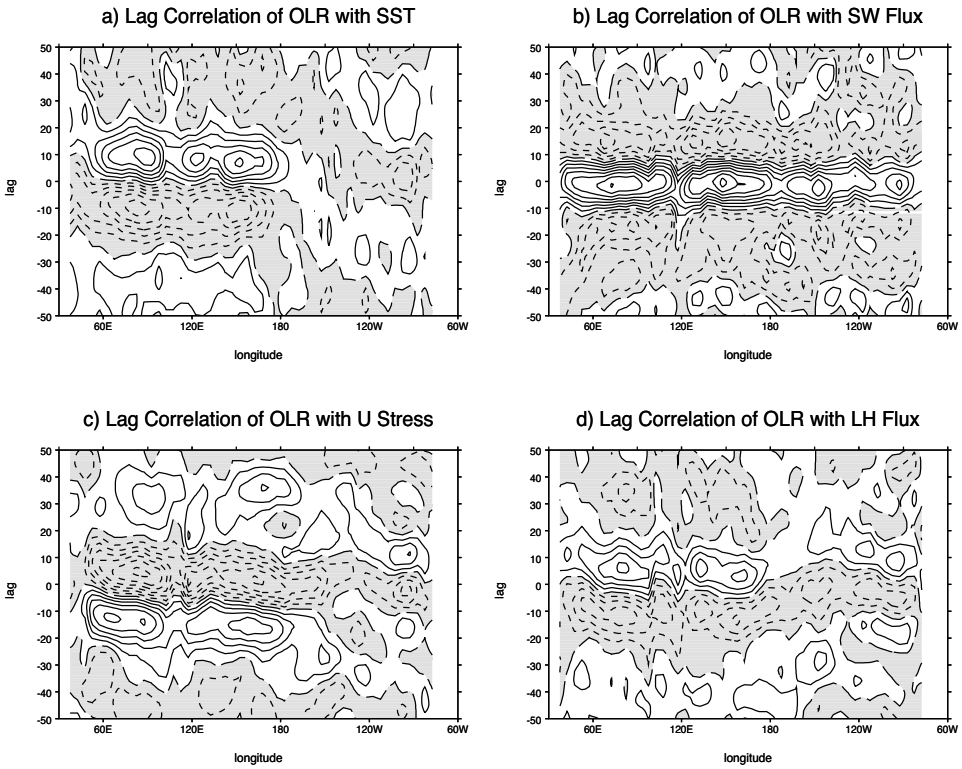

Figure 5.13. Lag correlations between OLR (convection) and surface fields (SST, short-wave flux (SWF), latent heat flux (LHF), zonal wind stress (UST)). Negative lags indicate that the convection lags the surface field; positive lags indicate that the convection leads the surface fields. The sign convention is such that positive correlations indicate that enhanced convection (a negative OLR anomaly) is correlated with a negative SST anomaly, reduced SWF at the surface, a negative LHF anomaly at the surface (enhanced evaporation), or an easterly wind stress anomaly. Negative correlations are shaded; contour interval is 0.1, with negative contours dotted; and the zero contour is dashed. Correlation coefficients above 0.103 at zero lag and 0.116 at 50-day lag are significant at the 95% level based on $N/10$ degrees of freedom, the minimum number of points required to resolve variations with the largest retained frequency.
From Woolnough *et al.* (2000).

minimum, the MJO strongly modulates air–sea fluxes and SST on the intraseasonal timescale. For example, Figure 5.13, taken from Woolnough *et al.* (2000), shows a very robust relationship between convection and each of the following: SST, wind stress, and surface latent and short-wave flux, over much of the eastern hemisphere tropical oceans. The plots show that positive anomalies in convection lead positive anomalies in wind stress and latent heat flux and lag positive anomalies in SST and short-wave flux. Put another way, to the east of the convection, surface easterly anomalies within a westward mean state and subsidence driven clear skies imply

SST-warming flux anomalies for both evaporation and short-wave fluxes. As the convection passes over the anomalously warm water the cloud-induced negative short-wave anomalies and enhanced surface westerly anomalies imply SST-cooling flux anomalies. To gain an appreciation of the magnitude of the variations, Figure 5.14, taken from Shinoda *et al.* (1998), shows the typical variations of these quantities during the TOGA COARE period. From this and the other studies above, it is well known that MJO-related surface latent and short-wave flux variations can easily exceed $\pm 50\,\mathrm{Wm}^{-2}$, SST variations often exceed 0.5°C, and zonal wind (stress) variations can exceed $5\,\mathrm{m\,s}^{-1}$ ($0.4\,\mathrm{N\,m}^{-2}$). Along with these intraseasonal changes, there is even an indication that the MJO strongly modulates the character and size of the diurnal variations of these quantities (Weller and Anderson, 1996; Shinoda and Hendon, 1998).

Given the observational developments described above, the reigning interest and understanding of the close ocean–atmosphere coupling that exists in the tropics (e.g., TOGA COARE, ENSO), and the recurrent shortcomings in AGCM representations of the MJO, the community began to hypothesize a role for air–sea coupling in the manifestation of the MJO (e.g., Kawamura, 1988, 1991; Li and Wang, 1994; Jones and Weare, 1996; Waliser, 1996; Sperber *et al.*, 1997). In particular, the question was raised how do the intraseasonal variations in SST and surface heat fluxes – which to first order appear driven by the MJO – feedback and influence the MJO itself? Given the nature of this problem involves testing a feedback, the most suitable, albeit limiting, framework for its examination is in a modeling context. The first studies having some relevance to this problem were by Lau and Shen (1988) and Hirst and Lau (1990). Stemming from an intense period of theoretical ENSO research, they developed theoretical coupled ocean–atmosphere models to explore the instability of high-frequency coupled equatorial disturbances. The ocean coupling in these models was limited to a simplified interactive SST based only on thermocline dynamics. While the results of these studies showed a particular regime of high-frequency coupled instabilities, it came at the expense of unrealistic treatments of dissipation and/or neglect of the Coriolis force. The idealized form of the coupling in these studies severely limited the thermodynamic influence of the ocean mixed layer, an interaction that would be expected to be important given the nature of the Indo–Pacific warm pool and observational studies mentioned above.

Wang and Xie (1998) extended these studies (or rather the frictional wave–CISK studies discussed above) by adding a fairly sophisticated mixed layer feedback that takes into account MJO-forced variations in surface heat and ocean mixed layer entrainment fluxes. Their model indicated that the feedback from wind-driven entrainment/evaporation, and to a lesser extent by the clouds/radiation, were largely responsible for slowing and destabilizing what would otherwise be a neutral moist Kelvin wave in the uncoupled model. In their analysis, slow disturbances with low wavenumbers were preferentially destabilized, since they would be the most effective at modifying and interacting with SST. The results of their study provide a theoretical basis for the suggestion that SST variations provide an important feedback on the MJO, and in particular, that ocean mixed layer physics are an important element in this feedback.

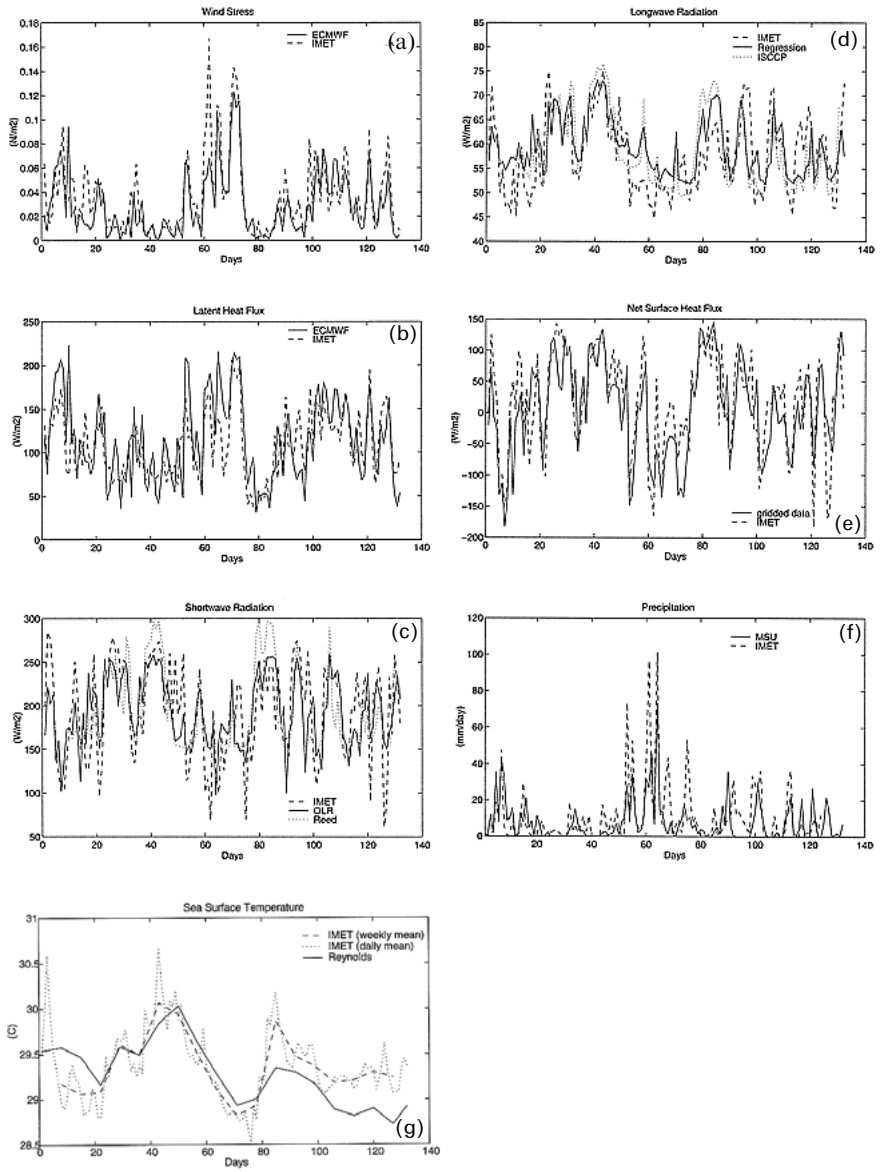

Figure 5.14. Time series of (a) wind stress, (b) latent heat flux, (c) short-wave radiation, (d) long-wave radiation, (e) net surface heat flux, (f) precipitation, and (g) SST for TOGA COARE on 22 October 1992 through to 2 March 1993. Dashed lines in (a)–(f) indicate daily mean flux estimates from the IMET mooring observations sited at 1°45′S, 156°E. The dashed line in (g) indicates the weekly mean SST from the IMET mooring observations. Thick lines indicate estimates from gridded data centered at 2.5°S, 155°E. The dotted line in (c) indicates the short-wave flux estimated from the formula by bulk formula. The dotted line in (d) indicates net long-wave flux estimated from bulk formula using ISCCP total cloudiness. The dotted line in (g) indicates the daily mean SST from the IMET mooring observations. From Shinoda *et al.* (1998).

Over the past few years a number of numerical studies have addressed the role of SST coupling and the MJO. For example, Flatau *et al.* (1997) employed a simplified GCM (e.g., Lau and Peng, 1987) coupled to an empirically derived slab ocean mixed layer feedback. They found that the addition of the SST feedback produced a stronger and more organized form of intraseasonal variability. They proposed that the zonal gradients in SST anomalies near the region of convection can create zonal gradients in surface moist static energy which favors the formation of convection in the wave convergent region and thus helps to amplify the power of the oscillation. They termed the mechanism Air–sea Convective Intraseasonal Interaction (ASCII). Unfortunately, the simplicity of the GCM used in their study prevented any conclusive analysis (e.g., on the surface heat flux or planetary boundary layer (PBL) moisture budget) that would directly support this hypothesis.

Waliser *et al.* (1999a) found that when their AGCM was coupled to a (50 m) slab ocean mixed layer the interactive SSTs had modest but important impacts in the simulation of the MJO, with the characteristics of the coupled model's MJO being closer to those observed. These impacts included (1) the increased variability associated with the MJO, (2) the tendency for the timescales of modeled intraseasonal variability to be around those found in the observations, (3) a reduced eastward phase speed in the eastern hemisphere and (4) an increased seasonal signature in the MJO with relatively more events occurring in the December–May period. They attributed the better simulation to the feedback with the SSTs. They suggested that the enhanced SSTs, forced by decreased latent heating and increased short-wave flux to the east of the positive convective anomalies tended to reinforce the meridional convergence associated with the frictional wave–CISK mechanism working within the AGCM. This meridional convergence increased the moist static energy that acts to destabilize the model's MJO. It is interesting to note that in both the above numerical studies, some element of the MJO did exist without coupling – as is often the case with AGCMs (Slingo *et al.*, 1996; see Section 5.6), yet in Wang and Xie's theoretical study, the instability only exists upon coupling. This raises an important question regarding whether the MJO is inherently a coupled phenomena or whether interactive SST simply provides a modulating feedback (see Waliser *et al.* 1999a for further discussion).

In another GCM study, Hendon (2000) explored the impact of air–sea coupling on the dynamics of the MJO in a GCM coupled to a 1-D ocean mixed layer model. In that study, Hendon found that coupling had no significant influence on the simulation of the MJO. However, analysis of the model results showed that the simulated MJO-induced latent heat flux anomalies were relatively incoherent and did not exhibit the proper (i.e., observed) phase relationship relative to the convection, in part due to the model's basic state (see evaporation–wind feedback discussion above). Thus, the latent heat flux anomalies did not constructively interact with the MJO-induced short-wave anomalies to produce the needed/observed systematic changes in the anomalous SST that in turn could influence the MJO. Thus, to some degree, this study's findings highlight the necessity for a proper representation of the basic state when simulating the MJO rather than have implications on the SST–MJO coupling question directly (see also Gualdi *et al.*, 1999b). Additional important work

in this area includes the studies by Inness and Slingo (2003), Inness *et al*. (2003), and Sperber (2004) that emphasize the proper simulation of the basic state in terms having low-level westerly zonal winds present in regions where eastward propagation is observed/expected (e.g., Indian and western Pacific Ocean).

Wu *et al*. (2002) analyzed a particularly strong MJO event within observations and from 10-member ensemble simulations with 10 different AGCMs forced with the same observed (1996–1998) weekly SSTs but with different initial atmospheric conditions. One of the main findings in that analysis relevant to the present discussion is that while the observed convection anomalies were in quadrature with, and lagging, the associated intraseasonal anomaly in SST, the simulated MJO convection events were nearly in phase with the SST anomaly. Based on the results of the studies mentioned above, the observed relationship is understood to come about – to first order – via MJO-driven heat flux variations imparting an intraseasonal signal on SST. However, given the specified SST framework in the simulations, the modeled relationship is more accurately depicted as a 'forced' signal whereby the MJO event is responding to the SST variations in the boundary conditions. Additional support for this finding comes from the modeling study of Zheng *et al*. (2004) who compared the simulation of the MJO between a coupled GCM (CGCM) simulation and the corresponding AGCM simulation that used the SSTs from the CGCM simulation. In the coupled case, the model convection lags the SST anomalies by about 1/4 cycle (consistent with observations), while for the specified SST case, the convection and SST are nearly in phase. These results help to emphasize the importance of including air–sea coupling in the context of numerical simulations and predictions.

Additional studies supporting the notion that interactive SSTs are important to the character of the MJO include Sobel and Gildor (2003), Watterson (2002), and Maloney and Sobel (2004). These studies emphasize the sensitivity of the SST feedback to the depth of the ocean mixed layer, with the implication that the depth has to be shallow enough to provide sufficient sensitivity to the intraseasonal timescale and associated size of surface fluxes (e.g., Figure 5.14) and yet deep enough to provide a sufficient time lag between SST anomaly development and the passage of the MJO convection – considered together these imply that a mixed layer depth induces the greatest feedback to the MJO when it is O (10 m). Finally, the study by Maloney and Kiehl (2002) illustrate analogous feedbacks between SST and MJO-like variability in the eastern Pacific Ocean. Taken together, the studies highlighted in this subsection strongly suggest that a proper and complete physical description of the MJO has to take into account its interaction with the near-surface ocean, namely the SST. For a more thorough review of this area, the reader is referred to Hendon (2005).

5.5.3 Boreal summer ISO

The above two subsections provide pertinent background information on the theoretical developments associated with the MJO. While there has yet to be widespread acceptance of a single theory for the MJO, it is becoming increasingly clear at least what the main physical elements are that need to be considered. As discussed

previously, the ISO and MJO could be considered essentially the same phenomena modified by the annually changing background state. For the case of the MJO, this tends to simplify the issue somewhat since during the period it is most strongly exhibited; the warm SSTs and large-scale circulation are more symmetrically aligned with the equator. This results in a background state that has a more straightforward zonal structure and a lower boundary made up almost entirely of ocean. However, for the case of the ISO, all the same issues relevant to the MJO need to be considered but in addition it is necessary to deal with the asymmetric and off-equatorial circulations prevalent around south-east Asia in boreal summer and possibly consider a larger role for land surface interactions. In addition, the ISO's influence on, and from, the oceans and seas surrounding south-east Asia is also more complex than for the MJO, which interacts more directly with the more uniform, basin-scale oceanography of the equatorial Pacific and Indian Ocean (e.g., Waliser *et al*., 2003b, 2004).

Taking the above discussion into account, it is not surprising that theoretical and air–sea interaction studies for the boreal summer ISO analogous to those described above for the MJO are considerably fewer. However, in recent years there has been significantly more research in these areas as they pertain to the boreal summer ISO. For example, Vecchi and Harrison (2002), Sengupta *et al*. (2001), Sengupta and Ravichandran (2001), and Kemball-Cook and Wang (2001) all document similar relations between convection, surface heat fluxes, and SST as described above for the MJO – the principal difference being that the large-scale propagation includes a northerly component in addition to the eastward component (see Figure 5.4). Figure 5.15, taken from Sengupta *et al*. (2001), succinctly illustrates the fact that ahead of the northward propagating convection are clear skies, calm winds, and warming SSTs, and that upon arrival of the convection comes cloudy skies, high winds, and cooling SST. Additional evidence suggests the importance of the ocean–atmosphere coupling implied by this relationship to understand and properly model the ISO. For example, similar to the study by Wu *et al*. (2002) discussed above, the studies by Fu and Wang (2004) and Zheng *et al*. (2004) both illustrate that it is not just the intraseasonal oscillations in SST that are important but rather the inclusion of actual interactive SST coupling. The contour plots in Figure 5.16, taken from Fu and Wang, compare the spectral power in the northward propagating ISO components from a CGCM, the corresponding AGCM where the SSTs were specified from the CGCM simulation, and from observations. For this model, it is clear that the coupling has a profound and positive impact on the modeled ISO. The line plot in Figure 5.16, taken from Zheng *et al*., shows that the observed (quadrature) phase relationship between convection and SST is properly represented in their CGCM. However, the relationship becomes incorrectly represented in the corresponding AGCM simulations that use specified SSTs taken from the CGCM simulations. Nearly identical results regarding this aspect of the ISO phase relationship were also found by Fu and Wang. The results from studies such as these indicate that interactive SSTs, namely via mixed layer physics, are a crucial part of the physical makeup of the ISO and, as with the MJO, will need to be accounted for in any comprehensive theory for the ISO.

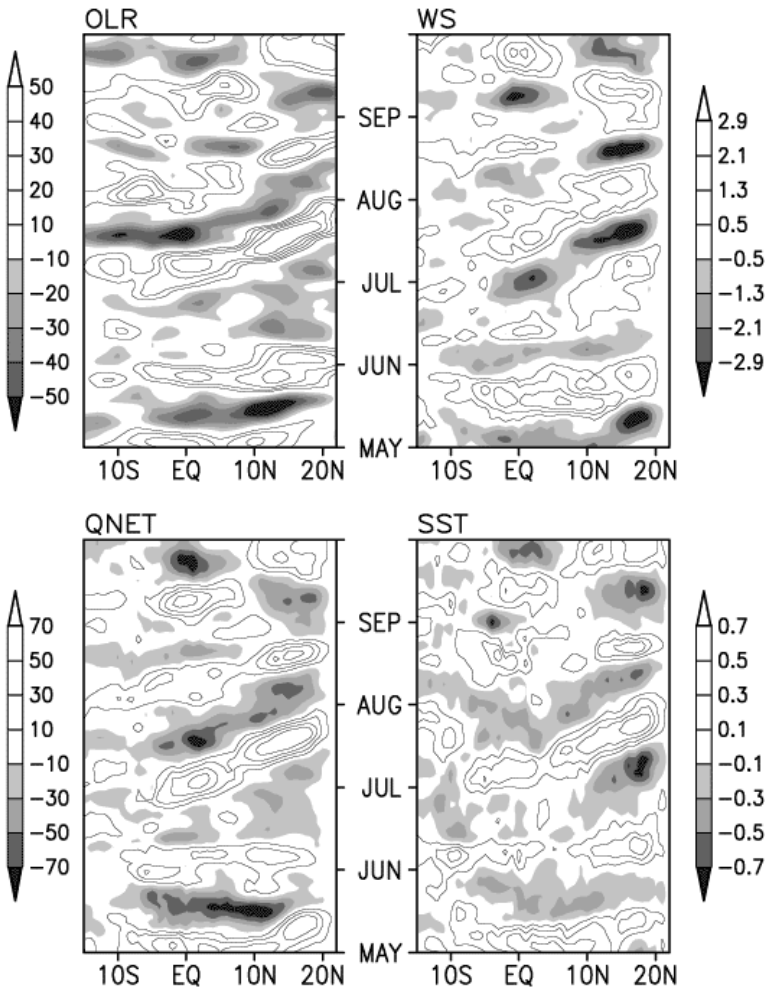

Figure 5.15. Time–latitude sections of 10–80-day filtered anomalies of OLR (Wm^{-2}), windspeed (ms^{-1}), net surface heat flux (Wm^{-2}), and SST (°C) averaged over 85°–90°E in the summer of 1998.
From Sengupta *et al.* (2001).

In terms of theoretical constructions for the boreal summer ISO, one of the most important distinctions or additions that need to be accounted for over the MJO is the ISO's northward propagation and the off-equatorial westward propagation of large-scale disturbances within the planetary-scale eastward moving structure (Figures 5.4 and 5.6). The earliest hypotheses regarding northward propagation did not require or account for any aspect of zonal asymmetry in the ISO pattern – which at that point was probably not that well defined. For example, Webster (1983) suggested that positive surface sensible heat flux anomalies into the atmosphere,

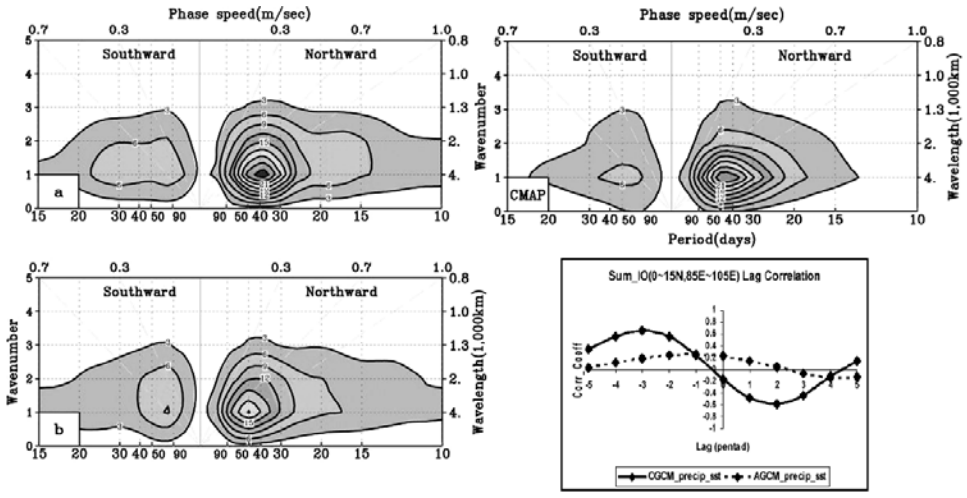

Figure 5.16. (Contour plots from Fu and Wang, 2004) Wavenumber–frequency power spectra of north–south propagation characteristics of rainfall from longitude range 65°E–95°E from a (U. Hawaii) CGCM (*upper left*), the corresponding AGCM using SSTs specified from the CGCM simulation (*lower left*), and CMAP rainfall data (Xie and Arkin, 1997) (*upper right*). (Line plots from Zheng *et al.*, 2004) Lagged correlation values between SST and rainfall anomalies averaged over 85°–105°E, 0°–15°N from a (GFDL) CGCM (solid line) and the corresponding AGCM using SSTs specified from the CGCM simulation (dotted line).

driven by ground temperature anomalies to the north of the convection, could destabilize the atmospheric column and promote northward movement of the convection. Gadgil and Srinivasan (1990) and Nanjundiah *et al.* (1992) suggested a similar mechanism but in their case it was the gradient in *moist* static energy that promoted the northward propagation. Based on a zonally symmetric model, Goswami and Shukla (1984) suggested that the interaction between convection, dynamics, and ground surface evaporation (the model oscillation diminished considerably over the ocean) can result in an oscillatory behavior of about the right timescale.

Inclusion of wave-like features and zonal asymmetry to the problem started with Lau and Peng's study (1990), which, based on numerical experiments, showed that the interaction between equatorial moist Kelvin waves could interact with the large-scale monsoon flow and produce quasigeostrophic baroclinic waves that would influence the south-east Asian region. The study by Hsu and Weng (2001) suggests that the north-westward propagating disturbances within the ISO complexes could develop from the interaction of an eastward propagating (MJO-like) convective disturbance and a subtropical westward propagating low-level convergence anomaly. As alluded to earlier, the combined works of Wang and Xie

(1997), Xie and Wang (1996), and Kemball-Cook and Wang (2001) help to explain some aspects of both the overall northward propagation of the large-scale complex and the westward moving variability embedded within it. Their studies suggest that as the near-equatorial ('MJO-like') convective complex moves eastward, with its attendant equatorial Kelvin and off-equatorial Rossby wave circulations, it develops weakened states upon encountering the heterogeneous Maritime Continent and the cooler central Pacific (Figure 5.6). At these stages, the relaxation process results in the emanation of north-westward propagating Rossby wave disturbances that account for the overall north-west–south-east tilt of the ISO 'rain bands' (Figure 5.4). Additional observational evidence for the connection between the emanation of Rossby waves and the rain band tilt was found by Annamalai and Slingo (2001) and Lawrence and Webster (2002). The eastward movement of these tilted rain bands thus results in a northward propagating feature when considered at a given longitude. Thus while most of the studies discussed above specifically tried to address the northward propagation of individual disturbances/rain bands, yet did not account for the overall structure and propagation of the ISO, they provided the latter but did not address why a given (Rossby wave) disturbance within the ISO complex has a northward propagating component.

Recently, the studies of Drbohlav and Wang (2004) and Jiang *et al.* (2004) have provided some possible answers to this question. Using much of the same model framework associated with the 'frictional CID' MJO analysis described above, but taking into account the strong easterly vertical shear occurring over the Asian monsoon region, these studies each concluded that this shear is a fundamental driver in the northward propagation. The easterly shear, along with the meridional gradient in vertical motion (i.e., ascending within the convective region and descending to the north), combine to form a vorticity twisting term that promotes the northward movement of the disturbed (i.e., cyclonic vorticity) regions. While the influence of easterly shear on northward propagation appeared crucial in these two studies, as well as in a GCM study (Kemball-Cook *et al.*, 2002), the study by Jiang *et al.* also indicated important contributions for promoting northward propagation from meridional advection of the low-level humidity gradient and from interactive SST. The nature of the latter process was discussed above and its importance to the development of northward propagation is also evident in the studies by Fu *et al.* (2003) and Fu and Wang (2004).

The discussion in this section is meant to highlight the theoretical developments associated with tropical subseasonal variability, namely the MJO/ISO phenomena (some treatment of the 10–20-day mode can be found in Goswami (2005)). While there is yet to be overall agreement on a given theory, it appears that most of the essential issues that need to be considered in developing and refining our theories have at least been identified. This achievement at least provides the means for the theory to help guide GCM model diagnosis and development aimed at improving their representation of the MJO/ISO, which, as will be discussed in the next section, remains an ongoing challenge.

5.6 NUMERICAL MODELING

Previous sections have outlined our observational and theoretical understanding of tropical ISV. At this point it is clear that the ISV, namely in the form of the ISO, is an inherent mode of variability within the Asian summer monsoon system, one that dictates its active and break periods, modulates the embedded synoptic variability, and possibly even helps to determine its interannual variability. In addition, the previous section suggests that we have gained considerable appreciation for the essential physical processes involved in its maintenance and evolution. Yet, in order to substantiate and further our theoretical understanding of the ISO, take advantage of what it can offer in terms of short-term monsoon prediction, ensure that our weather forecasts and climate simulations/predictions include all the necessary and important scale interactions, it becomes imperative to be able to simulate ISV in a numerical setting. Consistent with most of the topics discussed above, a majority of the research and development in this area has been done in association with the MJO. However, given the overall similarities between the MJO and the ISO, particularly in regards to their modeling successes and shortcomings, this chapter will focus primarily on boreal summer activity. In particular, it will tend to only highlight the state-of-affairs of ISO modeling, focusing on the main shortcomings and the recent attempts to overcome them. Keep in mind that some of the findings discussed in previous sections were derived from GCM studies and thus part of the material related to numerical modeling of the ISO has been discussed above. For a more thorough review of modeling issues related to both the MJO and ISO, the reader is referred to Slingo *et al.* (2005).

As discussed in the previous section, the theoretical understanding of the ISO is a more challenging prospect than that for the MJO. This is primarily due to the more complex mean flow that the ISO interacts with compared with the MJO, as well as the greater heterogeneity of the underlying surface conditions and topography in the Asian monsoon sector relative to the equatorial Indian and western Pacific Oceans where the MJO is most prominent. From this standpoint, it is not surprising that as difficult as it has been to simulate the MJO in numerical settings (Lau and Lau, 1986; Park *et al.*, 1990; Slingo and Madden, 1991; Slingo *et al.*, 1996; Wang and Schlesinger, 1999; Hendon, 2000; Inness *et al.*, 2001; Maloney and Hartmann, 2001; Maloney, 2002; Wu *et al.*, 2002; Inness and Slingo, 2003; Inness *et al.*, 2003; Lee *et al.*, 2003; Liess and Bengtsson, 2003; Liess *et al.*, 2003; Waliser *et al.*, 2003a; ECMWF, 2004), it has been even more infrequent that reasonable simulations of the ISO have been noted. Prominent shortcomings highlighted in the above MJO GCM studies include a tendency for weak variability, disturbances that tend to propagate too fast, sensitivity to mean state conditions – particularly in the Indian and western Pacific Ocean, a less than ideal representation of the modulation by the annual cycle, and in some cases improper phase relationships between convection and surface heat flux components. While some of these shortcomings hold for the ISO, recent diagnostic studies of the ISO in GCMs indicates that there are a number of problems that tend to be unique to the boreal summer activity.

In their examination of dynamical seasonal prediction of the Asian summer

monsoon, the study by Sperber *et al.* (2001) also included an assessment of how well seven AGCM models reproduced subseasonal modes of variability. Their results showed that for many models, the dominant dynamical pattern of subseasonal variability (i.e., dynamical analog to Figure 5.4), as depicted in observations, is reasonably well simulated. Beyond this however, the AGCMs had difficulty in representing the pattern of precipitation associated with the dominant mode (e.g., Figure 5.4) as well as difficulty in simulating most aspects of the higher order modes of subseasonal variability. In addition, that study found that the models usually failed to project the subseasonal modes onto the seasonal mean anomalies, even in cases where the mode may have been influenced by surface boundary conditions (see discussion in Section 5.4.1).

The study by Waliser *et al.* (2003e) examined ten AGCM simulations to assess their representation of ISO variability associated with the Asian summer monsoon. Figure 5.17 shows the spatial patterns of boreal summer ISV in the ten AGCMs analyzed and the observations. Evident is the very wide range of realism depicted by the models, with a couple of the models having virtually no ISV and a few having ISV that exceeds that exhibited in observations. In some cases, the spatial pattern of variability is somewhat realistic, at least away from the equator. Not surprising is the result that when considering maps such as that in Figure 5.17 for both winter and summer, the fidelity of a model to represent northern hemisphere summer vs. winter ISV appears to be strongly linked. In addition, their analysis showed that most of the model ISO patterns did exhibit some form of northward propagation. Figure 5.18 (color section) shows composite ISO patterns from the observations and seven of the ten AGCMs analyzed. While the seeds of northward propagation are apparent, the model ISO patterns are typically less coherent, lack sufficient eastward propagation, have smaller zonal and meridional spatial scales than the observed patterns, and are often limited to one side or the other of the Maritime Continent. In addition, for those models that do exhibit a large-scale variability, they often have a south-west–north-east tilt rather than the observed north-west–south-west tilt.

One of the most pervasive and problematic feature of the models' depiction of the ISO is the overall lack of variability in the equatorial Indian Ocean. In some cases, this characteristic appears to result due to the propensity of a number of models to form double convergence zones about the equator rather than one region of strong convergence on the equator. This shortcoming not only results in a poor representation of the local rainfall pattern but is also found to significantly influence the models' representations of the global-scale teleconnection patterns associated with the ISO (e.g., Figure 5.10). The results of Zheng *et al.* (2004) indicate that the lack of ocean coupling in the above AGCM simulations may be at least part of the reason for their reduced levels of ISV in the Indian Ocean. And, as discussed in the previous section, the results of Kemball-Cook and Wang (2002), Fu *et al.* (2003), and Fu and Wang (2004) all suggest that improvements in a model's representation of the northward propagation of the ISO can result from the inclusion of ocean coupling.

In another related study to the ISO, Kang *et al.* (2002b) examined how well AGCMs (the same ten as in the Waliser *et al.* (2003e) study discussed above)

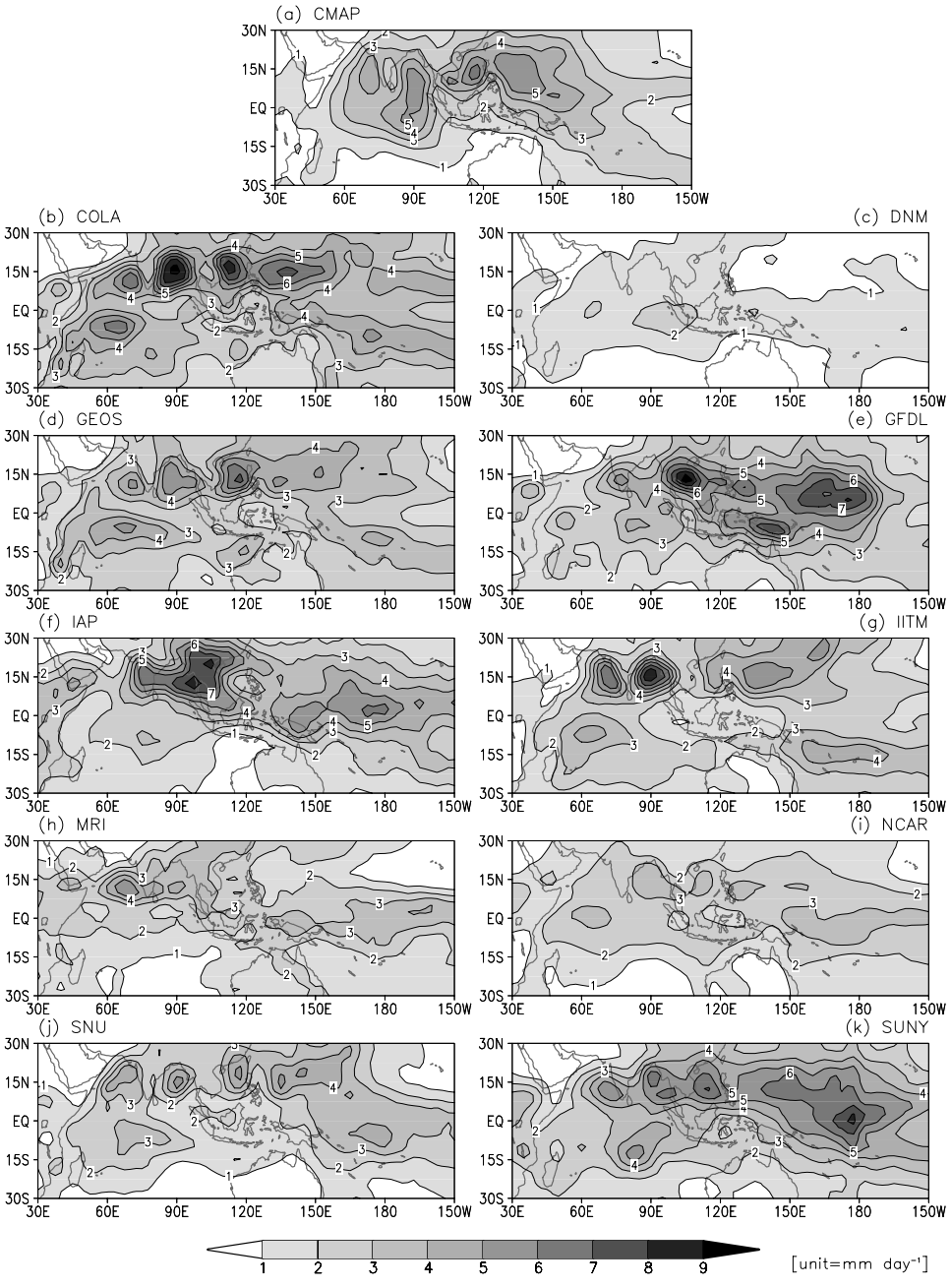

Figure 5.17. Standard deviation of 20–90-day filtered rainfall (mm day^{-1}) for Boreal from the CMAP observations (Xie and Arkin, 1997) (*top*) for 1979 to 1998 and for the ten AGCMs (*lower*). In the case of the models, there were 20 summer seasons of data (i.e., ten members each consisting of two years). From Waliser *et al.* (2003e).

simulate the climatological intraseasonal variation of the Asian summer monsoon (Section 5.2.4). Based on an EOF analysis of the high-frequency seasonal progression of the monsoon, their analysis showed that all the models generally failed to faithfully simulate the CISO. While this is certainly related to the models' poor representation of the ISO, it is also necessarily related to the lack of any model to realistically represent the slowly evolving seasonal pattern of monsoon rainfall. In addition, their study showed that the simulated northward propagation of the climatological intraseasonal oscillations (CISO) of precipitation occur 20–30 days earlier than the observations over the east Asian monsoon region. This result is in partial agreement with the studies by Wu *et al.* (2002), Fu and Wang (2004), and Zheng *et al.* (2004) which all indicate that for individual ISO events, the lag between positive SST anomalies and convection is reduced by about 5–10 days in AGCM simulations relative to the observations and CGCM simulations. One of the most important implications of this latter result is that if specified SSTs are used in a prediction environment, phase errors in tropical convection of the order of 5–10 days (or 5°–20° longitude) will occur. This is substantial when considering the local tropical prediction but also problematic when considering the impact on the extratropics. Thus, subseasonal (e.g., MJO/ISO) predictions must include ocean coupling (i.e., a 'two-tier' prediction framework is inadequate).

Based on the above brief summary of the state-of-affairs of ISO modeling, it is clear that a number of critical problems remain to be solved. Recognition of the need for better ISO simulations and the associated benefits that could be derived from accurate predictions, has led to some concerted efforts to try and remedy these problems. In June of 2003, a modeling workshop was held on MJO/ISO modeling (Waliser *et al.*, 2003a; see also ECMWF, 2004) to assess current capabilities, recent developments, and to determine future directions. From the workshop presentations and the results such as those discussed above, the following summarizing remarks in terms of modeling can be made. In contrast to a decade ago (e.g., Slingo *et al.*, 1996), specific model problems are not as generic. For example, many models have variability stronger than observed or even have propagation speeds than are slower than observed. In addition, there seems to be more models getting something in the way of an MJO/ISO, and fewer models that are completely absent of ISV phenomenon. Unfortunately, when a model does exhibit a relatively good MJO/ISO, we can at best only give vague or plausible explanations for its relative success. This inhibits the extension of individual model successes to other more ISV challenged models.

It has long been thought that the ISV problem likely relates to the treatment of the cumulus convection. This is because typically the greatest sensitivity that the MJO/ISO simulation exhibits to various model 'tunings' is associated with that of the convective parameterization – or closely related processes (e.g., Slingo *et al.*, 1996; Wang and Schlesinger, 1999; Lee *et al.*, 2001; Maloney and Hartmann, 2001; Maloney, 2002; Lee *et al.*, 2003). This was fairly evident from many of the presentations in the MJO/ISO modeling workshop mentioned above, which included a number of efforts illustrating that it was somewhat possible to 'tune in' better ISV via modifications such as the Tokioka 'fix' to the Arakawa-Schubert parameterization (Tokioka *et al.*, 1988), boundary layer inhibition, controls on free atmospheric

humidity, inclusion of gustiness, etc. While we still grapple with why certain changes lead to a better or worse MJO, it is expected or perceived that a more realistic parameterization of convection, or 'no' parameterization at all (Randall *et al.*, 2003; Kuang *et al.*, 2004), should/will lead to more realistic MJO simulations. In addition to the convection issue, it seems more of a certainty that SST coupling does play an important role in the quality of a MJO/ISO simulation. However, for this interaction to be properly represented, it is imperative the surface heat flux anomalies (mainly short-wave and latent) associated with the MJO/ISO be reproduced with some fidelity. This in turn involves the representation of clouds and the interactions between the heating profiles and the surface in producing a realistic boundary layer.

In regards to observations and their use in model development and improvement, it is clear that we have enough data to determine that our GCMs have poor ISV representations but probably not enough information to properly tune the models or to remove ambiguities regarding parameterization choices. At this stage, the most notable areas where we lack important constraining/verifying information are associated with the hydrological cycle (e.g., moisture, re-evaporation, microphysics, latent heating profiles) as well as boundary layer processes and cloud–radiative interactions. For example, how well do we represent the partition between deep and shallow heating associated with the MJO/ISO life cycle (e.g., Wu, 2003)? In addition, and as alluded to in Section 5.5.1, it is still to be determined how much cloud long-wave forcing influences the instability of the atmosphere during the convective phase of the MJO/ISO? Additional modeling problems that have to be rectified include achieving a proper representation of the basic state. Issues such as the tendency for models to produce double ITCZs, produce inadequate representations of the mean monsoon or the surface zonal wind structure in the Indo-Pacific warm pool, or exhibit biased coupled basic states can all produce limitations on the fidelity of a model's ISV representation. These basic state issues are extremely important in the forecasting context, discussed in the next section, since the models need to be initialized to the observed state but then will subsequently undergo an adjustment toward their own (poor) basic state which can wreak havoc on the forecasts.

5.7 PREDICTION AND PREDICTABILITY

As our understanding and modeling capabilities of ISV grow, it is natural to want to exploit this knowledge and ability in order to develop improved and expanded monsoon prediction resources. This section will review developments made regarding our capabilities for predicting tropical ISV, specifically the MJO/ISO, via empirical and dynamical means, our understanding of its predictability characteristics and present efforts at real time prediction. A more complete review of this material can be found in Waliser (2004).

5.7.1 Empirical models

By the late 1980s, many characteristics of the ISV were fairly well documented and it was clear that the dominant modes of ISV exhibited a number of reproducible features from one event to another and in events between years. Since numerical weather and climate models typically had a relatively poor representation of the ISV at the time, a natural avenue to develop was the use of empirical models. The first study along these lines was by von Storch and Xu (1990) who examined POPs (Hasselmann, 1988) of equatorial 200-hPa velocity potential (VP200) anomalies. They found that forecasts based on the first pair of POPs, which tended to emphasize the MJO, produced forecasts that had useful skill out to about 15 days. While this was an encouraging result, at least relative to 'weather', the limited length of data used ($\sim$5 yr) combined with the non-stationary characteristics of the MJO over interannual timescales (e.g., Section 5.3) necessitated some caution in over-interpreting it. Moreover, given the smoothly varying nature of VP200, and the fact that it is only loosely related to near-surface meteorological variables (e.g., precipitation), also suggested caution in generalizing this result to other years, variables, and/or different techniques. A number of years later, Waliser *et al.* (1999b) developed an empirical ISV forecasting method in order to benchmark numerical long-range forecasts and to begin exploring the feasibility of employing such a model to augment operational long-range forecasting procedures. The model was based on singular value decomposition (SVD) and used previous and present pentads of filtered OLR to predict future pentads of OLR. Separate models were developed for northern hemisphere winter and summer conditions and each exhibited temporal correlations against observed total anomalies of the order of 0.3 to 0.5 over the eastern hemisphere. While this result also promoted some optimism for making subseasonal predictions, the fact that the model utilized filtered data warranted caution and limited its immediate real time applicability.

Following the above were a number of empirical MJO forecasting efforts that each produced a unique and useful approach to the problem. For example, Lo and Hendon (2000) developed a lag regression model that uses as predictors the first two and first three principal components of spatially and intraseasonally filtered OLR and 200-hPa streamfunction (φ200), respectively, to predict the evolution of the OLR and φ200 anomalies associated with the MJO. Separate methods were used to remove the annual cycle, interannual, and high-frequency (i.e., $<$30 days) components, leaving only the ISV. When tested on independent data, the model exhibited useful skill for predictions of these principal components over at least 15 days, with greater skill during active vs. quiescent MJO periods. A somewhat different approach was taken by Mo (2001) who utilized empirical basis functions in time for the forecasting procedure. This was done by using a combination of singular spectrum analysis (SSA; Vautard and Ghil, 1989) for the filtering and identification of the principal modes of variability and the maximum entropy method (MEM; Keppenne and Ghil, 1992) for the forecasting component. The procedure was applied to monitor and forecast OLR anomalies (OLRAs) associated with the MJO, intraseasonal modes associated with the Asian monsoon, and

variability related to both of these that occurs over the US west coast. When tested on independent December–February and June–August OLRA data, the averaged correlation over the tropics between the predicted and the observed anomalies was 0.65 at the lead times of four pentads (20 days).

In a quite different approach, Wheeler and Weickmann (2001) utilized tropical wave theory (Matsuno, 1966) as the basis for their filtering and forecasting technique. Essentially, a space–time Fourier analysis is performed on daily OLR data for a given time–longitude section of interest in the tropics. In a previous study, Wheeler and Kiladis (1999) showed that the spectrum from such an analysis exhibits variability that is associated with the modes that one would expect from theoretical considerations (e.g., Kelvin, mixed Rossby–Gravity waves), as well as the expected peak of variability around wavenumbers 1–3 and 40–60 days associated with the MJO. In order to monitor and predict the evolution of a given mode of interest, the specific zonal wavenumbers and frequencies associated with the mode(s) of interest are retained and then the modified spectrum is inverse Fourier analyzed. The filtered values obtained for times before the end of the dataset are used for monitoring the activity of a given mode, while the filtered fields obtained for times after the end point may be used as a forecast. For prediction, the method exhibits useful skill for the MJO over about 15–20 days. An advantage is that the method readily provides predictions of other well-defined, typically higher frequency, modes of large-scale tropical variability, although it has little applicability to the Asian monsoon.

In an effort that focused on active and break conditions of the Indian summer monsoon, Goswami and Xavier (2003) noted that all active (break) conditions go over to a break (active) phases after about 15–20 days – albeit with a fair amount of event-to-event variability. Using a rainfall-based ISO index and a definition of active and break conditions, they calculated the typical (i.e., ensemble average) transition from active to break (and break to active) conditions as a function of lead time. This method exhibited apparent skill in predicting break-to-active (active-to-break) transitions over about 10 (20) days lead time, indicating that monsoon breaks are intrinsically more predictable than active monsoon conditions. Similar results in this regard were found by (Waliser *et al.*, 2003d) using an ensemble of twin-predictability GCM experiments (discussed below).

The above discussion gives a flavor of the types of empirical forecast models for ISV that have been developed to date. A number of additional approaches presently associated with real time efforts are discussed below. It is worth emphasizing that as yet numerical forecast models have not demonstrated the skill level associated with the above techniques. Moreover, it is worth reiterating that in no cases are these particularly complex techniques and thus it its likely that we may not develope models that have saturated the skill potential for empirical methods. In addition, it is also worth highlighting that ISV-related events are at best quasiperiodic, meaning conditions can be relatively quiescent and then an event suddenly develops. Each of the models above would tend to perform relatively poorly at forecasting this initial development, as they all tend to rely on the periodic nature of ISV to forecast its evolution. For these scenarios, as well as for dealing with the

inhomogeneity of ISV events, it will be vital to improve our dynamic models, as they are likely to be the best means to deal with these sorts of issues.

5.7.2 Dynamical forecast models

As yet, there have only been a handful of studies that have examined forecast skill (i.e., verified against observations) from dynamical models. This has probably stemmed from what amounted to considerably less overall interest in forecasting the intraseasonal timescale relative to weather and ENSO, the difficulty and resources required to produce an adequate sample of very long-range weather forecasts (at least 30 days), the pessimism and known challenges associated with tropical weather forecasting in general, and the indications that neither our forecast or climate simulation models were not very adept at simulating ISV. In any case, as part of a more generalized forecast skill study of the planetary-scale divergent circulation, Chen and Alpert (1990) examined MJO forecast skill from one year (June 1987–May 1988) of daily 10-day forecasts from the US National Meteorological Center's (NMC; now National Centers for Environmental Prediction (NCEP)) medium range forecast (MRF) model in terms of the VP200. In their analysis, the MRF's forecast skill, measured in terms of spatial correlations of VP200 between 50°N–50°S, declined to about 0.6 by forecast day 6 and 0.4 by forecast day 9. This relatively poor skill was attributed to: (1) the inability of the model to maintain MJO variability during a forecast, and (2) the model's tendency to propagate MJO anomalies too fast. Lau and Chang (1992) analyzed one season (14 Dec 1986–31 Mar 1987) of daily 30-day global forecasts derived from a set of Dynamical Extended Range Forecasts (DERFs) from a research version of the MRF model mentioned above. Their results showed that the forecast model had significant skill in predicting the global pattern of ISV in VP200 and streamfunction for up to 10 days lead time, with the error growth of tropical and extratropical low-frequency modes less than persistence when the amplitude of the MJO was large and vice versa when the amplitude was small.

Both Hendon *et al.* (2000) and Jones *et al.* (2000) analyzed a more recent DERF experiment which used the reanalysis version (Kalnay *et al.*, 1996) of the NCEP MRF model (Schemm *et al.*, 1996). This experiment included 50-day forecasts made once a day for the period January 1985 to February 1990. In both studies, the focus was on the MJO. Using different analysis and filtering techniques for identifying the MJO within the forecasts and thus for assessing forecast skill against observations, both studies concluded that this version of the NCEP MRF model still exhibited rather poor MJO forecast skill. Specifically, Jones *et al.* found that the anomaly correlations of intraseasonally filtered values of 200-hPa zonal wind, zonally averaged along the equator, declined from about 0.6 on day 3 to 0.2 by day 10 with some indication that the forecast skill was slightly better (worse) when the MJO was particularly active (weak). The rather poor forecast skill was attributed to the development of systematic errors in the forecast upper level winds, particularly over the eastern Pacific and, as above, due to the inability of this model to maintain/simulate a robust MJO phenomena itself. The analysis by Hendon *et al.*

showed that forecasts initialized during very active episodes of the MJO did not reproduce the observed eastward propagation of the tropical convection and circulation anomalies, rather the anomalies would typically weaken in places and even retrograde in some cases. Typically it was found that the convective anomalies would decay almost completely by day 7 of the forecast, and in nearly the same time considerable systematic errors in the extratropical 200-hPa streamfunction would develop. The above studies point to the need for the forecast models to not only have a proper representation of MJO anomalies but also to produce an unbiased mean state so initialization errors and their subsequent evolution/adjustment don't contaminate the forecast over these relatively long lead times.

The most prominent studies of forecast skill associated with the boreal summer ISO were based on the work of T. N. Krishnamurti in the early 1990s. In the first study, Krishnamurti *et al*. (1990) laid the groundwork for the method which argues that part of the loss of forecast skill associated with 'low-frequency modes' comes about from the errors and evolution of high wavenumber/frequency variability. If the objectives are the prediction of active and break monsoon periods, then it is plausible to filter the initial state in order to remove all but the recent (e.g., 45-day) 'mean' state and the low-frequency modes of interest (in this case, obtained via time filtering). Krishnamurti *et al*. argue that this will delay the 'contamination of the low-frequency modes as a result of the energy exchanges from the higher frequency modes'. This idea was tested in forecasts that used observed SST anomalies, filtered to include only 30–50-day variability. While the latter specification certainly provided the hindcast with information that a true forecast would not have, the results from the case study performed for 31 July 1979 were still encouraging. They showed that the model forecast exhibited considerable skill at predicting the meridional motion of the 850-mb trough–ridge system over Indian and the eastward propagation of the 200-mb divergence anomaly out to about 4 weeks. In Krishnamurti *et al*. (1992a, 1995), analogous experiments using two select case studies were performed for low-frequency 'wet and dry spells' over China and Australia for each of their associated summer monsoons with similar results. As in the first study, the SST anomalies were found to be vital to retaining the forecast skill. In both of these studies, simple empirical prediction of the SST anomalies was incorporated and found to provide much of the necessary SST information to retain most of the long-lead forecast skill found in this suite of experiments (see Fu and Wang, 2004; Zheng *et al*., 2004).

5.7.3 Predictability

The research highlighted in the previous two sections provides an indication of what the inherent predictability limit might be for principal modes of ISV. From the empirical model studies, this limit might be ascertained to be around 20–30 days. However, most empirical models are limited in the totality of the weather/climate system they can predict, their ability to adapt to arbitrary conditions, and their ability to take advantage of known physical constraints. Thus, one might conclude

that if dynamical models had a realistic representation of ISV, this limit might be extended. However, the information that can be ascertained from the above dynamical studies is limited due to the facts that they were either based on models with a relatively poor representation of ISV, they were based on only a few select cases, and since they were based on verification between models and observations all include model systematic bias in addition to the natural non-linear processes that limit predictability.

A complimentary avenue of research for ascertaining the inherent limits of prediction for ISV was taken by Waliser *et al.* (2003c, 2003d) who used so-called 'twin predictability' experiments. In this case, the model employed is presumed to be 'perfect' and forecast experiments are verified against others that only differ in the initial conditions (e.g., Lorenz, 1965; Shukla, 1985). The important consideration for a study such as this is that the model provides a relatively realistic representation of the phenomenon of interest. In this case, the experiments were performed with the NASA Goddard Laboratory for Atmospheres (GLA) GCM (Kalnay *et al.*, 1983; Sud and Walker, 1992). In a number of studies, this model has been shown to exhibit a relatively realistic ISV representation (Slingo *et al.*, 1996; Sperber *et al.*, 1997; Waliser *et al.*, 2003e) with reasonable amplitude, propagation speed, surface flux properties, seasonal modulation, and interannual variability (Waliser *et al.*, 2001). For these studies, a 10-year control simulation using specified annual cycle SSTs was performed in order to provide initial conditions from which to perform an ensemble of twin predictability experiments. The following discussion describes the boreal summer ISO study (Waliser *et al.*, 2003d) but the methods and results are quite similar for the MJO (Waliser *et al.*, 2003c). Initial conditions were taken from periods of strong ISO activity identified via EOF analysis of 30–90-day band-passed tropical rainfall during the May–September season. From the above analysis, 21 cases were chosen when the ISO convection was located over the central Indian Ocean, northern Indian Ocean, south-east Asia region, and north-west tropical Pacific, respectively, making 84 cases in total. Two different sets of small random perturbations, determined in a rather *ad hoc* and simplistic manner, were added to these 84 initial states. Simulations were then performed for 90 days from each of these 168 perturbed initial conditions.

A measure of potential predictability was constructed based on a ratio of the signal associated with the MJO, in terms of band-passed (30–90 day filter) rainfall or VP200 (VP200), and the mean square error between sets of twin (band-passed) forecasts. Predictability was considered useful if this ratio was greater than one, and thus if the mean square error was less than the signal associated with the MJO. The results indicate that useful predictability for this model's ISO extends over about 20–30 days for VP200 and about 10–15 days for rainfall (Figure 5.19). This is in contrast to the timescales of useful predictability for the model's weather that is about 12 days for VP200 and 7 days for rainfall. Predictability was shown to be sensitive to the amplitude of the events, with stronger events being more predictable. In addition and as indicated above, the predictability measure indicated greater predictability for the convective phase at short ($<\sim$5 days) lead times and for the suppressed phase at longer ($>\sim$15 days) lead times.

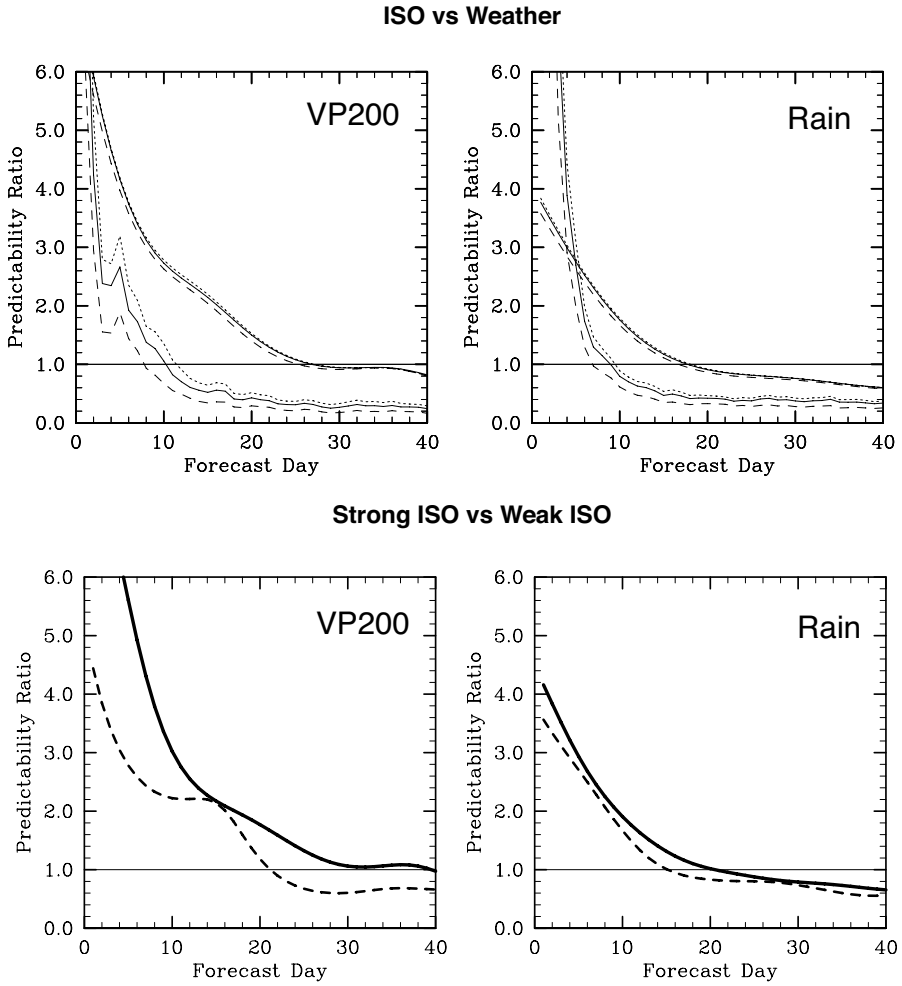

Figure 5.19. (*top*) ISO predictability vs. lead time for 200-hPa velocity potential (VP200; *left*) and rainfall (*right*) averaged over the region 4°N–24°N and 72.5°E–132.5°E. The results are based on all 168 northern hemisphere summertime cases from the dynamical forecasts. The rightmost (leftmost) group of lines are based on an evaluation using filtered (unfiltered) data to ascertain the predictability of the model's ISO (weather). (*bottom*) Same as (*top*), except that the solid (dashed) lines are based on forecasts using the 80 strongest (weakest) ISO cases.

In order to address the sensitivity of the above results to the model used and the analysis framework, an analogous study has recently been undertaken by Liess *et al.* (2004) using the ECHAM AGCM. The modeling and analysis framework is similar to that described above with two important exceptions. First, rather than select a large number of events (i.e., ~15–20) for each of the four phases of the ISO (i.e., as it propagates north-eastward) and performing two perturbation experiments for each,

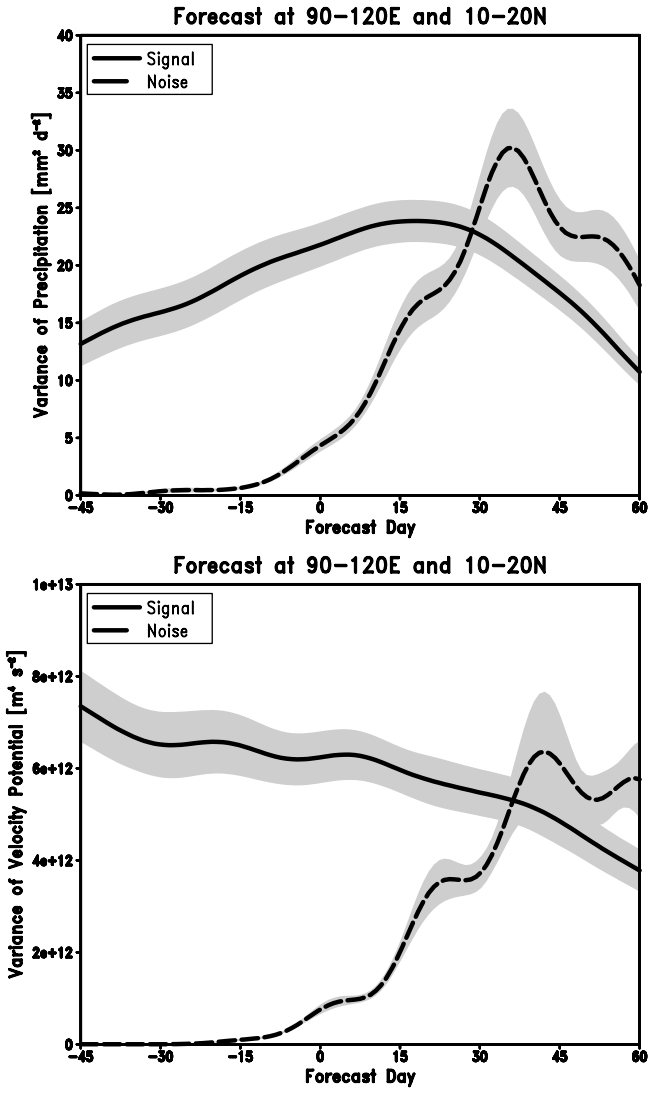

Figure 5.20. Signal-to-noise ratio of 30–90-day filtered precipitation (*top*) and 200-hPa velocity potential (*bottom*) predictions averaged over all four phases of three ISO events. Shadings represent the significance at the 95% interval based on all 12 15-member ensemble forecasts. All values are averaged over the region 90°–120°E and 10°–20°N.
Adapted from study by Liess *et al.* (2004).

this study has selected the strongest 3 events and performed a 15-member ensemble for each of the four phases. In addition, rather than use simply determined perturbations, this study uses the breeding method (Toth and Kalnay, 1993; Cai *et al.*, 2003). Figure 5.20 shows the combined results from all 12 15-member ensemble ISO

forecasts using the ECHAM5 AGCM. The data for the figure are taken from 90°E to 120°E and 10°N to 20°N for 30–90-day band-pass filtered rainfall (upper) and VP200 (lower) anomalies. These results suggest that the boreal summer MJO has dynamical predictability with lead times potentially up to and beyond 30 days. These lead times are at least as large, if not larger, than those found in Waliser *et al.* (2003c,d) studies highlighted above. However, it should be noted that the event analysed here is a particularly robust and strong one for the model, and those above were based on both strong and moderate sized events which could account for the difference. In any case, even though the above results do not take into account systematic model bias relative to the observations, they, along with many of the other studies discussed above, indicate that a promising avenue and timescale of operational monsoon prediction lies ahead.

5.7.4 Real time forecasts

Based on the qualified success of some of the prediction efforts discussed above, a number of forecast schemes have been implemented in real time. The first of these was associated with the Wheeler and Weickmann (2001) scheme described in Section 5.7.1[1] and is thus more strictly associated with the MJO as well as other coherent modes of tropical variability (e.g., Kelvin, mixed Rossby gravity). A second effort that has been developed more recently builds on the study by Lo and Hendon (2000) and utilizes what is referred to as an all-season real time multivariate MJO (RMM) index (Wheeler and Hendon, 2004).[2] The index results from projecting daily data onto the first two modes of a combined EOF of tropical OLR, and zonal winds at 850 and 200 hPa. This projection onto the EOF pair, along with the prior removal of an estimate of the data's very low-frequency components (e.g., ENSO) via their relationship to interannual SST variability, remove the need to perform time filtering to identify the MJO. The values of the index (actually two indices, one amplitude time series for mode 1 (RMM1) and one for mode 2 (RMM2)) at any given time can be used for monitoring. In addition, seasonally and time lag dependent regression can be used to forecast the evolution of these indices or any associated field, using as predictors RMM1 and RMM2 at the initial day. Skill scores in terms of spatial correlation are about 0.6 at 12-day forecast, and 0.5 for a 15-day forecast. The advantages of the method are that it has a seasonal dependence built in and it can be easily adapted for forecasting nearly any field.

Jones *et al.* (2004b) has also produced real time predictions of the MJO.[3] The scheme is based on band-passed (20–90 days) OLR, and zonal winds at 850 and 200 hPa. Upon filtering, a combined EOF of the three fields is computed and then the principle components (PCs) are separated into summer and winter. A seasonally dependent regression model is then formed at every given lead between 1 and 10 pentads. The model utilizes the first five PCs from the EOF analysis and the five most

[1] http://www.bom.gov.au/bmrc/clfor/cfstaff/matw/maproom/OLR_modes/index.htm
[2] http://www.bom.gov.au/bmrc/clfor/cfstaff/matw/maproom/RMM/index.htm
[3] http://www.icess.ucsb.edu/asr/mjo_forecasts.htm

recent values of the PCs. The model is found to exhibit winter and summer skills comparable to the other empirical models described in Section 5.7a.

In quite a different approach, stemming from a somewhat different and/or more comprehensive objective, Matt Newman and his colleagues have developed and implemented a real time forecasting scheme[4] that has applicability to the MJO based on what is often referred to as the Linear Inverse Model (i.e., LIM; Winkler *et al.*, 2001; Newman *et al.*, 2003). The LIM is based on NCEP/NCAR reanalysis data (Kalnay *et al.*, 1996) that has had the annual cycle removed, been smoothed with a 7-day running mean filter, gridded to T21 spatial resolution, and been reduced by EOF decomposition. The specific fields used include global 250 and 750-hPa streamfunction and tropical column integrated diabatic heating. For the northern hemisphere winter (summer) model, the first 30 (30) streamfunction and 7 (20) diabatic heating EOFs are used. In this model, historical data are used to define the relationship between a given state (i.e., a weekly average) and conditions one week later, with the process being iterated to produce multiweek forecasts. The advantage of the model is that it includes both tropical (in terms of diabatic heating – hence a prediction of the MJO) and extratropical (in terms of streamfunction) forecasts. In this way, the interaction between the two can be more readily examined and diagnosed. For tropical forecasts of diabatic heating, the LIM slightly outperforms a research version of the NCEP MRF model at lead times of 2 weeks, for both summer and winter.

It is almost a certainty that the greatest impact from ISV on society via direct impacts on day-to-day weather, agriculture, and associated economics is associated with the Asian summer monsoon. Motivated by this, Webster and Hoyos (2003) have developed an empirical model for predicting ISV in Indian district rainfall. The empirical model is physically based with predictors drawn from the composite structure of the boreal summer ISO (e.g., Indian Ocean SST, precipitation over India, upper level easterly jet). In essence, the model is Bayesian and uses a wavelet technique to separate significant spectral bands. The model illustrates considerable skill, even over 20–25 days, in predicting rainfall in hindcast mode. It was used for the first time during the summer of 2003 in a real time operational mode in the Climate Forecast Application in Bangladesh project. Since then, these forecasts of precipitation (and river discharge) have been integrated into the Bangladesh forecasting system on an experimental basis.

Based on the sorts of activities and success described above, along with the needs to take a more systematic approach to diagnosing problems in dynamical forecasts of the ISV, an experimental 'MJO' prediction program has recently been formulated.[5] The project's website has been operational since about late 2003 and is host to real time predictions of ISV from about 3–4 empirical methods and about 3–4 numerical forecast models. This effort continues to grow and evolve and during the winter and spring of 2004 began to also include 'synoptic' discussions of ISV conditions and their forecasts, with particular emphasis on the tropical–extratropical

[4] http://www.cdc.noaa.gov/map/images/mjo/

[5] http://www.cdc.noaa.gov/MJO/index.html

interactions. Additional information on this effort can be found in Waliser *et al.* (2003a) and Waliser (2005).

5.8 CONCLUSION

The literature reviewed here has shown that tropical intraseasonal variability makes up an extremely important part of the character and evolution of the Asian summer monsoon. While its most pronounced influence is associated with its direct connection to monsoon active and break periods, other important effects include its modulation of higher frequency variability and the role it may play in helping to determine interannual and longer term variability. A principal driver of the present enthusiasm for the subseasonal component of the monsoon is it offers a new – relative to the longstanding efforts at seasonal prediction – and unique form of predictive capability that is just beginning to be exploited. The principle roadblock to achieving the full potential that such predictability might offer is the development of a more robust and well-understood modeling capability, one that can withstand even modest observational scrutiny. Recent years have seen tangible progress in the form of theoretical hypotheses through the identification and narrowing of the major physical processes underlying ISV, as well as the acquisition of a wide variety of new data sets and field programs. The latter includes BOBMEX (Bhat *et al.*, 2001), JASMINE (Webster *et al.*, 2002), GAME-GEWEX (GAME, 1998), SCSMEX (Lau *et al.*, 2000), the CLIVAR/GCM Monsoon Intercomparison Project (Kang *et al.*, 2002a; Waliser *et al.*, 2003e), the development of an Indian Ocean moored array and drifter program (Meyers and Wijffels, 2004), as well as a number of new and exciting satellite programs (e.g., TRMM, AIRS, MODIS, MISR). At least in terms of intraseasonal variability of the monsoon, these additional resources and theoretical developments should make the coming decade a promising and productive one that will hopefully lead to a greatly improved modeling and predictive capability.

Relatively large uncertainties and/or gaps in our knowledge still exist in terms of the manner high-frequency (e.g., 10–30-day) and intraseasonal (40–60-day) variability interact, how ENSO or other low-frequency variations can modify ISV, and in turn, the degree that ISO variations contribute to interannual variability and the extent that this is chaotically driven. Theoretical and GCM efforts still struggle to define the role that multiscale interactions (e.g., cumulus, mesoscale, synoptic, planetary) might play in the manifestation of the ISO as well the degree and manner that cloud–radiative interactions might be important. While the land surface is an inherent part of the geographic extent of the boreal summer ISO, very little research has been performed to evaluate its role. In addition, there are clearly some very general numerical simulation problems that still need to be overcome that when solved will have a positive impact on the simulation of ISV. These include better mean states, undoubtedly the treatment of convection including the roles of stratiform/anvil clouds and shallow cumulus, when and where ocean coupling is important, etc. Finally, while the development and application of

empirical ISO forecast models is taking foot, the ability to exploit the details associated with a weather/climate prediction GCM is at best in its infancy. At this stage there are not only the difficulties associated with the simulation of ISV, there are still many uncertainties associated with how to carry out subseasonal predictions in terms of supplying initial conditions and supplying/modeling surface boundary conditions (Waliser *et al.*, 2003a). The development and improvement of subseasonal predictions, based on phenomena such as the ISO, offer a great opportunity to help bridge the present gap between weather and seasonal-to-interannual climate predictions.

5.9 ACKNOWLEDGEMENTS

This work was supported by the Human Resources Development Fund at the Jet Propulsion Laboratory, as well as the National Science Foundation (ATM-0094416), the National Oceanographic and Atmospheric Administration (NA16GP2021), and the National Atmospheric and Aeronautics Administration (NAG5-11033). The author would like to thank an anonymous reviewer and the editor for providing a number of useful comments and suggestions that improved the balance of material in this chapter along with its presentation. The author would also like to thank D. R. Chakraborty for contributing material for the section on Theory and Physical Processes.

6

Interannual variability of the Asian monsoon

Song Yang and William K.-M. Lau

6.1 INTRODUCTION

The Asian monsoon fluctuates with large amplitudes on various timescales. Among the wide ranges of timescales, the interannual variability is the most extensively studied. This is not surprising if we recall that the word monsoon is derived from the Arabic word 'mausam', which means season. In many Asian countries, summer monsoon precipitation accounts for a large part of the annual total precipitation and significantly affects the annual gross national product, an important index to measure the economic growth of individual countries. Many large-scale phenomena (e.g., El Niño/Southern Oscillation; ENSO) that interact with the monsoon also fluctuate significantly on interannual timescales. Thus, the conditions of the Asian monsoon in specific years and the change in these conditions from one year to another have large socioeconomic impacts within and outside the Asian region.

The interannual variability of the Asian monsoon is defined as the yearly deviation of seasonal transition from the mean annual cycle. The pronounced seasonal cycle of the Asian monsoon distinguishes it from other monsoon systems in the World that have much weaker annual cycles (e.g., the North American monsoon system; see Higgins *et al.*, 2003). Furthermore, substantial spatial variability exists in the Asian monsoon system so that several major regional monsoon components are usually needed in order to classify monsoon variability within Asia. That is to say, the interannual variability of the Asian monsoon is characterized by a set of seasonally and spatially varying characteristic features. In many cases, to describe monsoon variability clearly, it is necessary to specify the time and location of the monsoon phenomenon in question. In addition, monsoon variability refers not only to the changes in a specific location but also to the migration of the monsoon from one place to another. The latter, from which the concept of the Asian–Australian monsoon system is derived, is pivotal for

B. Wang (ed.), *The Asian Monsoon*.

understanding the relationship between monsoon and the tropospheric biennial oscillation (TBO; Section 6.4).

Early studies of the Asian monsoon were mainly conducted to understand and predict the regional features over India. During the past decades, increasing effort has been devoted to the understanding of monsoon phenomena outside south Asia. It is now recognized that the Asian monsoon is an integral part of the Earth's climate system and plays a critical role in determining the nature of the coupling among oceans, land, and the atmosphere. In this chapter, we discuss the large-scale monsoon over the entire tropical Asia and adjacent regions. For the interannual variability of the regional monsoons over south Asia and east Asia, readers may refer to the reviews by Shukla (1987a), Tao and Chen (1987), Chen *et al.* (1991), and Ding (1992). We focus on the summer monsoon, but the monsoon phenomena for other seasons will also be discussed when appropriate, to the extent they will enlighten the mechanisms for understanding the interannual variability of the monsoon. Specifically, we address several key issues regarding the interannual variability of the Asian monsoon, which include the principal modes of monsoon variability, dominant impacting factors, the TBO, and the relationship of the monsoon with global climate. It should be pointed out that the features presented in this chapter may undergo interdecadal and even longer variations, which are not covered here but are detailed in Chapter 7.

6.2 PRINCIPAL MODES

The variations of the Asian monsoon on different timescales are usually characterized by major features associated with different dominant modes, or spatial patterns, although these modes may be phase-locked as in the case for interannual and intraseasonal timescales (Ferranti *et al.*, 1997; Kang *et al.*, 1999; Goswami and Mohan, 2001). Here, we discuss the principal modes of the interannual variability, with a focus on the fields of precipitation and atmospheric circulation and on the essential features associated with several monsoon indices that have been developed to describe the Asian monsoon.

6.2.1 Precipitation

Figure 6.1 shows the distributions of climatological means (shadings) and standard deviations (contours) of precipitation for December–January–February (DJF), March–April–May (MAM), June–July–August (JJA), and September–October–November (SON). The data are available from the NOAA Climate Prediction Center Merged Analysis of Precipitation (CMAP; Xie and Arkin, 1997), for the period of 1979–2002. The standard deviations, computed from the departures of the seasonal means of each year from the seasonal climatology, are a measure of the degree of interannual variability of precipitation at each grid point for each season.

The precipitation patterns shown in Figure 6.1 have several important charac-

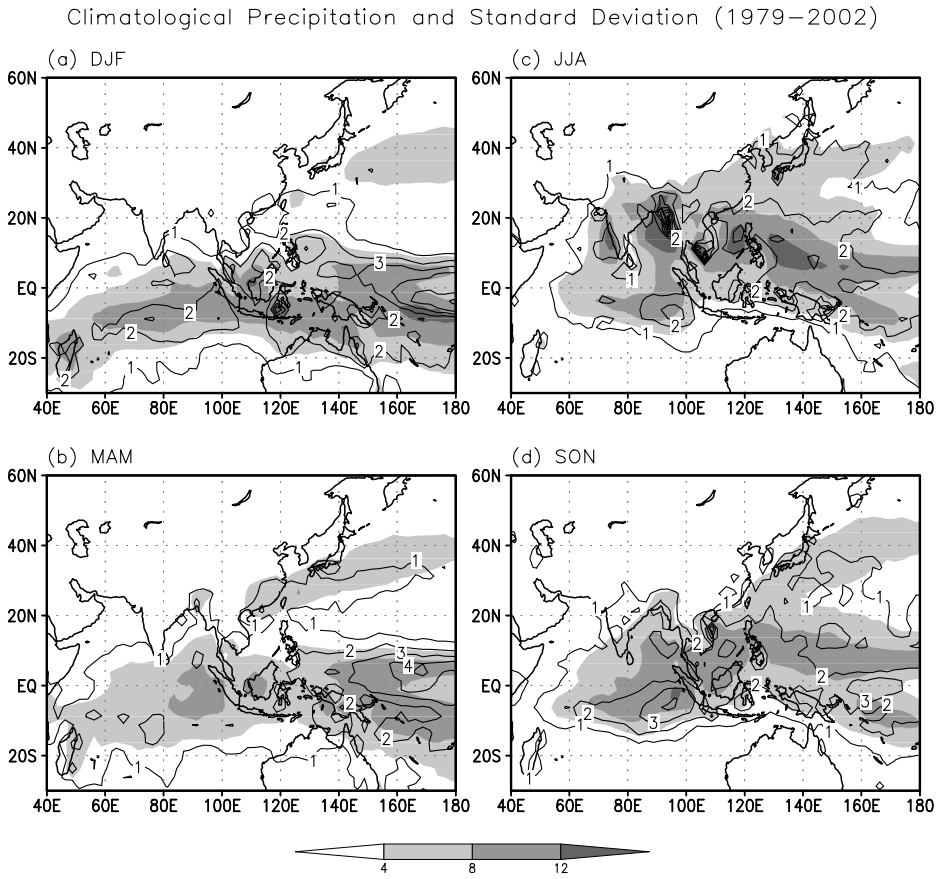

Figure 6.1. Climatology (1979–2002) of seasonal means (shadings) and standard deviations (contours) of CMAP precipitation (mm day^{-1}) for (a) DJF, (b) MAM, (c) JJA, and (d) SON.

teristic features. Climatologically, they represent the bands of heaviest seasonal rainfall in the World. These rain bands are associated with the World's strongest monsoon systems and warmest ocean domains. They represent the strongest annual cycle in the tropics, with centers of action shifting from tropical Asia to the Australian monsoon region from boreal summer to winter, and in an opposite direction from winter to summer. The strongest annual cycle is manifested not only by the largest difference in the magnitude of precipitation at given locations between summer and winter, but also by the largest distance that the heavy rain belts 'travel' between the two seasons. These features have been the subject matter of many studies on the dynamics and physics of the coupled ocean–atmosphere–land system. For example, the seasonal migration of the rain bands is one of the central issues of the underlying monsoon–ENSO and monsoon–TBO relationships

(Sections 6.3 and 6.4). The most dominant modes of the climatological variations of summer monsoon rainfall include the features associated with the precipitation over south Asia, south-east Asia, and east Asia. In particular, the east Asia precipitation is associated with the rain bands of Meiyu in China, Baiu in Japan, and Changma in Korea.

Figure 6.1 also shows significant variability in the precipitation patterns on interannual timescales. The precipitation over the tropical western Pacific is always characterized by large variations ($>$2–3 mm day^{-1}), and both the Australian monsoon in DJF and the Asian monsoon in JJA change significantly from one year to another. Interestingly, significant variability also exists over the tropical southern Indian Ocean and south-east Asia during most of the seasons. Large variability of precipitation is even found over the South China Sea and the Philippine Sea in winter, due partially to the influence of the east Asian winter monsoon, when the major centers of monsoon rainfall shift to the southern hemisphere.

The most dominant mode of the interannual variability of summer monsoon rainfall is associated with a dipole-like variation of precipitation between south Asia and south-east Asia (e.g., Goswami *et al.*, 1999; Lau *et al.*, 2000a). The change in precipitation over south Asia including India and the Bay of Bengal is usually accompanied by an opposite signal over the equatorial Indian Ocean. Analyses of more regional-scale precipitation patterns often reveals detailed features such as the precipitation variability over northern and southern China and the change in Meiyu over the Yangtze River valley (e.g., Lau and Weng, 2001). However, under the influence of ENSO, these features of precipitation may be significantly different from the normal conditions (Lau and Wu, 2001).

6.2.2 Atmospheric circulation

Shown in panels (a)–(d) of Figure 6.2 are the first modes of empirical orthogonal function (EOF) analysis of the 200-mb zonal wind (U200) for the analysis domain as shown in the figure. Data from the National Centers for Environmental Prediction (NCEP)–National Center for Atmospheric Research (NCAR) reanalysis (Kalnay *et al.*, 1996) for 1968–2003 were used to produce these plots. Note that the data of early years are not used here because of the potential problem of the product for studies of the Asian monsoon (see Yang *et al.*, 2002). In DJF (Figure 6.2(a)), the most dominant features are found over east Asia and regions from the Mediterranean to the Middle East, associated with the changes in the east Asian and Middle East jet streams. In JJA (Figure 6.2(c)), when the spatial structure is the weakest among all the seasonal EOF modes, the variability of the upper tropospheric monsoon easterlies over tropical Asia and the Indian Ocean, and that of the westerlies to the north, are pronounced. Associated with these easterlies and westerlies is the south Asian High, mainly over the Tibetan Plateau and Pakistan, which appears more clearly in the field of geopotential height (not shown). In spite of some shift in latitudes, the features of MAM (Figure 6.2(b)) resemble those of DJF, and the patterns of SON (Figure 6.2(d)) and JJA are similar to each other.

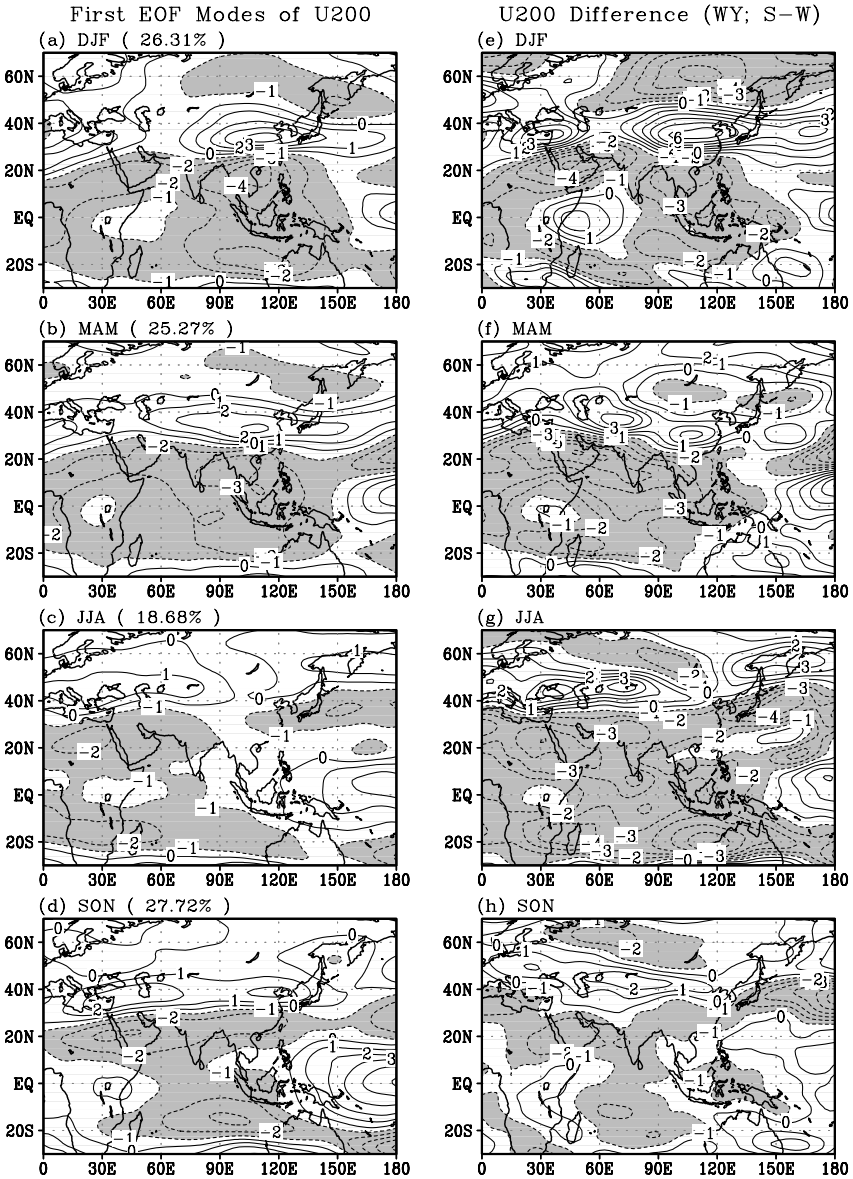

Figure 6.2. (a)–(d) First EOF modes of U200 for DJF, MAM, JJA, and SON based on the NCEP/NCAR reanalysis for 1968–2003. (e)–(h) Differences in U200 (ms^{-1}) between strong and weak Asian summer monsoon for the previous DJF and MAM, concurrent JJA, and following SON. The patterns are constructed with respect to the strong (1970, 1981, 1984–1985, 1990, 1994, 1999, and 2001) and weak (1972, 1974, 1979, 1983, 1987, 1992, 1995–1997) monsoon years based on the Webster–Yang monsoon index (Webster and Yang, 1992) in JJA. Values smaller than −1 are shaded.

One of the important features of Figure 6.2(a)–(d) is that there exists significant correlation between the principal components from one season to another, indicating a large persistence of these first EOF modes from DJF to MAM and from MAM to JJA.

Another important feature of Figure 6.2 is that, for each individual season, there is a strong relationship between panels (a)–(d) and panels (e)–(h), which show the differences in U200 between the years of strong and weak large-scale Asian summer monsoon measured by the Webster–Yang monsoon index (see discussion in Section 6.2.3). This is demonstrated by the close resemblance among the spatial patterns (e.g., Figures 6.2(a) and (e), Figures 6.2(b) and (f), etc.). The strong relationship is also demonstrated by the high temporal correlation between the principal component in each season and the corresponding major circulation feature such as the Middle East jet stream in DJF, the geopotential height condition (not shown) over the Tibetan Plateau in MAM, and the large-scale Asian monsoon in JJA. The above features indicate that the most dominant mode of each season and its seasonal evolution are associated with the variability of the Asian summer monsoon, suggesting that the interannual variability of the summer monsoon can also be described by the deviation of the atmosphere from its mean annual cycle, besides the changes from one summer to another. Because of the large persistence in the seasonal evolution of these dominant modes and the monsoon-related features, Figure 6.2 also suggests a potential for monsoon prediction. As it will be discussed in Section 6.3, a combination of the memory effects of sea surface temperature (SST), land surface processes, and other large-scale climate phenomena may provide a plausible explanation of the persistence of the atmospheric signals from one season to the next.

Besides the variability in the mean easterlies–westerlies and the south Asian High, the anomalous atmospheric circulation patterns over the southern Indian Ocean and the western North Pacific are also important elements in representing the nature of principal monsoon modes. As demonstrated by Wang *et al.* (2003b), who conducted an extended singular value decomposition analysis to depict these modes and their evolution by applying the concept of 'monsoon year' (Yasunari, 1991) and ENSO cycle, the evolution of the Asian–Australian monsoon is significantly characterized by the variations of two anticyclones over the Indian Ocean and the Pacific (Figure 6.3, color section). The developments of the southern Indian Ocean anticyclone in the autumn (Figure 6.3(b)) and the western North Pacific anticyclone in the winter (Figure 6.3(c)) are accompanied by the transition of monsoon anomalies from one summer to another. From the development of the southern Indian Ocean anticyclone in the autumn (Figure 6.3(b)) to the next spring (Figure 6.3(d)), the anomalous monsoon circulation shifts from the Indian Ocean to the Pacific. Figure 6.3 also shows a strong biennial oscillation in the dominant mode, in which monsoon anomalies reverse from one summer to the next (Figure 6.3(g)). This feature is especially apparent over the western North Pacific, the Maritime Continent, and the northern Indian Ocean. According to Wang *et al.* (2003b), a better understanding of the origin, development, and maintenance of these two anomalous anticyclones is important for advancing the knowledge of the

evolution of the Asian monsoon and for improving the theoretical understanding of the fundamental physics of the TBO.

6.2.3 Dominant modes associated with major monsoon indices

Because of the need of referring to monsoon variability with reference to specific features and the time of their occurrence, numerous monsoon indices have been developed (see Wang and Fan, 1999; Li and Zeng, 2003). Useful indices provide a simple characterization of the state of the monsoon. However, due to the distinct spatial features of monsoon and the diverse ways of representing monsoon (e.g., by different fields for different purposes), it is difficult to derive a 'universal' index to measure the interannual variability of the monsoon over all of Asia. Provided in Table 6.1 are attributes of a number of frequently used monsoon indices including their definitions and applications. They are 'all-India' monsoon rainfall (AIMR) index, Webster and Yang (W–Y) monsoon index, and regional monsoon indices for the south Asian monsoon (SAM), the east Asian monsoon (EAM), and the south-east Asian monsoon (SEAM). Assessments of these indices and their associated dominant features can be found in Wang and Fan (1999) and Lau *et al.* (2000a).

Perhaps the mostly widely applied index is AIMR, the rainfall over the whole of India averaged from June to September (Mooley and Parthasarathy, 1984; Parthasarathy *et al.*, 1992b). In spite of the spatial difference in rainfall within the country (Parthasarathy *et al.*, 1993; Parthasarathy and Yang, 1995), AIMR seems more appropriate for representing the variability of monsoons in India than the indices that are constructed correspondingly for representing the monsoons in other Asian countries of similar size.

Most of the indices summarized in Table 6.1 are dynamical indices. In particular, the W–Y monsoon index (Webster and Yang, 1992) measures the monsoon circulation by the vertical shear of zonal winds between 850 mb and 200 mb, averaged over tropical Asia and the adjacent oceans. It depicts the thermally driven nature of the monsoon and thus recognizes the importance of horizontal temperature gradient. Similarly, SAM (Goswami *et al.*, 1999) is defined as the vertical shear of meridional winds and measures the overturning over south Asia and the Indian Ocean associated with the local Hadley cell. It is argued that SAM is superior to AIMR, which does not include the rainfall variability over the Bay of Bengal where maximum monsoon heating is located. For south-east Asia, SEAM (Wang and Fan, 1999) is constructed based on the locations of local atmospheric convection and the characteristic low-level Rossby wave response to heat sources. The east Asian monsoon index EAM, as defined by Lau *et al.* (2000a), is based on the close relationship between the multicell structure of the monsoon and the wave-trains associated with the east Asian jet stream.

Figure 6.4 shows the regression of 850-mb winds and precipitation against the different dynamical monsoon indices. The main circulation feature associated with the W–Y index is a zonally elongated band of westerlies stretching from eastern Africa to the Philippines (Figure 6.4(a)). This westerly band and the easterlies

Table 6.1. Frequently used monsoon indices of the Asian summer monsoon.

Name of index	Type of index	Domain of application	Definition	Reference
AIMR	Precipitation	India	Rainfall over India	Parthasarathy *et al.* (1992b)
W–Y	Circulation	Tropical Asia	U850–U200 Over 0°–20°N, 40°–110°E	Webster and Yang (1992)
SAM	Circulation	South Asia	V850–V200 Over 10°–30°N, 70°–110°E	Goswami *et al.* (1999)
SEAM	Circulation	Southeast Asia	U850 (5°–15°N, 90°–130°E) – U850 (22.5°–32.5°N, 110°–140°E)	Wang and Fan (1999)
EAM	Circulation	East Asia	U200 (40°–50°N, 110°–150°E) – U200 (25°–35°N, 110°–150°E)	Lau *et al.* (2000a)

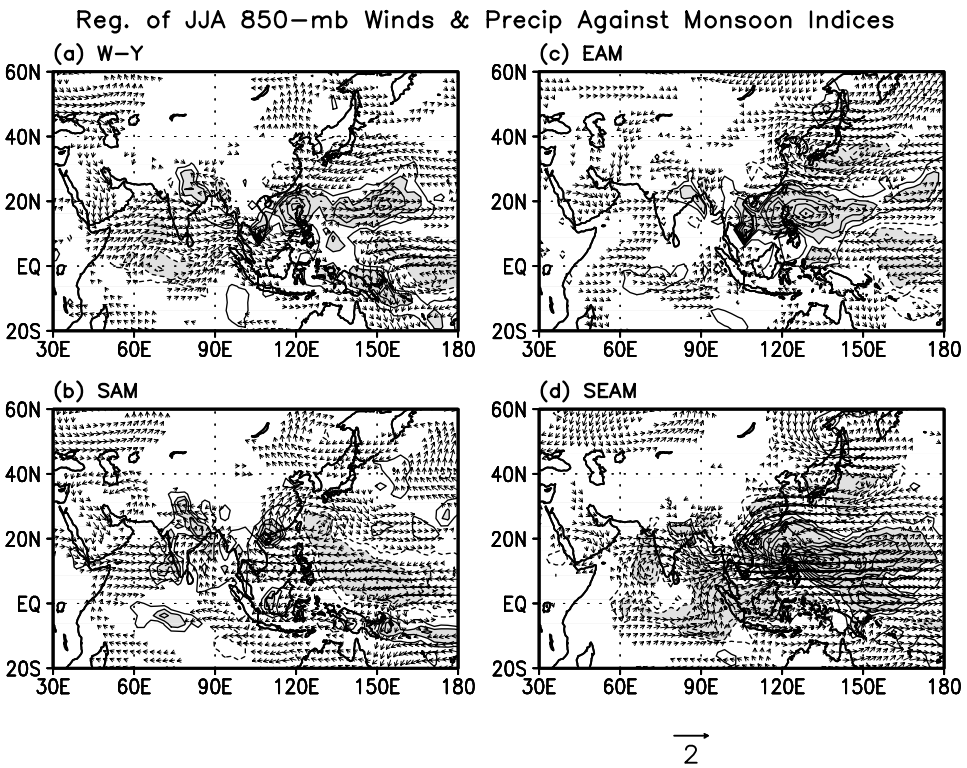

Figure 6.4. Patterns of regression of JJA 850-mb winds (vectors; 1968–2003) and precipitation (contours; 1979–2003) against various monsoon indices. Contour intervals are 0.3 with the zero contours omitted. Absolute values larger than 0.6 are shaded, and negative values are plotted by dashed contours.

from the western Pacific lead to major convergence over the Maritime Continent. Several other convergence centers also appear because of the cyclonic patterns over the northern Bay of Bengal and the South China Sea. A high W–Y index corresponds to an increase in precipitation over north-eastern India, the Bay of Bengal, south-east Asia, the South China Sea, and the western Pacific. It also signals a decrease in precipitation over the Arabian Sea and the equatorial Indian Ocean due to the cooling in SST associated with the strong monsoon flow (see Figure 15(c) of Lau *et al.*, 2000a). Apparently, the index does not capture the local monsoon rainfall center usually seen over western India (Figure 6.1(c)). Overall, the W–Y index measures the broad-scale monsoon circulation, contributed collectively by various regional components.

SAM captures the westerlies from the Arabian Sea to the western Bay of Bengal, with a strong cross-equatorial flow and meridional component of winds over the Bay of Bengal (Figure 6.4(b)). A key difference between Figure 6.4(b) and Figure 6.4(a) is that, in SAM, the tropical easterlies extend deeply westward, covering the entire south-east Asia. SAM represents the changes in precipitation over India and the

Bay of Bengal. Compared with the other indices examined, it portrays the weakest signals over south-east and east Asia especially the South China Sea and the Philippines. In general, the patterns of atmospheric circulation and precipitation variability associated with SAM are similar to those related to AIMR. Although EAM is also linked to the westerlies over tropical Asia, in a narrower band, the main features represented by the index appear in the longitude band of 110°–140°E, within which easterlies and westerlies occur alternatively within 0°–50°N (Figure 6.4(c)). Thus, EAM depicts the multiple cell structure of the east Asia monsoon, which is closely related to the north–south shift of the overlying jet stream. The multicell feature can be clearly seen from the positive–negative–positive pattern of the change in precipitation over east Asia and the western North Pacific. Compared with others, SEAM depicts the strongest features over south-east Asia and the western Pacific (Figure 6.4(d)). It also delineates a largest change in the southern portion of the subtropical western Pacific High. A very important feature here is that the intensification of monsoon rainfall is accompanied by the weakening of the subtropical high. It is also interesting to note that precipitation increases over south-east Asia and the western Pacific when it decreases over south Asia, which is largely opposite to the feature shown for SAM (see Figure 6.4(b)).

6.3 DOMINANT IMPACTING FACTORS

This section is devoted to discussions of major factors affecting the interannual variability of the Asian monsoon. Although the variability of the monsoon is largely controlled by the internal dynamics of the atmosphere, which is ultimately related to the amount and distribution of solar energy, the slowly varying boundary forcing from the underlying oceans and land also plays an important role in affecting the interannual variability of the monsoon. The classical concept of the monsoon, as a circulation system driven by the thermal contrast between oceans and continents, implies the importance of ocean and land surface processes for the monsoon and its variability. However, the Asian monsoon is also significantly influenced by large-scale climate phenomena such as the Arctic Oscillation (Gong and Ho, 2003; Yang *et al.*, 2004). These phenomena may themselves be the result of atmospheric internal dynamics; however, since their variability is characterized by low-frequency global variations outside the monsoon system, they are considered impacting factors of the monsoon as well (Section 6.3.3).

6.3.1 Sea surface temperatures

Among all the external causes of interannual variability of the Asian monsoon, SST is perhaps the leading impacting factor (Chao and Chen, 2001). The effect of SST on the monsoon can be divided into 'remote effect' by the tropical central eastern Pacific SST and 'local effect' by the regional SSTs of tropical–extratropical oceans near the Asian continent.

6.3.1.1 Tropical central eastern Pacific SST

The relationship between the tropical central eastern Pacific SST and Asian monsoon is the most popular topic in SST–monsoon studies because of the long history and the nature of ocean–atmosphere coupling associated with ENSO. In searching for predictors of the Indian monsoon, Walker (1923, 1924) defined the Southern Oscillation, which is closely related to the zonal circulation over the equator. Later, it was found that the so-called Walker circulation is strongly coupled with the underlying oceans, especially the SST in the tropical central eastern Pacific (Bjerknes, 1969). Thus, the relationship between the central eastern Pacific SST and the monsoon is generally regarded as a problem of ENSO–monsoon association. During the past decades, extensive studies have been carried out to understand the various aspects of the ENSO–monsoon association and the responsible physical mechanisms (Sikka, 1980; Rasmusson and Carpenter, 1983; Ropelewski and Halpert, 1987; Webster and Yang, 1992; Nigam, 1994; Ju and Slingo, 1995; Yang, 1996; Zhang *et al.*, 1996; Kawamura, 1998; Lau and Nath, 2000; Slingo and Annamalai, 2000; Wang, 2000; Lau and Wu, 2001; Chou *et al.*, 2003). One of the most important results is that the Indian summer monsoon is weaker (stronger) than normal before (after) the peak of an El Niño in winter, and that the relationship is opposite for the monsoon and La Niña. On a much broader scale, the monsoon circulation over southern Asia is generally weaker (stronger) than normal during El Niño (La Niña) summers (e.g., Webster and Yang, 1992; Lau and Yang, 1997).

However, the impact of ENSO on the east Asian monsoon is usually more complex and is often characterized by strong regional features (Huang and Wu, 1989; Lau and Weng, 2001). For example, during the El Niño years, the summer rainfall generally increases (decreases) in southern (northern) China but the signal in central China is less significant (Wang and Li, 1990; Chang *et al.*, 2000b; Wu *et al.*, 2003). This complex ENSO–monsoon relationship can be attributed partially to the complex features of the local precipitation pattern, which is related closely to the multicell structure of atmospheric circulation discussed above. In east Asia, the monsoon precipitation includes the rainfall amount of the early season rainfall and Meiyu in China, Baiu in Japan, and Changma in Korea (Ninomiya and Murakami, 1987; Tao and Chen, 1987; Kang *et al.*, 1999; Krishnan and Sugi, 2001; Lau and Weng, 2001; Chung *et al.*, 2004). These precipitation phenomena not only occur in different places at different times but also link to the influence of mid-latitude atmospheric process.

Table 6.2 shows the lag correlation between various Asian monsoon indices and Niño 3.4 (5°S–5°N, 170°–120°W) SST anomalies for different seasons. The table indicates that the winter condition of ENSO has little prediction potential for the following summer monsoons measured by the indices except for SEAM. Starting with MAM, ENSO is a reasonable precursor for the large-scale monsoon measured by the W–Y index. The largest values are found in the correlation between Niño 3.4 SST and AIMR, but only simultaneously and when the monsoon leads the SST. The lead of the monsoon to SST can also be seen for other monsoon components except the EAM. These features have led to the speculation that the Asian monsoon plays

Table 6.2. Correlation between various summer monsoon indices and Niño 3.4 SST of different lags (1968–2003; 1968–2000 for AIMR). Significant values exceeding 95% confidence level are emboldened and italicized.

	DJF−	MAM−	JJA0	SON+	DJF+
AIMR	0.25	−0.02	***−0.48***	***−0.49***	***−0.47***
W–Y	−0.17	***−0.40***	***−0.44***	***−0.35***	−0.28
SAM	0.09	−0.11	−0.30	***−0.33***	−0.30
SEAM	***−0.48***	−0.31	0.26	***0.39***	***0.40***
EAM	−0.16	−0.20	−0.14	−0.07	−0.11

an active role in driving monsoon–ENSO interaction (Section 6.5). The table also indicates that both the SAM and AIMR are linked to ENSO in a similar way but the AIMR–SST relationship is stronger. In addition, there is no significant linear relationship between ENSO and the east Asian monsoon measured by index EAM for the period examined. Interestingly, since JJA, Niño 3.4 SST is positively correlated with the SEAM. (The feature that the weakest SEAM–SST correlation appears in the simultaneous relationship may need to be confirmed by more data records.) This is different from the feature associated with the Indian monsoon, and the difference seems consistent with the notion that the Indian and south-east Asian monsoons are two relatively independent components of the Asian monsoon system although they are also connected to each other in fundamental ways (Jin and Chen, 1983; Zhu *et al.*, 1986; Guo and Wang, 1988; Yang and Gutowski, 1992; Kripalani and Kulkarni, 1997b, 1998; Wang *et al.*, 2001; Wu *et al.*, 2005).

Figure 6.5 shows the anomalous 850-mb summer monsoon circulation (vectors) arising from the impacts of ENSO related SST (contours) in DJF (a), MAM (b), and JJA (c). It can be seen that the increase in Niño 3.4 SST in DJF leads to a slight weakening of the summer monsoon flow over tropical south Asia. Changes in the monsoon are relatively stronger over south-east Asia. More significant weakening of the monsoon including the cross-equatorial flow in summer follows the tropical central eastern Pacific warming in MAM (Figure 6.5(b)). This is consistent with the result given in Table 6.2 for the monsoon defined by the W–Y index (row 3 for MAM). Associated with the increase in Niño 3.4 SST, moderate warming appears in the Indian Ocean in both DJF and MAM. Simultaneously, the increase in Niño 3.4 SST in summer weakens the monsoon flow over the tropical central western Indian Ocean (Figure 6.5(c)). In spite of the intensifying cross-equatorial flow over the eastern Indian Ocean and westerlies over south-east Asia, a broad anomalous anticyclonic pattern appears over tropical Asia and the Indian Ocean. It reduces the precipitation over the Arabian Sea, India, southern South China Sea, and Indonesia (result not shown). In the meantime, the Indian Ocean and the western Pacific are generally cooler. Figure 6.5(c) also indicates that much more significant weakening occurs in the trade winds over the tropical western central Pacific.

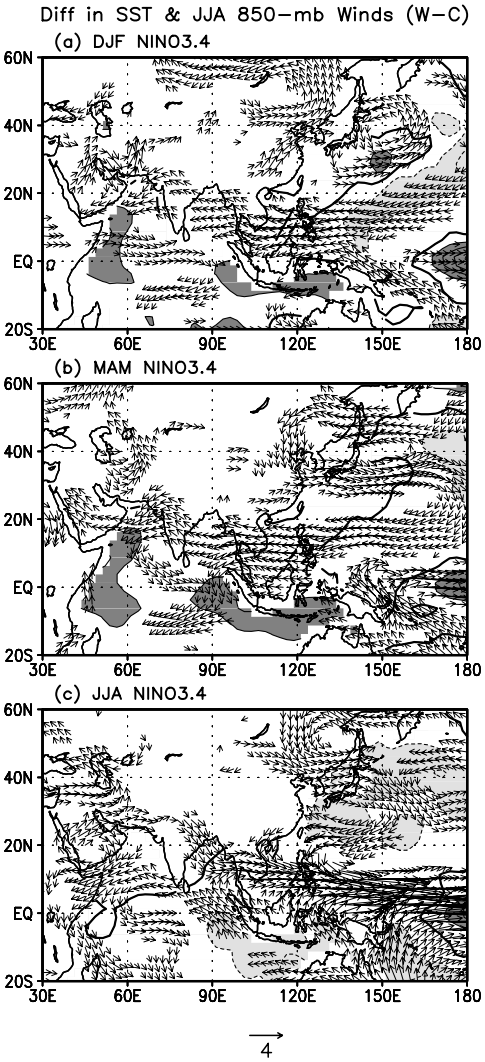

Figure 6.5. Patterns of differences in Niño 3.4 SST (contours) of respective seasons and in JJA 850-mb winds (vectors) between warm and cold cases (warm minus cold). The years are chosen (based on largest SST anomalies) for each season individually and are different among the various panels. For DJF, the warm cases include 1957/1958, 1965/1966, 1972/1973, 1982/1983, 1991/1992, and 1997/1998; and the cold cases include 1970/1971, 1973/1974, 1976/1977, 1988/1989, 1998/1999, and 1999/2000. For MAM, warm cases: 1958, 1969, 1983, 1987, 1992, 1993, and 1998; cold cases: 1950, 1955, 1971, 1974, 1985, 1989, and 1999. For JJA, warm cases: 1965, 1972, 1982, 1987, and 1997; cold cases: 1973, 1975, 1988, 1998, and 1999. That is, shown in (a) are the differences in DJF SST and in the JJA winds following those DJFs; and (b) are the differences in MAM SST and in the JJA winds following those MAMs. Shown in (c) are the differences in SST and in winds (simultaneously) for the JJAs specified above. Contour intervals are 0.5 and the zero contours are highlighted. Values larger than 0.5 (smaller than −0.5) are shaded heavily (lightly).

ENSO influences the Asian monsoon in many ways (see details in Chapter 12). As discussed above, the tropical central eastern Pacific SST is closely linked to the Walker circulation, whose upward branch and associated zonal cell over the Indian Ocean are within the longitudes of the monsoon. The Walker circulation and the monsoon features, over land regions further north, are connected by a third element: the local Hadley cell, which also varies forcefully with time. Thus, if the Asian land mass were located closer to the equator, the dynamics of the ENSO–monsoon association could be much simpler.

Changes in the atmospheric circulation over the tropical western North Pacific provide another physical explanation of the impact of ENSO on the east–south-east Asian monsoon. As shown by Wang *et al.* (2000), an anomalous anticyclonic pattern appears over the south-east of the Philippine Sea as a Rossby wave response to the SST anomalies during El Niño years. This anomalous circulation pattern exerts a significant impact on the weather and climate in Asia. The dynamical coupling of the anticyclonic circulation and oceans maintains the anomalies of the atmosphere and oceans for a large part of the year. The above features identified by Wang *et al.* (2000) and further explained by Wang and Zhang (2002) can also be found in Figure 6.5 (see the anomalous anticyclonic pattern over the western North Pacific), in spite of a shift in location.

ENSO can also exert an impact on the Eurasian continent before the monsoon season and the anomalous land surface conditions in turn affect the following monsoon (Yasunari and Seki, 1992; Meehl, 1997; Yang and Lau, 1998). Experiments with general circulation models can clearly depict this 'indirect impact' of ENSO related SST on the monsoon (Yang and Lau, 1998). Discussions of the influence of land surface process on the Asian monsoon will be given later in Section 6.3.2 (also see Chapter 11).

A better understanding of the ENSO–monsoon relationship requires considerations of the annual cycles of both ENSO and the monsoon. From the boreal winter to summer, as ENSO signals decrease gradually, the monsoon strengthens rapidly. From summer to winter, ENSO and the monsoon evolve in ways opposite to those described above. The importance of these processes, in which the back and forth migration of the monsoon between Asia and Australia occurs, has been recognized by Webster and Yang (1992). These considerations suggest the importance of the transitional seasons. For example, spring can be a very unique season in understanding the ENSO–monsoon association. First, spring is a season of monsoon rapid growth and a season of ENSO initiation or termination. Second, the monsoon convection shifting from Australia to Asia overlaps the convection associated with the Walker circulation, a critical component of ENSO. Spring is also an important season for understanding the mechanism for the TBO (Meehl and Arblaster, 2002a,b), in which both the monsoon and ENSO related SST play critical roles.

6.3.1.2 Regional SSTs

The SSTs in the western Pacific and Indian Oceans and other coastal water domains are also believed to be important for the Asian monsoon. Although the variability of these regional SSTs is not necessarily always independent from ENSO, there is considerable evidence that the local SSTs often vary differently from the SST over the tropical central eastern Pacific on interannual timescales. However, the fluctuations of these SSTs usually exhibit complex patterns and are sometimes well correlated among various ocean domains. These features have caused tremendous difficulties in understanding the relationship between the Asian monsoon and the local oceans.

Regional SSTs influence the Asian monsoon through changes in surface heat and moisture fluxes, direct moisture supply, thermal difference between land and oceans, and wavetrains generated anomalous atmospheric heat sources, spurred by ocean–atmosphere interactions. A rise in SST enhances evaporation and the moisture supply and latent heating in the atmosphere. As a result, monsoon rainfall increases. On the other hand, warming in oceans reduces the summertime land–sea thermal contrast and therefore the intensity of the monsoon circulation. The latter addresses an issue about SST as a forcing for the monsoon through changes in horizontal temperature gradients. To assess the relative importance of local SST forcing and moisture supply effects, which seem to offset each other, the geographic locations and their sizes of SST anomaly are critical. The Asian monsoon is a broad climate system and is likely to be driven by SST anomalies over large oceanic regions. For this reason, the small coastal water domains selected in some early studies (e.g., Shukla, 1975; Washington *et al*., 1977) may not be effective in influencing the monsoon.

Observational studies on the relationship between the Indian Ocean SST and the Asian monsoon mostly focus on the correlative aspect of the relationship (e.g., Saha, 1970; Cadet and Diehl, 1984; Joseph *et al*., 1994; Clark *et al*., 2000a). For example, a positive relationship has been found between the Indian summer monsoon and the SST throughout the tropical Indian Ocean in the preceding autumn and winter. One of the main objectives of modeling studies in the 1990s is to understand whether the Indian Ocean provides important forcing for the Asian monsoon (e.g., Palmer *et al*., 1992; Chen and Yen, 1994; Latif *et al*., 1994; Nagai *et al*., 1995; Zhu and Houghton, 1996; Soman and Slingo, 1997; Arpe *et al*., 1998), although the skills of monsoon simulations change from one model to another (Sperber and Palmer, 1996; Kang *et al*., 2002). Model experiments have also focused on the mechanisms for the relationship between the Indian Ocean SST and the monsoon and on the association of this relationship with ENSO (e.g., Lau and Nath, 2000, 2003; Wu and Kirtman, 2004a). Recently, much effort has been devoted to the understanding of the SST dipole mode in the tropical Indian Ocean because it has been claimed to exert an impact on the Asian summer monsoon (Saji *et al*., 1999; Webster *et al*., 1999; Ashok

et al., 2001). However, this tropical dipole mode grows fast in summer and reaches a maximum amplitude in the autumn, and there exists evidence indicating that the Asian monsoon is one of the forcing mechanisms for the SST dipole (Li *et al.*, 2003). Yet other studies have found that the large-scale maximum variance of Indian Ocean SST does not appear in the regions associated with the dipole and that the SST variability associated with the dipole does not represent the most dominant mode of the Indian Ocean SST (e.g., Yoo *et al.*, 2005). The Asian monsoon has also been strongly linked to the SST of the southern Indian Ocean (e.g., Zhu and Houghton, 1996; Terray *et al.*, 2005; Yoo *et al.*, 2005) where large SST variability appears, including the subtropical SST dipole (Behera and Yamagata, 2001; Qian *et al.*, 2002a). In spite of the limited effort, the relationships of the Asian monsoon to the maximum variance and the most dominant modes of Indian Ocean SST have not been fully understood.

The SST over the tropical western Pacific Ocean often influences the variability of the subtropical western Pacific High, an important factor for regulating the weather and climate in east and south-east Asia. Numerous studies (Huang, 1984, 1985; Nitta, 1987; Huang and Sun, 1992; Lau and Peng, 1992; Nitta and Hu, 1996) have clearly shown that the convective activity, which is usually related to the anomalies of local SSTs, over the tropical western Pacific including the South China Sea and the Philippine Sea excites Rossby wavetrains that affect east–south-east Asia and other regions. It has been proposed that the impact of tropical western Pacific SST on the Asian monsoon is more significant during La Niña years than El Niño years (Soman and Slingo, 1997). According to Ailikun and Yasunari (2001), these SST anomalies persist from winter to late spring and further maintain the associated convective activity in the atmosphere until the early summer. These features of persistence explain the influence of precursory SST anomalies on the Asian summer monsoon and the memory effect on ENSO even after the monsoon season.

Figure 6.6 shows the impact of the tropical western Pacific SST on the climate anomalies in east–south-east Asia during the JJAs of 1993 and 1994. Presented in panels (a)–(c) are the patterns of difference in surface temperature, precipitation, and atmospheric circulation between two experiments that are forced, respectively, by the monthly global SST of 1994 and 1993 (Experiment-1994 minus Experiment-1993). The model used is the atmospheric general circulation model of the Seoul National University, Korea, which captures successfully many features observed in these fields. Compared with 1993, hot and dry conditions are found in east Asia for 1994. Associated with these features is a wavetrain in which an anomalous high emerges over northern–north-eastern China, Korea, and Japan, and anomalous lows appear to the northern and southern sides (Figure 6.6(c)). The features discussed above do not resemble the climate signals caused by ENSO. Shown in panels (d)–(f) of Figure 6.6 are the perturbations in the various fields forced by the difference in SST between 1994 and 1993 over the tropical western Pacific only (Figure 6.6(d)). Substantial similarities exist between (d)–(f) and (a)–(c) in east and south-east Asia, signifying that the SST anomalies over the tropical western Pacific may explain a considerable portion of the regional climate features during

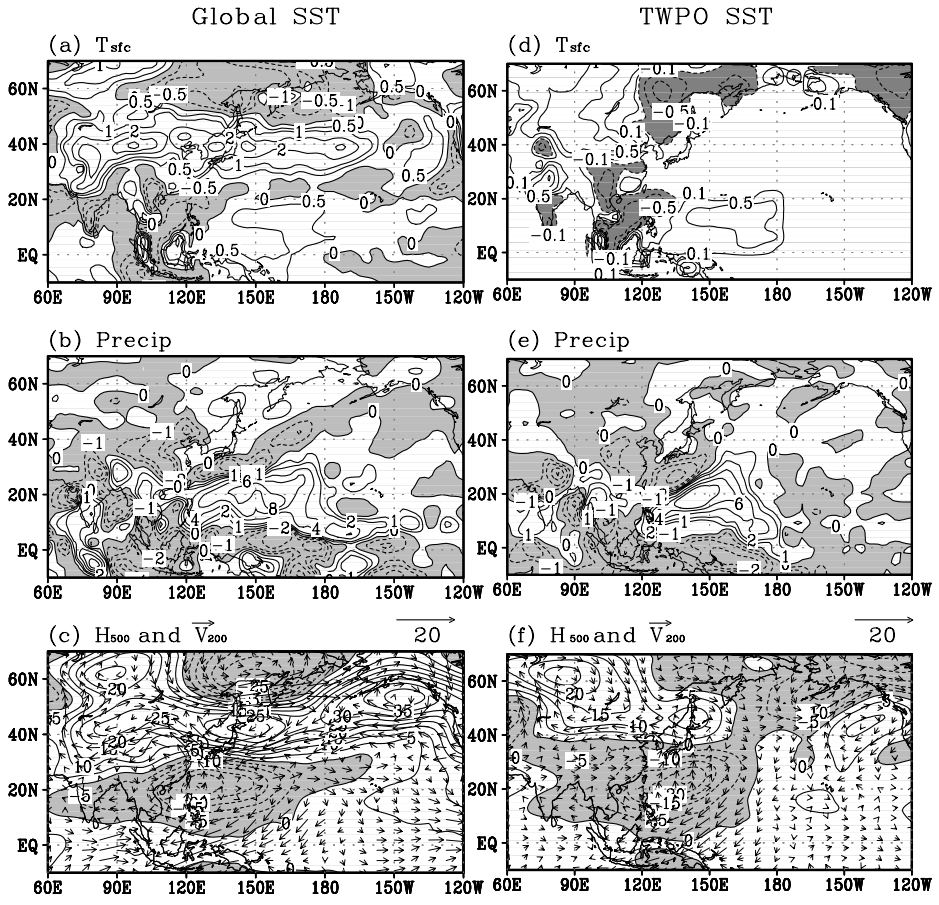

Figure 6.6. JJA differences (1994 minus 1993) in land–sea surface temperature, precipitation, 500-mb geopotential height, and 200-mb winds. Panels (a)–(c) show the differences between two experiments in which the model is forced by the monthly SSTs observed in 1994 and 1993. In the two experiments for (d)–(f), SST observed values of 1994 and 1993 are used, respectively, for the tropical western Pacific but monthly climatological SSTs are applied elsewhere. There are five ensemble members for all experiments. Negative values of temperature, precipitation, and geopotential height are shaded.
Modified from Yoo *et al.* (2004).

the two summers. For this particular case, the experiment forced by the SST anomalies over the extratropical Pacific yields features significantly different from the observed, indicating that the extratropical SST does not play a major role in explaining the climate anomalies examined (figures not shown; see Yoo *et al.* (2004) for more details). However, additional experiments in which the atmospheric model is coupled with an oceanic mixed layer model indicate that the ocean–atmosphere coupling in the extratropical Pacific Ocean are important for improving the simulations of the climate over east Asia.

6.3.2 Land surface process

Land surface process affects the Asian monsoon in a very complex way because the interaction between the atmosphere and land surface involves complicated coupling of hydrologic and energy cycles. As shown in the left-hand portion of Figure 6.7, an increase in soil moisture enhances evaporation, which moistens and destabilizes the atmospheric boundary layer and causes the growth of atmospheric convection and precipitation. The release of associated latent heat warms the troposphere, leads to low-level moisture convergence, and further intensifies precipitation. Thus, this local process involves a positive feedback of the hydrologic cycle of the atmosphere and land surface.

The evaporation due to increased soil moisture also cools the land surface directly and leads to highly reflective clouds (because of the increase in evaporation-related convection), which in turn cool the land surface as well. The cooling of land reduces the thermal contrast between the land and the oceans and weakens the monsoon circulation and thus moisture supply. NF2 (negative feedback 2) shown in the center of Figure 6.7 illustrates this process, which is reinforced by the sensible heat flux and long-wave emission from the land surface as indicated by NF1 (negative feedback 1) in the figure.

Snow cover may have an important effect on the interannaul variability of the

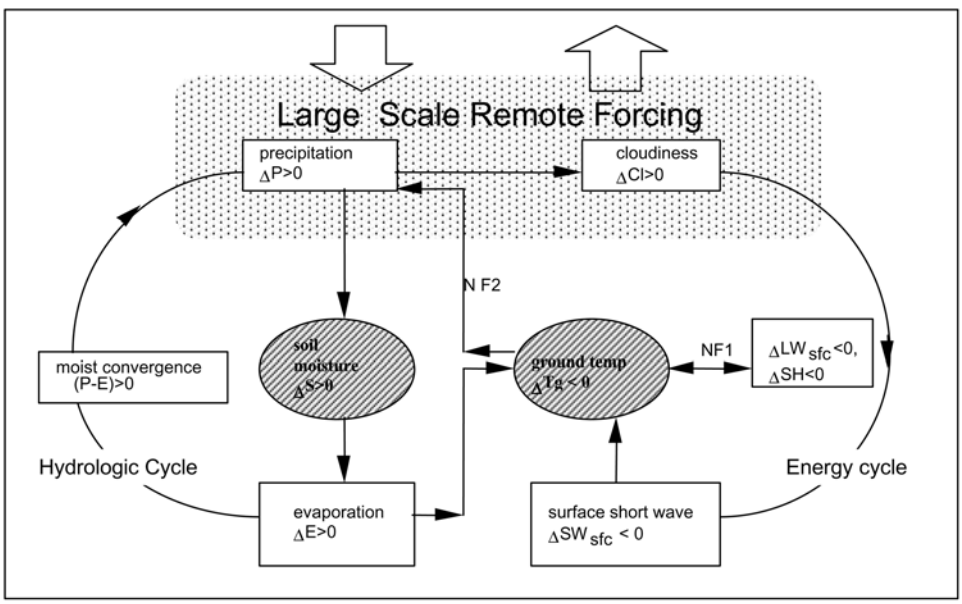

Figure 6.7. Schematic diagram showing the fast response of the hydrologic and energy cycles and the influence of large-scale circulation induced by slowly varying forcing in the atmosphere–land coupling over the east Asian monsoon region. See text for more details.
From Lau and Bua (1998).

monsoon because of its ability to alter the surface albedo and to regulate soil moisture (Hahn and Shukla, 1976; Barnett *et al*., 1989; Yasunari *et al*., 1991; Zwier, 1993; Vernekar *et al*., 1995; Sankar-Rao *et al*., 1996; Shen *et al*., 1998; Bamzai and Shukla, 1999; Kripalani *et al*., 2003). Signals of snow and soil moisture variability are often characterized by a feature of persistence. Because snow cover persists from winter through late spring, proving additional memory to the overlying atmosphere, it is one of the first predictors applied in the seasonal forecast of the Indian monsoon (Blanford, 1884; Normand, 1953), which may be among the earliest seasonal predictions of the Earth's climate. The major feature of the snow–monsoon connection is a generally negative relationship: the Indian summer monsoon is weaker (stronger) than normal following more (less) extensive snow cover in Eurasia. However, the relationship differs in other Asian regions (Lau and Li, 1984; Yang and Xu, 1994; Wu and Qian, 2003). For example, following more extensive snow over Eurasia, summer rainfall decreases in central China but increases more significantly in northern and southern China (Yang and Xu, 1994). This result also implies an in-phase relationship between the variations of summer rainfall over India and central China (see Kripalani and Kulkarni, 2001), and suggests a positive–negative–positive (or opposite) pattern of rainfall variability over northern, central, and southern China. Recent studies have also identified localized regions of Eurasia where snow variations have an impact on the subsequent monsoon. In particular, the wintertime snow depth variations over western (eastern) Eurasia are negatively (positively) related to the monsoon over south Asia (Kripalani and Kulkarni, 1999). Furthermore, high lands such as the Tibetan Plateau are often covered by snow in the cold seasons and their role in the Asian monsoon is an important issue in monsoon studies (Luo and Yanai, 1984; He *et al*., 1987; and Li and Yanai, 1996).

Figure 6.7 also indicates that the atmosphere–land coupling is affected by remote forcing such as ENSO (see the large arrows in the figure). ENSO affects monsoon precipitation and radiation directly through large-scale forced descending and ascending motions over the monsoon region. It also causes changes in land surface conditions, whose persistence influences the following monsoon, before the monsoon season. Based on experiments with a general circulation model, Yang and Lau (1998) depict clearly the process in which ENSO produces antecedent signals in the Eurasian continent in winter and spring. These land surface anomalies in turn affect the development and intensity of the Asian monsoon. This feature, also discussed by Yasunari and Seki (1992) and Meehl (1997) using observational data, is referred to as the SST's indirect impact on the monsoon.

The study of Yang and Lau (1998) reveals several other important features. First, the impact of snow and soil moisture on the Asian monsoon mainly occurs over the tropical land portion and coastal water domains (Figure 6.8(a)). This is different from the impact of SST, which causes changes in a more extensive scale, especially over oceans (see figures 9 and 12 in Yang and Lau). Second, land surface processes mainly influence the monsoon in May and June (Figure 6.8(b)), but less significantly during July–September (not shown). In addition, compared with SST, land surface processes exert a relatively weaker impact on the tropical Asian

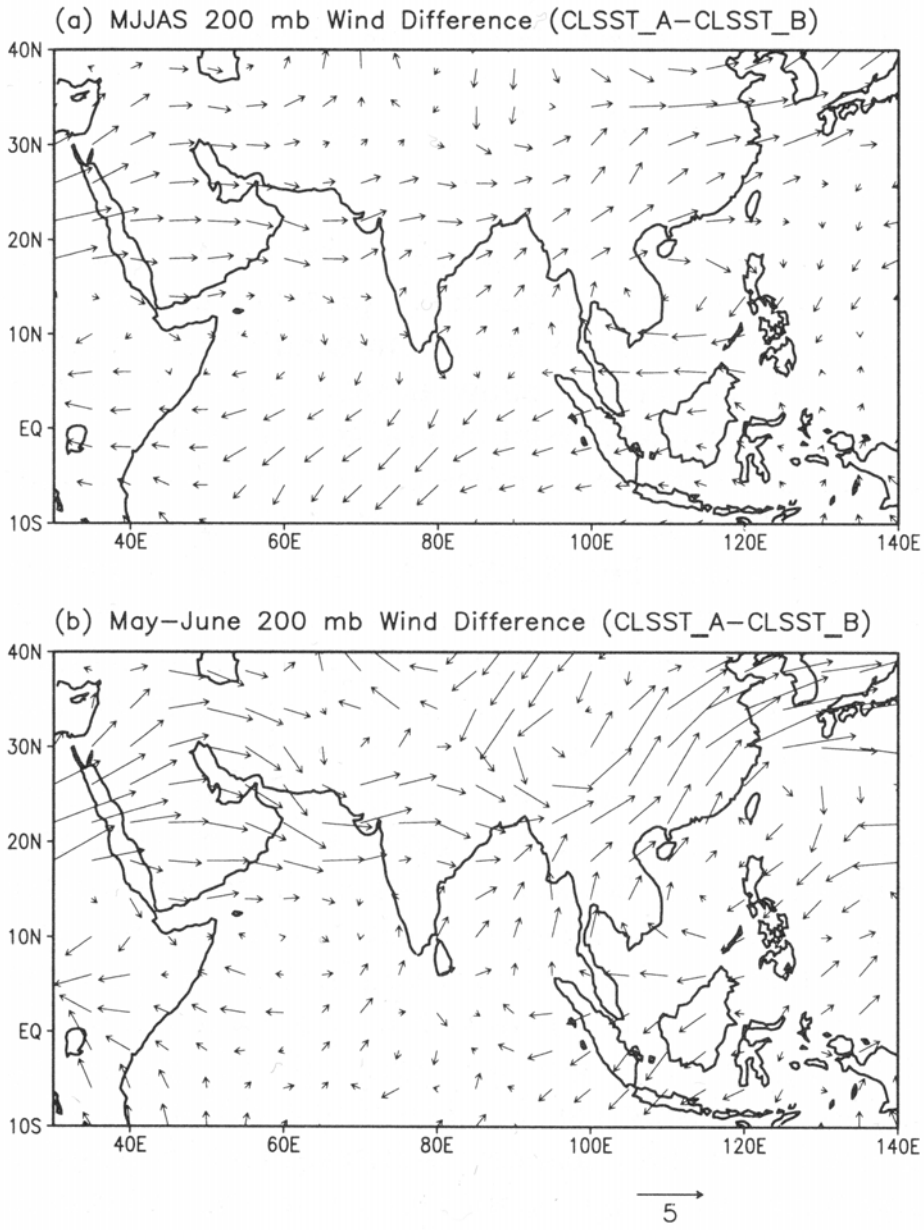

Figure 6.8. (a) Pattern of differences in May–September 200-mb winds between experiment A and experiment B (A minus B) with a NASA general circulation model. In both A and B the model is forced by monthly SST climatology. However, while the atmosphere and land surface are interactive in B, the soil moisture and snow from an AMIP-type experiment (forced by observed monthly SST) are used in A. (b) Same as (a) but for May and June only.
From Yang and Lau (1998).

monsoon, which is consistent with the result obtained by Koster and Suarez (1995) and Xue *et al.* (1996) who found that over relatively wet (dry) areas, SST (land surface process) affects the climate more significantly.

Compared with SST, soil moisture has a shorter memory. Thus, it is generally more difficult to explain the persistence of atmospheric perturbation caused by land surface processes. However, as emphasized by Yang *et al.* (2004), the interaction between land surface and the overlying atmosphere and the relationship between land surface processes and large-scale climate phenomena can prolong the signals in the coupled atmosphere–land system.

6.3.3 Basic flow and broad-scale climate phenomena

The relationship between monsoon and ocean–atmosphere interaction, or land–atmosphere interaction, is also determined by the directions of the basic flow. For example, a SST-generated wind anomaly that intensifies the total wind under a westerly basic flow background will weaken the total wind if the basic state is an easterly flow. The ocean–atmosphere interaction under westerly and easterly basic flow conditions exerts different impacts on the variability of the monsoon (see further discussions in Section 6.4). Also, during the cold seasons, the basic flow over subtropical–extratropical Asia is a westerly wind, and a cooling in the extratropics resulted from extensive snow increases the meridional temperature gradient and thus intensifies the basic flow in the subtropics. As discussed above, a prolonged maintenance of these processes, which is usually characterized by a frequent southward intrusion of cold air from higher latitudes, influences the development of the Asian monsoon.

There is now emerging evidence suggesting that the Asian summer monsoon is also linked to the North Atlantic Oscillation (NAO) and the Arctic Oscillation (AO), as discussed by Yasunari and Seki (1992), Chang *et al.* (2001a), Gong and Ho (2003), and Yang *et al.* (2004). Within this context, several features can be seen from Figure 6.9, which show the difference in DJF U200 before strong and weak W–Y index. First, over the eastern Pacific, a wavetrain emanates from the equator and extends into North America. This feature mimics that shown in the composite pattern of U200 based on Niño 3.4 SST (figure not presented), indicating a relationship between the Asian monsoon and ENSO. Second, an increase in westerlies appears over east Asia in the latitude band of 25°–48°N, associated with the decreases in the winds to the north and the south, and is linked to the changes in the westerlies over the extratropical North Pacific. Clearly, these features over east Asia and the western Pacific are closely related to the variability of the east Asian jet stream, especially its east–west shift, and thus imply a relationship between the monsoon and the jet stream. Third, a clear wavetrain pattern emerges from the eastern Atlantic and western European–African region, which seems to be associated with the AO and the NAO. More interestingly, another wavetrain appears to the east and south-east of the above-mentioned pattern, extending from western Europe, the Mediterranean Sea, and the Middle East, to the western Arabian Sea. It seems to be a subset of the AO and the NAO related pattern. However, the key characteristic

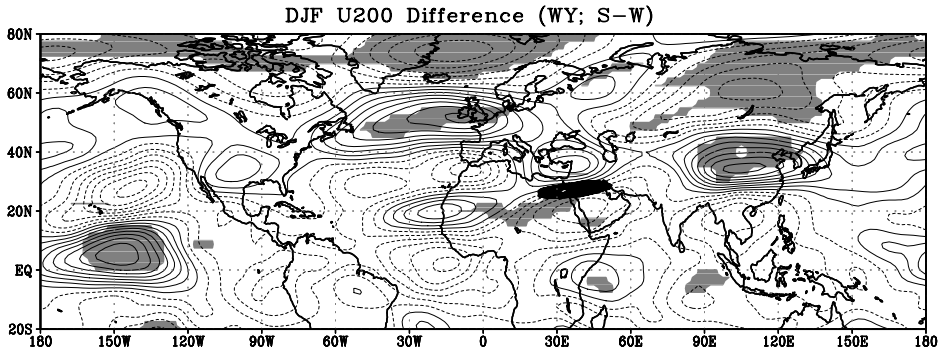

Figure 6.9. Difference in the previous DJF U200 (ms^{-1}) between a strong (1970, 1981, 1984–1985, 1990, 1994, 1999, and 2001) and a weak (1972, 1974, 1979, 1983, 1987, 1992, 1995–1997) Asian monsoon in the summer. The darkly shaded portion near Egypt indicates the climatological location of the Middle East jet stream. Significant values exceeding the 90% confidence level are shaded.
Modified from Yang *et al.* (2004).

here is the south-east–north-west shift of the Middle East jet stream, which is located climatologically over northern Egypt and Saudi Arabia, as highlighted by the heavily shaded area in Figure 6.9. More discussions about the relationship between this jet stream and the following Asian summer monsoon can be found in Yang *et al.* (2004).

6.4 TROPOSPHERIC BIENNIAL OSCILLATION AND THE MONSOON

A unique component of the interannual variability of the Asian monsoon is its pronounced biennial tendency. The tropospheric biennial oscillation (TBO) should be distinguished from the stratospheric quasibiennial oscillation (QBO; Reed *et al.*, 1961). Here, it refers to the variability in the coupled system of tropospheric atmosphere, land, and oceans in the region of Asia–Australia and the Indian and western Pacific Oceans on the quasibiennial timescale.

Strong TBO signals exhibit in the variability of both precipitation and circulation of the Asian monsoon (e.g., Mooley and Parthasarathy, 1984; Meehl, 1987; Lau and Sheu, 1988; Yasunari, 1990; Ropelewski *et al.*, 1992; Shen and Lau, 1995; Webster *et al.*, 1998; Li *et al.*, 2001a; Li and Zhang, 2002). TBO signals also exhibit in the relationship between the Asian monsoon and other climate phenomena such as ENSO and snow (Shukla and Paolino, 1983; Yasunari, 1990; Lau and Yang, 1996a,b; Kripalani and Kulkarni, 1999). Figure 6.10 presents the correlation between the June–September AIMR and monthly SST along 5°N–5°S, and between the monsoon rainfall and monthly surface winds along 6°N–6°S, before and after the monsoon period. It can be

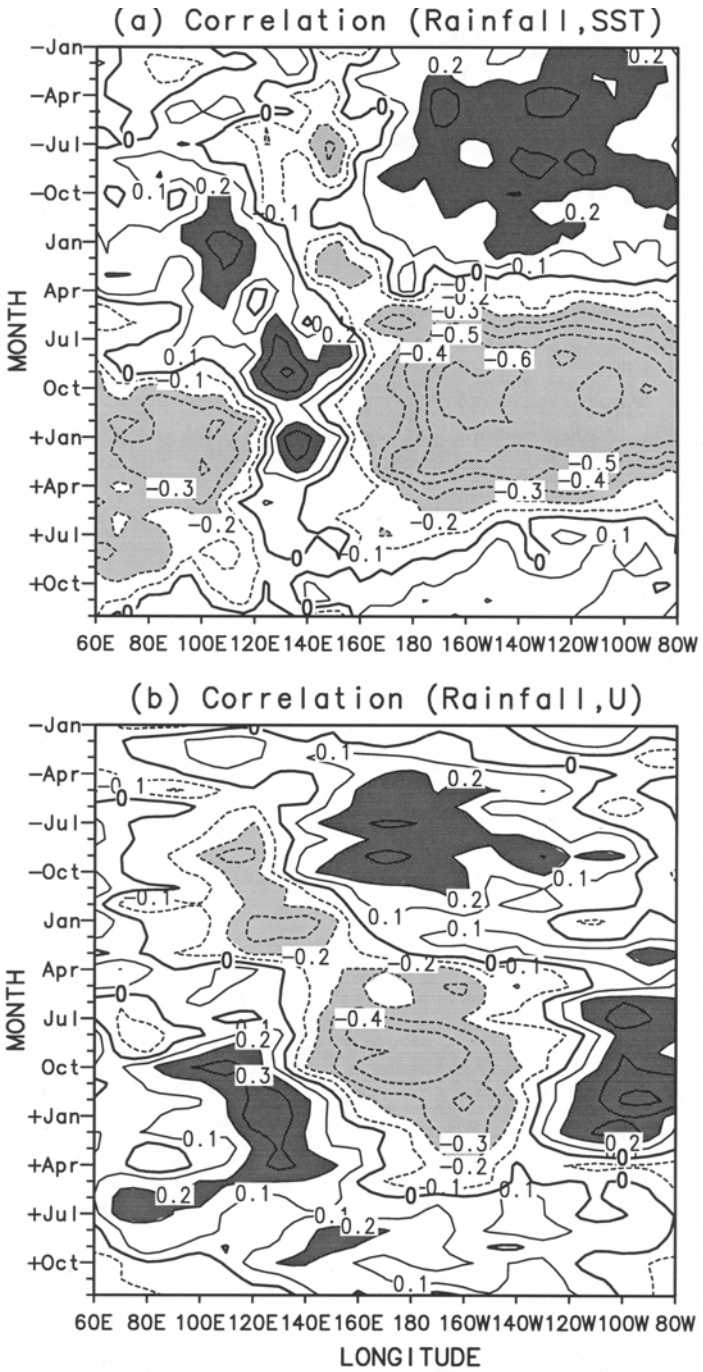

Figure 6.10. Lag correlation of Indian summer monsoon rainfall with (a) SST along 5°S–5°N and (b) surface winds along 6°S–6°N of different months.
From Lau and Yang (1996b).

found that values of opposite signs usually appear between the equatorial Pacific Ocean and the longitudinal band including the eastern Indian Ocean and the Maritime Continent (see features along the x-coordinate). TBO features appear as indicated by the reversal of the signs of correlation on quasibiennial timescale (see features along the y-coordinate).

Understanding the TBO in the Asian–Australian, the Pacific Ocean, and the Indian Ocean sector often relies on the knowledge of the variations of Asian–Australian monsoons, ENSO, and Indo-Pacific SST as well as the transitions of these phenomena with seasons and geographic locations. The existing theories on the TBO emphasize the importance of the following three aspects of ocean–atmosphere–land coupling: (a) local air–sea interaction (Brier, 1978; Nicholls, 1978; Meehl, 1987; Clarke *et al*., 1998), (b) remote ocean–atmosphere interaction (Meehl, 1987; Chang and Li, 2000; Kim and Lau, 2001; Li *et al*., 2001b), and (c) tropical–extratropical teleconnection (Yasunari and Seki, 1992; Meehl, 1994a, 1997; Tomita and Yasunari, 1996; Ogasawara *et al*., 1999). Here, we discuss some major features of the TBO especially those closely related to monsoon variability. For a more comprehensive review of the theories for the TBO, readers should refer to Li *et al*. (2001c).

(a) The local air–sea interaction theory emphasizes the importance of the basic flow and the interactive processes of atmospheric and oceanic anomalies (see Nicholls, 1978). A westerly anomaly superimposed on the westerly basic flow intensifies the total wind and cools the ocean, as in the case of the winter season. By the same argument, the westerly anomaly weakens the easterly basic flow and warms the upper ocean in summertime. The later change in the atmosphere associated with these changes is considered a delayed feedback of the SST anomaly. It is understood that the time delay between SST forcing and atmospheric response is necessary for the transition of the biennial oscillation from one year to the next. On the other hand, Meehl (1987, 1993) stressed the importance of *initial* SST anomalies in explaining the TBO. A positive SST anomaly in tropical oceans enhances local convective activity, and the enhanced convection leads to stronger winds, which cool the upper ocean through the processes of evaporation and ocean vertical mixing. In turn, the negative SST anomaly leads to weaker convection in the atmosphere. Later, a similar idea of explaining the TBO is proposed with an emphasis on the interaction between the atmosphere and land surface processes (Meehl, 1997). In this atmosphere–land mechanism, soil moisture is treated as an analogue of SST. Figure 6.11 schematically illustrates the scenarios for both the atmosphere–ocean (Figure 6.11(a)) and atmosphere–land (Figure 6.11(b)) interactions, starting from the upper central panels, with conditions of the first year on the left-hand side and second year on the right-hand side.

(b) One of the prominent features of the Asian–Australian monsoon system is that monsoon convection migrates from northern Australia to southern Asia from boreal winter to summer, and moves in an opposite direction from summer to winter. In this migrating process, a strong (weak) Asian monsoon is followed by a strong (weak) Australian monsoon, although it is more difficult to establish a link from the Australian monsoon to the Asian monsoon (Meehl, 1987; Gregory, 1991; Joseph *et al*., 1991; Matsumoto, 1992; Hung *et al*., 2004). To explain the quasibien-

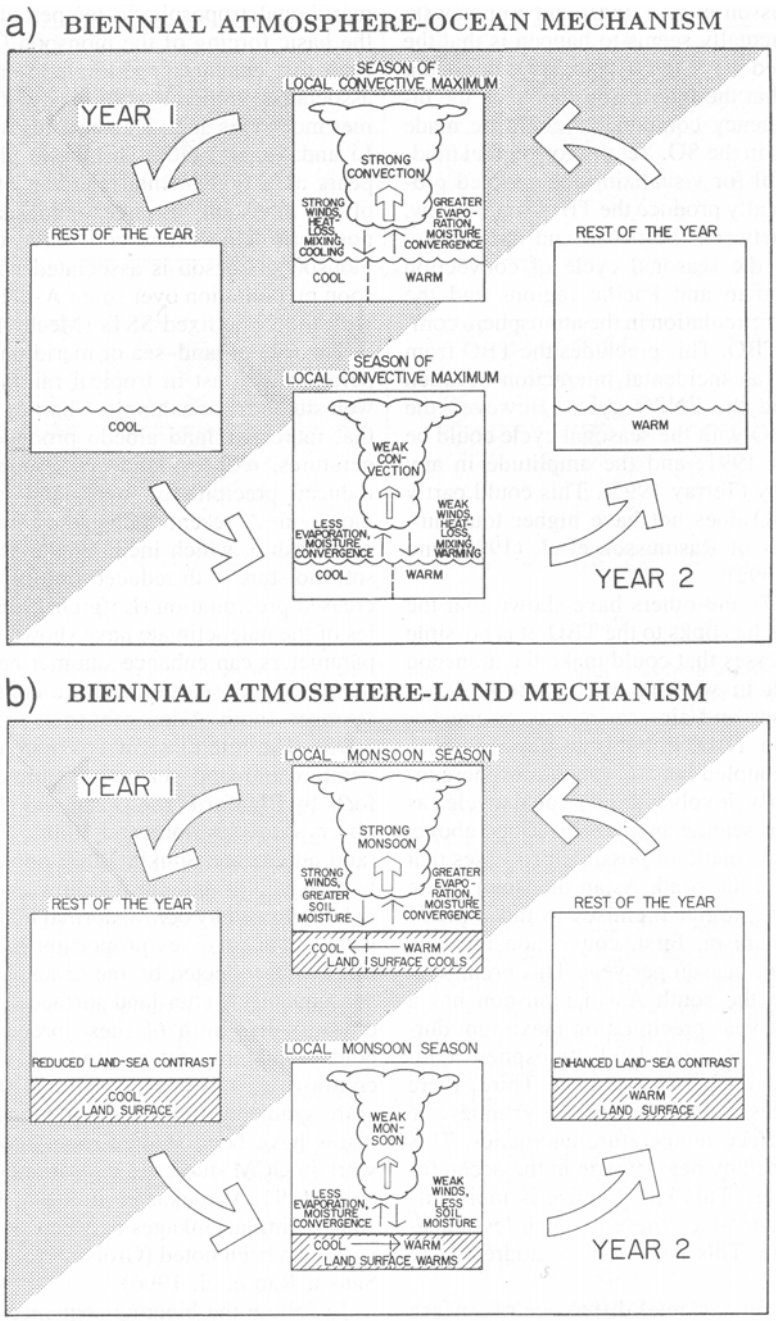

Figure 6.11. (a) Schematic illustration of an ocean–atmosphere mechanism for the TBO. (b) Same as (a) but for a land–atmosphere mechanism in which soil moisture acts like SST. From Meehl (1997).

nial feature of the monsoon transition between Asia and Australia, Meehl (1987) proposed a remote-forcing mechanism emphasizing the importance of eastern Pacific SST for the large-scale east–west circulation and the Asian monsoon. Within this remote ocean–atmosphere interaction mechanism, the south-eastward migration of a strong Asian monsoon through Australia weakens the South Pacific High and thus the trade winds. This increases the eastern Pacific SST and decreases the zonal SST gradient and the east–west atmospheric cell across the tropical Pacific. As a result of the diminished ascending motion over the far western Pacific, the following Asian monsoon appears weaker.

From a different approach, Chang and Li (2000) put forward a multiocean domain interactive mechanism with a specific emphasis on the role of the Asian monsoon and the Indian Ocean (Figure 6.12, color section). The authors started the scenario from a warm Indian Ocean (see the central top of Figure 6.12 – left of the ribbon) and assumed that the warm ocean anomaly leads to a strong Asian monsoon because of the increase in water vapor supply. The strong monsoon induces strong westerlies over the Indian Ocean and intensifies the east–west circulation over the Pacific. (The key difference between this mechanism and Meehl's mechanism discussed above seems to be that the latter emphasizes the role of eastern Pacific SST while the former puts more emphasis on the Asian monsoon.) Because of the intensifying westerlies, negative SST anomalies appear in the Indian Ocean whose persistence favors a weak monsoon in the coming year. However, this mechanism also emphasizes the importance of the increase in western Pacific SST, which is caused by the deepening ocean thermocline due to the strong east–west circulation, because it favors a strong Australian monsoon later (see the central bottom section of Figure 6.12). In addition, the strong trade winds over the Pacific decrease the eastern Pacific SST, which helps maintain the western Pacific warming through easterly anomalies and the shoaling of the thermocline. The reversed phase, starting from a cold SST in the Indian Ocean, is shown on the upper right-hand side of the ribbon.

(c) Tropical SST and extratropical land surface processes exert not only a local but also a remote effect on the atmospheric process associated with the TBO. This notion leads to the tropical–extratropical teleconnection mechanism (Meehl, 1997), which is introduced to emphasize the importance of the response of the extratropical atmosphere to tropical forcing for the TBO. The response of extratropical atmospheric circulation causes anomalies in the land surface temperature, which affects the onset and intensity of the Asian summer monsoon. According to Ogasawara *et al.* (1999), the convective activity around Indonesia and northern Australia is the main tropical forcing and the anomalous atmospheric circulation over Asia is a direct Rossby wave response to the tropical heating. This mechanism, in which the persistence of land surface signals from one season to another is a key issue, is supported by a number of observational and modeling analyses. For example, during the boreal winter, more active convection over Indonesia and northern Australia leads to a stronger east Asian westerly jet stream (Yang and Webster, 1990), which is accompanied by colder weather and climates in east Asia (Yang *et al.*, 2002). Favorable interactions between the atmosphere and land surface process prolongs the

anomalies of the coupled atmosphere–land system (e.g., Yang *et al.*, 1996; Yang and Lau, 1998; Yang *et al.*, 2004).

In brief, the variability of the Asian–Australian monsoons and its relationships with other processes of the coupled tropical ocean–atmosphere–land system are characterized by strong biennial features. Discussions of the TBO usually underline the important roles of the monsoons, the Indian Ocean and Pacific SSTs, and Asian land surface conditions (also see Loschnigg *et al.*, 2003; Meehl *et al.*, 2003; Yu *et al.*, 2003; Wu and Kirtman, 2004b), although the role of the land surface process is not emphasized by some models. Figure 6.13 shows an idealized consequence of the major features of the mechanisms for TBO discussed above. Starting with DJF (Figure 6.13(a)) of a weak Australian monsoon, warm SSTs appear in the Indian and central eastern Pacific Oceans while cold SSTs appear to the north of Australia. This SST distribution and related changes in the overlying east–west cells resemble the conditions of El Niño events. Under these circumstances, the Eurasian continent is characterized by less snow and warmer conditions as a result of an atmospheric Rossby wave response to the tropical heating. In the following MAM (Figure 6.13(b)) when a transition from DJF to JJA occurs, many of the above signals in the coupled ocean–atmosphere–land system persist because of the memories in the SST and the associated thermocline conditions (see more detailed discussion by Meehl and Arblaster (2002b)). As a consequence, the summer monsoon rainfall increases over south Asia and the dynamically consistent changes in the zonal circulation are similar to the La Niña conditions (Figure 6.13(c)). Because of these, the Eurasian land surface is cool (because of heavy rainfall) and SST decreases in the Indian and central Pacific oceans and increases in the western Pacific (consistent with the anomalous atmospheric circulation). The above summertime features are largely maintained to the coming SON (Figure 6.13(d)) owing to the strong zonal cells and coupled wind–ocean response from the previous seasons. The above conditions lead to a strong Australian monsoon in the next DJF (Figure 6.13(e)). The strong convection associated with the Australian monsoon and weak convection over the western Indian Ocean and the central Pacific contribute an anomalous trough and cold land temperature over Eurasia (as a Rossby wave response), which are followed by a weak south Asian monsoon in summer.

Difficulties in fully understanding the relationship between the TBO and monsoon arise at least partially from the lack of understanding the internal and external features of the TBO. The TBO in Asia, Australia, and the adjacent tropical regions can perhaps be considered an inherent mode of the monsoon itself. However, the variability of SST in the tropical central Pacific, which is commonly used to measure ENSO and generally considered to be coupled with the Asian–Australian monsoon, is also characterized by a quasibiennial signal. The dynamical processes for the TBO and lower frequency (3–7 years) components of ENSO are different (Li *et al.*, 2001a) and how these components interact with each other is not fully clear. It is even more difficult to understand the relationship between the internal monsoon characteristics and the 'external' ENSO features of the TBO, which may be a phenomenon arising from the interaction between the annual and ENSO cycles (e.g., Goswami, 1995). Whether to treat the TBO as

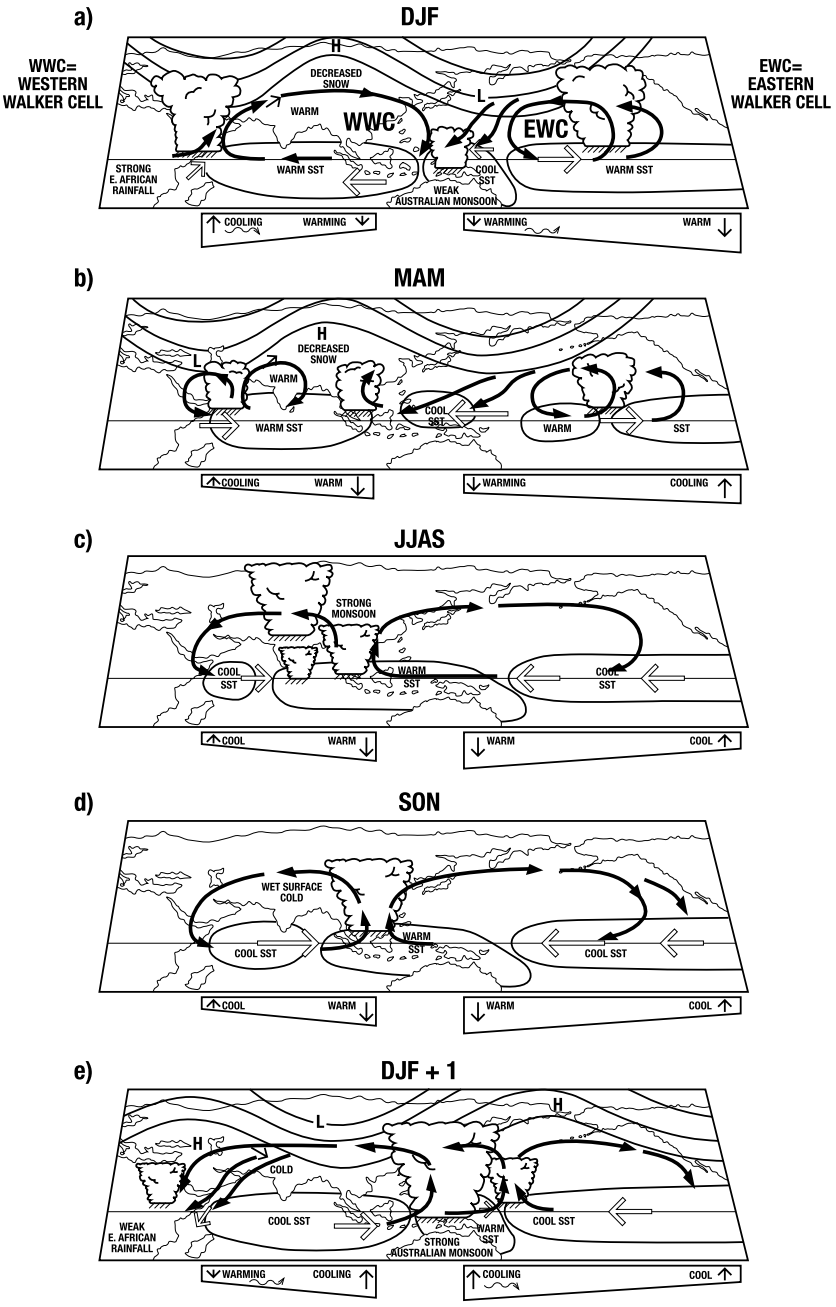

Figure 6.13. Schematic diagram illustrating the TBO features associated with anomalies of convective activity, SST, surface winds, extratropical circulation, and equatorial Indian and Pacific Ocean thermocline orientations. See text for details.
From Meehl and Arblaster (2002b).

an internal or external mode will substantially affect the approach of studying the TBO–monsoon relationship.

6.5 MONSOON AND GLOBAL CLIMATE VARIABILITY

6.5.1 Role of the monsoon in ENSO and atmospheric teleconnection

As discussed above, the Asian monsoon varies significantly from one year to another, and to a certain extent, this variability is accounted for by slowly varying surface forcing. On the other hand, the giant monsoon system also plays an important role in affecting the weather and climate in many regions of the World. It has long been understood that the variability of the Indian summer monsoon can lead to changes in the Southern Oscillation (see Normand, 1953). In particular, Shukla and Paolino (1983) showed that large anomalies of pressure in Darwin, Australia, occur during and after, rather than before, the monsoon season. Within this scope, numerous studies have attempted to identify signals in the monsoon region that are prior to ENSO events. For example, Xu and Chan (2001) indicated that the Asian–Australian monsoon system affects the onset time of El Niño events. Model simulations have also demonstrated the impact of monsoon on ENSO (Wainer and Webster, 1996; Kirtman and Shukla, 2000; Wu and Kirtman, 2003b). The importance of the monsoon in forcing ENSO can be seen from the discussions in which the monsoon is considered an active part in the TBO as well (Section 6.4).

The influence of the Asian monsoon on ENSO can be understood from the strong interaction between the westerlies over the tropical Indian Ocean and the trade winds over the Pacific Ocean (Barnett, 1984a; Webster and Yang, 1992), because the westerlies are closely related to the monsoon and the trade winds are generally linked to ENSO. Such a feature has also been suggested by Figure 6.10, which links the monsoon to both Indian Ocean westerlies and ENSO. General circulation models and simple climate models have shown that monsoon related forcing in the wind and heat flux leads to changes in the intensity and phase of the ENSO cycle (Wainer and Webster, 1996; Chung and Nigam, 1999; Kirtman and Shukla, 2000; Kim and Lau, 2001; Wu and Kirtman, 2003b). There exist also indications that the precursory signals of ENSO exist in the Eurasian continent (Barnett *et al.*, 1989). It is even claimed that strong and persistent activities of the east Asian winter monsoon may trigger or terminate ENSO events (e.g., Li, 1990). Recently, it has been shown that the degree of coupling from the Asian monsoon to ENSO changed around the middle of the 1970s (Kinter *et al.*, 2002) but that from ENSO to the monsoon did not change significantly (Miyakoda *et al.*, 2003).

As showed by Yasunari (1990), the changes in the Asian monsoon are significantly correlated with subsequent ENSO signals shown in SST, ocean subsurface temperature, and tropical east–west circulation. Although the results are mainly based on linear correlation analysis and often exhibit a quasibiennial behavior, a

scenario starting from the monsoon consists of a sound sequence of the physical processes of monsoon and ENSO evolutions. Within this context, Yasunari and Seki (1992) provided further evidence arguing for the important role of the Asian monsoon in leading to the zonal asymmetry in the tropical circulation (see Krishnamurti, 1971b; Krishnamurti *et al.*, 1973a) and in triggering ENSO events. The authors argued that the monsoon, through its interaction with the extratropical land–atmosphere process, and the NAO excite variability in ENSO, at least the biennial feature, and suggested that the irregular ENSO cycle may result from the interaction between the monsoon related coupled ocean–atmosphere system and the NAO. The above observational features have been better explained recently by Wu and Kirtman (2003b) whose modeling study shows that the monsoon variability unrelated to ENSO induces noticeable SST anomalies in the equatorial central Pacific in the following winter. A strong (weak) monsoon leads to cold (warm) SST anomalies. The impact of the monsoon on ENSO is manifested in the change of surface zonal wind stress.

The heating associated with the Asian summer monsoon is also linked to the variability of westerly jet streams in the southern hemisphere winter (Yang and Webster, 1990) and the climate signals in Africa and Europe, which may not necessarily be part of ENSO signals. The mid-latitude westerly jet streams during the northern hemisphere summer are also believed to play an important role in linking the climate anomalies in different locations through the associated teleconnection patterns, although they become weakened significantly from winter to summer (Lu *et al.*, 2002; Enomoto *et al.*, 2003). The large vorticity gradients associated with the jet streams generate a waveguide with limited meridional dimension and confine wave activity in a relatively narrow zonal band so that it can be transported downstream a long distance before being dispersed (Hoskins and Ambrizzi, 1993). For the tropics and subtropics, Yang *et al.* (1992), Webster *et al.* (1992), Webster *et al.* (1998), and Chen (2003) have emphasized the importance of the lateral component of the Asian monsoon in which a strong sinking motion affects the African monsoon and climate over the Sahara desert. While the equatorward portion of the subtropical western Pacific High to the east of the Asian monsoon can be viewed as the Kelvin wave response to monsoon heating, Rossby wave response is believed to lead to decent motions and explain the Mediterranean-type climate to the west of the monsoon heating (Rodwell and Hoskins, 1996, 2001). On longer timescales, the cause of decadal climate change over the North Atlantic Ocean may also be found in the Indo-Pacific sector (Hoerling *et al.*, 2001).

6.5.2 Asian monsoon and Pacific–American climate

It is known that the anomalies in the western tropical Pacific SST and its associated atmospheric heating generate atmospheric wavetrains that affect east Asia, the North Pacific, and North America (e.g., Huang, 1984, 1985; Nitta, 1987; Lau and Peng, 1992). Many climate anomalies in North America may have their origins in the

variability of western Pacific SST (e.g., Trenberth *et al.*, 1990) and Eurasian snow cover (e.g., Cohen *et al.*, 2001).

Yang *et al.* (2002) have recently established a relationship between the wintertime climate in east Asia and North America through the variability of the east Asian westerly jet stream. They have shown that the changes in surface temperature and precipitation in the two regions can be explained by the fluctuations of the jet stream and associated stationary waves. When the jet stream is strong, cold and dry climates appear in east Asia. In the meantime, while precipitation generally decreases in the USA, surface temperature decreases in the east but increases in the west of the country (see figure 11 in Yang *et al.*, 2002). We depict this teleconnection pattern and its potential source in Figure 6.14 by showing the 3-D flux of stationary wave activity (see Plumb, 1985; Yang and Gutowski, 1994). The figure indicates that a stronger jet stream is associated with a stronger source (vertical component) over east Asia and larger eastward energy propagation. When the snow cover in the Asian continent is more extensive and the meridional temperature gradient between the tropical western Pacific and the extratropical land and oceans to the north is larger in the previous autumn season, the jet stream intensifies in winter. The variability of the atmosphere over east Asia, the North Pacific, and North America shows features coupled with the variations of North Pacific SST. In fact, the changes in the jet stream, the underlying SST, and the climate of east Asia and North America are represented clearly by the second most dominant EOF mode of the tropical–extratropical atmosphere and oceans. These changes are not necessarily influenced by ENSO, which is generally associated with the first EOF mode of interannual variability of the atmosphere and oceans in the Asian–Pacific–American sector.

Although the active role of the Asian monsoon in global climate was noticed a long time ago, it is only until recently that the relationship between summer rainfall over China and the USA has been demonstrated explicitly (Lau and Weng, 2002; Lau *et al.*, 2004; Lau *et al.*, 2005; Li *et al.*, 2005; Zhang *et al.*, 2005). For example, the drought in central eastern China (the Yangtze River basin) together with the wet conditions to the north and south, one of the typical climate patterns in China, is associated with the deficit rainfall in eastern–south-eastern USA (Lau and Weng, 2002; see their figure 6). The climate patterns between the two regions are linked by atmospheric teleconnection with pronounced signals in the extratropical Pacific SST.

Figures 6.15 and 6.16 show the two most dominant modes that link rainfall variability over east Asia and North America to SST and atmospheric circulation patterns. The singular value decomposition analysis of rainfall over the USA and 500-mb geopotential height indicates that the most dominant mode (the first mode) is associated with a relatively zonally elongated pattern in the atmosphere (Figure 6.15(a)). The related pattern of 200-mb velocity potential and divergent winds (Figure 6.15(b)) exhibits a wavenumber one structure, reflecting the fluctuation of the Walker circulation driven by the heat source over the western Pacific and the Maritime Continent. The associated SST pattern also signifies a zonal structure in the North Pacific (see Lau and Weng, 2002). This teleconnection associated with the first mode links rainfall anomalies of the same sign over Japan, western Canada, and the northern Great Plains and the Midwest of the USA, and is referred to as

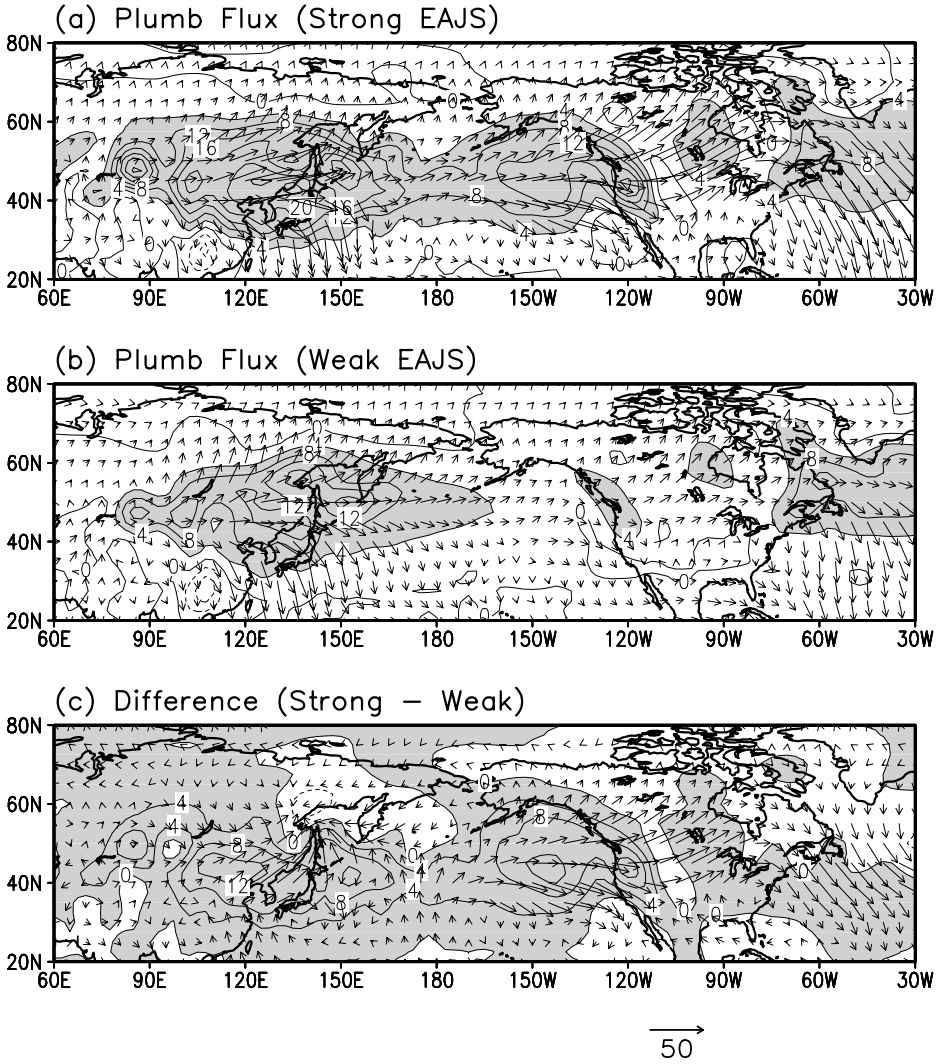

Figure 6.14. DJF stationary wave activity flux for (a) a strong east Asian jet stream, (b) a weak jet stream, and (c) the difference between the strong and weak jet streams. The vectors ($m^2\,s^{-2}$) and contours ($\times 10^4\,m^2\,s^{-2}$) represent the horizontal component at 300 mb and vertical component at 850 mb (with values larger than $4 \times 10^4\,m^2\,s^{-2}$ shaded in (a)–(b) and positive values shaded in (c), respectively.
From Yang *et al.* (2002).

'Tokyo–Chicago Express'. The teleconnection may be related to the ENSO condition in the preceding spring. However, it becomes increasingly decoupled from the tropical SST during summer and autumn. The air–sea coupling in the North Pacific may play a critical role in maintaining and amplifying the signals in both the atmosphere and the ocean.

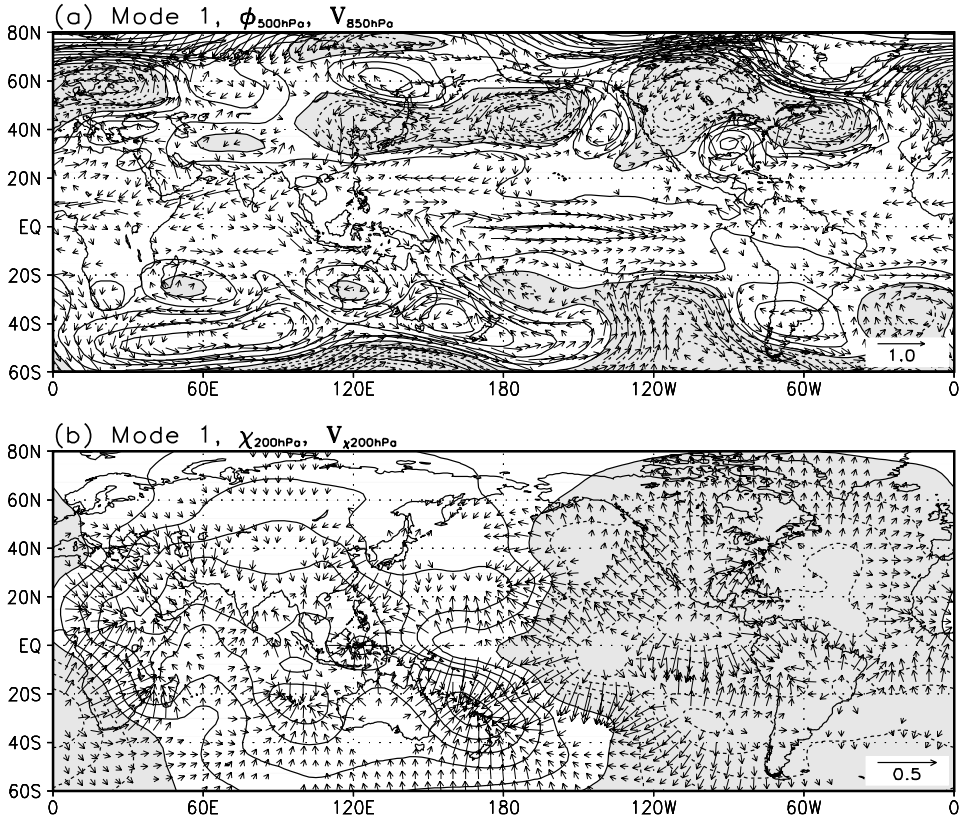

Figure 6.15. Regression of the principal component of the first mode of North America summer rainfall against (a) 500-mb geopotential height and 850-mb winds and (b) 200-mb velocity potential and divergent winds.
From Lau *et al.* (2005).

The atmospheric teleconnection pattern associated with the second mode of the singular value decomposition analysis is shown in Figure 6.16. Compared with the first mode, this mode is characterized by a circumglobal Rossby wave pattern spanning the northern hemisphere. An apparent heat source is found over the Indo-Pacific monsoon region. This teleconnection, linking opposite rainfall anomalies over eastern China and central USA, is referred to as the 'Shanghai–Kansas Express'. This second mode is not correlated with ENSO. This feature is similar to the condition of boreal winter when the atmospheric and oceanic processes associated with the second mode do not seem to vary closely with ENSO (Yang *et al.*, 2002).

During the northern hemisphere summer, the climate teleconnection in the Asian–Pacific–American sector is apparently part of the circumglobal teleconnection pattern (Lau and Weng, 2002; Ding and Wang, 2005). While it is only indirectly

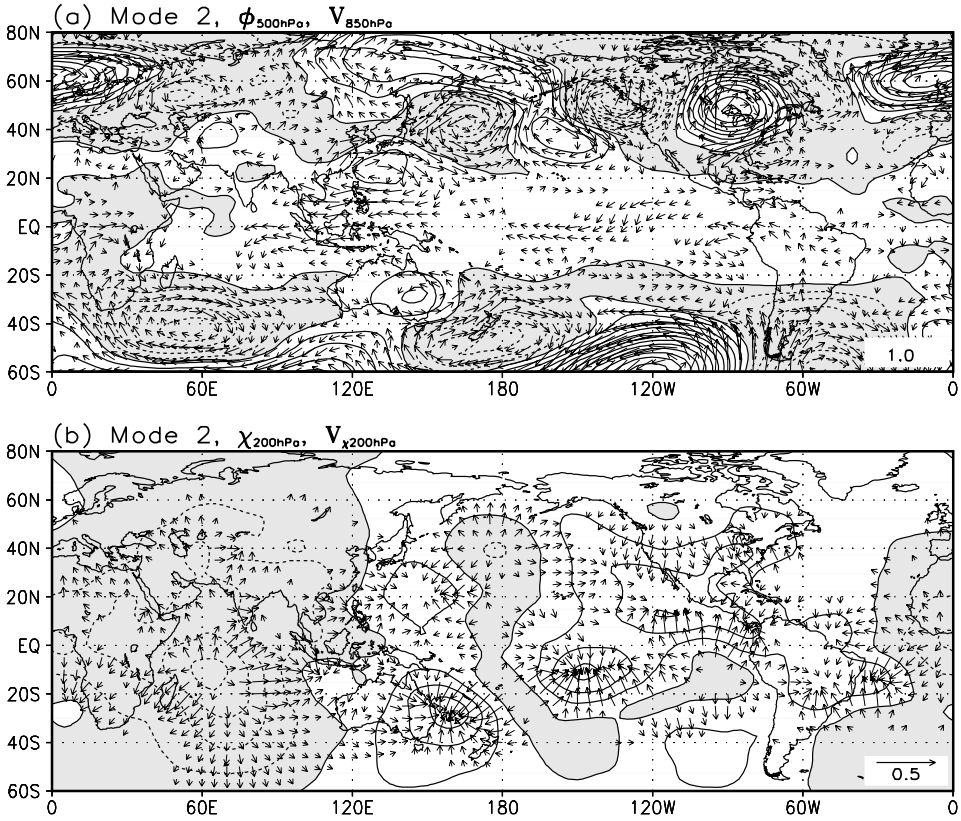

Figure 6.16. Regression of the principal component of the second mode of North America summer rainfall against (a) 500-mb geopotential height and 850-mb winds and (b) 200-mb velocity potential and divergent winds.
From Lau *et al.* (2005).

linked to ENSO and insignificantly related to the AO and the western North Pacific monsoon, this circumglobal teleconnection pattern is maintained by the interaction between the global wavetrains and the South Asian summer monsoon (Ding and Wang, 2005).

6.6 SUMMARY

In this chapter, we have discussed the interannual variability of the Asian monsoon, with a focus on the summer monsoon over all of tropical Asia. Major effort has been devoted to documenting the principal modes, dominant impacting factors, biennial variability, and the relationship between monsoon and the global climate. We have in particular focused on the advances in monsoon studies since the reviews by Ramage (1971), Shukla (1987a), Tao and Chen (1987), and Asnani (1993).

The Asian monsoon is a coupled ocean–atmosphere–land system and its interannual variability is determined by the dynamic processes of interaction among the Eurasian continent, the Pacific and Indian Oceans, and the overlying atmosphere. An important feature of the dominant modes of monsoon variability is their dependence on the seasonal and spatial transition of the coupled system, in which the Asian and Australian monsoons are closely related to each other. The Pacific and Indian Ocean SSTs and the Eurasian land surface processes provide a major slowly varying forcing for the Asian monsoon. Other large-scale climate phenomena such as the AO and the NAO are also factors that seem to influence the monsoon. The variability of the Asian–Australian monsoons and their associated coupled ocean–atmosphere–land processes is characterized by a distinct biennial tendency, which is usually explained by local air–sea interaction, forcing by SSTs of remote ocean domains, and tropical–extratropical interaction in which the land surface process is involved. A better understanding of the back and forth transition of the monsoon between Asia and Australia, the coupling of tropical ocean–atmosphere–land system including that in transitional seasons such as spring, and the role of the annual cycles of the monsoon and SSTs are critical for improving the skill of predicting the interannual variability of the Asian monsoon.

There is now growing evidence indicating that the Asian monsoon plays an active role in the variability of the global climate. The monsoon affects the global climate through its influence on ENSO. It also affects the climate through ocean–atmosphere–land coupling and changes in atmospheric wavetrains that are quite distinct from those forced by ENSO. However, despite that the impact of the Asian monsoon on global climate was realized decades ago, such an impact has not been demonstrated and explained as thoroughly as the influence of ENSO on the monsoon. This can be accounted for by several reasons including the substantial regional features of the monsoon and the difficulties in representing and integrating these regional features in numerical models as forcing functions. Therefore, to gain an insight into the global impact of the Asian monsoon, it is necessary to improve the understanding of the monsoon's spatial features such as the relative dominance of regional monsoon components. It is likely that, during a specific period of time, one regional monsoon is more powerful in affecting the large-scale climate than the others. Furthermore, a better understanding of the global impact of monsoons relies largely on the availability of better general circulation models in which the meteorological elements measuring the atmospheric and land surface conditions over the Eurasian continent, such as the land surface temperature, can be accurately specified as forcing for the monsoon.

6.7 ACKNOWLEDGEMENTS

The authors are thankful to Miss Soo-Hyun Yoo and Drs Kyu-Myong Kim, Tim Li, and Renguang Wu for preparing some of the figures used in this chapter. They are also thankful to the four anonymous reviewers for their comments, which were helpful in improving the quality of this chapter.

7

The Asian monsoon: Interdecadal variability

B. N. Goswami

7.1 INTRODUCTION

Prediction of the seasonal mean monsoon at least one season in advance is one of the most important problems in tropical climate study. It also happens to be one of the most difficult problems. The Asian monsoon climate exhibits variability on a variety of timescales. The predictability of the seasonal mean monsoon depends on the nature of the interannual variability (IAV) of the monsoon. Extensive studies on IAV of different components of the Asian monsoon have led to better documentation and better understanding of the physical mechanisms responsible for IAV of the monsoon (Chapter 6). Various components of the Asian monsoon also exhibit significant interdecadal variability (Mooley and Parthasarathy, 1984; Kripalani *et al*., 1997; Mehta and Lau, 1997; Chang *et al*., 2001b, 2000b; Parthasarathy *et al*., 1991; Wu and Wang, 2002). Modulation of IAV by the interdecadal variability influences predictability of the seasonal mean monsoon. One example of the role of interdecadal variability on the predictability of the summer monsoon is seen in the change in usefulness of several predictors used in statistical prediction of the Indian summer monsoon precipitation (Gowarikar *et al*., 1989, 1991; Thapliyal and Rajeevan, 2003). The correlation between several of these predictors and the Indian summer monsoon precipitation has been found to undergo interdecadal variations (Kumar *et al*., 1999; Krishnamurthy and Goswami, 2000) forcing the Indian Meteorological Department to drop many of the original predictors in their recent statistical model (Rajeevan *et al*., 2004). A better understanding of the interdecadal variability may, therefore, be very important in improving the predictability of the seasonal monsoon climate. However, the space–time structure of the monsoon interdecadal variability is less well documented than the IAV and mechanisms responsible for it are poorly understood. This problem is largely related to the lack of availability of good quality data for a sufficiently long period. While the instrumented record of surface climate (e.g., temperature, surface pressure, and

B. Wang (ed.), *The Asian Monsoon*.

precipitation) could be extended to about 150 years, upper air data is available for only about 50 years. In this chapter, we shall attempt to highlight the temporal and spatial characteristics of the surface climate associated with the dominant interdecadal variability of the Asian monsoon making use of long records of rainfall, sea surface temperature (SST), and sea level pressure (SLP). Further, we shall endeavor to unravel the 3-D structure of the dominant mode of interdecadal variability from available upper air circulation data. Connections between interdecadal variability of the monsoon and that of other climate regimes around the globe will be made and indicated that the monsoon interdecadal variability may be manifestations of a global coupled ocean–atmosphere mode of interdecadal variability. A positive feedback mechanism involving air–sea interaction will be proposed for intensification of the oscillation. An attempt will be made to understand the observed relationship between the Indian monsoon and the El Niño/Southern Oscillation (ENSO) on an interdecadal timescale within the context of the global 3-D structure of the dominant mode of monsoon interdecadal variability. The data sets used and methods of analysis are described in the Appendix of this chapter.

7.2 INTERDECADAL VARIABILITY OF THE SOUTH ASIAN SUMMER MONSOON

Based on the availability of long records of reliable rainfall observations over the Indian continent, epochal variation of Indian summer monsoon rainfall has been noted previously (e.g., Mooley and Parthasarathy, 1984; Parthasarathy *et al*., 1991). Normalized anomalies of June–September (JJAS) rainfall over all-India (AIR), the homogeneous Indian region (HMR), and the west central Indian region (WCR) between 1871 and 2000 are shown in Figure 7.1(a–c), respectively (bars). Also, normalized JJAS SST anomalies in the Niño 3 region (150°W–90°W, 5°S–5°N) are shown in Figure 7.1(d). The solid curve in each figure represents the normalized 11-year running mean of each variable. Standard deviation of IAV as well as that of the running mean (i.e., low-pass filtered data, l.s.p.d.) are also noted in each figure. All three indices of Indian summer monsoon rainfall show a lack of trend or climate change signal but contain coherent multidecadal variability with an approximate periodicity of 55–60 years. The tridecades between 1871 and 1900 and between 1930 and 1960 generally saw more above than below normal rainfall over the country. Frequency of occurrence of large-scale floods were also higher during these periods. Similarly, the tridecades between 1901 and 1930 and between 1971 and 2000 saw more below than above normal rainfall over the country. These periods were also characterized by a higher frequency of droughts. The eastern equatorial Pacific SST (Niño 3) also shows a similar interdecadal variability but is approximately out of phase with that of the summer monsoon rainfall. High correlations between the interdecadal component of variability of the three summer monsoon indices as well as with that of Niño 3 SST are shown in Table 7.1. Such epochal behavior of Indian summer monsoon rainfall with multidecadal quasi-periodicity has been noted in many studies (Parthasarathy *et al*., 1994; Kripalani

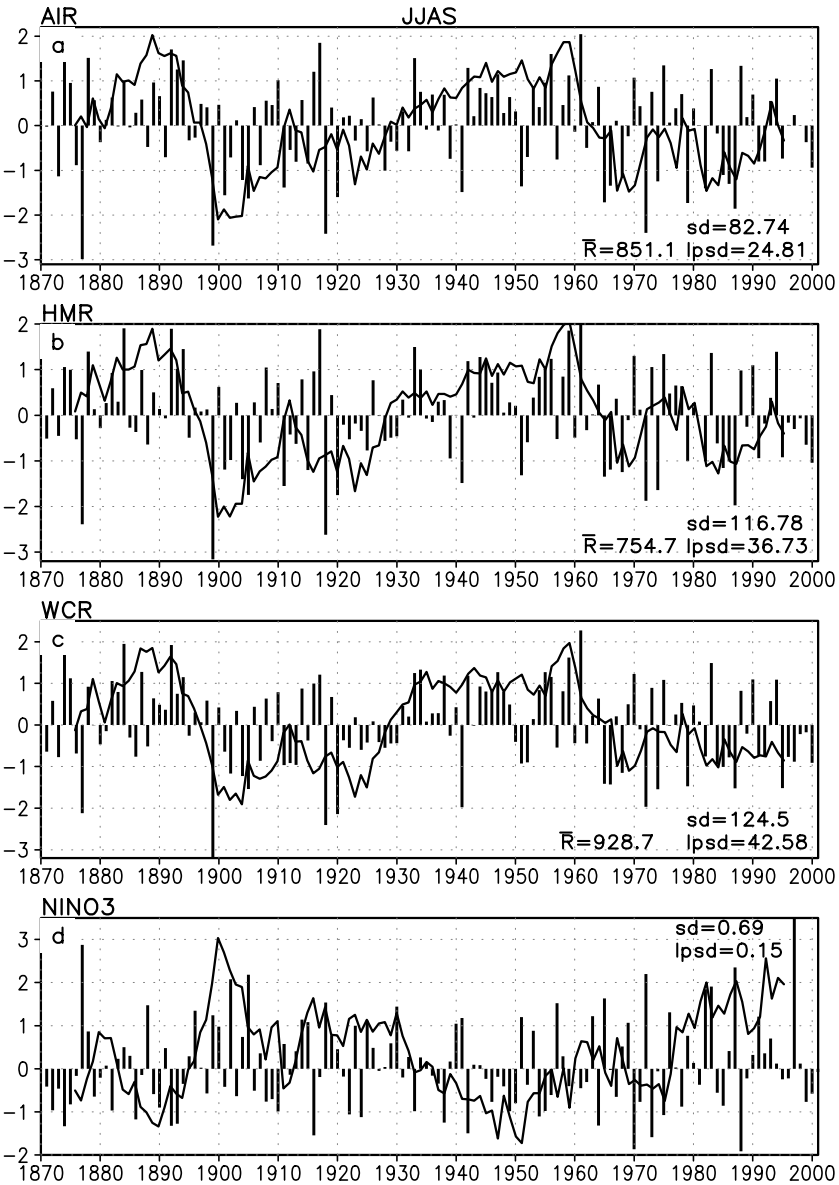

Figure 7.1. Interannual (bar) and interdecadal (solid) variability of three Indian summer (JJAS) rainfall indices (a–c) and summer (JJAS) SST over Niño 3 (170°–90°W, 5°S–5°N). (a) AIR, (b) HMR, and (c) WCR. Low-pass filtered seasonal anomalies are obtained by using an 11-year running mean. For the rainfall time series, long-term mean seasonal rainfall ($\bar{R}$), interannual standard deviation (s.d.), and standard deviation of the low-pass filtered seasonal anomalies (l.p.s.d.) are shown (in millimeters). Interannual as well as low-pass filtered anomalies are normalized by their own standard deviations.

Table 7.1. Correlations between low-pass filtered JJAS indices.

CORR	AIR	HMR	WCR	Niño 3
AIR	1			
HMR	0.96	1		
WCR	0.95	0.96	1	
Niño 3	−0.77	−0.76	−0.77	1

AIR = all-India rainfall; HMR = homogeneous Indian region; WCR = west central Indian region.

et al., 1997; Kripalani and Kulkarni, 1997; Mehta and Lau, 1997; Krishnamurthy and Goswami, 2000).

In order to examine the spatial coherence of the interdecadal variability of summer monsoon rainfall, composites of the JJAS precipitation anomalies over 29 meteorological subdivisions over the Indian continent during a below normal epoch (1900–1925) and an above normal epoch (1940–1965) were constructed (Figure 7.2(a–b)). The anomalies were calculated with respect to means of individual subdivisions. The rainfall tends to be above (below) normal over most of the country during these above (below) normal interdecadal epochs indicating a large spatial scale for the interdecadal variability of the Indian summer monsoon rainfall. The rainfall over the easternmost part and the southern tip of the country tend to go out of phase with the rest of the country. It is interesting to note that the spatial pattern of the interdecadal variability of rainfall over the Indian continent has a similarity with the dominant pattern of IAV over India (Shukla, 1987b; Krishnamurthy and Shukla, 2001).

The annual mean of daily mean surface temperature as well as that of daily maximum surface temperature over India are known to have a trend representing the climate change signal, while the daily minimum surface temperature over India does not show such a trend (Rupakumar *et al.*, 1994). As the interdecadal variability of summer monsoon precipitation has a large continental scale (Figure 7.2), it is likely to influence the summer mean surface temperature averaged over the Indian continent. During the wet (dry) interdecadal phase of the Indian summer monsoon rainfall, increased (decreased) cloudiness and evaporative cooling of the surface is expected to lead to day maximum temperature cooler (warmer) than normal. Increased cloudiness and enhanced moisture content in the atmosphere during the same phase is expected to result in reduced long-wave cooling during the night leading to a higher than mean minimum temperature. Using available data between 1901 and 1990, the interdecadal variability of the summer season (JJAS) mean maximum and minimum surface temperature was examined. It was found that they do have a trend. However, after detrending them using a simple least square linear fit, both minimum and maximum temperature show significant interdecadal variability (after passing through an 11-year running mean) similar to that of AIR (Figure 7.3). It is noteworthy that the interdecadal variation of the maximum summer surface temperature is coherently negatively correlated ($r = -0.88$) with that of the AIR. The interdecadal variation of summer minimum surface temperature is positively correlated with that of AIR after about 1930. The existence of

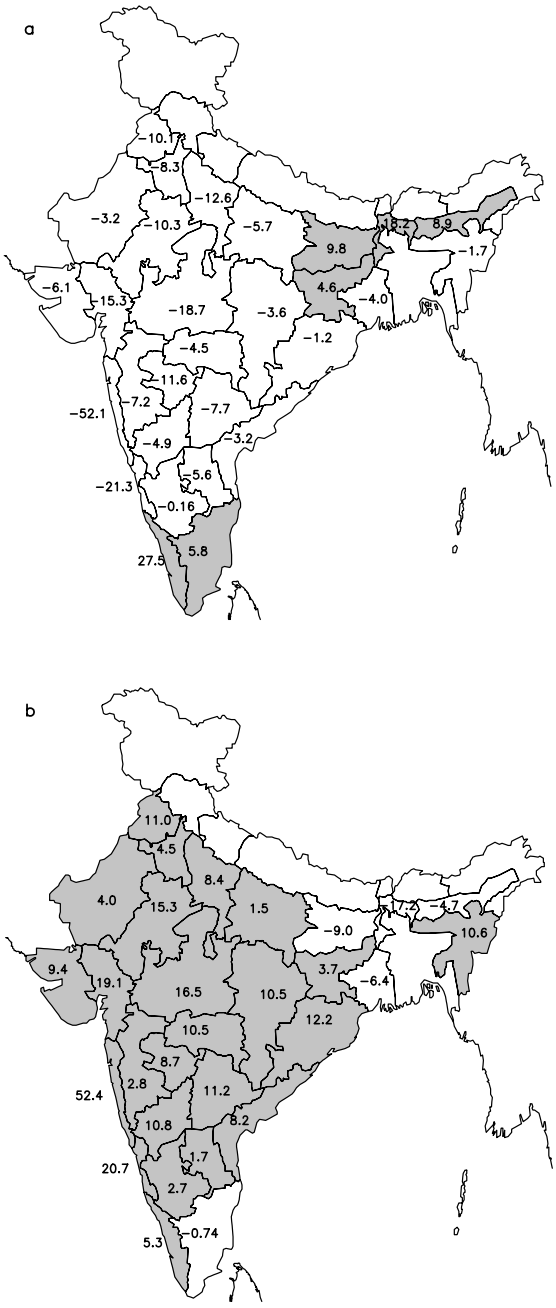

Figure 7.2. Spatial distribution of rainfall anomalies within the Indian continent during two contrasting interdecadal epochs. June–September rainfall anomaly (mm) over individual meteorological subdivisions of India averaged over (a) a below normal epoch, 1900–1925, and (b) an above normal epoch, 1940–1965. Positive anomalies are shaded.

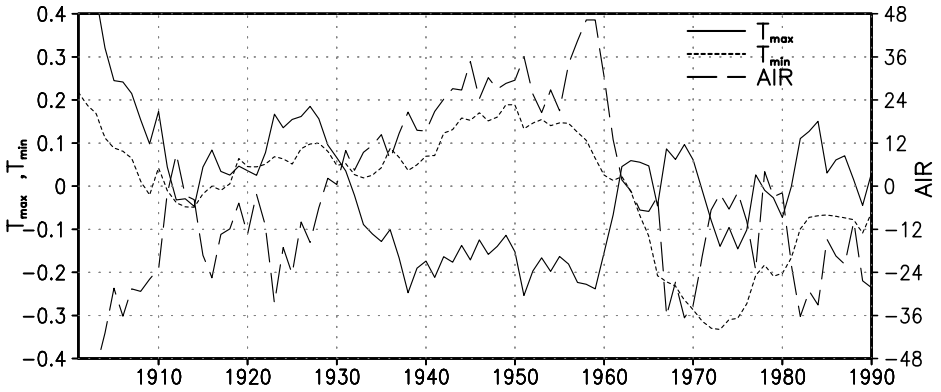

Figure 7.3. Interdecadal variation of June–September maximum surface temperature (T_{max}) and minimum surface temperature (T_{min}) over India in K (scale on the left) together with that for AIR (mm; scale on the right).

similar interdecadal variability in the maximum and minimum surface temperature and consistency between the precipitation and surface temperature indicates a certain amount of robustness for the quasi 60-year interdecadal mode.

The quasi 60-year oscillation of the Indian summer monsoon system is evident in many other parameters as well. Joseph (1976b) showed that interdecadal changes in monsoon rainfall are associated with interdecadal changes in the tracks of storms and cyclones in the Bay of Bengal. He found that during the period between 1931 and 1960, severe cyclonic storms in the Bay of Bengal had more westward tracks than during the periods 1891–1920 and 1965–1974 when the tracks of the storms were more northward than westward. He attributed the interdecadal change in storm tracks to modulations of background mean flow on interdecadal timescales. Agnihotri *et al.* (2002) analyzed a sediment core in the eastern Arabian Sea dating back to 1,200 years and found an approximate 60-year periodicity in several parameters related to surface productivity such as organic carbon (C_{org}), N, and Al, which in turn are related to the strength of the south-west monsoon winds. All these observations indicate that the quasi 60-year oscillation may be an intrinsic mode of oscillation of the monsoon system.

ENSO-like interdecadal variability of Pacific SST has been noted in several recent studies (Zhang *et al.*, 1997a; Kachi and Nitta, 1997; Graham, 1994; Tanimoto *et al.*, 1993; Graham *et al.*, 1994; Kawamura, 1994). The close association between the interdecadal variability of the summer monsoon and Niño 3 (Figure 7.1) indicates a strong link between interdecadal variability of Pacific SST and that of the Indian summer monsoon. The IAV of both the Indian monsoon rainfall as well as that of the ENSO seems to be coherently modulated by the interdecadal variability. Interdecadal variability of the IAV of AIR and Niño 3 SST were calculated using a 21-year moving window (Figure 7.4). IAV of both the Indian monsoon and the ENSO also show a quasi 60-year interdecadal fluctuation. Strong correlation ($r = 0.82$) between the two indicates that the quasi 60-year oscillation is a global

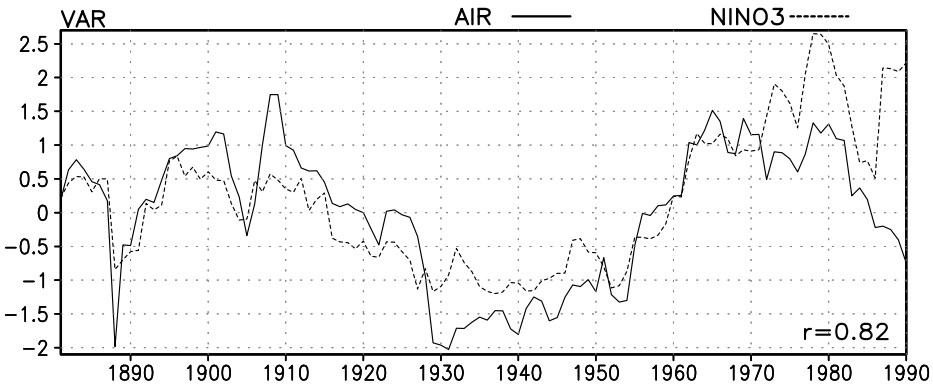

Figure 7.4. Interdecadal variability of interannual variance of normalized AIR (solid) and JJAS Niño 3 SST (dotted) using a 15-year moving window. The correlation (r) between the two is shown.

mode of variability that modulates activity of both the Indian monsoon and the ENSO. Similar interdecadal variability of variance of the 2–7-year band of AIR and Niño 3 SST anomalies (SSTAs) and the coherence between the two have also been noted by Torrence and Webster (1999).

Here, we contrast the strong negative relationship between the interdecadal variability of the Indian summer monsoon and the ENSO with the ENSO–monsoon relationship on interannual timescales. The ENSO–monsoon relationship on an interannual timescale has been studied extensively (Sikka, 1980; Pant and Parthasarathy, 1981; Rasmusson and Carpenter, 1983; Shukla and Paolino, 1983; Parthasarathy and Pant, 1985; Shukla, 1987b; Goswami, 1998; Lau and Wu, 2001; Lau and Nath, 2000). The simultaneous correlation between JJAS Niño 3 SSTAs and AIR has remained significantly negative over a long period of time (Figure 7.5(a)). However, it has decreased sharply over the last two decades and is currently insignificantly small (Figure 7.5(a)). Another aspect of this relationship is that even when correlation was strong (e.g., between 1871 and 1971), the largest correlation between AIR and Niño 3 SST occurs with Niño 3 SST following the monsoon season (Figure 7.5(b)). This observation prompted a hypothesis that the large-scale circulation changes associated with the Indian monsoon may play an important role in determining the evolution and strength of the ENSO on interannual timescales (e.g., Nigam, 1994; Kirtman and Shukla, 1997). During recent decades, however, the largest correlation between the Indian summer monsoon rainfall and eastern Pacific SST takes place not with SST following the monsoon but with SST one year prior to the Indian monsoon (Figure 7.5(b)). This indicates a qualitative change in the ENSO–monsoon relationship during recent years.

The fact that the relationship between Indian summer monsoon and ENSO has the same sign on interannual (over a large fraction of the historical data) as well as

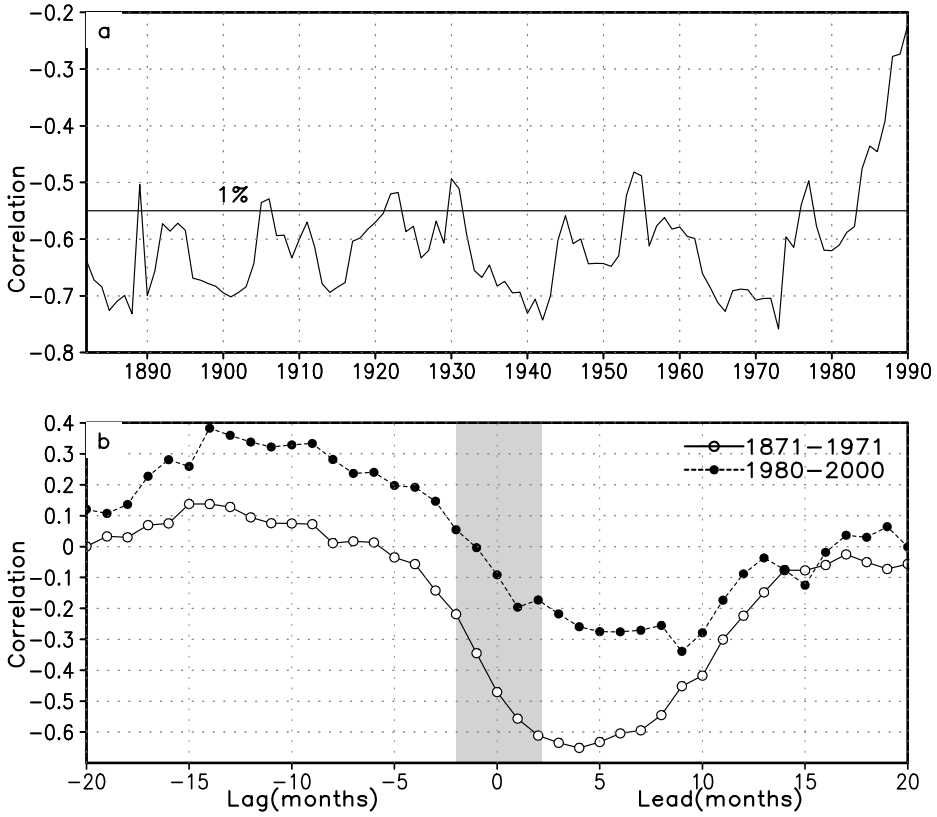

Figure 7.5. (a) 21-year moving correlation between AIR and JJAS Niño 3 SST, the horizontal line representing significance at the 1% level. (b) Lag correlations between AIR and monthly mean SSTAs over the Niño 3 region using data between 1871 and 1971 (open circles) and the recent period between 1980 and 2000 (filled circles).

on interdecadal timescales indicates that the mechanism through which the two interact may be similar on both timescales. The physical linkage between the two on interdecadal timescales will be examined later in the chapter and compared with that between the two on interannual timescales. The rapid weakening of the ENSO–monsoon relationship on interannual timescales during the recent decades has also been a subject of considerable attention (Kumar *et al.*, 1999; Krishnamurthy and Goswami, 2000; Chang *et al.*, 2001a; Torrence and Webster, 1998; Kinter *et al.*, 2002). It will be explored whether the changing relationship between the ENSO and Indian monsoon could be understood in terms of modulation of the ENSO–monsoon relationship on interannual timescales by the large-scale circulation changes associated with the interdecadal variability.

7.3 INTERDECADAL VARIABILITY OF THE EAST ASIAN SUMMER MONSOON

The east Asian summer monsoon (EASM) encompasses both the tropics and subtropics. It is distinct from the south Asian (Indian) monsoon and has a complex space–time structure ranging from tropical baroclinic systems to middle latitude barotropic systems. The EASM also experiences a quasibiennial tendency on interannual timescales (Shen and Lau, 1995) like the south Asian monsoon. However, the EASM is influenced by ENSO in a distinctly different way than the south Asian monsoon. While the Indian summer monsoon precipitation correlates strongly with eastern Pacific SST during the evolving phase of the ENSO (Figure 7.5(b)), the EASM correlates strongly with eastern Pacific SST during the decaying phase of the ENSO (Shen and Lau, 1995; Chang *et al.*, 2001b, 2000b; Wang *et al.*, 2001; Wu and Wang, 2002). The EASM also exhibits interdecadal variability somewhat similar to that observed in the Indian monsoon rainfall. In order to get an idea of the temporal scale of the interdecadal variability of the EASM, May–August (MJJA) precipitation over two regions for the period between 1901 and 1998 were extracted from historical rainfall records compiled by Dr. Mike Hulme of the University of East Anglia, UK. The climatological precipitation during MJJA over east China around the Yangtze River valley (27.5°–37.5°N, 100°–122.5°E) and over north-eastern China (37.5°–47.5°N, 115°–125.5°E) are 56 cm and 40.4 cm respectively. The interannual and interdecadal (11-year running mean of interannual anomalies) variations normalized by their own standard deviations are shown in Figure 7.6. A quasi 50–60-year interdecadal periodicity is evident in both time series similar to that observed in the south Asian monsoon rainfall (Figure 7.1(a–c)). Roughly after 1920, the phase of the interdecadal variability of the EASM precipitation also has a similarity with that of the south Asian summer monsoon. It is noteworthy here that a 65–70-year periodicity of the global temperature record was found by Schlesinger and Ramankutty (1994) after removing the trend. Thus, the quasi 60-year oscillation in both the south Asian summer monsoon and the EASM may be a manifestation of a global mode of interdecadal variability.

The EASM goes through a major interdecadal transition in the mid-1970s concurrent with the major climatic transition in the tropical Pacific. While this is clearly seen in the east China precipitation (Figure 7.6(a)), the complex spatial structure associated with this interdecadal transition influences the whole EASM region. The spatial structure and possible causative mechanisms for this interdecadal transition of the EASM has been examined in several studies (Hu, 1997; Wu and Wang, 2002; Chang *et al.*, 2001b, 2000b) using station rainfall data over China, Japan, and Korea and National Centers for Environmental Prediction/National Center for Atmospheric Research (NCEP/NCAR) reanalysis. A negative–positive–negative precipitation pattern over south-eastern China, the Yangtze River valley, and northeastern China during the pretransition (1962–1977) period seems to go over to a positive–negative–positive pattern during the post-transition (1978–1993) period (Wu and Wang, 2002). Significant interdecadal changes of large-scale circulation are also found consistent with the interdecadal changes in precipitation pattern.

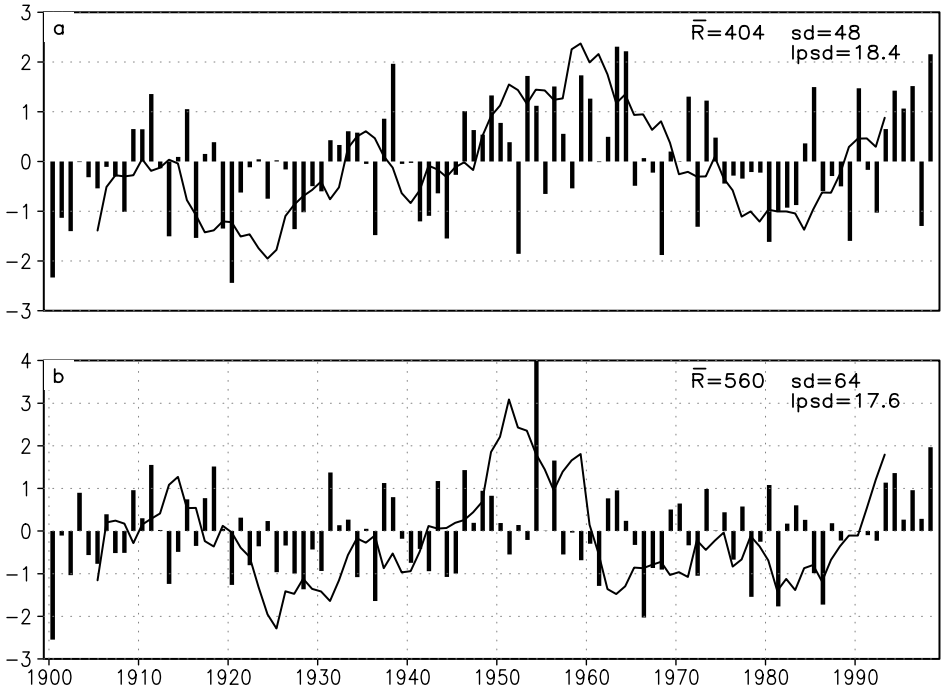

Figure 7.6. Interannual (bar) and interdecadal (solid) variability of the EASM (May–August) rainfall over two areas in China. (a) North-eastern China between 37.5°–47.5°N, 112.5°–125.0°E, (b) the Yangtze River valley between 27.5°–37.5°N, 105.5°–115.0°E. Low-pass filtered seasonal anomalies are obtained by using an 11-year running mean. The long-term mean seasonal rainfall ($\bar{R}$), interannual standard deviation (s.d.) and standard deviation of the low-pass filtered seasonal anomalies (l.p.s.d.) are shown (in millimeters). Interannual as well as low-pass filtered anomalies are normalized by their own standard deviations.

The low-level anticyclone is stronger and located at higher latitudes in 1978–1993 than in 1962–1977. Also the barotropic anticyclonic anomaly over the Japan Sea during the earlier epoch turned into cyclonic during the later epoch. The circulation over the EASM region could be influenced by western north Pacific convection through a low-level response and by the Indian summer monsoon heating through an upper level wave response. It appears that during 1978–1993, the western north Pacific convection was largely responsible for the interdecadal anomalies while during the earlier epoch both processes contributed to it (Wu and Wang, 2002). Significant change in summertime typhoon tracks were also found by Ho *et al.* (2004) between two interdecadal periods, namely between 1951–1979 and 1980–2001 consistent with the westward and northward extension of the subtropical north-western Pacific High.

Table 7.2. Correlations between low-pass filtered NDJF indices.

CORR	AIR	PEN	EQIO	Niño 3
AIR	1			
PEN	0.85	1		
EQIO	0.6	0.5	1	
Niño 3	0.41	0.46	0.72	1

AIR = all-India rainfall; PEN = Indian peninsula rainfall; EQIO = equatorial Indian Ocean.

7.4 INTERDECADAL VARIABILITY OF THE SOUTH ASIAN WINTER MONSOON

During winter (November–February, NDJF) monsoon rainfall over India primarily comes from the rainfall over the peninsular region. Therefore, the variability of NDJF rainfall averaged over all India (Figure 7.7(a)) is very similar to that over the peninsular of India (Figure 7.7(b)). The interdecadal variability of the two time series is also highly correlated ($r = 0.85$, Table 7.2). As in Figure 7.1, these time series are also normalized by their own standard deviations. NDJF SSTAs averaged over the equatorial Indian Ocean (EQIO; 50°–110°E, 15°S–10°N) and over the Niño 3 area are presented in Figure 7.7(c) and (d) respectively. A comparison of Figure 7.1(a) with Figure 7.7(b), reveals that the interdecadal variability of the winter monsoon is nearly out of phase with that of the summer monsoon (Figure 7.1(a)). Consistent with this observation, the interdecadal variability of the winter monsoon is positively correlated with that of the Niño 3 SST as well as with that of the EQIO (Table 7.2). Somewhat weaker correlation between interdecadal variability of winter monsoon rainfall and either EQIO or Niño 3 SST is partly due to the fact that the two time series are phase shifted during the earlier part of the record between 1871 and 1920. Between 1920 and 2000, they are strongly correlated.

How are Indian monsoon and ENSO linked on interdecadal timescales? Why is the interdecadal variability of the Indian summer monsoon negatively correlated with that of the equatorial Pacific SST while it is positively correlated with the interdecadal variability of the Indian winter monsoon? We explore some of these questions in the next section.

7.5 MECHANISM FOR THE INTERDECADAL VARIABILITY OF THE ENSO–MONSOON RELATIONSHIP

The annual cycle and IAV of the Asian monsoon are described and discussed in Chapters 2 and 6 of this book respectively. A framework is described here that may be used as a basis through which we may attempt to understand the observed interdecadal variability. The climatological mean June–September precipitation

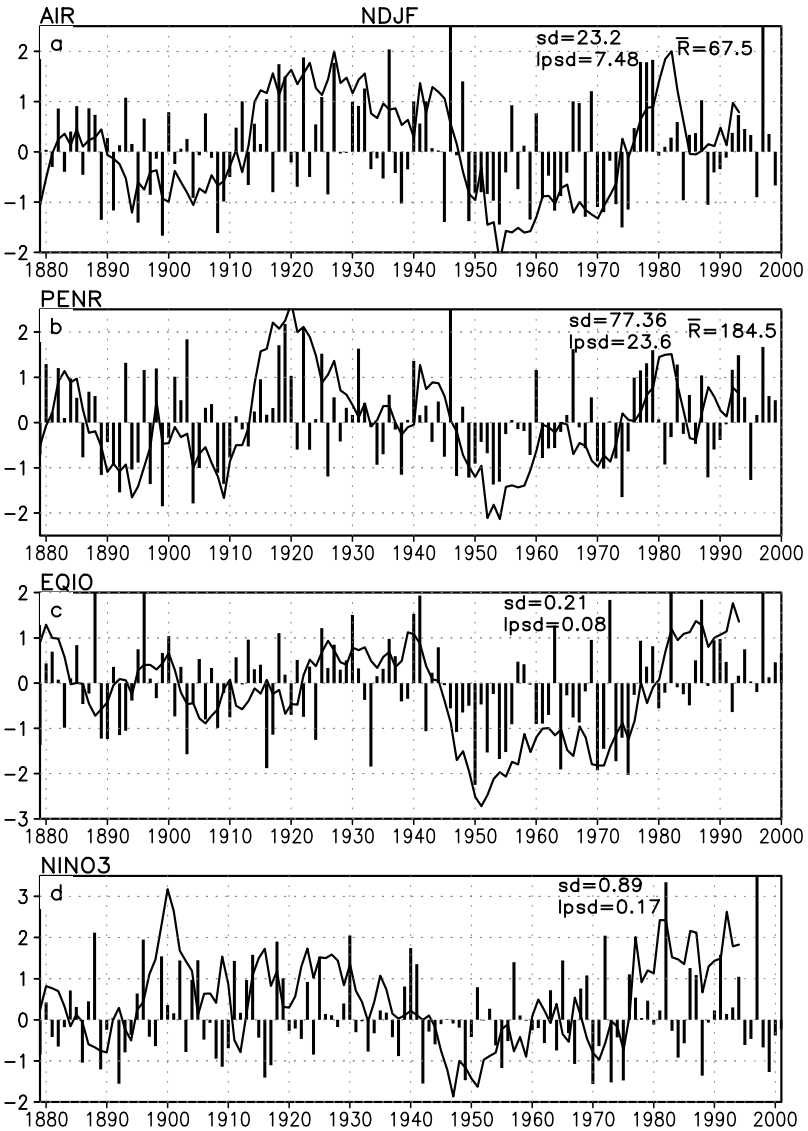

Figure 7.7. Interannual (bar) and interdecadal (solid line) variability of two Indian winter (November–February, NDJF) rainfall indices (a–b) and winter (NDJF) SST over the EQIO (50°–110°E, 15°S–10°N) and over Niño 3 (170°–90°W, 5°S–5°N). (a) Winter all-India rainfall (AIR(W)), (b) monsoon rainfall over the peninsular region (PENR), (c) NDJF SSTAs over the EQIO, and (d) NDJF SST over Niño 3. Low-pass filtered seasonal anomalies are obtained by using an 11-year running mean. For the rainfall time series, long-term mean seasonal rainfall ($\bar{R}$), interannual standard deviation (s.d.), and standard deviation of the low-pass filtered seasonal anomalies (l.p.s.d.) are shown (in millimeters). Interannual as well as low-pass filtered anomalies are normalized by their own standard deviations.

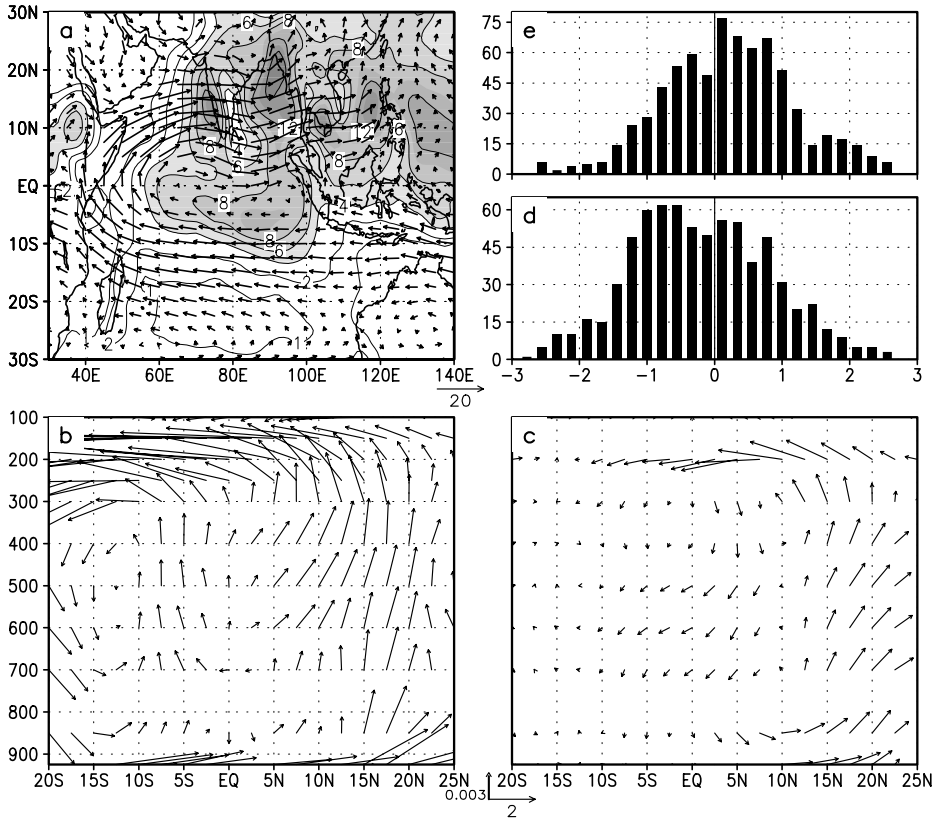

Figure 7.8. (a) Climatological seasonal mean (JJAS) precipitation (mm day^{-1}) and vector wind at 850 hPa. The unit of wind vector is shown at the bottom of the panel. (b) Climatological JJAS mean MH circulation constructed with meridional velocity and vertical pressure velocity (with a negative sign) averaged between 70°–100°E. Scale for the vertical velocity (Pa s^{-1}) and meridional velocity (m s^{-1}) are shown at the bottom of the panel. (c) Same as (b) but with anomalous meridional and vertical pressure velocity during an active condition. Scale is the same as in (b). (d) Frequency distribution of normalized 10–90-day filtered precipitation anomalies during 1 June–30 September for 6 strong monsoon years averaged over the monsoon trough region (10°–25°N, 70°–90°E). (e) Same as in (d) but for anomalies averaged over the equatorial Indian Ocean (5°S–5°N, 70°–100°E).

and low-level winds over the Asian monsoon region are shown in Figure 7.8(a). The mean summer precipitation has a primary maximum in the monsoon trough (MT) region between 10°N and 25°N with a secondary maximum in the equatorial Indian Ocean. Low-level cyclonic vorticity, arising through interaction of low-level converging flow with the Himalayan mountain range, helps organize convection through frictional moisture convergence and makes the MT a preferred location of the tropical convergence zone (TCZ). The eastern equatorial Indian Ocean with a

maximum of SST between the equator and 10°S during the summer season represents another preferred location of the TCZ (Goswami *et al.*, 1984). The meridional circulation is characterized by a regional monsoon Hadley (MH) circulation (Figure 7.8(b)) with ascending motion around 25°N and descending motion south of the equator (Webster *et al.*, 1998; Gadgil, 2003). Within the summer monsoon season, vigorous intraseasonal oscillations (ISOs) in the form of active/break cycles ride on the seasonal mean monsoon. The ISOs are characterized by a competition of the TCZ to fluctuate between the two preferred locations with repeated northward propagation from the equatorial position to the MT (Yasunari, 1979; Sikka and Gadgil, 1980). The active (break) phase is associated with increased (decreased) rainfall over the MT and decreased (increased) rainfall over the equatorial location. The anomalous MH circulation associated with the active condition (Figure 7.8(c)) enhances the ascending branch of mean MH circulation over the MT but weakens the ascending motion near the equator. The seasonal mean precipitation is influenced by the statistical average of the ISOs of the TCZ over the season (Goswami and Ajayamohan, 2001a). During a strong seasonal mean monsoon the frequency of occurrence of active conditions over the MT is higher than break conditions (Figure 7.8(e)) while over the oceanic region breaks are more frequent than active conditions (Figure 7.8(d)).

Thus, processes that influence the frequency of occurrence of the TCZ over the equatorial Indian Ocean (IO) preferred region could influence the seasonal mean monsoon Hadley circulation and seasonal mean monsoon precipitation. The strength and distribution of SST over the equatorial IO as well as the convergences and divergences associated with the equatorial Walker circulation could influence the equatorial ISOs and thereby influence the seasonal mean monsoon precipitation. Therefore, a link between the Pacific SST and that of the Indian monsoon rainfall could be expected through modification of the equatorial Walker circulation and the regional monsoon Hadley circulation. The answer to the questions raised in the previous section may become clearer once we have a reasonable idea of the changes of the Walker and monsoon Hadley circulation associated with the interdecadal variability.

In order to bring out the robust global patterns of SST and SLP associated with the interdecadal variability of the Indian summer monsoon as well as with that of the ENSO, long records of AIR, SST, and SLP since 1871 are used. The spatial pattern associated with interdecadal variability of the Indian summer monsoon is obtained by regressing global SST and SLP fields on the low-pass filtered AIR (solid curve in Figure 7.1(a)) and shown in Figure 7.9(a) and (c) respectively. Similarly, the spatial pattern associated with the interdecadal variability of ENSO is obtained by regressing the global SST and SLP field on the low-pass filtered Niño 3 (negative of the solid curve in Figure 7.1(d)) and shown in Figure 7.9(b) and (d) respectively. These patterns are similar to those associated with the ENSO-like interdecadal variability noted in some earlier studies (Kachi and Nitta, 1997; Zhang *et al.*, 1997; Enfield and Mestas-Nunez, 1999). Some minor differences between patterns shown in Figure 7.9 and those obtained by Zhang *et al.* (1997) are due to the fact that while the patterns shown here were obtained by regressing northern hemisphere summer mean (JJAS)

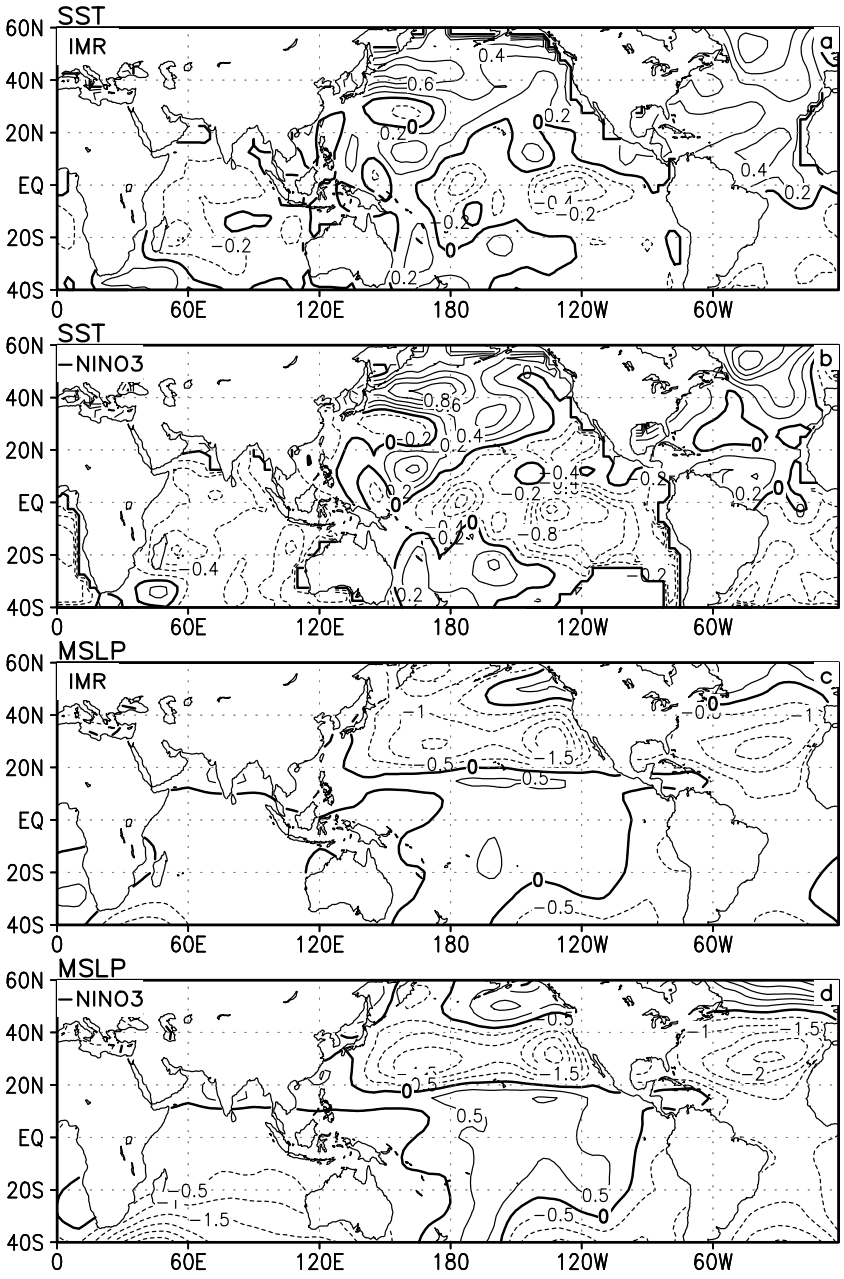

Figure 7.9. Spatial pattern obtained by regressing global SST (top two panels) and global SLP (bottom two panels) on low-pass filtered AIR and Niño 3 (shown in Figure 7.1), respectively. Negative contours are dashed and the contour interval is 0.1 K per standard deviation for SST and 0.1 hPa for SLP, respectively.

anomalies, their patterns were obtained by regressing monthly mean anomalies for the entire period which resulted in more weighting from northern hemispheric winter SST pattern associated with the interdecadal mode. The global spatial patterns of SST associated with interdecadal variability of the AIR and ENSO (Figure 7.9(a) and (b)) are almost identical, the pattern correlation between the two being 0.86. Similarly the global spatial pattern of SLP associated with the interdecadal variability of AIR and ENSO (Figure 7.9(c) and (d)) are also almost identical, the pattern correlation between the two being 0.85. A possible implication of this observation is that the interdecadal variability of the monsoon and ENSO are manifestations of a global coupled ocean–atmosphere mode of interdecadal variability.

It may be possible to gain some insight regarding the relationship between the ENSO and Indian monsoon on interdecadal timescales by examining the 3-D structure of the global interdecadal mode of variability during 1948–2002 for which circulation data is available. Hence, a multivariate empirical orthogonal function (EOF) analysis of low-pass filtered SST, precipitation, winds at 850 hPa and 200 hPa, and velocity potential at 200 hPa was carried out. The first EOF explaining 41.5% of the variance of the low-pass filtered fields together with the corresponding principal component (PC1) are shown in Figure 7.10 and Figure 7.11, respectively. The global SST pattern associated with the EOF1 (Figure 7.10(a)) is similar to the pattern associated with the interdecadal variability of ENSO (Figure 7.9(b)) based on long data of SST (spatial correlation between the two patterns being -0.7). The time evolution of PC1 is quite similar to the low-pass filtered Niño 3 time series (Figure 7.1(d)) during the period 1948–2002. The EOF1 essentially represents the interdecadal modulation of ENSO from a La Niña preferred regime in the 1950s and 1960s to an El Niño preferred regime during the 1980s and 1990s with a transition around the mid-1970s. Therefore, the 3-D structure associated with the EOF1 may be representative of that of the interdecadal variability of the ENSO and the Indian monsoon discussed earlier with an approximate period of 55–60 years. While the EOF1 explaining 41.5% of the low-pass filtered variance is quite distinct from the other EOFs and could be considered a natural mode of oscillation representative of the multidecadal amplitude modulation of the ENSO, the EOF2 and EOF3 explaining the 10.1% and 9.8% variance of low-pass filtered fields are not distinct from each other and could not be considered as independent modes of oscillation. Hence, we focus our attention primarily on EOF1 representing the multidecadal component of the variability.

Associated with the EOF1, the ENSO-like SST warming (cooling) in the eastern tropical Pacific is in phase with SST over the tropical IO (Figure 7.10(a)). The spatial pattern of precipitation associated with the interdecadal mode (Figure 7.10(b)) consists of enhancement of precipitation over two major regions, namely, northern south America and the eastern equatorial IO and Indonesia and decrease in precipitation over two major regions, namely, the central and eastern Pacific and central Africa. Consistent with the precipitation pattern, the wind patterns show low-level convergence and upper level divergences over equatorial central America and northern south America and Indonesia while low-level divergence is seen over equatorial eastern Africa and the central Pacific around the Date Line

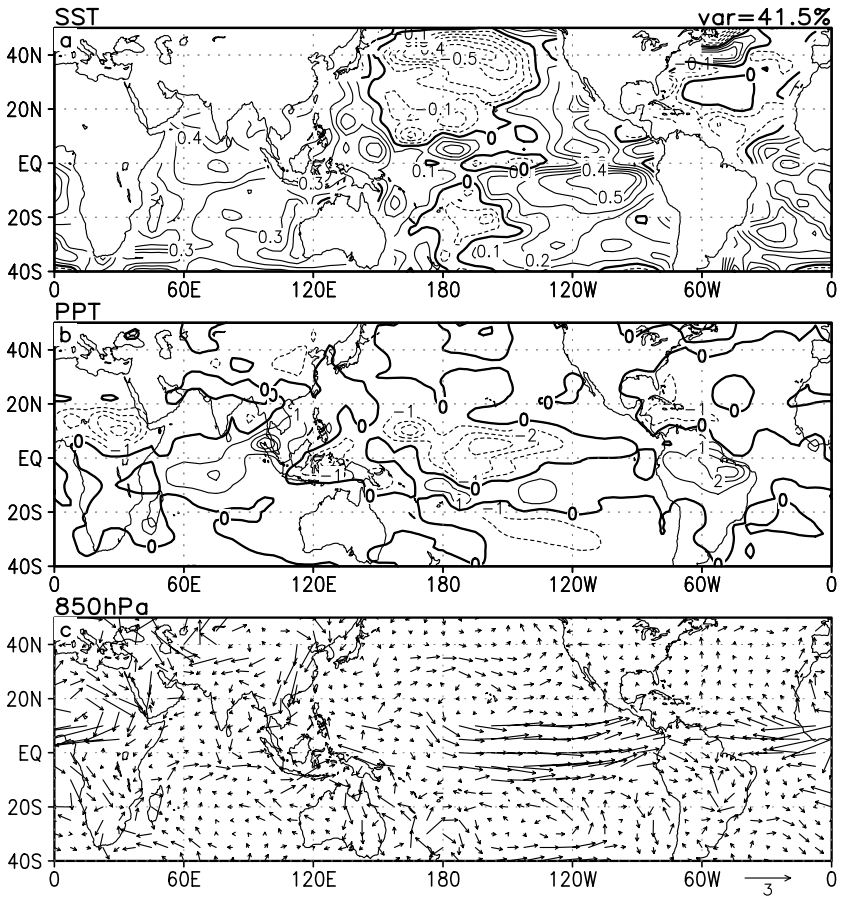

Figure 7.10. Spatial pattern of the first combined EOF (CEOF) of low-pass filtered fields of (a) SST (K), (b) precipitation (mm day^{-1}), and (c) vector winds at 850 hPa (ms^{-1}). Scale for the vector winds is shown.

(Figure 7.10(c)). A comparison between Figure 7.10(c) and Figure 7.11(a) shows that in the equatorial region, low-level convergence (divergence) is always associated with upper level (200-hPa) divergence (convergence). The upper level velocity potential field of the interdecadal mode (Figure 7.11(b)) is consistent with the divergent circulation associated with the precipitation anomalies (Figure 7.10(b)). The vertical structure of the oscillation in the equatorial region is, therefore, that of a first baroclinic mode. The precipitation pattern and the equatorial circulation are indicative of a three cell Walker circulation and are consistent with the velocity potential field at 200 hPa (Figure 7.11(b)). The upper level easterly jet in the equatorial IO (Figure 7.11(a)) is weakened during the warm phase of the interdecadal variability. This is a signature of a weakened Indian monsoon.

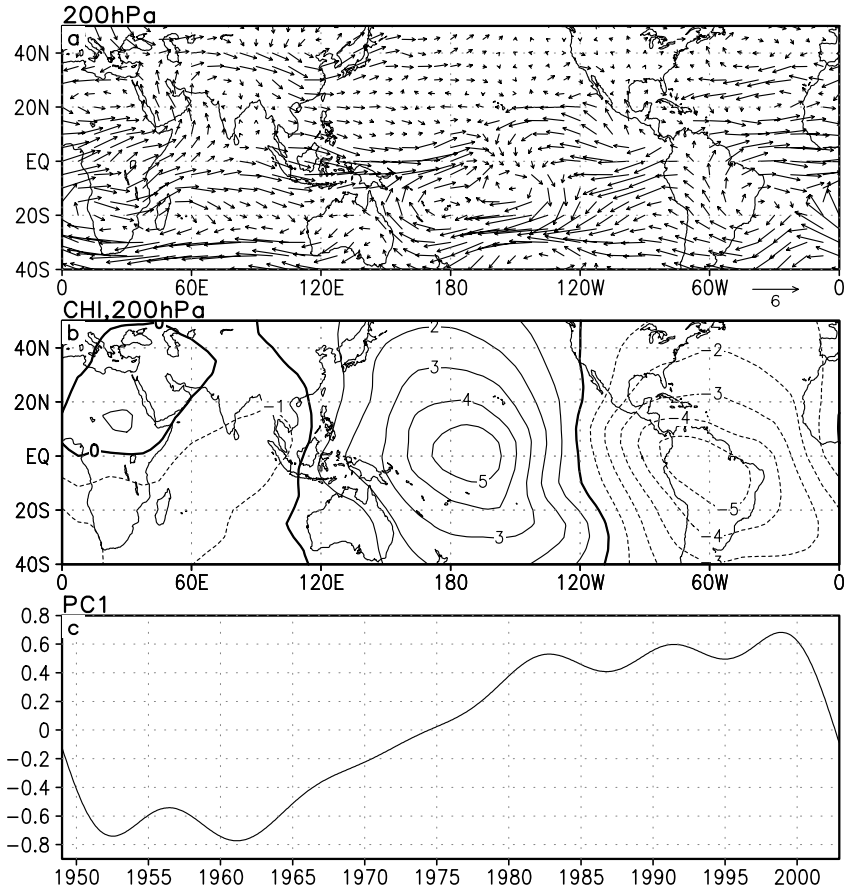

Figure 7.11. Continuation of spatial pattern of the first CEOF of low-pass filtered fields for (a) vector winds at 200 hPa (ms^{-1}). Scale for the vector winds is shown. (b) Velocity potential at 200 hPa ($10^6\,s^{-1}$), and (c) time evolution of PC1 for CEOF1 in arbitrary units.

To gain a better understanding of the ENSO–monsoon relationship on interdecadal timescales, a comparison of the spatial structure and strength of the MH circulation and the Walker circulation associated with the interdecadal and interannual timescales is required. For an estimate of the MH and Walker circulation associated with the interdecadal timescale, a warm (1982–1995) minus cold (1952–1965) composite of low-pass filtered zonal and meridional winds and vertical pressure velocity were created. The low-pass filtered fields are slowly varying and have no seasonal variations. Therefore, all months within each period were taken in these composites. The interdecadal MH circulation is represented as a pressure–latitude section of vector winds constructed with meridional winds and negative of vertical pressure velocity averaged over 70°–110°E (Figure 7.12(a)). The interdecadal

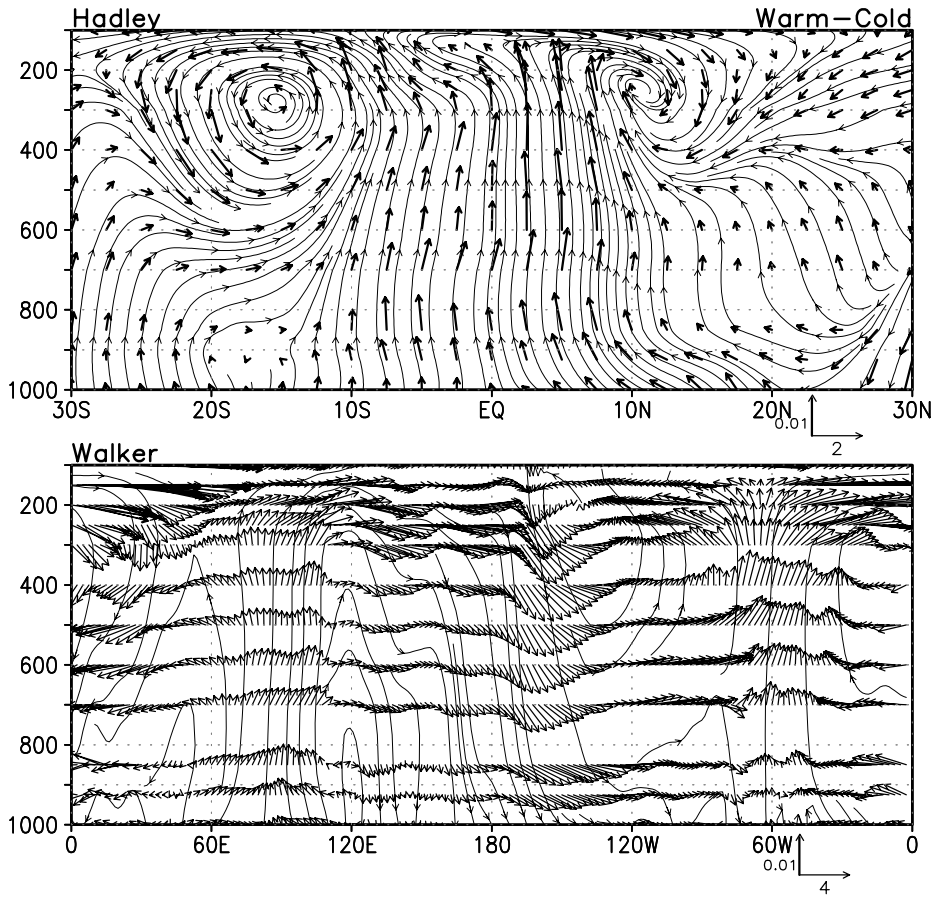

Figure 7.12. MH and equatorial Walker circulation associated with the interdecadal mode. (*top*) Latitude–height section of meridional winds ($m\,s^{-1}$) and negative of vertical pressure velocity ($Pa\,s^{-1}$) averaged over 70°–110°E of warm minus cold composites of low-pass filtered fields at 12 vertical levels. The warm (cold) composite was created by averaging low-pass filtered fields between January 1952 and December 1965 (January 1982 and December 1995). (*bottom*) Longitude–height section of zonal winds (ms^{-1}) and negative of vertical pressure velocity ($Pa\,s^{-1}$) averaged over 10°S–10°N of warm minus cold composites of low-pass filtered fields at 12 vertical levels. Unit vector in the vertical direction is $0.01\,Pa\,s^{-1}$ and 2 and 4 $m\,s^{-1}$ for the top and bottom panels respectively.

Walker circulation is represented as a pressure–longitude section of vector winds constructed with zonal wind and negative of vertical pressure velocity averaged over 10°S–10°N (Figure 7.12(b)). A similar estimate of MH and Walker circulation associated with the interannual ENSO mode was made by constructing a JJAS composite of El Niño minus La Niña from the interannual anomalies (after

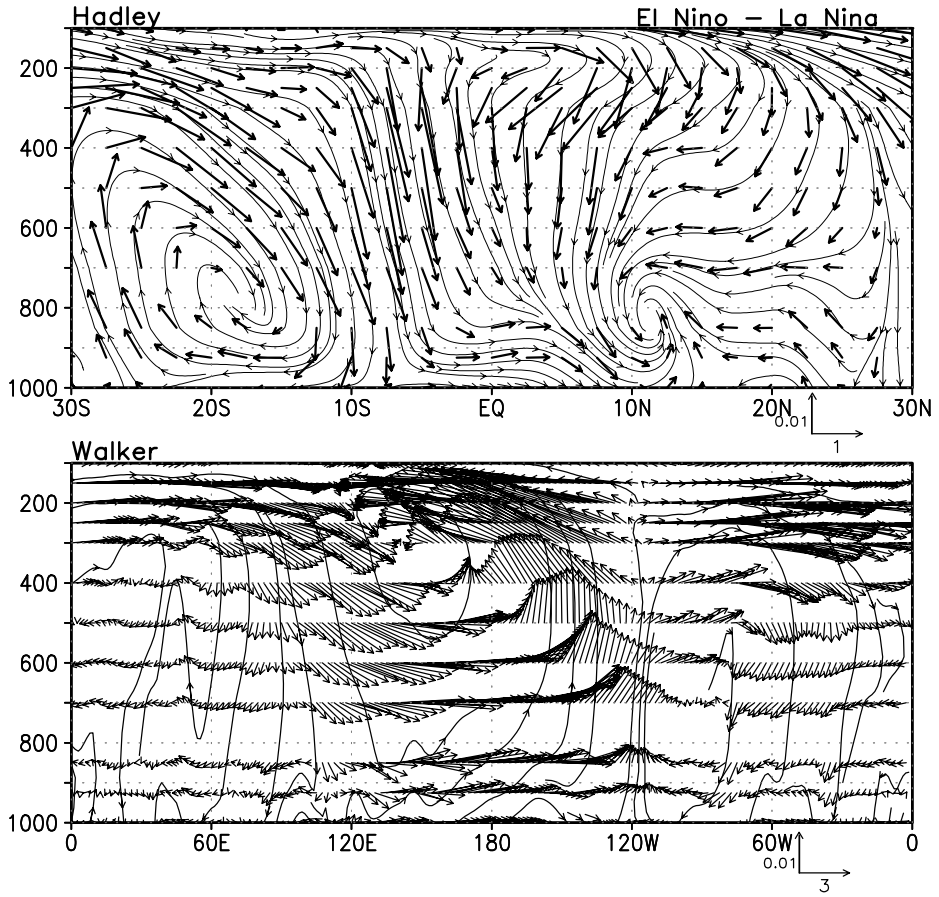

Figure 7.13. MH and equatorial Walker circulation associated with the interannual ENSO mode during northern summer (JJAS). (*top*) Latitude–height section of meridional winds ($m\,s^{-1}$) and negative of vertical pressure velocity ($Pa\,s^{-1}$) averaged over 70°–110°E of El Niño minus La Niña composites of residual (interannual) anomaly fields at 12 vertical levels. The El Niño (La Niña) composite was created by averaging JJAS anomalies for the years 1957, 1965, 1972, 1976, 1982, 1983, 1987, and 1997 (1964, 1970, 1973, and 1988). (*bottom*) Longitude–height section of zonal winds ($m\,s^{-1}$) and negative of vertical pressure velocity ($Pa\,s^{-1}$) averaged over 10°S–10°N of El Niño minus La Niña composites of residual (interannual) anomaly fields at 12 vertical levels. Unit vector in the vertical direction is 0.01 $Pa\,s^{-1}$ and 1 and $3\,ms^{-1}$ for the top and bottom panels respectively.

removal of the low-pass filtered component). 1957, 1965, 1972, 1976, 1982, 1983, 1987, and 1997 were used for the El Niño composite while 1964, 1970, 1973, and 1988 were used for the La Niña composite. The El Niño (La Niña) years were selected based on the JJAS Niño 3 SST anomaly being greater than +1 (less than −1) standard deviation. The MH and Walker circulation associated with the interannual ENSO mode are shown in Figure 7.13.

The interdecadal MH circulation is characterized by significant deep ascending motion over the equatorial IO between 10°S and 10°N and upper level subsidence extending down to 500 hPa north of 10°N. The large-scale persistent upper level subsidence inhibits convective activity over the Indian summer monsoon region leading to an overall decrease in monsoon rainfall. This appears to be responsible for the negative correlation between interdecadal variability of the ENSO and the summer monsoon. Since the Indian winter monsoon is associated with precipitation only over the southern tip of India extending to about 12°N, the winter convection (or rainfall) is facilitated by the enhanced upward motion in this region. This is consistent with the positive correlation between the Indian winter monsoon rainfall and the ENSO on interdecadal timescales. As could be derived from the EOF1 (Figure 7.10), the Walker circulation associated with interdecadal variability has a three east–west cell structure with ascending motion in the eastern equatorial IO and around 60°W and descending motion in the eastern Pacific between the Date Line and 120°W and over central Africa. A point of some significance is to note that the anomalies of the MH and Walker circulation associated with the interdecadal and interannual ENSO variability are comparable in magnitude. During a warm eastern Pacific phase of the interdecadal mode, the upward motion associated with the MH circulation over the equatorial IO (Figure 7.12(a)) is opposed by the descending motion associated with the interannual El Niño (Figure 7.13(a)) while both the modes reinforce the descending motion over the Indian monsoon region. During the same warm phase of the interdecadal mode, the MH circulation associated with interannual La Niña would result in an enhancement of the equatorial ascending motion while compensating the decadal descending motion over the Indian summer monsoon region. This means that during the warm interdecadal phase (e.g., 1965–1995), the El Niños are likely to have a stronger negative influence on the Indian summer monsoon while the La Niñas may not have any significant positive influence. Similarly, during a cold phase of the interdecadal mode (e.g., 1948–1965), the La Niñas is likely to have stronger positive effect on the Indian summer monsoon while the El Niños are likely to have no significant negative influence on the summer monsoon. With the exception of 1997, this conclusion appears to be generally born out by the observed Indian summer monsoon rainfall (Figure 7.1; also see Kripalani and Kulkarni, 1997). During 1997, the expected negative influence on the Indian monsoon by the strong El Niño on a warm interdecadal phase of ENSO appears to have been countered by some strong regional influence of opposite sign.

7.6 DECADAL CHANGES IN MONSOON INTRASEASONAL ACTIVITY

Intraseasonal oscillations (ISOs) are an integral part of the Asian monsoon. The Indian summer monsoon is characterized by a northward propagating 30–60-day oscillation (Yasunari, 1979; Sikka and Gadgil, 1980; Goswami, 2004) and a quasi-biweekly oscillation (Krishnamurti and Bhalme, 1976; Chen and Chen, 1993; Chatterjee and Goswami, 2004). The basic characteristics of the summer monsoon

ISOs and a mechanism for their genesis and scale selection have been studied extensively (for a summary see Webster *et al.*, 1998; Goswami, 2005; Wang, 2004). The ISOs essentially arise from internal dynamics, namely feedback between convection and dynamics (Goswami *et al.*, 1984; Chatterjee and Goswami, 2004). As this feedback is a function of the background mean flow and thermal structure, the statistics (e.g., frequency of occurrence, amplitude, etc.) of monsoon ISOs may be modulated by the modulation of the large-scale background flow on interdecadal timescales. Does any characteristic statistical property of the monsoon ISOs change significantly from the cold interdecadal phase of ENSO in the pre-1970s to the warm interdecadal ENSO phase of the post-1970s? This question is examined here using daily NCEP/NCAR reanalysis data between 1948 and 2002. The amplitude of intraseasonal variability (ISOV) during the Indian summer monsoon season is represented by the standard deviation of the 10–90-day filtered intraseasonal anomalies between 1 June and 30 September at each grid point. The climatological mean ISOV based on all the years for zonal winds and relative vorticity at 850 hPa and vertical pressure velocity at 500 hPa over the Indian monsoon region are shown in Figure 7.14. Interannual standard deviation of the ISOV of the three fields are shown in Figure 7.15. Existence of significant IAV of the ISOV is evident from Figure 7.15 (15–20% of the climatological mean). The interdecadal variability of ISOV is constructed from an average interannual anomaly standard deviation of 10–90-day filtered zonal winds and relative vorticity at 850 hPa over 40°–100°E, 10°–35°N using an 11-year moving window and is shown in Figure 7.16 together with the PC1 of the multivariate EOF of the low-pass filtered fields (Figure 7.11). The interdecadal variability of the ISOV in the 500-hPa vertical velocity (not shown) is also similar to that of the other two variables shown in Figure 7.15. It is interesting to note that the interdecadal variability of ISO activity over the Indian summer monsoon region has a close correspondence with the interdecadal variability of the ENSO–monsoon mode. The periods between 1955–1975 and between 1980–1995 were characterized by systematically higher and lower than normal ISO activity over the Indian monsoon region, respectively. The transition from higher than normal to lower than normal ISO activity took place simultaneously with that of the coupled interdecadal mode in the mid-1970s. The correlation between the low-pass filtered ISOV of zonal winds and relative vorticity at 850 hPa is 0.92 while that between PC1 and the low-pass filtered ISOV of relative vorticity at 850 hPa is −0.73.

These results are similar to those obtained by Zveryaev (2002) who examined the decadal–interdecadal variability of ISO activity in zonal winds at 850 hPa over the Asian monsoon region and showed that the decadal–interdecadal contributes significantly to the total variability of ISO intensity (20–35%). Using a singular value decomposition (SVD) analysis, the study also showed a strong link between the interdecadal variability of SST over the IO and that of the ISO intensity over the Asian monsoon region. As the interdecadal variability of the tropical IO is strongly linked with that in the Pacific (Figure 7.10), we believe that the interdecadal ISOV intensity is essentially modulated not merely by the IO SST but by the global-scale circulation associated with the interdecadal mode of tropical variability.

Why does the ISOV decrease over the Indian summer monsoon region during

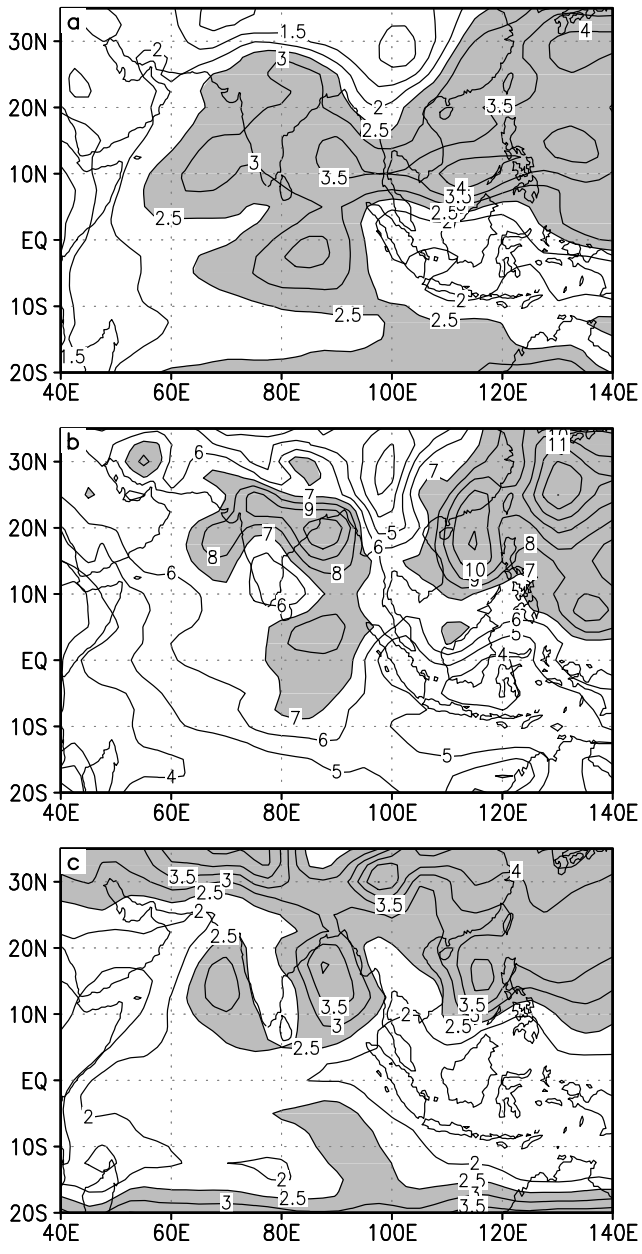

Figure 7.14. Climatological mean (based on 55 years) ISO activity during northern summer (1 June–30 September). (a) Climatological mean of standard deviation of 10–90-day filtered zonal winds at 850 hPa ($m\,s^{-1}$). (b) Climatological mean of standard deviation of 10–90-day filtered relative vorticity at 850 hPa ($10^{-6}\,s^{-1}$). (c) Climatological mean of standard deviation of 10–90-day filtered vertical pressure velocity at 500 hPa ($0.01\,Pa\,s^{-1}$).

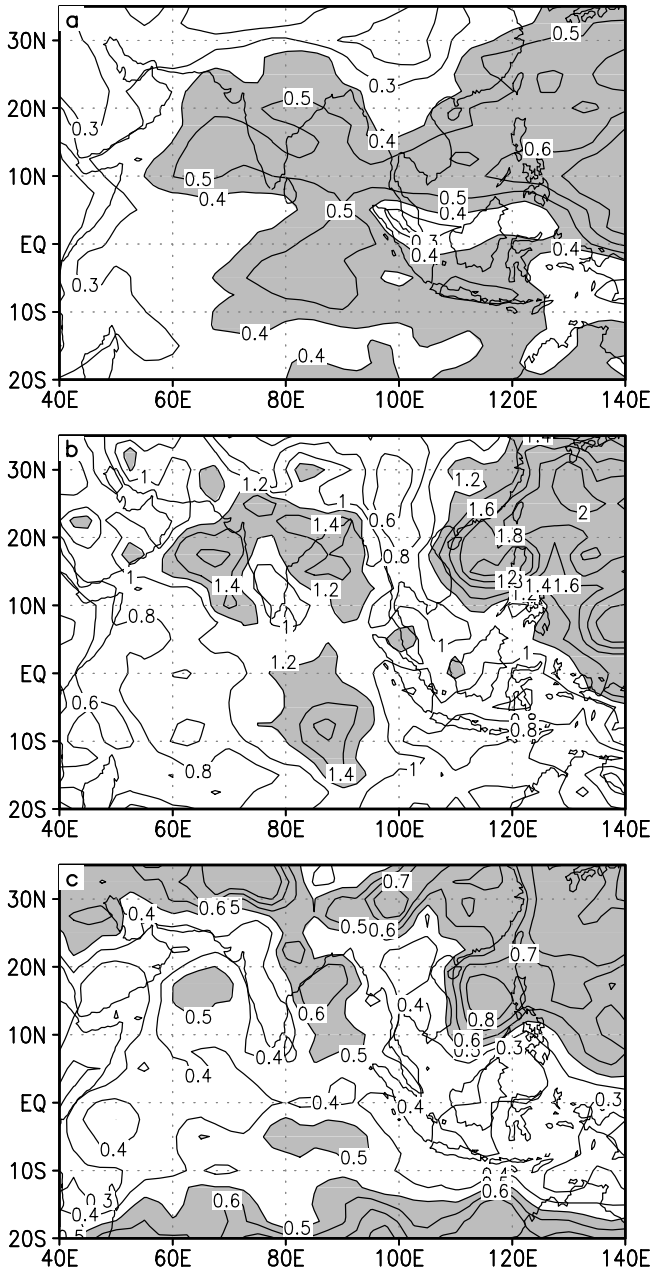

Figure 7.15. Amplitude of IAV of ISO activity. Interannual standard deviation of amplitude of 10–90-day filtered anomalies during 1 June–30 September of: (a) zonal winds at 850 hPa ($m\,s^{-1}$), (b) relative vorticity at 850 hPa $10^{-6}\,s^{-1}$, and (c) vertical pressure velocity at 500 hPa ($0.01\,Pa\,s^{-1}$).

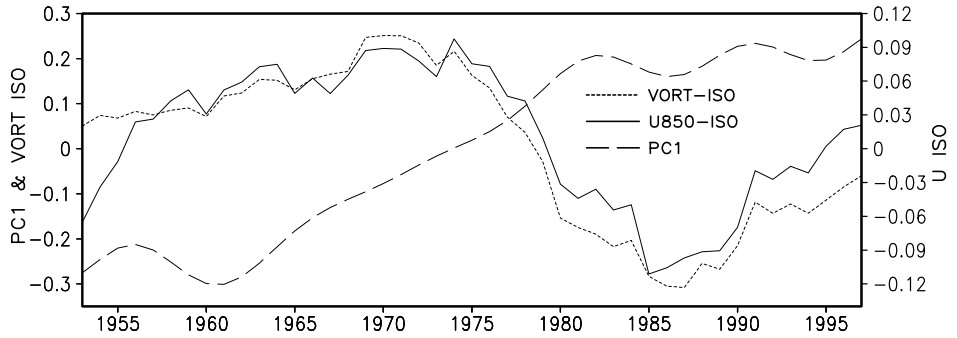

Figure 7.16. Low-pass filtered (11-year running mean) interannual standard deviation of ISO activity averaged over 40°–100°E, 10°–35°N of zonal winds at 850 hPa (solid) and relative vorticity at 850 hPa (dotted) together with PC1 of the interdecadal mode (dashed) scaled down by a factor of 5.1. The unit for standard deviation of zonal winds is $m\,s^{-1}$ while that for relative vorticity is $10^{-6}\,s^{-1}$.

the warm phase of the interdecadal mode when the SST over both the equatorial eastern Pacific as well as that over the equatorial IO are above normal (Figure 7.9(b))? To understand this, we must remember that the Indian summer monsoon ISO is a manifestation of fluctuations of convection over the two preferred positions, one over the equatorial eastern IO and the other over the MT. This results in a bimodal meridional structure of the dominant ISO mode in outgoing long-wave radiation (OLR) or in vertical velocity (see Goswami and Ajayamohan, 2001). Persistent warmer than normal SST over the equatorial IO leads to persistently enhanced convection and ISO activity in the equatorial IO. Enhanced convection over the equatorial IO gives rise to subsidence over the MT region and leads to suppression of convection and ISO activity over the MT region. Rajeevan *et al.* (2000) indeed show that the recent warm interdecadal phase of the ENSO (the post-1975 period) is associated with an increase in low cloud amount in the equatorial IO and a decrease of the same over the northern Bay of Bengal. This bimodal meridional structure of ISO activity on interdecadal timescales is seen in the first EOF of low-pass filtered ISOV of vertical velocity at 500 hPa (Figure 7.17). This pattern of interdecadal variability of ISO activity is quite similar to the SVD pattern of Zveryaev (2002). Following the same argument, we may also expect even the synoptic activity to show a similar interdecadal variability. The frequency of occurrence of monsoon depressions and storms in the northern Bay of Bengal has indeed changed from above normal during the pre-1970s to below normal during the post-1970s (Rajeevan *et al.*, 2000).

Using 40-year NCEP/NCAR reanalysis (1958–1997), Slingo *et al.* (1999) found an indication of variability of the Madden–Julian Oscillation (MJO) activity in the tropics at decadal or longer timescales. For this time period the index of MJO activity appears to have a positive 'trend', possibly with a transition to greater activity around the late 1970s and/or a very low frequency oscillation (their

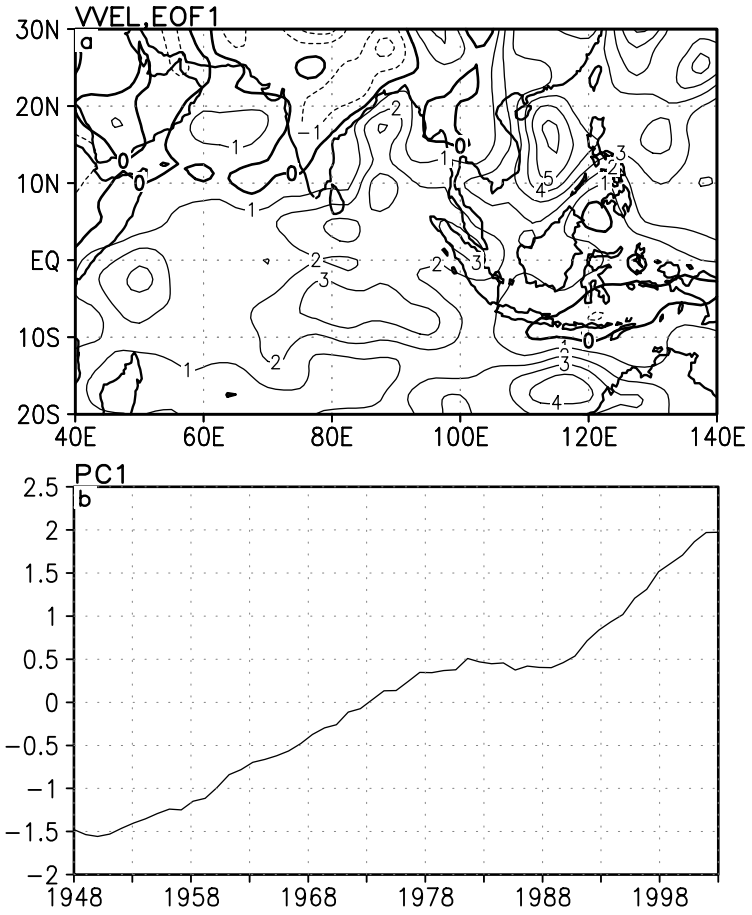

Figure 7.17. Spatial pattern of the first EOF low-pass filtered vertical pressure velocity at 500 hPa (Pa s^{-1}) and time evolution of the PC1.

figure 7). The decadal variability of MJO activity is similar to that of ISO activity observed over the Asian monsoon region and consistent with the findings of Rajeevan *et al.* (2000) over the equatorial IO and our findings over the equatorial Pacific (Figure 7.18(c)). Slingo *et al.* (1999) discussed the possible reasons for this low-frequency variability. One likely possibility is that it may be an artifact associated with additional global data into the reanalysis via the arrival of the weather-satellite era. Another is that the 'trend' may be real, possibly associated with the low-frequency SST warming of the IO. As a test, they carried out a 4-member ensemble of long integrations of an AGCM with observed SSTs as boundary conditions to examine the ability of the AGCM to simulate the very low-frequency variability. Each of the 4 members also exhibited evidence of a

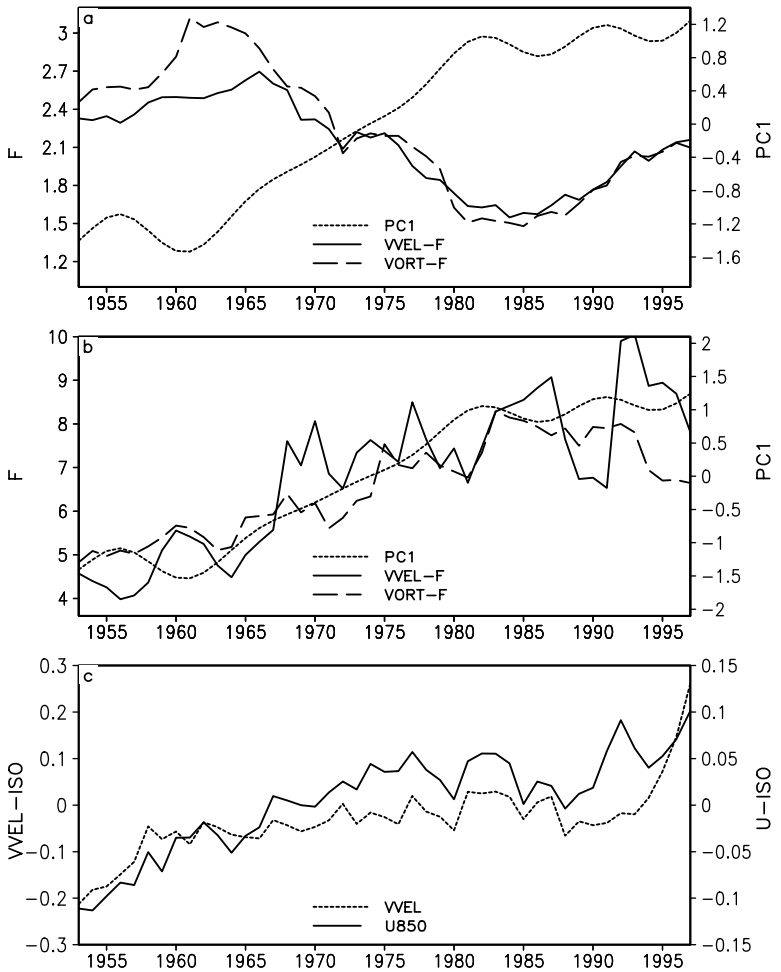

Figure 7.18. (a) Variation of predictability index (F) of relative vorticity at 850 hPa and vertical pressure velocity at 500 hPa averaged over the Indian summer monsoon region (40°–100°E, 10°–35°N) based on an 11-year moving window together with the PC1 of the interdecadal mode. (b) Variation of predictability index (F) of relative vorticity at 850 hPa and vertical pressure velocity at 500 hPa averaged over the central Pacific (160°E–160°W, 10°S–10°N) based on an 11-year moving window together with the PC1 of the interdecadal mode. (c) 11-year running mean of ISO activity of zonal winds at 850 hPa and vertical pressure velocity at 500 hPa over the central Pacific (160°E–160°W, 10°S–10°N).

similar low-frequency variability of MJO activity indicating that quite possibly the upward trend in activity is real and/or that the 'observed' SST record used for model boundary conditions may have possibly been influenced by the introduction of satellite SSTs.

7.7 DECADAL CHANGES IN MONSOON PREDICTABILITY

Significant modulation of the background mean flow (Section 7.5) and ISO activity (Section 7.6) on interdecadal timescales indicates that the predictability of the Indian summer monsoon may also undergo interdecadal variability. Foundation for this conjecture lies in the realization that the predictability of the Indian monsoon depends on the relative contribution of (or ratio between) slowly varying external forcing and the internal low-frequency (LF) variability to the observed IAV of the monsoon (Charney and Shukla, 1981; Goswami, 2004; Ajaya Mohan and Goswami, 2003). The internal LF variability of the Indian summer monsoon essentially arises from the summer monsoon ISOs (Ajaya Mohan and Goswami, 2003) while the interdecadal variability of the background mean flow would modulate the external contribution. Following Ajaya Mohan and Goswami (2003), estimates of the variance associated with the external and internal components of the IAV of zonal winds and relative vorticity at 850 hPa and vertical velocity at 500 hPa during June–September were made from daily NCEP/NCAR reanalysis and a predictability index F is defined as the ratio between the external and internal variances. In order to see the variation of the predictability index (F), an 11-year moving window is used starting from 1948 so that the first F value corresponds to 1953. The variation of the predictability index (F) for zonal winds and relative vorticity at 850 hPa averaged over the Indian summer monsoon region (40°–100°E, 10°–35°N) is shown in Figure 7.18(a) together with the PC1 of the interdecadal mode (Figure 7.11(c)). The correlation between PC1 and F for relative vorticity and zonal winds is −0.88 and −0.84, respectively (Goswami, 2004). In order to contrast the variation of predictability over the Indian monsoon region with that over the center of ENSO activity (equatorial central and eastern Pacific), F for relative vorticity at 850 hPa averaged over (170°E–110°W, 10°S–10°N), and F for vertical pressure velocity at 500 hPa averaged over (170°E–110°W, 5°S–5°N) are shown in Figure 7.18(b) together with the PC1 of the interdecadal mode (Figure 7.11). The correlation between PC1 and F for relative vorticity and vertical velocity over the central and eastern Pacific is 0.89 and 0.82, respectively.

Consistent with the findings in some earlier studies (Shukla, 1998; Ajaya Mohan and Goswami, 2003), the climate over the central and eastern Pacific is highly predictable (with F being much larger than 1) while the Indian summer monsoon climate is only marginally predictable (F only slightly larger than 1) where the contribution of internal LF variability is comparable in amplitude to that from the external slowly varying forcing. The other interesting point to note from Figure 7.18 is the following. While the predictability over the central and eastern Pacific is increasing almost monotonically, the value of F in recent years reaching almost double its value during the early 1950s, the predictability of the Indian monsoon has decreased significantly during the recent warm phase of the interdecadal ENSO compared with the pre-1970s colder phase. Strong correlation between the PC1 of the interdecadal mode and the predictability over the central and eastern Pacific as well as that over the Indian summer monsoon indicates that the interdecadal variability of predictability over both the regions is strongly linked

with interdecadal changes in the background mean flow and intraseasonal activity over the two regions. The internal variability is related to the ISO activity. Compared with the decades between 1950 and 1970, while the ISO activity during the recent decades has decreased over the Asian monsoon region (Figure 7.17(a)), it has increased over the equatorial central Pacific (Figure 7.18(c)). The resulting decrease in internal variability over the Asian monsoon region should have helped enhance the predictability over the region during recent years. The observed decrease in predictability of the Asian summer monsoon during recent decades (Figure 7.18(a)) is essentially due to a much larger decrease in external variability in recent decades due to modulation of the mean circulation by the interdecadal mode (Figure 7.3 in Goswami, 2004).

7.8 DISCUSSION AND CONCLUSION

Epochal amplitude modulation of the Indian monsoon with approximately three decades of below-normal seasonal mean rainfall followed by approximately three decades of above-normal seasonal mean rainfall has been known for a while. Physical mechanisms responsible for this interdecadal variability are poorly understood. Some studies (Mehta and Lau, 1997; Agnihotri *et al*., 2002) indicate a possibility of a forcing of the quasi 60-year variability of the monsoon by solar forcing variability over the same timescale. A temporal record of total solar irradiance (TSI) has been reconstructed since 1610 based on parameterization of sunspot darkening and facular brightening (Lean *et al*., 1995). Recently, the TSI reconstruction has been extended to 843 AD based on a quantitative estimate of common variations of production rates of ^{14}C and ^{10}Be (Bard *et al*., 2000). While spectral analysis of TSI derived from sunspot numbers do show a significant peak with a periodicity of 53 years (see Agnihotri *et al*., 2002), the TSI data derived from ^{14}C and ^{10}Be show significant peaks only at periods longer than 100 years. Therefore, existence of a significant oscillation of the solar flux at the 50–60-year timescale itself needs to be established beyond reasonable doubt. Moreover, the absolute changes in solar intensity on interdecadal timescales is very small. Hence, the direct forcing by solar flux changes on the climate in general, and the Indian monsoon in particular on interdecadal timescales, is not well established. Some evidence is presented in this chapter to support an alternative hypothesis that the interdecadal variability of the monsoon is a manifestation of a global coupled ocean–atmosphere mode of variability. It is shown that the interdecadal variability of the ENSO (amplitude modulation mode) is strongly negatively correlated with the interdecadal variability of the Indian summer monsoon while being positively correlated with the Indian winter monsoon. Using long records of Indian monsoon rainfall, global SST, and SLP data, it is shown that interdecadal variability of both AIR and ENSO (Niño 3 SST) are associated with almost identical global patterns of SST and SLP. Thus, the interdecadal variability of the Indian monsoon and that of the ENSO are likely to be parts of a global-scale oscillation on quasi 60-year timescales. Schlesinger and Ramankutty (1994) found that there exists a 65–70-year oscillation of global

surface temperature. Using a fully coupled ocean–atmosphere model, Delworth *et al.* (1993) showed ocean–atmosphere interaction can indeed give rise to a climatic oscillation with a period of approximately 50 years. These findings support our hypothesis that the quasi 60-year oscillation of the Asian monsoon and ENSO is a manifestation of a global coupled ocean–atmosphere mode of oscillation.

The ENSO is known to have had a major interdecadal transition in the mid-1970s with the period between 1950–1977 and that between 1978–2002 representing two opposite phases of the interdecadal oscillation. Using NCEP/ NCAR reanalysis data, it is shown that a coherent 3-D circulation pattern is associated with the interdecadal mode of ENSO variability with a first baroclinic mode vertical structure and a distinct three cell equatorial Walker circulation in the equatorial region. It is also found that the anomalies of the MH and Walker circulation associated with the interdecadal variability are comparable in magnitude to those associated with the IAV of ENSO. A distinct regional MH circulation associated with the interdecadal mode has significant persistent ascending motion in the equatorial IO between 10°S and 10°N with upper level subsidence over the summer monsoon region. Suppression of convection by the persistent upper level subsidence associated with the interdecadal ENSO mode explains the negative correlation between Indian summer monsoon and ENSO on interdecadal timescales. It also explains the positive correlation between Indian winter monsoon and ENSO on interdecadal timescales as the Indian winter monsoon rainfall comes from the southern tip of India which is directly under the influence of the equatorial interdecadal ascending motion. The 3-D structure of the MH and Walker circulation associated with the interdecadal mode of variability indicates that the mechanism through which ENSO influences the Indian monsoon on interannual timescales also operates on interdecadal timescales.

Strong association between variation of precipitation and low-level winds and the first baroclinic vertical structure of wind fields associated with it indicates that the interdecadal mode of variability is strongly convectively coupled. The following positive feedback between the atmosphere and the ocean may be envisaged for generating the interdecadal mode of variability. Enhanced precipitation over northern South America and Indonesia (Figure 7.10(b)) gives rise to low-level convergence and weakens the easterlies in the eastern Pacific and south-eastern equatorial IO. Decrease of latent heat (LH) flux associated with the weakened mean winds lead to a positive net heat flux to the ocean in the eastern Pacific and eastern IO resulting in positive SST anomalies in these regions (Figure 7.10(a)). Higher SSTs in these regions further weakens the easterlies and leads to a further increase in SST. However, the exact mechanism for controlling this positive feedback and for leading to an oscillatory behavior is not quite clear. More analysis and modeling studies are required to better understand the air–sea interaction associated with this mode.

In these attempts to gain insight regarding the interdecadal variability of the ENSO–monsoon relationship through examination of the 3-D structure of the interdecadal variability, precipitation and vertical pressure velocity from the NCEP/ NCAR reanalysis project have been used. As precipitation is not an assimilated

variable, it is influenced by physical parameterizations of the model used in the analysis system. As a result, a certain amount of concern has been raised (Kinter *et al.*, 2004) for use of precipitation (and also vertical velocity as it is forced by precipitation) from NCEP/NCAR reanalysis for study of interdecadal variability. This is a genuine concern. However, low-level horizontal winds from NCEP/NCAR reanalysis are assimilated variables and are more reliable. The consistency between the low-level convergence and the precipitation anomalies for the interdecadal mode (Figure 7.10(b) and (c)) indicates that the large-scale pattern of interdecadal variability of precipitation is probably still reasonable in NCEP/NCAR reanalysis. However, it may not be useful to compare interdecadal variability of precipitation from NCEP/NCAR reanalysis at small locations such as a station. The CEOF1 of SST (Figure 7.10(a)) including NCEP/NCAR reanalyzed variables during the period 1948–2002 compares well with SST regressed on low-pass filtered Niño 3 SSTAs over a much longer period between 1871 and 1995 (Figure 7.9(b)) with the PC1 of the CEOF agreeing very well with low-pass filtered Niño 3 SSTA over that period. It is believed that the interdecadal mode described by the CEOF1 including NCEP data is reasonable as it appears to be forced by the SST variations.

Intraseasonal oscillations in the tropics arise from interaction between convection and dynamics which in turn depends on the background mean flow. It is shown that the modulation of large-scale mean flow on interdecadal timescales is associated with modulation of intraseasonal activity in the tropics. The cold (warm) interdecadal phase during the pre-1970s (post-1970s) is shown to be associated with a decrease (increase) in ISO activity over the equatorial central Pacific and IO but an increase (decrease) in ISO activity over the Indian summer monsoon region. Increase in ISO activity over the central and eastern Pacific and equatorial IO associated with a warm interdecadal phase is consistent with systematically higher SSTs in these regions. This is also consistent with a decrease in ISO activity over the Indian summer monsoon region as an increase in convection over the equatorial IO leads to suppression of convection and hence ISO activity over the summer monsoon region.

As the predictability of the monthly mean and seasonal mean climate in the tropics is determined by the relative contribution of external forcing (slow modulation of the mean) and internal LF oscillations (primarily arising from ISO activity), it is also expected to be modulated by the interdecadal oscillation. It is shown that the Indian summer monsoon predictability has reduced significantly during the warm interdecadal phase of the post-1970s compared with the cold interdecadal phase of the pre-1970s. This is in contrast to the climate over the central Pacific where the predictability has increased significantly from pre-1970s to post-1970s. Increase of predictability over the core ENSO region in the Pacific and decrease of the same over the Indian monsoon region during the post-1970s is strongly correlated with increase and decrease of ISOV in the two regions during the phase of interdecadal variability. Since these estimates are based on NCEP reanalyzed data, there may be a certain amount of uncertainty in the estimates. Small changes in the potential predictability may therefore be questionable. However, it is noted from Figure 7.18 the changes in potential predictability both in the Asian monsoon region and central Pacific are

very large. Therefore, we believe that the basic signal is correct while the exact magnitude of change may be subject to revision with availability of more reliable data.

7.9 ACKNOWLEDGEMENTS

I thank Department of Ocean Development (DOD), Government of India, New Delhi and Indian National Centre for Ocean Information Services (INCOIS) for a grant partially supporting this work. I also thank M. S. Madhusoodanan and R. Vinay for help in the analysis of data and preparation of the figures for the article. Comments by two anonymous reviewers were helpful in improving the presentation of the chapter.

7.10 APPENDIX

7.10.1 Data used and method of analysis

For long records of precipitation, we use June–September (JJAS) rainfall over all India (AIR) based on 306 land stations distributed uniformly over the Indian continent (Parthasarathy *et al*., 1995). In addition to the AIR, we also examine JJAS precipitation over two large regions within India, namely the homogeneous monsoon region (HMR) and the western central Indian region (WCR) (for a definition of these regions, see Parthasarathy *et al*. (1995)). In order to show the spatial homogeneity of the interdecadal variability of summer monsoon rainfall, summer precipitation over 29 meteorological subdivisions over the Indian continent are also used (Parthasarathy *et al*., 1995). Winter monsoon rainfall over India during November to February (NDJF) mainly comes from the peninsular region. Therefore, winter monsoon rainfall is represented by peninsular Indian rainfall (PENR). The variability of NDJF AIR and that over the peninsular India (PENR) is almost identical. The time series originally constructed by Parthasarathy *et al*. (1995) has been extended to cover the period 1871 to 2000. Historical monthly precipitation for global land areas from 1901 to 1998 at 2.5 latitude by 3.75 longitude constructed and supplied by Dr. Mike Hulme of the University of East Anglia, U.K. (gu23wld0098.dat, version1 available at *http://www.cru.uea.ac.uk/mikeh/datasets/* (Hulme *et al*., 1998)) is used to extract long records over the east Asian monsoon region. Monthly mean maximum and minimum temperature over the Indian continent based on 121 uniformly distributed stations has been collected from the Indian Institute of Tropical Meteorology, Pune, India (Rupakumar *et al*., 1994; available at *http://www.tropmet.res.in/data.html*). For long records of SST, we have used the analysis of global SST for the period 1856–1996 created by Kaplan *et al*. (1997). The global SST analysis is obtained through application of reduced space optimal estimation to the global SST anomalies. For SLP data, we have used the GMSLP2 data set developed by the Commonwealth Scientific and Industrial

Research Organization (CSIRO) and the UK Meteorological Office (Allan *et al.*, 1996; Bassnett and Parker, 1997) covering the period between 1871 and 1995. The data set has been developed by blending a combination of existing mean SLP analysis with marine and land observations using a Laplacian interpolation technique. NCEP/NCAR reanalysis has been used for circulation (Kalnay *et al.*, 1996; Kistler *et al.*, 2001). Due to the fact that the analysis system and the forecast model remains unchanged throughout the reanalysis period and that it uses a database as complete as possible, NCEP/NCAR reanalysis provides a homogeneous research quality data set devoid of artificial climate jumps.

We obtained monthly mean horizontal winds and vertical velocities at standard pressure levels for the period 1948–2002. Although reanalyzed precipitation may have some bias arising from inadequacy of the forecast model used in the reanalysis, only NCEP/NCAR reanalyzed precipitation can provide some insight regarding the relationship between circulation and convective activity on interdecadal timescales. For this purpose, monthly mean reanalyzed precipitation for the period was also extracted. Although 55 years is not a long period for studying interdecadal variability, this period contains a major transition of tropical interdecadal variability in the late 1970s. Therefore, we expect the reanalysis data set to provide important insight regarding the 3-D structure of the monsoon interdecadal variability. In order to study variation of intraseasonal oscillations on interdecadal timescales and for the study of change in predictability of the monsoon, daily zonal and meridional winds at 850 hPa and vertical velocity at 500 hPa were extracted from NCEP/NCAR reanalysis for the entire 55 years. Monthly anomalies of different variables were calculated by removing the climatological mean annual cycle from the monthly means. While the climatological mean annual cycle for SST was constructed based on data between 1951 and 1980, the climatological mean annual cycle of all other variables were constructed based on entire periods of respective data. We also constructed seasonal mean anomalies for summer (JJAS) and winter (NDJF). Interdecadal components of the seasonal mean SST and SLP fields were obtained by using an 11-year running mean of the seasonal anomalies. It was earlier found that the 11-year running mean of the seasonal mean anomalies is closely similar to the interdecadal variability extracted by a harmonic filter retaining only periods greater than 7 years. To separate interdecadal variations from the IAV of the global NCEP/NCAR reanalysis at all levels, a harmonic filter is used. A low-pass filtered field is created by reconstructing it from all the harmonics with periods longer than 7 years. A residual field representing IAV is obtained by subtracting the low-pass filtered field from the original monthly anomaly time series. For characterization of intraseasonal activity, daily anomalies are required. Daily anomalies of zonal winds at 850 hPa, relative vorticity at 850 hPa, and vertical velocity at 500 hPa are calculated by subtracting a climatological daily annual cycle from the daily observations. The climatological daily annual cycle is defined as the climatological mean of annual cycles of each year constructed as the sum of the annual mean and first three harmonics of each year. The intraseasonal anomalies are then extracted using a 10–90-day band-pass Lanczos filter.

Part Three

8

Mesoscale processes

Richard H. Johnson

8.1 INTRODUCTION

Within Asia and other monsoon regions of the World, most significant weather events are localized or *mesoscale* in nature. The term mesoscale generally refers to horizontal scales between ten and several hundreds of kilometers, which lie between the scale height of the atmosphere and the Rossby radius of deformation (Ooyama, 1982). The latter scale can become quite large in equatorial regions owing to the weakness in background rotation, hence mesoscale processes in the tropics can occur over a broad range of horizontal scales. Although local weather is influenced by processes ranging from the largest scales to the smallest, those on the mesoscale have the most direct impact.

In the Asian monsoon region, there are a multitude of mesoscale processes that influence the weather. Convection is arguably the most important, contributing through latent heat release to the energetics of the large-scale monsoon circulation. Its far-reaching effects impact short-term weather, the diurnal cycle, as well as intraseasonal, seasonal, and interannual variability of the monsoon. Convection responds to and modulates its environment through a wide range of processes that can be classified as local, advective, or dynamical (Johnson and Mapes, 2001). These processes are associated with convective preconditioning and triggering, as well as the feedback of convection onto its environment and larger scales of motion.

In addition to convection, a wide range of other mesoscale processes influence the Asian monsoon. Notable among these are topographically forced local circulations (including flow blocking, sea and land breezes, and mountain and valley circulations), jets, surface-atmosphere interactions, gravity currents and gravity waves, coastally trapped disturbances, and mesoscale instabilities. Most of these phenomena are significantly modulated by the diurnal cycle. In this chapter we review mesoscale atmospheric processes and provide some examples that occur in

B. Wang (ed.), *The Asian Monsoon*.

the Asian monsoon region, many of which are relevant to other monsoon regions of the World.

8.2 CONVECTION

Atmospheric convection is one of nature's most complex and multifaceted phenomena (e.g., Ludlam, 1980; Cotton and Anthes, 1991; Emanuel, 1993; and Houze, 1993). Considerable insight into tropical and monsoon convection has been gained from field experiments such as the GATE (GARP Atlantic Tropical Experiment), MONEX (Monsoon Experiment), and TOGA/COARE (Tropical Ocean–Global Atmosphere/Coupled Ocean–Atmosphere Response Experiment) (Houze and Betts, 1981; Johnson and Houze, 1987; Godfrey *et al.*, 1998); however, many aspects of convection are still not well understood.

A map of the global distribution of precipitation based on data from the Tropical Rainfall Measuring Mission (TRMM) is presented in Figure 8.1 (color section). Much of the World's heaviest rainfall occurs in the regions of the Asian–Australian monsoon. The largest annual totals occur in proximity to coastlines, suggesting possible roles of sea and land breezes and topographic effects in the precipitation mechanisms. To understand this distribution or other aspects of monsoon rainfall, we need to first examine the precipitation characteristics and structural properties of moist convection.

8.2.1 Distribution, organization, and structure of tropical convection

There is growing evidence from field experiments over the past three decades that convective systems in the various monsoon and tropical regions of the World bear a close resemblance to each other. In particular, deep convection tends to organize on the mesoscale and undergo an evolution characterized by a dominance of convective precipitation (localized heavy rainfall) early in the life cycle followed by an upscale growth and development of stratiform precipitation (lighter rainfall) on a timescale of 2–4 hours and longer (Zipser, 1977; Houze, 1977; Leary and Houze, 1979). The stratiform precipitation is partly a result of the transfer of hydrometeors from the convective region and partly a result of *in situ* condensation and deposition in the stratiform region. The net result is a mesoscale convective system or MCS, defined by Houze (1993) as a cloud system that occurs in connection with a cluster of showers and produces a contiguous precipitation area $\sim$100 km or more in horizontal scale in at least one direction.

Global climatologies of MCSs in the monsoon regions were first carried out using satellite studies of mesoscale convective complexes or MCCs (Maddox, 1980), the largest and longest lived of MCS populations. Laing and Fritsch (1997) present a map of MCC locations using satellite data (Figure 8.2). They found that MCCs are (1) mostly continental, (2) tend to occur in gradient zones between OLR maxima and minima (i.e., they are normally not in the most frequently raining areas), and (3) tend to occur in the lee (relative to the prevailing mid-level flow) of

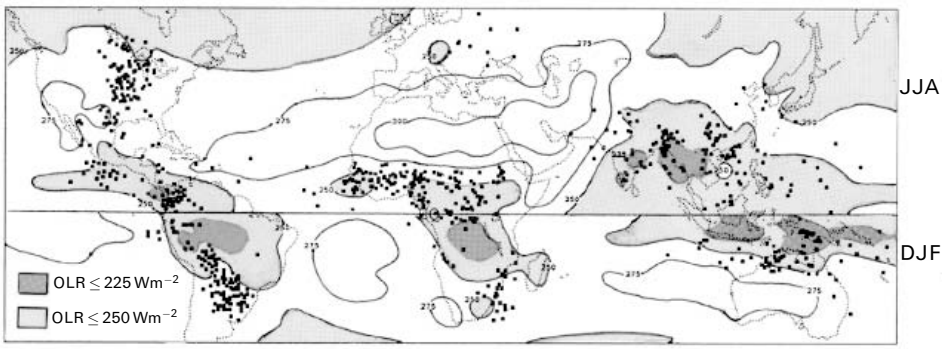

Figure 8.2. MCC locations based on 1980s satellite data for JJA in the northern hemisphere and DJF in the southern hemisphere. Outgoing long-wave radiation (OLR) values are shaded. From Laing and Fritsch (1997) Royal Meteorological Society.

elevated terrain. Figure 8.2 shows that MCCs are common not only over the region of the Asian–Australian monsoon (China, India, Bangladesh, and northern Australia) but also over South America to the lee of the Andes and West Africa. These findings have recently been confirmed and extended by TRMM microwave measurements (Nesbitt *et al.*, 2000).

The structure and dynamics of MCSs have been the subject of intensive study for the past 30 years (Houze, 1993). A recent investigation of the evolution of nearly 100 MCSs over the central USA has revealed new characteristics of such systems (Parker and Johnson, 2000). Three main patterns of MCS organization have been identified (Figure 8.3). The three modes are convective lines with trailing (TS), leading (LS), and parallel (PS) stratiform precipitation. TS systems were the most common, accounting for ~60% of the cases, with the LS and PS each accounting for about 20%. TS systems have received considerable attention (e.g., Houze *et al.*, 1990), but the occurrence of LS and PS systems is not insignificant, and there is evidence they are important in monsoon regions. For example, MCSs in the Baiu front appear to have these precipitation structures (Ninomiya and Muarkami, 1987). Wang (2004) recently found LS organization of MCSs to be commonplace over the northern South China Sea during the 1998 South China Sea Monsoon Experiment (SCSMEX). TS systems normally propagate rapidly (~10–15 $m\,s^{-1}$) and, as such, produce brief, heavy rainfall but usually not flash floods. LS and PS systems, on the other hand, move more slowly and are often implicated in flash flooding as a result of slow-moving, 'training', and/or back-building cells. For example, heavy rainfall over Taiwan has been attributed to back-building cells associated with the Mei-yu front (Li *et al.*, 1997).

It has long been known that the organization of tropical convection is influenced predominantly by the vertical shear and convective available potential energy or CAPE (Moncrieff and Green, 1972). Various observational studies in the eastern Atlantic and northern Australia have confirmed the strong influence of environmental winds on the structure, orientation, and propagation of convective bands

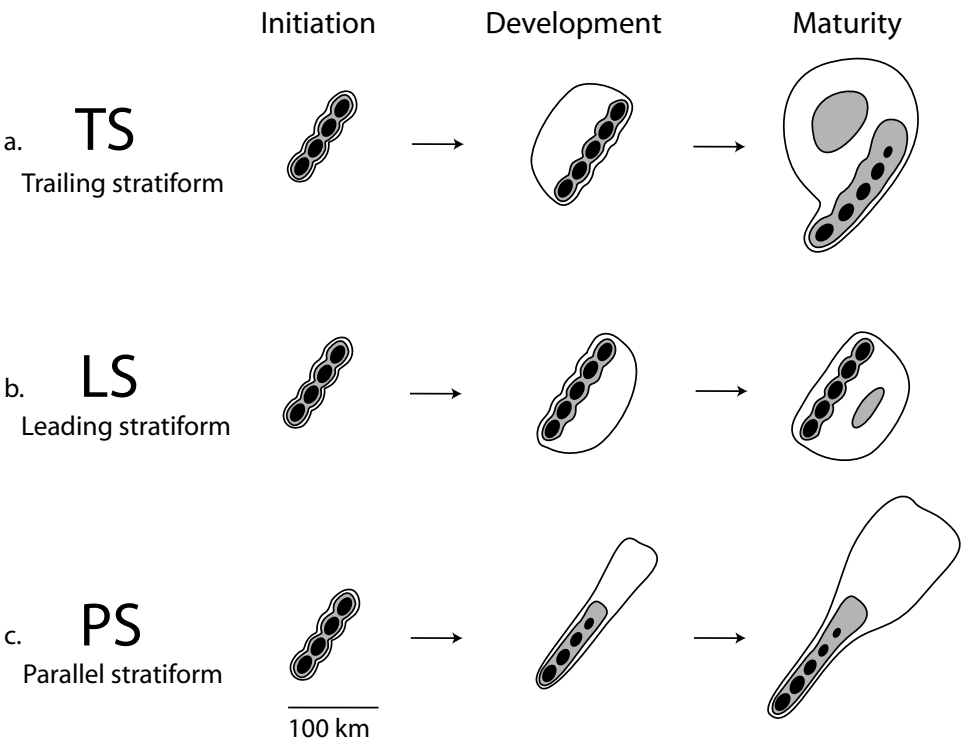

Figure 8.3. Schematic reflectivity drawing of idealized life cycles for three linear MCS archetypes: (a) TS, (b) LS, and (c) PS. Approximate time intervals between phases: for TS 3–4 h; for LS 2–3 h; for PS 2–3 h. Levels of shading roughly correspond to, 20, 40, and 50 dBZ. From Parker and Johnson (2000).

(e.g., Barnes and Sieckman, 1984; Alexander and Young, 1992; Keenan and Carbone, 1992). LeMone *et al.* (1998) investigated the organization of convection over the western Pacific warm pool using aircraft data from the TOGA/COARE. In agreement with Alexander and Young (1992) they found that vertical shear in the low to mid-troposphere is a key factor in determining the orientation of convective bands, while CAPE influences their depth and longevity. Their results have been recently supported by numerical simulations of convection in shear by Robe and Emanuel (2001).

The results of LeMone *et al.* (1998) have been recently extended to the Asian summer monsoon by Johnson *et al.* (2005). The modes of organization of convection over the northern South China Sea during the onset of the 1998 east Asian summer monsoon have been determined using the BMRC C-POL radar located on Dongsha Island (Figure 8.4). This figure, adapted from LeMone *et al.* (1998), is a summary of the findings from SCSMEX. In general, the organizational modes for SCSMEX were consistent with those determined by LeMone *et al.* (1998) for the western Pacific warm pool. It is found that when the shear in the lowest 200 hPa exceeds 4 m s^{-1} and

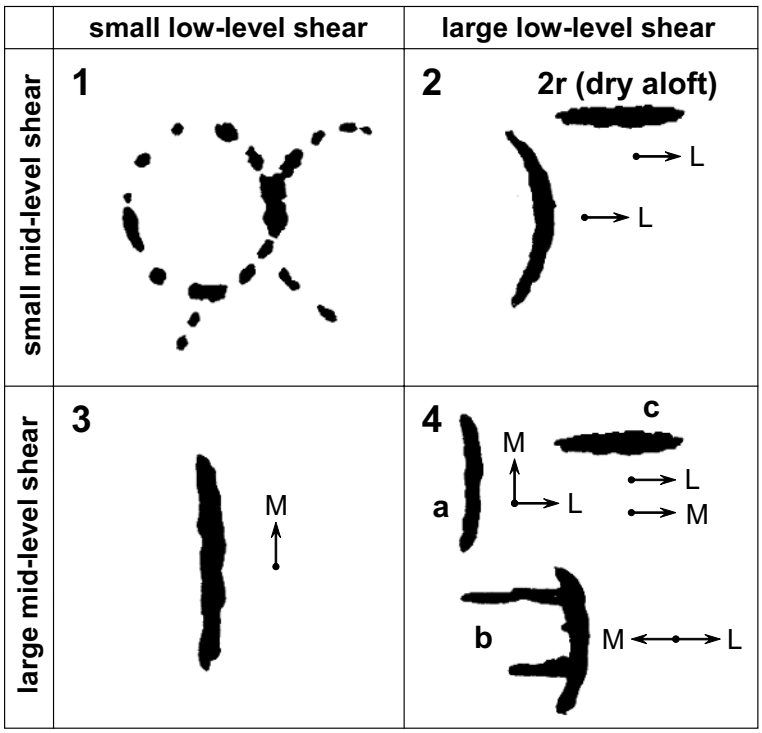

Figure 8.4. Schematic depiction adapted from LeMone *et al.* (1998) of four main categories of convective structures for given vertical shears in the lower troposphere (1,000–800 hPa) and at middle levels (800–400 hPa) based on COARE observations, but modified to include results from SCSMEX (modes 2r and 4c added). Length of schematic convective bands is ~100–300 km; line segments in upper left frame are up to 50 km in length. Cutoff between 'strong' and 'weak' shear for the lower layer (1,000–800 hPa) is $4\,m\,s^{-1}$ and for the middle layer (800–400 hPa) is $5\,m\,s^{-1}$. Arrows marked L and M are shear vectors for lower and middle layers, respectively. See text for description of convective modes.
From Johnson *et al.* (2005).

the shear from 800–400 hPa is less than $5\,m\,s^{-1}$, the orientation of the primary convective band in MCSs is perpendicular to the low-level shear (type 2 in Figure 8.4). Secondary lines parallel to the low-level shear are found in some cases ahead of these bands. In the absence of strong low-level shear, lines form parallel to the 800–400 hPa shear when its magnitude exceeds $5\,m\,s^{-1}$ (3 in the lower left frame of Figure 8.4). When the vertical shear exceeds the thresholds in both layers and the shear vectors are not in the same direction, the primary band is normal to the low-level shear (4a or 4b in the lower right frame of Figure 8.4). Trailing secondary bands parallel to the mid-level shear occur if the mid-level shear is opposite the low-level shear (4b). When the shear in both layers is weak, convection develops in arcs along outflow boundaries (1). Two additional modes of convection have been identified

from analysis of SCSMEX C-POL radar data (Figure 8.4): shear-parallel bands (2r) for strong low-level shear and weak mid-level shear when the air is dry aloft, and shear-parallel bands (4c) for strong shears in both layers when the shear vectors are in the same direction. The latter two modes are related to the passage of mid-latitude troughs (Johnson *et al.*, 2005).

8.2.2 Latent heating profiles and the monsoon

MCSs produce areas of convective and stratiform precipitation that vary over the life cycle of the storms. These two precipitation features have strongly contrasting latent heating profiles, as illustrated in Figure 8.5 for the mature stage of a westward-propagating tropical squall line. The convective region is characterized by a single, condensational heating peak in the low to mid-troposphere. The stratiform region has a peak in the upper troposphere associated with condensation or deposition aloft, and a cooling peak in the lower troposphere associated with melting and evaporation (Houze, 1982; Johnson, 1984). The dynamical effects of latent heating can be assessed through the potential vorticity equation for frictionless flow:

$$\frac{dP}{dt} = -(\varsigma_\theta + f)\frac{\partial \dot{\theta}}{\partial p} - \left[\mathbf{k} \times \nabla_\theta \dot{\theta} \times \frac{\partial \mathbf{v}}{\partial \theta}\right]\frac{\partial \theta}{\partial p} \tag{8.1}$$

where $\dot{\theta}$ is the diabatic heating rate, $\varsigma_\theta + f$ is the absolute vorticity on an isentropic surface, and $P \equiv -(\varsigma_\theta + f)\partial\theta/\partial p$ is the potential vorticity. From the first term on the RHS of equation (8.1), the increase with height of diabatic heating at mid-levels within the stratiform region of an MCS (Figure 8.5) produces a positive potential vorticity anomaly in the mid-troposphere. This heating distribution often leads to the generation of a mid-level mesoscale convective vortex or MCV (Zhang and

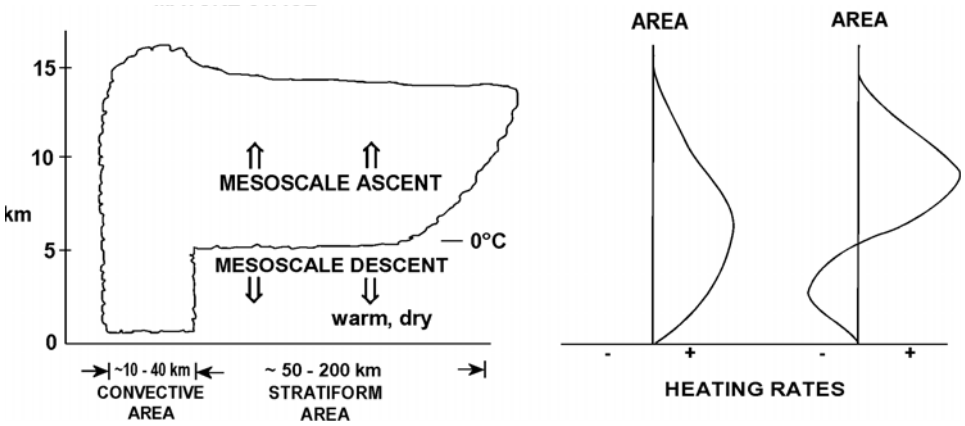

Figure 8.5. Idealized mature stage of MCS illustrating convective and stratiform precipitation areas along with associated heating profiles.
From Johnson (1986) Meteorological Society of Japan.

Fritsch, 1987; Raymond and Jiang, 1991; Hertenstein and Schubert, 1991). MCVs appear to be common over China in the Yangtze valley during the Mei-yu season, potentially contributing to long-lived precipitation systems, heavy rainfall, and flash floods (e.g., Akiyama, 1984a,b). They have also been observed in the Australian summer monsoon (Keenan and Rutledge, 1993). In addition, MCVs are thought to be potential precursors or contributors to tropical cyclogenesis (Velasco and Fritsch, 1987; Montgomery and Enagonio, 1998).

The mesoscale characteristics of convection have an important impact on the temporal and spatial distribution of monsoon heat sources and sinks. Yanai *et al.* (1973) introduced the following notation and terminology in connection with the conservation laws for heat and moisture:

$$Q_1 = \frac{\partial \bar{s}}{\partial t} + \bar{\mathbf{v}} \times \nabla \bar{s} + \bar{\omega} \frac{\partial \bar{s}}{\partial p} = Q_R + L(\bar{c} - \bar{e}) + \frac{\partial}{\partial p} \overline{s'\omega'} \tag{8.2}$$

$$Q_2 = -L\left(\frac{\partial \bar{q}}{\partial t} + \bar{\mathbf{v}} \times \nabla \bar{q} + \bar{\omega} \frac{\partial \bar{q}}{\partial p}\right) = L(\bar{c} - \bar{e}) + L \frac{\partial}{\partial p} \overline{q'\omega'} \tag{8.3}$$

where $s = c_p T + gz$ is the dry static energy, Q_R the radiative heating rate, c the condensation rate, e the evaporation rate, q the specific humidity, and the deviations from horizontal averages (indicated by overbars) are denoted by primes. Q_1 and Q_2 are the residuals of heat and moisture budgets of the 'resolvable' motion, first introduced by Yanai (1961). They are called the 'apparent' heat source and moisture sink, respectively, because they include true sources and sinks (condensation and evaporation) as well as correlation terms resulting from unresolved eddies (Yanai and Johnson, 1993). Comparing equations (8.2) and (8.3), it can be seen that for precipitation systems possessing negligible eddy transports (i.e., stratiform precipitation systems), the profiles of $Q_1 - Q_R$ and Q_2 should closely match (Luo and Yanai, 1984; Arakawa and Chen, 1987). When deep convection is present, the peaks in Q_1 and Q_2 are separated (e.g., as in the tropical western Pacific study of Yanai *et al.* (1973)).

Luo and Yanai (1984) computed heat and moisture budgets over and around the Tibetan Plateau for the period 26 May to 4 July 1979 using sounding data from the First GARP Global Experiment (FGGE). Their results are shown in Figure 8.6 for four regions. Region I, which is centered over the western Plateau near 34°N, 80°E, shows a pattern of mean upward motion with a maximum Q_1 just above the surface and negligible Q_2. This structure is indicative of a strong sensible heat flux in this region with very little precipitation. Recently, Ueda *et al.* (2003a) found a somewhat different result using 1998 GAME (GEWEX Asian Monsoon Experiment) reanalysis data, namely, that heating by deep convection nearly equaled that due to the sensible heat flux over the western Plateau. This finding may indicate important interannual variability in this region, or it may point to the difficulty in using reanalysis data, which are sensitive to convective parameterizations, to assess heating profiles. Over the eastern Plateau (Region II, centered near 34°N, 95°E) the mean vertical motion is still upward, but latent heat release is more important, contributing to nearly half the apparent heat source. Region III, centered over the Yangtze valley

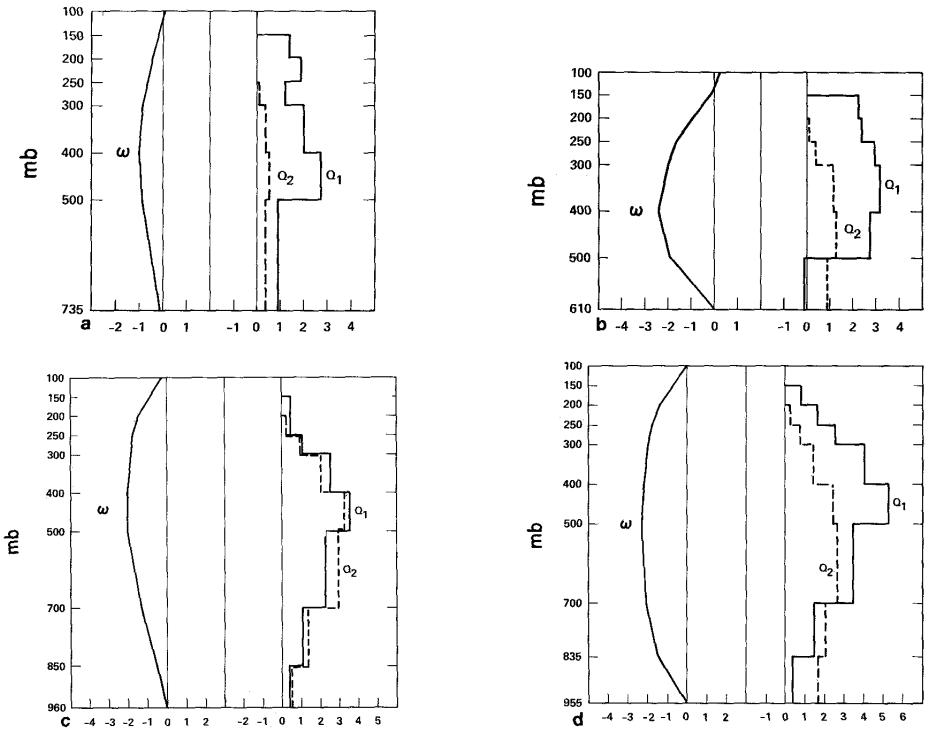

Figure 8.6. Forty-day mean vertical distributions of areal mean vertical p-velocity ($\mathrm{hPa\,h^{-1}}$), heating rate Q_1, and drying rate Q_2 for (a) Region I, (b) Region II, (c) Region III, and (d) Region IV.
From Luo and Yanai (1984).

(near 28°N, 115°E), exhibits large Q_1 and Q_2 which are virtually coincident in the mid-troposphere, suggestive of a predominance of stratiform precipitation in that region. Finally, Region IV, centered in the Assam–Bengal area near 25°N, 85°E, shows large Q_1 and Q_2 peaks, but displaced from each other, indicative of the prevalence of deep convection.

There have been other studies of the latent heating profiles over China during the summer monsoon for the FGGE year (Nitta, 1983; Kato, 1985) and later years (Ding and Hu, 1988; Ding and Wang, 1988; Johnson *et al.*, 1993), and over Taiwan during the 1987 Taiwan Area Mesoscale Experiment or TAMEX (Johnson and Bresch, 1991). Johnson *et al.* (1993) found that during the pre-Mei-yu and Mei-yu periods of 1987, 1988, and 1989, precipitation type over the Yangtze region was a mixture of convective and stratiform, whereas over southern China deep convection predominated. Inferences from satellite data support these findings (e.g., Ninomiya, 1989), but it has only been in recent years that radar data (including Doppler observations) have been available to document in detail the convective and stratiform properties of MCSs over Tibet and within the Mei-yu and Baiu frontal zones

(Uyeda *et al.*, 2001; Shinoda and Uyeda, 2002; Chen *et al.*, 2003; Yamada *et al.*, 2003).

As noted earlier, the vertical distribution of latent heating determines the generation of potential vorticity anomalies. On the other hand, the generation of available potential energy A_E can be written as:

$$\frac{\partial A_E}{\partial t} = -\frac{[\nu' T']}{\sigma}\frac{\partial [T]}{\partial y} - \frac{[\omega' T']}{\sigma}\frac{\partial [T]}{\partial p} + \frac{R}{gp}[\omega' T'] + \frac{[Q_1' T']}{c_p \sigma} \tag{8.4}$$

where brackets refer to a zonal average and σ is the static stability. Thus, there is a generation of positive A_E where positive heating anomalies coincide with warm anomalies. Hence, an accurate determination of the vertical and horizontal distribution of Q_1 as well as the temperature field is needed to properly represent both the dynamics and energetics of monsoon circulations and disturbances in prediction models.

Since the heating profiles in the convective and stratiform regions contrast greatly (Figure 8.5), the relative amounts of convective and stratiform precipitation in cloud systems should impact the large-scale response to convection. A climatology of the relative contributions of convective and stratiform precipitation to total rainfall has been carried out by Schumacher and Houze (2003) using the TRMM precipitation radar. Their results (Figure 8.7, color section) show a wide variation in the stratiform rain fraction over the globe, with greatest amounts (50–60%) over the central and western Pacific and Indian Ocean. Low stratiform rain fractions (20–30%) are observed over Africa, parts of the Maritime Continent, and the Caribbean. This variability is not fully understood, but is likely related to the differing instability, humidity, and wind shear profiles in the different locations. Schumacher *et al.* (2004) have recently used the observed stratiform rain fractions in Figure 8.7 in an idealized general circulation model to show that the strong zonal gradient in the stratiform rain fraction across the equatorial Pacific, from ~30% over Indonesia to ~60% over the eastern Pacific, accounts for the observed tilted structure of the east–west Walker circulation.

The impact of convection on the modeled large-scale circulation appears to be critically sensitive to the heating distribution. The theoretical basis for this sensitivity is discussed in Hartmann *et al.* (1984). Early modeling studies of the Madden–Julian Oscillation (MJO) have shown an important sensitivity of the characteristics of this global-scale wave to the vertical heating distribution (e.g., Lau and Peng, 1990). In particular, when the heating peak is in the upper troposphere, the wave appears to move too fast, whereas when the peak is in the lower troposphere, the phase speed is more in line with observations (e.g., Sui and Lau, 1989). However, more recently, Lin and Johnson (1996a), Tung *et al.* (1999), Mapes (2000), and Lin *et al.* (2004) have presented Q_1 profiles for TOGA/COARE MJO events indicating a 'top-heavy' structure to the heating and suggesting (from Figure 8.5) a large contribution from stratiform precipitation. Using TRMM data, Lin *et al.* (2004) confirmed that the MJO for the COARE region has an anomalously large stratiform rain fraction of 60%, much larger than the long-term mean of ~40%. They also found a significant

tilt in the heating profile in the MJO over the western Pacific, with heating in stratiform anvils (latent plus radiative) lagging the surface precipitation maximum by a few days. Kiladis *et al.* (2005) also found this tilted structure over the western Pacific (but not the Indian Ocean) and noted that the evolution of the heating field leads to a temperature structure that favors MJO growth. Yanai *et al.* (2000) recently computed the generation of A_E for the MJO observed during TOGA/COARE and found a strong generation by deep convection in the upper troposphere in the active part of this disturbance, while 'convective damping' (a negative value of the last term in equation (8.4)) was found in the lower troposphere.

The latent heating profiles within MCSs also have a profound influence on the mesoscale environment of convection. In particular, convective heating generates gravity waves which propagate away from the convective source (Nicholls *et al.*, 1991; Mapes, 1993). In the work of Nicholls *et al.* (1991) thermally forced gravity waves were considered in the context of a 2-D, linear, incompressible, hydrostatic, and Boussinesq fluid. The thermal forcing was considered to consist of contributions from both convective and stratiform precipitation (as illustrated in Figure 8.5). The sum of the two modes of heating yields positive heating at mid and upper levels and cooling near the surface. This form of heating produces two prominent gravity wave modes, the first internal or $n = 1$ mode and the second internal or $n = 2$ mode. For an atmosphere at rest, the horizontal phase speeds of internal modes are given by $c = NH/n\pi$, where N is the Brunt–Väisälä frequency and H is the fluid depth. Using a typical value of N from 2 to 8 km of $1.1 \times 10^{-2}\,\mathrm{s}^{-1}$ and $H = 12$ km, then c for the $n = 1$ and $n = 2$ modes is $\sim$42 and 21 $\mathrm{m\,s}^{-1}$, respectively. Thus, the waves rapidly disperse.

Both modes produce subsidence in the upper troposphere as the waves propagate away from the source, as shown in Figure 8.8 for a superposition of the solutions with a rigid upper lid two hours after the heating has been turned on. Relative to the initial state, the heating produces positive buoyancy in the upper troposphere and negative buoyancy in the lower troposphere. Near the source there is a positive pressure perturbation in the upper troposphere and a minimum in the mid-troposphere. The flow is away from the source in the upper and lower troposphere and toward the source at mid-levels. The latter feature occurs near the melting level since the base of the stratiform anvil is there (Figure 8.5) (i.e., the node in the $n = 2$ profile is near the 0°C level). This mid-level inflow has been referred to by Mapes and Houze (1995) as 'melting convergence.' The solutions are modified somewhat when the rigid lid is removed such that gravity wave energy propagates upwards into the stratosphere and the intensity of the circulations in the troposphere are reduced away from the source, but the overall qualitative results are unchanged (Nicholls *et al.*, 1991; Pandya *et al.*, 1993). Outside the tropics (e.g., in the MCV-forming region of China), the Earth's rotation leads to geostrophic adjustment for a heat source on the scale of MCSs such that the warming is trapped near the source rather than propagating away as shown in Figure 8.8 (Johnson and Mapes, 2001), which could lead to the formation of MCVs. The upward displacement at low levels near the source caused by the $n = 2$ or 'stratiform' mode can reduce convective inhibition and also by cooling,

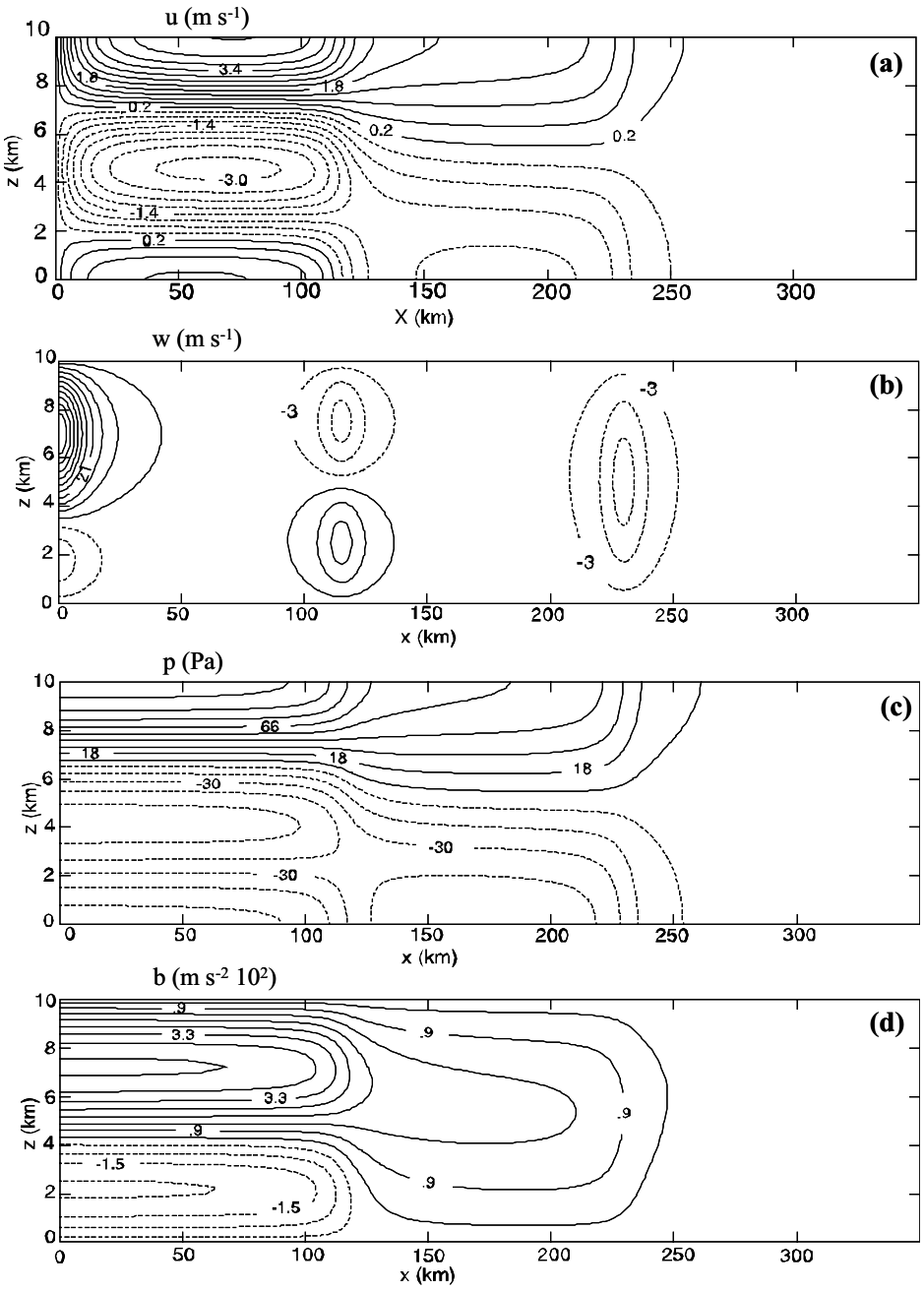

Figure 8.8. Rigid-lid solutions (top to bottom) for perturbations of u, w, p, and buoyancy b for superposition of $n = 1$ and 2 modes. The magnitude of the heat source at the origin is $1.0\,\mathrm{J\,kg^{-1}}$ with a half-width of 10 km, $H = 10\,\mathrm{km}$, $N = 0.01\,\mathrm{s^{-1}}$, and $t = 2\,\mathrm{h}$.
From Nicholls *et al.* (1991).

increase the relative humidity. Both effects favor new convection adjacent to old, possibly explaining why convection in the tropics and monsoon regions tends to cluster together or be 'gregarious' (Mapes, 1993). This concept has been generally supported by modeling studies of the clustering of deep convection (Lac *et al.*, 2002), but in a 4-D setting with many MCS heat sources growing and decaying, detailed patterns of vertical displacement are very complex (Mapes, 1998).

It has been pointed out by Mapes (2000) that the top-heaviness of deep-convective heating profiles is inadequate to balance radiative cooling, which is large through the lower troposphere. This finding implies that in the tropics there must be abundant precipitating shallow cumulus and cumulus congestus clouds to provide lower tropospheric heating, essentially to offset widespread cooling beneath stratiform anvils. This finding has been borne out by radar observations of clouds in TOGA/COARE (DeMott and Rutledge, 1998; Johnson *et al.*, 1999; Short and Nakamura, 2000). This topic leads us to a consideration of cloud populations in the tropics and Asian monsoon.

8.2.3 Cloud populations

It has long been known that trade wind cumulus and deep cumulonimbus represent primary components of the broad spectrum of cumulus clouds in the tropics (e.g., Riehl, 1979). Observations from TOGA/COARE have provided new evidence concerning the distribution of tropical clouds (DeMott and Rutledge, 1998; Rickenbach and Rutledge, 1998; Johnson *et al.*, 1999). Johnson *et al.* showed cumulus echo top statistics from the 5-cm radar aboard the R/V *Vickers* indicating that cumulus congestus clouds are the most abundant of all precipitating clouds over the western Pacific warm pool. Specifically, congestus with tops between 4.5 and 9.5 km represent 57% of the precipitating convective clouds in COARE and account for 28% of the total rainfall. Radar studies from GATE reveal a similar result (Houze and Cheng, 1977; Cheng and Houze, 1979). The prevalence of congestus clouds is related to processes that restrict the development of deep convection: entrainment of dry air, precipitation loading, and the existence of a stable layer near the melting layer (Johnson *et al.*, 1996; Mapes and Zuidema, 1996; Redelsperger *et al.*, 2002). The growth of congestus clouds in COARE was often limited to just above the 0°C level, which limited enhancement of cloud buoyancy through glaciation (Zuidema, 1998). The existence of a congestus maximum in the cloud population, along with the well-known maxima of shallow and deep cumulus, has led to the concept of a 'trimodal distribution' of tropical convective clouds (Johnson *et al.*, 1999), which is schematically depicted in Figure 8.9.

While deep convective clouds are the dominant rain producers in the tropics and monsoon regions, shallower clouds serve an important role in moistening the environment and preconditioning it for deep convection. For example, Johnson *et al.* (1999) used shipboard radar observations in TOGA/COARE to document increasing populations of shallow cumulus and cumulus congestus clouds, along with a deepening moist layer in the lower troposphere prior to the active phase of the December 1992 MJO. While such clouds detected by radar

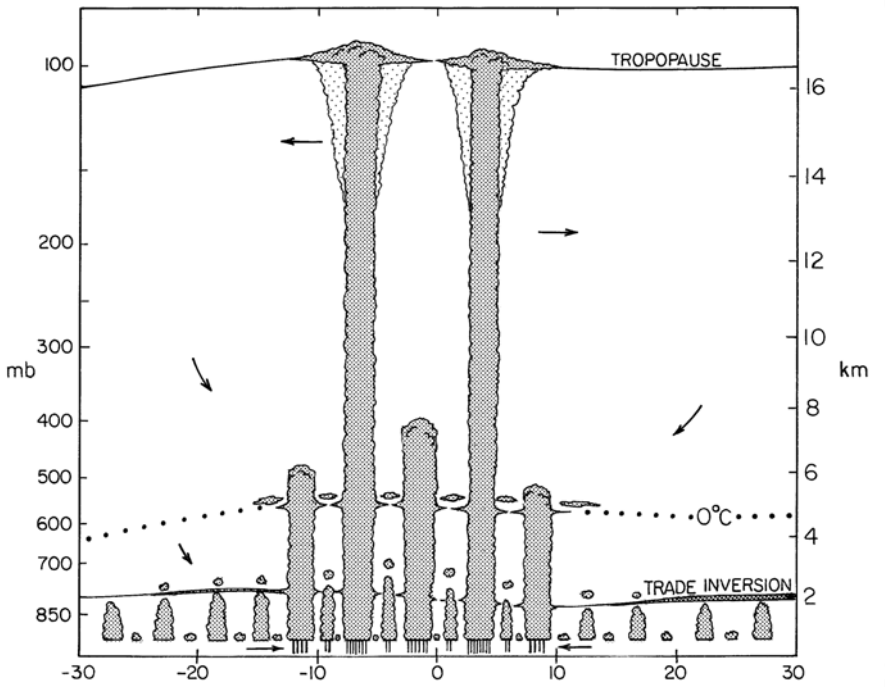

Figure 8.9. Conceptual model of tropical cumulus cloud distributions from 30°N to 30°S based on COARE mean radar data and thermal stratification. Three main cloud types are indicated: shallow cumulus, cumulus congestus, and cumulonimbus. Within the shallow cumulus classification, there are two subdivisions: forced and active cumulus. Three stable layers are indicated: the trade inversion, the 0°C layer, and the tropopause. Shelf clouds and cloud debris near the trade and 0°C stable layers represent detrainment there. Cirrus anvils occur near the tropopause. Considerable overshooting of the trade and 0°C stable layers occurs in the equatorial trough zone. Arrows indicate meridional circulation. Although a double intertropical convergence zone (ITCZ) is indicated, representing Intense Observing Period (IOP)-mean, this structure is transient over the warm pool and a single ITCZ often exists.
From Johnson *et al.* (1999).

produce rain, they do so inefficiently, thereby moistening the low to mid-troposphere (Raymond and Torres, 1998). Moreover, a large amplitude diurnal cycle of the SST (2–3°C) over the western Pacific warm pool during the light-wind phase of the MJO contributes to a deepening of the boundary layer (Johnson *et al.*, 2001) and the development of afternoon showers (Chen and Houze, 1997; Rickenbach and Rutledge, 1997; Sui *et al.*, 1997). Without this diurnal enhancement, precipitation over the warm pool and its associated lower tropospheric moistening would likely be far less during the suppressed phase of the MJO (Webster *et al.*, 1996). This preconditioning likely plays a key role in setting the timescale for the MJO (Bladé and Hartmann, 1993; Hu and Randall, 1994; Kemball-Cook and

Weare, 2001). In a simulation using the Hadley Center HadAM3 model, Inness *et al.* (2001) obtained an improved simulation of the MJO when they increased the vertical resolution in the model. Higher resolution allowed the melting layer to be better resolved, leading to more congestus clouds and an improved representation of the moistening and preconditioning of the lower troposphere in advance of the active phase of the MJO.

There is also evidence from the Asian monsoon of the importance of shallow cumulus clouds in the development of convection along the Mei-yu front. Shinoda and Uyeda (2002) found that in the southern part of the Mei-yu front where there is moist southerly flow, shallow cumulus can develop into deep convection because the clouds do not dissipate through evaporation. In addition, they found that the shallow cumulus serve an important moistening role for the mid-troposphere, transporting water vapor upward from the boundary layer.

8.2.4 Convective momentum transports

In addition to their roles in heating and moistening the atmosphere, deep convection has an important impact on the momentum field. Part of this impact arises through the gravity wave response to convective heating. For example, Pandya and Durran (1996) show that the time-averaged, tilted dipole heating structure in squall lines with trailing stratiform precipitation (a relatively narrow, tilted band of heating followed by a broader, tilted region of cooling in the lower troposphere) can explain the essential circulation features of squall lines: an upward-sloping, front-to-rear flow followed by a descending rear-inflow jet. However, convective clouds also serve to transport momentum vertically. There is evidence to suggest that the momentum transport is a function of convective organization with up-gradient transport in the line-normal direction and down-gradient transport in the line-perpendicular direction (LeMone, 1983; Wu and Yanai, 1994; Tung and Yanai, 2002; Moncrieff, 2004). Over much of the Asian monsoon it is expected that the greatest role for convective momentum transport is simple damping by down-gradient transport.

The MJO, which is a fundamental component of the intraseasonal variability of the Asian monsoon, appears to be influenced significantly by convective momentum transports. By placing aircraft observations from COARE in the context of a Kelvin–Rossby wave paradigm for the MJO, Houze *et al.* (2000) found that very large MCSs, referred to as superconvective systems, located within and to the west of the region of maximum heating have broad mid-level inflows that transport westerly momentum downward, serving to enhance the westerly wind bursts associated with the MJO (see also Moncrieff and Klinker, 1997; Tung and Yanai, 2002). To the east, near the boundary between westerlies and easterlies, the mid-level inflows transport environmental easterly wind downward, thereby enhancing low-level convergence in the MJO. Biello and Majda (2005) developed a multiscale model of the MJO that includes congestus heating in the eastern part of the disturbance and heating by westward-tilted superconvective systems to the west. The superconvective systems drive westerly momentum downward while the congestus heating enhances easterly flow in the leading portion of the MJO envelope, and the model reproduces many of

the observed structural features of the MJO. Moncrieff (2004) and Kiladis *et al.* (2005) also found evidence of substantial vertical fluxes of zonal momentum in the MJO, and the latter study provides evidence of similar heating and momentum transports in other propagating convectively coupled equatorial waves.

8.2.5 Diurnal cycle of convection

The diurnal cycle of precipitation is a dominant feature of the Asian monsoon. On the large scale the Tibetan Plateau generates significant diurnally varying circulations, vertical motion, and diabatic heating features (Luo and Yanai, 1983; Nitta, 1983; Krishnamurti and Kishtawal, 2000). On the mesoscale there are local land and sea breezes, mountain/valley circulations, and surface heterogeneities that influence precipitation patterns over the monsoon regions of the World.

There have been numerous studies of the diurnal cycle of convection over Asia (Murakami, 1983; Nitta and Sekine, 1994; Chen and Takahashi, 1995; Ohsawa *et al.*, 2001; Fujinami and Yasunari, 2001; Kurosaki and Kimura, 2002). Over land, many areas exhibit an afternoon maximum of convection, as expected from daytime heating; however, certain regions such as the base of the Himalayas and mountain basins (e.g., the Sichuan Basin) have a late night, early morning maximum (Akiyama, 1989; Johnson *et al.*, 1993; Ohsawa *et al.*, 2001). Over the open ocean, an early morning maximum of precipitation has been observed, which has been attributed to horizontal gradients in radiative cooling between cloud systems and their environment (Gray and Jacobson, 1977), daytime stabilization of the upper troposphere by short-wave heating (Kraus, 1963; Randall *et al.*, 1991), and/or the life cycle effects of MCSs (Chen and Houze, 1997). While an early morning maximum has been found over some ocean areas around Asia, the diurnal cycle there is rather complex. Ohsawa *et al.* (2001) find late night, early morning maxima near the coastlines of south Asia, Thailand, Sumatra, Malaysia, and Borneo which they attribute to an interaction of mountain or land breezes with the prevailing wind.

During the 1978 WMONEX, the diurnal cycle of convection off the north coast of Borneo was studied in detail using radar and sounding data. Houze *et al.* (1981) documented the development of nocturnal MCSs off Borneo, arguing they were a result of low-level convergence of the night-time land breeze with the north-east monsoon flow. The MCSs (discussed in detail in Chapter 3) typically began as a group of convective cells near the coastline and later expanded to a several hundred-km scale dimension with both convective and stratiform components, later dissipating after sunrise as the sea breeze developed.

In a study of convection over Taiwan during the TAMEX, Johnson and Bresch (1991) suggested that the land breeze flow at night was augmented by evaporation of the previous evening's precipitation over the interior elevated terrain. Mapes *et al.* (2003) proposed that the land breeze by itself was inadequate to account for nocturnal convection that regularly occurs offshore Columbia in the Panama Bight. They argued that thermally forced gravity waves (produced by elevated terrain and propagating at about $15\,\mathrm{m\,s^{-1}}$) are an essential part of the process, and that they produce a warm anomaly offshore during the daytime, thereby

capping convection, while a cooling is produced at night, thus allowing convection to develop.

Understanding the diurnal cycle of convection in coastal environments is important because so much precipitation occurs there and global models do not properly represent the diurnal cycle of convection (Yang and Slingo, 2001). There are possible global consequences of this deficiency, as the Maritime Continent heat source is too weak in the mean (Neale and Slingo, 2003). In the region of the Asian monsoon, satellite data indicate southward propagation of precipitation systems from India over the Bay of Bengal. This propagation is evident in a time–latitude diagram of brightness temperatures over the Bay of Bengal (Webster *et al.*, 2002, their figure 4). Precipitation systems (inferred from the cold cloud tops) were found to propagate all the way from the India coast near 20°N to the equator. Radar data from the R/V *Ron Brown* in the Bay of Bengal indicate that the convection associated with the diurnal signal has characteristics of TS systems described in Section 8.2.1.

A southward propagation of convective systems over the South China Sea was also observed during the 1998 SCSMEX, similar to that over the Bay of Bengal. The monsoon onset over the northern South China Sea (near 20°N) occurred around mid-May and is characterized by a regular signal of southward propagation of convection (low values of IR brightness temperature) at an approximate speed of $15\,\mathrm{m\,s^{-1}}$ (Figure 8.10, color section). In late May the convection shifts southward to the central South China Sea (10–15°N) with a diurnal propagating signal still present, indicating that the diurnal pattern is independent of coastal effects. Then in June the convection shifts back again to China, and diurnal propagation persists.

Propagation tied to the diurnal cycle is also present over land in monsoon regions. Wang *et al.* (2004) documented a diurnal cycle of convection over the eastern Tibetan Plateau, peaking in the late afternoon or early evening then propagating eastward. Kousky (1980) and Molion (1987) presented sequences of satellite images illustrating the afternoon coastal genesis and subsequent inland propagation of squall lines in the Amazon basin. Squall lines over West Africa propagate westward over great distances in association with African easterly waves (see review by Houze and Betts (1981)), and a maximum in convective cloud coverage has been found to occur near or shortly after midnight over West Africa (McGarry and Reed, 1978).

The diurnal cycle of precipitation systems over the ocean has been related to their size by Chen *et al.* (1996). Using satellite data from COARE, they found that the diurnal cycle of accumulated cloudy area of cold cloud tops (clouds with infrared temperatures less than 208 K) is a function of the size of the cloud system (Figure 8.11). The area covered by the smallest cloud clusters (Class 1) had a very small diurnal amplitude, whereas the largest clusters (Class 4) had a strong diurnal variation (nearly 10 : 1 amplitude) with a peak in the early morning hours and a minimum in the afternoon (as also found by Mapes and Houze, 1993). This diurnal cycle reflects the upscale growth of convection to MCS dimensions during the nighttime hours.

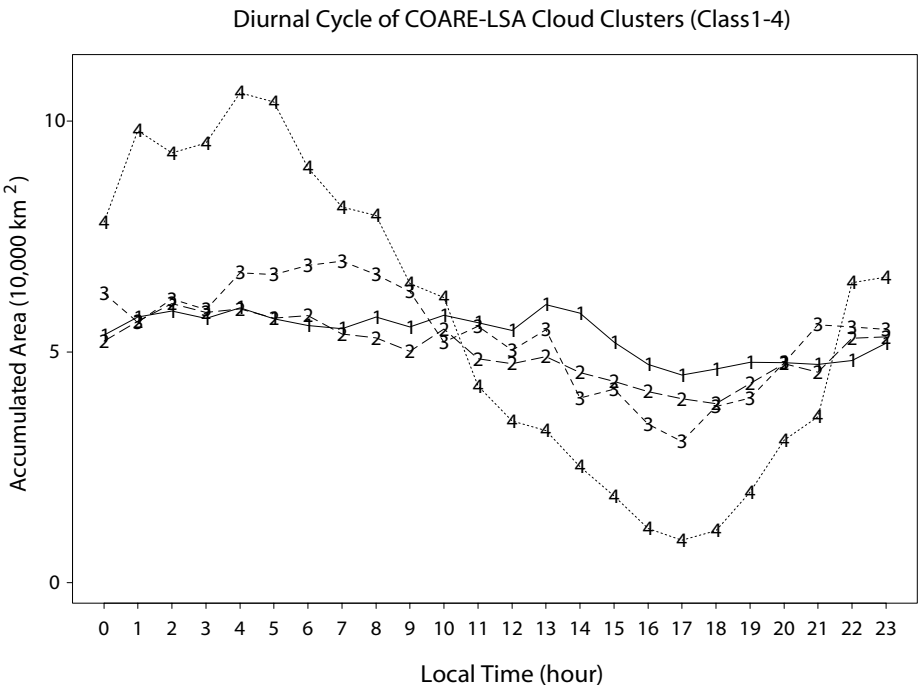

Figure 8.11. Diurnal cycle of accumulated cloudy area covered by the 208 K cloud clusters over the domain of 10°N–10°S, 152°E–180° for each of the four class sizes.
From Chen *et al.* (1996).

8.3 TOPOGRAPHICALLY FORCED LOCAL CIRCULATIONS

Throughout the Asian monsoon region, topography has a significant impact on local weather and precipitation (Riehl, 1954; Ramage, 1971; Ding, 1994). In Figure 8.1, the heavy rainfall at the foot of the Himalayas and adjacent to mountainous coastal regions (e.g., western India, Myanmar, Thailand, and Sumatra) is linked to topographic effects. Although not obvious from Figure 8.1, much of the heavy coastal rainfall occurs just offshore rather than over the windward slopes of the coastal ranges. This behavior has been noted and studied for the heavy rain along the coast of western India upstream of the western Ghats by Krishnamurti *et al.* (1983b) and Grossman and Durran (1984). Grossman and Durran carried out a modeling study explaining this phenomenon in terms of upstream blocking. However, Smith (1985) argued that their study did not include important physics such as the effects of wind shear, air–sea interaction, Coriolis force, and latent heat release. A modeling study of Ogura and Yoshizaki (1988) included those effects and concluded that the positioning of the heaviest rainfall just offshore is dependent on the strong vertical wind shear (low-level westerlies and upper level easterlies) and strong surface fluxes over the ocean. Upper level easterlies advect the cirrus aloft

westward over the open oceans (Krishnamurti *et al*., 1983b), so there is the impression from infrared satellite imagery that the heavy rainfall is spread far offshore; however, most of it is confined near the coast. Similar flow reversals occur during the boreal summer monsoon off Myanmar and the west coast of the Philippines, possibly helping to explain the similar behavior in those regions. Other possible factors contributing to the offshore precipitation are land breeze effects and coastal frictional convergence.

Recently, Chang *et al*. (2005b) studied the relationship of rainfall to the monsoon flow and topography over Indo-China and the Maritime Continent using the TRMM precipitation radar (PR) and QuikSCAT data. A map of topography over this region along with DJF and JJA QuikSCAT winds is shown in Figure 8.12 (color section). Over most of the region there is a marked seasonal reversal of the flow. During boreal winter, there is onshore flow toward coastal mountain ranges in Vietnam, Malaysia, and along the east side of the Philippines. This onshore flow contributes to boreal winter monsoon rainfall maxima in these regions, as seen in Figure 3.9 (DJF minus JJA TRMM PR rainfall and QuikSCAT winds). Positive (negative) anomalies indicate maximum precipitation in boreal winter (summer). In addition to the positive anomalies in boreal winter, there are negative anomalies off the west coasts of Myanmar, Cambodia, and the Philippines indicating maximum rainfall during boreal summer in association with south-westerly monsoon flow (the reverse of that shown in Figure 3.9). These results emphasize the important role of topography on precipitation distributions in the Asian monsoon region.

There are many other mesoscale topographic effects in the monsoon regions of the World affecting local precipitation patterns. For example, flow blocking by Taiwan during the summer monsoon often leads to a low-level jet through the Taiwan Straits north-west of the island and lee vortices downstream, both of which can affect precipitation patterns around Taiwan (e.g., Chen and Yu, 1988; Wang and Chen, 2002). Watanabe and Ogura (1987) found that flow deflection by a mountain range contributed to extreme rainfall within the Baiu front in a 23 July 1983 storm along the west coast of Japan.

A particularly complex topographic effect reported by Xie *et al*. (2003) concerns the impact of the Annam Cordillera (the north–south mountain range on the east coast of Indo-China shown in Figure 8.12 (color section)) on the flow over the South China Sea. During the summer months the south-westerly monsoon flow impinging on the Annam Cordillera creates a strong low-level jet off the south Vietnam coast (Figure 8.13). This jet leads to coastal upwelling of cool water, which is enhanced by Ekman upwelling due to the cyclonic curl of the wind stress on the north side of the jet. Figure 8.13 shows the coolest water displaced just north of the jet axis. The development of this cold filament in midsummer disrupts the summer warming of the South China Sea and causes a pronounced semiannual cycle in the SST. There is considerable interannual variability in this cold filament (e.g., it did not develop during the 1998 SCSMEX year).

Mountain and valley flows and sea and land breezes are important manifestations of the impact of the diurnal cycle of solar heating on terrain features. These

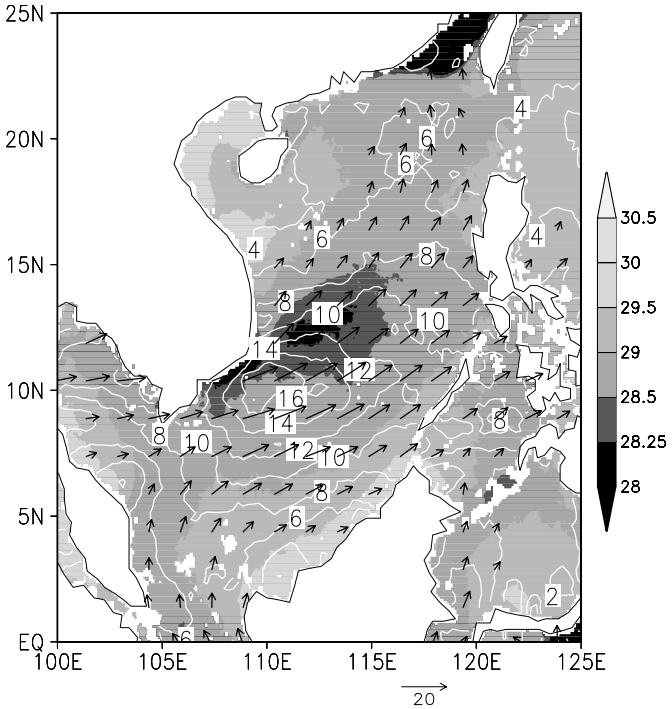

Figure 8.13. 1985–1999 SST climatology (shading in °C) along with QuikSCAT wind vectors and stress magnitude (contours in $10^{-2}\,\mathrm{N\,m^{-2}}$).
From Xie *et al.* (2003).

flows account for the daytime maximum of convection over hills and mountains, and inland of coastlines, as well as the nocturnal maxima in precipitation in mountain basins and just offshore the coastlines of Asia. An interesting example of the impact of mountain and valley flows on convection can be found in a recent study by Fujinami *et al.* (2004). Using geostationary meteorological satellite (GMS) IR data, they found that over the Tibetan Plateau convection is closely tied to two major east–west mountain ranges, indicated by the topographic cross section along 90°E in the left panel of Figure 8.14. A time–latitude plot of cloud cover frequency (right panel) shows clouds developing along these ranges around 09 UTC (15 LT) and then shifting to the valley between them by 13 UTC (19 LT). This shift is presumably a consequence of the development of drainage flow convergence into the valley in the evening augmented by downdraft outflows.

8.4 JETS

As previously noted, the topography of the monsoon regions often contributes to flow deflection or blocking and mesoscale low-level jets. The low-level jet through the

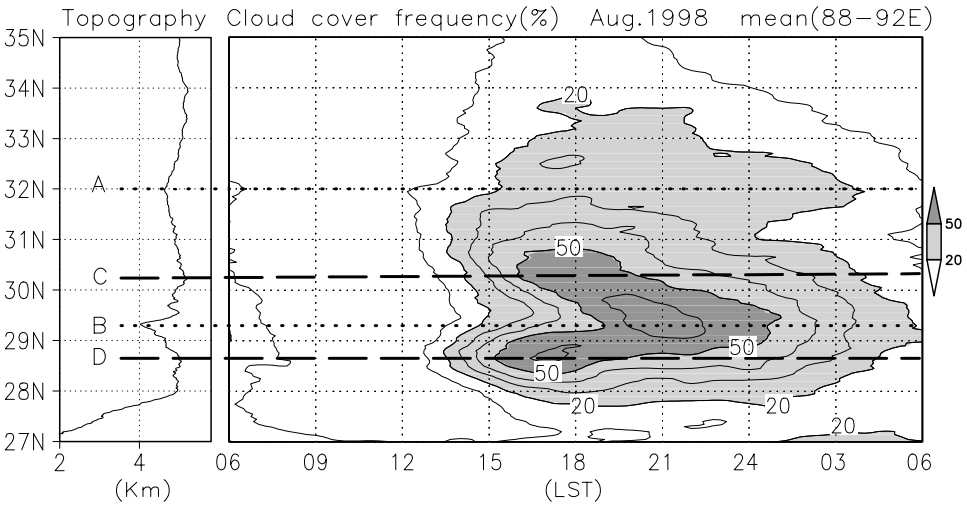

Figure 8.14. Latitude–time section of cloud cover frequency along 90°E for August 1998. Left panel indicates cross section of topography along 90°E.
From Fujinami *et al.* (2004).

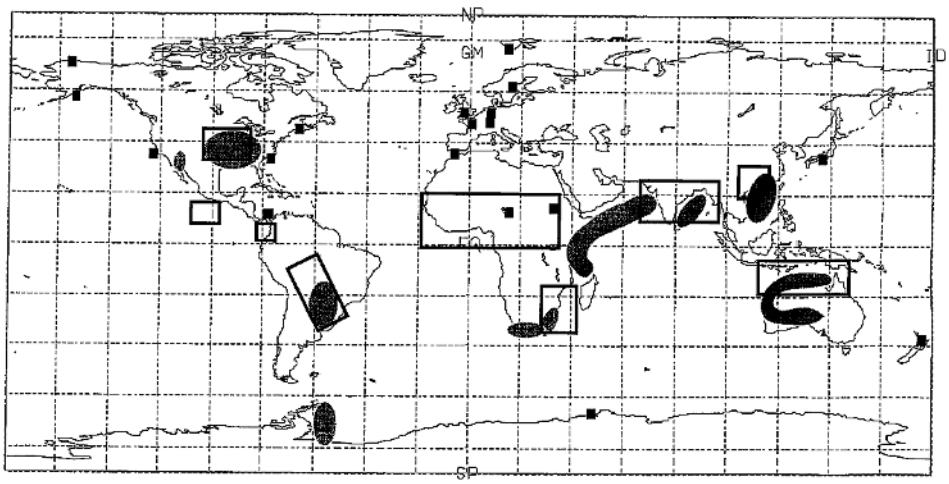

Figure 8.15. Regions where low-level jets are known or suspected to occur with some regularity (shaded) and where mesoscale convective complexes are known to occur frequently during the summer (open boxes). Squares denote locations where low-level jets have been occasionally observed.
From Stensrud (1996).

Taiwan Straits is but one example. However, there are other low-level jets of mesoscale and larger dimensions in the Asian monsoon. A map showing the global distribution of low-level jets is presented in Figure 8.15 (Stensrud, 1996). Within the tropical monsoon regions, low-level jets are observed over the Indian Ocean/Arabian Sea (the Somali jet), the Bay of Bengal, the South China Sea,

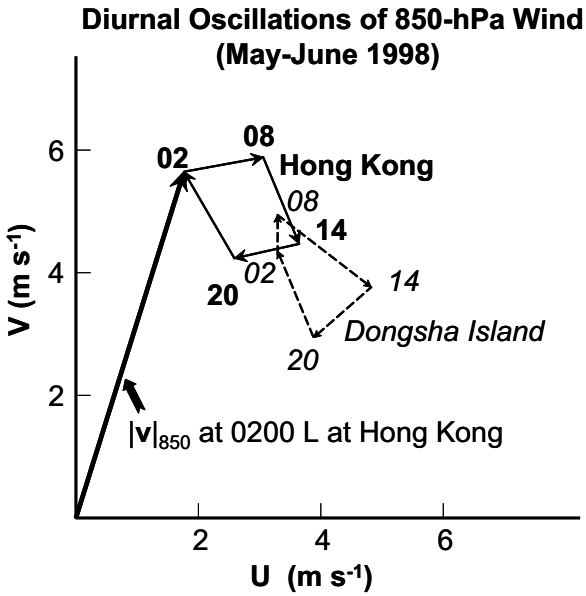

Figure 8.16. Diurnal wind oscillations at Hong Kong and Dongsha Island during SCSMEX.

Australia, and South America. Topography plays an important role in a number of these jets (e.g., the South American low-level jet occurs downstream of the Andes, the Somali jet is influenced by the east African mountains (Krishnamurti *et al.*, 1976)). Many of the areas of significant MCC activity are colocated with low-level jets, indicating the important role these jets play in transporting moisture into the convection thereby promoting large, long-lived systems (Maddox, 1983; Laing and Fritsch, 2000).

Low-level jets can also develop in response to boundary layer nocturnal cooling and an associated inertial oscillation, as observed in the African monsoon region (Blackadar, 1957) and elsewhere. Other mechanisms that can contribute to the formation of low-level jets are the diurnal heating cycle over sloping terrain (producing a diurnal oscillation in the low-level thermal wind), flow blocking by terrain, shallow baroclinic zones due to surface contrasts, and isallobaric forcing in connection with upper level jet streaks (see review by Stensrud (1996) for a detailed discussion of these mechanisms).

To illustrate the nocturnal low-level jet (LLJ), consider the findings from SCSMEX shown in Figure 8.16. An inertial oscillation is present as in Blackadar (1957) characterized by a clockwise turning of the wind, with maximum amplitudes at both Hong Kong and Dongsha Island at 08 LT. The amplitude of the ageostrophic wind oscillation ($\sim 1\,\mathrm{m\,s^{-1}}$), is considerably less than the $\sim 5\,\mathrm{m\,s^{-1}}$ found over the summertime central USA (Whiteman *et al.*, 1997), but is not insignificant. Over the USA the nocturnal LLJ has been linked with a nocturnal precipitation maximum in the Great Plains associated with eastward propagation of convective

systems (e.g., Wallace, 1975; Carbone *et al*., 2002). Similar low-level jets and nocturnal precipitation maxima have been found over South America by Virji (1981) and Velasco and Fritsch (1987); over southern China and Taiwan by Chen and Yu (1988) and Chen and Li (1995); and over Australia by Allen (1981).

In addition to low-level jets, meso-to-synoptic scale processes associated with upper level jets occur in monsoon regions. Keenan and Brody (1988) found that banded cloud structures in the Australian summer monsoon are associated with secondary circulations in the equatorial entrance region of a subtropical, 200-hPa trough. Chang and Lau (1980, 1982) found linkages between the transverse circulations associated with the east Asian jet streak and the strength of the local Hadley circulation and northern winter monsoon. Chang and Lum (1985) found that tropical convective activity during the northern winter monsoon can influence the strength of the mid-latitude jet. This coupling can often take the form of 'tropical plumes' (McGuirk *et al*., 1988), which can amplify and spread poleward as a result of convectively generated inertial instability (Mecikalski and Tripoli, 1998). Blanchard *et al*. (1998) have identified inertial instability, often occurring on the anticyclonic side of jet streaks, as a mechanism for the upscale development of MCSs.

8.5 SURFACE–ATMOSPHERE INTERACTIONS

Throughout the monsoon regions of the World, surface exchanges represent important components of both the forcing of, and response to, the monsoon system (Ding, 1994). For example, studies have shown that strong surface sensible heat flux over the Tibetan Plateau during the spring helps set the stage for the onset of the Asian summer monsoon by heating the upper troposphere, thereby contributing to an eventual reversal in the north–south temperature gradient (e.g., Flohn, 1968; Luo and Yanai, 1984; Li and Yanai, 1996). After the summer rains begin, diabatic heating contributes further to this reversal and the overall energetics of the monsoon circulation.

Vigorous air–sea exchanges over the Arabian Sea and Indian Ocean have significant effects on the rainfall distribution over India as well as on the upper ocean. A prominent feature of the Indian summer monsoon is the abrupt cooling of the Arabian Sea following the onset of a strong south-westerly flow in June. This phenomenon was recently studied by Rudnick *et al*. (1997) using surface mooring data from the west-central portion of the Arabian Sea. A sudden onset of strong south-westerlies around June 1 is accompanied by a sharp drop in the SST and air temperature. The SST–air temperature difference decreases to near zero after onset and there is a period of upward net heat fluxes, primarily due to latent heat losses from the strong winds. The strong low-level jet over the Arabian Sea leads to a pattern of coastal upwelling (north of the jet axis) and downwelling (south of the jet axis) and an overall southward Ekman transport (Chapter 1). This upwelling contributes to the Arabian Sea cooling, and it also brings nutrient-rich water to the surface, supporting increased productivity in the upper ocean.

During the Asian winter monsoon, cold air often streams off the east coast of

Asia, leading to strong sensible heat fluxes over the bordering oceans. The boundary layer over the East China Sea during cold air outbreaks was sampled during the 1975 Air Mass Transformation Experiment (AMTEX). A visible satellite image of the cloud fields associated with a cold air outbreak over the East China Sea is shown in Figure 8.17 (color section). Narrow cloud lines are seen to expand in scale to closed cellular patterns downstream. Surface sensible heat fluxes in these cold air outbreaks can reach 1,200 $W\,m^{-2}$ (Agee, 1984), thus having a dramatic impact on the downstream circulation. Changes in the boundary layer accompanying cold surges were also sampled during the 1978 Winter Monsoon Experiment or WMONEX (Johnson and Zimmerman, 1986).

There are a number of complex mesoscale processes involving air–sea interactions during the monsoons. A remarkable example occurs over the East China Sea during winter (Figure 8.18 (color section), from Xie, 2004). As cold air streams off China in the winter, it cools the upper ocean. Shallower water cools more than deep water, so the SST field closely matches the bathymetry (Figure 8.18(a)). The SST field in turn influences the surface wind field. Warmer water enhances the vertical mixing, so stronger surface winds are observed over warmer waters, and a pattern of surface divergence and convergence is established (Figure 8.18(b)). Over the offshore area of convergence there is increased cloudiness, as indicated by the TRMM Microwave Imager (TMI) cloud liquid water shown in Figure 8.18(c).

8.6 GRAVITY CURRENTS AND GRAVITY WAVES

Gravity currents are horizontal flows generated by density differences in a fluid (Simpson, 1997). They commonly occur when a cool, thunderstorm downdraft reaches the Earth's surface and spreads out horizontally in a neutrally stratified boundary layer. The ensuing outflow or *gust front* often leads to the triggering of new convection throughout the Asian monsoon region. In the absence of low-level shear, the new convection occurs in arcs along the advancing outflow boundary, as illustrated in the upper left panel of Figure 8.4. When low-level shear is present, new convection is favored along the portion of the gust front that is perpendicular to the low-level shear vector (upper right panel of Figure 8.4).

If the atmosphere is stably stratified, the downdraft will generate a series of gravity waves rather than a gravity current (Haertel *et al.*, 2001). On the other hand, if the downdraft impinges on a stable layer near the surface, such as a nocturnal inversion, it can generate a *bore*. A bore consists of an increase in the depth of a fluid (or stable layer near the ground) with a series of waves on its surface that typically separate from the leading edge of the outflow and move ahead of it. Bores have the characteristic of a significant surface pressure rise and rapid propagation, such as has been observed for undular bores (called 'Morning Glories') over northern Australia in the Gulf of Carpenteria (e.g., Clarke *et al.*, 1981) and the Japan Kanto Plain (Ogura and Hoshino, 2001).

Cold fronts passing Taiwan display gravity current characteristics on the west side of the island, which impacts the properties of frontal convection there (Trier

et al., 1990). Farther to the south as the cold fronts (or cold surges in the winter monsoon) move equatorward, their gravity current characteristics diminish and their propagation is explained more by gravity wave dynamics (Chang *et al.*, 1983).

8.7 COASTALLY TRAPPED DISTURBANCES

The (northward) southward movement of cold air to the west (east) of mountain barriers in the northern hemisphere contributes to sudden changes in local weather conditions in monsoon regions. These disturbances often exhibit characteristics of coastally trapped gravity waves, Kelvin waves, or Rossby waves (Skamarock *et al.*, 1999), and their dynamics are still a subject of investigation. Douglas and Leal (2003) have used sounding data from the west coast of Mexico to demonstrate that Gulf of California surges during the south-west monsoon have characteristics of coastal gravity currents (coincident sharp wind shift, temperature drop, and pressure rise in the lowest kilometer). Cold fronts moving southward past Taiwan also exhibit properties of coastally trapped disturbances, with rapid propagation on the east side of the mountainous island, as illustrated in Figure 8.19 (Chen *et al.*, 2002). This rapid southward propagation along the east side of the barrier can be explained in terms of shallow-water equations. For a north–south barrier, the meridional component of the wind is given by $-fv = -g\,\partial h/\partial x$, where h is the free surface height. As the easterly geostrophic flow piles up cool air along the east coast of Taiwan, $\partial h/\partial x$

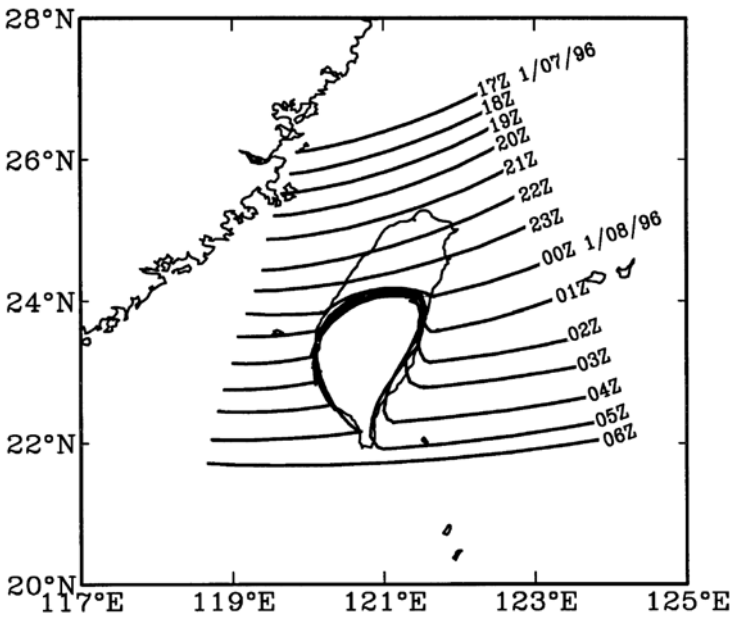

Figure 8.19. Locations of a cold front at hourly intervals on 7–8 January 1996.
From Chen *et al.* (2002).

becomes negative, yielding $v < 0$ or a northerly flow. Similar effects are seen along the east coast of China during the winter monsoon as cold fronts surge southward just along the coastline.

8.8 MESOSCALE INSTABILITIES

Numerous mesoscale instabilities exist throughout the monsoon regions, many of which influence cloud and precipitation patterns. In the boundary layer, shear-modified Rayleigh instability, inflection point instability, and Ekman layer instability may help explain the cloud streets and closed cell patterns seen in Figure 8.17. Kelvin–Helmholtz (vertical shear) instability is prevalent in many regions and accounts for closely spaced ($\sim$10 km) banded structures in precipitation systems in sheared environments. Larger scale banded structures in Mei-yu or Baiu precipitation systems which have some baroclinicity may be associated with conditional symmetric instability (Bennetts and Hoskins, 1979) or slantwise convection (Emanuel, 1983). Inertial instability has been invoked by Toyoda *et al.* (1999) to explain a series of anticyclonic vortices in a cloud band over Japan, where the instability is envisaged as arising from the vertical transport of momentum within deep convection. Cho and Chen (1995) have presented a theory for Mei-yu frontogenesis that invokes conditional instability of the second kind (CISK), arguing that in contrast to the traditional Ekman layer CISK theory, boundary layer convergence is partly induced by friction and partly by latent heat release in deep convection. To a large degree, the study of the role of mesoscale instabilities in Asian monsoon precipitation systems is still in its infancy.

8.9 SUMMARY AND OUTSTANDING ISSUES

In this chapter we have examined mesoscale processes that influence weather in the region of the Asian monsoon. Precipitation is the most important of these processes from a societal perspective, and it is also the most complex. There are a multitude of mesoscale processes that influence the location, intensity, and duration of precipitation. Field experiments in the past three decades in the tropics and monsoon regions have shed considerable light on the properties and mechanisms of deep convection. One of the most important findings is the tendency for convection to organize into cloud systems of several hundreds of kilometers in horizontal dimension (mesoscale convective systems or MCSs), such that they last considerably longer than the $\sim$30 min lifetime of individual cells. This organization has significant consequences for the distribution, intensity, and duration of precipitation, as well as the impact of convection on the large-scale flow. Various aspects of convection have been reviewed: the structure and properties of convective systems, cloud populations, latent heating profiles, convective momentum transports, and the diurnal cycle of convection.

In addition to convection, a wide range of other mesoscale processes influence the Asian monsoon. Among these are topographically forced local circulations (including flow blocking, sea and land breezes, and mountain and valley circulations), jets, surface–atmosphere interactions, gravity currents and gravity waves, coastally trapped disturbances, and mesoscale instabilities. Most of these phenomena are significantly modulated by the diurnal cycle. We have reviewed these processes and given examples that apply to the Asian monsoon. However, this list of mesoscale phenomena is not exhaustive and a number of phenomena and processes have unavoidably been omitted.

Despite progress in understanding the mechanisms of monsoon mesoscale phenomena, there remain a number of outstanding problems warranting further research, some of which are listed below:

- What determines the organization and propagation characteristics of mesoscale convective systems?
- What are the organizational patterns and life cycle characteristics of convective storms that produce flash floods?
- What roles do mesoscale convective vortices play in prolonged heavy rainfall in the Mei-yu/Baiu frontal zone?
- What are the mechanisms by which the low-level and upper level jets modify convective rainfall?
- How does convection interact with synoptic-scale disturbances (e.g., equatorial waves, monsoon depressions, etc.) to modify their development?
- What are the mechanisms for upstream development of convection along coastlines in monsoon regions?
- What processes account for the diurnal evolution and propagation of convection over oceans?
- What are the dynamics of coastally trapped disturbances in monsoon regions (e.g., coastal fronts during the winter monsoon)?
- How does the environmental flow affect the structure and organization of convective systems and their associated latent heating profiles?
- What roles do convective systems play in the onset and intraseasonal variability of the monsoon?

These are just a few of many questions pertaining to monsoon mesoscale processes which undoubtedly will motivate future observational, theoretical, and modeling studies of the Asian monsoon.

8.10 ACKNOWLEDGEMENTS

This research has been supported under NSF Grant No. ATM-0071371, NASA Grant No. NAG5-9665, and NOAA Office of Global Programs Grant No. NA17RJ1228. Thanks go to Brian Mapes for his careful review of the manuscript.

9

Large-scale atmospheric dynamics

Brian Hoskins and Bin Wang

9.1 INTRODUCTION

Monsoons are a response of the coupled atmosphere–ocean–land system to annual variation of solar radiation forcing. Physical processes governing monsoon climate involve not only atmospheric dynamical processes but also extremely complex interactions among the atmosphere, ocean, and land surface processes. This chapter deals with atmospheric internal dynamical processes that are fundamental to understanding large-scale monsoon circulation. Even with a specific focus on the large-scale monsoon dynamics, choice of topics for a concise chapter remains a challenge, because the dynamics of the Asian monsoon involves nearly all aspects of tropical dynamics and climate dynamics. Two previous monsoon books edited by Fein and Stephens (1987) and Chang and Krishnamurti (1987) provided a number of chapters that are very useful for understanding the basic mechanisms of the monsoon, in particular, the chapters written by Webster (1987) and Young (1987). Our present chapters are built on, and complementary to, these previous works with emphasis on more advanced dynamical aspects relevant to the Asian monsoon and the progress that has been made during the last two decades.

This chapter begins with a brief review of the properties of equatorial wave motions (Section 9.2) and how the tropical atmosphere responds to given idealized heating patterns (Section 9.3). The subsequent Sections 9.4 through 9.6 discuss mechanisms that are pertinent to comprehend the major Asian monsoon circulation systems, especially during summer when the Asian monsoon is a dominant feature of the global atmospheric circulation. The major circulation features of the lower troposphere include the continental monsoon lows (and the monsoon troughs) and the oceanic subtropical anticyclones, and the cross-equatorial Somalia jet. Above and to the north of the monsoon trough is located a huge anticyclonic circulation called the Tibetan High. The clockwise flow around this anticyclone contains an easterly jet stream in its southern flank called tropical easterly jet. In

B. Wang (ed.), *The Asian Monsoon*.

this chapter we examine how the monsoon low and subtropical anticyclones are generated by the diabatic heating and mountains (Section 9.4), how the Tibetan High and easterly jet form and their possible feedback on the distribution of monsoon rainfall (Section 9.5), and the dynamics of the cross-equatorial flow and its impacts on monsoon rainfall (Section 9.6). Together, these sections examine why the monsoon rainfall in south-east Asia is sandwiched by the desert and semi-arid climate associated with the two adjacent oceanic subtropical anticyclones. Sections 9.7 through 9.9 are devoted to understanding large-scale monsoon variability driven by atmospheric internal dynamics. The monsoon variability involves a variety of space and timescales. The atmospheric processes play a significant role probably only at timescales of days to months. Given the limited space, we will examine only at a rudimentary level how the monsoonal basic flows could impact the behavior of tropical waves and heat-induced steady circulation (Section 9.7), the nature of the interaction between large-scale waves and convection on an intraseasonal timescale (Section 9.8), and the teleconnection dynamics associated with the monsoon (Section 9.9).

To motivate those who are new to the subjects we normally begin with a brief summary of the observed phenomena and relevant physical issues. Emphasis is placed on explanation of the processes and mechanisms that are involved in these phenomena. A more detailed account is also given, as to how these processes are represented mathematically, in Section 9.10 (Appendix). Those who do not want mathematical derivations can skip the Appendix, while those who are interested can find enough guidance to dig further into the papers referenced therein.

9.2 EQUATORIAL WAVES

Basic theory shows that if weather systems are going to grow by converting potential to kinetic energy, their vertical scale H and horizontal scale L must scale as:

$$H/L \sim f/N$$

where $f = 2\Omega \sin\varphi$, with Ω the rotation rate of the Earth, is the Coriolis parameter and N is the buoyancy frequency, a measure of the vertical stratification of the atmosphere. In middle latitudes this gives an aspect ratio of about 1/100. However as the equator is approached, the aspect ratio would tend to zero, so that weather systems of a fixed horizontal scale would become shallower and shallower in the vertical. This does not occur because organized deep convection rather than potential energy is the dominant energy source for tropical motion. It determines that the vertical scale for motions is essentially that of the troposphere.

When the tropical atmosphere is subject to diabatic heating, the pressure (mass) and wind fields will experience an adjustment process. Atmospheric waves play an essential role in this adjustment process. In general, these waves propagate both horizontally and vertically. The vertically propagating equatorial waves have important consequences for the circulation of the equatorial middle atmosphere (stratosphere). However, for our purpose of understanding tropospheric large-

scale motion, it is convenient to simplify the problem by neglecting vertical propagation and focusing on horizontally propagating waves.

As shown in Appendix A.1, tropical waves, in a resting atmosphere without diabatic heating and friction, can be simplified as standing waves in the vertical direction. Their vertical structure can be described by appropriate summation of a family of vertical ('normal') modes (equation A.1.6). Each vertical mode satisfies the same set of wave equations called 'shallow-water equations' but with different propagation speeds (equations A.1.5 and A.1.7).

The properties of tropical waves are primarily controlled by two fundamental geophysical parameters. One is the Earth's rotation and the other is atmospheric density stratification. The Earth's rotational effect in the tropics is most conveniently represented by assuming the Coriolis parameter f varies linearly with distance from the equator (y) so that $f = \beta y$, where $\beta \equiv df/dy = 2\Omega/a$ is the Rossby parameter where a is the radius of the Earth. The change of sign of the Coriolis parameter f at the equator results in a special class of large-scale atmospheric waves, which are trapped laterally in the equatorial region as demonstrated by Matsuno (1966). For this reason, these tropical waves are referred to as equatorial waves.

The atmospheric stratification determines the vertical structure of the horizontal propagating equatorial waves (A.1.6) and the corresponding gravity wave propagation speed C_0 for individual vertical mode (A.1.7). For a given typical stratification profile, the vertical velocity profiles of the lowest four vertical modes ($m = 1$, 2, 3, and 4) calculated by using (A.1.6) are shown in Figure 9.1. The gravest baroclinic mode ($m = 1$) has maximum vertical velocity in the middle of the atmosphere. The higher baroclinic modes have more nodes and shorter vertical wavelengths. For a typical stratification parameter value of the dry atmosphere, the phase speed computed for the lowest four vertical modes using (A.1.7) are approximately 50, 26, 18, and 13 $\mathrm{m\,s^{-1}}$, respectively. Higher vertical modes have slower phase speeds.

To the lowest order, the large-scale tropospheric motion stimulated by deep convective heating can be described by the lowest baroclinic mode ($m = 1$) for which the internal gravity wave speed for the dry atmosphere is $C_0 = 50\,\mathrm{m\,s^{-1}}$. Matsuno (1966) and Gill (1980) have used the shallow-water model that describes this most important vertical mode to discuss the basic dynamics of the equatorial waves and the atmospheric response to specified heating. The two parameters, β and C_0, which reflect the Earth's rotational and gravitational effects, respectively, determine an equatorial trapped length scale $R_e = (C_0/\beta)^{1/2}$ called the equatorial Rossby radius of deformation. A value of $C_0 = 50\,\mathrm{m\,s^{-1}}$ corresponds to an equatorial Rossby radius of deformation of about 15 degrees of latitude.

9.2.1 Equatorial Kelvin wave

The eastward-propagating Kelvin wave is a possible free solution to the perturbation equations of the shallow-water model (A.1.5) provided that the meridional velocity vanishes or the motion is exactly in the along-equator direction. The resultant solution of the Kelvin wave is given in dimensional form by (A.2.3).

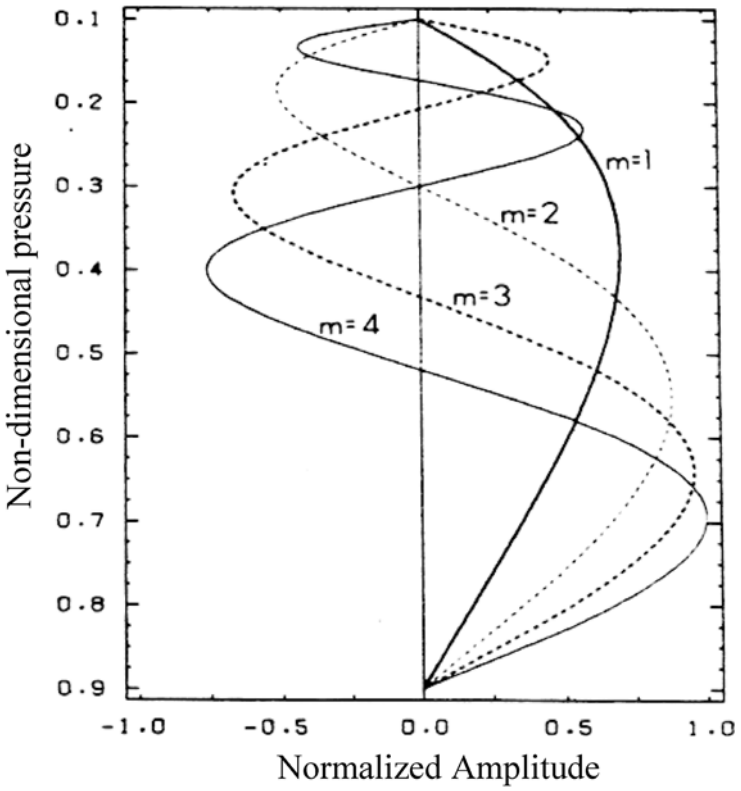

Figure 9.1. Vertical structures of the vertical pressure velocity for the first four internal modes computed for an isothermal atmosphere in which the static stability parameter is proportional to the inverse of the pressure squared. The vertical pressure velocity vanishes at the upper ($p = 0.1$) and lower ($p = 0.9$) boundary.
From Wang and Chen (1989).

In general, the Kelvin wave is a special type of gravity wave that is affected by the Earth's rotation and trapped at the equator or along lateral vertical boundaries such as coastlines or mountain ranges. The existence of the equatorial Kelvin wave relies on (i) gravity and stable stratification for sustaining a gravitational oscillation, (ii) significant Coriolis acceleration, and (iii) the presence of the equator. The Coriolis force acting on a westerly flow in the equatorial region tends to turn it toward the equator in both hemispheres. This acts to pile up fluid in the equatorial region and forms a pressure maximum at the equator. The associated poleward pressure gradient force then balances the equatorward Coriolis force (i.e., it leads to the westerly flow being geostrophic). Thus the equator acts like a lateral wall to support the Kelvin wave. The high (low) pressure is in phase with westerly (easterly) flows (Figure 9.2(a)). The fact that the equatorial trapping demands that the pressure and westerly flow are in phase means that it works only for the eastward propagating gravity wave, which gives the unique nature of the equatorial Kelvin wave.

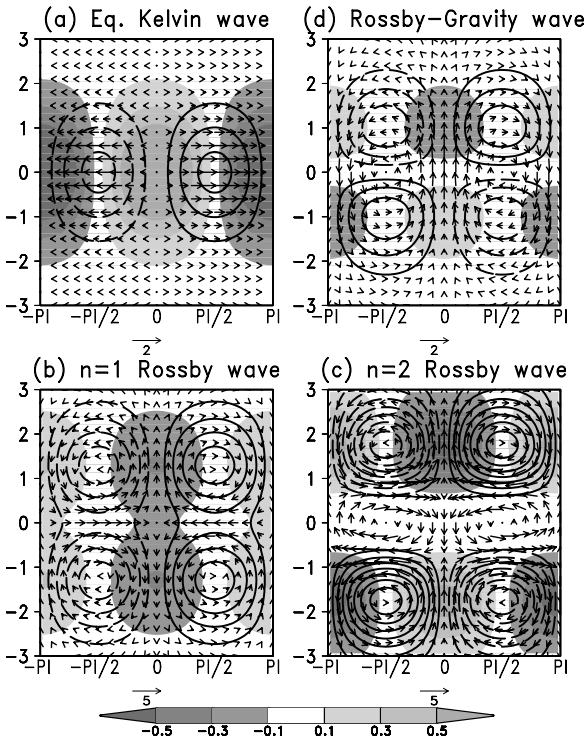

Figure 9.2. Horizontal structures of the equatorial wave solution to the shallow water equations on equatorial β-plane for (a) equatorial Kelvin wave $k = 1$, (b) $n = 1$ Rossby wave $k = -1$, (c) $n = 2$ Rossby wave $k = -1$, and (d) $n = 0$ Rossby–gravity wave $k = -1$. All scales and fields are dimentionless. The dimension for latitude y is the Rossby radius of deformation $R_c = (C_0/\beta)^{1/2}$. Contours are geopotential with intervals of 0.2 units. Solid (dashed) contours are positive (negative) and zero contours are omitted. The largest wind vectors are given in the bottom-right corner. Shading indicates divergence with a 0.2 unit interval.

At the Equator, Kelvin waves always propagate eastward and have zonal velocity and pressure perturbations that decay with latitude on an e-folding scale of $\sqrt{2}R_c$ (A.2.3). Figure 9.2(a) shows the horizontal structure of the equatorially trapped Kelvin wave solution for a simplified mode 1 vertical structure. Of note is that the Kelvin wave propagates without dispersion as for non-rotating gravity waves.

9.2.2 General dispersion relation

In addition to the equatorial Kelvin wave solution, other equatorial wave solutions exist. The general dispersion relation is derived in Appendix A.2 and given by (A.2.6). The dispersion relation describes the fundamental property of the wave

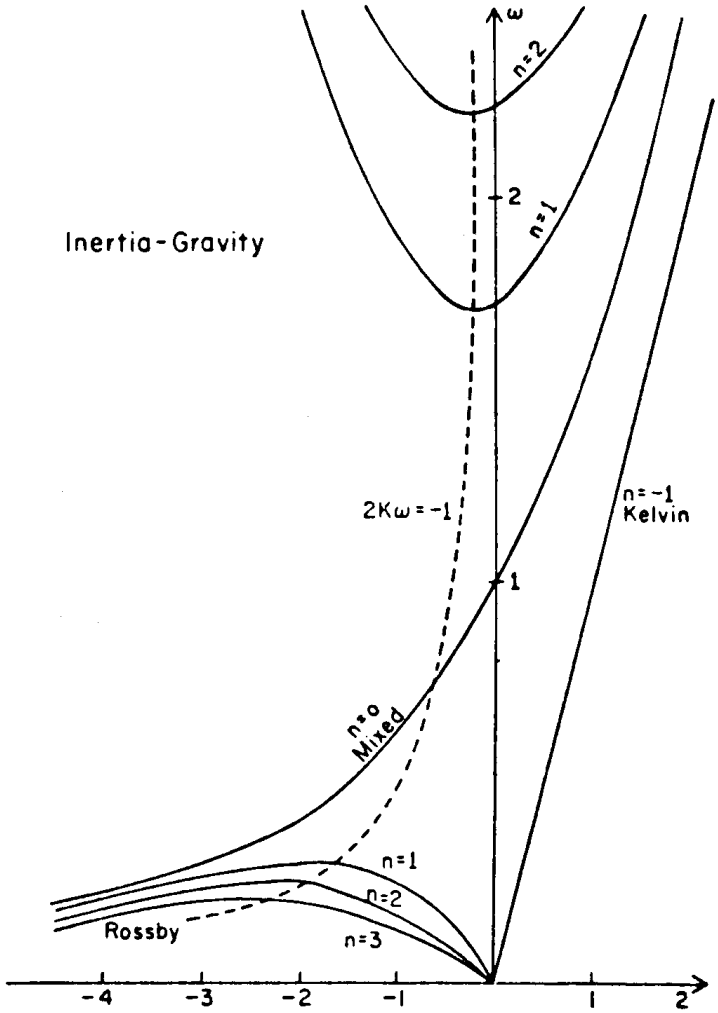

Figure 9.3. Dispersion curves for equatorial waves (up to $n = 3$) in a resting basic state as a function of non-dimentional zonal wavenumber k and frequency ω. Positive (negative) wavenumber k means eastward (westward) propagating waves. The dotted curve indicates zero group velocity.

motion by relating the wave frequency ω and zonal wavenumber k. Here ω is assumed to be always positive so that $k > 0$ implies eastward propagation relative to the ground with phase speed $C_x = \omega/k$.

Figure 9.3 shows schematically the dispersion relation for all types of equatorial waves derived by Matsuno (1966). The special Kelvin wave is represented by the straight line in the $k > 0$ domain. The general dispersion relation reflects a family of infinite number of meridional modes, each associated with an integer index n. When

$n \geq 1$, there are two distinct groups of waves: high-frequency and low-frequency waves (A.2.6). Taking $C_0 = 50\,\mathrm{m\,s^{-1}}$, the high-frequency waves have a period shorter than 1.26 days. The low-frequency waves have a period longer than 7.3 days.

9.2.3 Low-frequency equatorial Rossby waves

For low-frequency waves, it is shown in Appendix A.2 that the dimensional dispersion equation (A.2.6) can be approximated by:

$$\frac{\omega_*}{k_*} = -\frac{\beta}{k_*^2 + (2n+1)\beta/C_0}$$

This is the same dispersion relation as a Rossby wave in a β-plane channel except that the quantized y-wavenumber has a slightly different form due to the meridional boundary conditions. These low-frequency modes are, therefore, called **equatorial Rossby waves**. They occur because f varies with latitude. The higher the index of the meridional mode n, the lower the frequency ω.

In contrast with equatorial Kelvin waves, equatorial Rossby waves always propagate westward as shown by the negative sign in the above dispersion relation. However, the group speed, which represents the speed at which wave energy propagates, can be either eastward or westward. In the dispersion diagram (Figure 9.3), the slopes of the dispersion curves represent the corresponding group speed. A positive slope (frequency increases with increasing wavenumber) indicates an eastward group speed. The dashed curve in Figure 9.3 highlights the zero group speed. To the right-hand side of the curve of the zero group speed, energy associated with Rossby waves propagates westward as indicated by the negative slope. These waves have small wavenumbers or long wavelengths. Thus, the energy associated with *long Rossby waves* propagates westward while the energy associated with *short Rossby waves* propagates eastward. This property is important when considering reflection of Rossby waves at the oceanic lateral boundaries and thermocline adjustment in a finite ocean basin.

For long Rossby waves $k \to 0$ so that $\omega/k \approx -C_0/(2n+1)$ $(n = 1, 2, \ldots)$, implying that they are approximately non-dispersive. The dimensional westward phase speed is $(2n+1)^{-1}$ times the long gravity wave speed C_0. Thus, the fastest long Rossby wave $(n = 1)$ speed is about one-third of the Kelvin wave speed (and in the opposite direction).

Figures 9.2(b) and 9.2(c) depict the horizontal structure for $n = 1$ and $n = 2$ equatorial Rossby waves. Here the axes are in units of R_e. Rossby waves are characterized by a geostrophic relationship between pressure and the meridional as well as the zonal wind. Strong zonal winds are found near the equator for the $n = 1$ mode, which is expected from an approximate balance between pressure gradient and Coriolis forces (both of them approach zero as $y \to 0$). For the $n = 1$ mode, zonal wind u and geopotential height ϕ are symmetric about the equator, while v is antisymmetric. On the other hand, for the $n = 2$ mode, u and ϕ fields are antisymmetric about the equator but v is symmetric. At the equator, there is no meridional motion for the $n = 1$ mode, while no zonal motion for $n = 2$ mode.

The maximum convergence/divergence are located at $y = 1.25$ for the $n = 1$ mode and $y = 1.75$ for the $n = 2$ mode.

The high-frequency waves are inertio-gravity waves. The behavior of these waves is not discussed here. Interested readers are referred to Matsuno (1966).

9.2.4 Mixed Rossby–gravity waves

When $n = 0$, the dispersion equation $\omega^2 - k^2 - k/\omega = 1$ yields only one meaningful root $k = \omega - 1/\omega$ (the curve $n = 0$ in Figure 9.3). Of note is that for large ω, one has $k = \omega$, which is the asymptotic limit of high-wavenumber gravity waves. On the other hand, for small ω, one has $k = -1/\omega$, which is the high-wavenumber limit of the Rossby waves. For this reason, this particular $n = 0$ mode is called the (mixed) **Rossby–gravity wave**. This mixed mode is unique in the equatorial region. The crossover point from k positive to negative, corresponds to a dimensional period of about 2.1 days for $C_0 = 50\,\mathrm{m\,s^{-1}}$, and represents a stationary wave in the y direction; the waves with periods shorter than 2.1 days ($k > 0$) propagate eastward while waves with periods longer than 2.1 days ($k < 0$) propagate westward. The energy associated with the Rossby–gravity waves, however, always propagates eastward (Figure 9.3).

Figure 9.2(d) shows the horizontal distribution of velocity and pressure for a westward moving Rossby–gravity wave. The pressure and zonal velocity are anti-symmetric about the equator while the meridional component v is symmetric. The largest meridional flow occurs at the equator (cross-equatorial flow). The largest convergence/divergence occurs at $y = 1$.

The high-frequency waves (large ω) are inertio-gravity waves. These are almost symmetric in their eastward and westward propagation.

9.3 FORCED STEADY MOTION

The latent heat released during convection drives the tropical circulation while the strength and the location of convection depends on large-scale circulation. In this section, this complex interaction is simplified to a one-way problem as we examine how the tropical atmosphere responds to a *given* heat source (pattern and strength).

9.3.1 The wave perspective

To illustrate the fundamental physical processes, Gill (1980) used a single sinusoidal vertical mode, shallow-water equation model on an equatorial β-plane (A.2.1). This simplification is based on the consideration that the heating released in the middle troposphere stimulates primarily the lowest baroclinic vertical mode. Gill considered a steady-state motion in a resting basic state forced by a given heating Q. The forced motion is sufficiently weak that it can be treated using linear dynamics. The friction takes the form of Raleigh damping (a linear drag that is proportional to wind speed) and the thermal damping takes the form of Newtonian cooling (a heating rate

proportional to the temperature perturbation from its basic equilibrium state). For simplicity, the momentum and thermal damping rates are assumed to have the same timescale ε^{-1} everywhere. Taking the long-wave approximation (i.e., neglecting the high-frequency inertio-gravity waves, Rossby–gravity waves, and the short Rossby waves), the non-dimentional governing equations can then be derived from (A.2.1), which takes the following form:

$$\varepsilon u - yv = -\frac{\partial \phi}{\partial x} \tag{9.3.1a}$$

$$yu = -\frac{\partial \phi}{\partial y} \tag{9.3.1b}$$

$$\varepsilon \phi + \left(\frac{\partial u}{\partial x} + \frac{\partial v}{\partial y}\right) = -Q \tag{9.3.1c}$$

Here Q is a non-dimensional heating rate. A positive sign for Q gives u, v, and ϕ at the surface of the model atmosphere. The tropopause u, v, and ϕ have opposite signs from their corresponding low-level counterparts. The vertical velocity is given by:

$$\omega = -\left(\frac{\partial u}{\partial x} + \frac{\partial v}{\partial y}\right) = Q + \varepsilon \phi \tag{9.3.2}$$

The analytical free wave solutions can be derived from (9.3.1) after replacing damping terms with local rates of change and dropping the heating term. The free wave solutions consist of equatorial Kelvin waves, long Rossby waves and the long Rossby–gravity wave. It is expected that these types of waves will adjust the geopotential and winds toward the imposed diabatic heating and reach a steady state under the damping. This steady state is the solution of (9.3.1).

To derive the analytical solution of (9.3.1), it is sufficient to eliminate u and ϕ from (9.3.1), which leads to a single equation for v:

$$\varepsilon \frac{\partial^2 v}{\partial y^2} + \frac{\partial v}{\partial x} - \varepsilon y^2 v = y \frac{\partial Q}{\partial x} - \varepsilon \frac{\partial Q}{\partial y} \tag{9.3.3}$$

The series solution for v under a given heat forcing Q can be expressed as:

$$v(x, y) = \sum_{n=1}^{\infty} v_n(x) D_n(y) \tag{9.3.4a}$$

$$Q(x, y) = \sum_{n=1}^{\infty} Q_n(x) D_n(y) \tag{9.3.4b}$$

In (9.3.4) $D_n(y)$ is the weber–Hermite function (see A.2.7). It can be shown that the coefficients $v_n(x)$ can be solved from the following equation by assuming the

coefficients for each order of n vanish:

$$\sum_{n=1}^{\infty}\left\{\begin{array}{r}\dfrac{dv_n}{dx}-\varepsilon(2n+1)v_n-\dfrac{d}{dx}\left[\dfrac{1}{2}Q_{n-1}+(n+1)Q_{n+1}\right]\\ +\dfrac{\varepsilon}{2}Q_{n-1}-\varepsilon(n+1)Q_{n+1}\end{array}\right\}=0 \tag{9.3.5}$$

Gill presented two basic solutions, one for an equatorially symmetric isolated heating Q_s and the other for an equatorially antisymmetric dipole heating Q_{as}, i.e.:

$$Q_s(x,y)=D_0(y)F(x)=e^{-y^2/2}F(x) \tag{9.3.6}$$

$$Q_{as}(x,y)=D_1(y)Q_1(x)=2ye^{-y^2/2}F(x) \tag{9.3.7}$$

where

$$F(x)=\cos kx \qquad (|x|<L)$$

$$F(x)=0 \qquad (|x|>L)$$

Figure 9.4(a) shows the solution of the Gill model for the symmetric heating (9.3.6). The upward vertical motion basically coincides with the imposed heating field as implied by (9.3.2). Gill interpreted this circulation pattern in terms of the propagation of the large-scale equatorial Kelvin and Rossby waves. The low-level easterlies to the east of the heating are due to a Kelvin wave propagating eastward in the presence of the damping. The low-level westerlies to the west of the heating are

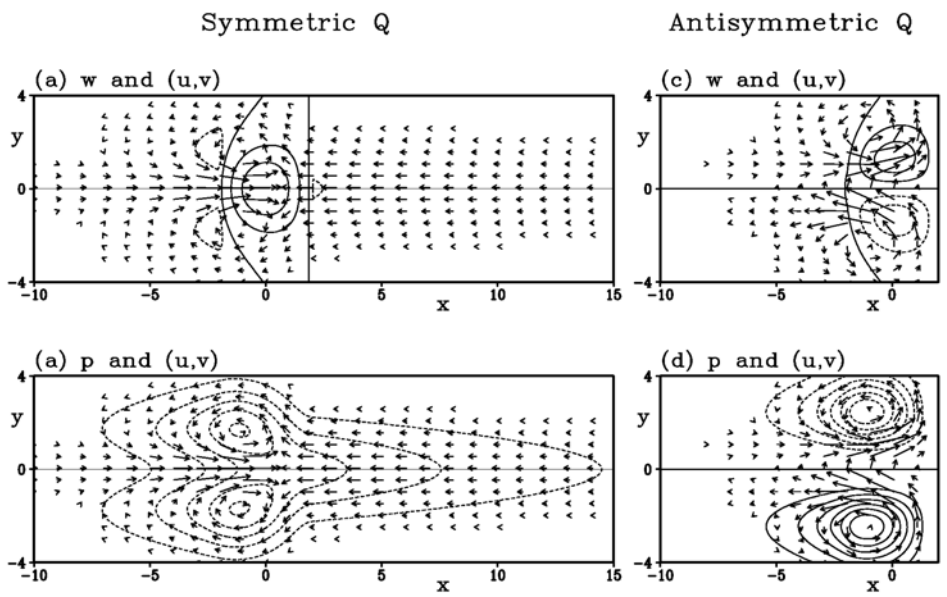

Figure 9.4. Gill's solution for (*left panels*) heating symmetric about the equator and (*right panels*) heating antisymmetric about the equator.

the result of westward propagation of the damping $n = 1$ Rossby wave. Since the Kelvin wave has no meridional component, the easterlies are more tightly trapped to the equator. On the other hand, the Rossby wave consists of two cyclonic gyres symmetric and straddling the equator.

Along the equator ($v' \cong 0$) (9.3.1) can be approximated as:

$$-\varphi_x - \varepsilon u' = 0$$

Integrating along the equator, we obtain:

$$\int_0^{2\pi a} u' dx = -\int_0^{2\pi a} \varphi_x \, dx/\varepsilon = 0$$

The above constraint means that the integral of the zonal wind due to the Rossby waves is balanced by the integrated zonal wind associated with the Kelvin waves. Since Kelvin waves move eastward at a speed roughly three times that of the fastest moving Rossby wave, when a steady state is reached, the damping distance of the Kelvin waves is about three times larger than the damping distances of the Rossby waves. This creates a wider region of easterly winds to the east of the heating than the westerly wind region to its west. The above equation also implies that the zonal winds associated with Rossby waves must be stronger than the zonal winds associated with Kelvin waves.

Under the long-wave approximation, Rossby waves occur only to the west of the forcing region and Kelvin waves only to the east. In the presence of the short Rossby waves, their energy can propagate eastward because of dispersion. Also, if the damping is not too strong, the eastward propagating Kelvin waves and the westward propagating Rossby waves can travel far enough to interact with each other due to the cyclic nature of the real domain.

Figure 9.4(c) and (d) shows Gill's solution for the antisymmetric heating. The major ascent and descent regions tend to coincide with imposed heating and cooling, respectively. There is a cyclonic circulation in the heated hemisphere and anticyclonic circulation in the cooled hemisphere at low levels. In this case the excited Rossby–gravity waves are confined within the forcing region, and the Rossby waves propagate westward. There is no response to the east of the heat source because of the absence of equatorially symmetric eastward propagating Kelvin waves. Along the equator there are northerly (southerly) winds in the lower (upper) level, which means that mass is transported from the cooling (heating) hemisphere to the heating (cooling) hemisphere in the lower (upper) level.

A circulation pattern more relevant to the Asian summer monsoon may be obtained using a thermal forcing that is the sum of the symmetric and antisymmetric forcings. In this situation, the imposed heating field is asymmetric about the equator with the heating mainly in the northern hemisphere. If the equatorial Rossby radius of deformation R_c is taken to be 10° of latitude, the solution corresponds to a maximum heating at 10°N covering 40° of longitude. This heat source is similar to the summer monsoon heating in the Bay of Bengal and the Philippines, except that the latter is centered near 15°N. The solution corresponding to this 'summer

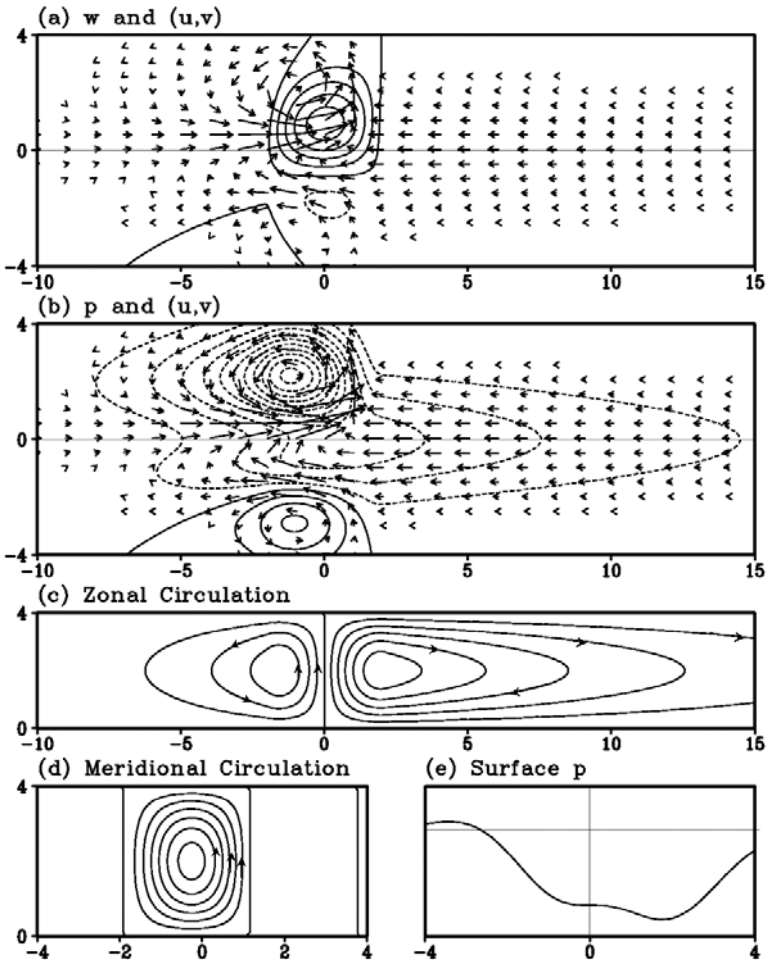

Figure 9.5. Gill's solution for asymmetric heating which is the sum of the heatings shown in Figure 9.4(a) and (b). Shown also is the zonal mean circulation and meridional mean zonal circulation.

monsoon' heating can be obtained by adding the solution shown in Figure 9.4(a) and (b) and is shown in Figure 9.5(a) and (b).

There is a low-level cyclonic circulation in the heating hemisphere to the west of the heating, due to westward propagation of the long Rossby waves. The flow pattern to the east of the heating region is due to the eastward propagation of the Kelvin waves. Thus, the winds are easterlies toward the heat source and tend to be parallel to the equator and symmetric about the equator. As stated above, they move three times faster than the long Rossby waves, and thus cover a larger longitudinal range.

In the southern hemisphere the cooling and equatorial warming induced solution shows a weak trough close to the equator and an anticyclonic circulation poleward of this. The entire circulation pattern bears close similarity to the summer circulation in the Indian–Pacific sector.

Figure 9.5(c) and (d) show the meridionally and zonally averaged circulations associated with the asymmetric heating, respectively. The meridionally averaged zonal circulation is referred to as a Walker cell (Bjerknes, 1969), which comprises east–west atmospheric circulation cells along the equatorial belt. Analogous to observations, the dominant component is the Pacific branch, which consists of easterly winds at the lower troposphere, westerly winds at the upper troposphere, rising motion over the western Pacific, and subsidence over the eastern Pacific. The zonal mean meridional circulation is referred to as the 'Hadley cell' (Lorenz, 1967). The Hadley circulation exhibits a rising branch over the northern hemisphere monsoon trough latitude (the major surface low pressure) and sinking branch over the southern hemisphere cooling region. It is of interest to note a secondary low pressure just south of the equator (Figure 9.5(e)). This Hadley cell is a result of the antisymmetric component of heat forcing.

It has already been said that the longitudinal extent of the Rossby wave structures to the west, and the Kelvin wave structure to the east, depend on the wave speeds and the damping timescale, and that if this timescale is not short enough there will be interference through propagation around the equator. It is also clear from (9.3.2) that outside the heating region, the vertical motion is totally dependent on the damping. Therefore, the whole meridionally averaged structure shown in Figure 9.5(c), and in particular the Walker cell, depends on the damping. The figures shown here assume a dimensional damping timescale of about 2.5 days. It is interesting that to produce realistic pictures this simple model requires such large thermal and momentum damping, not just in the boundary layer but throughout the depth.

9.3.2 The vorticity and thermodynamic equation perspective

Assuming that advection by any basic state may be neglected, the undamped vorticity equation may be written in z-coordinates:

$$\frac{\partial \zeta}{\partial t} + \beta v = f \frac{\partial w}{\partial z} \tag{9.3.8}$$

Here ζ is the vertical component of relative vorticity, the β term represents the meridional advection of planetary vorticity, and the term on the right-hand side represents the creation of cyclonic (anticyclonic) vorticity by the stretching (shrinking) of the vorticity due to the Earth's rotation. Scale analysis shows that the thermodynamic equation may be written as:

$$N^2 w = Q \tag{9.3.9}$$

Here the left-hand-side term represents adiabatic cooling (warming) due to ascent

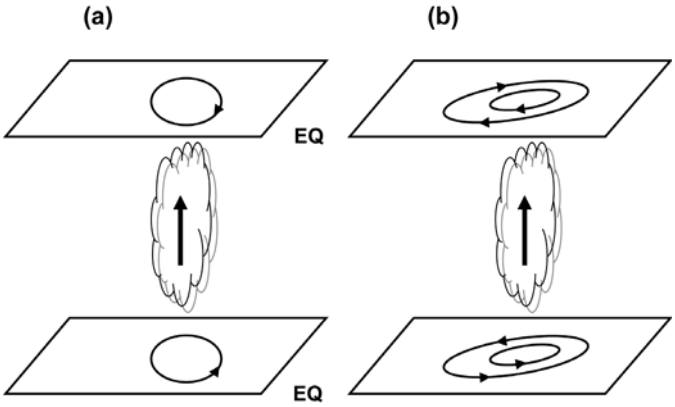

Figure 9.6. Schematic diagram showing response of the tropical atmosphere to an imposed deep cumulus heating: (a) initial tendency and (b) equilibrium solution. If the heating were located in the southern hemisphere, the resultant flows would be a mirror image.

and expansion (descent and compression). The heating is again represented by Q, which would be proportional to the value used before in (9.3.1c).

Consider a region of large-scale, deep convective heating in the equatorial region as sketched in Figure 9.6. Equation (9.3.9) shows that there is ascent in the region of heating, with adiabatic cooling balancing the diabatic heating. The stretching term in the vorticity equation then implies the tendency to create cyclonic circulations in the lower troposphere and anticyclonic circulations in the upper troposphere, as shown in Figure 9.6(a). Under the action of the β-effect, which is described in the vorticity equation, these circulations tend to drift westward just as occurs in Rossby waves. The equilibrium situation is reached when they have drifted to the point shown in Figure 9.6(b) where there is a balance in the convective region:

$$\beta v = f \frac{\partial w}{\partial z} \tag{9.3.10}$$

This is often referred to as Sverdrup balance. For example, in the upper troposphere, the shrinking of vortex tubes is balanced by the advection of larger basic vorticity from higher latitudes. Combining (9.3.9) and (9.3.10) leads to the approximate relationship:

$$\beta v \approx f \frac{\partial}{\partial z}\left(\frac{Q}{N^2}\right) \tag{9.3.11}$$

As discussed by Wu *et al.* (1999) and Liu *et al.* (2001) this form emphasizes the importance of the vertical distribution of heating.

If the heating is away from the equator then the vortex stretching is only in that hemisphere and so the circulations are only created there.

In terms of the solutions determined using the wave approach, it is clear that the vorticity arguments have given a complementary perspective on the formation of the

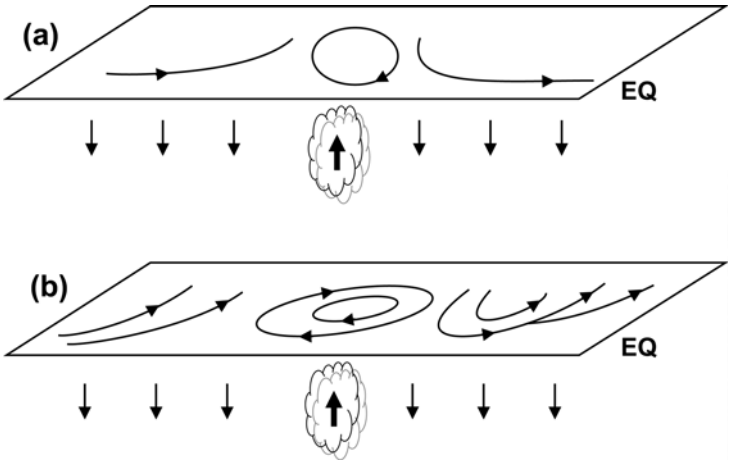

Figure 9.7. Schematic diagram showing the upper level circulation induced by both an imposed heating and the corresponding compensated cooling outside of the heating region: (a) initial tendency and (b) equilibrium solution. The lower level circulation would be the same except with an opposite sense. If heating spreads into the southern hemisphere the circulation would be a mirror image.

Rossby wave circulations to the west of the heating. For a different perspective on the Kelvin wave response to the east we take account of the cyclic nature of the equatorial domain and consider a case with zero zonally averaged heating. In this case small, uniform cooling at other longitudes compensates the local convective heating. As illustrated in Figure 9.7(a), the cooling then leads to descent in this region, and vortex stretching at upper levels and shrinking at lower levels. The consequent zonally elongated upper level cyclones and lower level anticyclones are dominated by westerly and easterly winds, respectively. These circulations again tend to drift westwards to give Sverdrup balance with, in the cooling region, poleward components of the winds in the upper troposphere (to the east of the heating region) and equatorward components in the lower troposphere. Damping in the vorticity equation would act to reduce the westward drift of all the circulations. The equilibrium state is shown in Figure 9.7(b).

These vorticity arguments give a perspective on the motions forced by large-scale, deep convective heating that is complementary to that given by the wave approach. They also show the generality of the nature of the particular solutions obtained using that approach.

9.4 MONSOON AND SUBTROPICAL ANTICYCLONES

Belts of high pressure dominate the winter subtropics in the lower troposphere in both hemispheres. These can be associated with the descending branch of the Hadley

cell in the winter hemisphere. In some of the ocean basins, particularly the South Pacific, the anticyclones are strong enough to have closed circulations. In summer these oceanic subtropical anticyclones are stronger and the tropical and subtropical atmospheric circulations in the lower troposphere are dominated by them and by monsoon lows and associated monsoon troughs over the continents (Figure 2.5(a)). Associated with these circulation systems are the heavy rains in the monsoon trough and desert to its west in the eastern flanks of the subtropical anticyclone (Figure 2.4(a)).

9.4.1 Winter hemisphere subtropical anticyclone: the effects of mountains

The subtropical anticyclone has been traditionally related to the sinking branch of the zonally mean meridional circulation, which was envisioned first by Hadley (1735). The annual zonal mean meridional circulation consists of a pair of thermally driven cells, one in each hemisphere. The Hadley cell varies considerably with season and, except near the equinoxes, is dominated by a cross-equatorial cell with low-level flow from the winter tropics to the summer tropics and reversed upper level meridional flow (Newell *et al.*, 1972). Linzden and Hou (1988) characterized the seasonal varying Hadley cell as a 'solsticial pattern'. Their theoretical analysis suggested that small equatorial asymmetries in the imposed temperature of the underlying surface, say a displacement of the thermal equator from the geodetic equator by a few degrees of latitude, would give rise to a strong equatorial asymmetric mean meridional circulation. Consistent with (9.3.9), the descent in the winter hemisphere is associated with diabatic cooling there. This cooling is related to the suppression of deep convection with its associated heating and the consequent dominance of radiative cooling. In the lower troposphere, in the region of descent, there is vortex shrinking and the generation of anticyclonic vorticity leading to the winter subtropical anticyclone belt.

In the winter hemisphere, the relatively symmetrical nature of the cooling and also the equatorward shift and strengthening of the deep westerly winds means that the strong non-linear interaction between the zonal-mean circulation and the mountains can be important for defining the large-scale features of the subtropical circulation as well as in the higher latitudes. In particular the blocking effect of the longitudinal mountain chains has been shown to be very important (Bolin, 1950; Yeh, 1950) for the formation of the winter hemisphere planetary stationary wave patterns.

Rodwell and Hoskins (2001) used an idealised numerical model to elucidate how mechanical forcing of the mountains can act to divide the winter subtropical anticyclonic belt into distinct anticyclones over the ocean basins. They considered the mountain-zonal mean flow interactions according to both linear and non-linear theoretical frameworks. Based on the linear theory, when a westerly or easterly flow climbs over the mountain (Figure 9.8(a)), one would expect ascent on the 'upslopes' and descent on the 'downslopes. Below an isentrope passing smoothly over the mountain there is vortex shrinking and anticyclonic tendency on the upslope, leading to an anticyclone over the mountain (or moved slightly to the

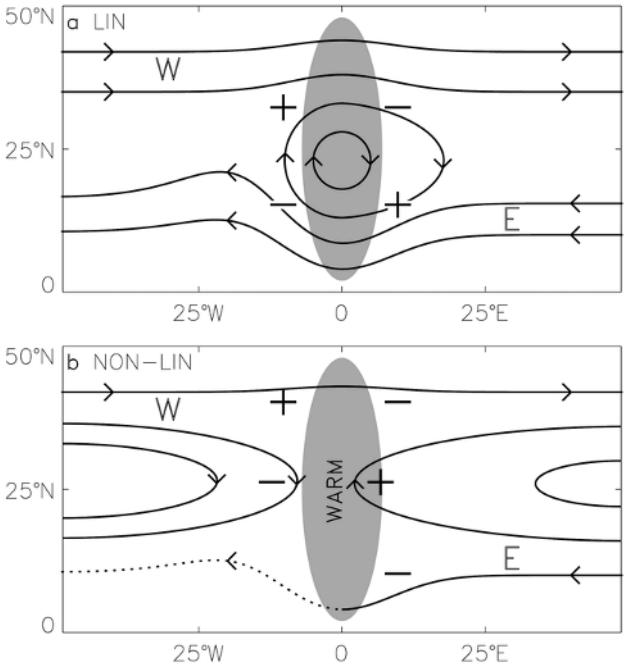

Figure 9.8. Schematic diagrams depicting the adiabatic interaction between the zonally averaged flow and an idealized mountain (shaded) based on (a) the linear theory in which isentropes do not intersect the mountain in the zonal plane and (b) the non-linear theory in which isentropes can intersect the mountain in the zonal plane. Contours depict low-level streamfunction. Here '+' indicates ascent and '−' indicates descent.
From Rodwell and Hoskins (2001).

west like a Rossby wave, under the action of the beta effect). On the downslope there is vortex stretching and a cyclonic tendency. The westerly and easterly flows deviate as they pass over the mountain in the manner shown in Figure 9.8(a). However, observation shows that many lower tropospheric isentropes intersect with mountain sides (Rodwell and Hoskins, 2001) with the downward displacement of the isentropes over the mountains implying anomalously warm temperatures in these regions. This implies that the flow in these lower isentropes is blocked by the mountain, a behaviour that can only be simulated in a non-linear model in which the whole response is very different.

Figure 9.8(b) represents schematically how the northern hemisphere atmosphere can respond to a north–south oriented mountain forcing in a non-linear theory. For simplicity, assume a situation in which the isentrope heights are constant with longitude. Assuming that the atmosphere is warmer toward the equator, the isentropes will slope upwards towards the pole. As the low-level easterly trade winds ('E' in Figure 9.8(b)) approach the eastern slope of the mountain, they must be deflected equatorward and/or poleward since the mountain blocks the isentropes. The

equatorward deflected flow will descend on the meridionally sloping isentropes (minus sign in Figure 9.8(b)) and be blocked by the mountain. The poleward deflected flow will arise on the isentropes and attain anticyclonic relative vorticity, leading to further poleward turning. Thus, a large proportion of the easterly flow must actually turn poleward. This is an explanation for what actually occurs for the case of North America and south Asia during winter (Figure 2.5(b)) or for the case of South America during boreal summer (Figure 2.5(a)). The low-level flow impinging on the mountain from the west ('W' in Figure 9.8(b)) must also be deflected equatorward or poleward. The flow that is deflected poleward in the extratropics rises up the sloping isentropes; so that the mountain does not so effectively block it. The subsequent descent occurs in the eastern slope, much as suggested by linear theory. Such an extratropical flow can be seen over the Tibetan Plateau and Rockies (Figure 2.5(b)). On the other hand, the westerly flow that turns equatorward descends on the isentropes. Such a partial blocking of westerly flow to the west side of the mountain can be seen over the Rockies (Figure 2.5(b)).

9.4.2 Processes determining the summer monsoon and subtropical anticyclones

Hoskins (1996) pointed out that the descending arm of the Hadley cell explanation in Section 9.4.1 for the winter anticyclone belt is not applicable in the summer, the subtropical anticyclones are in most measures actually stronger, as well as being more longitudinally localized (Figure 2.3). In the summer hemisphere the monsoons are important aspects of the flow, and in particular the Asian summer monsoon dominates the global circulation. The vertical motion exhibits a strong stationary wave pattern (Figure 2.9(a)) and there is practically no zonal-mean subtropical descent.

Hoskins and Rodwell (1995) used a time-dependent primitive equation model to investigate the effects of diabatic heating, in particular that associated with the Asian summer monsoon, and topography on the June–August large-scale global circulation. The prescribed heating was calculated as a residual in the time-mean thermodynamic equation from European Centre for Medium-Range Weather Forecast (ECMWF) data. The integration was initiated with an observed June–August zonal-mean flow that was maintained throughout the integration. Their initial value integrations yielded a realistic response to the imposed heating fields in the presence of mountains. In particular, the low-level flow was well simulated, including the cross-equatorial flow into the Asian monsoon and the subtropical anticyclonic flows.

Hoskins and Rodwell (1995) demonstrated that in a linear version of their model, forced with the same diabatic heating but with no mountains, the upper tropospheric circulation was similar. This linear heating-only model also gave the subtropical highs of the lower tropospheric circulation, although their definition and amplitudes were improved when mountains and the non-linear interactions of the orographic and thermal responses were included. They demonstrated that the resolved transients played little role in the model simulation, and the realism of

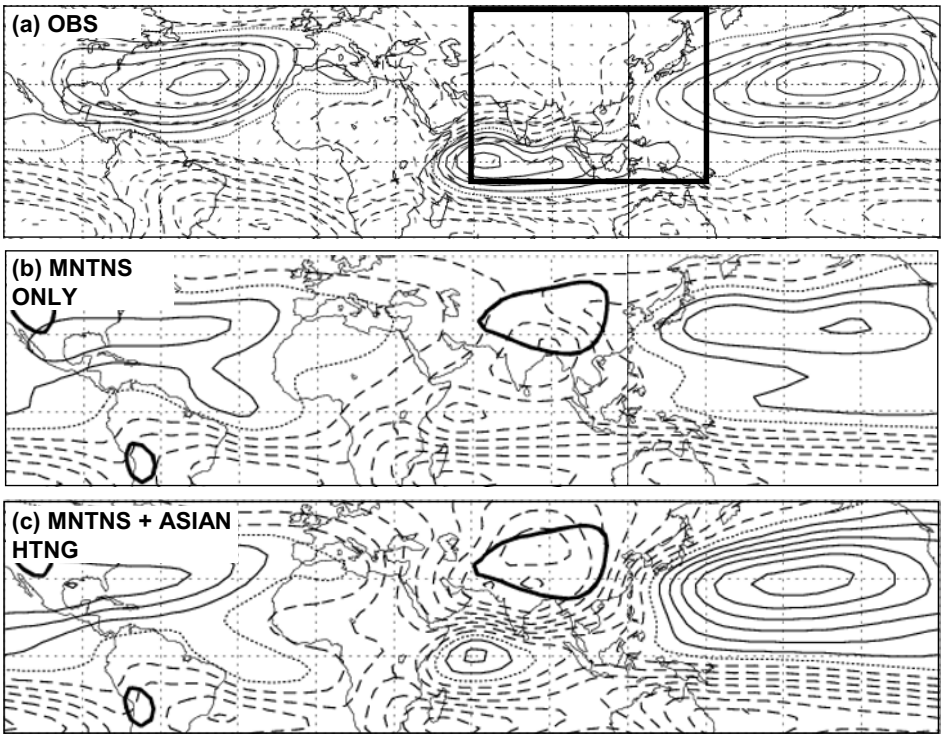

Figure 9.9. June–August mean 887-hPa streamfunctions (for (a) horizontal wind vectors are also included). (a) From European Centre for Medium-Range Weather Forecasts (ECMWF) operational analyses for the period 1990–1994. (b) For day 16 of an integration of a primitive equation model with orography but no zonally asymmetric diabatic forcing. (c) For day 16 of an integration of the same primitive equation model with orography and prescribed observed diabatic forcing. The contour interval is $2 \times 10^{-6}\,\mathrm{m^2\,s^{-1}}$ with positive contours solid, the zero contour dotted, and negative contours dashed. The largest wind vector is approximately $10\,\mathrm{ms^{-1}}$.
From Rodwell and Hoskins (2001).

the simulation implied that transient motions are not of vital importance to the large-scale time-mean global circulation during this season.

Figure 9.9 shows the impacts of the Asian monsoon heating on the northern hemisphere subtropical circulation. The $5\,\mathrm{mm\,day^{-1}}$ precipitation contour in the boxed region (Figure 9.9(a)) delimits well the south-east Asian and western North Pacific monsoon rainfall regions (Figure 2.4(a)). The Asian monsoon heating forcing alone induces some very realistic low-level circulation features (Figure 9.9(c)), which include cross-equatorial flows off the east coast of Africa and the North Pacific subtropical anticyclone. The response to only orographic forcing shows much weaker subtropical anticyclones compared with those produced in the heating-only simulation (Figure 9.9(b)). In fact, the addition of the South Asian monsoon strengthens the descent associated with the North Pacific subtropical anticyclone by

around 70%. The interactions between topography and thermal response are found to be important for realistic simulation of the low-level monsoon inflow. Their results suggested that the blocking effect of mountains on the low-latitude easterlies and mid-latitude westerlies are even more important in summer, but that the monsoon heatings are also vital.

9.4.3 Mechanisms of the summer monsoon and subtropical high

The Asian monsoon heating gives a response similar to that discussed in Section 9.3 from the wave and vorticity equation perspectives. The strengthened easterlies in the equatorward portion of the North Pacific subtropical anticyclone can be interpreted as the Kelvin wave response to the Asian monsoon heating to the west. The low-level poleward flow between 90° and 150°E at about 10–40°N is consistent with Sverdrup balance and the mid-tropospheric ascent associated with the heating. Over the Pacific this forms the western flank of the subtropical high.

How does the Asian monsoon heating affect the deserts to its west and the eastern portion of the Atlantic subtropical anticyclone? Or how does monsoon heating contribute to the summer 'Mediterranean type' of desert to its west? A similar question would be: could the heating in the eastern North Pacific and Mexico enhance the eastern portion of the North Pacific subtropical anticyclone? Hoskins and Rodwell identified a number of mechanisms, which are summarized as follows.

Monsoon–desert mechanism

Hoskins (1996) suggested that in addition to the blocking of the flow by longitudinal mountain chains, the basic cause of the summer subtropical anticyclones is the monsoonal latent heat release over the neighboring continents to the east. Using an idealized model, Rodwell and Hoskins (1996) show that the descent results from the interaction between westward propagating Rossby waves and the mean westerly flow on its poleward side. As discussed in Section 9.3.2, the diabatic heating in the Asian monsoon region induces a Rossby wave pattern to the west. This has an anticyclone at upper levels and a cyclone at lower levels, and so from hydrostatic balance there must be warmth in the mid-troposphere. When this thermal structure is far enough poleward to interact with the southern flank of the mid-latitude westerlies, this air moves down the isentropes on the western side of it and backs up on the eastern side. Trajectories indicate that the monsoon–desert mechanism does not represent a simple 'Walker-type' overturning cell. Instead, the descending air is seen to be mainly of mid-latitude origin.

The descent is highly sensitive to the latitude of heating, being negligible for the pre-monsoon heating that is centered at 10°N. As this diabatic heating pushes poleward to near 25 degrees latitude, deep descent is induced poleward and westward of it. Thus, the intensity of the summer subtropical anticyclones, particularly in the eastern oceanic regions, is due to the poleward excursion of the monsoon convective heating over the continent to the east. The observed dramatic strengthen-

ing of descent over the Mediterranean and east Sahara during the onset of the Asian monsoon supports this conclusion. It should be noted that the ascent on the north-eastern side of the warm, mid-tropospheric region will encourage the extension of the monsoon heating over eastern China.

The monsoon–desert mechanism may not be confined to the Asian monsoon alone. The monsoon–desert mechanism can explain, in a similar way, the observed summertime strengthening of the oceanic subtropical anticyclones over the Pacific Ocean and the existence of western continental deserts in the regions such as United States (western mountain area and California) and South America (Chilean desert).

Radiative enhancement mechanism

The Asian monsoon-forced adiabatic descent is likely to result in clear air over the Sahara and Mediterranean and, therefore, a local diabatic enhancement may further double the strength of descent. The enhanced radiative cooling and suppressed convection are then viewed as amplifiers of the descent. The adiabatic descent, which has a warm thermal anomaly associated with it, would act to reduce relative humidity and suppress convection and its associated latent heat release. In addition, it may lower the level of long-wave radiative emission and increase radiative cooling. The combined effects result in net cooling of the atmosphere and hence an increase in the strength of the descent. The observed cooling over the eastern Mediterranean and Sahara is explained by this diabatic enhancement mechanism. Note, however, that this mechanism is seen as a passive response to monsoon heating; the cooling in the descent region has little direct feedback on the Asian monsoon.

Figure 9.9(b) shows that orographic effects can act to localize the monsoon-induced descent to the west. The adiabatic descent is localized over the eastern Sahara and Mediterranean, and over the Kyzylkum desert to the south-east of the Aral Sea, by the mountains of North Africa and south-west Asia.

In addition to the afore-mentioned diabatic enhancement mechanism, Charney (1975) proposed a biosphere–albedo feedback mechanism whereby local anthropogenic effects related to overgrazing could affect the radiative balance, enhancing summertime diabatic descent in general. In the long term, the Charney type rainfall–vegetation–albedo–radiation feedback over the desert may cause desertification. Hahn and Manabe's (1975) numerical experiments also demonstrated that the elevated Tibetan heat source during summer could be a cause of the Gobi deserts to its north. These processes work in a north–south meridional plane, which differ from the Monsoon–desert mechanism but could be complementary in explaining the World's largest North Africa–western central Asian desert.

Rodwell and Hoskins (1996) estimated that in the eastern subtropical Pacific High, about 40% of the total descent is adiabatic – accounted for by the remote monsoon and mountain forcing. Much of the remaining part was *diabatic enhancement* to this remote forced descent through local radiative cooling, which is discussed further below.

Air–sea interaction

Air–sea interaction may give additional enhancing factors. A small percentage for the oceanic descent regions in the North Pacific subtropical anticyclone off California could come from a positive feedback involving air–sea interaction (Rodwell and Hoskins, 2001). Philander *et al.* (1996) has argued that the tilt of the coastlines of North and South America is essential in creating the hemispheric asymmetry and keeping the intertropical convergence zone (ITCZ) in the northern hemisphere. This argument applies to the tropical region. Off the coast of Baja, California along-shore north-west winds prevail in the intense eastern portion of the subtropical high. These equatorward winds result from the vortex shrinking accompanying the Mexican monsoon-induced descent, according to the Sverdrup balance. On the other hand, the equatorward along-shore wind stress will lead to offshore Ekman transport (Anderson and Gill, 1975), inducing oceanic upwelling, leading to cold sea surface temperatures. The decreased surface temperature, in turn reinforces the suppression of convection through changes to the moist static energy (Neelin and Held, 1987) and the formation of marine stratus clouds. Below the descending motion, and associated with it, lies the vast marine stratus cloud deck (Klein and Hartmann, 1993), which, owing to its persistence, low altitude and high reflectivity, in turn enhances local radiative cooling (Ma *et al.*, 1996). The effects of radiative cooling seem to be a very important contributor to enhancement of the subtropical anticyclone (Liu *et al.*, 2004).

9.5 THE TIBETAN HIGH AND THE TROPICAL EASTERLY JET

In the upper troposphere, say 200 hPa, a prominent circulation system of the Asian summer monsoon is the planetary-scale high-pressure system and associated anticyclonic circulation (Figure 2.6(a)). This system is centered over the Tibetan Plateau and is often referred to as the Tibetan High (TH) or south Asian High. The ridge of the elongated TH is around 30°N and spans the entire eastern hemisphere from North Africa to the Date Line with the core region between roughly 50°E to 130°E and 15°N to 40°N. Evidently, this TH dominates the global upper tropospheric circulation (Figure 2.6(a)). A similar anticyclone exists over the North America sector but with about 1/3 of the longitudinal span and 1/2 of the amplitude in geopotential departure (from the zonal mean). This North American counterpart is called the Mexican High. In between the TH and the Mexican High are two troughs located in the mid-Pacific and mid-Atlantic Ocean, respectively (Figure 2.6(a)).

The clockwise flow (anticyclone) around the TH contains an easterly jet stream in its southern flank called the tropical easterly jet (Figure 2.6(a)). The core of the easterly jet is attained in the north Indian Ocean between 5°N and 10°N with the maximum speed exceeding $30\,\mathrm{m\,s^{-1}}$ (Figure 9.10(a), color section). The jet stretches from the western Pacific (150°E) all the way to the west coast of North Africa. Pronounced cross-equatorial flow in the Indian Ocean is a major component of

the upper level branch of the Hadley cell. It is notable that the zonal wind component of the easterly jet, although located in the deep tropics, is nearly in geostrophic balance with the meridional pressure gradient force. Scale analysis shows that this is because the Rossby number V/fL for the jet is small, where L is the long zonal length scale for this jet and V is a typical meridional wind.

9.5.1 Formation and maintenance of the Tibetan High

The formation and maintenance of the TH and the upper tropospheric circulation are primarily attributed to the diabatic heating processes associated with deep convective rainfall in south-east Asia and the western North Pacific and also to the sensible and convective heating over the elevated Tibetan Plateau.

As already discussed, the general convective heating in the Asian monsoon region leads to a response similar to that shown in Figures 9.6(b) and 9.7(b). Above and to the west of the Plateau the cyclone at low levels and the anticyclone at upper levels are associated hydrostatically with a warm troposphere that has spread westwards from the heating region as a long Rossby wave.

It has also been recognized for many years that the Plateau itself acts as an elevated heat source in summer (Flohn, 1957; Ye *et al.*, 1979; Yanai *et al.*, 1992; Ye and Wu, 1988; see also Chapter 13 for reviews). In particular, the strong surface sensible heat flux makes the boundary layer very unstable and produces strong near-surface convergence and upper level divergence/negative vorticity. As a result, the TH has a warm and moist core over the Plateau. The mean upper tropospheric (500–200 hPa) temperature over south Asia and the Tibetan Plateau is the highest on the planet (Figure 1.10 and Chapter 13). This remarkable warmth is directly associated with the intensity of the high pressure in the upper troposphere.

9.5.2 The upper level easterly jet and its impact on the precipitation distribution

Over the Tibetan Plateau, the local mean temperature is more than 5°C higher than at the equator at the same longitude (Figure 1.10). This reversed poleward temperature gradient is consistent with a strong easterly thermal wind and the existence of the upper level easterly jet (Figure 9.10(a), color section).

When thinking about vertical circulations associated with the easterly jet, it is of interest to consider an alternative partition of the wind to the rotational and divergent split so far used. The quasigeostrophic version of the zonal momentum equation may be written:

$$\frac{du_g}{dt} = f(v_g + v_a) - \frac{1}{\rho}\frac{\partial p}{\partial x} = fv_a \tag{9.5.1}$$

Here the meridional wind component has been decomposed into a geostrophic (v_g) and an ageostrophic (v_a) component (i.e., $v = v_g + v_a$). Evidently, on the north side of the entrance region of the easterly jet (i.e., the monsoon trough from the Bay of Bengal to the Philippine Sea) (Figure 9.10(a), color section), a parcel moving through the jet will experience an increase in easterly wind speed ($du_g/dt < 0$, where u_g is the

zonal component of the geostrophic wind). Equation (9.5.1) implies that in this entrance region of the jet there must be a northerly ageostrophic flow, and consequently upper level divergence and mid-level ascent over the south-east Asian monsoon trough region, as shown in Figure 9.10(b) (color section). The ascent along with the upper level northerly ageostrophic flow forms a secondary circulation which consists of a southerly flow crossing the equator and a sinking motion just south of the equator. This secondary circulation is an enhancement of the monsoon Hadley cell and consistent with the ascent in the monsoon trough (Figure 9.10(b)). On the other hand, North Africa is located in the exit region of the northern side of the easterly jet where the easterly decreases in intensity, resulting in upper level southerly ageostrophic winds and convergence on the northward side (Figure 9.10). The resultant secondary circulation is consistent with subsidence over the North African region on the poleward side of the easterly jet, which may restrict the northward extension of the Sahel monsoon rainfall and confine the rain belt to the coastal zone of North Africa. In summary, the easterly jet favors ascent in the jet entrance region in the south-east Asia monsoon trough and descent in the exit region of the jet over the Sahara in North Africa. However the strongest descent occurs over the Mediterranean Sea, as explained by the monsoon–desert mechanism. The importance of radiative cooling as a positive feedback on the descent should also be stressed again.

Webster *et al.* (1998) visualized that the divergent circulation associated with the Asian monsoon consists of not only the conventional cross-equatorial circulation (the lateral monsoon or Hadley type cell) but also two types of zonally oriented transverse divergent circulation cells: the transverse cell between the south-east Asian ascent and the North African descent and the Walker cell between the south-east Asian ascent and the eastern Pacific sinking motion. They argued that the south-east Asia–North Africa transverse cell is driven by the longitudinal contrast in the latent and radiative heating between North Africa and south Asia. The transverse divergent circulation cell can be understood in terms of the dynamics of the easterly jet associated with the TH discussed in this section and the Hoskins–Rodwell theory. Since in general the latent heat difference is a factor of two larger than the difference in columnar radiative heat flux divergence (Webster, 1994), to a large degree, the transverse divergent cell and the corresponding rotational circulation system of the Asian monsoon can be understood as resulting from the deep convective heating in the south-east Asian monsoon rainfall and the sensible/convective heating over the Tibetan Plateau.

9.5.3 A possible positive feedback between the Tibetan High/easterly jet and the monsoon convection

The Hoskins–Rodwell theory takes the diabatic heating as given and focuses on how it, together with the mountains, affects the summer subtropical circulation. While the latent heat released in monsoon precipitation can produce realistic large-scale monsoon circulation, the monsoon rainfall itself also needs support from, and

must be consistent with, the large-scale flow. The interactive nature of the monsoon rains and circulation leaves an open question regarding what determines the preferred geographic location of the monsoon rains.

The effects of land–sea thermal contrast and topographic effects have been traditionally considered as important factors in determining the location of monsoon rainfall. It has also been argued that boundary layer frictional convergence should draw rainfall into the central low-pressure system that is induced by the land surface warming contrasting with the adjacent cool oceans. However, the Asian monsoonal rains do not tend to coincide with the central regions of monsoon lows. Rather, the heavy rains prefer to concentrate in the south-east portion of the continent and adjacent marginal seas. This is in sharp contrast to the desert and semi-arid regions to the west of the Eurasian continent and North Africa. In general, a typical monsoon rainfall distribution is characterized by a dipole pattern consisting of an east 'wet' region and a west 'dry' region with respect to the major body of the land mass. This east/wet–west/dry dipole pattern is generally observed over all continental monsoon lows including Eurasia, North America, South America, South Africa, and Australia. This prominent continental monsoonal precipitation pattern can be readily recognized from Figure 2.4.

There should be a preferred fundamental reason for the location of monsoon rains and the east/wet–west/dry dipole rainfall distribution with respect to the land–sea configuration. It is hypothesized that this dipole pattern may be due to a positive feedback between the rainfall-induced heating and the heating-induced, large-scale circulation. The following discussion takes the Asian summer monsoon as an example, but in principle it may apply to other continental monsoon regions.

On the one hand, according to Hoskins–Rodwell theory, the diabatic heating released by rainfall in the south-east Asian monsoon region sets up the subtropical anticyclone to the east in the North Pacific and the descent to its west in the Sahara and Mediterranean regions. A particular point that is noteworthy is that the south-east Asian heating not only induces the North Pacific subtropical anticyclone and associated easterly trades but also contributes to the formation and maintenance of the TH and the upper tropospheric easterly jet. On the other hand, the upper level easterly jet has an associated secondary circulation, shown in Figure 9.10(a) (color section), which, in turn, favors development of deep convection, synoptic disturbance, and mesoscale systems in the south-east Asian monsoon trough (the poleward side of the entrance region of the easterly jet) and descent over North Africa. In the lower troposphere, the south-easterly trades associated with the North Pacific subtropical anticyclone meet the south-westerly monsoon, forming a confluence zone – the monsoon trough over the Philippines. Thus, the heating-induced, large-scale circulation is in favor of the maintenance of heavy monsoon rains in south-east Asia where low-level flows converge and upper level flows diverge. The above argument implies that the dynamical forcing provided by the heating-induced, large-scale circulation feeds back positively to reinforce the strength of the convection in the south-east Asian monsoon trough. Arguably, this positive feedback may play a critical role in selecting the preferred location for the monsoon trough and heavy monsoon rainfall.

It should be noted that the TH and easterly jet are not solely due to the effect of the south-east Asian monsoon rainfall. The Tibetan Plateau is also a major factor determining the character of the TH and easterly jet. The location of the elevated heat source to the north of 25°N over the Plateau is perhaps sufficiently strong to provide an anchor for the central location of the TH, which in turn, sets the location of the tropical easterly jet and the ascent region influenced by the secondary circulation in the jet entrance region (Figure 9.10, color section). The latter favor heavy rains establishing in the Asian monsoon trough region. Thus, the Tibetan Plateau may make a considerable contribution in determining the location of the whole monsoon structure.

9.6 CROSS-EQUATORIAL FLOW AND INERTIAL INSTABILITY

The low-level cross-equatorial flow in the western Indian Ocean stands out as the strongest low-level jet on Earth during boreal summer (Figure 2.5(a)). It has been recognized in early studies of the south-west Indian monsoon that the monsoon flows originate south of the equator (e.g., Blandford, 1874). Findlater (1966, 1967, 1969) found that the low-level monsoon airflow is organized into a relatively narrow high-speed trans-equatorial current in the western periphery of the monsoon region. The wind speed in the core of the Somalia jet exceeds $25\,\mathrm{m\,s^{-1}}$ (Findlater, 1969a). The jet core is located about 1.5 km above sea level, 200–400 km in width, and 1 km in depth and lies about 200 km east of the Aast African Highlands (EAH). Associated with this jet is active air–sea interaction.

This cross-equatorial flow, which is now referred to as the Findlater jet or Somalia jet, is an essential component of the Asian monsoon system. It transports moisture from the southern Indian Ocean to south Asia, connects the Mascarene High and Indian monsoon trough, and completes the lower branch of the Hadley cell of the Asian monsoon. The jet stream also drives a strong seasonal cross-equatorial ocean current, the Somalia Current. In addition, the along-shore winds induce intense upwelling farther up the coast, resulting in a SST drop of around 3–4°C in the eastern Arabian Sea. The decreased SST has significant impacts on the Indian monsoon and its variability (Krishnamurti and Bahme, 1976; Love, 1985). Relations between the cross-equatorial flow and the rainfall have been recognized in other monsoon regions such as over Central America (Pena and Douglas, 2002), the western Amazon (Wang and Rong, 2002), and North Africa.

Two different perspectives on the cross equatorial flow and the Somalia jet will be presented. In the first, a cross-equatorial pressure gradient will be assumed to exist and the steady flow associated with it will be discussed. The second perspective will focus on the occurrence of inertial instability in cross-equatorial motion and the consequences of this.

9.6.1 Steady flow in an imposed pressure gradient

The discovery of the Somalia jet stimulated great interest in understanding the physical processes determining the location and structure of the cross-equatorial

flow in general and the Findlater jet in particular. To understand the basic dynamics of the cross-equatorial flow, let us focus on a large-scale, steady boundary layer flow. The equation governing the vertically averaged boundary flow on an equatorial β-plane may be written as (Hastenrath, 1987):

$$u\frac{\partial u}{\partial x} + v\frac{\partial u}{\partial y} = -\alpha\frac{\partial p}{\partial x} + fv + \kappa_s u \tag{9.6.1a}$$

$$u\frac{\partial v}{\partial x} + v\frac{\partial v}{\partial y} = -\alpha\frac{\partial p}{\partial y} - fu + \kappa_s v \tag{9.6.1b}$$

In (9.6.1), α is the specific volume of the air. The effects of transient eddies have been neglected since they are small. Boundary layer friction is represented by a linear drag with κ_s^{-1} being a time constant associated with surface stress and being typically about 2 days. Equation (9.6.1) depicts a balance among the pressure gradient force (the 1st right-hand-side (RHS) term), Coriolis force (the 2nd RHS term), friction (the 3rd RHS term), and inertial acceleration (the left-hand-side (LHS) terms). This equation can be used to indicate the influence of the pressure field on the recurvature of the south-east trades and cross-equatorial flow.

Equatorially asymmetric thermal forcing leading to a cross-equatorial pressure gradient is an essential driver for cross-equatorial flow. Consider now a constant meridional pressure gradient extending from wintertime southern subtropics to the low pressure over the heated northern subtropics. At the equator ($y = 0$) the Coriolis force vanishes so that if the inertial (advective) terms are negligible then $v = \kappa_s^{-1}\alpha\,\partial p/\partial y$ and the flow is directly across the isobars toward low pressure. For a strong cross-equatorial flow, however, the advective accelerations in the near-equatorial balance of forces are essential. If the frictional terms are neglected an inertial regime exists with the LHS of (9.6.1) balanced by the pressure gradient force (Young, 1987). Thus, the zonal momentum equation (9.6.1a) at the equator yields a flow that is directly across the equator, namely, $v = -\alpha(\partial p/\partial x)/(\partial u/\partial y)$ and $u(0) = 0$. This indicates that zonal pressure differences are essential for a strong cross-equatorial flow such as the Somalia jet.

9.6.2 Inertial instability and the location of the ITCZ

Krishnamurti *et al.* (1983c), in their numerical study of the low-level flow in the Indian monsoon region, noted that in the boundary layer there is geostrophic balance to the north of the ITCZ and an advective balance (i.e., parcels accelerating) to the south of the ITCZ. They stated, '...just north of the equator the flow is accelerated, with little impediment, toward lower pressure...'. The acceleration of the cross-equatorial Asian monsoon circulation toward the coast of India may be under the influence of inertial instability.

Consider now a perturbation to a zonal flow $U(y)$, which is in geostrophic balance. In contrast to the previous subsection we will consider unsteady motion

but assume that the perturbation pressure gradient and the friction are negligible. Then the equations are:

$$\frac{du}{dt} = \zeta v \tag{9.6.2a}$$

$$\frac{dv}{dt} = -fu \tag{9.6.2b}$$

where $\zeta = f - \partial U/\partial y$ is the absolute vorticity of the basic flow. If the relative vorticity of the basic flow is negligible compared with f, (9.6.2a) shows that in the northern hemisphere a velocity in the x direction, u, leads to an acceleration in the negative y direction. Once this negative y velocity, v, has developed, according to (9.2.6b), this leads to a negative x acceleration opposing the original motion. In turn, once this negative u has developed, it leads to a positive acceleration in the y direction. Solution of the equations indeed shows that the air moves anticyclonically in so-called inertial circles with a frequency f.

If the relative vorticity of the basic flow is anticyclonic, (9.6.2a) shows that the generation of u is weakened. Consistent with this, solutions indicate that the trajectories of parcels become ellipses elongated in the y direction and the frequency of the motion around them decreases. If however the basic relative vorticity is so anticyclonic that the absolute vorticity reverses sign, then the restoring effect of the Coriolis parameter in the x momentum equation is lost and there is inertial instability. To show this, if we set $\gamma = (-\zeta/f)^{1/2}$, which is now a positive real number, and add γ times the y momentum equation in (9.6.2) to the x momentum equation using $u = dx/dt$ and $v = dy/dt$, the result can be written:

$$\frac{d^2}{dt^2}(x - \gamma y) = \gamma f \frac{d}{dt}(x - \gamma y) \tag{9.6.3}$$

This shows that the motion in the direction of $x - \gamma y$ grows on a timescale of $(\gamma f)^{-1}$. Negative absolute vorticity is found in the northern hemisphere in the air that has crossed the equator on the eastern side of the EAHs.

As discussed by Hoskins (1974), the more general instability criterion depends on the potential vorticity (PV) rather than the absolute vorticity. There is instability if f^*PV is negative (i.e., if there is negative (positive) PV in the northern (southern) hemisphere). Since PV is materially conserved in the absence of diabatic and frictional sources, this makes a non-linear discussion, as opposed to imposing a basic state, possible. If air from the southern hemisphere, with the ambient negative PV of that hemisphere, crosses the equator and conserves its PV then it will be inertially unstable in the northern hemisphere and will accelerate. As demonstrated by Rodwell and Hoskins (1995), this is what occurs in the cross-equatorial flow forced by the Indian monsoon and leads to the Somalia jet. The only way such an effect can be limited is if the PV of the air is made positive by diabatic and frictional processes. In the absence of such processes, the air eventually moves back to the southern hemisphere. The appearance of the low-level flow almost trying to avoid India (see Figure 4.1) is a manifestation of the tendency for this return before the

PV of the air becomes sufficiently positive for it to remain in the northern hemisphere.

The EAH act as a mechanical barrier to the southern Indian Ocean south-east trades and concentrate the low-level flow intercepting the mountains while crossing the equator. Presence of the stable inversion layer forces the incident flow to go around rather than over the EAHs barrier (Hart, 1977). The concentrated, rapid flow of the air into the northern hemisphere means that it tends to maintain its southern hemisphere PV and therefore is crucial to the existence of the Somali jet. However even there PV is changed on fluid parcels and, as discussed above, the PV of the Indian monsoon inflow has to be made positive if the air is to remain in the northern hemisphere. In Rodwell and Hoskins (1995) it was shown that frictional material PV tendencies are particularly important in the flow along the east African coast where the land/sea contrast in friction is large and over the northern Indian Ocean where relative vorticity anomalies within the jet are significant. The diabatic modification of PV is important over the southern Indian Ocean and eastern Africa, where shallow heating of more than $3\,\mathrm{K\,day^{-1}}$ exists. Thus, both the surface friction and local diabatic heating provide mechanisms for material modification of PV and both are important for maintenance of the jet.

Numerical experiments performed by Rodwell and Hoskins (1995) showed that without the EAH, but still imposing the Asian monsoon heating, the inflow into India is fed from cross-equatorial flow in a broad longitudinal band. However, there must then be a question over whether the existence of the imposed heating is actually consistent with the flow that is generated by it. It might be expected that without the EAH to localize the cross-equatorial flow there would be moisture transport into the African continent and the moisture supply to the south Asian monsoon would be substantially reduced. To answer these questions and others, full general circulation experiments have been performed with and without the EAH, as described in Slingo *et al.* (2005). Without the EAH in June–August the south-east trades in the southern Indian Ocean were found to penetrate the African continent. However, they did not lead to more precipitation there as they were capped by an increased flow of dry air from the north-west. There was little sign of a Somali jet and the inflow of air to the south Asian monsoon was found to arise from a weaker cross-equatorial flow but in a much broader region from Africa through the western Indian Ocean. The total precipitation over southern Asia was similar but with a slightly modified distribution.

Tomas *et al.* (1999) gave a complementary physical explanation as to why inertial instability is associated with cross-equatorial anticyclonic flow. The large-scale flow in the boundary layer is somewhat subgeostrophic and thus contains a cross-isobaric component. The effect that the cross-isobaric flow has on the along-isobar flow depends strongly on the sign of the local absolute vorticity. When the absolute vorticity is locally anticyclonic, cross-isobaric flow drives the along-isobar flow away from geostrophic balance. This in turn leads to increased cross-isobaric flow; thus, there is a positive feedback and the total flow tends toward a state that is more subgeostrophic and has a significantly stronger

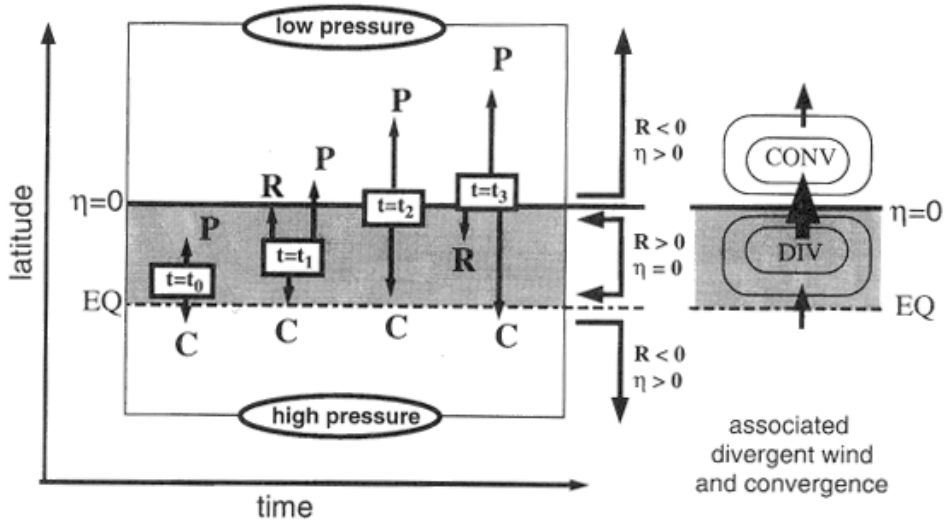

Figure 9.11. Schematic diagram showing the forces acting on a parcel of air under the influence of a cross-equatorial pressure gradient. Flow in the region is assumed to be inertially unstable. Axes representing time and latitude are drawn with orientation appropriate for northern hemisphere (boreal) summer, P, C, and R represent the pressure gradient force, Coriolis force, and residual force respectively. The region where the local absolute vorticity (here denoted by η) is negative is stippled. On the right-hand side is the divergence–convergence distribution consistent with an inertially unstable flow.
From Tomas and Webster (1997).

cross-isobaric component. The situation with locally cyclonic absolute vorticity is just the opposite.

Tomas and Webster (1997) show a strong association between the local cross-equatorial pressure gradients and the position of the zero absolute vorticity (AV) contours in the lower troposphere, suggesting that the location of the zero AV contour is determined by the macroscale cross-equatorial pressure gradient. The zero AV contours in the lower troposphere are located north of the equator in the western Indian Ocean in summer, indicating that the flow is inertially unstable. Figure 9.11 shows the forces acting on a parcel as it passes through a region that is inertially unstable. The parcel is drawn with orientation appropriate for northern summer conditions with low pressure to the north of the equator and high pressure to the south. Consider a parcel at time $t = t_0$ that is located just north of the equator, in geostrophic balance, in a region where the AV is negative, and that it is then displaced northward at time $t = t_1$. The zonal velocity changes as a result of this displacement but, because the environment is inertially unstable, the new zonal velocity of the parcel is subgeostrophic. The unbalanced pressure gradient force R acts to accelerate the parcel northward. At time $t = t_2$, the parcel reaches the zero AV contour. At this stage, the acceleration is zero ($R = 0$). Further northward motion (time $t = t_3$) results in the parcel experiencing a southward restoring force

($R < 0$). Thus, when the zero AV contour is found some distance from the equator, the wind will be accelerated on the equatorward side and decelerated on the poleward side of the zero AV contour. They argue that the atmospheric response to this AV distribution is a convergence–divergence couplet in the boundary layer (i.e., the divergent wind is being accelerated on the equatorward side of the zero AV contour and decelerated on the poleward side); thus the general collocation of divergent wind maxima and the zero AV contour away from the equator results from inertial instability. It was hypothesized that the divergence–convergence couplets of inertial instability appear to play an important role in determining the location of near-equatorial convection and the mean latitude of the ITCZ.

9.7 THE EFFECTS OF MEAN FLOWS ON EQUATORIAL WAVES AND FORCED MOTION

The theories of Matsuno (1966) and Gill (1980) discussed in Sections 9.2 and 9.3 deal with perturbation motions in a resting environment. In reality, the equatorial waves induced by deep convective heating penetrate the entire troposphere where the 3-D background flows can have significant modification on the behavior of the waves. Observed anomalies associated with monsoon variability are departures from monsoon background flow. Thus, understanding of how the planetary-scale background flows alter the properties of the equatorial waves is fundamental for explaining the various aspects of monsoon variability.

While the tropical seasonal mean flow has a complicated 3-D structure, to the lowest order of approximation, one may consider it a basic zonal flow, $U(y,p)$, that is in geostrophic balance and varies with height and latitude. The question to be addressed is how the meridional and vertical shears of the zonal mean flow affect the properties of the horizontally propagating low-frequency waves. The separation of variables to give a vertical mode and the shallow-water equations in the horizontal is only possible for a resting atmosphere basic state. The possible effects introduced by horizontal and vertical shears will be discussed in this section.

The likely effects of the meridional shear of such a zonal flow are suggested by the use of a modified shallow-water model. The modified model would be the same as (A.1.5) except that the β-term in the zonal momentum equation should be replaced by the meridional gradient of the absolute vorticity of the basic flow, $(\beta - \partial^2\bar{u}/\partial y^2)$. Thus, the meridional shear influences the equatorial waves through latitude-dependent zonal advection (Doppler shift) and through changing the basic state vorticity gradients. Theoretical analysis indicates that the effect of the realistic meridional shear on low-frequency waves is generally moderate. The shear-induced change of the absolute vorticity gradients makes baroclinic Rossby modes more tightly trapped near the equator (Wilson and Mak, 1984). The trapping effect is significant for short waves but negligible for planetary-scale (wavenumber 1 to 4) waves (Wang and Xie, 1996). The Doppler shift effect at the latitude where the geopotential reaches maximum amplitude affects the wave propagation speed and has a major impact on the group velocity (Hoskins and Jin, 1991). The meridional

shear affects equatorial Kelvin waves in a way similar to that in which it affects the Rossby waves except that the Kelvin waves are more trapped near the equator if $\partial^2\bar{u}/\partial y^2 > 0$, whereas they may be less trapped when $\partial^2\bar{u}/\partial y^2 < 0$. The meridional shear can also make Kelvin waves become weakly dispersive due to the wavelength-dependent modification of their meridional structure and latitude-dependent zonal advection (Wang and Xie, 1996).

In contrast to the effects of the meridional shear, the vertical shear of the zonal mean flow can considerably change the behavior of the equatorial waves in a resting atmosphere and atmospheric response to a given heat source without mean flows. In the presence of a summer mean flow, Webster (1972) showed that the atmospheric response in the vicinity of heat forcing has a baroclinic structure but displays a barotropic structure away from the forcing region. Kasahara and Silva Dias (1986) noticed the vertical shear of the basic flow permits a coupling of the external and internal modes. Lim and Chang (1986) demonstrated this coupling process using an f-plane model.

In this section, an idealized model of equatorial β-plane is used to examine the impacts of a vertically sheared zonal flow $U(p)$ on low-frequency equatorial waves. In the presence of vertical shear, the different vertical modes are coupled by the shear and no longer separable. Wang and Xie (1996) have developed a simple two-level model describing equatorial waves propagating through a zonal flow with a constant vertical shear. The derivation is presented in Appendix A3.

The two-level model represents two vertical modes, a barotropic mode and a baroclinic mode (A.3.2), which are governed by equations (A.3.3) and (A.3.4), respectively. The barotropic mode is essentially a Rossby wave modified by a forcing arising from the baroclinic mode acting on the vertical shear. The baroclinic mode is governed by a modified shallow-water equation including the feedback from the barotropic mode. The forcing terms on the RHS of equations (A.3.3) and (A.3.4) indicate interactions between the barotropic and baroclinic modes in the presence of vertical shear.

Linear wave solutions of the form:

$$(u_-, v_-, \phi_-, \psi) = \mathrm{Re}(U, V, \Phi, \Psi)e^{i(kx-\omega t)}$$

can be shown to satisfy a set of ordinary differential equations. With Matsuno's (1966) meridional boundary conditions, one can determine the meridional structures of the barotropic and baroclinic modes and the dispersion relation can also be determined.

9.7.1 The effects of vertical shear on the Rossby wave structure and propagation

Figure 9.12 shows meridional structures of the geopotential (thickness) field of the barotropic (baroclinic) modes for the $n = 1$ (most equatorial trapped) Rossby waves. Here a westerly vertical shear means that westerly wind increases with height or easterly wind decreases with height. In the presence of the vertical shear, the baroclinic mode remains equatorially trapped (Figure 9.12(a)). In contrast, the

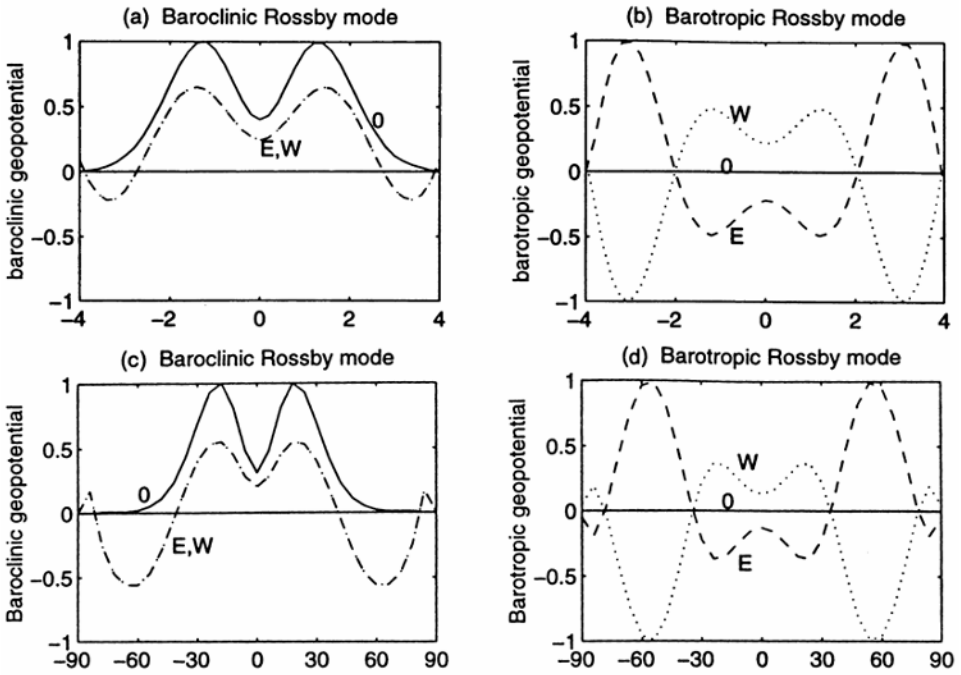

Figure 9.12. Meridional structures of the geopotential field for (a) baroclinic and (b) barotropic Rossby wave mode ($n = 1$) calculated using an equatorial β-plane. Panels (c) and (d) are the same as in (a) and (b) except computed from a spherical coordinates model. From Wang and Xie (1996).

barotropic mode extends poleward with geopotential extremes occurring in the extratropics around three Rossby radii of deformations away from the equator (Figure 9.12(b)). To confirm the results derived from the equatorial β-plane, a parallel analysis using spherical coordinates was carried out (Wang and Xie, 1996). The results show that the maximum geopotential perturbation of the barotropic mode is found near 57° latitude in the spherical coordinate model (Figure 9.12(d)). Due to the feedback of the barotropic mode, the baroclinic mode also has significant amplitude around 60° latitude (Figure 9.12(c)).

The lowest baroclinic mode in the absence of mean flow vertical shear exhibits a precisely out-of-phase flow field in the upper and lower levels. The presence of the vertical shear modifies the vertical structure of the waves dramatically.

Figure 9.13 presents a 3-D structure of the $n = 1$ Rossby waves in a westerly vertical shear (Figure 9.13(a)) and an easterly vertical shear (Figure 9.13(b)) in comparison with the case without vertical shear (Figure 9.13(c)). In a westerly (easterly) shear, the Rossby waves have larger amplitude at the upper (lower) troposphere. This is particularly evident in the tropical regions. Poleward by about two Rossby radii of deformation, the barotropic mode dominates and the sign of the

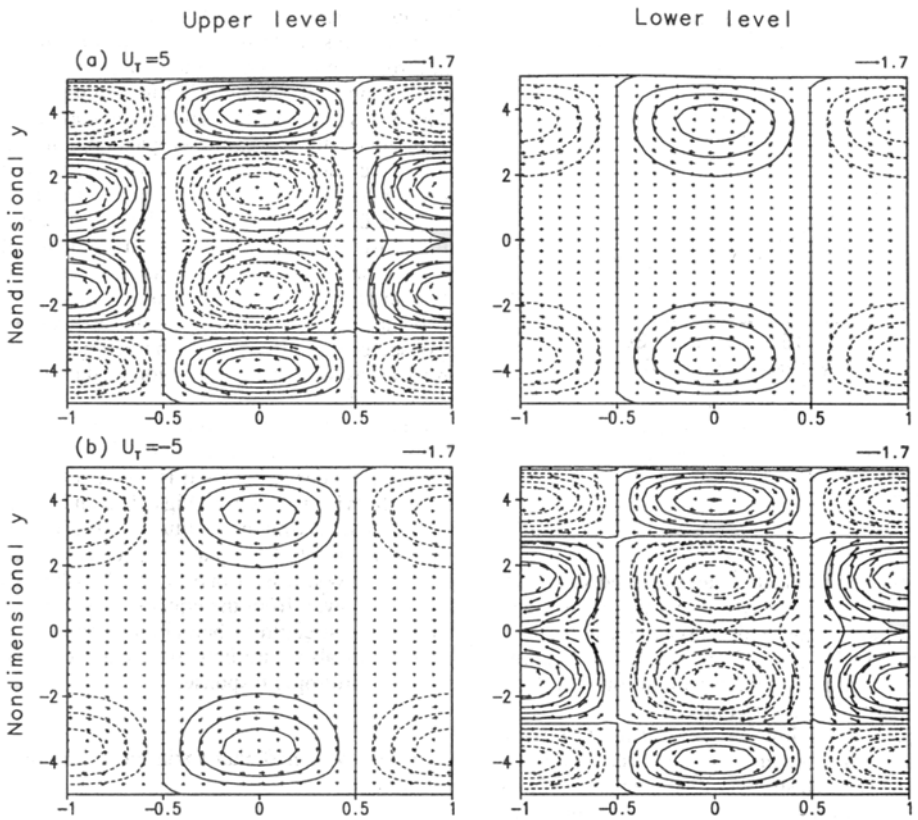

Figure 9.13. Horizontal structure of the $n = 1$ Rossby waves with a wavelength of 10,000 km. Geopotential and wind patterns in the upper and lower troposphere are displayed for (a) $U_T = 5\,\mathrm{m\,s^{-1}}$ (westerly vertical shear) and (b) $U_T = -5\,\mathrm{m\,s^{-1}}$ (easterly vertical shear). The abscissa denotes zonal phase in units of π.
From Wang and Xie (1996).

geopotential perturbation tends to be out of phase with that in the tropical region. Obviously, the vertical shear has changed the vertical structure of the Rossby wave drastically. The reason is that the nature of coupling of the two vertical modes depends on the sign of the vertical shear ((A.3.3) and (A.3.4)). Wang and Xie (1996) have shown that for a constant vertical shear, one of the vertical modes may have a structure that is independent of the sign of the shear, but the remaining mode must then have a structure that is dependent on the sign of the vertical shear. However, no matter which mode is assumed to be independent of the sign of the vertical shear, the two vertical modes are in phase in the westerly shears, whereas they are 180° out of phase in easterly shears. Thus, the vertical shear creates a vertical asymmetry with respect to the mid-troposphere in the Rossby wave structure.

The presence of vertical shears also slow down the westward propagation of the Rossby waves regardless of the sign of the vertical shear. The reason is that Rossby waves tend to have an elevated (lowered) steering flow level in a westerly (easterly) shear. If the vertical mean zonal flow vanishes, the resultant mean zonal steering flow is thus eastward in both the westerly and easterly shears, which acts to reduce propagation speed of the Rossby waves.

The modification of the structure and propagation depends on the strengths of the vertical shear and the wavelength. For a given shear, the structures of the short waves are more significantly modified and so are their phase speeds. In reality, the vertical shear of the zonal mean flow may also change with latitude. In the presence of meridional variation of the vertical shear, the Rossby waves will be enhanced in the vicinity of the latitudes where the vertical shear is strengthened, suggesting the importance of regional vertical shear in modification of the *in situ* wave characteristics.

The above discussion applies to stable Rossby waves. Further analysis has shown that vertical shear has profound influences on the instability of the moist equatorial Rossby waves (Xie and Wang, 1996). When the vertical shear of the mean zonal flow exceeds a certain critical value, the most trapped equatorial Rossby waves become unstable by extracting mean flow available potential energy. When convective heating is organized by, and fed back to, the equatorial Rossby waves, the preferred most unstable wavelength increases with increasing vertical shear and decreases with increasing heating intensity, ranging typically from 3,000 to 5,000 km.

Without boundary layer friction the Rossby wave instability does not depend on the sign of the vertical shear. However, in the presence of a boundary layer, easterly (westerly) shears enhance (suppress) the moist Rossby wave instability considerably. The reason is that an easterly shear confines the wave to the lower level, generating a stronger Ekman pumping-induced heating and meridional heat flux, both of which reinforce the instability. The opposite is true for a westerly shear. The effects of vertical shear on the westward propagating Rossby–Gravity waves are similar to those for Rossby waves. However, the vertical shear has little impact on the equatorial Kelvin waves (Wang and Xie, 1996).

9.7.2 Extratropical barotropic response induced by equatorial heating

One of the fundamental impacts of vertical shear is excitation of prominent barotropic Rossby wave motion through interaction with the gravest baroclinic Rossby waves. This vertical shear mechanism may help explain how an equatorial heating generates a significant extratropical barotropic response.

An internal heating sitting on the equator can directly generate a baroclinic Rossby mode (A.3.4). It can be shown from (A.3.3) that the vorticity equation of the barotropic mode is given by:

$$\frac{D\zeta_+}{Dt} = -v_+ + U_T\left(\frac{\partial D_-}{\partial y} - \frac{\partial \zeta_-}{\partial x}\right) \tag{9.7.1}$$

Thus, the meridional variation of baroclinic divergence and longitudinal variation of the baroclinic vorticity acting on the vertical shear of the mean flow represents a source of forcing for the barotropic motion. Figures 9.12(c) and 9.12(d) show that the barotropic Rossby waves are not equatorially trapped; rather they have maximum amplitudes in the extratropics. Hence, an equatorial heating can indirectly generate extratropical barotropic Rossby waves, providing a mechanism by which equatorial heating can generate extratropical teleconnection patterns. The discussion on Rossby wave source in Section 9.9 will give an alternative perspective on this.

9.7.3 Asymmetric Rossby wave response to equatorial symmetric heating

In a resting atmosphere, an equatorial symmetric heating can only induce an equatorial symmetric response in the pressure and zonal wind field. As discussed earlier, the vertical shear can induce remarkable equatorial asymmetry for the $n = 1$ Rossby waves, which in the absence of the vertical shear has equatorial symmetric pressure and zonal winds. The Asian summer monsoon is characterized by significant vertical easterly shears over south Asia. Because the monsoon easterly shear is primarily confined to the northern hemisphere, the unstable $n = 1$ Rossby wave can become markedly trapped in the northern hemisphere (Xie and Wang, 1996). Under the influence of such a summer mean monsoon circulation, even a heating that is symmetric about the equator can possibly induce a considerable asymmetric Rossby wave response with major circulation located in the easterly vertical regions (i.e., the northern hemisphere).

To validate the inference deduced from the theoretical model, a numerical experiment with an anomaly atmospheric general circulation model (AGCM) was performed (Wang *et al.*, 2003). A multilevel linearized AGCM is chosen because more realistic 3-D basic states can be specified. 3-D summer (JJA) and winter (DJF) mean basic states were prescribed in an equally spaced five-level sigma coordinate. A strong momentum damping with a decay timescale of one day is applied in the lowest model level to mimic the planetary boundary layer dissipation, while a Newtonian damping with an e-folding timescale of 10 days is applied to all levels in both momentum and thermodynamic energy equations.

Figure 9.14 illustrates the response of the lowest level winds to a prescribed ideal equatorial symmetric cooling. This cooling is motivated by mimicking the anomalous cooling associated with the Maritime Continent subsidence during El Niño. In the presence of the northern summer mean flow, the atmospheric response is obviously asymmetric to the equator: a strong low-level anticyclone anomaly appears to the north of the equator (Figure 9.14(a)). The anomalous anticyclone extends to the west of the heat sink, covering the entire south Asian monsoon region. On the other hand, with specification of a resting background flow, the model produces a symmetric response with twin anticyclones residing on each side of the equator similar to that in Figure 9.4 (figure omitted). When the mean winter (DJF) basic flow is specified, the model simulated anticyclonic response in the southern hemisphere tends to be extended more westward, consistent with the distribution of the easterly vertical shear (Figure 9.14(b)). The numerical results

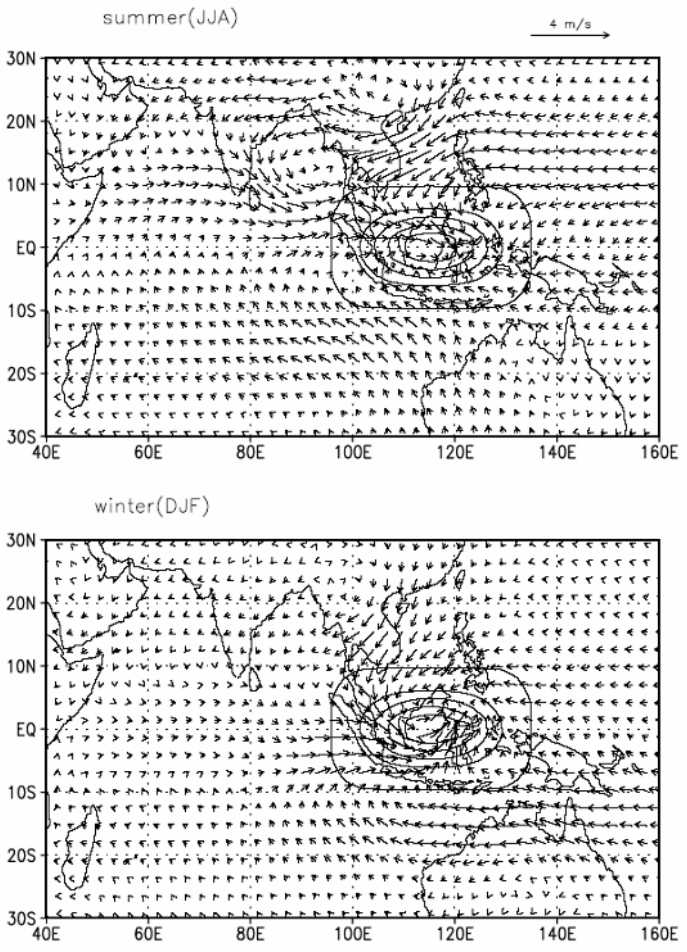

Figure 9.14. The low-level wind response to an equatorially symmetric heat sink simulated using an anomaly atmospheric general circulation model with specified basic states of (a) boreal summer (JJA) mean and (b) boreal winter (DJF) mean climatological flow. The contours represent horizontal distribution of the heat sink strength at an interval of $0.4^{\circ}\mathrm{C\,day^{-1}}$ with a maximum amplitude of heating rate of $-2^{\circ}\mathrm{C\,day^{-1}}$, which is located in the middle troposphere.

shown in Figure 9.14(a) provide an explanation why during an El Niño/Southern Oscillation (ENSO) developing phase (JJA) the major monsoon anomalies are dominated by an anticyclonic ridge located north of the equator, while the response in the southern hemisphere is weak (Wang *et al.*, 2003). Using an intermediate atmospheric model, Wang and Xie (1997) identified that the equatorial asymmetric response is primarily produced by the effects of the vertical shear in the seasonal mean state. On the other hand, during the mature phase of El Niño

(DJF), the suppressed convection over the Maritime Continent and Australian monsoon region favors anomalous anticyclones forming over the tropical southern Indian Ocean, similar to the solution shown by Figure 9.14(b).

9.7.4 Northward propagation of Rossby waves due to monsoon easterly shear

Lau and Lau (1990) have documented the detailed statistical behavior of vorticity disturbances over the Bay of Bengal and the Philippine Sea–South China Sea. They showed the horizontal and vertical structures and preferred wavelength (4,000 km), as well as the peculiar north-westward propagation (4–5 m s^{-1}) of these disturbances. It is proposed that these vorticity waves are a manifestation of the unstable equatorial Rossby waves, because the horizontal and vertical structure of the most unstable moist Rossby waves predicted by the linear analysis compare favorably to the observed vorticity waves in terms of the horizontal and vertical structure and westward propagation phase speed.

A puzzling question is what causes the Rossby waves to have a northward propagation component? In addition to the advective effect of the mean flow, which is probably more significant in the Philippine Sea region, the effect of the easterly vertical shear of the mean flow is a potentially important internal dynamic factor that drives Rossby waves moving northward. This has been demonstrated by the numerical experiments using an intermediate atmospheric model (Wang and Xie, 1997).

To illustrate this mechanism, let us consider a simplified 2-D version of the model shown in Appendix A.3, in which the zonal variations of the basic state and the dependent variables are neglected. The vorticity equation for the barotropic component (denoted by the subscript '+') (9.7.1) becomes:

$$\frac{\partial \varsigma_+}{\partial t} = -v_+ - U_T\left(\frac{\partial \omega}{\partial y}\right) \tag{9.7.2}$$

where U_T denotes the constant vertical shear of the basic zonal flow. Equation (9.7.2) indicates that in the presence of easterly vertical shear $U_T < 0$, a northward decrease in the perturbation upward motion can generate positive barotropic vorticity to the north of the convection. This process is illustrated in Figure 9.15. A mean flow with easterly vertical shear has a large equatorward horizontal relative vorticity (order of 10^{-5} s^{-1}) which the perturbation motion can tap. The Rossby wave-induced heating generates a perturbation vertical motion that decreases away from the convection center (low-level cyclonic center). This vertical motion field twists the mean flow horizontal vorticity and generates vorticity with a positive vertical component north of the convection region as shown by (9.7.2) and illustrated by Figure 9.15. The positive vorticity in turn induces convergence in the boundary layer, which destabilizes the atmosphere and triggers new convection to the north of the original convection (low-pressure center). For the same reasons, negative vorticity and divergence in the boundary layer develop south of the cyclonic circulation, suppressing convection. Thus, the twisting of the mean flow horizontal vorticity by the meridional differential vertical motion associated with the Rossby

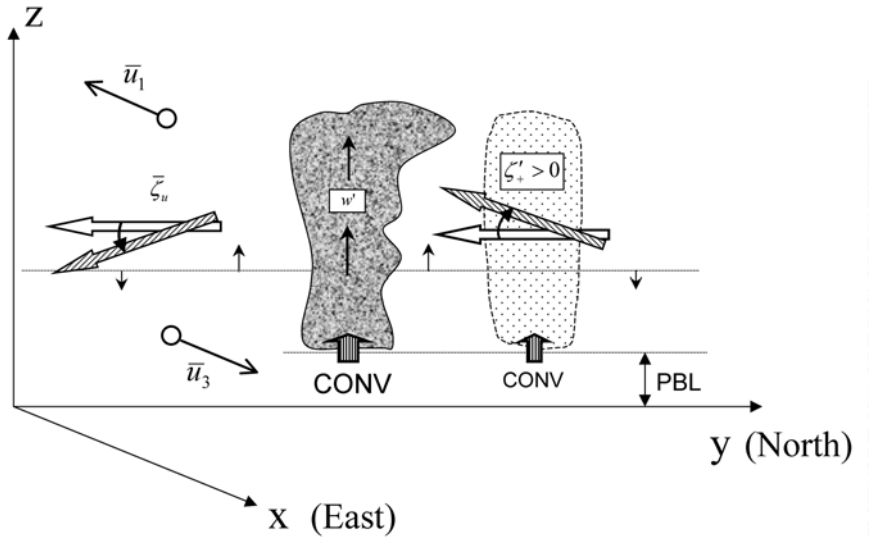

Figure 9.15. Schematic diagram showing the mechanism by which an easterly vertical shear of the mean flow generates a northward propagation component for moist Rossby waves. From Wang (2005).

waves creates conditions that favor northward movement of the enhanced rainfall. This explanation is supported by observations made by Jiang *et al.* (2004) who showed that the barotropic vorticity in the free troposphere is located about 4° to the north of the northward propagating convection anomalies for the intraseasonal disturbances.

9.7.5 Wave energy accumulation in the equatorial westerly duct

One of the important impacts of the vertical shear on equatorial Rossby waves is that the westerly (easterly) shear favors trapping wave kinetic energy in the upper (lower) troposphere (Figure 9.13). This may be pertinent to interpretation of the in-phase relationship between the transient kinetic energy and the equatorial mean flow in the upper troposphere as observed by Arkin and Webster (1985), which is also known as the accumulation of wave energy in the upper tropospheric westerly duct (a zonal flow with westerly vertical shear). On the other hand, in a region of easterly vertical shear (monsoon regions), the Rossby waves tend to be trapped in the lower troposphere, which agrees with the behavior of perturbations in the summer monsoon trough region.

9.8 CONVECTIVELY COUPLED EQUATORIAL WAVES AND THE TROPICAL INTRASEASONAL OSCILLATION

Latent heating released in convection is the principal source of energy for monsoons and tropical circulations. Radiative heating plays an important but secondary role.

The convective heating is directly associated with motions on the scale of individual convective clouds and the mesoscale and synoptic-scale systems into which they are sometimes organized. Radiative heating and cooling are influenced by the properties of clouds. Practically, the statistical effects of subgrid convective heating must be parameterized in terms of large-scale variables when the large-scale flow itself is considered. The importance of the convective/large-scale feedback in producing transient variability on synoptic to intraseasonal timescales is an area of controversy and remains an active and very important topic of research. A recent attempt to document the structure of observed convectively coupled equatorial waves has been made by Yang *et al.* (2003). They used the horizontal wave structures given by equatorial wave theory (Section 9.1), but did not assume any other part of the theory. They found coupled Kelvin, mixed Rossby–gravity (MRG), and Rossby waves but with vertical structures and phase speeds different from those given by the simple theory.

9.8.1 CISK and wave–CISK

Charney and Eliassen (1964) and Ooyama (1964) introduced the concept of CISK (conditional instability of the second kind) to explain development of tropical cyclones (TCs). CISK refers to a positive feedback between deep convection and the large-scale circulation in which it is embedded. The surface friction helps to induce low-level convergence into a TC, enhancing deep convection and latent heating that in turn amplify the TC. Yamasaki (1969) extended the CISK idea and proposed a possible feedback between deep convection and large-scale equatorial waves. In their model, under certain circumstances convection could intensify the waves through inviscid processes without involving feedbacks with surface drag or thermodynamic fluxes. Lindzen (1974b) referred to this destabilization as wave–CISK to distinguish it from Charney and Eliassen's Ekman–CISK. An important feature of CISK models is that shorter wavelengths will grow fastest when instability occurs. Thus, the CISK might be expected to manifest itself at the shortest scale, but this violates the original conceptual assumption that the large-scale wave motion interacts with an ensemble of convective heating.

While theoretical models that predict wave–CISK are based on somewhat dubious parameterizations of cumulus convection, observed evidences suggest that moist convection may practically destabilize some large-scale waves through additional mechanisms not considered in conventional wave–CISK. The impact of surface friction associated with convectively coupled equatorial Kelvin waves and a Kelvin–Rossby wave couplet were examined by Wang (1988) and Wang and Rui (1990b). They demonstrate that in a regime where the wave–CISK modes are damped the addition of surface drag could stimulate a pattern of convective heating that helps destabilize equatorial waves, there being a preferred large-scale instability. The results of these eigenmode analyses with linear heating were later supported by initial value solutions with non-linear heating (Wang and Li, 1994). The roles of wind-evaporation feedback or wind-induced surface heat exchange (WISHE) were examined by Emanuel (1987) and Neelin *et al.* (1987). The role of

radiative feedbacks on waves associated with convectively produced anvils or moisture redistribution has also been examined recently (e.g., Raymond, 2001; Lin and Mapes, 2004). These additional mechanisms differ from the wave–CISK and may be termed as convective interaction with large-scale dynamics (CID) as suggested by Neelin and Yu (1994). To understand how equatorial boundary layer friction may contribute to wave selection, we start with a discussion of basic equatorial boundary layer dynamics.

9.8.2 Equatorial boundary layer convergence

The boundary layer has an important influence on the behavior of atmospheric motion throughout the troposphere, especially in the tropics. This layer not only determines the drag between the atmosphere and the surface by which a large part of the energy in the large-scale motion is dissipated but also plays a critical role in determining the moisture flux entering the base of deep convective clouds. Boundary layer dynamics also plays a central role in determining the occurrence of low-level cloud within the boundary layer and the consequent effects on radiation budgets. Thus, boundary layer dynamics should be viewed as a vital ingredient in considering CID.

The Coriolis force always acts perpendicularly to the wind and turbulent drag acts in the opposite direction to the wind. In the subtropical or extratropical boundary layer a force balance can be achieved only if the wind has a component directed across the isobars towards low pressure. This produces a net boundary layer inflow into surface low-pressure systems, which by transporting mass toward the pressure minimum acts to 'spin down' the circulation. The vertical velocity induced by boundary layer friction called Ekman pumping is determined by the vorticity at the top of the boundary layer (Eliassen, 1971).

Near the equator, however, due to a change of sign of the Coriolis parameter, boundary layer dynamics differs considerably from quasigeostrophic Ekman theory. The solution of the boundary equation, (9.6.1), for a linear steady motion yields (Wang and Li, 1994):

$$D = -\frac{E}{E^2 + \beta^2 y^2}\left(\nabla^2 \phi_e + \beta u_b + \frac{\beta^2}{E} y v_b\right) \tag{9.8.1}$$

where D is the boundary layer divergence, E is proportional to the linear drag coefficient κ_s, ϕ_e denotes the geopotential height on the top of the boundary layer $p = p_e$, and u_b and v_b denote the vertical mean zonal and meridional winds in the boundary layer. Equation (9.8.1) indicates that the frictional convergence in the equatorial region is determined by the Laplacian of the pressure at the top of the boundary layer (a term similar to the mid-latitude Ekman pumping) and the strengths of the eastward and poleward surface winds. Equation (9.8.1) implies that equatorial boundary layer convergence prefers to occur in association with low-pressure centers/troughs (the first RHS term), and westerlies (the second RHS term) and off-equatorial poleward flows (the third RHS term). Thus, the

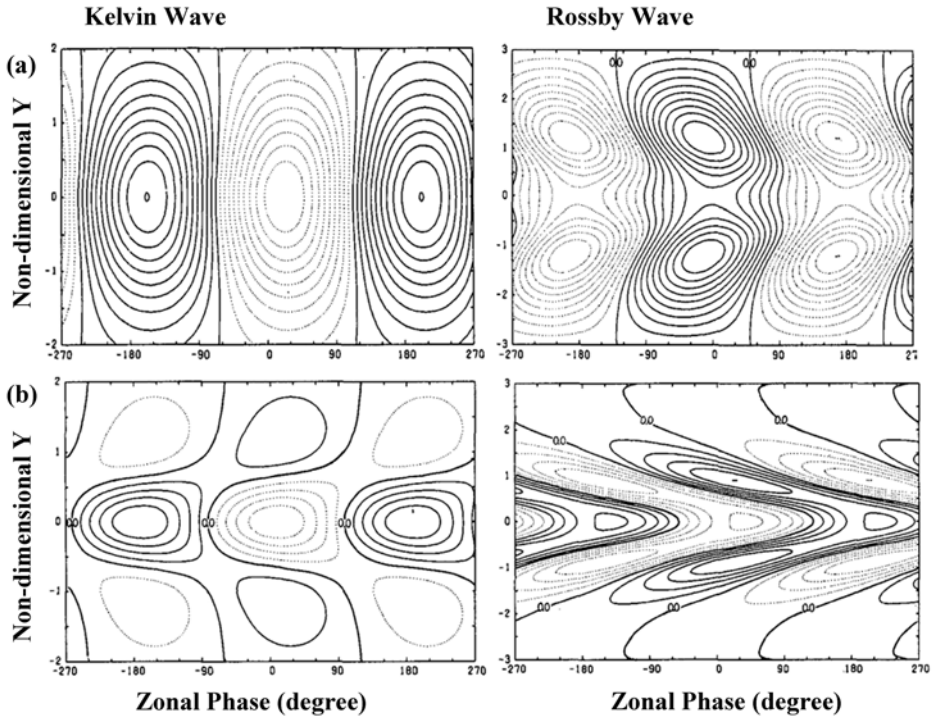

Figure 9.16. Horizontal structures of the equatorial Kelvin wave (*left*) and the most trapped equatorial Rossby wave (*right*) in the presence of boundary layer damping: (a) geopotential height (*upper panels*), and (b) vertical pressure velocity at the top of the boundary layer (*lower panels*). The meridional scale is Rossby radius of deformation, whose unit corresponds to about 1,500 km.

equatorward side of an off-equatorial monsoon trough is a preferred location for frictional convergence, partly because the β-effect acting on the south-westerly on the equatorward side of a monsoon trough provides additional convergence in the trough. This agrees with observations (Section 9.6).

It is of interest to examine Ekman pumping associated with the low-frequency equatorial waves. Figure 9.16(a) illustrates the horizontal structure of the pressure fields for Kelvin waves and the most equatorially trapped Rossby wave in the presence of a boundary layer. These 'dry' waves are slightly damped due to the presence of friction. Their structures are similar to their corresponding inviscid counterparts (Figure 9.2(a,c)). Figure 9.16(b) shows vertical motions at the top of the boundary layer associated with these waves. The calculations were based on (9.8.1). For these waves, the Laplacian of pressure terms generally dominates the total frictional convergence. Thus, for Kelvin waves the friction-induced upward motion is located in its low pressure or its easterly phase, while for the most trapped equatorial Rossby waves, the ascending motion occurs in both the off-equatorial low pressures and the equatorial trough between the two off-equatorial

anticyclones to the east of the double low-pressure cells. As a result, the maximum ascent (descent) along the equator leads the corresponding westerly (easterly) by about one-eighth of a wavelength. Overall, the upward motion associated with the Rossby wave is generally shifted eastward compared with the minimum pressure and strongest equatorial westerlies. This feature has important ramifications for the selection of the eastward propagating unstable mode in the presence of interactive heating.

9.8.3 A theoretical model of friction CID for the MJO

At the center of CID is the non-linear interaction among condensational heating, large-scale equatorial waves, the boundary layer frictional moisture feedback, and wind-induced heat exchanges at the surface (Wang, 1988). A theoretical model for frictional CID is described in Appendix A.4. It is based on a time-dependent primitive equation model on an equatorial β-plane that has two levels of free troposphere and a well-mixed boundary layer. It describes the gravest baroclinic mode in the free troposphere and the barotropic mode in the boundary layer and their interaction with convective heating. The model incorporates effects of sea surface temperature (SST) gradients (the Lindzen–Nigam (1987) mechanism), frictional moisture feedback, and surface wind-induced heat fluxes. This steady version of the layer frictional CID model has been demonstrated to simulate realistic tropical atmospheric response to given SST and land surface temperature distributions (Wang and Li, 1993).

Figure 9.17 represents schematically the major characteristics of the Madden–Julian Oscillation (MJO): an east–west circulation that spans the global tropics and

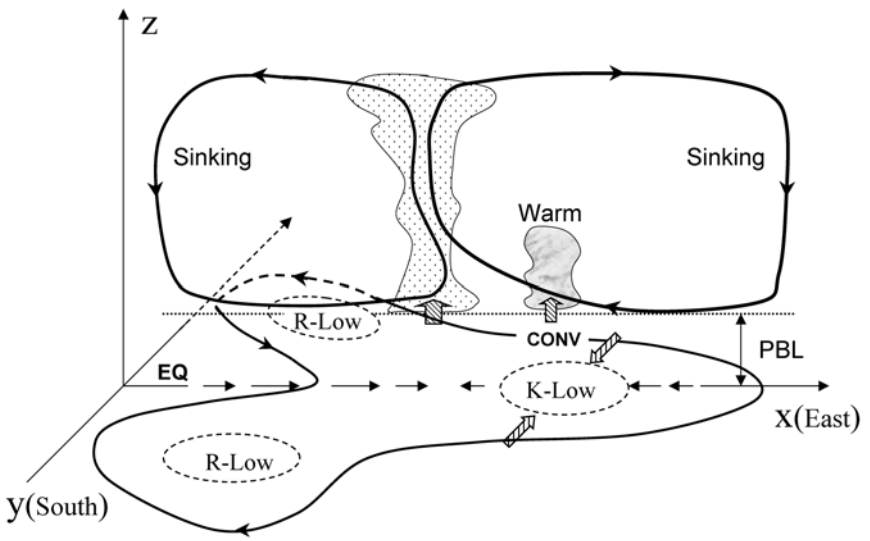

Figure 9.17. Schematic diagram for the Madden–Julian (intraseasonal) Oscillation in the tropical atmosphere.

is coupled to a large-scale complex of convective cells (Madden and Julian, 1972); a gravest baroclinic structure in the troposphere with winds converging in the boundary layer in front of the main precipitation (Hendon and Salby, 1994); a horizontal circulation featuring a coupling of both equatorial Kelvin and Rossby waves (Rui and Wang, 1990), and a slow eastward (about 5–10 ms^{-1}) movement that gives rise to an intraseasonal timescale (30–60 days).

Regardless of its simplicity and limitations, the frictional CID model is able to reproduce atmospheric disturbances that closely resemble features of the observed MJO. For instance, the disturbance originating from the fastest growing frictional CID mode has the following characteristics resembling the MJO: an east–west circulation that spans the globe and is coupled to a large-scale complex of convective cells; a baroclinic structure, with winds converging in the boundary layer in front of the main precipitation; a horizontal circulation consisting of both equatorial Kelvin and Rossby waves, and a slow eastward (about 5–10 $m\,s^{-1}$) movement that gives rise to an intraseasonal timescale (30–60 days) (Wang and Rui, 1990b; Wang and Li, 1994). In addition, given the seasonally varying basic circulation and SST distribution, the simulated intraseasonal oscillation (ISO) shows appropriate seasonality, having prominent northward propagation and off-equatorial westward propagation of disturbances in the Asian monsoon region during the boreal summer (Wang and Xie, 1997). These resemblances enable frictional CID theory to be helpful in understanding the basic dynamics of the MJO and the boreal summer monsoon ISO, which will be discussed in the next two subsections.

9.8.4 Dynamics of MJO and monsoon intraseasonal oscillation

It is straightforward to explain the free tropospheric, vertical, and horizontal structures of the MJO provided the heating associated with the convective complex in the MJO is *given*. The Matsuno–Gill theory predicts that deep convective heating released in the MJO convective region may stimulate large-scale eastward-moving Kelvin waves and westward-moving equatorial Rossby waves. These waves are dissipated away from the heating region, leaving an equatorial low-pressure trough of Kelvin wave response (K–L) east of the main convection and two off-equatorial lows of the Rossby wave (R–L) response (Figure 9.17). However, without the boundary layer, the convectively interactive Kelvin and Rossby waves would soon decouple and propagate in opposite directions. The key questions that a theory for MJO must address is what mechanism can hold the convective heating and the Kelvin and Rossby waves together and give eastward propagation (or favor the eastward propagating tendency of the Kelvin waves over the westward propagating tendency of the Rossby waves).

The frictional CID theory is instrumental in addressing the above questions. As shown in Figure 9.16(b), the Rossby wave-induced boundary layer convergence favors the development of moist Kelvin waves by producing equatorial convergence in its easterly phase, but the Kelvin wave-induced frictional convergence favors only

its own growth. Therefore, the frictional organization of convective heating has a maximum on the equator which couples the Kelvin and Rossby waves together but favors eastward propagation. As such, the frictional coupling creates a realistic mixed Kelvin and Rossby wave structure. In addition, the boundary layer convergence coincides with the low-pressure (easterly) of the Kelvin wave response to the east of precipitation heating, thus leading the eastward propagating precipitation anomalies by a fraction of a wavelength, which is an important feature of the observed MJO (Figure 9.17).

The spatial phase shift between the frictional convergence and the convection is also essential for generation of the CID instability that distinguishes it from wave–CISK and Ekman–CISK. In wave–CISK and Ekman–CISK the convection is in phase with low-level convergence, which, without additional mechanisms, leads to the fastest growth of the shortest wavelengths. In frictional CID, however, the frictional convergence that supplies a large amount of moisture is not in phase with the wave-induced moisture convergence. This effectively reduces the strength of the interaction between the wave-induced heating and the circulation, prohibiting unstable wave–CISK modes. The energy source driving the frictional CID instability comes from generation of the eddy available potential energy, which is proportional to the covariance between the warming and heating. As shown in Figure 9.17, the upper level return flow associated with the eastward spreading of Kelvin waves descends and warms the atmosphere to the east of the major convection. The frictional convergence to the east of the major convection induces condensational heating that overlaps the positive temperature anomaly, thereby generating eddy available potential energy for the growth of the unstable CID mode. Because the frictional convergence leads the main convective region, this energy source for instability is not directly converted to kinetic energy as is the case in the wave–CISK or Ekman–CISK, avoiding the short-wave blowup. Wang (1988) has shown that the rate of generation of eddy available potential energy by frictional moisture convergence increases with increasing zonal scale so that the planetary-scale mode is preferred.

What gives rise to the slow propagation speed giving an intraseasonal timescale for this oscillation? A primary reason is that the condensational heating induced by the free tropospheric waves acts to reduce the 'effective' static stability and thus the gravity wave speed. The moist tropical atmosphere normally has a reduced gravity wave speed of about $20\,\mathrm{m\,s^{-1}}$, much slower than that in a dry atmosphere. The slow eastward propagation is also attributed to frictional coupling of the moist Kelvin and Rossby waves, because the eastward movement of the Kelvin wave is slowed down by the westward tendency of the Rossby waves that result from the β-effect (Wang and Tui, 1990b). Therefore, the coupled Rossby–Kelvin wave couplet takes on the approximate eastward speed of $10\,\mathrm{m\,s^{-1}}$. Higher vertical modes have slower phase speeds, and these modes may also contribute to the slow eastward propagation of the MJO (Mapes, 2000).

Why does the circulation have a planetary zonal scale while the core convection has a large scale of a few thousand kilometers? A portion of the eddy energy generated by convective heating is carried away from the convective regions by

fast moving, dry Kelvin and Rossby waves, which spread perturbed circulation rapidly around the globe (Wang and Li, 1994). This energy dispersion may account for the planetary circulation scale of the MJO, while the moist core remains to be confined to a limited region (several thousands of kilometers).

9.8.5 Roles of atmosphere–ocean interaction and other processes

With seasonally varying basic circulation and SST distributions, an extended, frictional CID model is able to simulate the ISO in the Asian monsoon region during the boreal summer, which is characterized by prominent northward propagation and off-equatorial westward propagation (Wang and Xie, 1997). The model results suggest that the northward propagation of the ISO in the Asia–Pacific summer monsoon region is due to north-westward emanation of moist Rossby waves from the equatorial disturbances when the latter decay over Indonesia and near the Date Line. The vertical shear mechanism discussed in Section 9.7 induces a northward component for the westward propagating Rossby waves in the northern summer monsoon region.

The interactive SST and surface heat fluxes may also contribute to the eastward propagation of the MJO and the northward propagation of the summer monsoon ISO. The coupled model results suggest that, while atmospheric internal dynamics are essential in generating the ISO, interaction between the atmosphere and ocean mixed layer may further enhance and better organize the eastward propagating MJO and northward propagating monsoon ISO through an additional coupled instability that amplifies moist atmospheric low-frequency perturbations. The basic state of the warm pool is conducive to the occurrence of the coupled unstable mode on intraseasonal timescales (Wang and Xie, 1998). The wind–evaporation–SST feedback is central to this coupled instability.

Limitations of the theory and outstanding issues concerning the complex GCM simulation of the MJO have been discussed in detail by Wang (2005). The major drawback of the frictional CID theory lies in its simple representation of diabatic heating which cannot deal with the interactions among scales, and only allows for a direct coupling between the large-scale equatorial waves and convection. In reality, the MJO involves a multiscale interaction. The planetary-scale MJO does not directly organize convection and the convective latent heat release is largely consumed directly by mesoscale and synoptic-scale disturbances. In GCMs, correct representation of this energy cascade process and the partitioning of convective and stratiform heating may be critical for modeling the MJO. The theoretical model's simplicity does not allow description of the complex cloud–radiation feedback process, which may also play an important role in sustaining oscillations on intraseasonal timescales (Hu and Randall, 1994; Raymond, 2001). Studies such as that of Woolnough *et al.* (2000) raise the hypothesis that interaction with the top few metres of the ocean and associated small temperature changes may also play a role in the observed MJO behaviour.

9.9 TELECONNECTIONS

The fact that there is a relationship between large-scale phenomena occurring in separated regions of the globe is often referred to as a teleconnection between them. Wallace and Gutzler (1981) explored teleconnections in observed monthly data and investigated them for the particular case of ENSO. The theory of such teleconnections as developed by Hoskins and Karoly (1981) depends on Rossby wave propagation. This and the initiation of such Rossby waves by large-scale tropical convection will be summarized here.

9.9.1 Rossby wave propagation

The dispersion relation for barotropic Rossby waves on a uniform zonal wind U may be written:

$$\left.\begin{aligned} \omega &= Uk - \frac{\beta k}{K^2} \\ c &= U - \frac{\beta}{K^2} \end{aligned}\right\} \tag{9.9.1}$$

where ω is the frequency, c the x phase speed, k the x wavenumber, l the y wavenumber, and $K = (k^2 + l^2)^{1/2}$ the total wavenumber. Therefore, stationary Rossby waves $\omega = c = 0$ are possible for U greater than zero (a westerly wind) and these have a total wavenumber:

$$K = K_s = (\beta/U)^{1/2} \tag{9.9.2}$$

Because it is the total wavelength of these stationary Rossby waves that is determined, their wavelength is independent of the direction of the wave crests and troughs.

The propagation of the wave activity, as opposed to the individual crests and troughs, is determined by the group velocity, which is given by the derivative of the frequency by the relevant wavenumber. For Rossby waves the 2-D horizontal group velocity is:

$$\vec{c}_g = \left(\frac{\partial \omega}{\partial k}, \frac{\partial \omega}{\partial l}\right) = (c, 0) + \frac{2\beta k}{K^2}(k, l) \tag{9.9.3}$$

For Rossby waves that are stationary this can be written:

$$\vec{c}_g = 2U \cos\alpha \hat{K}$$

where $\hat{K} = K^{-1}(k, l)$ denotes the vector total wavenumber and α is the angle between this vector and the eastward direction.

The activity of stationary Rossby waves always propagates normal to the crests and troughs. When the ray path is in the eastward direction, the speed of propagation of the activity is twice that of the zonal flow, and it is equal to the zonal flow when the ray path is oriented at 60° to the north or south of the eastward direction.

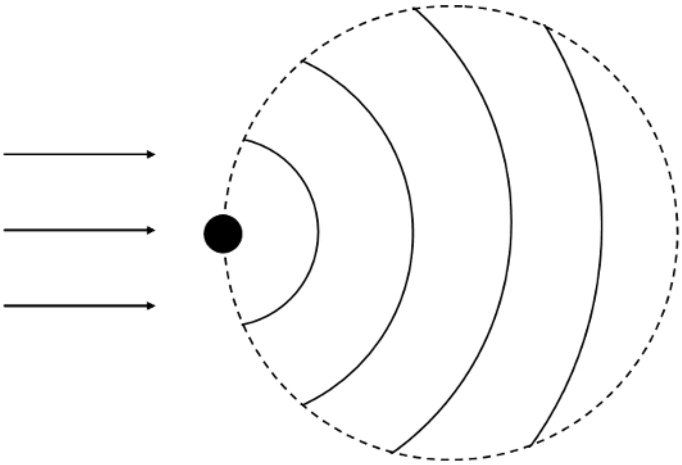

Figure 9.18. Schematic diagram for stationary Rossby waves from a point source filling a circle when the ray path is in the eastward direction.

It is straightforward to show that, in a system with damping on a timescale of T, the waves from a point source fill a circle centered a distance UT downstream from it and of radius UT, as shown in Figure 9.18.

When propagation on the sphere is considered, Hoskins and Karoly (1981) showed that the straight-line ray paths are replaced by great circles. As shown in Figure 9.19, waves triggered in the tropics can propagate into higher latitudes, and so influence events there. Equally, waves triggered in higher latitudes, perhaps by a stronger than normal flow over a mountain chain can influence the tropics.

When the ambient flow is not a uniform westerly then Rossby waves are refracted like light shining through a non-uniform medium. As shown in Hoskins and Karoly (1981) and further discussed in Hoskins and Ambrizzi (1993), in general the waves are refracted toward larger values of K_s. A strong westerly flow can act as a partial waveguide (the effective β increases more than U). In regions of the tropics where westerlies occur, propagation into the deep tropics is possible. Where there are tropical easterlies, as waves propagating toward the tropics approach the critical line at which $U = 0$ their wavelength becomes vanishingly small, their ray path becomes almost meridional and their group velocity tends to zero. In reality, non-linear effects would be important in such a region, and local convection could be generated.

9.9.2 Rossby wave source associated with tropical convection

Numerical solutions of idealized primitive equation models suggest that stationary Rossby waves have an equivalent barotropic structure in middle latitudes, with significant amplitude and the same sign throughout the troposphere. However, the

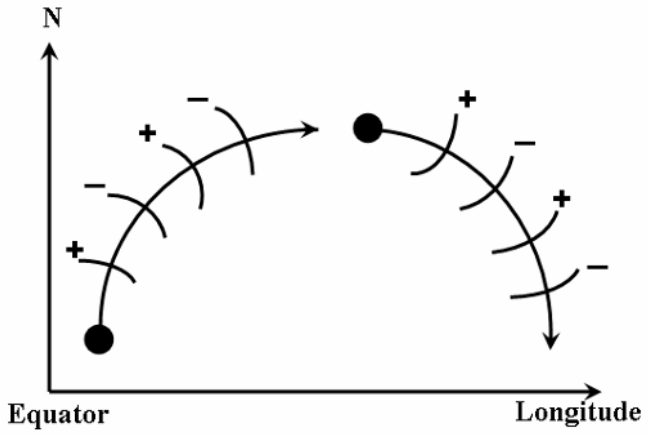

Figure 9.19. Schematic diagram for teleconnections between the tropics and higher latitudes caused by propagation of stationary Rossby waves along great circle ray paths.

propagation and significant amplitude tend to occur in the upper troposphere in the tropics. Therefore, the triggering of stationary Rossby waves by long-lasting, large regions of tropical convection appears at first sight to be unlikely as these are usually found in regions of ambient upper tropospheric easterlies. However, as shown by Hoskins and Sardeshmukh (1988), there is a mechanism for possible triggering of a stationary Rossby wave by such a tropical heating. The relevant theory will now be summarized.

The horizontal wind may be considered as the sum of its divergent and rotational components:

$$\vec{v} = \vec{v}_\psi + \vec{v}_\chi$$

Here the dominant rotational component of the wind may be defined in terms of a streamfunction:

$$\vec{v}_\psi = \hat{k} \times \nabla\psi \tag{9.9.4}$$

($\hat{k}$ is a unit vertical vector) and the divergent component in terms of a velocity potential:

$$\vec{v}_\chi = \nabla\chi \tag{9.9.5}$$

The streamfunction and the velocity potential are related, respectively, to the relative vorticity and the horizontal divergence by:

$$\zeta = \frac{\partial^2\psi}{\partial x^2} + \frac{\partial^2\psi}{\partial y^2} \tag{9.9.6a}$$

$$-\frac{\partial\omega}{\partial p} = \nabla\cdot\vec{v} = \nabla\cdot\vec{v}_\chi = \frac{\partial^2\chi}{\partial x^2} + \frac{\partial^2\chi}{\partial y^2} \tag{9.9.6b}$$

The full equation for the vertical component of vorticity at a level at which the vertical velocity is zero may be written:

$$\frac{\partial \zeta}{\partial t} + \vec{v} \cdot \nabla(f + \zeta) = -(f + \zeta)\nabla \cdot \vec{v}_\chi$$

At large length scales, in the upper troposphere near the tropopause this is a good approximation to the full equation. (A much more approximate form of this equation was given in (9.3.8) and used in the discussion there.) Splitting the velocity field into its rotational and divergent components, and putting all the purely rotational terms on the left-hand side gives:

$$\frac{\partial \zeta}{\partial t} + \vec{v}_\psi \cdot \nabla(f + \zeta) = \text{RWS} \tag{9.9.7}$$

where

$$\text{RWS} = -(f + \zeta)\nabla \cdot \vec{v}_\chi - \vec{v}_\chi \cdot \nabla(f + \zeta) \tag{9.9.8}$$

$$= -\nabla \cdot [\vec{v}_\chi(f + \zeta)] \tag{9.9.9}$$

The left-hand side of (9.9.7) comprises the terms that are relevant in a description of barotropic Rossby waves. The right-hand side terms therefore describe the generation of such Rossby waves, as well as the modification of barotropic Rossby waves associated with a full baroclinic atmosphere. The former identification is why the term Rossby wave source (RWS) is used for them. It can be seen that the divergent motion in the upper troposphere associated with tropical convection generates Rossby waves not only through the stretching term, the first term in (9.9.8), or its simplified form in (9.3.8), but also through its advection of the absolute vorticity field. The two terms can be combined in (9.9.9).

Hoskins and Sardeshmukh (1988) investigated the generation of rotational motion by specified divergence sources in a variety of situations. In particular they showed that when tropical convection occurs in upper level easterlies so that the stretching term cannot directly lead to stationary Rossby waves, then on the poleward side of this the divergent advection term tends to be strong in the subtropical westerly region and acts as an efficient generator of stationary Rossby waves in that region. The combination of the two terms in RWS given in (9.9.9) can be useful in a discussion of the area average of RWS which is seen to be given by a boundary integral of the normal component of the flux of absolute vorticity associated with the divergent motion, the term inside the square brackets (Figure 9.20).

9.10 APPENDIX

A.1 Vertical modes and shallow-water equations

Governing equations on the equatorial β-plane

The Earth's rotational effects on dynamic processes in the tropics are most easily analyzed by utilizing an equatorial β-plane approximation, in which the Coriolis

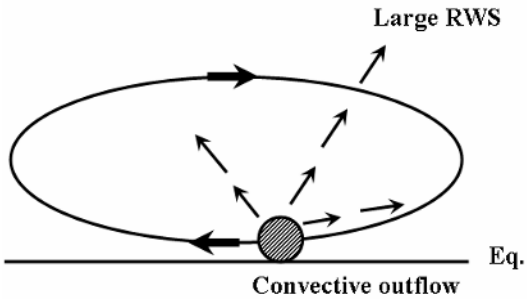

Figure 9.20. Schematic diagram showing the generation of rotational motion when tropical convection occurs in upper level easterlies. Polewards of the easterlies the strong divergent advection of vorticity in the subtropical westerly region acts as an efficient generator of stationary Rossby waves.

parameter $f = \beta y$, where $\beta \equiv df/dy = 2\Omega/a$ is the Rossby parameter with Ω and a the rotation rate and the radius of the Earth, respectively.

The physical principles that govern the hydrostatic *perturbation* motion consist of conservations of momentum (A.1.1a,b), mass (A.1.1c), thermodynamic energy (A.1.1d), and water vapor (A.1.1e). These principles expressed in a vertical pressure (p) coordinates on an equatorial β-plane are:

$$\frac{\partial u}{\partial t} - \beta y v = -\frac{\partial \phi}{\partial x} + F_x + N(u) \tag{A.1.1a}$$

$$\frac{\partial v}{\partial t} + \beta y u = -\frac{\partial \phi}{\partial y} + F_y + N(v) \tag{A.1.1b}$$

$$\frac{\partial u}{\partial x} + \frac{\partial v}{\partial y} + \frac{\partial \omega}{\partial p} = 0 \tag{A.1.1c}$$

$$\frac{\partial}{\partial t}\frac{\partial \phi}{\partial p} + S(p)\omega = -\frac{R}{C_p p} Q_c(p) + N\left(\frac{\partial \phi}{\partial p}\right) \tag{A.1.1d}$$

$$\frac{\partial}{\partial t} M_c + \frac{1}{g}\int_{p_u}^{P_s} \nabla \times (\bar{q}\vec{V}) dp = E_v - P_r + N(q) \tag{A.1.1e}$$

In Equation (A.1.1) (x, y) is the distance in the eastward and northward direction; the dependent variables, u, v, ω, and ϕ, denote zonal and meridional wind, vertical pressure velocity, and geopotential height, respectively; F_x and F_y denote frictions; and the terms $N(u)$, $N(v)$, $N(\partial\phi/\partial p)$, and $N(q)$ represent non-linear advections. The static stability parameter $S(p)$ describes the effects of atmospheric stratification; Q_c expresses diabatic heating rate per unit mass; and R and C_p are the gas constant of the air and the specific heat at constant pressure, respectively. A more detailed explanation of diabatic heating and moisture equations will be given in Section A.4.

The vertical mode and the shallow-water equation

To better understand the 3-D, large-scale tropical atmospheric motion, it is helpful to begin with an idealized model in which the vertical structure of the 'normal' modes can be determined and the corresponding horizontal motion can be described by simple equations. For this purpose, consider frictionless, dry, adiabatic and small amplitude perturbation motion in a quiescent environment, so that (A.1.1) becomes:

$$\frac{\partial u}{\partial t} - \beta y v = -\frac{\partial \phi}{\partial x} \tag{A.1.2a}$$

$$\frac{\partial v}{\partial t} + \beta y u = -\frac{\partial \phi}{\partial y} \tag{A.1.2b}$$

$$\frac{\partial u}{\partial x} + \frac{\partial v}{\partial y} + \frac{\partial \omega}{\partial p} = 0 \tag{A.1.2c}$$

$$\frac{\partial}{\partial t}\frac{\partial \phi}{\partial p} + S(p)\omega = 0 \tag{A.1.2d}$$

Because the static stability parameter S varies primarily in the vertical direction, let us assume $S(p)$ is a function of pressure only that can be quite well approximated by $S(p) = C_s^2/p^2$. Here $C_s = p_s S(p_s)^{1/2}$ represents a reference gravity wave speed at the surface $p = p_s$, which is about $70\,\mathrm{m\,s^{-1}}$ for a typical dry tropical atmosphere. Then the solutions of (A.1.2) can be expressed as separable forms:

$$\omega = \Omega \times W(p) \tag{A.1.3a}$$

$$(u, v, \Phi) = (U, V, \Phi)\frac{dW}{dp}(p) \tag{A.1.3b}$$

where $W(p)$ describes the vertical structure of the motion, whereas U, V, Φ, and Ω are only functions of x, y, and t. Substituting (A.1.3) into (A.1.2), one finds that $W(p)$ satisfies:

$$C_0^2 \frac{d^2 W}{dp^2} + S(p)W = 0 \tag{A.1.4}$$

and the horizontal motion U, V, and Φ, satisfy:

$$\frac{\partial U}{\partial t} - \beta y V = -\frac{\partial \Phi}{\partial x} \tag{A.1.5a}$$

$$\frac{\partial V}{\partial t} + \beta y U = -\frac{\partial \Phi}{\partial y} \tag{A.1.5b}$$

$$\frac{\partial \Phi}{\partial t} + C_0^2\left(\frac{\partial U}{\partial x} + \frac{\partial V}{\partial y}\right) = 0 \tag{A.1.5c}$$

where C_0^2 is a 'separation constant'. Equation (A.1.5) describes horizontal wave propagation and is referred to as the 'shallow-water equation' because it is similar to the equation that describes the propagation of the long gravity surface waves with a speed C_0.

Of note is that the vertical structure of atmospheric motion may be expressed in terms of the sum of many vertical 'normal' modes. For simplicity, assume an atmosphere being confined by a lower surface at $p = p_s$ and a 'lid' at the tropopause $p = p_u$ at which we impose $\omega = 0$. The normal mode solution of (A.1.4) with the given boundary conditions yields (A.1.6) a family of an infinite number of vertical modes $W_m(p)$ with an arbitrary amplitude A_m (Wang and Chen, 1989):

$$W_m(p) = Am(p^{1/2+b_m} - p_u^{2b_m} p^{1/2-b_m}), \quad m = 1, 2, 3 \ldots \tag{A.1.6}$$

where

$$b_m = im\,\pi(\ln p_s/p_u) \tag{A.1.6a}$$

The phase speed corresponding to the mth vertical mode is:

$$C_0(m) = C_s(\tfrac{1}{4} - b_m^2)^{-1/2} \tag{A.1.7}$$

We note that the vertical structures and the gravity wave phase speed of each vertical mode are solely determined by the basic state stratification.

A.2 Equatorial waves

Using $R_c = (C_0/\beta)^{1/2}$ (the equatorial Rossby radius of deformation), $\tau = (\beta C_0)^{-1/2}$, and C_0^2 as characteristic scales for the horizontal length, time, and geopotential height, respectively, one can obtain the following non-dimensional shallow-water equation for the description of a single vertical mode:

$$\frac{\partial u'}{\partial t'} - y'v' = -\frac{\partial \phi'}{\partial x'} \tag{A.2.1a}$$

$$\frac{\partial v'}{\partial t'} + y'u' = -\frac{\partial \phi'}{\partial y'} \tag{A.2.1b}$$

$$\frac{\partial \phi'}{\partial t'} + \frac{\partial u'}{\partial x'} + \frac{\partial v'}{\partial y'} = 0 \tag{A.2.1c}$$

where the prime denotes non-dimensional quantities. The dimensional variables may be returned by multiplication of their corresponding characteristic scales.

Consider first the wave motion without meridional wind (Kelvin waves). The system of equation (A.2.1) becomes:

$$\frac{\partial u'}{\partial t'} = -\frac{\partial \phi'}{\partial x'} \tag{A.2.2a}$$

$$y'u' = -\frac{\partial \phi'}{\partial y'} \tag{A.2.2b}$$

$$\frac{\partial \phi'}{\partial t'} + \frac{\partial u'}{\partial x'} = 0 \tag{A.2.2c}$$

The combination of (A.2.2a) and (A.2.2c) yields a wave equation, which has a general solution $u' = F(x' \mp t')Y(y')$, where F is an arbitrary function. From (A.2.2a) $\phi' = \pm u'$. Using (A.2.2b) one can obtain $Y(y') = Y(0)e^{\mp y'^2/2}$. Only the minus sign is valid because the other choice leads to an unbounded solution for large y. The solution of the system is in dimensional form:

$$u = \phi/C_0 = F(x - C_0 t)e^{-\beta y^2/2C_0} \quad \text{and } v \equiv 0 \tag{A.2.3}$$

In addition to the equatorial Kelvin wave solution, (A.2.1) has other equatorial wave solutions. Since the coefficients of (A.2.1) only depend on y, the solution for a zonally propagating wave disturbance can be expressed as the form of normal modes:

$$(u', v', \phi') = \mathrm{Re}(U(y), V(y), \Phi(y))e^{i(kx-\omega t)}$$

where 'Re' means taking the real part; k is zonal wavenumber; and ω the frequency which is assumed to be always positive so that $k > 0$ implies eastward propagation relative to the ground with a phase speed $C_x = \omega/k$; and $U(y), V(y)$, and $\Phi(y)$ denote the meridional structure – assumed to be bounded as $y \to \pm\infty$ (Matsuno, 1966). This condition is necessary as the equatorial β-plane is not a valid approximation to spherical geometry for large y.

Substituting the normal mode solution into (A.2.1) and eliminating $U(y)$ and $\Phi(y)$ leads to an equation for $V(y)$:

$$\frac{d^2V}{dy^2} + \left[(\omega^2 - k^2) - \frac{k}{\omega} - y^2\right]V = 0 \tag{A.2.4}$$

Note that in deriving (A.2.4) $k^2 \neq \omega^2$ was assumed, which excluded the equatorial Kelvin waves.

Equation (A.2.4) along with the boundary condition ($V(y)$ is bounded as $y \to \pm\infty$) poses an eigenvalue problem, which is the same as the Schrödinger equation for a simple harmonic oscillator. The solution of (A.2.4) satisfying the condition of equatorial trapping exists if and only if:

$$\omega^2 - k^2 - k/\omega = 2n + 1, \quad n = 0, 1, 2, \ldots \tag{A.2.5}$$

Equation (A.2.5) is the non-dimensional dispersion equation, which describes the relationship between the frequency ω and wavenumber k. Figure 9.3 shows the dispersion curve of the equatorial waves. When $n \geq 1$, the exact dispersion relation is given by:

$$k_n = -\frac{1}{2\omega} \pm \sqrt{\omega^2 + 1/4\omega^2 - (2n+1)} \quad n = 1, 2, 3, \ldots \tag{A.2.6}$$

A real (number) k, which corresponds to propagating neutral waves (non-decaying), requires that either $\omega \geq \sqrt{(n+1)/2} + \sqrt{n/2} \geq 1 + 1/\sqrt{2}$ or $\omega \leq 1 - 1/\sqrt{2}$. Thus, there are two distinct groups of waves: high-frequency waves, $\omega \geq 1 + 1/\sqrt{2} = 1.71$, and low-frequency waves, $\omega \leq 1 - 1/\sqrt{2} = 0.29$ (Figure 9.3). When $n = 0$, the dispersion equation $\omega^2 - k^2 - k/\omega = 1$ yields only one meaningful root $k = \omega - 1/\omega$ (the curve $n = 0$ in Figure 9.3).

Differentiating the dispersion equation, (A.2.5) with respect to k, one finds that the group speed in the x direction is:

$$C_{gx} \equiv \frac{\partial w}{\partial k} = \frac{2k\omega + 1}{2\omega^2 + k/\omega}$$

which vanishes at $2k\omega = -1$ (if $2\omega^2 + k/\omega \neq 0$). The curve $\omega = -1/2k$ is shown in Figure 9.3 by the dashed line, which represents zero group speed.

The meridional structures of the zonal propagating Rossby, inertio-gravity and Rossby–gravity waves are described by the solutions of (A.2.4), which are the Weber–Hermite functions:

$$V(y) = D_n(y) = e^{-y^2/2} H_n(y) \quad n = 0, 1, 2, \ldots, \tag{A.2.7}$$

where the $H_n(y)$ denotes the Hermite polynomial of order n (the meridional mode index):

$$H_n(y) \equiv \sum_{l=0}^{[n/2]} \frac{(-1)^l n!}{l!(n-2l)!} (2y)^{n-2l} \tag{A.2.7a}$$

The solutions for $U(y), \Phi(y)$ can be obtained from (A.2.1) in terms of (A.2.7).

The solution for the $n = 0$ mode (the mixed Rossby–gravity waves), $k = \omega - 1/\omega$, and the structure is given by:

$$\nu_0' = \mathrm{Re}\, e^{-y^2/2}\, e^{i[(\omega - 1/\omega)x - \omega t]} \tag{A.2.8a}$$

$$u_0' = \phi_0' = \mathrm{Re}\, i\omega e^{-y^2/2} y e^{i[(\omega - 1/\omega)x - \omega t]} \tag{A.2.8b}$$

A.3 Theoretical model for study of mean flow effects on equatorial waves

Assume that the zonal mean flow $\bar{u}(p)$ satisfies geostrophic balance $\beta y \bar{u} = -\partial\phi/\partial y$. The equations governing inviscid, hydrostatic perturbation motions are (A.3.1), in which the meanings of the other symbols are the same as in (A.1.1) except $\bar{u}(p)$.

$$\frac{\partial u}{\partial t} + \bar{u}\frac{\partial u}{\partial x} + \omega\frac{\partial \bar{u}}{\partial p} - \beta y v = -\frac{\partial \phi}{\partial x} \tag{A.3.1a}$$

$$\frac{\partial v}{\partial t} + \bar{u}\frac{\partial v}{\partial x} + \beta y u = -\frac{\partial \phi}{\partial y} \tag{A.3.1b}$$

$$\frac{\partial u}{\partial x} + \frac{\partial v}{\partial y} + \frac{\partial \omega}{\partial p} = 0 \tag{A.3.1c}$$

$$\frac{\partial}{\partial t}\left(\frac{\partial \phi}{\partial p}\right) + \bar{u}\frac{\partial}{\partial x}\left(\frac{\partial \phi}{\partial p}\right) - \beta y v \frac{\partial \bar{u}}{\partial p} + S\omega = 0 \tag{A.3.1d}$$

To illustrate the basic mechanisms, a simple two-level model is adopted. Writing the momentum and continuity equation (A.3.1a,b,c) at the upper (p_1) and lower (p_3) levels and the thermodynamic equation in the middle (p_m) level, one can obtain a set of governing equations in this two-level model. To facilitate elaboration of dynamic

mechanisms, it is more convenient to introduce a barotropic and a baroclinic component (mode) defined by:

$$A_+ = (A_1 + A_3)/2 \quad A_- = (A_1 - A_3)/2 \tag{A.3.2}$$

where the quantity A represents any dependent variable and A_+ and A_- are referred to as the corresponding barotropic and baroclinic mode, respectively. For the wind and geopotential fields, they describe, respectively, the vertical mean wind (geopotential) and the thermal wind (thickness). The governing equations are then written using the two vertical modes and are non-dimensionalized using the same scale as those used in deriving (A.2.1). In the two-level model, the internal gravity wave speed $C_m = (\Delta p^2 S_m/2)^{1/2}$.

Since the barotropic mode is non-divergent, a barotropic streamfunction ψ can be introduced so that $u_+ = -\partial\psi/\partial y$ and $v_+ = \partial\psi/\partial x$. It can be shown that the barotropic streamfunction satisfies:

$$\frac{D}{Dt}\nabla^2\psi + \frac{\partial\psi}{\partial x} = U_T\left(\frac{\partial^2}{\partial y^2} - \frac{\partial^2}{\partial x^2}\right)v_- + 2U_T\frac{\partial^2 u_-}{\partial x \partial y} \tag{A.3.3}$$

where

$$\frac{D}{Dt} \equiv \frac{\partial}{\partial t} + \bar{U}\frac{\partial}{\partial x} \tag{A.3.3a}$$

$$\bar{U} = (\overline{u_1} + \overline{u_3})/2 \quad U_T = (\overline{u_1} - \overline{u_3})/2 \tag{A.3.3b}$$

The baroclinic mode is governed by (A.3.4):

$$\frac{Du_-}{Dt} - yv_- + \frac{\partial\phi_-}{\partial x} = -U_T\frac{\partial u_+}{\partial x} \tag{A.3.4a}$$

$$\frac{Dv_-}{Dt} + yu_- + \frac{\partial\phi_-}{\partial y} = -U_T\frac{\partial v_+}{\partial x} \tag{A.3.4b}$$

$$\frac{\partial\phi_-}{\partial x} + \frac{\partial u_-}{\partial x} + \frac{\partial v_-}{\partial y} = yv_+U_T \tag{A.3.4c}$$

A.4 A one and a half layer model including interactive diabatic heating

Representation of interactive diabatic heating is an extremely challenging problem. Here we try to represent the convective heating effect in a rudimentary way, mainly for the convenience of theoretical analysis. This model, as will be shown, is an extension of the Matsuno model that includes diabatic heating and boundary layer dynamics.

In the thermodynamic equation (A.1.1d), two diabatic heating terms are included: the condensational latent heat and a simplest form of radiation cooling, Newtonian cooling, with a constant coefficient μ. The condensational heating rate Q_c must be constrained by the precipitation rate (i.e., the column integrated

condensational heating rate is linked with the precipitation rate):

$$\delta L_c P_r = \frac{1}{g}\int_{p_u}^{p_s} Q_c(p)\, dp \tag{A.4.1}$$

where L_c is latent heat of condensation and δ represents a switch-on tracer for non-linear heating in the absence of basic state rainfall: δ equals unity in the region of positive precipitation and zero otherwise. The heating is linear when $\delta \equiv 1$.

Equation (A.1.1e) describes the conservation of water vapor, which requires the local rate of change in the column-integrated water vapor M_c to be balanced by the sum of the column integrated moisture convergence, perturbation precipitation rate P_r, and the perturbation surface evaporation rate E_v. In the moisture convergence term $\vec{V}$ represents the horizontal wind and p_u and p_s are the pressures at the upper and lower boundary, respectively. The moisture convergence depends on the basic state specific humidity $\bar{q}$, which provides latent energy for the perturbation motion. We assume that the absolute humidity of the basic state atmosphere falls off with height exponentially with a water scale height $H_1 = 2.2\,\text{km}$. The mean specific humidity in an arbitrary vertical layer between pressure p_1 and p_2 where $p_2 > p_1$ is (Wang, 1988):

$$\bar{q}(p_1, p_2) = q_0 \frac{(p_2^m - p_1^m)}{m(p_2 - p_1)} \tag{A.4.2}$$

where $m = H/H_1$ is the ratio of the density scale height H to the water vapor scale height H_1, and q_0 is the air specific humidity at the surface. Over ocean and on the timescale of a few weeks or longer, q_0 is well correlated with SST and may be approximated by the following empirical formula (Li and Wang, 1994):

$$q_0 = q_0(\text{SST}) = (0.94 \times \text{SST}(^\circ\text{C}) - 7.64) \times 10^{-3} \tag{A.4.2a}$$

Since large-scale tropical motion is stimulated by condensational heating in the middle troposphere, the vertical structure of the motion is dominated by the gravest baroclinic mode. Thus, the simplest model should consist of two layers in the free troposphere. In the absence of basic flows, all advection terms in (A.1.1) can be neglected for perturbation motion. As shown in Section A.3, the motion in the two-level free atmosphere can be represented by a baroclinic and a barotropic mode. In the presence of boundary layer friction, these two vertical modes are coupled through frictional convergence induced vertical motion at p_e, the top of the boundary layer. To save space, the equations for this two-level system are not given here. The interested readers can find them, for example, in Wang and Rui (1990a). Note that only the baroclinic mode is subjected to diabatic heating. The condensational heating is linked to the precipitation rate (A.4.1). With the limited vertical resolution of the two-level system, the precipitation rate is expressed by:

$$\delta P_r' = \delta b\{[-\omega_2 \bar{q}_3 - \omega_e(\bar{q}_e - \bar{q}_3)]/g + \rho_s C_E |V_b|(q_s - q_0)\} \tag{A.4.3}$$

where ω_e and ω_2 represent, respectively, vertical pressure velocities at the top of the boundary layer (p_e) and the mid-troposphere (p_2); g, ρ_s, and C_E are gravity, surface air density, and heat exchange coefficient, respectively; V_b the wind speed at surface

$p = p_s$ that will be approximated by the model boundary layer wind; and q_s the saturation specific humidity at the SST, which can be calculated from the Clausius–Clapeyron equation. Equation (A.4.3) enables the governing equations to be a closed system.

It has been demonstrated that *in the absence of basic flows* the magnitude of the barotropic mode is an order of magnitude smaller than that of the baroclinic mode (Wang and Rui, 1990a; Wang and Li, 1993). Thus, a simplification can be made to neglect the barotropic mode by assuming a vanishing column integral of divergence in the free troposphere. The baroclinic mode in the free troposphere is then governed by the following equations on an equatorial β-plane (after ω_2 and ω_e are eliminated by using the continuity equation):

$$\frac{\partial u}{\partial t} - \beta y v = -\frac{\partial \phi}{\partial x} \tag{A.4.4a}$$

$$\frac{\partial v}{\partial t} + \beta y u = -\frac{\partial \phi}{\partial y} \tag{A.4.4b}$$

$$C_0^{-2}\frac{\partial \phi}{\partial t} + (1 - \delta I)\nabla \cdot \vec{V} = d(\delta B - 1)\nabla \cdot \vec{V}_b - \delta F C_E |\vec{V}_b|/h \tag{A.4.4c}$$

where u, v, and ϕ represent the lower troposphere zonal and meridional wind and geopotential height, respectively (the upper tropospheric zonal and meridional wind are $-u$ and $-v$, respectively); $\vec{V}_b$ denotes the boundary layer barotropic wind whose components (u_b, v_b) satisfy a linear version of (9.6.1); $C_0 = 50\,\mathrm{m\,s^{-1}}$ denotes a dry gravity wave speed of the free-troposphere baroclinic mode (corresponding to the gravest baroclinic mode in a vertically continuous model); $d = (p_s - p_e)/\Delta p$ is the dimensionless depth of the boundary layer; and $h = \Delta p/\rho_e g$, where Δp is one-half pressure depth of the free troposphere. In the thermodynamic equation (A.4.4c) there are three non-dimensional heating parameters, which are defined by:

$$I = \bar{q}_3/q_c \qquad \text{heating coefficient due to wave convergence} \tag{A.4.5a}$$

$$B = \bar{q}_e/q_c \qquad \text{heating coefficient due to frictional convergence} \tag{A.4.5b}$$

$$F = (q_s - q_0)/q_c \qquad \text{heating coefficient associated with evaporation} \tag{A.4.5c}$$

where $q_c = 2C_p p_s C_0^2/(bR\Delta p L_c)$ represents a vertical mean specific humidity in the lower tropospheric layer, corresponding to a vanishing effective static stability in the presence of convective heating. The standard values of model parameters used in this chapter are listed in Wang and Li (1994).

Note that, in a two-level free atmospheric model, the heating is released in the middle of the troposphere; the closure assumption for condensational heating is provided solely by conservation laws for moisture and thermal energy through the linkage between vertical integrated condensational heating rate and the precipitation rate in the same column (A.4.1). Any type of cumulus parameterization, when reduced to a two-level approximation, must obey the same physical principles. Therefore, use of (A.4.3) should not be considered a version of Kuo or any other

specific parameterization schemes. The only approximation made in (A.4.3) is the neglect of the local change of moisture and the moisture in the upper tropospheric layer. An adjustable parameter b is introduced to compensate the omission of the moisture storage in the atmosphere. The parameter b represents the condensation efficiency measuring the fraction of total moisture convergence that condenses out as precipitation. This simplification facilitates eigenvalue analysis. A two-level version of the time-dependent moisture equation (A.1.1e) and a transient boundary layer (rather than steady boundary layer) had also been used; the results are not qualitatively different from those derived with these simplifications.

The equations (A.4.4a–c) and (9.8.1) (with the assumption $\phi_e = \phi$) consist of a closed set of equations, which describes moist dynamics of a single free troposphere baroclinic mode that is coupled with the boundary layer motion. Such a model is referred to as a one and one half ($1\frac{1}{2}$) layer model.

9.11 ACKNOWLEDGEMENTS

We would like to thank Zhuo Wang for plotting Figure 9.10, Bo Yang for plotting Figures 9.6 and 9.7, Na Lan for plotting Figures 9.2, 9.18, 9.19, and 9.20, and Hway-Jen Chen for providing Figure 9.8.

10

Variation of the Asian monsoon water vapor budget: Interaction with the global-scale modes

Tsing-Chang Chen

10.1 INTRODUCTION

More than half of the World's population resides in the Asian monsoon region. Because of its importance to the well-being of such a large population, various aspects of monsoon rainfall have been the focus of Asian monsoon studies. Thus, numerous research efforts were attracted to perform regional water vapor budget analyzes over different areas: Japan (e.g., Yoshino, 1965, 1966; Akiyama, 1975), east Asia (e.g., Chen *et al*., 1988a), the South China Sea (e.g., Lau *et al*., 1998), the Tibetan Plateau (e.g., Luo and Yanai, 1983; Bollasina and Benedict, 2004), the Indo-China Peninsula (e.g., Kiguchi and Matsumoto, 2005), and other regions within the Asian monsoon system. In order to understand the water supplied by monsoon rainfall, the regional hydrological cycles/water vapor budgets were stressed by monsoon research. Although these regional hydrological cycles/water vapor budgets in the Asian monsoon system are part of the global hydrological cycle, we are still lacking a global perspective of the role played by the Asian monsoon in this hydrological cycle. On the other hand, it was uncommon for the studies of the global hydrological cycle/water vapor budget analysis (e.g., Chen and Pfaendfner, 1993; Ziegler *et al*., 2003) to explore its effect on the regional hydrological cycle. Because the Asian summer monsoon is embedded in the global circulation, the regional hydrological cycles/hydrological processes in Asia must be linked to the global circulation through some special relationship. The concern of this relationship leads us to raise the following two issues:

(1) What is the contribution of the Asian monsoon system to the global hydrological cycle/water vapor budget?
(2) How does the global circulation affect the hydrological cycle/water vapor budget of the Asian monsoon region?

B. Wang (ed.), *The Asian Monsoon*.

Issue (1) deals with the upscale interaction, while issue (2) tackles the downscale processes.

The Asian monsoon system is characterized by the Asian continental thermal low encircled by monsoon southerlies in south Asia and south-westerlies in south-east and east Asia. Within this continental-scale monsoon circulation, the Asian monsoon system consists of several distinguishable regional monsoon components: south Asia, the South China Sea and western tropical Pacific, east Asia, and north-east Asia. Due to differences in their response to diabatic heating, the monsoon circulations in these regions exhibit different characteristics, including timing of onset, life cycle, and interaction with synoptic disturbances. The south Asian monsoon circulation includes the Indian monsoon trough, which is modulated by the northward migration of the intraseasonal monsoon trough and ridge (Sikka and Gadgil, 1980; Krishnamurti and Subrahmanyam, 1982), and westward propagation of monsoon depressions (Saha *et al.*, 1981; Chen and Weng, 1999). The south-east Asian monsoon circulation is characterized by a south-east-extended monsoon trough that interacts with the northward-migrating monsoon trough/ridge (Chen and Chen, 1995), westward-propagating easterly waves (Lau and Lau, 1990), and tropical cyclones (Chen *et al.*, 2004). The east Asian monsoon circulation, which is characterized by the Meiyu–Baiu rain belt, receives contributions of rainfall from extratropical fronts before the monsoon break and tropical cyclones after the break (Ramage, 1952; Chen *et al.*, 2004a).

As for the contribution of the Asian monsoon to the global hydrological cycle, it may be difficult, if not impossible, to combine water vapor budget analyzes of all the individual monsoon components. Based on the rainfall and its variance (of different timescales), the Asian monsoon covers areas stretching from 60°E to near the Date Line (e.g., Chen *et al.*, 1995a). For convenience, let us designate the hemisphere of 60°E–120°W as the Asian monsoon hemisphere and the one of 120°W–60°E as the extra-Asian hemisphere (which covers the North American and west African monsoons). Therefore, the contrast between the water vapor budgets of these two hemispheres will be used to illustrate the contribution of the Asian monsoon system to the global hydrological cycle.

Numerous attempts have been made to explore the impact of global-scale propagating modes on the regional circulations of the Asian monsoon. However, few of these efforts gave attention to the effect of these propagating modes on the hydrological cycle over a particular region within the Asian monsoon system. As pointed out previously, the regional monsoon circulations over different areas of the Asian monsoon system are characterized by different features. Of course, it may not be possible for the regional hydrological cycles to respond to the global-scale propagating modes in a uniform manner. The east Asian monsoon will be used to illustrate the downscale processes of how the global-scale propagating mode regulates the regional hydrological cycle.

10.2 THEORETICAL BACKGROUND OF THE WATER VAPOR BUDGET

The atmospheric branch of the hydrological cycle is usually depicted in terms of the water vapor budget equation (e.g., Peixoto and Oort, 1992):

$$\frac{\partial W}{\partial t} + \nabla \cdot Q = E - P \tag{10.1}$$

where $W \equiv \frac{1}{g}\int_0^{p_S} q dp$, $Q \equiv \frac{1}{g}\int_0^{p_S} Vq\, dp$, E, P, g, q, p, p_s, and V are precipitable water, water vapor flux, gravity, specific humidity, pressure, surface pressure, and the velocity vector, respectively. Water vapor, which resides primarily in the lower troposphere, is largely transported by the low-level atmospheric circulation. Therefore, low-level atmospheric flow is reflected through water vapor flux. Without a phase change, water vapor behaves like a passive atmospheric constituent. According to (10.1), water vapor converges ($\nabla \cdot Q < 0$) toward its sink region ($E - P < 0$). Consequently, the residence of water vapor in the atmosphere is maintained by the imbalance between $\nabla \cdot Q$ and $(E - P)$, and represented by the water vapor storage $\partial W/\partial t$.

According to the Helmholtz theorem, water vapor flux (Q) may be split into rotational (Q_R) and divergent (Q_D) components:

$$Q = Q_R + Q_D \tag{10.2}$$

These two components of water vapor flux (Q_R, Q_D) may be expressed in terms of the streamfunction (ψ_Q; Rosen *et al.*, 1979) and potential functions (χ_Q; Chen, 1985) of water vapor flux:

$$Q_R = \hat{k} \times \nabla \psi_Q \qquad Q_D = \nabla \chi_Q. \tag{10.3}$$

These two water vapor flux functions can be obtained by the following two inverse transforms:

$$\psi_Q = \nabla^{-2}(\hat{k} \times \nabla \cdot Q) \qquad \chi_Q = \nabla^{-2}(\nabla \cdot Q) \tag{10.4}$$

The water vapor budget equation can therefore be expressed as either

$$\frac{\partial W}{\partial t} + \nabla \cdot Q_D = E - P \tag{10.1$'$}$$

or

$$\frac{\partial W}{\partial t} + \nabla^2 \chi_Q = E - P \tag{10.1$''$}$$

Since water vapor is largely transported by low-level atmospheric flows, the spatial structure of the global ψ_Q and χ_Q distributions resemble those of the low-level streamfunction (ψ) and velocity potential (χ). After depictions of the global ψ (200 mb) and χ (200 mb) fields introduced by Krishnamurti (1971b) and Krishnamurti *et al.* (1973a), the global atmospheric circulation is often portrayed by these two variables. Thus, the water vapor transport by the global atmospheric circulation

can be well delineated by ψ_Q and χ_Q. As indicated by the water vapor budget, $(E - P)$ is only the local source/sink of water vapor. It may be inferred from (10.1″) that the link between this source and sink of water vapor is established by the global divergent circulation depicted in terms of the χ_Q field.

Despite their local nature, hydrological processes included in the water vapor budget can be coupled with the global divergent circulation through the χ_Q field and the regional water vapor flux linked to the global atmospheric circulation through both the ψ_Q and χ_Q fields. Using this link between local hydrological processes and the global atmospheric circulation, the contribution of the Asian monsoon to the global hydrological cycle will be illustrated in terms of the hemispheric water vapor budget, and the possible impact/effect of the global atmospheric circulation on the Asian monsoon rainfall will be demonstrated in terms of the ψ_Q and χ_Q fields.

10.3 CONTRIBUTION OF THE ASIAN MONSOON TO THE GLOBAL HYDROLOGICAL CYCLE

The Asian monsoon rainfall undergoes variations on three different timescales: diurnal, intraseasonal, and interannual. Can the contribution of the Asian monsoon to the global hydrological cycle be reflected in these variations? We shall illustrate them from two different perspectives: climatological and temporal variations.

10.3.1 Climatology

During the northern summer, there are three major monsoon systems in the northern hemisphere: the Asian, North American, and west African monsoons. The summer rainfall in these monsoon regions and along the intertropical convergence zone (ITCZ) is maintained by the convergence of water vapor flux carried out by global divergent circulation inferred from the Q_D distribution in Figure 10.1(a) (Chen, 1985). As revealed from summer precipitation in this figure, the amount and spatial coverage over the Asian monsoon region and the western tropical Pacific is much larger than the other two monsoon regions. Following Chen *et al.* (1995a), let us divide the globe into two hemispheres: the Asian monsoon hemisphere (60°E–120°W) and the extra-Asian monsoon hemisphere (120°W–60°E). For convenience, any variable ( ) averaged over the former hemisphere is designated by $(\,)_A$, over the latter hemisphere by $(\,)_E$, and over the globe by $(\,)_G = \frac{1}{2}[(\,)_A + (\,)_E]$. Based on the water vapor budget (10.1), the water vapor budgets of the two hemispheres may be written as:

$$\frac{\partial W_A}{\partial t} + (\nabla \cdot Q)_A = E_A - P_A \tag{10.5a}$$

and

$$\frac{\partial W_E}{\partial t} + (\nabla \cdot Q)_E = E_E - P_E \tag{10.5b}$$

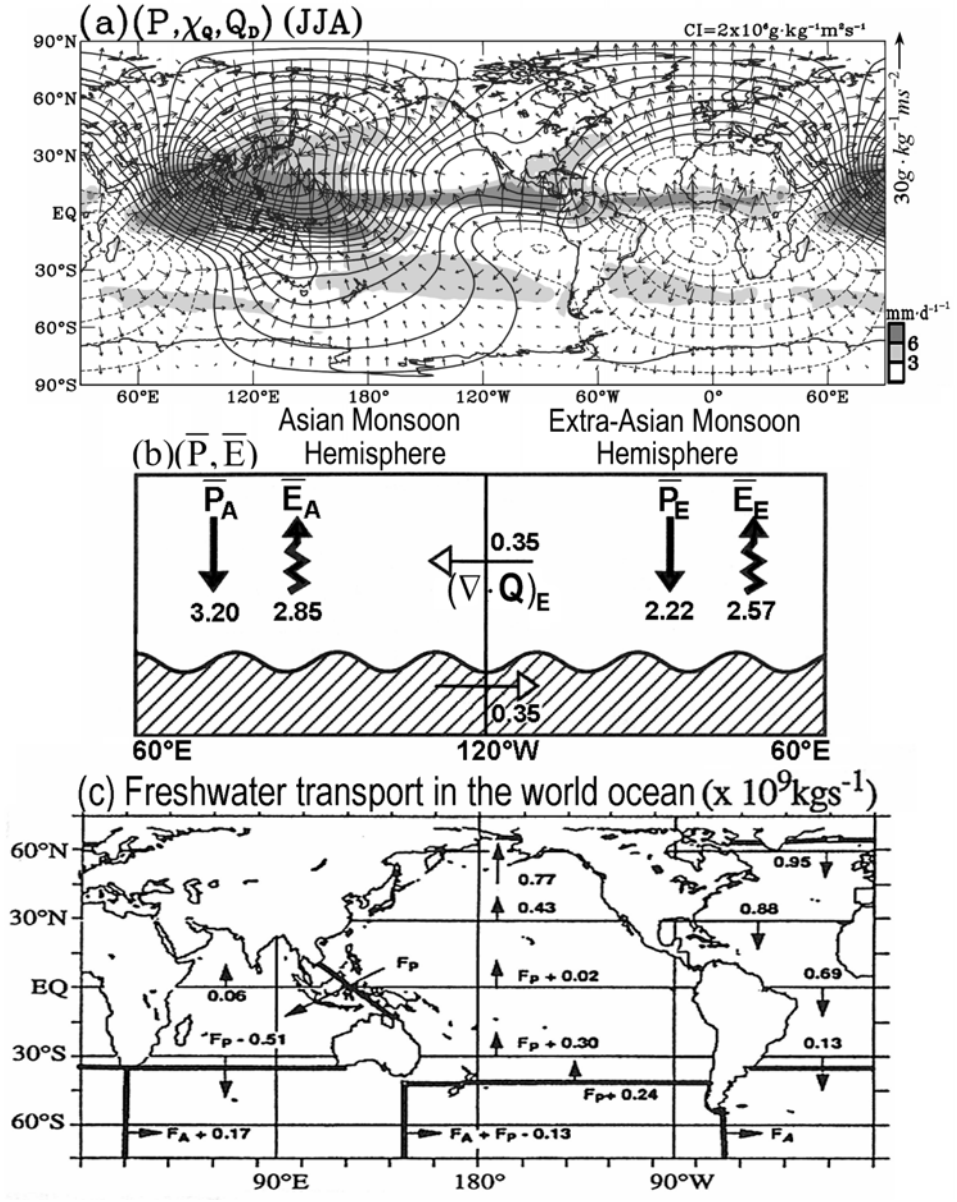

Figure 10.1. The global hydrological cycle: (a) precipitation P, potential function of water vapor flux χ_Q, and divergent water vapor flux Q_D for the northern summer (JJA), (b) the long-term mean hemispheric water vapor budgets of the Asian monsoon hemisphere $(\,)_A$ and the extra-Asian monsoon hemisphere $(\,)_E$, and (c) the long-term mean freshwater transport of the global ocean from Wijffels *et al.* (1992). Units of all hydrological variables in the hemispheric water budget are mm day^{-1}.

Because $(\nabla \cdot Q)_G = 0$:

$$(\nabla \cdot Q)_A = -(\nabla \cdot Q)_E \tag{10.6}$$

The water vapor budgets of the two hemispheres are displayed in Figure 10.1(b). The contrasts in the water vapor budgets between these two hemispheres may be summarized as follows:

(1) Values of P_A and E_A are larger than those of P_E and E_E, respectively. It is suggested by the contrast between hemisphere averaged E and P values that the intensity of the hydrological cycle in the Asian monsoon hemisphere is larger than that in the extra-Asian monsoon hemisphere.
(2) Rainfall in the Asian monsoon hemisphere ($P_A = 3.2\,\text{mm day}^{-1}$) is larger than evaporation ($E_A = 2.85\,\text{mm day}^{-1}$), while rainfall in the extra-Asian monsoon hemisphere ($P_E = 2.22\,\text{mm day}^{-1}$) is smaller than evaporation ($E_E = 2.57\,\text{mm day}^{-1}$). Evidently, $E_A - P_A < 0$ and $E_E - P_E > 0$. In other words, the Asian monsoon hemisphere is a water vapor sink and the extra-Asian monsoon hemisphere is a water vapor source. The deficit of water vapor in the former's hemisphere is supplied by the latter's hemisphere, as indicated by $(\nabla \cdot Q)_E > 0$ (or $(\nabla \cdot Q)_A < 0$).

In view of the contrasting characteristics of the water vapor budget between the two hemispheres shown in Figure 10.1(b), several questions are raised: (1) Can the contrast of the water vapor budget between the two hemispheres always be maintained? (2) How is the water vapor surplus supplied in the extra-Asian monsoon hemisphere? (3) Where does the excessive rainfall in the Asian monsoon hemisphere go? Question (1) will be discussed later in Section 3.2, but questions (2) and (3) are answered here. The salinity is higher in the Atlantic Ocean than the Pacific Ocean (Levitus, 1986; Chen *et al.*, 1994) because evaporation is larger over the former ocean than the latter (Figure 10.1(b)). The excessive water vapor generated by evaporation in the Atlantic Ocean converges toward the Pacific Ocean (Bryan and Oort, 1984; Chen *et al.*, 1994) to make up for its deficit of water vapor. If this water vapor supply is ceaseless, the contrast between the water vapor budgets of the two hemispheres in Figure 10.1(b) may become sharper. Despite interannual variations in the global and hemispheric hydrological cycle, it will be shown in Section 3.2 that the water vapor budget contrast between the two hemispheres is always maintained. It is implied by this contrast that there must be a path for water vapor to exit the Asian monsoon hemisphere. Compiling the interocean freshwater transport shown in Figure 10.1(c), Wijffels *et al.* (1992) showed that freshwater is routed from the Pacific Ocean through the Bering Sea and Arctic Ocean to the Atlantic Ocean. Based on the contrast between the Q_D distribution in Figure 10.1(a) and the interocean freshwater transport in Figure 10.1(c), the path of water vapor exiting the Asian monsoon hemisphere is through the interocean freshwater transport shown in Figure 10.1(c) (Chen *et al.*, 1994). The basic role played, and the contribution made, by the Asian monsoon hemisphere to the global hydrological cycle is revealed by the contrast

between the water vapor budgets of the Asian monsoon and extra-Asian monsoon hemispheres in Figure 10.1.

10.3.2 Temporal variation

As previously shown in Figure 10.1(b), the Asian monsoon hemisphere produces about 50% more rainfall than the extra-Asian monsoon hemisphere. Since the global atmospheric circulation exhibits variation with different timescales, ranging from diurnal to interannual, does the global hydrological cycle undergo variations within these timescales? Can these variations of the global hydrological cycle follow those of the Asian monsoon hemisphere? This question may be answered in terms of three different statistical analyzes. *First*, time series of globally and hemispherically long-term precipitation averaged every three hours for a half month of June, daily mean precipitation for the entire year of 1991, summer mean precipitation (JJA) for the 1979–2002 period, and the corresponding hemispheric mean divergence of water vapor flux. The hemispheric mean divergence of water vapor flux are also shown in Figure 10.3. It is clearly revealed that variations of P_G in all timescales concerned in this study follow those of P_A. *Second*, power spectra of the first two types of time series are displayed in Figure 10.3. Signals of diurnal cycle $()'$ and intraseasonal [$30 \sim 60$ day ($\tilde{}$) and $12 \sim 24$ day ($\hat{}$)] modes clearly stand out. For time series of summer rainfall, interannual variations of summer precipitation closely follow summer sea surface temperature (SST) (Niño 3.4) departures. It is of interest to note that amplitudes of rainfall variations shown in Figure 10.2 are of the same order of magnitude, regardless of their timescales. *Third*, in order to understand where significant signals of rainfall variations identified above are located, and to verify whether the separation of these signals into two hemispheres is appropriate, rainfall variance distributions of these signals are shown in Figure 10.4. Despite the detailed spatial structure in their variance distributions, it is clearly indicated that these rainfall variation modes exhibit larger values over the Asian monsoon hemisphere as inferred from their time series shown in Figure 10.2. The Asian monsoon hemisphere not only contributes more rainfall to the global hydrological cycle, but also affects temporal variations of the global hydrological cycle more significantly than the other hemisphere. In addition, to substantiate this inference with the hemispheric water vapor budget, we shall also explore the hydrological implication of the possible contrast of roles played by the Asian and extra-Asian monsoon hemispheres in the global hydrological cycle.

Diurnal variation

Several interesting features emerge from the comparison of the 3-hour time series of P_G, P_A, and P_E in Figure 10.3(a):

(1) P_A is always larger than P_E.
(2) Standard deviations of P_G, P_A, and P_E diurnal variations are 0.2, 0.5, and $0.3\,\mathrm{mm\,day^{-1}}$, respectively. The amplitude of the P_A diurnal variation is generally larger than that of the P_E diurnal variation. This contrast is consistent

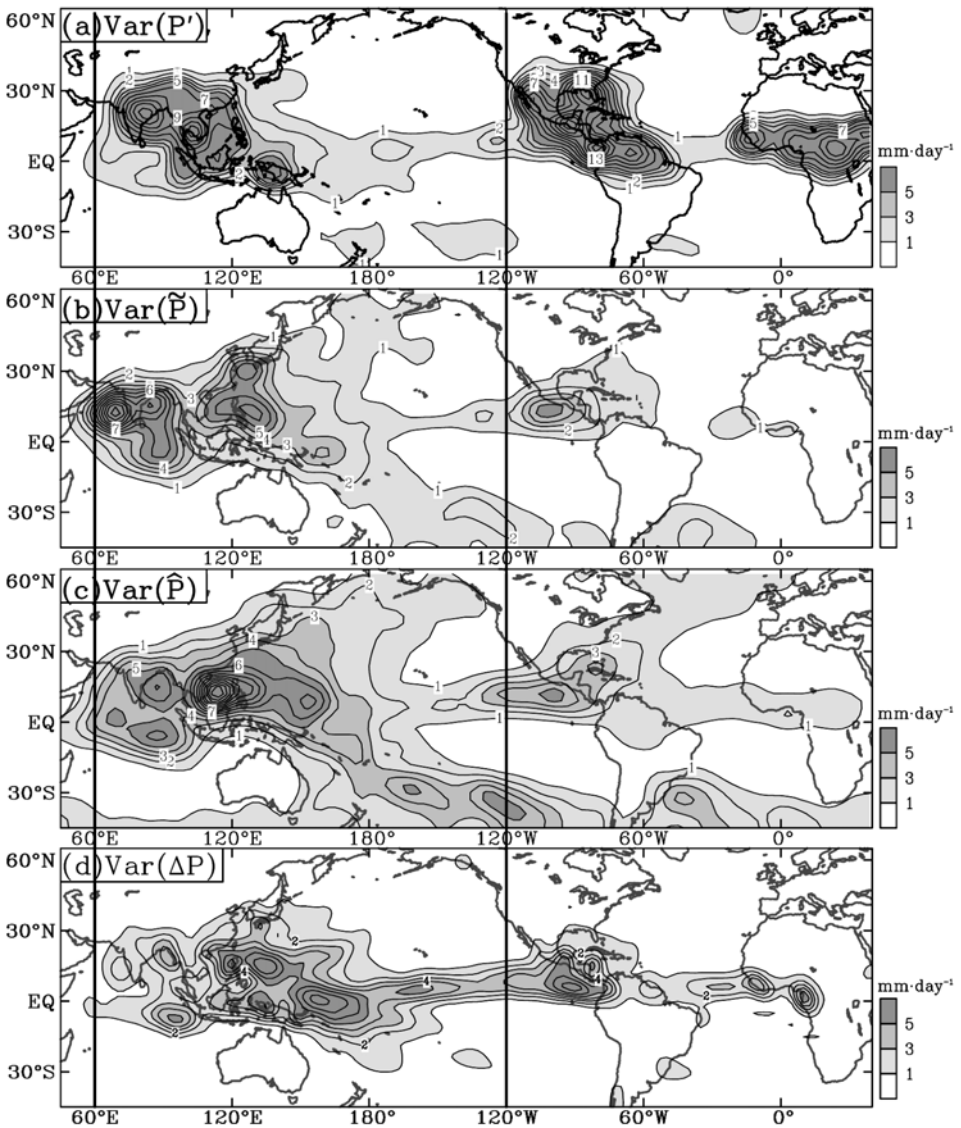

Figure 10.2. Variance (Var) of global precipitation fluctuations: (a) diurnal cycle P', (b) 30–60-day mode $\tilde{P}$, (c) 12–24-day mode $\hat{P}$, and (d) interannual variation mode ΔP. Contour intervals of these precipitation variances are shaded according to the right-hand scales.

with the variance distributions of diurnal variations of rainfall shown in Figure 10.4(a).

(3) Diurnal variations of P_G and P_A are *in phase* (with a correlation coefficient $r_{P_A \cdot P_G} = 0.95$; where $r_{x \cdot y}$ is the correlation coefficient between the time series

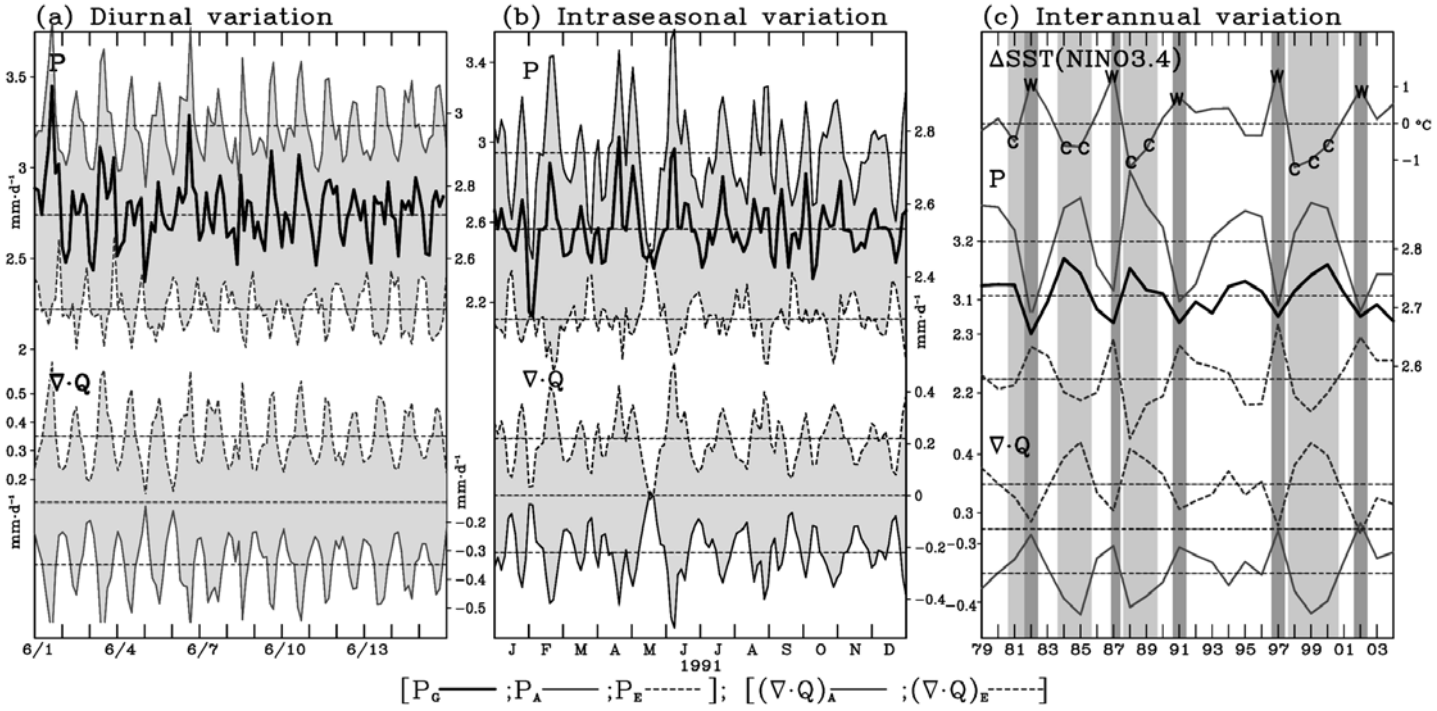

Figure 10.3. Temporal variations of hemispheric mean P and $\nabla \cdot Q$ and global mean precipitation P_G: (a) diurnal variation, (b) intraseasonal variation, and (c) interannual variation. $(\,)_G$, $(\,)_A$, and $(\,)_E$ are variables $(\,)$ averaged over the globe (thick solid line), Asian monsoon (thin solid line), and extra-Asian monsoon (short dashed line) hemisphere, respectively. Global and hemispheric mean values of hydrological variables are denoted by thin dashed lines.

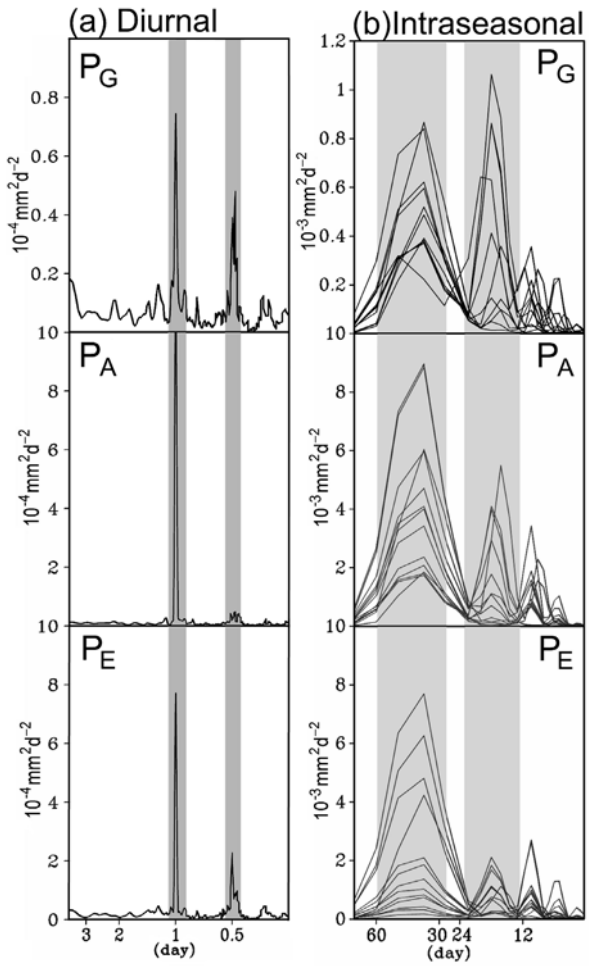

Figure 10.4. Power spectra of P_G, P_A, and P_E time series shown in Figure 10.3(a) and (b): (a) diurnal, and (b) intraseasonal. Diurnal variation is dominated by the diurnal cycle, while intraseasonal variation is contributed to by both the 30–60-day and 12–24-day modes.

of variables x and y), but are out of phase with P_E (with correlation coefficients $r_{P_A \cdot P_E} = -0.93$ and $r_{P_G \cdot P_E} = -0.94$). It is inferred from these statistical relationships that the diurnal variation of global rainfall follows closely that of the Asian monsoon hemisphere.

Both the Asian monsoon and extra-Asian monsoon hemispheres contribute to global precipitation. Why should the diurnal variation of global precipitation follow the former hemisphere? What roles are played by these two hemispheres in the global hydrological cycle? The hemispheric water vapor budget analyzes will be discussed further to answer these questions. Observations of evaporation are not available and

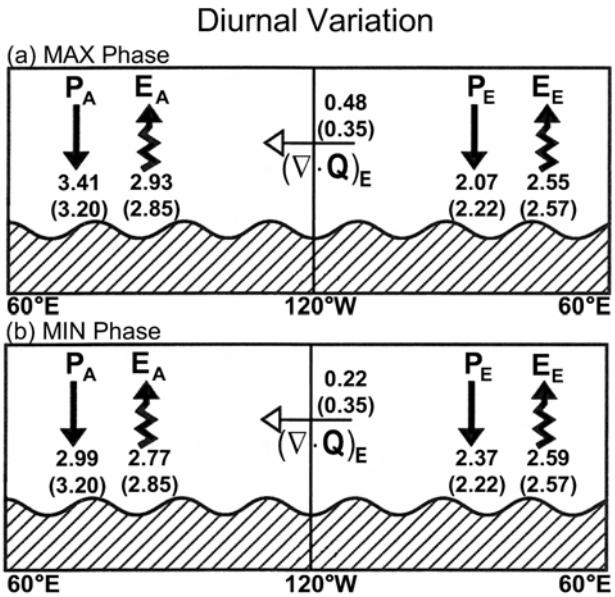

Figure 10.5. Same as Figure 10.1(b) except for the maximum and minimum phase of the diurnal cycle. The long-term climatological values of all hydrological variables shown in Figure 10.1(b) are parenthesized in this figure for comparison.

estimations of evaporation using the residual method of the water vapor budget are inaccurate. Therefore, it is difficult, if not impossible, to perform a complete water vapor budget analysis. Because rainfall is primarily maintained by the water vapor supply through the convergence of the water vapor flux, an inference of the roles played by the Asian monsoon and the extra-Asian monsoon hemispheres may be made by the following hydrological relationship:

$$P_A \sim -(\nabla \cdot Q)_A = (\nabla \cdot Q)_E \sim -P_E$$

The 3-hour time series of $(\nabla \cdot Q)_E$ are displayed at the bottom of Figure 10.2(a). The P_A (P_E) variation is in phase (out of phase) with $(\nabla \cdot Q)_E$. As shown in Figure 10.1(b), the summer rainfall in the Asian monsoon hemisphere is supplied by the water vapor flux diverged from the extra-Asian monsoon hemisphere, in addition to the *in situ* evaporation. On the other hand, the 3-hour time series of P_A, P_E, and $(\nabla \cdot Q)_E$ in Figure 10.2(a) reveal that water vapor from the Asian monsoon hemisphere is supplied (depleted) by (from) the extra-Asian monsoon hemisphere through divergence (convergence) of the water vapor flux to maintain the diurnal variation of the Asian monsoon hemisphere rainfall.

Roles played by the two hemispheres in the diurnal variation of the global hydrological cycle may be summarized by the composite hemispheric water vapor budget during P'_G maximum and minimum phases (Figure 10.5). Hemispheric evaporation is estimated by the residual, although the estimation may contain bias from

the data assimilation system and computational errors. It is of interest to note that the summer mean hemispheric water vapor budgets in both hemispheres are modulated by the diurnal variation, but the contrast of the water vapor source and sink between the two hemispheres revealed from the climatological water vapor budget shown in Figure 10.1(b) is not changed by the diurnal variation.

At the surface, the short-wave radiative heating of the diurnal hemisphere and the long-wave radiative cooling of the nocturnal hemisphere roughly form a spatially wavenumber-1 structure around the globe. The direct atmospheric response to this east–west differential heating/cooling is reflected by the global divergent circulation which may exhibit a low-level structure similar to χ_Q shown in Figure 10.1(a). As inferred from the spatial structure of χ_Q, the global divergent circulation in response to the surface radiative heating/cooling also exhibits a wavenumber-1 structure. Because the Earth rotates in an eastward direction, the response of the atmospheric divergent circulation propagates westward. First, the division of the global circulation into the Asian monsoon and extra-Asian monsoon hemisphere matches well with the wavenumber-1 structure of the global divergent circulation. Second, the Asian monsoon region may be more convectively unstable than the other hemisphere. The atmospheric response to the surface radiative heating is more dramatic over the Asian monsoon hemisphere. This hemispheric difference of rainfall in response to this diurnal variation of heating will be illustrated in Section 10.4.

Intraseasonal variation

Numerous research efforts have been devoted to exploring the impact and modulation of intraseasonal modes on the onset and life cycle of monsoons in different regions within the Asian monsoon system: the Indian monsoon by Murakami (1976), Krishnamurti and Bhalme (1976), Krishnamurti and Subrahmanyam (1982); the South China Sea monsoon by Chen and Chen (1995); and the east Asian monsoon by Chen and Murakami (1988). The effect of intraseasonal modes on the hydrological cycle of the entire Asian monsoon system has not been a research focus. The lack of previous research attention on this effect may be attributed to the lack of uniform rainfall observations available. Therefore, previous research efforts along this direction were largely concentrated on regions of particular concern (e.g., east/south-east Asia by Lau *et al.* (1988), Chen *et al.* (1988a), Chen *et al.* (2004b); India by Chen *et al.* (1988b) and Chen and Chen (1993)). It may be difficult to obtain an overview of the possible effect of the global intraseasonal modes on the Asian monsoon system by merging its impacts on several regional monsoons. As revealed from the $\mathrm{Var}(\tilde{P})$ and $\mathrm{Var}(\hat{P})$ distributions in Figure 10.2, large variances of these two variables cover the entire Asian monsoon hemisphere. In order to obtain a coherent impact of intraseasonal modes over the entire Asian monsoon and the contribution of the Asian monsoon system to the possible intraseasonal variation of the global hydrological cycle, we need to examine the intraseasonal variation of the global and hemispheric water vapor budget.

Time series of daily P_G, P_A, P_E, $(\nabla \cdot Q)_A$, and $(\nabla \cdot Q)_E$ are displayed in

Figure 10.3(b). Certain interesting features of the global and hemispheric hydrological cycles are reflected in these time series:

(1) Variation of P_E is out of phase with P_A, but variation of P_G is coincident with P_A. Since $P_G = \frac{1}{2}(P_A + P_E)$ and the time series of P_G and P_A are in phase, it is obvious that the amplitude of P_A is larger than P_E. The intraseasonal variation of global precipitation follows the Asian monsoon hemispheric rainfall. It was observed that monsoon breaks in south Asia (e.g., Krishnamurti and Subrahmanyam, 1982), the South China Sea (e.g., Chen and Chen, 1995), Indo-China (e.g., Kihuchi and Matsumoto, 2005), and east Asia (e.g., Chen *et al.*, 2004a) occur in late June and early July when monsoon onset takes place in south-western North America (e.g., Douglas *et al.*, 1993) and west Africa (e.g., Sultan *et al.*, 2003; Sultan and Janicot, 2003). The contrast of these monsoon rainfall variations is well revealed from the out-of-phase variations between P_A and P_E during the northern summer.
(2) Regardless of intraseasonal variations in both $(\nabla \cdot Q)_A$ and $(\nabla \cdot Q)_E$, water vapor always diverges out of the extra-Asian monsoon hemisphere (i.e., $(\nabla \cdot Q)_E > 0$) and converges toward the Asian monsoon hemisphere ($(\nabla \cdot Q)_A < 0$). Evidently, the former hemisphere is a water vapor source, while the latter hemisphere is a water vapor sink. Since precipitation is maintained by the convergence of water vapor, it is expected that intraseasonal variations of hemispheric precipitation and convergence of water vapor flux should be related in a coherent way. As shown in Figure 10.3(b), intraseasonal variation of $(\nabla \cdot Q)_E$ [$(\nabla \cdot Q)_A$] is in phase [out of phase] with P_E. Thus, water vapor is exchanged between these two hemispheres in such a way that an increase (decrease) of P_A follows that of $(\nabla \cdot Q)_E$ which results in the decrease (increase) of P_E.

It was shown in Figure 10.4 that intraseasonal variations of global and hemispheric precipitation exhibit two pronounced modes: 30–60-day and 12–24-day. How do these two low-frequency modes contribute to the global and hemispheric hydrological cycles? Time series of hydrological variables corresponding to Figure 10.3(b) for these two intraseasonal modes are shown in Figure 10.6. First, let us explore how significant are the contributions of these two low-frequency modes to intraseasonal variations of all hydrological variables shown in this figure. This contribution is measured by the ratio $R(\,)$ between variance of any variable $(\,)$ and variance of its 30–60-day and 12–24-day modes combined $(\tilde{}) + (\hat{})$. $R(P_G) = 70\%$, $R(P_A) = 75\%$, $R(P_E) = 72\%$, and $R[(\nabla \cdot Q)_E] = 84\%$. Apparently, intraseasonal variations of these hydrological variables are well contributed to by the two intraseasonal modes.

The life cycles of both the 30–60-day and 12–24-day modes are different. Therefore, both modes may occasionally be in phase. We shall illustrate separately their roles in the global hydrological cycle. Variation of $\tilde{P}_G(\hat{P}_G)$ is in phase with $\tilde{P}_A(\hat{P}_A)$ but out of phase with $\tilde{P}_E(\hat{P}_E)$. Variation of $(\nabla \cdot \tilde{Q})_E[(\nabla \cdot \hat{Q})_E]$ is in phase with $\tilde{P}_A(\hat{P}_A)$, while out of phase with $\tilde{P}_E(\hat{P}_E)$. The phase relationships of these hydrological variables indicate that the roles played by these two intraseasonal modes on

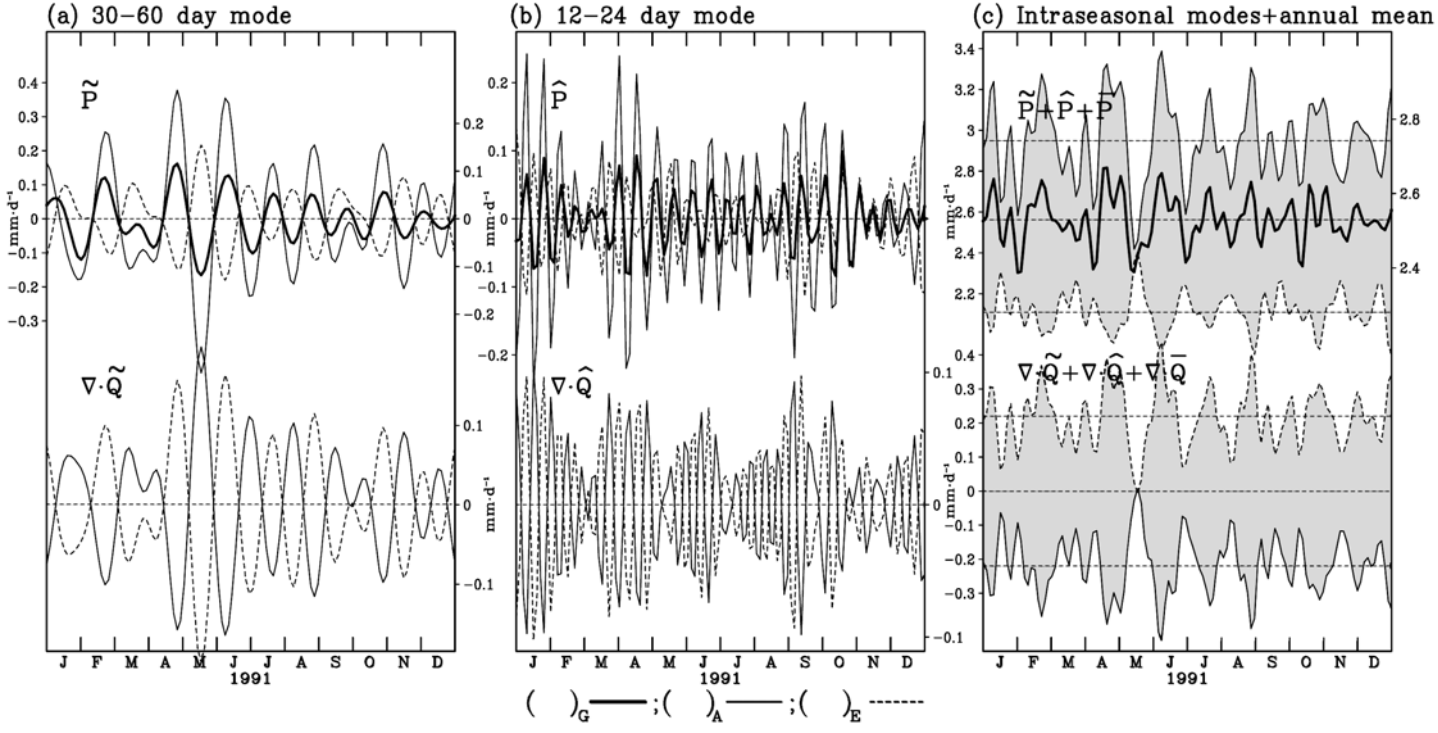

Figure 10.6. Intraseasonal variations of $P'_{()}$s and $(\nabla \cdot Q)'_{()}$s: (a) 30–60-day mode ($\tilde{}$), (b) 12–24-day ($\hat{}$), and (c) combination of ($\tilde{}$) + ($\hat{}$) + ($\bar{}$), where ($\bar{}$) = annual mean of ( ).

the global hydrological cycle behave in the same manner. During the minimum phase, the 30–60-day (12–24-day) mode enables the extra-Asian monsoon hemisphere to diverge water vapor to the Asian monsoon hemisphere in supporting maximum $\tilde{P}_A(\hat{P}_A)$. During the $\tilde{P}_E$ and $\hat{P}_E$ maximum phases, and $\tilde{P}_A$ and $\hat{P}_A$ minimum phases, the two intraseasonal modes reverse their function in the divergence of water vapor flux. It was shown by Chen *et al.* (1995a,b) that the potential function of water vapor flux of these two intraseasonal modes, $\tilde{\chi}_Q$ and $\hat{\chi}_Q$, are mainly depicted by a wavenumber-1 pattern. The eastward propagation of these two intraseasonal modes results in the seesaw exchange of water vapor flux (reflected by $(\nabla\cdot\tilde{Q})_E$ and $(\nabla\cdot\hat{Q})_E$) and the corresponding seesaws of both $\tilde{P}_A(\hat{P}_A)$ and $\tilde{P}_E(\hat{P}_E)$. The impacts of global $\tilde{\chi}_Q$ and $\hat{\chi}_Q$ modes on the regional Asian monsoon rainfall will be further illustrated in Section 10.4. In addition, the coherent variation between $\tilde{P}_G(\hat{P}_G)$ and $\tilde{P}_A(\hat{P}_A)$ indicates that the hydrological responses of the Asian monsoon hemisphere to the eastward-propagating intraseasonal modes are more sensitive than the extra-Asian monsoon hemisphere.

The roles played by the two intraseasonal modes in the global hydrological cycle are concisely summarized in the composite hemispheric water vapor budgets during their maximum and minimum phases in Figure 10.8. The major features of these water vapor budgets can be highlighted as follows:

(1) Regardless of the seesaw precipitation variation and exchange of water vapor flux between the Asian monsoon and the extra-Asian monsoon hemisphere, a clear distinction between water vapor source and sink is always maintained.
(2) Although evaporation is estimated, it is indicated that $\Delta P[\equiv P(\max) - P(\min)]$ is always larger than $\Delta E[\equiv E(\max) - E(\min)]$ for both intraseasonal modes in the two hemispheres. It suggests that precipitation/convection is more sensitive to the eastward propagation of the intraseasonal modes, despite the possible effect of intraseasonal modes on the latent heat energy flux from oceans by previous studies (e.g., Krishnamurti *et al.*, 1988).
(3) Recall that the Asian monsoon hemisphere is a water vapor sink. It was pointed out in Section 10.3.1 that the freshwater flow from the Indian and the Pacific Oceans (generated by monsoon rainfall) across the Bering Strait and the Arctic Sea returns back to the Atlantic. Can this returning freshwater to the Atlantic undergo intraseasonal variations? Although it may be difficult to substantiate this argument with existing observational data, simulations of a coupled global climate model may offer an alternative.

Interannual variation

The interannual variation of Indian monsoon rainfall has a long history as a research subject. The two most compelling mechanisms causing this interannual variation are the Southern Oscillation (an east–west surface pressure seesaw between the Indian–western Pacific and the central eastern Pacific) (Walker, 1923, 1924) and the interannual variation of snowfall over central Asia and the Himalayan mountains (Blanford 1884). These two mechanisms have been extensively explored and analyzed in the past several decades with data generated by modern data assimila-

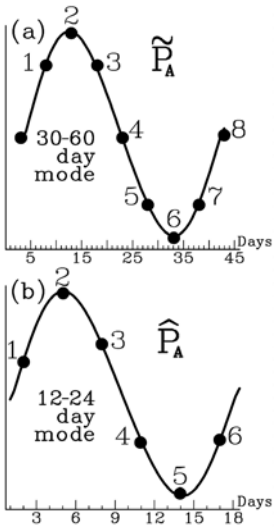

Figure 10.7. Phase of (a) 30–60-day mode and (b) 12–24-day mode defined in terms of $\tilde{P}_A$ and $\hat{P}_A$ time series.

tion systems. The interannual variation of the east/south-east Asian monsoon rainfall has also stimulated a surge of research activity in recent decades (e.g., Wu and Wang, 2000, 2002). The main focus of these research endeavors include the possible impact of the El Niño/Southern Oscillation (ENSO) cycle on the east/south-east Asian monsoon. Over Indo-China, only a few studies (e.g., Chen and Yoon, 2000) have explored the interannual variation of monsoon rainfall. The variance distribution of interannual rainfall departures from their long-term summer mean rainfall in Figure 10.2(d) indicates that the major global interannual variation of summer rainfall is primarily contributed to by the Asian monsoon hemisphere. A more concise perspective of the ENSO effect on the Asian monsoon system and the contribution of the Asian monsoon system to the interannual variation of the global hydrological cycle may be gained through hemispheric water budget analysis.

It was suggested that the global hydrological cycle is intensified (weakened) during ENSO warm (cold) events (Chahine, 1992; Soden, 2000). Analyzing the interannual variation of the global and hemispheric hydrological cycle, Chen and Huang (2005) recently showed that the impact of the ENSO cycle on the global hydrological cycle is opposite to Chahine's suggested impact. Does the summer global and hemispheric water vapor budget undergo interannual variation in concert with the ENSO cycle? This concern is clarified by time series of various hydrological variables in Figure 10.3(c). In order to compare these variables with the ENSO cycle, the summer ΔSST (Niño 3.4) is also included in Figure 10.3(c). The summer warm and cold events are classified based on the criterion $\Delta\text{SST (Niño 3.4)} \geq 0.5^{\circ}\text{C}$ warm and $\Delta\text{SST (Niño 3.4)} \leq -0.5^{\circ}\text{C}$ cold. Since ΔSST anomalies

over the western tropical Pacific and the central/eastern tropical Pacific exhibit an interannual seesaw following the ENSO cycle, the convective activity/rainfall in the western tropical Pacific has an interannual variation opposite to that in the central/eastern tropical Pacific. Therefore, it is expected that rainfall over the western tropical Pacific and the Asian monsoon region becomes larger (smaller) during the cold (warm) summer over the eastern tropical Pacific.

The inference of the interannual variation in the hemispheric water vapor budget is confirmed by time series of various hydrological variables shown in Figure 10.3(c):

(1) Interannual variation of P_A is out-of-phase with summer ΔSST (Niño 3.4) anomalies, while that of P_E is in phase.
(2) Interannual variation of P_G follows that of P_A, because the amplitude of P_A is larger than P_E.
(3) Water vapor is always diverged out of the extra-Asian monsoon hemisphere (i.e., $(\nabla \cdot Q)_E > 0$) and converges toward the Asian monsoon hemisphere (i.e., $(\nabla \cdot Q)_A < 0$). This hemispheric water vapor exchange is always larger (smaller) during cold (warm) events.

It will be shown in Section 10.4 that the interannual mode of χ_Q exhibits a dominant wavenumber-1 structure and eastward propagation (as shown by Barnett (1983, 1984a,b, 1985, 1988)). The convective activity/rainfall over the Asian monsoon hemisphere is more sensitive in response to the eastward propagation of the ENSO interannual mode. Divergence of interhemispheric water vapor flux is therefore regulated by this interannual mode in concert with the P_A interannual variation. Consequently, the global rainfall variation follows the P_A variation. The relationship between the summer ΔSST (Niño 3.4) and the global hemispheric water vapor essentially contradicts Chahine's (1992) suggested relationship.

The composite hemispheric water vapor budgets for those warm and cold summers marked on the ΔSST (Niño 3.4) time series in Figure 10.3(c) are displayed in Figure 10.9 to summarize the interannual variation in the global/hemispheric hydrological cycle. It was suggested that the global hydrological cycle is regulated by the central eastern tropical Pacific SST anomalies in such a way that it is accelerated (decelerated) during the ENSO warm (cold) events. As revealed from the composite hemispheric water budgets, it works opposite to this suggestion. Recall that the ΔSST anomalies over western tropical Pacific exhibit a seesaw with the ΔSST (Niño 3.4) anomalies. The convective activity/rainfall in the Asian monsoon hemisphere is enhanced (suppressed) during the cold (warm) ΔSST (Niño 3.4) anomalies. Regardless of interannual variations in hemispheric hydrological variables, the hydrological roles played by the extra-Asian monsoon hemisphere as a water vapor source and the Asian monsoon hemisphere as a water vapor sink are not affected by the ENSO activity. Finally, it may be difficult to measure short timescale variations in the ocean freshwater flux. However, it may be possible to explore whether the global freshwater flux route suggested by Wijffels *et al.* (1992) undergoes an interannual variation in response to that of the water vapor flux exchange between the Asian monsoon and the extra-Asian monsoon hemisphere.

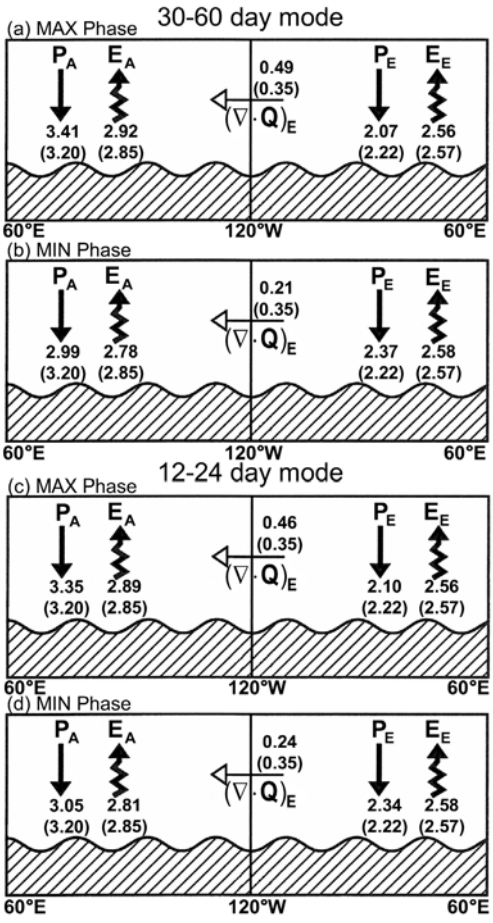

Figure 10.8. Same as Figure 10.1(b), except for 30–60-day mode ((a) maximum phase and (b) minimum phase) and 12–24-day mode ((c) maximum phase and (d) minimum phase). The maximum and minimum phases of these two intraseasonal modes are determined according to the phase schematic shown in Figure 10.7.

10.4 MODULATION OF THE WATER VAPOR TRANSPORT AND RAINFALL IN THE EAST ASIAN MONSOON REGION BY GLOBAL MODES

The contribution of the Asian monsoon system to the global hydrological cycle was illustrated in terms of the hemispheric water vapor budget of the Asian monsoon. This hemisphere contributes 50% more than the extra-Asian monsoon hemisphere to the global rainfall. Since the rainfall of the Asian monsoon hemisphere undergoes variations of different timescales, the global rainfall is also subjected to the same variations. It was observed that the extra-Asian monsoon hemisphere is a water

vapor source. Therefore, the rainfall and interhemispheric divergent water vapor flux in this hemisphere vary out-of-phase with the extra-Asian monsoon hemisphere. These east–west seesaw variations of hemispheric hydrological variables are caused by the propagation of global-scale oscillations. In this section, the effect/modulation of these global modes on the rainfall and water vapor transport of the regional monsoon circulation will be illustrated by means of downscale processes.

10.4.1 Diurnal variation

Because of the lack of sufficient station observations, particularly over oceans, satellite observations around the tropical belt were often used as proxies for tropical rainfall; for example, the tropical rainfall estimations by a threshold value of the National Oceanic and Atmospheric Administration (NOAA) outgoing long-wave radiation (Janawiak *et al.*, 1994), the Tropical Rainfall Measuring Mission (TRMM) Satellite measurements (Nesbitt and Zipser, 2003), and the combination of the oceanic rainfall observed by the Special Sensor Microwave Imager (SSM/I) and TRMM measurements (Imaoka and Spencer, 2000). On the other hand, Dai (2001) analyzed the diurnal variation of global precipitation using the merged station observations over the globe with the comprehensive ocean–atmosphere data set (CODAS; Woodruff *et al.*, 1987). Common features of the diurnal variation in tropical rainfall observed by these studies are: (1) rainfall/convection tends to reach its maximum over the oceans in the early morning and over land in the evening, and (2) amplitude of the diurnal variation of tropical rainfall/convection is much larger over land than over the oceans.

The direct atmospheric response to any change in diabatic heating is the divergent circulation (Chen and Yen, 1991a,b). Because the Earth rotates eastward, the immediate atmospheric response to the diurnal variation of the solar heating is reflected by the westward propagation of the diurnal component of the global divergent circulation. Most studies of diurnal variation in the global rainfall, including those referred to above, focused primarily on precipitation in the tropical belt. It is difficult for us to infer from these studies how the diurnal variation of tropical rainfall is coupled with that of the global atmospheric circulation. This concern may be addressed by the following approach. Recall that $\nabla \cdot Q = \nabla^2 \chi_Q$. Convergence (divergence) of water vapor flux is coupled with a positive (negative) center of the χ_Q field. As shown by (10.1), precipitation is maintained (suppressed) by convergence (divergence) of the water vapor flux. Although these two variables are local hydrological processes, they can be linked to the global divergent circulation through the potential function of the water vapor flux. Based on this argument, it is expected that diurnal components of both variables (χ'_Q, P') propagate westward. This inference is substantiated by composite charts of these two variables every three hours in Figure 10.10. In order to distinguish the day and night, noon and midnight are marked by open thin solid and thick solid lines, respectively. The westward propagation of solar heating is clearly indicated by these time lines.

The land–ocean contrasts of P' amplitudes (larger over land than ocean) are

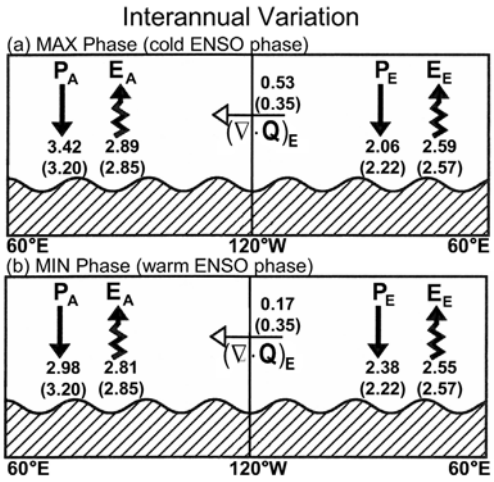

Figure 10.9. Same as Figure 10.1(b), except for the interannual ENSO mode: (a) maximum phase and (b) minimum phase determined by ΔP_A and ΔSST (Niño 3.4) time series. An example is shown in Figure 10.3(c).

clearly evident in Figure 10.9. The phase of maximum P' (over land in the afternoon/evening; over ocean in early morning) is well presented. The best example shown in Figure 10.9 to support this observation would be rainfall at 12Z–15Z over the central western tropical Pacific and 12Z–18Z over the Asian Maritime Continent. In addition to these traditional observations of tropical rainfall diurnal variation, it is also of interest to note that the spatial coverage of P' anomalies over the Asian monsoon hemisphere is much larger than that over the extra-Asian monsoon hemisphere.

The westward propagation of (χ'_Q, P') anomalies is clearly discernable in Figure 10.10. As expected, positive (negative) P' anomalies are always coincident with a positive (negative) χ'_Q center. It was shown in Figure 10.3(a) that a diurnal seesaw oscillation exists between P_A and P_E: P_A (P_E) gains its maximum (minimum) at 12Z and minimum (maximum) at 00Z. This east–west diurnal seesaw oscillation of rainfall between the two hemispheres coincides with the centers of χ'_Q anomalies. Evidently, this diurnal seesaw oscillation of rainfall is a result of the hemispheric hydrological cycle modulated by the westward propagation of the global divergent circulation reflected by the global χ'_Q anomalies. Recall that the spatial coverage of P' over the Asian monsoon hemisphere is larger than that of the extra-Asian monsoon hemisphere. It is not surprising to see that diurnal variation of P_G follows P_A. Because positive (negative) P' anomalies coincide with positive (negative) χ'_Q centers, diurnal variation of $(\nabla \cdot Q')_E$ is in phase with P'_A, but out of phase with P'_E.

The atmospheric diurnal tidal wave may be divided into *migrating* and *non-migrating* components (Chapman and Lindzen, 1970). The migrating component displays a wavenumber-1 structure, while the non-migrating component exhibits the regional-scale structure. Do χ'_Q anomalies (shown in Figure 10.10) behave like

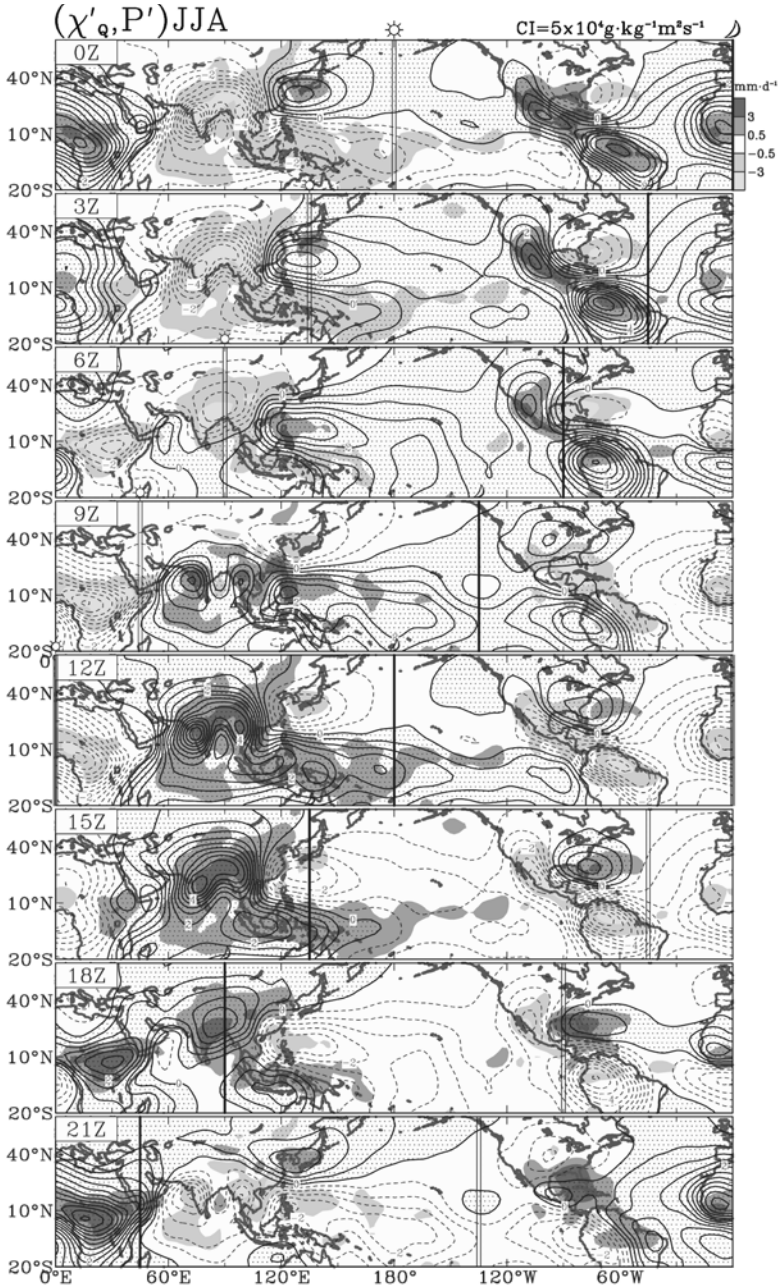

Figure 10.10. Composite charts of (χ'_Q, P') (JJA) every three hours: χ'_Q anomalies are contoured while P' anomalies are stippled. Local noon and midnight are marked by an open strip and thick solid line, respectively. The contour interval of χ'_Q anomalies is $5 \times 10^4\,\mathrm{g\,kg^{-1}\,m^2\,s^{-1}}$ and P' anomalies are colored with the gray colors shown in the lower right side of the top panel of (χ'_Q, P') at 00 UTC.

diurnal tidal waves? In addition to its westward propagation, a clear clockwise rotation of the (χ'_Q, P') anomalies appears over Asia and the Americas. To obtain a better view of the clockwise (χ'_Q, P') anomalies over the Asian continent and the western Pacific, these two variables in the Asian monsoon hemisphere are extracted out every three hours from Figure 10.10 and are shown in Figure 10.11. What is the cause of such an interesting rotation of (χ'_Q, P') anomalies around a major continent and its surrounding oceans? The tropical troposphere is generally conditionally unstable (Riehl, 1979), while the troposphere of middle to high latitudes is stable. Convection can be triggered by diabatic heating faster in the warm tropics than in the cool middle to high latitudes. On the other hand, soil and rock have smaller heat capacities than air. Because the Himalayas and the Rockies are located west of the Pacific and the Atlantic, respectively, the east–west land–ocean contrast results in an east–west differential response to the solar heating which is enhanced by these major mountain ranges. The response of the tropical troposphere, which has a lower land–ocean contrast and fewer major mountain ranges, is dominated by the westward-propagating wave-1 migrating component of diurnal variation. In contrast, the tropospheric response in the subtropics–mid-latitudes is dominated by the non-migrating component, whose scale is primarily determined by the effect of the land–ocean contrast and whose response is faster over land than ocean. The clockwise rotations of (χ'_Q, P') anomalies over Asia and North America, and their surrounding oceans are essentially formed by the north–south difference in the tropospheric response to the westward moving solar heating.

Analyzing the diurnal mode of the Asian summer monsoon, Krishnamurti and Kishtawal (2000) found that the diurnal component of divergent circulation in the afternoon hours has an ascending center over north central India with its divergent air descending around the surrounding regions. The reverse occurs in the morning hours. The χ'_Q anomalies at 12Z and 00Z in Figure 10.11 match their finding over south Asia. Actually, the diurnal χ'_Q mode (which is a reflection of χ' (850 mb) or $-\chi'$ (200 mb)) exhibits not only the diurnal pulsation of the continental-scale divergent circulation, but a clockwise rotation over the Asian continent and its surrounding oceans. This rotation of (χ'_Q, P') anomalies is further confirmed by the phase (timing) of the diurnal variation of rainfall observed/compiled by the GEWEX (Global Energy and Water Cycle Experiment) Asian Monsoon Experiment (GAME). Two approaches were adopted to depict the phase of the diurnal rainfall variation: universal coordinated time (UTC) and local solar time (LST). The Cressman (1959) scheme was applied to project station observations of GAME rainfall on $2.5^\circ \times 2.5^\circ$ boxes. A clear clockwise rotation in the phase of the diurnal rainfall variation emerges from both approaches.

The diurnal variation of any meteorological variable is one of the most regular and significant climate signals (next to annual variation). Diurnal variations of the Asian monsoon rainfall and hydrological processes in maintaining this rainfall are results of multiple complex downscale hydrological processes of the atmosphere in response to the westward migration of solar heating. This response includes not only the westward propagation of a global-scale migrating component, but also the clockwise rotation of a continental-scale non-migrating component.

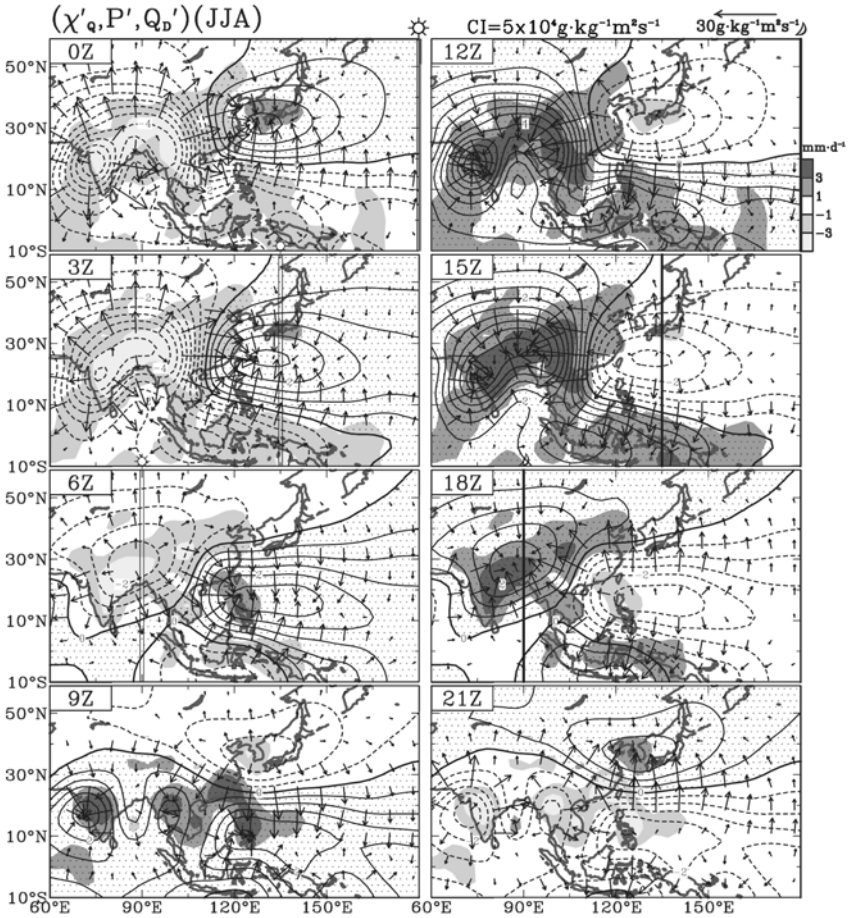

Figure 10.11. Enlarged regional composite charts of (χ'_Q, Q', P') (JJA) anomalies in the Asian monsoon hemisphere every three hours extracted out of the corresponding global composite charts in Figure 10.10: P' anomalies are stippled in terms of the grayscale shown in the lower right-hand side of the (χ'_Q, Q', P') composite chart at 12 UTC. Local noon and midnight are marked by an open strip and thick solid line, respectively. The contour interval of χ'_Q is $5 \times 10^4\,\mathrm{g\,kg^{-1}\,m^2\,s^{-1}}$.

10.4.2 Intraseasonal variation

The intraseasonal (30–60-day and 12–24-day) seesaws of P_A and P_E were caused by eastward propagation of these two global intraseasonal modes (Chen *et al.*, 1995a,b) which will be illustrated later in this section. On the other hand, one may question how these two global intraseasonal modes affect the local monsoon circulation and local weather systems (which are embedded in the monsoon circulation) which are effective producers of monsoon rain. The monsoon rainfall and the activity of the

rainfall-generating synoptic systems in south Asia are generated/modulated by the coupling of the global intraseasonal modes with the regional 30–60-day monsoon trough/ridge (Krishnamurti and Subrahmanyam, 1982; Chen *et al*., 1988b), and the westward propagation of the 12–24-day monsoon mode (Chen and Chen, 1993). How do these global intraseasonal modes modulate the summer monsoon rainfall in east Asia? Water vapor transport in this region, particularly along the Meiyu rainfall belt is fluctuated by the 30–60-day mode (Chen *et al*., 1988b). The regional monsoons in the South China Sea and east Asia are coupled by the 30–60-day and 12–24-day monsoon modes (Chen *et al*., 2000). This interaction is reflected by the intraseasonal variation of east Asian rainfall observed by Lau *et al*. (1988). It is inferred from these studies that variation of the east Asian monsoon rainfall is profoundly affected by global intraseasonal modes through certain downscale interactions with the regional circulation and rainfall-producing synoptic systems.

Using station measurements of rainfall in south China, Hong Kong, Taiwan, and Japan, Ramage (1952) pointed out that major rainfall in east Asia was generated by cold fronts before the monsoon break and by tropical cyclones after the break. Because rainfall observations over the ocean by satellites and reanalysis data became available, Ramage's suggestion was confirmed by an extensive study performed by Chen *et al*. (2004a). The east Asian summer monsoon is characterized by the northward migration of the Meiyu rain belt, the monsoon life cycle (including its onset in mid-May, break in late June-early July, and revival in late July), and the active typhoon season after the monsoon break. These characteristics are revealed from the y–t diagram of rainfall at 120°E–125°E (Figure 10.13(a)). In addition to the monsoon life cycle, both the Meiyu rain belt and the ITCZ also undergo intraseasonal variation with a timescale smaller than the monsoon life cycle. The rainfall time series of every summer season at (22.5°–25°N, 120°–125°E) were subjected to a power spectral analysis. The 30–60-day and 12–24-day intraseasonal modes emerge from the averaged power spectra (Figure 10.13(b)). After removing the yearly mean, annual and semiannual components from the rainfall y–t diagram (Figure 10.13(a)), the y–t diagram of rainfall departure (δP) is shown in Figure 10.13(c). Evidently, the monsoon life cycle and intraseasonal variation of shorter timescales are largely determined by 30–60-day and 12–24-day modes. It is revealed from Figure 10.13 that intraseasonal variations of the east Asian monsoon rainfall are modulated by the global intraseasonal modes through certain downscale processes.

In order to illustrate this downscale process, let us first understand how the global intraseasonal modes affect intraseasonal variations of the hemispheric water vapor budgets. This local impact of the global intraseasonal modes is depicted by composite charts of the two global intraseasonal modes. The composite procedure is as follows:

(1) *Selection of 30–60-day and 12–24-day cycles*: using $(\tilde{P}_A)$ and $(\hat{P}_A)$ as indices, we select these half cycles with their amplitudes larger than 0.8 or smaller than -0.8 of the corresponding standard deviations over the summer (May–September) season.

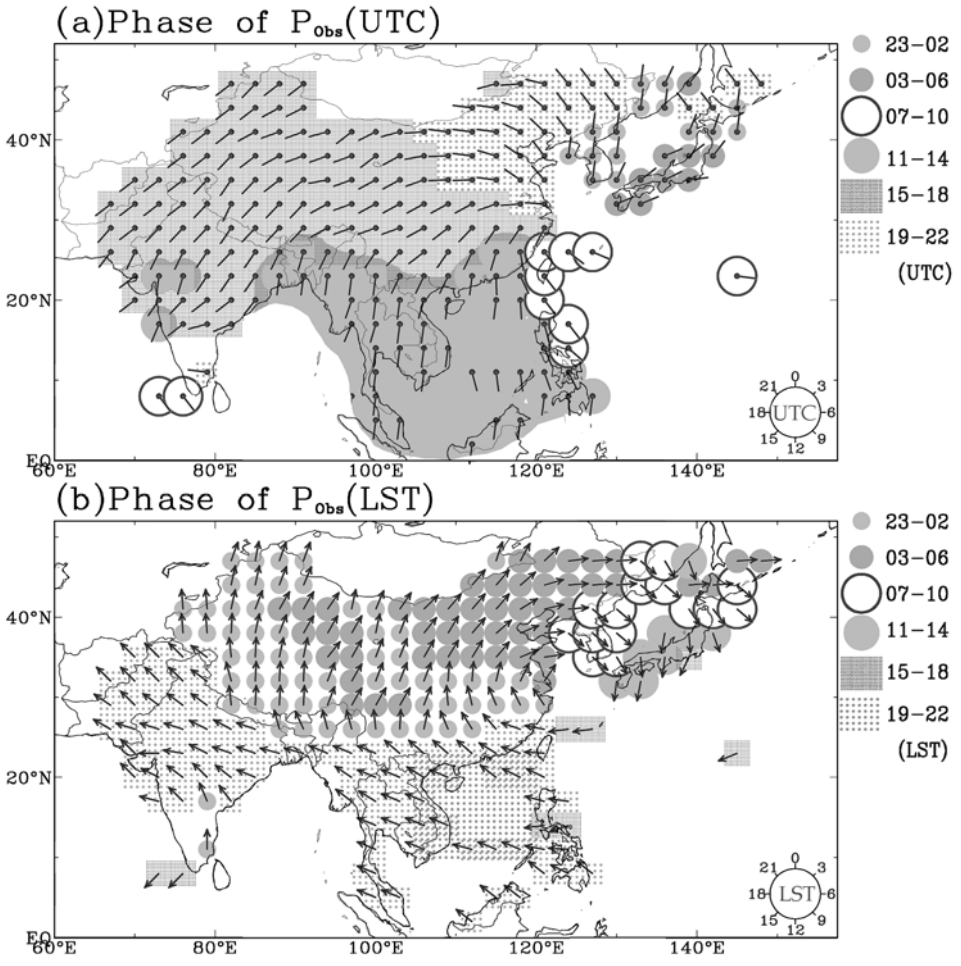

Figure 10.12. Maximum phase of the P diurnal cycle expressed in terms of (a) UTC and (b) LST. The maximum P phase is indicated by a stick with a dot on its root (UTC) or an arrow (LST).

(2) *Definition of phases*: a cycle of the 30–60-day mode is divided into eight phases (Figure 10.7(a)), while a cycle of the 12–24-day mode is split into six phases (Figure 10.7(b)). Composite charts of $(\tilde{\chi}_Q, \tilde{P})$ and $(\hat{\chi}_Q, \hat{P})$ at each phase are prepared with five and three-day averages, respectively, centered on the date of the selected phase.

Composite charts of $(\tilde{\chi}_Q, \tilde{P})$ and $(\hat{\chi}_Q, \hat{P})$ over their entire life cycles are shown in Figure 10.14(a) and (b), respectively. Both the $\tilde{\chi}_Q$ and $\hat{\chi}_Q$ anomalies exhibit a wavenumber-1 structure and relatively regular eastward propagation. $\tilde{P}_A$ and $\hat{P}_A$ attain their maxima at phase 2, when positive $\tilde{\chi}_Q$ and $\hat{\chi}_Q$ centers are located over the

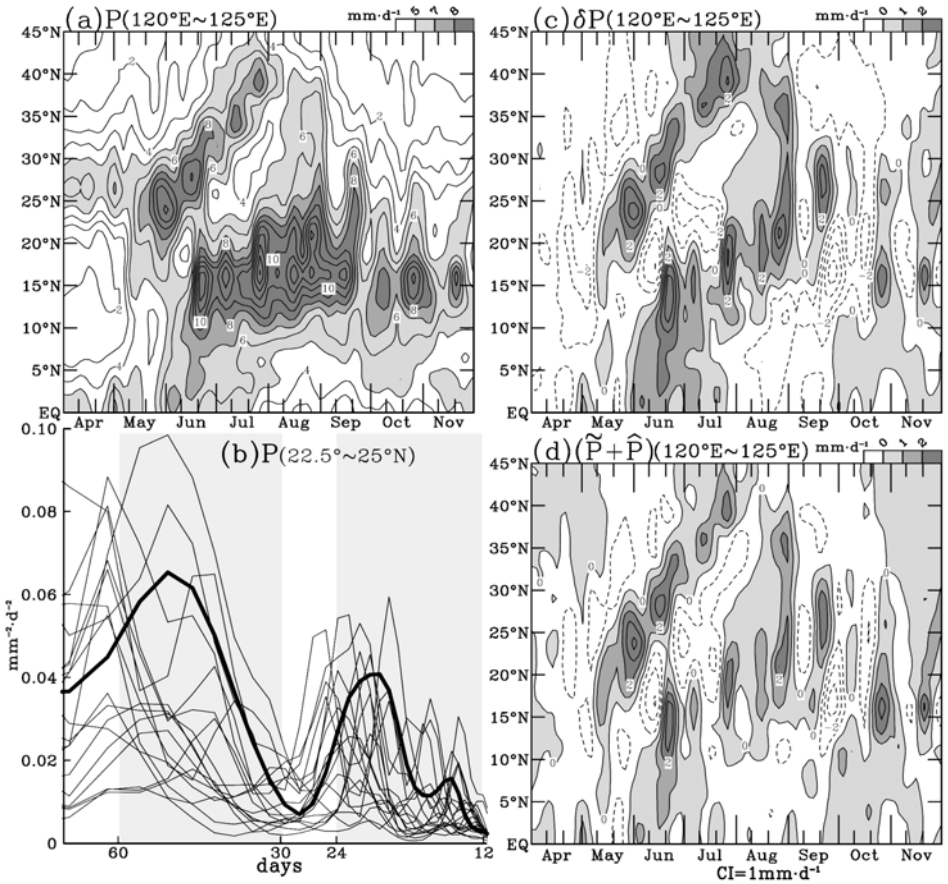

Figure 10.13. *y–t* diagrams of various P anomalies at 120°–125°E and power spectra of δP anomalies (P anomalies with their annual mean, annual, and semiannual components removed): (a) P, (b) δP, and (c) $\tilde{P} + \hat{P}$. Power spectra of δP at (22.5°–25°N) for every summer (thin solid lines) and averaged power spectra (thick solid line) are shown. Contour intervals of P, δP, and $\tilde{P} + \hat{P}$ are shown on the top of each panel.

western tropical Pacific (the Asian monsoon hemisphere). During this phase, $\tilde{P}_E$ and $\hat{P}_E$ obtain their minima, when negative $\tilde{\chi}_Q$ and $\hat{\chi}_Q$ centers are located over northeast Brazil (the extra-Asian monsoon hemisphere). Spatial phase structures of both $\tilde{\chi}_Q$ and $\hat{\chi}_Q$ are reversed when ($\tilde{P}_A$ (phase 6), and $\hat{P}_A$ (phase 5)) and ($\tilde{P}_E$ (phase 2), $\hat{P}_E$ (phase 2)) reach their minima and maxima, respectively. According to time series of hydrological variables shown in Figure 10.6, $\tilde{P}_A$ maxima (minima) and $\tilde{P}_E$ minima (maxima) are coupled with $(\nabla \cdot \tilde{Q})_A$ minima (maxima)/$(\nabla \cdot \tilde{Q})_E$ maxima (minima). The same contrast is also applicable to the 12–24-day mode. Comparing variations in time series of P_A, P_E, $(\nabla \cdot Q)_A$, and $(\nabla \cdot Q)_E$ with $(\tilde{\chi}_Q, \tilde{P})$ and $(\hat{\chi}_Q, \hat{P})$ composite charts, it becomes clear that intraseasonal variations of P_A and P_E are caused by eastward propagation of these two global intraseasonal modes. In addition,

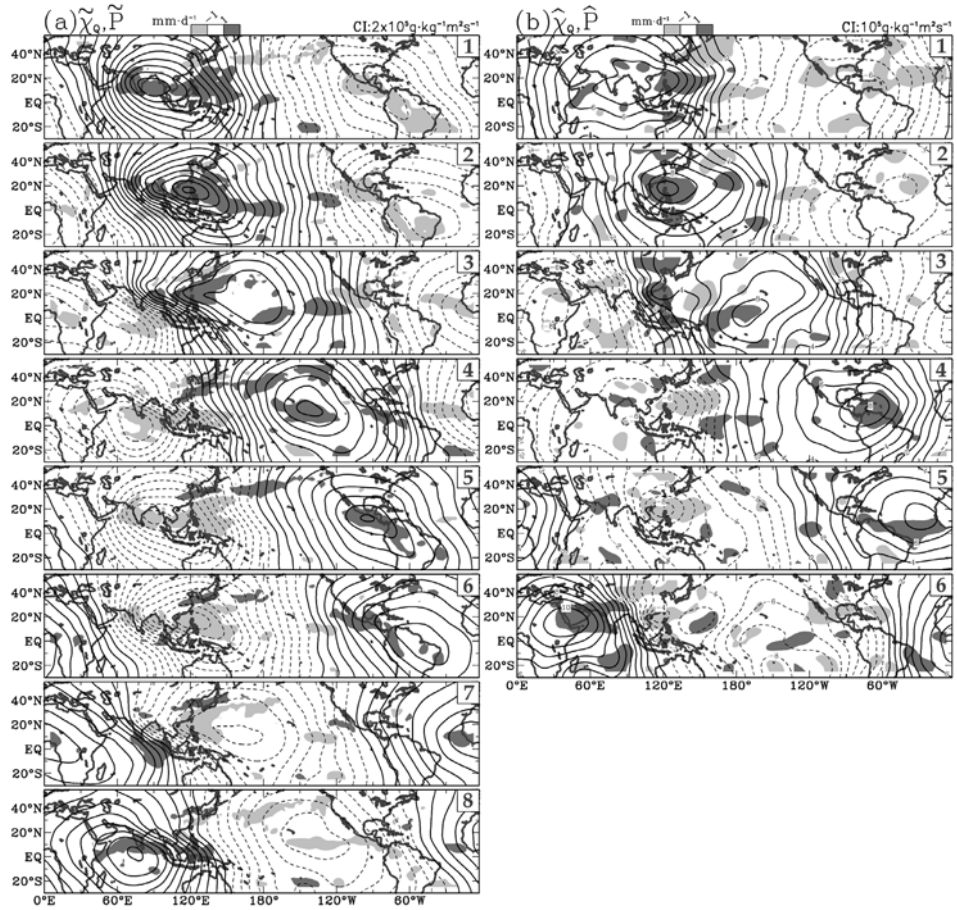

Figure 10.14. Summer (May–September) composite charts of (a) $(\tilde{\chi}_Q, \tilde{P})$ and (b) $(\hat{\chi}_Q, \hat{P})$ anomalies based on phases defined by $\tilde{P}_A$ and $\hat{P}_A$ indices shown in Figure 10.7. Contour intervals of $\tilde{\chi}_Q$ and $\hat{\chi}_Q$, and scales of $\tilde{P}$ and $\hat{P}$, are shown at the top of the first panel in each column.

hemispheric divergence of water vapor flux is also perturbed by these two global intraseasonal modes in such a way that water vapor diverges from the hemisphere of rainfall decrease and converges toward the hemisphere of rainfall increase.

Because rainfall and divergence of water vapor flux are local hydrological processes, how do the two global intraseasonal modes affect these local processes? As shown in Figure 10.13(a), the majority of east Asian summer rainfall is generated along the Meiyu rain belt before the monsoon break and tropical cyclones after the break. It is revealed from the contrast between Figure 10.13(c) and (d) that rainfall variations in east Asia are caused by the two intraseasonal modes. The impact of the global intraseaonsal modes on east Asian rainfall should be achieved through the downscale interaction of these global modes with the regional monsoon circulation/

synoptic weather systems. This downscale interaction will be illustrated in terms of the regulation of the two intraseasonal modes on the northward migration of the Meiyu rain belt/frontal activity and on the tropical cyclone occurrence frequency as indicated by the y–t diagrams of $\tilde{P}$ and $\hat{P}$. Note that the atmospheric circulation is well depicted by the rotational component of atmospheric flow. For this reason, we shall use the intraseasonal modes of the streamfunction of water vapor flux to illustrate the downscale interaction.

30–60-day mode

In southern south-east Asia and the western tropical Pacific, the eastward-propagating global 30–60-day mode couples with the monsoon trough/ridge through the local Hadley circulation (Chen *et al*., 1988b; Chen and Chen, 1995). The eastward propagation of this global 30–60-day mode migrates the monsoon ridge/trough northward from the equator, and regulates the monsoon life cycle over this region (Krishnamurti and Subahmanyan, 1982; Lorenc, 1984; Krishnamurti *et al*., 1985; Chen *et al*., 1988b). The eastern end of the 30–60-day monsoon trough/ridge generally exhibits a cyclonic/anticyclonic cell over the South China Sea and the western tropical Pacific. This local intraseasonal circulation, which is well depicted by $\tilde{\psi}_Q$ anomalies in Figure 10.15, migrates northward from the vicinity of the equator to 30°–35°N, as shown by the y–t diagram of $\tilde{\psi}_Q$ anomalies at 120°E for the 1996 summer. The frontal activity (shaded areas) and locations of tropical cyclones (dots) during different phases of the 30–60-day monsoon mode are superimposed on $\tilde{\psi}_Q$ anomalies (Figure 10.15(a)). Tropical cyclone occurrence is enhanced over the intraseasonal $\tilde{\psi}_Q$ cyclonic cell, while frontal activity is intensified along the northern rim of the intraseasonal $\tilde{\psi}_Q$ anti-cyclonic cell, where water vapor flux along the Meiyu rain belt is increased. The contrast between tropical cyclone/frontal activity (Figure 10.15(a)) and rainfall anomalies (Figure 10.15(b)) over the entire life cycle of the local 30–60-day intra-seasonal mode indicates that the east Asian monsoon rainfall is primarily generated by these two types of synoptic disturbances. In turn, the activity and occurrence locations of these synoptic disturbances are regulated by the regional intraseasonal mode which is coupled with the eastward-propagating 30–60-day mode. Evidently, the intraseasonal variation of P_A in east Asia is formed by such a downscale interaction.

12–24-day mode

In Figure 10.13, a 12–24-day signal along the Meiyu rain belt and the ITCZ stands out in the y–t diagram of east Asian summer rainfall at 120°–125°E. What are the possible synoptic disturbances generating this rainfall variation signal? Cold surges are the most pronounced synoptic activities in the east Asian winter monsoon system. The cold front associated with a cold surge is coupled with the eastward propagating upper level short-wave trough in north-east Asia (e.g., Lau and Lau, 1990; Chen *et al*., 2002). Following the cold surge front, the cold air intrusion brings precipitation across east Asia. In late spring, the upper level east coast jet becomes

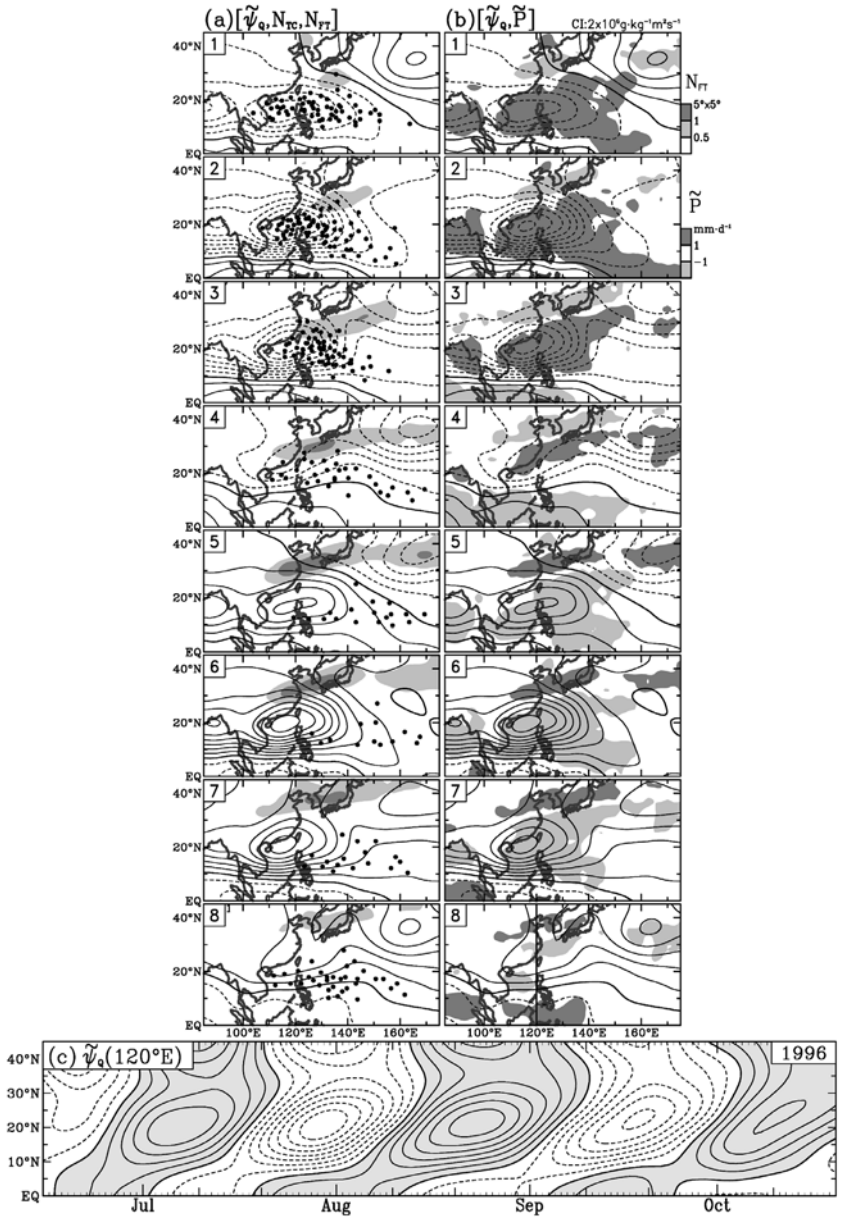

Figure 10.15. Composite charts of $\tilde{\psi}_Q$ anomalies in the east Asian region for all eight phases of the 30–60-day cycle corresponding to those shown in Figure 10.14(a) and superimposed with N_{FT} (frontal occurrence frequency) and N_{TC} (dot; tropical cyclone locations) in (a) and with $\tilde{P}$ anomalies in (b). The northward migration of the 30–60-day $\tilde{\psi}_Q$ mode, which may be perceived from composite charts of $\tilde{\psi}_Q$ over its entire life cycle (eight phases), can be summarized by (c) the y–t diagram of $\tilde{\psi}_Q$ (120°E) anomalies in 1996 summer. The contour interval of $\tilde{\psi}_Q$, numerical values of N_{FT}, and scale of $\tilde{P}$ are shown around the top right corner.

weaker. At this time, the passage of cold fronts over east Asia are usually slow because the eastward propagation speed of the mid-latitude short-wave trough is reduced by the weakening of mid-latitude westerlies. Therefore, the slowly moving cold fronts form the Meiyu rain belt. This circulation evolution will not stop until the east Asian monsoon break. It was shown by Compo *et al.* (1999) that the cold front/surge activity in east Asia exhibits a 12–24-day signal of surface pressure. This signal of rainfall along the Meiyu rain belt is a reflection of the frequent passage of cold fronts. On the other hand, the rainfall variation along the ITCZ is caused by tropical cyclone activity. Chen *et al.* (2004b) observed that approximately 70% of tropical cyclogeneses over the western tropical Pacific are linked to monsoon gyres (Lander, 1994). The occurrence of monsoon gyres is evolved from the perturbation of the NW–SE oriented monsoon trough (which extends from Indo-China across the northern part of the South China Sea to the Philippine Sea) by the intraseasonal monsoon trough/ridge (Chen *et al.*, 2005). Since the monsoon gyre occurrence shows a preferred timescale of 12–24 days, it is not surprising that tropical cyclogenesis in the western tropical Pacific undergoes such a temporal variation.

The mechanisms generating the 12–24-day rainfall signal in east Asia *before* and *after* the monsoon break in late June and early July defined by Chen *et al.* (2004a) differ from each other. The modulation of the regional 12–24-day modes on rain-producing synoptic systems and the link between these regional modes and the global mode are illustrated in Figure 10.16 in terms of composite charts of $\hat{\psi}_Q$ anomalies for all six phases determined by the $\hat{P}_A$ index (Figure 10.13(b)). The rain-producing systems are cold fronts along the Meiyu rain belt *before* the monsoon break and tropical cyclones *after* the break. Therefore, the cold front (N_{FT}) and tropical cyclone (N_{TC}) occurrence frequencies are superimposed on $\hat{\psi}_Q$ anomalies in Figure 10.16(c). As indicated by the y–t diagram of $\hat{\psi}_Q$ anomalies in Figure 10.16(e), the cellular $\hat{\psi}_Q$ structure migrates south-eastward before the monsoon break. This propagation characteristic is a reflection of the south-eastward movement of synoptic disturbances associated with cold fronts. The SW–NE oriented strip of $\hat{P}$ anomalies (Figure 10.16(b)) are coincident with the frontal occurrence frequency N_{FT} in Figure 10.16(a). Both positive (negative) values of $\hat{\psi}_Q$ and maximum (minimum) N_{FT} appear when the $\hat{P}_A$ index reaches its maximum (minimum). Evidently, the east Asian rainfall variation modulated by the regional 12–24-day mode coincides with the hemispheric water vapor budget and the eastward propagation of the global 12–24-day mode.

After the break, the Meiyu rainbelt no longer exists in East Asia, and tropical cyclones become the major rainfall producer. The y–t diagram of $\hat{\psi}_Q$ anomalies (Figure 10.16(e)) exhibits a northeastward propagation opposite to that which occurred before the break by the south-easterlies along the southwest rim of the North Pacific anticyclone. It is of interest to note that the tropical cyclone occurrence frequency (*TC* locations denoted by dots) is suppressed by a positive (anticyclonic) $\hat{\psi}_A$ cell, but enhanced by a negative (cyclonic) $\hat{\psi}_A$ cell. Therefore, we can find in Figure 10.16(d) that positive (negative) $\hat{P}$ anomalies appear over negative (positive) cells of $\hat{\psi}_Q$ anomalies when $P_A(P_E)$ reaches a maximum (minimum) during phase 2(5) of the 12–24-day mode. The link between this regional 12–24-day mode activity

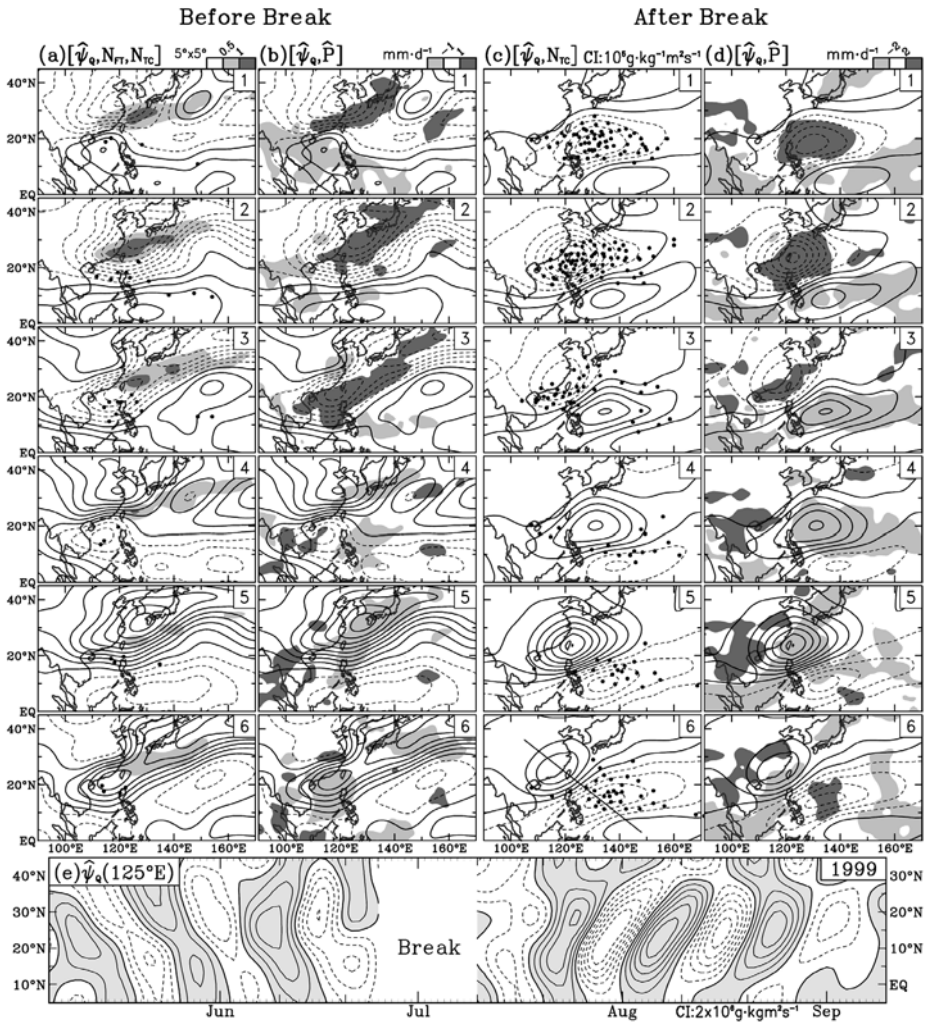

Figure 10.16. Same as Figure 10.15, except for six phases of the 12–24-day mode of $\tilde{\psi}_Q$ before (a, b) and after (c, d) the Asian monsoon break, and (e) the y–t diagram of $\hat{\psi}_Q$ (125°E) in the 1999 summer before the monsoon break, and in the 1999 summer after the break. The contour interval of $\tilde{\psi}_Q$, scale of N_{FT}, and $\hat{P}$ anomalies are shown on the top of each column.

and the hemispheric/global hydrological cycle is revealed through composite charts of N_{TC}, $\hat{\psi}_Q$, and $\hat{P}$ anomalies over the 12–24-day cycle.

10.4.3 Interannual variation

As pointed out previously, interannual variations of rainfall in different regions of the Asian monsoon may be caused by different mechanisms. It may seem unlikely to

bring out a coherent interannual variation of rainfall over the entire Asian monsoon system by combining these variations in different monsoon regions. On the other hand, within the context of the ENSO cycle, the contrast of time series of hydrological hemispheric variables and ΔSST (Niño 3.4) in the two hemispheres provides a systematic perspective of the hydrological cycle of the Asian monsoon hemisphere: its contribution to the global hydrological cycle, and its relationship with the hydrological cycle of the extra-Asian monsoon hemisphere. Actually, our main concern here is how the interannual variation of rainfall in the two hemispheres is related to the global circulation. To address this concern, the tropical x–t diagram of $\Delta(\chi_Q, P)$ is shown in Figure 10.17(a). The extreme summers of the ENSO cycle are defined by the following criteria: *warm* when ΔSST (Niño 3.4) $\geq 0.5^{\circ}$C and *cold* when ΔSST (Niño 3.4) $\leq -0.5^{\circ}$C. The warm and cold summers are marked by thick (thin) solid lines on the x–t diagrams of $\Delta(\chi_Q, P)$.

The ENSO cycle is often depicted in the tropics by an east–west seesaw oscillation of surface pressure between the Indo-western tropical Pacific and the central eastern tropical Pacific, or an east–west seesaw variation of SSTs between the two sides of the tropical Pacific. It was observed by Barnett (1983, 1984a,b, 1985, 1988) that following the ENSO cycle, tropical surface winds and pressure exhibit a clear eastward propagation from the Indian Ocean to the central Pacific. The interannual variation of summer ΔSST (Niño 3.4) may not always follow that of *winter* ΔSST (Niño 3.4). A clear eastward propagation emerges from the tropical x–t diagram of summer $\Delta(\chi_Q, P)$ anomalies. P_A and P_E gain their maximum and minimum in Figure 10.3(c), when positive and negative $\Delta\chi_Q$ centers are located over the Asian and extra-Asian monsoon hemispheres, respectively. In contrast, P_A and P_E reach their minimum and maximum, when the reversed spatial structure of $\Delta\chi_Q$ occurs. It becomes clear that interannual variations of P_A and P_E are modulated by the ENSO cycle through the eastward propagation of the global divergent circulation in response to the interannual variation of the tropical Pacific SST anomalies. This eastward propagation of summer $\Delta(\chi_Q, P)$ anomalies is further illustrated by the transition of the global $\Delta(\chi_Q, P)$ distribution from the 1982 summer warm episode, through the 1984–1985 summer cold episodes, to the 1987 summer warm episodes (Figure 10.18). As shown by Chen and Yoon (2000), a positive (negative) center of $\Delta(\chi_Q, P)$ is located over the Asian monsoon hemisphere during cold (warm) summers. The transition between them is not caused by an east–west seesaw oscillation, but by the eastward propagation of $\Delta(\chi_Q, P)$ anomalies. Note that $P_G = \frac{1}{2}(P_A + P_E)$. The in-phase interannual variations of P_G and P_A indicate once again that rainfall/convection in response to the global ENSO mode is more sensitive over the Asian monsoon hemisphere than the extra-Asian monsoon hemisphere.

Our next concern is how the global ENSO mode affects interannual variation of regional monsoon rainfall in the Asian monsoon system. We shall illustrate its impact on the east Asian monsoon rainfall as an example of downscale interaction. Because the atmospheric circulation is largely depicted by the rotational flow, the interannual variation of the east Asian summer circulation to positive SST anomalies over the western tropical Pacific is a short-wave train (emanating from this region) along the rim of the North Pacific with an anticyclonic cell over Korea and Japan.

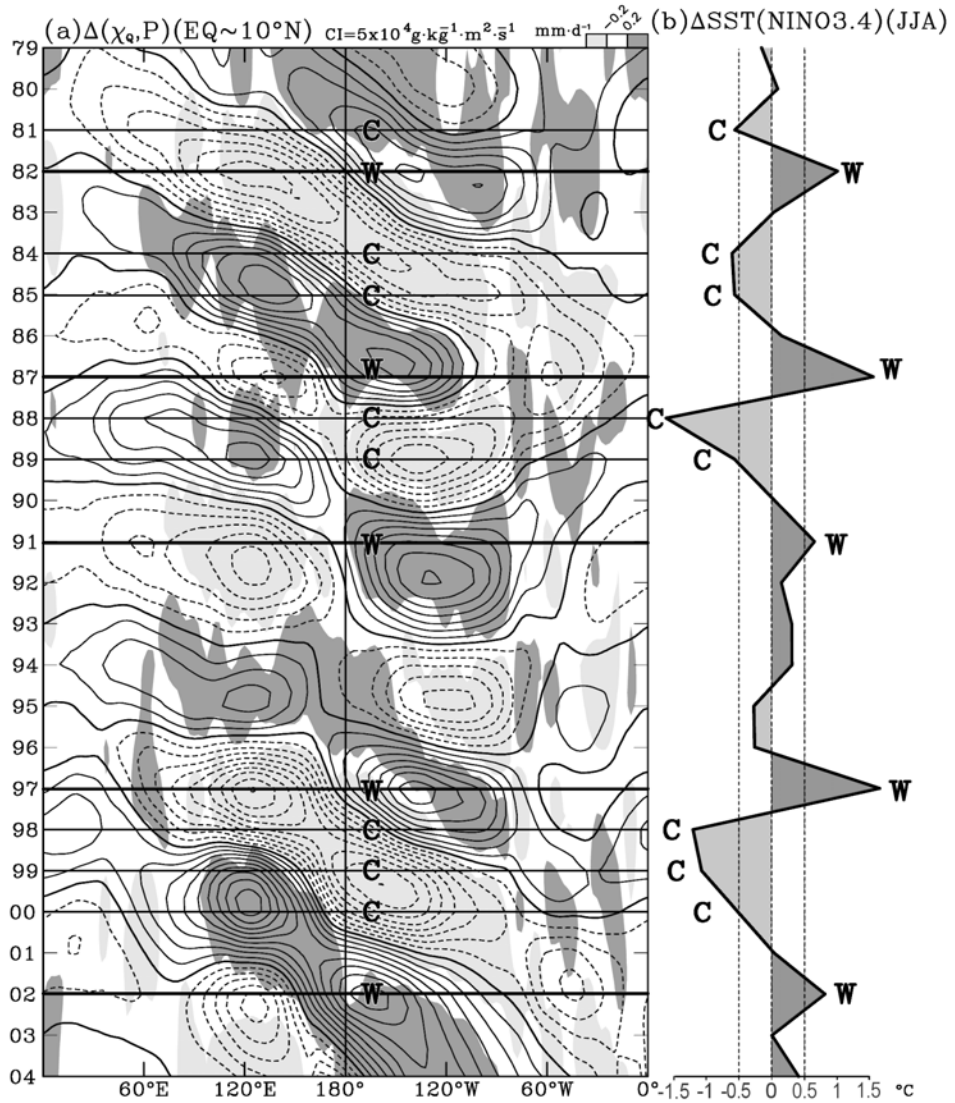

Figure 10.17. (a) The x–t diagram of $\Delta(\chi_Q, P)$ (eq–10°N) anomalies and (b) time series of ΔSST (Niño 3.4) (JJA). Warm (cold) extreme summers are defined by ΔSST (Niño 3.4) $\geq -0.5^\circ$ (≤ -0.5°C) and marked by W (C). The contour interval of $\Delta\chi_Q$ is 5×10^4 g kg^{-1} m^2 s^{-1} and the grayscale of ΔP is shown at the top of (a).

The reversed phase anomalous short-wave train appears during cold western tropical SST anomalies. The dipole of anomalous circulation in the western Pacific was named by Nitta (1986, 1987) as the *Pacific–Japan pattern*. Later, it was shown by Chen *et al*. (1998) that the southern cell of this pattern not only shifts northward, but also enhances the tropical cyclone occurrence frequency when SST anomalies in the

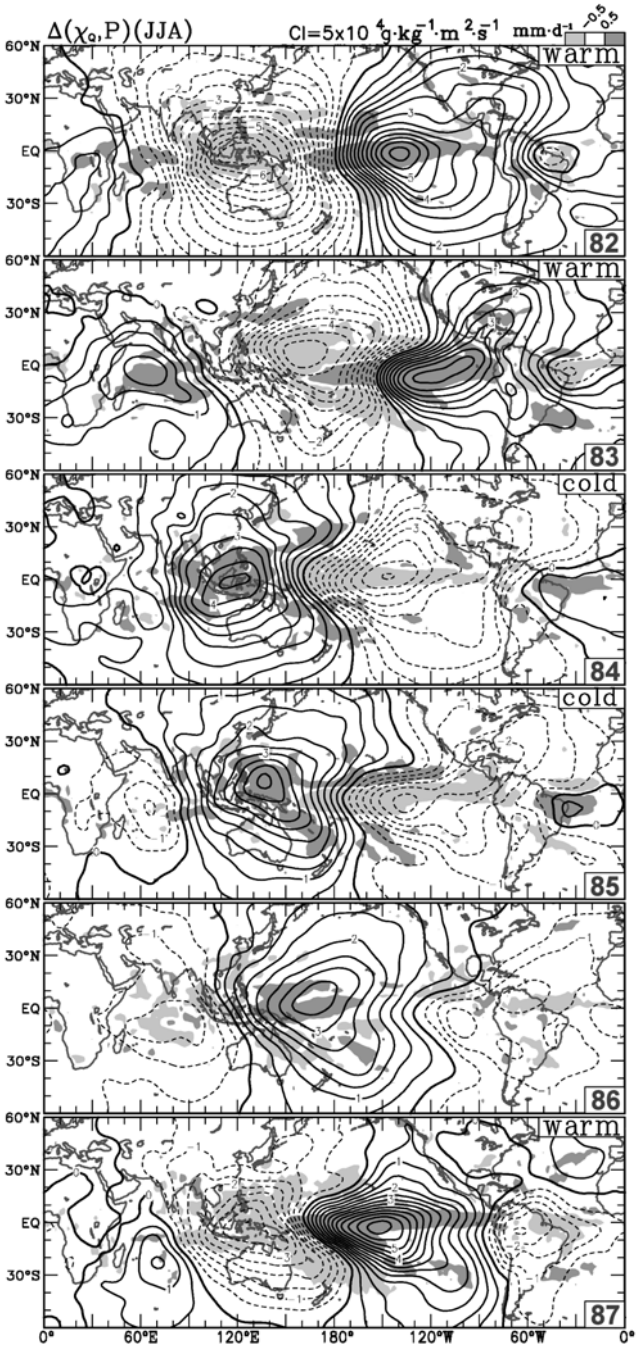

Figure 10.18. The eastward propagation of summer $\Delta(\chi_Q, P)$ anomalies is illustrated by the warm-cold-warm ENSO cycle (1982–1987).

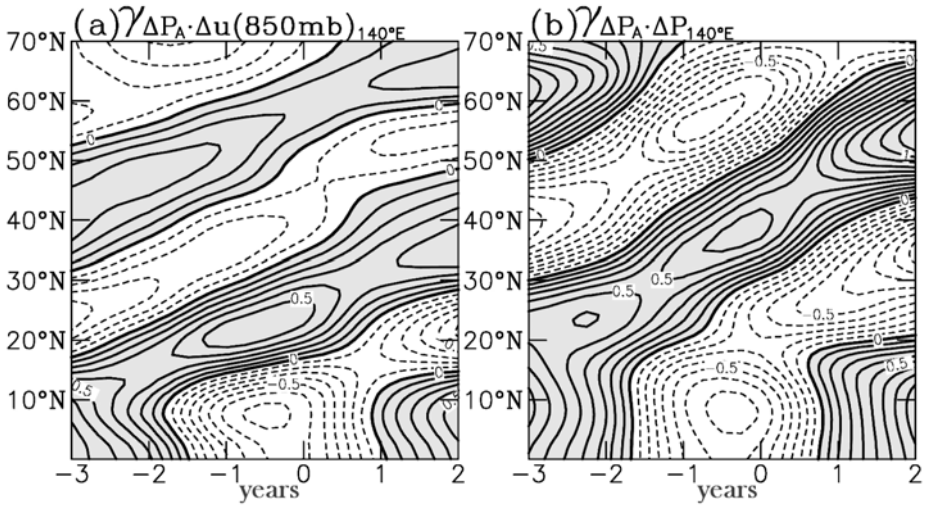

Figure 10.19. The y–t diagram of lagged correlation coefficients (a) $r_{\Delta P_A \cdot \Delta u(850\,\mathrm{mb})140°\mathrm{E}}$ between ΔP_A and $\Delta u(850\,\mathrm{mb})_{140°\mathrm{E}}$ and (b) $r_{\Delta P_A \cdot \Delta P_{140°\mathrm{E}}}$ between ΔP_A and $\Delta \mathrm{P}_{140°\mathrm{E}}$.

western tropical Pacific become warmer. In contrast, tropical cyclone activity is weakened and migrates southward during cold SST anomalies of the western tropical Pacific.

The transition of summer global $\Delta(\chi_Q, P)$ anomalies between the warm and cold ΔSST (Niño 3.4) phases is achieved by the eastward propagation of summer $\Delta(\chi_Q, P)$ anomalies. What are the responses of the east Asian summer hydrological processes to this eastward-propagating ENSO mode? The interannual variation of the east Asian summer monsoon is often portrayed by the Pacific–Japan pattern accompanied by the east–west oriented anomalous rain belts (e.g., Samel *et al.*, 1999). Because the east Asian monsoon circulation is characterized by the Meiyu rain belt and tropical cyclone activity, can the aforementioned response of the east Asian monsoon be reflected by a north–south oscillation of the Pacific–Japan pattern and an alternation of the accompanied anomalous rain belts? This question is answered by the y–t diagrams of lagged correlation coefficients between ΔP_A and Δu (850 mb) at 140°E (Figure 10.19(a)) and between ΔP_A and ΔP (140°E) (Figure 10.19(b)). As inferred from these two y–t diagrams, the response of the east Asian monsoon circulation and its rainfall should be a northward migration of the Pacific–Japan pattern (indicated by Δu (850 mb)) with its accompanied rainfall anomalies (indicated by ΔP), instead of the north–south oscillation of this anomalous circulation pattern.

The major rain producers of the east Asian monsoon are the Meiyu rain belt and tropical cyclones. Because of the spatial relationship between the Meiyu rain belt, tropical cyclone activity, and the North Pacific anticyclone, it is expected that frontal and tropical cyclone activities are modulated by the northward propagation of the Pacific–Japan pattern. Following this anomalous circulation pattern and its

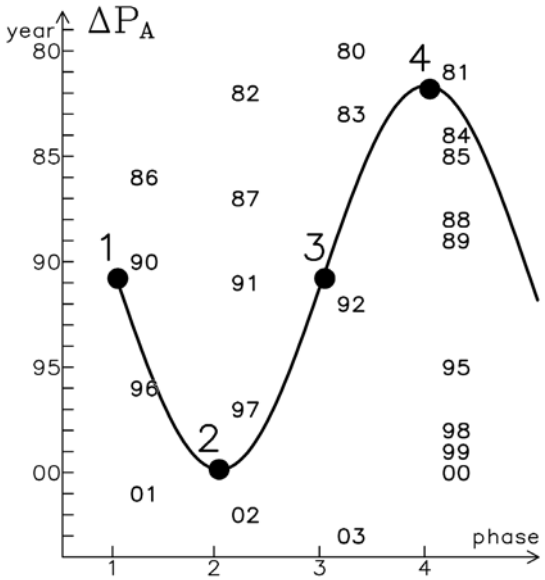

Figure 10.20. Composite cycle of warm and cold extreme summers (condensed from Figure 10.17) determined by ΔP_A. Summers between 1979 and 2004 that are projected on different phases of this composite cycle are indicated by the last two numbers of a given year. Schematic cycles of ΔSST (Niño 3.4) and ΔSST (WTP) matched with the ΔP_A composite cycle are shown by phase number along the abscissa. WTP represents an area (120°E–140°E, 5°N–15°N) of the western tropical Pacific.

accompanied rainfall anomalies, can interannual variations of cold fronts along the Meiyu rain belt and tropical cyclone activity also undergo a northward migration? First, let us use ΔP_A, ΔSST (Niño 3.4) and ΔSST (WTP) (an area covering 120°E–140°E, 5°N–15°N) as interannual variation indices of the northern summer monsoon circulation. Four phases of these indices are designated in Figure 10.20. Composite charts of $\Delta(\psi_Q, P)$, $\Delta(\psi_Q, N_{FT})$, and $\Delta(\psi_Q, N_{TC})$ for these four designated phases of the warm–cold extreme summer of the ENSO cycle identified with summer interannual variation indices are shown in Figure 10.21. Salient features of these composite charts are summarized as follows:

(1) A distinct Pacific–Japan pattern and east–west oriented strips of rain anomalies emerge from composite charts of $\Delta(\psi_Q, P)$ during warm and cold summers. The $\Delta(\psi_Q, P)$ anomalies of two transition phases (1, 3) juxtaposed with those of the two extreme phases (2, 4) form a clear northward migration of the $\Delta(\psi_Q, P)$ wave train.
(2) The Meiyu rain belt extending from east China to southern Japan is established by the eastward propagation of cold fronts which are advected by monsoon south-westerlies. These monsoon south-westerlies are intensified (weakened) when the anticyclonic (cyclonic) $\Delta\psi_Q$ cell of the Pacific–Japan pattern is centered over the Philippine Sea (phase 2) and east of Taiwan (phase 3).

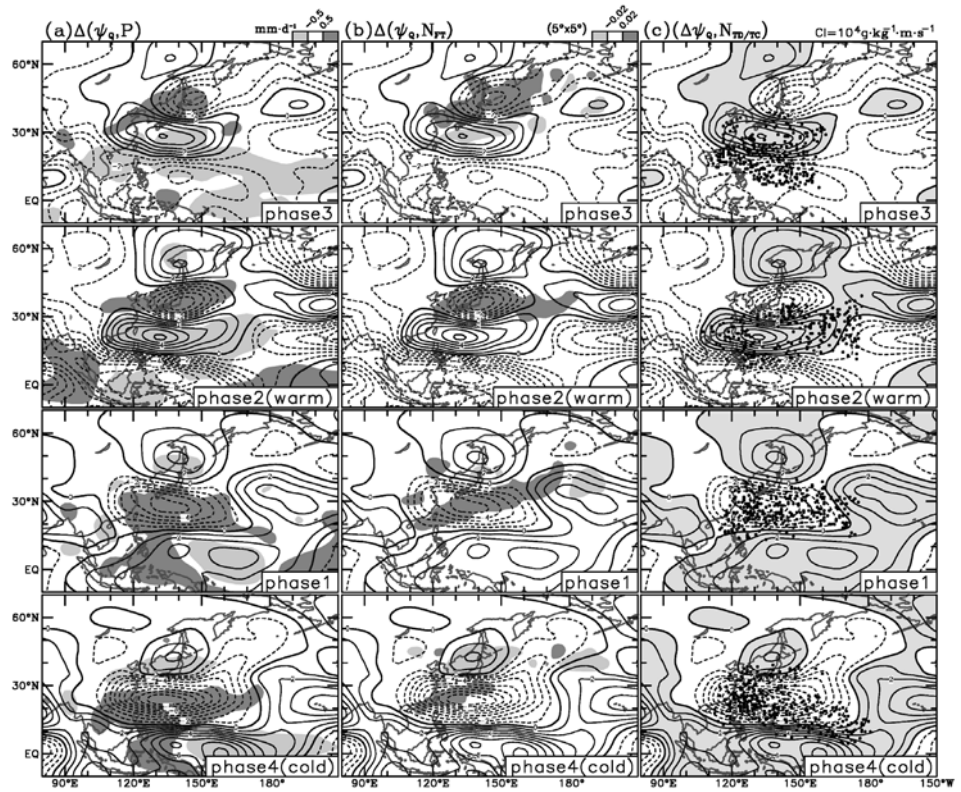

Figure 10.21. Composite charts of (a) $\Delta(\psi_Q, P)$, (b) $\Delta(\psi_Q, N_{FT})$, and (c) $\Delta(\psi_Q, N_{TC/TD})$ over four phases of the extreme warm–cold summer cycle (based on summers shown in Figure 10.20). The contour interval of $\Delta\psi_Q$ is $2 \times 10^6\,\mathrm{g\,kg^{-1}\,m^2\,s^{-1}}$. Grayscales of ΔN_{FT} and $N_{TC/TD}$ are shown on tops of columns (a) and (b).

Therefore, frontal activity and the Meiyu rain belt can be enhanced (reduced) by intensification (weakening) of these monsoon south-westerlies which is a reflection of the east Asian monsoon intensity. Frontal activity is clearly modulated by the northward propagation of the Pacific–Japan pattern. It was observed by Nitta (1987) that Japan becomes dry/hot (wet/cool) during the warm (cold) ΔSST (Niño 3.4) summer. The intensity modulation of monsoon south-westerlies by the Pacific–Japan pattern also affects rainfall in south China and Taiwan.

(3) The occurrence frequency of tropical cyclones is enhanced (suppressed) by the cyclonic (anticyclonic) southern cell of the Pacific–Japan pattern (Chen *et al.*, 1998). It is shown in Figure 10.21 that tropical cyclone activity is covered by the cyclonic southern cell of the Pacific–Japan pattern during phase 1 and 4 (cold). In contrast, tropical cyclone activity is expelled from the anticyclonic southern cell during phases 2 (warm) and 3 to appear along the southern rim of this cell

where strong anomalous easterlies exist. Because tropical cyclones are major rain producers, rainfall is therefore increased (reduced) over the cyclonic (anti-cyclonic) southern cell of the Pacific–Japan pattern.

In summary, we conclude that the modulation of the east Asian hydrological processes by the eastward propagation of the global ENSO mode depicted by $\Delta(\chi_Q, P)$ anomalies can be accomplished through its downscale interaction with the regional monsoon circulation reflected by the northward migration of the Pacific–Japan pattern and the regulation of the frontal and tropical cyclone activity by this northward propagation property.

10.5 SUMMARY AND CONCLUDING REMARKS

Because of the importance of summer rainfall to the monsoon region, monsoon research has long been focused on the search for mechanisms of the onset, life cycle, and interannual variation of monsoon rainfall. During the northern summer, major global rainfall is actually produced in the Asian monsoon–western tropical Pacific region. This special feature of northern summer rainfall leads us to explore two issues of the global/hemispheric hydrological cycle in the present study: (1) the role played by the Asian monsoon in the global hydrological cycle, and (2) effects of the propagating global modes, including diurnal, intraseasonal, and interannual modes, on hydrological processes in the Asian monsoon region. Results of these two issues are summarized below.

The role played by the Asian monsoon in the global hydrological cycle

As indicated by the global distribution of seasonal mean values and variance, northern summer (JJA) rainfall occurs largely over the Asian monsoon–western tropical Pacific region. The water vapor budget analysis of the hemisphere (60°E–120°W) covering this region (which is designated as the Asian monsoon hemisphere) was used to illustrate the contribution of the Asian monsoon to the global hydrological cycle. *Climatologically*, the Asian monsoon hemisphere contributes 50% more than the extra-Asian monsoon hemisphere (120°W–60°E) to global precipitation. Therefore, part of this excessive rainfall in the former hemisphere is supported by water vapor diverged out of the latter hemisphere and converged toward the former hemisphere. Eventually, the excessive rainfall in this hemisphere is transported from the Pacific, across the Bering Strait and the Arctic Ocean, into the Atlantic. Based on this hemispheric water vapor budget, it is clear that the Asian monsoon hemisphere is a sink region of water vapor and the extra-Asian monsoon hemisphere is a source region of water vapor. The water vapor budgets of both hemispheres exhibit temporal variations of different timescales. Variations of three time scales, including diurnal, intraseasonal, and interannual modes, were analyzed in this study. Several interesting features of these variations emerge. Amplitudes of these three variation modes are of the same order of magnitude (which is an order of

magnitude smaller than that of precipitation itself). An out-of-phase, east–west seesaw of precipitation and water vapor flux exchange is observed between the two hemispheres. The variations of global precipitation follow those of the Asian monsoon hemisphere because it contributes more to global precipitation than the extra-Asian monsoon hemisphere. Nevertheless, roles played by the two hemispheres in the global hydrological cycle are not changed by the variation of any timescale at all. The upscale interaction of the Asian monsoon with the global hydrological cycle is revealed through the water vapor budget of the Asian monsoon hemisphere.

Effects of global propagating modes on Asian monsoon hydrological processes

Regional processes involved in the evolution of the Asian monsoon were the major concern of previous monsoon research. In contrast, the coupling between the global and regional monsoon modes has not been a focus of this research. Actually, it was shown in this study that variations of the hemispheric water vapor budget and hydrological processes over the Asian monsoon region are modulated by the propagating global modes.

Diurnal variation

Because the Earth rotates in an eastward direction, the immediate atmospheric response to the wave-1, east–west differential solar heating/cooling at the surface is the westward propagation of the global divergent circulation. Diurnal seesaw variations in hydrological variables of the hemispheric water vapor budgets between the Asian monsoon and the extra-Asian monsoon hemisphere are caused by this westward propagation of the diurnal mode of global divergent circulation. The tropical atmosphere is conditionally unstable, while the troposphere in middle to high latitudes is climatologically stable. Thus, the atmospheric response to the surface solar heating in triggering convection/rainfall is faster in the tropics than in middle to high latitudes. On the other hand, the heat capacity contrast between east–west land and ocean, and between land (mountain range) and air enables the land to be warmed up by the solar heating faster than water and air. A collaboration of these two differential responses to the surface solar heating forms a clockwise rotation of diurnal variation in the continental-scale rainfall.

Intraseasonal variation

The intraseasonal variations of northern summer rainfall are contributed to by 30–60-day and 12–24-day modes. Both global modes exhibit a clear eastward propagation, but couplings between these two modes and the corresponding regional monsoon modes differ from each other.

- *30–60-day mode*. Maximum (minimum) $\tilde{P}_A$ and minimum (maximum) $\tilde{P}_E$ occur at phase 2(6) of the $\tilde{P}_A$ index, when the positive (negative) $\tilde{\chi}_Q$ center appears in the western tropical Pacific and the negative (positive) $\tilde{\chi}_Q$ center covers the Amazon basin. Over east Asia, the regional circulation in response to the

eastward propagating 30–60-day mode is reflected by the alternate northward migration of positive and negative $\tilde{\psi}_Q$ cells. The east Asian monsoon rainfall produced by cold fronts along the Meiyu rain belt before the monsoon break and by tropical cyclones after the break is regulated by the northward-migrating $\tilde{\psi}_Q$ cells.

- *12–24-day mode*. $\hat{P}_A$ reaches its maximum (minimum) and $\hat{P}_E$ attains its minimum (maximum) at phase 2(5) of the $\hat{P}_A$ index, when the positive (negative) $\hat{\chi}_Q$ center moves to the western tropical Pacific and the negative (positive) $\hat{\chi}_Q$ center propagates to Central America. The response of the east Asian monsoon to the global $(\hat{\chi}_Q, \hat{P})$ mode before the monsoon break is a south-eastward propagation of $\hat{\psi}_Q$ cells which modulate the cold air intrusion following the eastward propagation of cold fronts. After the monsoon break, tropical cyclone activity is modulated by the north-westward propagation of a 12–24-day $\hat{\psi}_Q$ short wave train. East Asian monsoon rainfall is regulated by the global 12–24-day mode through these regional monsoon modes.

Interannual variation

The east–west seesaw variation of the water vapor budgets between the Asian monsoon and the extra-Asian monsoon hemispheres is caused by the eastward propagation of the interannual $\Delta(\chi_Q, P)$ mode. This propagating $\Delta\chi_Q$ mode follows the ΔSST (Niño 3.4) index in the following manner: ΔP_A gains its maximum (minimum) and ΔP_E attains its minimum (maximum) when the positive (negative) $\Delta\chi_Q$ center is located over the tropical western Pacific and the negative (positive) $\Delta\chi_Q$ center is situated over the tropical central eastern Pacific during phase 4(2) of the ΔP_A index and ΔSST (Niño 3.4) $\leq -0.5^{\circ}$C ($\geq 0.5^{\circ}$C). It was suggested by previous studies (e.g., Chahine, 1992; Soden, 2000) that warm (cold) ΔSST (Niño 3.4) anomalies intensify (weaken) the tropical/global hydrological cycle. Our results show otherwise because the convective activity/rainfall in the Asian monsoon hemisphere is more sensitive to the eastward propagation of the interannual $\Delta\chi_Q$ mode. The regional response to this interannual variation mode was often portrayed as a flip-flop oscillation between the warm and cold Pacific–Japan pattern. It was found in this study that this response is a northward migration of the Pacific–Japan pattern. Frontal and tropical cyclone activities are modulated by this pattern to produce the north–south juxtaposition of the east–west oriented rainfall anomalies.

The global and regional hydrological processes presented in this study offer a new perspective of the east Asian monsoon hydrological cycle: (1) its relationship with the extra-Asian monsoon hemisphere and contribution to the global hydrological cycle, (2) its role in the temporal variations of the global hydrological cycle, and (3) the hydrological interaction between the global and regional monsoon modes with various timescales. Numerous previous studies of the Asian monsoon focused primarily on either the special features of this monsoon's evolution or a given timescale (e.g., diurnal, intraseasonal, interannual, etc.). Therefore, numerical simulations of the Asian monsoon often pay special attention to either a special regional phenomena (e.g., Rajendran *et al*., 2004) or a special timescale (e.g., Lau and Yang,

1996; Lau *et al.*, 2000a). In fact, the Asian monsoon simulated by global climate models can possibly include all temporal and spatial scales. So far, no comprehensive analyzes of the Asian monsoon simulations have attempted to cover timescales ranging from diurnal to interannual, and both the upscale and downscale interaction with the propagating global modes. The global/regional water vapor budgets and hydrological processes presented in this study provide a new way to validate Asian monsoon simulations using global climate models.

10.6 ACKNOWLEDGEMENTS

The technical assistance provided by Judy Huang, Simon Wang, Paul Tsay, and Adam Clark in preparing the manuscript is gratefully acknowledged.

11

Land–atmosphere interaction

Tetsuzo Yasunari

11.1 FUNDAMENTAL PROCESSES IN THE SEASONAL CYCLE

The monsoon is manifested as a land–atmosphere–ocean interaction between continents and oceans in the seasonal cycle. The ocean has a large heat content with a longer climate memory of more than a year, but the land has a small heat content and its climate memory is believed to be short (less than a season). Some of the recent model studies emphasized the relative importance of the ocean–atmosphere interaction (OAI) compared with land–atmosphere interaction (LAI), particularly focusing on the strong impact of large-scale sea surface temperature (SST) anomalies in the tropical oceans nearby the continent. It should be noted, however, that to specify or distinguish the roles of LAI from those of OAI and vice versa is very difficult or, particularly in the Asian–Australian monsoon system, because these two processes are strongly coupled to each other. In other words, the LAI (or OAI) in the monsoon system should be understood as part of the full land–atmosphere–ocean interactive system.

The land shows strong and rapid heating (and cooling) in the seasonal cycle which in turn has a large impact on seasonal atmospheric differential heating (and cooling) processes between the land and the ocean. The land surface processes which modulate the seasonal heating, therefore, are likely to be responsible, to some extent, for the interannual variability of the monsoons. The snow cover and soil moisture anomalies over the Eurasian continent in the pre-monsoon seasons have been thought to have a large impact on the Asian summer monsoon variability (Section 11.2).

Seasonal land surface heating and the resultant atmospheric heating over Eurasia manifests itself in the surface or lower tropospheric pressure field. Figure 11.1 shows the difference of the monthly mean geopotential field at 850 hPa from April to May. A remarkable decrease of pressure is seen over southern Eurasia centered over the India/Tibetan Plateau area. Similar patterns of

B. Wang (ed.), *The Asian Monsoon*.

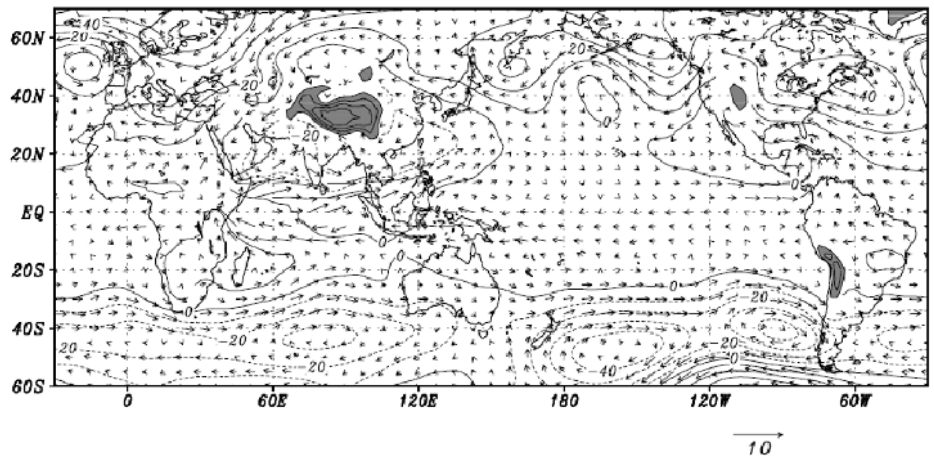

Figure 11.1. Difference of climatological mean height and U, V field for May values minus April values. Dashed line shows negative values.

pressure change are seen over Eurasia from month to month for the period of March through July. In contrast, the pressure change over the tropical and subtropical oceans are very small and positive (increase in pressure). The large decrease of pressure over Eurasia is indicative of the seasonal heating of land, presumably centered over the Tibetan Plateau and Mongolia. The decrease of pressure over North America centered over the Rockies is very small, suggesting smaller heating compared with the Tibetan Plateau area.

The low-pressure area over southern Eurasia (called the 'monsoon trough') at the surface and lower troposphere induces moist south-westerly wind from the Indian Ocean (the south-west monsoon flow) toward India, south-east Asia and east Asia, and dry northerly wind from the interior of the Eurasian continent. The moist monsoon flow, in turn, induces convection and precipitation over the south-eastern part of the continent, which plays a dominant role in atmospheric latent heating as a 'moist LAI' during the monsoon season.

An important issue may be how this moist LAI starts in the interior of the continent. The sensible heating over the Tibetan Plateau may be one of the important factors for triggering this process. In other continents, dry LAI based on sensible heating from the land surface cannot produce the continental-scale monsoons. Figure 11.2 shows a schematic diagram of this dry and shallow LAI. This process is dominant over the Australian continent and west Africa (to the north of the west African monsoon) where desert area prevails and large-scale downward motion dominates. The existence of the desert and the downward motion are self-perpetuating through a positive feedback of surface albedo and radiation balance (Otterman, 1974; Charney, 1975; Webster *et al.*, 1998). This dry LAI cannot induce deep atmospheric heating in the interior of the continents, but can trigger shallow coastal monsoon circulation along the periphery of the continent. This shallow monsoon circulation, however, is likely to trigger deep convection when the

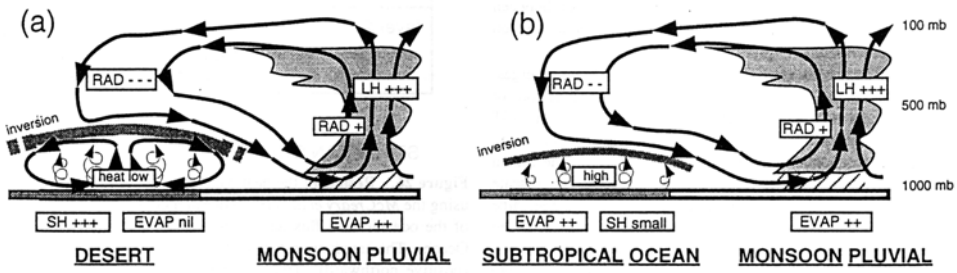

Figure 11.2. Schematic of the circulation between (a) the desert region of North Africa and the Near East; and (b) the subtropical ocean regions and the precipitating (pluvial) part of the monsoon circulation, respectively. The components of the monsoon match the transverse and lateral monsoon components shown in Figure 11.9. The dominant heating or cooling terms are shown in the boxes. 'SH' and 'LH' refer to sensible and latent heating. 'RAD' and 'EVAP' refer to radiational heating and evaporation, respectively. The pluses and minuses represent the sign of the processes and their relative intensities.
Webster *et al.* (1998).

continents are surrounded by warm tropical oceans (e.g., the warm water pool of the Arafura and Timor Seas neighboring the Australian continent) (Kawamura *et al.*, 2002). The land heating process over the Australian continent is thus important for triggering the Indonesian–Australian monsoon.

Over the elevated land surface of the Tibetan Plateau, in contrast, sensible heating plays a dominant role in atmospheric diabatic heating of the whole troposphere particularly in the onset phase of the Asian monsoon. Figure 11.3 (color section) shows diabatic heating rate (Q1) in May over the Tibetan Plateau based upon the GEWEX Asian Monsoon Experiment (GAME) reanalysis data, showing strong heating of the whole troposphere over the Plateau through deep, dry convection (Ueda *et al.*, 2003a). This diagram suggests that latent heating through shallow convection in the pre-monsoon season may also play some role in the heating process even in the preonset phase. The simulation of Asian monsoon by a coupled ocean–atmosphere general circulation model (GCM) also suggests that without the Tibetan Plateau orography the monsoon precipitation cannot penetrate into the interior of the continent (Abe *et al.*, 2003). The role of the Tibetan Plateau is discussed in more detail in Chapter 13.

Diabatic heating over the Tibetan Plateau in the pre-monsoon phase causes horizontal temperature (pressure) gradients in the upper (lower) troposphere between the surrounding Indian and Pacific Oceans and the interior of the continent, which facilitates large-scale convective activity over the South China Sea through the strengthening of the south-west monsoon flow intrusion (Ueda and Yasunari, 1998). Very recently, Jiang *et al.* (2004) and Wang *et al.* (2005) pointed out an important role of the existence of a strong vertical easterly wind shear over south Asia to the south of the Tibetan Plateau in the northward migration of the convective zone with intraseasonal timescales (including the monsoon onset phase) from the equatorial Indian Ocean toward the Himalayas.

This may imply that the atmospheric diabatic heating over and around the Tibetan Plateau (which is primarily responsible for producing the meridional thermal contrast and the vertical easterly shear over south Asia) is one of the essential elements, which characterize the variability as well as the mean state of the Asian summer monsoon system.

11.2 LAND SURFACE QUANTITIES CONTROLLING MONSOONS

The physical quantities of the land surface which may posses anomalous atmospheric forcing or climate memory effects can be (1) snow cover, (2) soil moisture, and (3) vegetation. The land surface layer is generally thought to have a small heat capacity compared with the ocean surface layer, the non-linear processes of these quantities in seasonal and interannual variations effectively produce a relatively longer memory effect, even compatible with SST as shown in Figure 11.4 (Walsh

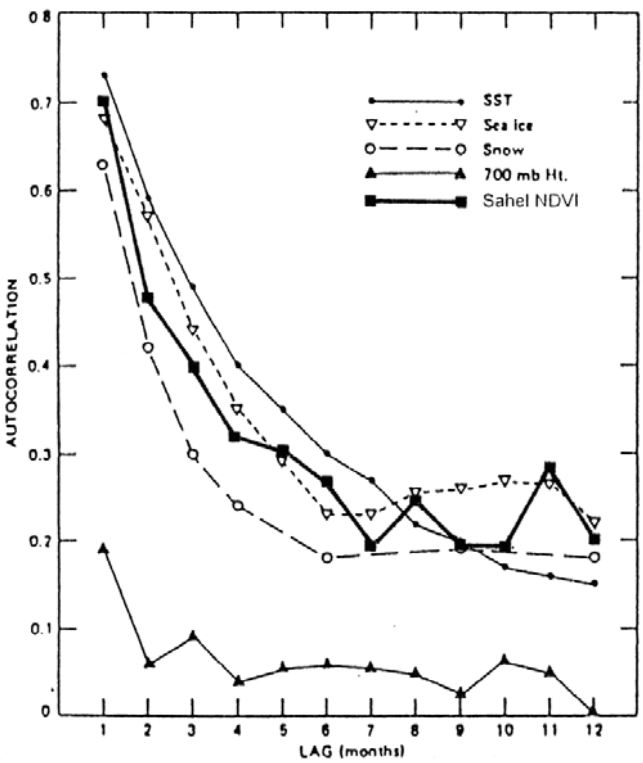

Figure 11.4. Autocorrelations of monthly SST anomalies in the northern Pacific, sea ice in the Arctic Sea, snow cover over Eurasia, geopotential height at 700 hPa depicted from Walsh *et al.* (1985), and NDVI in the Sahel region, North Africa obtained from Shinoda and Gamo (2000). From Shinoda *et al.* (2003).

et al., 1985; Shinoda and Gamo, 2000). The seasonal and interannual variability of these quantities play a significant role in LAI by producing anomalous surface and atmospheric heating or cooling, which in turn affects the monsoon circulation and convection. One should keep in mind that these quantities are interactive with the atmospheric conditions so that detection of a simple cause–result relationship is sometimes difficult. However, due to a lack of adequate observational data, and a lack of understanding of the actual physical processes particularly relevant to climate studies, large uncertainties still exist in the relationship between variabilities of these quantities and the monsoon activity. Comprehensive and interactive observational and modeling strategies are of significant importance to this study.

11.2.1 The role of continental snow cover

Snow cover has several effects which produce anomalous atmospheric conditions as follows: (a) the albedo effect controlling incoming solar radiation, (b) the insulation of heat between the atmosphere and land surface by a snow mass with a small heat conductivity, (c) a heat sink effect resulting from the melting process, and (d) a water source resulting from the melting process (Shinoda *et al.*, 2003). The first three effects can work to change the surface energy transfer process while snow cover exists on the surface. Only the fourth effect possibly has a climate memory even after snowmelt, by affecting the soil moisture content near the surface – called the 'snow–hydrological effect' as shown in Figure 11.5 (Yasunari *et al.*, 1991).

The data sets for validating these effects of snow cover are still limited. Most of the observational studies have been made based on the snow cover extent (of frequency) data from the National Oceanic and Atmospheric Administration (NOAA) operational meteorological satellites. Some studies also used ground-based snow depth measurements for limited areas (e.g., the former USSR, USA, Canada etc.). The continental-scale snow mass (water equivalent depth) information retrieved from satellite-based microwave data have become available over the last one or two decades (e.g., Koike *et al.*, 2001) though some accuracy problems still exist due to biases from vegetation and melting processes.

Blanford (1884) first noted the relationship between the Himalayan winter snow cover anomaly and the succeeding 'all-India' monsoon rainfall (AIMR). Walker (1910) followed up this study and reconfirmed this negative correlation. Since the 1960s satellite-based snow cover extent data became available. Many studies have addressed this issue as a typical example of the role of LAI on the interannual variability of Asian monsoon. Hahn and Shukla (1976) showed an apparent negative correlation between the satellite-based winter snow cover extent anomaly over Eurasia and the following AIMR, though the data used were only for 9 years (Figure 11.6). Since then numerous similar studies have been undertaken using some different indices of snow cover for winter and/or spring, and some different indices of the Indian or Asian summer monsoon activity (Dey and Bhanu Kumar, 1982; Dickson, 1984; Bhanu Kumar, 1987, 1988; Chattopadhay and Singh, 1995; Kripalani *et al.*, 1996; Shankar-Rao *et al.*, 1996; Morinaga *et al.*, 1997, 2000; Bamzai and Shukla, 1999; Kripalani and Kulkarni, 1999; Kripalani *et al.* 2003;

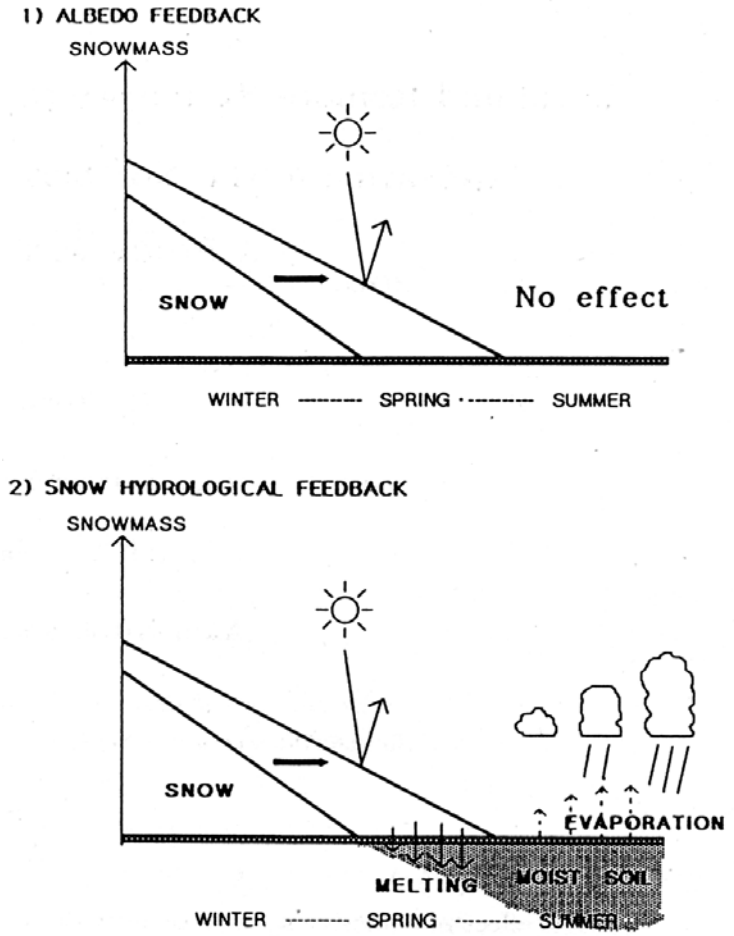

Figure 11.5. Schematic diagram for the albedo feedback and the hydrological feedback of snow cover during the seasonal march from winter to summer.
Yasunari *et al.* (1991).

Robock *et al.*, 2003). Some studies also discussed the Eurasian snow–AIMR relationship relating to the El Niño/Southern Oscillation (ENSO)–monsoon relationship (Yasunari, 1987; Kahndekar, 1991; Yasunari and Seki, 1992; Yang, 1996; Yang and Lau, 1998; Kawamura, 1998; Ye and Bao, 2001; Liu and Yanai, 2002). Some of these studies concluded that the snow cover–AIMR correlation might result from a common large-scale atmospheric circulation pattern that is responsible both for the snow cover anomaly and the AIMR anomaly. One possible idea is that ENSO-related teleconnection induces anomalous atmospheric circulation over Eurasia, which may fundamentally be responsible for anomalous Asian summer monsoon activity (Webster *et al.*, 1998). The snow cover anomaly induced by the anomalous circulation may be partly reinforced to produce a weaker monsoon

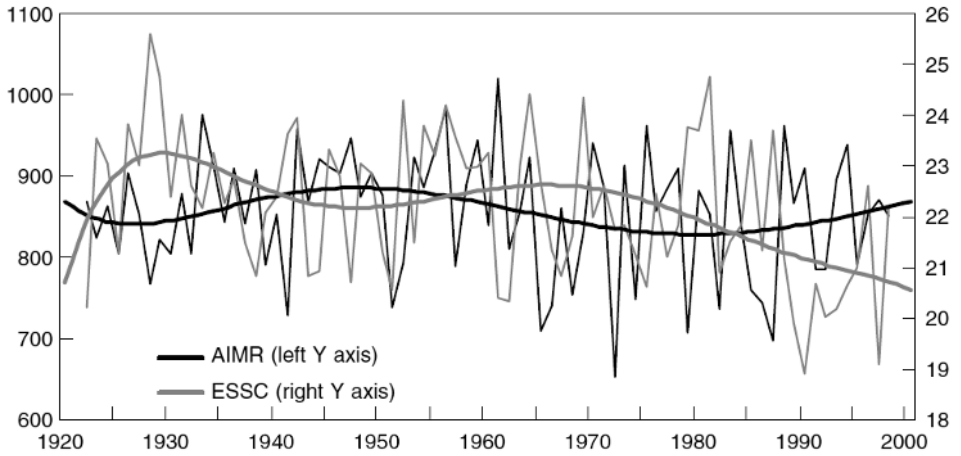

Figure 11.6. Year-to-year variations of the AIMR and ESSC. The thick solid lines represent the trends fitted with sixth-order polynomials.
Liu and Yanai (2002).

through radiation and energy flux processes as suggested in the observational study of Yang *et al.* (2004) and in a GCM experiment of Shen *et al.* (1998).

A central issue for the snow cover–AIMR connection may be how the climate memory of the snow cover anomaly in winter (or spring) can be conveyed to the following summer. Some GCM studies attempted to address this issue (Barnett *et al.*, 1989; Yamazaki, 1989; Yasunari *et al.*, 1991; Vernekar *et al.*, 1995; Douville and Royer, 1996). Though some of these GCM experiments have given unrealistically large anomalous snow covers (snow mass) as an initial condition, both the albedo and the snow–hydrological effect of anomalous snow cover could play, to some extent, the role of producing monsoon anomalies in the summer. Some studies emphasized that the albedo and snow-melting effect on the Tibetan Plateau in spring showed a relatively large impact on weakening of the summer monsoon through suppressing the net radiation and sensible heat flux (Yasunari, 1991; Douvelle and Royer, 1996). In contrast, a recent large-ensemble GCM experiment has suggested that in the northern part of the continent (e.g., Siberia), snow mass anomaly may be more important for producing an atmospheric anomaly than snow cover (albedo) forcing (Gong *et al.*, 2004). Takata and Kimoto (2000) pointed out the importance of seasonal freezing (and melting) of the surface permafrost layer in the northern part of the continent on thermal and hydrological processes of the surface. Full inclusion of these processes causes higher surface temperatures (due to suppressed evaporation) and stronger monsoon circulation in south-east Asia.

The recent precise observational studies on the seasonal march of temperature and circulation fields over Eurasia from spring to summer have shown that the influence of snow cover and related soil moisture anomalies on the temperature and circulation anomalies in the lower troposphere is limited primarily when and where snow cover exists seasonally as schematically shown in Figure 11.7

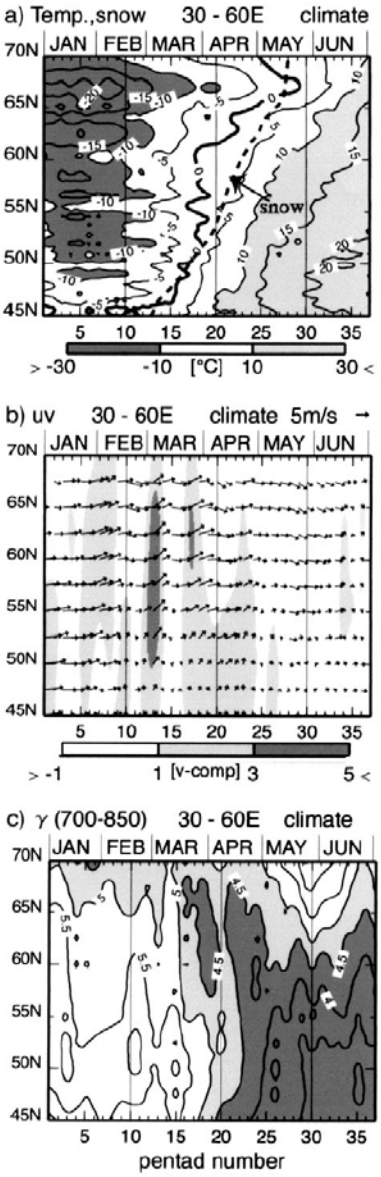

Figure 11.7. Latitude–time sections showing (a) mean (1966–1990) seasonal evolution of the surface temperature (°C) along a longitude of 30°–60°E. Thick black contour indicates a surface temperature of 0°C. The dashed contour denotes climatological snow disappearance pentads. (b) The same as in (a), except for 850 hPa horizontal wind obtained from ECMWF reanalysis (1980–1990). The southerly wind component greater than 1 m s^{-1} is denoted by two-tone shading. (c) The same as in (a), but for static stability γ between 850 and 700 hPa. Shading represents the region of γ less than 5.0 K km^{-1}.
Ueda *et al.* (2003b).

(Shinoda *et al.*, 2003; Ueda *et al.*, 2003; Robock *et al.*, 2003). The long-term surface energy flux observation on the Tibetan Plateau as part of GAME in 1998 suggested that the anomalous heavy snow cover in spring on the central Plateau resulted in a considerable decrease of sensible heating and delayed the monsoon onset over the Plateau (Tanaka *et al.*, 2004). The observational study (Ohta *et al.*, 2001) of seasonal surface energy and water flux in east Siberia conducted as part of GAME–Siberia also proved the important processes noted by Takata and Kimoto (2000).

11.2.2 The role of soil moisture

Soil moisture is a key parameter for LAI in the climate system. The anomaly of surface and near-surface soil moisture is likely to have a persistence of several days to several months, which may cause climate memory through anomalous surface energy and moisture fluxes. However, this quantity is very difficult to measure adequately. The long-term, *in situ* measurement of soil moisture is very limited both in time and space (Robock *et al.*, 2000, 2003). The recent satellite-based indirect measurement using microwave sensors is a promising method for large-scale soil moisture monitoring, but it has still been limited for soil moisture or wetness of the very near surface soil layer. The climate memory effect of soil moisture has, therefore, been discussed basically based upon climate model experiments.

Delworth and Manabe (1988, 1989) firstly assessed the climate memory effect of soil moisture in GCMs using the so-called bucket model (Manabe, 1969) interacting with the atmosphere through a surface water balance. Their bucket model consisted of one soil layer with a 15-cm water holding capacity (field capacity). They noticed that the persistency (measured by autocorrelation) of the soil moisture anomaly was small whereas in higher latitudes its value was large, depending upon the ratio of P/Ep (P, precipitation; Ep, potential evapotranspiration) as shown in Figure 11.8. In the humid tropics or monsoon regions where P is large enough to saturate the soil layer, the soil moisture anomaly does not function as a climate memory. The distribution of persistency in Figure 11.8 can be generally described in the form $1/\lambda = W^*/Ep$, where λ is e-folding time of exponential decay of soil moisture anomaly, and W^* the field capacity. Though their definition of soil moisture and assumption of soil layer model were so simple, this relation between soil moisture anomaly persistency, field capacity of soil layer, and Ep was partly proved in observations in central Eurasia (Vinnikov and Yeserkepova, 1991).

In recent years, more realistic and sophisticated land surface models (LSMs) have been developed, and many sensitivity experiments with GCMs have been conducted using different types of LSMs under different experimental designs. For example, Douville *et al.* (2001) and Douville (2002) assessed the influence of soil moisture on seasonal and interannual variability of the Asian and African monsoons. Through some ensemble experiments with and without an interactive LSM (named ISBA; Interaction between Soil Biosphere and Atmosphere model), they found that the impact of soil moisture anomaly through the LAI process is significant in relatively dry monsoon regions (e.g., the Indian subcontinent and

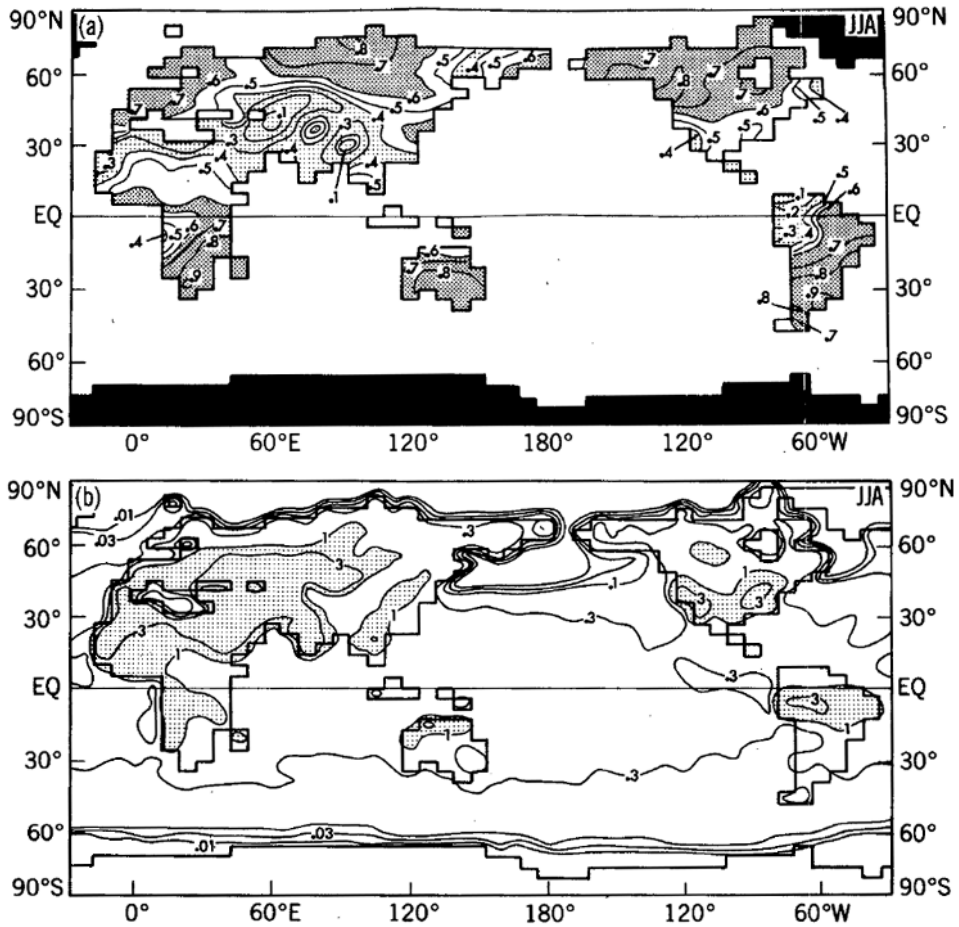

Figure 11.8. (a) Lag one autocorrelation values of soil moisture for the months of June, July, and August (JJA) for SMI. At each grid point, deviations of monthly mean soil moisture from the long-term mean for that month were correlated with data from the same grid point, but lagged by one month. Coefficients greater than 0.16 (0.3) are significantly different from zero at the 95% (99.9%) confidence level (see Chatfield, 1984, p. 63). Values greater than 0.6 are densely stippled, while values less than 0.4 are lightly stippled. Permanently ice covered regions are black. (b) Potential evaporation ($cm\,d^{-1}$) for JJA in SMI.
From Delworth and Manabe (1989).

north-east Asia) but not in the humid monsoon regions (e.g., south-east Asia). They also noticed that in the significantly impacted regions soil moisture anomaly primarily plays a role as an initial condition (at the monsoon onset phase) rather than the boundary condition. Kanae *et al.* (2004) also performed a set of hindcast GCM simulations (with prescribed SST) on the boreal summer hydroclimate for about 40 years (1951–1998), with and without realistic soil moisture anomalies,

and noticed that only semiarid regions in the peripheries of monsoon regions showed reasonably good simulated precipitation compared with that observed. It is interesting to note that all the GCM experiments, though the LCM performance and simulation design are quite different from each other, have shown a relatively high impact of soil moisture anomaly in dry or semiarid regions. This general tendency of soil–precipitation feedback has comprehensively been confirmed by the recent Global Land Atmosphere Coupling Experiment (GLACE) (Koster *et al.*, 2004), where twelve GCMs with different LCMs participated. For example, in the Asian monsoon region, the sensitivity of precipitation change to soil moisture condition is large only in relatively dry areas (e.g., the Indian subcontinent and the Yellow River/inner Mongolia in China) as shown in Figure 11.9 (color section). In humid monsoon and tropical regions, the impact seems to be small or insignificant primarily due to already saturated soil moisture conditions. However, this characteristic nature of the weak soil moisture memory effect in the humid tropics may, to some extent, counteract with the relatively long memory effect in the humid tropics (Wu and Dickinson, 2004). In addition, the soil moisture anomaly may be important as an initial condition to switch on the interaction with precipitation in these relatively dry regions.

11.2.3 The role of vegetation and landuse/land cover changes

Some new aspects from observational studies

Another important aspect of LAI in addition to soil moisture (and snow cover) may be the role of vegetation. In the Asian monsoon region, most of the areas are heavily covered by vegetation, including tropical rain and monsoon forests, water-fed paddy fields, grass lands, and boreal forests, etc. The roles of vegetation in LAI may be classified as follows:

(1) control of radiation and energy fluxes through albedo and surface roughness;
(2) control of transpiration through stomatal resistance; and
(3) control of the substantial field capacity of soil with root depth and structure.

Due to a lack of observations particularly of the large-scale vegetation and its impact on climate and the water cycle, this aspect has been noted only in the recent years. LSMs including these vegetation processes have also been developed and improved in the most recent few decades (e.g., Dickinson and Henderson-Sellers, 1988; Sellers *et al.*, 1986), though these models need numerous numbers of tuning parameters. To improve and fully utilize these sophisticated models, however, observational studies are also essential, including optimal determination of these parameter values. In the Asian monsoon region, intensive field campaigns related to some international projects such as GAME have been conducted, and have revealed new aspects of the role of vegetation in terms of energy and water cycle processes.

In the evergreen tropical forest in Thailand, energy and water flux measurements at several sites with different types of vegetation were conducted for more than two years as part of GAME–Tropics. The evapotranspiration estimated by a multilayer

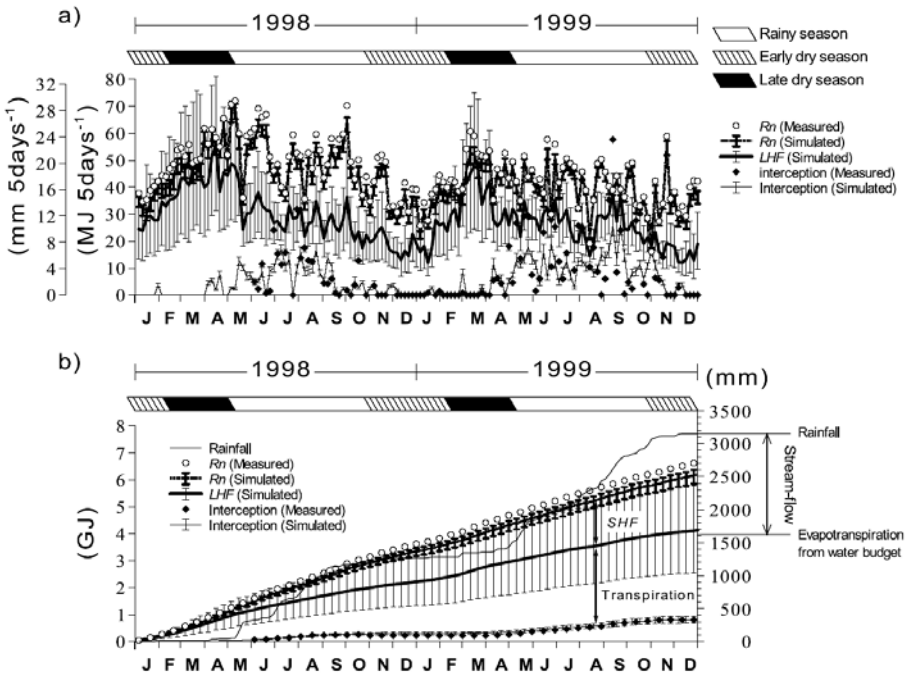

Figure 11.10. (a) Simulation of the seasonal variation in the net radiation and latent heat over an evergreen forest and rainfall interception in 1998 and 1999. (b) The cumulative result. In the figure the tops and bottoms of the vertical bars indicates the maxima and minima, respectively, of the 32 simulated values. The line in between shows the average.
Tanaka *et al.* (2003).

model forced by the observed radiation, leaf area index (LAI), and other realistic parameters revealed that a seasonally maximum evapotranspiration appeared in the late dry season (Figure 11.10) just before the monsoon onset when the ground surface was at its driest for the year (Tanaka *et al.*, 2003). An LSM study including the effects of root depth (to pump up the water in the deep soil layer) was found to simulate this seasonal feature well when the mean root depth was set to 6 m (Tanaka *et al.*, 2004). This implies that effective field capacity must be set at an extremely large value in this case. In the deciduous monsoon forest in Thailand, in contrast, the seasonal maximum of evapotranspiration appeared in the late monsoon season, associated with a seasonal photosynthetic activity and water availability (Toda *et al.*, 2002). These dependencies of the seasonal variation of evapotranspiration (i.e., latent heating) on dominant vegetation types may have a great impact on the modeling of the regional and large-scale climate and water cycle, particularly in the tropics.

In the boreal forests of Siberia, similar long-term flux measurements were made in the Lena River basin as part of GAME–Siberia (Ohta *et al.*, 2001) as shown in Figure 11.11. Here, surface energy partition (sensible vs. latent energy) is strongly

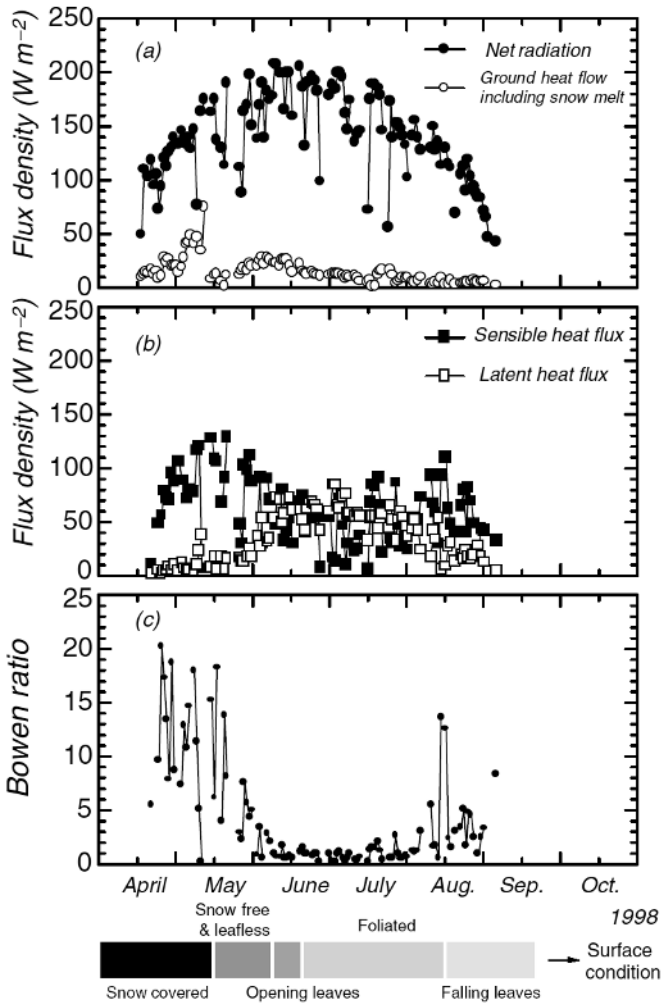

Figure 11.11. Time series for the daily net 'all-wave' radiation and the ground heat flow (a), the sensible heat flux and the latent heat flux (b), and the Bowen ratio (c). The energy balance components and the Bowen ratio indicated in this figure are for a dry canopy only.
Ohta *et al.* (2001).

controlled by the phenology of the (larch) forest coupled with seasonal melting (and freezing) conditions of the permafrost beneath the forest. Namely, in May during and after the snowmelt, sensible heating greatly increased, which was mostly used for melting the frozen ground. At the beginning of June when the melt layer of the ground surface reached about 20 cm depth or so, the foliation of trees suddenly started, which at the same time triggered transpiration (latent heating) from the trees. During mid-summer (June, July and the beginning of August) latent heating

rate was comparable with, or more than, the sensible heating rate. Most of the annual precipitation occured in this period. This condition prevailed for a broad area of the Siberian boreal forest zone, which contributes to water recycling as well as maintenance of permafrost, by limiting the melting of permafrost within the near-surface layer. Thus, the boreal forest and permafrost of this region are likely to coexist as a symbiotic ecoclimate system through energy and water cycles.

Some new aspects from modeling studies

The potential role of large-scale vegetation and land cover on the Asian monsoon has recently also been investigated by some GCM experiments. Xue *et al.* (2004) showed that some characteristic features of the east Asian summer monsoon (e.g., the abrupt northward jump of the rainfall belt in the seasonal march and low-level monsoon circulation) are far better simulated when a more sophisticated vegetation scheme is introduced (a simplified simple biosphere (SSiB) with realistic vegetation distribution) rather than a simple vegetation scheme without physiological processes (i.e., photosynthesis and stomatal control of transpiration). The abrupt northward jump of rainfall could occur due to strong sensible heating in the interior of east Asia which would induce horizontal temperature and pressure gradients in the pre-monsoon season. This would probably relate to stomatal control of evapotranspiration in the dry and hot season, resulting in enhancement of sensible heating. Suh and Lee (2004) also showed in the regional climate model experiment that temperature and rainfall biases over east Asia have improved considerably as a result of including the biospheric processes of realistic vegetation over the east Asian land mass. These experiments have suggested that physiological control of surface energy flux partitioning (i.e., Bowen ratio) greatly affects the pressure gradients over land, and in turn, circulation and rain systems. However, the reality of these biospheric processes needs to be validated through *in situ* and satellite-based comprehensive observations.

Very recently, we have conducted a series of GCM experiments assessing the role of the continental land surface with and without vegetation, and relative importance of topography and vegetation on the formation of the Asian summer monsoon. In this case, various vegetation types are simply represented by differences in albedo, roughness, and field capacities of surface soil layers (Yasunari *et al.*, 2005; Saito *et al.*, 2005). These experiments do not explicitly include the physiological processes of vegetation in the model, but the difference in field capacity of the soil layer is expected to simulate the important nature of vegetated or non-vegetated surfaces since the soil layer is basically formed by plants. The results suggest the role of vegetation is generally significant in producing a strong monsoon, and relative roles of albedo and field capacities of soil appear to be different from region to region. In east Asia both the Tibetan Plateau's topography and vegetation are important for the penetration of the moist monsoon flow and precipitation. In addition, the relative importance of albedo vs. field capacity seems to be different from region to region. In east Asia the albedo effect of vegetation is more important, but in south/south-east Asia the role of a large field capacity has proved to be more important in producing stronger monsoons particularly in the mid-monsoon season,

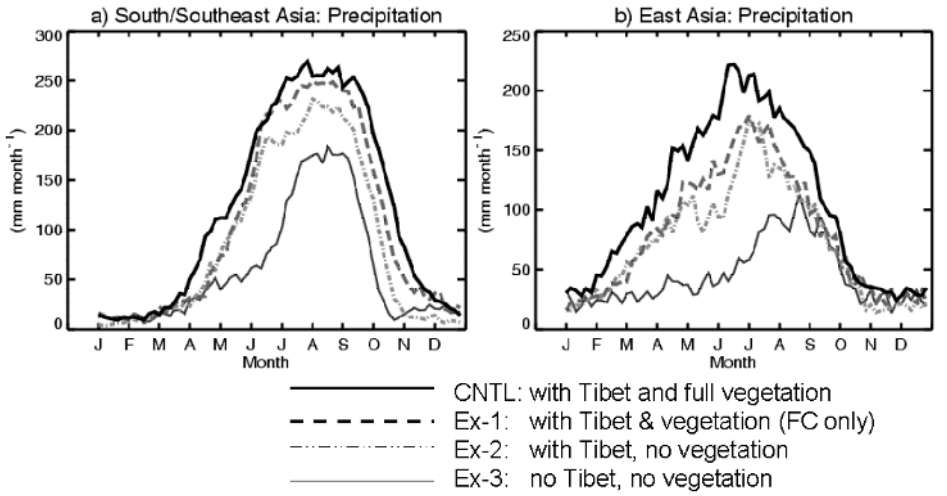

Figure 11.12. Changes of seasonal precipitation for (a) south/south-east Asia and (b) east Asia for different boundary conditions: (1) with no Tibetan Plateau, no vegetation (bared surface with rock albedo and roughness) (thin solid line); (2) with the Tibetan Plateau, but no vegetation (dotted and dashed line); (3) with the Tibetan Plateau and vegetation (soil only) (thick dashed line); and (4) with the Tibetan Plateau and full vegetation (with soil and realistic vegetation albedo and roughness) (thick solid line).
From Yasunari *et al.* (2005).

as shown in Figure 11.12. These numerical experiments have strongly suggested that in the Asian monsoon region the role of vegetation is essential for the formation of monsoon circulation and precipitation through strong latent heating of the atmosphere. The evapotranspiration from vegetated surfaces plays a crucial role in forming a thick moist boundary layer and convection for latent heating, as will be described in the next section.

11.3 THE CONNECTION BETWEEN THE LAND SURFACE, THE ATMOSPHERIC BOUNDARY LAYER, AND CLOUD/ PRECIPITATION PROCESSES

The Impacts of land surface processes on the atmosphere are brought about through the modification of the atmospheric boundary layer (ABL), and relevant cloud processes at or above the ABL. Betts *et al.* (1998) reviewed the overall possible interactive processes between land surface conditions and the ABL, and emphasized the importance of vegetation and related land cover/use differences on the ABL structure and cloud/precipitation process. In the monsoon region, the advection or inflow of moist air from oceans to the land is sometimes emphasized to produce monsoon rainfall in the interior of the land area. However, through some continental-scale experiments (CSEs) under GEWEX (e.g., GAME in Asian monsoon region,

LBA in Amazon basin) moisture supply from wet land surfaces has also been proved to be important particularly in the late monsoon season when the surface becomes wetter than in the earlier stage of the monsoon season. Shinoda and Uyeda (2002) examined a possible impact of water-fed paddy fields in east Asia, using a cloud-resolving atmospheric model. They forced the model using latent and sensible heat fluxes over the paddy field observed in GAME–Huaihe Basin Experiment (HUBEX), and found that mesoscale cloud systems embedded in the Meiyu (Baiu) front developed through the moisture supply to the ABL and the change of the moist static stability of the lower troposphere. This change of LAI and its impact on cloud/precipitation systems through the seasonal change of soil moisture conditions was also observed over the Tibetan Plateau during GAME–Tibet (Yamada and Uyeda, 2004). In fact, these characteristic changes of the water balance or the recycling process of water vapor between land surface and atmosphere through the seasonal march of the summer monsoon have been noticed in various parts of the continent (Yasunari and Kozawa, 2005). Understanding of these non-linear feedbacks from precipitation to land surface conditions may have some clue for the prediction of seasonal as well as interannual variations of precipitation in the Asian monsoon region.

11.4 THE POSSIBLE IMPACT OF ANTHROPOGENIC LANDUSE/LAND COVER CHANGES ON THE ASIAN MONSOON CLIMATE

The Asian monsoon region is heavily populated with nearly 60% of the World's population. Therefore, the anthropogenic landuse and land cover changes have been significant. These landuse/land cover changes from the original vegetation have the significant possibility to change the regional climate and water cycle. Fu (2003) investigated the potential impacts of human-induced land cover change on the east Asian monsoon, assuming the present and the potential vegetation (Ojima, 2000). Using a regional model (MM5) with a land surface scheme (BATS), he noticed that the land cover change which occurred over the history of China may have weakened the east Asian summer monsoon and strengthened the winter monsoon. The weakened monsoon trough in the interior of the continent presumably induced by a decreased latent heating is responsible for the weakened summer monsoon.

Xue (1996) focused on the impact of desertification in the Mongolian and the inner Mongolian grassland on the east Asian monsoon climate, by changing the area of desertification in the GCM. He found that the desertification is further intensified by altering from the grassland-type to a desert-type land surface due to the reduction in evaporation and convective latent heating above the surface layer. This process seems to be contrastive to the positive feedback of desertification in the Sahel, west Africa where enhanced radiative cooling and an associated sinking motion induced by increased albedo is likely to be a main mechanism (Charney, 1975).

In the Indo-China peninsula, a decreasing trend of monsoon rainfall has remarkably only been seen in September during the past several decades. Kanae

et al. (2001) tried to explain this feature as a result of deforestation in the central part of the peninsula using a regional climate model (RAMS). They noticed that the effect of deforestation by changing albedo, roughness, and soil moisture conditions significantly reduced rainfall only in September when the monsoon westerly flow seasonally became weak as shown in Figure 11.13 (color section). In other monsoon months, the effects of deforestation were negligible because the effect of a strong inflow and convergence of the moist monsoon flow dominated over this region. These results suggested that the impact of land surface conditions (i.e., vegetation cover, soil moisture etc.) change depending upon the atmospheric conditions including large-scale wind fields, thermal stability, etc.

11.5 THE FEEDBACK PROCESSES THROUGH THE ENERGY AND WATER CYCLES

A key process of regional climate and water cycle change by the landuse/land cover change including deforestation may be a process by which the land surface change induces changes of moisture convergence (C) and *in situ* evapotranspiration (E) which results in a change in precipitation (P). This issue can be more generally interpreted as a fundamental energy and water cycle process of an interaction between an area-limited land surface condition and large-scale atmospheric environment or circulation. This issue was discussed in terms of deforestation in the Amazon basin by Zeng *et al.* (1996) and Zeng (1998). Figure 11.14 shows a schematic diagram of the two feedback loops in the perturbed land surface area for the atmospheric water cycle. Change in P is controlled by two mechanisms: C feedback (right-hand side) and E feedback (left-hand side). In the first mechanism, an increase in P releases latent heat that drives large-scale upward motion (w), which causes more moisture convergence, leading to more P. In the E feedback, higher P leads to a

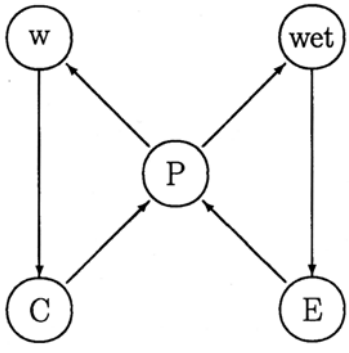

Figure 11.14. The two major feedback loops in the perturbed region: moisture convergence feedback and evaporation feedback. Here, P is precipitation, w is large-scale upward motion, C is large-scale moisture convergence, wet is surface wetness, and E is evapotranspiration. From Zeng (1998).

wetter surface and more evaporation, which in turn contributes to even more P. If these two positive feedbacks overlap and work at the same time, a higher sensitivity of P to land surface changes appears. However, if the P increase causes a decrease in radiation through, for example, cloud cover increase, the increase of C is partially compensated by a decrease of E due to decrease of radiation. An essential issue in the C feedback may be how a P increase contributes to an increase of large-scale upward motion (w).

Assuming thermodynamic balance and neglecting horizontal temperature advection, radiative heating approximated by Newtonian cooling, convective latent heating proportional to P, the moisture closure (i.e., $P = E + C$), and C proportional to w and humidity q in the boundary layer, the P change (ΔP) can be approximated as a simple equation (Zeng *et al.*, 1996; Zeng, 1998):

$$\Delta P = q\eta\Delta T^*/(1 - q - \beta) \tag{11.1}$$

where q is a measure of moist static stability (unstable if $q > 1$), T^* is an atmospheric equilibrium temperature, $\beta(\equiv Ep/P_0)$ is the ratio of potential evaporation Ep to a threshold precipitation rate P_0, above which soil is saturated, and η is a constant relevant to the radiation relaxation and atmospheric latent heat profile.

In the tropics near the equator, this positive C feedback roughly depends upon whether the horizontal scale of the perturbed area is larger than the equatorial radius of deformation (Zeng, 1998). In the off-equatorial monsoon region, however, the influence of large-scale moisture advection is dominated and the feedback loops (as shown in Figure 11.14) may not be so simple. The impact of deforestation may be apparent through the two positive feedback loops when the environmental monsoon flow is weak, as demonstrated in the September case in Thailand (Kanae *et al.*, 2001). In the relatively dry or marginal monsoon region (e.g., the north-west part of the Indian subcontinent, Mongolia, and northern China) where the sensitivity of P to the soil moisture anomaly is large (as discussed in Section 11.2.2), the positive feedback loops as shown in Figure 11.14 may be strong mostly due to large β under relatively dry conditions. We should keep in mind that relatively humid regions under the Asian summer monsoon climate, the ABL, and the lower troposphere are close to saturated (i.e., q is relatively large). This condition also increases the sensitivity of P to slight changes of surface conditions (e.g., albedo) and in turn changes of radiational forcing. The large impact of water-fed paddy fields in China on the development of cloud/precipitation systems in the Meiyu frontal zone may correspond to this situation.

This simple model of energy and water balance can be applied to understanding the role of the LAI of the large-scale Asian monsoon system. For example, when we compare the pre-onset phase and the mature phase of the monsoon season, we notice that ΔP between the two season is basically due to the change of T^* derived from the seasonal change of solar radiation, but the enhancement of ΔP is due to a change of q and β, derived from moisture convergence and *in situ* evaporation, respectively (Yasunari and Kozawa, 2005). Through these moist processes, the large-scale Asian monsoon system, with a huge P particularly over the land area, could be formed as it is now.

11.6 CONCLUDING REMARKS

This chapter has discussed the role of LAI in the Asian monsoon system. Particular emphasis and focus has been placed on what is the essential and primary role of the 'land' of the Asian (or Eurasian) continent in the Asian monsoon system as a huge coupled ocean–land–atmosphere system.

The role of the Tibetan Plateau is emphasized as a means of triggering the atmospheric heating over the continent. At the onset or pre-monsoon phase of the monsoon, sensible heating over the elevated land surface plays an important role in forming the continental-scale heat low in the lower troposphere. This circulation system in turn produces a moist south-westerly flow penetrating into south, south-east, and east Asia. This moist monsoon flow induces convection and precipitation over the south-eastern part of the continent, which further intensifies atmospheric diabatic heating through latent heat release.

As major land surface parameters controlling the Asian monsoon variability, we have discussed the roles of snow cover, soil moisture, and vegetation. The snow cover and soil moisture are internal factors of the climate system particularly in the seasonal to interannual timescales, and are likely to play some important roles in changing the large-scale surface energy and water balance, which in turn affects the monsoon circulation and precipitation. One big problem is that the data available on these two quantities as internal parameters of the climate system is still limited, though new satellite data are considerably improving this situation. The quantitative estimates of the impact of these parameters on the monsoon-related fields needs further study, but it may be concluded that both the extent of these parameters and what role they play in the variability of the monsoon system depends strongly on the basic climatic conditions and seasonality.

Another parameter, vegetation, has been noted as an important variable for the formation of moist monsoon flow over the continent. Vegetation has several functions for controlling atmospheric energy and water vapor conditions, such as albedo, roughness, stomatal conductance, and water-holding capacity (of the root/soil structure). In fact, through the recent observations and modeling studies, the atmospheric latent heating over land has been noticed fundamentally through vegetation control of evapotranspiration. The anthropogenically induced change of land cover/landuse, including deforestation, has had a great impact on the regional precipitation and water cycle of the monsoon region by changing some characteristics of the vegetation's control of the energy and water cycles, which in turn affect the ABL and cloud/precipitation processes on regional-scales.

Finally, a general discussion has been made on how the land surface changes could induce changes in precipitation through the feedback processes of moisture convergence and *in situ* evapotranspiration processes. In this simple discussion the critical role of moisture amount near the surface and in the ABL is emphasized, to induce a positive feedback to change precipitation over land in the monsoon region.

In the Asian monsoon system, the fundamental heating centers are located over the warm oceans near the continent, which also prove to result from the strong thermal and thermodynamic effect of the Tibetan Plateau (Kitoh, 2004; Abe *et al.*,

2004). In addition, we emphasize that the moist land surface could play an important role for the penetration of precipitation into the deep interior of the continent. This moist land surface process has proved to be essentially attributed to the existence of vegetation. In this sense, the heavily vegetated land surface may be another key factor of the strong Asian summer monsoon in addition to the Tibetan Plateau.

12

Interactions between the Asian monsoon and the El Niño/Southern Oscillation

Ngar-Cheung Lau and Bin Wang

The other chapters in this book have devoted considerable attention to the significant role of the sea surface temperature (SST) conditions over the Pacific and Indian Oceans in climatological aspects as well as variability of the Asian monsoon. The El Niño/Southern Oscillation (ENSO) phenomenon is known to exert a strong influence on the SST patterns throughout the World's oceans. The nature of the interactions between ENSO and the atmospheric circulation over different parts of the Asian–Australian region is obviously of primary importance in understanding many facets of the monsoon system. Of particular interest is the response of the monsoon flows to local and remote SST changes that emerge during ENSO, as well as the impact of monsoon fluctuations on the evolution of ENSO episodes.

The principal goal of the present chapter is to offer a synopsis of the basic characteristics of the ENSO phenomenon, its relationships with monsoonal features in the south Asian and east Asian–western Pacific sectors in different stages of the ENSO cycle, physical mechanisms that contribute to covariability between ENSO and the monsoon system, the effects of monsoon anomalies on the oceanic temperature and circulation fields, and the implications of such feedbacks on the subsequent development of ENSO. This review of the linkages between ENSO and the Asian monsoon is based on the available observational records of the last half-century, as well as output from general circulation model (GCM) experiments that are designed to delineate pertinent aspects of atmosphere–ocean coupling.

12.1 AIR–SEA INTERACTIONS RELATED TO ENSO

Detailed historical accounts of the discovery of a myriad of oceanic and atmospheric features associated with ENSO, as well as the mechanisms contributing to ENSO variability, have been given by Rasmusson (1985), Enfield (1989), Philander (1990), Glantz *et al.* (1991), Cane (1992), Wallace *et al.* (1998), Neelin *et al.* (1998), Jin (2004)

B. Wang (ed.), *The Asian Monsoon*.

and Wang and Picaut (2004), among others. The term 'El Niño' (the child) was originally used by natives of the Peru–Ecuador coasts to refer to a warm ocean current that appears in that region during the Christmas season. It has been known for centuries that the intensity of this annual coastal warming fluctuates from year to year (Quinn and Neal, 1978). The data from an expanded monitoring network established during the International Geophysical Year (1957–1958), which coincided with an unusually strong El Niño, indicate that the warm SST anomaly associated with this episode extended westward to as far as the Date Line. Composite analyses of recent outstanding El Niño events (e.g., Rasmusson and Carpenter, 1981) confirm the large spatial extent of the SST signal associated with El Niño. These empirical studies also reveal that the anomalous SST episodes in the equatorial Pacific often exhibit cyclical characteristics, with warm events being followed by cold ('La Niña') events, and vice versa. The SST anomaly typically emerge in the eastern equatorial Pacific during the boreal spring, attaining maximum strength in the central Pacific 6–9 months later, and attenuating in the northern spring or summer of the following year.

The term 'Southern Oscillation' was coined by Walker and Bliss (1932) to refer to a global-scale east–west seesaw pattern in the sea level pressure (SLP) field. This pattern primarily depicts the out-of-phase relationship between interannual SLP variations over the western Pacific/Indian Oceans, and those over the eastern Pacific (e.g., Troup, 1965; Trenberth and Shea, 1987). This phenomenon was documented by Sir Gilbert Walker in his pursuit to improve monsoon prediction in the Indian region.

A significant milestone in our understanding of the El Niño and Southern Oscillation phenomena was reached when Bjerknes (1966, 1969) pointed out that they are strongly coupled to each other. The basic processes considered in Bjerknes' hypothesis may be summarized as follows. The marked climatological thermal contrast between the 'warm pool' in the western Pacific and cold temperatures in the equatorial eastern Pacific is accompanied by relatively low (high) SLP west (east) of the Date Line. This thermal contrast drives a thermally direct atmospheric circulation loop (the 'Walker Cell') along the equatorial zonal plane, with ascending (descending) motion over the western (eastern) Pacific, a westward air current near the surface, and eastward return flow at upper levels. An anomalous cold event in the eastern tropical Pacific (i.e., La Niña) would enhance the zonal SST and SLP gradients across the Pacific basin, which would correspond to a positive swing of the Southern Oscillation (i.e., higher SLP to the east, lower to the west). The stronger Walker Cell would be accompanied by above-normal easterly winds at the surface, which further amplify the east–west SST gradient through the effects of oceanic advection, upwelling and thermocline displacement (see description of the latter oceanic processes by Cane (1992)). Conversely, the slackened thermal and pressure contrasts across the Pacific basin during an El Niño event would be associated with a negative phase of the Southern Oscillation and weakened easterly trades at the equator, which is conducive to still further oceanic warming. The anomalous episodes of either polarity are hence sustained by the cooperative feedbacks between the atmospheric and oceanic components of the coupled system (see

schematic diagrams in McPhaden *et al.* (1998; figure 1)). In recognition of the intimate relationship between El Niño and the Southern Oscillation, the term 'ENSO' has been widely adopted since the 1980s to refer to the myriad of phenomena mentioned above.

The characteristic spatial patterns of atmospheric and oceanic anomalies during the peak stage of ENSO are portrayed in Figure 12.1(a) (color section). This panel has been constructed by subtracting the composite over ten La Niña events (1950, 1954, 1955, 1964, 1970, 1973, 1975, 1988, 1998, 1999; see blue markers along the time axis in Figure 12.1(b)) from that over ten El Niño events (1957, 1965, 1969, 1972, 1976, 1982, 1987, 1991, 1997, 2002; see red markers in Figure 12.1(b)). This composite procedure has been performed for the three-month period from December of the year when the events initiated ('year 0') to February of the following year ('year 1'). We shall henceforth refer to a specific time period within the ENSO time frame by grouping the first letter of the months in that period, followed by the year(s) in parentheses. For instance, the northern winter period considered in Figure 12.1(a) is abbreviated as DJF(0/1). The patterns generated by the above procedure will be referred to as the 'warm-minus-cold composites'. The distributions of SLP (contours) and surface vector wind (arrows) in Figure 12.1(a) have been obtained from the National Centers for Environmental Prediction (NCEP) reanalysis data set (Kalnay *et al.*, 1996). The SST pattern (shading) in this figure has been computed using the data set compiled by Hurrell *et al.* (2005). These charts indicate that, when the ENSO events are fully developed, the zonal extent of the near-equatorial SST anomaly is more than 90° of longitude, and its peak-to-peak amplitude exceeds 3°C. Concurrent with the warm SST anomaly are negative (positive) SLP changes east (west) of the Date Line, with peak-to-peak amplitudes approaching 2 hPa near the two poles of the Southern Oscillation (i.e., subtropical central south Pacific and northern Australia). Anomalous westerly surface flow prevails near the equator during warm events, thus indicating a weakened Walker circulation. The composite patterns in Figure 12.1(a) also indicate considerable convergence of the surface wind to the warm SST anomaly.

The variations of the key atmospheric and oceanic features in Figure 12.1(a) (color section) are depicted in the panels below that figure, for anomalies of (b) SST in the eastern/central equatorial Pacific, (c) SLP over the central subtropical south Pacific and over northern Australia, and (d) surface zonal wind over the central/western equatorial Pacific. These indicators are obtained by averaging the monthly data over the rectangular regions shown in Figure 12.1(a). The temporal fluctuations displayed in Figures 12.1(b–d) illustrate the relationships between the SST and atmospheric changes as noted by Bjerknes.

Bjerknes' hypothesis has offered a good explanation for the amplification of ENSO-related atmospheric and oceanic anomalies through mutual reinforcement. However, further research is needed to elucidate the mechanisms responsible for the cyclical nature of ENSO events. One of the most influential paradigms that addresses this important aspect of ENSO was proposed by Schopf and Suarez (1988), Suarez and Schopf (1988), and Battisti and Hirst (1989). The essential processes considered by these investigators are shown in Figure 12.2. During an

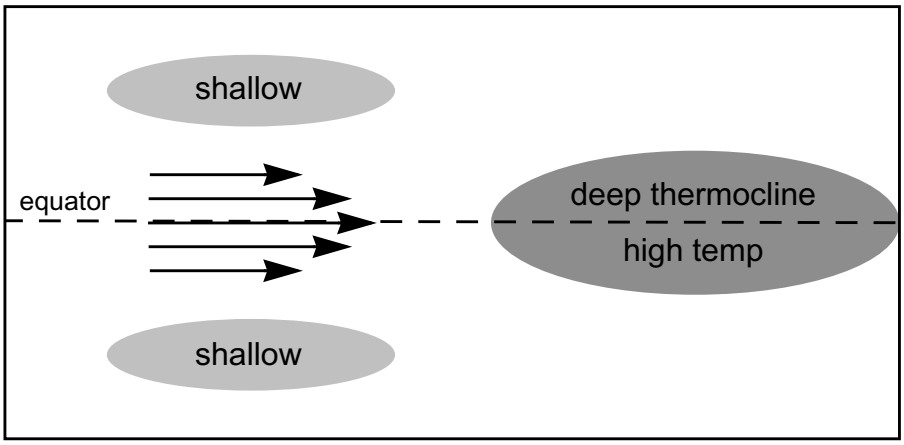

Figure 12.2. Schematic representing the spatial structures of the delayed oscillator mode during El Niño. Anomalies in surface wind and thermocline depth are indicated by arrows and shading, respectively.
From Philander and Fedorov (2003).

El Niño event, the above-normal SST and deepened thermocline in the central and eastern equatorial Pacific is accompanied by westerly surface wind anomalies in the western part of the basin (see Figure 12.1(a), color section). The curl of the wind stress associated with the latter feature leads to shoaling of the thermocline on both sides of the equator. The spatial structure of this pair of off-equatorial oceanic signals resembles that of a Rossby wave packet, which tends to carry the thermocline anomalies westward. When these wave motions encounter the western edge of the basin, a portion of their energy is converted to that associated with Kelvin waves, which first propagate equatorward near the western coast and then eastward along the equatorial Pacific. The shoaling thermocline tendency is preserved in this process at the western boundary. The oceanic signals returned by the Kelvin waves to the central and eastern Pacific are hence opposite in sign to the deep thermocline anomaly that originally resides in that region, and thereby facilitates the transition in the ENSO cycle from a warm phase to a cold phase. In this context, the behavior of the tropical atmosphere–ocean system is analogous to that of a delayed oscillator, with the SST anomaly of a given polarity 'sowing the seed' for its own demise some time later by instigating a host of atmospheric and oceanic changes that eventually generate a new anomaly of the opposite polarity. Observational evidence (e.g., Wyrtki, 1975, 1985) and diagnosis of coupled models (e.g., Zebiak and Cane, 1987) are in support of the applicability of this general paradigm for understanding certain facets of ENSO dynamics. Other oscillator modes highlighting the roles of a charging/recharging of the upper ocean heat content (Jin, 1997), zonal temperature advection in the central Pacific (Picaut *et al.*, 1996), and various aspects of air–sea interaction over the western Pacific (Weisberg and Wang, 1997a; Wang *et al.*, 1999) have also been proposed.

Philander and Federov (2003) proposed that the ENSO events observed in

nature may be viewed as a hybrid of the delayed oscillator mode illustrated in Figure 12.2, and other modes arising from local air–sea interactions (e.g., the 'SST mode' examined by Neelin (1991)). Fedorov *et al*. (2003) further noted that random atmospheric disturbances, such as westerly wind bursts over the western tropical Pacific, could play a crucial role in determining the unique characteristics of individual events. The predictability of ENSO is hence limited by the amount of atmospheric 'noise' that is ever present in the climate system.

12.2 PRECIPITATION ANOMALIES IN THE ASIAN–AUSTRALIAN MONSOON REGION DURING ENSO EVENTS

The typical evolution of precipitation anomalies in the Asian–Australian monsoon region in various phases of the ENSO cycle has been documented by Ropelewski and Halpert (1987) using station records. Various other empirical studies on the impacts of ENSO on the monsoon rainfall intensity over the Indian subcontinent, east Asia, and Australia have also been reviewed recently by Webster *et al*. (1998) and Wang *et al*. (2003).

The development of the anomalous rainfall pattern through different stages of ENSO is illustrated using the warm-minus-cold composites from JJA(0) to JJA(1) in Figure 12.3. These charts have been constructed using the data set produced by the Global Precipitation Climatology Project (GPCP; see Huffman *et al*., 1997), which incorporates measurements of both rain gauges and satellites. Due to the somewhat limited duration of this data set, only three El Niño events (1982, 1991, 1997) and two La Niña events (1988, 1998) have been included in the present composite procedure. The composite charts in Figure 12.3 bear some correspondence to the correlation maps presented by Navarra *et al*. (1999) and Miyakoda *et al*. (1999).

Through much of the JJA(0)–DJF(0/1) period (Figure 12.3(a–c)), the precipitation patterns in the equatorial zone are dominated by negative anomalies over the Indonesian archipelago and eastern Indian Ocean, and by positive anomalies from $\sim 150^{\circ}$E to the Date Line. These features are indicative of the eastward displacement of the Walker circulation during warm ENSO events (Section 12.1). Over the Arabian Sea/India/southern Bay of Bengal region, below-normal rainfall prevails during the summer and autumn of 'year 0' (Figure 12.3(a,b)). This deficiency of Indian monsoon rainfall during the summer of warm events is a well-known phenomenon (e.g., Rasmusson and Carpenter, 1983; Shukla and Paolino, 1983). Comparison between Figure 12.3(a) and (e) suggests that the summertime precipitation anomalies over the Arabian Sea and Bay of Bengal tend to change sign from year(0) to year(1). During SON(0) and DJF(0/1) (Figure 12.3(b,c)), the precipitation changes over the equatorial and southern Indian Ocean are characterized by dry conditions in the east, and wetness in the west. This rainfall pattern is evidently related to a recurrent mode of SST variability in the Indian Ocean basin, which also exhibits distinct east–west contrasts in northern autumn (Section 12.3.1 and Figure 12.5, color section).

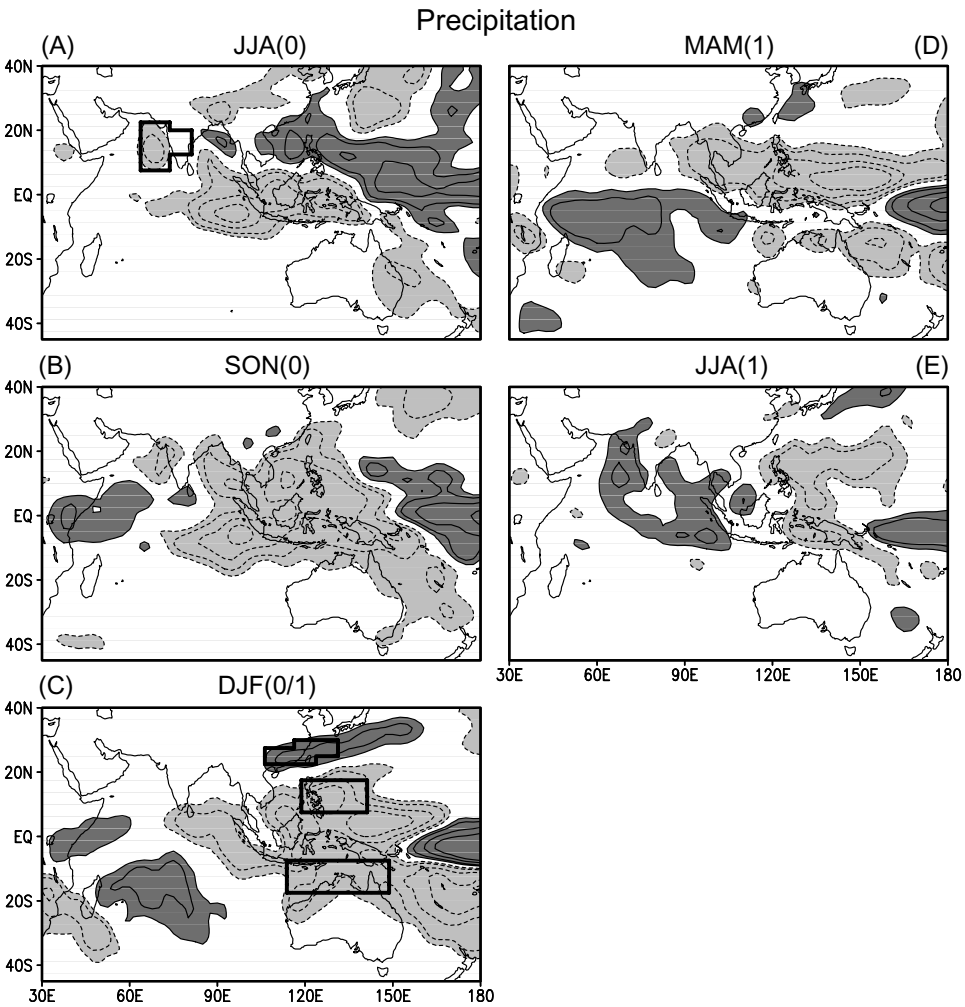

Figure 12.3. Distributions of the warm-minus-cold composites of precipitation during (a) JJA(0), (b) SON(0), (c) DJF(0/1), (d) MAM(1) and (e) JJA(1), as computed using GPCP data for the warm ENSO events of 1982, 1991 and 1997 and the cold events of 1988 and 1998. Contours are shown for ± 1, ± 2, ± 3, ± 4 and $\pm 6\,\mathrm{mm\,d^{-1}}$, respectively. The zero contours are not shown. The sites used for computing the areal averages displayed in Figure 12.4 are indicated in (a) and (c).

The most prominent precipitation anomalies in the east Asian and Australian monsoon regions appear in DJF(0/1) (Figure 12.3(c)). Below-normal rainfall is observed over the Philippines and the nearby oceans, as well as northern Australia. An elongated wet zone is also seen to extend north-eastward from southern China to the waters south of Japan. The dry anomaly in the vicinity of the Philippines is first established in SON(0) over the South China Sea

(Figure 12.3(b)). This feature migrates eastward with time, with its main center being located over the tropical western Pacific in MAM(1) (Figure 12.3(d)). Remnants of the wet anomaly over southern China and Japan are still discernible in MAM(1).

The robustness of the composite precipitation signals identified in Figure 12.3 may be assessed by inspecting the anomalies in various key regions for a larger number of individual warm and cold ENSO events, and comparing the rainfall estimates based on different data sources. In Figure 12.4 are plotted the precipitation anomalies occurring in each of six selected warm events (left panels) and six cold events (right panels), as obtained using the data sets provided by GPCP, Climate Prediction Center Merged Analysis of Precipitation (CMAP; see Xie and Arkin, 1997) and Dai *et al.* (1997). The CMAP fields are based on a combination of rain gauge observations, satellite measurements and numerical model outputs. Both the GPCP and CMAP data have global coverage, and are available from 1979 onwards. Dai's product consists of gridded analyses of rain gauge records exclusively, and covers land points over the period of 1950–1995. The data values shown in Figure 12.4 are areal averages taken at four individual monsoon regions: central India–Arabian Sea (IND), southern China and the East China Sea (CHI), the Philippine Sea (PHI), and northern Australia (AUS). The boundaries chosen for these regions are depicted in Figure 12.3(a) (for IND) and Figure 12.3(c) (for CHI, PHI, and AUS). The seasons used in computing the anomalies (i.e., JJA(0) for IND, and DJF(0/1) for CHI, PHI, and AUS) correspond to those periods in the ENSO cycle when the rainfall signals attain maximum strength in the respective sites (Figure 12.3).

The observational data points displayed in Figure 12.4 confirm the dry conditions in the IND, PHI, and AUS regions, and wet conditions in CHI in a majority of the warm events. These precipitation anomalies are reversed during most of the cold events. The consistency among individual warm and cold events is particularly strong for the PHI region (Figure 12.4(e,f)). A notable exception to the general relationship between ENSO and monsoon rainfall over IND is seen during the warm events in the post-1980 era (Figure 12.4(a)), when some of the observational data sets indicate wet anomalies in that region. Such occurrences evidently contribute to the weakened correlation between ENSO and Indian rainfall during the past two decades, as pointed out by Krishna Kumar *et al.* (1999b). For a given region considered in Figure 12.4, the estimates by the GPCP and CMAP data sets in each event are mostly in good agreement with each other. The corresponding estimates by Dai's data set deviate noticeably from the GPCP/CMAP values in some cases, partially due to the incorporation of other sources of information in the latter data sets, and to the voids in Dai's station data over the maritime portion of the four regions examined here.

The observational rainfall estimates in Figure 12.4 are displayed in juxtaposition with corresponding areal averages based on output from two experiments with a 30-wavenumber, 14-level GCM developed at the Geophysical Fluid Dynamics Laboratory (GFDL). Details of these integrations have been given by Alexander *et al.* (2002) and Lau and Nath (2003). In the control (CTRL) experiment, the observed monthly SST variations throughout the 1950–1999 period have been

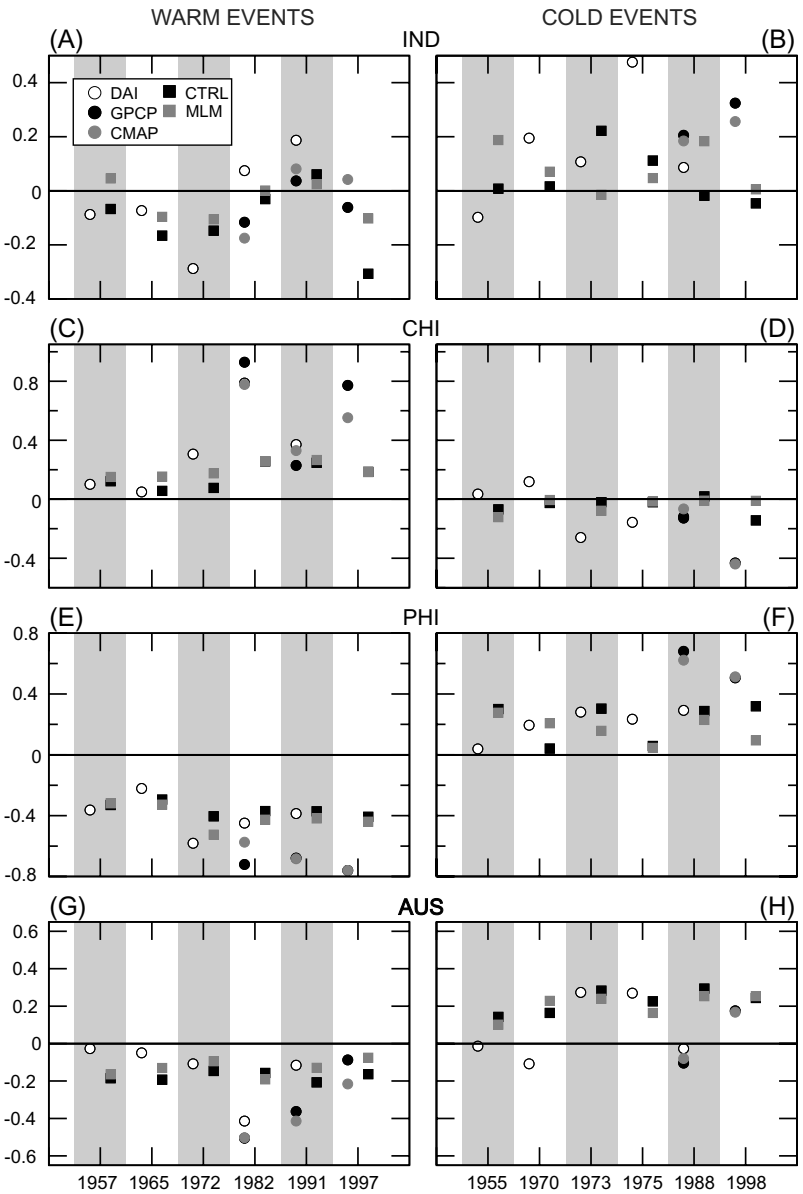

Figure 12.4. Areal averages of precipitation anomalies during six selected warm ENSO events (*left panels*) and six cold events (*right panels*), for (a, b) India–Arabian Sea (IND) in JJA(0); and for (c, d) southern China–East China Sea (CHI), (e, f) the Philippine Sea (PHI), and (g, h) northern Australia (AUS), all in DJF(0/1). Results are computed based on various observational data sets (Dai, GPCP, and CMAP, indicated by circles) and on output from the MLM and CTRL experiments (indicated by squares). All results are expressed as fractions of the local climatological mean precipitation. The regions used in computing the areal averages are indicated in Figure 12.3(a) (for IND) and Figure 12.3(c) (for CHI, PHI and AUS).

inserted in the deep tropical eastern/central Pacific (DTEP; 5°S–5°N, 172°E to the South American coast). The SST at all ocean points outside of the DTEP has been fixed at their climatological seasonal values, with no interannual variability. In the mixed-layer model (MLM) experiment, the identical sequence of temporally varying SST changes has been prescribed in the DTEP, whereas the SST conditions at remaining ice-free maritime sites have been predicted using a variable-depth oceanic mixed-layer model. A detailed description of this mixed-layer model has been provided by Alexander *et al.* (2000). Altogether eight and sixteen independent integrations have been performed using the designs for the CTRL and MLM experiments, respectively. The results presented in this chapter are based on ensemble averages over these individual realizations.

Inspection of the data entries in Figure 12.4 for the CTRL and MLM experiments reveals considerable model skill in reproducing the observed ENSO-monsoon rainfall relationships in various regions. The fidelity of the simulations is particularly evident in the PHI and AUS regions, where the polarity of model-generated precipitation anomalies is the same for all six warm events for each site (Figure 12.4(e) and (g)), and is reversed for all six cold events (Figure 12.4(f) and (h)). In accord with the weakening of the correlation between ENSO and the observed Indian monsoon rainfall in recent decades, the model simulations for the IND region (Figure 12.4(a,b)) also exhibit a relatively broader scatter among the individual events. For the CHI, PHI, and AUS regions, the precipitation anomalies for a given event in the CTRL and MLM experiments are mostly in close agreement with each other. This result suggests that the rainfall variations in these regions during the DJF(0/1) season are mostly forced by SST anomalies in the DTEP region, and that the additional air–sea feedbacks incorporated in the MLM experiment do not significantly alter the remote response to this primary forcing originating from the tropical Pacific. On the other hand, the more notable differences between the CTRL and MLM signals for some ENSO events in the IND region (Figure 12.4(a,b)) are indicative of a stronger role of local air–sea interactions in rainfall variability at that location.

In view of the demonstrable capability of the GCM to mimic the impact of ENSO on monsoon rainfall, we shall henceforth make use of the output from the CTRL and MLM experiments to delineate the mechanisms linking ENSO to the variability of the coupled atmosphere–ocean system in the Asian–Australian monsoon region.

12.3 ENSO-RELATED VARIABILITY IN THE INDIAN OCEAN BASIN

12.3.1 Atmospheric and SST anomalies

The typical atmospheric and oceanic changes in the Indian Ocean (IO) sector during ENSO episodes are illustrated in Figure 12.5 (color section), which shows the warm-minus-cold composites of the 850-hPa vector wind (arrows) and SST (shading) fields for the JJA(0), SON(0), and DJF(0/1) seasons. These patterns are based on the six

warm and six cold events examined in Figure 12.4, and have been constructed using the NCEP data (left panels) and model data generated in the MLM experiment (right panels).

The most coherent atmospheric signal in both the reanalysis and MLM patterns for JJA(0) (Figure 12.5(a,b), color section) is the anticyclonic 850-hPa circulation anomaly that prevails over the Arabian Sea and the surrounding land areas. This feature is seen to extend toward the Bay of Bengal and Indo-China during the SON(0) season (Figure 12.5(c,d)). The easterly wind anomalies over much of the northern IO that accompany the anticyclone oppose the climatological westerlies over this region (see climatological streamline charts shown in Lau and Nath (2000)), and is indicative of below-normal intensity of the summer monsoon circulation over south Asia during warm ENSO events. Also evident in the composite patterns for the northern summer and fall seasons is the emergence of warm SST anomalies in both the Arabian Sea and Bay of Bengal. As noted in Lau and Nath (2000, 2003), two factors contribute to these SST changes. First, reduction in the monsoon intensity during warm ENSO episodes is accompanied by lowered wind speeds over these oceanic regions, which result in less latent and sensible heat loss to the atmosphere. Second, the decreased amount of cloud cover due to the generally dryer conditions in these areas (Figure 12.3(a,b)) leads to more heating of the ocean surface by incoming solar radiation. The observed SST increase near the Somali and Arabian coasts could also be partially caused by the reduced oceanic upwelling associated with weakened monsoon flows, an effect that is not considered in the MLM experiment.

Another noteworthy SST signal in the JJA(0) and SON(0) seasons is the cold anomaly that develops off the Sumatra–Java coasts. This feature is collocated with low-level south-easterly or easterly wind anomalies, which are parallel to the local climatological circulation (e.g., see Lau and Nath, 2000). Budget analysis performed by Lau and Nath (2003) indicates that the increased surface wind speeds in this region lead to increased latent and sensible heat loss from the ocean, as well as deepening of the local oceanic mixed layer. Both effects are conducive to SST cooling. The stronger upwelling driven by the intensified winds along the shores of Sumatra and Java, and by anomalous easterlies in the eastern equatorial IO, could further enhance the observed cold SST anomaly in those sites. This oceanic cooling in the eastern IO is in distinct contrast with the warming in the western portion of the basin described in the preceding paragraph. The occurrence of this zonal asymmetric SST anomaly pattern, which is most evident in SON(0), has been noted by Webster *et al.* (1999) and Saji *et al.* (1999). A corresponding east–west contrast in the precipitation field is also discernible in the same season (Figure 12.3(b)). These investigators have attributed this mode of variability mostly to processes operating within the IO sector. However, the appearance of the same pattern in the ENSO composites shown in Figure 12.5(c,d; color section) indicates that the remote forcing from the tropical Pacific could also influence the SST field in the IO.

During the DJF(0/1) period (Figure 12.5(e,f), color section), the cold SST anomaly in the tropical eastern IO is no longer discernible. The climatological low-level flow over this region switches from easterly to westerly in this season

(e.g., Lau and Nath, 2000; Schott and McCreary, 2001), so that the easterly wind anomalies would lead to reduction of both wind speed and heat loss from the ocean. The below-normal rainfall in this area results in decreased cloud amounts and increased incoming solar radiation. Both effects contribute to warming in the eastern IO. The processes contributing to the reversal of the SST tendency in the tropical eastern IO during the JJA(0)–DJF(0/1) period have also been noted by Nicholls (1984), Hendon (2003), Li *et al.* (2003), and Shinoda *et al.* (2004). The SST anomalies in other parts of the IO remain positive in DJF(0/1), with notable amplification in the Bay of Bengal and the central IO between, 20°S and 30°S. These two sites are overlain by wind anomalies that oppose the local climatological circulation, which is oriented south-westward over the Bay of Bengal, and north-westward over southern IO during the DJF season. The resulting decrease in wind speed and in oceanic heat loss are hence consistent with the more pronounced SST warming over these areas. The basin-wide atmospheric circulation anomaly in DJF(0/1) is characterized by strong easterlies along the tropical IO, and a pair of anticyclonic cells straddling the equator, with centers located over the north-western Australia and the South China Sea. The MLM pattern (Figure 12.5(f)) is suggestive of a tendency for the anomalous wind vectors to be directed from the eastern equatorial IO (where SST is near normal) to the primary sites of warm SST anomalies (i.e., western IO, Arabian Sea, Bay of Bengal, and central IO south of 20°S). Composite SST patterns for the MAM(1) and JJA(1) seasons, as shown in Alexander *et al.* (2004) and later in this chapter (Figure 12.7(b,c), color section) using observed and MLM data, respectively, indicate that the principal warm SST anomalies in the IO basin persist through the northern summer season of year(1).

There is general agreement between the broad-scale features of the wind anomaly pattern deduced from the reanalysis data and the model output. The magnitude of the wind vectors in the JJA(0) and SON(0) seasons is noticeably larger in the reanalysis results than in the model simulation (note the different scales used plotting the left and right panels of Figure 12.5, color section). The discrepancies between the observed and model patterns are more evident in the SST field. During the SON(0) season, the cold anomaly simulated in the MLM experiment (Figure 12.5(d)) extends too far to the central and western IO as compared with the observed pattern (Figure 12.5(c)). The observed warming of the equatorial waters in the central and eastern IO in DJF(0/1) is also less evident in the model pattern (compare Figure 12.5(e) with (f)). Such discrepancies may partially be attributed to the effects of ocean dynamics that are not incorporated in the MLM experiment.

12.3.2 Atmospheric response to anomalous tropical heating

We next evaluate the extent to which the atmospheric wind anomalies depicted in Figure 12.5 (color section) may be attributed to remote forcing by ENSO-related precipitation changes in the tropical zone. By invoking analytic solutions presented by Matsuno (1966) and Gill (1980) for tropical circulations induced by heating,

several investigators (e.g., Chen and Yen, 1994; Kawamura, 1998; Lau and Nath, 2000; Wang *et al*., 2003) have interpreted the low-level anticyclones over south Asia and the southern IO (Figure 12.5) as Rossby wave responses to anomalous cooling over the Indonesian archipelago and the equatorial western Pacific. The latter heat sink is in turn linked to the eastward displacement of the Walker circulation during warm ENSO events, which results in below-normal precipitation in the equatorial zone between 90°E and 150°E (Figure 12.3(a–c)). The atmospheric responses to diabatic heating in various monsoon regions have also been examined by Rodwell and Hoskins (2001).

The effects of the altered diabatic forcing over the western Pacific on the atmospheric flow pattern have been demonstrated by Wang *et al*. (2003) and Lau *et al*. (2004) using solutions of stationary wave models for the JJA(0) and DJF(0/1) seasons, respectively. We hereby adopt the same approach to diagnose the atmospheric response to heating anomalies in the Indo-Pacific region. The stationary wave model examined in the current work is based on the dynamical framework of the GFDL GCM used for the MLM experiment (see Ting and Yu, 1998, for details). The 2-D basic state in the latitude–height plane has been incorporated in the stationary wave models using climatological data for the corresponding season. Anomalous diabatic forcing, as obtained from the warm-minus-cold composites of the heating rates generated in the MLM experiment for JJA(0) and DJF(0/1), has been applied to the stationary wave model, and linear steady-state solutions were then computed. Only composite cooling rates in the Indonesia–western Pacific sector have been considered in the calculations to be presented here. During JJA(0), there exists some cancellation between the solution in Figure 12.6(a) and the corresponding response to the enhanced heating over the central equatorial Pacific during warm ENSO events (not shown). In DJF(0/1), the response to central Pacific heating is much weaker than that displayed in Figure 12.6(b) (see Lau *et al*., 2004).

The vector wind response in the lower troposphere (sigma level 0.935) of the stationary wave model (arrows) to the prescribed cooling anomaly (contours) is displayed in Figure 12.6, for (a) JJA(0) and (b) DJF(0/1) seasons. Some similarity exists between the wind anomaly patterns in Figure 12.5 (color section) and the stationary wave model solutions for the corresponding season in Figure 12.6, thus suggesting that the diabatic forcing in the vicinity of the tropical western Pacific accounts for some of the circulation changes appearing in the IO sector of the GCM atmosphere. Of particular interest is the generation by the stationary wave model of strong anticyclonic flow over south Asia during JJA(0), which is located to the north-west of the prescribed cooling center over the equatorial western Pacific (Figure 12.6(a)). The center of this anticyclone in the stationary wave solution is situated to the east of the corresponding features in Figure 12.5(a) and (b) (color section). Analogously, the anticyclonic centers over the east Asian and northern Australia–southern IO during DJF(0/1) are situated to the north-west and south-west, respectively, of the extensive heat sink over the tropical and subtropical western Pacific (Figure 12.6(b)). These spatial relationships between the atmospheric flow pattern and the heating field are in accord with those for the Rossby wave solutions in the Matsuno–Gill models. It is also noteworthy that the pronounced

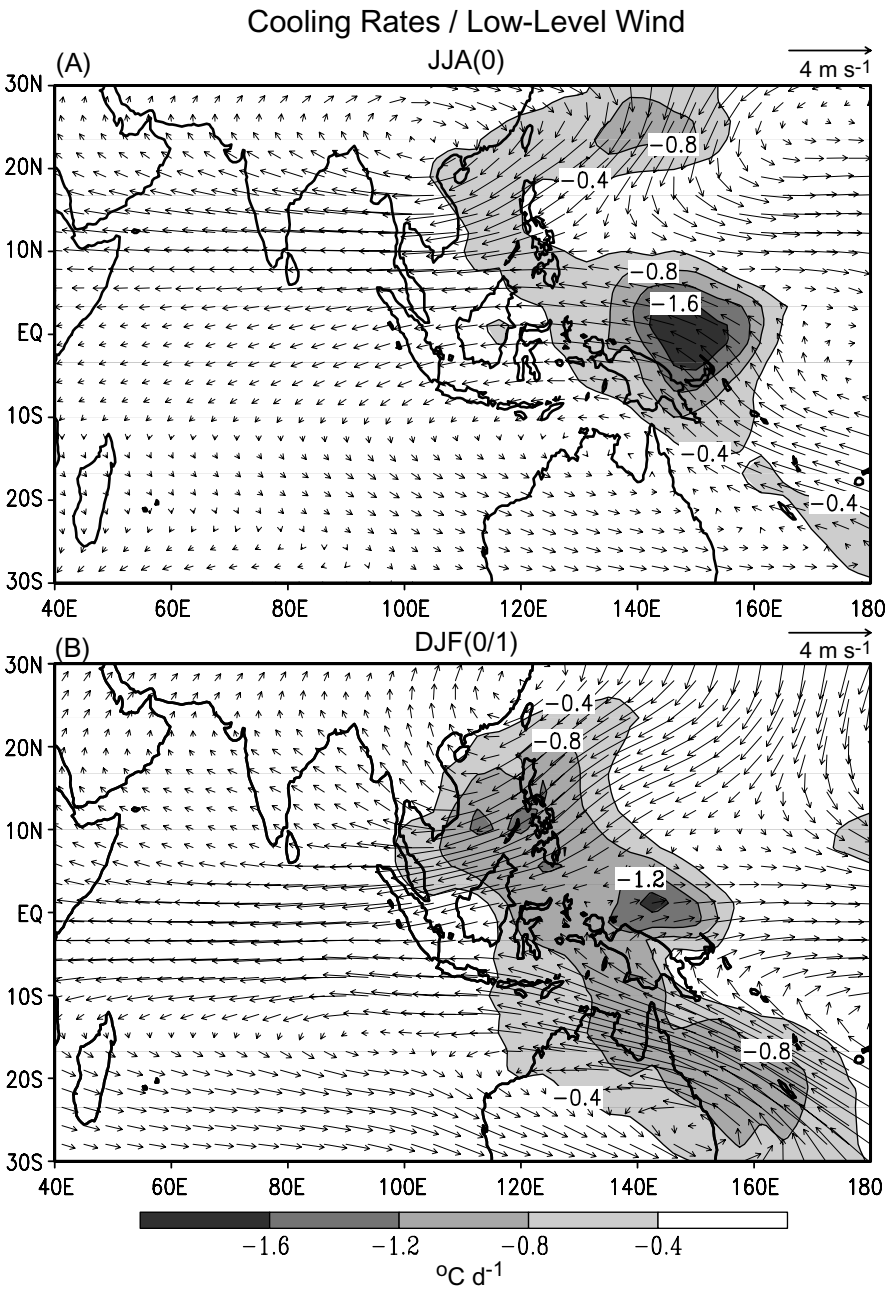

Figure 12.6. Distributions of wind response (arrows) in the lower troposphere (sigma level 0.935) to cooling in the Maritime Continent and western Pacific, as simulated by a linear stationary wave model with specified 2-D basic state for (a) JJA and (b) DJF. Warm-minus-cold composites of the cooling rates from the MLM experiment are shown in contours and shading (units: $^{\circ}\mathrm{C\,d^{-1}}$) for the (a) JJA(0) and (b) DJF(0/1) periods.

near-equatorial easterlies over the IO basin, as seen in the observed and MLM patterns in Figure 12.5, are also evident in the patterns based on the stationary wave model.

The stationary wave solution for JJA(0) in Figure 12.6(a) exhibits a considerable degree of asymmetry about the equator, with strong anticyclonic signals over south Asia, and much weaker responses over the southern hemisphere. This interhemispheric difference in the response patterns during the boreal summer is partially related to the spatial distribution of the cold sink imposed in this season (see contour pattern in Figure 12.6(a)). As noted by Wang *et al.* (2003), another contributing factor to the asymmetry of the cooling-induced circulation anomaly about the equator is the distinct vertical structure of the basic state over the IO region in JJA. During this season, strong easterly shears with increasing height occur over the south Asian monsoon region north of the equator. The normal mode analyses by Wang and Xie (1996) and Xie and Wang (1996) indicate that moist Rossby wave responses are amplified in the presence of easterly vertical shears in the background flow, and vice versa. These theoretical results are consistent with the relative strength of the response signals in the two hemispheres for the JJA season.

12.3.3 Atmosphere–ocean feedbacks in the IO basin

The cumulative evidence presented in Figures 12.3–12.6 highlights the following chain of processes linking ENSO events in the tropical Pacific to SST variations in the IO basin: eastward displacement of the Walker circulation during warm ENSO episodes, reduced precipitation and latent heat release over Indonesia and the tropical western Pacific, generation of atmospheric Rossby wave responses to the north-west and south-west of the heat sink, and atmospheric driving of the SST field in the IO sector through modulation of surface latent and radiative fluxes as well as ocean currents. Hence the atmospheric circulation serves as a 'bridge' communicating the ENSO forcing in the DTEP to oceanic changes elsewhere (Klein *et al.*, 1999; Alexander *et al.*, 2002). In the early stages of ENSO development (i.e., during the JJA(0)–SON(0) period), the impact of the atmospheric bridge is not yet fully felt in the IO sector, and the SST anomalies in that basin are still relatively weak (Figure 12.5(b) and (d), color section). As noted in Section 12.3.1, the SST changes over the IO in this period may be interpreted as the oceanic response to ENSO-related atmospheric driving; whereas the emerging SST anomalies do not exert a strong influence on the atmospheric circulation. It is only after the ENSO-induced SST anomalies are better established (in DJF(0/1) and thereafter) that the feedbacks of the oceanic changes on the atmosphere become more evident. We shall henceforth focus on such feedbacks in the period starting from DJF(0/1). The nature of these effects could be delineated by diagnosing the model output from the MLM experiment in conjunction with that from the CTRL experiment (Section 12.2). The CTRL experiment has been designed to yield the global atmospheric responses to SST forcing prescribed in the tropical Pacific only. In addition to this 'direct' response to ENSO, the MLM experiment also incorporates two-way, air–sea interactions induced by the atmospheric bridge mechanism outside of the tropical Pacific.

Hence, the atmospheric signals that are associated with the latter feedback processes may be estimated by removing the direct ENSO response as simulated in the CTRL experiment from the MLM data. This strategy has been adopted by Lau and Nath (2000, 2003) and Lau *et al.* (2004) to isolate the impact of ENSO-induced SST anomalies in different parts of the World's oceans on the atmospheric circulation.

The distributions of SST (shading), precipitation (contours), and 850-hPa wind vector (arrows), as obtained by subtracting the warm-minus-cold composites based on output of the CTRL experiment from the corresponding composites based on MLM data, are shown in Figure 12.7 (color section) for (a) DJF(0/1), (b) MAM(1), and (c) JJA(1) seasons. On the basis of the above arguments, we shall henceforth interpret these 'MLM-minus-CTRL' patterns in terms of local feedbacks between the atmospheric and SST anomalies in the IO basin. During DJF(0/1) (Figure 12.7(a)), the 850-hPa wind vectors are directed toward the warm SST anomalies in the Arabian Sea, Bay of Bengal, and the central portion of the southern IO. The predominantly south-westerly (north-westerly) wind vectors over the northern IO (south-western IO) are oriented against the climatological flow in these regions (see Lau and Nath, 2000), so that the decreased surface wind speeds over these regions would reduce oceanic heat loss to the atmosphere, thus resulting in SST warming. These results are indicative of positive feedbacks in the atmosphere–ocean coupled system in the IO (i.e., wind responses to SST changes in the northern and southern IO tend to reinforce the SST anomalies in these locations).

Also evident in Figure 12.7(a) (color section) is a cyclonic (clockwise wind vectors) pattern centered at 20°S–55°E. The placement of this feature to the west of the warm SST site in the southern IO suggests that it is an atmospheric response to the thermal forcing associated with the latter oceanic anomaly (e.g., see arguments by Hoskins and Karoly, 1981). This circulation signal is seen to persist through the MAM(1) season (Figure 12.7(b)), with its center being shifted south-westward relative to the DJF(0/1) position. The appearance of the anomalous cyclonic center over the south-western IO in the boreal winter and spring of year(1), and its effects on local Ekman upwelling and ocean circulation, have been noted in the observational study of Xie *et al.* (2002).

The pattern in Figure 12.7(a) indicates enhanced cyclonic circulation and precipitation over the warmer waters in the vicinity of Sumatra in the MLM run as compared with the CTRL run. The presence of a positive precipitation signal in that region in the DJF(0/1) phase of the observed warm ENSO events has previously been studied by Chang *et al.* (2004c). The model finding presented here illustrates that air–sea feedbacks outside of the tropical Pacific could contribute to the rainfall signal over the western part of the Maritime Continent during ENSO events.

The warm SST anomalies in the Arabian Sea, Bay of Bengal, and South China Sea attain maximum amplitudes in MAM(1), and are still discernible in JJA(1) (Figure 12.7(b,c), color section). The corresponding wind vector and precipitation patterns in these seasons are characterized by south-westerly flows toward these warm ocean sites, and positive precipitation centers over India and Indo-China. These results imply that air–sea coupling in the IO basin tends to strengthen the summer monsoon over south Asia in year(1) of warm ENSO events. This perturba-

tion is in opposition to that simulated in the MLM experiment in year(0), when the monsoon flow over the same region is weaker than normal (Figure 12.5(b)), and dry conditions generally prevail (see data points for MLM in Figure 12.4(a,b)). The reversal of the precipitation anomalies over the Indian monsoon region from JJA(0) to JJA(1) is also supported by the observational data shown in Figures 12.3(a,e). This tendency for some monsoonal variations to switch polarity from one year to the next may be viewed as one facet of the tropospheric biennial oscillation (TBO) (e.g., see Meehl, 1997; Meehl and Arblaster, 2002b). The model evidence shown in this section indicates that biennial changes of the south Asian monsoon may partially be the consequence of the following chain of processes: remote responses to ENSO forcing in JJA(0) (Figure 12.6(a)), generation of SST anomalies in the IO basin during SON(0)–DJF(0/1) (Figure 12.5(d,f), color section) by the atmospheric bridge, and feedback of these oceanic perturbations on the atmosphere in MAM(1)–JJA(1) (Figure 12.7(b,c)).

12.4 ENSO-RELATED VARIABILITY OVER EAST ASIA, AUSTRALIA AND THE WESTERN PACIFIC

The essential atmospheric and oceanic changes in the eastern portion of the Asian–Australian monsoon system during ENSO events are summarized in Figure 12.8 (color section), which shows the warm-minus-cold composites of (a, b, e, f) surface wind vector (arrows) and SST (shading), and (c, d, g, h) SLP (contours) and precipitation (shading), for the (top half) DJF(0/1) and (bottom half) MAM(1) seasons. Results based on NCEP and MLM output are displayed in the left and right panels, respectively. The most prominent features over the western Pacific are organized about the pair of positive SLP anomalies over the Philippine Sea and off the eastern Australian seaboard. These pressure perturbations are coincident with anomalous anticyclonic flows at the surface (see arrow patterns) and below-normal rainfall. The stationary wave solution presented in Figure 12.6(b) indicates that the two high-pressure centers are responses to the heat sink over the tropical western Pacific. Comparison between the MLM composites for the DJF(0/1) and MAM(1) periods reveals considerable eastward displacement with time of the SLP, wind, and precipitation anomalies associated with two anticyclones.

As has been pointed out by Wang *et al.* (2000), the evolution of the anomalous SST pattern is closely related to changes in the local surface circulation. For instance, the south-westerly wind anomalies to the west of the Philippine Sea anticyclone (hereafter abbreviated as PSAC) oppose the climatological north-easterly winter monsoon over that region (see Lau and Nath, 2000). The reduction in the wind speed leads to suppression of oceanic heat loss and warm SST anomalies. Conversely, the intensification of the north-easterly monsoon flow by the wind anomalies to the east of this anticyclone brings about oceanic cooling in the subtropical north-western Pacific. The resulting SST anomaly pattern with characteristic east–west contrast is seen to migrate eastward from winter to spring, in concert with the movement of the overlying PSAC. Analogous considerations of the super-

position of the local wind anomalies on the south-easterly time-mean flow also account for the SST anomaly pattern off the eastern coast of Australia. Besides its impact on the underlying SST field, the weakening of the dry winter monsoon over east Asia in DJF(0/1) is also accompanied by above-normal precipitation over south China and the East China Sea. This wet anomaly is seen to persist through the following spring season. The large-scale signals in the NCEP and MLM patterns are in general agreement with each other.

The strong relationship between the temporal evolution of the anomalous PSAC and the SST pattern over the South China Sea and north-western Pacific is illustrated in greater detail in Figure 12.9, which shows the time–longitude variations of the warm composites of SLP (contours) and SST (shading), as computed using monthly mean data from (a) NCEP and (b) MLM that are averaged over latitudes between 10° and 20°N. In the summer of year(0), below-normal SLP and SST prevail over the subtropical north-western Pacific. The amplitude of the negative SLP anomaly centered near 170°E is markedly stronger in the MLM experiment as compared to observations. For both model and observations, the positive SLP anomaly emerges in September(0) over the South China Sea. The NCEP data indicate that the eastward migration of this feature is most notable during the autumn of year(0); whereas the corresponding signal in the MLM pattern exhibits the strongest zonal movement in the DJF(0/1) and MAM(1) periods. This difference between model and observation in the timing of the spatial displacement of the pressure anomaly is also discernible in the patterns of Figure 12.8 (color section), in which the eastward march of this anomaly during the winter and spring seasons is more evident in the MLM than in the NCEP composites. The patterns in Figure 12.9 indicate that, for both observed and simulated data, the establishment of the PSAC is followed by oceanic warming to its west, and cooling to its east. Corresponding to the zonal evolution of the SLP anomaly, this warm–cold SST couplet also spreads eastward with time, particularly in the MLM pattern. The SST changes attain maximum strength in January(1)–February(1) in the observed pattern, and in March(1)–May(1) in the MLM experiment.

12.5 EVOLUTION OF THE PHILIPPINE SEA ANTICYCLONE ANOMALY

The results in Figure 12.9 highlight the following stages of evolution of the PSAC: the pre-establishment phase in the summer of year(0), the onset phase in the autumn of year(0), and the fully developed phase that persists from late winter of year(0/1) to the following spring. We proceed to examine the phenomena prevailing in each of these stages by further diagnosing the MLM output for the corresponding time periods, so as to identify the processes contributing to the development of the PSAC.

12.5.1 Atmospheric preconditions in JJA(0)

The atmospheric environment prior to the onset of the PSAC is depicted by the warm-minus-cold composites in Figure 12.10, for (a) 850-hPa wind vector,

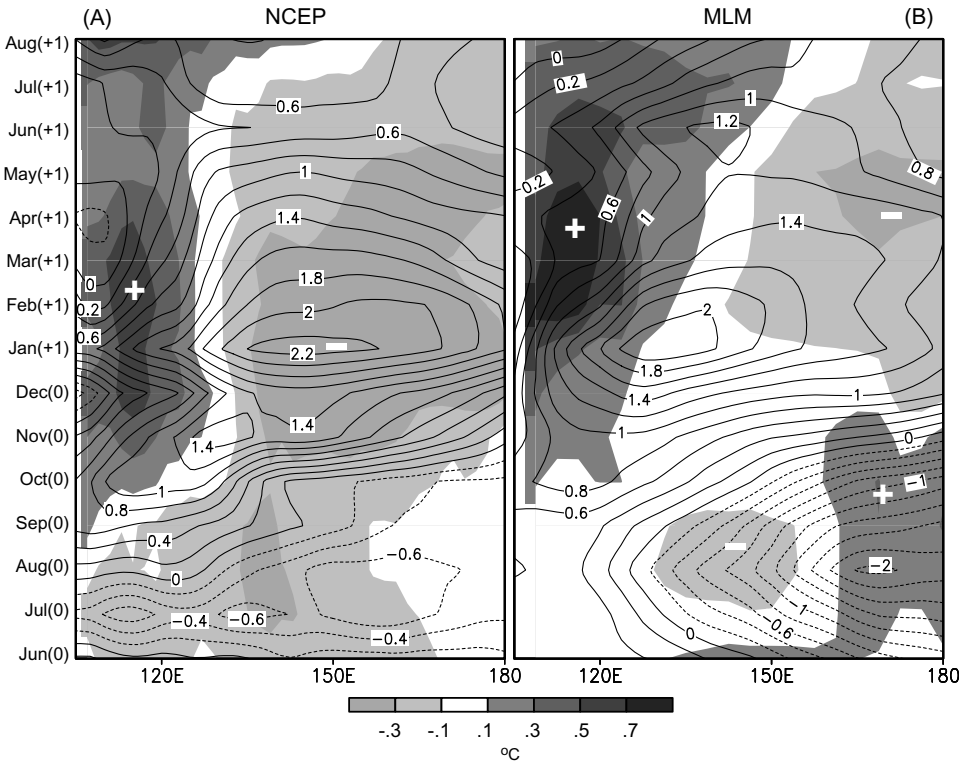

Figure 12.9. Time–longitude distributions of the warm composites of SLP (contour intervals: 0.2 hPa) and SST (shading), as computed by averaging (a) NCEP data and (b) output from the MLM experiment over the zonal belt between 10°N and 20°N.

(b), 200-hPa wind vector, (c) 500-hPa height (contours) and precipitation (shading), and (d) surface air temperature for the MLM simulation in the JJA(0) season. The circulation in this phase of the ENSO cycle is characterized by an anomalous 850-hPa cyclone and 200-hPa anticyclone over the western North Pacific. Results from stationary wave modeling (Lau and Nath, 2005) analogous to those presented in Figure 12.6 indicate that these features are essentially Rossby wave responses to enhanced condensational heating over the equatorial central Pacific, which results from displacement of the rising branch of the Walker circulation to that region during warm ENSO events. Also evident in Figure 12.10(b) is the cyclonic anomaly over northeastern Asia and the intensified westerlies within the 30°–40°N zone over east Asia. These upper tropospheric signals are indicative of a deepened trough and southward displacement of the climatological jetstream over that region. The relationships between these features at the upper level and other circulation changes over east Asia are further examined in the following paragraphs.

The northerly or north-westerly wind anomalies at 850 hPa off the south-eastern Asian seaboard (Figure 12.10(a)) are in opposition to the climatological south-

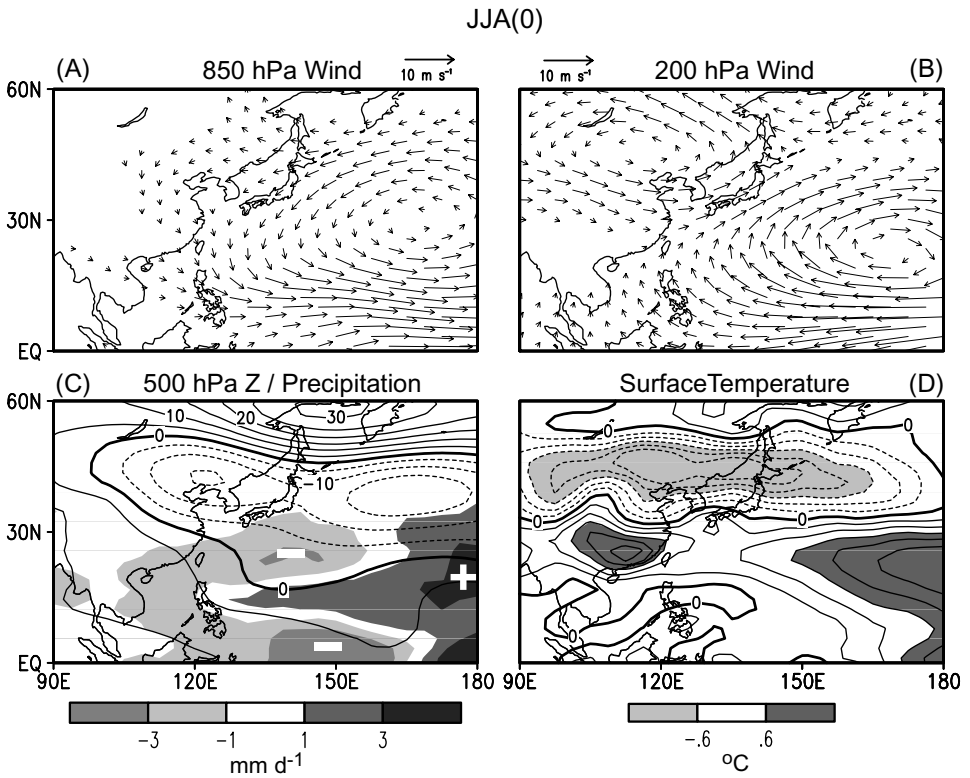

Figure 12.10. Distributions of the warm-minus-cold composites of the anomalous (a) 850-hPa vector wind; (b) 200-hPa vector wind; (c) 500-hPa height (contour interval: 5 m) and precipitation (shading); and (d) surface air temperature (contour interval: 0.2°C). Results are based on output for the JJA(0) season from the MLM experiment. Solid and dashed contours indicate positive and negative values, respectively.

easterly monsoon flow in that region. This weakening of the monsoon circulation is seen to be accompanied by below-normal precipitation over the area in 15°–25°N 120°–150°E (shading in Figure 12.10(c)). The contour pattern in Figure 12.10(c) shows an elongated negative 500-hPa anomaly extending eastward from northern China to the western Pacific, and a positive anomaly centered over the Sea of Okhotsk. The spatial relationship between the 500-hPa height pattern and the suppressed rainfall over the western Pacific in the 15°–25°N zone is reminiscent of that between the changes in atmospheric circulation and convective activity associated with the summertime 'Pacific–Japan' pattern documented by Nitta (1987), who has interpreted such a relationship in terms of Rossby wave responses to subtropical heat sources and sinks. The most prominent feature in the composite chart for surface air temperature (Figure 12.10(d)) is the cold anomaly that extends from the Asian interior to the North Pacific between 35° and 55°N. These below-normal temperatures are coincident with onshore wind anomalies at 850 hPa, as well as negative geopotential height changes and enhanced vorticity at upper levels.

The corresponding composite charts for the September(0)–October(0) period (not shown) indicate that the summertime surface temperature and circulation anomalies seen in Figure 12.10 are still evident in the early autumn. A similar set of atmospheric conditions preceding the establishment of the PSAC has been described using observational data by Wang and Zhang (2002). These investigators pointed out that such changes in the temperature and circulation environments are favorable for more intense cold air outbreaks over east Asia in early autumn. As will be demonstrated in the following subsection, the formation of the PSAC is often preceded by increased cold air activity in this region.

12.5.2 Synoptic development during PSAC onset

In order to study the synoptic phenomena associated with the onset of the PSAC, the time series of pentadal (five day) averages of selected fields simulated in each of the 16 individual runs of the MLM experiment during the six warm ENSO years (1957, 1965, 1972, 1982, 1991, 1997) have been analyzed. Following a procedure similar to that described in Wang and Zhang (2002), those MLM runs in which the SLP field over the South China Sea and Philippine Sea made a distinct transition to a persistent positive anomaly during the individual warm events were noted, and the specific pentad (hereafter referred to as the 'onset pentad', or T_o) in which this transition occurred was identified for each of such runs and El Niño episodes. By averaging the calendar dates of T_o for individual runs and ENSO events, it is found that the onset of PSAC typically occurs in early October. The SLP anomaly associated with this feature remains to be above-normal for more than four months in all cases considered here. More detailed results of the composite analyses are reported in Lau and Nath (2005).

Composites of various model fields at different temporal leads relative to the onset pentad for individual cases were constructed. The composite patterns for anomalous SLP (contours), surface wind vector (arrows), and precipitation (shading) are displayed in Figure 12.11 (color section) for the pentads centered at (a) 20 days before T_o, (b) 10 days before T_o, and (c) T_o. The most pronounced features in Figure 12.11(a) are the anticyclonic wind pattern and dryness associated with the high-pressure anomaly over the interior of the Asian land mass, the cyclonic flow and wet conditions accompanying the low center over the Philippine Sea, and the prevalent northerly wind anomalies over south-eastern China, the East China Sea, and southern Japan. These atmospheric signals bear a strong similarity to the characteristic behavior of cold air outbreaks over this region. The continental high-pressure anomaly migrates south-eastward to the Philippine Sea, so that anticyclonic flows and dry conditions are established in the latter area at about 4 pentads after T_o (Figure 12.11(c)). This sequence of simulated events during the PSAC onset is in broad agreement to that reported by Wang and Zhang (2002) using observational data. These investigators have pointed out that the deepening of the upper level trough and below-normal air temperature over east Asia in the preceding months (Figure 12.10) constitute a favorable environment for the incidence of cold air outbreaks and the subsequent PSAC formation. They have also considered the

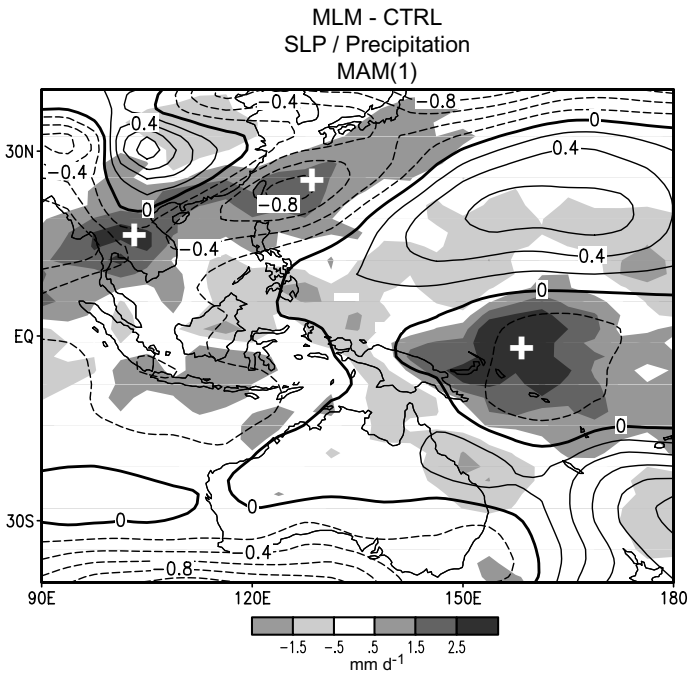

Figure 12.12. Distributions of the differences between the outputs from the MLM and CTRL experiments for the warm-minus-cold composites of SLP (contour interval: 0.2 hPa) and precipitation (shading), for MAM(1). Solid and dashed contours indicate positive and negative values, respectively.

effects of intraseasonal oscillations on the rather abrupt reversal of the wind, pressure, and rainfall anomalies over the Philippine Sea during T_o (Figure 12.11), and the role of atmosphere–ocean interactions in the seasonal dependence of the amplitude of such oscillations.

12.5.3 Air–sea feedbacks in MAM(1)

The simulated SST changes associated with the PSAC development, as illustrated in Figure 12.9(b), are seen to attain maximum amplitudes in MAM(1). By invoking the same reasoning as that applied in interpreting Figure 12.7 (color section), the local feedback of these mature SST anomalies in the western Pacific sector on the overlying atmospheric circulation may be inferred by subtracting the output of the CTRL experiment from that of the MLM experiment. The MLM-minus-CTRL pattern of the warm-minus-cold composites of SLP (contours) and precipitation for the MAM(1) season is shown in Figure 12.12. It is seen that the warm SST anomaly near the 10°–20°N, 110°–140°E region (see Figure 12.8(f), color section) is coincident with negative values of SLP and positive values of precipitation in Figure 12.12, and with a cyclonic low-level wind pattern in Figure 12.7(b). Hence, the air–sea feedbacks attendant to this warm SST anomaly leads to stronger cyclonic

development and more abundant springtime precipitation along the climatological rain belt extending north-eastward from the southern coast of China to the western Pacific. Conversely, the cold SST anomaly at 10°–20°N, 150°–180°E is overlain by increased SLP and reduced rainfall in the MLM simulation relative to the CTRL experiment. The SLP couplet over the subtropical north-western Pacific in Figure 12.12, with falling (rising) pressures west (east) of the center of the PSAC (see Figures 12.8(d,h)), is conducive to the eastward migration of this anomaly. The role of air–sea interaction in the spatial displacement of PSAC has previously been noted by Wang *et al.* (2000). Analogous relationships between the SLP and precipitation signals in Figure 12.12 and the SST anomalies in Figure 12.8(f) are also discernible in the south-western Pacific. The SLP rise over the SST anomaly near the Date Line at 30°S due to local air–sea feedbacks (Figure 12.12) may contribute to the eastward tendency of the high-pressure anomaly situated off the eastern Australian coast (Figures 12.8(d,h)).

12.6 IMPACT OF THE ASIAN MONSOON ON ENSO

How ENSO affects the Asian monsoon is better understood than the influence of the Asian monsoon on ENSO. The Asian monsoon covers one-third of the area of the tropics, and is an interactive component of the climate system that can impact the slowly varying lower boundary conditions (Webster *et al.*, 1998). In the following subsections, we shall separately consider the effects of the Indian and western North Pacific monsoons on ENSO.

12.6.1 Effects of the Indian summer monsoon on the development of El Niño

The all-Indian summer rainfall anomaly is most negatively correlated with the central tropical Pacific SST anomaly occurring three to six months after the summer monsoon, implying that a weak (strong) monsoon leads the mature phase of an El Niño (La Niña) event by about one to two seasons (Yasunari, 1990). This result suggests that the Indian summer monsoon could play an active role in ENSO development. However, ENSO is primarily governed by its intrinsic coupled ocean–atmospheric dynamics in the tropical Pacific. Regardless of monsoon variability, the mature phases of El Niño or La Niña tend to occur toward the end of the calendar year. This phase-locking behavior of ENSO is largely determined by the climatological seasonal cycle in the Pacific Ocean (Wang and Fang, 1996; Tziperman *et al.*, 1998; An and Wang, 2000). Thus, the above-mentioned lag relationship between Indian monsoon and ENSO does not necessarily imply a cause-and-effect relationship. Nevertheless, it is plausible that the monsoon variability could potentially add irregularity to ENSO as suggested by Yasunari and Seiki (1992) and illustrated by Wainer and Webster (1996).

If the Indian monsoon indeed exerts an influence on ENSO, what are the key processes involved? Barnett (1984b) noted that ENSO-related westerly anomalies in the western/central Pacific originate from the Indian Ocean. It has been speculated that the eastward propagation of the westerly anomalies from the Indian monsoon

region to the Pacific Ocean could serve as a trigger for ENSO events. Moreover, Webster and Yang (1992) showed that when the broad-scale south Asian summer monsoon is stronger (weaker) than normal, the tropical Pacific trade winds are also stronger (weaker) than average. This result suggests that an anomalous Indian monsoon could affect ENSO through changing the trade winds over the Pacific. However, it is difficult to determine the causal relationship between the monsoon and ENSO based on observations alone, because the two components are integral parts of the coupled climate system.

Using the Center for Ocean–Land–Atmosphere Studies (COLA) atmospheric GCM, Kirtman and Shukla (2000) examined a 50-year simulation forced by climatological mean SST to determine the tropical Pacific wind anomalies that are associated with a variable monsoon. Since the ENSO phenomenon and SST anomalies have been excluded in this experiment, the simulated monsoon variability is attributed to atmospheric internal dynamics and atmosphere–land interactions. The monsoon variability was measured by a monsoon rainfall index for south Asia (5°–25°N, 60°–100°E). Figure 12.13 shows the regressed global zonal wind in the model with reference to this monsoon index. During a strong south Asian monsoon, the Walker circulation over the tropical Pacific is indeed enhanced (Figure 12.13(a)). The opposite is true for a weak monsoon. With an enhanced summer monsoon the westerly flows in the vicinity of India and the associated monsoon cross-equatorial gyre in the tropical Indian Ocean are stronger than normal; along the equatorial Indian Ocean there are easterly anomalies (Figure 12.13(b)). Of note is that the easterly wind stress anomalies prevail throughout most of the central and eastern Pacific. This pattern indicates that a weak (strong) monsoon results in a weakening (strengthening) of the trade winds over the equatorial Pacific. This is consistent with the observed contemporaneous ENSO–monsoon relationship (Webster and Yang, 1992), even though the model wind anomalies are independent of ENSO. These numerical experimental results indicate the remote influence of the south Asian summer monsoon on the North Pacific trade winds, mainly by perturbing the climatological Walker cell over the Pacific.

In order to assess the impacts of monsoon variability on ENSO, various types of coupled atmosphere–ocean models have been used. Chung and Nigam (1999) examined the feedback of Asian monsoon on ENSO using a modified Cane–Zebiak (CZ) model (Zebiak and Cane, 1987). The original CZ model has not incorporated monsoon influence. In the modified CZ model, Chung and Nigam used Asian summer monsoon heating anomalies as an additional forcing, and referred to this suite of experiments as 'monsoon runs'. The monsoon heating anomalies were parameterized empirically by using rotated principal component analysis of tropical Pacific SSTs, residually diagnosed tropical diabatic heating, and surface winds during northern summer. In the monsoon runs, the 'interactive' summer heating anomalies in the Asian sector are included, and the ENSO events in the model occur more frequently. The presence of monsoonal interaction results in a broader frequency distribution of ENSO variability and a population shift in amplitude towards stronger El Niño events. The causes for these changes remain to be ascertained.

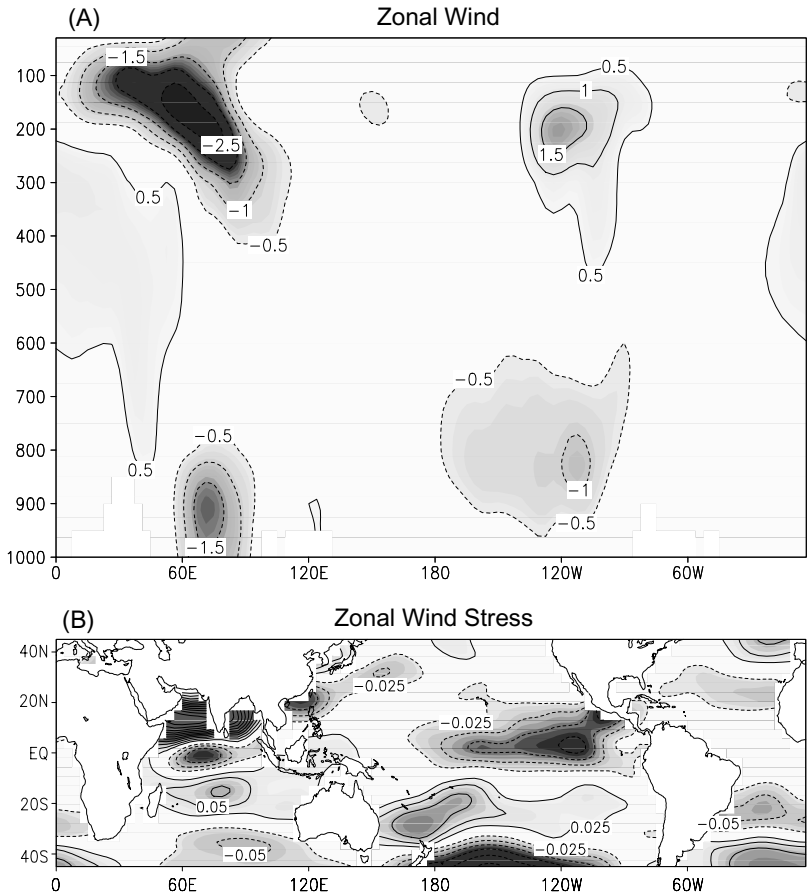

Figure 12.13. Distributions of the linear regression coefficients vs. the south Asian monsoon rainfall index of (a) zonal wind along the equatorial zonal plane (contour interval: $0.5\,\mathrm{m\,s^{-1}}$) and (b) zonal wind stress (contour interval: $0.025\,\mathrm{dynes\,cm^{-2}}$). The amplitude of the pattern corresponds to a rainfall anomaly of $2\,\mathrm{mm\,d^{-1}}$. Solid and dashed contours indicate positive and negative values, respectively. Results are based on output from the COLA atmospheric GCM.
From Kirtman and Shukla (2000).

Kirtman and Shukla (2000) implemented the CZ model by adding the effects of monsoon anomalies derived from their atmospheric GCM experiments mentioned earlier. Note that these monsoon anomalies are independent of ENSO. Their model reproduces realistically the observed lag relationship between ENSO and Asian monsoon. Their results suggest that a variable monsoon enhances ENSO variability, particularly three to six months after the summer monsoon ends. An ongoing warm (cold) event is made even warmer (colder) by a weak (strong) monsoon. They also presented model evidence on the role of a variable summer monsoon as a trigger mechanism for ENSO.

In reality, the monsoon variability is not independent of ENSO. It is thus necessary to distinguish between the impacts of monsoon variability that is related to ENSO from those that are independent of ENSO. Wu and Kirtman (2004) have examined simulations based on the COLA coupled GCM. The effects of monsoon variability that are related and unrelated to ENSO were separated using a composite approach based on simulated SST in the Niño 3.4 region (5°S–5°N, 120°–170°W) and Indian rainfall anomalies. They found that the ENSO-related monsoon variability has significant impacts on warm events but not the cold events. A weak (strong) monsoon enhances (weakens) an ongoing warm event. The monsoon impacts are manifested in the surface zonal wind stress over the western/central equatorial Pacific. The monsoon variability that is unrelated to ENSO also induces noticeable SST anomalies in the equatorial central Pacific in the following winter. A weak (strong) monsoon induces noticeable warm (cold) SST anomalies.

12.6.2 Effects of the western North Pacific monsoon on the turnabout of the ENSO cycle

The delayed oscillator paradigm (Section 12.1) attributes the reversal of the SST anomaly during the mature phases of ENSO cycles to the reflection of oceanic Rossby waves at the western boundary in a delayed manner. However, this mechanism does not explicitly explain the seasonal preference of the ENSO phase transitions. McBride and Nicholls (1983) showed that SST anomalies in the Indonesian region lead those in the eastern Pacific by 4–6 months. They speculated that air–sea interaction in the Indonesian region might in part be responsible for the turnabout of the ENSO.

In Sections 12.4 and 12.5, the observational evidence suggests, and the model results confirm, that a large-scale anomalous surface anticyclone forms over the northern Philippines in September–October during a strong El Niño episode. This feature rapidly develops from autumn to winter over the Philippine Sea and the western North Pacific (WNP), and has been referred to as the Philippine Sea anticyclone (PSAC). To focus on the turnabout during the peak phase of major El Niño events in the last 50 years, we display in Figure 12.14 the time series of ENSO anomalies within an 18-month time window centered in the November of El Niño years. In all six strong events, the maximum SST anomalies in the Niño 3.4 region occurred in boreal winter from November to January. Note that a sharp increase in SLP over the Philippine Sea (10°–20°N, 120°–150°E) preceded the corresponding warm SST peak by about one to three months. In conjunction with this pressure rise, strong anticyclonic surface wind anomalies appear over the Philippine Sea, with enhanced easterlies prevailing north of New Guinea (5°S–10°N, 120°–150°E). This temporal development is different from that inferred from the argument made by Weisberg and Wang (1997a,b), who suggested that the atmospheric high-pressure anomaly could be induced by the cooling due to oceanic upwelling Rossby waves. As discussed by Wang and Zhang (2002) and in Section 12.5, the establishment of large-scale WNP SLP and surface wind anomalies may be attributed to multiple factors: the remote forcing from heat sources and sinks over the tropical Pacific (thus

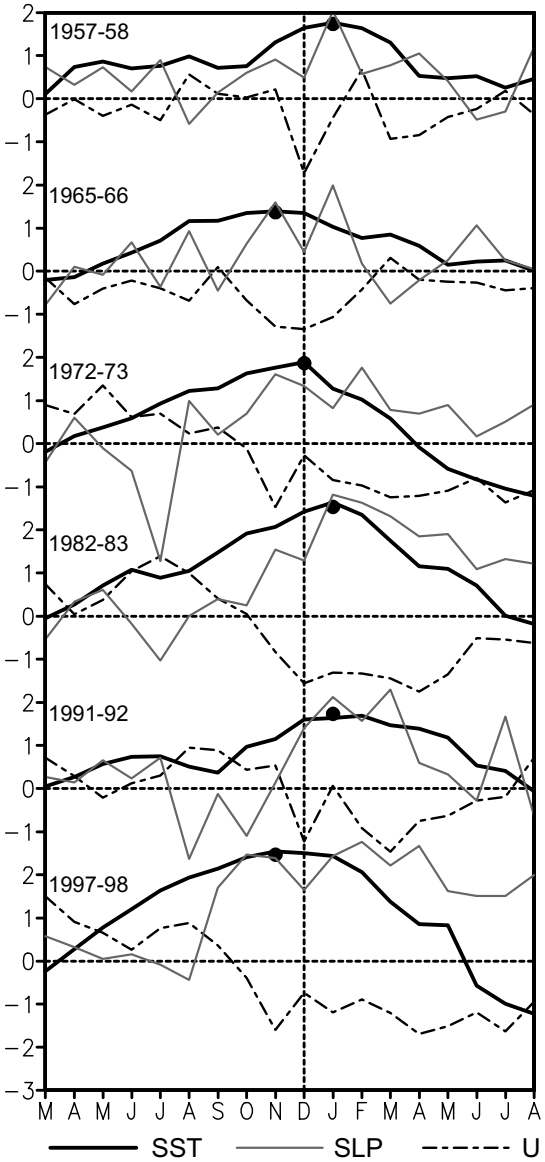

Figure 12.14. Time series of SST and atmospheric anomalies in the WNP during the six strongest warm episodes in the 1950–2003 period. The bold black curves show Niño 3.4 (5°S–5°N, 120°–170°W) SST anomalies (°C) with a heavy circle indicating the time of the maximum SST anomaly. A three-month running mean has been applied to the SST anomalies. The thin gray and dashed curves show, respectively, SLP anomalies (hPa) over the Philippine Sea (10°–20°N, 120°–150°E) and the zonal wind anomalies ($m\,s^{-1}$) north of New Guinea (4°S–4°N, 120°–150°E). The abscissa denotes a time window spanning 18 months centered in November of the year during which the warm event matures. Results are based on NCEP data.

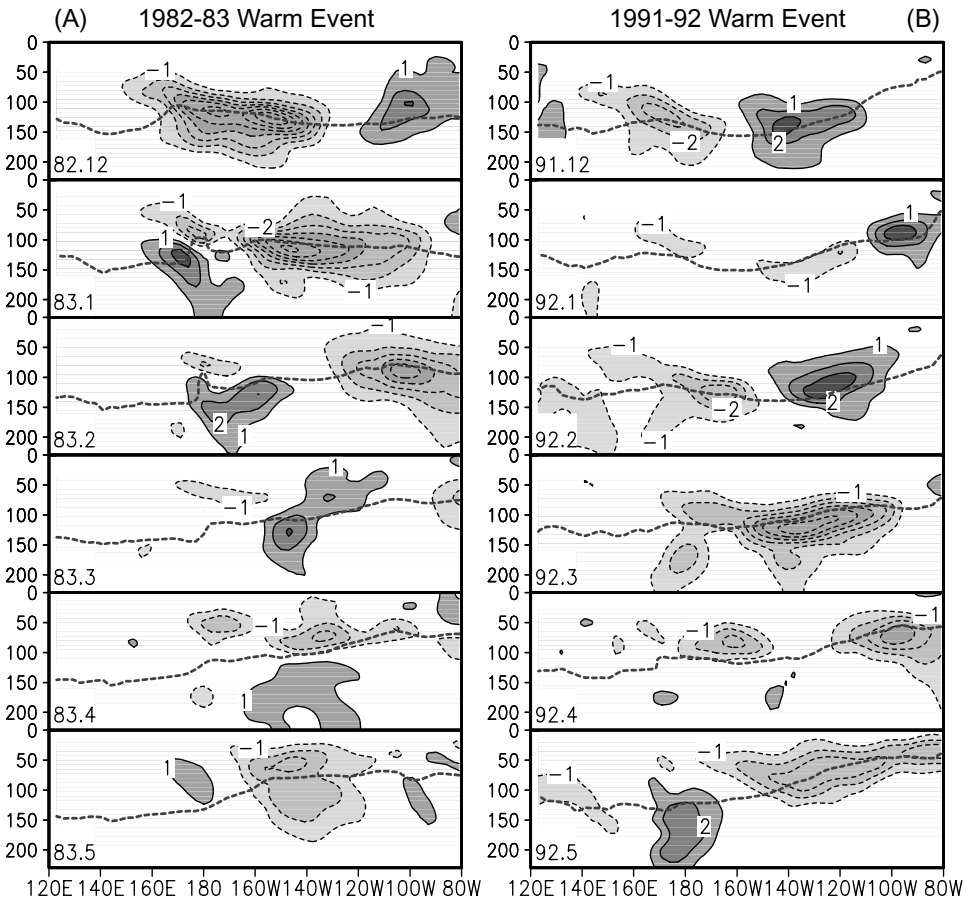

Figure 12.15. Distributions of the monthly mean local rate of change of subsurface ocean temperature in a vertical section along the equator during the turnabouts of the warm events of (a) 1982–1983 and (b) 1991–1992. The ordinate denotes the depth (m) below the surface. The dashed gray lines are the 20°C isotherm which corresponds approximately to the position of the thermocline during each month. The contour interval is 1°C per month. Solid and dashed contours indicate positive and negative values, respectively. Results are obtained from NCEP (Ji *et al.*, 1995).

contributing to the atmospheric bridge effect), extratropical–tropical interaction, and local air–sea interaction.

The sudden emergence of the equatorial easterly anomalies over the western equatorial Pacific may generate oceanic upwelling Kelvin waves that propagate along the equator into the eastern Pacific. This process might significantly perturb the slow variation of the coupled ocean–atmosphere system. Figure 12.15(b) shows local rates of change of the subsurface temperature (referred to as temperature tendency hereafter) in vertical cross sections along the equator for the 1991–1992 warm event. The tendencies of the subsurface temperature result primarily from a

vertical displacement of the thermocline. In December 1991, one month before the peak of the warm event, a sudden increase of easterlies over the equatorial western Pacific (Figure 12.14) induced upwelling and raised the local thermocline, causing negative temperature tendencies at the thermocline depth (Figure 12.15). The cold temperature anomaly then migrated eastward at a speed of about 40–50 degrees of longitude per month ($\sim 1.9\,\mathrm{m\,s^{-1}}$) along the thermocline, which suggests an association with upwelling Kelvin waves. The enhancement of anomalous easterlies in February 1992 triggered a second set of cold Kelvin waves that propagated again into the equatorial eastern Pacific. Similar sequences occurred in the 1982–1983 (Figure 12.15(a)) and 1997–1998 (not shown) events. Given that the establishment of the PSAC is about two months earlier than the peak warming of El Niño, this atmospheric feature may play a role in the El Niño turnabout. Once the PSAC is established, it can persist due to positive feedback between atmospheric Rossby waves and the underlying SST dipole through wind-induced evaporation and entrainment, as well as SST-related processes in the atmospheric boundary layer (Wang *et al.*, 2000; see also Sections 12.4–12.5).

Note that both the persistent equatorial easterly anomalies and the fluctuations in these easterlies on intraseasonal timescales contribute to turnabout of the ENSO. A rise of the thermocline in the eastern Pacific due to the arrival of forced upwelling Kelvin waves may initially offset local warming, which would in turn restore the SST gradients and associated equatorial easterlies, thereby triggering a slow thermocline shoaling and SST decrease in the eastern Pacific. The consecutive generation and passage of Kelvin waves, which are forced by the wind fluctuations of a variety of timescales over the western Pacific, may facilitate slow eastward migration of the negative heat content anomalies through the 'fetch extension' mechanism (Kessler and McPhaden, 1995) or zonal advection process (Lukas *et al.*, 1984; Picaut *et al.*, 1996). These heat content anomalies act to restore the thermocline slope from a flat state during El Niño to the normal downward incline from east to west. Model simulation of the 1997–1998 warm event indicates that the upwelling Kelvin waves generated by the easterly anomalies in the western Pacific contributed to the shoaling of the thermocline and the demise of the warming (McPhaden and Yu, 1999).

The development of the PSAC may facilitate the turnabout of ENSO at the end of the calendar year, thereby enhancing the biennial tendency of ENSO events (Wang *et al.*, 1999). The positive feedback between the atmospheric Rossby wave and ocean mixed layer thermodynamics, which plays a key role in development of the PSAC, depends on the presence of climatological north-easterly trades. In the WNP this favorable basic state exists only from late autumn through the following early summer. This seasonal dependence implies that persistent western Pacific easterly anomalies occur preferentially in autumn and winter, thus favoring ENSO turnabout towards the end of the calendar year. This temporal evolution also explains why strong El Niño episodes tend to decay quickly after their mature phase, leading to a biennial tendency of SST variation.

Kim and Lau (2001) have shown that a strong biennial tendency in the ENSO cycle could result from the occurrence of wind anomalies in the western Pacific six months after the SST anomaly peaks in the eastern Pacific. The analysis of Lau and

Wu (2001) suggests that a stronger monsoon–ENSO relationship tends to occur in boreal summer immediately after a peak El Niño and before a pronounced La Niña (i.e., 1983, 1988, and 1998). Their result appears to support the idea that the summer monsoon could influence ENSO variability via the development of the PSAC. The wind forcing associated with the PSAC may be instrumental in enhancing the biennial component of the natural ENSO cycle.

It is worthwhile to mention that the above process operates mostly during strong warm events. There are three moderate warm events (1986–1987, 1968–1969, and 1976–1977) with no reversal of the warming trend at the end of the year of El Niño development. The easterly anomalies in the equatorial western Pacific were not well established and did not persist in the boreal winter of these El Niño years. An important feature common to all three prolonged events is the insufficient strength of the central Pacific warming (Niño 3.4 SST anomaly less than 1.5 standard deviation by the end of the El Niño year), whereas during the six strong events considered in Figure 12.14, the corresponding anomalies were all above 1.5 standard deviations. This suggests that the strong warming in the equatorial central Pacific is probably necessary for the robust establishment of the western Pacific wind anomalies.

12.6.3 Effects of the east Asian winter monsoon in triggering the onset of El Niño

Li (1990, 1996) noticed, for the period 1950–1979, that during the winter prior to El Niño events the Mongolian cold highs tended to be stronger and surface temperature in eastern China tended to be lower than normal. This relationship prompted him to hypothesize that a strong east Asian winter monsoon leads to development of warm episodes in the equatorial eastern Pacific. He argued that strong cold surges associated with a strengthened Asian winter monsoon could penetrate into the South China Sea and equatorial western Pacific regions (Chang and Lau, 1980; Lau *et al.*, 1982), triggering deep convection over the warm tropical ocean. The anomalous convection could further induce westerly wind anomalies to its west, which might excite downwelling oceanic Kelvin waves, thus resulting in anomalous warming in the eastern Pacific.

We have examined the above relationship between the east Asian winter monsoon and ENSO by analyzing NCEP/NCAR reanalyses data for the more extended period of 1948–2002. To avoid the possible influence of decadal variations, we have analyzed the interannual component of the data by retaining variations shorter than 8 years. The leading empirical orthogonal function (EOF) mode of the winter 925-hPa temperature field over east Asia (Figure 12.16(a)) represents the strength of the east Asian winter monsoon, which is characterized by a temperature extremum centered over northern China. The winters with strong winter monsoons are signified by large negative temporal coefficients for this mode. The time series in Figure 12.16(c) indicates that during some years in the pre-1986 period (e.g., 1950, 1956, 1962, 1967, 1971, 1975, and 1985) a strong winter monsoon indeed preceded an El Niño event. However, several prominent La Niña events such as those in 1955, 1970, and 1984 were also preceded by strong winter monsoons. In

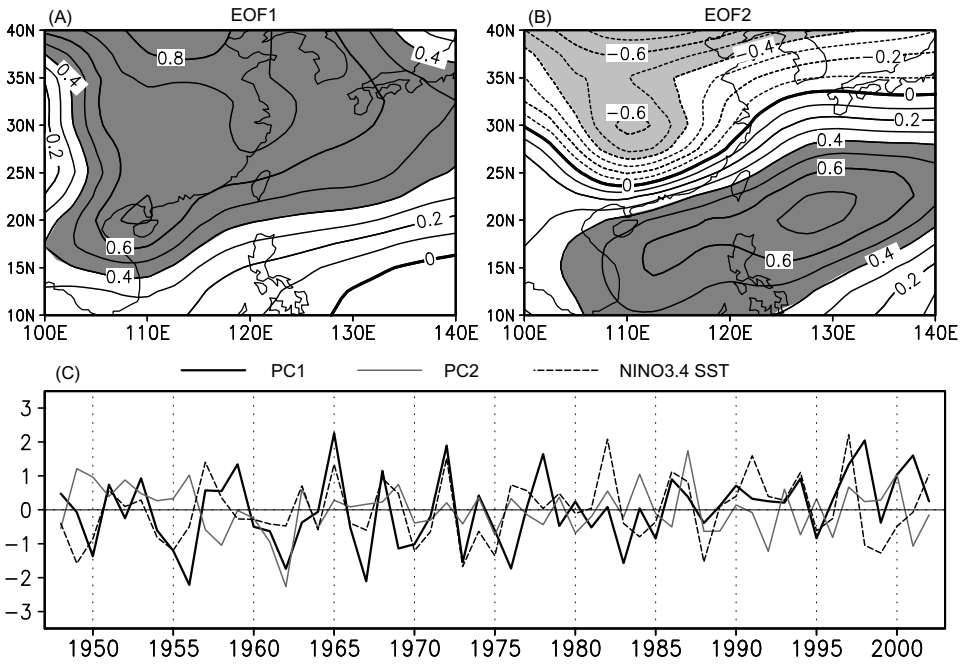

Figure 12.16. Spatial patterns (*top panels*) and temporal coefficients (*bottom panel*) of the first and second EOF modes of the winter (November–March) mean air temperatures at 925 hPa in the 1948–2002 period. The dashed curve in the bottom indicates the Niño 3.4 SST anomalies. In panel (c) the time labels refer to the calendar years for November and December of five-month winter seasons (e.g., '1950' denotes the November 1950–March 1951 period).

addition, prior to the strong El Niño events of 1965 and 1982, the east Asian winter monsoons were normal. It is also worth noting that none of the recent El Niño events (i.e., 1991, 1994, 1997, and 2002), were preceded by stronger than normal winter monsoons. The maximum correlation between the principal component of the leading EOF and SST over the Niño 3.4 region (5°S–5°N, 120°–170°W) occurs at zero lag (0.45), indicating that the Asian winter monsoon weakens during the mature phase of an El Niño and vice versa. However, when the first principal component leads Niño 3.4 SST by one year, the correlation coefficient drops to 0.18, which is not statistically significant at the 95% confidence level. Thus, the principal mode of the east Asian winter monsoon tends to vary with ENSO in tandem, but is not a reliable precursor of ENSO one year in advance. Analysis of unfiltered data yields the same conclusion.

The second EOF pattern (Figure 12.16(b)) is characterized by opposing centers of extremes over central China and the South China Sea. The time coefficient of EOF 2 negatively correlates with Niño 3.4 SST in the following year (−0.27, which is significant at the 95% level), suggesting that a strong (weak) winter monsoon over South China Sea tends to lead warming (cooling) in the central equatorial Pacific by

about one year. Cooling over the South China Sea and warming over the middle Yangtze River valley may be a result of mature La Niña forcing and an indication of subsequent transition from a La Niña to an El Niño state. In view of the difficulty in predicting ENSO transition in boreal spring, the search for precursors of the eastern Pacific warming continues to be a meaningful endeavor.

12.7 DISCUSSIONS AND OUTSTANDING ISSUES

The Asian monsoon is one of the most significant signals in the climatological seasonal cycle, whereas ENSO is a principal contributor to interannual variability. The mutual interactions between these two powerful components of the climate system have important implications on monsoon predictability (see pertinent discussion in Chapters 14 and 15 of this book), as well as frequency characteristics and seasonal phase-locking of ENSO episodes. We shall conclude this chapter by discussing outstanding issues that pertain to various facets of the ENSO–monsoon relationship.

12.7.1 Biennial tendency

Perhaps one of the important consequences of the ENSO–monsoon interaction is the resultant biennial tendency of the atmosphere–ocean system. Precipitation records in Asian monsoon regions exhibit a strong biennial tendency (i.e., a strong monsoon tends to be followed by a weak monsoon), and vice versa (e.g., see Figure 12.3). A biennial spectral peak is also discernible in ENSO indices. The biennial tendency of ENSO is particularly linked to turnabouts of El Niño and La Niña episodes from one summer to the following summer, with amplitudes of these episodes peaking during the boreal winter between the two summers. Still more study is required to clarify the origin of the biennial oscillation of the monsoon–ENSO system. However, this phenomenon is likely related to the interplay between the Asian monsoon, the ENSO cycle, and myriad of oceanic and land surface processes (e.g., Meehl and Arblaster, 2002b), as well as regulation of these interactive processes by the climatological seasonal cycle.

12.7.2 Interdecadal changes

The correlation between Indian rainfall and the Southern Oscillation Index has experienced significant fluctuations in the past 120 years (Webster *et al.*, 1998). It was high during 1880–1920 and 1960–1980 (ranging from 0.5 to 0.6) but low in 1920–1940 (ranging from 0.2 to 0.3) and after the 1980s. The relationship between the east Asian monsoon and ENSO has also experienced significant changes in the mid-1970s (Chang *et al.*, 2000b; Wu and Wang, 2002). The precise causes for these secular changes are still unclear, but it may be related to changes in global-scale circulation patterns (Krishna Kumar *et al.*, 1999b), changes in the circulation over the North Atlantic (Chang *et al.*, 2001), or sampling fluctuations (Gershunov *et al.*, 2001).

ENSO properties experienced a significant change in the late 1970s (Wang, 1995), when the North Pacific experienced a notable climate shift (Trenberth and Hurrell, 1994). In model simulations of the global warming scenario, the tropical Pacific undergoes ENSO-like warming, similar to the decadal shift in the Pacific Ocean in the late 1970s (Meehl and Washington, 1996). Whether the secular change of the ENSO–monsoon relationship is related to the changes in the spatial–temporal structure of ENSO, or to global warming, remains uncertain. Further investigations are needed to identify the physical processes responsible for the interdecadal changes of ENSO–monsoon relationships.

12.7.3 Effects of atmosphere–ocean interaction

Monsoon–ocean interaction can considerably modify the monsoon–ENSO relationship in several ways. As noted in Section 12.3.2, the anomalous Walker circulation induced by eastern Pacific warming has a descending branch over the vicinity of the Maritime Continent. The suppressed deep convection over that region can generate westward propagating, descending atmospheric Rossby waves that are conducive to a weak Indian summer monsoon (Figure 12.6). However, the weakening monsoon can induce local warming in the Bay of Bengal (Figure 12.5, color section). As a result of this SST change, the Indian summer monsoon would tend to intensify (Figure 12.7, color section). Thus, through local atmosphere–ocean interaction, the ENSO-induced monsoon anomalies in turn offset the 'direct' ENSO impacts (Lau and Nath, 2000). Another example is the Indian Ocean dipole. During an eastern Pacific warming, the low-level anticyclonic pattern over the southern Indian Ocean enhances the cross-equatorial flow along the west coast of Sumatra (Figure 12.5), which subsequently enhances coastal and equatorial upwelling and decreases the SST off Sumatra. The resultant SST cooling in the equatorial eastern Indian Ocean, along with concomitant warming in the western Indian Ocean, forms a dipolar SST anomaly pattern (Saji *et al*., 1999; see also Section 12.3.1). This dipole pattern tends to increase Indian rainfall and thus opposes the direct ENSO impacts on the Indian monsoon in year(0) (Figure 12.7). Over the WNP, the local air–sea interaction can maintain the ENSO-induced anticyclonic anomalies from the mature phase of El Niño to its decay phase, thus leading to a prolonged impact of ENSO on the east Asian summer monsoon (Section 12.5). On interannual timescales, Wang *et al*. (2003) have proposed that local monsoon–ocean interaction is one of the fundamental driving mechanisms for the biennial variability of the Asian–Australian monsoon. Questions remain regarding how the anomalies over the WNP and southern Indian Ocean interact to yield the biennial tendency of the continental-scale monsoon system.

12.7.4 Effects of atmosphere–land interactions

Land surface processes can significantly influence monsoon variability and monsoon–ENSO relationships. The snow cover and snow depth over the Tibetan Plateau and Eurasian interior might impact the strength of the Indian summer

monsoon (e.g., Bamzai and Shukla, 1999). Increased snow pack increases surface albedo and reflects more solar energy from the land surface. Melting of excessive snow consumes additional heat energy. Thus, the land surface heats up slower than normal during the following spring and summer, thereby reducing land–sea thermal contrast and weakening the summer monsoon. While changes in snow pack over the Tibetan Plateau and Eurasia may be due to atmospheric internal dynamics, it may also be related to ENSO (Yang, 1996). Land surface processes could affect the ENSO–monsoon relationship by altering the energy and water cycles within the monsoon system (Chapter 11). The quantitative importance of such influences, however, has yet to be assessed.

12.7.5 Roles of intraseasonal oscillations

The Asian monsoon system exhibits prominent intraseasonal oscillations with timescales of 30–60 days. The intraseasonal variations arise primarily from internal atmospheric moist dynamics, but could be considerably modified by air–sea interaction and land surface feedback. Anomalous behavior of these oscillations may have strong impacts on the seasonal mean monsoon climate. There exists considerable evidence for the covariability of intraseasonal activity and ENSO (Li and Long, 2002). In some regions (e.g., over the western Pacific), ENSO can influence the monsoon through regulating the Madden–Julian Oscillation (MJO) (e.g., Tam, 2003) and westward propagating biweekly oscillations (Chen and Weng, 1998). On the other hand, the intraseasonal oscillations in the Indian monsoon region could move into the western central Pacific Ocean and influence ENSO transitions through excitation of eastward propagating oceanic Kelvin waves, which can change thermal conditions in the eastern Pacific. Whether the intraseasonal oscillations of the monsoon system can trigger ENSO development or are more passive responses to ENSO remains a topic of debate.

The scientific issues raised in the above discussion can be best addressed by a combination of theoretical understanding of the basic processes involved, diagnosis of observational data, and experimentation with a hierarchy of numerical models. The history of progress in ENSO–monsoon research has shown that these alternative approaches are highly complementary to each other. For instance, insights gained from theoretical investigations have fostered fresh interpretations of empirical results and guided model experimental designs, whereas observational and model evidence has spurred theoretical advances. It is anticipated that improved analytical, observational, and modeling tools, in conjunction with coordinated intercomparison of findings derived from such diverse tools, will continue to enhance our understanding of ENSO–monsoon interaction.

12.8 ACKNOWLEDGEMENTS

We would like to thank Mary Jo Nath for performing many of the computations for this work, Hailan Wang for providing the stationary wave solutions displayed in Figure 12.6, John Lanzante for conducting the suite of MLM and CTRL experi-

ments, Ben Kirtman for providing Figure 12.13, Renguang Wu for plotting Figures 12.14 and 12.15, and Yongsheng Zhang for computing and plotting Figure 12.16. We are also grateful to Mike Alexander, Ben Kirtman, Chongyin Li, and George Philander for their insightful comments on previous drafts of this chapter.

13

Effects of the Tibetan Plateau

Michio Yanai and Guo-Xiong Wu

The Tibetan Plateau (Qinghai–Xizang Plateau) extends over the latitude–longitude domain of 25–45°N, 70–105°E, with a size of about one-quarter of the Chinese territory and a mean elevation of more than 4,000 m above sea level (Figure 13.1, color section). Surface elevation changes rapidly across the boundaries of the Plateau, especially the southern boundary, and strong contrasts exist between the western and eastern parts in land surface features, vegetation, and meteorological characteristics (e.g., Ye and Gao, 1979b; Smith and Shi, 1995). At these altitudes the mass of the atmosphere over the surface is only 60% that at sea level. Because of the lower densities, various radiative processes over the Plateau, particularly in the boundary layer, are quite distinct from those over lower elevated regions (e.g., Liou and Zhou, 1987; Smith and Shi, 1992; Shi and Smith, 1992). Therefore, the Tibetan Plateau exerts profound thermal and dynamical influences on atmospheric circulation.

13.1 INTRODUCTION

Before the 1950s, most of the studies concerned with the influence of large-scale topography upon atmospheric circulation and climate focused on its mechanical aspects. Queney (1948) summarized the studies on airflow over mountains and brought forward three critical scales to distinguish different mountain waves by using linearized equations. He showed that gravity waves, inertial gravity waves, or Rossby waves will be forced when atmospheric current flows over mountains with various spatial scales. In the early 1950s, Bolin (1950) and Yeh (1950) suggested that the Tibetan Plateau splits the westerlies into two branches in winter and thus favors of the generation of the Great Trough over east Asia. The numerical simulations based on a new atmospheric model developed by Charney and Eliassen (1949) also concentrated on understanding the mechanical forcing of large-scale

B. Wang (ed.), *The Asian Monsoon*.

topography on the formation of mean troughs and ridges in the mid-latitude westerliers.

In 1957, Yeh *et al.* and Flohn respectively found that the Tibetan Plateau is a heat source to the atmosphere in summer. Since then the temporal and spatial distributions of the heating field over the Plateau and their impacts on weather and climate have become an important research field in meteorology. Earlier, the thermal influences of the Plateau upon atmospheric circulation were inferred from: (1) the shift of the mid-tropospheric westerly jet stream from the south side to the north side of the Plateau in early summer; (2) the presence of a huge warm-core anticyclone in the upper troposphere centered over the Plateau in summer; and (3) the pronounced diurnal variations in the surface meteorological elements on and along the periphery of the Plateau.

13.1.1 The jet stream

The earliest work that related the presence of the Himalayas to the onset of the summer monsoon was that of Yin (1949), a Burmese meteorologist visiting the University of Chicago and conducting research with Herbert Riehl. Yin recognized the westward shift of a trough, originally located to the east of India, in summer. He found that this movement is comparatively rapid and coincides with the 'burst of the monsoon' over India. The movement of the trough is explained as being due to 'changes in the long-wave pattern brought about by the presence of the Himalayan mountain complex combined with seasonal variation in the latitude of the circumpolar jet stream of the northern hemisphere.' The work of Yin was included in the textbook *Tropical Meteorology* by Riehl (1954) with an illustration (Yin, figure 6) of splitting and shifting of the westerly jet stream from the south side to the north side of the Tibetan Plateau. (Also, it is interesting to note that T. C. Yeh (i.e., Duzheng Ye), another visitor to the University of Chicago and Riehl's colleague, published his famous theoretical paper on dispersion of Rossby waves (Yeh, 1949) in the same year as Yin's.)

In 1951, Murakami published a paper entitled, 'Mechanism of Tsuyu-Ake (end of Baiu)'. In this paper, he showed splitting of the jet stream over Japan during Baiu (Meiyu in China) and the disappearance of the southern branch at the end of the Baiu season. The work of Yin and Murakami were followed by Suda and Asakura (1955) and Dao and Chen (1957). They showed that the onset of Baiu (Meiyu) and the south-west monsoon coincides with the time of the jet stream shifting from the south side to the north side of the Tibetan Plateau.

The role of the Tibetan Plateau on the withdrawal of the Asian monsoon has also been studied. Staff Members of Academia Sinica (1957) described that the sudden shift of jet stream from the north of Tibet (40°N) to the south (32°N) occurred in mid-October of 1956 along 125°E. Yeh *et al.* (1959) discussed the abrupt change of the upper air circulation over the northern hemisphere in June and October. The southward retreat of the jet stream around Tibet in October was shown by cross sections. Matsumoto (1988, 1990) studied the withdrawal of the Indian summer monsoon and its relation to the seasonal transition from summer

to autumn over east Asia. He described sudden temperature drops over the Eurasian continent in late September and October, which coincided with the sudden southward shift of the jet steam around the Tibetan Plateau.

13.1.2 Warm anticyclone

During the Second World War, a study of pilot-balloon data above northern India in summer showed the shift from westerlies to easterlies and the increase of easterlies with height. Considering the thermal wind relation, the presence of a warm anticyclone north of the Himalayas in the 300–100-hPa layer was inferred (Flohn, 1981). After the war, Flohn investigated the surface and upper air data and established the presence of the warm anticyclone on the Tibetan Plateau. He further pointed out the concurrent occurrence of 'reversal' of meridional temperature gradient south of the Himalayas and the onset of the Indian monsoon (Flohn, 1957, 1960, 1968, 1981). Koteswaram (1958), in his pioneering paper on the easterly jet stream in the tropics, concluded that the greatly elevated surface of the vast Tibetan Plateau serves to heat directly the middle troposphere and to produce a strong solenoid field in the upper troposphere.

Our knowledge of the 'Tibetan anticyclone (or south Asian High)' was greatly enhanced by Krishnamurti's analysis of the, 200-hPa streamline charts based on his extensive collection of commercial aircraft data (Krishnamurti and Rodgers, 1970; Krishnamurti, 1971a,b). A word of caution is needed here, however. The Tibetan anticyclone is not a purely thermally driven system maintained on the Plateau. As Krishnamurti (1985) has demonstrated, its center is located over the western tropical Pacific during northern winter and moves over south-east Asia in May. In their recent studies, Wu and his colleagues (Liu *et al*., 2001; Zhang *et al*., 2002; Wu and Liu, 2003) refer the term 'south Asian High (SAH)' only to the huge upper tropospheric anticyclone that appears over south Asia in the summer half year, and showed that the SAH possesses bimodality that is composed of the Tibetan mode and the Iran mode, with each corresponding to distinct climate anomaly patterns.

13.1.3 Early progress of Tibetan Plateau research in China

The systematic research of Tibetan Plateau meteorology in China started from 1950. On analysing the upper tropospheric circulation over Asia in the winter from 1945 to 1946, Yeh (1950) found that due to the Tibetan Plateau forcing, the westerly jet is split into two branches with the south branch established in mid-October, and the downstream trough becoming strongly tilting from the north-east to south-west. This is in good accordance with the theoretical results of Bolin (1950). Koo (1951) further emphasizes such a splitting impact of the Tibetan Plateau, and showed that downstream of the Plateau, the north and south branches of the westerly merge into one jet stream, which becomes the strongest in the World. In 1951 in a study of the onset and retreat of the jet stream over Asia, Yeh *et al*. (1951) already noticed the 'abrupt seasonal change' of circulation over Asia in 1945–1946. Yeh (1952) also pointed out that the influence of the Tibetan Plateau on the atmosphere depends

on the circulation patterns it encounters, and varies from one season to another. At the same time, Chu (1957a,b) used a two-layer numerical model to simulate the impacts on stationary waves of large-scale heating sources/sinks and orography, and found that both the Tibetan Plateau and Rockies can generate the ridge/trough pattern along the westerlies reasonably well. Cao (1957) treated the impacts of the Tibetan Plateau and Rockies as the lower boundary conditions of an atmospheric dynamic system and obtained similar conclusions in his analytical solutions. Together with many other studies, the early research on the dynamical impacts of the Plateau on general circulation by Yeh and his colleagues led to the establishment of the meteorology of the Tibetan Plateau in the 1950s.

In 1957, Yeh and his colleagues published a paper entitled 'the wind structure and heat balance in the lower troposphere over the Tibetan Plateau and its surrounding' to show the wind field and heat balance in the lower troposphere over the Plateau. They found that in winter the westerlies are split to the west of the Plateau but converge to its east; whereas in summer the wind field is featured by a cyclonic circulation in the lower layer, which turns to anticyclonic at high levels. In winter most of the Plateau region is dominated by a descending motion except its south-eastern part, whereas in summer ascending motion prevails. More importantly they used for the first time the air–ground temperature difference, instead of the air temperature itself, to study the thermal status of the Tibetan Plateau in different seasons and revealed the fact that in summer the Plateau is a thermal source and in winter is a thermal sink, except for its south-eastern part. This study was followed by the classic 3-part paper by 'Staff Members of Academia Sinica' (1957, 1958a,b, with Yeh as the principle author) published in *Tellus*. In Part II of this paper, the influence of the Tibetan Plateau on the circulation over Asia was discussed dynamically, and a brief discussion of 'likely' heat sources in summer and heat sinks in winter were inferred. As evidence, the observed 'plateau-scale' diurnal variation was illustrated. In Part III, influence of topography on the general circulation was discussed using the quasigeostrophic vorticity equation with orographic forcing. In the *Rossby Memorial Volume*, Yeh *et al.* (1959) emphasized the global nature of the abrupt change of the upper air circulation in the northern hemisphere in June and October. They also discussed the changes in relation to the south-west monsoon in India and of Meiyu in China and Japan.

Since then, efforts have been made to find the thermal state of the Tibetan Plateau and to understand how such an elevated heating source and sink affect the local and global weather and climate. Ye *et al.* (1974) found that in the summer half year, the convective activities over the Plateau are well developed, and the non-linear interaction between large-scale systems and small-scale systems are important for maintaining the aforementioned summertime circulation patterns over the Plateau. Chen (1964) and Ye *et al.* (1979b,c,d, 1981) showed that strong ascending air over the Plateau flows eastward along the westerlies in the upper troposphere toward the eastern Pacific and North America. In summertime, the ascending air flows westward along the easterlies then subsides over Iran and other middle Asia regions, resulting in a dry climate. They also showed that in the meridional direction the summertime Tibetan Plateau ascending air subsides in

mid-latitudes to its north and in the southern hemisphere to its south, influencing the climate in these areas.

During the last 30 years, annular experiments, numerical modeling, and field experiments have been employed to investigate the climate impacts of the Tibetan Plateau. Based on various annulus experiments, Ye and Chang (1974), Chang *et al.* (1977), and Yang (1980) demonstrated that the Plateau not only split the westerlies into north and south branches, but also changed the propagation speed of large-scale waves along the westerlies in winter months. In summer, weak heating of the Plateau with strong background westerlies only affect the intensity of stationary waves, whereas strong heating over the Plateau contributes to the establishment of the Tibetan High, and weak westerlies can generate vortices on the eastern flank of the Plateau under its mechanical and thermal perturbation (Li *et al.*, 1976). Their experimental results also implied that the strong heating over the Tibetan Plateau in summer produces a super moist adiabatic lapse rate near the surface. This, together with strong lower layer convergence, leads to the general development of convections over the Plateau in summer.

It is clear from the description made above, the Tibetan Plateau has been considered important for both its dynamical and thermal impact on the large-scale circulation by keen analysis of upper level charts and by theoretical consideration. The subsequent work by Chinese meteorologists before the First GARP Global Experiment (FGGE) (including preliminary work on heat budgets and laboratory experiments) were summarized by Ye and Gao (1979b) in *Meteorology of the Tibetan Plateau.*

13.2 LARGE-SCALE FEATURES OF THE ATMOSPHERE NEAR THE TIBETAN PLATEAU

13.2.1 Large-scale flow and temperature fields

The stream fields at the upper, middle, and lower tropospheric levels for January (left) and July (right) are shown in Figure 13.2. The data are from the National Centers for Environment Prediction/National Center for Atmospheric Research (NCEP/NCAR) reanalysis (Kalnay *et al.*, 1996) from 1958–1997. The most striking feature of the stream field at 1,000 hPa in January is the divergence of air flow from the Tibetan Plateau to the surrounding areas, in particular to the southern hemisphere over the Indian and western Pacific Oceans. In July, although the pattern of stream field at 1,000 hPa looks similar to its wintertime counterpart in general, the directions of flow around the Tibetan Plateau are completely reversed. This implies the important impacts on the atmospheric circulation of the land–sea heating contrast (Chou, 2003) and the Tibetan Plateau (e.g., Tang and Reiter, 1984; Hsu *et al.*, 1999). Air converges toward the Tibetan Plateau from the surrounding areas, particularly from the southern hemisphere. The reversal of wind directions over the Arabian Sea and India, the eastern Bay of Bengal (BOB) and western Indo-China peninsula, South China Sea (SCS), and the western Pacific corresponds, respectively,

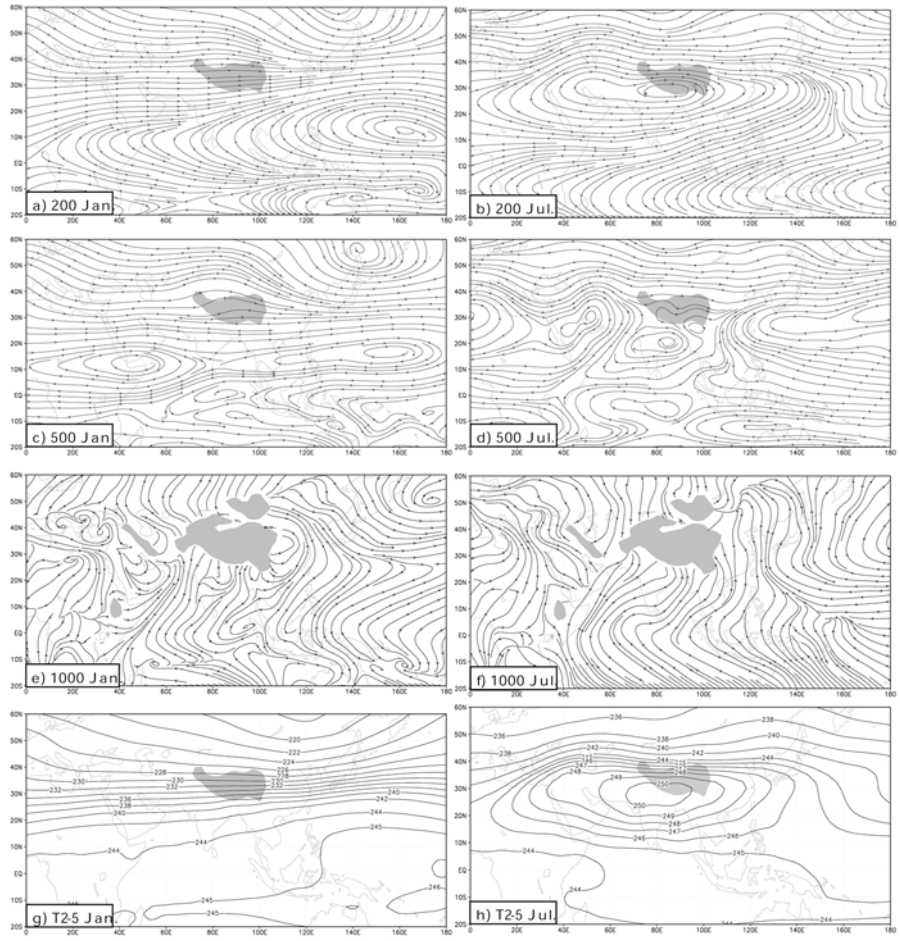

Figure 13.2. January (*left*) and July (*right*) mean stream fields at 200 hPa ((a) and (b)), 500 hPa ((c) and (d)), and 1,000 hPa ((e) and (f)) and the mean temperature fields averaged from 200–500 hPa ((g) and (h)) based on the NCEP/NCAR reanalysis and averaged over the period from 1958 to 1997.

to the south Asian, BOB, SCS, and western Pacific monsoons (e.g., Wu and Zhang, 1998; Ueda and Yasunari, 1998; Wang and Lin, 2002).

At 500 hPa, the mechanical influence of the Tibetan Plateau on the impinging westerlies in January is evident, although not as prominent as at 700 hPa (figure not shown), and most part of the Plateau is controlled by a high ridge. This then contributes to the formation of the wintertime semipermanent planetary-scale ridge between 40° and 120°E in high latitudes. In July, the anticyclone belt that goes around the subtropics in the northern hemisphere is broken over the Tibetan Plateau domain. A strong cutoff cyclone exists to its south and over the North

Indian Ocean, India, and the Indo-China Peninsula area. These are associated with the Tibetan Plateau heating and the Asian monsoon as will be discussed later.

At 200 hPa in January, a strong east Asian trough in the north and a huge subtropical anticyclone in the south dominate the north-western Pacific, forming a 'wind tunnel' along the subtropics. Westerly jets initiate from the Mediterranean Sea, penetrate the Asian subtropics, and merge into the tunnel, forming the strong east Asian jet. By July, the westerly jet retreats northward to high latitudes. In the subtropics, although a tropical upper troposheric trough is located over the North Pacific, a huge anticyclone is observed over the entire Afro-Asian continental area. This upper tropospheric continental anticyclone exists only in the summer half year, and is usually named as the Tibetan or south Asian High (SAH). It differs in nature from the aforementioned upper tropospheric anticyclone over the western Pacific in the winter half year (e.g., Krishnamurti, 1985). As reported by many studies (e.g., Flohn, 1957, 1960; Mason and Anderson, 1963; Tao and Zhu, 1964; Krishnamurti, 1971a,b; Krishnamurti *et al.*, 1973b; Luo *et al.*, 1982; Wang, 1987; Zhang *et al.*, 2002), the formation of the SAH is associated with the strong summertime continental heating and the latent heat release associated with the Asian monsoon. Based on the NCEP/NCAR reanalysis, Wu and Liu Y. (2003) and Liu Y. *et al.* (2004) found that the subtropical anticyclonic circulation exists over each of the continents in summer mainly due to the summertime continental heating. The SAH becomes the strongest because of the larger scale of the Eurasia continent, the existence of the Tibetan Plateau, and the strong latent heat release associated with the east Asian monsoon (Wu *et al.*, 1999; Liu Y. *et al.*, 1999, 2001). On the other hand, the formation of the upper tropospheric anticyclone over the western Pacific in winter is in association with the warm sea surface temperature (SST) of the warm pool in the western Pacific. Deep convections are widespread over this area, and their latent heat release contributes greatly to the formation of the upper tropospheric anticyclone.

The mean upper tropospheric temperature averaged from 200 to 500 hPa for January and July are shown, respectively, in Figure 13.2(g) and (h). In January (Figure 13.2(g)), the area warmer than 246 K is over the western equatorial Pacific, and the cold trough is over the eastern Siberia in high latitudes. A baroclinic belt with strong meridional temperature gradient along the subtropics is then intensified over east Asia just between the warmest center to the south and the coldest center to the north. These are in good coordination with the wintertime 200-hPa geopotential configuration as demonstrated in Figure 13.2(a) (i.e., a strong westerly jet stream, which is intensified over east Asia, is sandwiched by an anticyclone to the south and a trough to the north). In July, the warmest center of over 250 K is observed to the south of the Tibetan Plateau where the maximum summer monsoon rainfall occurs. It is also in good coordination with the center of the huge SAH as demonstrated in Figure 13.2(b).

The circulation features around the Tibetan Plateau, as presented in Figure 13.2, are closely related to the Tibetan Plateau forcing. Figure 13.3 shows cross sections along 30°N and 90°E of the January (a and b) and July (c and d) mean potential temperature and wind vector projected on the corresponding cross sections in which

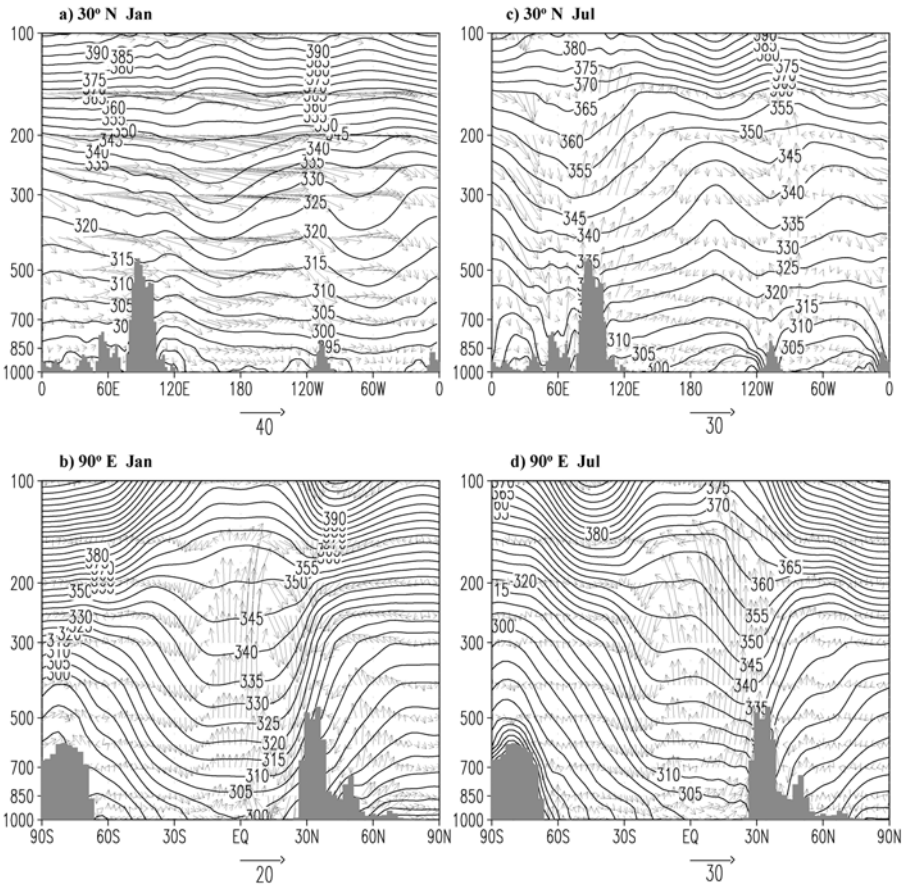

Figure 13.3. January (*left*) and July (*right*) mean (1986–1995) cross sections of potential temperature (contour interval: 10 K) and vertical circulation (vectors) along 30°N ((a) and (c)) and 90°E ((b) and (d)).

the vertical velocity w has been multiplied by 10^3. These cross sections are based on NCEP/NCAR reanalysis from 1986–1995. In January along 30°N, cold temperatures over continents and warm temperatures over oceans are prominent. Atmospheric cooling indicated by air descent ($\vec{V} \times \nabla\theta < 0$) prevails in the free troposphere. Along 90°E, the strongest cooling is over the Tibetan Plateau and to its south, whereas the strongest heating exist between 15°S and 10°N, corresponding to the intertropical convergence zone (ITCZ) rain belt with rainfall rate more than 4 mm per day (figure not shown). An enhanced local Hadley cell is therefore observed between 20°S and 30°N. During summer, the warmest center of potential temperature is just over the Tibetan Plateau. This is in agreement with the existence of the warm temperature center in July over the Plateau (Figure 13.2(h)). Strong ascent prevails in the area from the Tibetan Plateau to eastern China on the east and

to the BOB to the south, penetrating the isentropic surfaces almost perpendicularly and indicating the existence of a strong heating source over the area in summer (Kuo and Qian, 1981, 1982; Zheng and Liou, 1986; Liu X. *et al*., 2002; Wu, 2004). The cooling and descent of the air column over the Tibetan Plateau in winter accounts for the existence of surface divergence flow, whereas the heating and ascent of the air column over the Plateau in summer explains the existence of the surface flow convergence and accounts partly for the intensification of the SAH over the Plateau, as shown in Figure 13.2.

13.2.2 Mechanical effects of the Tibetan Plateau on large-scale motion

'The Tibetan Plateau is roughly of ellipsoidal shape with a major axis oriented in west–east direction. This will split the westerlies and force them to flow around it. The splitting of the westerlies is very pronounced on daily 500-mb charts. Due to the fact that in a rotating fluid the motion has a strong tendency to be quasi-2-D the splitting is also observed well high above the Plateau.' (Staff Members of Academia Sinica, 1958a.) This unique orographic influence of the Tibetan Plateau on the large-scale circulation has also been emphasized by Murakami (1981a,b, 1987).

Tokioka and Noda (1986) studied the effects of large-scale orography on January atmospheric circulation using a general circulation model (GCM). They performed four experiments under the perpetual January condition to isolate the orographic effects of the Tibetan Plateau and those of the Rockies and Greenland. They showed that the large-scale mountains tend to divert flows around the orography. The ascending (descending) center shifts poleward (equatorward) in the upwind (downwind) side of mountains. As for the zonal wavenumber 1, the surface vertical motions are very different from what are expected from the linear kinematical surface boundary condition (e.g., Charney and Eliassen, 1949).

Trenberth and Chen (1988) discussed the planetary-scale response of the atmosphere to the kinematic effects of orographic forcing by the Tibetan Plateau–Himalayan mountain complex. The key point of this analysis is to retain a term related to the perturbation in the horizontal motion in the kinematic lower boundary condition (LBC). From a scaling analysis they deduced a critical mountain height h_c beyond which the component of flow 'around' will dominate that 'over' the orography. The h_c is proportional to the meridional scale of the orography and depends on latitude. For a north–south scale appropriate for the Himalayan complex $h_c \sim 1.5$ km, which is much less than the actual height of the Plateau ($\sim$4 km), implying that the 'around' component will dominate. On the other hand, while the westerly flow impinges on a large-scale orography such as the Tibetan Plateau and goes around in the lower layers, the atmospheric westerly angular momentum is lost due to the reaction of the mountain. At the same time, the orography also plays an important role by drawing on the zonal mean kinetic energy and converting it into eddy kinetic energy. By considering the conservation constrains of both energy and angular momentum, Wu (1984) deduced a critical mountain height h_c as a function of the phase difference between the pressure perturbation and orography (λ_0) and the frictional coefficient (α):

$h_c = 8\sqrt{2}\alpha(3\sin\lambda_0)^{-1}$. Taking $\alpha = 230\,\text{m}$ and λ_0 from $\pi/2$ to $\pi/6$, h_c varies from 870 m to 1.5 km. When a mountain height is $h < h_c$, the climbing effect of the mountain is important, and the linear theory of planetary waves is acceptable. When $h > h_c$ the deflection effect becomes important, and the response of the atmosphere to the mountain forcing is non-linear.

In a following paper, Chen and Trenberth (1988a) studied the orographically forced planetary waves in the northern hemisphere winter, using a linear steady-state model with the wave-coupled lower boundary formulation. They demonstrated that the wave-coupled LBC has significant impact on the forced planetary waves. The most noticeable difference in response of the planetary wave appears near the Himalayas. The wave-coupled LBC allows the total flow at the lower boundary to circumvent the Himalayas, unlike the traditional LBC. The kinematic effects of the Himalayas alone form the basis for a quite realistic Siberian High and Aleutian Low, and the resulting east Asian trough is close to the observed position. In Cheng and Trenberth (1988b) they included thermal forcing in the model. When both orographic and thermal forcings are included, the simulation produces excellent results which are compared in detail with observations.

13.2.3 Winter cold surge and the role of the Tibetan Plateau

During winter, the thermal effect becomes less important than the mechanical effect of the Tibetan Plateau. The low-level westerlies split into two main streams that flow around the Plateau. A phenomenon unique to the east of the Tibetan Plateau is the frequent occurrence of low-level cold surges bursting out of Siberia and reaching as far south as the South China Sea and even Indonesia (e.g., Boyle and Chen, 1987; Murakami, 1981b, 1987).

The generation mechanisms of the cold surges were investigated by Nakamura and Murakami (1983) and by Murakami and Nakamura (1983), using a ten-layer hemispheric model. Since the thermal effect is not significant during winter, the diabatic heat source is simplified to the form of Newtonian cooling. A hypothetical Tibetan Plateau was prescribed to be elliptic (40 degrees in longitude and 30 degrees in latitude) and Gaussian-shaped in the vertical with a maximum height of 5 km. They confirmed that the orography of the Tibetan Plateau has a dominant effect on lee cyclogenesis and associated northerly surges. These phenomena were preceded by the development of a small-scale edge anticyclone trapped in a shallow layer near the north-east corner of the Plateau. Nakamura and Doutani (1985) extended the work and examined the detailed structure of the edge front associated with the cold surge, using a higher resolution model with a 1×1 degree horizontal grid interval and 16 vertical levels. A strong cold front was formed at the north-east corner of the elliptic-shaped model mountain. The ageostrophic northerly wind with a magnitude of 20 to $25\,\text{m s}^{-1}$ appeared across the cold front. This edge front was trapped along the mountain boundary and propagated clockwise with a speed of 20 to $25\,\text{m s}^{-1}$. This behavior indicates the similarity between edge waves and coastal Kelvin waves.

Sumi (1985) investigated cold surges around the Tibetan Plateau obtained in a numerical prediction model. Cold surges trapped in the periphery of the mountain

and in the lower troposphere were well simulated in the model. To investigate the mechanism of cold surges, momentum budget analyses at the 850-mb level were performed on two cases showing increases in northerly winds. Initially, an increase of the northerly wind was associated with the southward passage of a cold front. However, this northerly wind weakened gradually at the south-eastern corner of the Tibetan Plateau. The major increase of the northerly wind occurred in the cold air behind the cold front and was propagated further southward. Although the effect of the ageostrophic component played a dominant role in the early stage of propagation, the effect of the non-linear advection term became important in the late stage. Because of this effect, the northerly wind left the mountain and traveled farther southward. Sumi and Toyota (1988) made a detailed observational study of the edge disturbances around the Tibetan Plateau which were found in the numerical simulations. Two types of orographic effects are found: one is the effect upon synoptic disturbances, which corresponds to the main cold surge events; and the other is the excitation of the edge disturbances. A relationship between the intensity of a trough ahead of the Plateau and the excitation of edge disturbances is suggested.

Lu and Zhu (1991) developed a theory in terms of the linear shallow-water wave equation involving a huge topographic effect. Two kinds of gravitational wave solutions are derived with the assumption that the plateau in question is a vast topography, inclined at a constant slope from west to east. One set of solutions corresponds to two high-frequency inertia–gravitational waves, another solution is one of a low-frequency, orographic gravitational wave excited by the huge topography. The latter is similar to Kelvin waves in some respects. The path of gravitational wave rays is described by a hypocycloid equation. The result agrees quite well with the fact that the center of the cold surge strong wind moves in a curved path along the eastern fringe of the Tibetan Plateau.

13.2.4 Summertime negative vorticity source over the Tibetan Plateau

Figure 13.4 shows the July mean cross sections of geopotential height deviation from the corresponding zonal means (a) along 30°N and (b) along 90°E. A unique feature over the Tibetan Plateau is clearly seen: in summer, there is a strong but very shallow lower tropospheric low underlying a strong and deep high in the upper troposphere. The maintenance mechanism concerning such a peculiar large-scale circulation feature has attracted continuous efforts (Yeh, 1950; Yeh *et al.*, 1957; Ye and Gao, 1979b; Luo and Yanai, 1984; Yanai *et al.*, 1992; Yang *et al.*, 1992; Ye and Wu, 1998). In this section, the theory of Ertel potential vorticity is employed to provide new insights into the problem (Wu *et al.*, 2004).

As demonstrated in Figure 13.3, in the boreal summer the isentropic surfaces between 315 to 335 K intersect with the Tibetan Plateau while remaining continuous surfaces over the other parts of the World. A study by Haynes and McIntyre (1987) has shown that there is no net creation and destruction of potential vorticity between two complete isentropic surfaces. The intersection of those isentropic surfaces with the plateau as shown in Figure 13.3 then suggests that *the Tibetan Plateau is an*

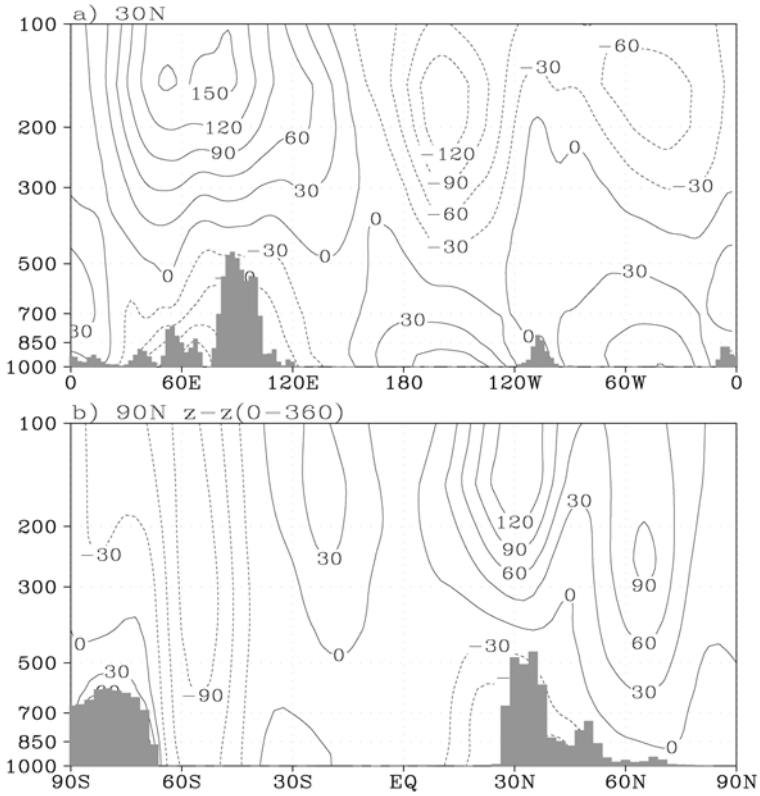

Figure 13.4. 1980–1997 July mean cross sections of geopotential height deviation from the corresponding zonal mean (a) along 30°N and (b) along 90°E (in units of geopotential meter (gpm)).

important source of potential vorticity for atmospheric motions in summer. The land surface sensible flux over the Tibetan Plateau in summer can be more than $100\,\mathrm{Wm}^{-2}$. This heat source is transferred to the atmospheric column by diffusion and produces a maximum heating of about $10\,\mathrm{Kd}^{-1}$ near the surface. Since the diffusive sensible heating is very strong near the surface and decreases gradually with increasing height, the atmospheric thermal adaptation (Hoskins, 1991; Wu and Liu, 2000) to such a heating should produce cyclonic vorticity in a shallow lower layer, but negative vorticity in the deep upper layers aloft. Therefore, it would be instructive to employ the flux form of the Ertel potential vorticity equation (Ertel, 1942) to gain new insights on the maintenance of the circulation pattern shown in Figure 13.4. For this purpose, Liu *et al.* (2001) and Wu *et al.* (2004) took the monthly average of the equation:

$$\frac{DW}{Dt} = \frac{\partial W}{\partial t} + \nabla \times (\vec{V} W) = \vec{F}_\zeta \times \nabla\theta + \vec{\zeta}_a \times \nabla Q \tag{13.1}$$

where $Q(=\dot{\theta})$ denotes diabatic heating; $\vec{\zeta}_a$ the 3-D absolute vorticity; $\vec{F}_\zeta$ the frictional dissipation rate of $\vec{\zeta}_a$; ∇ the 3-D Hamilton operator; and

$$W = \rho P = \vec{\zeta}_a \times \nabla\theta \tag{13.2}$$

is the amount of Ertel potential vorticity (P) per unit volume (Haynes and McIntyre, 1987). Liu *et al.* (2001) and Wu *et al.* (2004) then performed diagnosis by using the 12-hour (00Z and 12Z) NCEP/NCAR reanalysis data for July from 1986 to 1995. In such circumstances, the local time change is small and can be omitted. Let the overbars indicate the monthly mean and the primes indicate the deviation from it. Equation (13.1) can then be written as:

$$\nabla \times \overline{\vec{V}\,\overline{W}} = \overline{\vec{\zeta}}_a \times \nabla\overline{\dot{\theta}} + R \tag{13.3}$$

where the term on the left denotes the divergence of the potential vorticity flux; the first term on the right is the generation of potential vorticity due to diabatic heating; and

$$R = \overline{\vec{\mathbf{F}}_\zeta \times \nabla\theta} + \overline{\vec{\zeta}'_a \times \nabla\dot{\theta}'} - \nabla \times \overline{\vec{\mathbf{V}}' W'} \tag{13.4}$$

is the residual which represents the effects of frictional dissipation and transient processes with timescales of less than 12 hours. Since transient heating data are absent from the reanalysis, the diabatic heating rate ($\dot{\theta} = d\theta/dt$) is inversely computed from the distribution of θ at each time step, and R is calculated as the difference between the two other terms in (13.3). The σ coordinate system is used in the calculation. The two levels of $\sigma = 0.435\,7$ and $\sigma = 0.995$ are chosen to represent the upper and lower layers of the atmosphere. The former is near 250 hPa and the latter is near the ground over the Tibetan Plateau. Due to the large diurnal variation in diabatic heating over the Plateau (Ye and Gao, 1979b; Yanai *et al.*, 1992), the usage of the 12-hour analysis may present a sampling problem in calculating the magnitudes of those terms contained in (13.3) and (13.4). However, this will not affect the qualitative evaluation of the potential vorticity balance from (13.3).

The potential vorticity (PV) budget at $\sigma = 0.435\,7$ is shown in Figure 13.5(a) and (b). The distribution of the divergence of the PV flux (Figure 13.5(a)) exhibits two strong negative centers with intensities of more than $2 \times 10^{-12}\,\mathrm{Km^{-1}\,s^{-2}}$ on the eastern and north-western flanks of the Tibetan Plateau. They are in good agreement with the distribution of the generation of negative PV (Figure 13.5(b)) that is due to the decrease with height of diabatic heating. Thus, we can infer that the effects of the frictional dissipation and the transient processes are small in the upper troposphere, although cumulus friction can exist when cumulus convection is active (e.g., Tung and Yanai, 2002). It is somewhat strange that in Figure 13.5(b) no center exists over the heavy rain regions such as at the head of the BOB and southern China. One possible explanation is that over these regions the $\sigma = 0.435\,7$ surface is just close to the level of maximum rainfall so that $\partial\dot{\theta}/\partial z$ becomes small.

The PV budget at the $\sigma = 0.995$ level is shown in Figure 13.5(c–e). The strong center of positive potential vorticity generation is due to the increase of diabatic heating with height on the southern side of the Tibetan Plateau, from 25°N to 31°N

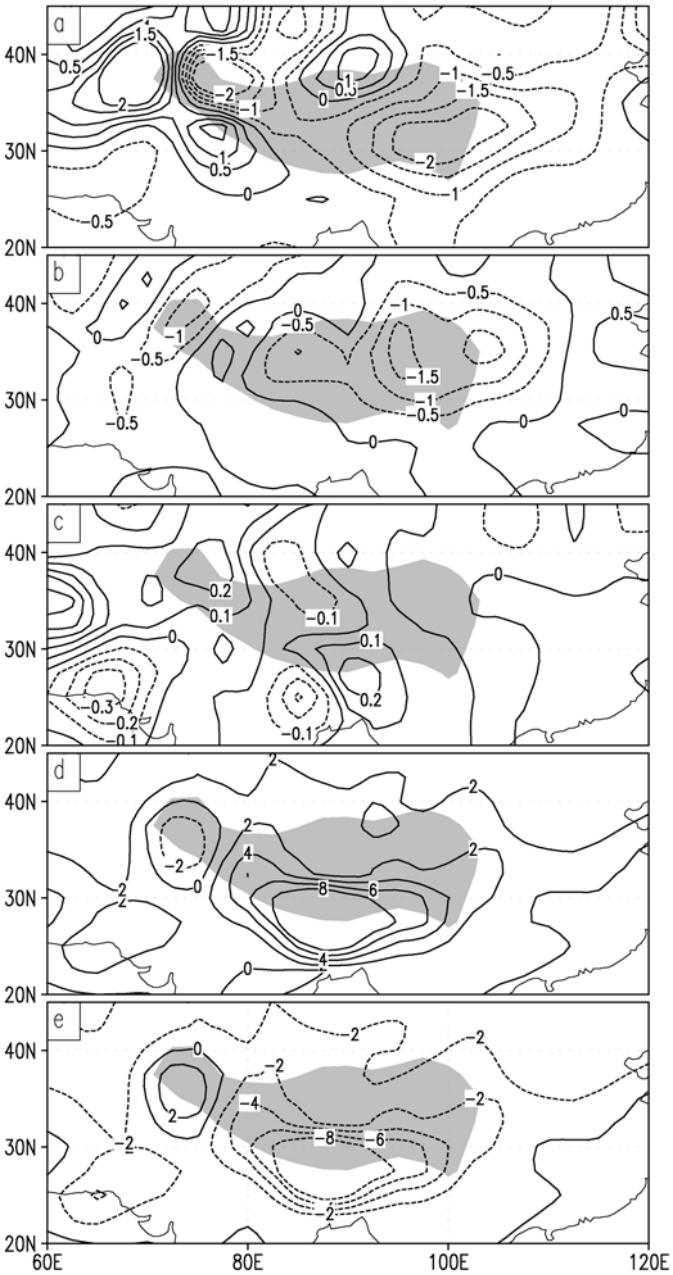

Figure 13.5. The July mean (1986–1995) PV budget calculated from the PV equation (13.3) at the $\sigma = 0.4357$ level ((a) and (b)) and at the $\sigma = 0.995$ level ((c), (d), and (e)). Regions higher than 3,000 m above sea level are shaded. Panels (a) and (c) are the divergence of the W flux; (b) and (d) are the generation of W due to diabatic heating; and (e) is the residual term R. The units are $10^{-12}\,\mathrm{Km}^{-1}\,\mathrm{s}^{-2}$.

(Figure 13.5(d)), revealing the importance of near-surface sensible heating in the maintenance of the lower layer cyclone over the Tibetan Plateau. On the other hand, the divergence of vorticity flux (Figure 13.5(c)) is too small to balance the vorticity generation. The heating term must be balanced mainly due to the frictional and transient processes (Figure 13.5(e)). The results obtained from the above analysis not only confirm the thermal adaptation theory, but also provide an interpretation for the formation of the atmospheric circulation over the Tibetan Plateau. It is mainly due to the strong surface sensible heating over the plateau that the shallow and strong surface cyclone and deep anticyclone aloft are maintained.

Further diagnosis of the cross-boundary flux of vorticity shows that the Tibetan Plateau area is a negative vorticity source in summer, and the negative vorticity is transferred outwards through its northern and eastern boundaries (Liu Xin *et al.*, 2001), affecting the circulation anomalies in the northern hemisphere. This will be discussed further in Section 13.4.

13.3 HEAT SOURCES ON THE TIBETAN PLATEAU

13.3.1 Various estimates of heating over the Tibetan Plateau

Ye and Gao (1979b) showed the monthly mean values of net heating of the air column of a unit cross section $\langle Q_1 \rangle$ (in notation used by Yanai *et al.*, 1973):

$$\langle Q_1 \rangle = \langle Q_{SR} \rangle + LR_1 - LR_2 + S + LP \tag{13.5}$$

where $\langle Q_{SR} \rangle$ is the absorption of solar radiation by the air column; LR_1 is the effective long-wave radiation from the ground surface; LR_2 the outgoing long-wave radiation at the tropopause; S the sensible heat flux at the surface; P the precipitation rate; and L the latent heat of condensation, for the western and eastern Plateau separately. In the western Plateau, the sensible heat flux dominates, and in the eastern Plateau the condensation heating becomes dominant after the onset of summer rains. These general features have not changed during the large numbers of subsequent studies.

Since the FGGE (December 1978–November 1979), renewed attempts have been made to examine the heat sources over the Tibetan Plateau and surrounding areas. Parallel with the FGGE, Chinese scientists conducted the Qinghai–Xizang Plateau Meteorology Experiment (QXPMEX) from May to August 1979. During QXPMEX, temporary surface, upper air, and radiation stations were added to the previously data-void region of the western and central Tibetan Plateau (see e.g., Shen, *et al.*, 1984; Liou and Zhou, 1987; Zhang *et al.*, 1988; Yanai and Li, 1994).

Yanai *et al.* (1992) tabulated 16 papers on the Tibetan heat sources published since 1979, according to the type of method used.

(1) Method A (Q_1: *apparent heat source*, and Q_2: *apparent moisture sink* as residuals of the large-scale atmospheric heat and moisture budgets, following Yanai *et al.*

(1973)). We can show that the vertically integrated Q_1 and Q_2 satisfy:

$$\langle Q_1 \rangle = \langle Q_R \rangle + LP + S \ldots \tag{13.6}$$

and

$$\langle Q_2 \rangle = L(P - E) \ldots \tag{13.7}$$

where Q_R is the radiative heating rate; and E the rate of evaporation at the surface.

(2) Method B (surface and radiation measurements using (13.5) (e.g., Ye and Gao (1979b)).
(3) Method C (surface energy balance: estimates of $S + LE$ only).

Nitta (1983) was the first to use Method A to discuss the heating profiles over the Tibetan Plateau. Using the FGGE station data, he obtained the mean vertical profiles of the tropospheric heat source Q_1 and moisture sink Q_2 over several parts of the eastern Tibetan Plateau for a 100-day period from the end of May to early September 1979. He found that, over the eastern Plateau, heating occurs in a deep tropospheric layer and that the sensible heat flux from the surface and the release of latent heat of condensation contributes nearly equally to the total heating in this period.

Luo and Yanai (1983), using an objectively analyzed FGGE data set, studied the time evolution of the large-scale precipitation, low-level (850-hPa) wind, moisture and vertical motion fields, and horizontal moisture transport over the Tibetan Plateau and the surrounding areas during a 40-day period (26 May–4 July 1979) which included the onset of the Indian summer monsoon. They showed that the mean 850-hPa wind field exhibits a pronounced inflow toward the Plateau with diurnally varying intensity, confirming the earlier finding of Yeh *et al.* (1957) (also see Staff Members, 1958a,b). Subsequently, Luo and Yanai (1984) examined the large-scale heat and moisture budgets of the Plateau region during the 40-day period. They found that there is a deep heating layer over the Plateau and the mean heating rate in the 200–500 hPa layer above the Plateau is as intense as that over the Assam–Bengal region. They identified the principal components of the heat source as the sensible heat flux from the ground surface and the additional condensation heat from the summer rains, supporting the classical studies of Flohn (1968) and Ye and Gao (1979). They also showed that a deep, nearly mixed layer with high potential temperature is observed over the Plateau in the evening (1200 UTC) (upper level soundings were available only at 0000 and 1200 UTC). The mixed layer was especially pronounced during the dry preonset period.

He *et al.* (1987) extended the heat and moisture budget analysis to an 80-day period (16 April–4 July 1979) and over a larger domain (0–50°N, 40–130°E). They showed that, from spring to summer 1979, the general circulation over south Asia underwent two distinct stages of abrupt transitions, resulting in the successive onsets of the south-east Asian and Indian monsoons (e.g., Krishnamurti, 1985). The two onsets were related to a similar two stages of upper tropospheric warming over the Asian land mass. The rapid warming occurred first over longitudes east of

85°E (the eastern Tibetan Plateau–south China), and then over longitudes west of 85°E (Iran–Afghanistan–western Plateau). The successive warming over these regions is the primary cause of the successive reversals of the meridional temperature gradient on the south sides of these regions. They also showed the presence of the large-scale vertical circulation that is thermally induced by the Tibetan Plateau. The existence of the Plateau-induced vertical circulation is also evident in the distribution of subsidence in the surrounding desert areas (see also Manabe and Broccoli, 1990). In a case study of the Asian summer monsoon onset in 1989 based on the European Centre for Medium-Range Weather Forecasts (ECMWF) analysis, Wu and Zhang (1998) obtained the similar result that before the monsoon onset, the upper tropospheric temperature over the eastern Plateau and along the Yangtze River is several degrees celsius warmer than over the western Plateau. They demonstrate that this is mainly due to the strong westerlies over the Tibetan Plateau before the monsoon onset, which advects cold air from the west to compensate the local heating of 2 to 4°C per day over the Plateau.

Using the FGGE and QXPMEX data, Yanai *et al.* (1992) further studied the seasonal changes in the large-scale circulation, thermal structure, and heat sources and moisture sinks over the Tibetan Plateau and the surrounding areas for a 9-month period from December 1978 to August 1979. They showed that the air above the Tibetan Plateau is warmer than the air over the surrounding areas when compared at the same level and the same latitude (Figure 13.2(h)). They also described the seasonal change of a large-scale vertical circulation that is thermally induced by the Plateau (Figure 13.3). In northern summer, this circulation merges with the circulation associated with the monsoon rain belt which has migrated from the Indian Ocean. Both the warm air and the vertical circulation over the Plateau exhibit pronounced diurnal variations. They also verified that the Plateau is a heat sink in winter and becomes a heat source in spring as shown previously by Ye and Gao (1979b).

Li and Yanai (1996) studied the onset and interannual variability of the Asian summer monsoon in relation to land–sea thermal contrast using a 14-year (1979–1992) set of the global analyses prepared by the ECMWF. The onset of the Asian summer monsoon is concurrent with the reversal of the meridional temperature gradient in the upper troposphere south of the Tibetan Plateau, as suggested by Flohn (1957). The reversal is the result of large temperature increases in May to June over Eurasia centered on the Plateau with no appreciable temperature change over the Indian Ocean (see Figure 13.10). In spring the Tibetan Plateau is a heat source that is distinctly separate from the heat source associated with the rain belt in the equatorial Indian Ocean (see Figures 13.9 and 13.10). The Tibetan heat source is mainly contributed to by the sensible heat flux from the ground surface, while the oceanic heat source is due to the release of the latent heat of condensation. It is the sensible heating over the Plateau region in spring that leads to the reversal of the meridional temperature gradient. Despite its intensity the condensational heating over the Indian Ocean does not result in tropospheric warming because it is offset by the adiabatic cooling of ascending air.

Recently, Ueda *et al*. (2003a,b) examined the heat source (Q_1) and moisture sink (Q_2) over the western and eastern Tibetan Plateau for a 4-month period from May to August 1998, using the Global Energy and Water Cycle Experiment (GEWEX) Asian Monsoon Experiment (GAME) 4-D data assimilation (4DDA) upper air data. In addition, they utilized the Climate Prediction Center Merged Analysis of Precipitation (CMAP) data (Xie and Arkin, 1997). They showed that there is substantial rainfall along the western and south-western slopes of the western Tibetan Plateau in May and June, contributing condensation heating to the western Plateau.

13.3.2 Heating over the Tibetan Plateau and the onset of Asian Monsoon

Here we show recent estimates of Q_1 and Q_2 using the 15-year (1979–1993) ECMWF reanalysis. This data set has been used in a study of the Australian summer monsoon (Hung and Yanai, 2004) and a study of the relationship between the Asian and Australian summer monsoons (Hung *et al*., 2004).

Figure 13.6 shows the horizontal distributions of the vertically integrated heat source $\langle Q_1 \rangle$ (top) and $\langle Q_2 \rangle$ (bottom) for December–February (DJF) and for June-August (JJA). In DJF, pronounced belts of heating exist along the southern side of the equator (South Africa, the South Indian Ocean, and the south-western Pacific) and off the east coast of Asia (Figure 13.6(a)). The essential nature of these heating belts becomes evident when we see the $\langle Q_2 \rangle$ field of the same season (Figure 13.6(c)). The south-of-equator heating belt is mainly due to condensation heating. On the other hand, over the region off east Asia, heating must come from sensible heating over the warm ocean, because $\langle Q_2 \rangle$ is negative, indicating that evaporation is exceeding precipitation.

During JJA, most of the major regions of heating including the two centers of heavy rain (the BOB–Bangladesh, and the western coast of the Indian subcontinent) associated with the Asian summer monsoon (positive $\langle Q_1 \rangle$ in Figure 13.6(b)) are also the regions of large moisture sink (positive $\langle Q_2 \rangle$ in Figure 13.6(d)). Exception is over the western Eurasian continent where $\langle Q_1 \rangle$ is positive but $\langle Q_2 \rangle$ is negative. A notable feature seen from Figure 13.6(b) and (d) is a well-known desert region of the Arabian peninsula where both $\langle Q_1 \rangle$ and $\langle Q_2 \rangle$ are negative, consistent with radiative cooling and evaporation exceeding precipitation in this region of subsidence.

In Figure 13.7 we show the annual cycles of the vertically integrated heat source $\langle Q_1 \rangle$ and moisture sink $\langle Q_2 \rangle$ for the western (top) and eastern (bottom) parts of the Tibetan Plateau separately. In this calculation, the Plateau (above 4,000 m) is divided into two parts (west of 90°E, and east of 90°E). The results for $\langle Q_1 \rangle$ for the two parts of the Plateau are qualitatively similar to those obtained by Ye and Gao (1979b) but the magnitudes are smaller than those given by Ye and Gao. For most of the year the Tibetan Plateau acts as a heat source. Only in winter months does the Plateau become a heat sink. Over the western Plateau, the sensible heat dominates except in July–September when the condensation heating becomes comparable and then dominant. In the eastern Plateau, the significance of condensation heating for May–October is evident. These results generally confirm the previous results (Nitta, 1983; Luo and Yanai, 1984; Yanai *et al*., 1992; Ueda *et al*., 2003b).

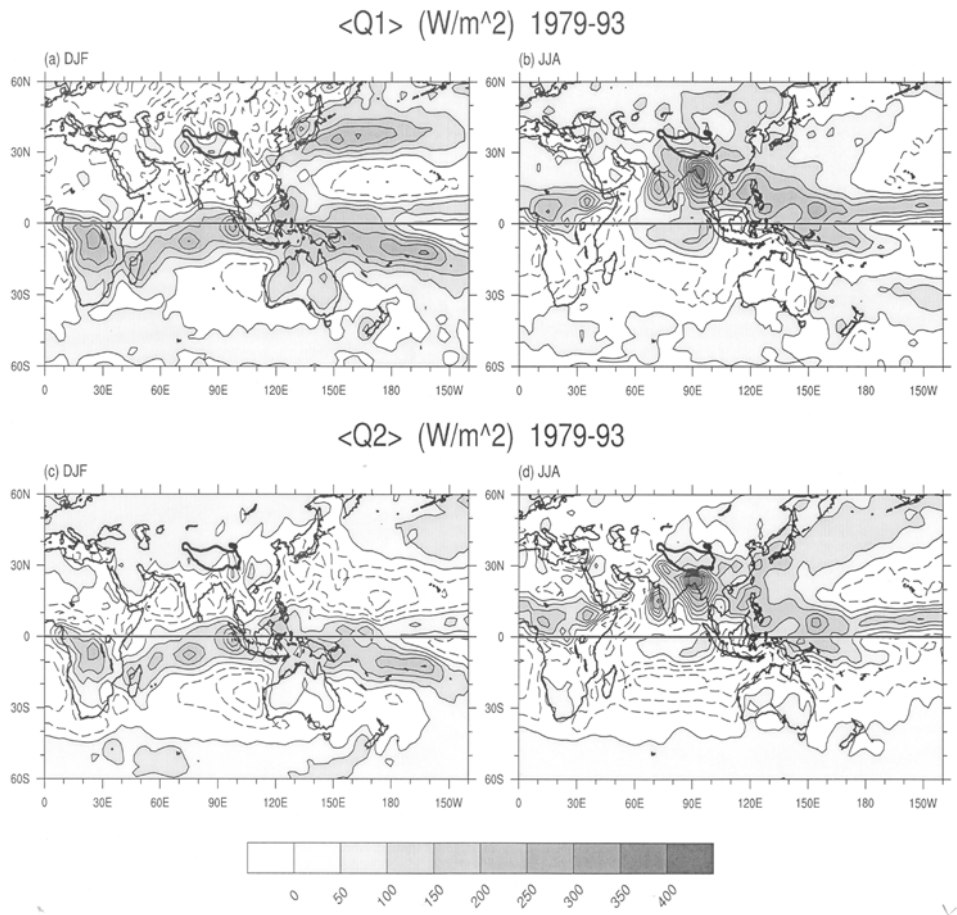

Figure 13.6. Vertically integrated heat source $\langle Q_1 \rangle$ (*top*) and moisture sink $\langle Q_2 \rangle$ (*bottom*), averaged for 1979–1993 for December–February (DJF) and June–August (JJA). (Units: $\mathrm{W\,m^{-2}}$.)

Figures 13.8(a) and (b) display the vertical–longitudinal distributions of Q_1 and Q_2 averaged between 27.5°N and 37.5°N in four seasons, respectively. There are three major regions of interest:

(a) The first is over the Tibetan Plateau. Figure 13.8(a) clearly indicates that there is a column of heating (positive Q_1) on the Plateau throughout the four seasons. But only in JJA and SON is the heating clearly related to Q_2 (condensation heating) of comparable magnitude. The lower half of the air above the Plateau is heated even in DJF and MAM, but there is very little contribution from Q_2, again suggesting the dominance of sensible heating in winter and spring.
(b) The mostly oceanic region east of the Tibetan Plateau is dominated by intense heating ($Q_1 > 0$). The strong heating in DJF just above the sea surface

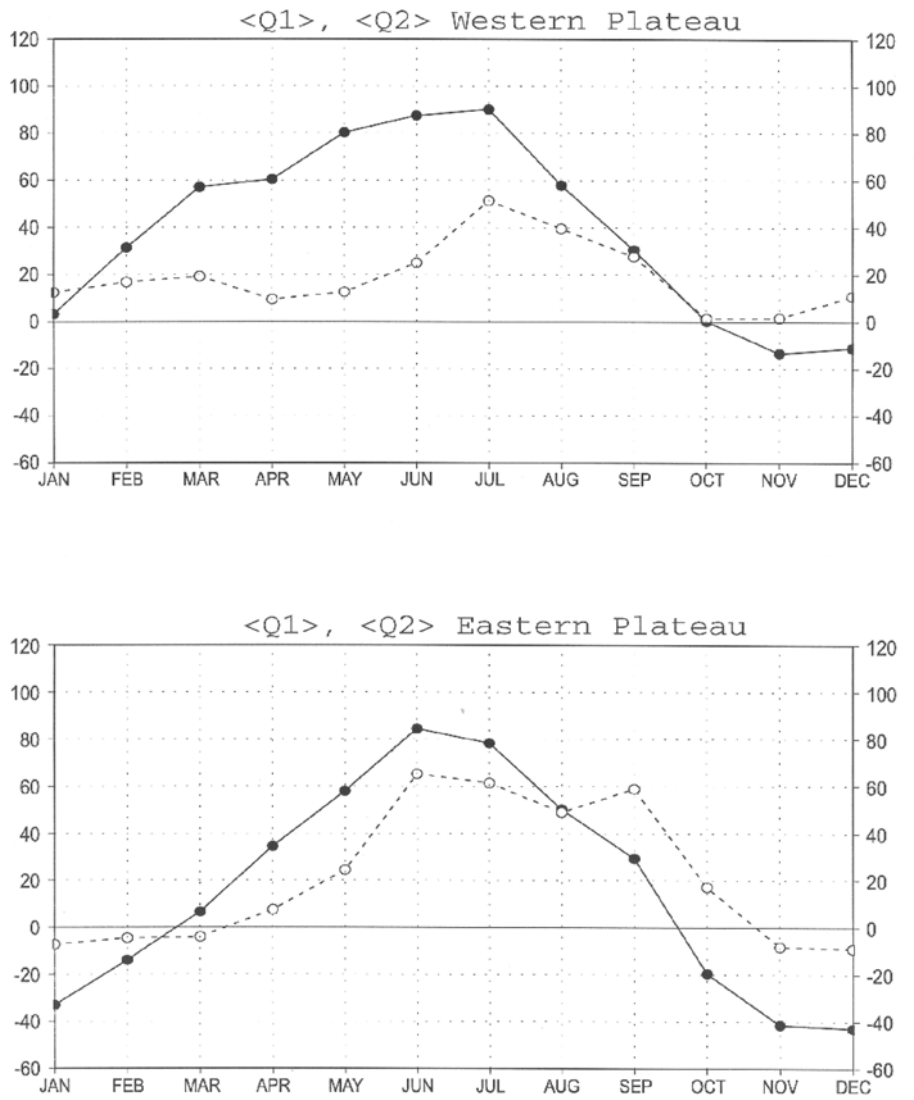

Figure 13.7. Annual cycles of the 1979–1993 mean vertically integrated heat source $\langle Q_1 \rangle$ (solid) and moisture sink $\langle Q_2 \rangle$ (dashed) over the western Tibetan Plateau (*top*) and over the eastern Tibetan Plateau (*bottom*). (Units: $\mathrm{W\,m^{-2}}$.)

(Figure 13.8(a), part (i)) is clearly related to the oceanic heat source off the east coast of Asia (Figure 13.6(a)). For the other three seasons, heating in this region is dominated by rain (Figure 13.8(b), parts (ii)–(iv)).

(c) The third region of interest is located to the west of the Tibetan Plateau. Especially during and after the monsoon season (JJA and SON), this region is

dominated by negative Q_1 and Q_2 (Figure 13.8(a), parts (iii–iv) and (b), parts (iii–iv)). As discussed by He *et al.* (1987) and Yanai *et al.* (1992), strong subsidence prevails in this region. Rodwell and Hoskins (1996) discussed the dynamics of desert formation in terms of a Rossby wave response to the monsoonal heating to the east.

Figure 13.9(a) and (b) display the vertical distributions of Q_1 and Q_2 averaged between 70°–100°E over four seasons, respectively. The large values of Q_1 and Q_2 seen near the equator are associated with the migrating ITCZ involving deep convection throughout the year. On the other hand, during spring (MAM), large values of Q_1 are seen from the surface to 250 hPa above the Tibetan Plateau (Figure 13.9(a), part (ii)). This heat source does not accompany Q_2 (Figure 13.9(b), part (ii)). This shows that the heating above the Tibetan Plateau in northern hemisphere spring is mainly contributed to by a sensible heat flux from the surface (e.g., Yanai *et al.*, 1992; Yanai and Li, 1994). After the onset of the Asian summer monsoon, heating from condensation in the ITCZ and heating over land merge together. In summer (JJA), large heating between surface and 200 hPa is centered over the southern edge of the Tibetan Plateau, although weak peaks of Q_1 and Q_2 are still observed between 10°S and the equator (Figures 13.9(a), part (iii) and 13.9(b), part (iii)).

Figure 13.10(a,b,c) shows the latitude–time sections of $\langle Q_1 \rangle$, $\langle Q_2 \rangle$ and the mean upper tropospheric (200–500 hPa) temperature averaged in the sector (70°–100°E) from 1979 to 1993. The daily $\langle Q_1 \rangle$ and $\langle Q_2 \rangle$ are averaged from the original 6-hourly estimates, and the upper tropospheric mean temperature is from ECMWF reanalysis. The thick curves in the figure indicate the solar declination angle.

We note a large region of positive values of $\langle Q_1 \rangle$ between 30° and 70°N from April to September in Figure 13.10(a) without corresponding features in $\langle Q_2 \rangle$ (Figure 13.10(b)). This region of positive $\langle Q_1 \rangle$ at high latitudes shows the sensible heating over the Asian continent including the Tibetan Plateau. On the other hand, large positive values in $\langle Q_1 \rangle$ between 20°S and 30°N are with large $\langle Q_2 \rangle$ and rainfall (not shown). A prominent rain belt is associated with the ITCZ moving between the two hemispheres (Figure 13.10(a) and (b)). During northern autumn (SON), the ITCZ propagates smoothly from north to south with some delay from the seasonal forcing. However, the ITCZ stays between 15°S–5°N from January to May without any north–south movement. Then, it shows a sudden northward jump in May–June at the onset of the Asian summer monsoon. The onset is concurrent with the reversal of the meridional temperature gradient in the upper troposphere over the BOB region (Flohn, 1957; Li and Yanai, 1996).

13.3.3 Mechanism of heating

Since Ye and Gao (1979b) it has been well recognized that the western and eastern Plateau have different heating characteristics (see Figure 13.7). For the western Plateau sensible heating dominates during spring, whereas for the eastern Plateau condensation heating dominates after the monsoon onset. This east–west contrast is related to the marked difference in the surface properties (e.g., Shi and Smith, 1992).

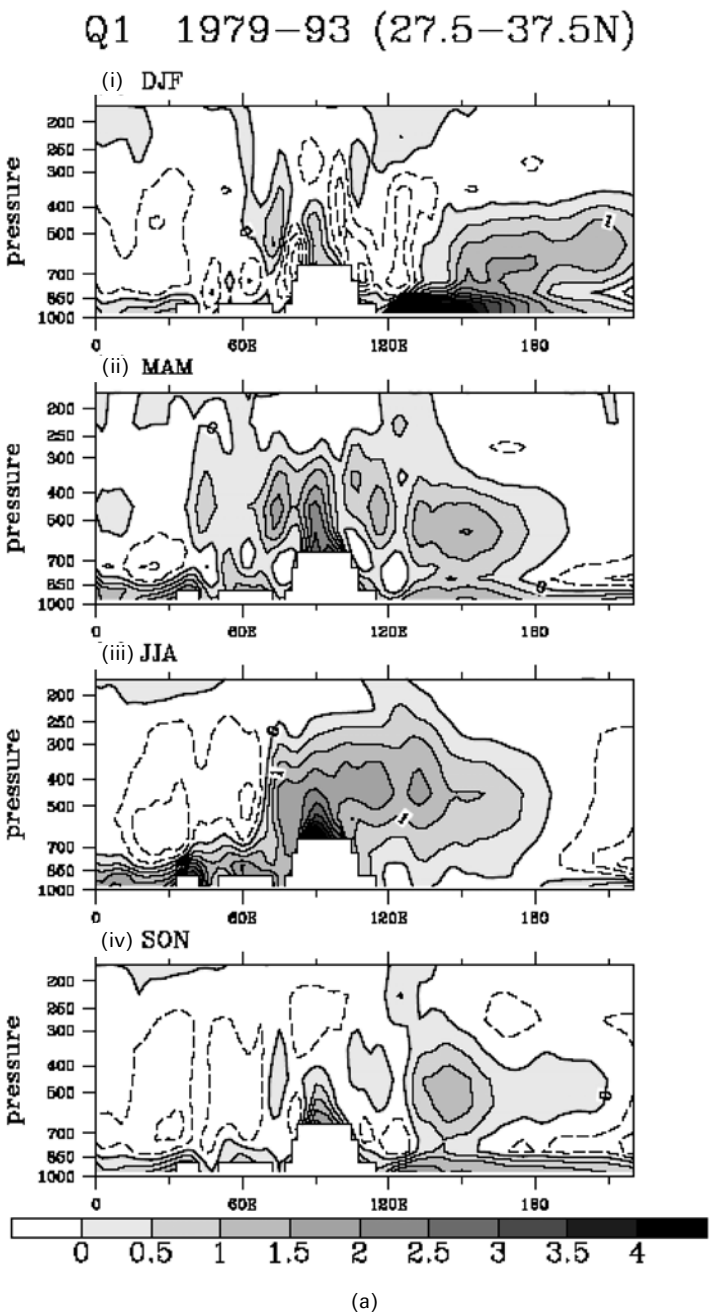

Figure 13.8. (a) Longitude–height sections of the 1979–1993 mean apparent heat source Q_1 for (i) DJF, (ii) MAM, (iii) JJA, and (iv) SON, averaged between 27.5°N and 37.5°N. (Expressed in units of K per day.) (b) Similar to (a), but for the 1979–1993 mean apparent moisture sink Q_2.

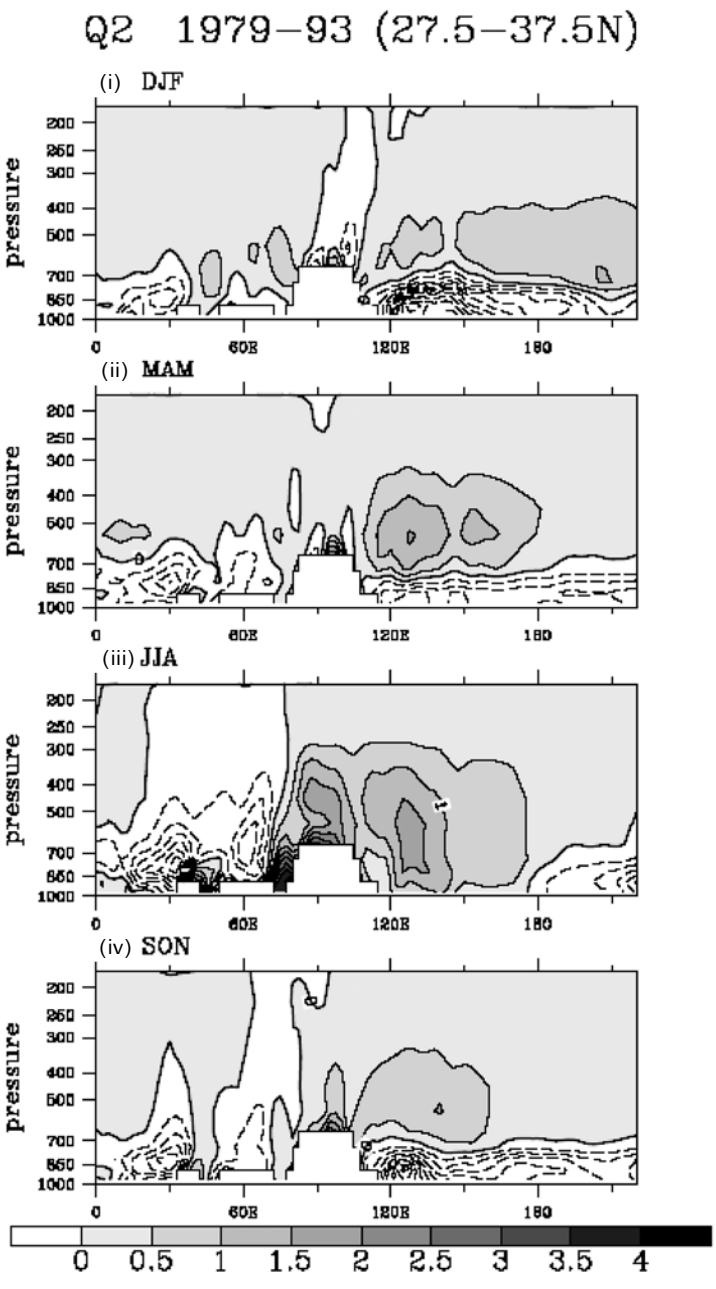
Q2 1979–93 (27.5–37.5N)
(i) DJF
(ii) MAM
(iii) JJA
(iv) SON
pressure
200
250
300
400
500
700
850
1000
0
60E
120E
180
0 0.5 1 1.5 2 2.5 3 3.5 4

(b)

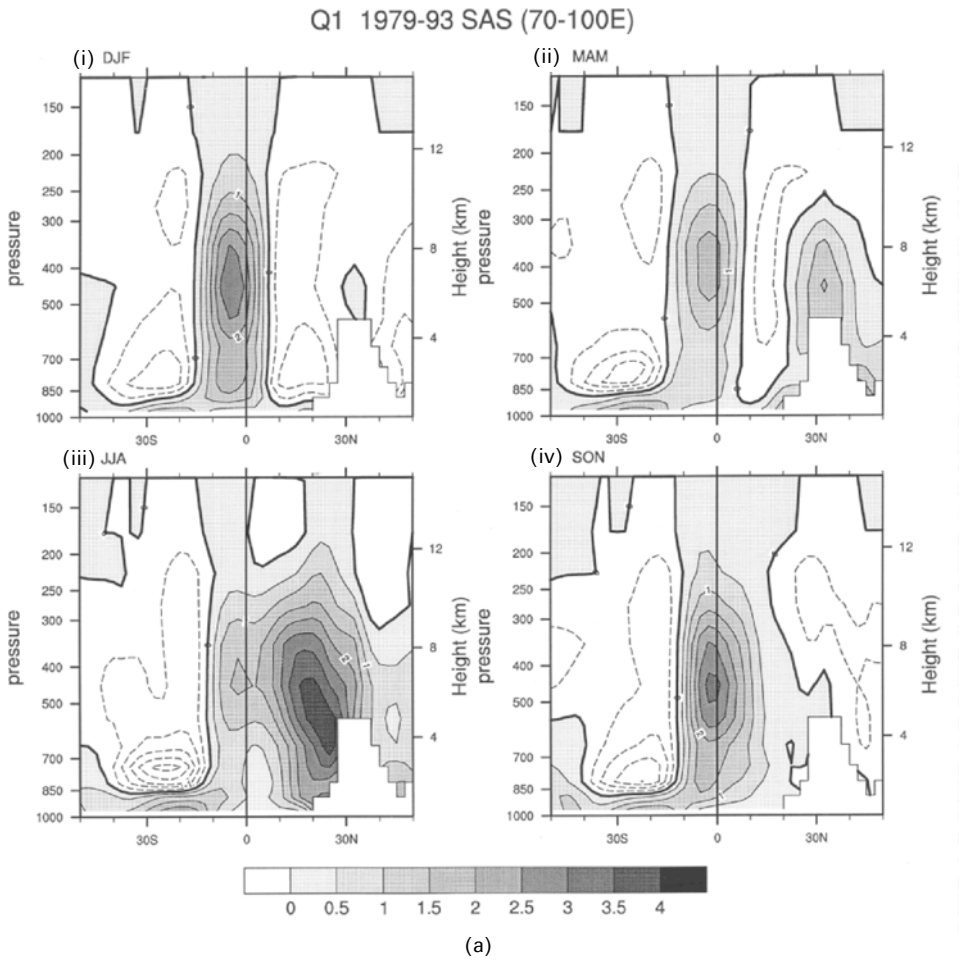

Figure 13.9. (a) Latitude–height sections of the 1979–1993 mean Q_1 for (i) DJF, (ii) MAM, (iii) JJA, and (iv) SON (K per day), averaged between 70°E and 100°E. (b) Similar to (a) but for the 1979–1993 mean Q_2.

Recently, the atmospheric response to different surface properties and vegetation has become an active area of research (e.g., Xue *et al.*, 2004).

Luo and Yanai (1984), Yanai *et al.* (1992), and Yanai and Li (1994) reported the observation of diurnal formation of a deep mixed layer (in terms of potential temperature) on the Tibetan Plateau (especially on the western Plateau) in the pre-monsoon period. The mixed layer was very deep at Shiquanhe (elevation 4,279 m) on the western Plateau (4-month mean top: near 400 hPa) and becomes shallower toward the central Plateau (Naqu) and the eastern Plateau (Jimai). They speculated on the role of 'dry plumes' rising from the heated surface. More detailed observations of the mixed layer formation were reported by Endo *et al.* (1994) using 1993

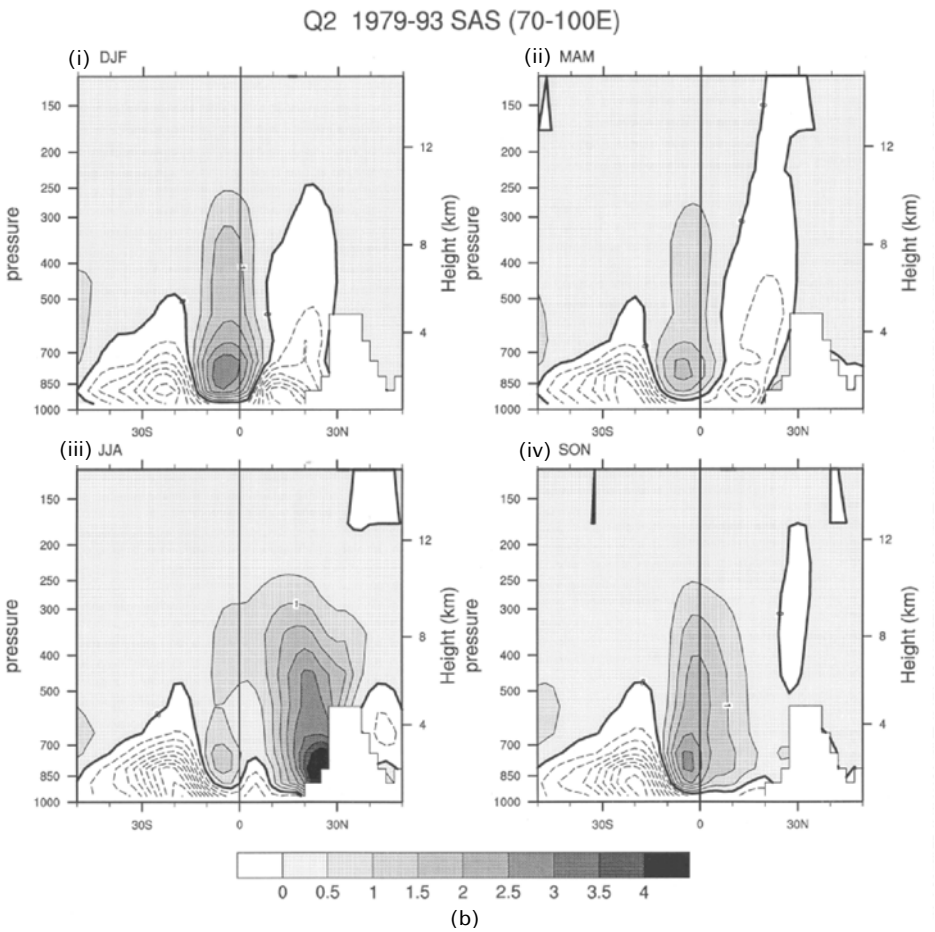

data and by Kuwagata *et al.* (2001) using the GAME–Tibet data. The behavior of the mixed layer is very similar to that found over the heated land such as the famous 'Wangara' boundary layer over Australia (Clarke *et al.*, 1971; Stull, 1988; Garratt, 1992).

We must be careful, however, in the interpretation of heating mechanism on the western Plateau. Satellite observation suggests that there are rains during the preonset period even on the western Plateau especially along the western and southwestern slopes, thus contributing to condensation heating (e.g., Ueda *et al.*, 2003a).

Luo and Yanai (1984), Yanai *et al.* (1992), and Yanai and Li (1994) also found that the mixing ratio q of water vapor is not well mixed and shows a decrease with height. Furthermore, q is smaller during the evening (1200 UTC) than in the morning (0000 UTC). This was confirmed by an extensive study by Kuwagata *et al.* (2001) using various data sources. Earlier, Mahrt (1976) reported similar observations in the high plains region of the USA and explained the decrease of moisture with height

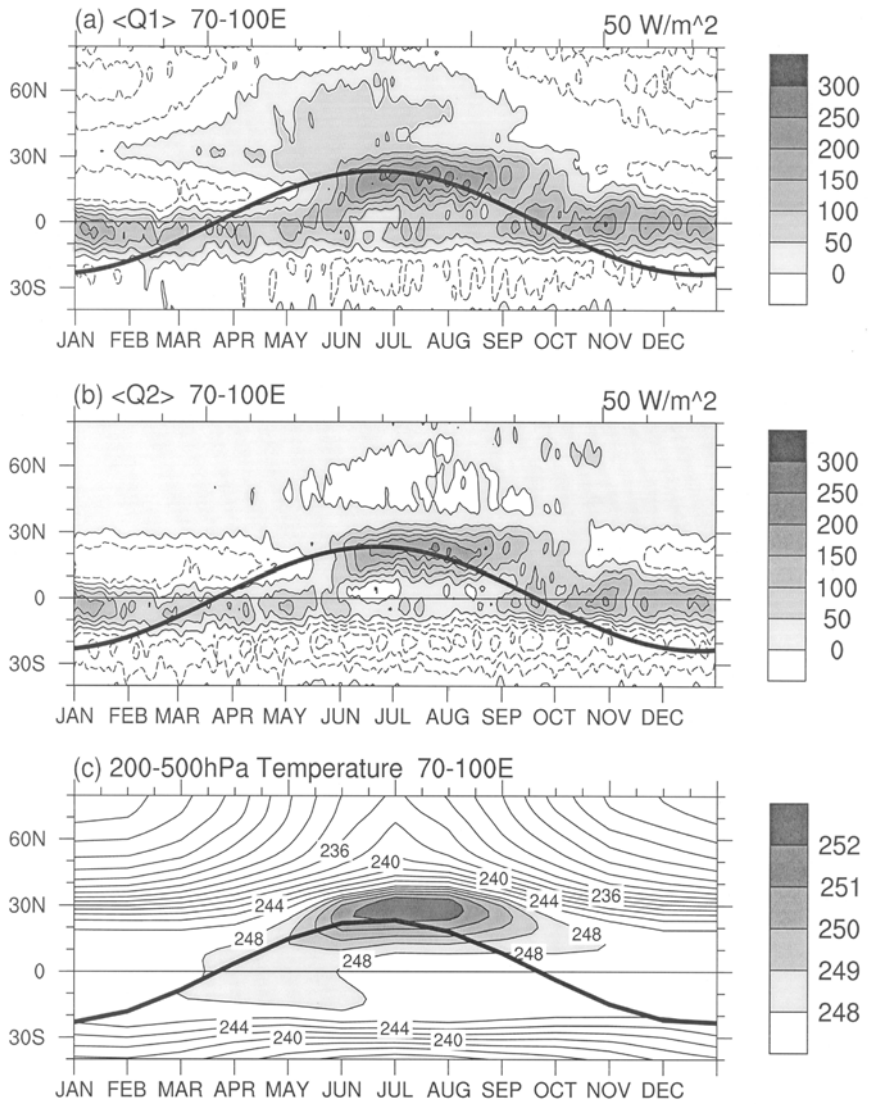

Figure 13.10. Time–latitude sections of the 1979–1993 mean (a) $\langle Q_1 \rangle$, (b) $\langle Q_2 \rangle$, and (c) upper tropospheric (200–500 hPa) temperature, averaged over 70°–100°E. The contour interval for (a) and (b) is 50 W m^{-2}. For (c) the contour interval is 1 K (2 K) when the values are larger (smaller) than 248 K. The thick solid curve is the solar declination angle.

as a result of entrainment of dry air aloft into the rapidly growing mixed layer (see also Mahrt, 1991). On the other hand, Kuwagata *et al.* (2001) considered this a result of local circulation because most of the sounding stations on the Tibetan Plateau are located in valleys.

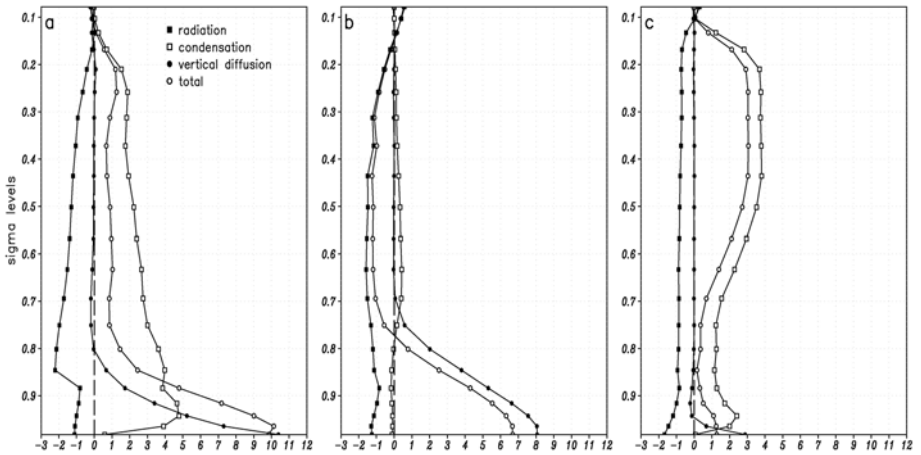

Figure 13.11. July mean area-averaged profiles of the total diabatic heating rate and its components over (a) the Tibetan Plateau region (75°–105°E, 27.5°–37.5°N); (b) middle Asia region (55°–70°E, 30°–42.5°N); and (c) east China region (110°–120°E, 27.5°–37.5°N). Units are K per day. Data are from the monthly mean NCEP/NCAR reanalysis from 1980–1999.

Our knowledge of the detailed heating mechanisms over the Tibetan Plateau is still limited. Although reanalysis data can provide temporal and spatial distributions of different components of heating (Figure 13.11) they are model dependent. More definitive observations are needed to resolve the various problems found by preliminary studies. Since the Topography Experiment for Ocean Circulation (TOPEX)/GAME–Tibet (1998) there have been extensive boundary layer, convection, and precipitation measurements over the Tibetan Plateau. Preliminary results from the field experiments and satellite observations, as well as numerical simulations, show some promise in clarifying these questions (e.g., Zhou *et al.*, 2000; Tanaka *et al.*, 2001; Ueno *et al.*, 2001; Uyeda *et al.*, 2001; Ma *et al.*, 2003; Yang *et al.*, 2003, 2004a,b).

13.4 THERMAL INFLUENCES OF THE TIBETAN PLATEAU ON THE SEASONAL TRANSITION OF CIRCULATION AND ASIAN MONSOON ONSET

13.4.1 Sensible heat driven air-pump over the Tibetan Plateau

Tao and Chen (1987) pointed out that due to the existence of the Tibetan Plateau, the east Asian monsoon onset occurs about two to three weeks earlier than the Indian monsoon onset. Wu and Zhang (1998) further showed that it is due to the mechanical as well as thermal forcing of the Tibetan Plateau that the Asian monsoon onset is composed of three consequential stages: the earliest over the eastern BOB to

the western Indo-China peninsula in early May. The BOB monsoon onset creates favorable conditions for the SCS monsoon onset in mid-May (Liu *et al.*, 2002). These lead to the great changes in both large-scale circulation and diabatic heating over Asia. Finally, the Indian monsoon onset appears in early June.

In Section 13.2, it is demonstrated that in winter the air over the Tibetan Plateau sinks in the free atmosphere (Figure 13.3(a) and (b)) and diverges from the Plateau to the surrounding areas near the surface (Figure 13.2(e)), whereas in summer it arises in the free atmosphere (Figure 13.3(c) and (d)) and converges from the surrounding areas to the plateau near the surface (Figure 13.2(f)). Using a nine-layer GCM, Wu and his collaborators (1997a, 1998, 2004) studied how the elevated heating of the Tibetan Plateau affects the local climate and global circulation. They indicated that due to the surface cooling in winter and heating in summer, the air column over the Tibetan Plateau descends strongly in winter and ascends strongly in summer. It acts as a huge air-pump and regulates the seasonal evolution of the lower layer circulation over the surrounding areas, contributing to the occurrence of the south Asian, BOB, SCS, and the western Pacific monsoons. However, were there no surface sensible heating, such an air-pump would not expel or suck the surface airflow. This is because in the absence of surface sensible heating, the surface air parcel has to stay on the same isentropic surface and cannot penetrate the surface downward or upward along the Tibetan Plateau slopes. In other words, such an air-pump must be driven by the surface sensible heating and is defined as the sensible heat driven air-pump, or SHAP for short (Wu *et al.*, 1997a, 2002b and Wu, 2004).

It is important to note that the SHAP affects not only the airflow near the surface, but also the circulation in the upper layers. As was discussed in Section 13.2, the Tibetan Plateau is a negative vorticity source in summer. Since in the upper troposphere the northern Tibetan Plateau is located within the westerlies, this negative vorticity source may trigger perturbations along the westerlies and affect the circulation anomalies. To verify this, numerical experiments were designed. The model used is the climate model Global–Ocean–Atmosphere–Land–System (GOALS) that was developed at the Laboratory of Atmospheric Sciences and Geophysical Fluid Dynamics (LASG), Institute of Atmospheric Physics (IAP) (Wu *et al.*, 1997b; Zhang *et al.*, 2000). Its atmospheric component (Wu *et al.*, 1996a) has 9 levels in the vertical and is rhomboidally truncated at wavenumber 15 in the horizontal. The ocean component (Zhang *et al.*, 1996) has 20 layers in the vertical with a horizontal resolution of 4° latitude by 5° longitude. The land component uses the simplified simple biosphere (SSiB) model (Xue *et al.*, 1991; Liu and Wu, 1997). The K-distribution scheme developed by Shi (1981) is used for the parameterizing radiation processes. This model has been used in the Atmospheric Model Intercomparison Program (AMIP), Coupled Model Intercomparison Program (CMIP), and Task I of the Intergovernmental Program for Climate Change (IPCC, 2001). There are two experiments in this study. In the first experiment, cloud distributions are prescribed using satellite remote sensing data for the calculation of radiation. There is no cloud–radiation feedback. The observed distributions of SST and sea ice from 1979 to 1988, which were set for the AMIP experiments, are introduced as the prescribed lower boundary conditions to integrate the model for 10 years. This is

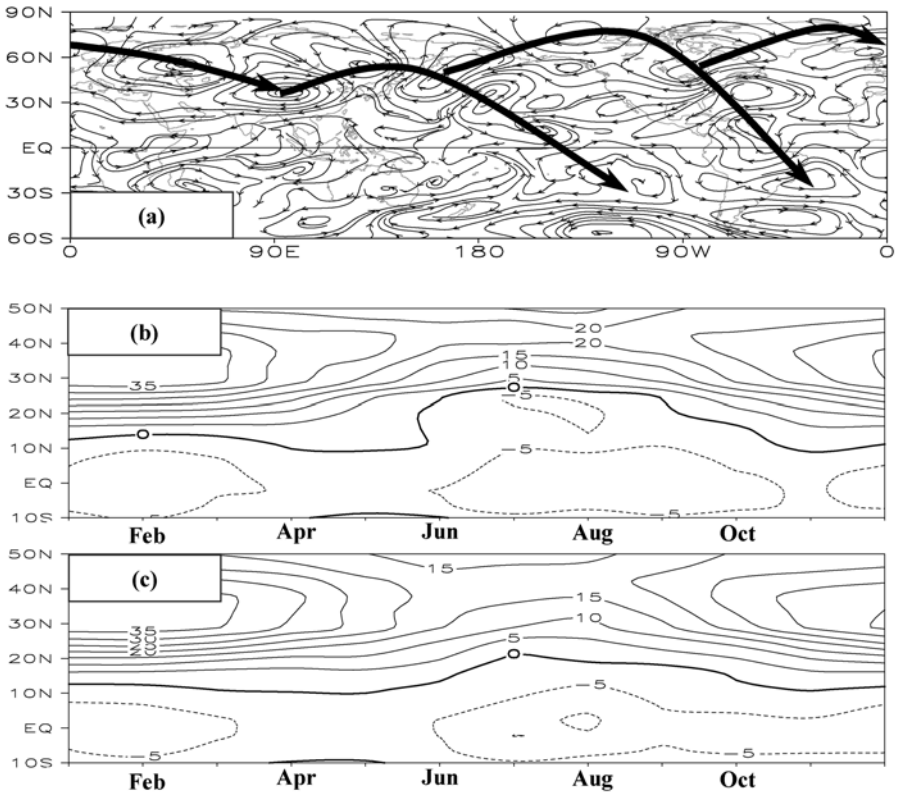

Figure 13.12. The difference of July mean stream field at 200 hPa between the experiments of CON and NSH (a), and the simulation results of the seasonal evolutions of the zonal wind u and the ridge line of the subtropical anticyclone ($u = 0$) along 90°E in the experiments CON (b) and NSH (c).

defined as the CON run. The second experiment is the same as the CON except that the sensible heating over the Tibetan Plateau region that is above 3 km is not allowed to heat the atmosphere aloft. This is achieved by switching off the sensible heating term in the thermodynamic equation at the grid points over the plateau region. This experiment is then defined as the NSH run. Since there is no cloud–radiation feedback in the model and the cloud amounts are prescribed, and since the ground surface temperature in the model is calculated based on the thermal equilibrium assumption, the energy budgets at the ground surface in the two experiments are kept unchanged. Therefore, the difference between the two experiments can be considered as resulting purely from the sensible heating over the plateau.

The difference in stream field at 200 hPa between CON and NSH shown in Figure 13.12(a) demonstrates that the sensible heating over the Tibetan Plateau does generate anticyclonic vorticity in the upper troposphere as was discussed in Section 13.2. More importantly, such a sensible heat-induced vorticity source over the Plateau forces a series of stream field anomalies in the form of a ray of Rossby

waves. Although this result is obtained through numerical experimentation, it is also supported by observational evidence. Based on the NCEP/NCAR monthly mean data, Liu X. *et al.* (2002) analyzed the correlation between the July heating over the Tibetan Plateau area and the corresponding 200-hPa geopotential height, and obtained a similar pattern of Rossby wave rays. This implies that the effective working of the SHAP over the Tibetan Plateau affects not only the climate anomaly in the surrounding area but also the circulation over the northern hemisphere.

Furthermore, such a SHAP has significant impacts on the seasonal transition of the atmospheric circulation at least over the Asian monsoon areas. Yeh *et al.* (1959) found that the seasonal transition between winter and summer patterns is abrupt: in late May and early June, the westerly jet retreats quickly from the south of the Tibetan Plateau to its north, and the associated ridge line of the subtropical anticyclone and the circulations over south Asia also jump northward; whereas in October the circulation experiences the opposite abrupt seasonal transition. These abrupt seasonal transitions are closely linked with the Asian monsoon onset and retreat. In Figure 13.12(b) and (c) are demonstrated the seasonal evolutions of the 500-hPa zonal wind at 90°E based on the results of the aforementioned numerical experiments CON and NSH, respectively. In CON, in which the surface sensible heating over the Tibetan Plateau exists (Figure 13.12(b)), the easterly axis in winter is maintained near the equator, the westerly axis at 35°N, and the ridge line of the subtropical anticyclone identified by $u = 0$ near 12°N. By the end of May and early June, the tropical easterly axis suddenly jumps northward, the westerly axis settles to the north of the Tibetan Plateau at about 42°N, and the abrupt change in the location of the ridge line of the subtropical anticyclone is the most evident. In October, the seasonal transition in circulation experiences the opposite direction. All this is in good agreement with Yeh *et al.* (1959). On the other hand, in the experiment NSH, in which the sensible heating over the Tibetan Plateau area where elevation is above 3 km is not allowed to heat the atmosphere, the seasonal transition between the winter and summer patterns becomes smooth, and the abrupt transition disappears (Figure 13.12(c)). This is because the strong surface sensible heating over the Tibetan Plateau and the strong latent heat release associated with the east Asian monsoon in May greatly intensify the SAH (Wu *et al.*, 1999; Liu Y. *et al.*, 1999, 2001). As a result, the wintertime westerlies to the south of the Tibetan Plateau are substantially weakened, whereas the westerlies to its north are intensified – abrupt changes in circulation thus occur. After the withdrawal of the Asian monsoon, the SAH is weakened, and the circulation returns to its winter pattern.

13.4.2 Thermal impacts of the Tibetan Plateau on seasonal transition and Asian monsoon onset

As demonstrated in Figure 13.10(a), during the spring months while the Tibetan Plateau domain has become a heating region, the areas over the Indian Ocean to its south and over the land surface to its north are still experiencing cooling. The heating over the Tibetan Plateau starting from early spring will then help the over-

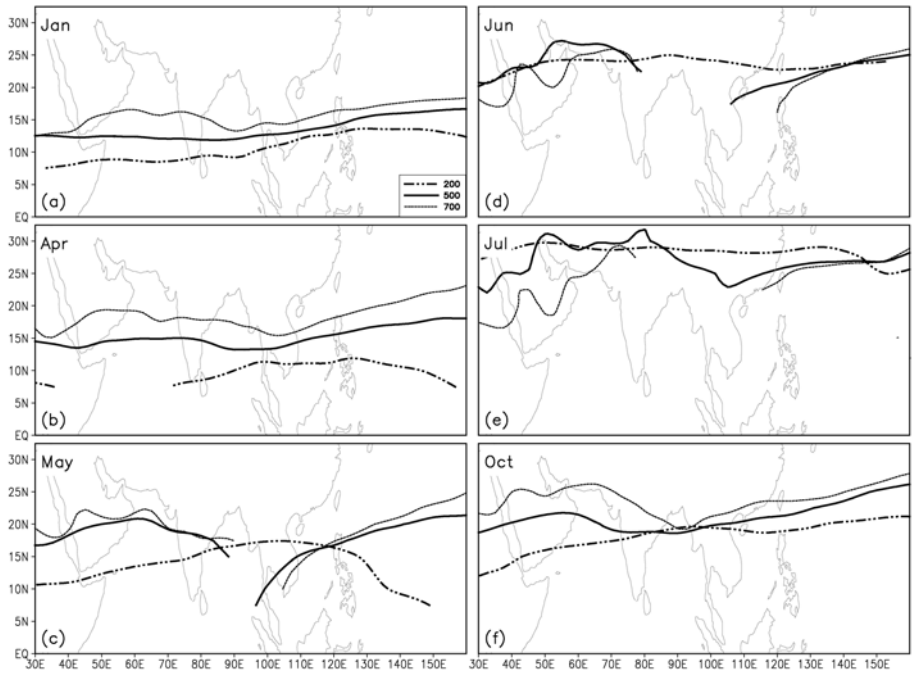

Figure 13.13. Distributions in different months of the ridge lines of the subtropical anticyclone at 700 hPa (dashed curve), 500 hPa (solid curve), and 200 hPa (dotted curve) averaged from 1980 to 1997.

turning of the meridional temperature gradient in the region (Figure 13.10(c)) in favor of the Asian monsoon onset (Flohn, 1957; Li and Yanai, 1996). This can be viewed by diagnosing the configuration of the subtropical anticyclone ridge surface.

In winter months from October to April, the ridge lines of the subtropical anticyclone in the troposphere are all zonally located (Figure 13.13). These ridge lines then comprise a surface. It becomes a continuous boundary that separates the westerlies to the north and the easterlies to the south, and can be defined as WEB (westerlies and easterlies boundary) for short. On the other hand, the tilting of the WEB can be measured by the vertical shear of zonal wind across the WEB surface (i.e., $\partial u/\partial z$). Subject to the thermal wind relation, the reversal of meridional temperature gradient across the WEB must be accompanied by a change in vertical tilting of the WEB. In winter, the tropical air temperature to the south of the WEB is warmer than to its north, and the WEB surface tilts southward with increasing height (Figure 13.13). In summer, the Asian continent to the north of the WEB is warmer than the ocean to its south. As a result, the sector of the WEB surface over the Asian monsoon area tilts northward, while other parts of the WEB surface still keep tilting southward. The lower part of the WEB surface is then broken. Therefore, the monsoon onset index of the reversal in the prevailing wind direction in the lower troposphere can be viewed as the breaking of the lower part

of the WEB where the wintertime easterlies to the south of the WEB are replaced by westerlies after the monsoon onset. Figure 13.13 indicates that on monthly scales the onset of the Asian monsoon is in May and its withdrawal is in October.

When the ridge lines at different levels intersect at one point (e.g., Point C or D in Figure 13.14), the WEB surface at that point becomes perpendicular to the Earth's surface. The vertical axis at this point on the surface can then be defined as a seasonal transition axis, or STA for short. The appearance of an STA then implies the start of the seasonal transition. Since it is usually accompanied by the occurrence of severe convective rainfall, it is also the time of monsoon onset. Figure 13.14 shows the pentad-mean evolution of the ridge lines at different levels calculated from the NCEP/NCAR reanalysis and averaged from 1980 to 1997 (Mao *et al.*, 2002a and b). Before the end of April (Figure 13.14(a–d)), the ridge lines from 700 hPa upwards all tilt southward with increasing height, presenting a typical winter pattern. By 1–5 May (Figure 13.14(e)), the WEB surface becomes perpendicular between point C (105°E) and point D (90°E) along 12°N, just over the eastern BOB and western Indo-China peninsula, and the 850-hPa wind direction south of 12°N over the BOB area has changed from easterly to westerly, indicating the BOB monsoon onset. Afterwards, the STA point C propagates eastward quickly. By 16–20 May (Figure 13.14(h)), it reaches the eastern SCS, and the wind directions at 850 and 700 hPa to the south of 16°N over most of the SCS have been overturned from easterly to westerly. This corresponds to the SCS monsoon onset. The arrival of the STA point C by 135°E in early June (Figure 13.14(k)) is well coordinated with the western Pacific monsoon onset (Wang and Lin, 2002). Meanwhile, the STA point D moves westward gradually. By early June, it arrives in western India (Figure 13.14(k) and (l)), in accordance with the Indian monsoon onset. By this time, the monsoon onset procedure is completed, and the summer circulation pattern over Asia is established. These results are also in good agreement with the results of Wu and Zhang (1998) that the Asian monsoon onset continues for about forty days, and is composed of three consequential stages: the earliest in the early May over the eastern BOB, then the SCS monsoon onset by 20 May, and the Indian monsoon onset in early June. They showed that in early spring, partly due to the Tibetan Plateau heating and the westerly advection over the plateau, the air over its eastern part is warmer than over its western part. The meridional thermal contrast between the eastern part of the Tibetan Plateau in the north and the North Indian Ocean in the south then becomes strongest. This is in favor of the earliest overturning of the meridional temperature gradient over the eastern part of the BOB and the western Indo-China peninsula. Therefore, the Asian monsoon onset occurs firstly over this area.

To verify this result, the time series of the BOB monsoon onset is constructed for the BOB domain (90°–100°E, 5°–15°N) based on the following criteria:

(a) The meridional temperature gradient ($\partial T/\partial y$) across the WEB surface has changed its sign from negative to positive and maintained this change for 5 consecutive days;
(b) The vertical shear of the zonal wind ($\partial u/\partial z$) across the WEB surface has changed its sign from positive to negative; and

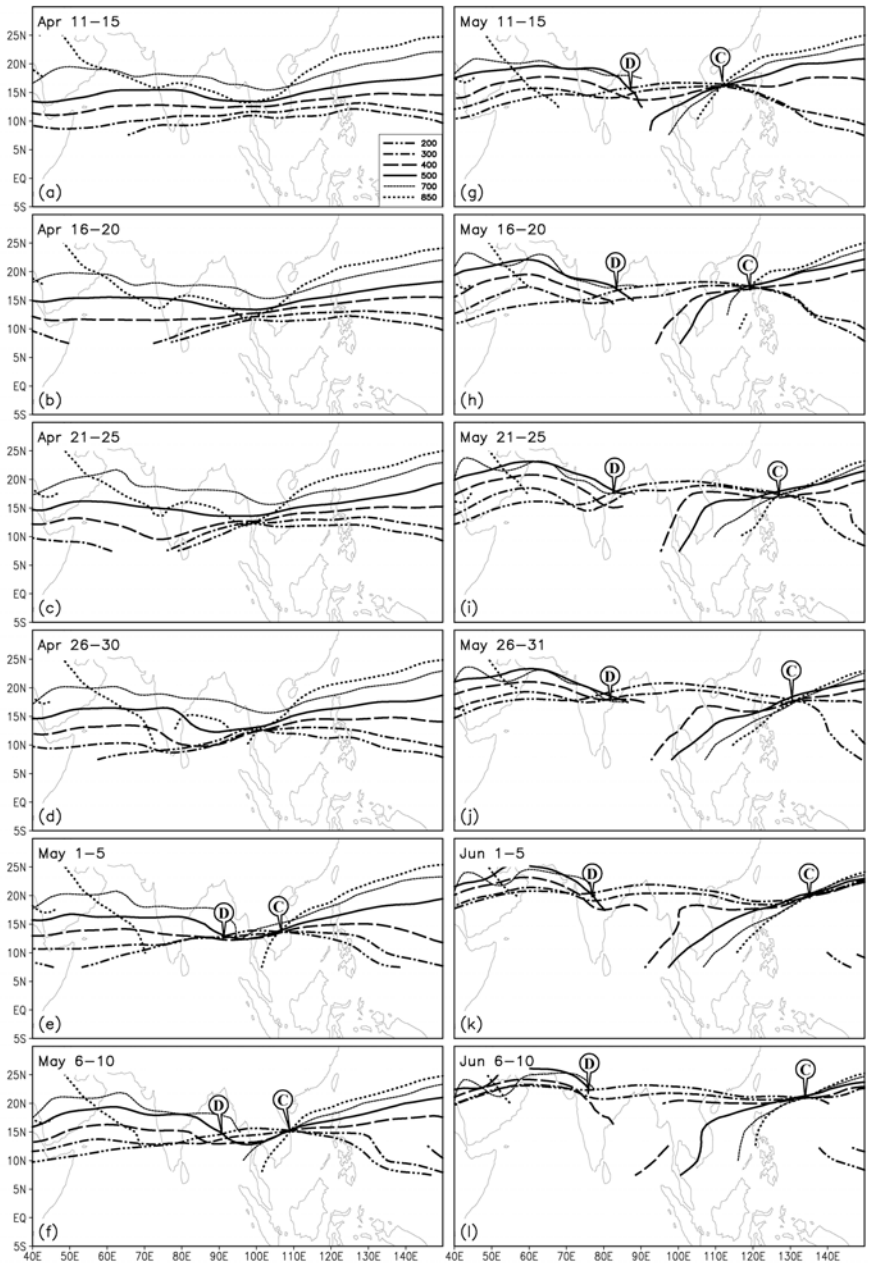

Figure 13.14. The projection of the subtropical anticyclone ridge line ($u = 0$) at the levels from 850 hPa to 200 hPa during the season transition (from the third pentad of April to the second pentad of June) (a) 11–15 April, (b) 16–20 April, (c) 21–25 April, (d) 26–30 April, (e) 1–5 May, (f) 6–10 May, (g) 11–15 May, (h) 16–20 May, (i) 21–25 May, (j) 26–31 May, (k) 1–5 June, (l) 6–10 June.

(c) The outgoing long-wave radiation (OLR) at the site under examination has decreased to below 230 Wm^{-2}.

This time series of the BOB monsoon onset is then used to calculate its time lag correlations with temperature and geopotential height fields. Figure 13.15 displays the time lag correlation between the BOB monsoon onset and the monthly mean geopotential height at 200 hPa, in which the statistically significant correlation higher than 95% is shaded. It shows that in the years with early/late BOB monsoon onsets, the 200-hPa monthly mean geopotential heights over the Tibetan Plateau before the onset (from December to April) are continuously higher/lower than normal. In other words, the warmer the air over the eastern Tibetan Plateau, the earlier the BOB monsoon onset. This result supports our earlier conclusion that the Tibetan Plateau heating in spring contributes substantially to the earliest monsoon onset over the eastern BOB and western Indo-China peninsula.

13.5 CONCLUDING REMARKS

In this chapter, we have briefly reviewed the study of the effects of the Tibetan Plateau during the last half century. However, there are issues this chapter did not discuss because of textual extent limitations. These include:

- **The effects of mountain uplift**
  Raising the altitude of large-scale mountains can increase the non-linear atmospheric response to mechanical forcing and planetary waves (Wu, 1984; Trenberth and Chen, 1988). Early GCM results with and without an account of mountains (e.g., Hahn and Manabe, 1975; Kutzbach *et al.*, 1989) established the role of mountains in enhancing the Asian monsoon. Liu and Yin (2002) showed that the evolution of the east Asian monsoon may be more sensitive to the uplift of the Tibetan Plateau than that of the south Asian monsoon. Recently, Abe *et al.* (2004) and Kitoh (2004) used a coupled atmosphere–ocean GCM and showed that the mountain uplift causes changes in the SST of the surrounding oceans, resulting in a larger sensitivity of the east Asian monsoon to the uplift than previously obtained using the atmospheric GCM alone.
- **The effects of snow cover**
  Many observational studies and GCM experiments (e.g., Hahn and Shukla, 1976; Barnett *et al.*, 1989; Yasunari *et al.*, 1991) examined the relationship between the Eurasian–Tibetan Plateau snow cover and the subsequent Asian monsoon. An inverse relation between the winter snow cover and the subsequent summer monsoon rainfall was generally noted. However, a detailed study (Bamzai and Shukla, 1999) revealed that western Eurasia is the region for which a significant inverse correlation exists between winter snow cover and subsequent summer monsoon rainfall. They did not find a significant relation between the Himalayan snow cover and subsequent monsoon rainfall. Ueda *et al.* (2003b) studied factors contributing to the spring northward retreat of

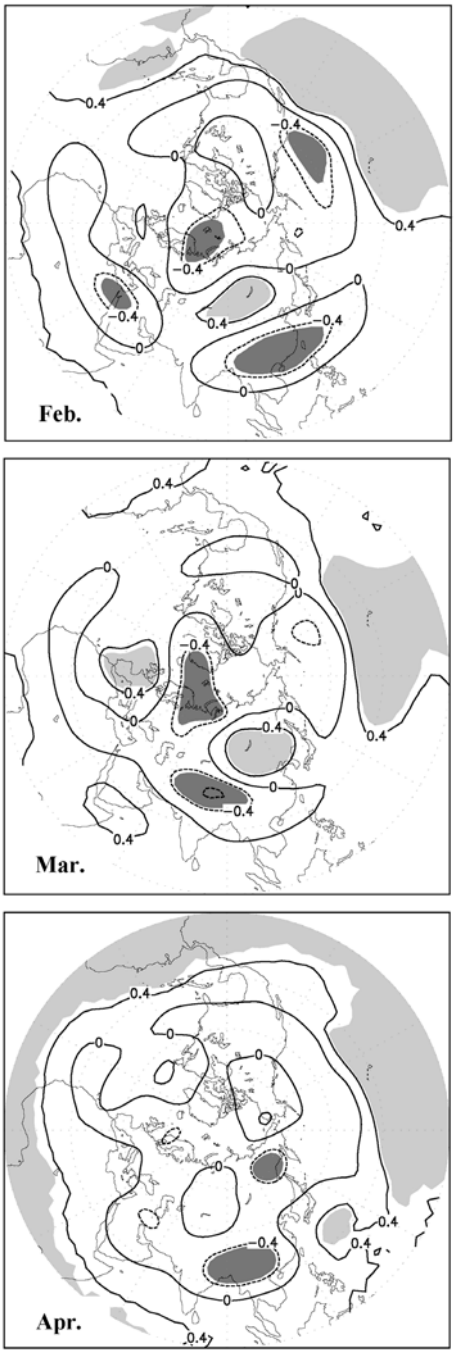

Figure 13.15. The time lag correlation coefficients between the monsoon onset over the eastern part of the BOB and the monthly mean 200-hPa geopotential height.

Eurasian snow cover. They showed that the surface air temperature anomalies produced during the snow disappearance period diminishes in May, suggesting a rather weak dynamic link between the snow cover and Asian summer monsoon. Recently, Zhang *et al.* (2004) discussed the decadal change of spring snow depth over the Tibetan Plateau and its influence on the east Asian summer monsoon.

- **Climatic warming**
  Liu and Chen (2000) discussed the observed warming trend over the Tibetan Plateau during recent decades. Chen *et al.* (2003) made a model study of the climatic warming in the Tibetan Plateau due to a doubling of CO_2.

Now we can make brief conclusions about the studies on the effects of the Tibetan Plateau. Mechanically the Tibetan Plateau, representing a huge obstacle, can block atmospheric basic flows and split the wintertime westerlies into the northern and southern branches. It also has a dominant effect on lee cyclogenesis and associated northerly cold surges in winter. Since Ye h *et al.* (1957) and Flohn (1957) discovered the heating nature of the Tibetan Plateau, a new field of research (i.e., the Tibetan Plateau meteorology) has been established. During the past decades, many efforts have been devoted to understanding its heating features and the consequent weather and climatic impacts. Much new light has been shed on the associated mechanisms. It has become certain that the Tibetan Plateau is a heat sink in winter but a heat source in summer. Recent studies also show that the Tibetan Plateau is a strong negative vorticity source in summer, which, via energy dispersion, affects the anomaly of the atmospheric circulation at least in the northern hemisphere. Strong descending in winter and ascending in summer of the air column over the Tibetan Plateau represents a huge air pump, and regulates the annual cycle of the global circulation and the monsoon climate over Asia, Africa, and Australia. Furthermore, due to it having a larger 'memory' than the underlying surface, the Tibetan Plateau heating in late winter and spring can exert both simultaneous and delayed impacts on the weather and climate anomalies in summer in the surrounding areas (Chen and Yan, 1981; Wu *et al.*, 1996a,b; Hsu and Liu, 2003), and can be used as a prediction indicator.

However, most of these conclusions are still qualitative in nature. Our further understanding on the Tibetan Plateau forcing and its impacts on weather and climate are hampered by various limitations. First of all the sparseness and the lack of representativeness in observational data over the complex topography shadows the heating details over the plateau. Due to a lack of knowledge about the land–air–sea interaction in this area, questions concerning how the Tibetan Plateau and its heating nature affect the local and global climate remain unclear, and the use of such a knowledge for quantitative climate prediction is still unavailable. To move forward, we need to plan our coordinated research to take in many aspects, such as:

- Expanding our understanding from summer months to other months. Most of the existing research is focused on the impact of the Tibetan Plateau on circulation and climate in the summer months. To achieve a coherent understanding we need to study how the Tibetan Plateau cooling in winter affects the weather and

climate, and how the annual variation of the Plateau heating is associated with the seasonal evolution of the atmospheric circulation.

- Revealing all the mechanisms related to the Asian monsoon onset. The climate system is a non-linear, dissipative, and open system, and the timing and location of the Asian monsoon onset is influenced by many factors not just the Tibetan Plateau heating, such as the persistently external forcing and low-frequency oscillations in the atmosphere (e.g., the MJO).
- Detailing the heating feature over the Tibetan Plateau. Up to now, our knowledge of the Tibetan Plateau heating is rather limited. Although reanalysis data can provide temporal and spatial distributions of different heating, they are model dependent. The provision of vertical profiles of different heating over the Tibetan Plateau and its neighboring regions will enable the study of the circulation formation and its impacts on regional as well as global climate.
- Analysing the response of the Tibetan Plateau thermal status to global change. Most of the existing research concerns how the Tibetan Plateau thermal status affects the global climate. However, the changes in global climate will in return influence the thermal status over the Tibetan Plateau and its contrast with those over the Indian Ocean and western Pacific, eventually exerting different forcing on the global climate.
- Revealing the physical processes associated with the interactions between the Tibetan Plateau and the atmosphere. To achieve this, more field observation experiments and numerical modeling are required.

All these and other related research issues demand great efforts and will continue in the coming decades.

13.6 ACKNOWLEDGEMENTS

We would like to thank Professor Duzheng Ye for his help and encouragement during writing. Thanks are also due to the editor, and to Professor T. Murakami, Dr. Akio Kitoh, and Dr. Jun Matsumoto for kindly offering useful comments and help on improving our original draft. The first author thanks Drs. Chih-wen Hung, Xiaodong Liu, and Hui Su for their useful discussions and assistance with the illustrations; the second author thanks Drs. Xin Liu, Jiangyu Mao, and Anmin Duan for producing the relevant figures. This work was partially supported by the Chinese Academy of Sciences under Grant No. ZKCX2-SW-210, the National Natural Science Foundation of China under Grant Nos 40135020 and 40475027, the National Oceanic and Atmospheric Administration under Grant NA96GP0331, and by the National Science Foundation under Grant ATM-9902838.

Part Four

14

Seasonal climate prediction of Indian summer monsoon

T. N. Krishnamurti, T. S. V. Vijaya Kumar, and A. K. Mitra

This chapter provides a review of some aspects of the numerical weather prediction of the Indian summer monsoon. Here we address the data issues, state of monsoon forecasts of the current major global models, some results from regional high-resolution models, the area of cumulus parameterization, and how perhaps we might cope with its difficulties. The major issues of the organization of convection and how high-resolution models are addressing this is also discussed and the promise of multimodel ensembles and the superensemble for improving the state of forecasting of the monsoon is described. These procedures provide insights to the performance of various cumulus parameterization schemes. A short review of the month-long forecasts of low-frequency motions such as the Madden–Julian Oscillations (MJO) and the intraseasonal oscillation (ISO) of the monsoon are included in this chapter. Finally, a summary is provided on the possible areas of future work emphasizing the need for more detailed observations over regions of steep orography and heavy rain and the modeling issues related to these regions.

14.1 INTRODUCTION

A short review of the current state of monsoon forecasts over the Indian region is presented here. Monsoon forecasts span timescales of a few days to a season. Here the emphasis is on numerical weather prediction (NWP) methods and numerous groups in North America, Japan, Australia, China, Europe, and India have made major contributions in this area of research and operational practice. In this review of the NWP of the monsoon, we show the current performance of several numerical models. In recent years, major advances have occurred in data quality (those from the ground surface, aircraft, and space), assimilation, modeling in terms of resolution, representation of orography, physical parameterizations of shallow and deep convection, radiative transfer (treatment of clouds, details of diurnal changes, and

B. Wang (ed.), *The Asian Monsoon*.

surface energy balance), surface and planetary boundary layer physics for the fluxes of heat, moisture, and momentum, and the inclusion of land surface processes. Both high-resolution global, and very high-resolution regional non-hydrostatic microphysical models have been employed by numerous scientists to address the issues of the monsoon life cycle and forecast skill has been gradually improving during the last two decades. Prediction of precipitation on different timescales over the monsoon region is one of the central scientific issues and has been a challenge for several research and operational weather prediction centers in the World. Weather and climate prediction over the monsoon region is particularly important because of its greater role and influence on the global general circulation, apart from its socio-economic impacts. Major weather forecasting groups in Asia, Europe, Australia, and North America have undertaken significant work and achieved significant progress in understanding and prediction of the monsoon system and several review papers on monsoon prediction are available in the literature (e.g., Webster *et al*., 1998; Shukla 1998; Chang and Krishnamurti, 1987). In this chapter, further details on the status of the Indian summer monsoon prediction is provided with emphasis on short-to-medium range and seasonal timescales.

Improvements in forecasting daily rainfall on the medium-range time frame of 5–7 days have come about from the use of improved physical initialization and ensemble forecast approaches and in this review, we shall provide a short account of monsoon forecasts from this perspective. Physical initialization is a means for the improvement of the nowcasting of rain and this has been formulated for different models that use different cumulus parameterization schemes (Krishnamurti *et al*., 1991; Treadon, 1996). It has been possible to improve the nowcasting skill of precipitation, which provides a correlation between the modeled initial rain and the satellite-based estimates to around 0.9, in a very consistent manner. The physical initialization has been shown to have a major impact on the short-range forecasts of the monsoon while studies on models' sensitivity to other physical parameterizations have been somewhat limited. In the context of the multimodel ensemble and super-ensemble forecasts (Krishnamurti *et al*., 1999, 2000a,b, 2001, 2002), we show the current performance of a number of lead models over the monsoon domain. We present here the skill scores for medium-range forecasts of winds, sea level pressure, and precipitation, all part of a real time global forecast model intercomparison. We note here that a measurable improvement in skill between 10 to 30% is achievable, compared with all member models, from the construction of a multimodel super-ensemble.

Next we show some results on forecasts of the ISO of the monsoon that are carried out using a frequency filter within a low-resolution global model (Krishnamurti and Subrahmanyam, 1982; Krishnamurti *et al*., 1990a, 1992b). The frequency filter is only employed at the initial state to remove all high-frequency motions, the initial state thus includes only a time mean state and a low-frequency state, and the sea surface temperature (SST) anomalies are prescribed. We show that the prediction of one cycle at low frequency has some skill. Such information can be used to provide some guidance for the occurrence of the wet and dry spells of the monsoon roughly a month in advance.

In the context of monsoon climate prediction, in recent years, a number of papers have addressed seasonal forecasts of the Indian monsoon. These studies have examined impacts from a range of parameters such as the role of land surface processes on interannual variability. Shen *et al.* (1998), Douville *et al.* (2001), and Douville (2002) addressed soil moisture impacts, and Molteni *et al.* (2003) addressed the impacts of SST anomalies. Most of these studies utilized atmospheric general circulation models (AGCMs) where the SST anomalies and sea ice were prescribed. The important message from these studies was a clear sensitivity of the Asian summer monsoon to the lower boundary physics such as land surface processes, soil moisture, and SST anomalies, especially over the equatorial Pacific and the Indian Ocean. Slingo and Annamalai (2000) looked at the response of the Indian summer monsoon to the major El Niño SST anomalies for 1997. They also compared their results with another major El Niño event (i.e., 1982). They noted that strong El Niño events do not always affect the Indian monsoon rainfall in the same manner. Monsoon 1982 was a year of very deficient rainfall, whereas the year 1997 encountered heavier than normal rains. They attributed such differences to the manner of excitation of the Hadley and Walker circulations and noted that the Walker circulation responses for the two contrasting years were affected by the latitudinal location of the rising branch of the Hadley circulation, factors other than the equatorial Pacific SST anomalies.

Multimodel based ensemble and superensemble forecasts of the monsoon have been addressed by Krishnamurti *et al.* (2000a), Wang *et al.* (2004a), Kang *et al.* (2002), Wu *et al.* (2002), and Krishnamurti *et al.* (2005). Several of these studies were based on AGCMs with prescribed lower boundary conditions. The coupled model based studies, such as Fu *et al.* (2002) and Krishnamurti *et al.* (2003), concluded that these are promising for better prediction of the MJO and hence of the ISOs that have a large control on the monsoonal dry and wet spells. The use of a multimodel ensemble mean has shown some improvement in monsoon forecasts over single models. The Florida State University (FSU) superensemble appears to do better than an ensemble mean since it deploys weights (for combining models) that are based on past performance and do vary three dimensionally for each model and for each variable at each geographical and vertical coordinate. By deploying as many as 10^7 weights for the training phase, it seems to reduce r.m.s. errors of forecasts.

A host of studies have addressed the monsoon predictability issues over seasonal timescales (Schubert and Wu, 2001; Sperber *et al.*, 2001; Ji and Vernekar, 1997; and several others). All these studies note the poor performance of forecasts in predicting the Indian monsoon a season in advance and they attribute these difficulties to the large internal variability of the monsoon with somewhat less of a control for the local boundary forcings. In recent observational studies on monsoon seasonal climate, much emphasis has been placed on the combined roles of the Pacific and Indian Ocean SST anomalies (Anderson, 1999; Ashok *et al.*, 2001; Gadgil *et al.*, 2003). Exploring the monsoon climate from a coupled model is worthwhile to study the mutual interactions of the atmosphere and ocean over these different basins. A number of recent studies on the MJO/ISO simulations related to the monsoon

climate have also emphasized the need for coupled models (Kemball-Cook *et al.*, 2002; Fu *et al.*, 2002; Inness and Slingo 2003). One purpose of the present study is to demonstrate that the use of multimodel superensembles (especially a variant called the synthetic superensemble) using the coupled models can reduce the errors of seasonal climate forecasts somewhat. Given the current uncertainties of the model forecasts, we feel that this may be an avenue for future practical applicability.

14.2 WEATHER AND CLIMATE MODELING OF THE MONSOON USING REGIONAL MODELS

14.2.1 Limited area models

For a number of regions of the World, regional mesoscale models at high resolution have shown that they can provide useful short-range forecasts with higher skill than their global counterparts. Developed nations have put huge resources into real time regional NWP. With the availability of enhanced computing and communication resources, efforts on regional numerical prediction for the monsoon also have increased in Asia. At the India Meteorological Department (IMD), New Delhi, the FSU Limited Area Model (FSULAM) (Krishnamurti *et al.*, 1990b) has been run operationally for short-range weather prediction and for tropical storm prediction over the monsoon region. A host of community based regional mesoscale models is available freely for research and real time use. With the increasing demands for high-resolution (horizontal and vertical) forecasts, the need for non-hydrostatic computations is becoming common.

Numerical modeling for the tropical low latitudes and especially for the Indian summer monsoon was initiated at FSU about 3–4 decades ago. Those studies were carried out with the FSULAM at various horizontal and vertical resolutions, having detailed computations for physical processes (Krishnamurti, 1969, 1987a; Krishnamurti *et al.*, 1990b). The semilagrangian advection scheme coupled with the semi-implicit time integration scheme for the tropical weather systems were appropriate and computationally economical while use of generalized normal mode initialization for high-resolution (50 km) tropical monsoon modeling was introduced for FSULAM. This state-of-the-art limited area model could simulate the movement/landfall of tropical storms and was capable of predicting monsoon rainfall events. However, during those initial years, lack of proper observational data and assimilation schemes to produce mesoscale analyses were major hurdles for the more accurate prediction of monsoon systems as the model prediction skill is quite sensitive to initial and boundary conditions. With the availability of unique high-quality data sets from various observational campaigns, the FSULAM was capable of predicting the genesis, and tracking movement, of monsoon disturbances. The importance of soil moisture and associated feedbacks was realized for monsoon prediction using FSULAM (Dastoor and Krishnamurti, 1991).

The FSULAM at the IMD has been used on a daily basis for the Indian monsoon region for the last two decades. It consists of 1° lat./long. horizontal

resolution with 12 vertical sigma levels. The boundary conditions and the initial analysis are taken from the operational version of Indian National Centre for Medium-Range Weather Forecasting (NCMRWF) global spectral model. The flow field and precipitation from real time, short-range forecasts associated with the summer and winter monsoon for the Indian region is represented well by this limited area model (Roy Bhowmik and Prasad, 2001). However, as expected, at this low resolution, the orographic rainfall associated with the western Ghat Mountains of India is underpredicted. During the post-monsoon period, when the orographic rain decreases and the rainfall belt moves to the Indian peninsular, the skill of this model is found to be much higher. By prescribing a realistic initial moisture field from the Indian National Satellite (INSAT) infrared (IR) data over the Bay of Bengal and Arabian Sea, the skill of the precipitation forecast associated with movements of the monsoon depression was improved considerably (Rao *et al.*, 2001). When the model resolution is enhanced to 50 km and 16 vertical levels, it could capture the mesoscale convective organization associated with cyclonic storm and monsoon depressions more realistically (Roy Bhowmik, 2003). With enhanced resolution, the model could capture the heavy rainfall belt along the western Ghats as well.

A version of the National Centers for Environmental Prediction (NCEP) mesoscale ETA model is being used operationally at NCMRWF, India for the monsoon region (Rajagopal and Iyengar, 2002) for producing forecasts of up to 3 days. The horizontal resolution is 32 km, and in the vertical, it has 38 layers. The mean layer depth in the planetary boundary layer (PBL) is roughly 20 m and the initial and the boundary conditions are interpolated from the NCMRWF global spectral model analysis and forecasts. However, real time SST, snow depth, and snow cover analyzed by NCEP are used in real time as other surface boundary conditions. It produced more details of rainfall distribution and intensity associated with the west coast and the Himalayan orography.

14.2.2 Nested regional models

Nested regional models for the monsoon are useful for providing regional details both of weather and climate predictions. Kanamitsu and Juang (1994) simulated the Indian monsoon by nesting the NCEP regional spectral model (40 km horizontal resolution with 18 levels in the vertical) to the NCEP global spectral model at a resolution T62/18L (triangular truncation at 62 waves and 18 levels in the vertical). The onset and progress of the monsoon for the year 1992 and the associated rainfall distribution was more realistic in the regional nested model simulation. In another study, the NCEP ETA model (80-km horizontal resolution with 38 levels in the vertical) was nested to the spectral Center for Ocean–Land–Atmospheric Studies (COLA) general circulation model at R40/18L resolution (rhomboidal truncation at 40 waves and 18 levels in the vertical) to simulate the contrasting 1987/1988 monsoons. The nested high-resolution ETA model could simulate the anomalous distribution of rain in a more realistic way (Ji and Vernekar, 1997).

14.2.3 Very high-resolution mesoscale regional models

The fifth generation Penn State University/National Center for Atmospheric Research (PSU/NCAR) non-hydrostatic mesoscale model (MM5) has been used for real time application over the Indian monsoon domain since 2002 (Das, 2002). The model has been tested for the region with triple nesting at 90 km (Asia), 30 km (India), and 10 km resolutions. The innermost domain of the 10-km resolution was placed over the different orographic regions and regions of special interest to predict the weather over mountainous regions and severe weather events. The model was also tested at cloud-resolving scales (1-km resolution) for a heavy rainfall episode. Several weather systems during active monsoon conditions, heavy rainfall events, tropical cyclones, and western disturbances have been simulated by the model with interpolated initial conditions taken from the T80 global model analysis produced operationally at the NCMRWF. At present, a variational data assimilation system developed for MM5 at NCAR (Barker *et al.*, 2004) is being adopted at the NCMRWF for operational use to produce mesoscale regional analysis. Mesoscale analysis from this system will help in evaluating the model's skill for the monsoon systems.

A version of the Advanced Regional Prediction System (ARPS) model of Oregon State University (OSU) was also used to simulate two cases of monsoon systems (Vaidya *et al.*, 2004) at two different resolutions of 50-km and 25-km grid spacing with 25 vertical levels. The 1.25° lat./long. resolution analysis was used for the initial and boundary conditions. The details of the flow fields and precipitation associated with the features of the subsynoptic patterns are verified reasonably well with observed analysis.

14.3 MONSOON FORECASTS USING GLOBAL MODELS

14.3.1 Sensitivity to global model resolution

A summary of monsoon modeling related to the resolution issue is presented here. Krishnamurti (1990) carried out forecasts at various resolutions with a global model (triangular truncation at different zonal wavenumbers T21, T31, T42, T63, T106, and T170) ranging in their resolutions of transform grid spacing between 6 degrees to roughly 0.7° lat./long. In this example the location of a monsoon depression at day 5 of the forecast was examined. It was noted that as the resolution increased, the location of the monsoon depression was placed by the forecasts close to the observed location. This is illustrated in Figure 14.1, where the observed flow field on day 5 at the 850 hPa is used as a reference, and dark points indicate the locations of the centers of circulation for the various experiments with different horizontal resolutions. Since organized convection is a very important process for the evolution of the monsoon, it is not surprising that increased resolution would improve these forecasts. In a later study (Krishnamurti *et al.*, 1998a), the global model resolution was increased to T255 (triangular truncation at 255 waves, which is equivalent to a

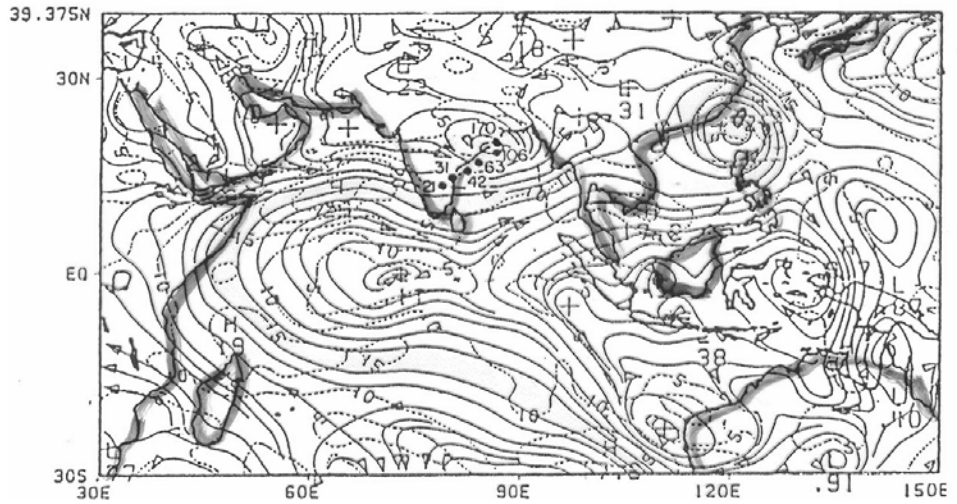

Figure 14.1. 120-hour forecasts of streamlines at 850 hPa using a global model at varying horizontal resolutions of T21, T31, T42, T63, T106, and T170. The black dots along the east coast of India denote the positions of the monsoon depression. The flow field shown via streamlines is the observed field on day 5.

transform grid separation of around 45 km near the equator). In these experiments, improved monsoon circulation forecasts included the distribution of an organized convection of mesoscale precipitating rain elements that resembled closely the observed precipitation signatures, which are illustrated in Figure 14.2(a,b) (color section). In this context, it should be noted that it is not imperative to have a mesoscale non-hydrostatic microphysical model for accurate forecasts of the large-scale monsoon, it is the ability of the model to predict the organization of mesoscale precipitating clusters that is more important. The dimensions of the mesoscale precipitating clusters are of the order of 300 km, and at a global resolution of T255, those are resolved by at least 8 transform grid points, thus a good cumulus parameterization scheme within a high-resolution global model can carry and predict their organization – as was seen in this study. Predicting accurately each and every cloud may be important for defining the detailed structure of the mesoscale cluster, but a high-resolution global model can effectively predict the organization of convection out to at least 3 days.

14.3.2 Month-long forecasts of monsoonal ISOs and MJOs

The pioneering work of Madden and Julian (1971) has seen a major push of research toward ISOs in the last 30 years. The MJO (as it is properly named) is a planetary-scale wave that traverses from west to east in roughly 40 days. It has the largest amplitude in the equatorial latitudes and is discernible over the tropics and sub-tropics. Its signature is seen in most variables, such as the sea level pressure, zonal

wind, and divergent circulation. The issue of climate model simulation of the MJO has been a topic of great interest in recent years. Summaries of recent contributions on the topic may be found in Kemball-Cook *et al.* (2002) and Maloney (2002). The consensus seems to be that models with prescribed SSTs are not able to simulate realistic features of the MJO, whereas the coupled atmosphere–ocean models are somewhat more successful in this respect. Maloney (2002) explored the effects of wind-induced surface heat exchange (WISHE) following Emanuel (1987) in the simulation of the MJO. He noted that a removal of WISHE in the NCAR Climate Community Model (CCM3.6) led to an improved simulation of the MJO. He concluded that WISHE might contribute to the growth of modes outside of the MJO frequencies. This is just one aspect of the details of a cumulus parameterization to which MJO sensitivity has been addressed. A more recent unpublished work from Colorado State University (David Randal, pers. commun.) points to the importance of cloud-resolving models where explicit, rather than parameterized, cumulus convection have been very successful in the mapping of the MJO. Some of the earlier work of Manabe *et al.* (1965) where moist convective adjustment was used has provided some evidence of ISOs. Further work is clearly warranted to identify the scope of models that resolve the MJO and its variability.

Simulation of the MJO is regarded as one of the most important components for the medium-range and long-range forecasts of the Asian summer monsoon. In many GCM studies, it has been observed that the simulation of tropical ISOs highly depends on the choice of cumulus convection parameterization scheme (Wang and Schlesinger, 1999). In some recent studies, Lee *et al.* (2001) emphasized the influence of cloud–radiation interaction and cumulus entrainment constraint in simulating tropical ISOs with the aqua-planet version of the Seoul National University GCM (SNUGCM). In another study, Maloney and Hartman (2001) pointed out that the boundary layer relative humidity thresholds control the variability of the tropical MJO. However, most atmosphere-only GCMs forced with a slowly varying SST annual cycle are unable to represent the eastward propagation of convection from the Indian Ocean to the West Pacific. Waliser *et al.* (1999a) have compared the MJO in coupled and atmosphere-only versions of the same GCM and showed an improvement in many aspects of simulation of the MJO. Due to the complex interaction between large-scale dynamics and convection, and between convection and the ocean surface, representation of the MJO presents a challenge for a coupled model (Inness and Slingo, 2003).

Other promising parallel efforts on the prediction of dry and wet spells of the monsoon have emerged from statistical rather than deterministic efforts by many authors. In a recent study, Goswami and Xavier (2003) noted from an analysis of historical data sets that there exists a potential predictability of up to 20 days in advance for break periods of the monsoon. The potential predictability of active spells is only of the order of 10 days. The former appears to have large-scale controls (Krishnan and Kasture, 1996), whereas the latter seem to have thermodynamic control as well.

In a series of papers (Krishnamurti and Subrahmanyam, 1982; Krishnamurti *et al.*, 1990a, 1992) a methodology for predicting the monsoonal ISO on the

timescale of 30–50 days was addressed. Because of the relationships of the ISO to the dry and wet spells of the monsoon, this topic is of considerable practical interest. This series of papers addressed forecasts over India, China, and Australia. The methodology consists of prescribing an initial state for an atmospheric global model at a resolution of T21 (triangular truncation at 21 waves) and is derived from roughly 120 days of past data sets. A band-pass filter is employed to extract the ISO timescale anomalies (i.e., perturbation on the timescale of 30 to 50 days). Let us call it Q_{ISO}. There is also a 120-day average value $\bar{Q}$ that denotes a recent time mean of that variable. The initial state for any variable Q is simply $\bar{Q} + Q_{ISO}$ and this essentially filters out all high-frequency motions. The SSTs are similarly extracted to define the initial values. Since this is an atmospheric model, the future oceanic states of the SSTs are simply obtained from an extrapolation of the SST anomalies from the past 120 days into the future. Here the future projection is done by extrapolation of the phase and amplitude of the harmonic wave time series of the SST anomalies at each grid point. This permits the slight movement of the SST anomaly over a one-month period with the range of forecast being studied here.

The initial state of the model was so designed because the highest frequency modes have predictability for a period of only one week. There are some very strong interactions between the ISO timescale motion and the high-frequency motions. Thus, the errors in the latter, after a one-week's integration, lead to large errors for the ISO. Filtering out these higher frequencies initially suppressed growth of such errors at least through one cycle of the dry and wet spell, and it was thus possible to push the forecasts of the ISO to well past one month. Even in these experiments where the higher frequencies are initially absent, they still grow after a few cycles; see Figure 14.3. Here results of integration over several cycles and a rapid growth of the higher frequencies are clearly apparent after a few cycles of ISO timescales. In these integrations we noted a marked predictability for the ISO on a one-month timescale, thus making it possible to address the issues of monsoonal dry and wet spells.

Figure 14.4 illustrates the ISO based on observations and the model forecasting for days 5, 10, 15, 20, 25, and 30. These are the wind fields at the 800-hPa levels on the timescale of the ISO. In this example the analyzed (observed) and the model

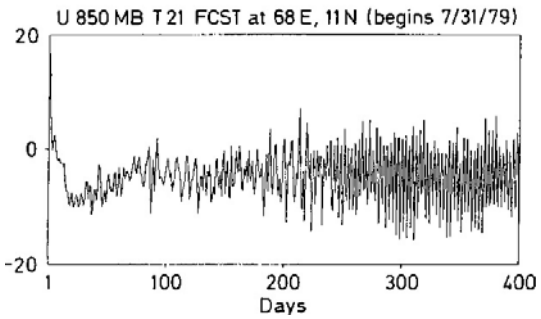

Figure 14.3. Time history of the zonal wind at 850 hPa along 68°E from the anomaly experiment (ms^{-1}) using the FSU global model at T21 resolution.

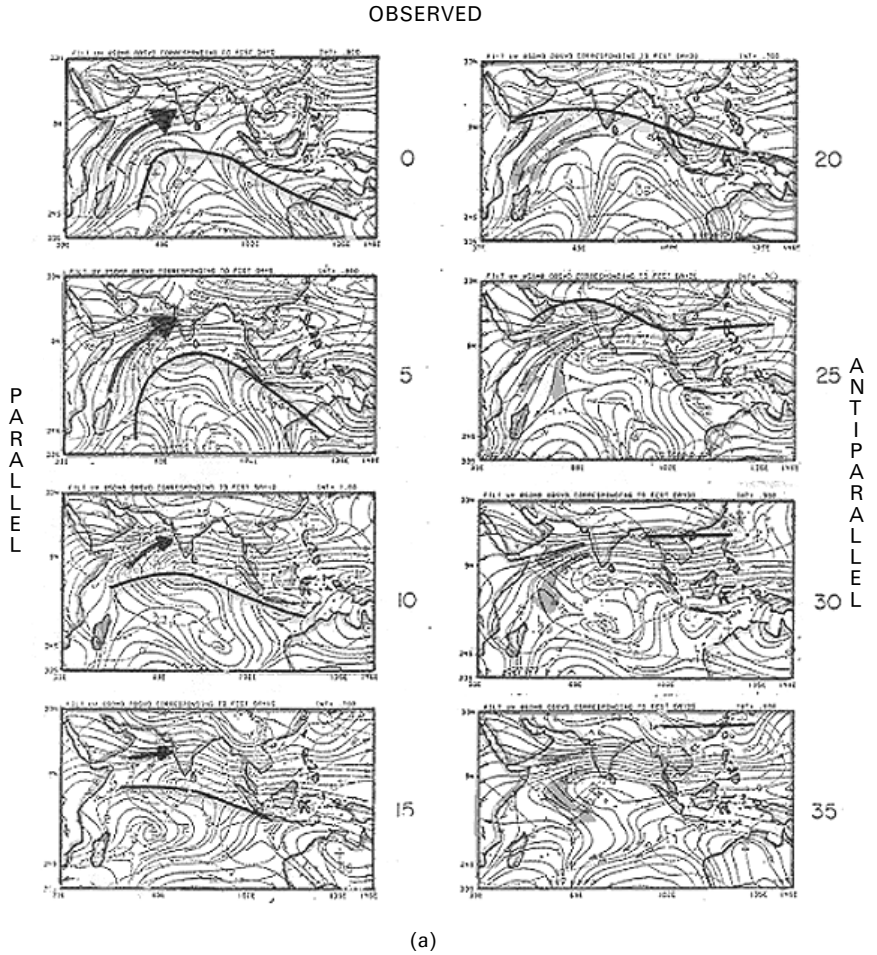

Figure 14.4. (a) A sequence of 850-hPa observed flow fields (time filtered on the scale of 30 to 50 days) for the experiment on a dry spell over India. Streamlines (solid lines) and isotachs (ms^{-1}) are shown here. (b) Same as (a) but for predicted fields.

predicted fields show a great degree of similarity during an entire one-month forecast. The cyclonic and anticyclonic lobes of the low-frequency motion move meridionally and the predictability of the ISO appears quite high. The dry and wet spells of the monsoon relate to the presence of parallel and antiparallel flows. If these predicted anomalies are parallel to the climatological monsoon circulations, they tend to enhance the monsoon and a wet spell prevails. Generally, the anti-parallel geometry favors a dry spell. In that sense this one-month forecast was very successful in predicting the intraseasonal wet and dry spells during the first month of this forecast.

It is also possible to assess this skill quantitatively. For this purpose, an anomaly

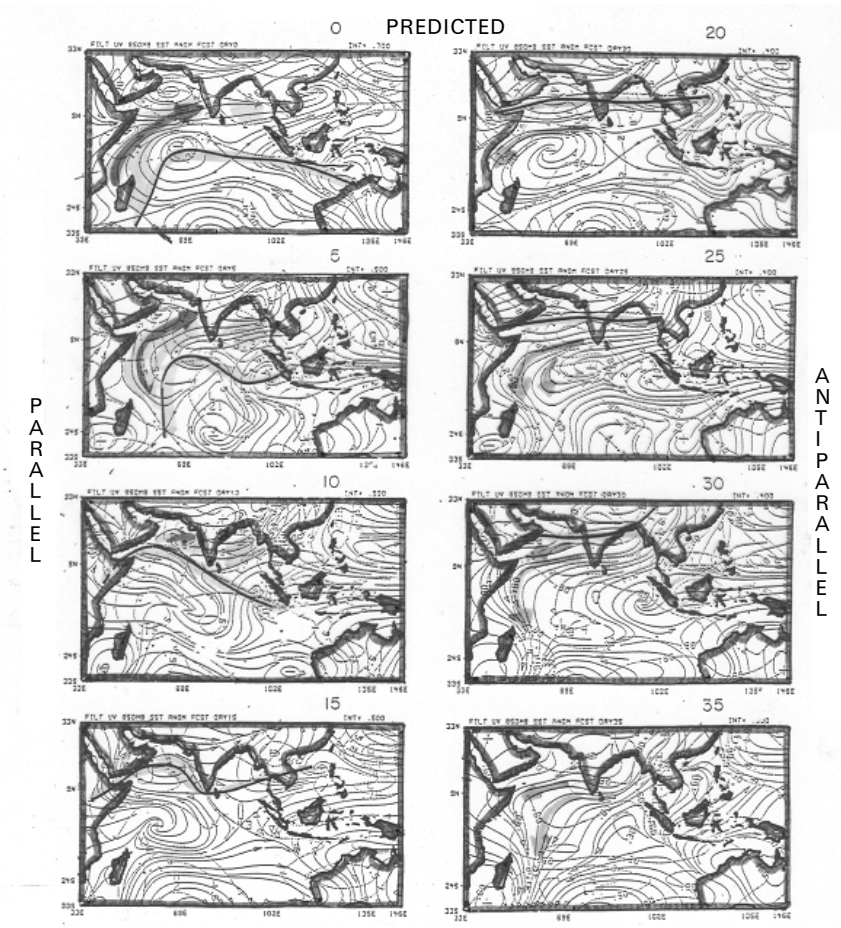

(b)

correlation of these forecasts was estimated from the 850-hPa streamfunction and is shown in Figure 14.5. The anomalies over the global domain (Figure 14.5(a)) and for the tropical region (Figure 14.5(b)) were predicted here at an anomaly correlation of 0.6. This is a reasonably high value for the forecast of an anomaly for the first few days of the forecast. Overall, this appears to be a promising method for predicting the passage over a month-long period of ISO anomalies. One obvious limitation of this model is the initial loss of skill in the first five days, which is clearly apparent in Figure 14.3. The loss of skill is attributed to a lack of proper initialization of the low-frequency initial state. The low frequencies were extracted from past data for all variables but no effort was made to establish any kind of a balance for the different

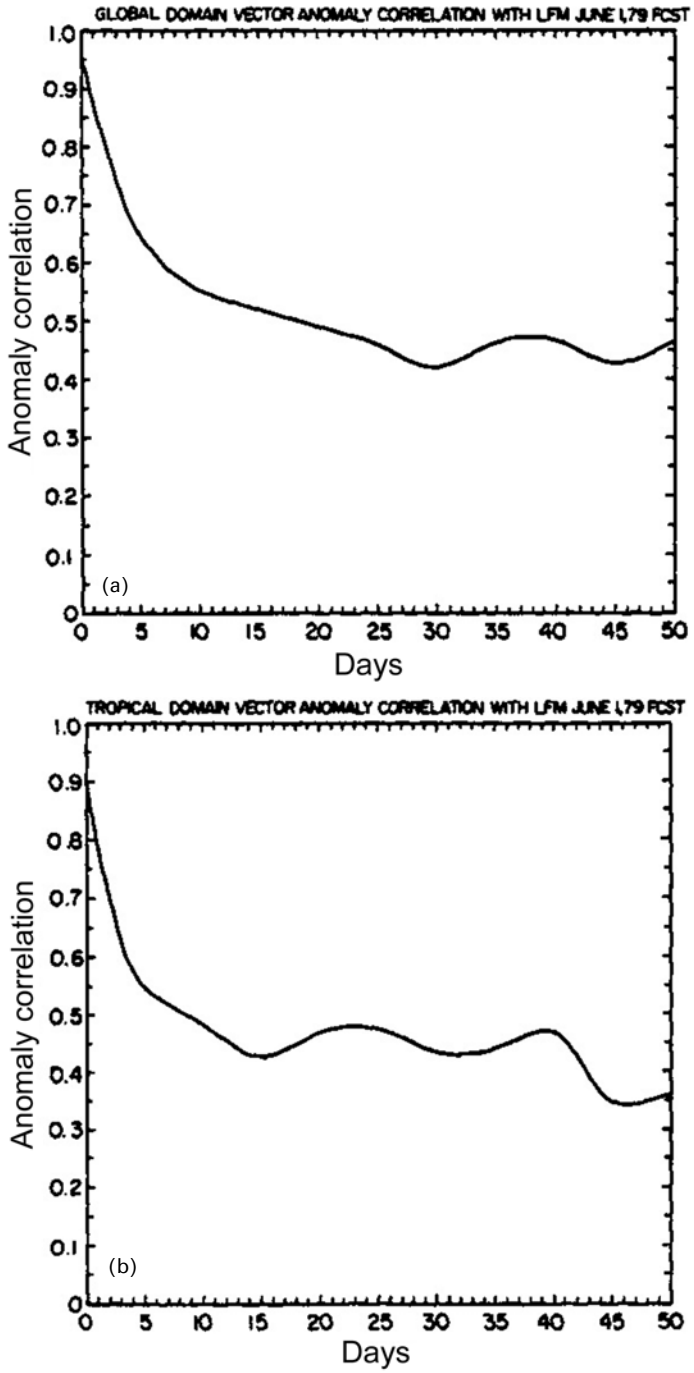

Figure 14.5. Anomaly correlations of forecasts as a function of days of forecasts for (a) the globe and (b) tropics.

variables. Relating first the low frequencies and assuring a balance among variables is not a trivial task and requires further research. If such a balance were possible, we may be able to prevent the initial loss of skill and produce even better forecasts than the one displayed here.

14.4 MONSOON FORECASTS AND SENSITIVITY TO PHYSICAL PARAMETERIZATION SCHEMES

A number of recent studies have addressed the issues of physical parameterization to the modeling of the monsoon. Among many different areas of research, that of cumulus parameterization has drawn the most interest (Eitzen and Randall, 1999; Alapaty *et al.*, 1994; Slingo *et al.*, 1994; Zhang, 1994; Rajendran *et al.*, 2002; etc.). Alapaty *et al.* (1994) used the Naval Research Laboratory (NRL)/North Carolina State University (NCSU) regional nested model (Madala *et al.*, 1987) to study the impact of two different convection schemes (Kuo and Betts-Miller) on the prediction of the winds and precipitation for one case of a monsoon depression. In this experiment, the finer resolution grid was 0.5° lat./long. and was nested to a coarser 1.5° lat./long. grid. Their conclusion was that the Kuo scheme performed better for that case. Inclusion of parameterization for the land surface processes made the simulations better in one case study (Raman *et al.*, 1998). In another case study, using the same model in a triple nested set-up the importance of orography in the west coast was shown for heavy rainfall events (Wu *et al.*, 1999). Cumulus parameterization is still somewhat *ad hoc* and does not blend with a large-scale model in a very natural way (i.e., the dynamics and physics are somewhat unconnected in the sense that they are different components of separate computations that are carried out sequentially within the time step of a model). It is however quite apparent that monsoon evolutions in prediction models are very sensitive to the particular cumulus parameterization one deploys. A cumulus parameterization scheme within a certain model behaves somewhat differently if the same scheme is used in a different model. This has to do with the fact that model resolutions, mathematical treatment of dynamics and rest of the physics, and the boundary conditions and the treatment of orography all end up dictating how a particular scheme equilibrates with that cumulus parameterization scheme within one model. Thus it is somewhat meaningless to state that scheme A is superior to scheme B from tests performed with a single model. However, there are some gross distinctions on the formulations of different schemes that do spell out the superiority of one scheme over another regardless of what diverse models they are tested with. For example, a hard convective adjustment does not properly represent the effects of an ensemble of clouds. Some schemes do not describe the vertical structure of heating or moistening very well. Such deficiencies can be explored using semiprognostic tests using well-established field experimental data sets such as those from Global Atmospheric Research Program (GARP) Atlantic Tropical Experiment (GATE) or Tropical Ocean–Global Atmosphere (TOGA)/Coupled Ocean–Atmosphere Response Experiment (COARE).

For the monsoon systems, a number of case studies have been undertaken to study the impact of parameterization procedures available for different physical processes. Unfortunately, the results are heavily dependent on model formulation, model resolution, and the weather system itself. Any particular model at a fixed resolution behaves in a particular way for one type of weather system. Each tropical monsoon weather system is unique in its structure, evolution, and interactions. It becomes very difficult to conclude the impact of parameterization of physical processes on precipitation forecasts. Observed data from field campaigns (Monsoon Trough and Boundary Layer Experiment – MONTBLEX, Indian Ocean Experiment – INDOEX, Bay of Bengal Monsoon Experiment – BOBMEX, Arabian Sea Monsoon Experiment – ARMEX) will perhaps be useful to understand the physical processes associated with different monsoon weather systems. Then, depending on the scale of interest, a particular set of parameterization algorithms can perhaps be combined for optimum performance for a model. In this section, a review of various physical parameterization schemes and their impact on monsoon forecasts is presented.

14.4.1 Land surface processes

Demand for more realistic treatment of the land surface processes, in the vegetation and the soil, have led to the development of increasingly elaborate and explicit schemes. The most rudimentary of treatments employs a prescribed moisture function for the calculation of the evaporation rate as a fraction of the potential evaporation. Such models have obvious shortcomings, especially for long-term integrations, since they do not respond to rain or drought in the course of the integration, and therefore evaporation feedback is lost. A step up from these are bucket models, first introduced by Manabe (1969), linking the ground wetness to the past rainfall through a simple empirical relationship. Such models do not explicitly model what happens in the soil below, or in the vegetation above, the surface.

A number of sophisticated land–surface schemes have been developed in recent decades. The best known of which are the BATS (biosphere–atmosphere transfer scheme) of Dickinson *et al.* (1986) and SiB (simple biosphere) of Sellers *et al.* (1986), later succeeded by a simplified version (SSiB) (Xue *et al.*, 1991). A number of similar land surface schemes have been developed recently, such as Interactions Soil–Biosphere–Atmosphere (ISBA; Mahfouf *et al.*, 1995) and a simple parameterization of the hydrologic exchanges between the soil–vegetation system and the atmosphere (SECHIBA; Ducoudre *et al.*, 1993). All these models calculate the fluxes from the soil and canopy using similar principles with somewhat different formulations. Most have several soil layers and one or two vegetation layers; some use a mosaic approach in which several types of vegetation are assigned fractional coverage of a grid box. A comprehensive summary of the different land surface schemes used in the scientific community can be found in Henderson-Sellers (1993) and the issues associated with them in Garratt (1993). An intercomparison project – PILPS (Project for Intercomparison of Land Surface Parameterization Schemes) (Henderson-Sellers, 1993, 1995) – has been undertaken to evaluate the relative performances of

a wide spectrum of land surface schemes (LSS). Due to the limited amount of *in situ* observations (and the difference in the GCMs into which the different LSS are introduced) it has proved impossible to name one superior scheme. It has been noted that the introduction of complex LSS has resulted in a significant disagreement between the different models, even if their underlying physical concepts are similar (Mahfouf *et al.*, 1996; Gates *et al.*, 1996). These differences (in the surface fluxes and in the energy and hydrology balances) are present both in offline experiments and in GCM simulations (Henderson-Sellers, 1995). The performance of the LSS depends heavily on the atmospheric models they are introduced into (Garratt, 1993). The partitioning of the incoming radiation at the surface into fluxes of sensible and latent heat and absorbed and emitted radiation is highly dependent on the properties of the land surface and its vegetation cover. Despite the significant progress in the development of detailed parameterizations of land surface processes over the last few decades, the relative importance of the degree of sophistication of the land surface treatment remains an open question in forecasts on seasonal timescales.

In the context of monsoon forecasts, this aspect of modeling is clearly more important for climatic timescales of a season or longer. However, since the land surface parameterization has considerable impact on the diurnal change, it is worthy of examinination in the context of medium-range weather prediction. A semiarid region has a very large diurnal change in its surface physics in the pre-monsoon period; soon after the onset of the monsoon that region becomes greener and has a much smaller amplitude regarding its diurnal changes. Modeling of such differences are important.

14.4.2 Parameterization of the planetary boundary layer

The mixing of heat, moisture, momentum, and passive scalars is brought about by turbulence in the atmospheric boundary layer. In numerical models, the large-scale atmospheric flow determines to a large extent the properties of the PBL, and the PBL in turn reacts to these external forcings and modifies the large-scale flow. In order to explicitly resolve the boundary layer structure, several computational levels in the PBL of the numerical model are introduced. The formulations require turbulent terms of heat, momentum, and moisture at all these levels. Thus, in order to approximate or parameterize these turbulence terms, some kind of closure assumption is necessary to relate turbulent fluxes to mean quantities. Such closure assumptions can be classified by their statistical order and the degree of non-locality. While no parameterization is perfectly accurate, they offer a range of physical details and computational economies from which to choose. Basic closure schemes for all practical purposes are presently limited to the first, one and a half, second, and third order. Second and third order closure schemes involve more physics of the boundary layer through increased formulation and numerical complexity. By and large, the closure assumptions used in numerical models are confined up to 1.5 orders.

There are certain basic limitations of the mixing length theory (Stull, 1988) involved with the local K approach. The most important drawback is its inability

to realistically represent mixing in the convective boundary layer involving the 'counter gradient fluxes' since the influence of large eddy transports are not accounted for (Holtslag and Moeng, 1991). This affects the profiles of mean quantities especially in locations where dry convection is of importance in the PBL. One of the possibilities to overcome this problem is to utilize higher order closure approaches, which are computationally more expensive. In the modified gradient approach or *non local* corrected, the fluxes are still allowed to flow down the local gradient, but an artificial gradient is added to the gradient during convective conditions.

An improvement on the simplicity of first-order closure could be achieved by introducing more of the physics of the atmosphere while accounting for the formulation of the eddy diffusivity coefficient, keeping in mind computational economy. One such scheme is the Turbulent Kinetic Energy (TKE) closure where the K coefficient is determined by the TKE available in the atmosphere obtained prognostically. While Prandtl (1932) considered only mechanically induced turbulence, the TKE approach can also include buoyant turbulence and turbulence that is transported in from other locations. Within this approach, one needs a forecast equation for the TKE. Thus, knowing the TKE as well as the mean gradients, it is then possible to parameterize the fluxes. Second and third-order closure carries forecast equations for not only all the mean variables but also for all the second-order and third-order terms respectively. Some also include forecast equations for the dissipation rate. Third and higher order correlations and pressure correlation terms must be parameterized. Most of these parameterizations utilize down-gradient local diffusion. The scope of including one such higher order PBL scheme for this work is also important for monsoon studies.

Many scientists have studied the performance of different PBL schemes in monsoon prediction. Basu *et al.* (2002) compared the performance of a non-local closure PBL scheme following Hong and Pan (1996) with that of the local closure scheme (Kanamitsu 1989) in the NCMRWF global spectral model used for real time forecasts over India. Using a version of the NCMRWF model, Sanjay *et al.* (2002) analyzed the temporal and spatial variability of simulated PBL height, based on Troen and Mahrt (1986), within the non-local scheme. A similar non-local K PBL scheme was introduced by Holtslag and Boville (1993) in the NCAR CCM2 model used for climate simulations. The formulation differs from that of Troen and Mahrt (1986) in the specification of surface turbulent scales and in the non-local turbulent effects. All these studies indicated a relatively higher skill from the non-local schemes compared with the local closure schemes, suggesting the impact of treatment of the PBL on monsoon forecasts.

14.4.3 Parameterization of cumulus convection

An interesting example of the sensitivity of monsoon forecasts to cumulus parameterization was illustrated by Krishnamurti *et al.* (1987b). Here two versions of Kuo's scheme were used to examine the onset of the monsoon for 1979. During this year, the onset was preceded by the formation of a tropical cyclone (called the onset

vortex) in the Arabian Sea, thus the prediction required forecasting the formation and motion of this tropical cyclone and the development of a strong moist current to its south as the monsoon over India became established. This was a medium-range forecast experiment using the First GARP Global Experiment (FGGE) data sets. Figure 14.6(a,b,c) illustrates the 850-hPa level winds at the initial time and those at hour 144 for the two versions of the cumulus parameterization schemes – also shown are the day 5 observed fields (Figure 14.6(a)). It is apparent that one version of Kuo's scheme, called a classical Kuo scheme (Kuo, 1965), failed in this monsoon simulation while a second one that was a modified scheme (Krishnamurti *et al.*, 1983a) provided a very promising simulation. The former scheme was noted to provide strong moistening and was deficient in its definition of heating and rainfall rates. The latter scheme had been statistically improved to reduce that deficiency. The message here was clearly that monsoon simulations were strongly affected by the cumulus parameterization scheme one deploys.

In a recent paper Krishnamurti and Sanjay (2003) addressed the impacts of six different cumulus parameterization schemes (see Table 14.1 for a description of these schemes) in a large number of numerical forecast experiments. All of these experiments utilized the same model, the FSU global spectral model, described in Appendix 14.1. All these runs utilized the same initial states and a total of some 120 experiments were carried out from each of the 6 models. This provided a large sample of experiments to investigate the behavior of the different cumulus parameterization schemes. These were all one-to-two-day long integrations. Since the only differences were in the cumulus parameterization, the premise here was that the differences that arise in a one- or at most two-day forecast might largely reflect the behavior of the cumulus parameterization schemes, since all other factors were the same in all the models. The most important variable for these tests was the predicted rainfall. Skills such as the r.m.s. errors and anomaly correlations were evaluated for this large number of experiments to assess the performance of the different schemes. We also constructed a multimodel ensemble mean forecast and a superensemble (discussed in section 5 of this paper) from these same data sets of day 1 and day 2 of the forecasts. In addition to these we also designed a synthetic cumulus parameterization scheme (named the unified scheme) that included within one single model the weighted sums of all of the six cumulus parameterization schemes. Those weights were simply borrowed from the day one forecast weights of the multimodel superensemble. Since the six cumulus parameterizations are based on different physically based features, the unified scheme carries all of these features in a weighted sense. Figure 14.7 illustrates the skill of one- and two-day forecasts of precipitation from the member models, from the ensemble mean of these models, those from the unified model, and those from the multimodel superensemble. It is clear from this large volume of experiments that the performance of the different cumulus parameterization schemes are not drastically different from one another. One of these schemes (i.e., the relaxed Arakawa–Schubert scheme) did seem to perform slightly better than most of the other schemes. However, when we examined the day-to-day performance, we did find that the daily skill curves of these member models did intersect often, implying that a superior or inferior

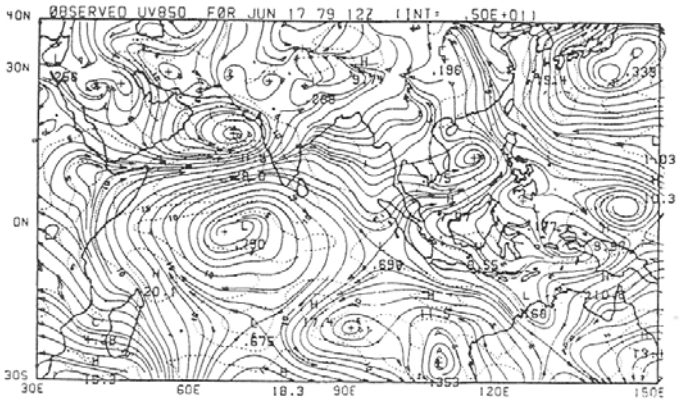

(a)

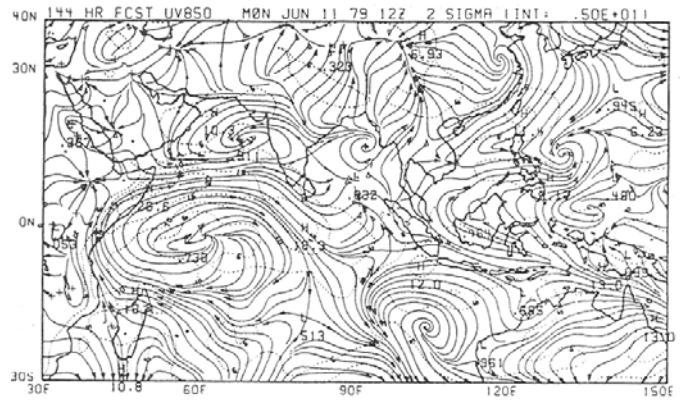

(b)

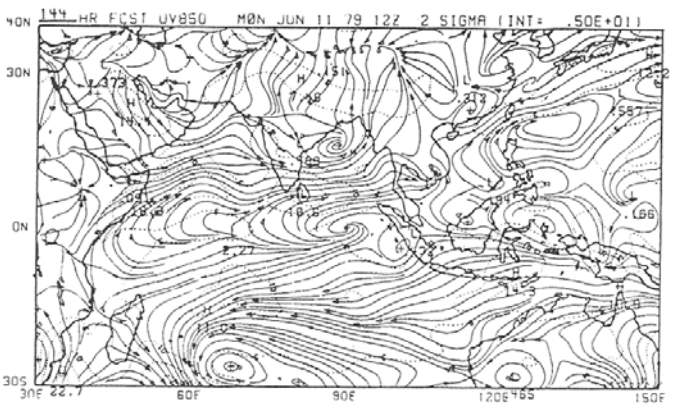

(c)

Figure 14.6. The 850-hPa flow field for 17 June 1979 (12 UTC). (a) Observed flows, (b) a six-day forecast from a modification of Kuo's scheme, and (c) a corresponding six-day forecast made from the classical scheme of Kuo.

Table 14.1. Features of different cumulus parameterization schemes.

	Cumulus scheme	Environmental trigger (*Modulation of convection by large-scale*)	Cloud model (*Treatment of cloud thermodynamic properties*)	Final state of the atmosphere (*Quantitative effects of convection on environment*)
1.	FSU Modified Kuo	Integrated vertical advection of moisture.	Moist adiabatic lapse rate. No downdrafts.	Tends toward local moist adiabat.
2.	GSFC Relaxed Arakawa–Schubert	Rate of destabilization by advective changes.	Entraining plume model. Invokes single members of a cloud ensemble one after the other. Normalized cloud updraft mass flux linear function of height. No downdrafts.	Relaxes to steady-state clouds in prescribed time.
3.	NRL relaxed Arakawa–Schubert	Rate of destabilization by advective changes.	Includes evaporation of falling rain. With downdrafts.	Relaxes to steady-state clouds in a prescribed time.
4.	NCEP simplified Arakawa–Schubert	Rate of change of stability. Upward vertical velocity at cloud base.	Only the deepest cloud considered. Moisture detrainment from convective clouds. Warming from environmental subsidence. Downdrafts and evaporation of falling rain included.	Adjusts toward an equilibrium cloud work function within a specified time.
5.	NCAR Zhang and McFarlene	Plumes of updraft ensemble need to be sufficiently buoyant to penetrate through locally conditional unstable lower troposphere.	Ensemble of entraining updrafts with associated saturated downdrafts.	Removes CAPE at an exponential rate with a specified time. Neutrally buoyant for undiluted reversible ascent of a parcel.
6.	NRL Emanuel	First level of neutral buoyancy for the undiluted, reversible ascent of near-surface air is at a higher altitude than the level of the cloud base.	Subcloud-scale drafts using a buoyancy-sorting technique. Determines mass flux prognostically. Stochastic coalescence and Bergeron–Findeisen mechanism. Cloud water in excess of a threshold amount converted to precipitation. Saturated and unsaturated downdrafts.	Adjusts to a local quasi-equilibrium situation, does not depend on the relaxation of cloud work function.

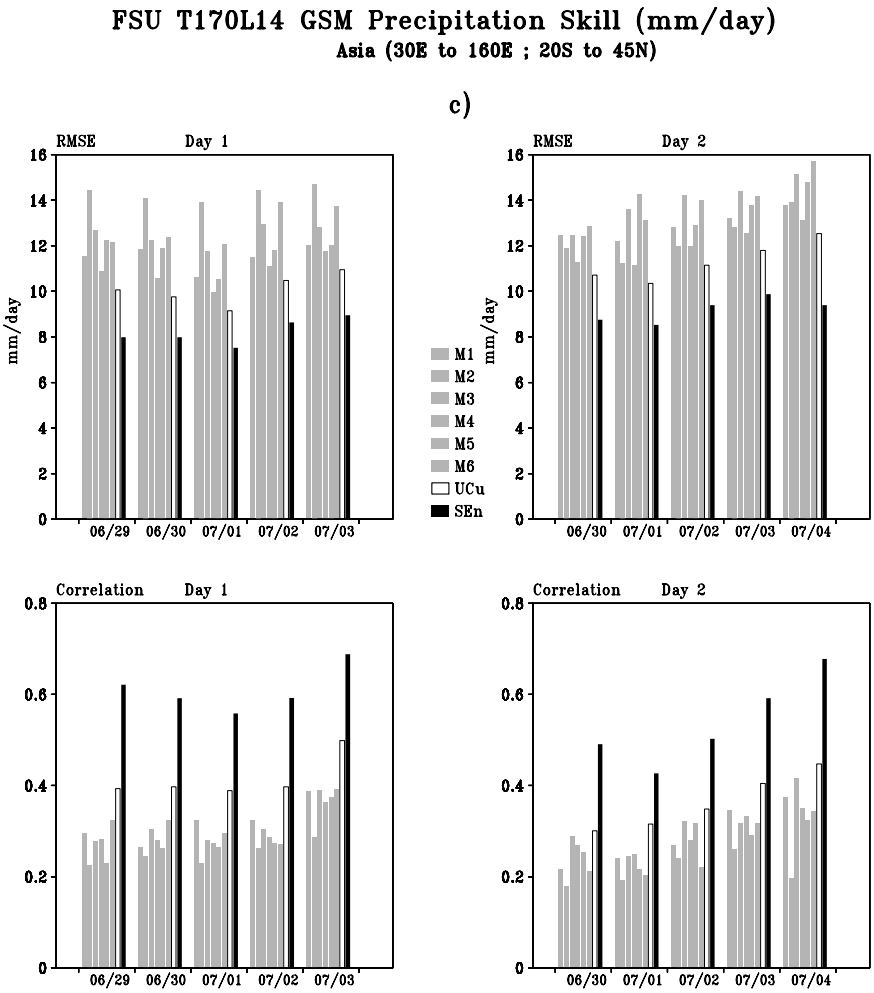

Figure 14.7. r.m.s. error skill (mm per day) and anomaly correlation of precipitation forecasts at day 1 (*left panels*) and day 2 (*right panels*) of forecasts from the FSU Global Spectral Model at T170 resolution, using different cumulus convection parameterization schemes (M1 through M6), Unified Convection Scheme (UCu), and the Superensemble (SEn).

performance on a given day by a certain scheme did show an initial state dependence. The unified model did perform better than each of the member models, implying that a collection of physically based processes that call for cumulus convection is better than the use of one single scheme that does not include all the possible processes. The result from the multimodel superensemble stands out as far superior to all others shown here. This is due to the fact that the superensemble technique is based on a training phase, where the collective bias errors of the member models are corrected in the construction of the superensemble forecast (see Section 14.5).

14.4.4 Organization of convection and monsoon forecasts

The organization of monsoon convection is an important model simulation problem. It has been shown that one needs almost a mesoscale resolution over the globe to simulate these features. We had noted that if we perform physical initialization of precipitation at a very high global resolution, such as T255 (which has a transform grid separation of roughly 45 km), it is possible to fully retain the organization of convection described by mesoconvective precipitating elements (with a scale of the order of 300 km). Furthermore, we find that such an organization of convection is in fact carried into the future in medium-range forecasts by this high-resolution model. This is an important issue for various scientific reasons. Gill (1980) provided a fundamental rationale for associating tropical motions to the distribution of heat sources and sinks. In the tropics, that relationship is very strong, the monsoon being an excellent example. These so-called heating forced solutions were extended over the entire global tropics by Zhang and Krishnamurti (1996). There it was shown that the climatological flows of the lower troposphere for the summer monsoon could be obtained as an exact solution from prescribed heating using parabolic cylinder functions and trigonometric functions as basis functions within a linearized shallow-water framework. The lower tropospheric monsoon circulation of the Asian summer monsoon is described by an inverted 'letter S'. The inverted S starts from the southern trades, then on to the cross-equatorial flows across the equator along the Kenya–Somalia coast, and then follows the south-west monsoon flows terminating in a monsoon low south of the Himalayas. Along this inverted S a steady growth of convection can be seen with the heaviest convection in the foothills of the Himalayas. Along the inverted S an organization of convection can be seen paralleling these low-level flows. We believe that this organization of convection is central to the maintenance of a robust monsoon. Thus, the modeling of this organization is very important. It turns out that, with a parameterized cumulus convection, instead of explicitly resolving each cloud and its organization, we can resolve the organization in medium-range forecasts if the hydrostatic model has a sufficiently high resolution.

14.4.5 Radiative interactions for monsoon modeling

There are three well known schemes for the parameterization of radiative transfer that are used in most models for the prediction of the monsoon. These are the classical emissivity/absorptivity based model (Chang, 1979), the Band model (Lacis and Hansen, 1974), and explicit cloud models (Zhao, 1997). The importance of radiative transfer for the modeling of the monsoon became clearly evident from Yanai *et al.* (1973), who studied the heat sources and sinks and showed that the apparent heat source Q_1 minus the apparent moisture sink Q_2 is of the order of the radiative heating R. The vertical eddy flux of heat that is central for monsoon simulation is directly proportional to $Q_1 - Q_2 - R$, thus an inclusion of the radiative forcing is important even for short to medium-range prediction of the monsoon. Having said that, when one looks at the literature on this topic, we find

that not many studies have been devoted to the issue of monsoon modeling sensitivity to radiative transfer. Further work is needed to address this problem considering the importance of differential heating of the monsoon that requires an accurate modeling of the radiative forcing over regions of the heat sinks. Another major monsoon issue is the modeling of the diurnal change that shows up in the surface fluxes and in the phase of convection and rainfall. Over a short distance of several hundred kilometers from the eastern Tibetan Plateau and the foothills of the Himalayas, the phase of the diurnal change varies from an afternoon convection to an early morning convection. These appear to be driven by cloud radiative and surface flux processes. A careful modeling of the phase of the diurnal change is important for the monsoon forecasts. The scales of the monsoonal diurnal change can be very large (up to several thousand kilometers, Kishtawal and Krishnamurti 2001), and on that scale a direct coupling of the diurnal cycle with the monsoon circulation seems to be apparent.

14.5 MULTIMODEL FORECASTS FOR WEATHER AND CLIMATE

One of the most powerful approaches to weather and seasonal climate forecasts utilizes a multimodel superensemble and was described in Krishnamurti *et al.* (1999, 2000a,b, 2001, 2002, 2005). The superensemble methodology utilizes a vast collection of past forecasts by member models to assess their collective biases. The statistics thus generated are used toward the correction of future model forecasts. Given some ten such member models providing forecasts over an array of roughly 100,000 locations at ten vertical levels for ten variables, that statistic ends up including some 10^6 correction weights. Examination of those weights show that most models have some areas of major skill, thus a superensemble is in some sense the collective wisdom of the multimodels. We use somewhat different methods for obtaining this statistic for weather or the seasonal climate forecast; these are briefly described in the next two sections.

The superensemble technique produces a single consensus forecast derived from a multimodel set of forecasts. Superensemble forecasts carry the highest skill compared with participating member models, their ensemble mean and the bias-removed ensemble mean representations. The methodology to construct the multimodel superensemble consists of partitioning the time line into two components – the training phase and the forecast phase. During the training period, the multimodel forecasts and the benchmark observed (analysis) fields are utilized to derive model performance statistics, which are then passed on to the forecast phase where multimodel forecasts are weighted as per their past performance to obtain superensemble forecasts.

In the training phase it is possible to derive statistics on the past behavior of the multimodel with respect to the observed analysis. Using a multiple linear regression technique, in which the model forecasts were regressed against an observed (analysis) field through a least squares minimization of the difference between anomalies of the model and the analysis fields, distribution of weights is determined for each member model. These regression coefficients associated with each individual model concei-

vably can be interpreted as a measure of that model's relative reliability for a given point over the training period.

The definition of the conventional superensemble forecast is given by:

$$S = \bar{O} + \sum_{i=1}^{N} a_i (F_i - \bar{F}_i) \tag{14.1}$$

where S is the superensemble prediction, $\bar{O}$ is the observed time mean (during the training phase), a_i are the weights for individual models i, F_i is the predicted value from model i, $\bar{F}_i$ is the time mean of prediction by model i for the training period, and N is the number of models. The weights are computed at each of the transformed grid points by minimizing the objective function G using least square minimization of the error of the forecasts:

$$G = \sum_{t=0}^{t=train} (S_t - O_t)^2 \tag{14.2}$$

where 't' denotes the length of a training period.

In this conventional superensemble methodology for weather and season climate forecasts, a sequence of individual forecasts from several models are collected and subjected to multiple linear regression against the observed (or assimilated) counterpart fields and the coefficients are stored for each of the member models. The length of the training data varies for each type of forecast. For medium-range (1–6 days into the future) forecasts, about 120 days of training is found to be required while for seasonal climate forecasts about 10 years of multimodel forecast data sets would be necessary. The weights collected during the training phase are passed on to the forecast phase of the superensemble. In the forecast phase, the member model forecasts are corrected collectively, using the regression weights. This type of local bias removal is more effective compared with a conventional bias-removed ensemble mean where a weight of 1.0 is assigned to all models after bias removal. The superensemble procedure assigns fractional and even negative weights to the model forecasts depending on their past behaviors.

In order to achieve higher skills for seasonal climate forecasts, a variant of the above conventional superensemble formulation was proposed by Yun *et al.* (2004). In this procedure, additional 'synthetic data sets' are constructed from the member model forecast data using a combination of the past observations and past forecasts. A consistent spatial pattern is determined among the observations and forecasts using a linear regression relationship in the EOF (empirical orthogonal function) space. Sets of such synthetic forecasts are then obtained for each available member model forecast and used for the creation of superensemble forecasts. The synthetic data generation and the associated statistical procedure are described below.

The time series of any observation field x can be written as a linear combination of EOFs such as:

$$O(x, t) = \sum_{n} P_n(t) \times \phi_n(x) \tag{14.3}$$

where n is the number of modes selected. The two terms on the right-hand side of the equation correspond to the time (principal component, PC) and space (EOF) decomposition, respectively. PC time series $P(t)$ represents how EOFs (spatial patterns) evolve in time. These PCs are independent of each other. In a similar manner the forecast time series is projected into the PCs and EOFs for m member models:

$$F_i(x, T) = \sum_n F_{i,n}(T) \times \varphi_{i,n}(x) \tag{14.4}$$

Here index i represents a particular member model. Using a regression relationship between the observation PC time series and a number of PC time series of forecast data, it is possible to deduce the spatial patterns of forecast data, which evolve in a consistent way with the EOFs of the observation for the time series considered. The regression relationship is given by:

$$P(t) = \sum_n \alpha_{i,n} F_{i,n}(t) + \varepsilon(t) \tag{14.5}$$

Here the observation time series $P(t)$ is expressed in terms of a linear combination of forecast time series $F(t)$ in EOF space. The regression coefficients α_n are found such that the residual error variance $E\ (\varepsilon^2)$ is minimum. Once the regression coefficients are determined, the PC time series of synthetic data can be written as:

$$F_i^{\text{reg}}(T) = \sum_n \alpha_{i,n} F_{i,n}(T) \tag{14.6}$$

Then the synthetic data set is reconstructed with EOFs and PCs as:

$$F_i^{\text{syn}}(x, T) = \sum_n F_{i,n}^{\text{reg}}(T) \times \phi_n(x) \tag{14.7}$$

These synthetic data (m sets) generated from m member model forecasts are now subjected to the conventional FSU superensemble technique (Krishnamurti *et al.*, 2000a) described in this section.

14.5.1 Performance of multimodels for weather and seasonal climate forecasts

Here we shall illustrate some of the current skills of weather forecasts for the Indian summer monsoon. The domain extends from 50°E to 110°E and 10°S to 35°N. These are typical real time forecast results for a year (this covers the skills for June, July, and August 2001). We illustrate in Figure 14.8 the skills of forecasts through days 3 (for precipitation) and 5 (for winds and mean sea level pressure). Part (a) shows the bias of the equitable threat scores for precipitation forecasts for rainfall rates in excess of 5 mm per day. The skill metrics are described in Appendix 14.2. A bias score near 1.0 is a perfect score. There are 6 member models included here, these are in fact some of the major operational models that carry out monsoon forecasts on a daily basis, these include models from the UK, USA, Japan, Australia, and Canada. Bias errors of the various models range from 1.0 to 2.3. The dark barb shows that it is possible to consistently reduce the bias errors to a value around 1.0 from the construction of the superensemble. Parts (b) and (c) show the precipitation

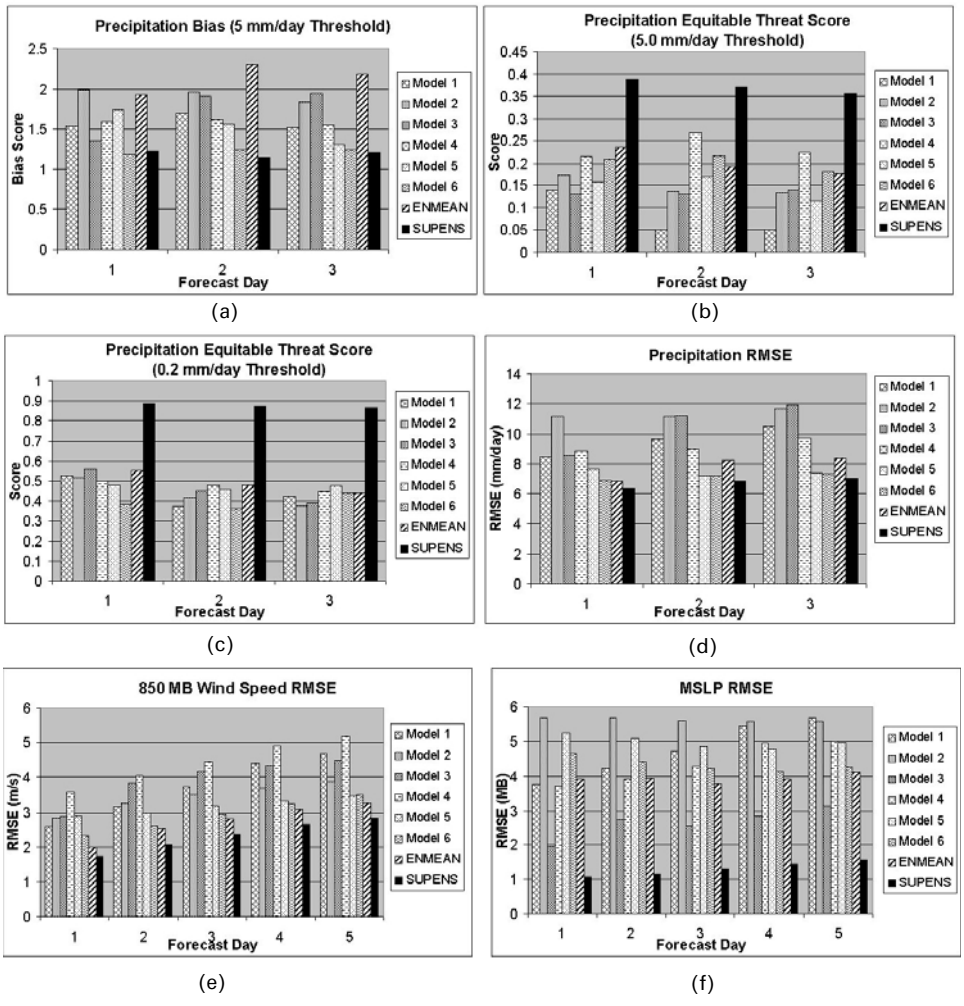

Figure 14.8. Various skill scores for the Asian summer monsoon region (10°S to 35°N, 50°E to 110°E) from different member models, their ensemble mean, and the superensemble. (a) Precipitation bias score at the 5 mm per day threshold; (b) equitable threat score at the 5 mm per day threshold; (c) precipitation equitable threat score at the 0.2 mm per day threshold; (d) precipitation r.m.s. error (mm per day); (e) 850-hPa wind r.m.s. error (ms^{-1}); and (f) mean sea level pressure r.m.s. error (hPa).

forecast skills for thresholds of rain rates greater than 5 and 0.2 mm per day respectively. These are skills for days 1, 2, and 3 of the forecasts. The superensemble skills clearly stand out over the monsoon region. For thresholds of precipitation rates above 0.2 mm per day the 3-day skills of around 0.7 are indeed most impressive, considering that most member models have values generally below 0.5. For heavier rains – thresholds greater than 5 mm per day – the superensemble is still quite impressive with equitable threat values around 0.35 or above, whereas the member

models have values closer to 0.2. We also present the r.m.s. errors of precipitation forecasts of the member models and of the superensemble in part (d), where we can see a reduction of the error from the superensemble compared with each of the member models. Shown in part (e) are the r.m.s. errors of the vector wind at the 850-hPa level. These are again slightly better for the superensemble compared with all the member models. The corresponding results for the r.m.s. errors for the sea level pressure are shown in part (f) where we note a major reduction of sea level pressure errors from the multimodel superensemble. Over all, in NWP of the monsoon this degree of improvement is generally possible for 3 to 5 days of forecast lengths from the deployment of the superensemble.

The results of the seasonal forecasts for the Asian summer monsoon are described here. These results are based on 11 member models, and the data sets cover the period from 1987 to 2001 (15 years). The length of this data set is still insufficiently long to separate the training period from the forecast phase distinctly, for this reason a cross-validation technique is used here that uses all forecasts in the training phase successively, always excluding the particular season that is being forecast. This enabled us to obtain a reasonable data length for the training phase. When more and more years are included, this use of cross-validation would not be necessary. Forecasts are made at the start day of each month and overall we have a total of 17 seasonal forecasts on which the skills are being prepared, for details see Krishnamurti *et al.* (2004). Tables 10.2 and 10.3 describe briefly the basic ingredients of the 11 models, among which 7 belong to a European family called DEMETER (Development of a European Multimodel Ensemble system for seasonal to inTERannual prediction; Palmer *et al.*, 2004). The remaining 4 models are variants of a single FSU model where different permutations of physical parameterizations are employed in the otherwise identical model. All eleven of these are coupled global atmosphere–ocean models. Coupled models are better suited for seasonal timescales since the temperature anomalies do change over timescales of 3 to 4 months. Here we shall provide a summary on the performance of single models, their ensemble mean performance, and that of the synthetic superensemble for the seasonal Asian summer monsoon rainfall. The results are presented in terms of the standard skill scores (see Appendix 14.2) such as the r.m.s. errors over the monsoon domain and the anomaly correlations. We shall also present comparative maps on the performance of models for a selected season for illustrative purposes.

In Figure 14.9(a,b) (color section) we present the seasonal forecast errors for each year of forecast for the Asian summer monsoon; Figure 14.9(a) shows the results from the DEMETER models and Figure 14.9(b) shows those from the FSU suite of models. Within each panel the top diagram carries the r.m.s. errors of the 7 member models, the results of the ensemble mean of the DEMETER member models, the ensemble mean for the synthetic models, and finally the synthetic superensemble. We also show the anomaly correlations within each panel. These are the seasonal skills for precipitation forecasts over a domain covering 50°E to 110°E and 30°S to 30°N. The member model's r.m.s. errors in seasonal precipitation are around 2.6 mm per day and are reduced from the deployment of the synthetic superensemble to around 1.7 mm per day. The corresponding

Table 14.2. Details of the seven DEMETER coupled models.

	CERFACS France	ECMWF	INGV Italy	LODYC France	M-France	UKMO	MPI Germany
Atmos. model	ARPEGE	IFS	ECHAM-4	IFS	ARPEGE	ARPEGE	ECHAM-5
Resolution	T63 31 Levs	T95 40 Levs	T42 19 Levs	T95 40 Levs	T63 31 Levs	$2.5^\circ \times 3.75^\circ$ 19 Levs	T42 19 Levs
Atmos. IC	ERA-40	ERA-40	Coupled AMIP-type	ERA-40	ERA-40	ERA-40	Coupled run relax to obs. SST
Ocean Model	OPA 8.2	HOPE-E	OPA 8.1	OPA 8.2	OPA 8.0	GloSea OGCM HadCM3 based	MPI-OMI
Resolution	$2^\circ \times 2^\circ$ 31 Levs	$1.4^\circ \times 0.3^\circ - 1.4^\circ$ 29 Levs	$2^\circ \times 0.5^\circ - 1.5^\circ$ 31 Levs	$2^\circ \times 2^\circ$ 31 Levs	182×152 GP 31 Levs	$1.25^\circ \times 0.3^\circ - 1.25^\circ$ 40 Levs	$2.5^\circ \times 0.5^\circ - 2.5^\circ$ 23 Levs
Ocean IC	Forced by ERA40	Forced by ERA40	Forced by ERA40	Forced by ERA40	Forced by ERA40	Forced by ERA40	Coupled run relax to obs. SST

Further details of the above coupled models can be found in Palmer *et al.* (2004).

Table 14.3. Details of the versions of the FSU coupled models.

	KOR	KNR	AOR	ANR
Atmos. model	FSUGSM	FSUGSM	FSUGSM	FSUGSM
Resolution	T63/14 Levs	T63/14 Levs	T63/14 Levs	T63/14 Levs
Atmos. IC	ECMWF with phy. init	ECMWF with phy. init	ECMWF with phy. init	ECMWF with phy. init
Atmos. Physics	Kuo Radiation old (emissivity/ absorbtivity based)	Kuo Radiation new (band model)	SAS Radiation old (emissivity/ absorbtivity based)	SAS Radiation new (band model)
Ocean Model	HOPE Global	HOPE Global	HOPE Global	HOPE Global
Resolution	$5^\circ \times 0.5^\circ - 5^\circ$ 17 Levs	$5^\circ \times 0.5^\circ - 5^\circ$ 17 Levs	$5^\circ \times 0.5^\circ - 5^\circ$ 17 Levs	$5^\circ \times 0.5^\circ - 5^\circ$ 17 Levs
Ocean IC	Coupled assimilation relax obs. SST	Coupled assimilation relax obs. SST	Coupled assimilation relax obs. SST	Coupled assimilation relax obs. SST

improvements for the anomaly correlations go from around 0.3 to 0.4 from the synthetic superensemble. The results for the FSU suite of models show a somewhat greater degree of improvement compared with the DEMETER suite. Thus, it is clear that monsoon forecasts can be improved somewhat beyond the performance of individual models by having a suite of multimodels and constructing a synthetic superensemble. We shall next display a geographical plot of this performance.

In Figure 14.10 (color section) we show in different panels the seasonal precipitation for June, July, and August 2000. Here they are expressed in the units of mm per day. The first panel (Figure 14.10(a)) shows the observed rainfall – obtained from the satellite/raingauge mix. The other panels show the seasonal forecasts for the member models of DEMETER, followed by the ensemble mean of the DEMETER models, the ensemble mean of the FSU suite of models, and finally the synthetic superensemble. This is generally representative of the results from this collection of models. It is clear from this example that the synthetic superensemble matches more closely the observed totals compared with any of the member models. Results of several other such fields, besides precipitation, are shown in Krishnamurti *et al*. (2000a,b). These are not shown here, but they show a similar enhancement of the skill of forecasts for the synthetic superensemble compared with the member models.

14.6 SUMMARY AND FUTURE WORK

Monsoon forecasting is a very difficult area of science since the circulations are so intimately connected to distributions of observations over the ocean and land,

parameterization of cumulus convection, orography, and differential heating. Large errors arise very quickly in medium-range forecasts from any of these areas. The current observational network needs to be enhanced over the orographic regions where the most intense monsoon rainfall occurs. The mix of observations from satellites over the ocean and from the conventional World Weather Watch (WWW) need to be critically examined in the context of adaptive observation based Observing System Simulation Experiments (OSSEs), an area that deserves future modeling studies toward improving the predictability of the monsoon. Here a major difficulty exists in defining a 'Nature Run' (a model forecast that is considered realistic or absolute), since that too may have to be based on a data deficient model that does not see all the possible scales adequately, such as for instance the mesoscale orographic ascent in regions of steep mountains and heavy rains. These are important areas for future modeling research that can provide insights on data requirements and modeling issues. We have illustrated that it is very difficult to pin down a cumulus parameterization scheme and label it as the most desirable. Most current schemes are somewhat comparable and are sensitive to initial states such that one or the other can easily have a superior performance on a given day. A way out of this difficulty seems to be a multimodel approach. Here one can construct a multimodel superensemble that utilizes a suite of cumulus parameterizations in the different models and the consensus so constructed (from a superensemble), provides a weighted bias corrected product for these member models that seems to perform the best.

With the available regional mesoscale models and a benchmark analysis, an intercomparison study (under simulated operational conditions) to assess the skill of models in predicting various weather systems associated with the monsoon will be quite useful for practical applicability and will also provide further insight into the issues related to the modeling of the monsoon. Such intercomparison studies have been undertaken for other regions (Cox *et al.*, 1998). Further improvements in all of the areas of physical parameterizations are essential in order to enhance the performance of individual models. As the models improve so will the multimodel superensemble, which always performs somewhat better than the member models.

There is increasing recognition of the important role of the MJO/ISO in its effects on the dry and wet spells of the monsoon. Thus, it may be necessary to be cognizant of the phase and amplitude of the MJO/ISO and to be able to bring in these features correctly at the start of a medium range forecast. Large errors in the representation of the MJO/ISO by the model data sets can be expected to effect the medium range monsoon forecasts.

Since moisture data sets are evidently most important during the onset phase and during the transitions between the dry and the wet spells of the monsoon, it may be worthwhile to explore newer moisture profiling data sets such as those provided by the AIRS/AQUA satellites for the data assimilation. Impacts of improved moisture distributions on medium-range monsoon forecasts deserve to be studied.

14.7 APPENDIX 14.1: OUTLINE OF THE FSU GLOBAL SPECTRAL MODEL

The global model used in this study is identical to that used in Krishnamurti *et al.* (1998b). The following is an outline of the global model:

(a) Independent variables: (x, y, σ, t).
(b) Dependent variables: vorticity, divergence, surface pressure, vertical velocity, temperature, and humidity.
(c) Horizontal resolution: triangular truncation at different wavenumbers.
(d) Vertical resolution: 15 layers between roughly 10 and 1,000 mb.
(e) Semi-implicit time differencing scheme.
(f) Envelope orography (Wallace *et al.*, 1983).
(g) Centered differences in the vertical for all variables except humidity, which is handled by an upstream differencing scheme.
(h) Fourth-order horizontal diffusion (Kanamitsu *et al.*, 1983).
(i) Kuo-type cumulus parameterization (Krishnamurti *et al.*, 1983a).
(j) Shallow convection (Tiedtke, 1984).
(k) Dry convective adjustment.
(l) Large-scale condensation (Kanamitsu, 1975).
(m) Surface fluxes via similarity theory (Businger *et al.*, 1971).
(n) Vertical distribution of fluxes utilizing diffusive formulation where the exchange coefficients are functions of the Richardson number (Louis, 1979).
(o) Long and short-wave radiative fluxes based on a band model (Harshvardan and Corsetti, 1984; Lacis and Hansen, 1974).
(p) Diurnal cycle.
(q) Parameterization of low, middle, and high clouds based on threshold relative humidity for radiative transfer calculations.
(r) Surface energy balance coupled to the similarity theory (Krishnamurti *et al.*, 1991).
(s) Non-linear normal mode initialization – 5 vertical modes (Kitade, 1983).
(t) Physical initialization (Krishnamurti *et al.*, 1991).

14.8 APPENDIX 14.2: DEFINITIONS OF STATISTICAL PARAMETERS (SKILL METRICS)

$$\text{r.m.s. error} = \left[\frac{1}{N}\sum_{n=1}^{N}(f_n - o_n)^2\right]^{1/2}$$

$$\text{Systematic error (bias)} = \frac{1}{N}\sum_{n=1}^{N}(f_n - o_n)$$

$$\text{Anomaly correlation} = \frac{\sum_{n=1}^{N}[(f_n - c_n)(o_n - c_n)]}{\left[\sum_{n=1}^{N}(f_n - c_n)^2 \sum_{n=1}^{N}(o_n - c_n)^2\right]^{1/2}} \quad (\text{AC} > 0.6 \text{ for useful forecast skill})$$

$$\text{Correlation coefficient} = \frac{\sum_{n=1}^{N}[(f_n - \bar{f})(o_n - \bar{o})]}{\left[\sum_{n=1}^{N}(f_n - \bar{f})^2 \sum_{n=1}^{N}(o_n - \bar{o})^2\right]^{1/2}} \quad (-1 \le c \le 1)$$

$$\text{Equitable threat score} = \frac{H - \left(F \times \frac{O}{N}\right)}{F + O - H - \left(F \times \frac{O}{N}\right)} \quad (0 \le \text{ETS} \le 1) \text{bias} = \frac{N_f}{N_o}$$

In these expressions:
N = number of grid points.
f_n = forecast value at grid point n.
o_n = observed value at grid point n.
c_n = climatological (mean) value at grid point n.
$\bar{f}$ = area mean of the forecasted values.
$\bar{o}$ = area mean of the observed values.
F = area where event is forecasted.
O = area where event is observed.
H = hit area, or overlap of areas F and O.
N_f = number of grid points where event is forecasted.
N_o = number of grid points where event is observed.

15

Dynamic seasonal prediction and predictability of the monsoon

In-Sik Kang and Jagadish Shukla

In this chapter we present a historical review of the hypothesis of boundary forced predictability of the monsoon and the limitations and challenges in dynamical seasonal prediction of monsoon rainfall. We also present an assessment of multi-model seasonal predictability of summer mean precipitation over the Asian monsoon–western Pacific region by using a set of 21-year (1979–1999) hindcast predictions of 5 models participating at the Asia–Pacific Economic Cooperation Climate Network (APCN). The five models consist of the current operational seasonal prediction models of NCEP, NASA, JMA, KMA, and SNU. The potential predictabilities of individual models are shown by various methods including the signal-to-noise ratio and anomaly correlations. Statistical methods for correcting the bias of model prediction are developed and applied to individual model predictions. We demonstrate that statistical correction is effective for enhancing the predictability, particularly for the Asian monsoon–Pacific region, where the models have a large bias. It is shown that a reasonably good seasonal prediction can be achieved when multimodel predictions are combined based on a composite of the individual predictions, after applying a statistical correction to each of them separately.

Although this chapter describes mainly the current status of tier-2 seasonal prediction systems, the present skills of tier-1 systems, utilizing coupled ocean–atmosphere models are also examined using the data from the Development of a European Multimodel Ensemble System for seasonal to inTERannual prediction (DEMETER). We show that the tier-1 system has an advantage in producing better seasonal mean predictions, particularly in the western Pacific and Indian Ocean where air–sea interaction is active during the summer. The spatial correlation skill of the DEMETER multimodel ensemble prediction is 0.47 for monsoon precipitation over the region of 40–180°E, 20°S–30°N.

B. Wang (ed.), *The Asian Monsoon*.

15.1 INTRODUCTION

15.1.1 Historical review

Variations in monsoon rainfall affect agriculture, drinking water, transportation, health, power, and the very livelihood of billions of people living in the monsoon region. It is no surprise therefore that for over a hundred years a number of countries in the region have tried to issue long-range forecasts of monsoons (The India Meteorological Department started issuing long-range forecasts of monsoon rainfall in 1886). The operational long-range forecasts of monsoon rainfall were based on empirical relationships derived from past observations of atmospheric pressure, temperature, and wind. Blanford (1884) was the first to suggest the use of a surface boundary condition (snowfall over the Himalayas in the preceding winter) to predict the summer monsoon rainfall over India.

Charney and Shukla (1981) presented a conceptual hypothesis of monsoon predictability based on the influence of boundary forcing at the Earth's surface. A brief historical perspective on this hypothesis is given here. Charney *et al.* (1977) had conducted atmospheric general circulation model (AGCM) experiments with the NASA/GISS AGCM to investigate the influence of changes in albedo on rainfall over the Sahel. In these experiments it was found that the summer rainfall variance among the three ensemble members (each member was integrated only for 45 days) was quite small over the Indian monsoon region, indicating that the boundary conditions mainly control the Indian monsoon rainfall. In the same year, Shukla and Misra (1977) had shown empirical evidence of a possible relationship between the Arabian Sea surface temperature (SST) and Indian rainfall, and Shukla (1975) had shown that in the Geophysical Fluid Dynamics Laboratory (GFDL) AGCM, specification of (large) positive SST anomalies over the Arabian Sea produced an increase in monsoon rainfall over India. Hahn and Shukla (1976) revived Blanford's hypothesis of a snow–monsoon relationship by showing, using satellite derived snow cover data, an inverse relationship between the winter season snow cover over Eurasia and the subsequent summer monsoon rainfall over India. These results, combined with the results from the GISS model, in which variance of seasonal rainfall among ensemble members was quite small, led Charney and Shukla (1981) to hypothesize that the predictability of the monsoon depends on the influence of boundary conditions at the Earth's surface.

The Charney–Shukla hypothesis has been the central paradigm for monsoon predictability research during the past 25 years. However, dynamical models have included large systematic errors in their simulations of the seasonal mean anomalies associated with changes in boundary conditions, and therefore their predictability for summer monsoon rainfall has been relatively low. Whether our inability to capture the boundary forced signals is due to inadequate models and modeling strategies or due to intrinsic limits to the predictability of seasonal mean rainfall because of the large natural intraseasonal variability of monsoons remains an open question and a topic of vigorous debate. In the following section we present a critical

retrospective of the Charney–Shukla hypothesis and describe the barriers to realizing its potential predictability.

For the boundary conditions to have a useful influence on the prediction of monsoon rainfall, the following three conditions need to be satisfied: (1) there must be a large and persistent anomaly at the Earth's surface, (2) there must be a well defined dynamical mechanism through which changes in the boundary conditions will produce a corresponding change in the seasonal mean monsoon rainfall, and (3) the seasonal mean response (signal) must be sufficiently large and reproducible so that it can be distinguished from the intrinsic variability (noise) of the model due to internal dynamics alone. A large number of model simulations during the past decade with high-resolution AGCMs using advanced parameterizations have clearly shown that the internal variability over the monsoon region is much larger than that found by Charney and Shukla. This implies that large member ensembles are needed to distinguish the boundary forced response from internal dynamics variability. If the internal variability is spatially small-scale and high-frequency, then large-scale spatio–temporal averages (viz. the seasonal mean over the whole of India) could be predicted if the boundary forcings were indeed important, and if the models were able to simulate the appropriate physical effects.

The current generation of AGCMs have such large systematic errors in simulating both the mean and the variance of summer monsoon rainfall that it is not possible to conclude whether our current inability to make useful dynamical seasonal prediction is due to the lack of boundary forced predictability or the inadequacy of the current models and modeling strategies. Recent research works carried out with coupled ocean–atmosphere models, suggest that the prescription of SST anomalies in AGCM experiments is an inadequate modeling strategy because SST anomalies in the Indian Ocean and the adjoining western Pacific Ocean are either forced by the atmosphere or evolve as a strongly coupled ocean–atmosphere process (Wang *et al.*, 2004a). If ocean–atmosphere coupling is indeed crucial for the Indian Ocean and western Pacific SST anomalies, the predictability of monsoons must be investigated with coupled ocean–atmosphere models, which currently have large systematic errors. The problem is further compounded by the fact that atmosphere–land interactions are also quite important for the simulation and prediction of monsoon rainfall. Even if SST anomalies force significant changes in large-scale circulation, local land–atmosphere interactions will modulate the ocean-forced remote response and determine the actual changes in rainfall over land. Therefore, realistic models of the total climate system (ocean–land–atmosphere) are required to understand the variability and to make useful predictions of monsoon rainfall.

15.1.2 Current dynamic seasonal predictions

In spite of the many challenges described above, dynamic seasonal predictions using general circulation models (GCMs) have been implemented by several operational centers in recent years. In particular, possible improvement of seasonal prediction has been attempted with the use of multimodel ensembles to remove the uncertainties

associated with the spread of ensemble predictions with different initial conditions and the uncertainties associated with model parameterizations (Krishnamurti *et al.*, 1999; Palmer *et al.*, 2004). This chapter describes the present status of dynamical multimodel ensemble seasonal prediction systems, particularly for the monsoon precipitation.

In an ensemble simulation, all ensemble members are forced by the same SST but start from slightly different atmospheric initial conditions (Dix and Hunt, 1995; Kumar and Hoerling, 1995; Stern and Miyakoda, 1995; Zwiers, 1996; Kang *et al.*, 2004). The basic idea of this approach is that the differences among the ensemble members can be used to quantify the noise due to internal dynamics, whereas the relative similarity between ensemble members can be considered as the atmospheric response to external forcing. Thus, the ensemble mean (signal) can be considered as the component of the prediction forced by the SST, and the deviation from the ensemble mean as the stochastic internal component of the prediction. In this approach, the potential predictability is measured as the ratio between the externally forced SST signal and the internal noise, using a standard statistical tool for this kind of problem: 'analysis of variance' (ANOVA), which has been detailed in many previous studies (Shukla, 1981; Rowell *et al.*, 1995; Rowell, 1998).

Recently, attempts have also been made to reduce the uncertainty of models by simply compositing multimodel solutions (Kang *et al.*, 2002) or by using the so-called 'superensemble' method (Krishnamurti *et al.*, 1999). The present performance of dynamical seasonal prediction is poor, unless some form of post-processing is applied. This poor performance is not only due to the inherent complexity of atmospheric internal processes but also due to the present models' inability to reproduce the actual atmospheric responses to external forcings, particularly the SST anomalies. This model bias in the external component arises from imperfect formulation and parameterization of the various physical processes in the model. Different parameterizations produce different solutions. Assuming that the errors of those solutions are independent of each other and that various model solutions spread randomly but close to the observation are used, the composite of many model solutions can reduce the random errors of the models.

Model error can also be reduced by statistical correction methods. A major part of the non-system error of each model can be corrected by incorporating a statistical relationship between the predicted and observed anomalies. The most commonly used methodology is the so-called coupled pattern technique (Graham *et al.*, 1994), based on singular value decomposition (SVD) analysis and canonical correlation analysis (CCA). Ward and Navarra (1997) applied SVD to simultaneous fields of GCM simulated precipitation and observed precipitation to correct the errors in the model response to SST forcing. CCA has been widely used in a statistical seasonal prediction system (Barnett and Preisendorfer, 1987; Barnston, 1994). A recent study by Feddersen *et al.* (1999) demonstrated that post-processed results are not sensitive to the choice of method, whether based on the CCA, SVD, or empirical orthogonal function (EOF) decompositions. In this chapter, the post-processing procedures of error correction are developed based on the SVD analysis and a pointwise statistical downscaling method. By comparing the potential predictabilities with and without

the correction, we can evaluate how the post-processing of error correction enhances predictability in the regions of interest.

At present, dynamical seasonal prediction procedures are categorized as tier-2 and tier-1 systems. The tier-2 system treats the atmosphere and the ocean (specifically SST) separately. This system relies on an AGCM integrated with a prescribed (either observed or predicted) SST boundary condition and atmospheric initial condition. The potential predictability of tier-2 systems have been examined internationally by the Seasonal Model Intercomparison Project (SMIP II) initiated by the Climate Variability and Predictability Program (CLIVAR)/Working Group on Seasonal to Interannual Prediction (WGSIP). The purpose of SMIP II is to evaluate the current dynamical seasonal prediction systems within a framework in which the lower boundary conditions are prescribed from the observed SSTs for the 20 years between 1979–1998. On the other hand, SMIP/Historical Forecast Project (HFP) uses predicted SST conditions instead of past observations, and therefore the SMIP/HFP evaluates the real seasonal predictability of current operational prediction systems.

The tier-1 system utilizes a coupled ocean–atmosphere model. At present, the climatology of coupled models has a large systematic bias. However, as mentioned before, the coupled model has some advantages in simulating monsoon anomalies, particularly in the subtropical western Pacific and Indian Oceans, where air–sea interaction plays an important role in producing seasonal mean anomalies. Recently, the European community has established the DEMETER based on the seven coupled models used in European countries (Palmer *et al.*, 2004). The aim of DEMETER is to develop a multimodel tier-1 seasonal prediction system and evaluate the skill of the prediction system. At present the European Centre for Medium-Range Weather Forecasts (ECMWF) produces a regular seasonal prediction based on the DEMETER. This chapter also shows the capability of the tier-1 DEMETER system.

Section 15.2 describes a prediction experiment and the data utilized in the present chapter. The potential predictabilities of tier-2 systems are examined in terms of the signal-to-noise ratio in Section 15.3, and in terms of anomaly correlation in Section 15.4. The potential predictability is defined here as the predictability obtained by prescribing the observed (not predicted) SST boundary conditions in the model. Section 15.5 introduces a statistical correction method and shows how the prediction skill is improved after the correction. Section 15.6 shows the potential predictability of various multimodel ensemble prediction systems. In contrast to the potential predictability examined in the previous sections, real predictabilities are assessed in Section 15.7 using a tier-2 system with predicted SSTs and tier-1 systems (DEMETER coupled models). Summary and concluding remarks are given in Section 15.8.

15.2 MODELS AND EXPERIMENT

The data utilized in the present study have been obtained from the APCN. The APCN aims to produce and disseminate a multimodel ensemble seasonal prediction

Table 15.1. Description of the five models used in the present study.

Institute	Resolution		Physical parameterizations
JMA	T63L40	Convection	Prognostic Arakawa–Schubert scheme (JMA, 2002)
		Radiation	JMA (2002)
		Land surface	Simple Biosphere Model (Sellers *et al.*, 1986)
KMA	T106L21	Convection	Kuo scheme (Kuo, 1974)
		Radiation	Lacis and Hansen (1974)
		Land surface	Simple Biosphere Model (Sellers *et al.*, 1986)
NASA	$2^\circ \times 2.5^\circ$L34	Convection	Relaxed Arakawa–Schubert scheme (Moorthi and Suarez, 1992)
		Radiation	Chou and Suarez (1994, 1996)
		Land surface	Mosaic LSM (Koster and Suarez, 1992)
NCEP	T62L28	Convection	Relaxed Arakawa–Schubert scheme (Moorthi and Suarez, 1992)
		Radiation	Chou (1992) and Chou and Suarez (1996)
		Land surface	OSU two-layer model (Pan and Mahrt, 1987)
SNUT	63L21	Convection	Relaxed Arakawa–Schubert scheme (Moorthi and Suarez, 1992)
		Radiation	2-stream k-distribution scheme (Nakajima and Tanaka, 1986)
		Land surface	NCAR LSM (Bonan, 1995)

based on operational prediction products of APEC member countries. Among the products used are the dynamical seasonal prediction data produced by the Japan Meteorological Agency (JMA), Korea Meteorological Administration (KMA), National Aeronautical Space Agency (NASA), National Centers for Environment Prediction (NCEP), and Seoul National University (SNU), as part of SMIP II, led by the CLIVAR WGSIP. The observed SSTs are prescribed for integration. Therefore, the SMIP II can estimate the upper bound of seasonal predictability but not the actual predictability. The initial conditions are obtained from their own initialization scheme or the NCEP reanalysis data. See the details of SMIP II on *http://www-pcmdi.llnl.gov/projects/smip/smip2.php*. The above models consist of different combinations of physical parameterizations, listed and summarized in Table 15.1. The DEMETER data has also been used in the present study. Details of DEMETER can be found in Palmer *et al.* (2004) and the participating models of DEMETER are listed in Table 15.2.

The present study focuses on the predictability of seasonal mean rainfall for boreal summer. For brevity, hereafter 'boreal summer' is abbreviated to 'summer'. The prediction data of each model consists of 10 member predictions of summer mean precipitation for the 21 summers of 1979–1999, except the NASA and JMA models, consisting of 9 and 6 members, respectively. The 10 members were generated with the observed initial conditions at 00:00 Z and 12:00 Z 27–31 May. The horizontal resolution of all data is converted to 2.5° in longitude and 2.5° in latitude. Since

Table 15.2. Brief description of the seven ocean–atmosphere coupled models of DEMETER.

Institute	AGCM	Resolution	OGCM	Resolution
CERFACS	ARPEGE	T63 31 levels	OPA 8.2	2.0×2.0 31 levels
ECMWF	IFS	T95 40 levels	HOPE-E	$1.4 \times 0.3 - 1.4$ 29 levels
INGV	ECHAM-4	T42 19 levels	OPA 8.1	$2.0 \times 0.5 - 1.5$ 31 levels
LODYC	IFS	T95 40 levels	OPA 8.2	2.0×2.0 31 levels
Meteo-France	ARPEGE	T63 31 levels	OPA 8.0	$182GP \times 152GP$ 31 levels
Met Office	HadAM3	2.5×3.75 19 levels	GloSea OGCM based on HadCM3	$1.25 \times 0.3 - 125$
MPI	ECHAM-5	T42 19 levels	MPI-OM1	$2.5 \times 0.5 - 2.5$ 23 Levels

the climatological mean precipitation of each model was presented in Kang *et al.* (2002) and documented elsewhere, we will focus on the deviation (anomaly component) from the 21-year predicted climatology of each model. The anomalies thus obtained do not contain the systematic error of each model climatology. The observed precipitation data for verification is obtained from the Climate Prediction Center Merged Analysis of Precipitation (CMAP) data set (Xie and Arkin, 1997).

15.3 LIMIT OF SEASONAL PREDICTABILITY

In this chapter, the interannual variance in model prediction is decomposed into the external (signal) part, related to the SST forcing, and the internal (noise) part, related to the atmospheric non-linear internal dynamics, and the theoretical limit of seasonal predictability is examined in terms of the signal-to-noise ratio. Figure 15.1(a) shows the variance in observed summer mean precipitation for the 21 years. The spatial pattern of Figure 15.1(a) is similar to that of the climatological summer mean shown in Kang *et al.* (2002), indicating that large variability appears in regions of large mean precipitation. Figure 15.1(b–f) are the corresponding variances of each model. Each model variance is estimated based on the predictions of all members for the 21 years, and it will be referred to as the total variance. As in the observation, the spatial distribution of the simulated variance appears to be similar to that of the corresponding climatological mean. However, the magnitudes of the simulated variances are quite different for different models. The NCEP variance is particularly large and about 10 times larger than that of the JMA over Indo-China, south China, and Indian regions. The NCEP model has much larger interannual variances than those actually observed, and the JMA model has much less variance in most of the

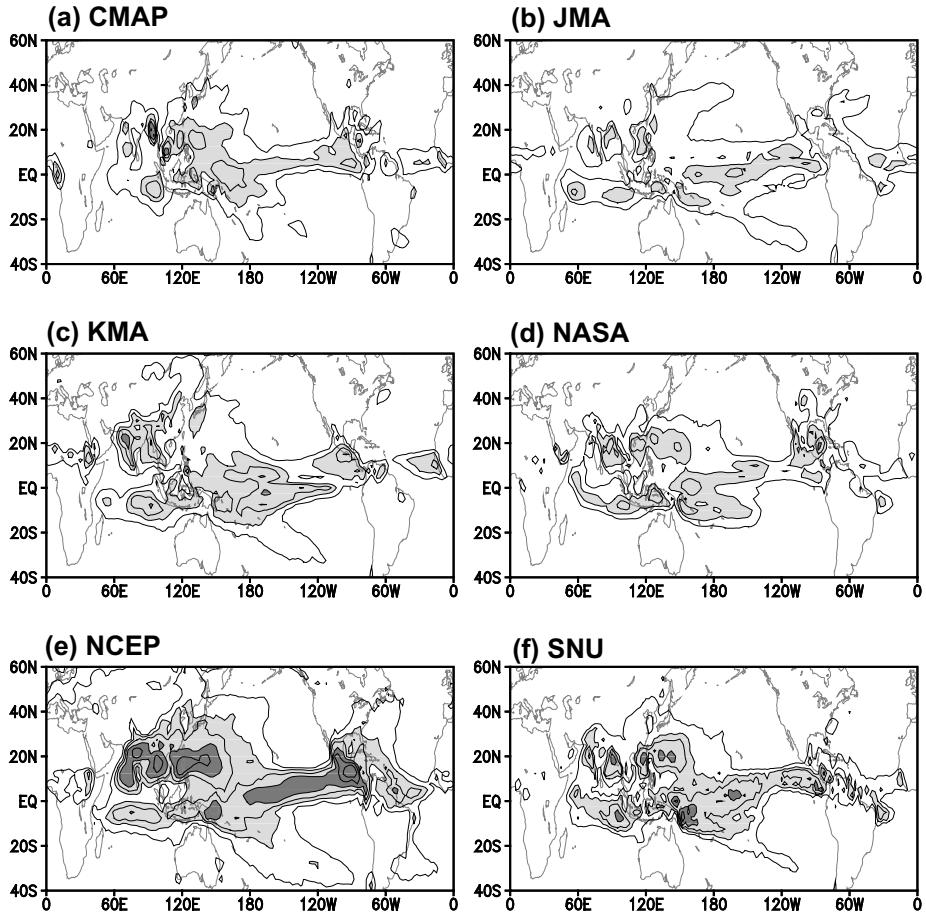

Figure 15.1. Variances of summer mean precipitation anomalies for the 21-year period (1979–1999). (a) CMAP observation precipitation, (b) JMA, (c) KMA, (d) NASA, (e) NCEP, and (f) SNU prediction models. The variance of each model is computed using all the ensemble members of the 21-year predictions. The contour interval is 1, 3, 6, 12, 24, and 48 $mm^2\,day^{-2}$ and light and dark shadings indicate a variance of more than 3 and 12 $mm^2\,day^{-2}$, respectively.

regions, particularly over the Asian monsoon region. The difference among the model variances is partly related to the difference in the mean climatology and to the different combinations of model physics. But, it is difficult to identify the model physics responsible for generating such large differences.

The total variance (σ^2_{TOT}) is divided into the external (σ^2_{SST}) and internal variances (σ^2_{INR}; Rowell, 1998). The ensemble mean is considered to be the external component of the prediction forced by the SST forcing, and the deviation from the ensemble mean is the stochastic internal component of the prediction. The

internal variance can then be expressed as:

$$\sigma^2_{INR} = \frac{1}{N(n-1)} \sum_{i=1}^{N} \sum_{j=1}^{n} (x_{ij} - \overline{x_i})^2 \tag{15.1}$$

where x is the precipitation, i indicates the individual year, $N = 21$, j is the ensemble member, and n is 6 to 10 for different models. $\bar{x}_i$ is the ensemble mean. The external variance is obtained by the mean square of the deviation of each year's ensemble mean from the climatological mean and with a consideration of bias correction, as in Rowell (1998):

$$\sigma^2_{SST} = \sigma^2_{EN} - \frac{1}{n}\sigma^2_{INR} \quad \text{and} \quad \sigma^2_{EN} = \frac{1}{N-1} \sum_{i=1}^{N} (\overline{x_i} - \overline{\overline{x}})^2 \tag{15.2}$$

where $\overline{\overline{x}}$ is the climatological mean and $\overline{\overline{x}} = 1/(Nn) \sum_{i=1}^{N} \sum_{j=1}^{n} x_{ij}$. It should be noted that the sum of external and internal variances expressed above is equal to the total variance.

Figure 15.2(a–e) show the external variances of various models, and Figure 15.2(f–j) the internal variances. The signal-to-noise ratio, the ratio of the external part to the internal part of the corresponding model, is shown in Figure 15.2(k–o). All the models produce large external variances over the tropical oceans that are much larger than the internal variance of the same model, particularly the ENSO region. This result indicates that tropical rainfall is less controlled by atmospheric internal processes and is thus less predictable for a given SST condition. In the extratropics, on the other hand, the internal variances are bigger than the external variances of the same model (Figures 15.2(k–o)), and therefore the extratropical atmosphere is more controlled by non-linear stochastic processes and less predictable.

Over the Asian monsoon–western Pacific region, the external and internal parts appear to be equally important for all models, although some models (JMA, NASA, and SNU) have relatively large values of the signal-to-noise ratio over the region (Figures 15.2(k–o)) compared with those of the KMA and NCEP models. It is interesting to note that the internal variance is generally proportional to the external variance. In particular, the large variance of the NCEP model shown in Figure 15.1 is partly due to a large internal variance, particularly over the Asian monsoon region. On the other hand, the internal variance of the JMA model is very weak. As a result, the JMA model has relatively large values of signal-to-noise ratio, although its forced variance is significantly weaker than those of the other models. It should also be noted that the internal variance is very model dependent, indicating that the internal variations are not only controlled by the dynamics but also by the model's physics.

Seasonal predictability is limited by the non-linear stochastic processes in the atmosphere, shown in terms of internal variance in Figure 15.2. Therefore, the seasonal prediction could not be perfect even if we had a perfect GCM and perfect boundary conditions and almost perfect initial conditions. Here, the theoretical limit of seasonal predictability is examined by separating the observation

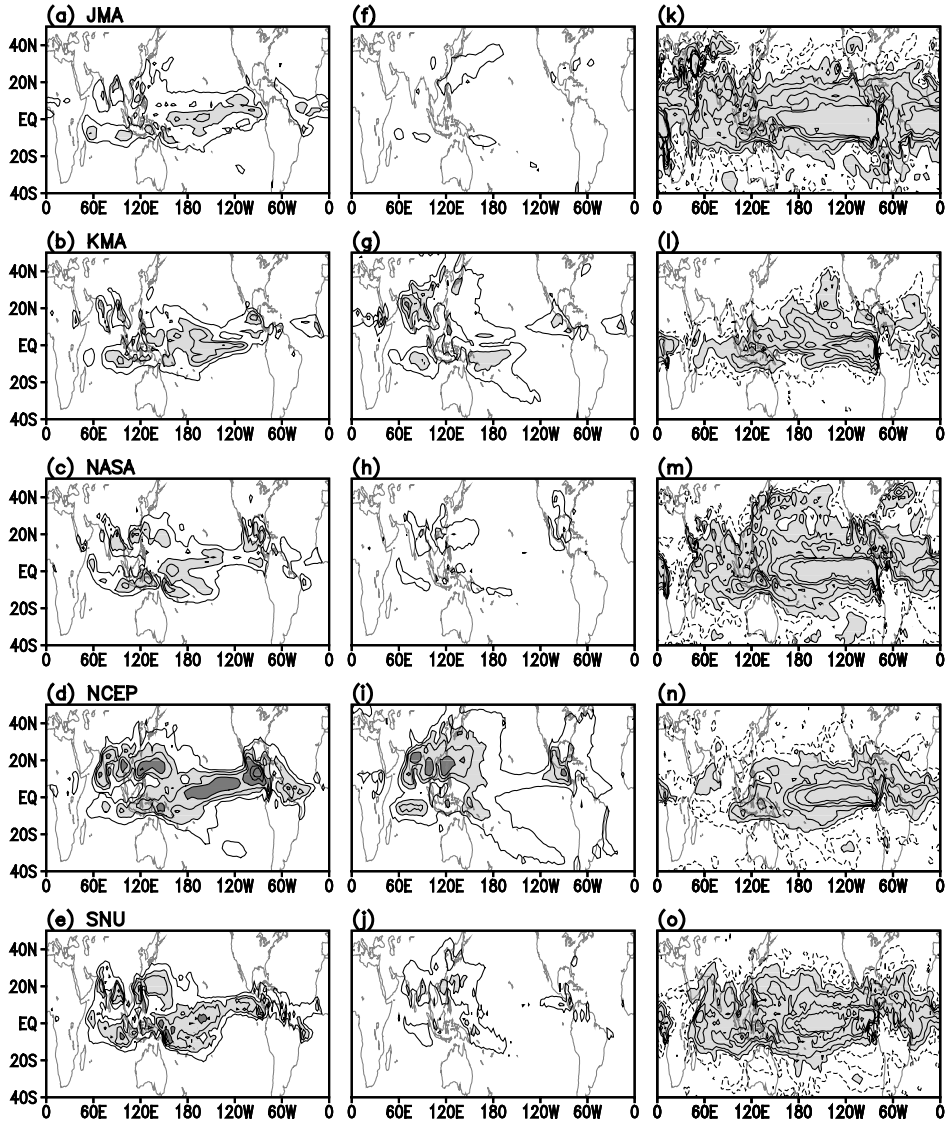

Figure 15.2. (a)–(e) External variance of precipitation based on the ensemble average of each year. (f)–(j) Internal variance based on the deviation of individual members from the ensemble average. Contour interval is 1, 3, 6, 12, 24, and 36 $mm^2\,day^{-2}$ and light and dark shadings indicate a variance of more than 3 and 12 $mm^2\,day^{-2}$, respectively. (k)–(o) Signal-to-noise ratio defined by the ratio of the forced variance to the free variance. Contour levels are 1, 2, 4, 8, and 16 and the dashed line indicates 0.5. Shading indicates a signal-to-noise ratio bigger than 1. Each model is marked at the upper left corner of panels (a)–(e).

(x) into a signal (x_S) and noise (x_N). The signal is related to the slowly varying boundary conditions. The corresponding model variable is then expressed as $y = y_S + y_N$. Assuming that the model signal is $y_S = \alpha x_S + y_e$ as in Sugi (2004), where α is the linear regression coefficient between x_S and y_S, and y_e is the model error. Then, the model variable $y = \alpha x_S + y_e + y_N$. The correlation coefficient between the observation and model variable can be expressed as:

$$R = \frac{\alpha V(x_S)}{V(x)^{1/2}(\alpha^2 V(x_S) + V(y_e) + V(y_N))^{1/2}} \tag{15.3}$$

where $V(x)$ is the variance of x. The above equation can be driven by assuming that the signal, noise, and error are independent of each other, and therefore all covariances of $\mathrm{Cov}(x_S, x_N)$, $\mathrm{Cov}(x_S, y_e)$, $\mathrm{Cov}(x_N, y_e)$, $\mathrm{Cov}(y_e, y_N)$, and $\mathrm{Cov}(x_N, y_N)$ are zero. Then the correlation skill can be maximized by minimizing the model error and the noise part. The noise part can be reduced by the ensemble mean procedure – the mean of many predictions with slightly different initial conditions. The model error can be corrected by statistical correlation methods, discussed in Section 15.5, and by using a multimodel composite, discussed in Section 15.6. The theoretical limit of seasonal prediction correlation skill can be expressed as:

$$R_{\mathrm{Limit}} = \sqrt{\frac{V(x_S)}{V(x)}} = \sqrt{\frac{\rho}{\rho + 1}} \tag{15.4}$$

As in (15.4), the theoretical limit can also be expressed in terms of the signal-to-noise ratio (ρ). Figure 15.3(a) shows the distribution of R_{Limit} estimated using the SNU AGCM. We can also examine the predictability limit using a hypothetical perfect model (a model with no systematic error). The correlation skill of the perfect model is usually estimated by considering one of the ensemble members as observation and correlating the member with the ensemble mean of the other members. Figure 15.3(b) shows the distribution of perfect model correlation as estimated with the SNU AGCM. As seen in the figure, the theoretical limit of correlation skill is very similar to the perfect model correlation. The relatively small amplitude of perfect model correlation in the extratropics is due to the sampling error associated with an insufficient number of ensemble members. The zonal means of predictability limits of various models are shown in Figure 15.4. The figure indicates that the predictability limit in the tropics is relatively high (correlation skill of about 0.8–0.9), but it rapidly drops in the subtropics near 30°N and is fairly low in the extratropics and polar regions (correlation of about 0.2–0.4). These correlation values are the upper limit of the dynamical seasonal prediction skill that can be achieved with a perfect model and perfect boundary conditions.

15.4 POTENTIAL PREDICTABILITY OF VARIOUS MODELS

The potential predictability, defined as the predictability of the model measured with perfect boundary (observed SST) conditions, should be lower than the theoretical limit because of the incompleteness of the models. The model error is estimated as

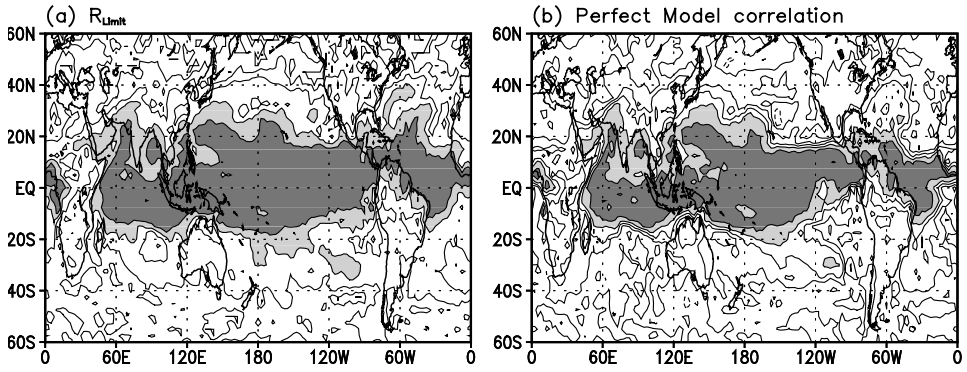

Figure 15.3. (a) The spatial distribution of the limit of correlation skill estimated by using the SNU AGCM. (b) Same as in (a) except for the perfect model correlation.

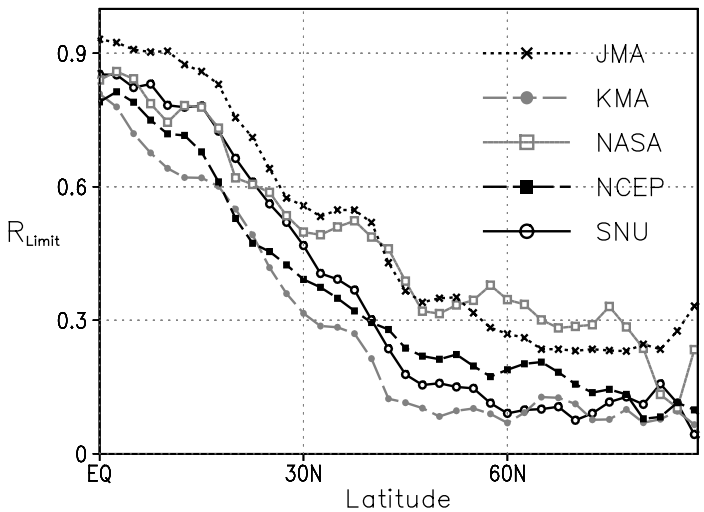

Figure 15.4. Zonal mean distribution of theoretical limit of correlation skill for five models in the northern hemisphere. Each line corresponds to each model.

the difference between the ensemble mean of model predictions and the corresponding observations. The error variances of each model are shown in Figure 15.5(a–e). It is interesting to note that the spatial distributions of the errors for all models are similar. All models produce large systematic errors in the Asian monsoon region and along the intertropical convergence zone (ITCZ). The ratio of the external variance to the error variance is shown in Figure 15.5(f–j) for individual models. A ratio exceeding 1 indicates that the prediction signal can be considered to be larger than the error. In the Asian monsoon and western Pacific, all the models produce errors

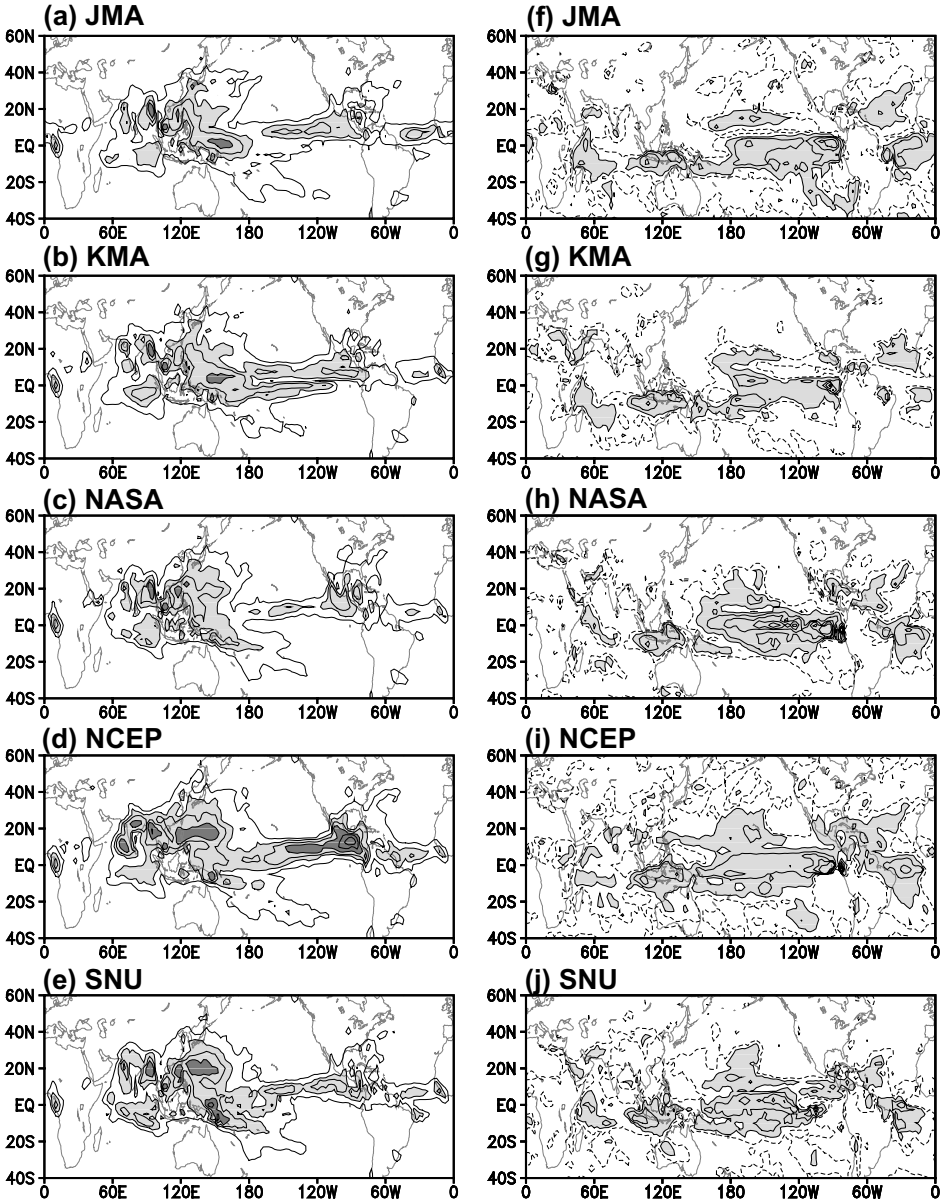

Figure 15.5. (a)–(e) Variance of the systematic error – the difference between the ensemble average of prediction and the corresponding observation. Contour interval is 1, 3, 6, 12, 24, and 36 $mm^2\,day^{-2}$ and light and dark shadings indicate a variance of more than 3 and 12 $mm^2\,day^{-2}$, respectively. (f)–(j) Ratio between the variances of ensemble mean and systematic error. Contour levels are 1, 2, 4, and 8 and the dashed line indicates 0.5. Shadings indicates a ratio bigger than 1. Model identification is marked at the upper left corner of each panel.

which are bigger than the signals. This result indicates that the large prediction signals in the monsoon region are biased by the poor performance of the models. In the next section, we investigate whether it is possible to make a reliable monsoon prediction, if the systematic errors are corrected.

The prediction skill of each model is measured by using the correlation between the anomalies of the ensemble mean predictions and the observations for 21 years. Since the observed SST was prescribed in the hindcast predictions, this prediction skill is a measure of potential predictability. Figure 15.6 (color section) shows the global distribution of correlation coefficients between the observed and predicted ensemble mean precipitation at each grid point for the 21 summers. The correlations of various models are shown in Figure 15.6(b–f), and Figure 15.6(a) shows the correlations between observations and the composite of five models. As expected from the previous section, all the models show a large correlation over the ENSO region, where the external (forced) variance exceeds the internal variance and the model error variance. By contrast, over the monsoon region, the correlation skill is very poor for all models. It should be noted that the model composite does not help improve the correlation skill. In the subtropical western Pacific and the Atlantic Ocean, all the models and the composite have large negative correlation values. The negative correlation in the western Pacific is due to model bias, whereas the external response has large systematic errors (Figure 15.5). Recently, Wang *et al.* (2004a) suggested that the poor simulations of precipitation over the western Pacific are due to the tier-2 prediction system, in which atmospheric feedback to the ocean does not exist. This provides additional evidence that ocean–atmosphere coupled processes are important for the summer precipitation anomalies in the western Pacific.

The spatial correlation over the monsoon region (40°–160°E, 20°S–30°N) between the anomalies of the ensemble mean seasonal prediction and the corresponding observed precipitation at each year is shown in Figure 15.7. With a few exceptions, all the models predict the monsoon precipitation poorly for most of the summers. The model composite shows correlation values below 0.3 for most of the summers, except the years 1981, 1986, and 1987. To examine the SST impact on monsoon prediction, the SSTs are averaged for the four cases of good prediction (the years 1981, 1986, 1987, and 1990) and for the cases of bad prediction (the years 1980, 1982, 1994, and 1997). The averaged SST anomalies are shown in Figure 15.8. Comparison between Figure 15.8(a) and (b) clearly demonstrate that monsoon precipitation is indeed closely related to SST anomalies, particularly over the oceans surrounding the Asian monsoon region and the eastern tropical Pacific.

15.5 PREDICTION SKILL AFTER ERROR CORRECTION

15.5.1 Error correction and verification methods

The model bias in the external component appears in a systematic way, in both the climatological mean and the anomaly component. The mean bias can be corrected

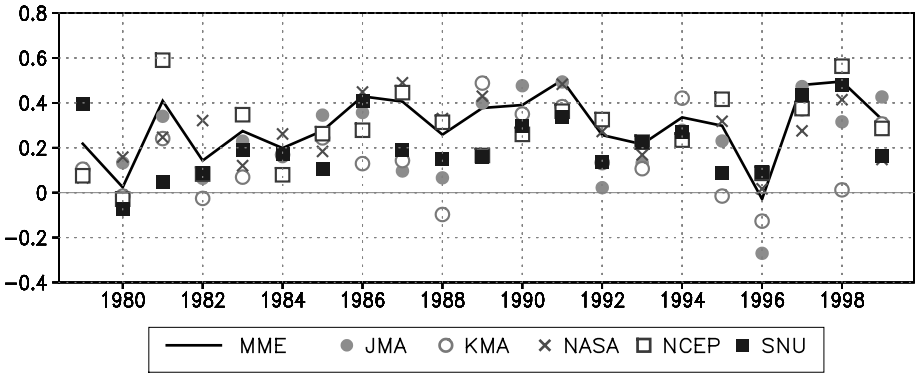

Figure 15.7. Pattern correlation coefficients between the observed and predicted precipitation over the monsoon region (40°–160°E, 20°S–30°N). Correlation values of each model and model composite are shown by various marks denoted in the figure.

by subtracting the predicted climatology from the prediction for an individual year. The systematic error of the anomaly component is related to the incorrect performance of the GCM in simulating the anomalies, predominantly forced by the SST anomalies. It should be noted that a slight shift in the spatial pattern of the model anomaly can result in a substantial drop in skill scores when the skill is measured based on the performance at individual grid points. Here, two statistical correction methods are introduced. The first method is based on the SVD (Ward and Navara, 1997; Feddersen *et al.*, 1999; Kang *et al.*, 2004). As in Kang *et al.* (2004), the systematic errors of the predicted anomaly are corrected by replacing the SVD modes of prediction by the corresponding observed modes. The transfer function for the replacement can be constructed as follows:

$$X(x,t) = \sum_{i=1}^{P} \alpha_i Y_i(t) R_i(x) \tag{15.5}$$

where $X(x,t)$ is the corrected field; $Y(t)$ is the time coefficient of the SVD mode for the predicted field; $R(x)$ is the projection of the SVD singular vector onto the observed field; i is the mode number; P the total number of the SVD modes; and α is the correlation coefficient between the time series of the SVD mode of prediction and the corresponding SVD time series of observations. It should be noted that before obtaining the SVD modes, the EOF analysis is applied to the predicted and observed anomalies separately, and the observed and predicted fields are reconstructed by retaining the leading 10 EOF modes of each field. This process filters out small-scale anomalies and smoothes the spatial fields.

It should be noted that the SVD-based correction method can not correct a bias which is not related to leading SVD modes and/or has a local character. Another correction method, used in this chapter, is the so-called 'point-wise downscaling (PDS)' method which is based on the large-scale patterns of model variables

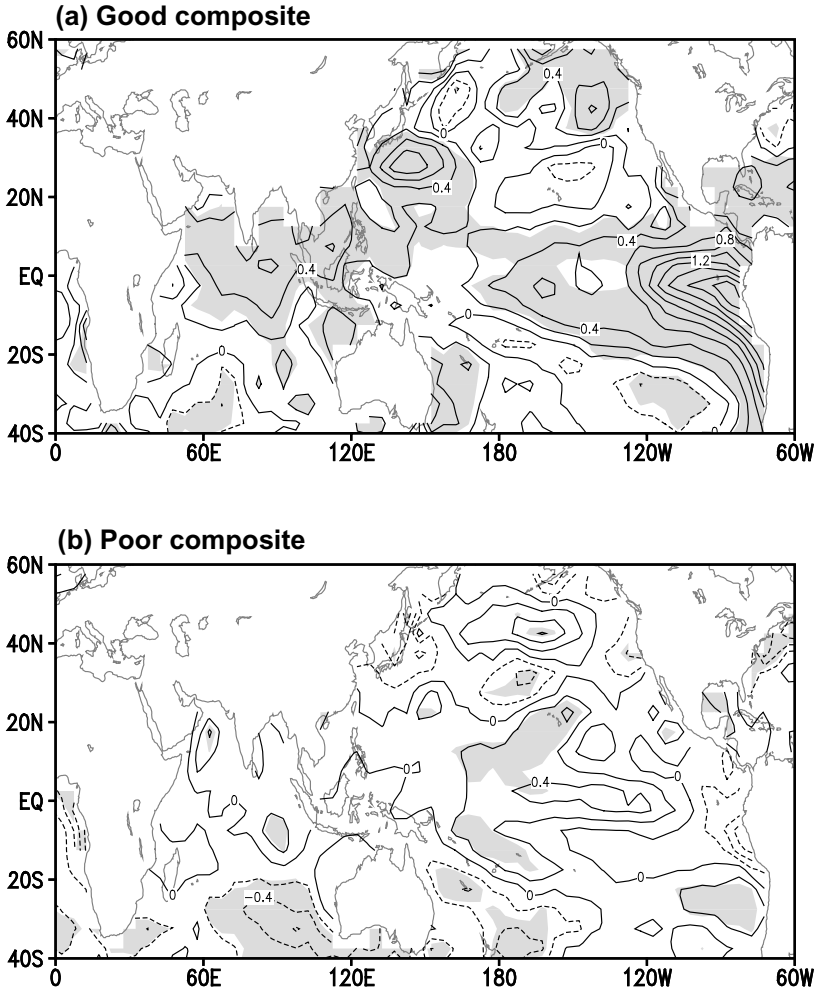

Figure 15.8. (a) Composite SST anomalies for the years of good monsoon prediction (1991, 1997, and 1998). (b) Those for the years of poor monsoon prediction (1980, 1982, and 1996). Selected cases exceeding one standard deviation of the correlation coefficient of a composite prediction are shown as solid lines in Figure 15.6(b). Shadings denote the anomalies that are significant at the 99% level of each grid point (Student t-test).

correlated to local (grid point) observed precipitation. Once the model patterns have been determined from hindcast prediction data, the local precipitation can be predicted by a linear combination of the predictors obtained by projecting the patterns onto the dynamical prediction data. The idea of PDS is similar to statistical prediction using indices of large-scale patterns. The detailed procedure is as follows.

Suppose the predictand and predictor field are $Y(t)$ and $X(\lambda, \phi, t)$, respectively. Here Y is a local observed precipitation and X model predicted variables. λ and ϕ

are longitude and latitude, respectively. The spatial pattern of the predictor field associated with the predictand can be expressed as:

$$C(\lambda, \phi) = \overline{Y(t)X(\lambda, \phi, t)} \tag{15.6}$$

and

$$\hat{C}_i = CW_i \quad W_i(\lambda, \phi) = \begin{cases} 1 & \text{inside window} \\ 0 & \text{outside window} \end{cases}$$

The overbar denotes the time mean for the hindcast period. The window W specifies the positions of the spatial patterns of the predictor field. Having obtained the patterns ($\hat{C}_i$), a local predictand (the corrected prediction) can be obtained by projecting the patterns to the predictor variables of the model predicted data, as in the following equation:

$$Y_C(t) = \frac{1}{k}\sum_{i}^{k}\left(a_i\left\{\sum_{\lambda,\phi} C(\lambda, \phi)W_i(\lambda, \phi) \times X(\lambda, \phi, t)\right\} + b_i\right) \tag{15.7}$$

The regression coefficients (a, b) are obtained by minimizing the error variance of Y using the hindcast prediction data. By applying this technique in a cross-validative manner, one can obtain an independently corrected forecast ($Y_i(t)$) for a particular ith window. The most important procedure of the PDS method is the selection of optimal windows. For this purpose, we generate a large number of corrected predictions corresponding to the windows by moving the position and changing the size. The window sizes changed are from 30° longitude × 20° latitude (the minimum size) to 120° longitude × 50° latitude (the maximum size). The optimal windows are selected by comparing the temporal correlation skill of corrected forecasts for corresponding windows with a double cross-validation procedure (Kaas *et al.*, 1996). The final corrected forecast is not determined by a single pattern with the highest cross-validated correlation skill but the ensemble mean of several corrections with several different patterns. The correlation coefficient of each pattern is divided into several categories based on the statistical significance of the correlation between observation and corrected forecasts. We use 6 categories whose lower bounds of significance level are 99.9%, 99%, 97%, 95%, 92.5%, and 90%. Among the 6 categories, only the patterns in the category with the highest significance level are used. If there are five patterns in the first category, the final correction is made by the composite of five corrections based on those patterns. In this case, $k = 5$ in equation (15.7). If there is no pattern in the first category then the patterns of the next category are used, and so on. For the correction of predicted precipitation, the predictor variables used here are precipitation and 850-hPa temperature.

It should be noted that the corrections of prediction toward observation, based on both the SVD and PDS methods, lead to a loss of variability in absolute magnitude. Thus, it may be necessary to apply some sort of inflation [method] to the adjusted field. The most common method of inflation is to multiply the adjusted values by the ratio between the standard deviation of the observations and that of the adjusted values. In the present study, the inflation factor has been obtained by

combining the common method of inflation and the weighting factor considered by Feddersen *et al.* (1999) and used by Kang *et al.* (2004).

15.5.2 Predictability after error correction

The error correction method introduced above has been applied to the SNU predictions here, and the applicability of the method to seasonal prediction is examined based on this single model's results. It has then been applied to the other models in the next section. Before making the correction, we examined how well the SNU model reproduces the EOF modes of precipitation variability over the globe. Figure 15.9(a) shows the first eigenvector of observed summer mean precipitation, which explains 24.3% of the total variance, and Figure 15.9(c) is the predicted counterpart, explaining 39.0% of the total variance. Both figures are characterized by an east–west seesaw pattern between the anomalies in the tropical central Pacific and Indonesian subcontinent, although the model centers are shifted to the east. Other noticeable differences include sign differences in the subtropical western Pacific and the Indian Ocean eastward of 60°E. The poor performance of the model in those regions has already been mentioned in the previous section. The time series associated with the eigenvectors, shown in Figure 15.9(e), vary in a similar way and are related to El Niño/Southern Oscillation (ENSO) SST anomalies. The difference between the model and observed eigenvectors in the subtropical western Pacific and Indian Ocean is due to a failure of the model to simulate the responses of ENSO SST anomalies.

The second eigenvector of the observed summer mean precipitation, shown in Figure 15.9(b), explains 15.7% of the total variance. The model counterpart, shown in Figure 15.9(d), shows that the model reproduces the western Pacific center but with a much weaker amplitude. It also produces anomalies in other regions in the Pacific and Indian Ocean that are somewhat different from observation. However, the similarity between the time series associated with observed EOF modes and the corresponding time series of predicted modes provides hope for error correction in the predicted field. The error correction has been completed using equation (15.5) and the SVD modes. The two leading SVD singular vectors (not shown) are very similar to the corresponding EOF eigenvectors shown in Figure 15.9. This similarity could be expected from Figures 15.9(e) and (f), where the two time series of the observed and predicted modes vary almost simultaneously, indicating that the two EOF modes are coupled to each other. The first four SVD modes are used for the correction. The fifth and higher modes consist of small-scale patterns and explain a small fraction of the variance. The sum of the four modes accounts for 41.2% of the total variance.

Figure 15.10(a) shows the spatial distribution of the correlation coefficient between observations and the corrected seasonal predictions based on the SVD method. The correlation coefficients of corrected predictions are replaced by those without correction, if the former is smaller than the latter. Those locations are in the central tropical Pacific, where the correlation coefficient of the original prediction

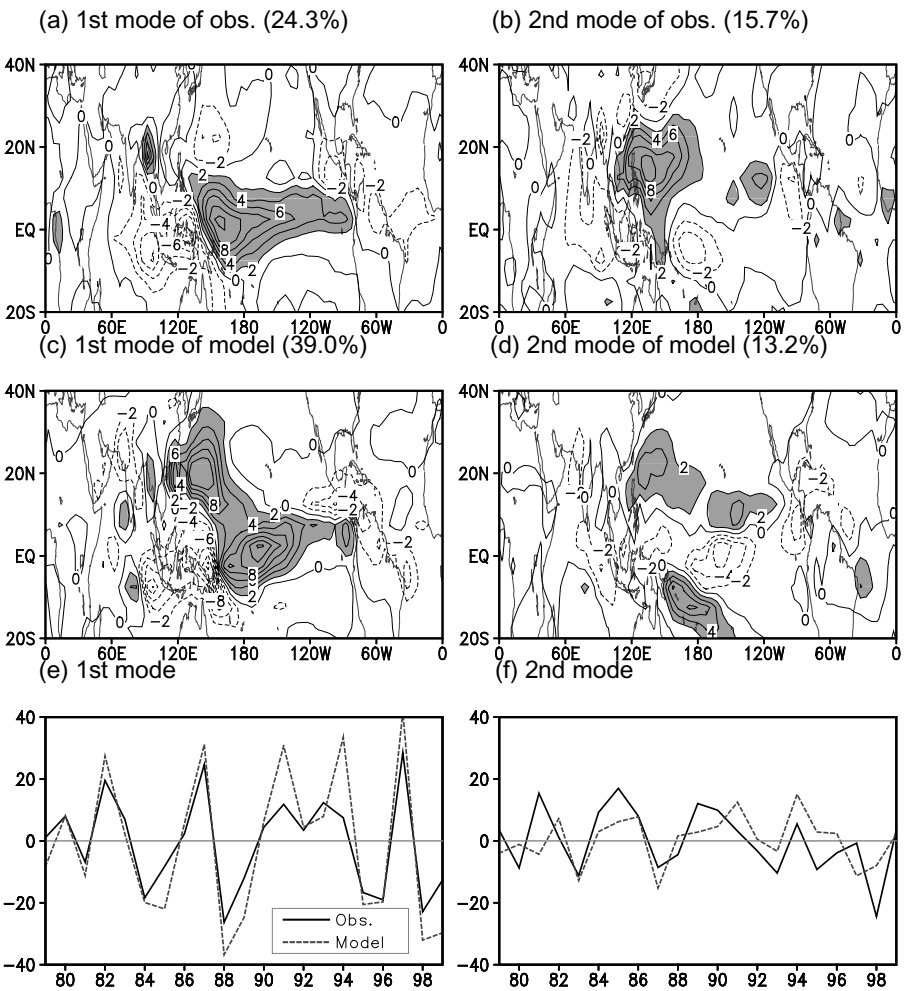

Figure 15.9. EOF modes of the observed and simulated ensemble mean precipitation. (a) and (b) are the observed first and second eigenvectors and (c) and (d) the simulated counter parts. (e) and (f) are the time series associated with the eigenvectors. Solid and dashed lines indicate the observed and simulated time series, respectively.

(Figure 15.3) is already very large. Clearly, in most of the regions, the predictability is greatly enhanced by statistical correction. The enhancement of predictability is particularly pronounced in the western Pacific where the prediction skill is negative without correction (Figure 15.5(f)) but has relatively large positive values after correction. The correlation skill of the corrected prediction based on PDS is shown in Figure 15.10(b). The double cross-validation procedure is applied to obtain the correlation skill. In the tropics, both correction methods produce similar results. In the subtropics and extratropics, however, the PDS method has a superior ability to correct errors, particularly in the western Pacific.

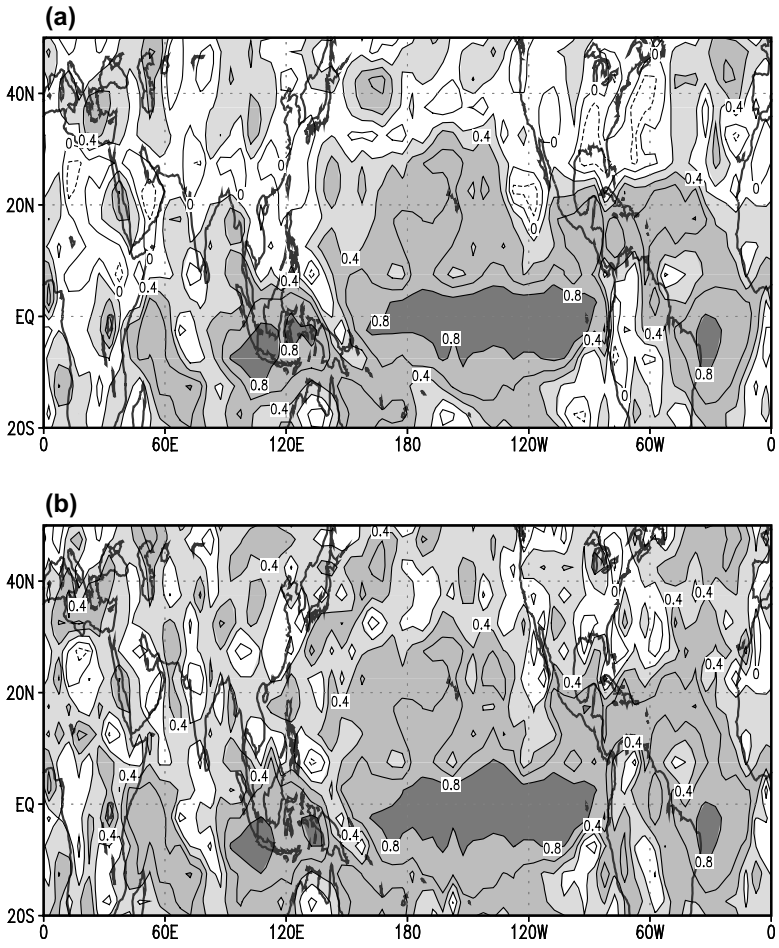

Figure 15.10. As in Figure 15.5 except the predicted precipitation of the SNU SMIP after correction of the systematic error using (a) SVD and (b) PDS.

The prediction skill of monsoon precipitation is shown in Figure 15.11 in terms of the spatial pattern correlation between the observed and predicted fields of each year for the monsoon domain of 20°S–30°N and 40°–160°E. In the figure, the open bar indicates the pattern of correlations without correction, and the shaded and black bars indicate those with the corrections based on the SVD and PDS methods, respectively. The predictability is greatly enhanced by the corrections for most of the years. The 21-year averages of correlation values are 0.24 for the prediction without correction, and 0.37 and 0.42 for the predictions with the SVD and PDS correction methods, respectively. Since the PDS method exhibits a better performance than the SVD method, hereafter all corrections are made based on the PDS method.

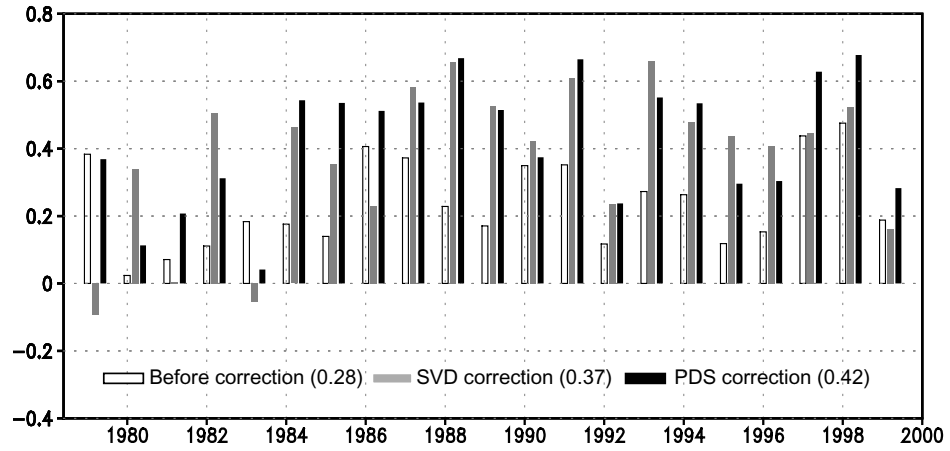

Figure 15.11. Pattern correlation coefficients between the observed and predicted precipitations of the SNU SMIP before (open bar) and after the bias correction by the SVD (gray shaded bar) and PDS (black shaded bar) over the monsoon region (40°–160°E, 20°–30°N).

15.6 MULTIMODEL POTENTIAL PREDICTABILITY

There are several ways of combining the multimodel outputs. The simplest way is a composite. The basic idea of a multimodel composite is that the errors of the individual models can cancel each other out. However, the multimodel composite may not be necessarily better than the best single model. The superiority condition of the multimodel composite to the best simple model is given here. After normalizing all anomalies with respect to their corresponding variance, the skill score S (here defined as $S = 1 - (V(error)/V(obs))$ can be expressed as:

$$\left.\begin{aligned} S_S &= 2R - 1 \\ S_M &= 2R_M - r_M \end{aligned}\right\} \tag{15.8}$$

Where S_S is the skill score of a single model and R is a correlation coefficient between the observation and the single model S_M is the skill score of a multimodel composite, $R_M = 1/N \sum_{i=1}^{N} R_i$ is the mean correlation skill of the N models used in the multimodel composite, and $r_M = 1/N^2 \sum_{i=1}^{N} \sum_{j=1}^{N} r_{ij}$ is the mean of inter-model correlations r_{ij}. The above equation indicates that the multimodel composite has its best skill when several of the best models are chosen to maximize R_M and the models are least dependent on each other to minimize r_M. In reality, the multimodel composite is not necessarily better than the single (best) model, mainly because of the inter-model dependency. The difference in the skills, $D = S_M - S_S$, can then be expressed as:

$$D = (1 - r_M) - 2(R - R_M) \tag{15.9}$$

The multimodel composite is better than a single model if D has a positive value. By

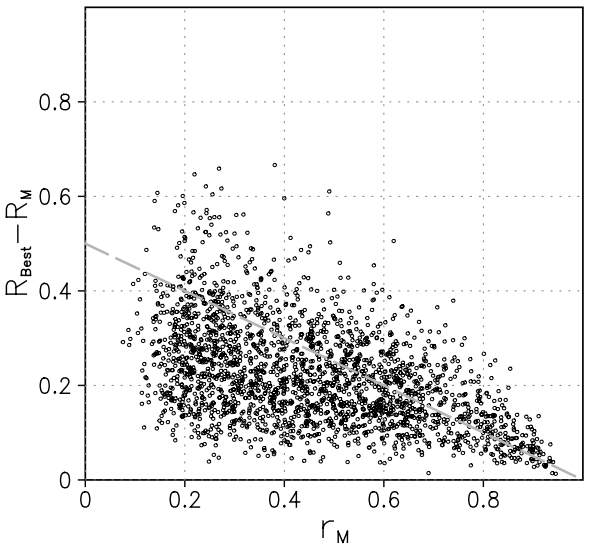

Figure 15.12. Distribution of r_M and $R_{\text{Best}} - R_M$, which are computed using five-model precipitation data. Each dot corresponds to each grid point. The thick dashed line indicates the threshold of superiority of the multimodel composite against the single best model. The multimodel composite is better than the single best model below this line.

denoting R_{Best} as the correlation skill of the best model, r_M and $R_{\text{Best}} - R_M$ at each grid point are computed using the five-model precipitation data – these values are plotted in Figure 15.12. The best model at each grid point is determined by comparing the prediction skills of the five models, obtained based on the 21-year hindcast data. In the figure, the multimodel composite is better than the single best model if the skills of the best model and the multimodel are in the region below the thick line. The figure indicates that the multimodel composite is better than the single best model at most of the grid points, although there are many exceptions.

There are several ways of combining the multimodel outputs other than as a composite. After Krishnamurti *et al.* (1999, 2000a), scientists have tried to improve weather and climate forecasts using an approach called the 'superensemble.' The skill of the superensemble method depends strongly on a post-processing algorithm for the multiple regression of multimodel solutions toward observed fields during a training period. For post-processing, the respective weights for individual models are generated using a multiple regression technique. The conventional superensemble forecast (Krishnamurti *et al.*, 2000a) can be constructed using the following formula.

$$S = \bar{O} + \sum_{i=1}^{N} a_i (F_i - \bar{F}_i) \tag{15.10}$$

Where F_i is the ith model forecast, $\bar{F}_i$ is the mean of the ith forecast over the training period, $\bar{O}$ is the observed mean over the training period, a_i is the weighting factor of

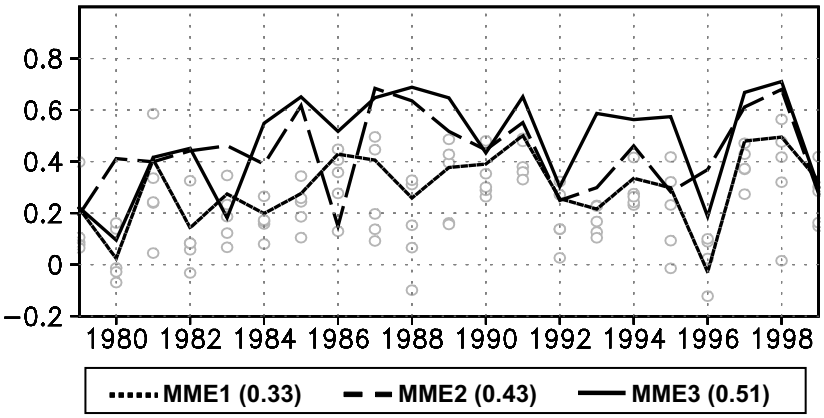

Figure 15.13. Time series of the spatial pattern correlations over the monsoon region (40°–160°E, 20°S–30°N) between the observed and the predicted precipitations of MME1 (dotted line), MME2 (dashed line), and MME3 (solid line). MME1, MME2, and MME3 are the multimodel predictions based on a simple composite, SVD based superensemble, and the composite of correction predictions by PDS, respectively. The open gray dots are spatial pattern correlation values of individual models.

the ith model, and N is the number of forecast models involved. The design of an optimal weighting function for a long-term forecast is the key to the development of a multimodel superensemble system. Here, the weighting factors are obtained based on the SVD method proposed by Yun *et al.* (2003).

In the present section, the multimodel predictions are a combination of three methods: a simple composite (MME1), the superensemble (MME2), and the composite of model predictions after each model prediction corrected by the statistical PDS method (MME3). It has been mentioned that the superensemble method is also applied to the predictions after error correction. However, the superensemble in this case does not provide better skill compared with the composite of the corrected predictions. This may be because of double fitting to the observation: the first fit of the prediction to the observation for the correction and the second fit for the superensemble.

The spatial pattern correlations over the monsoon region for 1979–1999 were obtained by using MME1, MME2, and MME3, and are plotted in Figure 15.13. As shown in Figure 15.6(b), the composite is not always better than the best individual model prediction, but the average skill of the composite is comparable to that of the best individual model. Therefore, the choice of a multimodel composite prediction will generally be a safe one since we do not know the best model for the prediction. On the other hand, the superensemble skill (MME2) appears, with a few exceptions, to be better than that of the best individual model. However, as shown in the previous section, the prediction skill of individual models after error correction is usually much better than that of the raw prediction. The correlation skill of MME2 appears to be comparable to that of the best individual model after correction. The

composite of corrected predictions (MME3) usually has a superior correlation skill than any of the corrected individual models. The MME3, which is the best system among the prediction systems used here, produces a 21-year average correlation skill of 0.51 for the monsoon summer prediction, which is statistically significant. The correlation skills in other regions and other seasons must be different, and their usefulness should be examined separately. In conclusion, dynamical monsoon seasonal prediction requires a multimodel system with statistical post-processing, which needs further research efforts.

15.7 COUPLED MODEL PREDICTABILITY

In the previous sections, seasonal predictability was investigated using AGCM simulations with prescribed observed SST conditions. However, a real operational prediction should use predicted SST as a boundary condition of model integration. The methods of SST prediction currently being used are a persistence model, ocean–atmosphere coupled models, and various statistical models. As indicated in the introduction, however, the tier-2 system (AGCM simulation with prescribed SST) has limits in simulating correctly the atmospheric response to local SST anomalies in the region of active ocean–atmosphere interaction (Wang *et al.*, 2004a). As in Wang *et al.*, the local ocean–atmosphere relationships in the tier-1 and tier-2 systems are examined here, before showing the real seasonal predictability of tier-1 systems.

In contrast to a commonly accepted view that a warmer SST produces more precipitation in the tropics, Wang *et al.* (2004a) showed that observed summer mean precipitation over the tropical western Pacific is negatively correlated with the local SST and atmospheric feedback to the ocean is an important mechanism for determining the western Pacific SST. This atmospheric feedback mechanism is not included in the tier-2 system. As a result, the tier-2 system produces incorrect precipitation anomalies over the western Pacific, as seen in Figure 15.3. Figure 15.14(a) shows the lead-lag relationship (correlation) between the pentad mean rainfall and SST averaged over the western Pacific of 5°–30°N, 110°–150°E for the summer season. The observed relationship, shown with a black line, indicates that rainfall leads the negative SST anomaly with a lead time of about 10 days. Such a relationship may be due to the reduction of solar radiation that comes with more cloud and the increase of surface fluxes associated with an increase of surface wind. This observed relationship is reasonably well simulated with a prototype ocean–atmosphere coupled model – the AGCM coupled with an ocean mixed layer. The mixed layer model used here is a slap model with a fixed 50 m depth and the SST is controlled only by the surface heat fluxes. On the other hand, the tier-2 AGCM simulations show that the rainfall has a weak positive correlation with the SST. The AGCM used for the two experiments is the same (SNU AGCM), and the results strongly suggest the use of an ocean–atmosphere coupled model for the correct prediction of summer rainfall over the western Pacific. We notice that for the winter season, the winter mean precipitation is positively correlated with the SST

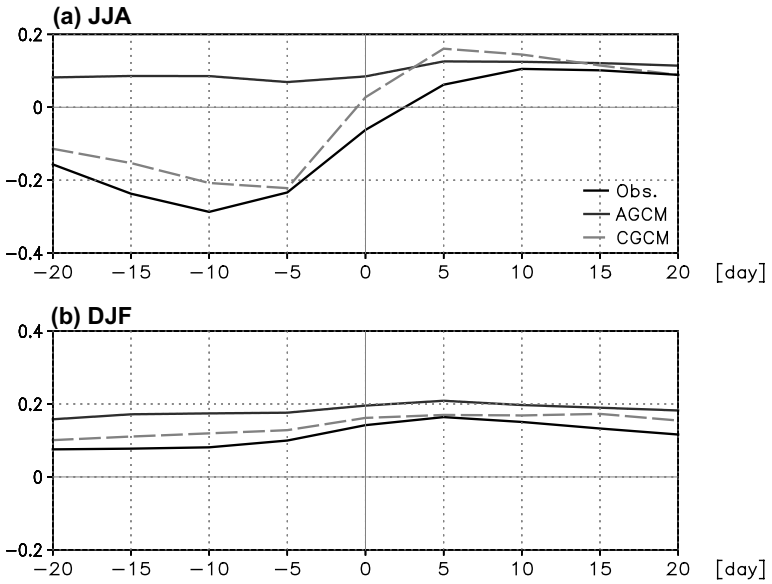

Figure 15.14. Lead-lag correlation coefficient between pentad rainfall and SST averaged over the western North Pacific (5°–30°N, 110°–150°E) for June/July/August (*upper panel*; 31–48 annual pentad) and December/January/February (*lower panel*; 1–12 and 68–73 pentad). The black solid line denotes the observed correlation coefficients between pentad CMAP and weekly OISST data during 1982–1999; the dotted line denotes AGCM (1950–1999); and the gray dashed line is for CGCM (25 years), respectively.

and that the tier-2 system can mimic the rainfall–SST relationship in the western Pacific (Figure 15.14(b)). The seasonal dependency of atmosphere–ocean feedback deserves further research.

The local rainfall and SST relationship during the summer was further examined using a fully coupled ocean–atmosphere model and the relationship compared with those of observations and AGCM alone (Figure 15.15, color section). The coupled model used here is the one developed at the Climate Environment System Research Center of SNU which uses the SNU AGCM coupled with a GFDL MOM2 ocean model and the ocean mixed layer model developed by Noh and Kim (1999). Figure 15.15 shows the distribution of local correlation coefficients between the summer mean precipitation and SST at the same grid point for the 21-year observations of 1979–1999 (Figure 15.15(a)), the AMIP AGCM simulation for 1950–1999 (Figure 15.15(b)), and the 25-year simulation of the coupled model (Figure 15.15(c)). Over the ENSO region, all three figures show that the summer mean precipitation is highly positively correlated with local SST, indicating that the atmosphere responds directly to the SST in the region. Over the western tropical Pacific and extratropical Pacific, on the other hand, the observed relationships are well reproduced by the coupled model, but are quite different (having a different sign) from those of the AGCM, again indicating that coupled ocean–atmosphere processes are important for simulating the summer rainfall over the regions.

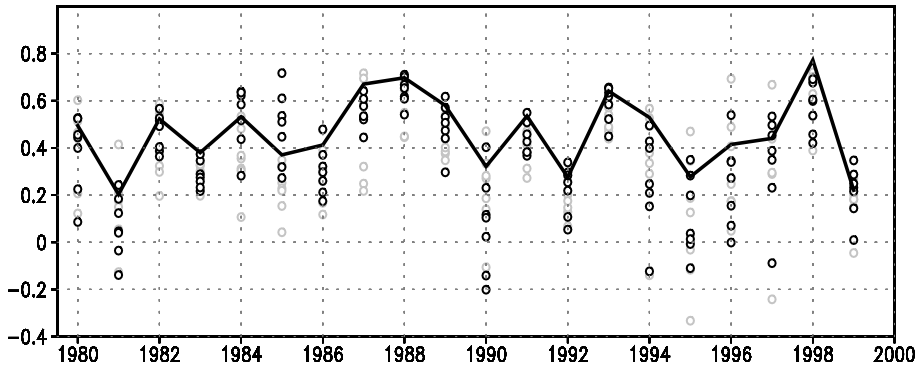

Figure 15.18. The interannual variation of the averaged value of pattern correlation of the individual DEMETER models before (gray) and after (black) the bias correction over the monsoon region. The thick solid line is the spatial pattern correlation of the multimodel composite after the correction (MME3).

The coupled model produces precipitation anomalies in a similar manner as observed. But it does not guarantee a high prediction skill, which can be achieved only if its SST prediction is reasonably good. We now examine the prediction skill of tier-1 systems using the seven coupled ocean–atmosphere models participating in the DEMETER project, listed in Table 2. Figure 15.16 (color section) shows the correlation skills of summer mean SST for the individual models and the multimodel ensemble over the globe. All models have a relatively high correlation skill over the tropical Pacific and a relatively low correlation skill in the extratropical oceans. The correlation skill of the multimodel composite, shown in Figure 15.16(a), is higher than those of individual models in most of the regions and is particularly high (over 0.8) in the tropical Pacific. The prediction skills for precipitation of the coupled models, shown in Figure 15.17 (color section), are relatively high in the tropical Pacific but poor in other regions. The skill of the multimodel composite (Figure 15.17(a)) is similar to that of the best model. As expected, the tier-1 systems produce slightly better prediction skills over the western Pacific compared with the negative correlation skills that the tier-2 systems produce in the region.

The year-to-year variations of spatial pattern correlation for the monsoon region, between the predicted and observed precipitation, are shown in Figure 15.18. Shaded and dark circles indicate the correlation values of raw and corrected predictions, respectively. A statistical correction based on the PDS method improves the correlation skill in most cases. The MME3 multimodel ensemble method (composite of the corrected predictions), shown to be the best method among the several multimodel ensemble methods treated in Section 15.5, is now applied to the DEMETER predictions. The solid line in the figure shows year-to-year variations of the spatial pattern correlation between the observed and the MME3 precipitation for the monsoon region. The 21-year average of the MME3

correlation values is 0.47. This value may represent the best prediction skill of summer monsoon precipitation that we can achieve at present.

15.8 SUMMARY AND CONCLUDING REMARKS

This chapter reviewed the present status of state-of-the-art dynamical seasonal prediction systems and demonstrated a possible improvement to the predictions based on statistical correction and a combination of several independent predictions. In particular, the seasonal predictability of summer mean precipitation over the Asian monsoon–western Pacific region was assessed by using the 21-year hindcast predictions of five models for 1979–1999. The five models consisted of the operation seasonal prediction models of the Japan Meteorological Agency (JMA), Korea Meteorological Administration (KMA), National Aeronautical Space Agency (NASA), National Centers for Environment Prediction (NCEP), and Seoul National University (SNU). The historical prediction data were produced as part of the CLIVAR/Seasonal Prediction Model Intercomparison Project II (SMIP II). In this experiment, the SST boundary conditions during the prediction period were prescribed with observed SSTs, and thus the potential predictability was assessed. The potential predictabilities of individual models and a multimodel ensemble system were shown by various methods including the signal-to-noise ratio, based on the analysis of variance and anomaly correlations. In addition to the potential predictability of the tier-2 systems, the real seasonal predictabilities of tier-1 systems were examined based on the coupled model predictions of the DEMETER project.

The signal-to-noise ratio of seasonal mean precipitation over the monsoon region is lower than that of other tropical regions. In addition to a lot of noise, all tier-2 models produce large systematic errors in the Asian monsoon region, particularly in the western Pacific. As a result, all models exhibit very poor correlation skill over the monsoon region. The model composite prediction does not help to improve the correlation skill. For the subtropical western Pacific and the Atlantic Ocean, all models and their composites show correlation skills with relatively large negative values. The negative skill in the western Pacific is due to model bias, where the external response has a large systematic error. Recently, Wang *et al.* (2004a) suggested that the poor simulations of precipitation over the western Pacific are due to the tier-2 prediction system, where the atmosphere is forced by the prescribed SST, but in nature the ocean–atmosphere coupled processes are active and atmospheric feedback to the ocean, which is missing in the tier-2 approach, is important in the western Pacific.

To correct the model bias, statistical methods based on the SVD and a PDS method were developed and applied to individual model predictions. It has been shown that statistical correction is effective in enhancing predictability, particularly for the Asian monsoon–Pacific region, where a large model bias is included in the forced signal (Kang *et al.*, 2004). The enhancement of predictability is particularly pronounced in the western Pacific where the correction skill is negative without correction but has relatively large positive values after correction. It has been

shown that point-wise correction is generally better than the correction with leading SVD modes.

The errors of individual models can be reduced by combining them into multimodel predictions. A theoretical case was made for the superiority of a multimodel composite over the single best model. It was shown that the multimodel composite has a good skill when several best models are chosen and the models are least dependent on each other. Intermodel dependency is a crucial problem at present for multimodel prediction, whose performance is better than that of the single best model. The seasonal predictability of multimodel ensemble prediction was assessed by using several multimodel methods including simple composite, superensemble, and composite of corrected individual predictions. It has been shown that a reasonably good dynamical seasonal prediction can be achieved when we use the multimodel composite after applying statistical correction to individual predictions.

The multimodel seasonal prediction based on coupled models was also examined by using the hindcast prediction data of DEMETER. It has been anticipated that the tier-1 system will often produce large systematic errors, particularly in the extratropical region, compared with those of the tier-2 system with the prescribed SST anomalies obtained from the same tier-1 system. However, this study shows that the tier-1 system can predict summer mean precipitation better, particularly over the monsoon–western Pacific region, where the atmosphere–ocean feedback is active. The DEMETER tier-1 systems appear to produce better prediction skills over the globe compared with tier-2 systems with predicted SST (not shown). The spatial correlation skill of the DEMETER MME3 for summer mean precipitation, the best among the multimodel ensemble systems treated in this chapter, is 0.47 over the monsoon region. These values may represent the best summer mean precipitation prediction skills that we can achieve with dynamical prediction models at present.

15.9 ACKNOWLEDGEMENTS

The authors would like to express their appreciation to their SNU colleagues and students, Dr. Jong-Sung Kug, Ms. Kyung Jin, Mrs. Jin Ho Yoo, Doo-Young Lee, and Ho-Yong Jeong, and Dr. June-Yi Lee at NASA/GSFC, who contributed their work to the materials presented in this chapter. The present study was supported by the Climate Environment System Research Center at Seoul National University and the Korea Meteorological Administration.

Part Five

16

Extending the historical record by proxy

S. Clemens

16.1 INTRODUCTION

Instrumental records of meteorological and oceanographic variables critical to understanding monsoon variability extend back in time only a century or so. These historical data allow evaluation of seasonal to interdecadal variability in the Asian monsoon system. Extending the historical record through development of terrestrial and marine-based proxies is a useful means of better understanding monsoon variability across all timescales – seasonal to tectonic. The utility of developing monsoon records from geological archives lies in the fact that monsoon variability during older intervals takes place in the context of boundary conditions very different from the modern system. For example, Earth-orbital variations lead to cyclical changes in the amount of radiation received at a given latitude over time (Figure 16.1(a)). In addition to climate change driven by these orbital radiation cycles, the Earth has undergone large, and currently unexplained, changes in the extent of its high-latitude ice sheets; changes of such magnitude that global sea level ranged from +6 m to −120 m relative to the present day within the last few hundred thousand years (Figure 16.1(b)). On the same timescales occurred large changes in the concentration of atmospheric greenhouse gasses such as carbon dioxide and methane as well as atmospheric dust content (Petit *et al*., 1999; Rea, 1994) indicating a very close coupling between the atmosphere, hydrosphere, cryosphere, and biosphere. Superimposed on the long-term orbital and glacial–interglacial climate cycles are abrupt climate events which occur on centennial to millennial timescales (Figure 16.2(a)). Evaluating the role of the monsoon in the context of climate change on these differing timescales provides important information on how the ocean, atmosphere, and terrestrial components of the Earth's climate system interact as a function of changing boundary conditions.

Monsoon circulation is defined on the basis of seasonal changes in regional patterns of wind and precipitation. These primary meteorological variables are

B. Wang (ed.), *The Asian Monsoon*.

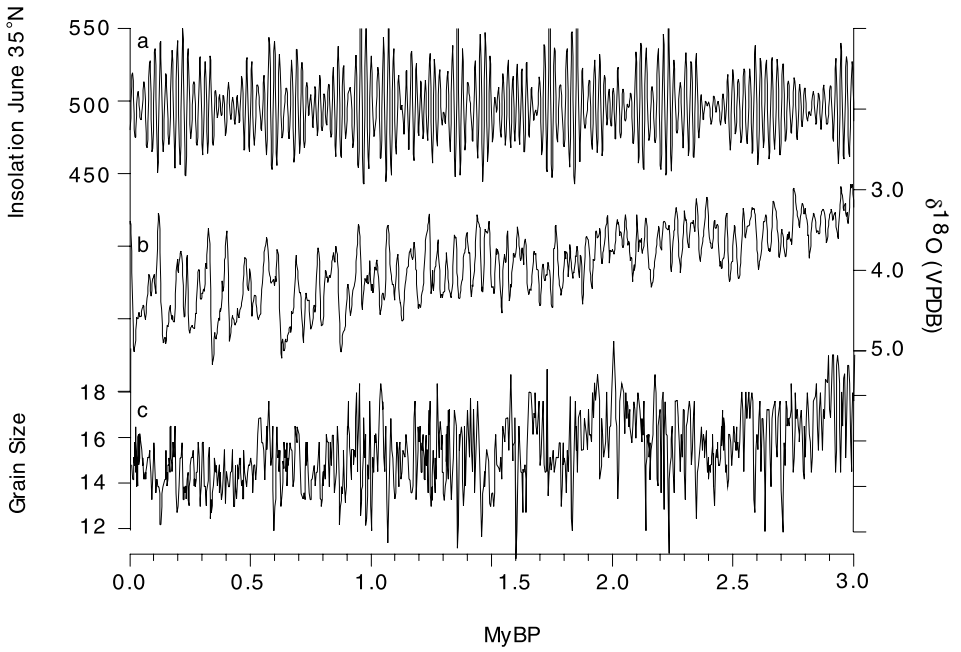

Figure 16.1. Climate change at orbital timescales; external forcing, internal boundary conditions, and monsoon climate change over the past three million years. (a) Time series of incoming solar radiation at 35°N in June (Laskar *et al.*, 1993); (b) the marine oxygen isotopic record of benthic foraminifera, a proxy for changes in global ice volume and sea level; and (c) lithogenic grain size, a proxy for changes in Indian summer monsoon wind strength (Clemens, 1998; Clemens *et al.*, 1996). Radiation variability driven by changes in the precession and obliquity of the Earth's orbit about the Sun is the primary external forcing for climate change at the 10^4 to 10^5-year timescale. Large-scale change in the amount of water stored as high-latitude ice (the Pleistocene ice ages) is a fundamental internal boundary condition associated with climate change on this timescale. Within the time frame of the past 3 million years, the oxygen isotopic (δ^{18}O) composition of benthic foraminifera are an excellent proxy for changing terrestrial ice volume; the maximum amplitude in the younger part of the record corresponds to ~126 m of sea level change (high values correspond to increased terrestrial ice and low sea level). The grain size of lithogenic material transported to the Arabian Sea is a proxy for changes in the strength of Indian summer monsoon winds; large grains correspond to increased circulation. The δ^{18}O record is a composite of three records from the equatorial Pacific Ocean, Vema 19–30 (Shackleton and Pisias, 1985), Ocean Drilling Program (ODP) Site 677 (Shackleton *et al.*, 1990), and ODP 846 (Shackleton *et al.*, 1995b). Isotope data available from *http://delphi.esc.cam.ac.uk/*.

not directly preserved in the geological record. However, they greatly influence the physics, chemistry, and biology of the associated ocean and land surface processes, aspects of which are readily preserved in geological archives such as deep-sea sediments, terrestrial sediments, corals, lakes, bogs, cave deposits, tree rings, and glaciers. As such, these geological archives preserve indirect, or proxy, measures of

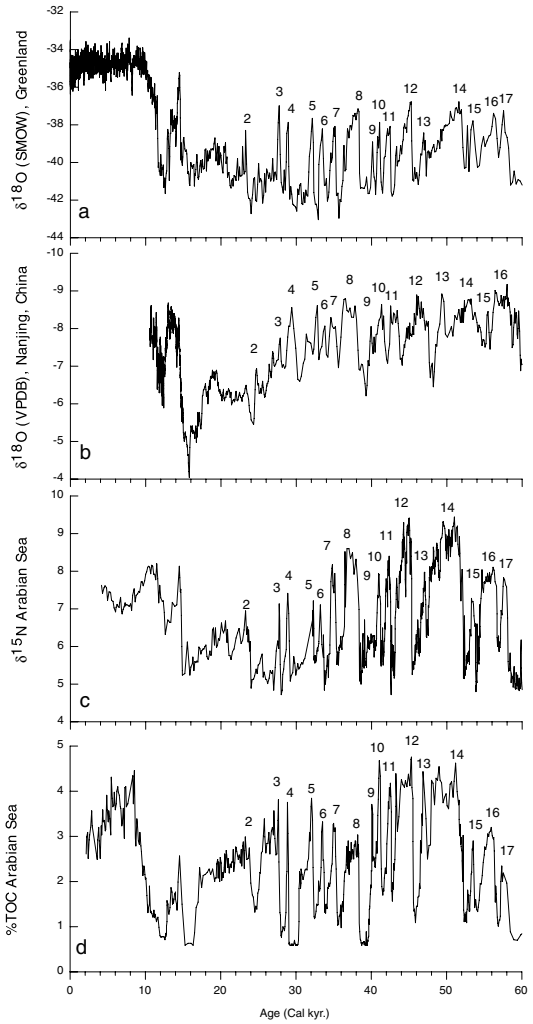

Figure 16.2. Climate change at millennial timescales. Superimposed on longer timescale climate change (Figure 16.1) are abrupt changes that occur at the centennial to millennial timescale. At the millennial timescale climate variability is thought to be largely internal to the climate system; there is no known source of solar variability at the millennial timescale. (a) The Greenland Ice Sheet Project 2 (GISP2) $\delta^{18}O$ record, a proxy for temperature change over Greenland (Dansgaard *et al.*, 1993). (b) Hulu Cave $\delta^{18}O$, a proxy for Asian summer monsoon strength as it impacts the oxygen isotopic composition of stalagmite calcite near Nanjing, China (Wang *et al.*, 2001b). (c) Total organic carbon, a proxy for the strength of the Indian summer monsoon as it impacts the strength of the oxygen minimum zone on the Pakistan Margin (Schulz *et al.*, 1998). (d) $\delta^{18}O^{15}N$, a proxy for the strength of the Indian summer monsoon as it impacts the productivity driven denitrification on the Oman Margin (Altabet *et al.*, 2002). Within the error of estimated ages, the numbered interstadial (warm) events are thought to be coincident, indicating strengthened Asian summer monsoons in association with abrupt warming events in the northern Atlantic region.

past monsoon variability. Depending on the proxy, changes in monsoon climate can be resolved on timescales ranging from seasonal (e.g., laminated sediment sections, corals, snow pits) to tectonic (e.g., marine and terrestrial sediment sections). Here we discuss paleomonsoon history at centennial (10^2 years) to tectonic (10^6 years) timescales. In terms of paleoclimate signals, monsoon circulation is exceptionally strong, often leaving a clear and dominant signal in the geological record. However, additional processes, sometimes unrelated to monsoon variability, may also influence the chemical, physical, and biological composition of these geological archives. For example, diagenesis, a post-depositional chemical and/or physical alteration of the archive, may take place under certain conditions, masking the monsoon signal. Such alterations are not always readily evident. For these reasons, paleoclimatologists often employ a multiproxy approach to evaluating climate variability preserved in the geological record (e.g., Clemens and Prell, 2003). The strategy is to develop a number of different proxies; each is physically, chemically, or biologically linked to changes in monsoon circulation but impacted differently by non-monsoon processes. Statistical techniques are then employed to extract the variance common to all the proxies, suppressing the variance unrelated to monsoon circulation. The common variance is taken as the best estimate of monsoon variability.

Another aspect of primary importance in evaluating paleomonsoon variability from geological archives is the development of accurate age models (chronostratigraphies) such that the time history of climate change recorded at different geographic locations can be compared with confidence. This is critical for evaluating temporal leads and lags in the system documenting how the monsoon initiates or responds to changes in other parts of the climate system. Sufficiently accurate chronostratigraphies are generally available for studies at the tectonic and orbital-scale. Sufficiently accurate chronostratigraphies are generally lacking for studies of abrupt climate change on millennial and finer scales although significant progress is being made in this area and a great deal of useful information is derived from the geological record in spite of current chronostratigraphic limitations (Sarnthein *et al.*, 2002).

The rapid increase in global-scale, instrument-based meteorological and oceanographic data has fueled tremendous advances in the understanding of modern monsoon variability and interactions among the various monsoon subsystems. However, the spatial coverage of paleomonsoon records is limited (Voelker, 2002). Thus, from a paleomonsoon perspective, the subsystems within the Asian monsoon have largely been studied independently both in terms of geographic variability and timescales of variability. While the number of high-quality paleomonsoon records is increasing, the coverage remains insufficient to fully assess regional differences in paleomonsoon circulation.

16.2 INTERNAL AND EXTERNAL FORCING

Potential mechanisms driving changes in the ancient monsoon can be broadly categorized as 'internal' or 'external'. External forcing is solar in origin, including

insolation cycles associated with eccentricity (100,000-year cycle), obliquity (41,000-year cycle), and precession (23,000-year cycle) of the Earth's orbit about the Sun (Hays *et al*., 1976; Imbrie *et al*., 1993; Imbrie *et al*., 1992; Imbrie *et al*., 1984; Laskar *et al*., 1993). External forcing at the suborbital scale is thought to be associated with sunspot, solar magnetic polarity, and cosmic ray activity (Beer *et al*., 2000; Bjorck *et al*., 2001; Bond *et al*., 2001; Solanki, 2002; Soon *et al*., 2000; Svensmark, 1998). In terms of radiation amplitude, the 23,000 and 41,000-year Earth-orbital cycles are very large, altering the incoming radiation at a given latitude by the order of 10% relative to present-day levels. Irradiance variability associated directly with the orbital eccentricity cycle and suborbital solar phenomenon are very much smaller, of the order of 0.1% of the present day (Beer *et al*., 2000; Imbrie *et al*., 1993; Solanki, 2002; Soon *et al*., 2000). Paleoclimate records indicate that the ancient monsoon does exhibit variability at timescales where the external radiation forcing is very small and, as well, exhibits orbital-scale variability significantly different in amplitude and phase from that of the primary radiation forcing at the 23,000 and 41,000-year cycles. This indicates that the ancient monsoon, like the modern, is strongly influenced by climatic feedback mechanisms internal to the climate system.

Potential internal forcing mechanisms include any interactions among the atmosphere, ocean, lithosphere, cryosphere, and biosphere which alter the seasonal pressure gradients between land and the ocean, thus altering monsoon circulation. Broadly defined, these internal mechanisms, or boundary conditions, range from the El Niño/Southern Oscillation (ENSO) system to plate tectonics.

16.3 TECTONIC VARIABILITY

The collision of the Indian continent with Asia in the early to middle Eocene, approximately 50 Myr (million years) ago, set the stage for what we experience as modern Asian monsoon circulation. Prior to collision, fossil evidence from the sedimentary basins of eastern China indicates that inland basins were characterized by arid environments whereas nearshore basins were under the influence of arid/humid climate cycles, most likely driven by eustatic changes in sea level. After collision and the initiation of plateau uplift in the late Eocene ($\sim$40 Ma), the inland basins came under the influence of humid or alternating arid/humid climates indicating the initiation of summer monsoon circulation penetrating the Asian interior (Chenggao and Renaut, 1994). While these data provide information regarding the initiation of monsoon circulation in terms of timing, they don't provide information regarding changes in circulation strength. Geological data indicating changes in monsoon strength between the late Eocene ($\sim$40 Ma) and late Miocene ($\sim$10 Ma) are currently lacking. However, general circulation model (GCM) experiments indicate that retreat of the Paratethys seaway and increased elevation and lateral extent of the Tibetan Plateau play important roles in strengthening monsoon circulation (Fluteau *et al*., 1999; Kutzbach *et al*., 1993; Prell and Kutzbach, 1992). Translating these model results into time histories of monsoon circulation awaits reliable estimates for the timing the Paratethys retreat and

plateau uplift (Fort, 1996). The long-term history of these events are recorded in land sections as well as the deep-sea fans off India and south-east Asia. These fans, including the Indus Fan and the Bengal Fan, are the largest on Earth, having accumulated and stored the erosional products of the Himalaya and the Tibetan Plateau for the past 50 Myr (Clift *et al.*, 2002; Curray *et al.*, 2003).

Reasonably well-dated geological records related to monsoon evolution have been generated for the last 11 Myr. These records, coupled with an array of evolving GCM experiments have begun to unravel the evolution of the monsoon as it relates to tectonism since the Miocene. A number of increasingly sophisticated GCM experiments examining the impact of plateau uplift on monsoon circulation have been generated since the late 1980s (deMenocal and Rind, 1993; Kutzbach *et al.*, 1989; Kutzbach *et al.*, 1993; Prell and Kutzbach, 1992; Prell and Kutzbach, 1997; Ruddiman and Kutzbach, 1989). These experiments are designed to understand the sign and magnitude of regional changes in surface variables (temperature, precipitation, precipitation minus evaporation, and runoff) as they relate to the elevation and lateral extent of the Himalayan–Tibetan Plateau complex and to changes in orbital forcing. Broadly, uplift enhances both the Asian summer and winter monsoon systems with regions south and east of the plateau becoming more humid and regions north and west of the plateau becoming more arid (Kutzbach *et al.*, 1993).

For south-east Asia in particular, the effects of solar radiation on the hydrological cycle are greatly amplified by increased plateau elevation and lateral extent (Prell and Kutzbach, 1997). Model results indicate that runoff in south-east Asia, a parameter which is readily recorded in marine deposits, is highly sensitive to uplift. For a plateau approximately 1/4 its modern elevation/extent, summer monsoon runoff in south-east Asia increases by 42% between intervals of radiation minima and maxima over orbital timescales. For a plateau of modern elevation/extent runoff increases by 118% between intervals of radiation minima and maxima. This represents a 180% increase in range, attributed to uplift from 1/4 to full modern plateau elevation/extent.

The impact of uplift on the wind regime in the north-west Arabian Sea is also important in terms of monitoring monsoon variability using the geological archive. The exceptionally strong south-west winds off Oman support open ocean and divergent upwelling which, in turn, drives high regional productivity. This upwelling-induced productivity signal is preserved in underlying sediments, serving as a proxy for the strength of summer monsoon circulation. GCM simulations by Prell and Kutzbach (1992) found that the south-west summer monsoon wind regime was not firmly established until plateau elevations reached $\sim$1/2 that of the modern plateau.

The effects of plateau uplift differ for central Asia and the east Asian Loess Plateau. The importance of these regions in defining the history of monsoon circulation derive from the geological record of eolian (wind-derived) deposition which created the Loess Plateau. These sediment sections are composed of an eolian red clay deposit overlain by alternating loess–soil horizons creating a combined sequence

of the order of 300 m thick. The loess is transported to the plateau from the north by winter monsoon winds. The interbedded soils are formed in situ by pedogenesis during periods of enhanced summer monsoon circulation (An, 2000). These processes have resulted in an extraordinary and well-dated archive of monsoon circulation. GCM simulations indicate that uplift results in drying within central Asia, the eolian source region, and increased precipitation within the east Asian region of eolian deposition (see An *et al.*, 2001, figure 3). These dynamics resulted in the development of the Loess Plateau with an areal extent of 500,000 km^2.

Given model results indicating strong hydrological sensitivity to tectonic uplift, one can use the well-dated geological record to piece together the monsoon response to uplift since the Miocene. A diverse multiproxy set of geological records indicate that monsoon circulation as we know it today, with strong summer and winter monsoons, initiated in a near threshold-like manner sometime between 9 and 7 Myr ago. The planktonic foraminifer *Globigerina bulloides* as well as the radiolaria *Actinomma spp* and *Collosphaera sp* are diagnostic of cold, nutrient-rich waters not found in the tropics except within upwelling regimes. In the Arabian Sea, off the coast of Oman, these upwelling indicators increased significantly, from near zero values, between 9 and 7 Myr ago indicating the initiation of strong south-west monsoon winds over the Arabian Sea (Kroon *et al.*, 1991; Nigrini and Caulet, 1991; Prell *et al.*, 1992). The record of lithogenic material transported from the Ganges/Brahmaputra River systems to the Bay of Bengal reflect erosion and runoff from the Himalayan–Tibetan orogen. Accounting for the effects of changing sea level on sediment transport (a signal unrelated to monsoon circulation), these records indicate a strong increase in precipitation, erosion, and runoff $\sim$9 Myr ago (Prell and Kutzbach, 1997). Changes in the carbon isotopic composition of soil carbonates indicate paleoecological changes in local plant cover while changes in the oxygen isotopic composition of soil carbonates reflect the isotopic composition of local rainfall. The combined shifts in the oxygen and carbon isotopic composition of soil carbonates in Pakistan at $\sim$7.4 Myr indicate a dramatic ecological shift marking the strengthening of the Asian monsoon system (Quade *et al.*, 1995; Quade *et al.*, 1989). In eastern Asia, the onset of red clay deposition at the base of the Loess Plateau ranges from 8.3 to 7.6 Myr ago depending on location, reflecting the onset of aridity in central Asia and monsoon circulation in east Asia (An *et al.*, 2001; An, 2000; Ding *et al.*, 1998b; Qiang *et al.*, 2001; Sun *et al.*, 1998). Simultaneously, eolian dust deposition peaked downwind of Asia in the North Pacific (Rea *et al.*, 1998).

Taken together, this diverse and independently dated set of proxy climate records indicate increasing seasonality across southern and eastern Asia, as would be predicted by the onset of strong summer and winter monsoon regimes in response to tectonic uplift and extension of the Tibetan Plateau. Evidence for the initiation of normal faulting in Tibet, suggesting that the plateau increased significantly in elevation at approximately 8 ± 3 Myr ago (Molnar *et al.*, 1993), is consistent with the inferred link between the proxy monsoon records and uplift based on GCM results.

16.4 EARTH-ORBITAL VARIABILITY

Orbital-scale paleoclimate studies enjoy a distinct advantage relative to tectonic and suborbital scale studies in that the external (solar) forcing function is accurately known (Laskar, 1999; Laskar *et al.*, 1993). Knowledge of the solar forcing function and the climate response allows one to evaluate the physics of the system using time series analytical approaches. In this regard, there are two important prerequisites. The time series records must have fine enough sample resolution to resolve orbital-scale cycles and chronostratigraphies sufficient to (1) compare variability in cores distributed across broad geographic regions and (2) compare the climate response to variability in external solar forcing. A number of continuous monsoon proxies meeting these requirements are available with lengths spanning the last few hundred thousand to a few million years (Wang *et al.*, 2005).

16.4.1 The Indian summer monsoon

Within the late Pleistocene interval, the two dominant boundary conditions influencing global climate change are variations in solar radiation and global ice volume (Figure 16.1). Figure 16.3 (color section) illustrates the cross-spectra of the Indian summer monsoon relative to insolation and global ice volume over the past 350,000 years (350 kyr). Earth-orbital periods associated with precession of the equinoxes (23-kyr period) and obliquity of the Earth's axis (41-kyr period) dominate the insolation and monsoon spectra whereas the ice volume spectrum is dominated by 100-kyr variance associated with the great ice ages. To a large extent, these 100-kyr ice age cycles are pervasive in paleoclimate records illustrating the global climatic impact of northern hemisphere ice volume. In this regard, the Indian summer monsoon is somewhat of an exception, being dominated largely by variability in the 41 and 23-kyr spectral bands. Much of the orbital-scale monsoon work has focused on understanding monsoon variability within the context of 41 and 23-kyr insolation cycles and changes in global ice volume, the two most obvious external and internal boundary conditions.

Since the mid-1980s a large variety of physical, chemical, isotopic, and biological proxies have been developed to evaluate the variability of the Indian summer monsoon using cores from the Arabian Sea (Almogi-Labin *et al.*, 2000; Altabet *et al.*, 1999; Altabet *et al.*, 1995; Anderson, 1991; Anderson *et al.*, 1992; Anderson and Prell, 1991; Anderson and Prell, 1993; Beaufort, 1996; Budziak *et al.*, 2000; Clemens *et al.*, 1996; Clemens and Prell, 1990; Clemens and Prell, 1991a; Clemens and Prell, 1991b; Clemens and Prell, 2003; Clemens *et al.*, 1991; Murray and Prell, 1991; Murray and Prell, 1992; Overpeck *et al.*, 1996; Prell, 1984a; Prell, 1984b; Prell and Kutzbach, 1987; Prell *et al.*, 1990; Prell and Van Campo, 1986; Reichart *et al.*, 1997; Reichart *et al.*, 1998; Rostek *et al.*, 1997; Shimmield and Mowbray, 1991; Shimmield *et al.*, 1990; Sirocko *et al.*, 1993; Street-Parrott and Harrison, 1984; van Campo *et al.*, 1982; Weedon and Shimmield, 1991). A subset of this proxy array have been shown to possess similar variance at orbital periods, indicating that the summer monsoon signal is not masked by unrelated physical, chemical, or biological processes (Budziak *et al.*, 2000; Clemens and Prell, 2003; Clemens

et al., 1991; Reichart *et al.*, 1998). This internally consistent subset of proxies are from cores spanning the past 250 to 400 kyr and is used to assess processed driving monsoon variability at the orbital timescale.

If summer monsoon variability were controlled only by changes in solar forcing over the Tibetan Plateau (sensible heating), monsoon maxima would be in phase with maximum northern hemisphere summer radiation (maximum obliquity and minimum precession; June 21 perihelion) (Figure 16.4). This would be consistent with atmospheric GCM results indicating that the summer monsoon is strongly influenced by changes in sensible heating at the latitude of the Tibetan Plateau (An *et al.*, 2001; Prell and Kutzbach, 1987; Prell and Kutzbach, 1992). Similarly, if summer monsoon variability were controlled only by high-latitude changes in global ice volume, then monsoon maxima should be in phase with minimum ice volume as suggested by atmospheric GCM results indicating weakened monsoons at times of increased global glaciation (Prell and Kutzbach, 1992; Prell and Kutzbach, 1997). Assuming equal sensitivity to both, the phase of the summer monsoon response would fall between northern hemisphere summer insolation maxima and global ice volume minima at both the obliquity and precession periods. The measured monsoon phase response does not entirely fit this simple conceptual model (Figure 16.4). Within each 41-kyr obliquity cycle, the Indian summer monsoon is strongest at the same time northern hemisphere summer insolation is strongest, ~8 kyr before global ice volume reaches a minimum (Clemens and Prell, 1990; Clemens and Prell, 2003; Clemens *et al.*, 1991). Within each 23-kyr precession cycle, the Indian summer monsoon is strongest ~8 kyr after northern hemisphere summer insolation is strongest, ~3 kyr after global ice volume reaches a minimum (Clemens and Prell, 1990; Clemens and Prell, 2003; Clemens *et al.*, 1991; Reichart *et al.*, 1998).

Two explanations have been put forth for these phase relationships. Reichart *et al.* (1998) suggest that the Indian summer monsoon is sensitive to late summer insolation forcing (August or September perihelion), resulting in longer although not necessarily stronger summer monsoons. Clemens *et al.* (2003, 1991), suggest that the observed phase relationships can be explained by the combined influence of sensible heating over the Tibetan Plateau (modulated by changes in ice volume) and the timing of latent heat export from the southern subtropical Indian Ocean. They hypothesize that orbital configurations characterized by warm southern hemisphere summers followed by cold winters (i.e., increased seasonality) precondition the ocean to release large amounts of latent heat at the onset of the Indian summer monsoon. This latent heat is transported to Asia in the low-level, cross-equatorial flow and released over Asia during precipitation, strengthening the monsoon. Only recently have fully coupled ocean–atmosphere GCM's become available that are capable of testing these hypotheses (Liu *et al.*, 2004; Liu *et al.*, 2003). Such experiments are in the planning phase.

16.4.2 The east Asian summer and winter monsoons

Proxy records of both summer and winter monsoon variability have been developed from the loess–paleosol sections of the east Asian Loess Plateau. Grain size and flux

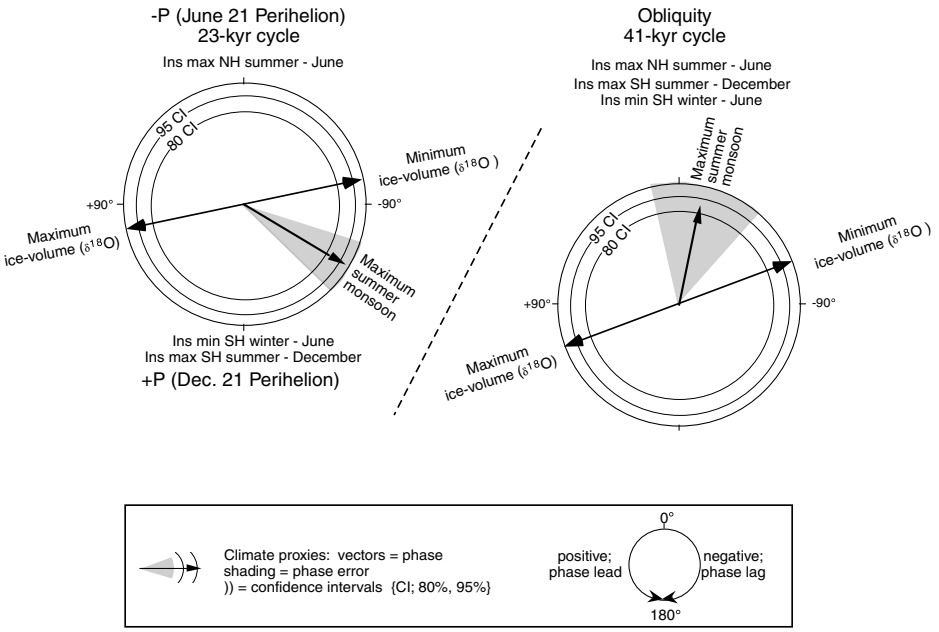

Figure 16.4. Indian summer monsoon phase wheels for precession and obliquity. Phase wheels display coherence and phase relationships among climate proxies and internal/external boundary conditions. The zero phase is set at June 21 perihelion for precession and at maximum obliquity; both correspond to maximum northern hemisphere summer insolation. The phase difference between an orbital component and a climate proxy is plotted as a vector whose angle is measured clockwise (positive, lag) or counterclockwise (negative, lead) from the zero point. The error associated with the phase is illustrated by the shaded area centered on the vector. The length of the vector indicates the degree of coherence between the climate proxy and the orbital parameter (below the 80% CI, between the 80% and 95% CI, or >95% CI). Text at 0° and 180° indicate seasonal insolation relationships associated with each orbital configuration for the southern hemisphere and northern hemisphere. 180° on the precession phase wheel and 0° on the obliquity phase wheel are characterized by warm southern hemisphere summers (December) followed by cold southern hemisphere winters (June), hypothetically ideal configurations for exporting latent heat from the southern Indian Ocean to Asia during the northern hemisphere summer monsoon. At both the precession and obliquity bands, summer monsoon maxima occur between the theoretical times of maximum latent heat export and global ice volume minima indicating that the monsoon is more sensitive to these internal boundary conditions than to direct sensible heating of the Asian Plateau.

measurements have been used extensively as winter monsoon proxies (An *et al.*, 1991a; Ding *et al.*, 1994; Liu *et al.*, 1999; Xiao *et al.*, 1995) while magnetic susceptibility, ^{10}Be, and chemical weathering indices have been used as summer monsoon proxies (An *et al.*, 1991b; Shen *et al.*, 1992). The coarse age models for these records is derived from the geomagnetic polarity reversal timescale, which is based on radio-

metric dating methods. The finely tuned age models are derived by correlation to the marine $\delta^{18}O$ record of global ice volume via astronomical tuning, assuming that loess deposition is in phase with the growth and decay of the northern hemisphere ice sheets (Ding *et al.*, 1995; Ding *et al.*, 2002; Shackleton *et al.*, 1995a). As such, there is no means of assessing changes in the timing (phase) of monsoon dynamics measured from the loess records relative to evolving glacial boundary conditions or insolation forcing; the monsoon response is phase locked to ice volume by virtue of the age model. Ding *et al.* (2002) address this issue, noting that the loess grain size and marine $\delta^{18}O$ record are more similar to one another over the past 1.8 Myr than prior to this time (see also Liu *et al.*, 1999). They suggest that the assumption of a phase lock between loess and $\delta^{18}O$ may not be appropriate prior to 1.8 Myr ago. This issue notwithstanding, the loess record provides an excellent means of assessing paleomonsoon variability. As summarized in An *et al.* (2001), proxies derived from the red clay and loess–soil sequences indicate that both the east Asian summer and winter monsoons strengthened between 3.6 and 2.6 Myr ago. After 2.6 Myr ago, the east Asian summer monsoon began to weaken while the winter monsoon strengthened. Within the interval of the large-amplitude 100-kyr ice age cycles, the summer and winter monsoon proxies are out of phase indicating an alternation between winter and summer monsoon dominance with stronger winter monsoons and weaker summer monsoons during glacial intervals and stronger summer monsoons and weaker winter monsoons during interglacial intervals (An *et al.*, 2001; An, 2000).

A large variety of east Asian monsoon proxies from marine cores indicate similar dynamics, strengthened winter monsoons and weakened summer monsoons during glacial intervals of the late Pleistocene. However, these inferences are largely based on visual inspection of monsoon proxies relative to the marine $\delta^{18}O$ record; very few present phase analyses of summer and winter monsoon variability at specific orbital frequency bands. When viewed in the context of spectral (amplitude and phase) analyses, the relationship between monsoon strength and ice volume is more complicated than that inferred from visual inspection alone. Beaufort *et al.* (2003) analyze a coccolithophore (*Florisphaera profunda*) proxy for winter monsoon productivity in the Sulu Sea. They report that strong winter monsoons are in phase with maximum ice volume at the 100-kyr band and lag maximum ice volume by 40° (~5 ky) in the obliquity band (Figure 16.5). The in-phase relationship at the 100-kyr period is consistent with the east Asian loess and marine records described previously. However, the significant lag at the 41-kyr obliquity period associated with the obliquity of the Earth's axis suggests that winter monsoon strength at this period responds to both high-latitude ice volume as well as decreased insolation during northern hemisphere winter. The *profunda* record has very little 23-kyr amplitude, the variance in this region of the spectrum is shifted toward the 29-kyr period. This 29-kyr period is interpreted as a heterodyne (beat) between ENSO-induced winter monsoon variance at the eccentricity frequency and insolation-induced variance at the precession frequency ($1/100 \pm 1/23 = 1/19$ and $1/30$; where frequency $= 1/$period) (Beaufort *et al.*, 2003; Beaufort *et al.*, 2001). Similarly, the charcoal record from the same core, used as a proxy for decreased summer monsoon precipitation (drought-induced fires), indicates 19

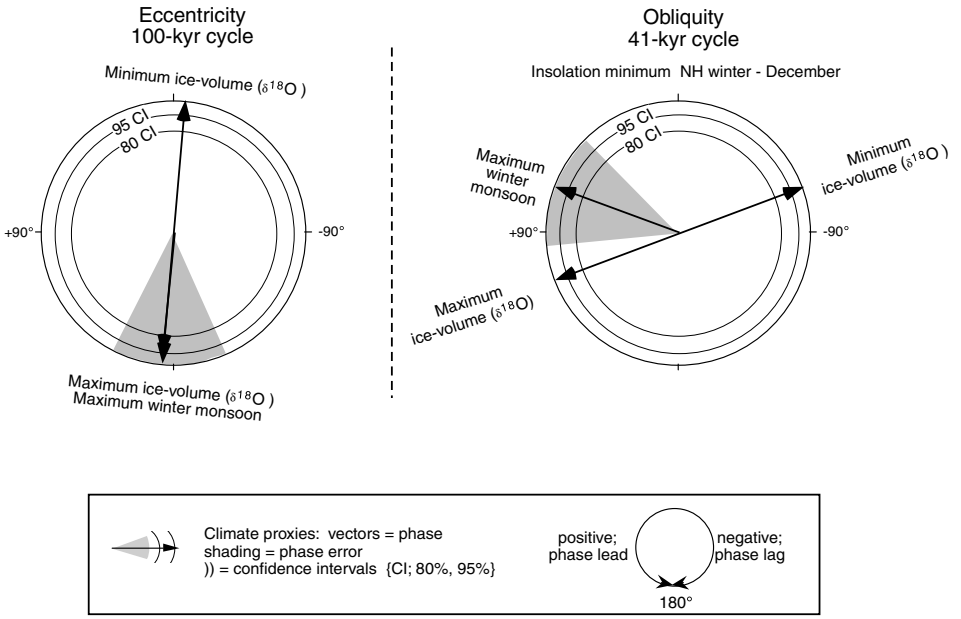

Figure 16.5. Asian winter monsoon phase wheels for eccentricity and obliquity. See Figure 16.4 caption for explanation of phase wheel construct. For the obliquity band, this record from the Sulu Sea indicates that the strongest winter monsoons are driven by a combination of decreased insolation heating over Asia during winter (0° on the obliquity phase wheel) and northern hemisphere ice volume maxima (111° on the obliquity phase wheel). The eccentricity band has no direct insolation forcing although eccentricity of the Earth's orbit modulates the amplitude of precession. At this band, the strongest winter monsoons coincide with times of greatest ice volume.

and 29-kyr periods (Beaufort *et al.*, 2003). These are also taken to represent an ENSO influence on the strength of the summer monsoon. This interpretation of the 19-kyr and 29-kyr periods stems from the work of Federov and Philander (2000) indicating strengthened and/or more frequent El Niño's during interglacial intervals. Monsoon pollen records from the southern hemisphere (north of Australia) also indicate significant amounts of variance at the 30-kyr period suggesting that this signal is pervasive throughout the Indonesian region (Kershaw *et al.*, 2003).

Morely and Heusser (1997) report phase estimates for a pollen-based proxy record of summer monsoon variability off Japan. They report a summer monsoon phase of -136° for the precession band, within error, the same as the Indian summer monsoon estimates from the Arabian Sea.

This sparse number of records analyzed in terms of amplitude and phase indicate that the summer and winter monsoons of the late Pleistocene ($\sim$0–400 ka) respond to processes beyond summer season radiation forcing over the Asian

continent and glacial–interglacial changes at the 100-kyr cycle. The Indian summer monsoon records indicate that latent heat export from the southern hemisphere Indian Ocean may also be an important feedback strengthening the monsoon low over Asia. The in-phase response with the summer monsoon index off Japan suggests that this feedback may be strong enough to drive the timing of the east Asian summer monsoon as well. These few records also suggest the beginning of a regional pattern in which monsoon records from outside the western Pacific Warm Pool (The Arabian Sea and off Japan) have variance concentrated at the primary (41 and 23-kyr) orbital periods, whereas those from within the Warm Pool exhibit a combination of orbital and heterodyne periods linked to an additional ENSO influence.

16.5 CENTENNIAL AND MILLENNIAL VARIABILITY

Superimposed on the longer term orbital-scale variations are abrupt centennial and millennial-scale events during which climate changes from one state to another within decades or less, remaining so for hundreds to one or two thousand years (Figure 16.2). Records with sufficient temporal resolution to resolve these scales of variability are typically from within the latest Pleistocene interval, usually from within the last 60 kyr.

Centennial-scale variations have been reported in a limited number of highly resolved Indian and east Asian paleomonsoon records (Agnihotri *et al.*, 2002; Buehring, 2001; Neff *et al.*, 2001; Thompson *et al.*, 1997; von Rad *et al.*, 1999; Wang *et al.*, 1999b; Wang *et al.*, 1999c). These records indicate a periodicity in the range of 84–102 years as well as at ~210 years and are interpreted as a monsoon response to the ~88-year solar (Gleissberg) cycle and the ~205-year solar (de Vries or Suess) cycle. The issue is that measured short-term solar irradiance variations are of the order of 0.1% ($1.5\,Wm^{-2}$), seemingly too small to drive significant climate change. However, there is some suggestion of climate sensitivity to parts of the solar spectrum that have larger amplitude variability. For example, Beer (2000, 2002), and references therein, suggest the possibility that variability in the UV portion of the spectrum may influence climate via changes in ozone production and the radiation balance at high latitudes. Specific mechanisms by which the monsoon might respond to this forcing at centennial (and millennial) scales are unknown. Lack of theory in this regard is not unique to the monsoon system; it is common to the climate field in general. Thus, while paleoclimate data indicate significant variance at the centennial and shorter timescales typically associated with solar variability, no unifying theory exists linking the two (Benestad, 2002).

Millennial-scale variability, sometimes referred to as Dansgaard–Oeschger (DO) variability was first recognized in Greenland ice cores (Dansgaard *et al.*, 1993; Johnsen *et al.*, 1992) but is now known to occur globally (Leuschner and Sirocko, 2000; Voelker, 2002). DO variability is characterized by a 1,470-year cyclicity (Grootes and Stuiver, 1997; Hinnov *et al.*, 2002; Rahmstorf, 2003; Schulz, 2002; Yiou *et al.*, 1997) although it appears sometimes to be manifest in terms of

harmonics at periods of ~700 to ~775 years (Sarkar *et al.*, 2000; Wang *et al.*, 1999a) as well as ~3,000 and ~4,500 years (Alley *et al.*, 2001). Based on currently available records, DO variability is best expressed during marine isotope stage 3 (MIS 3) spanning the interval ~30 to 60 kyr before present but has been documented in older intervals as well (to 400 kyr BP) although at considerably lower amplitude (de Garidel-Thoron *et al.*, 2001; Oppo *et al.*, 2003).

The direct (solar) forcing for orbital-scale variability (10^4 years) is well known and the chronology is generally sufficient to evaluate leads and lags among system components as previously described. For DO variability, the forcing is uncertain and the chronology at this point in time is insufficient to assess leads and lags among system components measured at globally distributed sites, information that would be very useful in deriving the underlying physics of millennial-scale climate variability. For example, the Greenland ice core records are very well dated (by layer counting) from the present to 40,000 years ago whereas the marine records rely on less accurate radiocarbon-based chronologies within this interval. This discrepancy in age model reliability precludes direct analysis of phase among records from these archives, information that might implicate high or low-latitude processes as initiating these abrupt climate change events.

Rahmstorf (2003) recently analyzed well-dated Greenland ice core records, finding that the 1,470-year cycle is stable to within a few percent, suggesting that the initial forcing may be solar in origin. In this case, the large-amplitude DO events of MIS3 might be thought of resulting from a stochastic resonant response to low-amplitude solar forcing. The geographic origin of this amplified signal and its mode of global transmission are unknown although two schools of thought exist: (1) that the signal initiates in the high-latitude North Atlantic in response to changes in freshwater influx and is transmitted globally by atmospheric and deep-ocean thermohaline circulation (e.g., Ganopolski and Rahmstorf, 2001); or (2) that the signal initiates in the tropical Pacific ocean–atmosphere system via ENSO-like physics and is transmitted globally via changes in atmospheric circulation (e.g., Cane and Clement, 1999).

In the first case, millennial-scale monsoon variability is likely a downstream response to changes in the North Atlantic transmitted across Eurasia by changes in snow and ice cover (Ganopolski and Rahmstorf, 2001; Overpeck *et al.*, 1996) leading to weakened winter and strengthened summer monsoons during Greenland interstadial (warm) periods and visa versa, strengthened winter and weakened summer monsoons during Greenland stadial (cold) periods. This general phasing, stronger summer monsoons during Greenland interstadials, is supported by the radiometrically-dated Hulu Cave $\delta^{18}O$ record from eastern China (Wang *et al.*, 2001b). In this case, given sufficient chronologies, monsoon proxies would lag North Atlantic proxies by a small amount.

An ENSO-like mechanism initiating in the tropical Pacific may result in monsoon proxies leading North Atlantic proxies at the millennial timescale. In general, the modern summer monsoon weakens in association with El Niño conditions although the strength of this relationship varies on decadal timescales (Clark *et al.*, 2000a; Kumar *et al.*, 1999; Wang *et al.*, 2001a) and the Indian and east Asian

subsystems respond somewhat differently to ENSO variability (Wang *et al.*, 2003a; Wang *et al.*, 2001a). Extrapolating the El Niño/weak summer monsoon relationship to paleoclimate timescales, Stott *et al.* (2002) interpret salinity records from the western pacific warm pool as indicating stronger and/or more frequent El Niños (weaker summer monsoons) during Greenland stadials. Again, this overall phasing is consistent with the Hulu Cave record. However, if the initial trigger for millennial-scale climate change resides in the tropical ENSO system, then monsoon proxies should lead North Atlantic proxies.

Current chronologies are not reliable enough to differentiate the small lead and lag relationships associated with these two hypotheses. The best that can be said at this point is that within the limitations of current chronologies, strong summer monsoons are generally coincident with Greenland interstadials as indicated by proxy records from the Arabian Sea (Altabet *et al.*, 2002; Schulz *et al.*, 1998), South China Sea (Wang *et al.*, 1999a), Sulu Sea (Dannenmann *et al.*, 2003), and Philippine Sea (Stott *et al.*, 2002) as well as terrestrial cave and loess profiles from Asia (Ding *et al.*, 1999; Ding *et al.*, 1998a; Wang *et al.*, 2001b) (Figure 16.2). Improved ability to accurately date geological archives is important to unraveling the origin of millennial-scale climate variability, including the role of monsoon circulation. Advances are being made in this area with the goal of eventually placing new and existing paleoclimate records on common age scales sufficient to evaluate phase relationships among globally distributed proxy records. Sarnthein *et al.* (2002) provide a brief review of these issues and advances.

16.6 SUMMARY

Geological archives contain records of paleomonsoon variability with temporal resolution ranging from seasonal to tectonic. These records offer the ability to evaluate monsoon climate change under boundary conditions different from the present and within intervals of time well beyond the reach of the instrumental record.

At the centennial to millennial scale (10^2 to 10^3 years), proxy records of east Asian and Indian monsoon circulation indicate that the summer monsoon strengthens during times of abrupt warming in the North Atlantic region as recorded in the GISP2 ice core. However, age control is not yet sufficient to assess the detailed timing of changes in monsoon circulation relative to high-latitude warming. As such it is not possible to determine if monsoon circulation changes prior to, coincident with, or after changes in the North Atlantic climate. At this point, enhanced understanding of the dynamics involved come from documenting the geographic distribution of millennial-scale variability in terms of the system components involved (atmosphere, cryosphere, biosphere, surface, intermediate, and deep-ocean circulation).

At orbital timescales (10^4 to 10^5 years), the late Pleistocene Indian summer monsoon is dominated by variance in the obliquity (41-kyr) and precession (23-kyr) bands. For both bands, the strongest summer monsoons take place between times of minimum northern hemisphere ice volume and maximum latent

heat export from the southern hemisphere Indian Ocean. The late Pleistocene east Asian winter monsoon is dominated by variance in the eccentricity (100-kyr) and obliquity (41-kyr) bands. Within the eccentricity band, the winter monsoon is strongest during times of maximum ice volume. Within the obliquity band, the winter monsoon is strongest between times of ice maxima and insolation minima during northern hemisphere winter. In spite of strong solar forcing at orbital timescales, proxy records of the east Asian and Indian monsoon systems indicate changes in monsoon circulation are driven at least as much by changing internal boundary conditions as by direct solar forcing. Limited geographic coverage suggests that monsoon circulation in regions outside the Pacific Warm Pool appear to be dominated by variance more closely associated with orbital forcing whereas those from within the Warm Pool appear to be influenced by variance associated with ENOS-like dynamics as well.

At tectonic timescales (10^6 to 10^7 years), monsoon circulation varies as a function of changes in location/extent of seaways and the location/elevation of continental landmasses. Monsoon circulation initiated with the collision of India and Asia approximately 40 Myr ago. Modeling results suggest that strengthened summer season circulation (similar to that of the modern) initiated between 9 and 7 Myr ago, likely in response to the Tibetan Plateau having achieved approximately half its modern elevation and lateral extent. Further strengthening of the winter monsoon and weakening of the summer monsoon took place as glacial conditions increased over the past three million years.

17

Asian monsoons in the future

Akio Kitoh

17.1 INTRODUCTION: GLOBAL ASPECTS

Climate models (specifically, global coupled atmosphere–ocean general circulation models (GCMs)) are the most useful tools for projecting future climate changes and variations across time. Several scenario experiments for future climate projections have been done recently, in addition to the 1% per year CO_2 increase experiments commonly used by the modeling community. These recent simulations used the marker scenarios identified by the Intergovernmental Panel on Climate Change (IPCC) Special Report on Emission Scenarios (SRES; IPCC, 2000) and shared many common results, including an increase in global mean surface temperature, an increase in global mean precipitation, greater increase in surface temperatures over land than over ocean, more temperature increases at high latitudes than at low latitudes, and more temperature increases in the northern hemisphere than in the southern hemisphere. However, there are still discrepancies among the models in terms of the geographical distribution of precipitation changes.

In order to get an idea of the global-scale temperature and precipitation trend and its uncertainty, it may be useful to use the 1% per year CO_2 increase experiments of the second phase of the Coupled Model Intercomparison Project (CMIP2; Meehl *et al.*, 2000). Figures 17.1 and 17.2 show the global distribution trends of the annual mean surface air temperature and annual mean precipitation for the next 100 years, as calculated by 11 climate models using the 1% per year CO_2 increase scenario (Noda *et al.*, 2003). The two figures show the mean values for the 11 models (the model ensemble mean) and the standard deviations among the models in order to illustrate the uncertainty.

The ensemble mean temperature trend clearly illustrates the differences in surface temperature changes already mentioned. Specifically, the regions with warming of at least 5°C per 100 years are seen only in the northern high latitudes, and the maximum temperature rise is seen in the Arctic region where sea ice

B. Wang (ed.), *The Asian Monsoon*.

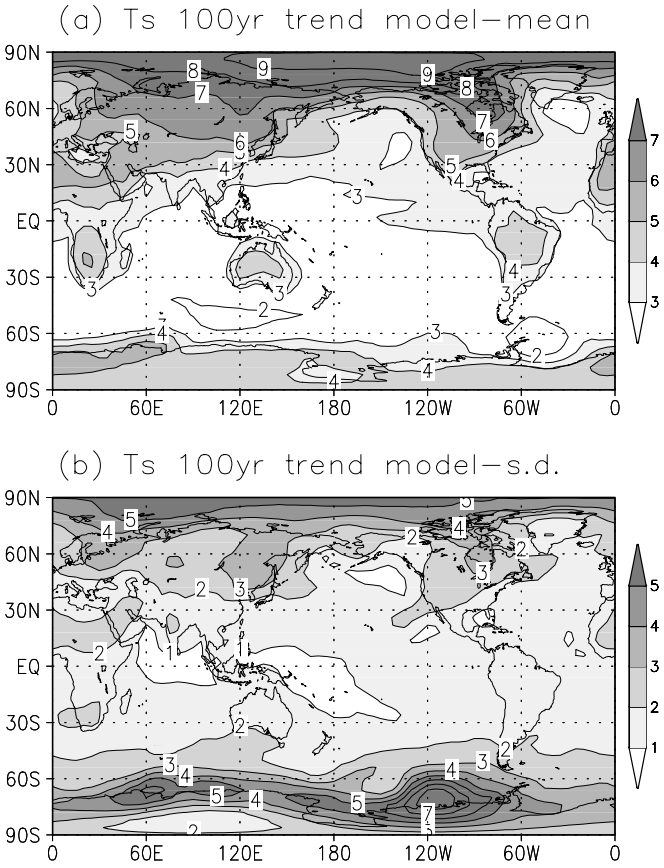

Figure 17.1. (a) Trend of the annual mean surface air temperature (°C/100 year) calculated as an ensemble mean of the 11 GCMs (CCC, CCSR/NIES, CSIRO, DKRZ, GFDL, HadCM, MPI, MRI, NCAR). Two different versions of the model are used for HadCM and MRI. (b) Standard deviation of the trend of the annual mean surface air temperature among 11 GCMs. After Noda *et al.* (2003).

reduction is eminent, according to the future climate projections. Over the Eurasian and North American continents, the temperature rise in the east is larger than in the west. It is thought that the temperature increase is larger over these regions due to a strong snow/ice–albedo feedback effect, because the snow line is located at relatively low latitudes (Noda *et al.*, 1996). The scatter among models was greater at higher latitudes than at lower latitudes, and in the southern hemisphere, the scatter was more pronounced around Antarctica.

The geographical distribution of predicted changes in annual mean surface temperatures by the end of the 21st century, as shown by the SRES-A2 and B2 scenario multimodel projections (IPCC, 2000), is quite similar to Figure 17.1. In these projections, the A2 and B2 storylines and scenarios reflect a very heterogeneous

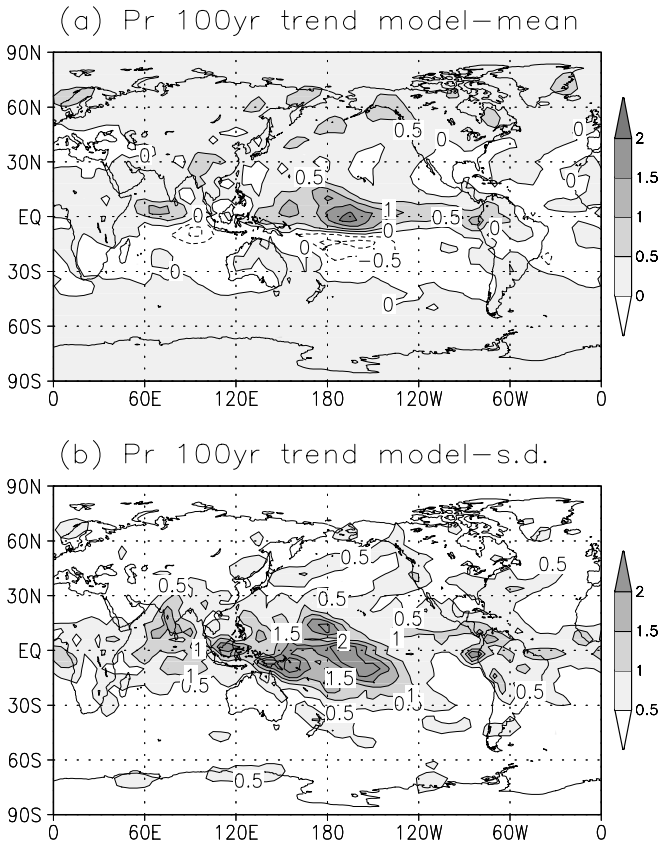

Figure 17.2. As in Figure 17.1 except for the annual mean precipitation (mm/day/100 year) After Noda *et al.* (2003).

world of self-reliance and preservation of local identities, and a world in which emphasis is on local solutions for economic, social, and environmental sustainability, respectively (IPCC, 2000). The average global mean surface air temperature increase is predicted to be 3.6°C over the next 100 years, but the increase over Asia is larger than the global average, and the increase over Japan in particular is 4–5°C (Noda *et al.*, 2003). Zhao *et al.* (2004) assembled the surface temperature projections averaged across east Asia (15°–60°E and 70°–150°E), using seven GCMs with various scenarios, and predicted that the surface temperature will increase between 3.4°C and 5.5°C by 2099.

The global annual mean precipitation is also increasing (Allen and Ingram, 2002), and large precipitation increases can be seen in the tropical Pacific (Figure 17.2). Trends of increasing precipitation in the equatorial Pacific and Indian Ocean and of decreasing precipitation in the subtropical South Pacific and South Indian Ocean are evident, but the scatter among models for these regions is

large. Over the Eurasian continent, the models predicted increased precipitation, with a larger increase to the south-east of the Tibetan Plateau. Over the Mediterranean region, precipitation was predicted to decrease.

The intermodel standard deviation of the projected precipitation trend is very large over the tropical oceans. The scatter is also large over India, which suggests caution in accepting the quantitative accuracy of Indian monsoon projections. It is evident that consistency among models is lower for precipitation than for temperature. Over the south Asia and east Asia regions the IPCC (2001) compared model consistency in the seasonal mean precipitation change, and found that models with the SRES-A2 scenario were consistent in showing increased precipitation in the summer months (June, July, and August), but were inconsistent in the winter months (December, January, and February).

One example of an MRI-CGCM2 simulation (Figure 17.3) showed changes in surface air temperature and precipitation for both the summer and winter months (Noda *et al.*, 2001; Ashrit *et al.*, 2005). An ensemble mean of the three-member SRES-A2 scenario simulations at the end of the 21st century (2071–2100) is compared with present-day simulations. The summertime temperature change is predicted to be large over dry regions in the Middle East and western China but relatively small over the Asian monsoon area. There is a minimal temperature increase over north-western India, where precipitation and soil moisture both increase. Precipitation increases over India, the Bay of Bengal, and south China through Japan, while it decreases over northern China. The increase in precipitation change over the arid area of the Persian Gulf/Pakistan and north-western India is in contrast to the decrease around the Caspian Sea to the north. In the winter, the simulated surface temperature change is large at high latitudes and over the Tibetan Plateau. There is also a large temperature increase over the Okhotsk Sea due to reduced sea ice cover. An increase in precipitation is seen over the Maritime Continent and is associated with intensified easterly trade winds from the western Pacific to the Indian Ocean.

17.2 SUMMER MONSOON

17.2.1 South Asian monsoon

Many climate model studies reported possible changes in the south Asian summer monsoon due to CO_2 increase. Although a few studies reported that the south Asian summer monsoon becomes weak or that there is no significant precipitation change (Zhao and Kellogg, 1988; Lal *et al.*, 1994, 1995; Lal and Singh, 2001), most models showed increases in both the seasonal mean precipitation and the interannual variability (Meehl and Washington, 1993; Bhaskaran *et al.*, 1995; Kitoh *et al.*, 1997; Giorgi and Francisco, 2000; Hu *et al.*, 2000a,b; Douville *et al.*, 2000a; May, 2002, 2004; Ashrit *et al.*, 2003; Meehl and Arblaster, 2003).

One of the earlier results (Figure 17.4) plotted the south Asian (5°–40°N, 60°–100°E) summer precipitation for $1 \times CO_2$ and $2 \times CO_2$ equilibrium experiments

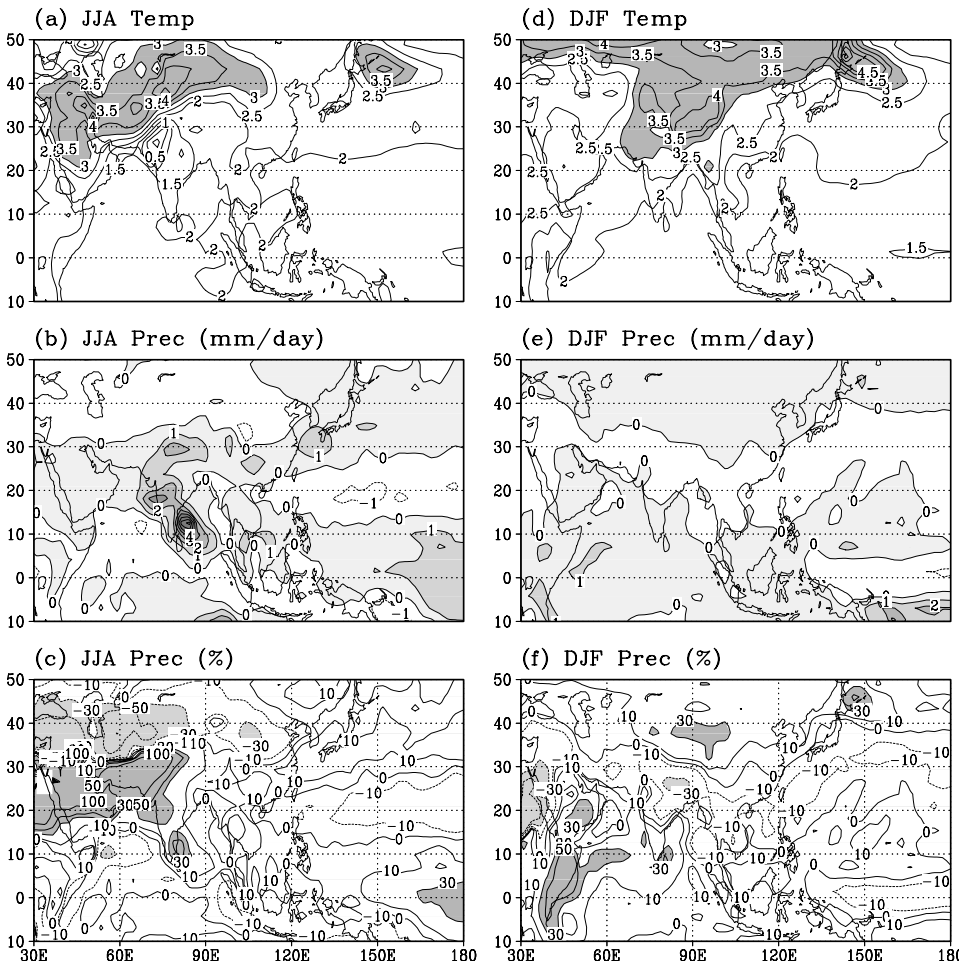

Figure 17.3. (a) JJA mean surface air temperature change between 2071–2100 and the present-day simulation (1971–2000) by the MRI-CGCM2. A three-member ensemble mean is shown with the SRES-A2 scenario. (b) JJA precipitation change. (c) JJA precipitation change as a ratio to the present value. (d–f) As in (a–c) except for DJF.

using the NCAR model (Meehl and Washington, 1993). Mean summertime precipitation increased 6.3% from 6.40 mm day^{-1} to 6.80 mm day^{-1}, while standard deviation (interannual variability) increased from 0.49 mm day^{-1} to 0.65 mm day^{-1}. Shown by the increase in both the mean value and standard deviation, the precipitation in wet years increased 11%; in dry years, the percentage changed slightly due to global warming. The researchers concluded that the precipitation increase is due to a larger increase of the Eurasian continental temperature than of the Indian Ocean temperature.

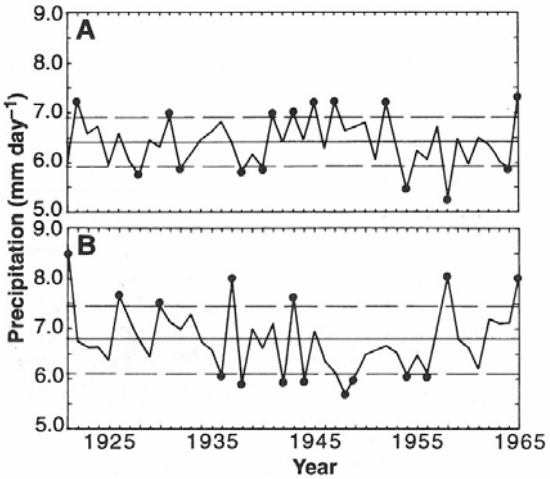

Figure 17.4. JJA mean precipitation in south Asia (60°–100°E, 5°–40°N) for (a) the control and (b) the $2 \times CO_2$ case of the NCAR model. Dashed lines indicate 1 standard deviation for each case.
Reprinted with permission from Meehl and Washington (1993) *Science*, **260**, 1101–1104. Copyright 1993 AAAS.

Using the 1% per year transient CO_2 increase experiments of the UKMO coupled model, Bhaskaran *et al.* (1995) found a 20% increase in the Indian summer monsoon precipitation at the time of CO_2 doubling. They concluded that the increase in precipitation is due to increased atmospheric moisture and increased land–sea temperature contrast. Also, from the 850 hPa wind system change, they found that monsoon circulation shifted to the north 10 degrees and was strengthened by 10%.

Kitoh *et al.* (1997) raised an issue about an apparent paradox between the south Asian summer monsoon's increasing precipitation and its decreasing circulation intensity. Figure 17.5 shows the two monsoon indices at the time of CO_2 doubling and quadrupling according to the MRI-CGCM 1 (Kitoh *et al.*, 1997): one is the all-India rainfall; the other is an averaged vertical zonal wind shear, which shows the difference in zonal wind between 850 hPa and 200 hPa, averaged over the region 40°–110°E, 5°–20°N (Webster and Yang, 1992). It is clear that the Indian summer monsoon precipitation increases with CO_2 increase. On the other hand, the monsoon wind index does not show a strengthening due to warming (Figure 17.5(b)); rather, the 850-hPa monsoon westerly jet and the 200-hPa easterly jet weakened in the summer months of July and August. Therefore, westerly wind shear becomes smaller with warming, which seems to be contradictory to the increase in the India summer monsoon precipitation. This paradox can be explained by the northward shift of the monsoon circulation. The lower tropospheric monsoon wind system shifts slightly to the north, thus leading to a weakening of the index defined over the 5°–20°N domain. The same is true for the CNRM GCM (Ashrit *et al.*, 2003) and the MRI-CGCM2 (Ashrit *et al.*, 2005).

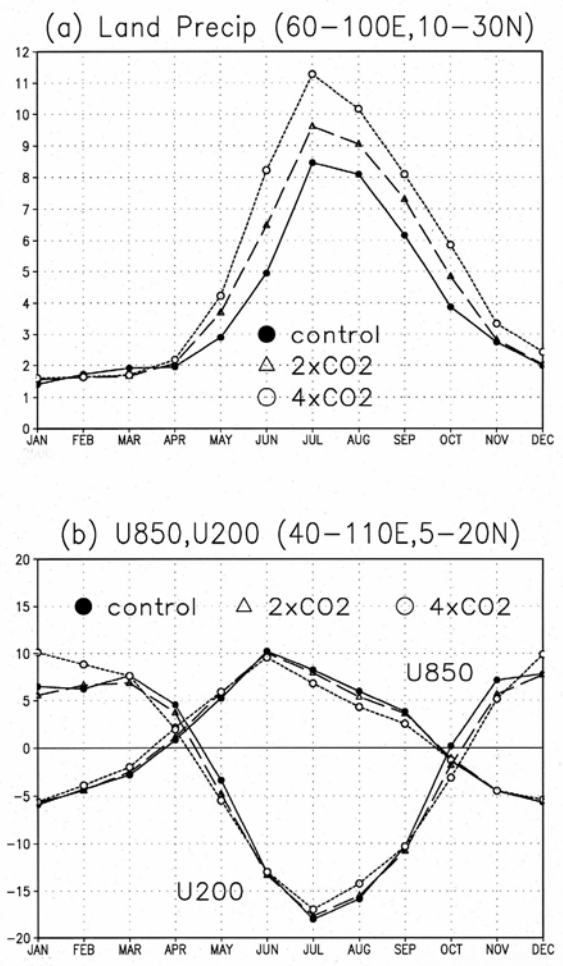

Figure 17.5. (a) Seasonal cycle of precipitation averaged over land for 60°–100°E, 10°–30°N. The solid line is the 20-year average in the control experiment, the dashed (dotted) line represents the times of the $2 \times CO_2$ ($4 \times CO_2$) in the MRI-CGCM1. (b) As in (a) except for zonal winds at 850 hPa and 200 hPa averaged for 40°–110°E, 5°–20°N.
After Kitoh *et al.* (1997).

Another analysis (Figure 17.6) showed the total atmospheric moisture flux and its change in the MRI-CGCM2. Although the monsoon westerly wind from the Arabian Sea to India became weak, the total moisture flux increased due to the increase of the atmospheric moisture content resulting from temperature increase, thus leading to increased precipitation in India. Bhaskaran *et al.* (1995), Douville *et al.* (2000b), Ashrit *et al.* (2003), and Meehl and Arblaster (2003) also reached the same conclusion. May (2002, 2004) used a higher horizontal resolution model (with a T106 time-slice experiment with ECHAM4 AGCM using the 1970–1999 and 2060–

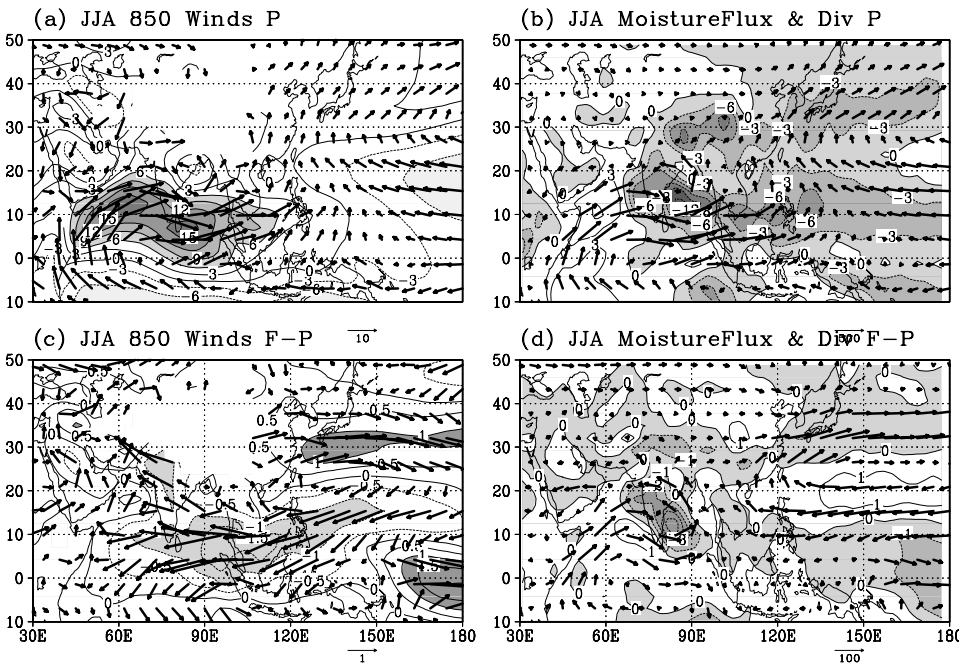

Figure 17.6. (a) JJA mean 850-hPa wind (vector) and its magnitude (contour) and (b) JJA mean column integrated moisture flux in $kg\,m^{-2}\,sec^{-1}$ and its convergence in $mm\,day^{-1}$ in the present-day simulation by the MRI-CGCM2. (c, d) As in (a, b) except for the change between 2071–2100 and the present simulation (1971–2000) by the MRI-CGCM2. A three-member ensemble mean is shown with the SRES-A2 scenario.

2099 sea surface temperature (SST) obtained by the T42 resolution ECHAM4/OPYC coupled GCM with IS92a scenario) and also showed a weakening of the monsoon circulation and an increase in the Indian summer monsoon precipitation due to strengthened moisture transport.

Using National Centers for Environmental Prediction/National Center for Atmospheric Research (NCEP/NCAR) reanalysis data, Stephenson *et al.* (2001) showed a decrease in the monsoon westerly wind shear index (Webster and Yang, 1992) and the meridional wind shear index (Goswami *et al.*, 1999) from −0.1 to −0.3% per year from 1958 to 1998, although the all-India summer precipitation showed no trend. Geological evidence based on the fossil record from the Arabian Sea shows an increase in the monsoon intensity over the past four centuries (Anderson *et al.*, 2002), but this does not contradict the northward shift of monsoon circulations (Figure 17.6).

Using the Centre National de Recherches Meteorologiques (CNRM) model results, Ashrit *et al.* (2003) showed that the rate of increase in precipitable water is larger than the rate of increase in precipitation, suggesting a decrease in the moisture recycling ratio. Douville *et al.* (2002) conducted a detailed analysis of this rain efficiency decrease. Moreover, since rain efficiency depends on soil moisture, the

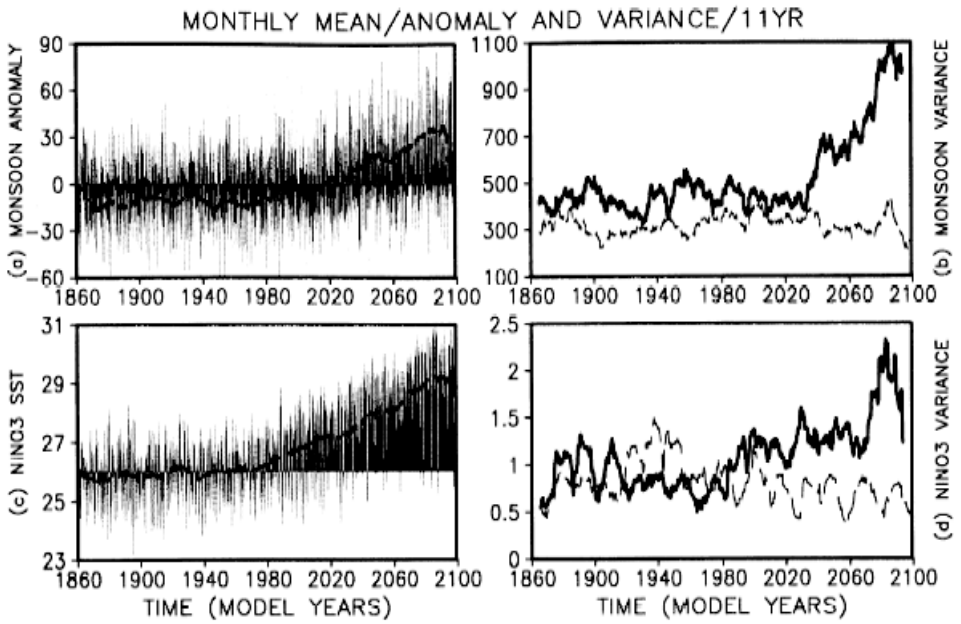

Figure 17.7. (a) Time series of the June–September precipitation anomalies in south Asia (40°–110°E, 0°–20°N) and its 11-year running mean of the IS92a run by the ECAHM4/OPYC3 CGCM. (b) Sliding variance of (a) using an 11-year window in the IS92a run (solid line) and control run (dashed line). (c, d) As in (a, b) except for the Niño 3 (150°–90°W, 5°S–5°N) SST.

Reproduced by permission of American Geophysical Union from figure 2 of Hu *et al.* (2000b).

regional change in monsoon precipitation resulting from a CO_2 increase is affected by the surface hydrological scheme (Douville *et al.*, 2000b).

Most model results projected an increase in interannual variability associated with an increase in mean precipitation (e.g., Meehl and Washington, 1993; Bhaskaran *et al.*, 1995; Kitoh *et al.*, 1997; Hu *et al.*, 2000b; Meehl and Arblaster, 2003). Bhaskaran *et al.* (1995) performed a frequency distribution analysis of daily precipitation in the UKMO model, and found an increase in the frequency of heavy rain. The result of the IS92a run by the MPI coupled model is shown in Figure 17.7 (Hu *et al.*, 2000b). The researchers calculated the time series of the variance in an 11-year running window (Figure 17.7(b)), which showed an increase in interannual variability of the Indian summer monsoon rainfall after 2030. Hu *et al.* (2000b) related this to the increased variability of the tropical Pacific SST (El Niño variability; Figure 17.7(d)). Meehl and Arblaster (2003) explored the cause of change in monsoon precipitation variability by separately examining SST anomalies in the Pacific and in the Indian Ocean. They found that the increased variability in evaporation and precipitation in the Pacific due to increased SST influenced the South Asian monsoon variability through Walker circulation; the role of the Pacific Ocean is dominant and that of the Indian Ocean is secondary.

The effect of aerosols on the monsoon system is a major controversy. If the direct effect of aerosol increase is considered, then the increase in surface temperature over Asia is lessened because the aerosol particles reflect solar insolation. For this reason, the land–sea temperature difference becomes smaller than without the aerosol effect, and the south Asian summer monsoon becomes weaker (Meehl *et al.*, 1996a). Using the UKMO model, Mitchell *et al.* (1995) and Mitchell and Johns (1997) reported that the south Asian (5°–30°N, 70°–105°E) summer monsoon rainfall decreased 5% when the direct effect of sulphate aerosol was considered, and it increased 5% when only the greenhouse gases (GHGs) were included. Rupa Kumar and Ashrit (2001) compared this UKMO model result with those of the MPI model. Although both models included the direct effect of sulphate aerosol, the MPI model showed an increase in precipitation while the UKMO model showed a decrease. Spatial patterns of monsoon precipitation were not sensitive to the magnitude of the forcing, if monsoon precipitation amount changes with warming. However, these model experiments have assumed that surface albedo change acts as a surrogate for the aerosol effect.

Other subsequent model results showed that the sulphate aerosol effect reduces the magnitude of precipitation change compared with the models with only GHGs, but the increase in south Asian summer monsoon precipitation remains (Roeckner *et al.*, 1999; Emori *et al.*, 1999). Furthermore, it was suggested that black carbon and dust, which absorb solar radiation, have a large influence on precipitation (Ramanathan *et al.*, 2001). These aerosol particles float in the atmosphere in south Asia mostly in the dry season (November–May), but when the rainy season begins they are washed away. Since aerosols with high absorptivity (such as black carbon) absorb solar radiation in the lower atmosphere, the solar radiation that reaches the surface decreases. This causes precipitation to increase in winter over the Indian Ocean, and to decrease in the surrounding Indonesian region and the western Pacific Ocean (Chung *et al.*, 2002). Black carbon also influences the summer monsoon, both in south Asia and east Asia (Menon *et al.*, 2002).

17.2.2 East Asian monsoon

A number of studies also looked at future climate projections in east Asia (Zhao *et al.*, 2004; and others discussed in this section). Using seven GCM results for $1 \times CO_2$ and $2 \times CO_2$ equilibrium experiments, Hulme *et al.* (1994) estimated that precipitation will increase over most of the east Asia region during all seasons. Giorgi and Francisco (2000) compared the local climatic change (2071–2100 compared with 1961–1990) using the IS92a transient experiment with five global climate models (HadCM2, CSIRO Mk2, CCCma/CGCM1, CCSR/NIES, and ECHAM/OPYC). They divided the World into 23 regions and investigated the temperature and precipitation changes in summer and winter. Although there were differences due to the aerosol effect and also among ensemble members, it was found that the intermodel difference was dominant. There was no summertime

precipitation change in east Asia when only the GHGs were considered, and no consensus among models was found when the effect of aerosol was included. Giorgi *et al.* (2001) summarized the nine global climate model results (CCCma/CGCM2, CSIRO Mk2, NCAR/CSM 1.3, ECHAM/OPYC, GFDL R30c, HadCM3, MRI-CGCM2, CCSR/NIES, and DOE PCM), which all used the SRES A2 and B2 scenarios and compared the periods of 2071–2100 and 1961–1990. According to this study, there was consensus among the models about the summer precipitation increase over east Asia (+5% to +20%). Hu *et al.* (2003) used the CMIP2 experiments with 16 models to show a trend of JJA increasing precipitation over almost all of China, except for the western part of Inner Mongolia at the time of CO_2 doubling. However, intermodel scatter was again very large.

There were some attempts to downscale climate change in east Asia by using regional climate models. Kato *et al.* (2001) investigated the east Asia climatic change in January and June at the time of CO_2 doubling using NCAR RegCM2.5 (50 km horizontal resolution), which is nested to NCAR CSM; one integration period covered ten years. They noted that in June, the subtropical anticyclone intensifies around 25°–30°N and extends westward; precipitation decreases near the Philippines, where the subtropical anticyclone belt intensifies, and increases around the Baiu rain area over south China and to the south of Japan. They also analyzed daily precipitation characteristics around Japan and showed that total precipitation increases, while there is no change in the frequency of wet days (daily precipitation greater than 1 mm day^{-1}), suggesting an increase in precipitation intensity. Gao *et al.* (2002) also showed an increase of heavy rain days in southern China at the time of CO_2 doubling by RegCM/China nested to CSIRO GCM.

Change in the above-mentioned Pacific anticyclone (i.e., the tendency for sea level pressure to become high in the region south of 30°N and become low in a 40°N–50°N belt, and the strengthening and southward movement of the Pacific anticyclone) has also appeared in the CO_2 increase experiment results by the MRI-CGCM1 (Kitoh *et al.*, 1997). Nishimori and Kitoh (2002) developed a statistical downscaling method to project high spatial resolution regional precipitation changes based on large-scale circulation features obtained by GCMs, and applied it to MRI-CGCM1, CCSR/NIES, HadCM3, and ECHAM4/OPYC3. Although the GCM results are scattered among the models, their statistical downscaling method found common features such as an increase in precipitation over the northern part of Japan and a decrease over the Pacific coastal side of Japan, which is associated with the intensification and south-west movement of the Pacific subtropical anticyclone.

Both the regional climate models and the statistical downscaling method are influenced greatly by the accuracy of the GCM in reproducing the present-day climate (mean and interannual variability). In a control experiment using the present climate model, the reproducibility of actual summertime precipitation is poor, particularly over the western Pacific region; this is common with many GCMs (Kang *et al.*, 2002). In order to predict the precipitation change in east Asia with sufficient accuracy, an improvement in the model climate is necessary.

17.2.3 Monsoon onset

Changes in the monsoon are not restricted to the seasonal mean precipitation but also include seasonality, such as monsoon onset and withdrawal dates. Figure 17.8(a,b) (color section) shows the distribution of onset dates of the summer rainy season according to the CMAP precipitation climatology and the present-day simulation by MRI-CGCM2 (Rajendran *et al.*, 2004). Following Wang and LinHo (2002), onset is defined as the first pentad in which the five-day mean precipitation increases more than the January average precipitation at the grid point of more than $4\,\mathrm{mm\,day^{-1}}$. Wang and LinHo (2002) observed that onset dates propagate over time from south-west to north-east over the Arabian Sea and from south-east to north-west over the Bay of Bengal. The MRI-CGCM2 effectively reproduced the observed characteristics of monsoon onset both in its spatial propagation and in its timing. The earliest onset takes place over the region around the Indo-China peninsula and the Bay of Bengal. The next onset occurs in mid-May over the South China Sea, and after that the onset dates propagate northward with the movement of the Meiyu/Baiu rain. Over the Philippine Sea and the western North Pacific, there are two jumps in the monsoon onset (Ueda and Yasunari, 1996). Although the movement of onset dates is generally well reproduced in the model, particularly over the Indian monsoon region, there remain some discrepancies in the western Pacific, showing that the models need further improvement in their climatology.

Figure 17.8(c) (color section) shows the predicted onset dates of the Asian summer rainy season at the end of the 21st century using the SRES-A2 scenario experiment of the MRI-CGCM2 (Kitoh, 2003). Earlier onset is more clearly seen in India than in other regions. Kitoh (2003) investigated regional differences in rainy seasons. In India, the model showed an overall increase in summertime precipitation, but the increase is larger in May and June, contributing to the earlier onset of the rainy season. In Indochina, although onset occurs one pentad earlier, the increase in the total amount of precipitation is not remarkable. On the other hand, the monsoon onset occurs later in the western North Pacific. In this area, the contrast between the decrease in May–June and the increase in July–August is remarkable, showing a clear onset. Around Japan, a change in the timing of onset is not seen, although precipitation increases. Although the Indian summer monsoon onset date becomes earlier in the MRI model, Bhaskaran and Mitchell (1998) presented another example showing a late Indian monsoon onset by the HadCM2 model where the seasonal average precipitation decreased. They also showed a delay in the onset in the western part of south-east Asia. Careful examination of other model results and the utilization of other methods is required.

In their projection of changes in the withdrawal of the rainy season, Uchiyama and Kitoh (2004) reported that the Baiu onset date does not change much, but the withdrawal near Japan clearly becomes later by the end of the 21st century in the MRI-CGCM2 SRES-A2 scenario experiment. They suggested that this delay of the Baiu withdrawal is caused by the large-scale circulation response associated with the El Niño-like mean SST change.

17.2.4 ENSO–monsoon relationship

The El Niño/Southern Oscillation (ENSO) affects interannual variability in the entire tropics through Walker circulation changes. Therefore, many are interested in how global warming changes the behavior of ENSO and the relationship between ENSO and the monsoon system. Many models so far have projected that the 'time-average' pattern of the tropical Pacific SST change due to global warming becomes El Niño-like (IPCC, 2001). That is, the SST rises more in the eastern tropical Pacific than in the western tropical Pacific, and the tropical Pacific rainfall distribution undergoes an eastward shift (Figure 17.2(a)).

So the question then is, what is the projected change in the amplitude, frequency, and spatial pattern of El Niño itself? IPCC (2001) concluded that the difference among the models is very large because in some models, ENSO activity becomes small and in others, it becomes large. This uncertainty is partly because these models are not able to reproduce ENSO with sufficient accuracy in their control experiment (Latif *et al.*, 2001).

It has been known that there is a significant correlation between ENSO and the monsoon, shown by the analysis of observational data (below-normal Indian monsoon rainfall in El Niño years, and above-normal rainfall in La Niña years). Recent analysis revealed that this correlation has a remarkable decadal fluctuation (Krishna Kumar *et al.*, 1999a). Variability in the relationship between the east Asian summer monsoon and ENSO is also reported (Wang, 2002). Moreover, since the correlation between ENSO and the Indian summer monsoon has recently collapsed, many hypotheses have looked for the reason; suggestions include decadal variability (Kripalani and Kulkarni, 1997b), a change in seasonality of the ENSO cycle (Kawamura *et al.*, 2003), the Indian Ocean Dipole mode (Ashok *et al.*, 2001), Atlantic Oscillation (Chang *et al.*, 2001a), and global warming. With respect to global warming, one hypothesis is that the Walker circulation accompanying ENSO shifted south-eastward, reducing the downward motion that originally suppressed precipitation in the Indian region at the time of El Niño, resulting in a normal precipitation (Krishna Kumar *et al.*, 1999b). Another explanation is that global warming raises the ground temperature of the Eurasian continent in the winter–spring season so that the temperature difference between the continent and the ocean becomes large; this causes more precipitation, and the Indian monsoon remains normal in spite of the occurrence of El Niño (Ashrit *et al.*, 2001). Although the climate models simulate increased Indian summer monsoon precipitation due to global warming, the reason may not be simply because monsoon circulation has strengthened but could possibly be because the amount of atmospheric moisture content has increased (Kitoh *et al.*, 1997; Douville *et al.*, 2000a).

It is reported that the MPI model (Ashrit *et al.*, 2001) and the CNRM model (Ashrit *et al.*, 2003) showed no global warming related change in the ENSO–monsoon relationship, although a decadal-scale fluctuation is seen, suggesting that a weakening in the relationship might be within natural variability. Ashrit *et al.* (2001) further showed that while the impact of La Niña does not change, the influence of El Niño on the monsoon becomes small, suggesting the possibility of

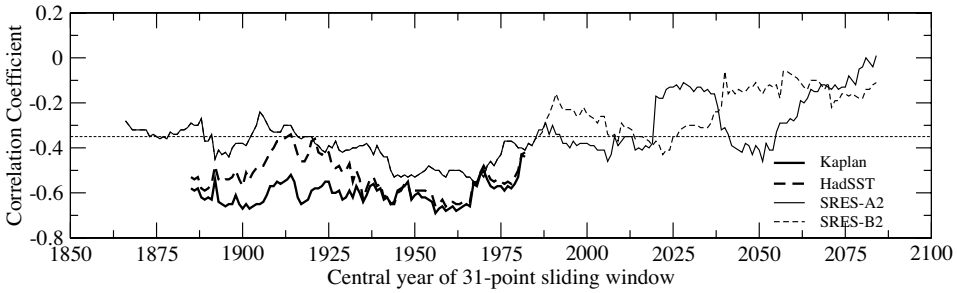

Figure 17.9. Observed and simulated changes in 31-year sliding window correlations between Indian monsoon rainfall and Niño 3 SST anomalies (JJA). For observations, two SST data are used. Model results are from the SRES-A2 and B2 scenario experiment with the MRI-CGCM2.
After Ashrit *et al.* (2005).

asymmetric behavior in the ENSO–monsoon relationship changes. Figure 17.9 shows long-term variations in the correlation between the JJAS Indian monsoon rainfall and the JJA Niño 3 SST anomalies found through observation and the MRI-CGCM2 simulations (Ashrit *et al.*, 2005). By comparing the model results with observed changes during the late 20th century, it seems that the simulations successfully captured the observed weakening of the teleconnection during that period. Further, the model indicates much weakening in the correlation in the 21st century, particularly after 2050. The MRI-CGCM2 model results support the above hypothesis: due to global warming, the Walker circulation no longer influences India at the time of El Niño because the interannual variability of El Niño is superimposed on an eastward movement of the Pacific circulation system that results from the baseline El Niño-like climate change response.

17.3 WINTER MONSOON

This section briefly reviews a possible change in the Asian winter monsoon due to global warming. Most model results agree that the surface air temperature in wintertime east Asia will rise more than the global average in the future (IPCC, 2001). In winter, the temperature rise over the Eurasian continent is more than that over the oceans, leading to a weakening of north-westerly winter monsoon flow from Siberia toward Japan (JMA, 2000). In particular, a reduction of sea ice in the Okhotsk Sea will bring a remarkable rise in the winter temperature in north-east Asia (Noda *et al.*, 1996; also see Figure 17.3(d)). At northern high latitudes, there is a wavenumber 3 structure in the lower troposphere with troughs over the Okhotsk Sea, the Barents Sea, and Hudson Bay, and the snow line is located closer to the equator than at other longitudes. Since these sea ice areas are located in lower latitudes that receive more solar radiation, the snow–albedo feedback is considered to increase with greater warming.

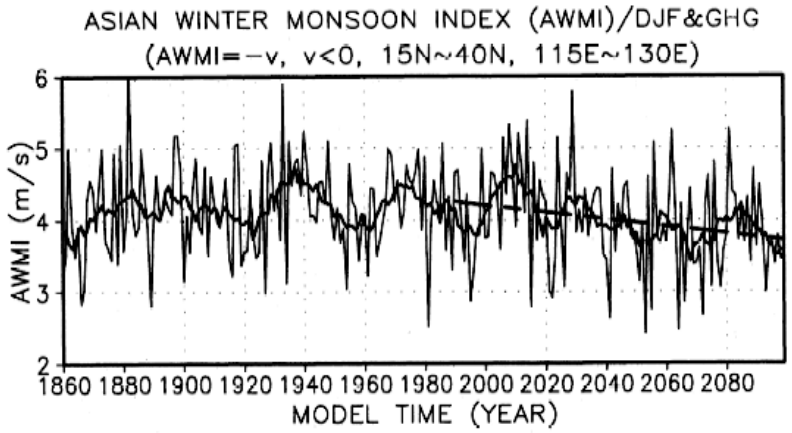

Figure 17.10. Variations of the Asian winter monsoon index (AWMI) defined as the DJF mean northerly wind averaged at 15°–40°N, 115°–130°E in the ECHAM4/OPYC3 CGCM IS92a experiment.
Reproduced by permission of American Geophysical Union from figure 2 of Hu *et al.* (2000a).

The time series of the intensity of the northerly wind from the East China Sea to the South China Sea (15°–40°N, 115°–130°E) by the MPI coupled model is shown in Figure 17.10 (Hu *et al.*, 2000a). A weakening in the winter north-easterly winds is seen along the Pacific coast of the Eurasian continent. In the global warming scenario, the contrast between the sea level pressure and the near-surface temperature in the area between the Asian continent and the Pacific Ocean became significantly smaller. The upper troposphere trough and jet stream were found to weaken and shift northward and eastward. The same index by the MRI-CGCM2 is shown in Figure 17.11(a); however, no trend can be seen in this model. When the surface northerly wind in the South China Sea was used as an index (Figure 17.11(b)), the MRI model showed an increasing trend in the latter half of the 21st century. Figure 17.12 shows the distribution of DJF mean surface wind, its magnitude at present, and its change by the end of the 21st century (2071–2100), as determined by the MRI-CGCM2. In the extratropics, there was a northward shift of the cyclone track and the position of the Aleutian Low, which resulted in a weakening of the north-westerly cold surge around Japan. This is similar to the study by Geng and Sugi (2003), which used the T106 JMA AGCM with 20-year time-slice experiments and found a decrease in DJF extratropical cyclone density in east Asia around Japan (south of 50°N) and an increase north of 50°N. Over the South China Sea, on the other hand, the north-easterly wind became strong. This resulted in increased precipitation in the South China Sea and the Indonesian region (Figure 17.3(e)).

Some models showed an increase in winter precipitation around Japan (e.g., Hu *et al.*, 2000a), while others predicted a decrease in precipitation (e.g., Boer *et al.*, 2000); the intermodel difference is large (Giorgi and Francisco, 2000; Lal and Harasawa, 2001; IPCC, 2001), and even the direction of regional change (+ or −) is in dispute when the effect of aerosols is considered (Lal and Harasawa, 2001).

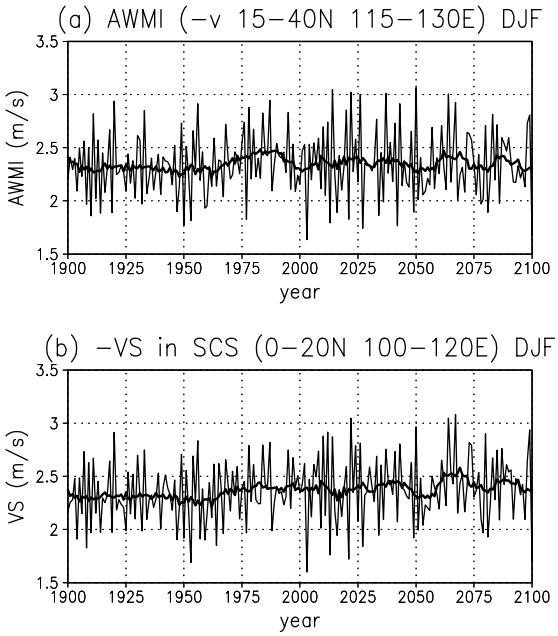

Figure 17.11. (a) As in Figure 17.10 except for the MRI-CGCM2 SRES-A2 experiment. (b) Time series of DJF mean surface northerly wind over the South China Sea (0°–20°N, 100°–120°E) in the MRI-CGCM2 SRES-A2 experiment. Thick solid lines are the 11-year running means.

Dai *et al.* (2001) showed the result of NCAR CSM and PCM. Although the CSM result is noisy, the five-member ensemble mean of PCM shows a 10% to 30% increase in precipitation north of 30°N, and a 10% decrease to the south of 30°N. As for the north-west monsoon in India, Pal *et al.* (2001), using the NCAR CCM3 CO_2 doubling experiment, reported an increase in the north-western monsoon precipitation from southern India and Sri Lanka to Indonesia through the Bay of Bengal. This corresponds to a northward shift of the Intertropical Convergence Zone (ITCZ) over the Indian Ocean due to warming. Lal *et al.* (2001) also reported a decline in the wintertime rainfall in India.

Three regional climate models (MRI, CRIEPI, and NIES) obtained climate change projections for the wintertime Japanese region (Ichikawa, 2004). Sato (2000) double-nested the regional climate models in the Asian region (RSM: horizontal resolution of 120 km) and the Japan region (JSM: 40 km) to the MRI-CGCM1. In a 20-year simulation of the January climate, the precipitation over Japan on the side toward the Japan Sea decreased when there was a decrease in the cold surge from Siberia, while the precipitation on the side toward the Pacific Ocean increased. Kato *et al.* (2001) performed a 10-year integration by NCAR RegCM2.5 (50 km resolution) nesting to NCAR CSM, and showed that a significant change in precipitation is not seen. On the other hand, in the NIES regional climate

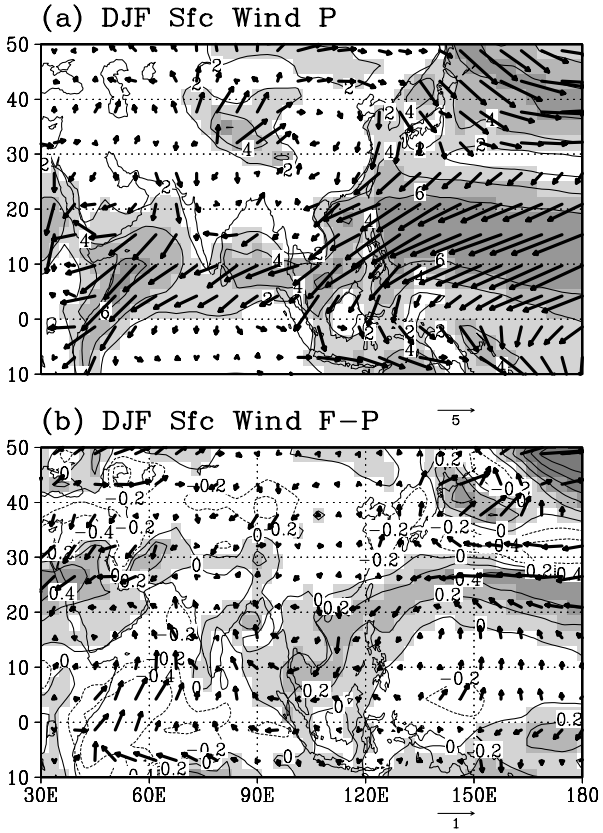

Figure 17.12. (a) DJF mean surface (10-m) wind and its magnitude in the present-day simulation by the MRI-CGCM2. (b) As in (a) except for the change between 2071–2100 and the present simulation (1971–2000) by the MRI-CGCM2. A three-member ensemble mean is shown with the SRES-A2 scenario.

model (50 km resolution), the precipitation from southern China to southern Japan decreased significantly (Emori *et al.*, 2000). Thus, the decreasing precipitation over Japan on the Japan Sea side, which corresponds to weaker cold surges from Siberia, is predicted similarly in the three models, but the models produce different results for the precipitation change over the Pacific side of Japan, suggesting a need to improve the global model.

17.4 OTHER ISSUES

Human beings have changed the land surface through fuel extraction and the expansion of farming areas. The potential (natural) vegetation and the existing vegetation differ greatly from each other in Asia, and further land use changes in

the future are highly probable. Wei and Fu (1998) performed sensitivity experiments looking at land surface change from grassland to desert in northern China, and found that such a land use change will weaken the monsoon circulation and reduce precipitation significantly. Similar results were also obtained when the potential vegetation was altered to reflect the present vegetation (Fu, 2003). Such a vegetation change was actually observed through changes in land surface and land use brought about by past human activity, which suggests the possibility that vegetation changes caused by future anthropogenic land use and climate changes will influence the monsoon circulation and precipitation pattern. Inclusion of the vegetation feedback will produce results showing different regional climate changes (Douville *et al*., 2000b). There are many GCM experiments that have investigated the impact of deforestation on the climate over various regions. In the south-east Asian monsoon region, Kanae *et al*. (2001) analyzed the probable precipitation decrease over Thailand due to deforestation over the last 40 years. Sen *et al*. (2004a) further showed that deforestation on the Indochina peninsula also affects the east Asian rainfall. Chen *et al*. (2004) and Sen *et al*. (2004b) discussed the effect of vegetation changes on the regional climate over China.

The influence of global warming on the tropical cyclone climatology, such as its intensity, frequency, and track, is also of great concern. Observed historical changes in some tropical cyclone characteristics have been reported recently (e.g., Yumoto and Matsuura, 2001; Ho *et al*., 2004). In order to determine future projections of changes in tropical cyclone characteristics, some experiments have used a high-resolution GCM (Bengtsson *et al*., 1996; Knutson and Tuleya, 2001; Sugi *et al*., 2002). Contrary to earlier low-resolution model results, they found a significant reduction in the frequency of tropical cyclones with CO_2 doubling. Sugi *et al*. (2002) showed a regional change in tropical cyclone frequency associated with the SST anomaly, and a significant decrease in typhoons over the North Pacific. The stabilization of the tropical atmosphere due to global warming seems to be responsible for such a change. Yoshimura *et al*. (2005) found an approximate 20% decrease in tropical cyclone numbers globally. They also showed that mean precipitation near the tropical cyclone centers is significantly larger in the warming experiments than in the present-day climate experiments, as compared with those with the same maximum wind speed. Wu and Wang (2004) estimated the tropical cyclone track changes in the western North Pacific using the Geophysical Fluid Dynamics Laboratory (GFDL) global warming experiments. Based on changes in the large-scale steering flow and in the formation locations in the GFDL model results, they predicted that tropical cyclone tracks will shift eastward in the western North Pacific during the mid-21st century. However, the spatial resolution of these GCMs is limited when representing tropical cyclone structures, and therefore an attempt with a much higher resolution model is needed (Mizuta *et al*., 2004; Oouchi *et al*., 2005).

17.5 SUMMARY

Future anthropogenic changes in GHGs, aerosols, and land use/land cover will inevitably alter the climate in Asia. As global warming leads to greater warming over land than over the oceans, the continental land–sea temperature contrast will become larger in the summer and smaller in the winter. Based on this prediction, a simple conclusion is that the Asian summer monsoon will be stronger and the winter monsoon will be weaker in the future. However, model results are not so straightforward and do not fit easily into such a simple view. For the south Asian summer monsoon, models suggest a northward shift of the lower tropospheric monsoon wind system with a weakening of the westerly flow over the northern Indian Ocean. However, atmospheric moisture buildup due to increased temperature will result in larger moisture flux and more precipitation over India. Changes in the winter monsoon will have different consequences from region to region. East Asia will have a weakened north-westerly cold surge, while south-east Asia could experience a stronger north-east monsoon. The projections of these regional climate changes, however, may still be highly model dependent, and should be considered carefully as there are large differences among models in projecting changes in wintertime precipitation, including even the direction of changes.

18

The Asian monsoon – agriculture and economy

Sulochana Gadgil and K. Rupa Kumar

Despite structural shifts and improvements of resilience to the vagaries of the monsoon, the kernel of the Asian economy is still very intricately and critically linked to the performance of the monsoon precipitation. In this chapter, we focus on rice, which is the major food crop of the region and provides more than half the calories and protein to the teeming millions. Asia accounts for about 90% of the area and about 92% of the production of rice in the World. We consider the links of the variation of the yield, area under cultivation, and the production of rice in several countries of the Asian monsoonal region to different facets of rainfall variability. We find that there is a strong link to interannual variation of seasonal rainfall for India and a somewhat weaker link for Thailand. We then consider the variability of the Indian monsoon and its relationship with rice production over the Indian region as a whole as well as in a major rice growing state. We also attempt to assess the impact of the monsoon on the Indian economy. We find that in general, the negative impact of a deficit of rainfall is larger than the positive impact of good rainfall. We then discuss the possible strategies for using knowledge and prediction of monsoon variability to enhance agricultural production.

18.1 INTRODUCTION

Over a third of the World's population resides in the region under the sway of the Asian monsoon. Agriculture has been described as the most weather dependent of all human endeavours, and naturally the impact of the vagaries of the monsoon rainfall on food production has been of great concern. The interannual variation of the Asian monsoon rainfall has an impact on the agricultural production, particularly under rain-fed conditions. The impact is large when at the lower end of the range of variation of seasonal rainfall – crops suffer from moisture stress leading to low crop yields. Floods due to heavy rainfall events (e.g., those caused by cyclones/typhoons)

B. Wang (ed.), *The Asian Monsoon*.

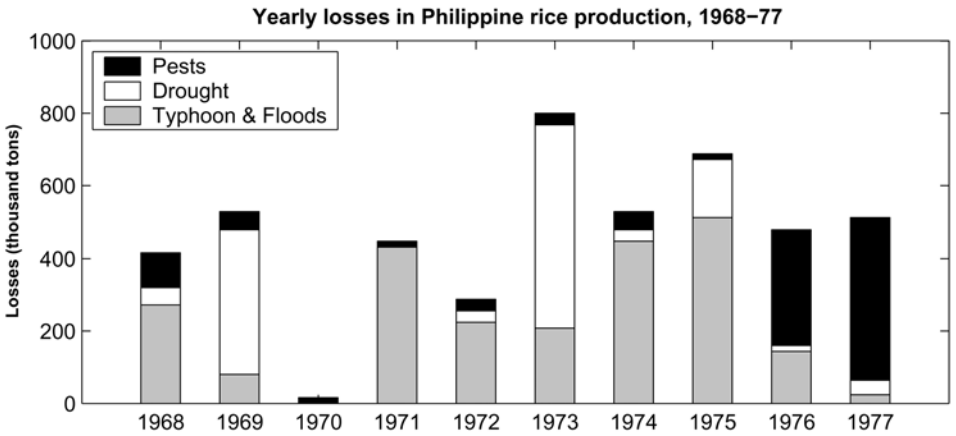

Figure 18.1. Yearly losses in Philippine rice production and their causes, 1968–1977.
After Pantastico and Cardenas (1980).

also lead to extensive crop damage. The phase of the intraseasonal variation between wet and dry spells within a season *vis-á-vis* the different phenological stages of the crop, also has an impact on the growth and yield of rain-fed crops (Gadgil *et al.*, 2002a). With similar cropping patterns over large areas (as is the case over a large part of monsoonal Asia) many pests and diseases have become endemic. In this situation whenever weather conditions are favorable (e.g., long dry spells for some insects such as leaf miner or wet spells for many fungal diseases) the population increase and incidence of the pests/diseases causes large losses (Gadgil *et al.*, 1999a, 2002a).

Pantastico and Cardenas (1980) have estimated the losses in rice yield in the Philippines due to such weather/climate related factors during 1968–1977 (Figure 18.1). The agricultural production of Bangladesh has been shown to be adversely affected by events ranging from synoptic to large scale such as floods caused by depressions and cyclones and large deficits in seasonal rainfall (Mowla, 1976). The large impact of monsoon variability over the agricultural production and hence the economy of countries such as India has been known for a very long time. In fact, the Indian economy was described as a gamble against the monsoon rains in the colonial era. A major impetus to research on the links between climate variability and agricultural production for application to the management of agriculture, particularly in the climate-sensitive areas of the tropics, came from the recommendations of the World Food Conference at Rome in 1974. Consequently, the activities of World Meteorological Organization (WMO) in the field of agrometeorology were intensified (WMO and IRRI, 1980). The recognition of the need to assess the probable impact of climate change around the mid-1970s also led to a large number of studies based on the understanding of the links between climate variability and agriculture (e.g., Takahashi and Yoshino, 1976; Mathews *et al.*, 1995). In the last decade, the major advances in the understanding of El Niño/Southern

Oscillation (ENSO) and hence in the ability to generate seasonal to interannual predictions led to a revival of interest in the atmospheric science community in application to agriculture. In view of the significant advances in the last decade in elucidating the nature of the interannual variation of the Asian monsoon (Chapter 6) and its links with ENSO (Chapter 12), the time is opportune to assess the extent to which these recent advances can contribute toward a higher productivity of the managed ecosystems.

The dominant component of the variation of agricultural production over monsoonal Asia from the 1960s or early 1970s is the enhancement in production associated with the Green Revolution. This increase in production resulted from a large increase in the yield per hectare due to the introduction of new dwarf, high-yielding, and fertilizer responsive varieties and also an increase in the area under cultivation (Abrol, 1996). The increase in the average yield over the Indian region during the Green Revolution was made possible by a substantial increase in irrigation and application of fertilizers and pesticides (Gadgil *et al*., 1999b). Despite the large investments in irrigation, at present more than 60% of the area under cultivation is rain-fed and we do not expect the rain-fed area to decrease to levels much below 50% in the foreseeable future (Katyal, 1998). Hence the interannual variation of the Indian monsoon has continued to have an impact on agricultural production (Krishna Kumar *et al*., 2004). The impact of the summer monsoon rainfall on the summer food grain production is particularly large (Figure 18.2). The variability of the monsoon also has an impact on irrigated crops because the quantity of water available for irrigation depends upon the monsoon rainfall. Whether our understanding of the nature of the variability of the Asian monsoon on different timescales and the enhanced ability of its prediction can contribute to the reduction of the negative impacts of monsoon variability and/or enhancement of the positive impacts on production needs to be explored.

In this chapter we consider only a few facets of the links between the Asian monsoon, agriculture, and the economy. Rather than attempting a comprehensive review (which would require an entire book) we present some results on the analysis of links of the Asian monsoon with rice production, assessment of the impact on the Indian economy, and suggest how understanding and prediction of the monsoon variability could be used for enhancing agricultural production. We focus on rice because it is the major food crop of the region and, on average, provides more than half the calories and nearly half the protein for the population. Asia accounts for about 90% of the area and about 92% of the production of rice in the World. We consider the links between the variation of yield, area under cultivation, and the production of rice in several countries of the Asian monsoonal region to different facets of rainfall variability (Section 18.2). We find that there is a strong link between the variability in rice production and interannual variation of the seasonal rainfall for India (and a somewhat weaker link for Thailand). We then consider some facets of the variability of the Indian monsoon (Section 18.3) and its relationship with the variability in rice production over the Indian region as a whole as well as in a major rice growing state of India (Section 18.4). We also attempt to assess the impact of the monsoon on the Indian economy (Section 18.5). We find that in general, the negative

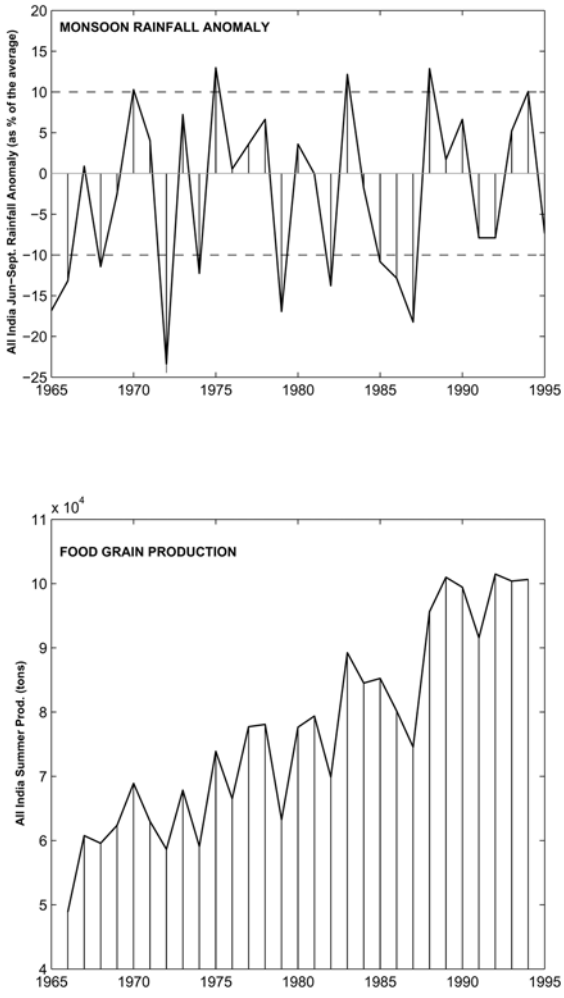

Figure 18.2. All-India summer monsoon rainfall anomalies and all-India summer foodgrain production during 1966–1994.

impact of deficit rainfall is larger than the positive impact of good rainfall. We then discuss possible strategies for using knowledge and prediction of monsoon variability for enhancing agricultural production in Section 18.6.

18.2 VARIABILITY OF RICE PRODUCTION IN ASIA AND ITS RELATION TO VARIATION IN RAINFALL

The rice production of Asia represents a very large fraction of the World's production. China, India and Indonesia are the major rice producing countries in Asia

(Figure 18.3, color section). We analyzed the variation of rice production of several countries in the region using the data from IRRI (1996) for the period 1961–1993.

18.2.1 Climatic aspects of rice production

The Asian cultivated rice (*Oryza sativa L.*) is the dominant rice of the World. Early archaeological evidences indicate that rice has come from India, China, and Thailand (Nair, 1999). Rice originated in a tropical rainy climate characterized by high temperature, high humidity, and low light intensity and abundant rainfall (Hardjawinata, 1980). Rainfall pattern is considered to be the most important limiting factor for rice production in south and south-east Asia, while temperature and radiation are more important for the higher latitude region in east Asia especially in the north-eastern and northern Japan. The total water requirement for cultivation of rice over rain-fed areas is 20 cm per month for wet season crops (Oldeman, 1980). An important feature of cultivation, which is special to rice, is transplantation, which is done after about one month of sowing (WMO and IRRI, 1980). The area under cultivation is, therefore, dependent on the rainfall in that period.

18.2.2 Observed variation of rice production: decadal-scale variation

A major component of variation in the area under rice cultivation as well as the yield per hectare (and hence the production), on the decadal scale, is the marked increase in association with the Green Revolution. However, depending on the socio-economic and political situations, there is considerable variation between the countries in the period over which the increase occurred and in the rate of increase (Figure 18.4, color section). Thus, over India, there has been an increase in the area under cultivation as well as the yield (and hence in the production) from the mid-1960s until the late 1980s; after which all three quantities seem to have reached a plateau. The variation over Thailand is similar to that over India. In Vietnam the increase in yield, area under cultivation, and production is seen only after the mid-1970s (i.e., after the end of the last war). Over Indonesia, the area under cultivation has increased steadily; the yield has increased from the mid-1960s with a more rapid increase in the early 1980s and the production has increased steadily throughout the period. Over China, the area under cultivation increased rapidly until the mid-1970s but declined thereafter; the yield has increased throughout the period (with a more rapid increase for the decade beginning in the mid-1970s) and the production has also increased throughout the period. The decadal-scale variation over the Philippines is similar to China's in that a steady increase in production is seen to be associated with a steady increase in yields although the area under cultivation declined in the early 1980s after attaining a maximum in the 1970s.

18.2.3 Interannual variation of the rice yield and cultivated area

Over and above these decadal-scale changes, there are changes on the interannual scale for the area under rice cultivation and/or the yield per hectare and hence the rice production for several countries. It is seen from Figure 18.3 that the interannual variation of the Indian rice production is large and the major dips in the Asian production (e.g., 1965, 1979, and 1987) coincide with those in the Indian production. On the other hand, the amplitude of interannual variation in rice production over China and Indonesia is rather small.

The frequency distributions of the change in yield from one year to the next (expressed as a percentage of the yield of the previous year) for several countries are shown in Figure 18.5 (color section). For each of these countries, the mode corresponds to an increase of up to 5% in the yield per year, which is a manifestation of the Green Revolution. In Indonesia, the yield can increase by more than 20% in a year, but it seldom decreases. The frequency distribution for rice yield in countries such as India and Sri Lanka is more symmetric, with long tails on both sides implying a large magnitude in the decrease/increase in yield in some years.

In the period considered here (viz. 1961–1993), the length of the runs of years with a continuing increase or decrease in the Indian rice yields is rather short (Table 18.1). For a majority of the years, an increase (decrease) in one year is followed by a decrease (increase) in the subsequent year. It is seen from Table 18.1 that the runs in the variation of the rice yield of Thailand are also short. For rice yields of China, the runs are longer with all the runs of three years or longer being characterized by increasing yield. For Indonesian rice yield, there are even longer runs with increasing yields and only one run of one year with a decreasing yield. Clearly the longer timescale variation associated with the Green Revolution dominates the rice variation over Indonesia and to somewhat less extent over China. There is a significant component of interannual variation in the rice yields of countries such as India and Thailand.

The frequency distribution of the year-to-year changes in the area under rice cultivation in different countries is shown in Figure 18.6, (color section). Over countries such as India and Thailand, there are large fluctuations of the areas under cultivation. While the fluctuations in area are well correlated with those in

Table 18.1. Lengths of runs of years with a continuing increase/decrease in rice yields.

	Runs with increasing yield					Runs with decreasing yield		
Country	1 yr	2 yrs	3 yrs	4 yrs	>4 yrs	1 yr	2 yrs	3 yrs
India	8	3	–	–		8	–	–
Thailand	6	3	–	–		6	2	–
China	3	3	1	1	1	4	1	–
Indonesia	1	1	1	1	1	1	–	–

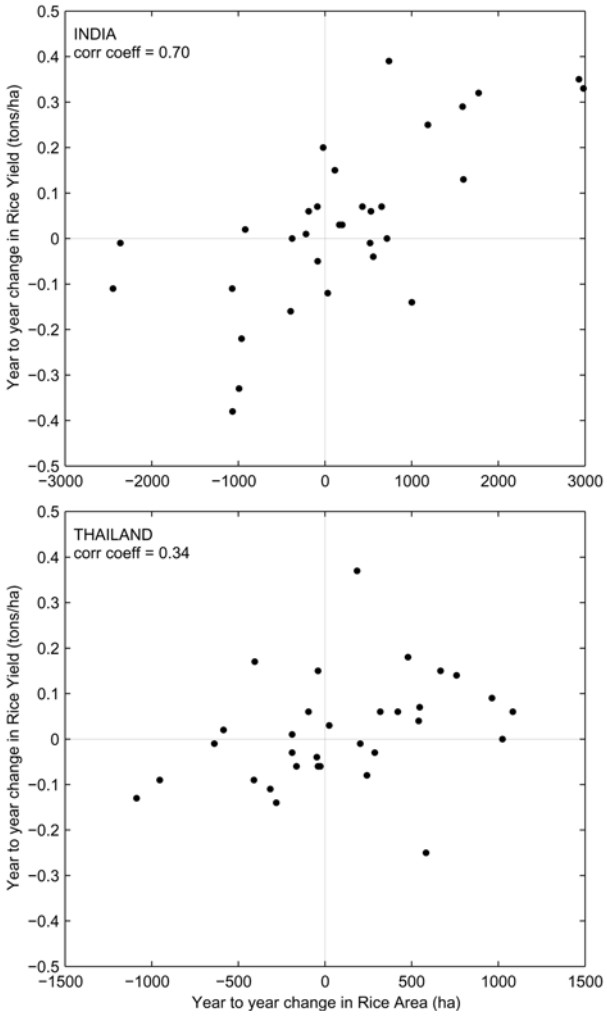

Figure 18.7. Change in yield from one year to the next vs. change in area from one year to the next for India and Thailand.

yield for India, the correlation between area and yield changes for Thailand is not as high (Figure 18.7); for Bangladesh, the correlation is in fact close to zero. It is interesting to note that there are large variations on the interannual scale in the area under cultivation, but not in yield, in Indonesia.

18.2.4 Relation between variation of rice production and variation of rainfall

In order to analyze the relationship between the interannual variation of the yield/production with rainfall, the trends on the longer timescales in the time series (such

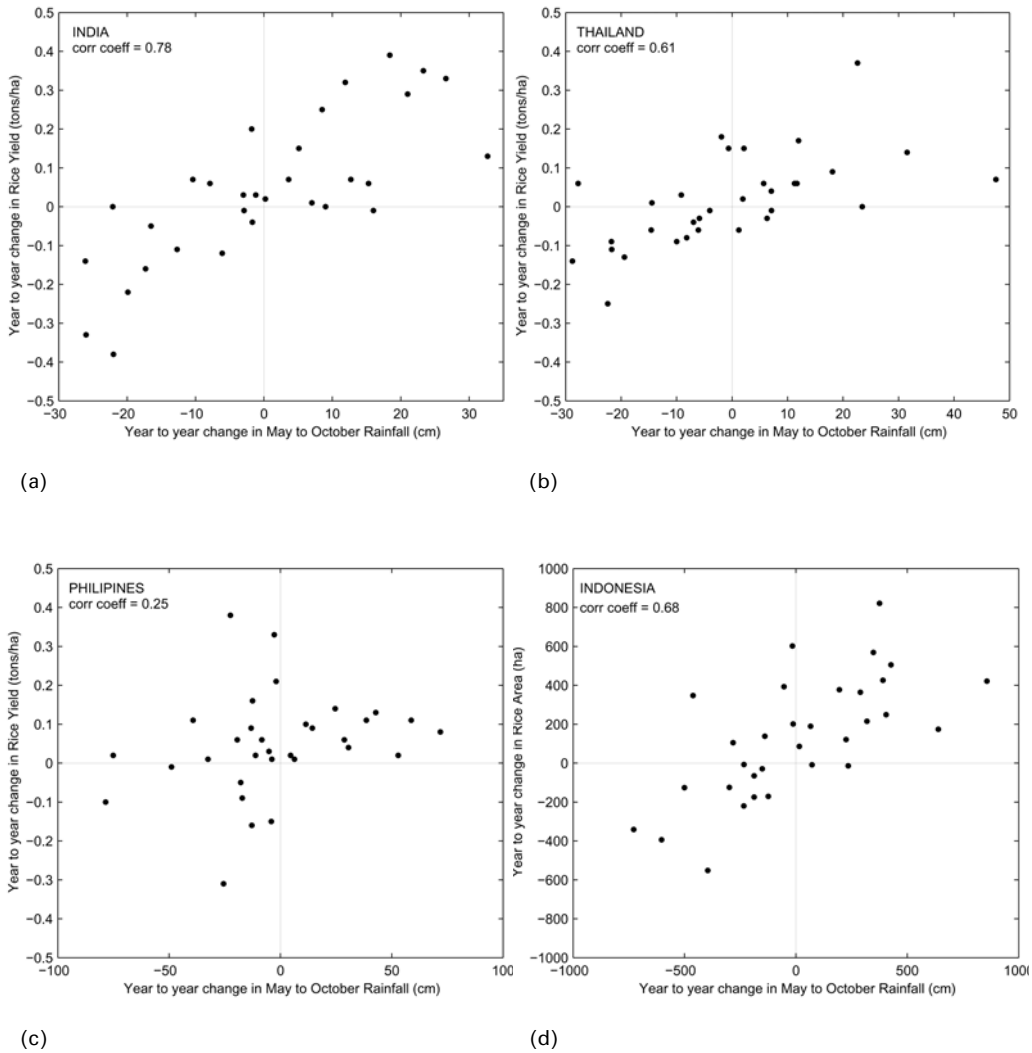

Figure 18.8. (a) Relationship between year-to-year changes in rice yield and those in May–October rainfall over India. (b), (c), and (d) – same as (a) but for Thailand, the Philippines, and Indonesia, respectively.

as those associated with the Green Revolution) have to be removed. A simple way of focusing on the shorter timescales is by considering the year-to-year difference in yield/production and their relation to the year-to-year difference in the seasonal rainfall (Krishna Kumar *et al.*, 2004). We expect the interannual variation in the yield to be related to that of the total seasonal rainfall and distribution within the

season. However, the variation in the area under cultivation is related to the rainfall received in the early part of the season, up to the time of transplantation. We consider here the relationship for India, Bangladesh, Sri Lanka, Myanmar, Thailand, Vietnam, and Indonesia using a countrywide means of monthly rainfall data for the period 1961–1993. These data have been prepared from the gridded monthly precipitation data sets of the Climatic Research Unit (CRU), University of East Anglia, UK (New *et al*., 2002) by taking the arithmetic means of all the land grid points within the respective countries.

For most of the countries considered here, the rainfall occurs primarily during May–October, and we consider the relationship of the yield to the rainfall during that season. The exceptions are Indonesia, over which the rainfall is less during June–September than in other months, and Sri Lanka, where most of the rainfall occurs during October–December. The year-to-year change in rice yield is highly correlated with the year-to-year change in the seasonal rainfall for India and Thailand (Figure 18.8(a,b)). The relationship of the rice yields of the Philippines to rainfall is rather complex (Figure 18.8(c)). It is seen that an increase up to 0.2 tons per hectare occurs irrespective of the change in seasonal rainfall in a majority of years. The decrease of the seasonal rainfall in the other years is associated with a decrease in yield in 6 out of 10 years and an increase beyond 0.2 tons per hectare in 4 out of 10 years. It appears that deficit rainfall could have a positive impact (perhaps because of absence of floods or suppression of some pests and diseases) whereas there is hardly any impact for the positive rainfall anomaly. We find that there is no discernable relationship between the year-to-year changes in rice yields over Vietnam, Bangladesh, and Myanmar and the change in seasonal rainfall.

In the period considered, while the Indonesian rainfall has fluctuated from year to year, the Indonesian yields have decreased only on one occasion and the year-to-year change in Indonesian rice yield is poorly correlated with that of the seasonal as well as the annual rainfall. Thus, despite the presence of the biennial component in the interannual variation of rainfall over the Asian monsoonal region (Chapter 6), there is hardly any variation on this timescale in the rice yield/production of some of the countries such as Indonesia. The rice season in Indonesia for the first crop begins during the dry period of May–October (Tanaka, 1976). There is no relationship between the rice yields and rainfall because the Indonesian rainfall is seldom less than the required amount (about 20 cm per month from transplanting to maturity stages) for good growth and yield of rice crops (Gadgil *et al*., 1999c). However, there is considerable variation in the area under rice cultivation in Indonesia with large decreases in the El Niño years of 1972, 1982, and 1991. This suppression in the area under cultivation could be because the Indonesian rainfall during May–October (i.e., the season in which transplantation occurs), is tightly coupled to ENSO with a deficit during El Niño (Hendon, 2003). In fact, the year-to-year variation in the area under rice cultivation in Indonesia is highly correlated with that of the May–October rainfall (Figure 18.8(d)).

Over India, the year-to-year change in the area under cultivation is correlated with the change in yield. This is because in most of the extreme years (with the amplitude of the summer monsoon rainfall anomaly being more than 10% of the

mean) the anomalies are coherent within the monsoon season. There are a few exceptions such as the drought of 1987 in which the impact on the area was much larger since the rainfall in June was highly deficient.

Thus, of the countries considered here, the relationship between rice yields, area, and production with seasonal rainfall is strongest for India, followed by Thailand.

Next we summarize what is known about the variability of some facets of the monsoon rainfall over the Indian region and then consider in detail the case of rice cultivation in the state of Andhra Pradesh in southern India, a major rice growing state, to illustrate the impact of the different facets of the monsoon on cultivation in irrigated areas.

18.3 SOME FACETS OF THE MONSOON VARIABILITY OVER THE INDIAN REGION

Rainfall has the most extensive and perhaps the longest data set available for analysis among all the meteorological parameters over India. A great deal is known about the space–time variation of rainfall (Pant and Rupa Kumar, 1997, and references therein). The focus of most of the studies has been the rainfall in the summer monsoon (June–September) season during which a large part of the country receives over 80% of the annual rainfall. The variation of the spatial average of the seasonal rainfall over the Indian region, widely known as the 'all-India' summer monsoon rainfall (ISMR), during 1871–2004 is depicted in Figure 18.9 (color section). The Indian summer monsoon is very stable in the longer term (Pant and Rupa Kumar, 1997), and is a dependable source of water for the region. The most prominent feature of the variation of ISMR is interannual variability, with the standard deviation being 10% of the long-term mean of ISMR. Annual countrywide mean ISMR anomalies beyond $\pm 10\%$ are associated with severe droughts and floods over extensive areas in the country. While the monsoon rainfall displays a very complex spatio–temporal variability, extreme situations have remarkable spatial coherence (Pant and Rupa Kumar, 1997) and demonstrate the existence of large-scale anomalies in the monsoon circulation. Hence, ISMR is considered to be a robust index for subcontinental-scale monsoon variability. The all-India production of foodgrain is highly correlated with ISMR (Parthasarathy *et al.*, 1988, 1992a). We find that the correlation of the year-to-year change in all-India rice yield is slightly better correlated with that of ISMR than with May–October rainfall shown in Figure 18.8(a).

The frequency of years with large deficits/excesses shows significant variation on the decadal scale. Figure 18.10 shows the 31-year moving averages of ISMR anomalies and also the variations in the standard deviations of the corresponding 31-year periods. The standard deviations are expressed as percentage departures from the overall standard deviation for the data period, to indicate decadal-scale decreases and increases in the variability. The moving average clearly shows two multidecadal periods of deficient (1900s to 1930s and late 1960s to present day) and

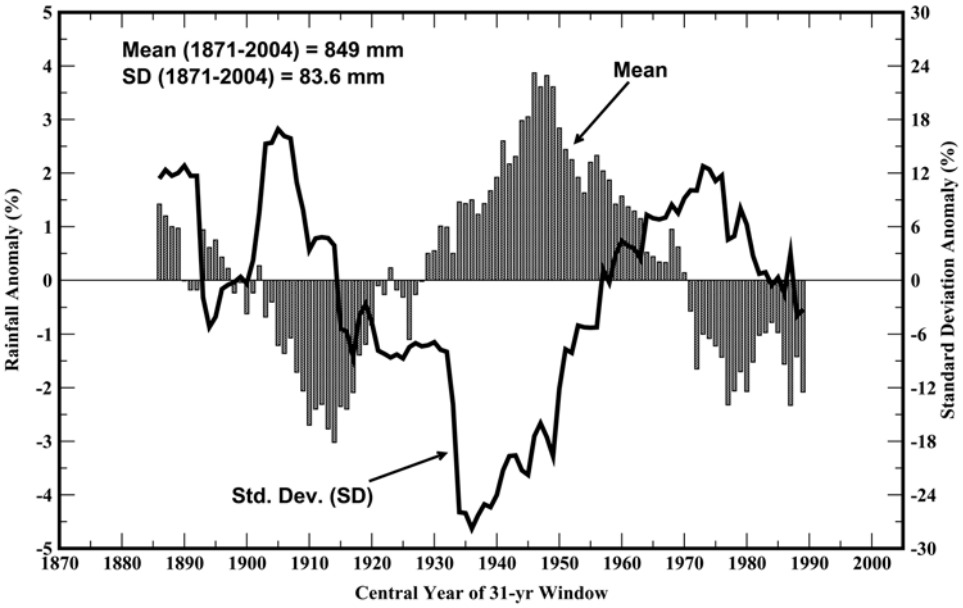

Figure 18.10. 31-year running means and standard deviations of all-India summer monsoon rainfall using the data period 1871–2004.

excess (1870s to 1900s and 1930s to early 1960s) monsoon rainfall, which is manifested in the actual data as frequent occurrences of droughts and floods. Interestingly, the variability in rainfall (see the standard deviation curve in Figure 18.10) increases during the dry epochs and decreases during the wet epochs.

The Green Revolution with phenomenal increase in agricultural production over India occurred in the last dry epoch during a high variability of the monsoon rainfall. As seen in the earlier section, droughts (defined as seasons with a larger than 10% deficit in ISMR) have continued to have a large impact throughout this period.

18.3.1 Extremes of seasonal rainfall: droughts and floods

A major advance in our understanding of the year-to-year variation of the monsoon rainfall occurred in the 1980s, with the discovery of a strong link with ENSO, the dominant signal of interannual variation of the coupled atmosphere–ocean system over the tropical Pacific. It was shown that there is an increased propensity of droughts during El Niño or the warm phase of this oscillation and of excess rainfall during the opposite phase (i.e., La Niña) (Sikka, 1980;

Table 18.2. El Niño/La Niña association with ISMR anomalies during 1871–2004 (number of years, category wise).

Number of years with...	Deficient monsoon	Normal monsoon (Negative)	Normal monsoon (Positive)	Excess monsoon	**Total**
El Niño	11	11	4	0	**26**
La Niña	0	1	9	8	**18**
Other	13	24	42	11	**90**
Total	**24**	**36**	**55**	**19**	**134**

Note: A year is classified as deficient, normal (negative), normal (positive), or excess monsoon year, when the ISMR is below −10%, between −10% and zero, between zero and +10%, or above +10%, respectively.

Pant and Parthasarathy, 1981; Rasmusson and Carpenter, 1983). Consistent with the nature of the links with ENSO, the La Niña event of 1988 was associated with a large excess in the ISMR, and the El Niño events of 1982 and 1987 were droughts. However, for 14 consecutive years beginning with 1988, there were no droughts despite the occurrence of El Niño. Further, during the strongest El Niño event of the century in 1997, the ISMR was even slightly higher than the long-term mean (Figure 18.9, color section) and Krishna Kumar *et al.* (1999b) suggested that the relationship between the Indian monsoon and ENSO had weakened in recent decades. Although a weak El Niño was known to be developing in 2002, none of the predictions for 2002 suggested a large deficit in the Indian monsoon rainfall. The experience of 1997 and 2002 suggests that we do not as yet understand adequately the response of the monsoon to El Niño. It should also be noted that droughts do occur in the absence of El Niño (e.g., 1979 in Figure 18.9). In fact, of the 24 droughts that occurred during 1871–2004, only 11 were associated with El Niño (Table 18.2, updated from Rupa Kumar *et al.* (2002)).

Gadgil *et al.* (2003, 2004) have suggested that the deficient and excess rainfall monsoon seasons are linked not only to ENSO, but also to events over the equatorial Indian Ocean involving an enhancement of deep convection over the western part with suppression over the eastern part of the equatorial Indian Ocean and vice versa. The oscillation between these two states, which is reflected in the pressure gradients and the wind along the equator, is termed as the Equatorial Indian Ocean Oscillation (EQUINOO). Gadgil *et al.* (2004) showed that every season with excess rainfall/drought during 1958–2003 can be 'explained' in terms of a favorable/unfavorable phase of either this oscillation or the ENSO or both. There is a strong relationship between large (of magnitudes larger than 10% of the mean) deficits/excesses of ISMR and a composite index based on indices of ENSO and EQUINOO (Figure 18.11).

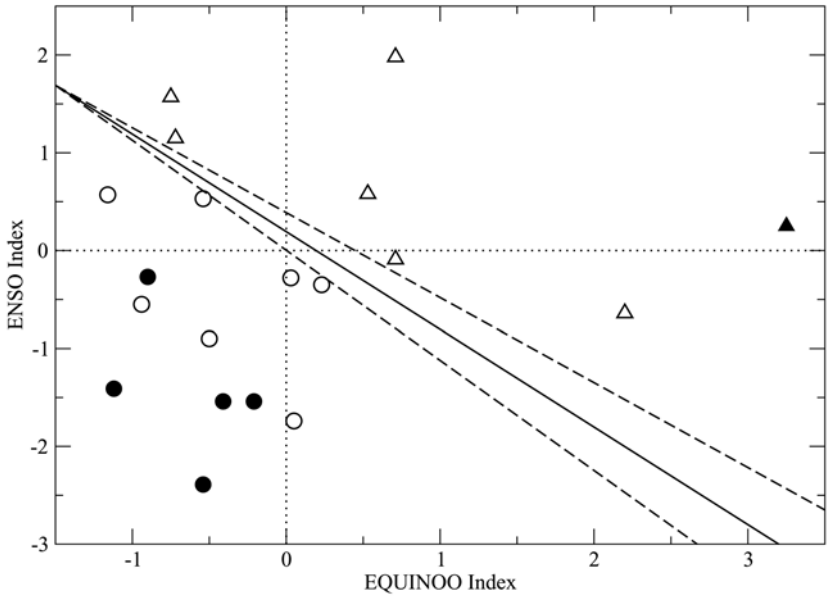

Figure 18.11. Extreme ISMR anomaly represented in the phase plane of the EQUINOO index and the ENSO index. Filled (open) circles represent the ISMR anomaly above (below) +(−) 1.5 s.d. and open (filled) triangles represent the ISMR anomaly between +(−)1 and +(−) 1.5 s.d.

18.3.2 Subseasonal patterns of monsoon anomalies

The months of July and August are generally the most active months of the summer monsoon season, contributing 60% of the monsoon rainfall. On an all-India scale, there is no significant correlation (Table 18.3) between the monthly rainfall within the season, mainly because synoptic situations of smaller timescales dominate the rainfall variability on a monthly scale. These synoptic situations are basically generated and developed independently, though broadly embedded in the monsoon circulation. Thus, the seasonal total rainfall cannot indicate the monthly distribution of rainfall. However, the highly significant correlations between the monthly rainfall and the seasonal total (Table 18.3) indicate that all the months substantially contribute to the variations in the seasonal rainfall.

To examine the monthly rainfall variations in extreme seasonal rainfall situations, the departures from the normal of monthly rainfall for deficient and excess years can be considered. There are several years in which the monthly rainfall anomalies are opposite to the seasonal anomalies (Table 18.4). In general, these subseasonal patterns indicate that the excessiveness or deficiency of the monsoon

Table 18.3. Correlations between monthly and seasonal ISMR.

Month	July	August	September	**Monsoon**
June	−0.05	−0.05	−0.07	**0.36****
July		0.11	0.23*	**0.57*****
August			0.26**	**0.61*****
September				**0.65*****

*Significant at 5% level.
**Significant at 1% level.
***Significant at 0.1% level.

Table 18.4. Subseasonal patterns of extreme ISMR anomalies (% departures from normal). From Pant and Rupa Kumar (1997).

Drought years						Flood years					
Year	June	July	August	September	JJAS	Year	June	July	August	September	JJAS
1873	−31	−3	−12	−3	−11	1874	39	12	−5	20	14
1877	−12	−43	−35	−13	−29	1878	−20	7	39	25	14
1899	20	−32	−41	−40	−26	1892	−3	15	26	24	16
1901	−29	−20	7	−27	−16	1893	48	−7	−5	32	12
1904	10	−10	−19	−26	−12	1894	33	14	−1	18	14
1911	18	−44	−14	5	−14	1916	23	−6	19	19	12
1918	11	−48	−10	−39	−24	1917	31	−11	14	57	18
1920	−12	6	−33	−29	−16	1933	24	−6	27	20	14
1928	−6	3	−19	−23	−10	1942	7	18	16	6	13
1941	1	−20	−14	−20	−14	1947	−25	6	21	37	11
1951	−5	−7	−15	−29	−13	1956	28	24	4	5	15
1965	−32	−3	−22	−18	−17	1959	−4	17	2	25	10
1966	2	−15	−19	−20	−14	1961	15	15	11	42	20
1968	−17	5	−20	−22	−11	1970	30	−19	23	21	10
1972	−25	−33	−11	−25	−23	1975	10	6	9	33	13
1974	−35	0	−7	−19	−12	1983	−15	0	21	47	12
1979	−12	−18	−18	−18	−17	1988	4	17	14	20	16
1982	−20	−21	10	−29	−14	1994	32	15	9	−18	10
1987	−29	−25	0	−19	−19						
2002	+5	−51	−16	−7	−19						
2004	0	−17	−5	−29	−13						

rainfall is more frequently realized in the later half of the season (Rupa Kumar *et al.*, 1992).

18.3.3 Dry spells – breaks in the monsoon

Though the mid-monsoon months July and August contribute most of the seasonal monsoon rainfall, the rainfall distribution is not spatio-temporally uniform over the

subcontinent even in these two months. There are significant variations on the intraseasonal scale between wet spells and dry spells. In some years during the 'breaks' in the monsoon the rainfall over the Indian monsoon zone is interrupted for several days in July–August (Gadgil and Joseph, 2003, and references therein). The phenomenon of break monsoon has been of interest because prolonged intense breaks often occur during droughts. For example, a prolonged break situation in the peak monsoon month of July in 2002 (Figure 18.12) resulted not only in a record deficit for the month of July, but also caused a seasonal-scale drought over the whole country.

18.3.4 Seasonal transitions: onset and retreat

The seasonal transition from the pre-monsoon to monsoon is so sudden (Figure 18.13(a)) that it is often termed as the 'burst' of the monsoon over the Indian subcontinent. The south-west monsoon over the Indian peninsula first arrives over the south Indian state of Kerala, while almost simultaneously the Bay of Bengal branch reaches west Bengal and the hills of the Assam region in the north-east of India. Kerala is widely known as the *gateway* of the Indian summer monsoon and its onset over the south Kerala coast is one of the most important meteorological events in the region that the public in general as well as the Indian meteorological community in particular eagerly look forward to every year. This event, with remarkable punctuality around the first week of June, heralds the rainy season for the region, ending the days of parching heat and bringing in much needed water for agricultural, industrial, and domestic use. This date also serves as an indicator of the timely or otherwise commencement of monsoon rains over the other parts of the subcontinent, which is very important for the start of agricultural operations for the main cropping season of the year known as *kharif*. The onset, advance, and withdrawal of the monsoon are particularly critical to the rain-fed agriculture during the *kharif* season.

Although the four-month period June through September is termed as the Indian summer monsoon season in a general large-scale sense, the actual rainy period differs widely over different parts of the subcontinent. Sustained increase in the rainfall and cessation of rainfall activity have been traditionally used to demarcate the beginning (or onset) and end (or withdrawal) of the monsoon circulation. The calendar dates of these seasonal demarcations also have considerable interannual variability, of the order of 1–2 weeks. The onset of the monsoon brings with it a dramatic change in the weather situation, associated with a conspicuous cloud cluster over a large area near the western part of the southern tip of the Indian peninsula. It gradually proceeds northwards and by the middle of July the whole of the Indian subcontinent comes under the grip of monsoon. However, the northward progress of the monsoon is not a smooth affair and takes place in surges, interspersed by periods of weakening or stagnation of monsoon activity. The retreat of the monsoon begins in the western parts of the north-west

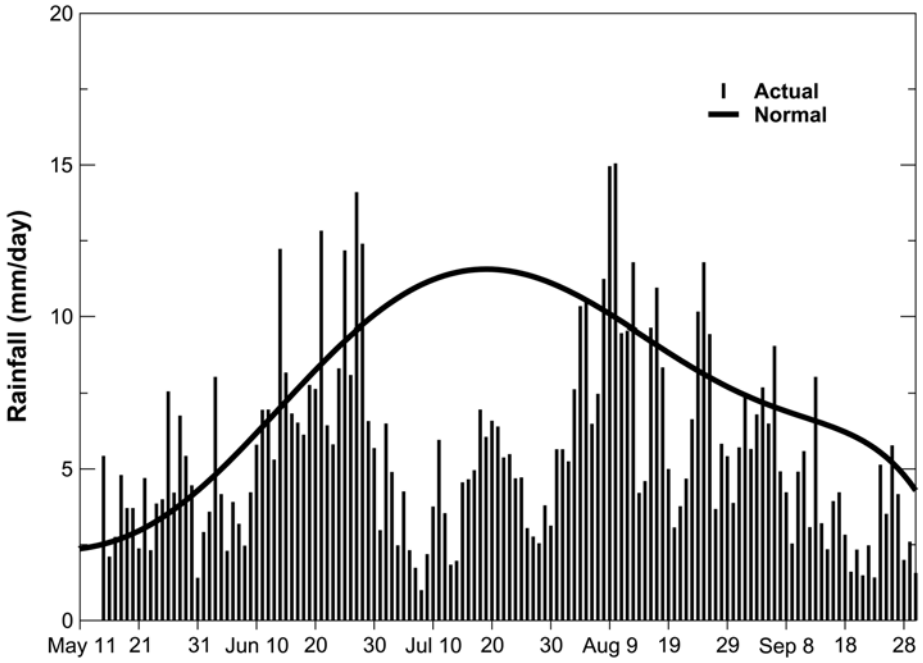

Figure 18.12. Daily variation of all-India summer monsoon rainfall during the recent drought year of 2002.
Source: Monsoon On Line (http://tropmet.res.in/~kolli/mol).

Indian state of Rajasthan in early September. Thus, the effective duration of the south-west monsoon rains over this area is only about $1\frac{1}{2}$ months. The southward retreat of the monsoon rains continues rapidly until about the middle of October, by which time it withdraws completely from the northern half of the Indian peninsula.

Ananthakrishnan and Soman (1988, 1989) have prepared long-term series of onset dates for south and north Kerala. They reported that the mean date of onset for south Kerala is 30 May, with a standard deviation of 8.5 days, while the mean onset date for north Kerala is 1 June, with a standard deviation of 8.4 days. The frequency distribution of the onset dates over south Kerala during the 100-year period 1891–1990 is shown in Figure 18.13(b). The onset of the monsoon over Kerala, although it may appear to be of local character, is generally considered to be a pointer for the advance of the monsoon over the entire Indian subcontinent. The time series of the onset dates of the south-west monsoon suggests considerable interannual variability. During the past century, there had been extremes in the dates of onset of the monsoon over Kerala which were as much as three weeks away from the normal.

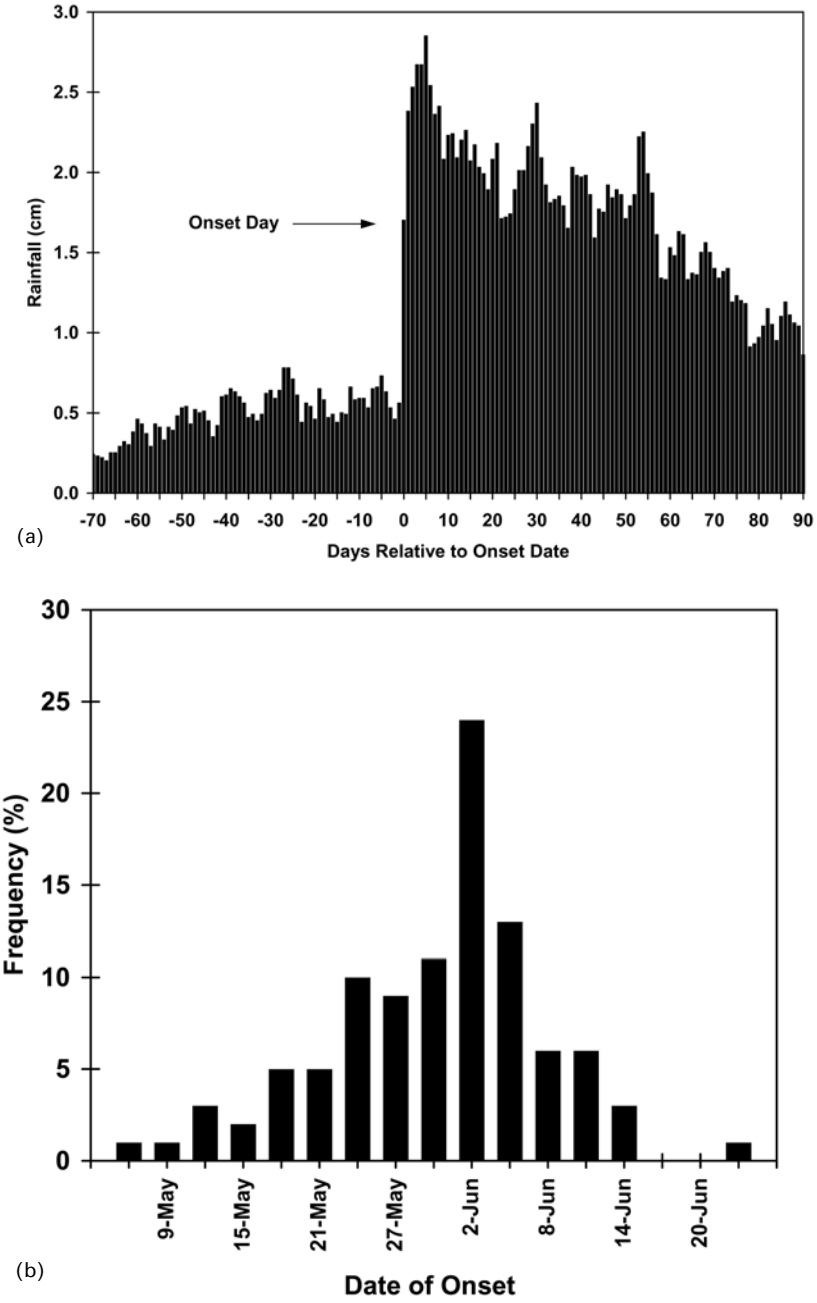

Figure 18.13. (a) Superposed-epoch composites of daily rainfall variation relative to the summer monsoon onset over south Kerala. (b) The frequency distribution of the onset dates of the south-west monsoon over south Kerala in three-day intervals for the period 1891–1990.

18.4 ROLE OF THE MONSOON IN RICE CULTIVATION IN THE STATE OF ANDHRA PRADESH IN INDIA

In India, rice is cultivated in the *Kharif* and *Rabi* seasons. *Kharif* rice is sown in July–August and harvested between October–January. The rice grown during the *Rabi* season is planted in winter (November–December) and is harvested in March–May. The rainfall during the summer monsoon determines to a large extent the availability of water for irrigation during the dry season. Hence, monsoon variability also has an impact on production of *Rabi* rice as the Indian rivers are mostly fed by the monsoon rainfall, with only a partial contribution from snowmelt in the northern regions.

To highlight the critical role of the summer monsoon variability in rice cultivation, we consider here rice production over the smaller spatial scales of the states of India. A large fraction of the area under rice in the state of west Bengal (which contributes by over 15% to the Indian production) is rain-fed, and large anomalies of the summer monsoon rainfall over the region have a large impact on the yield, area, as well as production (Gadgil *et al*., 1999a). On the other hand, a large fraction of the area under rice in Andhra Pradesh (Figure 18.14) is irrigated. Andhra Pradesh is a surplus rice growing state in India, which produces about 13% of the country's rice output with 9% of total rice area. Rice is the dominant staple food for about 70 million people in the state and a major source of livelihood for nearly 70% of rural households. Rice production and yields have nearly doubled with only a marginal expansion of cropped area since the introduction of modern rice varieties in the late 1960s (Janaiah, 2003). About 95% of the rice area in Andhra Pradesh under modern varieties is irrigated. However, this dramatic increase in rice production due to the use of modern varieties has almost plateaued during the last decade, once again bringing to the fore the weather (and consequently water) related stresses on rice production.

18.4.1 The impact of local and remote anomalies in seasonal rainfall

The interannual variation of the total kharif rice production in Andhra Pradesh and the seasonal rainfall (MJJASO) over three meteorological subdivisions of Andhra Pradesh, namely Coastal Andhra Pradesh, Telangana, and Rayalaseema (Figure 18.14) is shown in Figure 18.15 (color section). Of these, rice production is mainly concentrated over coastal Andhra Pradesh. In order to remove the technological trend from the production time series, a backward differencing filter is used (Stephenson *et al*., 2001), where the value for each year is expressed as the difference from the previous year. Similar differencing is also applied on the rainfall time series, to make them consistent with each other. All the correlation analyzes presented in this section are based on the difference filtered time series. All the major anomalies in the series closely agree with each other (Figure 18.15), highlighting the spatial coherence of season-scale rainfall anomalies over Andhra Pradesh and also their significant impact on the total rice production in the state. Figure 18.16 (color

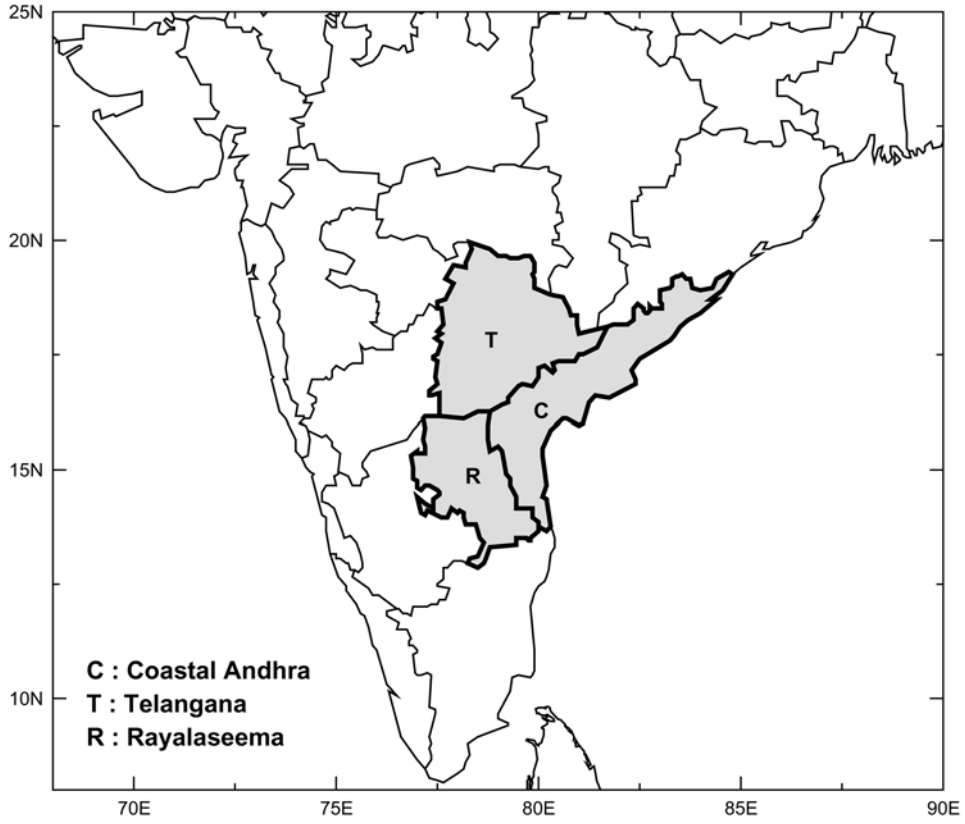

Figure 18.14. Andhra Pradesh state (shaded area) of India and its meteorological subdivisions.

section) presents the correlation between the monthly/seasonal rainfall over the three subdivisions of Andhra Pradesh with different rice production parameters (viz., area, production and yield of the kharif as well as the rabi crop). While almost all the rice parameters show significant correlation with the seasonal total rainfall, there are interesting differences on the monthly scale. The rainfall in the months of June, July, and August over both coastal Andhra Pradesh and Telangana is significantly correlated with the area as well as production of kharif rice, but not rabi rice. Rainfall in July and August over Rayalaseema significantly influences the kharif production in the state. Rainfall in the month of September appears to be more crucial for the rabi crop. Thus, the monsoon rainfall has a complementary influence on the kharif and rabi crops. In general, it can be seen that the correlations are the highest in the case of area and production of rice. However, the variations in yield per unit area do not seem to be sensitive to rainfall variability. This is possibly

because unviable cropping situations due to rainfall anomalies are abandoned. As already noted, the water required for rice cultivation also depends on the monsoon rainfall in catchment areas upstream in the western parts of the peninsula. Keeping this in view, we have examined the spatial patterns of correlations between the seasonal total rainfall and different rice parameters (Figure 18.17). For the kharif as well as rabi rice crops in Andhra Pradesh, the monsoon rainfall within the state as well as that over western Maharashtra and Karnataka is critical. As already seen, the rainfall has a limited impact on the yields. However, within the season, the kharif rice crop seems to be more dependent on local rainfall during the early part of the growing season, while in September the rainfall over the western peninsula is more favorable (Figure 18.18(a)). Interestingly, for the rabi crop, September rainfall over a large part of the peninsula stands out as the most important parameter affecting production (Figure 18.18(b)).

18.4.2 Impact of the timing of the onset of the monsoon

Rice cultivation involves transplantation of seedlings about one month after sowing. The seedlings are initially grown in nursery beds during the later part of the pre-monsoon season, with water from bore wells or by other methods of lifting water from the substantially reduced water available in the local canals/lakes. These nurseries are planned in such a way that the seedlings will be of transplantable age by the time the onset spells of the monsoon commence. Thus, even this operation is closely tied with the normal onset of the monsoon over the respective areas, which is typically in the later half of June. The transplantation activity is taken up during the onset phase, so that the cloudy and moist conditions help the young seedlings to establish. If the onset is delayed, transplantation cannot be taken up even if water for irrigation is available, as the high temperatures and intense solar radiation causes the seedlings to wilt. Consequently, the seedlings in nursery beds grow beyond the optimal age for transplantation, making the nursery beds unviable. Some farmers raise nursery beds with staggered dates to account for possible anomalies in the onset date, but such practices cannot be taken up on a large scale. Further, it is also essential that the rice fields have enough water available in the rivers for irrigation in the transplantation phase. Most of the rivers in Andhra Pradesh are dried up during the pre-monsoon season, and the release of water from the hydrological reservoirs initially helps to provide water at the time of transplantation. However, a weak onset spell in the upstream areas causes delays in the release of water, either delaying the transplantation or sometimes even causing a total abandonment of the activity. Thus, the onset phase not only over the state, but also over the western parts of the peninsula where the rivers fed by the summer monsoon originate, has a crucial impact on the initial phase of rice cultivation. For example, due to the late onset of the monsoon in 2003 which followed a severe drought in 2002, there was a substantial delay in the release of water for irrigation leading to large-scale abandonment of transplantation in the main rice-growing

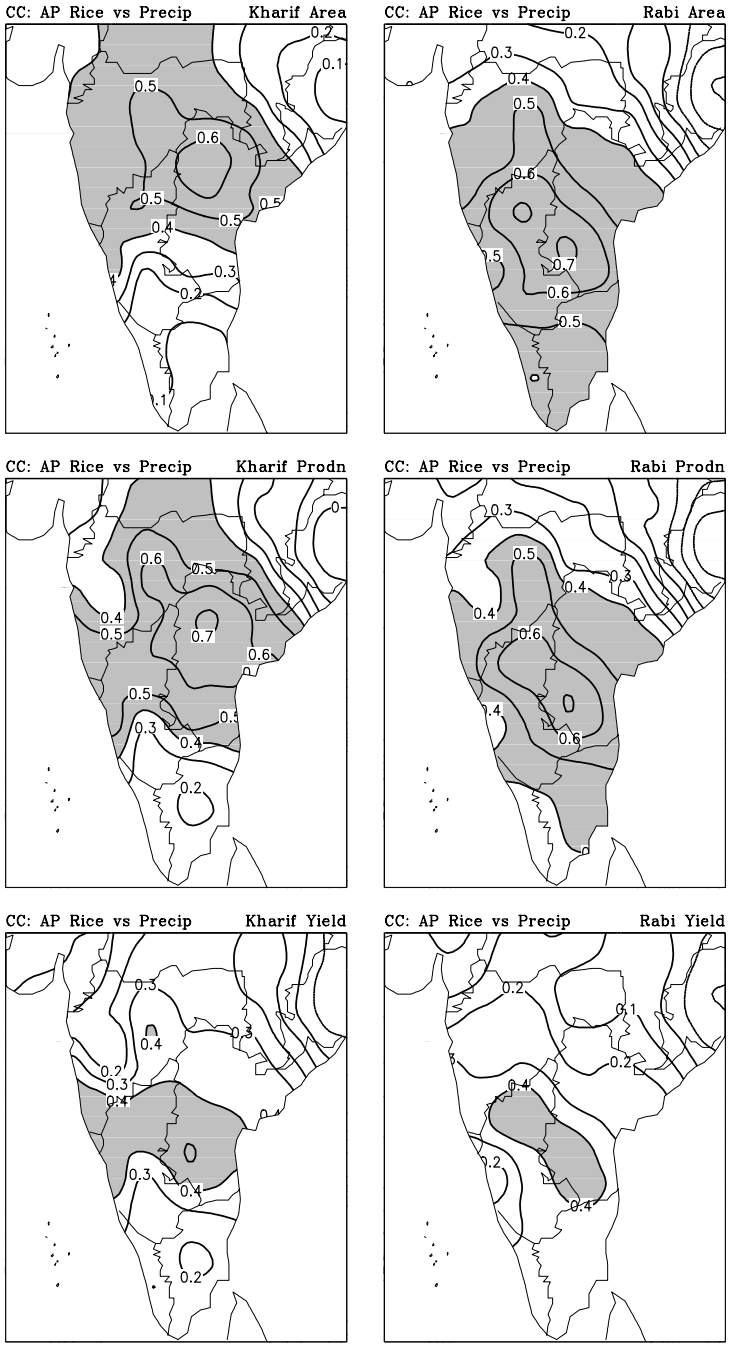

Figure 18.17. Spatial patterns of correlation between various rice production parameters over Andhra Pradesh and seasonal (MJJASO) rainfall over the peninsular of India.

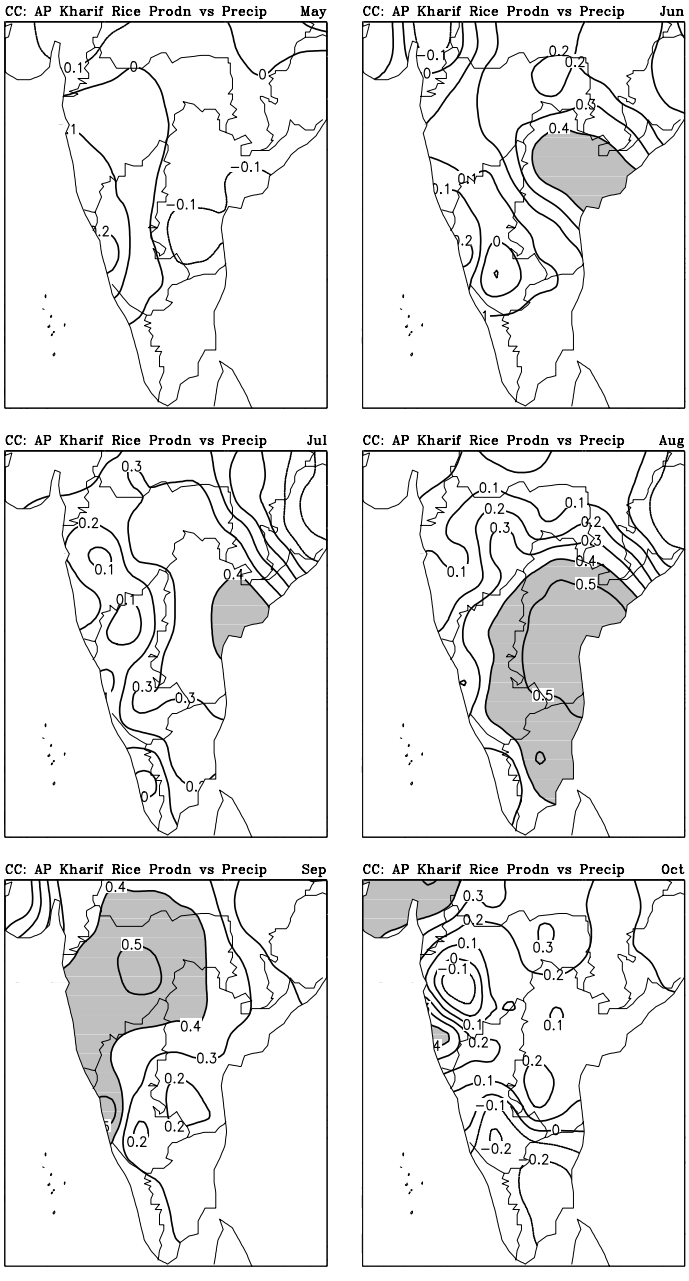

(a)

Figure 18.18. (a) Spatial patterns of correlation between kharif rice production in Andhra Pradesh and monthly rainfall during the monsoon season over the Indian peninsula. (b) Same as (a) but for rabi rice.

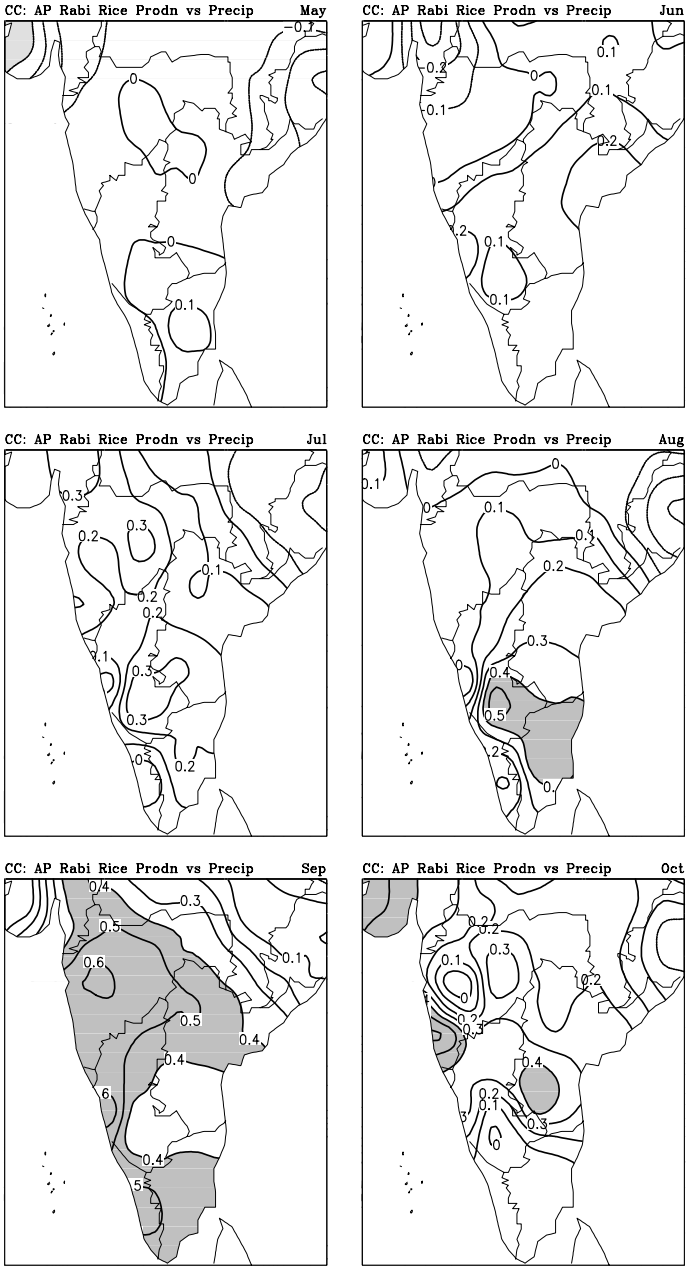
CC: AP Rabi Rice Prodn vs Precip May
CC: AP Rabi Rice Prodn vs Precip Jun
CC: AP Rabi Rice Prodn vs Precip Jul
CC: AP Rabi Rice Prodn vs Precip Aug
CC: AP Rabi Rice Prodn vs Precip Sep
CC: AP Rabi Rice Prodn vs Precip Oct

(b)

districts of Andhra Pradesh. Thus, monsoon variability has a significant influence on the area under the rice crop as well as production. Once the transplanted rice crop is established and enters a vegetative growth phase, the crop can withstand dry spells within the monsoon season. However, irrigation is still essential as the crop is grown under inundated conditions. Indeed, a few dry spells with bright sunshine may even help the crop to grow better and ward off pests and diseases which thrive under cloudy and humid conditions. Thus, intraseasonal variability may not be so crucial for irrigated crops, provided there is enough storage of water.

18.5 IMPACT OF THE MONSOON ON THE GROSS DOMESTIC PRODUCT – THE INDIAN CASE

It is well known that monsoon variability has a large impact on agricultural production in India. Since in the first half of the twentieth century, the contribution of the agricultural sector to the gross domestic product (GDP) was over 50%, the impact of monsoon variability on the economy was substantial. After freedom from colonial rule in 1947, there has been a rapid growth of other sectors and the share of the agricultural sector of the GDP has declined to about 22% (in 2000). However, the agricultural sector continues to be very important, since the livelihood of 70% of the working population is linked to agricultural activities and hence the Indian economy. Here we present an assessment of the impact of the monsoon on the agricultural component of the Indian GDP as well as the total Indian GDP (Gadgil and Gadgil, 2004).

The agricultural component of the GDP (GDP agriculture) has grown at an increasing rate with time (Figure 18.19). The rate of decrease in the contribution of the agricultural sector to GDP was rapid in the two decades following independence; smaller from the mid-1960s because of the Green Revolution but picked up again since 1980 with the commencement of liberalization of the economy (Figure 18.20). The Indian GDP has grown exponentially in the last five decades at a rate of about 3.8% before 1980 and 5.1% thereafter (Figure 18.21). We expect part of the fluctuations around the smoothly varying components of GDP agriculture and GDP (Figures 18.19 and 18.21) on the interannual scale to arise from the fluctuations in the monsoon.

The variation of the departure from the smoothly varying component (normalized by the actual value) with the anomalies of the ISMR is shown in Figure 18.22. It is seen that, for all the years characterized by the ISMR deficit of more than 10% (i.e., droughts), there is a negative departure of the GDP as well as GDP agriculture. Furthermore, for years with a deficit in the ISMR of over 5%, the magnitude of the dips in GDP agriculture and GDP increases with the magnitude of the ISMR anomalies, suggesting that deficits of ISMR have a large impact on the GDP

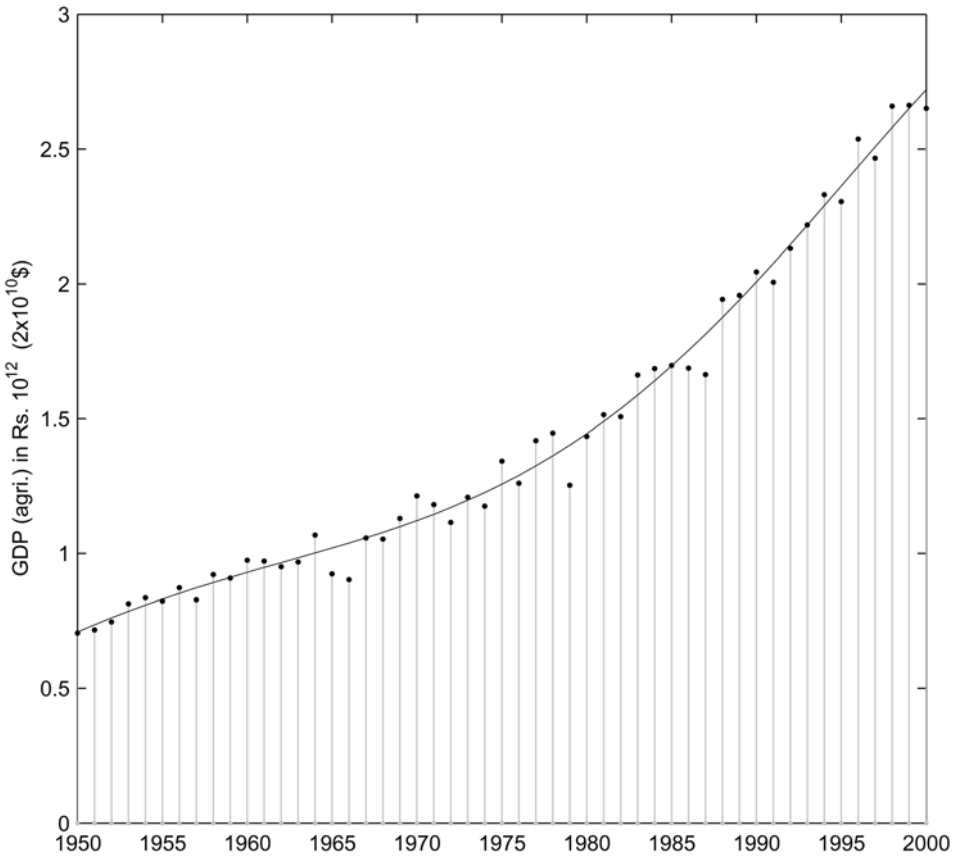

Figure 18.19. Variation of the agricultural component of the Indian GDP (observed and fitted).

agriculture as well as GDP. All the years for which rainfall is very good (the ISMR is in an excess by well over 10%) are characterized by positive departures of GDP agriculture as well as GDP. However, the magnitude of these departures does not appear to depend on the magnitude on the ISMR anomalies. When the monsoon rainfall is not as high, but still well above average (ISMR anomaly being positive between 5 and 10%), the values of the departure of the GDP and GDP agriculture are highly scattered. All but one such year are characterized by positive departures of GDP agriculture. However, the impact of above average monsoon rainfall on GDP agriculture does not seem to be commensurate with the magnitude of the rainfall anomaly; rather it seems to follow a law of diminishing returns. The relationship of

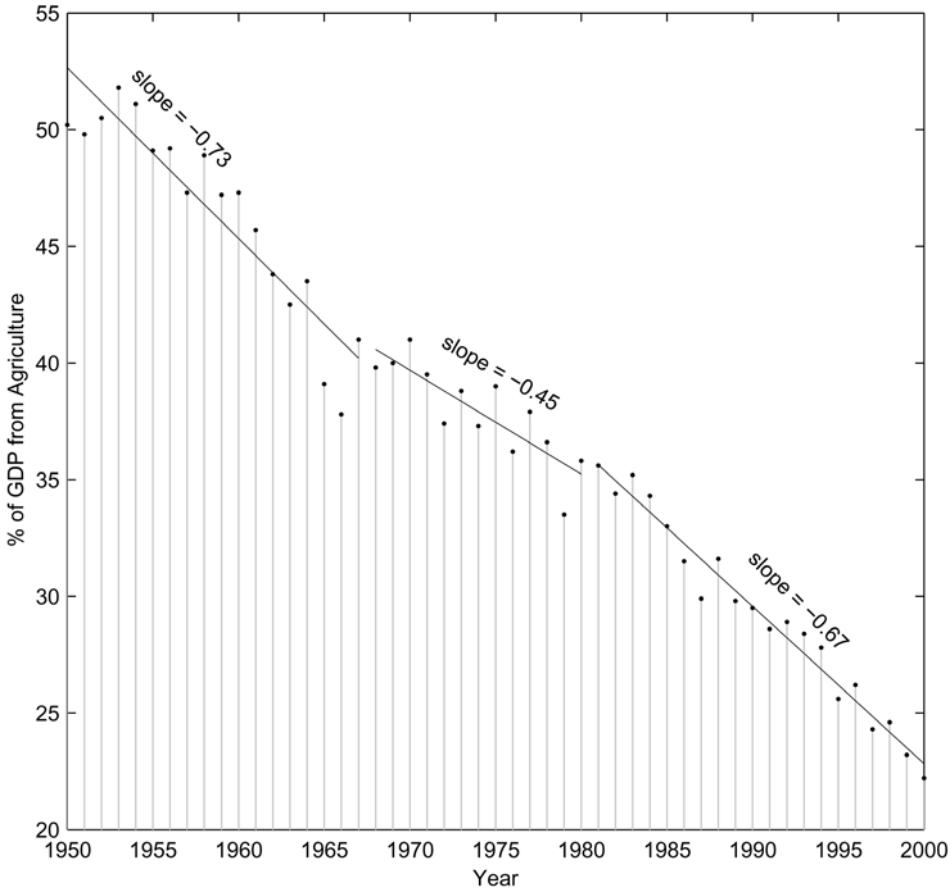

Figure 18.20. Variation of the percentage contribution of agriculture to the Indian GDP.

departures of GDP to positive rainfall anomalies in this range (5 to 10%) is more complex with more than half the years being characterized by negative departures.

Thus, for both GDP agriculture and GDP, there appears to be a large adverse impact of deficit monsoon rainfall, which increases with an increase in the magnitude of the deficit. However, when the rainfall is above average, the magnitudes of the GDP-agriculture as well as GDP departures are weakly related to that of the rainfall anomaly and the GDP-agriculture/GDP anomalies for such years are positive only for positive rainfall anomalies over 10 percent. Clearly, it has not been possible to reap as much benefit from good rainfall years in terms of enhanced agricultural production as the loss incurred in production in poor rainfall years.

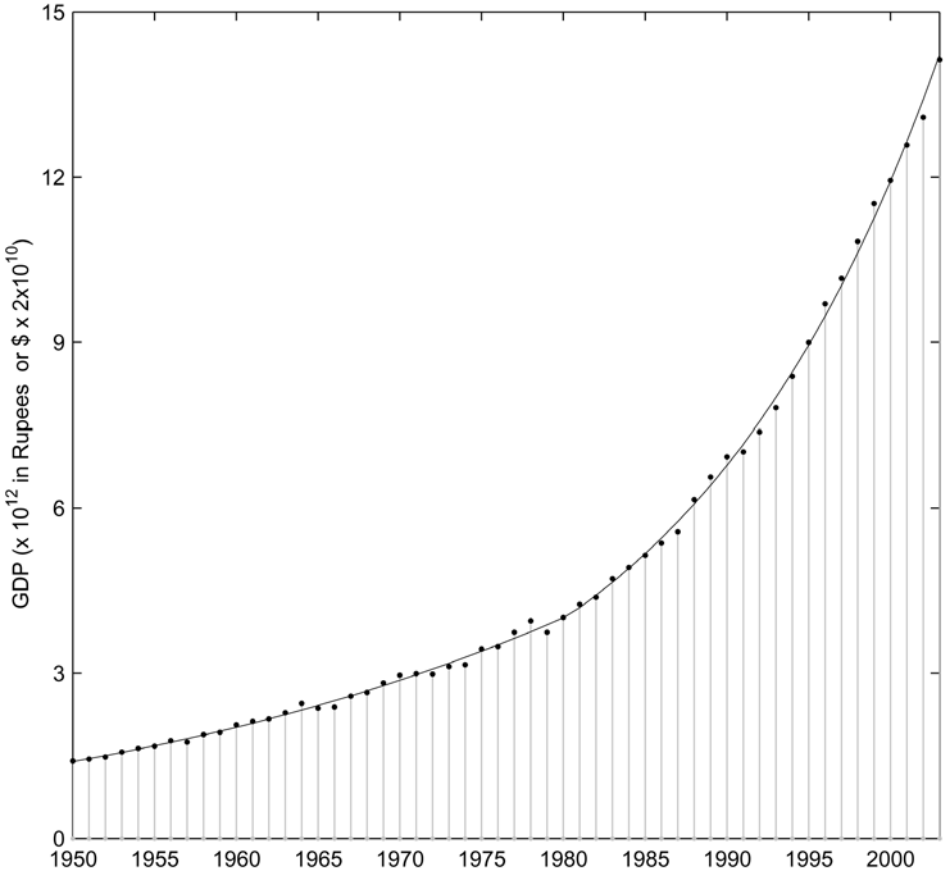

Figure 18.21. Variation of the Indian GDP (observed and fitted).

18.6 DISCUSSION ON THE USE OF METEOROLOGICAL INFORMATION AND PREDICTIONS FOR ENHANCEMENT OF AGRICULTURAL PRODUCTION IN A VARIABLE CLIMATE

We have seen that various facets of rainfall variability such as the interannual variation of the seasonal rainfall can have an impact on agricultural production and the economy. Such analyses can help in quantitative assessments of the impacts. In addition, we also need to derive the implications of the prediction of an event such as El Niño for the rainfall anomalies and hence the anomalies in agricultural production of the different regions, to provide advance information to enable mitigatory strategies. Also, if the aim is to use meteorological information or

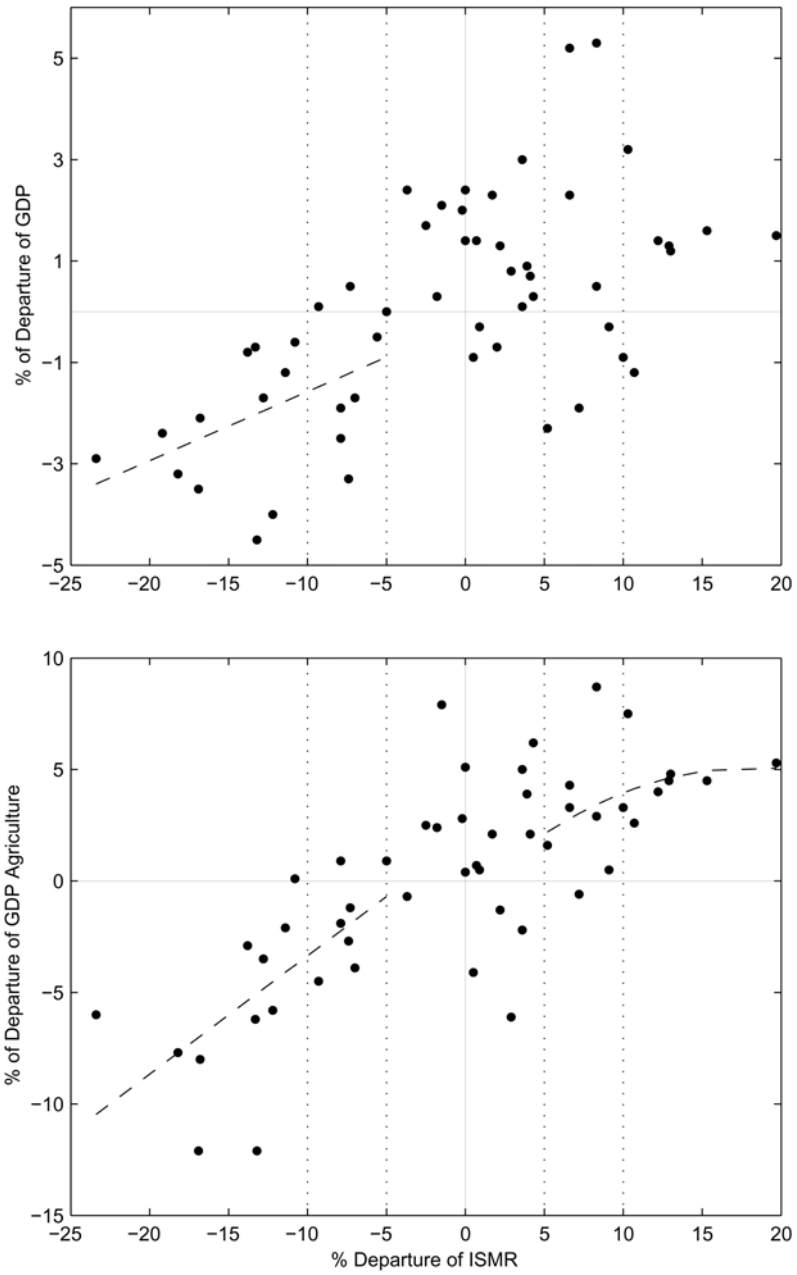

Figure 18.22. (*top*) Departure of the observed GDP from the fitted GDP (Figure 18.21) normalized by the fitted GDP vs. the ISMR anomalies normalized by the average ISMR for each year. (*bottom*) Departure of the observed GDP–agriculture from the fitted GDP–agriculture (Figure 18.21) normalized by the fitted GDP–agriculture vs. the ISMR anomalies normalized by the average ISMR for each year.

predictions for the enhancement of agricultural productivity, it is necessary to generate predictions that can directly impact farm level decisions.

18.6.1 Use of ENSO predictions

We have seen that the area under rice cultivation in Indonesia is highly correlated with the May–October rainfall which in turn depends on ENSO. However, the impact of different El Niños on crop yields of the region appear to differ considerably, as shown for the Australian wheat yield by Potgieter *et al.* (2004). The rainfall anomaly patterns for June–September for the two recent El Niño events of 1997 and 2002 are shown in Figure 18.23 (color section). The marked difference between the two seasons suggests that it may be important to predict/assess the phase of EQUINOO as well as ENSO for assessing the impact on rainfall and hence crop yields for the Asian region.

18.6.2 The Indian case

We have seen that the agricultural production of the country as a whole does not increase with ISMR when the rainfall is well above average. Some insight into the quantum of enhancement of agricultural production achieved in the years with good rainfall *vis-á-vis* that achievable with the current level of agricultural science and technology, is provided by Sivakumar *et al.* (1983), who compared the yields of several rainfed crops on the farmers' fields with the yields at 15 dry-land stations over semiarid parts of India (Figure 18.24). The major difference in the farming practices at the agricultural stations relative to those on the farmers' fields is in the application of fertilizers and pesticides. It is seen that the yield at the agricultural stations increases more rapidly with rainfall in the growing season. This is probably because when rainfall is not a limiting factor, the yields are limited by the degree to which the nutritional requirements are met. The yield gap (i.e., the difference between these yields) increases with good rainfall years because the farmers do not make the necessary additional investments in fertilizers and pesticides on their rainfed land. It is clear that this is not because of a lack of know-how, since the farmers do make these additional investments for irrigated patches with assured yields. This is because the cost–benefit ratio for such applications is favorable only in the years in which the level of rainfall and yields are reasonably good. If meteorologists could provide reliable forecasts of seasonal rainfall on the scale of agroclimatic zones, it would be possible to influence these farm-level decisions and enhance production within the years with good rainfall.

We consider the relationship of the variation of crop performance with the variation of rainfall in the growing season for two cases: (i) rice in Andhra Pradesh and (ii) rain-fed peanut for the Anantapur district of the Rayalaseema subdivision of Andhra Pradesh. The variation of rice production with the variation of rainfall during May–October for the three subdivisions of Andhra Pradesh is shown in Figure 18.25. It is seen that when the rainfall is very much below average (a deficit of over 250 mm) the production also tends to be below

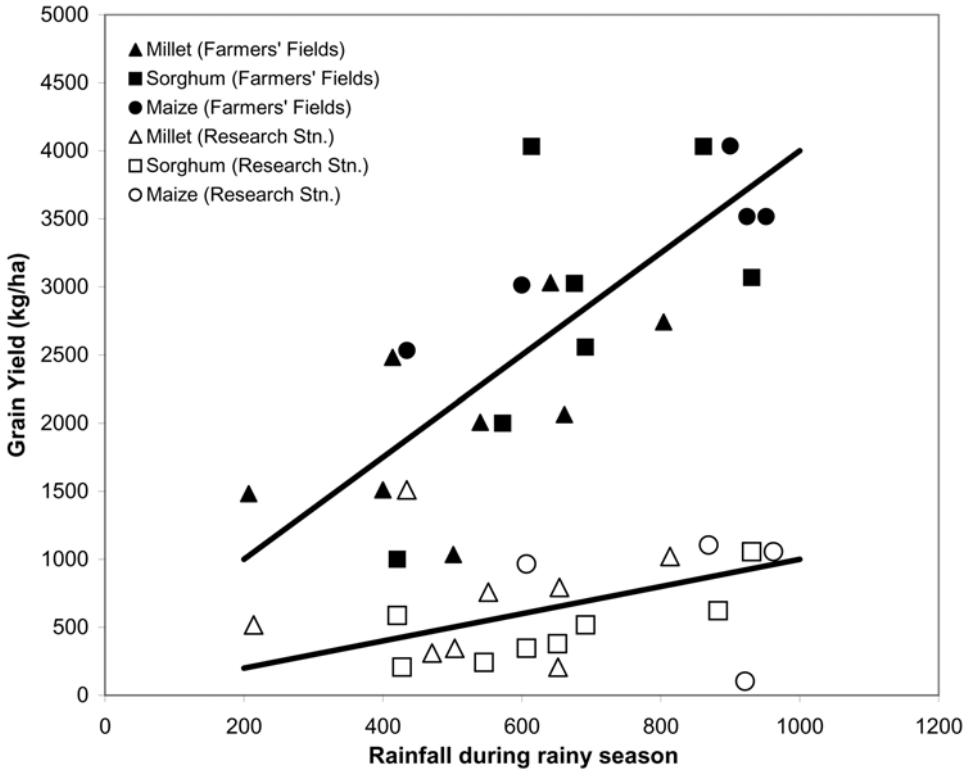

Figure 18.24. Relationship between rainfall during the rainy season and yield of maize, sorghum, and millet at 15 dryland locations in India.
After Sivakumar *et al.* (1983).

average; whereas when the rainfall is well above the average (an anomaly over 250 mm), the anomaly in production is almost always positive. Between these two limits there is a large spread. The variation during 1911–2000 of the peanut yield simulated by the PNUTGRO model (Boote *et al.*, 1987), which has been validated for the region (Singh *et al.*, 1994) and that of the observed district yield during 1975–2000, with rainfall during July–December at Anantapur station is shown in Figure 18.26. It is seen from Figure 18.26 that for every year in which the seasonal rainfall is above the threshold of 50 cm at Anantapur the model yield is above 700 kg per hectare. However, when the rainfall is less than 30 cm the chance of yield above this level is small. These two examples suggest that prediction of seasonal rainfall relative to the relevant thresholds for specific cropping systems would be of considerable use in farm-level decisions regarding application of fertilizers, pesticides, etc.

The impact of intraseasonal variation (i.e., the occurrence of dry spells on the crop yields) can also be high when they occur at critical stages of the crop (Rao *et al.*, 1999; Gadgil, 2003). This is illustrated in Figure 18.27 in which the daily rainfall at

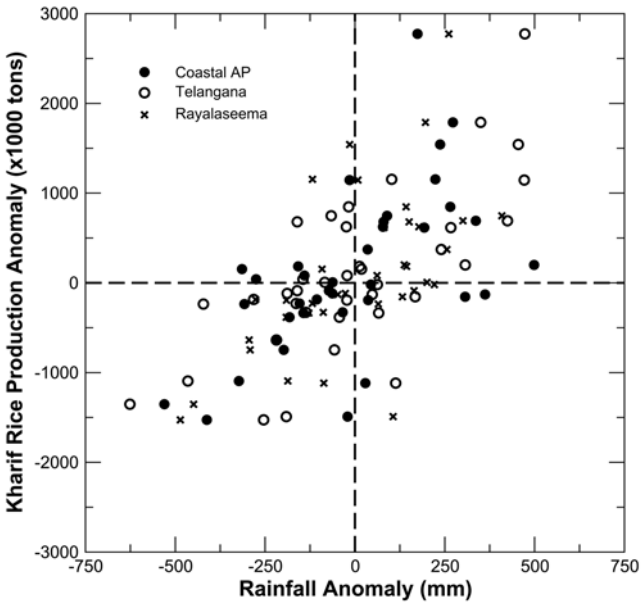

Figure 18.25. Variation of rice production anomalies with the variation of rainfall anomalies during May–October for the three subdivisions of Andhra Pradesh.

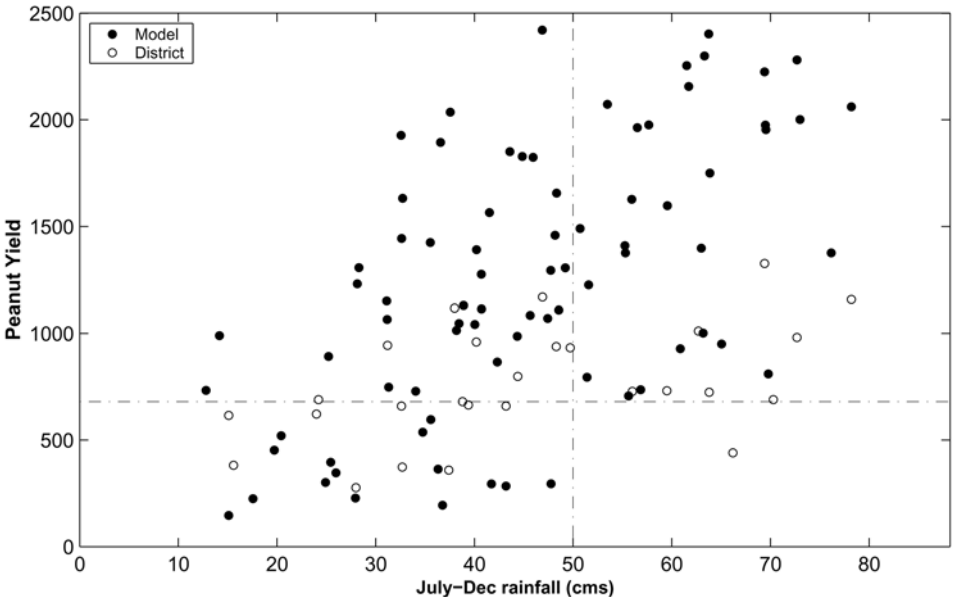

Figure 18.26. Simulated (PNUTGRO, 1911–2000; solid circles) and observed (1975–1998; open circles) peanut yield vs. July–December rainfall for the Anantapur district of Andhra Pradesh.

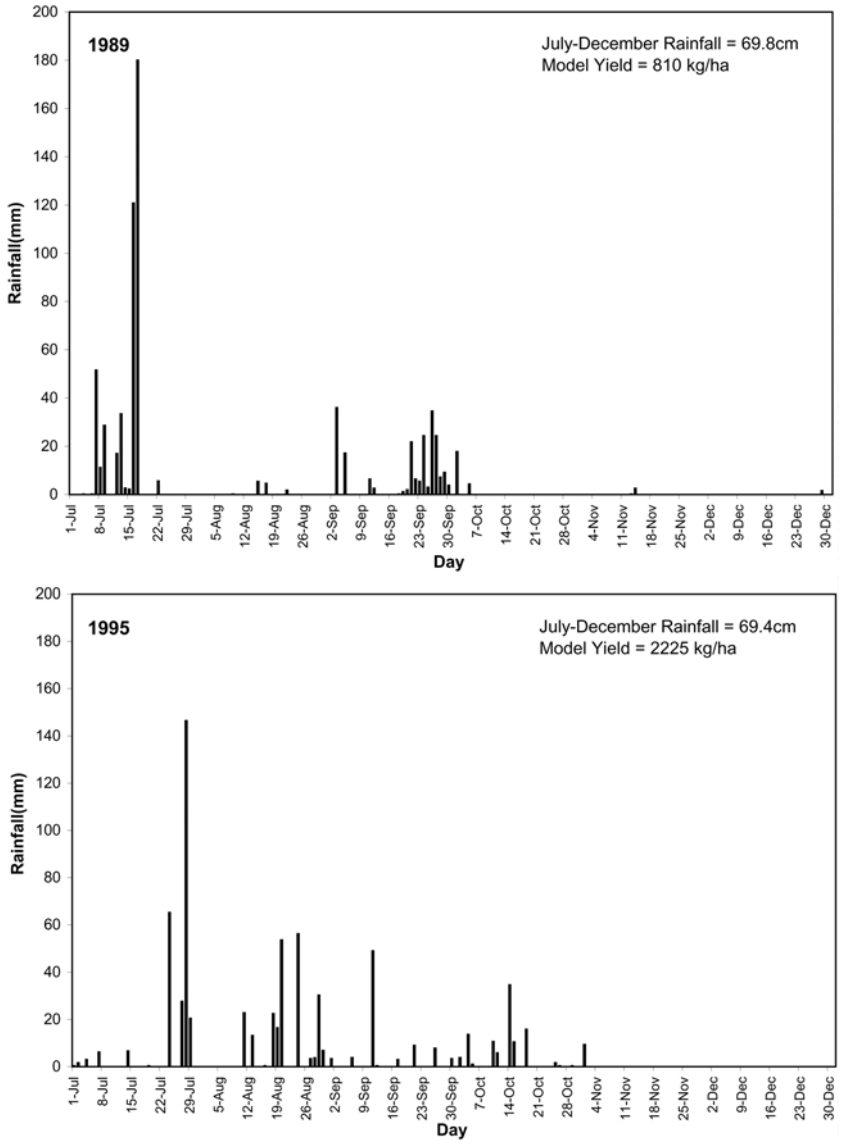

Figure 18.27. Daily rainfall at Anantapur during July to December in 1989 and 1995. Note that although the seasonal total rainfall is almost the same, the simulated yields are very different.

Anantapur for July–December 1989 and 1995 is shown. Although the total rainfall in the season is almost identical, the simulated yield for the latter year is more than twice that in the former year, which had a long dry spell in July–August. It appears unlikely that the detailed distribution of the rainfall in a season (i.e., the occurrence of such spells), can be predicted in the beginning of the season. However, available

information on climate variability can be used to choose the planting dates which imply a low probability of occurrence of such dry spells in the critical stages of the plant (Gadgil *et al.*, 2003).

A judicial use of information and prediction of important events should help in reducing adverse impacts and lead to better strategies of exploiting favorable conditions for enhancement of agricultural production.

18.7 ACKNOWLEDGEMENTS

The authors are grateful to Dr. G. B. Pant, Director, Indian Institute of Tropical Meteorology, for his keen interest in this field and the encouragement of this collaborative work. Much of the basic meteorological data used in the study has been provided by the India Meteorological Department. The authors are also thankful to Dr. Mark New for supplying the CRU gridded precipitation data and to IRRI for the data on rice crops. The authors have greatly benefited from many interesting discussions with Dr. K. Krishna Kumar of IITM. The authors place on record their deep appreciation of the excellent editorial review support provided by Dr. Bin Wang and the anonymous reviewers.

Bibliography

Abe, M., A. Kitoh and T. Yasunari (2003) An evolution of the Asian summer monsoon associated with mountain uplift: Simulation with the MRI atmosphere–ocean coupled GCM. *J. Meteorol. Soc. Japan*, **81**, 909–933.

Abe, M., T. Yasunari and A. Kitoh (2004) Effects of large-scale orography on the coupled atmosphere–ocean system in the tropical Indian and pacific oceans in boreal summer. *J. Meteorol. Soc. Japan*, **82**, 745–759.

Abrol, I. P. (1996) India's agriculture scenario. In: Y. P. Abrol, S. Gadgil and G. B. Pant (eds), *Climate Variability and Agriculture*. Narosa Publishing House, New Delhi, pp. 19–25.

Agee, E. M. (1984) Observations from space and thermal convection: A historical perspective. *Bull. Amer. Meteorol. Soc.*, **65**, 938–949.

Agnihotri, R., K. Dutta, R. Bhushan and B. Somayajulu (2002) Evidence for solar forcing on the Indian monsoon during the last millennium. *Earth and Planetary Science Letters*, **198**, 521–527.

Ailikun, B. and T. Yasunari (2001) ENSO and Asian summer monsoon: Persistence and transitivity in the seasonal march. *J. Meteorol. Soc. Japan*, **79**, 145–159.

Ajaya Mohan, R. S. and B. N. Goswami (2003) Potential predictability of the Asian summer monsoon on monthly and seasonal time scales. *Meteorol. Atmos. Phys.*, DOI 10.1007/s00703-002-0576-4.

Akiyama, T. (1975) Southerly transversal moisture flux into the extremely heavy rainfall zone in the Baiu season. *J. Meteorol. Soc. Japan*, **53**, 304–316.

Akiyama, T. (1984a) A medium-scale cloud cluster in a Baiu front. Part I: Evolution process and fine structure. *J. Meteorol. Soc. Japan*, **62**, 485–504.

Akiyama, T. (1984b) A medium-scale cloud cluster in a Baiu front. Part II: Thermal and kinematic fields and heat budget. *J. Meteorol. Soc. Japan*, **62**, 505–521.

Akiyama, T. (1989) Large, synoptic and mesoscale variations of the Baiu Front during July 1982, Part I: Cloud features. *J. Meteorol. Soc. Japan*, **67**, 57–81.

Alapaty, K., S. Raman, R. V. Madala and U. C. Mohanty (1994) Monsoon Rainfall Simulations with Kuo and Betts–Miller Schemes. *Meteorol. Atmos. Phys.*, **53**, 33–49.

Aldrian, E. and D. Susanto (2003) Identification of three dominant rainfall regions within Indonesia and their relationship to sea surface temperature. *Int. J. Climatol.*, **23**, 1435–1452.

Aldrian, E., L. Dumenil-Gates and F. H. Widodo (2003) *Variability of Indonesian Rainfall and the Influence of ENSO and Resolution in ECHAM4 Simulations and in the Reanalyses* (Report No. 346). Max-Planck Institute, Hamburg, Germany.

Alexander, G. D. and G. S. Young (1992) The relationship between EMEX mesoscale precipitation feature properties and their environmental characteristics. *Monthly Weather Review*, **120**, 554–564.

Alexander, G., R. N. Keshvamurthy, U. S. De, R. Chellapa, S. K. Das and P. V. Pillai (1978) Fluctuations of monsoon activity. *Ind. J. Meteorol. Hydro. Geophy.*, **29**, 76–87.

Alexander, M. A., J. D. Scott and C. Deser (2000) Processes that influence sea surface temperature and ocean mixed layer depth variability in a coupled model. *J. Geophys. Res.*, **105**, 16823–16842.

Alexander, M. A., I. Blade, M. Newman, J. R. Lanzante, N.-C. Lau and J. D. Scott (2002) The atmospheric bridge: The influence of ENSO teleconnections on air–sea interaction over the global oceans. *J. Climate*, **15**, 2205–2231.

Alexander, M. A., N.-C. Lau and J. D. Scott (2004) Broadening the atmospheric bridge paradigm: ENSO teleconnections to the tropical west Pacific-Indian Oceans over the seasonal cycle and to the North Pacific in summer. In: C. Wang, S.-P. Xie and J. A. Carton (eds), *Earth's Climate: the Ocean–Atmosphere Interaction* (AGU Geophysical Monograph No. 147). American Geophysical Union, Washington, D.C., pp. 85–103.

Ali, A. and J. U. Chowdhury (1997) Tropical cyclone risk assessment with special reference to Bangladesh. *Mausam*, **48**, 305–322.

Allan, R. J. (1991) Scientific basis and societal impact. In: M. H. Glantz, R. W. Katz and N. Nicholls (eds), *Teleconnections Linking Worldwide Climate Anomalies*. Cambridge University Press, Cambridge, UK, pp. 73–120.

Allan, R. J., J. A. Lindesay and D. E. Parker (1996) *El Niño, Southern Oscillation and Climatic Variability*. CSIRO Publishing, 405pp.

Allen, S. (1981) *Australian Low-level Jet Climatology* (Meteorological Note 119). Department of Science and Technology, Australian Bureau of Meteorology, 23 pp. [Available from Bureau of Meteorology, G.P.O. Box 1289K, Melbourne VIC 3001, Australia.]

Allen, M. R. and W. J. Ingram (2002) Constraints on future changes in climate and the hydrologic cycle. *Nature*, **419**, 224–232.

Alley, R. B., S. Anandakrishnan and P. Jung (2001) Stochastic resonance in the North Atlantic. *Paleoceanography*, **16**, 190–198.

Almogi-Labin, A., G. Schmield, C. Hemleben, R. Siman-Tov, M. Segl and D. Meischner (2000) The influence of the NE winter monsoon on productivity changes in the Gulf of Aden, NW Arabian Sea, during the last 530 ka as recorded by foraminifera. *Marine Micropaleontology*, **40**, 295–319.

Altabet, M., D. Murray and W. Prell (1999) Climatically linked oscillations in Arabian Sea denitrification over the last 1 m.y.: Implications for marine N Cycle. *Paleoceanography*, **14**, 732–743.

Altabet, M. A., R. Francois, D. W. Murray and W. L. Prell (1995) Climate-related variations in denitrification in the Arabian Sea from sediment $^{15}N/^{14}N$ ratios. *Nature*, **373**, 506–509.

Altabet, M. A., M. J. Higginson and D. W. Murray (2002) The effect of millennial-scale changes in Arabian Sea denitrification on atmospheric CO_2. *Nature*, **415**, 159–162.

An, S.-I. and B. Wang (2000) Interdecadal change of the structure of the ENSO mode and its impact on the ENSO frequency. *J. Climate*, **13**, 2044–2055.

An, S.-I. and B. Wang (2001) Mechanisms of locking the El Niño and La Niña mature phases to boreal winter. *J. Climate*, **14**, 2164–2176.

An, Z., J. E. Kutzbach, W. Prell and S. C. Porter, (2001) Evolution of Asian monsoons and phased uplift of the Himalaya–Tibetan Plateau since late Miocene times. *Nature*, **411**, 62–66.

An, Z. S. (2000) The history and variability of the East Asian paleomonsoon climate. *Quaternary Science Reviews*, **19**, 171–187.

An, Z. S., G. Kukla, S. C. Porter and J. L. Xiao (1991a) Late Quaternary dust flow on the Chinese Loess Plateau. *Catena*, **18**, 125–132.

An, Z. S., G. Kukla, S. C. Porter and J. L. Xiao (1991b) Magnetic susceptibility evidence of monsoon variations on the Loess Plateau of central China during the last 130,000 years. *Quaternary Research*, **36**, 29–36.

Ananthakrishnan, R. and M. K. Soman (1988) The onset of SW monsoon over Kerala. *Int. J. Climatol.*, **8**, 283–296.

Ananthakrishnan, R. and M. K. Soman (1989) The dates of onset of the southwest monsoon over Kerala for the period 1870–1900. *Int. J. Climatol.*, **9**, 321–322.

Anderson, D. L. T. and A. E. Gill (1975) Spin-up of a stratified ocean, with application to upwelling. *Deep-Sea Res.*, **22**, 583–596.

Anderson, D. L. T. and P. B. Rowlands (1976) Somali Current response to southwest monsoon: Relative importance of local and remote forcing. *J. Marine Sci.*, **34**(3), 395–417.

Anderson, D. M. (1991) Foraminiferal evidence of monsoon upwelling off Oman during the late Quaternary (Ph.D. thesis). Brown University, Providence.

Anderson, D. M. (1999) Extremes in the Indian Ocean. *Nature*, **401**, 337–338.

Anderson, D. M. and W. L. Prell (1991) Coastal upwelling gradient during the late Pleistocene. In: W. L. Prell, N. Niitsuma and K. Emeis (eds), *Proceedings of the Ocean Drilling Program* (Scientific Results 117 Ocean Drilling Program). College Station, pp. 265–276.

Anderson, D. M. and W. L. Prell (1993) A 300 KYR record of upwelling off Oman during the late Quaternary: Evidence of the Asian southwest monsoon. *Paleoceanography*, **8**, 193–208.

Anderson, D. M., J. C. Brock and W. L. Prell (1992) Physical upwelling processes, upper ocean environment, and the sediment record of the southwest monsoon. In: *Upwelling Systems: Evolution Since the Early Miocene*. UK Geological Society, London, pp. 121–130.

Anderson, D. M., J. T. Overpeck, and A. K. Gupta (2002) Increase in the Asian southwest monsoon during the past four centuries. *Science*, **297**, 596–599.

Anjaneylu, T. S. S. (1969) On the estimates of heat and moisture budgets over the Indian monsoon trough zone. *Tellus*, **21**, 64–74.

Annamalai, H. and J. M. Slingo (2001) Active/break cycles: Diagnosis of the intraseasonal variability of the Asian Summer Monsoon. *Climate. Dynamics*, **18**, 85–102.

Annamalai, H., J. M. Slingo, K. R. Sperber and K. Hodges (1999) The mean evolution and variability of the Asian summer monsoon: Comparison of ECMWF and NCEP–NCAR reanalyses. *Monthly Weather Review*, **127**, 1157–1186.

Arakawa, A. and J.-M. Chen (1987) Closure assumption in the cumulus parameterization problem. In: T. Matsuno (ed.), *Short- and Medium-Range Numerical Weather Prediction* (Special Volume of *J. Meteorol. Soc. Japan*, pp. 107–131).

Arkin, P. A. and P. J. Webster (1985) Annual and interannual variability of tropical–extratropical interaction: An empirical study. *Monthly Weather Review*, **113**, 1510–1523.

Arpe, K., L. Dumenil and M. A. Giogetta (1998) Variability of the Indian monsoon in the ECHAM3 model: Sensitivity to sea surface temperature, soil moisture, and the stratospheric quasi-biennial oscillation. *J. Climate*, **11**, 1837–1858.

Ashok, K., Z. Guan and T. Yamagata (2001) Impact of the Indian Ocean Dipole on the relationship between the Indian Monsoon rainfall and ENSO. *Geophys. Res. Lett.*, **28**, 4499–4502.

Ashrit, R. G., K. Rupa Kumar and K. Krishna Kumar (2001) ENSO–monsoon relationships in a greenhouse warming scenario. *Geophys. Res. Lett.*, **28**, 1727–1730.

Ashrit, R. G., H. Douville and K. Rupa Kumar (2003) Response of the Indian monsoon and ENSO–monsoon teleconnection to enhanced greenhouse effect in the CNRM coupled model. *J. Meteorol. Soc. Japan*, **81**, 779–803.

Ashrit, R. G., A. Kitoh and S. Yukimoto (2005) Transient response of ENSO–monsoon teleconnection in MRI-CGCM2 climate change simulations. *J. Meteorol. Soc. Japan.*, **83**, 273–291.

Asnani, G. C. (1993) *Tropical Meteorology* (Vols I and II). Noble Printers Pune, India.

Awade, S. T. and R. N. Keshvamurty (1975) Vertical motions in the Indian summer monsoon. *Ind. J. Meteorol. Geophys*, **26**, 384–390.

Bamzai, A. S. and J. Shukla (1999) Relation between Eurasian snow cover, snow depth and the Indian summer monsoon: An observational study. *J. Climate*, **12**, 3117–3132.

Banerjee, A. K., P. N. Sen and C. R. V. Raman (1978) On foreshadowing southwest monsoon rainfall over India with mid-tropospheric circulation anomaly of April. *Indian J. Meteorol. Hydrol. Geophys.*, **29**, 425–431.

Banerji, S. K. (1950) Methods of foreshadowing monsoon and winter rainfall in India. *Indian J. Meteorol. Geophys.*, **1**, 4–14.

Bao, C. L. (1987) *Synoptic Meteorology in China*. China Ocean Press, Beijing, pp. 82–117.

Bard, E., G. Raisbeck, F. Yiou and J. Jouzel (2000) Solar irradiance during the last 1200 years based on cosmogenic nuclides. *Tellus*, **52B**, 985–992.

Barker D. M., W. Huang, Y.-R. Guo, A. J. Bourgeois and Q. N. Xiao (2004) A three-dimensional variational data assimilation system for MM5: Implementation and initial results. *Monthly Weather Review*, **132**, 897–914.

Barnes, G. M. and K. Sieckman (1984) The environment of fast- and slow-moving tropical mesoscale convective cloud lines. *Monthly Weather Review*, **112**, 1782–1794.

Barnett, T. P. (1983) Interaction of the monsoon and Pacific trade wind system at interannual time scales. Part I: The equatorial zone. *Monthly Weather Review*, **111**, 756–773.

Barnett, T. P. (1984a) Interaction of the monsoon and Pacific trade wind system at interannual time scales. Part II: The tropical band. *Monthly Weather Review*, **112**, 2380–2387.

Barnett, T. P. (1984b) Interaction of the monsoon and Pacific trade wind system at interannual time scales. Part III: A partial anatomy of the Southern Oscillation. *Monthly Weather Review*, **112**, 2388–2400.

Barnett, T. P. (1985) Variations in near-global sea level pressure. *J. Atmos. Sci.*, **42**, 478–501.

Barnett, T. P. (1988) Variations in near-global sea level pressure: Another view. *J. Climate*, **1**, 225–230.

Barnett, T. P. (1991) The interaction of multiple time scales in the tropical climate system, *J. Climate*, **4**, 269–285.

Barnett, T. P. and R. Preisendorfer (1987) Origins and levels of monthly and seasonal forecast skill for United States surface air temperatures determined by canonical correlation analysis. *Monthly Weather Review*, **115**, 1825–1850.

Barnett, T. P., L. Dumenil, U. Schlese, E. Roecker and M. Latif (1989) The effect of Eurasian snow cover on regional and global climate variations. *J. Atmos. Sci.*, **46**, 661–685.

Barnston (1994) Linear statistical short-term climate predictive skill in the Northern Hemisphere. *J. Climate*, **7**, 1513–1564.

Bassnett, T. A. and D. E. Parker (1997) Development of global sea level pressure data set GMSLP2. *Climate Res. Tech. Note*, **79**, 54pp.

Basu, S., G. R. Iyengar and A. K. Mitra (2002) Impact of a Nonlocal Closure Scheme in a simulation of a monsoon system over India. *Monthly Weather Review*, **130**, 161–170.

Battisti, D. S. and A. C. Hirst (1989) Interannual variability in the tropical atmosphere–ocean model: Influence of the basic state, ocean geometry and nonlinearity. *J. Atmos. Sci.*, **46**, 1687–1712.

Beaufort, L. (1996) Dynamics of the monsoon in the Equatorial Indian Ocean over the last 260,000 years. *Quaternary International*, **31**, 13–18.

Beaufort, L., T. de Garidel-Thoron, A. C. Mix and N. G. Pisias (2001) ENSO-like forcing on oceanic primary production during the late Pleistocene. *Science*, **293**, 2440–2444.

Beaufort, L., T. de Garidel-Thoron, B. Linsley, D. Oppo and N. Buchet (2003) Biomass burning and oceanic primary production estimates in the Sulu Sea area over the last 380 kyr and the East Asian monsoon dynamics. *Marine Geology*, **201**, 53–65.

Beer, J., W. Mende and R. Stellmacher (2000) The role of the sun in climate forcing. *Quaternary Science Reviews*, **19**, 403–415.

Beer, J., R. Muscheler, G. Wagner, C. Laj, C. Kissel, P. W. Kubik and H.-A. Synal (2002) Cosmogenic nuclides during Isotope Stages 2 and 3. *Quaternary Science Reviews*, **21**, 1129–1139.

Behera, S. K. and T. Yamagata (2001) Subtropical SST dipole events in the southern Indian Ocean. *Geophys. Res. Lett.*, **28**, 327–330.

Bei, G. F. and L. Young (1993) A statistical analysis of cold waves in Inner Mongolia, *Inner-Mongolia Meteorology*, **2**, 4–9.

Benestad, R. (ed.) (2002) *Solar Activity and Earth's Climate*. Springer, New York, 288pp.

Bengtsson, L., M. Botzet and M. Rsch (1996) Will greenhouse gas-induced warming over the next 50 years lead to higher frequency and greater intensity of hurricanes? *Tellus*, **48A**, 57–73.

Bennetts, D. A. and B. J. Hoskins (1979) Conditional symmetric instability: A possible explanation for frontal rainbands. *Quart. J. Roy. Meteorol. Soc.*, **105**, 945–962.

Berbery, E. H. and J. Noguespaegle (1993) Intraseasonal Interactions between the Tropics and Extratropics in the Southern Hemisphere. *J. Atmos. Sci.*, **50**, 1950–1965.

Betts, A. K., P. Viterbo, A. Beljaars, H.-L. Pan, S.-Y. Hong, M. Goulden and S. Wofsy (1998) Evaluation of land–surface interaction in ECMWF and NCEP/NCAR reanalysis models over grassland (FIFE) and boreal forest (BOREAS). *J. Geophys. Res.*, **103**, 23079–23086.

Bhalme, H. N. and D. A. Mooley (1980) Large Scale droughts and monsoon circulation. *Monthly Weather Review*, **108**, 1197–1211.

Bhanu Kumar, O. S. R. U. (1987) Seasonal variation of Eurasian snow cover and its impact on the Indian summer monsoon. *IAHS Publ.*, **166**, 51–60.

Bhanu Kumar, O. S. R. U. (1988) Interaction between Eurasian winter snow cover and location of the ridge at the 500 hPa level along 75°E. *J. Meteorol. Soc. Japan*, **66**, 509–514.

Bhaskara Rao, N. S. and M. V. Dekate (1967) Effect of vertical wind shear on the growth of convective clouds. *Quart. J. Roy. Meteorol. Soc.*, **93**, 363–367.

Bhaskaran, B. and J. F. B. Mitchell (1998) Simulated changes in Southeast Asian monsoon precipitation resulting from anthropogenic emissions. *Int. J. Climatol.*, **18**, 1455–1462.

Bhaskaran, B., J. F. B. Mitchell, J. R. Lavery and M. Lal (1995) Climatic response of the Indian subcontinent to doubled CO_2 concentrations. *Int. J. Climatol.*, **15**, 873–892.

Bhat, G. S., S. Gadgil, P. V. Harish Kunmar, S. R. Kalsi, P. Madhusoodanan, V. S. N. Murty, C. V. K. Prasada Rao, V. Ramesh Babu, L. V. G. Rao, R. R. Rao, *et al.* (2001) BOBMEX: The Bay of Bengal Monsoon Experiment. *Bull Amer. Meteorol. Soc.*, **82**, 2217–2243.

Bhatla, R., U. C. Mohanty, P. V. S. Raju and O. P. Madan (2004) A study on dynamic and thermodynamic of break monsoon. *Int. J. Climatol.* [In press.]

Bhide, U. V., R. Muzamdar, S. P. Ghanekar, D. K. Paul, T. C. Chen and G. V. Rao (1997) A diagnostic study on heat sources and moisture sinks in the monsoon trough area during active break phase of the Indian monsoon of 1979. *Tellus, Ser. A–Dyn. Meteorol. Oceanol.*, **49**, 455–473.

Bhowmik, Roy R. K. (2003) An evaluation of cyclone genesis parameters over the Bay of Bengal using model analysis. *Mausam*, **54**, 351–358.

Bi, M. Y. (1990) Features and cause of droughts in northern China in recent 40 years. In: D. Z. Ye and R. H. Huang (eds), *Advances in the Disastrous Climate Research Series*. China Meteorol. Press, Beijing, pp. 23–32.

Biello, J. A. and A. J. Majda (2005) A new multi-scale model for the Madden–Julian Oscillation. *J. Atmos. Sci.* [Submitted.]

Bishop, J. K. B. and W. B. Rossow (1991) Spatial and temporal variability of global surface solar irradiance. *J. Geophys. Res.*, **96**, 16839–16858.

Biswas N. C., U. S. De and D. R. Sikka (1998) The role of Himalayan massif–Tibetan Plateau and the mid-tropospheric tropical ridge over north India during the advance phase of the southwest monsoon. *Mausam*, **49**, 285–298.

Bjerknes, J. (1966) A possible response of the atmospheric Hadley circulation to equatorial anomalies of ocean temperature. *Tellus*, **18**, 820–829.

Bjerknes, J. (1969) Atmospheric teleconnections from the equatorial Pacific. *Monthly Weather Review*, **97**, 163–172.

Bjerknes, J. (1971) Continued studies on atmospheric teleconnections from equatorial Pacific. *Bull. Amer. Meteorol. Soc.*, **52**, 929.

Bjorck, S., R. Muscheler, B. Kromer, C. S. Andersen, J. Heinemeier, S. J. Johnsen, D. Conley, N. Koc, M. Spurk and S. Veski (2001) High-resolution analysis of an early Holocene climate event may imply decreased solar forcing as an important climate driver. *Geology*, **29**, 1101–1110.

Blackadar, A. K. (1957) Boundary-layer wind maxima and their significance for the growth of the nocturnal inversion. *Bull. Amer. Meteorol. Soc.*, **38**, 283–290.

Bladé, I. and D. L. Hartmann (1993) Tropical intraseasonal oscillations in a simple nonlinear model. *J. Atmos. Sci.*, **50**, 2922–2939.

Blanchard, D. O., W. R. Cotton and J. M. Brown (1998) Mesoscale circulation growth under conditions of weak inertial instability. *Monthly Weather Review*, **126**, 118–140.

Blanford, H. F. (1874) The rainfall of northern India in relations to the temperature and the vapour constituents of the atmosphere. *Proc. Trans. Roy. Soc.*, **164**, 563–653.

Blanford, H. F. (1884) On the connexion of Himalayan snowfall and seasons of drought in India. *Proc. Roy. Soc.*, **37**, 3–22.

Blanford, H. F. (1886) Rainfall of India. *Mem. India Meteorol. Dept.*, **2**, 217–448.

Blanford, H. F. (1884) On the connection of the Himalayan snowfall with dry winds and seasons of drought in India. *Proc. Roy. Soc.*, **37**, 3–22.

Blanford, H. F. (1887) *The Indian Meteorologists Vade-Mecum. Part 2: Meteorology of India*. Government Printing Office, Calcutta.

Bolin, B. (1950) On the influence of the earth's orography on the westerlies. *Tellus*, **2**, 184–195.

Bollasina, M. and S. Benedict (2004) The role of the Himalayas and the Tibetan Plateau within the Asian monsoon system. *Bull. Amer. Meteorol. Soc.*, **85**, 1001–1004.

Bonan, G. B. (1995) Land–atmospheric interactions for climate system models: Coupling biophysical, biogeochemical and ecosystem dynamical processes. *Remote Sensing of Environment*, **51**, 57–73.

Bond, G., B. Kromer, J. Beer, R. Muscheler, M. N. Evans, W. Showers, S. Hoffmann, R. Lotti-Bond, I. Hajdas and G. Bonani (2001) Persistent solar influence on north Atlantic climate during the Holocene. *Science*, **294**, 2130–2136.

Boer, G. J., G. Flato and D. Ramsden (2000) A transient climate change simulation with greenhouse gas and aerosol forcing: Projected climate to the twenty-first century. *Climate Dynamics*, **16**, 427–450.

Boote, K. J., J. W. Jones, G. Hoogenboom and G. G. Wilkerson (1987) PNUTGRO v1.0, Peanut crop growth and yield model (Technical documentation). Department of Agronomy and Agricultural Engineering, University of Florida, Gainesville, 121pp.

Boyle, J. S. and T.-J. Chen (1987) Synoptic aspects of the wintertime East Asian monsoon. In: C.-P. Chang and T. N. Krishnamurti (eds), *Monsoon Meteorology*. Oxford University Press, New York, pp. 125–160.

Braak, C. (1919) Atmospheric variations of short and long duration in the Malay Archipelago and neighbouring regions, and the possibility to forecast them. *Verhandelingen*, **5**, Koninklijk Magnetisch en Meteorologisch Observatorium te Batavia, 57 pp.

Braak, C. (1921–1929) Het climaat van Nederlandsch Indië. *Magn. Meteorol. Observ. Batavia*, Indonesia, Verhandelingen **8**, parts 1 and 2, 787 and 802pp.

Brier, G. W. (1978) The quasi-biennial oscillation and feedback processes in the atmosphere–ocean–earth system. *Monthly Weather Review*, **106**, 938–946.

Bryan, K. and A. H. Oort (1984) Seasonal variability of the global water balance based on aerological data. *J. Geophys. Res.*, **89**(11), 717–730.

Budziak, D., R. R. Schneider, F. Rostek, P. Muller, E. Bard and G. Wefer (2000) Late Quaternary insolation forcing on total organic carbon and C37 alkenone variations in the Arabian Sea. *Paleoceanography*, **15**, 307–321.

Buehring, C. (2001) East Asian monsoon variability on orbital- and millennial-to-subdecadal time scales (Ph.D thesis). University of Kiel, Kiel.

Businger, J. A., J. C. Wyngard, Y. Izumi and E. F. Bradley (1971) Flux profile relationship in the atmospheric surface layer. *J. Atmos. Sci.*, **28**, 181–189.

Cadet, D. (1983) The Monsoon over the Indian Ocean during summer 1975. 2: Break and active monsoons. *Monthly Weather Review*, **111**, 95–108.

Cadet, D. (1986) Fluctuations of precipitable water over the Indian Ocean during the 1979 summer monsoon. *Tellus Ser. A-Dyn. Meteorol. Oceanol.*, **38**, 170–177.

Cadet, D. and B. Diehl (1984) Interannual variability of surface fields over the Indian Ocean during recent decades. *Monthly Weather Review*, **112**, 1921–1935.

Cadet, D. and G. Reverdin (1981) Water-vapor transport over the Indian Ocean during summer 1975. *Tellus*, **33**, 476–487.

Cai, M., E. Kalnay and Z. Toth (2003) Bred vectors of the Zebiak–Cane model and their potential application to ENSO predictions. *J. Climate*, **16**, 40–56.

Cane, M. A. (1992) Tropical Pacific ENSO models: ENSO as a mode of the coupled system. In: K. E. Trenberth (ed.), *Climate System Modeling*. Cambridge University Press, Cambridge, UK, pp. 583–614.

Cane, M. A. and S. E. Zebiak (1985) A theory of El Niño and the Southern Oscillation. *Science*, **228**, 1085–1087.

Cane, M. A. and A. C. Clement (1999) A role for the tropical Pacific coupled ocean–atmosphere system on Milankovitch and millennial timescales. Part II: Global impacts. In: P. U. Clark, R. S. Webb and L. D. Keigwin (eds), *Mechanisms of Global Climate Change at Millennial Time Scales*. American Geophysical Union, Washington DC, pp. 373–383.

Cao, Jiping (1957) On the dynamics of orographically produced finite perturbations in baroclinic westerlies. *Acta. Meteor. Sinica*, **28**, 303–314 [in Chineese].

Carbone, R. E., J. D. Tuttle, D. A. Ahijevych and S. B. Trier (2002) Inferences of predictability associated with warm-season precipitation episodes. *J. Atmos. Sci.*, **59**, 2033–2056.

Carr, F. H. (1977) Mid-tropospheric cyclones of the summer monsoon. *Pure Appl. Geophys.*, **115**, 1383–1412.

Chan, J. C. L. and C. Y. Li (2004) The East Asian winter monsoon. In: C.-P. Chang (ed.), *East Asian Monsoon* (World Scientific Series on Meteorology of East Asia. Vol. 2), pp. 54–106.

Chan, J. C. L. (2005) A review of the East Asia winter monsoon. In: C. P. Chang, B. Wang and N. C. G. Lau (eds), *The Global Monsoon System: Research and Forecast*. World Meteorological Organization, Geneva, pp. 139–155.

Chahine, M. T. (1992) The hydrological cycle and its influence on climate. *Nature*, **359**, 373–380.

Chandrapalla, L. (1996) Long-term trends of rainfall and temperature in Sri Lanka. In: Y. P. Aberol, S. Gadgil and G. B. Pant (eds), *Climate Variability and Agriculture*. Norosa Publishing House, New Delhi, pp. 153–162.

Chang, C. B. (1979) On the influence of solar radiation and diurnal variation of surface temperatures on African disturbances (Report 79-3). Dept. of Meteorology, Florida State University, Tallahassee, Fl 32306, 157pp.

Chang, C. P. and T. Chen (1995) Tropical ciculations associated with southwest monsoon onset and westerly surges over the South China Sea. *Monthly Weather Review*, **123**, 3254–3267.

Chang, C. P. and T. N. Krishnamurti (1987) *Monsoon Meteorology* (Oxford Monographs on Geology and Geophys. No. 7). Oxford University Press, 544pp.

Chang, C. P. and K.-M. Lau (1980) Northeasterly cold surges and near-equatorial disturbances over winter MONEX area during December 1974. Part II: Planetary scale aspects. *Monthly Weather Review*, **108**, 298–312.

Chang, C. P. and K.-M. Lau (1982) Short-term planetary-scale interaction over the tropics and the midlatitudes during northern winter. Part I: Contrast between active and inactive periods. *Monthly Weather Review*, **110**, 933–946.

Chang, C. P. and T. Li (2000) A theory for the tropospheric biennial oscillation. *J. Atmos. Sci.*, **57**, 2209–2224.

Chang, C. P. and H. Lim (1988) Kelvin wave–CISK: A possible mechanism for the 30–50-day oscillations. *J. Atmos. Sci.*, **45**, 1709–1720.

Chang, C. P. and K. G. Lum (1985) Tropical–midlatitude interactions over Asia and the western Pacific Ocean during the 1983–1984 northern winter. *Monthly Weather Review*, **113**, 1345–1358.

Chang, C.-P., J. E. Erickson and K. M. Lau (1979) Northeasterly cold surges and near-equatorial disturbances over the winter MONEX area during Dec. 1974. Part I: Synoptic aspects. *Monthly Weather Review*, **107**, 812–829.

Chang, C. P., J. E. Millard and G. T. J. Chen (1983) Gravitational character of cold surges during Winter MONEX. *Monthly Weather Review*, **111**, 293–307.

Chang, C. P., J. M. Chen, P. A. Harr and L. E. Carr (1996) Northwestward-propagating wave patterns over the tropical western North Pacific during summer. *Monthly Weather Review*, **124**, 2245–2266.

Chang, C. P., S. C. Hou, H. S. Kuo and C. T. J. Chen (1998) The development of an intense East Asian summer monsoon disturbance with strong vertical coupling. *Monthly Weather Review*, **126**, 2692–2712.

Chang, C. P., L. Yi and G. T. J. Chen (2000a) A numerical simulation of vortex development during the 1992 East Asian summer monsoon onset using the Naveys regional model. *Monthly Weather Review*, **128**, 1604–1631.

Chang, C. P., Y. Zhang and T. Li (2000b) Interannual and interdecadal variations of the east Asian summer and tropical Pacific SSTs. Part I: Roles of the subtropical ridge. *J. Climate*, **13**, 4310–4325.

Chang, C. P., Y. Zhang and T. Li (2000c) Interannual and interdecadal variations of the east Asian summer monsoon and the tropical Pacific SSTs. Part II: Meridional structure of the monsoon. *J. Climate*, **13**, 4326–4340.

Chang, C. P., P. Harr and J. Ju (2001) Possible roles of Atlantic circulations on the weakening Indian monsoon rainfall–ENSO relationship. *J. Climate*, **14**, 2376–2380.

Chang, C. P., C. H. Liu and H. C. Kuo (2003) Typhoon Vamei: An equatorial tropical cyclone formation. *Geophys. Res. Lett.*, **30**, 501–504.

Chang, C. P., P. A. Harr, J. McBride and H. H. Hsu (2004a) Maritime Continent monsoon: Annual cycle and boreal winter variability. In: C.-P. Chang (ed.) *East Asian Monsoon* (World Scientific Series on Meteorology of East Asia. Vol. 2), pp. 107–150.

Chang, C. P., Z. Wang, J. Ju and T. Li (2004b) On the relationship between western maritime continent monsoon rainfall and ENSO during northern winter. *J. Climate*, **17**, 665–672.

Chang, C. P., P. A. Harr and H. J. Chen (2005a) Synoptic disturbances over the equatorial South China Sea and western Maritime Continent during boreal winter. *Monthly Weather Review*, **133**, 489–503.

Chang, C. P., Z. Wang, J. McBride and C.-H. Liu (2005b) Annual cycle of Southeast Asia–Maritime Continent rainfall and the asymmetric monsoon transition. *J. Climate*, **18**, 287–301.

Chang, K. *et al.* (1977) The annulus simulation of the movement of Qinghai–Tibetan high and its application to the forecast of summer flow patterns of high troposphere. *Sci. Sinica*, **20**, 631–644.

Chao, Jiping (1957) On the dynamics of orographically produced finite perturbations in baroclinic westerlies. *Acta Meteorol. Sinica*, **28**, 303–314. [In Chinese.]

Chao, W. C. and B. Chen (2001) The origin of monsoons. *J. Atmos. Sci.*, **58**, 3497–3507.

Chapman, S. and R. S. Lindzen (1970) *Atmospheric Tides*. D. Reidel Publishing Co., Dordrecht.

Charney, J. G. (1975) Dynamics of deserts and droughts in Sahel. *Quart. J. Roy. Meteorol. Soc.*, **101**, 193–202.

Charney, J. G. and A. Eliassen (1949) A numerical method for predicting in the perturbation of the middle latitude westerlies. *Tellus*, **1**, 38–54.

Charney, J. G. and A. Eliassen (1964) On the growth of the hurricane depression. *J. Atmos. Sci.*, **21**, 68–75.

Charney, J. G. and J. Shukla (1981) Predictability of monsoons. In: J. Lighthill and R. P. Pearce (eds), *Monsoon Dynamics*. Cambridge University Press, Cambridge, UK, pp. 99–108.

Charney, J. G., W. J. Quirk, S.-H. Chow and J. Kornfield (1977) A comparative study of the effects of albedo change on drought in semi-arid regions. *J. Atmos. Sci.*, **34**, 1366–1385.

Chase, T. N., J. A. Knaff, R. A. Pielke Sr. and E. Kalnay (2003) Changes in global monsoon circulations since 1950. *Natural Hazards*, **29**, 229–254.

Chatterjee, P. and B. N. Goswami (2004) Structure, genesis and scale selection of the tropical quasi-biweekly mode. *Quart. J. Roy. Meteorol. Soc.*, **130**, 1171–1194.

Chattopadhyay, J. and G. P. Singh (1995) A reappraisal of relationships between northern hemispheric surface air temperatures and Indian summer monsoon rainfall. *Theor. Appl. Climatol.*, **52**, 169–175.

Chaudhuri, S. and S. Chatopadhyay (2001) Measure of CINE: A relevant parameter for forecasting pre-monsoon thunderstorms over Gangetic West Bengal. *Mausam*, **52**, 679–684.

Cheang, B. K. (1977) Synoptic features and structures of some equatorial vortices over the South China Sea in the Malaysian region during the winter monsoon of December 1973. *Pure Appl. Geophys.*, **115**, 1303–1333.

Chen, B., W. C. Chao and X. Liu (2003) Enhanced climatic warming in the Tibetan Plateau due to doubling CO_2: A model study. *Climate Dynamics*, **20**, 401–413.

Chen, G. T. J. and C.-P. Chang (1980) The structure and vorticity budget of an early summer monsoon trough ('Meiyu') over south eastern China and Japan. *Monthly Weather Review*, **108**, 942–953.

Chen, G. T. J. and C. C. Yu (1988) Study of low-level jet and extremely heavy rainfall over northern Taiwan in the Mei-Yu season. *Monthly Weather Review*, **116**, 884–891.

Chen, H. Y. (1957) The characteristics of circulation during the period of flood event in the Yangtze and Huaihe Rivers in 1954. *Acta Meteorol. Sinica*, **38**, 142–149.

Chen., J., H. Uyeda and D.-I. Lee (2003) A method using radar reflectivity data for the objective classification of precipitation during the Baiu season. *J. Meteorol. Soc. Japan*, **81**, 229–249.

Chen, L., Q. Zhu and H. Luo (1991) *East Asian Monsoon*. China Meteorological Press, Beijing, pp. 362. [In Chinese.]

Chen, L. S. and Y. H. Ding (1979) *An Introduction to Western Pacific Typhoons*. Science Press, Beijing, 491pp.

Chen, Lieting and Z. Yan (1981) A statistical study of the impacts on the early summer monsoon of the snow cover in winter and spring over the Tibetan Plateau. *Proceedings of the Tibetan Plateau Conference*. Chinese Science Press, Bejing, 151–161.

Chen, M., D. Pollard and E. J. Barron (2004) Regional climate change in East Asia simulated by an interactive atmosphere–soil–vegetation model. *J. Climate*, **17**, 557–572.

Chen, P., M. P. Hoerling and R. M. Dole (2001) The origin of subtropical anticyclones. *J. Atmos. Sci.*, **58**, 1827–1835.

Chen, Q. J. and A. F. Huang (1989) Some feature of the South China Sea cold surge during winter season. *Meteorological Monthly*, **15**, 49–53.

Chen, Qiushi (1964) The mean streamfield and meridional circulation over the southwesterly monsoon region in Southeast Asia and over the trade wind region in Pacific in July 1958. *Acta Meteorol. Sinica*, **34**, 51–61. [In Chinese.]

Chen, S.-C. and K. E. Trenberth (1988a) Orographically forced planetary waves in the Northern Hemisphere winter: Steady state model with wave-coupled lower boundary formulation. *J. Atmos. Sci.*, **45**, 657–680.

Chen, S.-C. and K. E. Trenberth (1988b) Forced planetary waves in the Northern Hemosphere winter: Wave-coupled orographic and thermal forcings. *J. Atmos. Sci.*, **45**, 682–704.

Chen, S. J. and L. Dell'Osso (1984) Numerial prediction of the heavy rainfall vortex over Eastern Asia monsoon region. *J. Meteorol. Soc. Japan*, **62**, 730–747.

Chen, S. J. and L. Dell'Osso (1987) A numerical case study of East Asian coastal cyclogenesis. *Monthly Weather Review*, **115**, 477–487.

Chen, S. S. and R. A. Houze (1997) Diurnal variation and lifecycle of deep convective systems over the tropical Pacific warm pool. *Quart. J. Roy. Meteorol. Soc.*, **123**, 357–388.

Chen, S. S., R. A. Houze Jr. and B. E. Mapes (1996) Multiscale variability of deep convection in relation to large-scale circulation in TOGA COARE. *J. Atmos. Sci.*, **53**, 1380–1409.

Chen, T.-C. (1985) Global water vapor flux and maintenance during FGGE. *Monthly Weather Review*, **113**, 1801–1819.

Chen, T.-C. (1987) 30–50 Day Oscillation of 200-mb Temperature and 850-mb Height during the 1979 Northern Summer. *Monthly Weather Review*, **115**, 1589–1605.

Chen, T.-C. (2003) Maintenance of summer monsoon circulations: A planetary-scale perspective. *J. Climate*, **16**, 2022–2037.

Chen, T.-C. and J. C. Alpert (1990) Systematic errors in the annual and intraseasonal variations of the planetary-scale divergent circulation in NMC medium-range forecasts. *J. Atmos. Sci.*, **118**, 2607–2623.

Chen, T.-C. and J.-M. Chen (1993) The 10–20-day mode of the 1979 Indian monsoon: Its relation with the time variation of monsoon rainfall. *Monthly Weather Review*, **121**, 2465–2482.

Chen, T.-C. and J. R. Chen (1995) An observational study of the South China Sea monsoon during the 1979 summer: Onset and life-cycle. *Monthly Weather Review*, **123**, 2295–2318.

Chen, T.-C. and W.-R. Huang (2005) Interannual variation of global precipitation. *J. Climate*. (submitted).

Chen, T.-C. and M. Murakami (1988) The 30–50-day variation of convective activity over the western Pacific Ocean with the emphasis on the northwestern region. *Monthly Weather Review*, **116**, 892–906.

Chen, T.-C. and J. Pfaendtner (1993) On the atmospheric branch of the hydrological cycle. *J. Climate*, **6**, 161–167.

Chen, T.-C. and K. Takahashi (1995) Diurnal variation of outgoing longwave radiation in the vicinity of the South China Sea. *Monthly Weather Review*, **123**, 566–577.

Chen, T.-C. and S.-P. Weng (1999) Interannual and intraseasonal variation in monsoon depression and their westward propagation predecessors. *Mon. Wea. Rev.*, **127**, 1005–1020.

Chen, T.-C. and M. C. Yen (1991a) Intraseasonal variations of the Tropical Easterly Jet during the 1979 northern summer. *Tellus Ser. A-Dyn. Meteorol. Oceanol.*, **43**, 213–225.

Chen, T.-C. and M. C. Yen (1991b) Interaction between intraseasonal oscillations of the midlatitude flow and tropical convection during 1979 northern summer: The Pacific Ocean. *J. Climate*, **4**, 653–671.

Chen, T.-C. and M. C. Yen (1991c) A study of the diabatic heating associated with the Madden–Julian oscillation. *J. Geophys. Res.*, **96**(D7), 13163–13177.

Chen, T.-C. and M. C. Yen (1994) Interannual variation of the Indian monsoon simulated by the NCAR Community Climate Model: Effect of the tropical Pacific SST. *J. Climate*, **7**, 1403–1415.

Chen, T.-C. and J.-H. Yoon (2000) Interannual variation in Indochina summer monsoon rainfall: Possible mechanism. *J. Climate*, **13**, 1979–1986.

Chen, T.-C. and S.-P. Weng (1998) Interannual variation of the summer synoptic-scale disturbance activity in the western tropic Pacific. *Monthly Weather Review*, **126**, 1725–1733.

Chen, T.-C. and S.-P. Weng (1999) Interannual and intraseasonal variations in monsoon depressions and their westward-propagating predecessors. *Monthly Weather Review*, **127**, 1005–1020.

Chen, T.-C., C.-B. Chang and D. J. Perkey (1983) Numerical Study of an AMTEX '75 Oceanic Cyclone. *Monthly Weather Review*, **111**, 1818–1829.

Chen, T.-C., C.-B. Chang and D. J. Perkey (1985) Synoptic study of a medium-scale oceanic cyclone during AMTEX '75. *Monthly Weather Review*, **113**, 349–361.

Chen, T.-C., M.-C. Yen and M. Murakami (1988a) The water vapor transport associated with the 30–50 day oscillation over the Asian monsoon regions during 1979 summer. *Monthly Weather Review*, **116**, 1983–2002.

Chen, T.-C., R.-Y. Tzeng and M.-C. Yen (1988b) Development and life cycle of the Indian monsoon: Effect of the 30–50 day oscillation. *Monthly Weather Review*, **116**, 2183–2199.

Chen, T.-C., J. Pfaendtner and S.-P. Weng (1994) Aspects of the hydrological cycle of the ocean-atmosphere system. *J. Physical Oceanography*, **24**, 1827–1833.

Chen, T.-C., J.-M. Chen and J. Pfaendtner (1995a) Low-frequency variations in the atmospheric branch of the global hydrological cycle. *J. Climate*, **8**, 92–107.

Chen, T.-C., J.-M. Chen, J. Pfaendtner and J. Susskind (1995b) The 12–24 day mode of global precipitation. *Monthly Weather Review*, **123**, 140–152.

Chen, T.-C., S.-P. Weng, N. Yamazaki and S. Kiehne (1998) Interannual variation in the tropical cyclone formation over the Western North Pacific. *Monthly Weather Review*, **126**, 1080–1090.

Chen, T.-C., M. C. Yen and S. P. Weng (2000) Interaction between the summer monsoons in East Asia and the South China Sea: Intraseasonal monsoon modes. *J. Atmos. Sci.*, **57**, 1373–1392.

Chen, T.-J. and C.-F. Lu (1997) On the climatological aspects of explosive cyclones over the western North Pacific and East Asia coastal areas. *TAO* (Taiwan), **8**, 427–442.

Chen, Y.-L. and J. Li (1995) Large-scale conditions favorable for the development of heavy rainfall during TAMEX IOP 3. *Monthly Weather Review*, **123**, 2978–3002.

Chen, X. Y., H. J. Wang, F. Xue and Q. C. Zeng (2001) Intraseasonal oscillation: The global coincidence and its relationship with ENSO cycle. *Adv. Atmos. Sci.*, **18**, 445–453.

Chen, T.-C., M.-C. Yen, W.-R. Huang and W. A. Gallus (2002) An East Asian cold surge: Case study. *Monthly Weather Review*, **130**, 2271–2290.

Chen, T.-C., S.-Y. Wang, W.-R. Huang and M.-C. Yen (2004a) Variation of the East Asian summer monsoon rainfall. *J. Climate*, **17**, 744–762.

Chen, T.-C., S.-Y. Wang, M.-C. Yen and W. A. Gallus Jr. (2004b) Role of the monsoon gyre in the interannual variation of tropical cyclone formation over the Western North Pacific. *Weather Forecasting*, **19**, 776–785.

Chen, T.-C., S.-Y. Wang, M.-C. Yen and W. A. Gallus Jr. (2005) Effect of monsoon gyre on the tropical cyclone activity in the tropical western Pacific. *Monthly Weather Review* [Submitted.]

Cheng, C.-P. and R. A. Houze Jr. (1979) The distribution of convective and mesoscale precipitation in GATE radar echo patterns. *Monthly Weather Review*, **107**, 1370–1381.

Chenggao, G. and R. W. Renaut (1994) The effect of Tibetan uplift on the formation and preservation of Tertiary lacustrine source-rocks in eastern China. *J. Paleolimnology* (Dordrecht, The Netherlands), **11**, 31–40.

Chirokova, G. and P. J. Webster 2005: Interannual variability in Indian Ocean heat transports. *J. Climate*. [In press.]

Cho, H. R. and G. T.-J. Chen (1995) Mei-Yu frontogenesis. *J. Atmos. Sci.*, **52**, 2109–2120.

Cho, H. R. and D. Pendlebury (1997) Wave–CISK of equatorial waves and the vertical distribution of cumulus heating. *J. Atmos. Sci.*, **54**, 2429–2440.

Chou, C. (2003) Land–sea heating contrast in an idealized Asian summer monsoon. *Clim. Dyn.*, **21**, 11–25.

Chou, M.-D. (1992) A Solar Radiation Model for Use in Climate Studies. *J. Atmos. Sci.*, **49**, 762–772.

Chou, Y. Y. (1985) *Medium-range Weather Prediction*. Science Press, Beijing, 420pp.

Chou, M.-D. and M. J. Suarez (1994) An efficient thermal infrared radiation parameterization for use in general circulation models. NASA Tech. Memo. 104606, 85pp.

Chou, M.-D. and M. J. Suarez (1996) A solar radiation parameterization (CLIRAD-SW) for atmospheric studies. NASA Tech. Memo. 104606, 39pp.

Chou, L. C., C.-P. Chang and R. T. Williams (1990) A numerical simulation of the Mei-yu front and the associated low level jet. *Monthly Weather Review*, **118**, 1408–1428.

Chou, C., J.-Y. Tu and J.-Y. Yu (2003) Interannual variability of the western North Pacific summer monsoon: Differences between ENSO and non-ENSO years. *J. Climate*, **16**, 2275–2287.

Chu, E. W. K. (1978) *A method for forecasting the arrival of cold surges in Hong Kong*. Tech. Note No. 43, Royal Observatory, Hong Kong, 31pp.

Chu, Pao-chen (1957a) The steady state perturbations of the westerlies by the lagre-scale heat sources and sinks and Earth's orography (part I). *Acta Meteorol. Sinica*, **28**, 122–140. [In Chinese.]

Chu, Pao-chen (1957b) The steady state perturbations of the westerlies by the lagre-scale heat sources and sinks and Earth's orography (part II). *Acta Meteorol. Sinica*, **28**, 198–224. [In Chinese.]

Chu, P.-S. (1988) Extratropical forcing and the burst of equatorial westerlies in the western Pacific: A synoptic study. *J. Meteorol. Soc. Japan*, **66**, 549–564.

Chu, P. C. and C.-P. Chang (1997) South China Sea warm pool in boreal spring. *Advances in Atmos. Sci.*, **14**, 195–206.

Chu, P. C., H. C. Tseng, C.-P. Chang and J. M. Chen (1997) South China Sea warm pool detected in spring from the Navy's Master Oceanographic Observational Data set (MOODS). *J. Geophys. Res.*, **102**(C7), 15761–15771.

Chung, C. and S. Nigam (1999) Asian summer monsoon–ENSO feedback on the Cane–Zebiak model ENSO. *J. Climate*, **12**, 2787–2807.

Chung, C. E., V. Ramanathan and J. T. Kiehl (2002) Effects of the South Asian absorbing haze on the northeast monsoon and surface-air heat exchange. *J. Climate*, **15**, 2462–2476.

Chung, Y.-S., M.-B. Yoon and H.-S. Kim (2004) On climate variations and changes observed in South Korea. *Climatic Change*, **66**, 151–161.

Clark, C. O., J. E. Cole and P. J. Webster (2000) Indian Ocean SST and Indian summer Rainfall: Predictive relationships and their decacal variability. *J. Climate*, **13**, 2503–2519.

Clark, C. O., P. J. Webster and J. E. Cole (2003) The Indian Ocean dipole and the prediction of East African precipitation. *J. Clim.*, **16**, 548–554.

Clark, M. P. and M. C. Serreze (2000) Effects of variations in East Asian snow cover on modulating atmospheric circulation over the North Pacific Ocean. *J. Climate*, **13**, 3700–3710.

Clarke, A., *et al.* (1971) The Wangara experiment (Tech. Paper 19). Div. Meteorol. Phys. CSIRO, Australia.

Clarke, A. J., X. Liu and S. V. Gorder (1998) Dynamics of the biennial oscillation in the equatorial Indian and far western Pacific Oceans. *J. Climate*, **11**, 987–1001.

Clarke, R. H., R. K. Smith and D. G. Reid (1981) The morning glory of the Gulf of Carpentaria: An atmospheric undular bore. *Monthly Weather Review*, **109**, 1726–1750.

Clemens, S. C. (1998) Dust response to seasonal atmospheric forcing: Proxy evaluation and calibration. *Paleoceanography*, **13**, 471–490.

Clemens, S. C. and W. L. Prell (1990) Late Pleistocene variability of Arabian Sea summer-monsoon winds and continental aridity: Eolian records from the lithogenic component of deep-sea sediments. *Paleoceanography*, **5**, 109–145.

Clemens, S. C. and W. L. Prell (1991a) Late Quaternary forcing of Indian Ocean summer-monsoon winds: A comparison of Fourier model and general circulation model results. *J. Geophys. Res.*, **96**, 22683–22700.

Clemens, S. C. and W. L. Prell (1991b) One-million year record of summer-monsoon winds and continental aridity from the Owen Ridge (Site 722B), northwest Arabian Sea, Ocean Drillling Program. *Sci. Results*, **117**, 365–388.

Clemens, S. C. and W. L. Prell (2003) A 350,000 year summer-monsoon multi-proxy stack from the Owen Ridge, Northern Arabian Sea. *Marine Geology*, **201**, 35–51.

Clemens, S. C., W. L. Prell, D. Murray, G. Shimmield and G. Weedon (1991) Forcing mechanisms of the Indian Ocean monsoon. *Nature*, **353**, 720–725.

Clemens, S. C., D. W. Murray and W. L. Prell (1996) Nonstationary Phase of the Plio-Pleistocene Asian Monsoon. *Science*, **274**, 943–948.

Clemens, S. C., P. Wang and W. Prell (2003) Monsoons and global linkages on Milankovitch and sub-Milankovitch time scales. *Marine Geology*, **201**, 1–3.

Clift, P., C. Gaedicke, R. Edwards, J. I. Lee, P. Hildebrand, S. Amjad, R. S. White and H.-U. Schluter (2002) The stratigraphic evolution of the Indus Fan and the history of sedimentation in the Arabian Sea. *Marine Geophys. Res.*, **23**, 223–245.

Climate Change (2001) The Scientific Basis, IPCC Third Assessment Report. WMO and UNEP.

Cobb, K. M., C. D. Charles, R. L. Edwards, H. Cheng and M. Kastner (2003) El Niño-Southern Oscillation and tropical Pacific climate during the last millennium. *Nature*, **424**, 271–276.

Cohen, J. and D. Entekhabi (2001) The influence of snow cover on Northern Hemisphere climate variability. *Atmosphere–Ocean*, **39**, 35–53.

Cohen, J., K. Saito and D. Entekhabi (2001) The role of the Siberian high in Northern Hemisphere climate variability. *Geophys. Res. Lett.*, **28**, 299–302.

Compo, G. P., G. N. Kiladis and P. J. Webster (1999) The horizontal and vertical structure of east Asian winter monsoon pressure surges. *Quart. J. Roy. Meteorol. Soc.*, **125**, 29–54.

Cotton, W. R. and R. A. Anthes (1991) *Storm and Cloud Dynamics*. Academic Press, 883pp.

Cox, R., B. L. Bauer and T. Smith (1998) A Mesoscale Model Intercomparison. *Bull. Amer. Meteorol. Soc.*, **79**, 265–283.

Cressman, G. P. (1959) An operational objective analysis system. *Monthly Weather Review*, **87**, 367–374.

Cressman, G. P. (1981) Circulation of the West Pacific jet streams. *Monthly Weather Review*, **109**, 2450–2463.

Curray, J. R., F. J. Emmel and D. G. Moore (2003) The Bengal Fan: Morphology, geometry, stratigraphy, history and processes. *Marine and Petroleum Geology*, **19**, 1191–1223.

Curry, J. (1987) The contribution of radiative cooling of the formation of cold-core anticyclones. *J. Atmos. Sci.*, **44**, 2572–2592.

Daggupathy, S. M. and D. R. Sikka (1977) On the vorticity budget and vertical velocity distribution associated with a life cycle of monsoon depression. *J. Atmos. Sci.*, **33**, 773–792.

Dai, A. (2001) Global precipitation and thunderstorm frequencies. Part II: Diurnal variations. *J. Climate*, **14**, 1112–1128.

Dai, A. and T. M. L. Wigley (2000) Global patterns of ENSO-induced precipitation. *Geophys. Res. Lett.*, **27**, 1283–1286.

Dai, A., I. Fung and A. D. Del Genio (1997) Surface observed global land precipitation variation during 1900–1988. *J. Climate*, **10**, 2943–2962.

Dai, A., G. A. Meehl, W. M. Washington and T. M. L. Wigley (2001) Climate changes in the 21st century over the Asia–Pacific region simulated by the NCAR CSM and PCM. *Adv. Atmos. Sci.*, **18**, 639–658.

Dakshinarmuti, J. and R. N. Keshavamurty (1976) On oscillations of period around one month in the Indian summer monsoon. *Indian J. Meteorol. Hydrol. Geophys*, **27**, 201–203.

Danielsen, E. F. (1993) In situ evidence of rapid, vertical irreversible transport of lower tropospheric air into the lower tropical stratosphere by convective cloud turrets and by large-scale upwelling in tropical cyclones. *J. Geophys. Res.*, **98**, 8665–8681.

Dannenmann, S., B. K. Linsley, D. W. Oppo, Y. Rosenthal and L. Beaufort (2003) East Asian monsoon forcing of suborbital variability in the Sulu Sea during Marine Isotope Stage 3: Link to Northern Hemisphere climate. *Geochemistry Geophysics Geosystems*, **4**, 1–13.

Dansgaard, W., S. J. Johnson, H. B. Clausen, D. Dahl-Jensen, N. S. Gundestrup, C. U. Hammer, C. S. Hvildberg, J. P. Steffensen, A. E. Sveinbjornsdottir, J. Jouzel and G. Bond (1993) Evidence for general instability of past climate from a 250-kyr ice-core record. *Nature*, **364**, 281–219.

Dao, S.-Y. and L.-S. Chen (1957) The structure of general circulation over the continent of Asia in summer. *J. Meteorol. Soc. Japan*, **75**, 215–229.

Das, P. K. (1986) Monsoon, 5th WMO Lecture, WMO No. 613, 155pp.

Das, P. K., M. C. Sinha and V. Balasubramanyan (1974) Storm surges in the Bay of Bengal. *Quart. J. Roy. Meteorol. Soc.*, **100**, 437–447.

Das, P. M., A. C. De and M. Gangopadhyay (1957) Radar study of movements of norwesters. *Ind. J. Meteorol. Geophys.*, **8**, 399–409.

Das, S. (2002) Real time mesoscale weather forecasting over Indian region using MM5 modeling system. *Research Report No. NMRF/RR/3/2002*, NCMRWF, New Delhi, India, 19pp.

Dastoor, A. and T. N. Krishnamurti (1991) The landfall and structure of a tropical cyclone: The sensitivity of model predictions to soil moisture parameterization. *Bound. Layer Meteorol.*, **55**, 345–380.

Davidson, N. E., J. L. McBride and B. J. McAvaney (1983) The onset of the Australian monsoon during Winter MONEX: Synoptic aspects. *Monthly Weather Review*, **111**, 496–516.

De, A. C. (1959) An unusually high nor'wester radar cloud. *Ind. J. Meteorol. Geophys.*, **10**, 359–362.

De Garidel-Thoron, T., L. Beaufort, B. K. Linsley and S. Dannenmann (2001) Millennial-scale dynamics of the East Asian winter monsoon during the last 200,000 years. *Paleoceanography*, **16**, 491–502.

De, U. S. and K. C. Sinha Ray (2000) Weather and climate related impacts in health in mega cities. *WMO Bulletin*, **49**, 340–348.

De, U. S. and R. K. Mukhopadhyay (2002) Breaks in monsoon and related precursors. *Mausam*, **53**, 309–318.

Delworth, T. and S. Manabe (1988) The influence of potential evaporation on the variabilities of simulated soil wetness and climate. *J. Climate*, **1**, 523–547.

Delworth, T. and S. Manabe (1989) The influence of soil wetness on near-surface atmospheric variability. *J. Climate*, **2**, 1447–1462.

Delworth, T., S. Manabe and R. J. Stouffer (1993) Interdecadal variations of the thermohaline circulation in a coupled ocean–atmosphere model. *J. Climate*, **6**, 1993–2011.

deMenocal, P. B. and D. Rind (1993) Sensitivity of Asian and African climate to variations in seasonal insolation, glacial ice cover, sea surface temperature, and Asian orography. *J. Geophys. Res.*, **98**, 7265–7287.

DeMott, C. A. and S. A. Rutledge (1998) The vertical structure of TOGA COARE convection. Part II: Modulating influences and implications for diabatic heating. *J. Atmos. Sci.*, **55**, 2730–2747.

Desai, B. N. and S. Mal (1938) Thunder squalls of Bengal. *Beiter Geophys.*, **52**, 285–304.

Dey, B. and O. S. R. U. Bhanu Kumar (1982) An apparent relationship between Eurasian spring snow cover and the advance period of the Indian summer monsoon. *J. Appl. Meteorol.*, **21**, 1929–1932.

Dhar, O. N. and S. S. Nandargi (1995) Some characteristics of seasonal rain storms of India. *Theor. Appl. Climatol.*, **50**, 205–212.

Dhar, O. N. and S. S. Nandargi (1998) Floods in Indian rivers and their meteorological aspects. *Mem. Geological Soc. India*, **41**, 1–125.

Dhar, O. N., P. R. Rakecha and B. N. Mandal (1981) Influence of tropical disturbances on the monthly rainfall of India. *Monthly Weather Review*, **109**, 188–190.

Dickinson, R. E. and A. Henderson-Sellers (1988) Modeling tropical deforestation: A study of GCM land-surface parameterizations. *Quart. J. Roy. Meteorol. Soc.*, **114**, 439–462.

Dickinson, R. E., A. H. Sellers, P. J. Kennedy and M. F. Wilson (1986) Biosphere–atmosphere Transfer Scheme (BATS) for the NCAR Community climate Model. National Center for Atmospheric Research, Boulder Co., *Tech. Note NCAR/TN-275+STR*, 69pp.

Dickson, R. R. (1984) Eurasian snow cover versus Indian monsoon rainfall: An extension of the Hahn-Shukla results. *J. Climate Appl. Meteorol.*, **23**, 171–173.

Ding, Q. and B. Wang (2005) Circumglobal teleconnection in the northern hemisphere summer. *J. Climate* (in press).

Ding, Y. H. (1981) A case study of formation and structure of a depression over the Arabian Sea. *Chinese J. Atmos. Sci.*, **5**, 267–280. [In Chinese.]

Ding, Y. H. (1990a) Build-up air mass transformation and propagation of Siberian high and its relation to cold surge in East Asia. *Meteorol. Atmos. Phy.*, **44**, 281–292.

Ding, Y. H. (1990b) A statistical study of winter monsoon in East Asia. *J. Tropical Meteor*, **6**, 119–128.

Ding, Y. H. (1992) Summer monsoon rainfalls in China. *J. Meteorol. Soc. Japan*, **70**, 373–396.

Ding, Y. H. (1993) *A Study of the Prolonged Heavy Rainfall in the Yangtze-Huaihe River Basins in 1991*. China Meteor Press, Beijing, 255pp.

Ding, Y. H. (1994) *Monsoons over China*. Kluwer Academic Publisher, Dordrecht/Boston/London, 419pp.

Ding, Y. H. (2004) Seasonal march of the East Asian summer monsoon in The East Asian Monsoon. In: C. P. Chang (ed.), *The East Asian Monsoon*, World Scientific Publisher, Singapore, 564pp.

Ding, Y. H. and J. Hu (1988) The variation of the heat sources in East Asia in the early summer of 1984 and their effects on the large-scale circulation in East Asia. *Advances in Atmos. Sci.*, **6**, 171–180.

Ding, Y. H. and T. N. Krishnamurti (1987) Heat budget of Siberian high and the winter monsoon. *Monthly Weather Review*, **115**, 2428–2449.

Ding, Y. H. and X. Mong (1994) A study of the cold surge following an outbreak of cold air in East Asia. *Acta Meteorol. Sinica*, **52**, 442–451.

Ding, Y. H. and E. R. Reiter (1982) A relationship between planetary waves and persistent rain and thunderstorm in China. *Arch. Meteorol. Geophys. Biocl., Ser. B*, **31**, 221–252.

Ding, Y. H. and E. R. Reiter (1983) Large-scale hemispheric teleconnections with the frequency of tropical cyclone formation over Northwest Pacific and North Atlantic Oceans. *Arch. Meteorol. Geophys. Biocl., Ser. A*, **32**, 311–337.

Ding, Y. H. and Y. Sun (2002) Seasonal march of the East Asian summer monsoon and related moisture transport. *Weather and Climate*, **1**, 18–23.

Ding, Y. H. and X.-F. Wang (1988) An analysis of the distribution of apparent heat sources and sinks over the middle reaches of Yangtze River during the Meiyu season in 1983. *Tropical Meteorology*, **4**, 134–145. [In Chinese.]

Ding, Y. H. and S. R. Wang (2001) *An Introduction to Climate, Ecology and Environment in Northwest China*. China Meteorological Press, Beijing, 204pp.

Ding, Y. H., H. J. Feng, Q. F. Xue and K. S. Chen (1977) A preliminary study on the simultaneous development of the multiple typhoons in the intertropical convergence zone. *Sci. Atmos. Sinica*, **1**, 89–98. [In Chinese.]

Ding, Y. H., H. Z. Li, Z. Y. Cai and J. S. Li (1980) On the physical conditions of occurrence of heavy rainfalls and severe convective weather. *Proceedings of the Eighth Conference on Weather Forecasting and Analysis, June 10–13, Denver, CO*. American Meteorological Society. Boston (12.8), pp. 371–377.

Ding, Y. H., X. Q. Fu and B. Y. Zhang (1984) A study of the structure of a monsoon depression over the Bay of Bengal during the summer MONEX. *Advances in Atmos. Sci.*, **1**, 62–75.

Ding, Y. H., S. G. Wen and Y. J. Li (1994) A study of dynamic structures of Siberian highs in winter. *Acta Meteorol. Sinica*, **52**, 430–439.

Ding, Y. H., Y. Zhang, Q. Ma and G. Q. Hu (2001) Analysis of the large scale circulation features and synoptic systems in East Asia during the intensive observation period of GAMD/HUBEX. *J. Meteorol. Soc. Japan*, **79**, 277–300.

Ding, Z., Z. Yu, N. W. Rutter and T. Liu (1994) Towards an orbital time scale for Chinese loess deposits. *Quaternary Science Reviews*, **13**, 39–70.

Ding, Z., T. Liu, N. W. Rutter, Z. Yu, Z. Guo and R. Zhu (1995) Ice-volume forcing of East Asian winter monsoon variations in the past 800,000 years. *Quaternary Research*, **44**, 149–159.

Ding, Z. L., N. W. Rutter, T. S. Liu, J. Z. Ren, J. M. Sun and S. F. Xiong (1998a) Correlation of Dansgaard–Oeschger cycles between Greenland ice and Chinese loess. *Paleoclimates*, **4**, 281–291.

Ding, Z. L., J. M. Sun, T. S. Liu, R. X. Zhu, S. L. Yang and B. Guo (1998b) Wind-blown origin of the Pliocene red caly formation in the central Loess Plateau, China. *Earth and Planetary Science Letters*, **161**, 135–143.

Ding, Z. L., J. Z. Ren, S. L. Yang and T. S. Liu (1999) Climate instability during the penultimate glaciation: Evidence from two high-resolution loess records, China. *J. Geophys. Res.*, **104**, 20123–20132.

Ding, Z. L., J. Wang and Z. Zhai (2001) Research on composite diagnosis and mechanisms of explosive cyclones. *Quart. J. Appl. Meteorol.* (Beijing, China), **12**, 30–40.

Ding, Z. L., E. Derbyshier, S. L. Yang, Z. W. Yu, S. F. Xiong and T. S. Liu (2002) Stacked 2.6-Ma grain size record from the Chinese loess based on five sections and correlation with the deep-sea d18O record. *Paleoceanography*, **17**, 5-1 to 5–21.

Dix, M. R. and B. G. Hunt (1995) Chaotic influences and the problem of deterministic seasonal predictions. *Int. J. Climatol.*, **15**, 159–164.

Douglas M. W. and J. C. Leal (2003) Summertime surges over the Gulf of California: Aspects of their climatology, mean structure, and evolution from radiosonde, NCEP reanalysis, and rainfall data. *Weather Forecasting*, **18**, 55–74.

Douglas, M. W., R. A. Maddox, K. Howard and S. Reyes (1993) The Mexican monsoon. *J. Climate*, **6**, 1665–1677.

Douville, H. (2002) Influence of soil moisture on the Asian and African monsoon. Part II. Interannual variability. *J. Climate*, **15**, 701–720.

Douville, H. and J.-F. Royer (1996) Sensitivity of the Asian summer monsoon to an anomalous Eurasian snow cover within the Meteo-France GCM. *Climate Dynamics*, **12**, 449–466.

Douville, H., J.-F. Royer, J. Polcher, P. Cox, N. Gedney, D. B. Stephenson and P. J. Valdes (2000a) Impact of CO_2 doubling on the Asian summer monsoon: Robust versus model-dependent responses. *J. Meteorol. Soc. Japan*, **78**, 421–439.

Douville, H., S. Planton, J.-F. Royer, D. B. Stephenson, S. Tyteca, L. Kergoat, S. Lafont and R. A. Betts (2000b) Importance of vegetation feedbacks in doubled-CO_2 climate experiments. *J. Geophys. Res.*, **105**(D11), 14,841–14,861.

Douville, H., F. Chauvin and H. Broqua (2001) Influence of soil moisture on the Asian and African monsoon. Part I: Mean monsoon and daily precipitation. *J. Climate*, **14**, 2381–2403.

Douville, H., F. Chauvin, S. Planton, J.-F. Royer, D. Salas-Melia and S. Tyteca (2002) Sensitivity of the hydrological cycle to increasing amounts of greenhouse gases and aerosols. *Climate Dynamics*, **20**, 45–68.

Drbohlav, H.-K. L. and B. Wang (2004) Mechanism of the northward propagating intra-seasonal oscillation in the south Asian monsoon region: Results from a zonally-averaged model. *J. Climate*. [In press.]

Drosdowsky, W. (1996) Variability of the Australian summer monsoon at Darwin: 1957–1992. *J. Climate*, **9**, 85–96.

Duan, A. M. and G. X. Wu (2004) Role of the Tibetan Plateau thermal forcing in the summer climate patterns over subtropical Asia. [Accepted by *Climate Dynamics*]

Dube, S. K., A. D. Rao, P. C. Sinha, T. S. Murty and N. Bahulayan (1997) Storm surges in the Bay of Bengal and Arabian Sea: The problem and its prediction. *Mausam*, **48**, 283–304.

Ducoudre, N., K. Laval and A. Perrier (1993) SECHIBA, a new set of parameterizations of the hydrologic exchanges at the land/atmosphere interface within the LMD atmospheric general circulation model. *J. Climate*, **6**, 248–273.

Duing, W. and A. Leetmaa (1980) Arabian Sea cooling: A preliminary heat-budget. *Journal of Physical Oceanography*, **10**, 307–312.

Duing, W., R. I. Molinari and J. C. Swallow (1980) Somali Current: Evolution of surface flow. *Science*, **209**, 588–590.

Dunkerton, T. J. and F. X. Crum (1991) Scale selection and propagation of wave–CISK with conditional heating. *J. Meteorol. Soc. Japan.,* **69**, 449–458.

ECMWF (2004) ECMWF/CLIVAR Workshop on Simulation and Prediction of Intra-Seasonal Variability with Emphasis on the MJO. 3–6 November 2003. ECMWF, Reading, UK, 269pp.

Edwards, C. A. and J. Pedlosky (1988) Dynamics of nonlinear cross-equatorial flow. Part I: Potential vorticity transformation. *J. Phys. Oceanol.*, **28**, 2382–2406.

Eitzen, Z. A. and D. A. Randall (1999) Sensitivity of the simulated Asian summer monsoon to parameterized physical processes. *J. Geophys. Res.*, **104**, 12177–12191.

Eliot, J. (1884) Accounts of southwest monsoon storms generated in the Bay of Bengal during 1877–1881. *Mem. Ind. Meteorol. Dept.*, **2**, 217–440.

Eliassen, A. (1971) On the Ekman layer in a circular vortex. *J. Meteorol. Soc. Japan*, **49** (special issue), 784–789.

Emanuel, K. A. (1983) The Lagrangian parcel dynamics of moist symmetric instability. *J. Atmos. Sci.*, **40**, 2368–2376.

Emanuel, K. A. (1987) An air–sea interaction model of intraseasonal oscillations in the tropics. *J. Atmos. Sci.*, **44**, 2324–2340.

Emanuel, K. A. (1988) An air–sea interaction model of intraseasonal oscillation in the tropics – reply. *J. Atmospheric Sci.*, **45**, 3528–3530.

Emanuel, K. A. (1993) *Atmospheric Convection*. Oxford University Press, 580pp.

Emori, S., T. Nozawa, A. Abe-Ouchi, A. Numaguti, M. Kimoto and T. Nakajima (1999) Coupled ocean–atmosphere model experiments of future climate change with an explicit representation of sulfate aerosol scattering, *J. Meteorol. Soc. Japan*, **77**, 1299–1307.

Emori, S., T. Nozawa, A. Numaguti and I. Uno (2000) A regional climate change projection over East Asia. *Preprint of the 11th Symposium on Global Change Studies*, 9–14 January 2000, Long Beach, California, pp. 15–18.

Endo, N., K. Ueno and T. Yasunari (1994) Seasonal change of the troposphere in the early summer of 1993 over Central Tibet observed in the Tanggula mountains. *Bull. Glacier Res.*, **12**, 25–30.

Enfield, D. B. (1989) El Niño, past and present. *Rev. Geophys.*, **27**, 159–187.

Enfield, D. B. and A. M. Mestas-Nunez (1999) Multiscale variabilities in global sea surface temperatures and their relationship with tropospheric climate patterns. *J. Climate*, **12**, 2719–2733.

Enomoto, T., B. J. Hoskins and Y. Matsuda (2003) The formation mechanism of the Bonin high in August. *Quart. J. Roy. Meteorol. Soc.*, **129**, 157–178.

Ertel, H. (1942) Ein neuer hydrodynamische wirbdsatz. *Meteorology. Z. Braunschweig.*, **59**, 277–281.

Farfán, L. M. and J. A. Zehnder (1994) Moving and stationary mesoscale convective systems over northwest Mexico during the Southwest Area Monsoon Project. *Weather Forecasting*, **9**, 630–639.

Fasullo, J. (2004) Biennial characteristics of Indian monsoon rainfall. *J. Climate*, **17**, 2972–2982.

Fasullo, J. T. and P. J. Webster (1999) Warm pool sea surface temperature variability in relation to the surface energy balance. *J. Climate*, **12**, 1292–1305.

Feddersen, H., A. Navarra and M. N. Ward (1999) Reduction of model systematic error by statistical correction for dynamical seasonal prediction. *J. Climate*, **12**, 1974–1989.

Federov, A. and S. Philander (2000) Is El Niño changing? *Science*, **288**, 1997–2001.

Fedorov, A. V., S. L. Harper, S. G. Philander, B. Winter and A. Wittenberg (2003) How predictable is El Niño? *Bull. Amer. Meteorol. Soc.*, **84**, 911–919.

Fein, J. S. and P. Stephens (1987) *Monsoons*. Wiley, New York, 384pp.

Feng, W. H., L. S. Cheng and M. H. Cheng (2001) Nonhydrostatic numerical simulation for the '96.8' extraordinary heavy rainfall and development of structure of mesoscale system. *Acta. Meteorol. Sinica*, **59**, 294–307.

Ferranti, L., T. N. Palmer, F. Molteni and K. Klinker (1990) Tropical–extratropical interaction associated with the 30–60-day oscillation and its impact on medium and extended range prediction. *J. Atmos. Sci.*, **47**, 2177–2199.

Ferranti, L., J. M. Slingo, T. N. Palmer and B. J. Hoskins (1997) Relations between interannual and intraseasonal monsoon variability as diagnosed from AMIP integrations. *Quart. J. Roy. Meteorol. Soc.*, **123**, 1323–1357.

Findlater, J. (1966) Cross-equatorial jet streams at low level over Kenya. *Meteorol. Magazine*, **95**, 353–364.

Findlater, J. (1967) Some further evidence of cross-equatorial jet streams at low level over Kenya. *Meteorol. Magazine*, **96**, 216–219.

Findlater J. (1969a) A major air current near the West Indian Ocean during the northern summer. *Quart J. Roy. Meteorol. Soc.*, **95**, 1251–1262.

Findlater J. (1969b) Interhemispheric transport of air in the lower troposphere over the western Indian Ocean. *Quart. J. Roy. Meteorol. Soc.*, **95**, 400–403.

Findlater J. (1977a) A numerical index to monitor the Afro-Asian monsoon during the northern summers. *Meteorol. Magazine*, **106**, 170–180.

Findlater J. (1977b) Observational aspects of the low-level cross-equatorial jet stream. *Pure and Appl. Geophys.*, **115**, 1251–1262.

Fink, A. and P. Speth (1997) Some potential forcing mechanisms of the year-to-year variability of the tropical convection and its intraseasonal (25–70-day) variability. *Int. J. Climatol.*, **17**, 1513–1534.

Flatau, M. K., P. J. Flatau, P. Phoebus and P. P. Niller (1997) The feedback between equatorial convection and local radiative and evaporative processes: The implications for intraseasonal oscillations. *J. Atmos. Sci.*, **54**, 2373–2386.

Flatau, M. K., P. J. Flatau and D. Rudnick (2001) The Dynamics of Double Monsoon Onsets. *J. Climate*, **14**, 4130–4146.

Flatau, M. K., P. J. Flatau, J. Schmidt and G. N. Kiladis (2003) Delayed onset of the 2002 Indian monsoon. *Geophys. Res. Lett.*, **30**, 1768, doi: 10.1029/2003GL017434.

Fleming, R. J., T. M. Kaneshige and W. E. McGovern (1979) The Global Weather Experiment. Part I: The observational phase through the first special observing period. *Bull. Amer. Meteorol. Soc.*, **60**, 649–661.

Flohn, H. (1957) Large-scale aspects of the 'summer monsoon' in South and East Asia. *J. Meteorol. Soc. Japan*, **35**, 180–186.

Flohn, H. (1960) Recent investigations on the mechanism of the 'summer monsoon' southern and eastern Asia. In: *Monsoons of the World*. India Meteorological Department, pp. 75–88.

Flohn, H. (1968) Contributions to a meteorology of the Tibetan Highlands. Atmos. Sci. Paper No. 130, Colorado State University, Fort Collins, 120pp.

Flohn, H. (1981) The elevated heat source of the Tibetan highlands and its role for the large-scale atmospheric circulation. *Geological and Ecological Studies of Qinghai-Xizang (Tibet) Plateau*. Vol. II (Proc. Symp. Qinghai-Xizang (Tibet) Plateau, Beijing), Beijing, 1463–1470.

Fluteau, F., G. Ramstein and J. Besse (1999) Simulating the evolution of the Asian and African monsoons during the past 30 Myr using an atmospheric general circulation model, *J. Geophys. Res.* (Washington, DC), **104**, 11995–12018.

Fort, M. (1996) Late Cenozoic environmental changes and uplift on the northern side of the central Himalaya: A reappraisal from field data. *Palaeogeography, Palaeoclimatology, Palaeoecology*, **120**, 123–146.

Francis, P. A. and S. Gadgil (2002) Intense rainfall events over the west coast of India. CAOS Report, IISC, AS-, Centre for Atmospheric and Oceanic Sciences, Bangalore, India, 76pp.

Fu, C.-B. (2003) Potential impacts of human-induced land cover change on East Asia monsoon. *Global and Planetary Change*, **37**, 219–229.

Fu, C. and J. Fletcher (1985) The relationship between Tibet-tropical ocean thermal contrast and interannual variability of Indian monsoon rainfall. *J. Clim. Appl. Meteorol.*, **24**, 841–847.

Fu, R., A. D. Del Genio, W. B. Rossow and W. T. Liu (1992) Cirrus-cloud thermostat for tropical sea surface temperatures tested using satellite data, *Nature*, **358**, 394–397.

Fu, X. H. and B. Wang (2004) Differences of boreal summer intraseasonal oscillations simulated in an atmosphere–ocean coupled model and an atmosphere-only model. *J. Climate*, **17**, 1263–1271.

Fu, X. H., B. Wang and T. Li (2002) Impacts of air–sea coupling on the simulation of mean Asian summer monsoon in the ECHAM4 Model. *Monthly Weather Review*, **130**, 2889–2904.

Fu, X. H., B. Wang, T. Li and J. McCreary (2003) Coupling between northward-propagating boreal summer ISO and Indian Ocean SST: Revealed in an atmosphere–ocean coupled model. *J. Atmos. Sci.*, **60**, 1733–1753.

Fukutomi, Y. and T. Yasunari (1999) 10–25 day intraseasonal variations of convection and circulation over East Asia and western North Pacific during early summer. *J. Meteorol. Soc. Japan.*, **77**, 753–769.

Fujinami, H. and T. Yasunari (2001) The seasonal and intraseasonal variability of diurnal cloud activity over the Tibetan Plateau. *J. Meteorol. Soc. Japan*, **79**, 1207–1227.

Fujinami, H., S. Nomura and T. Yasunari (2004) Space–time characteristics of diurnal variation in convection and precipitation over the Tibetan Plateau during the summer Monsoon. Sixth International Study Conference on GEWEX in Asia and GAME, 3–5 December 2004, Kyoto.

Gadgil, S. (2003) The Indian monsoon and its variability. *Annu. Rev. Earth Planet. Sci.*, **31**, 429–467.

Gadgil, S. and G. Siddhartha (2004) Monsoon and the GDP. [Submitted.]

Gadgil, S. and P. V. Joseph (2003) On breaks of the Indian monsoon. *Proc. Indian Acad. Sci.–Earth Planet. Sci.*, **112**, 529–558.

Gadgil, S. and S. Sajani (1998) Monsoon precipitation in the AMIP runs. *Climate Dynamics*, **14**, 659–689.

Gadgil, S. and J. Srinivasan (1990) Low-frequency variation of tropical convergence zones. *Meteorol. Atmos. Phys.*, **44**, 119–132.

Gadgil, S., Y. P. Abrol and P. R. Seshagiri Rao (1999a) On growth and fluctuation of Indian foodgrain production. *Current Science*, **76**, 548–556.

Gadgil, S., P. R. Seshagiri Rao and S. Sridhar (1999b) Modelling impact of climate variability on rainfed groundnut. *Current Science*, **76**, 557–569.

Gadgil, S., K. Narahari, and S. Pradeep (1999c) Rice production in variable climate: Problems and prospects. In: Y. P. Abrol and Sulochana Gadgil (eds), *Rice in a Variable Climate*. APC Publications, New Delhi, pp. 11–24.

Gadgil, S., P. R. Seshagiri Rao and K. Narahari Rao (2002a) Use of climate information for farm-level decision making: Rainfed groundnut in southern India. *Agricultural Systems*, **74**, 431–457.

Gadgil, S., J. Srinivasan, R. S. Nanjundiah, K. K. Kumar, A. A. Munot and K. R. Kumar (2002b) On forecasting the Indian summer monsoon: The intriguing season of 2002. *Curr. Sci.*, **83**, 394–403.

Gadgil, S., P. N. Vinayachandran and P. A. Francis (2003) Droughts of the Indian summer monsoon: Role of clouds over the Indian Ocean. *Curr. Sci.*, **85**, 1713–1719.

Gadgil, S., P. N. Vinayachandran, P. A. Francis and Siddhartha Gadgil (2004) Extremes of the Indian summer monsoon rainfall, ENSO and the equatorial Indian Ocean Oscillation. *Geophys. Res. Lett.*, **31**, L12213, doi: 10.1029/2004GL019733.

GAME (1998) GAME (GEWEX Asian Mosoon Experiment) Implementation plan, GAME National Project Office, Terrestrial Environmental Research Center, Tsukuba University, Tsukuba, Japan.

Ganopolski, A. and S. Rahmstorf (2001) Abrupt Glacial Climate Changes due to Stochastic Resonance. *Phys. Rev. Lett.*, **88**.

Gao, Y.-X., *et al.* (1981) Some aspects of recent research on the Qinghai–Xizang Plateau meteorology. *Bull. Amer. Meteorol. Soc.*, **62**, 31–35.

Gao, Y.-X., Z.-C. Zhao and F. Giorgi (2002) Changes of extreme events in regional climate simulations over East Asia. *Adv. Atmos. Sci.*, **19**, 927–942.

Garratt, J. R. (1992) *The Atmospheric Boundary Layer*. Cambridge University Press, 316pp.

Garratt, J. R. (1993) Sensitivity of climate simulations to land surface and atmospheric boundary layer treatments: A review. *J. Climate*, **6**, 419–449.

Garreaud, R. D. and J. M. Wallace (1997) The diurnal march of convective cloudiness over the Americas. *Monthly Weather Review*, **125**, 3157–3171.

Gates, W. L. (1992) AMIP: The Atmospheric Model Intercomparison Project. *Bull. Amer. Meteor. Soc.*, **73**(12), 1962–1970.

Gates, W. L., A. H. Sellers, G. J. Boer, C. K. Folland, A. Kitoh, B. J. McAvaney, F. Semazzi, N. Smith, A. J. Weaver and Q.-C. Zeng (1996) Climate models: Evaluation. In: J. T. Houghton, L. G. Meira Filho, B. A. Callander, N. Harris, A. Kattenberg and K. Maskell (eds), *Climate Change 1995*, 567 pp.

Geng, Q. and M. Sugi (2003) Possible change of extratropical cyclone activity due to enhanced greenhouse gases and sulfate aerosols: Study with a high-resolution AGCM. *J. Climate*, **16**, 2262–2274.

George, L. and S. K. Mishra (1993) An observational study on the energetic of the monsoon onset vortex 1979. *Quart J. Roy. Meteorol. Soc.*, **119**, 755–778.

George, P. A. (1956) Effect of off-shore vortices on rainfall along the west coast of India. *Ind. J. Meteorol. Geophys.*, **7**, 235–240.

Gershunov, A., N. Schneider and T. Barnett (2001) Low-frequency modulation of the ENSO–Indian monsoon rainfall relationship: Signal or noise? *J. Climate*, **14**, 2486–2492.

Ghosh S. K., M. C. Pant and B. N. Dewan (1978) Influence of Arabian Sea on Indian Summer Monsoon. *Tellus*, **30**, 117–125.

Gibson, J. K., P. Källberg, S. Uppala, A. Hernandez, A. Nomura and E. Serrano (1997) ERA description. ECMWF Reanalysis Proj. Rep. 1, 72 pp.

Gill, A. E. (1980) Some simple solutions for heat-induced tropical circulation. *Quart. J. Roy. Meteorol. Soc.*, **106**, 447–462.

Gilman, D. L., F. J. Fuglister, and J. M. Mitchel, Jr. (1963) On the power spectrum of 'red noise'. *J. Atmos. Sci.*, **20**, 182–184.

Giorgi, F. and R. Francisco (2000) Evaluating uncertainties in the prediction of regional climate change. *Geophys Res. Lett.*, **27**, 1295–1298.

Giorgi, F., P. H. Whetton, R. G. Jones, J. H. Christensen, L. O. Mearns, B. Hewitson, H. von Storch, R. Francisco and C. Jack (2001) Emerging patterns of simulated regional climatic changes for the 21st century due to anthropogenic forcings. *Geophys. Res. Lett.*, **28**, 3317–3320.

Glantz, M. H., R. W. Katz and N. Nicholls (eds) (1991) *Teleconnections Linking Worldwide Climate Anomalies*. Cambridge University Press, Cambridge, UK, 353pp.

Godbole, R. V. (1977) The composite structure of monsoon horizontal momentum in monsoon depression over India. *Pure and Appl. Geophys.*, **24**, 1–14.

Godfrey, J. S. (1995) The role of the Indian Ocean in the global climate system: Recommendations regarding the global ocean observing system. Report of the Ocean Observing System Development Panel, Background Report #6, 89pp. Texas A&M Univ., College Station, TX.

Godfrey, J. S., R. A. Houze Jr., R. H. Johnson, R. Lukas, J. L. Redelsperger, A. Sumi and R. Weller (1998) Coupled Ocean–Atmosphere Response Experiment (COARE): An interim report. *J. Geophys. Res.*, **103**, 14395–14450.

Gong, D.-Y. and C.-H. Ho (2003) Arctic Oscillation signals in the East Asian summer monsoon. *J. Geophys. Res.*, **108**(D2), 4066, doi: 10.1029/2002JD002193.

Gong, G., D. Entekhabi and J. Cohen (2002) A large-ensemble model study of the wintertime AO–NAO and the role of interannual snow perturbations. *J. Climate*, **15**, 3488–3499.

Gong, G., D. Entekhabi and J. Cohen (2003) Modeled northern hemisphere winter climate response to realistic Siberian snow anomalies. *J. Climate*, **16**, 3917–3931.

Gong G., D. Entekhabi, J. Cohen and D. Robinson (2004) Sensitivity of atmospheric response to modeled snow anomaly characteristics. *J. Geophys. Res.*, **109**, D06107, doi: 10.1029/2003JD004160.

Goswami, B. N. (1995) A multiscale interaction model for the origin of the tropospheric QBO. *J. Climate*, **8**, 524–534.

Goswami, B. N. (1998) Interannual variations of Indian summer monsoon in a GCM: External conditions versus internal feedbacks. *J. Climate*, **11**, 501–522.

Goswami, B. N. (2004) Interdecadal change in potential predictability of the Indian summer monsoon. *Geophys. Res. Lett.*, **31**, doi: 10.1029/2004-GL020337.

Goswami, B. N. (2005) Intraseasonal variability (ISV) of south Asian summer monsoon. In: K. Lau and D. Waliser (eds), *Intraseasonal Variability of the Atmosphere–Ocean Climate System*. Springer–Praxis, Chichester, UK.

Goswami, B. N. and R. S. Ajayamohan (2001) Intraseasonal oscillations and predictability of the Indian summer monsoon. *Proc. Ind. Nat. Acad. Sci.*, **67**A(3), 369–383.

Goswami, B. N. and R. S. Ajayamohan (2001a) Intraseasonal oscillation and inter-annual variability of the Indian summer monsoon, *J. Climate*, **14**, 1180–1198.

Goswami, B. N. and J. Shukla (1984) Quasi-periodic oscillations in a symmetric general-circulation model. *J. Atmos. Sci.*, **41**, 20–37.

Goswami, B. N. and P. Xavier (2003) Potential predictability and extended range prediction of Indian summer monsoon breaks. *Geophys. Res. Lett.*, **30**, 1966, doi: 10.1029/2003GL017.810.

Goswami, B. N., J. Shukla, E. K. Schneider and Y. Sud (1984) Study of the dynamics of the Inter tropical convergence zone with a symmetric version of the GLAS climatic model. *J. Atmos. Sci.*, **41**, 5–19.

Goswami, B. N., V. Krishnamurthy and H. Annamalai (1997) A broad scale circulation index for the interannual variability of the Indian summer monsoon, COLA Tech. Rep. 46, pp. 52, Center for Ocean-Land-Atmosphere Studies, Calverton, MD.

Goswami, B. N., D. Sengupta and G. S. Kumar (1998) Intraseasonal oscillations and interannual variability of surface winds over the Indian monsoon region. *Proc. Indian Acad. Sci.–Earth Planet. Sci.*, **107**, 45–64.

Goswami, B. N., V. Krishnamurthy and H. Annamalai (1999) A broad scale circulation index for interannual variability of the Indian summer monsoon. *Quart. J. Roy. Meteorol. Soc.*, **125**, 611–633.

Goswami, B. N., R. S. Ajayamohan, P. K. Xavier and D. Sengupta (2003) Clustering of synoptic activity by Indian summer monsoon intraseasonal oscillations. *Geophys. Res. Lett.*, **30**, 1431, doi: 10.1029/2002GL016734.

Goswami, P. and V. Mathew (1994) A mechanism of scale selection in tropical circulation at observed intraseasonal frequencies. *J. Atmos. Sci.*, **51**, 3155–3166.

Gowarikar, V., V. Thapliyal, R. P. Sarker, G. S. Mandel and D. R. Sikka (1989) Parametric and power regression models: New approach to long range forecasting of monsoon rain in India. *Mausam*, **40**, 115–122.

Gowarikar, V., V. Thapliyal, S. M. Kulshrestha, G. S. Mandel, N. SenRoy and D. R. Sikka (1991) A power regression model for long range forecast of southwest monsoon rainfall over India. *Mausam*, **42**, 125–130.

Graham, N. E. (1994) Decadal-scale climate variability in the 1970s and 1980s: Observations and model results. *Climate Dynamics*, **10**, 135–162.

Graham, N. E., T. Barnett, R. Wilde, M. Ponater and S. Schubert (1994) On the roles of tropical and midlatitude SSTs in forcing interannual to interdecadal variability in the winter northern hemisphere circulation. *J. Climate*, **7**, 1416–1441.

Grant, A. (1953) The application of correlation and regression to forecasting. *Aust. Meteorol. Mag.*, **1**, 1–15.

Gray, W. M. (1967) Global view of the origin of tropical disturbances and storms. *Monthly Weather Review*, **96**, 669–700.

Gray, W. M. (1978) Hurricanes: Their formation, structure and likely role in the tropical circulation. In: D. B. Shaw (ed.), *Meteorology Over The Tropical Oceans*. Royal Meteorology Society, pp. 155–218.

Gray, W. M. (1979) Hurricanes: Their formation, structure and likely role in the tropical circulation. In: D. B. Show (ed.), *Meteorology over the Tropical Oceans*. Royal Meteorological Society, Reading, UK, pp. 155–218.

Gray, W. M. and R. W. Jacobson (1977) Diurnal variation of deep cumulus convection. *Monthly Weather Review*, **105**, 104–188.

Gregory, S. (1991) Interrelationships between Indian and northern Australian summer monsoon rainfall values. *Int. J. Climatol.*, **11**, 55–62.

Grootes, P. and M. Stuiver (1997) Oxygen 18/16 variability in Greenland snow and ice with 10^3 to 10^5 year time resolution, *J. Geophys. Res.*, **102**(C12), 26455–26470.

Grossman, R. L. and D. R. Durran (1984) Interaction of the low-level flow with the Western Ghats Mountains and offshore convection in the summer monsoon. *Monthly Weather Review*, **112**, 652–672.

Gruber, A. (1974) Wavenumber–frequency spectra of satellite-measured brightness in the Tropics. *J. Atmos. Sci.*, **31**, 1675–1680.

Gualdi, S., A. Navarra and G. Tinarelli (1999a) The interannual variability of the Madden–Julian Oscillation in an ensemble of GCM simulations. *Climate Dynamics*, **15**, 643–658.

Gualdi, S., A. Navarra and M. Fischer (1999b) The tropical intraseasonal oscillation in a coupled ocean–atmosphere general circulation model. *Geophys. Res. Lett.*, **26**, 2973–2976.

Guo, Q. (1994) Relationship between the variations of East Asian winter monsoon and temperature anomalies in China. Quart. *J. Appl. Meteorol.*, **5**(2), 218–225. [In Chinese.]

Guo, Q. and J. Wang (1988) A comparative study on summer monsoon in China and India. *J. Trop. Meteorol.*, **4**, 53–60. [In Chinese.]

Guo, Q. Y. (1994) Change in the East Asian winter monsoon and its relationship with anomalous temperature in China. *J. Appl. Meteorol.*, **5**, 218–225.

Guo, Q. Y. and J. Q. Wang (1981) The distribution of precipitation in China during the summer monsoon period for recent 30 years. *Acta Geographica Sinica*, **36**, 187–195. [In Chinese.]

Gupta, A. and U. C. Mohanty (1997) Secondary convective rings in an intense asymmetric cyclone of the Bay of Bengal. *Mausam*, **48**, 273–282.

Gutzler, D. S. (1991) Interannual fluctuations of intraseasonal variance of near-equatorial Zonal Winds. *J. Geophys. Res.-Oceans*, **96**, 3173–3185.

Gyakum, J. R., J. R. Anderson, R. H. Grumm and E. L. Gruner (1989) North Pacific cold-season surface cyclone activity: 1975–1983. *Monthly Weather Review*, **117**, 1141–1155.

Hacker, P., E. Firing, J. Hummon, A. L. Gordon, and L. Kindle (1998) Bay of Bengal currents during the northeast monsoon. *Geophys. Res. Lett*, **25**, 2769–2772.

Hadley, G. (1735) Concerning the cause of the general trade-winds. *Philos. Trans. R. Soc. London*, **39**, 58–62.

Haertel, P. T., R. H. Johnson and S. N. Tulich (2001) Some simple simulations of thunderstorm outflows. *J. Atmos. Sci.*, **58**, 504–516.

Hahn D. G. and S. Manabe (1975) The role of mountains in the south Asian monsoon circulation. *J. Atmos. Sci.*, **32**, 1515–1541.

Hahn D. G. and Shukla, J. (1976) An apparent relationship between Eurasian snow cover and Indian monsoon rainfall. *J. Atmos. Sci.*, **33**, 2461–2462.

Hall, J. D., A. J. Matthews and D. J. Karoly (2001) The modulation of tropical cyclone activity in the Australian region by the Madden–Julian Oscillation. *Monthly Weather Review*, **129**, 2970–2982.

Halley, E. (1686) An historical account of the Trade Winds, and Monsoons, observable in the seas between the Tropics, with an attempt to assign the physical cause of the said Winds. *Philos. Trans. R. Soc. London*, **16**, 153–168.

Halpern, D., R. A. Knox, and D. S. Luther (1988) Observations of 20-day period meridional current oscillations in the upper ocean along the Pacific equator. *J. Phys. Ocean*, **18**(11), 1514–1534.

Hamada, J.-I., M. D. Yamanaka, J. Matsumoto, S. Fukao, P. A. Winarso and T. Sribimawati (2002) Spatial and temporal variations of the rainy season over Indonesia and their link to ENSO. *J. Meteorol. Soc. Japan*, **80**, 285–310.

Han, W., P. J. Webster, R. B. Lukas, P. W. Hacker and A. Hu (2004) Impact of atmospheric intraseasonal atmospheric variability in the equatorial Indian Ocean: Low-frequency rectification in equatorial surface current and transport. *J. Phys. Oceanogr.*, **34**, 1350–1372.

Hanson, H. P. and B. Long (1985) Climatology of Cyclogenesis over the East China Sea. *Monthly Weather Review*, **113**, 697–707.

Hardjawinata, S. (1980) Macroclimatic aspects of rice production in Southeast Asia in 'Agro-meteorology of the rice crop'. Proc. of the symposium IRRI, Los Banos, Laguna, Phillipines, pp. 50–57.

Harr, P. A. and J. C. L. Chan (2005) Monsoon impacts on tropical cyclone variability. In: C. P. Chang, B. Wang and N. C. G. Lau (eds), *The Global Monsoon System: Research and Forecast*. World Meteorological Organization, Geneva, pp. 512–542.

Harr, P. A. and R. L. Elsberry (1995) Large-scale circulation variability over the tropical western North Pacific. Part I: Spatial patterns and tropical cyclone characteristics. *Monthly Weather Review*, **123**, 1225–1246.

Harshvardan and T. G. Corsetti (1984) Longwave parameterization for the UCLA/GLAS GCM. *NASA Tech. Memo. 86072*, Goddard Space Flight Center, Greenbelt, MD 20771, **52**, 51pp.

Hart, J. E. (1977) On the theory of the East Africa low level jet stream. *Pure Appl. Geophys.*, **115**, 1263–1282.

Hartmann, D. L. and E. D. Maloney (2001) The Madden–Julian Oscillation, barotropic dynamics, and North Pacific tropical cyclone formation. Part II: Stochastic barotropic modeling. *J. Atmos. Sci.*, **58**, 2559–2570.

Hartmann, D. L. and M. L. Michelsen (1993) Large-scale effects on the regulation of tropical sea surface temperature. *J. Climate*, **6**, 2049–2062.

Hartmann, D. L., H. H. Hendon and R. A. Houze, Jr. (1984) Some implications of the mesoscale circulations in tropical cloud clusters for large-scale dynamics and climate. *J. Atmos. Sci.*, **41**, 113–121.

Hartmann, D. L., L. A. Moy and Q. Fu (2001) Tropical convection and the energy balance at the top of the atmosphere. *J. Climate*, **14**, 4495–4511.

Harzallah, A. and R. Sadourny (1997) Observed lead-lag relationships between Indian summer monsoon and some meteorological variables. *Clim. Dyn.*, **13**, 635–648.

Hastenrath, S. (1987) *Climate Dynamics of the Tropics: An Updated Edition of Climate and Circulation of the Tropics*. Kluwer Academic, Dordrecht, The Netherlands.

Hasselmann, K. (1988) Pips and pops: The reduction of complex dynamical systems using principal interaction and oscillation patterns. *J. Geophys. Res.–Atmos.*, **93**, 11015–11021.

Hastenrath, S. (1986a) On climate prediction in the tropics. *Bull. Amer. Meteorol. Soc.*, **67**, 692–702.

Hastenrath, S. (1986b) Tropical climate prediction: A progress report 1985–1990. *Bull. Amer. Meteorol. Soc.*, **67**, 819–825.

Hastenrath, S. (1987a) Predictability of Java monsoon rainfall anomalies: A case study. *J. Clim. Appl. Meteorol.*, **26**, 133–141.

Hastenrath, S. (1987b) On the Prediction of India Monsoon Rainfall Anomalies. *J. Clim. Appl. Meteorol.*, **26**, 847–857.

Hastenrath, S. (1994) *Climate Dynamics of the Tropics: An Updated Edition of Climate and Circulation of the Tropics*. Kluwer Academic Publishers, Norwell, MA, 488pp.

Hastenrath, S. and L. Greischar (1993) The monsoonal heat budget of the hydrosphere–atmosphere system in the Indian Ocean sector. *J. Geophys. Res.*, **98**, 6869–6881.

Hastenrath, S. and P. Lamb (1978) On the dynamics and climatology of surface flow over equatorial oceans. *Tellus*, **30**, 436–448.

Hayashi, Y. (1970) A theory of large scale equatorial waves generated by condensation heat and accelerating the zonal wind. *J. Meteorol. Soc. Japan*, **48**, 140–160.

Haylock, M. and J. McBride (2001) Spatial coherence and predictability of Indonesian wet season rainfall. *J. Climate*, **14**, 3882–3887.

Haynes, P. H. and M. E. McIntyre (1987) On the evolution of vorticity and potential vorticity in the presence of diabatic heating and frictional or other forces. *J. Atmos. Sci.*, **44**, 828–841.

Hays, J. D., J. Imbrie and N. J. Shackleton (1976) Variations in the Earth's orbit: Pacemaker of the ice ages. *Science*, **194**, 1121–1132.

He, C. and Y. H. Ding (2004) Relationship between variations of the Asian monsoon and the anomalous climate in China. In: D. H. Qin (ed.), *Evolution of Climate and Environment in China*. Science Press, Beijing, 562 pp.

He, H., J. W. McGinnis, Z. Song and M. Yanai (1987) Onset of the Asian monsoon in 1979 and the effect of the Tibetan Plateau. *Monthly Weather Review*, **115**, 1966–1995.

Henderson-Sellers, A., Z.-L. Yang and R. E. Dickinson (1993) The project for intercomparison of land–surface parameterization schemes. *Bull. Amer. Meteorol. Soc.*, **74**, 1335–1349.

Henderson-Sellers, A., J. Pitman, P. K. Love, P. Irannejad and T. H. Chen (1995) The project for intercomparison of land surface parameterization schemes (PILPS): Phases 2 and 3. *Bull. Amer. Meteorol. Soc.*, **76**, 489–503.

Hendon, H. H. (1988) A simple model of the 40–50-day oscillation. *J. Atmos. Sci.*, **45**, 569–584.

Hendon, H. H. (2000) Impact of air-sea coupling on the Madden–Julian Oscillation in a general circulation model. *J. Atmos. Sci.*, **57**, 3939–3952.

Hendon, H. H. (2003) Indonesian rainfall variability: Impacts of ENSO and local air–sea interaction. *J. Climate*, **16**, 1775–1790.

Hendon, H. H. (2005) Air–sea interaction. In: W. K. M. Lau and D. E. Waliser (eds), *Intraseasonal Variability of the Atmosphere–Ocean Climate System*. Springer–Praxis, Chichester, UK.

Hendon, H. H. and J. Glick (1997) Intraseasonal air–sea interaction in the tropical Indian and Pacific Oceans. *J. Climate*, **10**, 647–661.

Hendon, H. H. and B. Liebmann (1990a) A composite study of onset of the Australian summer monsoon. *J. Atmos. Sci.*, **47**, 2227–2240.

Hendon, H. H. and B. Liebmann (1990b) The intraseasonal 30–50-day oscillation of the Australian summer monsoon. *J. Atmos. Sci.*, **47**, 2909–2923.

Hendon, H. H. and M. L. Salby (1994) The life-cycle of the Madden–Julian Oscillation. *J. Atmos. Sci.*, **51**, 2225–2237.

Hendon, H. H., N. E. Davidson and B. Gunn (1989) Australian summer monsoon onset during AMEX 1987. *Monthly Weather Review*, **117**, 370–390.

Hendon, H. H., C. D. Zhang and J. D. Glick (1999) Interannual variation of the Madden–Julian Oscillation during austral summer. *J. Climate*, **12**, 2538–2550.

Hendon, H. H., B. Liebmann, M. Newman, J. D. Glick and J. E. Schemm (2000) Medium-range forecast errors associated with active episodes of the Madden–Julian oscillation. *Monthly Weather Review*, **128**, 69–86.

Hertenstein, R. F. A. and W. H. Schubert (1991) Potential vorticity anomalies associated with squall lines. *Monthly Weather Review*, **119**, 1663–1672.

Higgins, R. W., J. K. E. Schemm, W. Shi and A. Leetmaa (2000) Extreme precipitation events in the western United States related to tropical forcing. *J. Climate*, **13**, 793–820.

Higgins, R. W., A. Douglas, A. Hahmann and coauthors (2003) Progress in Pan American CLIVAR Research: The North American Monsoon System. *Atmosfera*, **16**, 29–65.

Hinnov, L. A., M. Schulz and P. Yiou (2002) Interhemispheric space–time attributes of the Dansgaard–Oeschger oscillations between 100 and 0 ka. *Quaternary Science Reviews*, **21**, 1213–1228.

Hirakuchi, H. and F. Giorgi (1995) Multiyear present-day and $2 \times CO_2$ simulations of monsoon climate over eastern Asia and Japan with a regional climate model nested in a general circulation model. *J. Geophys. Res.*, **100**, 21105–21125.

Hirst, A. C. and K. M. Lau (1990) Intraseasonal and interannual oscillations in coupled ocean–atmosphere models. *J. Climate*, **3**, 713–725.

Ho, C.-H., J.-J. Baik, J.-H. Kim, D.-Y. Gong and C.-H. Sui (2004) Interdecadal changes in summertime typhoon tracks. *J. Climate*, **17**, 1767–1803.

Hodges, K. I. and C. D. Thorncroft (1997) Distribution and statistics of African mesoscale convective weather systems based on the ISCCP Meteosat imagery. *Monthly Weather Review*, **125**, 2821–2837.

Hoerling, M. P., J. W. Hurrell and T. Xu (2001) Tropical origins for recent north Atlantic climate change. *Science*, **292**, 90–92.

Holtslag, A. A. M. and C.-H. Moeng (1991) Eddy diffusivity and countergradient transport in the convective atmospheric boundary layer. *J. Atmos. Sci.*, **48**, 1690–1698.

Holland, G. J. (1984) On the climatology and structure of tropical cyclones in the Australian Southwest Pacific Region. *Aus. Meteorol. Mag.*, **32**, 17–31.

Holland, G. J. (1986) Interannual variability of the Australian summer monsoon at Darwin: 1952–1982. *Monthly Weather Review*, **114**, 594–604.

Holtslag, A. A. M. and B. A. Boville (1993) Local versus nonlocal boundary layer diffusion in a global climate model. *J. Climate*, **6**, 1825–1847.

Hong, S.-Y. and H.-L. Pan (1996) Nonlocal boundary layer vertical diffusion in a medium-range forecast model. *Monthly Weather Review*, **124**, 2322–2339.

Hoskins, B. J. (1974) The role of potential vorticity in symmetric stability and instability. *Quart. J. Roy. Meteorol. Soc.*, **49**, 1233–1241.

Hoskins, B. J. (1982) Cloud clusters and large-scale vertical motions in the Tropics. *J. Meteorol. Soc. Japan*, **60**, 396–410.

Hoskins, B. J. (1991) Towards a PV-view of the general circulation. *Tellus*, **43AB**, 27–35.

Hoskins, B. J. (1996) On the existence and strength of the summer subtropical anticyclones. *Bull Amer. Meteorol. Soc.*, **77**, 1287–1292.

Hoskins, B. J. and T. Ambrizzi (1993) Rossby wave propagation on a realistic longitudinally varying flow. *J. Atmos. Sci.*, **50**, 1661–1671.

Hoskins, B. J. and A. K. Betts (1981) Convection in GATE. *Rev. Geophys. Space Phys.*, **19**, 541–576.

Hoskins, B. J. and C.-P. Cheng (1977) Radar characteristics of tropical convection observed during GATE: Mean properties and trends over the summer season. *Monthly Weather Review*, **105**, 964–980.

Hoskins, B. J. and F. Jin (1991) The initial value problem for tropical perturbations to a baroclinic atmosphere. *Quart. J. Roy. Meteorol. Soc.*, **117**, 299–317.

Hoskins, B. J. and D. J. Karoly (1981) The steady linear response of a spherical atmosphere to thermal and orographic forcing. *J. Atmos. Sci.*, **38**, 1179–1196.

Hoskins, B. J. and M. J. Rodwell (1995) A model of the Asian summer monsoon. Part I: The global scale. *J. Atmos. Sci.*, **52**, 1329–1340.

Hoskins, B. J. and P. D. Sardeshmukh (1988) Generation of global rotational flow by steady idealized tropical divergence. *J. Atmos. Sci.*, **45**, 1228–1251.

Hoskins, B. J., S. G. Geotis, F. D. Marks Jr. and A. K. West (1981) Winter monsoon convection in the vicinity of North Borneo. Part I: Structure and time variation of the clouds and precipitation. *Monthly Weather Review*, **109**, 1595–1614.

Hoskins, B. J., M. I. Biggerstaff, S. A. Rutledge and B. F. Smull (1989) Interpretation of Doppler weather radar displays of midlatitude mesoscale convective systems. *Bull. Amer. Meteorol. Soc.*, **70**, 608–619.

Hoskins, B. J. Jr., B. F. Smull and P. Dodge (1990) Mesoscale organization of springtime rainstorms in Oklahoma. *Monthly Weather Review*, **118**, 613–654.

Hoskins, B. J., R. Neale, M. J. Rodwell and G.-Y. Yang (1999) Aspects of the large-scale tropical atmospheric circulation. *Tellus*, **51A-B**, 33–44.

Hoskins, B. J., S. S. Chen, D. E. Kingsmill, Y. Serra and S. E. Yuter (2000) Convection over the Pacific warm pool in relation to the atmospheric Kelvin–Rossby wave. *J. Atmos. Sci.*, **57**, 3058–3089.

Houze, R. A. Jr. (1977) Structure and dynamics of a tropical squall-line system. *Monthly Weather Review*, **105**, 1540–1567.

Houze, R. A., Jr. (1982) Cloud clusters and large-scale vertical motion in the tropics. *J. Meteor. Soc. Japan.*, **60**, 396–410.

Houze, R. A. (1993) *Cloud Dynamics*. Academic Press, San Diego, 573 pp.

Houze, R. A. Jr., and A. K. Betts (1981) Convection in GATE. *Rev. Geophys. Space Phys.*, **19**, 541–576.

Houze, R. A., Jr. and C.-P. Cheng (1977) Radar characteristics of tropical convection observed during GATE: Mean properties and trends in the summer season. *Mon. Wea. Rev.,* **105**, 964–980.

Houze, R. A. Jr., S. G., Geotis, F. D. Marks Jr. and A. K. West (1981) Winter monsoon convection in the vicinity of North Borneo. Part I: Structure and time variation of the clouds and precipitation. *Monthly Weather Review*, **109**, 1595–1614.

Houze, R. A., Jr., B. F. Smull, and P. Dodge (1990) Mesoscale organization of springtime rainstorms in Oklahoma. *Mon. Wea. Rev.,* **118**, 613–654.

Houze, R. A., Jr., S. S. Chen, and D. E. Kingsmill (2000) Convection over the Pacific warm pool in relation to the atmospheric Kelvin–Rossby wave. *J. Atmos. Sci.*, **57**, 3058–3089.

Hsiung, J., R. E. Newell and T. Houghtby (1989) The annual cycle of oceanic heat storage and oceanic meridional heat transport. *Quart J. Roy. Meteorol. Soc.*, **115**, 1–28.

Hsu, H. H. (1987) Propagation of low-level circulation features in the vicinity of mountain ranges. *Monthly Weather Review*, **115**, 1864–1893.

Hsu, H. H. (2005) East Asian Monsoon. In: W. K. M. Lau and D. E. Waliser (eds), *Intraseasonal Variability of the Atmosphere–Ocean Climate System*. Springer–Praxis, Chichester, UK.

Hsu, H. H. and X. Liu (2003) Relationship between the Tibetan Plateau heating and East Asian summer monsoon rainfall. *Geophys. Res. Lett.*, **30(20)**, 2066.

Hsu, H. H. and C.-H. Weng (2001) Northwestward propagation of the intraseasonal oscillation in the western North Pacific during the boreal summer: Structure and mechanism. *J. Climate*, **14**, 3834–3850.

Hsu, H. H., B. J. Hoskins and F. F. Jin (1990) The 1985/86 intraseasonal oscillation and the role of the extratropics. *J. Atmos. Sci.*, **47**, 823–839.

Hsu, H. H., C.-T. Teng and C.-T. Chen (1999) Evolution of large-scale circulation and heating during the first transition of Asian summer monsoon. *J. Climate*, **12**, 793–810.

Hsu, H. H., C.-H. Weng and C.-H. Wu (2004) Contrasting characteristics between the northward and eastward propagation of the intraseasonal oscillation during the boreal summer. *J. Climate*, **17**, 727–743.

Hu, Q. (1995) Low-frequency oscillations in radiative convective systems. Part 2: An idealized model. *J. Atmos. Sci.*, **52**, 478–490.

Hu, Z. Z. (1997) Interdecadal variability of summer climate over east Asia and its association with 500 hPa height and global sea surface temperature. *J. Geophys. Res.*, **102**, 19403–19412.

Hu, Q. and D. A. Randall (1994) Low-frequency oscillations in radiative–convective systems. *J. Atmos. Sci.*, **51**, 1089–1099.

Hu, Q. and D. A. Randall (1995) Low-frequency oscillations in radiative–convective systems. *J. Atmos. Sci.*, **52**, 478–490.

Hu, Z. Z., L. Bengtsson and K. Arpe (2000a) Impact of the global warming on the Asian winter monsoon in a coupled GCM. *J. Geophys. Res.*, **105**, 4607–4624.

Hu, Z. Z., M. Latif, E. Roeckner and L. Bengtsson (2000b) Intensified Asian summer monsoon and its variability in a coupled model forced by increasing greenhouse gas concentrations. *Geophys. Res. Lett.*, **27**, 2681–2684.

Hu, Z. Z., S. Yang and R. Wu (2003) Long-term climate variations in China and global warming signals. *J. Geophys. Res.*, **108**(D19), 4614, doi: 10.1029/2003JD003651.

Huang, R. (1984) The characteristics of the forced planetary wave propagations in the summer Northern Hemisphere. *Adv. Atmos. Sci.*, **1**, 85–94.

Huang, R. (1985) Numerical simulation of the three-dimensional teleconnections in the summer circulation over the Northern Hemisphere. *Adv. Atmos. Sci.*, **2**, 81–92.

Huang, R. and F. Sun (1992) Impacts of the tropical western Pacific on the East Asian summer monsoon. *J. Meteorol. Soc. Japan*, **70**, 243–256.

Huang, R. and Y. Wu (1989) The influence of ENSO on the summer climate change in China and its mechanism. *Adv. Atmos. Sci.*, **6**, 21–32.

Huffman, G. J., R. F. Adler, P. Arkin, A. Chang, R. Ferraro, A. Gruber, J. Janowiak, A. McNab, B. Rudolf, and U. Schneider (1997) The Global Precipitation Climatology Project (GPCP) combined precipitation dataset. *Bull. Am. Meteorol. Soc.*, **78**(1), 5–20.

Hulme, M., Z.-C. Zhao and T. Jiang (1994) Recent and future climate change in East Asia. *Int. J. Climatol.*, **14**, 637–658.

Hulme, M., T. J. Osborn and T. C. Johns (1998) Precipitation sensitivity to global warming: Comparison of observations with HADCM2 simulations. *Geophys. Res. Lett.*, **25**, 3379–3382.

Hung, C.-W. and M. Yanai (2004) Factors contributing to the onset of the Australian summer monsoon. *Quart. J. Roy. Meteorol. Soc.*, **130**, 739–761.

Hung, C.-W., X. Liu and M. Yanai (2004) Symmetry and asymmetry of the Asian and Australian summer monsoons. *J. Climate*, **17**, 2413–2426.

Hurrell, J. W., J. J. Hack, D. Shea, J. Caron, and J. Rosinki (2005) A new sea surface temperature and sea ice boundary data set for the community atmospheric model. [Submitted to *J. Climate*.]

Ichikawa, A. (ed.) (2004) *Global Warming, The Research Challenges: A Report of Japan's Global Warming Research Initiative*. Kluwer, Dordrecht, The Netherlands, 159 pp.

IITM (1989) *One day P.M.P. Atlas of India*. Indian Institute of Tropical Meteorology, Poona, India.

IITM (1994) *Atlas on Severe Rain Storms of India*. Indian Institute of Tropical Meteorology, Poona, India.

Imaoka, Keiji and R. W. Spencer (2000) Diurnal variation of precipitation over the tropical oceans observed by TRMM/TMI combined with SSM/I. *J. Climate*, **13**, 4149–4158.

Imbrie, J., J. D. Hays, D. G. Martinson, A. McIntyre, A. C. Mix, J. J. Morley, N. G. Pisias, W. L. Prell and N. J. Shackleton (1984) The orbital theory of Pleistocene climate:

Support from a revised chronology of the marine $\delta^{18}O$ record. In: A. L. Berger *et al.* (eds), *Milankovitch and Climate* (Part 1). D. Riedel, Hingham, pp. 269–305.

Imbrie, J., E. A. Boyle, S. C. Clemens, A. Duffy, W. R. Howard, G. Kukla, J. Kutzbach, D. G. Martinson, A. McIntyre, A. C. Mix, *et al.* (1992) On the structure and origin of major glaciation cycles. Part 1: Linear responses to Milankovitch forcing. *Paleoceanography*, **7**, 701–738.

Imbrie, J., A. Berger, E. A. Boyle, S. C. Clemens, A. Duffy, W. R. Howard, G. Kukla, J. Kutzbach, D. G. Martinson, A. McIntyre, *et al.* (1993) On the structure and origin of major glaciation cycles. Part 2: The 100,000-year cycle. *Paleoceanography*, **8**, 699–735.

IMD (1943) *Climatological Atlas for Airmen*. Ind. Meteorol. Dept, Poona.

IMD (1944) *Norwesters of Bengal*. Ind. Meteorol. Dept. Tech. Note, 120, 11pp.

IMD (1973) North east monsoon. Forecasting Manual Report No. IV, 18.4, IMD, New Delhi, India.

IMD (1979) Tracks of Storms and depressions in the Bay of Bengal of the Arabian Sea IMD, New Delhi, India, 186pp.

Indian Ocean Panel Implementation Plan (2004) Avaialable in draft form from Chair of the Indian Ocean Panel, G. Meyers, CSIRO Division of Oceanography, Hobart, Tasmania, Australia.

Inness, P. M. and J. M. Slingo (2003) Simulation of the Madden-Julian oscillation in a coupled general circulation model. Part I: Comparison with observations and an atmosphere-only GCM. *J. Climate*, **16**, 345–364.

Inness, P. M., J. M. Slingo, S. J. Woolnough, R. B. Neale and V. D. Pope (2001) Organization of tropical convection in a GCM with varying vertical resolution: Implications for the simulation of the Madden–Julian Oscillation. *Climate Dynamics*, **17**, 777–793.

Inness, P. M., J. M. Slingo, E. Guilyardi and J. Cole (2003) Simulation of the Madden–Julian Oscillation in a coupled general circulation model. Part II: The role of the basic state. *J. Climate*, **16**, 365–382.

IOP (2005) Draft version of the Indian Ocean Panel Implementation Plan is available from the Chair of the IOP. Contact: *Gary.Meyers@csiro.au*

IPCC (1996) *Climate Change 1995: The Science of Climate Change*. J. T. Houghton, L. G. Meira Filho, B. A. Callander, N. Harris, A. Kattenberg and K. Maskell (eds). Cambridge University Press, Cambridge, UK, 572pp.

IPCC (2000) *Special Report on Emission Scenarios*. N. Nakicenovic and R. Swart (eds). Cambridge University Press, Cambridge, UK, 612pp.

IPCC (2001) *Climate Change 2001: The Scientific Basis. Contribution of Working Group I to the Third Assessment Report of the Intergovernmental Panel on Climate Change*. J. T. Houghton, Y. Ding, D. J. Griggs, M. Noguer, P. J. van der Linden, X. Dai, K. Maskell and C. A. Johnson (eds). Cambridge University Press, Cambridge, UK, 881pp.

IRRI (1996) World Rice Statistics 1993–1994. International Rice Research Institute, Los Baños, Philippines.

Jagannathan, P. (1960) *Seasonal Forecasting in India, A Review*. Meteorological Office, Poona, India, 79pp.

Janaiah, A. (2003) Hybrid rice in Andhra Pradesh. *Economic and Political Weekly*, June 21, 2513–2516.

Janawiak, J. E., P. A. Arkin and M. Morrissey (1994) An examination of the diurnal cycle in oceanic tropical rainfall using satellite and in situ data. *Monthly Weather Review*, **122**, 2296–2311.

Jayanthi, N. and S. Govindachari (1999) El Niño and NE monsoon rainfall over Tamil Nadu. *Mausam*, **50**, 217–218.

Jhun, J. and E. Lee (2004) A new East Asian winter monsoon index and associated characteristics of the winter monsoon. *J. Climate*, **17**, 711–726.

Ji, M., A. Leetmaa and J. Derber (1995) An ocean analysis system for seasonal to interannual climate studies. *Monthly Weather Review*, **123**, 460–481.

Ji, Y. and A. D. Vernekar (1997) Simulations of the Asian summer monsoons of 1987 and 1988 with a regional model nested in a global GCM. *J. Climate*, **10**, 1965–1979.

Ji, L., S. Sun and K. Arpe (1997) Model study on the interannual variability of Asian winter monsoon and its influence. *Adv. Atmos. Sci.*, **14**, 1–22.

Jia, J. and S. Zhao (1994) A diagnostic study of explosive development of extratropical cyclone over East Asia and West Pacific Ocean. *Adv. Atmos. Sci.* (Beijing, China), **11**, 251–270.

Jiang, S. C. (1988) The climate characteristics of the ITCZ over the globe. *Acta Meteorol. Sinica*, **46**, 241–245 [In Chinese.]

Jiang, X. N., T. Li and B. Wang (2004) Structures and mechanisms of the northward propagating boreal summer intraseasonal oscillation. *J. Climate*, **17**, 1022–1039.

Jin, F.-F. (1997) An equatorial ocean recharge paradigm for ENSO. Part I: Conceptual model. *J. Atmos. Sci.*, **54**, 811–829.

Jin, F.-F. (2004) Understanding the coupled ocean–atmosphere dynamics of ENSO. In: X. Zhu (ed), *Observation, Theory and Modeling of Atmospheric Variability*. World Scientific Series on Meteorology of East Asia, **3**, pp. 39–72.

Jin, Z. and L. Chen (1983) On the medium-range oscillation of the East Asian monsoon circulation system and its relation with the Indian monsoon system. In: *Proceedings of the Symposium on the Summer Monsoon in South East Asia*. Yunnan People's Press, Yunnan, pp. 204–217.

JMA (2000) *Information of Global Warming (Vol. 3): Climate Change Due to Increase of CO_2 and Sulphate Aerosol Projected with A Coupled Atmosphere–Ocean Model*. JMA, Tokyo, Japan, 70pp. [In Japanese.]

JMA (2002) *Outline of the Operational Numerical Weather Prediction at the Japan Meteorological Agency* (Appendix to WMO Numerical Weather Prediction Progress Report). JMA, Tokyo, Japan, 157pp.

Johnsen, S. J., H. B. Clausen, W. Dansgaard, K. Fuhrer, N. Gundestrup, C. U. Hammer, P. Iversen, J. Jouzel, B. Stauffer and J. P. Steffensen (1992) Irregular glacial interstadials recorded in a new Greenland ice core. *Nature*, **359**, 311–313.

Johnson, R. H. (1984) Partitioning tropical heat and moisture budgets into cumulus and mesoscale components: Implications for cumulus parameterization. *Monthly Weather Review*, **112**, 1590–1601.

Johnson, R. H. (1986) Implications of lower tropospheric warming and drying in tropical mesoscale convective systems for the problem of cumulus parameterization. *J. Meteorol. Soc. Japan*, **64**, 721–726.

Johnson, R. H. and J. F. Bresch (1991) Diagnosed characteristics of precipitation systems over Taiwan during the May–June 1987 TAMEX. *Monthly Weather Review*, **119**, 2540–2557.

Johnson, R. H. and R. A. Houze, Jr. (1987) Precipitating cloud systems of the Asian monsoon. *Monsoon Meteorology*, **X**, 298–353, C.-P. Chang and T. N. Krishnamurti, Eds., Oxford University Press.

Johnson, R. H. and B. E. Mapes (2001) Mesoscale processes and severe convective weather. *Severe Convective Storms, Meteorol. Monogr.*, **50**, Amer. Meteorol. Soc., 71–122.

Johnson, R. H. and J. R. Zimmerman (1986) Modification of the boundary layer over the South China Sea during a Winter MONEX cold surge event. *Monthly Weather Review*, **114**, 2004–2015.

Johnson, R. H., Z. Wang and J. F. Bresch (1993) Heat and moisture budgets over China during the early summer monsoon. *J. Meteorol. Soc. Japan*, **71**, 137–152.

Johnson, R. H., P. E. Ciesielski and K. A. Hart (1996) Tropical inversions near the 0° level. *J. Atmos. Sci.*, **53**, 1838–1855.

Johnson, R. H., T. M. Rickenbach, S. A. Rutledge, P. E. Ciesielski and W. H. Schubert (1999) Trimodal characteristics of tropical convection. *J. Climate.*, **12**, 2397–2433.

Johnson, R. H., P. E. Ciesielski and J. A. Cotturone (2001) Multiscale variability of the atmospheric mixed layer over the western Pacific warm pool. *J. Atmos. Sci.*, **58**, 2729–2750.

Johnson, R. H., P. Ciesielski and T. D. Keenan (2004) Oceanic East Asian monsoon convection: Results from the 1998 SCSMEX. In: C.-P. Chang (ed.), *East Asian Monsoon*. World Scientific, Singapore, pp. 436–459.

Johnson, R. H., S. L. Aves, P. E. Ciesielski and T. D. Keenan (2005) Organization of oceanic convection during the onset of the 1998 East Asian summer monsoon. *Monthly Weather Review*, **133**, 131–148.

Jones, C. (2004) A statistical forecast model of tropical intraseasonal convective anomalies. *J. Climate*, **17**, 2078–2095.

Jones, C. and B. C. Weare (1996) The role of low-level moisture convergence and ocean latent heat fluxes in the Madden and Julian oscillation: An observational analysis using ISCCB data and ECMWF analyses. *J. Climate*, **9**, 3086–3104.

Jones, C., D. E. Waliser and C. Gautier (1998) The influence of the Madden–Julian Oscillation on ocean surface heat fluxes and sea surface temperature. *J. Climate*, **11**, 1057–1072.

Jones, P. D., M. New, D. E. Parker, S. Martin and I. G. Rigor (1999) Surface air temperature and its variations over the last 150 years. *Rev. Geophysics*, **37**, 173–199.

Jones, C., D. E. Waliser, J. K. E. Schemm and W. K. M. Lau (2000) Prediction skill of the Madden and Julian Oscillation in dynamical extended range forecasts. *Climate Dynamics*, **16**, 273–289.

Jones, C., L. M. V. Carvalho, R. W. Higgins, D. E. Waliser, and J.-K. E. Schemm (2003) Climatology of Tropical Intraseasonal Convective Anomalies: 1979–2002. *J. Climate*, **17**, 523–539.

Jones, C., D. E. Waliser, K. M. Lau and W. Stern (2004a) The Madden–Julian Oscillation and its impact on Northern Hemisphere weather predictability. *Monthly Weather Review*, **132**, 1462–1471.

Jones, C., L. M. V. Carvalho, R. W. Higgins, D. E. Walliser, and K.-K. E. Schemm (2004b) A statistical forecast model of tropical intraseasonal convective anomalies. *J. Climate*, **17**, 2078–2095.

Joseph, P. V. (1976a) Climatic change in monsoon and cyclones 1891–1974. *Proc. Symp. Tropical Monsoons, IITM, Pashan, Poona, India*, pp. 378–387.

Joseph, P. V. (1976b) Climate cycles in monsoon and tropical cyclones 1871–1974. *Proc. Symp. Tropical Meteorology, IITM, Poona.*

Joseph, P. V. (1982) A tentative model of Andhi. *Mausam*, **33**, 417–422.

Joseph, P. V. and P. V. Pillai (1988) 40-day mode of equatorial trough for long-range forecasting Indian summer monsoon onset. *Current Sci.*, **57**, 951–954.

Joseph, P. V. and P. L. Raman (1966) Existence of low level westerly jet stream over Peninsular India during July. *Ind. J. Meteorol. Geophys.*, **17**, 407–410.

Joseph, P. V., D. K. Raipal and S. N. Daka (1980) Andhi, the convective dust storm of NW India. *Mausam*, **31**, 431–442.

Joseph, P. V., B. Liebmann and H. H. Hendon (1991) Interannual variability of the Australian summer monsoon onset: Possible influence of Indian summer monsoon and El Niño. *J. Climate*, **4**, 529–538.

Joseph, P. V., J. K. Eischeid and R. J. Pyle (1994) Interannual variability of the onset of the Indian summer monsoon and its association with atmospheric features, El Niño, and sea surface temperature anomalies. *J. Climate*, **7**, 81–105.

Ju, J. and J. M. Slingo (1995) The Asian summer monsoon and ENSO. *Quart. J. Roy. Meteorol. Soc.*, **121**, 1133–1168.

Kaas, E., T.-S. Li and T. Schmith (1996) Statistical hindcast of wind climatology in the North Atlantic and northwestern European region. *Climate Res.*, **7**, 97–110.

Kachi, M. and T. Nitta (1997) Decadal variations of the global ocean atmosphere system. *J. Meteorol. Soc. Japan*, **75**, 657–675.

Kahndekar, M. L. (1991) Eurasian snow cover, Indian monsoon and El Niño/Southern Oscillation: A synthesis. *Atmosphere–Ocean*, **29**, 636–647.

Kalnay, E., R. Balgovind, W. Chao, D. Edelmann, J. Pfaendtner, L. Takacs and K. Takano (1983) Documentation of the GLAS fourth order general circulation model, Volume 1. NASA Tech. Memo. No. 86064, NASA Goddard Space Flight Center, Greenbelt, MD.

Kalnay, E., M. Kanamitsu, R. Kistler, W. Collins, D. Deaven, L. Gandin, M. Iredell, S. Saha, G. White, J. Woollen, *et al.* (1996) The NCEP/NCAR 40-year Reanalysis Project. *Bull. Amer. Meteorol. Soc.*, **77**, 437–471.

Kalsi, S. R. (1999) Multiple eye wall structure in an Arabian Sea cyclone. *Current Science*, **77**, 1175–1180.

Kalsi, S. R. (2002) *Use of Satellite Imagery in Tropical Cyclone Intensity Analysis and Forecasting* (Meteorol. Monograph No. 1/2002). Cyclone Warning Division, Ind. Meteorol. Dept., New Delhi.

Kalsi, S. R. and R. C. Bhatia (1992) Satellite observations of thunder storm complexes in weakly forced environments, Vayu Mandal, 22.

Kalsi, S. R. and R. K. Jain (1989) On some aspects of marginal cyclones, *Mausam*, **40**, 47–50.

Kalsi, S. R., S. D. Kojal and S. R. Roy Bhowmik (2003) Decaying nature of super cyclone of Orissa after landfall. *Mausam*, **54**, 393–396.

Kanae, S., T. Oki and K. Musiake (2001) Impact of deforestation on regional precipitation over the Indochina Peninsula. *J. Hydrometeor.*, **2**, 51–70.

Kanae, S., Y. Hirabayashi, T. Yamada and T. Oki (2004) Influence of land-surface hydrologic conditions on inter-annual variability of precipitation in boreal summer. [Submitted to *J. Climate*.]

Kanamitsu, M. (1975) On numerical prediction over a global tropical belt. *Report No. 75-1*, Dept. of Meteorology, Florida State University, Tallahassee, Florida 32306, pp. 1–282.

Kanamitsu, M. (1989) Description of the NMC global data assimilation and forecast system. *Weather and Forecasting*, **4**, 335–342.

Kanamitsu, M. and H.-M. H. Juang (1994) Multi-month simulations of Indian Monsoon by the NMC nested regional spectral model. *Preprints, 10th conference on NWP*, Portland, OR, AMS, pp. 351–352.

Kanamitsu, M., K. Tada, K. Kuda, N. Sato and S. Isa (1983) Description of the JMA operational spectral model. *J. Meteorol. Soc. Japan*, **61**, 812–828.

Kang, I., S. An, C. Joung, S. Yoon and S. Lee (1989) 30–60-day oscillation appearing in climatological variation of outgoing longwave radiation around East Asia during summer. *J. Korean Meteorol Soc.*, **25**, 149–160.

Kang, I., S. An, C.-H. Ho, Y.-K. Lim and K.-M. Lau (1999) Principal modes of climatological seasonal and intraseasonal variations of the Asian summer monsoon. *Monthly Weather Review*, **127**, 322–340.

Kang, I. S., K. Jin, B. Wang, K.-M. Lau, J. Shukla, V. Krishnamurthy, S. D. Schubert, D. E. Wailser, W. F. Stern, *et al.* (2002a) Intercomparison of the climatological variations of Asian summer monsoon precipitation simulated by 10 GCMs. *Climate Dynamics*, **19**, 383–395.

Kang, I. S, K. Jin, B. Wang, K.-M. Lau, J. Shukla, V. Krishnamurthy, S. D. Schubert, D. E. Wailser, W. F. Stern, V. Satyan, *et al.* (2002b) Intercomparison of the climatological variations of Asian summer monsoon precipitation simulated by 10 GCMs. *Climate Dynamics*, **19**, 383–395.

Kang, I., S. An, J.-Y. Lee and C.-K. Park (2004) Potential predictability of a dynamical seasonal prediction system with systematic error correction. *J. Climate*, **17**, 834–844.

Kantha, L. H. and C. A. Clayson (1994) An improved mixed layer model for geophysical applications. *J. Geophys. Res.*, **99**, 25235–25266.

Kapala, A., K. Born and H. Flohn (1994) Monsoon anomaly or an El Niño event at the equatorial Indian Ocean? Catastrophic rains 1961/62 in east Africa and their teleconnections. In: *Proceedings of the International Conference on Monsoon Variability and Prediction. Tech. Doc. 619*, pp. 119–126. World Meteorological Organization, Switzerland.

Kaplan, A., Y. Kushnir, M. A. Cane and M. B. Blumenthal (1997) Reduced space optimal analysis of historical data sets: 136 years of Atlantic sea surface temperatures. *J. Geophys. Res.*, **102c**, 27835–27860.

Kasahara, A. and P. L. Silva Dias (1986) Response of planetary waves to stationary tropical heating in a global atmosphere with meridional and vertical Shear. *J. Atmos. Sci.*, **43**, 1893–1912.

Kato, K. (1985) On the abrupt change in the structure of the Baiu front over the China continent in late May of 1979. *J. Meteorol. Soc. Japan*, **63**, 20–36.

Kato, H., K. Nishizawa, H. Hirakuchi, S. Kadokura, N. Oshima and F. Giorgi (2001) Performance of RegCM2.5/NCAR-CSM nested system for the simulation of climate change in East Asia caused by global warming. *J. Meteorol. Soc. Japan*, **79**, 99–121.

Katyal, J. C. (1998) Soil, Water and Environmental Sciences, paper presented at Brainstorming Session on 'Scientists Perception for Agriculture – 2020' held at NBPGR Auditorium, 4–5 June 1998, New Delhi, India.

Kawamura, R. (1988) Intraseasonal variability of sea surface temperatures over the tropical western Pacific. *J. Meteorol. Soc. Japan*, **66**, 1007–1012.

Kawamura, R. (1991) Air–sea coupled modes on intraseasonal and interannual time scales over the tropical western Pacific. *J. Geophys. Res.–Oceans*, **96**, 3165–3172.

Kawamura, R. (1994) A rotated EOF analysis of global sea surface temperature variability with interannual and interdecadal time scale. *J. Phys. Oceanogr.*, **24**, 707–715.

Kawamura, R. (1998) A possible mechanism of the Asian summer monsoon–ENSO coupling. *J. Meteorol. Soc. Japan*, **76**, 1009–1027.

Kawamura, R., Y. Fukuta, H. Ueda, T. Matsuura and S. Iizuka (2002) A mechanism of the onset of the Australian summer monsoon. *J. Geophys. Res.*, **107**(D14), doi: 10.1029/2001JD001070.

Kawamura, R., T. Matsuura and S. Iizuka (2003) Equatorially symmetric impact of the El Niño–Southern Oscillation on the South Asian summer monsoon system. *J. Meteorol. Soc. Japan*, **81**, 1329–1352.

Keenan, T. D. and L. R. Brody (1988) Synoptic-scale modulation of convection during the Australian summer monsoon. *Monthly Weather Review*, **116**, 71–85.

Keenan, T. D. and R. E. Carbone (1992) A preliminary morphology of precipitation systems in northern Australia. *Quart. J. Roy. Meteorol. Soc.*, **118**, 283–326.

Keenan, T. D. and S. A. Rutledge (1993) Mesoscale characteristics of monsoonal convection and associated stratiform precipitation. *Monthly Weather Review*, **121**, 352–374.

Kelkar, R. R. (1997) Satellite based monitoring and prediction of tropical cyclone intensity and movement. *Mausam*, **48**, 157–168.

Kemball-Cook, S. and B. Wang (2001) Equatorial waves and air–sea interaction in the Boreal summer intraseasonal oscillation. *J. Climate*, **14**, 2923–2942.

Kemball-Cook, S. R. and B. C. Weare (2001) The onset of convection in the Madden–Jullian Oscillation. *J. Climate*, **14**, 780–793.

Kemball-Cook, S., B. Wang and X. H. Fu (2002) Simulation of the intraseasonal oscillation in the ECHAM-4 model: The impact of coupling with an ocean model. *J. Atmos. Sci.*, **59**, 1433–1453.

Keppenne, C. L. and M. Ghil (1992) Adaptive filtering and prediction of the Southern Oscillation Index. *J. Geophys. Res.–Atmos.*, **97**, 20449–20454.

Kershaw, A. P., S. van der Kaars and P. T. Moss (2003) Late Quaternary Milankovitch-scale climatic change and variability and its impact on monsoonal Australasia. *Marine Geology*, **201**, 81–95.

Keshvamurty, R. N. (1973) Power Spectra of large scale disturbances of the Indian South West Monsoon. *Ind. J. Meteorol. Geophys.*, **24**, 117–124.

Keshvamurty, R. N. and S. T. Awade (1970) On the maintenance of the mean monsoon trough over north India. *Monthly Weather Review*, **98**, 315–320.

Keshvamurty, R. N. and S. T. Awade (1974) Dynamical abnormality associated with droughts of the Asian summer monsoon. *Ind. J. Meteorol. Geophy*, **25**, 257–264.

Keshvamurty, R. N. and M. Shankar Rao (1992) *The Physics of Monsoon*. Allied Pubs., New Delhi, India.

Kessler, W. S. (2005) The oceans. In: W. K. M. Lau and D. E. Waliser (eds), *Intraseasonal Variability of the Atmosphere–Ocean Climate System*. Springer–Praxis, Chichester, UK.

Kessler, W. S. (2001) EOF representations of the Madden–Julian oscillation and its connection with ENSO. *J. Climate*, **14**, 3055–3061.

Kessler, W. S. and M. J. McPhaden (1995) Oceanic equatorial waves and the 1991–1993 El Niño. *J. Climate*, **8**, 1757–1774.

Kessler, W. S. and R. Kleeman (2000) Rectification of the Madden–Julian Oscillation into the ENSO cycle. *J. Climate*, **13**, 3560–3575.

Khole, M. and U. S. De (2003) A study on the northeast monsoon rainfall over India. *Mausam*, **54**, 419–426.

Kiguchi, M. and J. Matsumoto (2005) The rainfall phenomena during the pre-monsoon period over the Indochina peninsula in the GAME-IOP year. *J. Meteorol. Soc. Japan*, **83**, 89–106.

Kiladis, G. N. and H. F. Diaz (1989) Global climate anomalies associated with extremes in the Southern Oscillation. *J. Climate*, **2**, 1069–1090.

Kiladis, G. N. and K. M. Weickmann (1992) Circulation anomalies associated with tropical-convection during northern winter. *Monthly Weather Review*, **120**, 1900–1923.

Kiladis, G. N., K. H. Straub and P. T. Haertel (2005) Zonal and vertical structure of the Madden–Julian Oscillation. *J. Atmos. Sci.* [In press.]

Kim, K. M. and K. M. Lau (2001) Dynamics of monsoon-induced biennial variability in ENSO. *Geophys. Res. Lett.*, **28**, 315–318.

Kinter III, J. L., K. Miyakoda and S. Yang (2002) Recent changes in the connection from the Asian monsoon to ENSO. *J. Climate*, **15**, 1203–1215.

Kinter, J. L., M. J. Fennessy, V. Krishnamurthy and L. Marx (2004) An evaluation of the apparent interdecadal shift in the tropical divergent circulation in the NCEP–NCAR reanalysis. *J. Climate*, **17**(2), 349–361.

Kirono, D. G., C. N. J. Tapper and J. McBride (1999) Documenting Indonesian rainfall in the 1997/1998 El Niño event. *Phys. Geogr.*, **20**, 422–435.

Kirtman, B. P. and A. Vernekar (1993) On wave–CISK and the evaporation wind feedback for the Madden–Julian oscillation. *J. Atmos. Sci.*, **50**, 2811–2814.

Kirtman, B. P. and J. Shukla (1997) Influence of the Indian summer monsoon on ENSO. *Quart. J. Roy. Meteorol. Soc.*, **126**, 213–239.

Kishtawal, C. M. and T. N. Krishnamurti (2001) Diurnal variation of summer rainfall over Taiwan and its detection using TRMM observations. *J. Appl. Meteorol.*, **40**, 331–344.

Kistler, R., E. Kalnay, W. Collins, S. Saha, G. White, J. Woollen, M. Chelliah, W. Ebisuzaki, M. Kanamitsu, V. Kousky, *et al.* (2001) The NCEP NCAR 50-year reanalysis: Monthly means CD-ROM and documentation. *Bull. Amer. Meteorol. Soc.*, **82**, 247–267.

Kitade, T. (1983) Nonlinear normal mode initialization with physics. *Mon. Wea. Rev.*, **111**, 2194–2213.

Kitoh, A. (1988) Numerical experiment on sea surface temperature anomalies and warm winter in Japan. *J. Meteorol. Soc. Japan*, **66**, 515–533.

Kitoh, A. (2003) Paleo monsoon and future monsoon. *Kishou Kenkyu Note*, **204**, 189–218. [In Japanese.]

Kitoh, A. (2004) Effects of mountain uplift on East Asian summer climate investigated by a coupled atmosphere–ocean GCM. *J. Climate*, **17**, 783–802.

Kitoh, A., S. Yukimoto, A. Noda and T. Motoi (1997) Simulated changes in the Asian summer monsoon at times of increased atmospheric CO_2. *J. Meteorol. Soc. Japan*, **75**, 1019–1031.

Klein, S. A. and D. L. Hartmann (1993) The seasonal cycle of low stratiform clouds. *J. Climate*, **6**, 1587–1606.

Klein, S. A., B. J. Soden and N.-C. Lau (1999) Remote sea surface temperature variations during ENSO: Evidence for a tropical atmospheric bridge. *J. Climate*, **12**, 917–932.

Knox, R. A. (1987) The Indian Ocean. In: Fein and Stephens (eds), *Monsoons*. Wiley, New York, pp. 3–32.

Knutson, T. R. and R. E. Tuleya (2001) Impact of CO_2-induced warming on hurricane intensities and simulated in a hurricane model with ocean coupling. *J. Climate*, **14**, 2458–2468.

Koide, H. and K. Kodera (1999) A SVD analysis between the winter NH 500-hPa height and surface temperature fields. *J. Meteorol. Soc. Japan*, **77**, 47–61.

Koike, T., H. Fujii, T. Ohta and E. Togashi (2001) Development and validation of TMI algorithms for soil moisture and snow. *Remote Sensing and Hydrology 2000*, IAHS publication, **267**, 390–393.

Koo, Chen-chao (1951) On the importance of the dynamical influence of Tibetan Plateau on the circulation over East Asia. *Sci. Sinica*, **2**, 283–303. [In Chinese.]

Koster, R. D. and M. J. Suarez (1992) Modeling the land surface boundary in climate models as a composite of independent vegetation stands. *J. Geophys. Res.*, **97**, 2697–2715.

Koster, R. D. and M. J. Suarez (1995) The relative contributions of land and ocean processes to precipitation variability. *J. Geophys. Res.*, **100**, 13775–13790.

Koster, R. D. *et al.* (The GLACE Team) (2004) Regions of strong coupling between soil moisture and precipitation. *Science*, **305**, 1138–1140.

Koteswaram, P. (1950) Upper air law in low latitudes in the Indian area during south west monsoon season and breaks in the monsoon. *Ind. J. Meteorol. Geophys*, **2**, 162–164.

Koteswaram, P. (1958) Easterly jet stream in the tropics. *Tellus*, **10**, 43–57.

Koteswaram, P. and C. A. George (1958) On the formation of monsoon depression in the Bay of Bengal. *Ind. J. Meteorol. Geophys*, **9**, 9–22.

Koteswaram, P. and N. S. Bhaskar Rao (1963) Formation and structure of Indian summer monsoon depressions. *Aust Meteorol. Mag.*, **41**, 2–75.

Koteswaram, P. and S. Parthasarthy (1954) The mean jet stream over India in the pre-monsoon and post-monsoon seasons and vertical motions associated with sub-tropical jet streams. *Ind. J. Meteorol. Geophy*s., **51**, 129–156.

Kousky, V. E. (1980) Diurnal rainfall variations in northeast Brazil. *Monthly Weather Review*, **108**, 488–498.

Kraus, E. B. (1963) The diurnal precipitation change over the sea. *J. Atmos. Sci.*, **20**, 551–556.

Kripalani, R. H. and A. Kulkarni (1997a) Climatic impacts of El Niño/La Niña on the Indian Monsoon. *Weather*, **152**, 39–46.

Kripalani, R. H. and A. Kulkarni (1997b) Rainfall variability over southeast Asia – connections with Indian monsoon and ENSO extremes: New perspectives. *Int. J. Climatol.*, **17**, 1155–1168.

Kripalani, R. H. and A. Kulkarni (1998) The relationship between some large-scale atmospheric parameters and rainfall over South-east Asia: A comparison with features over India. *Theor. Appl. Climatol.*, **59**, 1–11.

Kripalani, R. H. and A. Kulkarni (1999) Climatology and variability of historical Soviet snow depth data: Some new perspectives in snow–Indian monsoon teleconnections. *Climate Dynamics*, **15**, 475–489.

Kripalani, R. H. and A. Kulkarni (2001) Monsoon rainfall variations and teleconnections over South and east Asia. *Int. J. Climatol.*, **21**, 603–616.

Kripalani, R. H., S. V. Singh, A. D. Vernekar and V. Thapliyal (1996) Empirical study on Nimbus-7 snow mass and Indian summer monsoon rainfall. *Int. J. Climatol.*, **16**, 23–34.

Kripalani, R. H., A. Kulkarni and S. V. Singh (1997) Association of the Indian summer monsoon with the northern hemisphere midlatitude circulation. *Int. J. Climatol.*, **17**, 1055–1067.

Kripalani, R. H., A. Kulkarni and S. S. Sabade (2003) Western Himalayan snow cover and Indian monsoon rainfall: A re-examination with INSAT and NCEP/NCAR data. *Theor. Appl. Climatol.*, **74**, 1–18.

Krishna Kumar, K., M. K. Soman and K. Rupa Kumar (1995) Seasonal forecasting of Indian summer monsoon rainfall. *Weather*, **50**, 449–467.

Krishna Kumar, K., R. Kleeman, M. A. Cane and B. Rajagopalan (1999a) Epochal changes in Indian monsoon–ENSO precursors. *Geophys. Res. Lett.*, **26**, 75–78.

Krishna Kumar, K., B. Rajagopalan and M. A. Cane (1999b) On the weakening relationship between the Indian Monsoon and ENSO. *Science*, **284**, 2156–2159.

Krishna Kumar, K., K. Rupa Kumar, R. G. Ashrit, N. R. Deshpande and J. W. Hansen (2004) Climate impacts on Indian agriculture. *Int. J. Climatol.*, **24**, 1375–1393.

Krishnamurti, T. N. (1969) An experiment in numerical prediction in equatorial latitudes. *Quart. J. Roy. Meteorol. Soc.*, **95**, 594–620.

Krishnamurti, T. N. (1971a) Observational study of the tropical upper tropospheric motion field during the Northern Hemisphere summer. *J. Appl. Meteorol.*, **10**, 1066–1096.

Krishnamurti, T. N. (1971b) Tropical east–west circulation during the northern summer. *J. Atmos. Sci.*, **28**, 1342–1347.

Krishnamurti, T. N. (1985) Summer monsoon experiment–A review. *Monthly Weather Review*, **113**, 1590–1626.

Krishnamurti, T. N. (1987) NWP in low latitudes. *Adv. in Geophysics*, **28**, 283–333.

Krishnamurti, T. N. (1990) Monsoon prediction at different resolutions with a global spectral model. *Mausam*, **41**, 234–240.

Krishnamurti, T. N. and P. Ardanuy (1980) The 10 to 20 day westward propagating mode and breaks in the monsoon. *Tellus*, **32**, 15–26.

Krishnamurti, T. N. and H. N. Bhalme (1976) Oscillations of monsoon system. Part I: Observational aspects. *J. Atmos. Sci.*, **45**, 1937–1954.

Krishnamurti, T. N. and S. Gadgil (1985) On the Structure of the 30 to 50 day mode over the globe during FGGE. *Tellus Ser. A–Dyn. Meteorol. Oceanol.*, **37**, 336–360.

Krishnamurthy, V. and B. N. Goswami (2000) Indian monsoon–ENSO relationship on interdecadal time scales. *J. Climate*, **13**, 579–595.

Krishnamurti, T. N. and C. M. Kishtawal (2000) A pronounced continental-scale diurnal mode of the Asian summer monsoon. *Monthly Weather Review*, **128**, 462–473.

Krishnamurti, T. N. and Y. Ramanathan (1982) Sensitivity of the monsoon onset to differential heating. *J. Atmos. Sci.*, **39**, 1290–1306.

Krishnamurti, T. N. and E. B. Rodgers (1970) 200-mb wind field June, July, August 1967. *Rept. No. 70-2*. Dept. of Meteorol., Florida State University, Tallahassee, 115pp.

Krishnamurti, T. N. and J. Sanjay (2003) A New Approach to the cumulus parameterization issue. *Tellus*, **55**, 275–300.

Krishnamurthy, V. and J. Shukla (2000) Intra-seasonal and inter-annual variations of rainfall over India. *J. Climate*, **13**, 4366–4375.

Krishnamurthy, V. and J. Shukla (2001) Observed and model simulated interannual variability of the Indian monsoon. *Mausam*, **52**, 133–150.

Krishnamurti, T. N. and D. Subrahmanyam (1982) The 30–50 day mode at 850 Mb during MONEX. *J. Atmos. Sci.*, **39**, 2088–2095.

Krishnamurti, T. N., M. Kanamitsu, W. J. Ross and J. D. Lee (1973a) Tropical east–west circulation during the northern winter. *J. Atmos. Sci.*, **30**, 780–787.

Krishnamurti, T. N., S. M. Daggupaty, J. Fein, M. Kanamitsu, and J. D. Lee (1973b) Tibetan High and upper tropospheric tropical circulation during Northern summer. *Bull. Amer. Meteorol. Soc.*, **54**, 1234–1249.

Krishnamurti, T. N., J. Molinari and H.-L. Pan (1976) Numerical simulation of the Somali jet. *J. Atmos. Sci.*, **33**, 2350–2362.

Krishnamurti, T. N., J. Molinari, H. L. Pant and V. Wong (1977) Downstream amplification and formation of monsoon disturbances. *Monthly Weather Review*, **105**, 1281–1297.

Krishnamurti, T. N., P. Ardanuy, Y. Ramanathan and R. Pasch (1981) On the onset vortex of the summer monsoon. *Monthly Weather Review*, **109**, 344–363.

Krishnamurti, T. N., S. Low-Nam and R. Pasch (1983a) Cumulus parameterization and Rainfall Rates – II. *Monthly Weather Review*, **111**, 815–828.

Krishnamurti, T. N., S. Cocke, R. Pasch and S. Low-Nam (1983b) *Precipitation Estimates from Raingauge and Satellite Observations: Summer MONEX*. Dept. of Meteorology, Florida State University, 373pp.

Krishnamurti, T. N., V. Wong, H. L. Pan, R. Pasch, J. Molinari and P. Ardanuy (1983c) A three-dimensional planetary boundary layer model for the Somali jet. *J. Atmos. Sci.*, **40**, 894–908.

Krishnamurti, T. N., P. K. Jayakumar, J. Sheng, N. Surgi and A. Kumar (1985) Divergent circulations on the 30 to 50 day time scale. *J. Atmos. Sci.*, **42**, 364–375.

Krishnamurti, T. N., S. Low-Nam, A. Kumar, J. Sheng and M. Sugi (1987) Numerical weather prediction of monsoons. In: C.-P. Chang and T. N. Krishnamurti (eds), *Monsoon Meteorology* (Oxford Monographs on Geology and Geophysics). Oxford University Press, pp. 501–544.

Krishnamurti, T. N., D. K. Oosterhof and A. V. Mehta (1988) Air Sea Interaction on the Time Scale of 30 to 50 Days. *J. Atmos. Sci.*, **45**, 1304–1322.

Krishnamurti, T. N., M. Subramaniam, D. K. Oosterhof and G. Daughenbaugh (1990a) Predictability of Low-Frequency Modes. *Meteorol. Atmos. Phys.*, **44**, 63–83.

Krishnamurti, T. N., A. Kumar, K. S. Yap, A. P. Dastoor, N. Davidson and J. Sheng (1990b) Performance of a high-resolution mesoscale tropical prediction model. *Advances in Geophysics*, **32**, 133–286.

Krishnamurti, T. N., J. Xue, H. S. Bedi, K. Ingles and D. Oosterhof (1991) Physical initialization for numerical weather prediction over the tropics. *Tellus*, **43**AB, 53–81.

Krishnamurti, T. N., M. Subramaniam, G. Daughenbaugh, D. Oosterhof and J. H. Xue (1992a) One-month forecasts of wet and dry spells of the monsoon. *Monthly Weather Review,* **120**, 1191–1223.

Krishnamurti, T. N., M. C. Sinha, R. Krishnamurti, D. K. Oosterhof and J. Comeaux (1992b) Angular momentum, length of day and monsoonal low frequency mode. *J. Meteorol. Soc. Japan*, **70**, 131–166.

Krishnamurti, T. N., S. O. Han and V. Misra (1995) Prediction of the Dry and Wet Spell of the Australian Monsoon. *Int. J. Climatol.*, **15**, 753–771.

Krishnamurti, T. N., H. S. Bedi and W. Han (1998a) Organization of convection and monsoon forecasts. *Meteorol. Atmos. Phys.*, **67**, 117–134.

Krishnamurti, T. N., H. S. Bedi and V. M. Hardiker (1998b) *An Introduction to Global Spectral Modeling*. Oxford University Press, 253pp.

Krishnamurti, T. N., C. M. Kishtawal, T. E. LaRow, D. R. Bachiochi, Z. Zhang, C. E. Willford, S. Gadgil and S. Surendran (1999) Improved weather and seasonal climate prediction forecasts from multimodel superensemble. *Science*, **285**, 1548–1550.

Krishnamurti, T. N., C. M. Kishtawal, Z. Zhang, T. LaRow, D. Bachiochi, C. E. Williford, S. Gadgil and S. Surendran (2000a) Multimodel ensemble forecasts for weather and seasonal climate. *J. Climate*, **13**, 4196–4216.

Krishnamurti, T. N., C. M. Kishtawal, D. W. Shin and C. E. Williford (2000b) Improving tropical precipitation forecasts from a multianalysis superensemble. *J. Climate*, **13**, 4217–4227.

Krishnamurti, T. N., S. Surendran, D. W. Shin, R. J. Correa-Torres, T. S. V. V. Kumar, C. E. Williford, C. Kummerow, R. F. Adler, J. Simpson, R. Kakar *et al.* (2001) Real-time multianalysis–multimodel superensemble forecasts of precipitation using TRMM and SSM/I products. *Monthly Weather Review*, **129**, 2861–2883.

Krishnamurti, T. N., L. Stefanova, A. Chakraborty, T. S. V. V. Kumar, S. Cocke, D. Bachiochi and B. P. Mackey (2002) Seasonal Forecasts of precipitation anomalies for North American and Asian Monsoons. *J. Meteorol. Soc. Japan*, **80**, 1415–1426.

Krishnamurti, T. N., A. K. Mitra, W. T. Yun, T. S. V. V. Kumar and W. K. Dewar (2005) Seasonal climate forecasts of the Asian monsoon using multiple coupled models. [Submitted to *Tellus*.]

Krishnan, R. and S. V. Kasture (1996) Modulation of low frequency intraseasonal oscillations of northern summer monsoon by El Niño and southern oscillation (ENSO). *Meteorol. Atmos. Phys*., **60**, 237–257.

Krishnan, R. and M. Sugi (2001) Baiu rainfall variability and associated monsoon teleconnection. *J. Meteorol. Soc. Japan*, **79**, 851–860.

Krishnan, R., C. Zhang and M. Surgi (2000) Dynamics of breaks in the Indian summer monsoon. *J. Atmos. Sci*., **57**, 1354–1372.

Kroon, D., T. N. Steens and S. R. Troelstra (1991) Onset of monsoonal related upwelling in the northern Arabian Sea, Ocean Drilling Program. *Scientific Results*, **117**, 257–264.

Kuang, Z., P. N. Blossey and C. S. Bretherton (2004) A DARE approach for 3D cloud resolving simulations of large scale atmospheric circulation. *Geophys. Res. Lett*. [Submitted.]

Kumar, A. and M. P. Hoerling (1995) Prospects and limitations of seasonal atmospheric GCM predictions. *Bull. Amer. Meteorol. Soc*., **76**, 335–345.

Kumar, A. and F. Yang (2003) Comparative influence of snow and SST variability on extratropical climate in northern winter. *J. Climate*, **16**, 2248–2261.

Kung, E. C. (1982) Long-range forecasting of the Indian-summer monsoon onset and rainfall with upper air parameters and sea-surface temperature. *J. Meteorol. Soc. Japan*, **60**, 672–681.

Kung, E. C. and T. A. Sharif (1980) Regression forecasting of the onset of the Indian-summer monsoon with antecedent upper air conditions. *J. Appl. Meteorol*., **19**, 370–380.

Kuo, H. L. (1965) On formation and intensification of tropical cyclones through latent heat release by cumulus convection. *J. Atmos. Sci*., **22**, 40–63.

Kuo, H. L. (1974) Further studies of the parameterization of the influence of cumulus convection on large-scale flow. *J. Atmos. Sci*., **31**, 1232–1240.

Kuo, H. L. and Y.-F. Qian (1981) Influence of the Tibetan Plateau on cumulative and diurnal changes of weather and climate in summer. *Mon. Wea. Rev*., **109**, 2337–2356.

Kuo, H. L. and Y.-F. Qian (1982) Numerical simulation of the development of mean monsoonal circulation in July. *Monthly Weather Review*, **110**, 1879–1897.

Kuo, Y. H., L. Cheng and R. A. Anthes (1986) Mesoscale analyses of Sichuan flood catastrophe, 11–15 July, 1981. *Monthly Weather Review*, **114**, 1984–2003.

Kurosaki, Y. and F. Kimura (2002) Relationship between topography and daytime cloud activity around Tibetan Plateau. *J. Meteorol. Soc. Japan*, **80**, 1339–1355.

Kutsuwada, K. (1988) Spatial characteristics of interannual variability in wind stress over the western north Pacific. *J. Climate*, **1**, 333–345.

Kutzbach, G. (1987) Concepts of monsoon physics in historical perspective: The Indian monsoon (seventeenth to early twentieth century). In: J. S. Fein and P. L. Stephens (eds), *Monsoons*. 632pp.

Kutzbach, J. E., P. J. Guetter, W. F. Ruddiman and W. L. Prell (1989) Sensitivity of climate to late Cenozoic uplift in southern Asia and the American West: Numerical experiments, *J. Geophys. Res*., **94**, 18393–18407.

Kutzbach, J. E., W. L. Prell and W. F. Ruddiman (1993) Sensitivity of Eurasian climate to surface uplift of the Tibetan plateau. *J. Geology*, **101**, 177–190.

Kuwagata, T., A. Numaguti and N. Endo (2001) Diurnal variation of water vapor over the Central Tibetan Plateau. *J. Meteorol. Soc. Japan*, **79**, 401–418.

Lac, C., J.-P. Lafore, and J.-L. Redelsperger (2002) Role of gravity waves in triggering deep convection during TOGA COARE. *J. Atmos. Sci.*, **59**, 1293–1316.

Lacis, A. A. and J. Hansen (1974) A parameterization for the absorption of solar radiation in the Earth's atmosphere. *J. Atmos. Sci.*, **31**, 118–133.

Laing, A. G. and J. M. Fritsch (1993a) Mesoscale convective complexes over the Indian monsoon region. *J. Climate*, **6**, 911–919.

Laing, A. G. and J. M. Fritsch (1993b) Mesoscale convective complexes in Africa. *Monthly Weather Review*, **121**, 2254–2263.

Laing, A. G. and J. M. Fritsch (1997) The global population of mesoscale convective complexes. *Quart. J. Roy. Meteorol. Soc.*, **123**, 389–405.

Laing, A. G. and J. M. Fritsch (2000) The large-scale environments of the global populations of mesoscale convective complexes. *Monthly Weather Review*, **128**, 2756–2776.

Lal, M. and H. Harasawa (2001) Future climate change scenarios for Asia as inferred from selected coupled atmosphere–ocean global climate models. *J. Meteorol. Soc. Japan*, **79**, 219–227.

Lal, M. and S. K. Singh (2001) Global warming and monsoon climate. *Mausam*, **52**, 245–262.

Lal, M., U. Cubasch and B. D. Santer (1994) Effect of global warming on Indian monsoon simulated with a coupled ocean–atmosphere general circulation model. *Current Science*, **66**, 430–438.

Lal, M., U. Cubasch, R. Voss and J. Waszkewitz (1995) Effect of transient increase in greenhouse gases and sulphate aerosols on monsoon climate. *Current Science*, **69**, 752–763.

Lal, M., T. Nozawa, S. Emori, H. Harasawa, K. Takahashi, M. Kimoto, A. Abe-Ouchi, T. Nakajima, T. Takemura and A. Numaguchi (2001) Future climate change: Implications for Indian summer monsoon and its variability. *Current Science*, **81**, 1196–1207.

Lander, M. A. (1994) Description of a monsoon gyre and its effects on the tropical cyclones in the Western North Pacific during August 1991. *Weather Forecasting*, **9**, 640–654.

Latif, M., A. Sterl, M. Assenbaum, and M. M. Maierreimer (1994) Climate variability in a coupled GCM. Part II: The Indian Ocean and monsoon. *J. Climate*, **7**, 1449–1462.

Latif, M., D. Dommenget, M. Dima *et al.* (1999) The role of Indian Ocean sea surface temperature in forcing east African rainfall anomalies during December–January 1997/98. *J. Climate*, **12**, 3497–3504.

Latif, M., K. Sperber, J. Arblaster, P. Braconnot, D. Chen, A. Colman, U. Cubasch, C. Cooper, P. Delecluse, D. DeWitt *et al.* (2001) ENSIP: The El Niño simulation intercomparison project. *Climate Dynamics*, **18**, 255–276.

Laskar, J. (1999) The limits of Earth orbital calculations for geological time-scale use. *Philosophical Transactions of the Royal Society of London, A*, **357**, 1735–1759.

Laskar, J., F. Jouzel and F. Boudin (1993) Orbital, precessional, and insolation quantities for the Earth from −20 Myr to +10 Myr. *Astronnomy and Astrophysics*, **270**, 522–533.

Lau, K.-H. and N.-C. Lau (1990) Observed structure and propagation characteristics of tropical summertime disturbances. *Monthly Weather Review*, **118**, 1888–1913.

Lau, K.-M. and W. Bua (1998) Mechanism of monsoon–southern oscillation coupling: Insights from GCM experiments. *Climate Dynamics*, **14**, 759–779.

Lau, K. M. and P. H. Chan (1983) Short-term climate variability and atmospheric teleconnections from satellite-observed outgoing longwave radiation. Part II: Lagged correlations. *J. Atmos. Sci.*, **40**, 2751–2767.

Lau, K.-M. and P. H. Chan (1986) Aspects of the 40–50 day oscillation during the northern summer as inferred from outgoing longwave radiation. *Monthly Weather Review*, **114**, 1354–1367.

Lau, K.-M. and P. H. Chan (1988) Intraseasonal and interannual variations of tropical convection: A possible link between the 40–50 day oscillation and ENSO. *J. Atmos. Sci.*, **45**, 506–521.

Lau, K. M. and C.-P. Chang (1987) Planetary scale aspects of winter monsoon and teleconnections. In: C.-P. Chang and T. N. Krishnamurti (eds), *Monsoon Meteorology*. Oxford University Press, New York, pp. 161–202.

Lau, K.-M. and F. C. Chang (1992) Tropical intraseasonal oscillation and its prediction by the NMC operational model. *J. Climate*, **5**, 1365–1378.

Lau, K.-M. and M.-T. Li (1984) The monsoon of East-Asia: A survey. *Bull. Amer. Meteorol. Soc.*, **65**, 114–125.

Lau, K.-M. and L. Peng (1987) Origin of low-frequency (intraseasonal) oscillations in the tropical atmosphere. 1: Basic theory. *J. Atmos. Sci.*, **44**, 950–972.

Lau, K.-M. and L. Peng (1990) Origin of low frequency (intraseasonal) oscillations in the tropical atmosphere. Part III: Monsoon dynamics. *J. Atmos. Sci.*, **47**, 1443–1462.

Lau, K.-M. and L. Peng (1992) Dynamics of atmospheric teleconnection during northern summer. *J. Atmos. Sci.*, **5**, 140–158.

Lau, K.-M. and T. J. Phillips (1986) Coherent fluctuations of extratropical geopotential height and tropical convection in intraseasonal time scales. *J. Atmos. Sci.*, **43**, 1164–1181.

Lau, K.-M. and S. H. Shen (1988) On the dynamics of intraseasonal oscillations and ENSO. *J. Atmos. Sci.*, **45**, 1781–1797.

Lau, K.-M. and P.-J. Sheu (1988) Annual cycle, quasi-biennial oscillation, and Southern Oscillation in global precipitation. *J. Geophys. Res.*, **93**, 10975–10988.

Lau, K.-M. and C. H. Sui (1997) Mechanisms of short-term sea surface temperature regulation: Observations during TOGA COARE. *J. Climate*, **10**, 465–472.

Lau, K.-M. and S. Yang (1996a) Seasonal variation, abrupt transition, and intraseasonal variability associated with the Asian summer monsoon in the GLA GCM. *J. Climate*, **9**, 965–985.

Lau, K.-M. and S. Yang (1996b) The Asian monsoon and predictability of the tropical ocean–atmosphere system. *Quart. J. Roy. Meteorol. Soc.*, **122**, 945–957.

Lau, K.-M. and S. Yang (1997) Climatology and interannual variability of the southeast Asian summer monsoon. *Adv. Atmos. Sci.*, **14**, 141–162.

Lau, K. M. and H. Weng (1995) Climate signal detection using wavelet transform: How to make a time series sing. *Bull. Am. Meteorol. Soc.*, **76**, 2391–2402.

Lau, K.-M. and H. Weng (2001) Coherent modes of global SST and summer rainfall over China: An assessment of the regional impacts of the 1997–1998 El Niño. *J. Climate*, **14**, 1294–1308.

Lau, K.-M. and H. Weng (2002) Recurrent teleconnection patterns linking summertime precipitation variability over East Asia and North America. *J. Meteorol. Soc. Japan*, **80**, 1309–1324.

Lau, K.-M. and H.-T. Wu (2001) Principal modes of rainfall–SST variability of the Asian summer monsoon: A reassessment of the monsoon–ENSO relationship. *J. Climate*, **14**, 2880–2895.

Lau, K.-M., C. P. Chang and P. H. Chan (1982) Short-term planetary scale interactions over the tropics and midlatitudes. Part I: Contrast between active and inactive periods. *Monthly Weather Review*, **110**, 933–946.

Lau, K.-M., G. J. Yang and S. H. Shen (1988) Seasonal and intraseasonal climatology of summer monsoon rainfall over East Asia. *Monthly Weather Review*, **116**, 18–37.

Lau, K.-M., T. Nakazawa and C. H. Sui (1991) Observations of cloud cluster hierarchies over the tropical western Pacific. *J. Geophys. Res.–Oceans*, **96**, 3197–3208.

Lau, K.-M., H.-T. Wu and S. Yang (1998) Hydrologic processes associated with the first transition of the Asian summer monsoon: A pilot satellite study. *Bull. Amer. Meteorol. Soc.*, **79**, 1871–1882.

Lau, K.-M., K.-M. Kim and S. Yang (2000a) Dynamical and boundary forcing characteristics of regional components of the Asian summer monsoon. *J. Climate*, **13**, 2461–2482.

Lau, K.-M., Y. H. Ding, J. T. Wang, R. Johnson, T. Keenan, R. Cifelli, J. Gerlach, O. Thiele, T. Rickenbach, S. C. Tsay *et al.* (2000b) A report of the field operations and early results of the South China Sea Monsoon Experiment (SCSMEX). *Bull. Amer. Meteorol. Soc.*, **81**, 1261–1270.

Lau, K.-M., J.-Y. Lee, K.-M. Kim and I.-S. Kang (2004) The North Pacific as a regulator of summertime climate over Eurasia and North America. *J. Climate*, **17**, 819–833.

Lau, K.-M., K.-M. Kim and J.-Y. Lee (2005) Interannual variability, global teleconnection, and potential predictability associated with the Asian summer monsoon. In: C.-P. Chang (ed.), *East Asian Monsoon*. World Scientific, Beijing. [In press.]

Lau, N.-C. (1985) Modeling the seasonal dependence of the atmospheric response to observed El Niño in 1962–1976. *Monthly Weather Review*, **113**, 1970–1996.

Lau, N.-C. and M. J. Nath (2000) Impact of ENSO on the variability of the Asian–Australian monsoons as simulated in GCM experiments. *J. Climate*, **13**, 4287–4309.

Lau, N.-C. and M. J. Nath (2003) Atmosphere–ocean variations in the Indo-Pacific sector during ENSO episodes. *J. Climate*, **16**, 3–20.

Lau, N.-C. and K. M. Lau (1986) The structure and propagation of intraseasonal oscillations appearing in a GFDL general-circulation model. *J. Atmos. Sci.*, **43**, 2023–2047.

Lau, N.-C. and M. J. Nath (2005) ENSO moodulation of the interannual and intraseasonal variability of the East Asian Monsoon: A model study. [Submitted to *J. Climate*.]

Lau, N.-C. and B. Wang (2005) Interactions between the Asian Monsoon and the El Niño–Southern Oscillation. [Chapter 12 of this book.]

Lau, N.-C., I. M. Held and J. D. Neelin (1988) The Madden–Julian Oscillation in an idealized general-circulation model. *J. Atmos. Sci.*, **45**, 3810–3832.

Lau, N.-C., M. J. Nath and H. Wang (2004) Simulations by a GFDL GCM of ENSO-related variability of the coupled atmosphere–ocean system in the East Asian Monsoon region. In: C.-P. Chang (ed.), *East Asian Monsoon*. World Scientific Series on Meteorology of East Asia No. 2. World Scientific, Singapore, pp. 271–300.

Lau, W. K. M. (2005) ENSO connections. In: W. K. M. Lau and D. E. Waliser (eds), *Intraseasonal Variability of the Atmosphere–Ocean Climate System*. Springer-Verlag, Heidelberg, Germany.

Lau, W. K. M. and D. E. Waliser (eds) (2005) *Intraseasonal Variability of the Atmosphere-Ocean Climate System*. Springer, Heidelberg, Germany, 474pp.

Lavery, B., G. Joung and N. Nicholls (1997) An extended high-quality historical rainfall data set for Australia. *Aust. Meteorol. Mag.*, **46**, 27–38.

Lawrence, D. M. and P. J. Webster (2001) Interannual variability of intraseasonal convection and the Asian monsoon. *J. Climate*, **14**, 2910–2922.

Lawrence, D. M. and P. J. Webster (2002) The boreal summer intraseasonal oscillation: Relationship between northward and eastward movement of convection. *J. Atmos. Sci.*, **59**, 1593–1606.

Leary, C. A. and R. A. Houze (1979) The structure and evolution of convection in a tropical cloud cluster. *J. Atmos. Sci.*, **36**, 437–457.

Lean, J., J. Beer and R. Bradley (1995) Reconstruction of solar irradiance since 1610: Implications for climatic change. *Geophys. Res. Lett.*, **22**, 3195–3198.

Lee, M. I., I. S. Kang, J. K. Kim and B. E. Mapes (2001) Influence of cloud–radiation interaction on simulating tropical intraseasonal oscillation with an atmospheric general circulation model. *J. Geophys. Res.–Atmos.*, **106**, 14219–14233.

Lee, M. I., I. S. Kang and B. E. Mapes (2003) Impacts of cumulus convection parameterization on aqua-planet AGCM simulations of tropical intraseasonal variability. *J. Meteorol. Soc. Japan*, **81**, 963–992.

Leetmaa, A. (1973) Response of the Somali Current at 2 degrees to southwest monsoon of 1971. *Deep-Sea Res.*, **20**, 397–400.

LeMone, M. A. (1983) Momentum transport by a line of cumulonimbus. *J. Atmos. Sci.*, **40**, 1815–1834.

LeMone, M. A., E. J. Zipser and S. B. Trier (1998) The role of environmental shear and thermodynamic conditions in determining the structure and evolution of mesoscale convective systems during TOGA COARE. *J. Atmos. Sci.*, **55**, 3493–3518.

Leuschner, D. C. and F. Sirocko (2000) The low-latitude monsoon climate during Dansgaard–Oeschger cycles and Heinrich Events. *Quaternary Science Reviews*, **19**, 243–254.

Levitus, S. (1986) Annual cycle of salinity and salt storage in the world ocean. *J. Phys. Oceanogr.*, **16**, 322–343.

Levitus, S. (1987) Meridional Ekman heat fluxes for the world ocean and individual ocean basins, *J. Phys. Oceanogr.*, **17**, 1484–1492.

Li, C. (1990) Interaction between anomalous winter monsoon in East Asia and El Niño events. *Adv. Atmos. Sci.*, **7**, 36–46.

Li, C. (1996) A further study on interaction between anomalous winter monsoon in East Asia and El Niño. *Acta Meteorol. Sinica*, **10**, 309–320.

Li, C. and Y. Ding (1989) A diagnostic study of an explosively deepening oceanic cyclone over the northwest Pacific Ocean. *Acta Meteorol. Sinica*, **47**, 180–190. [In Chinese with English abstract.]

Li, C. and G. Li (2000) The NAO/NPO and interdecadal climate variation in China. *Adv. Atmos. Sci.*, **17**, 551–561.

Li, C. and Z. Long (2002) Intraseasonal oscillation anomalies in the tropical atmosphere and El Niño events. *CLIVAR Exchanges*, **7**, No. 2, 12–15.

Li, C. Y. and P. Xian (2003) Interdecadal variation of SST in the North Pacific and anomalies of atmospheric circulation and climate. *Climatic and Environmental Research*, **8**, 258–273.

Li, C. and M. Yanai (1996) The onset and interannual variability of the Asian summer monsoon in relation to land–sea thermal contrast. *J. Climate*, **9**, 358–375.

Li, F. and Y. H. Ding (2004) A statistical study of blocking highs in Eurasia in summer by using 30-yr NCEP datasets. [To be published in *Acta Meteorologica Sinica*.]

Li, Guoqing *et al.* (1976) Modeling the formation of vortex over the southeastern flank of Tibetan Plateau. *Sci. Sinica*, 286-294. [In Chinese.]

Li, J. and Q. Zeng (2003) A new monsoon index and the geographical distribution of the global monsoons. *Adv. Atmos. Sci.*, **20**, 299–302.

Li, J., Y.-L. Chen and W.-C. Lee (1997) Analysis of a heavy rainfall event during TAMEX. *Monthly Weather Review*, **125**, 1060–1082.

Li, Q., S. Yang, V. E. Kousky, R. W. Higgins, K.-M. Lau and P. Xie (2005) Features of cross-Pacific climate shown in the variability of China and United States precipitation. *Int. J. Climatol.* [In press.]

Li, T. and S. G. H. Philander (1996) On the annual cycle of the eastern equatorial Pacific. *J. Climate*, **9**, 2986–2998.

Li, T. M. and B. Wang (1994) The influence of sea-surface temperature on the tropical intraseasonal oscillation: A numerical study. *Monthly Weather Review*, **122**, 2349–2362.

Li, T. and Y. Zhang (2002) Processes that determine the quasi-biennial and lower-frequency variability of the South Asian monsoon. *J. Meteorol. Soc. Japan*, **80**, 1149–1163.

Li, T., Y. Zhang, C.-P. Chang and B. Wang (2001a) On the relationship between Indian Ocean SST and Asian summer monsoon. *Geophys. Res. Lett.*, **28**, 2843–2846.

Li, T., C.-W. Tham and C.-P. Chang (2001b) A coupled air–sea–monsoon oscillator for the tropospheric biennial oscillation. *J. Climate*, **14**, 752–764.

Li, T., B. Wang and C.-P. Chang (2001c) Theories on the tropospheric biennial oscillation: A review. In: B. Wang (ed.), *Dynamics of Atmospheric and Oceanic Circulations and Climate*. China Meteorological Press, Beijing, pp. 252–276.

Li, T., B. Wang, C.-P. Chang and Y. Zhang (2003) A theory for the Indian Ocean dipole-zonal mode. *J. Atmos. Sci.*, **60**, 2119–2135.

Li, T., C. Zhou, X. Jiang, C.-P. Chang and B. Wang (2004) Effect of the annual cycle of SST on Asian–Australian monsoon intensity and phase transition. *Joint AOGS 1st Annual Meeting and 2nd APHW Conference, Singapore, July 2004*, Abstracts, Vol. I, pp. 552–553.

Liang. P. D (1990) Relation between the El Niño–Indian summer monsoon in summer rainfall in Northern China. *Marine Forecast*, **7**, 17–23.

Liao, Y. F., X. D. Yu and Q. Guo (2003) A case study of a series of severe convective storms based on China new generation (Doppler) weather rader data. *J. Appl. Meteorol.*, **14**, 656–661.

Liebmann, B. and C. A. Smith (1996) Description of a complete (interpolated) outgoing longwave radiation dataset. *Bull. Amer. Meteorol. Soc.*, **77**, 1275–1277.

Liebmann, B. and D. L. Hartmann (1984) An observational study of tropical midlatitude interaction on intraseasonal time scales during winter. *J. Atmos. Sci.*, **41**, 3333–3350.

Liebmann, B., H. H. Hendon and J. D. Glick (1994) The relationship between tropical cyclones of the Western Pacific and Indian Oceans and the Madden–Julian Oscillation. *J. Meteorol. Soc. Japan*, **72**, 401–412.

Liberti, G. L., F. Chéruy and M. Desbois (2001) Land effect on the diurnal cycle of clouds over the TOGA COARE area, as observed from GMS IR data. *Monthly Weather Review*, **129**, 1500–1517.

Liess, S. and L. Bengtsson (2003) The intraseasonal oscillation in ECHAM4. Part II: Sensitivity studies. *Climate Dynamics*. [Submitted.]

Liess, S., L. Bengtsson and K. Arpe (2003) The intraseasonal oscillation in ECHAM4. Part I: AGCM/CGCM standard version. *Climate Dynamics*. [In press.]

Liess, S., D. E. Waliser and S. Schubert (2004) Predictability studies of the intraseasonal oscillation with the ECHAM5 GCM. *J. Atmos. Sci.* [Submitted.]

Lighthill, M. J. (1969) Dynamic response of the Indian Ocean to the onset of the southwest monsoon. *Phil. Trans. Roy. Meteorol. Soc. Series A*, **265**, 45–92.

Lim, H. and C.-P. Chang (1981) A theory for midlatitude forcing of tropical motions during winter monsoon. *J. Atmos. Sci.*, **38**, 2377–2392.

Lim, H. and C. P. Chang (1986) Generation of internal- and external-mode motions from internal heating: Effects of vertical shear and damping. *J. Atmos. Sci.*, **43**, 948–960.

Lim, H., T. K. Lim and C. P. Chang (1990) Reexamination of wave–CISK theory: Existence and properties of nonlinear wave–CISK modes. *J. Atmos. Sci.*, **47**, 3078–3091.

Lin, E. L. and S. S. Wu (1998) Activity of cold waves in Guangdong province for recent 40 years. *J. Tropical Meteorol.*, **14**, 337–343.

Lin, J.-L. and B. E. Mapes (2004) Radiation budget of the tropical intraseasonal oscillation. *J. Atmos. Sci.*, **61**, 2050–2062.

Lin, J. W. B., J. D. Neelin and N. Zeng (2000) Maintenance of tropical intraseasonal variability: Impact of evaporation–wind feedback and midlatitude storms. *J. Atmos. Sci.*, **57**, 2793–2823.

Lin, J., B. E. Mapes, M. Zhang and M. Newman (2004) Stratiform precipitation, vertical heating profiles, and the Madden–Julian Oscillation. *J. Atmos. Sci.*, **61**, 296–309.

Lin, X. and R. H. Johnson (1996a) Heating, moistening and rainfall over the western Pacific warm pool during TOGA COARE. *J. Atmos. Sci.*, **53**, 3367–3383.

Lin, X. and R. H. Johnson (1996b) Kinematic and thermodynamic characteristics of the flow over the western Pacific warm pool during TOGA COARE. *J. Atmos. Sci.*, **53**, 695–715.

Lindzen, R. S. (1974a) Wave–CISK and tropical spectra. *J. Atmos. Sci.*, **31**, 1447–1449.

Lindzen, R. S. (1974b) Wave–CISK in tropics. *J. Atmos. Sci.*, **31**, 156–179.

Lindzen, R. S. and A. Y. Ho (1988) Hadley circulations for zonally averaged heating centered off the equator. *J. Atmos. Sci.*, **45**, 2416–2427.

Lindzen, R. S. and S. Nigam (1987) On the role of the sea surface temperature gradients in forcing low-level winds and convergence in the tropics. *J. Atmos. Sci*, **45**, 2440–2458.

Liou, K.-N. and X. Zhou (eds) (1987) Atmospheric radiation: Progress and prospects. *Proceedings of the Beijing International Radiation Symposium, Beijing, 26–30 August, 1986*. Science Press, Beijing, and American Meteorological Society, 699pp.

Liu, H. and G.-X. Wu (1997) Impacts of land surface on climate of July and onset of summer monsoon: A study with an AGCM plus SSiB. *Adv. Atmos. Sci.*, **14**(3), 289–308.

Liu, T. F. (1990) An assessment of cold waves in China. *Meteorological Monthly*, **16**, 40–43.

Liu, T., Z. Ding and N. Rutter (1999) Comparison of Milankovitch periods between continental loess and deep sea records over the last 2.5 Ma. *Quaternary Science Reviews*, **18**, 1205–1212.

Liu, X. and B. Chen (2000) Climatic warming in the Tibetan Plateau during recent decades. *Int. J. Climatol.*, **20**, 1729–1742.

Liu, X. and M. Yanai (2002) Influence of Eurasian spring snow cover on Asian summer rainfall. *Int. J. Climatol.*, **22**, 1075–1089.

Liu, X. and Z.-Y. Yin (2002) Sensitivity of East Asian monsoon climate to the uplift of the Tibetan Plateau. *Paleogeography, Paleoclimatology, Paleoecology*, **183**, 223–245.

Liu, Xin, G. X. Wu, Weiping Li and Yimin Liu (2001) Thermal adaptation of the large-scale circulation to the summer heating over the Tibetan Plateau. *Progress in Natural Science*, **11**(2), 1–7.

Liu, Xin, Li Weiping and G. X. Wu (2002) Interannual variations of the diabatic heating over the Tibetan Plateau and the northern hemispheric circulation in summer. *Acta Meteorol. Sinica*, **60**(3), 267–277.

Liu, Y. M., G. X. Wu, H. Liu and P. Liu (2001) Dynamical effects of condensation heating on the subtropical anticyclones in the Eastern Hemisphere. *Climate Dyn.*, **17**, 327–338.

Liu, Y. J., Y. H. Ding and J. H. He (2003) A study of a typical Meiyu front. *Acta Meteorol. Sinica*, **61**, 291–301.

Liu, Y. Q. and Y. H. Ding (1995) Reappraisal of the relationship between El Niño events and climate in China. *Acta Atmos. Sinica*, **19**, 200–208.

Liu, Yimin, G. X. Wu, and H. Liu (1999) The effect of spatially non-uniform heating on the formation and variation of subtropical high. III: Latent heating and the South Asia High and the West Pacific Subtropical High. *Acta Meteorol. Sinica*, **57**(5), 525–538.

Liu, Yimin, G. X. Wu, H. Liu and P. Liu (2001) Condensation heating of the Asian summer monsoon and the subtropical anticyclone in the Eastern Hemisphere. *Climate Dynamics*, **17**, 327–338.

Liu, Yimin, J. C. L. Chan, Jiangyu Mao and G. X. Wu (2002) The role of Bay of Bengal convection in the onset of the 1998 South China Sea summer monsoon. *Monthly Weather Review*, **130**, 2731–2744.

Liu, Yimin, G. X. Wu and Ren, Rongcai (2004) Relationship between the subtropical anticyclone and diabatic heating. *J. Climate*, **17**, 682–698.

Liu, Z., B. Otto-Bleisner, J. Kutzbach and C. Shields (2003) Coupled climate simulation of the evolution of global monsoons in the Holocene. *J. Climate*, **16**, 2472–2490.

Liu, Z., S. Harrison, J. Kutzbach and B. Otto-Bleisner (2004) Global monsoons in the mid-Holocene and oceanic feedback. *Climate Dynamics*, **22**, 157–182.

Lo, F. and H. H. Hendon (2000) Empirical extended-range prediction of the Madden–Julian oscillation. *Monthly Weather Review*, **128**, 2528–2543.

Lorenc, A. C. (1984) The evolution of planetary-scale 200-Mb divergent flow during the Fgge year. *Quart J. Roy. Meteorol. Soc.*, **110**, 427–441.

Lorenz, E. N. (1965) A study of the predictability of a 28-variable atmospheric model. *Tellus*, **17**, 321–333.

Lorenz, E. N. (1967) *The Nature and Theory of the General Circulation of the Atmosphere* (Tech. Doc. 218). World Meteorological Organization, Beijing, 161pp.

Loschnigg, J. and P. J. Webster (2000) A coupled ocean–atmosphere system of SST regulation for the Indian Ocean. *J. Climate*, **13**, 3342–3360.

Loschnigg, J., G. A. Meehl, P. J. Webster, J. M. Arblaster and G. P. Compo (2003) The Asian monsoon, the tropospheric biennial oscillation, and the Indian Ocean zonal mode in the NCAR GCM. *J. Climate*, **16**, 1617–1642.

Louis, J. F. (1979) A parametric model of vertical eddy fluxes in the atmosphere. *Boundary Layer Meteorology*, **17**, 187–202.

Love, G. (1985) Cross-equatorial influence of winter hemisphere subtropical cold surges. *Monthly Weather Review*, **113**, 1487–1498.

Lu, M.-M. (2005) *An Experimental Monthly Report on Southeast Asia Climate Analysis, January 2005* (Climate Program Report). Central Weather Bureau, Taipei, Taiwan.

Lu, R., J.-H. Oh and B.-J. Kim (2002) A teleconnection pattern in upper-level meridional wind over the North African and Eurasian continent in summer. *Tellus*, **54**, 44–55.

Lu, W. and Q. Zhu (1991) Theoretical research on the cold surge of the Qinghai–Xizang plateau as a huge orography. *Acta Meteorol. Sinica*, **49**, 385–393.

Ludlam, F. H. (1980) *Clouds and Storms*. Pennsylvania State University Press, 405pp.

Lukas, R. and E. Lindstrom (1991) The mixed layer of the western equatorial Pacific Ocean. *J. Geophys. Res.*, **96**, 3343–3357.

Lukas, R., S. P. Hayes and K. Wyrtki (1984) Equatorial sea level response during the 1981–1983 El Niño. *J. Geophys. Res.*, **89**, 10425–10430.

Lum, C. Y. (1976) *500 mb Troughs Passing over Lake Baikal and the Arrival of Surges at Hong Kong* (Tech. Note 31). Royal Observatory, Hong Kong, 22pp.

Luo, H. and M. Yanai (1983) The large-scale circulation and heat sources over the Tibetan Plateau and surrounding areas during the early summer of 1979. Part I: Precipitation and kinematic analyses. *Monthly Weather Review*, **111**, 922–944.

Luo, H. and M. Yanai (1984) The large-scale circulation and heat sources over the Tibetan Plateau and surrounding areas during the early summer of 1979. Part II: Heat and moisture budgets. *Monthly Weather Review*, **112**, 966–989.

Luo, S. W., Z. A. Qian and Q. Q. Wang (1982) The study for 100 mb South Asian High and its association with climate of East China. *Plateau Meteorology*, **1**(2), 1–10. [In Chinese.]

Luyten, J. R. and J. C. Swallow (1976) Equatorial undercurrents. *Deep-Sea Res.*, **10**, 999–1001.

Ma, C. C., C. R. Mechoso, A. W. Robertson and A. Arakawa (1996) Peruvian stratus clouds and the tropical Pacific circulation: A coupled ocean–atmosphere GCM study. *J. Climate*, **9**, 1635–1645.

Ma, H. N. (1980) Subsynoptic omega system and the region of occurrence of rainstorms. *Selected Papers on Rainstorms*. Jilin People's Press, Changchun, pp. 171–178.

Ma, Y., H. Ishikawa, O. Tsukamoto, M. Menenti, Z. Su, T. Yao, T. Koike and T. Yasunari (2003) Regionalization of surface fluxes over heterogeneous landscape of the Tibetan Plateau by using satellite remote sensing data. *J. Meteorol. Soc. Japan*, **81**, 277–293.

Madala, R. V., S. W. Chang, U. C. Mohanty, S. C. Madan, R. K. Paliwal, V. B. Sarin, T. Holt and S. Raman (1987) *Description of Naval Research Laboratory Limited Area Dynamical Weather Prediction Model* (NRL Tech. Rep. 5992). Naval Research Laboratory, Washington, DC, 131 pp. [Available from Naval Research Laboratory, Washington, DC 20375.]

Madden, R. A. (1994) Observations of the 40–50-day tropical oscillation: A review. *Monthly Weather Review*, **122**, 814–837.

Madden, R. A. and P. R. Julian (1971) Detection of a 40–50 day oscillation in the zonal wind in the tropical Pacific. *J. Atmos. Sci.*, **28**, 702–708.

Madden, R. A. and P. R. Julian (1972) Description of large-scale circulations cells in the tropics with a 40–50 day period, *J. Atmos. Sci.*, **29**, 1109–1123.

Madden, R. A. and P. R. Julian (2005) Historical perspective. In: W. K. M. Lau and D. E. Waliser (eds), *Intraseasonal Variability of the Atmosphere–Ocean Climate System*. Springer, Heidelberg, Germany, 474pp.

Maddox, R. A. (1980) Mesoscale convective complexes. *Bull. Amer. Meteorol. Soc.*, **61**, 1374–1387.

Maddox, R. A. (1983) Large-scale meteorological conditions associated with mid-latitude, mesoscale convective complexes. *Monthly Weather Review*, **111**, 1475–1493.

Mahfouf, J.-F., A. O. Manzi, J. Noilhan, H. Giordani and M. Deque (1995) The land surface scheme ISBA within the Meteo-France climate model ARPEGE. Part I: Implementation and preliminary results. *J. Climate*, **8**, 2039–2057.

Mahfouf, J.-F., C. Ciret, A. Ducharne, P. Iranejad, J. Noilhan, Y. Shao, P. Thornton, Y. Xue and Z.-L. Yang (1996) Analysis of transpiration results from the RICE and PILPS workshop. *Glob. and Planet. Change*, **13**, 73–88.

Mahrt, L. (1976) Mixed layer moisture structure. *Monthly Weather Review*, **104**, 1403–1407.

Mahrt, L. (1991) Boundary-layer moisture regimes. *Quart. J. Roy. Meteorol. Soc.*, **117**, 151–176.

Mak, M. K. (1975) The monsoonal mid-tropospheric cyclogenesis. *J. Atmos. Sci.*, **32**, 2246–2253.

Maloney, E. D. (2002) An intraseasonal oscillation composite life cycle in the NCAR CCM3.6 with modified convection. *J. Climate*, **15**, 964–982.

Maloney, E. D. and M. J. Dickinson (2003) The intraseasonal oscillation and the energetics of summertime tropical western North Pacific synoptic-scale disturbances. *J. Atmos. Sci.*, **60**, 2153–2168.

Maloney, E. D. and D. L. Hartmann (1998) Frictional moisture convergence in a composite life cycle of the Madden–Julian oscillation. *J. Climate*, **11**, 2387–2403.

Maloney, E. D. and D. L. Hartmann (2000a) Modulation of eastern North Pacific hurricanes by the Madden–Julian oscillation. *J. Climate*, **13**, 1451–1460.

Maloney, E. D. and D. L. Hartmann (2000b) Modulation of hurricane activity in the Gulf of Mexico by the Madden–Julian oscillation. *Science*, **287**, 2002–2004.

Maloney, E. D. and D. L. Hartmann (2001) The sensitivity of intraseasonal variability in the NCAR CCM3 to changes in convective parameterization. *J. Climate*, **14**, 2015–2034.

Maloney, E. D. and J. T. Kiehl (2002) Intraseasonal eastern Pacific precipitation and SST variations in a GCM coupled to a slab ocean model. *J. Climate*, **15**, 2989–3007.

Maloney, E. D. and A. H. Sobel (2004) Surface fluxes and ocean coupling in the tropical intraseasonal oscillation. *J. Climate*, **17**, 4368–4386.

Manabe, S. J. (1969) Climate and the ocean circulation. I: The atmospheric circulation and the hydrology of the earth's climate. *Monthly Weather Review*, **97**, 739–774.

Manabe, S. J. and A. J. Broccoli (1990) Mountains and arid climate of middle latitude. *Science*, **247**, 192–195.

Manabe, S. J. and T. B. Terpstra (1974) The effects of mountains on the general circulation of the atmosphere as identified by numerical experiments. *J. Atmos. Sci.*, **31**, No. 1, 3–42.

Manabe, S. J., J. S. Smagorinsky and R. F. Stricker (1965) Simulated climatology of a general circulation model with a hydrological cycle. *Monthly Weather Review*, **93**, 769–798.

Mandal, G. S. (1991) *Tropical Cyclones and Their Forecasting and Warning Systems in the North Indian Ocean* (WMO Report No. TCP 28). World Meteorological Organization, Geneva.

Mandal, J. C., S. R. Kalsi, S. R. Veeraraghavan and S. R. Haldar (1990) On some aspect of severe cyclonic storm in the Bay of Bengal. *Mausam*, **41**, 385–392.

Mao, Jiangyu, G. X. Wu and Yimin Liu (2002a) Study on modal variation of subtropical high and its mechanism during seasonal transition. Part I: Climatological features of subtropical high structure. *Acta Meteorol. Sinica*, **60**(4), 400–408.

Mao, Jiangyu, G. X. Wu and Yimin Liu (2002b) Study on modal variation of subtropical high and its mechanism during seasonal transition. Part II: Seasonal transition index over Asian monsoon region. *Acta Meteorol. Sinica*, **60**(4), 409–420.

Mapes, B. E. (1993) Gregarious tropical convection. *J. Atmos. Sci.*, **50**, 2026–2037.

Mapes, B. E. (1998) The large-scale part of tropical mesoscale convective system circulations: A linear vertical spectral band model. *J. Meteorol. Soc. Japan*, **76**, 29–55.

Mapes, B. E. (2000) Convective inhibition, subgrid-scale triggering energy, and stratiform instability in a toy tropical wave model. *J. Atmos. Sci.*, **57**, 1515–1535.

Mapes, B. E. and R. A. Houze Jr (1993) Cloud clusters and superclusters over the oceanic warm pool. *Monthly Weather Review*, **121**, 1398–1415.

Mapes, B. E. and R. A. Houze Jr (1995) Diabatic divergence profiles in western Pacific mesoscale convective systems. *J. Atmos. Sci.*, **52**, 1807–1828.

Mapes, B. E. and P. Zuidema (1996) Radiative–dynamical consequences of dry tongues in the tropical troposphere. *J. Atmos. Sci.*, **53**, 620–638.

Mapes, B. E., T. T. Warner and M. Xu (2003) Diurnal patterns of rainfall in northwestern South America. Part III: Diurnal gravity waves and nocturnal offshore convection. *Monthly Weather Review*, **131**, 830–844.

Mason, R. B. and C. E. Anderson, (1963) The development and decay of the 100 mb summertime anticyclone over Southern Asia. *Monthly Weather Review*, **91**, 3–12.

Mathews, R. B., M. J. Kropff, D. Bachelet (eds) (1995) *Modelling the Impact of Climate Change on Rice Production in Asia*. CAB International, Wallingford, UK.

Matsuno, T. (1966) Quasi-geostrophic motions in the equatorial area. *J. Meteorol. Soc. Japan*, **44**, 25–43.

Matsumoto, J. (1988) Large-scale features associated with the frontal zone over East Asia from late autumn to autumn. *J. Meteorol. Soc. Japan*, **66**, 565–579.

Matsumoto, J. (1990) Withdrawal of the Indian summer monsoon and its relation to the seasonal transition from summer to autumn over East Asia. *Mausam*, **41**, 196–202.

Matsumoto, J. (1992) The seasonal changes in Asian and Australian regions. *J. Meteorol. Soc. Japan*, **70**, 257–273.

Matsumoto J. (1997) Seasonal transition of summer rainy season over Indochina and adjacent monsoon region. *Adv. Atmos. Sci.*, **14**, 231–245.

Matsumoto, J. and T. Murakami (2000) Annual changes of tropical convective activities as revealed from equatorial symmetric OLR data. *J. Meteorol. Soc. Japan*, **78**, 543–561.

Matsumoto, J. and T. Murakami (2002) Seasonal migration of monsoon between the Northern and Southern Hemisphere as revealed from equatorially symmetric and asymmetric OLR data. *J. Meteorol. Soc. Japan*, **80**, 419–437.

Matthews, A. J. (2000) Propagation mechanisms for the Madden–Julian oscillation. *Quart. J. Roy. Meteorol. Soc.*, **126**, 2637–2651.

May, W. (2002) Simulated changes of the Indian summer monsoon under enhanced greenhouse gas conditions in a global time-slice experiment. *Geophys. Res. Lett.*, **29**(7), doi: 10.1029/2001GL013808.

May, W. (2004) Potential future changes in the Indian summer monsoon due to greenhouse warming: Analysis of mechanisms in a global time-slice experiment. *Climate Dynamics*, **22**, 389–414.

McBride, J. L. (1987) The Australian summer monsoon. In: C.-P. Chang and T. N. Krishnamurti (eds), *Monsoon Meteorology*. Oxford University Press, Oxford, UK, pp. 203–231.

McBride, J. L. (1995) Tropical cyclone formation. In: R. L. Elsberry (ed.), *Global Perspective on Tropical Cyclones* (Tech. Doc. 693) World Meteorological Organization, Geneva, pp. 63–105.

McBride, J. L. (1998) Indonesia, Papua New Guinea, and tropical Australia: The southern hemisphere summer monsoon. *Meteorology of the Southern Hemisphere* (Meteorol. Monogr. 49). American Meteorological Society, Boston, pp. 89–99.

McBride, J. L. and T. D. Keenan (1982) Climatology of tropical cyclone genesis in the Australian region. *J. Climatol.*, **2**, 13–33.

McBride, J. L. and N. Nicholls (1983) Seasonal relationships between Australian rainfall and the Southern Oscillation. *Monthly Weather Review*, **111**, 1998–2004.

McBride, J. L., M. R. Haylock and N. Nicholls (2003) Relationships between the maritime continent heat source and the El Niño–Southern Oscillation phenomenon. *J. Climate*, **16**, 2905–2914.

McCreary, J. P., P. K. Kundu and R. L. Molinari (1993) A numerical investigation of the dynamics, thermodynamics and mixed-layer processes in the Indian Ocean. *Progress in Oceanogr.*, **31**, 181–244.

McGarry, M. M. and R. J. Reed (1978) Diurnal variations in convective activity and precipitation during Phases II and III of GATE. *Monthly Weather Review*, **106**, 101–113.

McGuirk, J. P., A. H. Thompson and J. R. Schaefer (1988) An eastern Pacific tropical plume. *Monthly Weather Review*, **116**, 2505–2521.

McPhaden, M. J. and X. Yu (1999) Genesis and evolution of the 1997–1998 El Niño. *Science*, **283**, 950–954.

McPhaden, M. J., A. J. Busalacchi, R. Cheney, J.-R. Donguy, K. S. Gage, D. Halpern, M. Ji, P. Julian, G. Meyers, G. T. Mitchum, *et al.* (1998) The tropical Pacific Ocean–Global Atmosphere observing system: A decade of progress. *J. Geophys. Res.*, **103**, 14169–14240.

Mecikalski, J. R. and G. J. Tripoli (1998) Inertial available kinetic energy and the dynamics of tropical plume formation. *Monthly Weather Review*, **126**, 2200–2216.

Meehl, G. A. (1987) The annual cycle and interannual variability in the tropical Pacific and Indian Ocean region. *Monthly Weather Review*, **115**, 27–50.

Meehl, G. A. (1993) A coupled air–sea biennial mechanism in the tropical Indian and Pacific regions: Role of the ocean. *J. Climate*, **6**, 31–41.

Meehl, G. A. (1994a) Influence of the land surface in the Asian summer monsoon: External conditions versus internal feedbacks. *J. Climate*, **7**, 1033–1049.

Meehl, G. A. (1994b) Coupled land–ocean–atmosphere processes and south Asian monsoon variability. *Science*, **266**, 263–267.

Meehl, G. A. (1997) The south Asian monsoon and the tropospheric biennial oscillation. *J. Climate*, **10**, 1921–1943.

Meehl, G. A. and J. M. Arblaster (2002a) Indian monsoon GCM sensitivity experiments testing tropospheric biennial oscillation transition conditions. *J. Climate*, **15**, 923–942.

Meehl, G. A. and J. M. Arblaster (2002b) The tropospheric biennial oscillation and Asian–Australian monsoon rainfall. *J. Climate*, **15**, 722–744.

Meehl, G. A. and J. M. Arblaster (2003) Mechanisms for projected future changes in south Asian monsoon precipitation. *Climate Dynamics*, **21**, 659–675.

Meehl, G. A. and W. M. Washington (1993) South Asian summer monsoon variability in a model with doubled atmospheric carbon dioxide concentration. *Science*, **260**, 1101–1104.

Meehl, G. A. and W. M. Washington (1996) El Niño-like climate change in a model with increased atmospheric CO_2 concentrations. *Nature*, **382**, 56–60.

Meehl, G. A., W. M. Washington, D. J. Erickson III, B. P. Briegleb and P. J. Jaumann (1996a) Climate change from increased CO_2 and direct and indirect effects of sulfate aerosols. *Geophys. Res. Lett.*, **23**, 3755–3758.

Meehl, G. A., G. N. Kiladis, K. Weickmann, M. Wheeker, D. S. Gutzler and G. P. Compo (1996b) Modulation of equatorial subseasonal convective episodes by tropical–extratropical interaction in the Indian and Pacific Ocean regions. *J. Geophy. Res.*, **101**, 15033–15049.

Meehl, G. A., G. J. H. Boer, C. Covey, M. Latif and R. J. Stouffer (2000) The Coupled Model Intercomparison Project (CMIP). *Bull. Amer. Meteorol. Soc.*, **81**, 313–318.

Meehl, G. A., J. M. Arblaster and J. Loschnigg (2003) Coupled ocean–atmosphere dynamical processes in the tropical Indian and Pacific Oceans and the TBO. *J. Climate*, **16**, 2138–2158.

Mehta, A. V. and E. A. Smith (1997) Variability of radiative cooling during the Asian summer monsoon and its influence on intraseasonal waves. *J. Atmos. Sci.*, **54**, 941–966.

Mehta, V. M. and K. M. Lau (1997) Influence of solar irradiance on the Indian monsoon: ENSO relationship at decadal–multidecadal time scales. *Geophys. Res. Lett.*, **24**, 159–162.

Menon, S., J. Hansen, L. Nazarenko and Y. Luo (2002) Climate effects of black carbon aerosols in China and India. *Science*, **297**, 2250–2253.

Meyers, G. and S. Wijffels (2004) Indian Ocean Basin Report to GSOP. *First Meeting of the CLIVAR Global Synthesis and Observations Panel, NCAR, Boulder, Colorado, November*.

Michell, J. F. B. and T. C. Johns (1997) On modification of global warming by sulfate aerosols. *J. Climate*, **10**, 245–267.

Miller, D. and J. M. Fritch (1991) Mesoscale convective complexes in the western Pacific region. *Monthly Weather Review*, **119**, 2978–2992.

Miller, F. R and R. N. Keshvamurty (1968) *Structure of an Arabian Sea Summer Monsoon System* (IIOE Meteorological Monograph). East–West Centre Press, Hawaii.

Mitchell, J. F. B., T. C. Johns, J. M. Gregory and S. F. B. Tett (1995) Climate response to increasing levels of greenhouse gases and sulphate aerosols. *Nature*, **376**, 501–504.

Miyakoda, K., A. Navarra and M. N. Ward (1999) Tropical-wide teleconnection and oscillation. II: The ENSO–monsoon system. *Quart. J. Roy. Meteorol. Soc.*, **125**, 2937–2963.

Miyakoda, K., J. L. Kinter III and S. Yang (2003) The role of ENSO in the south Asian monsoon and pre-monsoon signals over the Tibetan Plateau. *J. Meteorol. Soc. Japan*, **81**, 1015–1039.

Mizuta, R., H. Yoshimura, K. Oouchi, J. Yoshimura, K. Katayama, A. Noda and Kyosei-4 Modeling Group (2004) Development of a super high-resolution global climate model on the Earth Simulator for the projection of global warming. *Proceedings of the International Conference on High-Impact Weather and Climate, March 22–24, Seoul, Korea*, pp. 240–243.

Mo, K. C. (2000) The association between intraseasonal oscillations and tropical storms in the Atlantic basin. *Monthly Weather Review*, **128**, 4097–4107.

Mo, K. C. (2001) Adaptive filtering and prediction of intraseasonal oscillations. *Monthly Weather Review*, **129**, 802–817.

Mohanty, U. C., S. K. Dube and M. P. Singh (1983) A study of the heat and moisture budgets over the Arabian Sea and their role in the maintenance of the summer monsoon, *J. Meteorol. Soc. Japan*, **61**, 208–221.

Mohanty, U. C., K. J. Ramesh and M. C. Pant (1996) Certain seasonal characteristic features of oceanic heat budget components over the Indian seas in relation to the summer monsoon activity over India. *Int. J. Climatol.*, **16**, 243–264.

Molion, L. C. B. (1987) On the dynamic climatology of the Amazon Basin and associated rain-producing mechanisms. In: R. Dickinson (ed.), *The Geophysiology of Amazonia: Vegetation and Climate Interactions*. Wiley Interscience, pp. 391–407.

Molnar, P., P. England and J. Martinod (1993) Mantle dynamics, uplift of the Tibetan Plateau, and the Indian monsoon. *Reviews of Geophysics, Washington, DC*, **31**, 357–396.

Molteni, F., S. Corti, L. Ferranti and J. M. Slingo (2003) Predictability experiments for the Asian summer monsoon: Impact of SST anomalies on interannual and intraseasonal variability. *J. Climate*, **16**, 4001–4021.

Moncrieff, M. W. (2004) Analytic representation of the large-scale organization of tropical convection. *J. Atmos. Sci.*, **61**, 1521–1538.

Moncrieff, M. W. and J. S. A. Green (1972) The propagation and transfer properties of steady convective overturning in shear. *Quart. J. Roy. Meteorol. Soc.*, **98**, 336–352.

Moncrieff, M. W. and E. Klinker (1997) Large mesoscale cloud systems in the tropical western Pacific as a process in general circulation models. *Quart. J. Roy. Meteorol. Soc.*, **123**, 805–827.

Montgomery, M. T. and J. Enagonio (1998) Tropical cyclogenesis via convectively forced vortex Rossby waves in a three-dimensional quasigeostrophic model. *J. Atmos. Sci.*, **55**, 3176–3207.

Mooley, D. A. (1957) The role of western disturbances in the prediction of weather over India during different seasons. *Ind. J. Meteorol. Geophys*, **8**, 253–260.

Mooley, D. A. and D. A. Paolino (1989) The response of the Indian monsoon associated with changes in SST over eastern and south equatorial Pacific. *Mausam*, **40**, 360–380.

Mooley, D. A. and B. Parthasarathy (1984) Fluctuation in all-India summer monsoon rainfall during 1871–1985. *Clim. Change*, **6**, 287–301.

Mooley, D. A. and J. Shukla (1989) Main features of the westward moving low pressure systems which form over the Indian region during the monsoon season and their relationship with the monsoon rainfall. *Mausam*, **40**, 137–152.

Mooley, D. A., B. Parthasarathy and G. B. Pant (1986) Relationship between Indian-summer monsoon rainfall and location of the ridge at the 500-Mb level along 75-degrees-E. *J. Clim. Appl. Meteorol.*, **25**, 633–640.

Moorthi, S. and M. J. Suarez (1992) Relaxed Arakawa–Schubert: A parameterization of moist convection for general circulation models. *Monthly Weather Review*, **120**, 978–1002.

Mori, S., J.-I. Hamada, Y. I. Tauhid, M. D. Yamanaka, N. Okamoto, F. Murata, N. Sakurai and T. Sribimawati (2004) Diurnal rainfall peak migrations around Sumatra Island: Indonesian maritime continent observed by TRMM satellite and intensive rawinsonde soundings. *Monthly Weather Review*, **132**, 2021–2039.

Morinaga, Y., M. Shinoda and T. Yasunari (1997) Relationships between spring snow cover over central Asia and Indian summer monsoon rainfall. *Proceedings of the Third USA/CIS Joint Conference on Environmental Hydrology and Hydrogeology*, pp. 245–250.

Morinaga, Y., K. Masuda, M. Nishimori and T. Yasunari (2000) Relationships between Eurasian snow cover and the Indian summer monsoon rainfall. *Proceedings of the International Conference on Climate Change and Variability: Past, Present and Future, Tokyo*, pp. 293–298.

Morita, T. and T. Masui (2000) Emission scenarios for climate change studies. *Tenki*, **47**, 696–701. [In Japanese.]

Morley, J. J. and L. E. Heusser (1997) Role of orbital forcing in east Asian monsoon climates during the last 350 kyr: Evidence from terrestrial and marine climate proxies from core RC14-99. *Paleoceanography*, **12**, 483–494.

Moskowitz, B. M. and C. S. Bretherton (2000) An analysis of frictional feedback on a moist equatorial Kelvin mode. *J. Atmos. Sci.*, **57**, 2188–2206.

Mowla, K. G. (1976) Relation between climatic fluctuations and rice production in Bangladesh. In: K. Takahashi and M. M. Yoshino (eds), *Cimate Change and Food Production*. University of Tokyo Press, pp. 137–146.

Mukherjee, A. K., D. K. Rakshit and A. K. Chandhury (1972) On the very high clouds around Calcutta. *Ind. J. Meteorol. Geophys*, **23**, 217–218.

Mulki, G. and A. K. Banerjee (1960) The mean upper wind circulation around monsoon depressions. *Ind. J. Meteorol. Geophys*, **17**, 8–14.

Murakami, M. (1983) Analysis of the deep convective activity over the western Pacific and Southeast Asia. Part 1: Diurnal cycle. *J. Meteorol. Soc. Japan*, **61**, 60–75.

Murakami, T. (1951) On the study of the change of the upper westerlies in the last stage of Baiu season (rainy season in Japan). *J. Meteorol. Soc. Japan*, **29**, 162–175.

Murakami, T. (1958) The sudden change of upper westerlies near the Tibetan Plateau at the beginning of summer season. *J. Meteorol. Soc. Japan*, **36**, 239–247.

Murakami, T. (1976a) Cloudiness fluctuations during the summer monsoon. *J. Meteorol. Soc. Japan*, **54**, 175–181.

Murakami, T. (1976b) Analysis of summer monsoon fluctuations over India. *J. Meteorol. Soc. Japan*, **54**, 15–31.

Murakami, T. (1977) Spectrum analysis relevant to Indian Monsoon. *Pure Appl. Geophys.*, **115**, 1145–1166.

Murakami, T. (1981a) Orographic influence of the Tibetan Plateau on the Asiatic winter monsoon circulation. Part I: Large-scale aspects. *J. Meteorol. Soc. Japan*, **59**, 40–65.

Murakami, T. (1981b) Orographic influence of the Tibetan Plateau on the Asiatic winter monsoon circulation. Part III: Sort-period oscillations. *J. Meteorol. Soc. Japan*, **59**, 173–200.

Murakami, T. (1983) Analysis of the deep convective activity over the western Pacific and Southeast Asia. Part 1: Diurnal cycle. *J. Meteorol. Soc. Japan*, **61**, 60–75.

Murakami, T. (1987a) Intraseasonal atmospheric teleconnection patterns during the northern hemisphere summer. *Monthly Weather Review*, **115**, 2133–2154.

Murakami, T. (1987b) Effects of the Tibetan Plateau. In: C.-P. Chang and T. Krishnamurti (eds), *Monsoon Meteorology*. Oxford University Press, New York, pp. 235–270.

Murakami, T. and Y. H. Ding (1982) Wind and temperature changes over Eurasia during the early summer of 1979. *J. Meteorol. Soc. Japan*, **60**, 183–196.

Murakami, T. and H. Nakamura (1983) Orographic effects on cold surges and lee-cyclogenesis as revealed by a numerical experiment. Part II: Transient aspects. *J. Meteorol. Soc. Japan*, **61**, 547–567.

Murakami, T. and T. Nakazawa (1985) Tropical 45 day oscillations during the 1979 northern hemisphere summer. *J. Atmos. Sci.*, **42**, 1107–1122.

Murakami, T., L.-X. Chen and A. Xie (1986) Relationship among seasonal cycles, low-frequency oscillations, and transient disturbances as revealed from outgoing longwave radiation data. *Monthly Weather Review*, **114**, 1456–1465.

Murray, D. W. and W. L. Prell (1991) Pliocene to Pleistocene variations in calcium carbonate, organic carbon, and opal on the Owen Ridge, northern Arabian Sea. In: W. L. Prell, N. Niitsuma et al. (eds), *Proceedings of the Ocean Drilling Program, Scientific Results* (Ocean Drilling Program). Texas A&M University, pp. 343–364,

Murray, D. W. and W. L. Prell (1992) Late Pliocene and Pleistocene climatic oscillations and monsoon upwelling recorded in sediments from the Owen Ridge, northwest Arabian Sea. In: C. P. Summerhayes, W. L. Prell and K. C. Emeis (eds), *Upwelling Systems: Evolution since the Early Miocene* (Special Publication #64). U.K. Geological Society, London, pp. 301–321.

Myers, D. and D. E. Waliser (2003) Three dimensional water vapor and cloud variations associated with the Madden–Julian oscillation during northern hemisphere winter. *J. Climate*, **16**, 929–950.

NA (1978) Fgge: Global weather experiment. *Meteorological Magazine*, **107**, 225–232.

Nagai, T., Y. Kitamur, M. Endoh and T. Tokioka (1995) Coupled atmosphere–ocean model simulations of El Niño/Southern Oscillation with and without an active Indian Ocean. *J. Climate*, **8**, 3–14.

Nagar, S. G., S. V. Singh and R. H. Kriplani (1992) Relationship between circulation and rainfall over India during the southwest monsoon. Part I: Surface pressure theory. *Appl. Climatol.*, **45**, 265–275.

Nair, N. M. (1999) Origins of rices. In: Y. P. Abrol and S. Gadgil (eds), *Rice in a Variable Climate*. APC Publications, New Delhi, pp. 1–10.

Nakajima, T. and M. Tanaka (1986) Matrix formulations for the transfer of solar radiation in a plane-parallel scattering atmosphere. *J. Quant. Spectrosc. Radiant. Transfer*, **35**, 13–21.

Nakamura, H. and T. Doutani (1985) Numerical study on the coastal Kelvin wave features about the cold surges around the Tibetan Plateau. *J. Meteorol. Soc. Japan*, **63**, 547–563.

Nakamura, H. and T. Murakami (1983) Orographic effects on cold surges and lee-cyclogenesis as revealed by a numerical experiment. Part I: Time mean aspects. *J. Meteorol. Soc. Japan*, **61**, 524–546.

Nakamura, H. and T. Yamagata (1999) Recent decadal SST variability in the northwestern Pacific and associated atmospheric anomalies. In: A. Navarra (ed.), *Beyond El Niño: Decadal and Interdecadal Climate Variability*. Springer, pp. 49–72.

Nakamura, H., T. Izumi and T. Sampe (2002) Interannual and decadal modulations recently observed in the Pacific storm track activity and east Asian winter monsoon. *J. Climate*, **15**, 1855–1874.

Nakazawa, T. (1986) Intraseasonal variations of OLR in the tropics during the FGGE year. *J. Meteorol. Soc. Japan*, **64**, 17–34.

Nakazawa, T. (1988) Tropical super clusters within intraseasonal variations over the western Pacific. *J. Meteorol. Soc. Japan*, **66**, 823–839.

Nakazawa, T. (1992) Seasonal phase lock of intraseasonal variation during the Asian summer monsoon. *J. Meteorol. Soc. Japan*, **70**, 257–273.

Nanjundiah, R. S., J. Srinivasan and S. Gadgil (1992) Intraseasonal variation of the Indian-summer monsoon. 2: Theoretical aspects. *J. Meteorol. Soc. Japan*, **70**, 529–550.

Navarra, A., M. N. Ward and K. Miyakoda (1999) Tropical-wide teleconnection and oscillation. I: Teleconnection indices and type I/type II states. *Quart. J. Roy. Meteorol. Soc.*, **125**, 2909–2935.

NCC (National Climate Center of China) (1998) *Heavy Flooding and Climate Anomalies in China in 1998*. China Meteorological Press, Beijing, 139 pp.

Neale, R. and J. Slingo (2003) The maritime continent and its role in the global climate: A GCM study. *J. Climate*, **16**, 834–848.

Neelin, J. D. (1988) An air–sea interaction model of intraseasonal oscillation in the tropics: Reply. *J. Atmos. Sci.*, **45**, 3526–3528.

Neelin, J. D. (1991) The slow sea surface temperature mode and the fast-wave limit: Analytic theory for tropical interannual oscillations and experiments in a hybrid coupled model. *J. Atmos. Sci.*, **48**, 584–606.

Neelin, J. D. and I. M. Held (1987) Modeling tropical convergence based on the moist static energy budget. *Monthly Weather Review*, **115**, 3–12.

Neelin, J. D. and J. Y. Yu (1994) Modes of tropical variability under convective adjustment and the Madden–Julian oscillation. 1: Analytical theory. *J. Atmos. Sci.*, **51**, 1876–1894.

Neelin, J. D., I. M. Held and K. H. Cook (1987) Evaporation–wind feedback and low-frequency variability in the tropical atmosphere. *J. Atmos. Sci.*, **44**, 2341–2348.

Neelin, J. D., D. S. Battisti, A. C. Hirst, F.-F. Jin, Y. Wakata, T. Yamagata and S. E. Zebiak (1998) ENSO theory. *J. Geophys. Res.*, **103**, 14261–14290.

Neff, U. J., S. J. Burns, A. Mangini, M. Mudelsee, D. Fleitmann and A. Matter (2001) Strong coherence between solar variability and the monsoon in Oman between 9 and 6 kyr ago. *Nature*, **411**, 290–293.

Neiman, P. J. and M. A. Shapiro (1993) The lifecycle of an extratropical marine cyclone. Part I: Frontal-cyclone evolution and thermodynamic air–sea interaction. *Monthly Weather Review*, **121**, 2153–2176.

Nesbitt, S. W. and E. J. Zipser (2003) The diurnal cycle of rainfall and convective intensity according to three years of TRMM measurements. *J. Climate*, **16**, 1456–1475.

Nesbitt, S. W., E. J. Zipser and D. J. Cecil (2000) A census of precipitation features in the Tropics using TRMM: Radar, ice scattering, and lightning observations. *J. Climate*, **13**, 4087–4106.

New, M. G., D. Lister, M. Hulme and I. Makin, (2002) A high-resolution data set of surface climate for terrestrial land areas. *Climate Research*, **21**, 1–25.

Newell, R. E., J. W. Kidson and D. G. Boer (1972) *The General Circulation of the Tropical Atmosphere and Interactions with Extratropical Latitudes* (Vol. 1). MIT Press, Cambridge, Massachusetts, 258pp.

Newman, M., P. D. Sardeshmukh, C. R. Winkler and J. S. Whitaker (2003) A study of subseasonal predictability. *Monthly Weather Review*, **131**, 1715–1732.

Newton, C. W. (1956) Mechanisms of circulation change during a lee cyclogenesis. *J. Meteorology*, **13**, 528–539.

Nichol, J. (1998) Smoke haze in Southeast Asia: A predictable recurrence. *Atmos. Environ*, **31**, 1209–1219.

Nicholls, M. E., R. A. Pielke Sr and W. R. Cotton (1991) Thermally forced gravity waves in an atmosphere at rest. *J. Atmos. Sci.*, **48**, 1869–1884.

Nicholls, N. (1978) Air–sea interaction and the quasi-biennial oscillation. *Monthly Weather Review*, **106**, 1505–1508.

Nicholls, N. (1981) Air–sea interaction and the possibility of long-range weather prediction in the Indonesian Archipelago. *Monthly Weather Review*, **109**, 2435–2443.

Nicholls, N. (1983) Air–sea interaction and the quasi-biennial oscillation. *Monthly Weather Review*, **106**, 1505–1508.

Nicholls, N. (1984) The Southern Oscillation and Indonesian sea surface temperature. *Monthly Weather Review*, **112**, 424–432.

Nicholls, N. (1985) Towards the prediction of major Australian droughts. *Int. J. Climatol.*, **5**, 553–560.

Nicholls, N. (1989) Sea surface temperatures and Australian winter rainfall. *J. Climate*, **2**, 965–973.

Nicholls, N., J. L. McBride and R. J. Ormerod (1982) On predicting the onset of the Australian wet season at Darwin. *Monthly Weather Review*, **110**, 14–17.

Nicholson, S. E. (1985) Sub-Saharan rainfall 1981–1984. *J. Clim. Appl. Meteorol.*, **24**, 1388–1391.

Nicholson, S. E. (1993) An overview of African rainfall fluctuations of the last decade. *J. Climate*, **6**, 1463–1466.

Nigam, S. (1994) On the dynamical basis for the Asian monsoon rainfall–El Niño relationship. *J. Climate*, **7**, 1750–1771.

Nigrini, C. and J. P. Caulet (1991) Composition and biostratigraphy of radiolarian assemblages from an area of upwelling (northwest Arabian Sea, Leg 117). In: W. L. Prell, N. Niitsuma and K. C. Emeis (eds.), *Proceedings of the Ocean Drilling Program*. College Station, Texas, pp. 89–126.

Ninomiya, K. (1989) Cloud distribution over east Asia during the Baiu period of 1979. *J. Meteorol. Soc. Japan*, **67**, 639–658.

Ninomiya, K. and T. Akiyama (1992) Multiscale feature of Baiu, the summer monsoon of Japan and the east Asia. *J. Meteorol. Soc. Japan*, **70**, 467–495.

Ninomiya, K. and C. Kobayashi (1999) Precipitation and moisture balance of the Asian summer monsoon in 1991: Part I, *J. Meteorol. Soc. Japan*, **76**, 855–877; Part II, **77**, 77–99.

Ninomiya, K. and H. Muraki (1986) Large-scale circulation over east Asia during Baiu period of 1979. *J. Meteorol. Soc. Japan*, **64**, 409–429.

Ninomiya, K. and T. Murakami (1987) The early summer rainy season (Baiu) over Japan. In: C.-P. Chang and T. N. Krishnamurti (eds), *Monsoon Meteorology*. Oxford University Press, pp. 93–121.

Ninomiya, K., T. Akiyama and M. Ikawa (1988a) Evolution and fine structure of a long-lived meso-α-scale convective system in Baiu frontal zone. Part I: Evolution and meso-α-scale characteristics. *J. Meteorol. Soc. Japan*, **66**, 331–350.

Ninomiya, K., T. Akiyama and M. Ikawa (1988b) Evolution and fine structure of a long-lived meso-α-scale convective system in Baiu frontal zone. Part II: Meso-γ-scale characteristics of precipitation. *J. Meteorol. Soc. Japan*, **66**, 351–371.

Nishimori, M. and A. Kitoh (2002) Estimate of precipitation change in East Asian summer by global warming derived from statistical downscaling method. *Proceedings of the 6th Symposium on Water Resources*, pp. 489–494. [In Japanese with English Abstract.]

Nitta, T. (1983) Observational study of heat sources over the eastern Tibetan Plateau during the summer monsoon. *J. Meteorol. Soc. Japan*, **61**, 590–605.

Nitta, T. (1986) Long term variations of cloud amount in the western Pacific region. *J. Meteorol. Soc. Japan*, **64**, 373–390.

Nitta, T. (1987) Convective activities in the tropical western Pacific and their impact on the northern hemisphere summer circulation. *J. Meteorol. Soc. Japan*, **65**, 373–390.

Nitta, T. and Z.-Z. Hu (1996) Summer climate variability in China and its association with 500 hPa height and tropical convection. *J. Meteorol. Soc. Japan*, **74**, 425–445.

Nitta, T. and S. Sekine (1994) Diurnal variation of convective activity over the tropical western Pacific. *J. Meteorol. Soc. Japan*, **72**, 627–640.

Noda, A. (2000) Projection of global climate change due to global warming. *Tenki*, **47**, 702–708. [In Japanese.]

Noda, A., S. Nakagawa, T. Motoi, S. Yukimoto and T. Tokioka (1996) Global warming induced by CO_2 and the Okhotsk Sea. *J. Remote Sensing Soc. Japan*, **16**, 89–99.

Noda, A., S. Yukimoto, S. Maeda, T. Uchiyama, K. Shibata and S. Yamaki (2001) *A New Meteorological Research Institute Coupled GCM (MRI-CGCM2): Transient Response to Greenhouse Gas and Aerosol Scenarios* (CGER's Supercomputer Monograph Report Vol. 7). Center for Global Environmental Research, National Institute for Environmental Studies, Tsukuba, Japan, 63pp.

Noda, A., H. Isobe, A. Kitoh, Y. Sato, M. Sugi, M. Nishimori and J. Matsumoto (2003) Climate change: Observations and projections. In: H. Harasawa and S. Nishioka (eds), *Global Warming: Potential Impacts on Japan* (Third Report). Kokon-Syoin, Tokyo, pp. 7–55. [In Japanese.]

Noh, Y. and H. J. Kim (1999) Simulations of temperature and turbulence structure of the oceanic boundary layer with the improved near-surface process. *J. Geophys. Res.*, **104**, 15621–15634.

Normand, C. W. B. (1953) Monsoon seasonal forecasting. *Quart. J. Roy. Meteorol. Soc.*, **79**, 463–473.

Nozawa, T., S. Emori, A. Numaguti, Y. Tsushima, T. Takemura, T. Nakajima, A. Abe-Ouchi and M. Kimoto (2001) Projections of future climate change in the 21st century simulated by the CCSR/NIES CGCM under the IPCC SRES scenarios. In: T. Matsuno and H. Kida (eds), *Present and Future of Modeling Global Environmental Change toward Integrated Modeling*. Terra Scientific Publishing, pp. 15–28.

NRC (National Research Council) (1994) *GOALS; Global Ocean–Atmosphere–Land System for Predicting Seasonal-to-Interannual Climate*. National Academic Press, Washington, D.C., 103pp.

NRC (National Research Council) (1998) *A Scientific Strategy for U.S. Participation in the GOALS (Global Ocean–Atmosphere–Land System) Component of CLIVAR*. National Academic Press, Washington, D.C., 69pp.

Oberhuber, J. M. (1988) *An Atlas Based on the COADS Data Set: The Budgets of Heat, Buoyancy and Turbulent Kinetic Energy at the Surface of the Global Ocean* (Rep. 15). Max-Planck Institut, Hamburg, 20 pp., 160 figures.

Ogasawara, N., A. Kitoh, T. Yasunari and A. Noda (1999) Tropospheric biennial oscillation of ENSO–monsoon system in the MRI coupled GCM. *J. Meteorol. Soc. Japan*, **77**, 1247–1270.

Ogura, Y. and K. Hoshino (2001) A bore-like disturbance observed in the Kanto Plain area. *J. Meteorol. Soc. Japan*, **79**, 1257–1268.

Ogura, Y. and M. Yoshizaki (1988) Numerical study of orographic–convective precipitation over the eastern Arabian Sea and the Ghat Mountains during the summer monsoon. *J. Atmos. Sci.*, **45**, 2097–2122.

Oh, T.-H, W.-T. Kwon and S.-B. Ryoo (1997) Review of the researches on Changma and future observational study (KORMEX). *Advances in Atmos. Sci.*, **14**, 207–222.

Ohsawa, T., H. Ueda, T. Hayashi, A. Watanabe and J. Matsumoto (2001) Diurnal variations of convective activity and rainfall in tropical Asia. *J. Meteorol. Soc. Japan.*, **79**, 333–352.

Ohta, T., T. Hiyama, H. Tanaka, T. Kuwada, T. C. Maximov, T. Ohata and Y. Fukushima (2001) Seasonal variation in the energy and water exchanges above and below a larch forest in eastern Siberia. *Hydro. Proc.*, **15**(8), 1459–1476.

Ojima, D. (2000) *Land Use/Lane Cover Change in Temperate East Asia: Current Status and Future Trends*. International START Secretariat, Washington, D.C., p. 228.

Oldeman, L. R. (1980) The agroclimatic classification of rice growing environments in Indonesia. In: *Agrometeorology of the Rice Crop: Proc. of the Symposium IRRI, Los Baños, Laguna, Philippines*, pp. 47–56.

Oochi, K., J. Yoshimura, H. Yoshimura, R. Mizuta, S. Kusunoki, and A. Noda (2005) Tropical cyclone climatology in a global-warming climate as simulated in a 20-km-mesh global atmospheric model. Submitted.

Ooi, S. H. (1999) *Impacts of ENSO on Monsoons over Malaysia* (ESCAP/WMO Typhoon Committee Annual Review 1998). World Meteorological Organization, Geneva, pp. 153–173.

Ooyama, K. (1964) A dynamic model for the study of tropical cyclone development. *Geofits. Int.*, **4**, 187–198.

Ooyama, K. V. (1982) Conceptual evolution of the theory and modelling of the tropical cyclone. *J. Meteorol. Soc. Japan*, **60**, 369–380.

Oppo, D., B. Linsley, Y. Rosenthal, S. Dannenmann and L. Beaufort (2003) Orbital and suborbital climate variability in the Sulu Sea, western tropical Pacific. *Geochemistry, Geophysics, Geosystems*, **4**, 1003, doi: 1010.1029/2001GC000260.

Otterman, J. (1974) Baring high-albedo soils by overgrazing: A hypothesized desertification mechanism. *Science*, **186**, 426–427.

Overpeck, J., D. Anderson, S. Trumbore and W. Prell (1996) The southwest Indian Monsoon over the last 18,000 years. *Climate Dynamics* (Vol. 12). Springer-Verlag, Berlin, pp. 213–225.

Pal, P. K., P. K. Thapliyal and A. K. Dwavedi (2001) Regional climate changes due to double CO_2 simulation by CCM3. *Mausam*, **52**, 221–228.

Palmer, T. N. (1994) Chaos and the predictability in forecasting the monsoons. *Proc. Ind. Nat. Sci. Acad., Part A*, **60**, 57–66.

Palmer, T. N., C. Brankovic, P. Viterbo and M. J. Miller (1992) Modeling interannual variations of summer monsoons. *J. Climate*, **5**, 399–417.

Palmer, T. N., A. Alessandri, U. Andersen, P. Cantelaube, M. Davey, P. Délécluse, M. Déqué, E. Díez, F. J. Doblas-Reyes, H. Feddersen *et al.* (2004) Development of a European multimodel ensemble system for seasonal-to-interannual prediction (DEMETER). *Bull. Amer. Meteorol. Soc.*, **85**, 853–872.

Pan, H.-L. and L. Mahrt (1987) Interaction between soil hydrology and boundary layer developments. *Bound.-Layer Meteor*, **38**, 185–202.

Pan, H. M., X. Jia and X. Z. Yang (1985) *The Climatological Features of Outbreaks of Cold Air in China* (Paper Collection). Beijing Meteorology Center, SMA, Beijing, pp. 120–131.

Pandya, R. E. and D. R. Durran (1996) The influence of convectively generated thermal forcing on the mesoscale circulation around squall lines. *J. Atmos. Sci.*, **53**, 2924–2951.

Pandya, R. E., D. R. Durran and C. Bretherton (1993) Comments on 'Thermally forced gravity waves in an atmosphere at rest'. *J. Atmos. Sci.*, **50**, 4097–4101.

Pant, G. B. and B. Parthasarathy (1981) Some aspects of an association between the southern oscillation and Indian summer monsoon. *Arch. Meteorol. Geophys. Bioklimatol.*, **1329**, 245–252.

Pant, G. B. and K. Rupa Kumar (1997) *Climate of South Asia*. John Wiley & Sons, Chichester, UK, 320pp.

Pant, P. S. (1983) A physical basis for changes in the phases of the monsoon over India. *Monthly Weather Review*, **111**, 487–495.

Pantastico, E. B. and A. C. Cardenas (1980) Climate constraints to rice production in the Phillipines. In: *Agrometeorology of the Rice Crop: Proc. of the Symposium IRRI, Los Baños, Laguna, Phillipines*, pp. 3–8.

Park, C. K., D. M. Straus and K. M. Lau (1990) An evaluation of the structure of tropical intraseasonal oscillations in three general-circulation models. *J. Meteorol. Soc. Japan*, **68**, 403–417.

Parker, M. D. and R. H. Johnson (2000) Organizational modes of midlatitude mesoscale convective systems. *Monthly Weather Review*, **128**, 3413–3436.

Parthasarathy, B. and G. B. Pant (1985) Seasonal relationship between Indian summer monsoon rainfall and Southern Oscillation. *J. Climatol.*, **5**, 369–378.

Parthasarathy, B. and S. Yang (1995) Relationships between regional Indian summer monsoon rainfall and Eurasian snow cover. *Adv. Atmos. Sci.*, **12**, 143–150.

Parthasarathy, B., A. A. Munot and D. R. Kothawale (1988) Regression model for estimation of Indian foodgrain production from summer monsoon rainfall. *Agric. For. Meteorol.*, **42**, 167–182.

Parthasarathy, B., K. Rupakumar and A. A. Munot (1991) Evidence of secular variations in Indian monsoon rainfall–circulation relationships. *J. Climate*, **4**, 927–938.

Parthasarathy, B., K. Rupa Kumar and A. A. Munot (1992a) Forecast of rainy-season food grain production based on monsoon rainfall. *Indian J. Agricul. Sci.*, **62**, 1–8.

Parthasarathy, B., K. R. Kumar and D. R. Kothawale (1992b) Indian summer monsoon rainfall indices: 1987–1990. *Meteorol. Mag.*, **121**, 174–186.

Parthasarathy, B., K. Rupa Kumar and A. A. Munot (1993) Homogeneous Indian monsoon rainfall: Variability and prediction. *Proc. Indian Acad. Sci. – Earth Planet. Sci.*, **102**, 121–155.

Parthasarathy, B., A. A. Munot and D. R. Kothawale (1994) All India monthly and seasonal rainfall series: 1871–1993. *Theor. Appl. Climatol.*, **49**, 217–224.

Parthasarathy, B., A. A. Munot and D. R. Kothawale (1995) *Monthly and Seasonal Rainfall Series for All India, Homogeneous Regions and Meteorological Subdivisions: 1871–1994* (Research Report No. RR-065). Indian Institute of Tropical Meteorology, Pune, India, 113 pp.

Pasch, R. J. (1983) *On the Onset of the Planetary Scale Monsoon* (Report No. 83–9). Dept of Meteorology, Florida State University, Tallahassee.

Pearce, R. P. and U. C. Mohanty (1984) Onset of the Asian summer monsoon 1979–1982. *J. Atmos. Sci.*, **41**, 1620–1639.

Pedlosky, J. (1979) Finite-amplitude baroclinic waves in a continuous model of the atmosphere. *J. Atmos. Sci.*, **36**, 1908–1924.

Peixoto, J. P. and A. H. Oort (1992) *Physics of Climate*. American Institute of Physics, 520pp.

Pena, M. and M. W. Douglas (2002) Characteristics of wet and dry spells over the Pacific side of central America during the rainy season. *Monthly Weather Review*, **130**, 3054–3073.

Petersen, W. A., S. W. Nesbitt, R. J. Blakeslee, R. Cifelli, P. Hein and S. A. Rutledge (2002) TRMM observations of intraseasonal variability in convective regimes over the Amazon. *J. Climate*, **15**, 1278–1294.

Petit, J. R., J. Jouzel, D. Raynaud, N. I. Barkov, J. M. Barnola, I. Basile, M. Bender, J. Chappellaz, J. Davis, G. Delaygue *et al.* (1999) Climate and atmospheric history of the past 420,000 years from the Vostok Ice Core, Antarctica. *Nature*, **399**, 429–436.

Philander, S. G. H. (1990) *El Niño, La Niña, and the Southern Oscillation*. Academic Press, 293pp.

Philander, S. G. H. and A. Fedorov (2003) Is El Niño sporadic or cyclic? *Ann. Rev. Earth Planet. Sci.*, **31**, 579–594.

Philander, S. G. H., D. Gu, D. Halpern, G. Lambert, N.-C. Lau, T. Li and R. C. Pacanowski (1996) Why the ITCZ is mostly north of the equator. *J. Climate*, **9**, 2958–2972.

Picaut, J., M. Loualalen, C. Menkes, T. Delcroix and M. J. McPhaden (1996) Mechanism of the zonal displacements of the Pacific warm pool: Implications for ENSO. *Science*, **274**, 1486–1489.

Pisharoty, P. R. (1996) Long-range forecasts of the total monsoon rainfall of India. *Current Science*, **71**, 729.

Pisharoty, P. R. and G. C. Asnani (1957) Rainfall around monsoon depressions in India. *Ind. J. Meteorol. Geophys*, **8**, 15–20.

Pisharoty, P. R. and B. N. Desai (1956) Western disturbances and Indian weather. *Ind. J. Meteorol. Geophys.*, **7**, 333–338.

Plumb, R. A. (1985) On the three-dimensional propagation of stationary waves. *J. Atmos. Sci.*, **42**, 217–229.

Potgieter, A. B., G. L. Hammer, H. Meinke, R. C. Stone and L. Goddard (2004) Spatial variability in impact on Australian wheat yields reveals three putative types of El Niño. [Submitted.]

Prandtl, L. (1932) Meteorologische Anwendungen der Stromungslchre. *Beitr. Phys. Atmos.*, **19**, 188–202. [In German.]

Prasad, K., S. R. Kalsi and R. K. Datta (1990) On some aspects of wind and cloud structure of monsoon upressions. *Mausam*, **41**, 365–370.

Prasad, K., Y. V. Rama Rao and S. Sen (1997) Tropical cyclone track prediction by a high resolution limited area model using synthetic observations. *Mausam*, **48**, 351–360.

Prell, W. L. (1984a) Monsoonal climate of the Arabian Sea during the Late Quaternary: A response to changing solar radiation. In: A. L. Berger *et al.* (eds), *Milankovitch and Climate*. D. Riedel, Hingham, pp. 349–366.

Prell, W. L. (1984b) *Variation of Monsoonal Upwelling: A Response to Changing Solar Radiation* (AGU Geophysical Monograph). American Geophysical Union, Washington, D.C., pp. 48–57.

Prell, W. L. and J. E. Kutzbach (1987) Monsoon variability over the past 150,000 years. *J. Geophys. Res.*, **92**, 8411–8425.

Prell, W. L. and J. E. Kutzbach (1992) Sensitivity of the Indian Monsoon to forcing parameters and implications for its evolution. *Nature*, **360**, 647–652.

Prell, W. L. and J. E. Kutzbach (1997) The impact of Tibet–Himalayan elevation on the sensitivity of the monsoon climate system to changes in solar radiation. In: W. F. Ruddiman (ed.), *Tectonic Uplift and Climate Change*. Plenum Press, New York, pp. 171–201.

Prell, W. L. and E. Van Campo (1986) Coherent response of Arabian Sea upwelling and pollen transport to late Quaternary monsoonal winds. *Nature*, **323**, 526–528.

Prell, W. L., R. E. Marvil and M. E. Luther (1990) Variability in upwelling fields in the northwestern Indian Ocean. 2: Data–model comparisons at 9000 years B.P. *Paleoceanography*, **5**, 447–457.

Prell, W. L., D. W. Murray, S. C. Clemens and D. M. Anderson (1992) Evolution and variability of the Indian Ocean summer monsoon: Evidence from the western Arabian Sea drilling program. In: R. A. Duncan *et al.* (eds), *The Indian Ocean: A Synthesis of Results from the Ocean Drilling Program*. American Geophysical Union, Washington D.C., pp. 447–469.

Puvaneswaran, K. M. and P. A. Smithson (1993) Control in precipitation distribution in Sri Lanka. *Theor. Appl. Climatol.*, **74**, 105–115.

Qian, W. H. (2000) Dry/wet alternation and global monsoon. *Geophys. Res. Letters*, **27**, 3679–3682.

Qian, W. H. and D. K. Lee (2000) Seasonal march of Asian summer monsoon. *Int. J. of Climatol.*, **20**, 1371–1378.

Qian, W., H. Hu, Y. Deng and J. Tian, (2002a) Signals of interannual and interdecadal variability of air–sea interaction in the basin-wide Indian Ocean. *Atmosphere–Ocean*, **40**, 293–311.

Qian, W. H., H.-S. Kang, and D.-K. Lee (2002b) Distribution of seasonal rainfall in the East Asian monsoon region. *Theor. Appl. Climatol*, **73**, 151–168.

Qian, Yongfu (1978) A numerical weather forecast model based on primitive equation with the consideration of the influence of large-scale orography. *Chinese J. Atmos. Sci.*, **2**, 91–102.

Qiang, X. K., Z. X. Li, C. M. Powell and H. B. Zheng (2001) Magnetostratigraphic record of the Late Miocene onset of the East Asian monsoon, and Pliocene uplift of northern Tibet. *Earth and Planetary Science Letters*, **187**, 83–93.

Quade, J., T. E. Cerling and J. R. Bowman, (1989) Development of Asian monsoon revealed by marked ecological shift during the latest Miocene in northern Pakistan. *Nature*, **342**, 163–166.

Quade, J., J. M. Cater, T. P. Ojha, J. Adam and T. M. Harrison (1995) Late Miocene environmental change in Nepal and the northern Indian subcontinent: Stable isotope evidence from paleosols. *Geological Society of America Bulletin*, **107**, 1381–1397.

Queney, P. (1948) The problem of air flow over mountains: A summary of theoretical studies. *Bull Amer. Meteorol. Soc.*, **29**, 16–29.

Quinn, W. and V. Neal (1978) El Niño occurrences over the past four and a half centuries. *J. Geophys. Res.*, **92**, 14449–14461.

Raghvan, K. (1965) Zone of rainfall ahead of a tropical depression. *Ind. J. Meteorol. Geophys.*, **16**, 631–634.

Raghvan, K. (1973) Break monsoon over India. *Monthly Weather Review*, **101**, 33–43.

Raghvan, S. (1990) Structure of tropical cyclones in the Bay of Bengal. *Mausam*, **41**, 325–328.

Raghvan, S. (1997) Radar observation of tropical cyclones over the Indian seas. *Mausam*, **48**, 169–188.

Rahmatullah, M. (1952) Synoptic aspects of the monsoon circulation and rainfall over Indo-Pakistan. *J. Meteorol.*, **9**, 176–179.

Rahmstorf, S. (2003) Timing of abrupt climate change: A precise clock. *Geophys. Res. Lett.*, **30**, 17-11–17-14.

Raisircar, N. C. (1957) Forecasting of norwesters. *Ind. J. Meteorol. Geophys*, **8**, 21–32.

Raisircar, N. C. and S. V. Datar (1963) Cold waves in northwest India. *Ind. J. Meteorol. Geophys.*, **14**, 315–320.

Raj, Y. E. A. (1992) Objective determination of northeast monsoon onset dates over coastal Tamil Nadu for the period 1901–1990. *Mausam*, **43**, 273–282.

Raj, Y. E. A. (2003) Onset, withdrawal and intra-seasonal variation of northeast monsoon over coastal Tamil Nadu, 1901–2000. *Mausam*, **54**, 605–614.

Rajagopal, E. N. and G. R. Iyengar (2002) *Implementation of Mesoscale Eta Model at NCMRWF* (Research Report No. NMRF/RR/4/2002). NCMRWF, India, pp. 28.

Rajeevan, M., D. S. Pai and V. Thapliyal (1998) Spatial and temporal relationships between global land surface air temperature anomalies and Indian summer monsoon rainfall. *Meteorol. Atmos. Phys.*, **66**, 157–171.

Rajeevan, M., U. S. De and R. K. Prasad (2000) Decadal variation of sea surface temperatures, cloudiness and monsoon depressions in the north Indian ocean. *Current Science*, **79**, 283–285.

Rajeevan, M., D. S. Pal and M. R. Das (2002) Asymmetric thermodynamic structure of monsoon depression revealed in microwave satellite data, *Current Science*, **81**, 448–450.

Rajeevan, M., D. S. Pai, S. K. Dikshit and R. R. Kelkar (2004) IMD's new operational models for long-range forecast of southwest monsoon rainfall over India and their verification for 2003. *Curr. Sci.*, **86**(3), 422–431.

Rajendran, K. R., R. S. Nanjundiah and J. Srinivasan (2002) Comparison of seasonal and intraseasonal variation of tropical climate in NCAR CCM2 GCM with two different cumulus schemes. *Meteorol. Atmos. Phys.*, **79**, 3921–3926.

Rajendran, K. R., A. Kitoh and S. Yukimoto (2004) South and East Asian summer monsoon climate and variation in MRI coupled model (MRI-CGCM2). *J. Climate*, **17**, 763–782.

Ramage, C. S. (1952) Variation of rainfall over South China through wet season. *Bull. Amer. Meteorol. Soc.*, **41**, 591–598.

Ramage, C. S. (1968) Role of a tropical 'maritime continent' in the atmospheric circulation. *Monthly Weather Review*, **96**, 365–369.

Ramage, C. S. (1971) *Monsoon Meteorology* (Int. Geophys. Ser., Vol. 15). Academic Press, San Diego, California, 296pp.

Ramanathan, V. and W. Collins (1991) Thermodynamic regulation of ocean warming by cirrus clouds deduced from observations of the 1987 El Niño. *Nature*, **351**, 27–32.

Ramanathan, V., P. J. Crutzen, J. T. Kiehl and D. Rosenfeld (2001) Aerosols, climate, and the hydrological cycle. *Science*, **294**, 2119–2124.

Ramamoorthy, K. (1969) Monsoon of India: Some aspects of the break in the Indian southwest during July and August. *Forecasting Manual* (No. IV, 18.3). Indian Meteorological Department, Poona.

Ramamurthy, K. (1969) Some aspects of the 'break' in the Indian southwest monsoon during July and August. *Forecasting Manual*. Indian Meteorological Department, New Delhi.

Raman, C. R. V. and Y. P. Rao (1981a) Blocking high over Asia and droughts over India. *Nature*, **289**, 271–273.

Raman, C. R. V., Y. P. Rao, S. K. Subramanian and J. A. Maliekal (1981) Tropospheric wind shear oscillations as a characteristic of the southwest monsoon atmosphere. *Monthly Weather Review*, **109**, 910–915.

Raman, S., U. C. Mohanty, N. C. Reddy, K. Alapaty and R. V. Madala (1998) Numerical simulation of the sensitivity of summer monsoon circulation and rainfall over India to land surface processes. *Pure Appl. Geophys.*, **152**, 781–809.

Ramana, G. R. (1969) Relationship between depressions in Bay of Bengal and tropical storms of the China Sea. *Ind. J. Meteorol. Geophys.*, **20**, 148–150.

Ramanadh, R., P. V. Rao and J. K. Patnaik (1973) Break in Indian summer monsoon. *Pure Appl. Geophys.*, **104**, 635–647.

Ramaswamy, C. (1962) Breaks in the Indian summer monsoon as a phenomenon of interaction between the easterly and westerly jet streams. *Tellus*, **14**, 337–349.

Randall, D. A., Harshvardhan and D. A. Dazlich (1991) Diurnal variability of the hydrological cycle in a general circulation model. *J. Atmos. Sci.*, **48**, 40–62.

Randall, D. A., M. Khairoutdinov, A. Arakawa and W. Grabowski (2003) Breaking the cloud parameterization deadlock. *Bull. Amer. Meteorol. Soc.*, **84**, 1547–1564.

Rao, K. V. (1963) A study of the Indian northeast monsoon season. *Ind. J. Meteorol. Geophys.*, **14**, 143–155.

Rao, K. V. and S. Rajamani (1970) Diagnostic study of a monsoon depression by geostrophic baroclinic model. *Ind. J. Meteorol. Geophys.*, **21**, 187–194.

Rao, Y. P. (1976) *Southwest Monsoon* (Meteorological Monograph Synoptic Meteorology No. 1). Indian Meteorological Department, New Delhi, 367pp.

Rao, N. K., S. Gadgil, Rao, S. P. R. and K. Savithri (2000) Tailoring strategies to rainfall variability: The choice of sowing window. *Current Science*, **78**, 1216–1230.

Rao, Y. V. R., K. Prasad and S. Prasad (2001) A case study of the impact of INSAT derived humidity profiles on precipitation forecast by limited area model. *Mausam*, **52**, 647–654.

Rasmusson, E. M. (1985) El Niño and variations in climate. *Am. Sci.*, **73**, 168–178.

Rasmusson, E. M. and T. H. Carpenter (1983) The relationship between eastern equatorial Pacific sea surface temperature and rainfall over India and Sri Lanka. *Monthly Weather Review*, **111**, 517–528.

Rasmusson, E. M., X. Wang and C. F. Ropelewski (1990) The biennial component of ENSO variability. *J. Mar. Sys.*, **1**, 71–96.

Raymond, D. J. (2001) A new model of the Madden–Julian oscillation. *J. Atmos. Sci.*, **58**, 2807–2819.

Raymond, D. J. and H. Jiang (1990) A theory for long-lived mesoscale convective systems. *J. Atmos. Sci.*, **47**, 3067–3077.

Raymond, D. J. and D. J. Torres (1998) Fundamental moist modes of the equatorial troposphere. *J. Atmos. Sci.*, **55**, 1771–1990.

Rea, D. K. (1994) The paleoclimatic record provided by eolian deposition in the deep sea: The geologic history of wind. *Reviews of Geophysics*, **32**, 159–195.

Rea, D. K., H. Snoeckx and L. H. Joseph (1998) Late Cenozoic eolian deposition in the North Pacific: Asian drying, Tibetan uplift, and cooling of the northern hemisphere. *Paleoceanograohy*, **13**, 215–224.

Reason C. J. C., R. J. Allan, J. A. Lindesay *et al.* (2000) ENSO and climatic signals across the Indian Ocean Basin in the global context. Part I: Interannual composite patterns. *Int. J. Climatol.*, **20**, 1285–1327.

Redelsperger, J.-L., D. Parsons and F. Guichard (2002) Recovery processes and factors limiting cloud-top height following the arrival of a dry intrusion observed during TOGA COARE. *J. Atmos. Sci.*, **59**, 2438–2457.

Reed, R., W. J. Cambell, L. A. Rasmusson and D. G. Rogers (1961) Evidence of a downward propagating annual wind reversal in the equatorial stratosphere. *J. Geophys. Res.*, **66**, 813–818.

Reichart, G. J., M. den Dulk, H. J. Visser, C. H. van der Weijden and W. J. Zachariasse, (1997) A 225 kyr record of dust supply, paleoproductivity and the oxygen minimum zone from the Murray Ridge (northern Arabian Sea). *Paleogeography, Paleoclimatology, Paleoecology*, **134**, 147–169.

Reichart, G. J., L. J. Lourens and W. J. Zachariasse (1998) Temporal variability in the northern Arabian Sea oxygen minimum zone (OMZ) during the last 225,000 years. *Paleoceanography*, **13**, 607–621.

Reiter, E. R. and M. Tang (1984) Plateau effects on diurnal circulation pattern. *Monthly Weather Review*, **112**, 617–637.

Reverdin, G., D. Cadet and D. Gutzler (1986) Interannual displacements of convection and surface circulation over the equatorial Indian Ocean. *Quart. J. Roy. Meteorol. Soc.*, **122**, 43–67.

Reynolds, R. W. (1988) A real-time global sea surface temperature analysis. *J. Climate*, **1**, 75–86.

Reynolds, R. and D. Marisco (1993) An improved real-time global sea surface temperature analysis. *J. Climate*, **6**, 114–119.

Reynolds, R. W., N. A. Rayner, T. M. Smith, D. C. Stokes and W. Wang (2002) An improved in situ and satellite sea surface temperature analysis for climate. *J. Climate*, **15**, 1609–1625.

Rickenbach, T. M. and S. A. Rutledge (1997) The diurnal variation of rainfall over the western Pacific warm pool: Dependence on convective organization. *22nd Conference on Hurricanes and Tropical Meteorology, Fort Collins, CO., Amer. Meteor. Soc.*, pp. 205–206.

Rickenbach, T. M. and S. A. Rutledge (1998) Convection in TOGA COARE: Horizontal scale, morphology, and rainfall production. *J. Atmos. Sci.*, **55**, 2715–2729.

Riehl, H. (1954) *Tropical Meteorology*. McGraw-Hill, New York, 392pp.

Riehl, H. (1979) *Climate and Weather in the Tropics*. Academic Press, New York, 611pp.

Robe, F. R. and K. A. Emanuel (2001) The effect of vertical wind shear on radiative–convective equilibrium states. *J. Atmos. Sci.*, **58**, 1427–1445.

Robock, A., K. Y. Vinnikov, G. Srinivasan, J. K. Entin, S. E. Hollinger, N. A. Speranskaya, S. Liu and A. Namkhai (2000) The Global Soil Moisture Data Bank. *Bull. Amer. Meteorol. Soc.*, **81**, 1281–1299.

Robock, A., M. Mu, K. Vinnikov and D. Robinson (2003) Land surface conditions over Eurasia and Indian summer monsoon rainfall. *J. Geophys. Res.*, **108**, 4131–4143.

Rodwell, M. J. (1997) Breaks in the Asian monsoon: The influence of southern hemisphere weather systems. *J. Atmos. Sci.*, **54**, 2597–2611.

Rodwell, M. J. (2005) Monsoon internal dynamics. In: C. P. Chang, B. Wang and N. C. G. Lau (eds), *The Global Monsoon System: Research and Forecast*. World Meteorological Organization, Geneva, pp. 326–341.

Rodwell, M. J. and B. J. Hoskins (1995) A model of the Asian summer monsoon. Part II: Cross-equatorial flow and PV behavior. *J. Atmos. Sci.*, **52**, 1341–1356.

Rodwell, M. J. and B. J. Hoskins (1996) Monsoons and the dynamics of deserts. *Quart. J. Roy. Meteorol. Soc.*, **122**, 1385–1404.

Rodwell, M. J. and B. J. Hoskins (2001) Subtropical anticyclones and summer monsoons. *J. Climate*, **14**, 3192–3211.

Roebber, P. J. (1984) Statistical analysis and updated climatology of explosive cyclones. *Monthly Weather Review*, **112**, 1577–1589.

Roeckner, E., L. Bengtsson and J. Feichter (1999) Transient climate change simulations with a coupled atmosphere–ocean GCM including the tropospheric sulfur cycle. *J. Climate*, **12**, 3004–3032.

Ropelewski, C. F. and M. S. Halpert (1987) Global and regional scale precipitation patterns associated with the El Niño/Southern Oscillation. *Monthly Weather Review*, **115**, 1606–1626.

Ropelewski, C. F., M. S. Halpert and X. Wang (1992) Observed tropospherical biennial variability and its relationship to the Southern Oscillation. *J. Climate*, **5**, 594–614.

Rosen, R. D., D. A. Salstein and J. P. Peixoto (1979) Streamfunction analysis of interannual variability in large-scale water vapor flux. *Monthly Weather Review*, **107**, 1682–1684.

Rostek, F., E. Bard, L. Beaufort, C. Sonzogni and G. Ganssen (1997) Sea surface temperature and productivity records for the past 240 kyr in the Arabian Sea. *Deep-Sea Research. Part II: Topical Studies in Oceanography* (Vol. 44). Oxford University Press, Oxford, UK, pp. 1461–1480.

Ropelewski, C. F. and M. S. Halpert (1987) Global and regional scale precipitation patterns associated with the El Niño/Southern Oscillation. *Monthly Weather Review*, **115**, 1606–1626.

Ropelewski, C. F., M. S. Halpert and X. Wang (1992) Observed tropospheric biennial variability and its relationship to the Southern Oscillation. *J. Climate*, **5**, 594–614.

Rowell, D. P. (1998) Assessing potential seasonal predictability with an ensemble of multidecadal GCM simulations. *J. Climate*, **11**, 109–120.

Rowell, D. P., C. K. Folland, K. Maskell and M. N. Ward (1995) Variability of summer rainfall over tropical North Africa (1906–92): Observations and modeling. *Quart. J. Roy. Meteorol. Soc.*, **121**, 669–704.

Roy Bhowmik, S. K. (2003) Monsoon rainfall prediction with a nested grid mesoscale limited area model over Indian region. *Proc. India Acad. Sci.*, **112**, 499–520.

Roy Bhowmik, S. K. and K. Prasad (2001) Some characteristics of limited area model precipitation forecast of Indian monsoon and evaluation of associated flow features. *Meteorol. Atmos. Phys.*, **76**, 223–236.

Ruddiman, W. F. and J. E. Kutzbach (1989) Forcing of late Cenozoic northern hemisphere climate by plateau uplift in southern Asia and the American west. *J. Geophys. Res.*, **94**, 18,409–418,427.

Rui, H. and B. Wang (1990) Development characteristics and dynamic structure of the tropical intraseasonal convective anomalies. *J. Atmos. Sci.*, **47**, 357–379.

Rupa Kumar, K. and R. G. Ashrit (2001) Regional aspects of global climate change simulations: Validation and assessment of climate response over Indian monsoon region to transient increase of greenhouse gases and sulfate aerosols. *Mausam*, **52**, 229–244.

Rupa Kumar, K., G. B. Pant, B. Parthasarathy and N. A. Sontakke (1992) Spatial and subseasonal patterns of the long-term trends of Indian summer monsoon rainfall. *Int. J. Climatol.*, **12**, 257–268.

Rupa Kumar, K., K. K. Kumar and G. B. Pant (1994) Diurnal asymmetry of surface temperature trends over India. *Geophys. Res. Lett.*, **21**(8), 677–680.

Rupa Kumar, K., K. Krishna Kumar, R. G. Ashrit, S. K. Patwardhan and G. B. Pant (2002) Climate change in India: Observations and model projections. In: P. R. Shukla, S. K. Sharma, and P. V. Ramana (eds), *Climate Change and India: Issues, Concerns and Opportunities*. Tata/McGraw-Hill, New Delhi, pp. 24–75.

Rupakumar, S., G. B. Pant, B. Parthasarathy and N. A. Sontakke (1992) Spatial and subseasonal patterns of the long-term trends of Indian monsoon rainfall. *Int. J. Climatol.*, **12**, 257–268.

Rudnick, D. L., R. A. Weller, C. C. Eriksen, T. D. Dickey, J. Marra and C. Langdon (1997) Moored instruments weather Arabian Sea monsoons, yield data. *Eos, Trans. AGU*, **78**, 120–121.

Rutledge, S. A., E. R. Williams and T. D. Keenan (1992) The Down Under Doppler and Electricity Experiment (DUNDEE): Overview and preliminary results. *Bull. Amer. Meteorol. Soc.*, **73**, 3–16.

Sadhuram, Y. (1997) Predicting monsoon rainfall and pressure indices from sea surface temperature. *Curr. Sci. India*, **72**, 166–168.

Saha, K. (1970) Zonal anomaly of sea surface temperature in equatorial Indian Ocean and its possible effect upon monsoon circulation. *Tellus*, **XXII**, 403–409.

Saha, K. R., F. Sanders and J. Shukla (1981) Westward propagating predecessors of monsoon depressions. *Monthly Weather Review*, **109**, 330–343.

Sahami, K. (2003) Aspects of the heat balance of the Indian Ocean on annual and interannual time scales. PhD thesis, University of Colorado, 155pp.

Saito, K., T. Yasunari and K. Takata (2005) Relative roles of large-scale orography and vegetation on global hydro-climate. Part II. [To be submitted to *J. Hydrometeor.*]

Saji, N. H., B. N. Goswami, P. N. Vinayachandran and T. Yamagata (1999) A dipole mode in the tropical Indian Ocean. *Nature*, **401**, 360–363.

Salby, M. L. and H. H. Hendon (1994) Intraseasonal behavior of clouds, temperature, and motion in the Tropics. *J. Atmos. Sci.*, **51**, 2207–2224.

Salby, M. L., H. H. Hendon and R. R. Garcia (1994) Planetary-scale circulations in the presence of climatological and wave-induced heating. *J. Atmos. Sci.*, **51**, 3365.

Samel, A. N., W.-C. Wang and X.-Z. Liang (1999) The monsoon rainband over China and relationships with the Eurasian circulation. *J. Climate*, **12**, 115–131.

Sanders, F. and J. R. Gyakum (1980) Synoptic–dynamic climatology of the 'bomb'. *Monthly Weather Review*, **108**, 1589–1606.

Sanjay, J., P. Mukhopadhyay and S. S. Singh (2002) Impact of nonlocal boundary layer diffusion scheme on forecasts over Indian region. *Meteorol. Atmos. Phys.*, **80**, 207–216.

Sankar-Rao, M., K.-M. Lau and S. Yang (1996) On the relationship between Eurasian snow cover and the Asian monsoon. *Int. J. Climatol.*, **16**, 605–616.

Sardeshmukh, P. D. and B. J. Hoskins (1988) The generation of global rotational flow by steady idealized tropical divergence. *J. Atmos. Sci.*, **45**, 1228–1251.

Sarkar, A., R. Ramesh, B. L. K. Somayajulu, R. Agnihotri, A. J. T. Jull and G. S. Burr (2000) *High Resolution Holocene Monsoon Record from the Eastern Arabian Sea* (Earth and Planetary Science Letters No. 177). New York, pp. 209–218.

Sarkar, R. P. and A. Choudhary (1988) A diagnostic study of monsoon depression. *Mausam*, **39**, 9–18.

Sarnthein, M., J. P. Kennett, J. R. M. Allen, J. Beer, P. Grootes, C. Laj, J. McManus and R. Ramesh (2002) Decadal-to-millennial-scale climate variability–chronology and mechanisms: Summary and recommendations. *Quaternary Science Reviews*, **21**, 1121–1128.

Sato, Y. (2000) Projection of regional climate change over Japan due to global warming. *Tenki*, **47**, 708–716. [In Japanese.]

Schemm, J. E., H. v. d. Dool and S. Saha (1996) A multi-year DERF experiment at NCEP. *11th Conference on Numerical Weather Prediction, August 19–13, Norfolk, Virginia*, pp. 47–49.

Schlesinger, M. E. and N. Ramankutty (1994) An oscillation in the global climate system of period 65–70 years. *Nature*, **367**, 723–726.

Schopf, P. and M. Suarez (1988) Vacillations in a coupled ocean–atmosphere model. *J. Atmos. Sci.*, **45**, 549–566.

Schott, F. A. and J. P. McCreary Jr (2001) The monsoon circulation of the Indian Ocean. *Prog. Oceanogr.*, **51**, 1–123.

Schubert, S. D. and M. L. Wu (2001) Predictability of the 1997 and 1998 South Asian summer monsoon low-level winds. *J. Climate*, **14**, 3173–3191.

Schulz, H., U. von Rad, and H. Erlenkeuser (1998) Correlation between Arabian Sea and Greenland climate oscillations of the past 110,000 years. *Nature*, **393**, 54–57.

Schulz, M. (2002) On the 1470-year spacing of Dansgaard–Oeschger warm events. *Paleoceanography*, **17**, 4-1 through 4-10.

Schumacher, C. and R. A. Houze Jr (2003) Stratiform rain in the tropics as seen by the TRMM precipitation radar. *J. Climate*, **16**, 1739–1756.

Schumacher, C., R. A. Houze Jr and I. Kraucunas (2004) The tropical dynamical response to latent heating estimates derived from the TRMM precipitation radar. *J. Atmos. Sci.*, **61**, 1341–1358.

Seager, R., R. Murtugudde, N. Naik, A. Clement, N. Gordon and J. Miller (2003) Air–sea interaction and the seasonal cycle of the subtropical anticyclones. *J. Climate*, **16**, 1948–1966.

Sellers, P. J., Y. Mintz, Y. C. Sud and A. Dalcher (1986) A simple biosphere model (SiB) for use within general circulation model. *J. Atmos. Sci.*, **43**, 505–531.

Sellers, P. J., F. Hall, H. Margolis, B. Kelly, D. Baldocchi, G. D. Hartog, J. Cihlar, M. G. Ryan, B. Goodison, P. Crill *et al.* (1996) The boreal ecosystem–atmosphere study (BOREAS): An overview and early results from the 1994 field year. *Bull. Amer. Meteorol. Soc.*, **76**, 1549–1577.

Sen, O. L., Y. Wang and B. Wang (2004a) Impact of Indochina deforestation on the East Asian summer monsoon. *J. Climate*, **17**, 1366–1380.

Sen, O. L., B. Wang and Y. Wang (2004b) Re-greening the desertification lands in northern China: Implications from a regional climate model experiment. *J. Climate*. [In press.]

Sen, R. S. and S. K. Roy Bhowmik (2003) Evolution of the atmosphere in relation to pre-monsoon convective activity over north India. *Mausam*, **54**, 397–405.

Sen, S. N. (1931) Mechanism of Bengal tornadoes in the norwester's season. *Nature*, **127**, 128–129.

Sengupta, D. and M. Ravichandran (2001) Oscillations of Bay of Bengal sea surface temperature during the 1998 summer monsoon. *Geophys. Res. Lett.*, **28**, 2033–2036.

Sengupta, D., B. N. Goswami and R. Senan (2001) Coherent intraseasonal oscillations of ocean and atmosphere during the Asian summer monsoon. *Geophys. Res. Lett.*, **28**, 4127–4130.

Shackleton, N. J. and N. G. Pisias (1985) Atmospheric carbon dioxide, orbital forcing, and climate. In: E. Sundquist and W. S. Broecker (eds), *The Carbon Cycle and Atmospheric CO_2: Natural Variations Archean to Present*. American Geophysical Union, Washington, D.C., pp. 303–317.

Shackleton, N. J., A. Berger and W. R. Peltier (1990) An alternative astronomical calibration of the Lower Pleistocene timescale based on ODP Site 677. *Transactions of the Royal Society of Edinburgh: Earth Science*, **81**, 251–261.

Shackleton, N. J., Z. S. An, A. E. Dodonov, J. Gavin, G. Kukla, V. A. Ranov and L. P. Zhou (1995a) Accumulation rate of loess in Tadjikistan and China: Relationship with global ice volume cycles. *Quaternary Proceedings*, **4**, 1–6.

Shackleton, N. J., M. A. Hall and D. Pate (1995b) Pliocene stable isotope stratigraphy of Site 846. In: N. G. Pisias *et al.* (eds), *Proceedings of the Ocean Drilling Program: Scientific Results*. Ocean Drilling Program, College Station, pp. 337–353.

Shankar-Rao, P., K. M. Lau and S. Yang (1996) On the relationship between Eurasian snow cover and the Asian summer monsoon. *Int. J. Climatol.*, **16**, 605–616.

Shen, C. D., J. Beer, T. S. Liu, H. Oeschger, G. M. Bonani, Suter and W. Wolfli (1992) 10-Be in Chinese loess. *Earth and Planetary Science Letters*, **109**, 169–177.

Shen, S. and K. M. Lau (1995) Biennial oscillation associated with the east Asian monsoon and tropical sea surface temperatures. *J. Meteorol. Soc. Japan*, **73**, 105–124.

Shen, X., M. Kimoto and A. Sumi (1998) Role of land surface processes associated with interannual variability of broad-scale Asian summer monsoon as simulated by the CCSR/NIES AGCM. *J. Meteorol. Soc. Japan*, **76**, 217–236.

Shen, Z., D. Weng and S. Pan (1984) *An Outline of the Qinghai–Xizang Plateau Heat Source Observation Experiment* (Collected Papers on the Qinghai–Xizang Plateau Meteorological Experiment No. I). Science Press, Beijing, pp. 1–9. [In Chinese.]

Shi, D. B., W. Q. Zhu, H. Q. Wang and Z. Y. Tao (1996) Cloud top blackbody temperature analysis of infrared satellite image for mesoscale convective system. *Acta Meteorol. Sinica*, **54**, 600–611.

Shi, G. Y. (1981) An accurate calculation and the infrared transmission function of the atmospheric constituents. Ph.D. thesis, Tohoku University of Japan, 191pp.

Shi, L. and E. A. Smith (1992) Surface forcing of the infrared cooling profile over the Tibetan Plateau. Part II: Cooling-rate variation over large-scale plateau domain during summer monsoon transition. *J. Atmos. Sci.*, **49**, 823–844.

Shi, N. (1996) Multiple time scale variations of the East Asian winter monsoon in recent 40 years and its relation to climate. *J. Appl. Meteorol.*, **7**, 175–182.

Shi, P. J., 2003, *Atlas of Natural Disasters System of China*. Science Press, Beijing, 218pp.

Shi, Y. F. (eds) (2003) *An Assessment of the Issues of Climatic Shift from Warm to Warm–Wet in Northwest China*. China Meteorological Press, 124 pp.

Shimmield, G. B. and S. R. Mowbray (1991) The inorganic geochemical record of the northwest Arabian Sea: A history of productivity variation over the last 400 k.y. *Ocean Drilling Program, Scientific Results*, **117**, 409–429.

Shimmield, G. B., S. R. Mowbray and G. P. Weedon (1990) A 350 ka history of the Indian southwest monsoon: Evidence from deep-sea cores, northwest Arabian Sea. *Transactions of the Royal Society of Edinburgh*, **81**, 289–299.

Shinoda, T. and M. Gamo (2000) Interannual variations of boundary layer temperature over the African Sahel associated with vegetation and upper-troposphere. *J. Geophys. Res.*, **105**, 12317–12327.

Shinoda, T. and H. H. Hendon (1998) Mixed layer modeling of intraseasonal variability in the tropical Western Pacific and Indian Oceans. *J. Climate*, **11**, 2668–2685.

Shinoda, T. and H. H. Hendon (2001) Upper-ocean heat budget in response to the Madden–Julian oscillation in the western equatorial Pacific. *J. Climate*, **14**, 4147–4165.

Shinoda, T. and H. H. Hendon (2002) Rectified wind forcing and latent heat flux produced by the Madden–Julian Oscillation. *J. Climate*, **23**, 3500–3508.

Shinoda, T. and H. Uyeda (2002) Effective factors in the development of deep convective clouds over the wet region of eastern China during the summer monsoon season. *J. Meteorol. Soc. Japan*, **80**, 1395–1414.

Shinoda, T., H. H. Hendon and J. Glick (1998) Intraseasonal variability of surface fluxes and sea surface temperature in the tropical western Pacific and Indian Oceans. *J. Climate*, **11**, 1685–1702.

Shinoda, T., H. H. Hendon and J. Glick (1999) Intraseasonal surface fluxes in the tropical western Pacific and Indian Oceans from NCEP reanalyses. *Monthly Weather Review*, **127**, 678–693.

Shinoda, T., Y. Morinaga and T. Yasunari (2003) The forefront of monsoon researches. *Kisho Kenkyu Notes,* **204**, 69–114. [In Japanese.]

Shinoda, T., M. A. Alexander and H. H. Hendon (2004) Remote response of the Indian Ocean to interannual SST variations in the tropical Pacific. *J. Climate*, **17**, 362–272.

Short, D. A. and K. Nakamura (2000) TRMM radar observations of shallow precipitation over the tropical oceans. *J. Climate.*, **13**, 4107–4124.

Shukla, J. (1975) Effect of Arabian sea surface temperature anomaly on Indian summer monsoon: A numerical experiment with the GFDL model. *J. Atmos. Sci.*, **32**, 503–511.

Shukla, J. (1976) Effects of Arabian Sea-surface temperature anomaly on Indian summer monsoon: Numerical experiment with G model – Reply. *J. Atmos. Sci.*, **33**, 2253–2255.

Shukla, J. (1978) CISK, barotropic and baroclinic instability and the growth of monsoon depressions. *J. Atmos. Sci.*, **35**, 495–500.

Shukla, J. (1981) Dynamical predictability of monthly means. *J. Atmos. Sci.*, **38**, 2547–2572.

Shukla, J. (1985) Predictability. *Adv. Geophys.*, **28B**, 87–122.

Shukla, J. (1987a) Interannual variability of monsoon. In: J. S. Fein and P. L. Stephens (eds), *Monsoons*. John Wiley & Sons, New York, pp. 399–464.

Shukla, J. (1987b) Long-range forecasting of monsoons. In: J. S. Fein and P. L. Stephens (eds), *Monsoons*. John Wiley & Sons, New York, pp. 523–548.

Shukla, J. (1998) Predictability in the midst of chaos: A scientific basis for climate forecasting. *Science*, **282**, 728–731.

Shukla, J. and M. J. Fennessy (1994) Simulation and predictability of monsoons. *Proceedings of the International Conference on Monsoon Variability and Prediction* (Tech. Rep. WCRP No. 84). World Climate Research Programme, World Meteorological Organization, Geneva, pp. 567–575.

Shukla, J. and B. M. Misra (1977) Relationships between sea surface temperature and wind speed over the central Arabian sea and monsoon rainfall over India. *Monthly Weather Review*, **105**, 998–1002.

Shukla, J. and D. A. Mooley (1987) Empirical prediction of the summer monsoon rainfall over India. *Monthly Weather Review*, **115**, 695–703.

Shukla, J. and D. A. Paolino (1983) The Southern Oscillation and long range forecasting of summer monsoon rainfall over India. *Monthly Weather Review*, **111**, 1830–1837.

Sikka, D. R. (1971) Evaluation of the use of satellite photography in determining the location and intensity changes of tropical cyclones in Arabian Sea and Bay of Bengal. *Ind. J. Meteorol. Hydrol. Geophys*, **22**, 305–312.

Sikka, D. R. (1975) Forecasting the movement of tropical cyclones in the Indian seas by non-divergent barotropic model. *Ind. J. Meteorol. Geophys.*, **26**, 323–325.

Sikka, D. R. (1977) Some aspects of the life history, structure and movements of monsoon depressions. *Pure Appl. Geophys.*, **115**, 1501–1529.

Sikka, D. R. (1980) Some aspects of large-scale fluctuations of summer monsoon rainfall over India in relation to fluctuations in planetary and regional scale circulation parameters. *Proc. Ind. Acad. Sci. – Earth Planetary Sciences*, **89**, 179–195.

Sikka, D. R. (1981) An appraisal of the onset of summer monsoon over India in the light of MONEX-79 data. *Results of Summer MONEX Field Phase Research. Part B* (FGGE Operations Report No. 9). ICSO/World Meteorological Organization, Geneva, pp. 87–95.

Sikka, D. R. (1999) *Monsoon Droughts* (Joint COLA/CARE Report No. 2). COLA, Calverton, Maryland.

Sikka, D. R. (2000) *Monsoon Floods* (Joint COLA/CARE Report No. 4). COLA, Calverton, Maryland.

Sikka, D. R. (2003) Monsoon monitoring and forecasting drought of 2002. *Proc. Ind. Nat. Sci. Acad.,* **69A**.

Sikka, D. R. and S. Gadgil (1978) Large scale rainfall over India during the summer monsoon and its relationship with the lower and upper troposphereic vorticity. *Ind. J. Meteorol. Hydrol. Geophys.*, **29**, 219–231.

Sikka, D. R. and S. Gadgil (1980) On the maximum cloud zone and the ITCZ over Indian longitude during southwest monsoon. *Monthly Weather Review*, **108**, 1840–1853.

Sikka, D. R. and W. M. Gray (1981) Genesis of monsoon disturbances in north Indian Ocean with the passage of baroclinic waves across the southern Indian Ocean. *Proc. Int. Conf. on. Sci. Results of the Monsoon Experiment, Bali, Indonesia, October*. World Meteorological Organization, Geneva, pp. 4-29 through 4-34.

Sikka, D. R. and S. M. Kulsherestha (2002) *Indian Droughts in the Context of History and Climate* (Joint COLA/CARE Tech. Report No. 6). COLA, Calverton, Maryland.

Sikka, D. R. and R. Narasimha (1995) Genesis of the monsoon trough boundary layer experiment *Proc. Ind. Acad. Sci.,* **104**, 157–187.

Sikka, D. R. and D. K. Paul (1994) Monsoon variability over the Asia–Pacific region in relation to ENSO events. *Proc. Int. Conf on Monsoon Variability and Prediction, May, Trieste* (WMO D-619). World Meteorological Organization, Geneva.

Sikka, D. R., T. S. S. Anjaneylu and G. Gurunadham (1965) Some aspects of the Bay of Bengal cyclone of October 1963. *Ind. J. Meteorol. Geophys.*, **16**, 539–556.

Sikka, D. R., S. Adhikari, R. L. Grossman, A. R. Subbiah and N. Natarajan (2004) *Rainfall of Nepal*. [Under publication by Asian Disaster Preparedness Centre, Bangkok.]

Simmonds, L., D. Bi and P. Hope (1999) Atmospheric water vapor flux and its association with rainfall over China in summer. *J. Climate*, **12**, 1351–1367.

Simpson, J. E. (1997) *Gravity Currents in the Environment and the Laboratory* (2nd edn). Cambridge University Press, Cambridge, UK, 244pp.

Singh, O. P. (2001) Long-term trends in the frequency of monsoonal cyclonic disturbances over the north Indian Ocean. *Mausam*, **52**, 655–658.

Singh, P., K. J. Boote, A. Yogeswara Rao, M. R. Iruthayaraj, A. M. Sheikh, S. S. Hundal, R. S. Narang and P. Singh (1994) Evaluation of the groundnut model PNUTGRO for crop response to water availability, planting dates, and seasons. *Field Crops Research*, **39**, 147–162.

Singh, S. S. (1985) Short-range prediction with multi-level primitive equation model. *Proc. Ind. Acad. Sci.,* **94**, 159–184.

Sirocko, F., M. Sarnthein, H. Erlenkeuser, H. Lange, M. Arnold and J. C. Duplessy (1993) Century-scale events in monsoonal climate over the past 24,000 years. *Nature*, **364**, 322–324.

Sivakumar, M. V. K., P. Singh and J. H. Williams. (1983) Agroclimatic aspects in planning for improved productivity of alfisols. *Alfisols in the Semi-arid Tropics: A Consultant's Workshop, 1–3 December, ICRISAT Centre, India*, pp. 15–30.

Skamarock W. C., R. Rotunno and J. B. Klemp (1999) Models of coastally trapped disturbances. *J. Atmos. Sci.*, **56**, 3349–3365.

Slingo, J. M. (1998) Extratropical forcing of tropical convection in a northern winter simulation with the UGAMP GCM. *Quart. J. Roy. Meteorol. Soc.*, **124**, 27–51.

Slingo, J. M. and H. Annamalai (1997, 2000) The El Niño of the century and the response of the Indian summer monsoon. *Monthly Weath. Review*, **128**, 1778–1797.

Slingo, J. M. and R. A. Madden (1991) Characteristics of the tropical intraseasonal oscillation in the NCAR Community Climate Model. *Quart. J. Roy. Meteorol. Soc.*, **117**, 1129–1169.

Slingo, J. M., M. Blackburn, A. Betts, R. Brugge, K. Hodges, B. Hoskins, M. Miller, L. Steenmanclark and J. Thuburn (1994) Mean climate and transience in the tropics of the UGAMP GCM: Sensitivity to convective parameterization. *Quart. J. Roy. Meteorol. Soc.*, **120**, 881–922.

Slingo, J. M., K. S. Sperber, J. S. Boyle, J. P. Ceren, M. Dix, B. Dugas, W. Ebisuzaki, J. Fyfe, D. Gregory, J. F. Gueremy *et al.* (eds) (1996) Intraseasonal oscillations in 15 atmospheric general circulation models: Results from an AMIP diagnostic subproject. *Climate Dynamics*, **12**, 325–357.

Slingo, J. M., D. P. Rowell, K. R. Sperber and E. Nortley (1999) On the predictability of the interannual behaviour of the Madden–Julian oscillation and its relationship with El Niño. *Quart. J. Roy. Meteorol. Soc.*, **125**, 583–609.

Slingo, J. M. and H. Annamalai (2000) The El Niño of the century and the response of the Indian summer monsoon. *Monthly Weather Review*, **128**, 1778–1797.

Slingo, J. M., P. Inness and K. Sperber (2005) Modeling. In: W. K. M. Lau and D. E. Waliser (eds), *Intraseasonal Variability of the Atmosphere–Ocean Climate System*. Springer-Verlag, Heidelberg, Germany.

Smith, E. A. and L. Shi (1992) Surface forcing of the infrared cooling profile over the Tibetan Plateau. Part I: Influence of relative longwave radiative heating at high altitude. *J. Atmos. Sci.*, **49**, 805–822.

Smith, E. A. and L. Shi (1995) Reducing discrepancies in atmospheric heat budget of Tibetan Plateau by satellite-based estimates of radiative cooling and cloud-radiation feedback. *Meteorol. Atmos. Phys.*, **56**, 229–260.

Smith, I. (2004) An assessment of recent trends in Australian rainfall. *Aust. Meteorol. Mag.*, **53**(3), 163–173.

Smith, R. B. (1985) Comment on 'Interaction of low-level flow with the western Ghat Mountains and offshore convection in the summer monsoon'. *Monthly Weather Review*, **113**, 2176–2177.

Sobel, A. H. and H. Gildor (2003) A simple time-dependent model of SST hot spots. *J. Climate*, **16**, 3978–3992.

Soden, B. J. (2000) The sensitivity of the tropical hydrological cycle to ENSO. *J. Climate*, **13**, 538–549.

Solanki, S. K. (2002) Solar variability and climate change: Is there a link? *Astronomy and Geophysics*, **43**, 5.9–5.13.

Soman, M. K. and K. Krishnakumar (1992) Some aspects of daily rainfall over India during the southwest monsoon season. *Int. J. Climatol.*, **10**, 299–311.

Soman, M. K. and K. Krishnakumar (1993) Space time evolution of meteorological features associated with the onset of the Indian summer monsoon. *Monthly Weather Review*, **121**, 1177–1194.

Soman, M. K. and J. Slingo (1997) Sensitivity of Asian summer monsoon to aspects of sea surface temperature anomalies in the tropical Pacific Ocean. *Quart. J. Roy. Meteorol. Soc.*, **123**, 309–336.

Soon, W. H., E. S. Posmentier and S. L. Baliunas (2000) Climate hypersensitivity to solar forcing? *Annales Geophysicae*, **18**, 583–588.

Sperber, K. R. (2004) Madden–Julian variability in NCAR CAM2.0 and CCSM2.0. *Climate Dynamics*, **23**, 259–278.

Sperber, K. R. and T. N. Palmer (1996) Interannual tropical rainfall variability in general circulation model simulations associated with the Atmospheric Model Intercomparison Project. *J. Climate*, **9**, 2727–2749.

Sperber, K. R., J. M. Slingo, P. M. Inness and W. K. M. Lau (1997) On the maintenance and initiation of the intraseasonal oscillation in the NCEP/NCAR reanalysis and in the GLA and UKMO AMIP simulations. *Climate Dynamics*, **13**, 769–795.

Sperber, K. R., J. M. Slingo and H. Annamalai (2000) Predictability and the relationship between subseasonal and interannual variability during the Asian summer monsoon. *Quart. J. Roy. Meteorol. Soc.*, **126**, 2545–2574.

Sperber, K. R., C. Brankovic, M. Deque, C. S. Frederiksen, R. Graham, A. Kitoh, C. Kobayashi, T. Palmer, K. Puri, W. Tennant *et al.* (2001) Dynamical seasonal predictability of the Asian summer monsoon. *Monthly Weather Review*, **129**, 2226–2248.

Srinivasan, J., V. K. Ramamurty and Y. R. Nene (1973) Discussion of typical synoptic weather situations, summer norwesters and large scale convective activity over the peninsula and central parts of the country. *Forecasting Manual* (Part III). Ind. Meteorol. Dept, Pune, 22 pp.

Srinivasan, J., S. Gadgil and P. J. Webster (1993) Meridional propagation of large-scale monsoon convective zones. *Meteorol. Atmos. Phys.*, **52**, 15–35.

Srivastava, A. K. and K. C. Sinka Ray (1999) Role of CAPE and CINE in modulating convective activities during April over India. *Mausam*, **50**, 257–262.

Staff Members of the Section of Synoptic and Dynamic Meteorology, Institute of Geophysics and Meteorology, Academia Sinica, Peking (1957) On the general circulation over eastern Asia (I). *Tellus*, **9**, 432–446.

Staff Members of the Section of Synoptic and Dynamic Meteorology, Institute of Geophysics and Meteorology, Academia Sinica, Peking (1958a) On the general circulation over eastern Asia (II). *Tellus*, **10**, 58–75.

Staff Members of the Section of Synoptic and Dynamic Meteorology, Institute of Geophysics and Meteorology, Academia Sinica, Peking (1958b) On the general circulation over eastern Asia (III). *Tellus*, **10**, 299–312.

State Science and Technology Commission of China (SSTC) (1990) Climate. *Blue Book of Science and Technology of China* (No. 5). China Meteorol. Press, Beijing, 367 pp.

Stensrud, D. J. (1996) Importance of low-level jets to climate: A review. *J. Climate*, **9**, 1698–1711.

Stephens, G. L. and T. Slingo (1992) An air-conditioned greenhouse. *Nature*, **358**, 369–370.

Stephens, G. L., P. J. Webster, R. H. Johnson, R. Englen and T. L'eculer (2004) Observational evidence for the mutual regulation of the tropical hydological cycle and tropical sea surface temperature. *J. Climate*, **17**, 2213–2224.

Stephenson, D. B., H. Douville and K. Rupa Kumar (2001) Searching for a fingerprint of global warming in the Asian summer monsoon. *Mausam*, **52**, 213–220.

Stern, W. and K. Miyakoda (1995) The feasibility of seasonal forecasts speculated from multiple GCM simulations. *J. Climate*, **8**, 1071–1085.

Stott, L., C. Poulsen, S. Lund and R. Thunell (2002) Super ENSO and global climate oscillations at millennial time scales. *Science*, **297**, 222–226.

Stout, J. R. and J. A. Young (1983) Low-level monsoon dynamics derived from satellite winds. *Monthly Weather Review*, **111**, 774–798.

Straub, K. H. and G. N. Kiladis (2003) Interactions between the boreal summer intraseasonal oscillation and higher-frequency tropical wave activity. *Monthly Weather Review*, **131**, 945–960.

Street-Parrott, F. A. and S. P. Harrison (1984) Temporal variations in lake levels since 30,000 yr. B.P.: An index of the global hydrological cycle. In: J. E. Hansen and T. Takahashi (eds), *Climate Processes and Climate Sensitivity*. American Geophysical Union, Washington, D.C., pp. 118–129.

Stull, R. B. (1988) *An Introduction to Boundary Layer Meteorology*. Kluwer Academic, Dordrecht, 666pp.

Suarez, M. and P. Schopf (1988) A delayed action oscillator for ENSO. *J. Atmos. Sci.*, **45**, 3283–3287.

Sud, Y. C. and G. K. Walker (1992) A review of recent research on improvement of physical parameterizations in the GLA GCM. In: D. R. Sikka and S. S. Singh (eds), *Physical Processes in Atmospheric Models*. Wiley Eastern, pp. 422–479.

Suda, K. and T. Asakura (1955) A study on the unusual 'Baiu' season in 1954 by means of northern hemisphere upper air mean charts. *J. Meteorol. Soc. Japan*, **33**, 233–244.

Sugi, M. (2004) Improving estimation of potential predictability using a multi-model ensemble method. *Proc. Workshop on Ensemble Methods, Exeter, UK*. WGSIP/WGNE/WGCM, CLIVAR, pp. 48–49.

Sugi, M., A. Noda and N. Sato (2002) Influence of the global warming on tropical cyclone climatology: An experiment with the JMA global model. *J. Meteorol. Soc. Japan*, **80**, 249–272.

Suh, M.-S. and D.-K. Lee (2004) Impact of land use/cover changes on surface climate over east Asia for extreme climate cases using RegCM2. *J. Geophys. Res.*, **109**, D020108, doi: 10.1029/2003JD003681.

Sui, C. H. (1992) Multiscale phenomena in the tropical atmosphere over the western Pacific. *Monthly Weather Review*, **120**, 407–430.

Sui, C. H. and K.-M. Lau (1989) Origin of low-frequency (intraseasonal) oscillations in the tropical atmosphere. Part II: Structure and propagation of mobile wave–CISK modes and their modification by lower boundary forcings. *J. Atmos. Sci.*, **46**, 37–56.

Sui, C. H., K.-M. Lau, Y. N. Takayabu and D. A. Short (1997) Diurnal variations in tropical oceanic cumulus convection during TOGA COARE. *J. Atmos. Sci.*, **54**, 639–655.

Sultan, B. and S. Janicot (2003) The West African monsoon dynamics. Part II: The 'preonset' and 'onset' of the summer monsoon. *J. Climate*, **16**, 3407–3427.

Sultan, B., S. Janicot and A. Diedhiou (2003) The West African monsoon dynamics. Part I: Documentation of intraseasonal variability. *J. Climate*, **16**, 3389–3406.

Sumathipala, W. L. and T. Murakami (1988) Intraseasonal fluctuations in low-level meridional winds over the south China Sea and the western Pacific and monsoonal convection over Indonesia and northern Australia. *Tellus*, **A40**, 205–219.

Sumi, A. (1985) Study on cold surges around the Tibetan Plateau by using numerical models. *J. Meteorol. Soc. Japan*, **63**, 377–396.

Sumi, A. and T. Toyota (1988) Observational study on airflow around the Tibetan Plateau. *J. Meteorol. Soc. Japan*, **66**, 113–124.

Sun, D., J. Shaw, Z. An, M. Chen and L. Yue (1998) Magnetostratigraphy and paleoclimatic interpretation of a continuous 7.2 Ma Late Cenozoic eolian sequence from the Chinese Loess Plateau. *Geophys. Res. Lett.*, **25**, 85–88.

Sun, J. H. and S. X. Zhao (2003) A study of special circulation during Meiyu season of the Yangtze River Basin in 1998. *Climatic and Enviromental Research*, **8**, 293–306.

Sun, Y. and Y. H. Ding (2002) Anomalous activities of tropical cyclones over the western North Pacific and related large-scale circulation features during 1998 and 1999. *Acta Meteorol. Sinica*, **60**, 527–537.

Suppiah, R. (1988) Relationship between the Indian Ocean sea surface temperature and the rainfall of Sri Lanka. *Int. J. Climatol.*, **9**, 601–618.

Suppiah, R. (1989) Relationships between the Southern Oscillation and the rainfall of Sri Lanka. *Int. J. Climatol.*, **9**, 601–618.

Suppiah, R. and M. M. Yoshino (1984) Rainfall variations of Srilanka. Part 2: Regional fluctuations. *Arch. Meteorol. Geophys. Bioclim.* Ser A., **35**, 81–92.

Svensmark, H. (1998) Influence of cosmic rays on Earth's climate. *Physical Review Letters*, **81**, 5027–5030.

Sverdrup, H. U. (1947) Wind-driven currents in a baroclinic ocean, with application to the equatorial currents of the eastern Pacific. *Proc. Natl. Acad. Sci. U.S.A.*, **33**, 318–326.

Swallow, J. C. (1980) The Indian Ocean experiment: Introduction. *Science*, **209**, 588–594.

Takahashi, M. (1987) A theory of the slow phase speed of the intraseasonal oscillation using the wave–CISK. *J. Meteorol. Soc. Japan*, **65**, 43–49.

Takahashi, K. and M. M. Yoshino (eds) (1976) *Cimate Change and Food Production*. University of Tokyo Press.

Takata, K. and M. Kimoto (2000) A numerical study on the impact of soil freezing on the continental-scale seasonal cycle. *J. Meteorol. Soc. Japan*, **78**, 199–221.

Tam, C.-Y. (2003) The impact of ENSO on tropical and extratropical atmospheric variability on intraseasonal and synoptic time scales as inferred from observations and GCM simulations. Ph.D. dissertation, Princeton University, 197pp.

Tanaka, A. (1976) Comparisons of rice growth in different environments. In: *Climate and Rice*. The International Rice Research Institute, Los Baños, Philippines, pp. 429–448.

Tanaka, M. (1994) The onset and retreat dates of the austral summer monsoon over Indonesia, Australia and New Guinea. *J. Meteorol. Soc. Japan*, **72**, 255–267.

Tanaka K., H. Ishikawa, T. Hayashi, I. Tamagawa and Y. Ma (2001) Surface energy budget at Amdo on the Tibetan Plateau using GAME/Tibet IOP98 data. *J. Meteorol. Soc. Japan*, **79**, 505–517.

Tanaka K., H. Takizawa, N. Tanaka, I. Kosaka, N. Yoshifuji, C. Tantasirin, S. Piman, M. Suzuki and N. Tangtham (2003) Transpiration peak over a hill evergreen forest in northern Thailand in the late dry season: Assessing the seasonal changes in evapotranspiration using a multilayer model. *J. Geophys. Res.*, **108**(D17), 4533, doi: 10.1029/2002JD003028.

Tanaka K., H. Takizawa, T. Kume, J. Xu, C. Tantasirin and M. Suzuki (2004) Impact of rooting depth and soil hydraulic properties on the transpiration peak of an evergreen forest in northern Thailand in the late dry season. *J. Geophys. Res.*, **109**, D23107, doi: 10.1029/2004JD004865.

Tanaka, M. (1992) Intraseasonal oscillation and onset and retreat dates of the summer monsoon over east, southeast Asia and the western Pacific region using GMS high cloud amount. *J. Meteorol. Soc. Japan*, **70**, 613–629.

Tanimoto, Y., N. Iwasaka, K. Hanawa and Y. Toba (1993) Characteristic variations of sea surface temperature with multiple time scales in the north Pacific. *J. Climate*, **6**, 1153–1160.

Tang, M. and E. R. Reiter (1984) Plateau monsoon of the northern hemisphere: A comparison between North America and Tibet. *Monthly Weather Review*, **112**, 617–637.

Tao, G., L. J. Su, Q. X. Ma, H. Y. Li, X. C. Li and X. Yu (2003) Climate analyses on increasing dust storm frequency in the springs of 2000 and 2001 in Inner Mongolia. *Int. J. Climatol.*, **23**, 1743–1755.

Tao, S. Y. (1955) *A Summary of Activities of Cold Airs in East Asia for Winter Half Year*. Central Meteorol. Observatory of China, Beijing.

Tao, S. Y. and L. Chen (1987) A review of recent research on East Asian summer monsoon in China. In: C.-P. Chang and T. N. Krishnamurti (eds), *Monsoon Meteorology*. Oxford University Press, London, pp. 60–92.

Tao, S. Y. and Y. H. Ding (1981) Observational evidence of the influence of Qinghai Xizang (Tibet) Plateau on the occurrence of heavy rain and severe convective storms in China. *Bull. Amer. Meteorol. Soc.*, **62**, 23–30.

Tao, S. Y. and C. Longxun (1987) A review of recent research on the East Asian summer monsoon in China. *Monsoon Meteorology*. Oxford University Press, UK, pp. 60–92.

Tao, S. Y. and F. K. Zhu (1964) The variation of 100 mb circulation over South Asia in summer and its association with march and withdraw of West Pacific subtropical high. *Acta Meteorol. Sinica*, **34**, 385–395. [In Chinese.]

Tao, S. Y., Q. Y. Zhang and S. L. Zhang (2001) An observational study of the behavior of the subtropical high over the West Pacific Ocean. *Acta Meteorological Sinica,* **59**, 745–758.

Taylor, S. C. (1998) Interactions of large-scale tropical motions systems during the 1996–1997 Australian monsoon. MSc. thesis, Naval Postgraduate School, Monterey, California.

Teng, H. Y. and B. Wang (2003) Interannual variations of the boreal summer intraseasonal oscillation in the Asian-Pacific region. *J. Climate*, **16**, 3572–3584.

Terray, P., S. Dominiak, and P. Delecluse (2005) Role of the southern Indian Ocean in the transitions of the monsoon–ENSO system during recent decades. *Climate Dynamics*, **24**, 169–195.

Thapliyal, V. and S. M. Kulshrestha (1992) Recent models for long-range forecasting of southwest monsoon rainfall in India. *Mausum*, **43**, 239–248.

Thapliyal, V. and M. Rajeevan (2003) Updated operational models for long-range forecasts of Indian summer monsoon rainfall. *Mausam*, **54**, 495–504.

Thompson, L. G., T. Yao, M. E. Davis, K. A. Henderson, E. Mosley-Thompson, P.-N. Lin, J. Beer, H.-A. Synal, J. Cole-Dal and J. F. Bolzan (1997) Tropical climate instability: The last glacial cycle from a Qinghai–Tibetan ice core. *Science*, **276**, 1821–1825.

Thorpe, A., M. Shapiro and R. Langland (2002) Presentation of THORPex Project to WMO/CAS, 13 February, 2002, Oslo. Available online at ⟨*http://www.mmm.ucar.edu/uswrp/powerpoint/thorpex/v3_document.htm*⟩.

Tian, S. C. and C. X. Du (1983) Some statistical features of temperature, humidity and wind during rainstorms in Beijing. *Sci. Atmos. Sinica*, **7**, 68–77.

Tian, S. F. and T. Yasunari (1992) Time and space structure of interannual variations in summer rainfall over China. *J. Meteorol. Soc. Japan*, **70**, 585–596.

Tiedtke, M. (1984) The sensitivity of the time-mean large-scale flow to cumulus convection in the ECMWF model. *Workshop on Convection in Large-scale Numerical Models, ECMWF, 28 November–1 December 1983*, pp. 297–316.

Ting, M. and L. Yu (1998) Steady response to tropical heating in wavy linear and nonlinear baroclinic models. *J. Atmos. Sci.*, **55**, 3565–3582.

Toda, M., K. Nishida, N. Ohte, M. Tani and K. Musiake (2002) Observation of energy fluxes and evapotranspiration over terrestrial complex land covers in the tropical monsoon region. *J. Meteorol. Soc. Japan*, **80**(3), 465–484.

TOGA COARE International Project Office (1994) *TOGA COARE International Data Workshop, Toulouse, France, 2–11 August 1994* (summary report). Univ. Corp. for Atmos. Res., Boulder, Colorado.

Tokioka, T. and A. Noda (1986) Effects of large-scale orography on January atmospheric circulation: A numerical experiment. *J. Meteorol. Soc. Japan*, **64**, 819–840.

Tokioka, T., K. Yamazaki, A. Kitoh and T. Ose (1988) The equatorial 30–60 day oscillation and the Arakawa–Schubert penetrative cumulus parameterization. *J. Meteorol. Soc. Japan*, **66**, 883–901.

Tomas, R. and P. J. Webster (1997) On the location of the intertropical convergence zone and near-equatorial convection: The role of inertial instability. *Quart. J. Roy. Meteorol. Soc.*, **123**, 1445–1482.

Tomas, R., J. R. Holton and P. J. Webster (1999) On the theory of the location of convection in strong cross-equatorial pressure gradient flows. *Quart. J. Roy. Meteorol. Soc.*, **125**, 1107–1127.

Tomita, T. and T. Yasunari (1996) Role of the northeast winter monsoon on the biennial oscillation of the ENSO/monsoon system. *J. Meteorol. Soc. Japan*, **74**, 399–413.

Torrence, C. and G. Compo (1998) A practical guide to wavelet analysis. *Bull. Amer. Meteorol. Soc.*, **79**, 61–78.

Torrence, C. and P. Webster (1998) The annual cycle of persistence in the El Niño/Southern Oscillation. *Quart. J. Roy. Meteorol. Soc.*, **125**, 1985–2004.

Torrence, C. and P. Webster (1999) Interdecadal changes in the ENSO–monsoon system. *J. Climate*, **12**, 2679–2690.

Toth, Z. and E. Kalnay (1993) Ensemble forecasting at NMC: The generation of perturbations. *Bull. Amer. Meteorol. Soc.*, **74**, 2330–2371.

Toyoda, E., H. Niino, K. Tsuboki, K. Kazuhisa, R. Kimura and M. Yoshizaki (1999) Midtropospheric anticyclonic vortex sheet associated with a cloud band near a cold front. *J. Atmos. Sci.*, **56**, 2637–2656.

Treadon, R. E. (1996) Physical initialization in the NMC global data assimilation system. *Meteorol. Atmos. Phys.*, **60**, 57–86.

Treloar, H. M. and A. M. Grant (1953) Some correlation studies of Australian rainfall. *Aust. J. Agric. Res.*, **4**, 423–429.

Trenberth, K. E. (1976) Spatial and temporal variations of the Southern Oscillation. *Quart. J. Roy. Meteorol. Soc.*, **102**, 639–653.

Trenberth, K. E. (1983) What are the seasons? *Bull. Amer. Meteorol. Soc.*, **64**, 1276–1282.

Trenberth, K. E. (1997) Using atmospheric budgets as a constraint on surface fluxes. *J. Climate*, **10**, 2796–2809.

Trenberth, K. E. and J. M. Caron (2001) Estimates of meridional atmosphere and ocean heat transports. *J. Climate*, **14**, 3433–3443.

Trenberth, K. E. and S.-C. Chen (1988) Planetary waves kinematically forced by Himalayan orography. *J. Atmos. Sci.*, **43**, 2934–2948.

Trenberth, K. E. and J. W. Hurrell (1994) Decadal atmosphere–ocean variations in the Pacific. *Climate Dynamics*, **9**, 303–319.

Trenberth, K. E. and D. J. Shea (1987) On the evolution of the Southern Oscillation. *Monthly Weather Review*, **115**, 3078–3096.

Trenberth, K. E. and A. Solomon (1994) The global heat balance: Heat transports in the atmosphere and ocean. *Climate Dynamics*, **10**, 107–134.

Trenberth, K. E. and D. P. Stepaniak (2003a) Co-variability of components of poleward atmospheric energy transports on seasonal and interannual timescales. *J. Climate*, **16**, 3690–3704.

Trenberth, K. E. and D. P. Stepaniak (2003b) Seamless poleward atmospheric energy transports and implications for the Hadley circulation. *J. Climate*, **16**, 3705–3721.

Trenberth, K. E. and D. P. Stepaniak (2004) The flow of energy through the Earth's climate system: Symons Lecture 2004. *Quart. J. Roy. Meteorol. Soc.*, **130**, 2677–2701.

Trenberth, K. E., G. Branstator and P. Arkin (1990) Origin of the 1988 North America drought. *Science*, **42**, 1640–1645.

Trenberth, K. E., D. P. Stepaniak and J. M. Caron (2000) The global monsoon as seen through the divergent atmospheric circulation. *J. Climate*, **13**, 3969–3993.

Trier, S. B., D. B. Parsons and T. J. Matejka (1990) Observations of a subtropical cold front in a region of complex terrain. *Monthly Weather Review*, **118**, 2449–2470.

Troen, I. and L. Mahrt (1986) A simple model of the atmospheric boundary layer: Sensitivity to surface evaporation. *Bound. Layer Meteorol.*, **37**, 129–148.

Troup, A. J. (1965) The Southern Oscillation. *Quart. J. Roy. Meteorol. Soc.*, **91**, 490–506.

Tung, W.-W. and M. Yanai (2002) Convective momentum transport observed during the TOGA-COARE IOP. Part I: General features. *J. Atmos. Sci.*, **59**, 1857–1871.

Tung, W.-W., C. Lin, B. Chen, M. Yanai and A. Arakawa (1999) Basic modes of cumulus heating and drying observed during TOGA-COARE IOP. *Geophys. Res. Lett.*, **26**, 3117–3120.

Tziperman, E., M. A. Cane, S. E. Zebiak, Y. Xue and B. Blumenthal (1998) Locking of El Niño's peak time to the end of the calendar year in the delayed oscillator picture of ENSO. *J. Climate*, **11**, 2191–2199.

Uchiyama, T. and A. Kitoh (2004) Changes in Baiu–Changma–Meiyu rain by global warming in MRI-CGCM. *Proceedings of the International Conference on High-Impact Weather and Climate, 22–24 March 2004, Seoul, Korea*, pp. 218–221.

Ueda, H. and T. Yasunari (1996) Maturing process of summer monsoon over the western North Pacific. *J. Meteorol. Soc. Japan*, **74**, 493–508.

Ueda, H. and T. Yasunari (1998) Role of warming over the Tibetan Plateau in early onset of the summer monsoon over the Bay of Bengal and the South China Sea. *J. Meteorol. Soc. Japan*, **76**, 1–12.

Ueda, H., T. Yasunari and R. Kawamura (1995) Abrupt seasonal change of large-scale convective activity over the western Pacific in the northern summer. *J. Meteorol. Soc. Japan*, **73**, 795–809.

Ueda, H., H. Yamada, J. Horikomi, R. Shirooka, S. Shimizu, L. Liu, K. Ueno, H. Fujii and T. Koike (2001) Characteristics of convective clouds observed by a Doppler radar at

Naqu on Tibetan Plateau during GAME–Tibet IOP. *J. Meteorol. Soc. Japan*, **79**, 463–474.

Ueda, H., H. Kamahori and N. Yamazaki (2003a) Seasonal contrasting features of heat and moisture budgets between the eastern and western Tibetan Plateau during the GAME IOP. *J. Climate*, **16**, 2309–2324.

Ueda, H., M. Shinoda and H. Kamahori (2003b) Spring northward retreat of Eurasian snow cover relevant to seasonal and interannual variations of atmospheric circulation. *Int. J. Climatol.*, **23**, 615–629.

Ueno, K., H. Fujii, H. Yamada and L. Liu (2001) Weak and frequent monsoon precipitation over the Tibetan Plateau. *J. Meteorol. Soc. Japan*, **79**, 419–434.

Uyeda, H., H. Yamada, J. Horikomi, R. Shirooka, S. Shimizu, L. Liu, K. Ueno, H. Fujii and T. Koike (2001) Characteristics of convective clouds observed by a Doppler radar at Naqu on Tibetan Plateau during the GAME–Tibet IOP. *J. Meteorol. Soc. Japan*, **79**, 463–474.

Vaidya, S. S., P. Mukhopadhyay, D. K. Trivedi, J. Sanjay and S. S. Singh (2004) Prediction of tropical systems over Indian region using mesoscale model. *Meteorol. Atmos. Phys.*, **86**, 63–72.

van Campo, E., J. C. Duplessy and M. Rossignol-Strick (1982) Climatic conditions deduced from a 150-kyr oxygen isotope–pollen record from the Arabian Sea. *Nature*, **296**, 56–59.

Vautard, R. and M. Ghil (1989) Singular spectrum analysis in nonlinear dynamics, with applications to paleoclimatic time-series. *Physica D*, **35**, 395–424.

Vecchi, G. A. and D. E. Harrison (2002) Monsoon breaks and subseasonal sea surface temperature variability in the Bay of Bengal. *J. Climate*, **15**, 1485–1493.

Velasco, I. and J. M. Fritsch (1987) Mesoscale convective complexes over the Americas. *J. Geophys. Res.*, **92**, 9591–9613.

Vernekar, A. D., J. Zhou and J. Shukla (1995) The effect of Eurasian snow cover on the Indian monsoon. *J. Climate*, **8**, 248–266.

Verver, G. H. L., D. R. Sikka, J. M. Lobert, G. Stossmeister and M. Zachariasse (2001) Overview of the meteorological conditions and atmospheric transport processes during INDOEX 1999. *J. Geophys. Res.*, **106**, 28399–28413.

Vialard, J. and P. Delecluse (1998) An OGCM study for the TOGA decade. Part II: Barrier layer formation and variability. *J. Phys. Ocean.*, **28**, 1089–1106.

Vinnikov, K. Y. and I. B. Yeserkepova (1991) Soil moisture: Empirical data and model results. *J. Climate*, **4**, 66–79.

Virji, H. (1981) A preliminary study of summer time tropospheric circulation patterns over South America from cloud winds. *Monthly Weather Review*, **109**, 599–610.

Voelker, A. (2002) Global distribution of centennial-scale records for Marine Isotope Stage (MIS) 3: A database. *Quaternary Science Reviews*, **21**, 1185–1212.

Vonder Haar, T. H. and A. H. Oort (1973) New estimate of annual poleward energy transport by the northern hemisphere ocean. *J. Phys. Oceanogr.*, **3**, 169–172.

Von Rad, U., M. Schaaf, K. H. Michels, H. Schulz, W. Berger and F. Sirocko (1999) A 5000-yr record of climate change in varved sediments from the oxygen minimum zone off Pakistan, northeastern Arabian Sea. *Quaternary Research*, **51**, 39–53.

von Storch, H. and J. Xu (1990) Principal oscillation pattern analysis of the 30- to 60-day oscillation in the tropical troposphere. *Climate Dynamics*, **4**, 175–190.

Wacongne, S. and R. C. Pacanowski (1996) Seasonal heat transport in the tropical Indian Ocean. *J. Phys. Ocean.*, **26**, 2666–2699.

Wainer, I. and P. J. Webster (1996) Monsoon/El Niño–Southern Oscillation relationships in a simple coupled ocean–atmosphere model. *J. Geophys. Res.*, **101**, 25599–25614.

Waliser, D. E. (1996) Formation and limiting mechanisms for very high sea surface temperature: Linking the dynamics and the thermodynamics. *J. Climate*, **9**, 161–188.

Waliser, D. E. (2004) Scientific issue topics: Intraseasonal variations. In: C. P. Chang (ed.), *WMO 3rd International Workshop on Monsoons*. [In Press.]

Waliser, D. E., K. M. Lau and J. H. Kim (1999a) The influence of coupled sea surface temperatures on the Madden–Julian oscillation: A model perturbation experiment. *J. Atmos. Sci.*, **56**, 333–358.

Waliser, D. E., C. Jones, J. K. E. Schemm and N. E. Graham (1999b) A statistical extended-range tropical forecast model based on the slow evolution of the Madden–Julian oscillation. *J. Climate*, **12**, 1918–1939.

Waliser, D. E., Z. Zhang, K. M. Lau and J. H. Kim (2001) Interannual sea surface temperature variability and the predictability of tropical intraseasonal variability. *J. Atmos. Sci.*, **58**, 2595–2614.

Waliser, D. E., S. Schubert, A. Kumar, K. Weickmann and R. Dole (2003a) *Proceedings of Workshop on 'Modeling, Simulation and Forecasting of Subseasonal Variability', 4–5 June 2003, University of Maryland, College Park, Maryland* (NASA/TM 2003-104606, Vol. 25, 67 pp.).

Waliser, D. E., R. Murtugudde and L. Lucas (2003b) Indo-Pacific Ocean response to atmospheric intraseasonal variability. Part I: Austral summer and the Madden–Julian oscillation. *J. Geophys. Res.–Oceans*, **108**, doi: 10.1029/2002JC001620.

Waliser, D. E., K. M. Lau, W. Stern and C. Jones (2003c) Potential predictability of the Madden–Julian oscillation. *Bull. Amer. Meteorol. Soc.*, **84**, 33–50.

Waliser, D. E., W. Stern, S. Schubert and K. M. Lau (2003d) Dynamic predictability of intraseasonal variability associated with the Asian summer monsoon. *Quart. J. Roy. Meteorol. Soc.*, **129**, 2897–2925.

Waliser, D. E., K. Jin, I. S. Kang, W. F. Stern, S. D. Schubert, M. L. Wu, K. M. Lau, M. I. Lee, J. Shukla, V. Krishnamurthy *et al.* (2003e) AGCM simulations of intra-seasonal variability associated with the Asian summer monsoon. *Climate Dynamics*, **21**, 423–446.

Waliser, D. E., R. Murtugudde and L. Lucas (2004) Indo-Pacific Ocean response to atmospheric intraseasonal variability. Part II: Boreal summer and the intraseasonal oscillation. *J. Geophys. Res.–Oceans*. [In Press.]

Waliser, D. E., K. Weickmann, R. Dole, S. Schubert, O. Alves, C. Jones, M. Newman, H.-L. Pan, A. Roubicek, S. Saha *et al.* (2005) The Experimental MJO Prediction Project. *Bull. Amer. Meteorol. Soc.* [Submitted.]

Walker, G. T. (1910) Correlation in seasonal variations of weather. *Mem. Indian Meteorol. Dept*, **21**, Part 2, 22–45.

Walker, G. T. (1923) Correlations in seasonal variations of weather. A preliminary study of world weather. *Mem. Indian Meteorol. Dept*, **24**, 75–131.

Walker, G. T. (1924) Correlation in seasonal variations of weather. IX: A further study of world weather. *Mem. Indian Meteorol. Dept*, **24**(9), 275–332.

Walker, G. T. (1928) World weather. Part III. *Mem. R. Meteorol. Soc.*, **4**, 97–106.

Walker, G. T. and E. W. Bliss (1932) World weather. *Mem. Roy. Meteorol. Soc.*, **4**, 53–84.

Walker, G. T. (1933) *Seasonal Weather and Its Prediction* (Rep. 103). British Association for Advancement of Science, pp. 25-44. [Reprinted by Smithsonian Institute in 1935, pp. 117–138].

Wallace, J. M. (1975) Diurnal variations in precipitation and thunderstorm frequency over the conterminous United States. *Monthly Weather Review*, **103**, 406–419.

Wallace, J. M. (1992) Effect of deep convection on the regulation of tropical sea surface temperatures. *Nature*, **357**, 230–231.

Wallace, J. M. and D. S. Gutzler (1981) Teleconnections in the geopotential height field during the Northern Hemisphere Winter. *Mon. Wea. Rev.*, **109**, 784–812.

Wallace, J. M., S. Tibaldi and A. J. Simmons (1983) Reduction of systematic forecast errors in the ECMWF model through the introduction of envelope orography. *Quart. J. Roy. Meteorol. Soc.*, **109**, 683–718.

Wallace, J. M., E. M. Rasmusson, T. P. Mitchell, V. E. Kousky, E. S. Sarachik and H. von Storch (1998) On the structure and evolution of ENSO-related climate variability in the tropical Pacific: Lessons from TOGA. *J. Geophys. Res.*, **103**, 14241–14260.

Walsh, J. E., W. H. Jasperson and B. Ross (1985) Influence of snow cover and soil moisture on monthly air temperature. *Monthly Weather Review*, **113**, 756–768.

Wang, B. (1987) The development mechanism for Tibetan Plateau warm vortices. *J. Atmos. Sci.*, **44**, 2978–2994.

Wang, B. (1988a) Comments on 'An air–sea interaction model of intraseasonal oscillation in the tropics'. *J. Atmos. Sci.*, **45**, 3521–3525.

Wang, B. (1988b) Dynamics of tropical low-frequency waves: An analysis of the moist Kelvin wave. *J. Atmos. Sci.*, **45**, 2051–2065.

Wang, B. (1994) On the annual cycle in the tropical eastern and central Pacific. *J. Climate*, **7**, 1926–1942.

Wang, B. (1995) Interdecadal changes in El Niño onset in the last four decades. *J. Climate*, **8**, 267–258.

Wang, B. L. (1997) An apparent increase in precipitation in June in Northwest China for recent 30 years. *Meteorological Monthly*, **23**, 39–44.

Wang, B. (1998) Coupled modes of the warm pool climate system. Part 1: The role of air–sea interaction in maintaining Madden–Julian oscillation. *J. Climate*, **11**, 2116–2135.

Wang, B. (2004) The Asian monsoon intraseasonal variability: Basic theories. In: K. Lau and D. Waliser (eds), *Intraseasonal Variability of the Atmosphere–Ocean Climate System*. Springer–Praxis, Chichester, UK.

Wang, B. (2005) Theories. In: K. M. Lau and D. E. Waliser (eds), *Intraseasonal Variability of the Atmosphere–Ocean Climate System*. Springer-Verlag, Heidelberg, Germany.

Wang, B. and S.-I. An (2001) Why the properties of El Niño changed in the late 1970s? *Geophys. Res. Lett.,* **28**, 3709–3712.

Wang, B. and J. C. L. Chan (2002) How strong ENSO events affect tropical storm activity over the western North Pacific. *J. Climate*, **15**, 1643–1658.

Wang, B. and J. K. Chen (1989) On the zonal-scale selection and vertical structure of equatorial intraseasonal waves. *Quart. J. Roy. Meteorol. Soc.*, **115**, 1301–1323.

Wang, B. and Z. Fan (1999) Choice of South Asian monsoon indices. *Bull. Amer. Meteorol. Soc.*, **80**(4), 629–638.

Wang, B. and Z. Fang (1996) Chaotic oscillations of tropical: A dynamic system theory for ENSO. *J. Atmos. Sci.*, **53**, 2786–2802.

Wang, B. and X. H. Fu (1997) Northern hemisphere summer monsoon singularities and climatological intraseasonal oscillation. *J. Climate*, **10**, 1071–1085.

Wang, B. and T. Li (1993) A simple tropical atmosphere model of relevance to short-term climate variations. *J. Atmos. Sci.*, **50**, 260–284.

Wang, B. and T. Li (1994) Convective interaction with boundary-layer dynamics in the development of a tropical intraseasonal system. *J. Atmos. Sci.*, **51**, 1386–1400.

Wang, B. and T. Li (2004) East Asian winter monsoon–ENSO interactions. In: C.-P. Chang (ed.), *East Asian Monsoon* (World Scientific Series on Meteorology of East Asia No. 2). World Scientific, Singapore, pp. 117–212.

Wang, B. and H. Lin (2002) Rainy season of the Asian–Pacific summer monsoon. *J. Climate*, **15**, 386–396.

Wang, B. and I. Orlanski (1987) Study of a heavy rain vortex formed over the eastern flank of the Tibetan Plateau. *Monthly Weather Review*, **115**, 1370–1393.

Wang, B. and H. Rui (1990a) Synoptic climatology of transient tropical intra-seasonal convective anomalies. *Meteorol. Atmos. Phys.*, **44**, 43–61.

Wang, B. and H. Rui (1990b) Dynamics of the coupled moist Kelvin–Rossby wave on an equatorial beta-plane. *J. Atmos. Sci.*, **47**, 397–413.

Wang, B. and Y. Wang (1999) Dynamics of the ITCZ–equatorial cold tongue complex and causes of the latitudinal climate asymmetry. *J. Climate*, **12**, 1830–1847.

Wang, B. and X. S. Xie (1996) Low-frequency equatorial waves in sheared zonal flow. Part I: Stable waves. *J. Atmos. Sci.*, **53**, 449–467.

Wang, B. and X. S. Xie (1997) A model for the boreal summer intraseasonal oscillation. *J. Atmos. Sci.*, **54**, 72–86.

Wang, B. and X. S. Xie (1998) Coupled modes of the warm pool climate system. Part I: The role of air–sea interaction in maintaining Madden–Julian Oscillation. *J. Atmos. Sci.*, **11**, 2116–2135.

Wang, B. and Y. Xue (1992) Behavior of a moist Kelvin wave packet with nonlinear heating. *J. Atmos. Sci.*, **49**, 549–559.

Wang, B. and Q. Zhang (2002) Pacific–East Asian teleconnection. Part II: How the Philippine Sea anomalous anticyclone is established during El Niño development. *J. Climate*, **15**, 3252–3265.

Wang, B., R. Wu and R. Lukas (1999) Roles of the western North Pacific wind variation in thermocline adjustment and ENSO phase transition. *J. Meteorol. Soc. Japan*, **77**, 1–16.

Wang, B., R. Wu and X. Fu (2000) Pacific–East Asian teleconnection: How does ENSO affect East Asian climate? *J. Climate*, **13**, 1517–1536.

Wang, B., R. Wu and K.-M. Lau (2001) Interannual variability of the Asian summer monsoon: Contrasts between the Indian and the western North Pacific–East Asian monsoons, *J. Climate*, **14**, 4073–4090.

Wang, B., S. C. Clemens and P. Liu (2003a) Contrasting the Indian and East Asian monsoons: Implications on geologic timescales. *Marine Geology*, **201**, 5–21.

Wang, B., R. Wu and T. Li (2003b) Atmosphere–warm ocean interaction and its impacts on the Asian–Australian monsoon variation. *J. Climate*, **16**, 1195–1211.

Wang, B., I.-S. Kang and J.-Y. Lee (2004a) Ensemble simulations of Asian–Australian monsoon variability during 1997/1998 El Niño by 11 AGCMs. *J. Climate*, **17**, 803–818.

Wang, B., P. J. Webster and H. Teng (2004b) Antecedents and perpetuation of the active-break Indian Monsoon cycles. [Accepted by *J. Climate*.]

Wang, C. and J. Picaut (2004) Understanding ENSO physics: A review. In: C. Wang, S.-P. Xie and J. A. Carton (eds), *Earth's Climate: The Ocean–Atmosphere Interaction* (AGU Monograph No. 147). American Geophysical Union, Washington, D.C., pp. 21–48.

Wang, C.-C. and G. T. J. Chen (2002) Case study of the leeside mesolow and mesocyclone in TAMEX. *Monthly Weather Review*, **130**, 2572–2592.

Wang, C.-C., G. T.-J. Chen and R. E. Carbone (2004) A climatology of warm-season cloud patterns over East Asia based on GMS infrared brightness temperature observations. *Monthly Weather Review*, **132**, 1606–1629.

Wang, H. (2000) The interannual variability of East Asian monsoon and its relationship with SST in a coupled atmosphere–ocean–land climate model. *Adv. Atmos. Sci.*, **17**, 31–47.

Wang, H. (2001) The interannual variability of East Asian monsoon and its relationship with SST in a coupled atmosphere–ocean–land climate model. *Adv. Atmos. Sci.*, **17**, 31–47.

Wang, H. (2002) The instability of the East Asian summer monsoon–ENSO relations. *Adv. Atmos. Sci.*, **19**, 1–11.

Wang, H. and R. Fu (2002) Cross-equatorial flow and seasonal cycle of prediction over South America. *J. Climate*, **15**, 1591–1608.

Wang, J.-J. (2004) Evolution and structure of the mesoscale convection and its environment: A case study during the early onset of the Asian summer monsoon. *Monthly Weather Review*, **132**, 1104–1120.

Wang, L., M. Sarnthein, H. Erlenkeuser, J. Grimalt, P. Grootes, S. Heilig, E. Ivanova, M. Kienast, C. Pelejero and U. Pflaumann (1999a) East Asian monsoon climate during the Late Pleistocene: High-resolution sediment records from the South China Sea. *Marine Geology*, **156**, 245–284.

Wang, L., M. Sarnthein, H. Erlenkeuser, P. M. Groots, J. O. Grimalt, C. Pelejero and G. Linck (1999b) Holocene variations in Asian Monsoon moisture: A bidecadal sediment record from the South China Sea. *Geophys. Res. Lett.*, **26**, 2889–2892.

Wang, L., M. Sarnthein, P. M. Grootes and H. Erlenkeuser (1999c) Millennial reoccurrence of century-scale abrupt events of East Asian monsoon: A possible heat conveyor for the global deglaciation. *Paleoceanography*, **14**, 725–731.

Wang, M. J. and Y. J. Zhou (2000) Weather and forecasting of cold waves in Helongjiang Province. *Helongjiang Meteorology*, **3**, 29–32. [In Chinese.]

Wang, P., S. C. Clemens, L. Beaufort, P. Braconnot, G. Ganssen, Z. Jian, P. Kershaw and M. Sarnthein (2005) Evolution and variability of the Asian monsoon system: State of the art and outstanding issues. *Quaternary Science Reviews*. [In press.]

Wang, W. and M. E. Schesinger (1999) The dependence on convection parameterization of the tropical intraseasonal oscillation simulated by the UIUC 11-layer atmospheric GCM. *J. Climate*, **12**, 1424–1457.

Wang, W., Y. H. Kuo and T. T. Warner (1993) A diabatically driven mesoscale vortex in the lee of the Tibetan Plateau. *Monthly Weather Review*, **121**, 2542–2561.

Wang, W.-C. and K. Li (1990) Precipitation fluctuation over semiarid region in northern China and the relationship with El Niño/Southern Oscillation. *J. Climate*, **3**, 769–783.

Wang, W. Q. and M. E. Schlesinger (1999) The dependence on convection parameterization of the tropical intraseasonal oscillation simulated by the UIUC 11-layer atmospheric GCM. *J. Climate*, **12**, 1423–1457.

Wang, Y. J., B. Wang and J. H. Oh (2001a) Impact of the preceding El Niño on the East Asian summer atmosphere circulation. *J. Meteorol. Soc. Japan*, **79**(1B), 575–588.

Wang, Y. J., H. Cheng, R. L. Edwards, Z. S. An, J. Y. Wu, C.-C. Shen and J. A. Dorale (2001b) A high-resolution absolute-dated Late Pleistocene monsoon record from Hulu Cave, China. *Science*, **294**, 2345–2348.

Wang, Z. L. and L. Fei (1987) *Manual of Typhoon Prediction*. China Meteoro Press, Beijing, 360pp.

Wang, Z. W., P. M. Zhai and H. T. Zhang (2003) Variation of drought over northern China during 1950–2000. *J. Geograph. Sci.*, **13**, 480–487.

Wang, Z. Y. and Y. H. Ding (2004) A study of long-term variations of winter monsoon in China. [To be submitted to *Acta Meteorol. Sinica*.]

Wang, Z. Y., Y. H. Ding, J. H. He and Y. Jun (2004) An updating analysis of the climate change in China in recent 50 years. *Acta Meteorol. Sinica*, **62**, 228–236.

Ward, M. N. and A. Navarra (1997) Pattern analysis of SST-forced variability in ensemble GCM simulations: Examples over Europe and the tropical Pacific. *J. Climate*, **10**, 2210–2220.

Wardle, R. and I. Smith (2004) Modeled response of the Autralian monsoon to changes in land surface temperatures. *Geophys. Res. Lett.*, **21**, L16205, doi: 10.1029/2004GL020157.

Washington, W. M. and S. M. Dagupatty (1975) Numerical simulation with the NCAR global circulation model of the mean conditions during the Asian–African summer monsoon. *Monthly Weather Rev.*, **103**, 105–114.

Washington, W. M., R. M. Chervin and G. V. Rao (1977) Effects of a variety of Indian Ocean surface temperature anomaly patterns on the summer monsoon circulation: Experiments with the NCAR general circulation model. *Pageoph*, **115**, 1335–1356.

Watanabe, H. and Y. Ogura (1987) Effects of orographically forced upstream lifting on mesoscale heavy precipitation: A case study. *J. Atmos. Sci.*, **44**, 661–675.

Watanabe, M. (2004) Asian jet waveguide and a downstream extension of the North Atlantic Oscillation. *J. Climate*, **17**, 4674–4691.

Watanabe, M. and T. Nitta (1998) Relative impacts of snow and sea surface temperature anomalies on an extreme phase in the winter atmospheric circulation. *J. Climate*, **11**, 2837–2857.

Watanabe, M. and T. Nitta (1999) Decadal changes in the atmospheric circulation and associated surface climate variations in the northern hemisphere winter. *J. Climate*, **12**, 494–509.

Watterson, I. G. (2002) The sensitivity of subannual and intraseasonal tropical variability to model ocean mixed layer depth. *J. Geophys. Res.–Atmos.*, **107**, No. D2, doi: 10.1029/2001JD000671.

WCRP (World Climate Research Programme) (1990) *Scientific Plan for the Global Energy and Water Cycle Experiment (GEWEX)* (WMO/TD 376). World Climate Research Programme, World Meteorological Organization, Geneva, 137 pp.

WCRP (World Climate Research Programme) (1995) *CLIVAR: A Study of Climate Variability and Predictability* (WMO/TD 690). World Climate Research Programme, World Meteorological Organization, Geneva, 157 pp.

WCRP (World Climate Research Programme) (1998) *CLIVAR Initial Implementation Plan* (WCRP Report 103, WMO/TD 869). World Climate Research Programme, World Meteorological Organization, Geneva, 195 pp.

Webster, P. J. (1972) Response of the tropical atmosphere to local steady forcing. *Monthly Weather Review*, **100**, 518–540.

Webster, P. J. (1983) Mechanisms of monsoon low-frequency variability: surface hydrological effects. *J. Atmos. Sci.*, **32**, 427–476.

Webster, P. J. (1987) The variable and interactive monsoon. In: J. S. Fein and P. Stephend (eds), *Monsoons*. Wiley, New York, 384 pp.

Webster, P. J. (1994) The role of hydrographic processes in ocean–atmosphere interactions. *Rev. Geophys.*, **32**, 427–476.

Webster, P. J. (2003) Lecture. *Workshop on Climate Forecasting and Applications to Bangladesh, Dhaka.*

Webster, P. J. and C. Hoyos (2004) Forecasting monsoon rainfall and river discharge variability on 20–25 day time scales. *Bull. Amer. Meteorol. Soc.* [In press.]

Webster, P. J. and R. Lukas (1992) TOGA-COARE: The Coupled Ocean–Atmosphere Response Experiment. *Bull. Amer. Meteorol. Soc.*, **73**, 1377–1416.

Webster, P. J. and R. A. Tomas (1997) *An Atlas of Precipitation and Boundary Layer Winds during Intraseasonal Oscillation Events in the Indian Ocean (1985–1995 Extended*

Summer Season) (Technical Report No. 2). Program in Atmospheric and Oceanic Sciences, University of Colorado, Boulder.

Webster, P. J. and S. Yang (1992) Monsoon and ENSO: Selectively interactive systems. *Quart. J. Roy. Meteorol. Soc.*, **118**, 877–926.

Webster, P. J., S. Yang, I. Wainer and S. Dixit (1992) Processes involved in monsoon variability. In: D. R. Sikka and S. S. Singh (eds), *Physical Processes in Atmospheric Models*. Wiley, New Delhi, pp. 492–500.

Webster, P. J., C. A. Clayson and J. A. Curry (1996) Clouds, radiation, and the diurnal cycle of sea surface temperature in the tropical western Pacific. *J. Climate*, **9**, 1712–1730.

Webster, P. J., V. O. Magaña, T. N. Palmer, J. Shukla, R. A. Tomas, M. Yanai and T. Yasunari (1998) Monsoons: Processes, predictability, and the prospects for prediction. *J. Geophys. Res.*, **103**, 14,451–14,510.

Webster, P. J., A. M. Moore, J. P. Loschnigg and R. R. Leben (1999) Coupled ocean–atmosphere dynamics in the Indian Ocean during 1997–1998. *Nature*, **401**, 356–360.

Webster, P. J., C. Clark, G. Cherikova, J. Fasullo, W. Han, J. Loschnigg and K. Sahami (2001a) The monsoon as a self-regulating coupled ocean–atmosphere system. *Meteorology at the Millennium*. Academic Press, New York. [In press.]

Webster, P. J., E. F. Bradley, C. E. Fairall, J. S. Godfrey, P. Hacker, R. A. Houze Jr, R. Lukas, Y. Serra, J. M. Humman, T. D. M. Lawrence *et al.* (2001b) JASMINE: The field phase. [Submitted to *Bull. Amer. Meteorol. Soc.*]

Webster, P. J., E. F. Bradley, C. W. Fairall, J. S. Godfrey, P. Hacker, R. A. Houze Jr, R. Lukas, Y. Serra, J. M. Hummon, T. D. M. Lawrence *et al.* (2002) The JASMINE pilot study. *Bull. Amer. Meteorol. Soc.*, **83**, 1603–1630.

Weedon, G. P. and G. B. Shimmield (1991) Late Pleistocene upwelling and productivity variations in the northwest Indan Ocean deduced from spectral analyses of geochemical data from Sites 722 and 724. *Ocean Drilling Program, Scientific Results*, **117**, 431–444.

Wheeler, M. and H. H. Hendon (2004) An all-season real-time multivariate MJO index: Development of an index for monitoring and prediction. *Monthly Weather Review*, **132**, 1917–1932.

Wheeler, M. and J. L. McBride (2005) Intraseasonal variability of the Australian–Indonesian monsoon region. In: K.-M. Lau and D. E. Waliser (eds), *Intraseasonal Variability of the Atmosphere–Ocean Climate System*. Springer–Praxis, Chichester, UK.

Wheeler, M., G. N. Kiladis and P. J. Webster (2000) Large-scale dynamical fields associated with convectively coupled equatorial waves. *J. Atmos. Sci.*, **57**, 613–640.

Wei, H. and C. Fu (1998) Study of the sensitivity of a regional model in response to land cover change over northern China. *Hydrological Processes*, **12**, 2249–2265.

Wei, J., Q. Y. Zhang and S. Y. Tao (2004) Physical causes of the 1999 and 2000 summer severe drought in North China. *Chinese J. Atmos. Sci.*, **28**, 125–137.

Weickmann, K. M. (1983) Intraseasonal circulation and outgoing longwave radiation modes during northern hemisphere winter. *Monthly Weather Review*, **111**, 1838–1858.

Weickmann, K. M., G. R. Lussky and J. E. Kutzbach (1985) Intraseasonal (30–60 day) fluctuations of outgoing longwave radiation and 250-Mb stream-function during northern winter. *Monthly Weather Review*, **113**, 941–961.

Weisberg, R. H. and C. Wang (1997a) A western Pacific oscillator paradigm for the El Niño–Southern Oscillation. *Geophys. Res. Lett.*, **24**, 779–782.

Weisberg, R. H. and C. Wang (1997b) Slow variability in the equatorial west–central Pacific in relation to ENSO. *J. Climate*, **10**, 1998–2017.

Weller, R. A. and S. P. Anderson (1996) Surface meteorology and air–sea fluxes in the western equatorial Pacific warm pool during the TOGA coupled ocean–atmosphere response experiment. *J. Climate*, **9**, 1959–1990.

Weston, K. J. (1972) The dry-line of northern India and its role in cumulonimbus convection. *Quart. J. Roy. Meteorol. Soc.*, **98**, 519–531.

Wheeler, M. and G. N. Kiladis (1999) Convectively coupled equatorial waves: Analysis of clouds and temperature in the wavenumber–frequency domain. *J. Atmos. Sci.*, **56**, 374–399.

Wheeler, M. and K. M. Weickmann (2001) Real-time monitoring and prediction of modes of coherent synoptic to intraseasonal tropical variability. *Monthly Weather Review*, **129**, 2677–2694.

Wheeler, M. and H. Hendon (2004) An all-season real-time multivariate MJO index: Development of an index for monitoring and prediction. *Monthly Weather Review* [In press.]

Wheeler, M. and J. L. McBride (2005) Australian-Indonesian monsoon region. In: K. M. Lau and D. E. Waliser (eds), *Intraseasonal Variability of the Atmosphere–Ocean Climate System*. Springer-Verlag, Heidelberg, Germany.

Whiteman, D. C., X. Bian and S. Zhong (1997) Low-level jet climatology from enhanced rawinsonde observations at a site in the southern Great Plains. *J. Appl. Meteorol.*, **36**, 1363–1376.

Wijffels, S. E., R. W. Schmitt, H. L. Bryden and A. Stigebrandt (1992) Transport of freshwater by the oceans. *J. Physical Oceanography*, **22**, 155–162.

Wilson, J. D. and M. Mak (1984) Tropical response to lateral forcing with a latitudinally and zonally nonuniform basic state. *J. Atmos. Sci.*, **41**, 1187–1201.

Winkler, C. R., M. Newman and P. D. Sardeshmukh (2001) A linear model of wintertime low-frequency variability. Part I: Formulation and forecast skill. *J. Climate*, **14**, 4474–4494.

WMO (2003) *The Global Climate System Review* (WMO No. 950). World Meteorological Organization, Geneva, 144 pp.

WMO and IRRI (1980) Agrometeorology of the rice crop. *Proc. of the Symposium IRRI, Los Baños, Laguna, Philippines*.

Woodruff, S. D., R. J. Slutz, R. L. Jenne and P. M. Steurer (1987) A comprehensive ocean–atmosphere data set. *Bull. Amer. Meteorol. Soc.*, **68**, 1239–1250.

Woolnough, S. J., J. M. Slingo and B. J. Hoskins (2000) The relationship between convection and sea surface temperature on intraseasonal timescales. *J. Climate*, **13**, 2086–2104.

Wu, B. and R. Huang (1999) Effects of the extremes in the North Atlantic Oscillation on East Asian winter monsoon. *Chinese J. Atmos. Sci.*, **23**, 641–651.

Wu, B. and J. Wang (2002) Possible impacts of winter Arctic oscillation on Siberian high, the East Asian winter monsoon and sea-ice extent. *Adv. Atmos. Sci.*, **19**, 297–320.

Wu, C., S. Yang, A. Wang, and S.-K. Fong (2005) Effect of condensational heating over the Bay of Bengal on the onset of the South China Sea monsoon. *Meteor. Atmos. Physics*, **90**, 37–47.

Wu, G. X. (1984) The nonlinear response of the atmosphere to large-scale mechanical and thermal forcing. *J. Atmos. Sci.*, **41**, 2456–2476.

Wu, G. X. (2004) Recent progress in the study of the Qinghai–Xizhang Plateau Climate Dynamics in China. *Quarternary Science*, **24**(1), 1–9.

Wu, G. X. and Y. M. Liu (2000) Thermal adaptation, overshooting, dispersion and subtropical anticyclone. I: Thermal adaptation and overshooting. *Chinese J. Atmos.*, **24**(4), 433–446.

Wu, G. X. and Liu Yimin (2003) Summertime quadruplet heating pattern in the subtropics and the associated atmospheric circulation. *Geophys. Res. Lett.*, **30**(5), 1201, 1–4.

Wu, G. X. and Zhang Yongsheng (1998) Tibetan Plateau forcing and the timing of the monsoon onset over South Asia and the South China Sea. *Monthly Weather Review*, **126**, 913–927.

Wu, G. X, H. Liu, Y. Zhao and W. Li (1996a) A nine-layer atmospheric general circulation model and its performance. *Adv. Atmos. Sci.*, **13**, 1–18.

Wu, G. X., J. S. Xue, Z. Z. Wang, H. Liu, A. G. He and Y. C. Zhao (1996b) Impacts on seasonal variation of the radiation anomaly associated with the spring snowmelt over the Tibetan Plateau. In: R. H. Huang *et al.* (eds), *Modeling and Prediction of Catastrophic Climate Events*. Chinese Meteorol. Press, pp. 151–161. [In Chinese.]

Wu, G. X, W. Li, H. Guo, H. Liu, J. Xue and Z. Wang (1997a) Sensible heat driven air-pump over the Tibetan Plateau and its impacts on the Asian summer monsoon. In: Ye Duzheng (ed.), *Collections on the Memory of Zhao Jiuzhang*. Chinese Science Press, Beijing, pp. 116–126.

Wu, G. X, X. Zhang *et al.* (1997b) The LASG global ocean–atmosphere–land system model GOALS/LASG and its simulation study. *J. Appl. Meteorol.*, **8**(spec.), 15–28.

Wu, G. X., Y. M. Liu and P. Liu (1999) Spatially inhomogeneous diabatic heating and its impacts on the formation and variation of subtropical anticyclone. I: Scale analysis. *Acta Meteorol. Sinica*, **57**, 257–263.

Wu, G. X., J. F. Chou, Y. M. Liu, J. H. He *et al.* (2002a) *Dynamics of the Formation and Variation of Subtropical Anticyclones*. China Science Press, Beijing, 314 pp.

Wu G. X., Sun Lan, Liu Yimin, Liu Hui, Sun Shufen and Li Weiping (2002b) Impacts of land surface processes on summer climate. In: C. P. Chang *et al.* (eds), *Selected Papers of the Fourth Conference on East Asia and Western Pacific Meteorology and Climate*. World Scientific, Singapore, pp. 64–76.

Wu, G. X., Liu Yimin, Mao Jiangyu, Liu Xin and Li Weiping (2004) Adaptation of the atmospheric circulation to thermal forcing over the Tibetan Plateau. In: Xun Zhu (chief ed.), *Observation, Theory, and Modeling of Atmospheric Variability* (selected papers of Nanjing Institute of Meteorology alumni in commemoration of Professor Jijia Zhang). World Scientific, Singapore, pp. 92–114.

Wu, L. and B. Wang (2004) Assessing impacts of global warming on tropical cyclone tracks. *J. Climate*, **17**, 1686–1698.

Wu, M. C. and J. C. L. Chan (1995) Surface features of winter monsoon surges over South China. *Monthly Weather Review*, **123**, 662–680.

Wu, M. C. and J. C. L. Chan (1997) Upper-level features associated with winter monsoon surges over South China. *Monthly Weather Review*, **125**, 317–340.

Wu, M. L. C., S. Schubert, I. S. Kang and D. E. Waliser (2001) Forced and free intra-seasonal variability over the South Asian monsoon region simulated by 10 AGCMs. *J. Climate*. [Submited.]

Wu, M. L. C., S. Schubert and I. S. Kang (2002) Forced and free intra-seasonal variability over the South Asian monsoon region simulated by 10 AGCMs. *J. Climate*, **15**, 2862–2880.

Wu, R. G. and B. Kirtman (2003a) *Biennial Oscillation of the Monsoon–ENSO System in an Interactive Ensemble Coupled GCM* (Tech. Report CTR 149). COLA, Calverton, Maryland.

Wu, R. G. and B. P. Kirtman (2003b) On the impacts of the Indian summer monsoon on ENSO in a coupled GCM. *Quart. J. Roy. Meteorol. Soc.*, **129**, 3439–3468.

Wu, R. G. and B. P. Kirtman (2004a) Impacts of the Indian Ocean on the Indian summer monsoon–ENSO relationship. *J. Climate*, **17**, 3037–3054.

Wu, R. G. and B. P. Kirtman (2004b) The tropospheric biennial oscillation of the monsoon–ENSO system in an interactive ensemble coupled GCM. *J. Climate*, **17**, 1623–1640.

Wu, R. G. and B. Wang (2000) Interannual variability of summer monsoon onset over the western North Pacific and the underlying processes. *J. Climate*, **13**, 2483–2501.

Wu, R. G. and B. Wang (2001) Multi-stage onset of the summer monsoon over the western North Pacific. *Clim. Dyn.*, **17**, 277–289.

Wu, R. G. and B. Wang (2002) A contrast of the east Asian summer monsoon–ENSO relationship between 1962–1977 and 1978–1993. *J. Climate*, **15**, 3266–3279.

Wu, R. G., Z.-Z. Hu and B. P. Kirtman (2003a) Evolution of ENSO-related rainfall anomalies in East Asia. *J. Climate*, **16**, 3742–3758.

Wu, S. S., J. Y. Lian and C. H. Li (2003b) Relationship between the intensity of South China Sea summer monsoon and the precipitation in raining seasons in China. *J. Tropical Meteorology*, **19**(Suppl.), 25–36.

Wu, T. and Z. Qian (2003) The relation between the Tibetan winter snow and the Asian summer monsoon and rainfall: An observational investigation. *J. Climate*, **16**, 2038–2051.

Wu, W. and R. E. Dickinson (2004) Time scales of layered soil moisture memory in the context of land–atmosphere interaction. *J. Climate*, **17**, 2752–2764.

Wu, X. and M. Yanai (1994) Effects of vertical wind shear on the cumulus transport of momentum: Observations and parameterization. *J. Atmos. Sci.*, **51**, 1640–1660.

Wu, Y., S. Raman and U. C. Mohanty (1999) Numerical investigation of Somali jet interaction with the western Ghat mountains. *Pure Appl. Geophys.*, **154**, 365–396.

Wu, Z. H. (2003) A shallow CISK, deep equilibrium mechanism for the interaction between large-scale convection and large-scale circulations in the tropics. *J. Atmos. Sci.*, **60**, 377–392.

Wu, Z. H. and Y. R. Bei (1982) A comparative analyses of the Ω-shaped energy system prior to occurrence of severe hailstorm and heavy rainfall. *Weather in North China* (No. 3). Beijing University Press, pp. 51–58.

Wyrtki, K. (1956) The rainfall over the Indonesian waters. *Lembaga Meteorologi dan Geofisik, Verhandelingen*, **49**, 24.

Wyrtki, K. (1973) Equatorial jet in Indian Ocean. *Science*, **181**, 264–266.

Wyrtki, K. (1975) El Niño: The dynamic response of the equatorial Pacific Ocean to atmospheric forcing. *J. Phys. Oceanogr.*, **5**, 572–584.

Wyrtki, K. (1985) Water displacements in the Pacific and the genesis of El Niño cycles. *J. Geophys. Res.*, **90**, 11710–11725.

Xiang, X. K. and J. X. Jiang (1995) Mesoscale convective complexes over the southern China mainland. *J. Appl. Meteorol.*, **6**, 9–17.

Xiao, J., S. C. Porter, Z. An, H. Kumai and S. Yoshikawa (1995) Grain size of quartz as an indicator of winter monsoon strength on the Loess Plateau of central China during the last 130,000 yr. *Quaternary Res.*, **43**, 22–29.

Xie, A., Y. Lu and S. J. Chen (1992) Development of the Siberian high prior to outbreak of winter monsoon. *Chinese J. Atmos. Sci.*, **16**, 677–685.

Xie, P. and P. A. Arkin (1996) Analyses of global monthly precipitation using gauge observations, satellite estimates, and numerical model predictions. *J. Climate*, **9**, 840–858.

Xie, P. and P. A. Arkin (1997) Global precipitation: A 17 year monthly analysis based on gauge observations, satellite estimates and numerical model outputs. *Bull. Amer. Meteorol. Soc.*, **78**, 2539–2558.

Xie, S. P. (1997) Unstable transition of the tropical climate to an equatorially asymmetric state in a coupled ocean–atmosphere model. *Monthly Weather Review*, **125**, 667–679.

Xie, S.-P. (2004) Satellite observations of cool ocean–atmosphere interaction. *Bull. Amer. Meteorol. Soc.*, **85**, 195–208.

Xie, S.-P., H. Annamalai, F. A. Schott and J. P. McCreary (2002) Structure and mechanisms of South Indian Ocean climate variability. *J. Climate*, **15**, 864–878.

Xie, S.-P., Q. Xie, D. Wang and W. T. Liu (2003) Summer upwelling in the South China Sea and its role in regional climate variations. *J. Geophys. Res.*, **108**(C8), 3261, doi: 10.1029/2003JC001867.

Xie, X. S. and B. Wang (1996) Low-frequency equatorial waves in vertically sheared zonal flows. Part II: Unstable waves. *J. Atmos. Sci.*, **53**, 3589–3605.

Xu, J. and J. C. L. Chan (2001) The role of the Asian/Australian monsoon system in the onset time of El Niño events. *J. Climate*, **14**, 418–433.

Xu, J. J., Q. G. Zhu and T. H. Zhou (1999) Abruptness and periodicity of the East Asian monsoon in recent 100 years. *J. Appl. Meteorology*, **10**, 1–8.

Xu, L.Y. and G. Gao (2003) Features of typhoon in recent 50 years and study to annual disaster assessment. *Weather and Climate*, **2**, 155–162.

Xu, Y. and M. Zhou (1999) Numerical simulations on the explosive cyclogenesis over the Kuroshio Current. *Adv. Atmos. Sci.*, **16**, 64–76.

Xu, Z. S. and C. J. Neumann (1984) *Frequency and Motion of Western North Pacific Tropical Cyclones* (Tech. Memo. NWS NHC 23). National Oceanic and Atmospheric Administration, Washington, D.C., 80 pp.

Xue Y. (1996) The impact of desertification in the Mongolian and the Inner Monglian grassland on the regional climate. *J. Climate*, **9**, 2173–2189.

Xue, Y., P. J. Sellers, J. L. Kinter and J. Shukla (1991) A simplified biosphere model for global climate studies. *J. Climate*, **4**, 345–364

Xue, Y., F. J. Zeng and C. A. Schlosser (1996) SSiB and its sensitivity to soil properties: A case study using HAPEX-Mobilhy data. *Global Planet. Change*, **13**, 183–194.

Xue, Y., H.-M. H. Juang, W.-P. Li, S. Prince, R. DeFries, Y. Jiao and R. Vasic (2004) Role of land surface processes in monsoon development: East Asia and West Africa. *J. Geophys. Res.*, **109**, D03105, doi: 10.1029/2003JD003556.

Yamada, H. and H. Uyeda (2004) Transition of the precipitation process over the central Tibetan Plateau during the summer of 1998. [Submitted to *Monthly Weather Review*]

Yamada, H., B. Geng, K. K. Reddy, H. Uyeda and Y. Fujiyoshi (2003) Three-dimensional structure of a mesoscale convective system in a Baiu-frontal depression generated in the downstream region of the Yangtze River. *J. Meteorol. Soc. Japan*, **81**, 1243–1271.

Yamasaki, M. (1969) Large-scale disturbances in conditionally unstable atmosphere in low latitudes. *Papers in Meteorology and Geophysics*, **20**, 289–336.

Yamazaki, K. (1989) A study of the impact of soil moisture and surface albedo changes on global climate using the MRI.GCM. *J. Meteorol. Soc. Japan*, **67**, 123–146.

Yan, H. M., W. Duan and Z. N. Xiao (2003) A study on relation between the East Asian winter monsoon and climate change during rainy seasons in China. *J. Tropical Meteorol.*, **19**, 367–376.

Yanai, M. (1961) Dynamical aspects of typhoon formation. *J. Meteorol. Soc. Japan*, **39**, 283–309.

Yanai, M. and R. H. Johnson (1993) Impacts of cumulus convection on thermodynamic fields. *Representation of Cumulus Convection in Numerical Models, Meteorol. Monogr.*, **46**, Amer. Meteorol. Soc., 39–62.

Yanai, M. and C. Li (1994) Mechanism of heating and the boundary layer over the Tibetan Plateau. *Monthly Weather Review*, **122**, 305–323.

Yanai, M., S. Esbensen and J.-H. Chu (1973) Determination of bulk properties of tropical cloud clusters from large-scale heat and moisture budgets. *J. Atmos. Sci.*, **30**, 611–627.

Yanai, M., S. Esbensen and J.-H. Chu (1973) Determination of bulk properties of tropical cloud clusters from large-scale heat and moisture budgets. *J. Atmos. Sci.*, **30**, 611–627.

Yanai, M., C. Li and Z. Song (1992) Seasonal heating of the Tibetan Plateau and its effects on the evolution of the Asian summer monsoon, *J. Meteorol. Soc. Japan*, **70**, 319–351.

Yanai, M., B. Chen and W.-W. Tung (2000) The Madden–Julian oscillation observed during the TOGA COARE IOP: Global view. *J. Atmos. Sci.*, **57**, 2374–2396.

Yang, G. Y. and J. Slingo (2001) The diurnal cycle in the tropics. *Monthly Weather Review*, **129**, 784–801.

Yang G., Wang Xingdong and Wang Guifang (1980) An annulus experimental simulation of the influence of the Chinghai–Tibetan Plateau on the wind field over its adjacent regions in winter. *Acta Meteorol. Sinica*, **38**(1), 16–26.

Yang, K., T. Koike and D. Yang (2003) Surface flux parameterization in the Tibetan Plateau. *Bound. Layer Meteorol.*, **106**, 245–262.

Yang, K., T. Koike, H. Ishikawa and Y. Ma (2004a) Analysis of the surface energy budget at a site of GAME/Tibet using a single-source model. *J. Meteorol. Soc. Japan*, **82**, 131–153.

Yang, K., T. Koike, H. Fujii, T. Tamura, X. Xu, I. Bian and M. Zhou (2004b) The daytime evolution of the atmospheric boundary layer and convection over the Tibetan Plateau: Observations and simulations. *J. Meteorol. Soc. Japan*, **82**, 1777–1792.

Yang, S. (1996) ENSO–snow–monsoon associations and seasonal–interannual predictions. *Int. J. Climatol.*, **16**, 125–134.

Yang, S. and W. J. Gutowski (1992) On the relationship between tropical Chinese rainfall and the Indian summer monsoon. *J. Meteorol. Soc. Japan*, **70**, 997–1004.

Yang, S. and W. J. Gutowski (1994) GCM simulations of the three-dimensional propagation of stationary waves. *J. Climate*, **7**, 414–433.

Yang, S. and K.-M. Lau (1998) Influences of sea surface temperature and ground wetness on Asian summer monsoon. *J. Climate*, **11**, 3230–3246.

Yang, S. and W. K. M. Lau (2006) Interannual variability of the Asian monsoon. In: B. Wang (ed), *The Asian Monsoon*. Springer–Praxis, Chichester, UK.

Yang, S. and P. J. Webster (1990) The effect of tropical heating in the adjacent hemisphere on the extratropical westerly jet stream. *J. Geophys. Res.*, **95**, 18705–18721.

Yang, S. and L. Xu (1994) Linkage between Eurasian snow cover and regional Chinese rainfall. *Int. J. Climatol.*, **14**, 739–750.

Yang, S., P. J. Webster and M. Dong (1992) Longitudinal heating gradient: Another possible factor influencing the intensity of the Asian summer monsoon circulation. *Adv. Atmos. Sci.*, **9**, 397–410.

Yang, S., K.-M. Lau and M. Sankar-Rao (1996) Precursory signals associated with the interannual variability of the Asian summer monsoon. *J. Climate*, **9**, 949–964.

Yang, S., K.-M. Lau and K.-M. Kim (2002) Variations of the East Asian jet stream and Asian–Pacific–American winter climate anomalies. *J. Climate*, **15**, 306–325.

Yang, S., K.-M. Lau, S.-H. Yoo, J. L. Kinter, K. Miyakoda and C.-H. Ho (2004) Upstream subtropical signals preceding the Asian summer monsoon circulation. *J. Climate*, **17**, 4213–4229.

Yang, W. Y., D. Z. Ye and G. X. Wu (1992b) Diagnosis study on the heating and circulation over the Tibetan Plateau in summer season. III: Mechanism for the maintenance of circulation. *Chinese J. Atmos.*, **16**(4), 409–426.

Yang, Y. M., Y. G. Zheng and Z. Y. Tao (2003) Analysis of tropical depression rainstorm in Shanghai. *J. Appl. Meteorol.*, **19**, 411–421.

Yang, Y. W (2001) The different effect of two types of blocking situation on major seasonal rain belt in China in July. *Acta Meteorologica Sinica*, **59**, 759–767.

Yano, J. and K. Emanuel (1991) An improved model of the equatorial troposphere and its coupling with the stratosphere. *J. Atmos. Sci.*, **48**, 377–389.

Yasunari, T. (1979) Cloudiness fluctuation associated with the northern hemisphere summer monsoon. *J. Meteorol. Soc. Japan*, **57**, 227–242.

Yasunari, T. (1980) A quasi-stationary appearance of the 30–40 day period in the cloudiness fluctuations during the summer monsoon over India. *J. Meteorol. Soc. Japan*, **58**, 225–229.

Yasunari, T. (1981) Structure of an Indian summer monsoon system with around 40-day period. *J. Meteorol. Soc. Japan*, **59**, 336–354.

Yasunari, T. (1985) Zonally propagating modes of the global east–west circulation associated with the Southern Oscillation. *J. Meteorol. Soc. Japan*, **63**, 1013–1029.

Yasunari, T. (1987) Global structure of the El Niño/Southern Oscillation. Part I: Time revolution. *J. Meteorol. Soc. Japan*, **65**, 81–102.

Yasunari, T. (1990) Impact of Indian monsoon on the coupled atmosphere/ocean system in the tropical Pacific. *Meteorol. Atmos. Phys.*, **44**, 29–41.

Yasunari, T. (1991) The monsoon year: A new concept of the climate year in the tropics. *Bull. Amer. Meteorol. Soc.*, **72**, 1331–1338.

Yasunari, T. and A. Kozawa (2005) Time–space characteristics of atmospheric water balance over Eurasia. [To be submitted to *J. Hydrometeor.*]

Yasunari, T. and Y. Seki (1992) Role of the Asian monsoon on the interannual variability of the global climate system, *J. Meteorol. Soc. Japan*, **70**, 177–188.

Yasunari, T., A. Kitoh and T. Tokioka (1991) Local and remote responses to excessive snow mass over Eurasia appearing in the northern spring and summer climate: A study with the MRI GCM. *J. Meteorol. Soc. Japan*, **69**, 473–487.

Yasunari, T., K. Saito and K. Takata (2005) Relative roles of large-scale orography and vegetation on global hydro-climate. Part I: Impacts on monsoon systems and tropics. [To be submitted to *J. Hydrometeor.*]

Ye, Duzheng (1981) Some characteristics of the summer circulation over the Qinghai–Xizang (Tibet) Plateau and its neighborhood. *Bull. Amer. Meteorol. Soc.*, **62**, 14–19.

Ye, Duzheng (1982) Some aspects of the thermal influences of the Qinghai–Tibetan Plateau on the atmospheric circulation. *Arch. Meteorol. Geophys. Biocl.*, **A31**, 205–220.

Ye, Duzheng and C.-C. Chang (1974) A preliminary experimental simulation on the heating effect of the Tibetan Plateau on the general circulation over eastern Asia in summer. *Sci. Atmos. Sinica*, **17**, 397–420.

Ye, D. Z. and D. Y. Gao (1979a) *The Influence on the Atmosphere of the Heating of Mount Qomolangma during Spring and Summer* (Report of Science Expedition to Mount Qomolangma in 1975). Meteorology and Environment, Chinese Science Press, Beijing.

Ye, Duzheng and Y. X. Gao (1979b) *Meteorology of the Qinghai–Xizang Plateau*. Chinese Science Press, Beijing, 278pp. [In Chinese.]

Ye, Duzheng and R. H. Huang (1991) Progress achievement and problems of study on cause and prediction of droughts and floods in Yellow River and the Yangtze River Basins. *Earth Science Advance*, **6**, 24–29.

Ye, Duzheng and R. H. Huang (1996) *Study on the Regularity and Formation Reason of Drought and Flood in the Yangtze and Huaihe River Regions*. Shandong Science and Technology Press, 387pp. [In Chinese.]

Ye, Duzheng and G. J. Yang (1979) The mean vertical circulation over the region of eastern Asia and Pacific Ocean (I): Summer. *Sci. Atmos. Sinica*, **3**, 1–11. [In Chinese.]

Ye, Duzheng and G. J. Yang (1981) The average summer vertical circulation to the south of 45°N of northern hemisphere and its relation to the distribution of heat sources and sinks in the atmosphere. *Acta Meteorol. Sinica*, **39**, 28–35. [In Chinese.]

Ye, Duzheng and G.-X. Wu (1998) The role of the heat source of the Tibetan Plateau in the general circulation. *Meteorol. Atmos. Phys.*, **67**, 181–198.

Ye, Duzheng, Li Jishun and Gao Dengyi (1974) *The Impact on the Maintenance of the Mean Summer Circulation of the Convectivity over Tibetan Plateau* (Collection of Tibetan Plateau Meteorology). Meteorology Press, Beijing, pp. 19–28. [In Chinese.]

Ye, Duzheng, G. J. Yang and X. D. Wang (1979) The mean vertical circulation over the region of eastern Asia and Pacific Ocean (II): Winter. *Sci. Atmos. Sinica*, **3**, 299–305. [In Chinese.]

Ye, H. and Z. Bao (2001) Lagged teleconnections between snow depth in northern Eurasia, rainfall in southeast Asia and sea-surface temperature over the tropical Pacific Ocean. *Int. J. Climatol.*, **21**, 1607–1621.

Yeh, T. C. (1949) On energy dispersion in the atmosphere. *J. Meteorol.*, **6**, 1–16.

Yeh, Tu-cheng (1950) The circulation of high troposphere over China in winter of 1945–1946. *Tellus*, **2**, 173–183.

Yeh, Tu-cheng (1952) The seasonal variation of the influence of Tibetan Plateau on the general circulation. *Acta Meteorol. Sinica*, **23**, 33–47. [In Chinese.]

Yeh, Tu-cheng, Y. H. Kao and K. N. Liu (1951) A study of the onset and retreat of the jet stream over southern Asia and SW United States of America in 1945–1946. *Acta Meteorol. Sinica*, **22**, 44–45. [In Chinese.]

Yeh, Tu-cheng, S.-W. Lo and P.-C. Chu (1957) The wind structure and heat balance in the lower troposphere over Tibetan Plateau and its surrounding. *Acta Meteorol. Sinica*, **28**, 108–121. [In Chinese.]

Yeh, Tu-cheng, S.-Y. Dao and M.-T. Li (1959) The abrupt change of circulation over the northern hemisphere during June and October. In: B. Bolin (ed.), *The Atmosphere and the Sea in Motion* (Scientific Contributions to the Rossby Memorial Volume). Rockefeller Institute Press, pp. 249–267.

Yi, Q. and Y. Ding (1992) A dynamic study of two explosively deepening cyclones over the East China Sea. *Acta Meteorol. Sinica*, **50**, 152–166. [In Chinese with English abstract.]

Yin, M. T. (1949) A systematic aerological study of onset of the summer monsoon over India and Burma. *J. Meteorol.*, **6**, 393–400.

Yiou, P., K. Fuhrer, L. D. Meeker, J. Jouzel, S. Johnsen and P. Mayewski (1997) Paleoclimatic variability inferred from the spectral analysis of Greenland and Antarctic ice-core data. *J. Geophys. Res.*, **102**(C12), 26441–26454.

Yoo, S.-H., C.-H. Ho, S. Yang, H.-J. Choi and J.-G. Jhun (2004) Influences of tropical–western and extratropical Pacific SSTs on the East and Southeast Asian climate in the summers of 1993–1994. *J. Climate*, **17**, 2673–2687.

Yoo, S.-H., S. Yang, and C.-H. Ho (2005) Variability of the Indian Ocean SST and its possible climate impact. *J. Geophys. Res.* [Accepted.]

Yoshimura, J., K. Oouchi, H. Yoshimura, R. Mizuta and A. Noda (2004) Tropical cyclone simulation by a 20-km mesh global atmospheric model: Influence of global warming (a

quick report). *Abstract of the Meeting of the Meteorol. Soc. Japan, October 2004, Fukuoka, Japan.* [In Japanese.]

Yoshimura, J., M. Sugi and A. Noda (2005) Influence of greenhouse warming on tropical cyclone frequency. [Submitted to *J. Meteorol. Soc. Japan*.]

Yoshino, M. M. (1965) Four stages of the rainy season in early summer over East Asia (Part I). *J. Meteorol. Soc. Japan*, **43**, 231–245.

Yoshino, M. M. (1966) Four stages of the rainy season in early summer over East Asia (Part II). *J. Meteorol. Soc. Japan*, **44**, 209–217.

Young, J. A. (1987) Physics of Monsoon: The current view. In: Fein and Stephens (eds), *Monsoon*. John Willey & Sons, New York, pp. 211–243.

Yu, L. and M. Rienecker (1999) Mechanisms for the Indian Ocean warming during the 1997–1998 El Niño. *Geophys. Res. Lett.*, **26**, 735–738.

Yu, L. S. and M. M. Rienecker (2000) Indian Ocean warming of 1997–1998. *J. Geophys. Res.–Oceans*, **105**, 16923–16939.

Yu, J.-Y., S.-P. Weng and J. D. Farrara (2003) Ocean roles in the TBO transitions of the Indian–Australian monsoon system. *J. Climate*, **16**, 3072–3080.

Yumoto, M. and T. Matsuura (2001) Interdecadal variability of tropical cyclone activity in the western North Pacific. *J. Meteorol. Soc. Japan*, **79**, 23–35.

Yun, W. T., L. Stefanova and T. N. Krishnamurti (2003) Improvement of the multimodel superensemble technique for seasonal forecasts. *J. Climate*, **22**, 3834–3840.

Yun, W. T., L. Stefanova, A. K. Mitra, T. S. V. V. Kumar, W. Dewar and T. N. Krishnamurti (2004) Multimodel synthetic superensemble algorithm for seasonal climate prediction using DEMETER forecasts. *Tellus*. [In press.]

Zangvil, A. (1975) Temporal and spatial behavior of large-scale disturbances in tropical cloudiness deduced from satellite brightness data. *Monthly Weather Review*, **103**, 904–920.

Zebiak, S. E. and M. A. Cane (1987) A model of El Niño–Southern Oscillation. *Monthly Weather Review*, **115**, 2262–2278.

Zeng, H. L., S. Q. Gao and S. G. Dai (2002) An analysis of interdecadal variation in sea-level pressure and 500 hPa fields in winter and summer over the last 20 years. *Meteor*, **21**, 66–73.

Zeng. N. (1998) Understanding climate sensitivity to tropical deforestation in a mechanistic model. *J. Climate*, **11**, 1969–1975.

Zeng. N., R. Dickinson and X. Zeng (1996) Climatic impact of Amazon deforestation: A mechanistic model study. *J. Climate*, **9**, 859–883.

Zhang, C. D. (1996) Atmospheric intraseasonal variability at the surface in the tropical western Pacific Ocean. *J. Atmos. Sci.*, **53**, 739–758.

Zhang, C. D. and H. H. Hendon (1997) Propagating and standing components of the intraseasonal oscillation in tropical convection. *J. Atmos. Sci.*, **54**, 741–752.

Zhang, C., H. H. Hendon, W. S. Kessler and A. Rosati (2001) A workshop on the MJO and ENSO. *Bull. Amer. Meteorol. Soc.*, **82**, 971–976.

Zhang, D. L. and J. M. Fritsch (1987) Numerical simulation of the meso-α-scale structure and evolution of the 1977 Johnstown Flood. Part II: Inertially stable warm-core vortex and the mesoscale convective complex. *J. Atmos. Sci.*, **44**, 2593–2612.

Zhang, G. J. (1994) Effects of cumulus convection on the simulated monsoon circulation in a general circulation model. *Monthly Weather Review*, **122**, 2022–2038.

Zhang, J. J. *et al.* (1988) *Advances in the Qinghai–Xizang Plateau Meteorology: The Qinghai–Xizang Meteorology Experiment (QXPMEX, 1979) and Research*. Chinese Science Press, Beijing, 268pp.

Zhang, L., G. Y. Reng and Y. H. Ding (2004) Long-term trend of sandstorm occurrence in North China and their climate cause. *Acta Meteorol. Sinica*. [Accepted.]

Zhang, P., S. Yang, and V. E. Kousky (2005) Remote influence of the Asian summer monsoon on Asian–Pacific–American climate. *Advances in Atmos. Sci.* [In press.]

Zhang, P. Z. and G. M. Chen (1999) A statistical study of cold highs affecting outbreaks of cold air in China. *Acta Meteorol. Sinica*, **16**, 312–325.

Zhang, Q., G. X. Wu and Q. Yongfu (2002) The bimodality of the 100 hPa South Asia high and its relationship to the climate anomaly over East Asia in summer. *J. Meteorol. Soc. Japan*, **80**(4), 733–744.

Zhang, Q. Y., S. Y. Tao and S. L. Zhang (2003) The persistent heavy rainfall over the Yangtze River Valley and its associations with the circulation over East Asia during summer. *Chinese J. Atmos. Sci.*, **27**, 1019–1030.

Zhang, R., A. Sumi and M. Kimoto (1996) Impact of El Niño on the East Asian monsoon: A diagnostic study of the '86/87 and '91/92 events. *J. Meteorol. Soc. Japan*, **74**, 49–62.

Zhang, X. H., K. M. Chen *et al.* (1996) Simulation of thermohaline circulation with a twenty layer oceanic general circulation model. *Theo. Appl. Climatol.*, **55**, 65–88.

Zhang, X. H., G. Y. Shi, H. Liu and Y. Q. Yu (2000) *IAP Global Ocean–Atmosphere–Land System Model*. Science Press, Beijing, 252pp.

Zhang, Y., J. M. Wallace and D. S. Battisti (1997a) ENSO-like interdecadal variability: 1900–1993. *J. Climate*, **10**, 1004–1020.

Zhang, Y., K. R. Sperber and J. S. Boyle (1997b) Climatology and interannual variation of the East Asian winter monsoon: Results from the 1979–1995 NCEP/NCAR Reanalysis. *Monthly Weather Review*, **125**, 2605–2619.

Zhang, Y., T. Li. and B. Wang (2004) Decadal change of the spring snow depth over the Tibetan Plateau: The associated circulation and influence on the East Asian summer monsoon. *J. Climate*, **17**, 2780–2793.

Zhang, Z. and T. N. Krishnamurti (1996) A generalization of Gill's heat-induced tropical circulation. *J. Atmos. Sci.*, **53**, 1045–1052.

Zhang, Z. Q., C. L. J. Chan and Y. H. Ding (2004) Characteristics, evolution and mechanisms of the summer monsoon onset over Southeast Asia. *Int. J. Climatol.* [Accepted.]

Zhao, H. G., X. G. Zhang and Y. H. Ding (1989) The El Niño and anomalous climate in China. *Acta Meteorol. Sinica*, **3**, 471–481.

Zhao, Q. (1997) A prognostic cloud scheme for operational NWP models. *Monthly Weather Review*, **125**, 1931–1953.

Zhao, Z. G. (1999) *Summer Droughts and Floods in China and Environmental Fields*. China Meteorological Press, Beijing.

Zhao, Z. and W. W. Kellogg (1988) Sensitivity of soil moisture to doubling of carbon dioxide in climate model experiments. Part II: The Asian monsoon region. *J. Climate*, **1**, 367–378.

Zhao, Z., A. Kitoh and D.-K. Lee (2004) Regional aspects of global warming in East Asia as the consequence of increasing of greenhouse gases. In: C. Fu (ed.), *Changes in the Human–Monsoon System of East Asia in the Context of Global Change*. John Wiley & Sons, New York, 297 pp.

Zheng, Q. and K.-N. Liou (1986) Dynamic and thermodynamic influences of the Tibetan Plateau on the atmosphere in a general circulation model. *J. Atmos. Sci.*, **43**, 1340–1354.

Zheng, X. J., S. Y. Tao, J. G. Luo and F. K. Zhu (2001) Characteristics of meso-scale cloud cluster during torrential rain process in Wuhan on 21–22 July 1998. *Acta Meteorol. Sinica*, **59**, 625–632.

Zheng, Y., D. E. Waliser, W. F. Stern and C. Jones (2004) The role of coupled sea surface temperatures in the simulation of the tropical intraseasonal oscillation. *J. Climate*, **17**, 4109–4134.

Zhou, L. T. and R. H. Huang (2003) Research on the characteristics of interdecadal variability of summer climate in China and its possible cause. *Climatic and Environmental Research*, **8**, 274–289.

Zhou, M. *et al.* (2000) *Observational, Analytical, and Dynamic Study of the Atmospheric Boundary Layer of the Tibetan Plateau*. Meteorology Press, Beijing, 125pp. [In Chinese.]

Zhu, Q., J. He and P. Wang (1986) A study of circulation differences between East-Asian and Indian summer monsoons with their interaction. *Adv. Atmos. Sci.*, **4**, 466–477.

Zhu, Y. and D. D. Houghton (1996) The impact of Indian Ocean SST on the large-scale Asian summer monsoon and the hydrological cycle. *Int. J. Climatol.*, **16**, 617–632.

Ziegler, A. D., J. Sheffield, E. P. Maurer, B. Nijssen, E. F. Wood and D. P. Lettenmaier (2003) Detection of intensification in global- and continental-scale hydrological cycles: Temporal scale of evaluation. *J. Climate*, **16**, 535–547.

Zipser, E. J. (1977) Mesoscale and convective-scale downdrafts as distinct components of squall line structure. *Monthly Weather Review*, **105**, 1568–1589.

Zuidema, P. (1998) On the 600–800-mb minimum in tropical cloudiness. *J. Atmos. Sci.*, **55**, 2220–2228.

Zveryaev, I. I. (2002) Interdecadal changes in the zonal wind and the intensity of intraseasonal oscillations during boreal summer Asian monsoon. *Tellus*, **54A**, 288–298.

Zwiers, F. W. (1993) Simulation of the Asian summer monsoon with the CCC GCM-1. *J. Climate*, **6**, 470–486.

Zwiers, F. W. (1996) Interannual variability and predictability in an ensemble of AMIP climate simulations conducted with the CCC GCM2. *Climate Dynamics*, **12**, 825–848.

Index

Colour plates

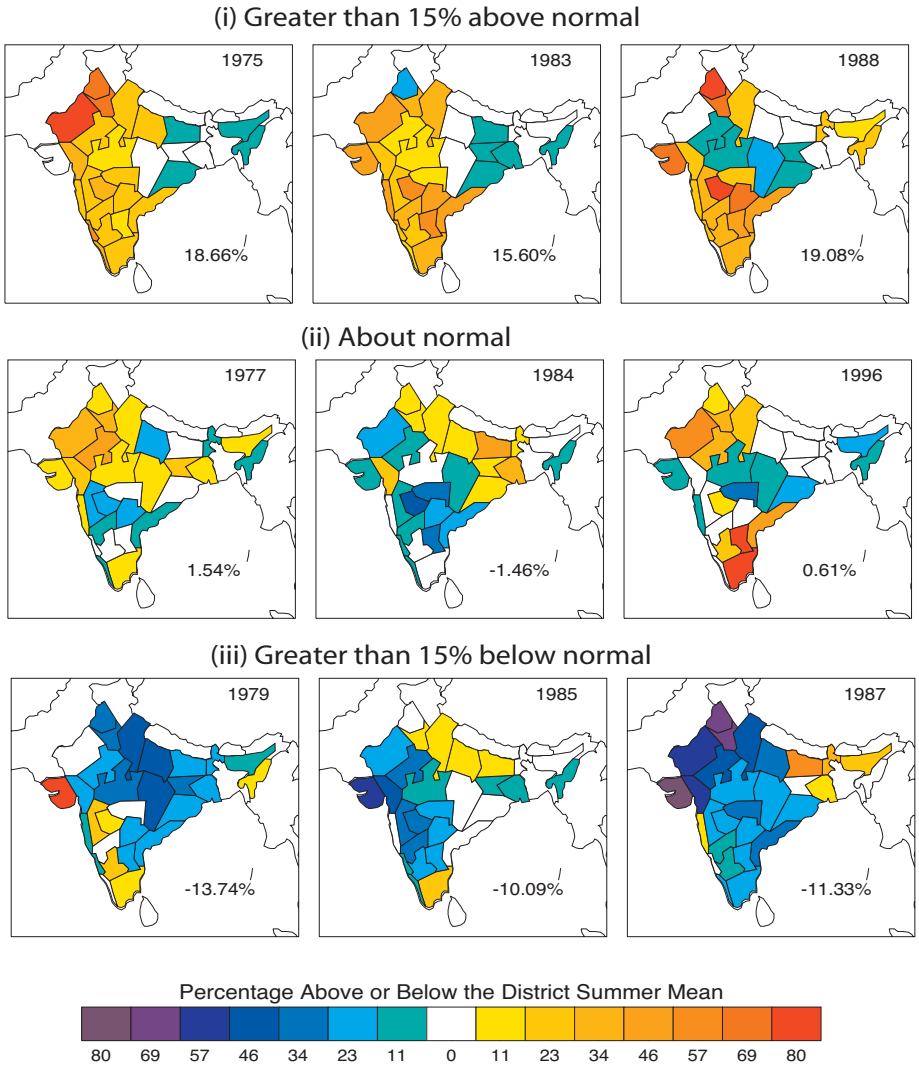

Figure 1.5. (b) Spatial variability of rainfall (% of district summer average) for years where the all-India seasonally precipitation averaged was (i) >115%, (ii) approximately normal and, (iii) <90%. Irrespective of category, there is great spatial variability throughout India.
Data provided courtesy of Dr. Rupa Kumar Kolli of the Institute of Tropical Meteorology, Pune, India.
From Webster and Hoyos (2004).

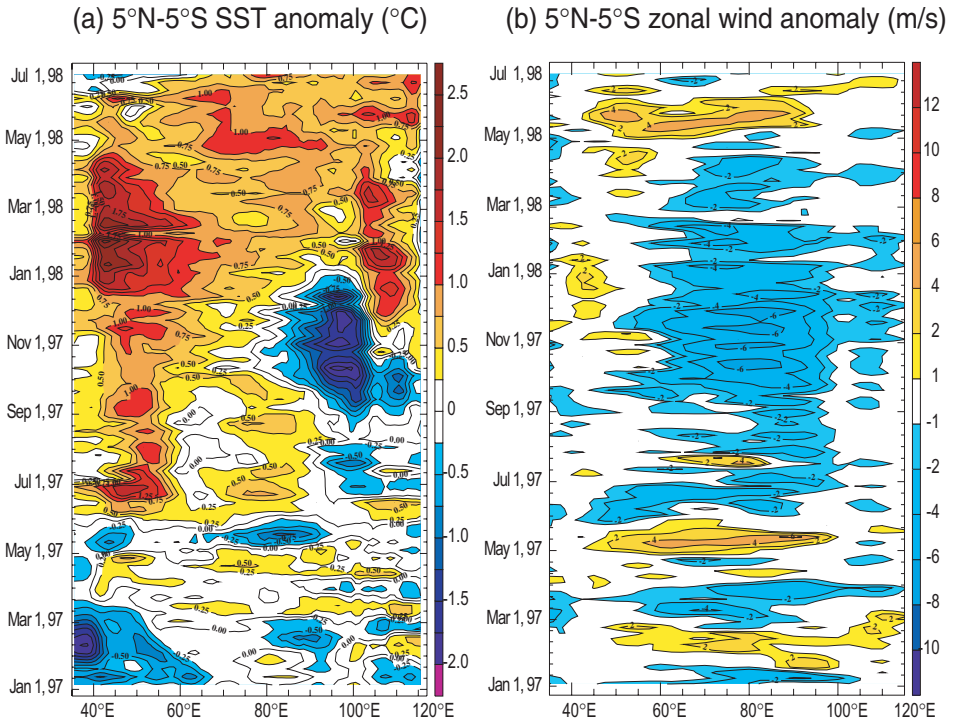

Figure 1.19. Time–longitude sections of (a) the SST and (b) the zonal wind anomaly averaged between 5°N and 5°S for the period January 1997 through July 1998. Units are °C and m s^{-1}, respectively.

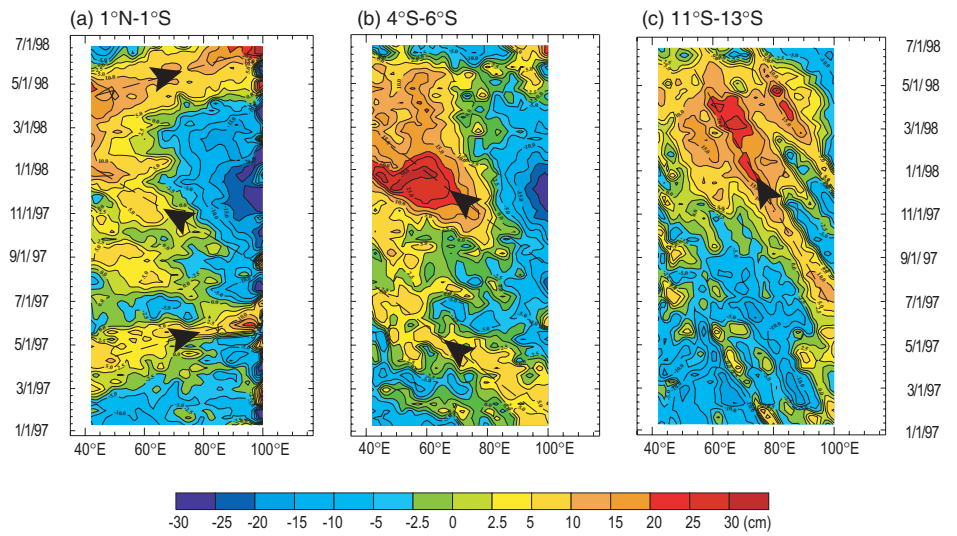

Figure 1.20. Time–longitude sections of the sea surface height anomalies (cm) between (a) 1°N and 1°S, (b) 4°S and 6°S, and (c) 11°S and 13°S, for the period using TOPEX/POSEIDEN altimeter data. Dashed black lines indicate the propagation speeds of westward propagating anomalies. The latitudinal dependence of phase speed indicates that the anomalies are associated with westward propagating and downwelling Rossby waves.

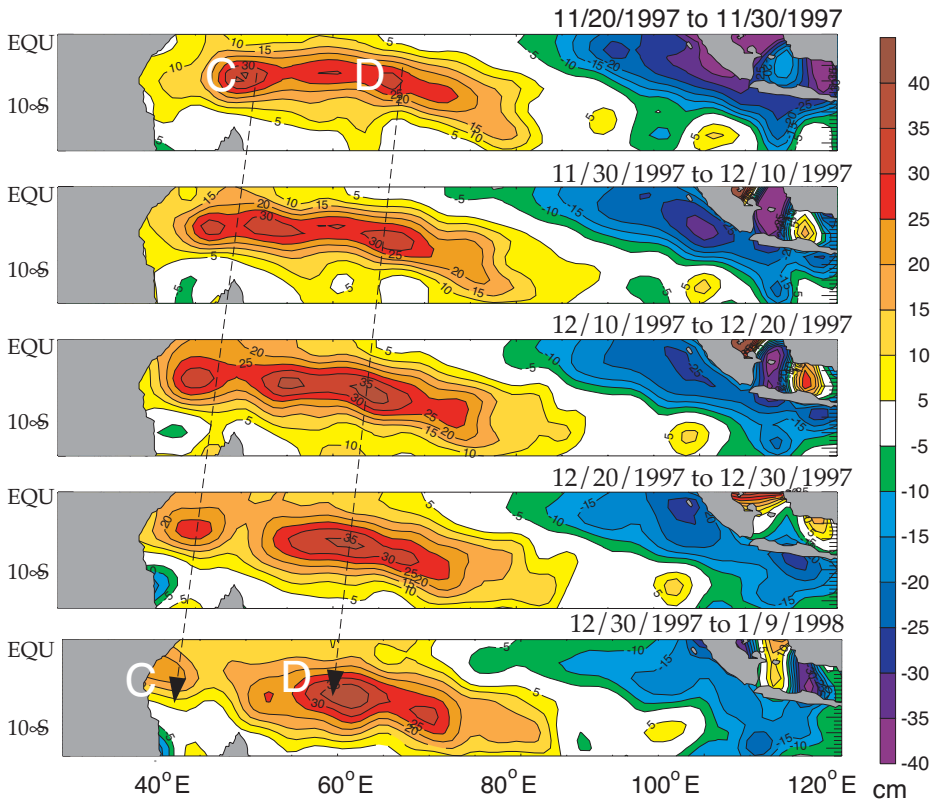

Figure 1.21. Five ten-day average latitude–longitude sections of the sea surface height (cm) from mid-November 1997 to early January 1998 using TOPEX/POSEIDEN altimeter data. 'C' and 'D' refer to locations identified in Figure 1.8(d). A steady westward propagation of anomalies is evident.
Date from TOPEX/POSEIDEN.

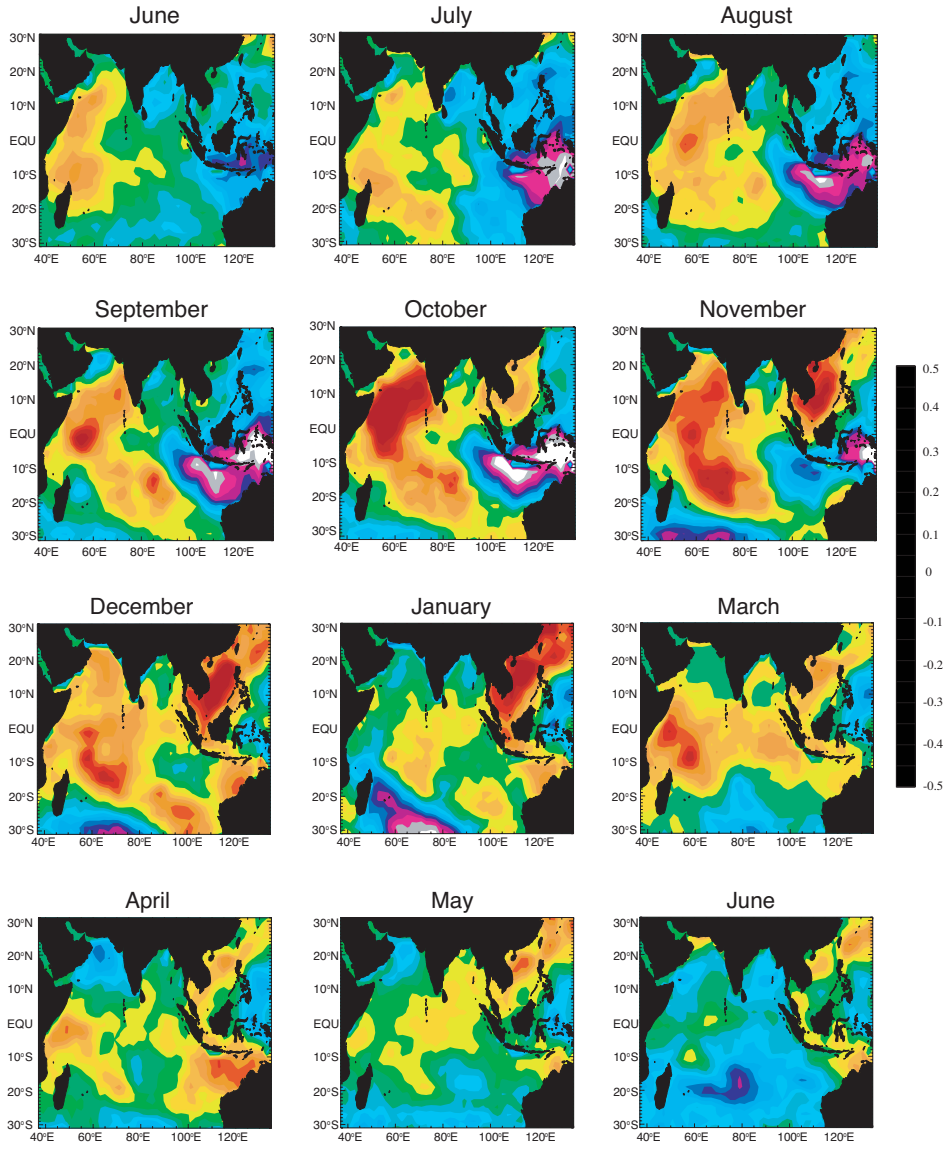

Figure 1.24. Composites of the SST anomaly during a positive phase (warmer than average SSTs in the western Indian Ocean, cooler than average in the east) of the IOZM. Evidence of a dipole appears in early to mid-summer and peaks in amplitude during the late-autumn/early-winter period, rapidly decaying in boreal spring.

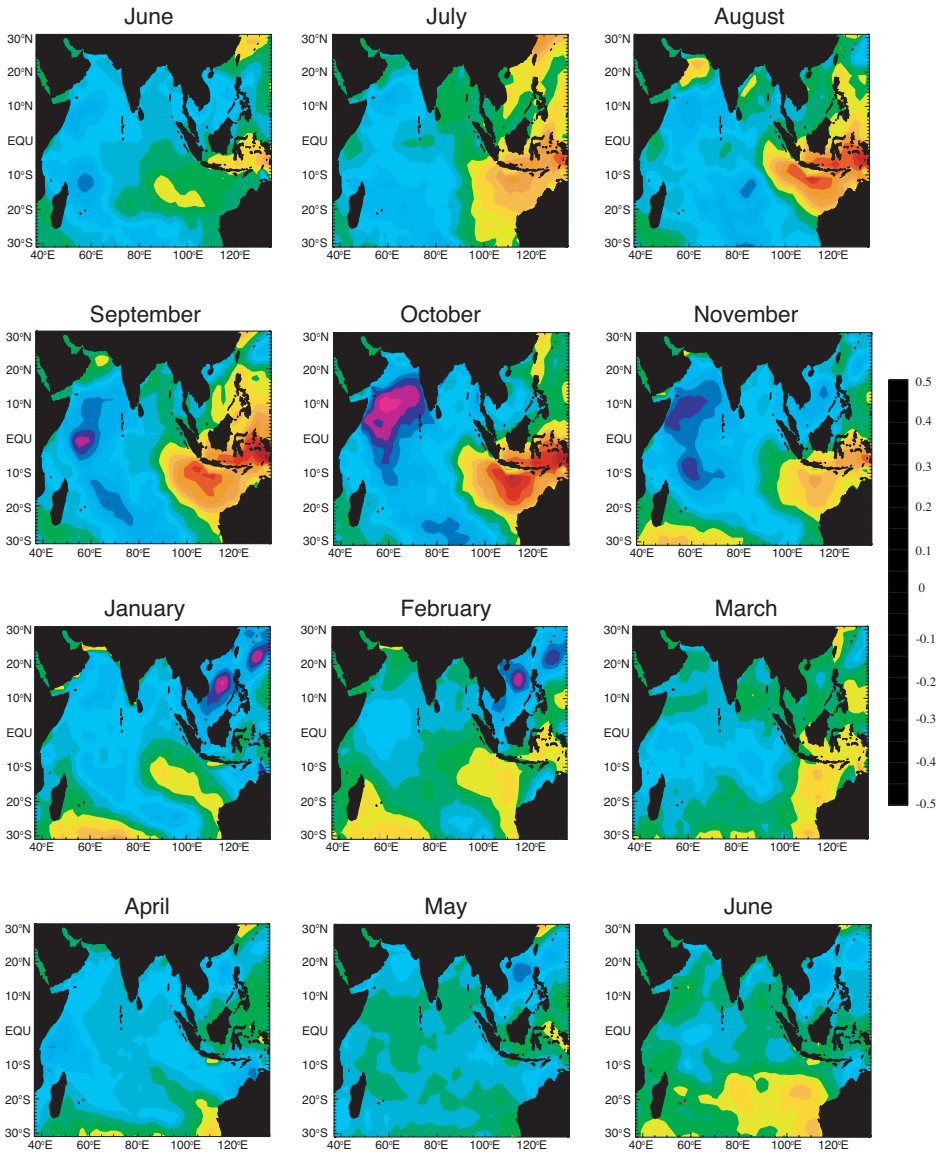

Figure 1.25. Same as Figure 1.24 but for the negative phase of the IOZM. Although the amplitude is somewhat smaller than the positive phase, the timing of appearance, maximum amplitude, and decay are much the same.

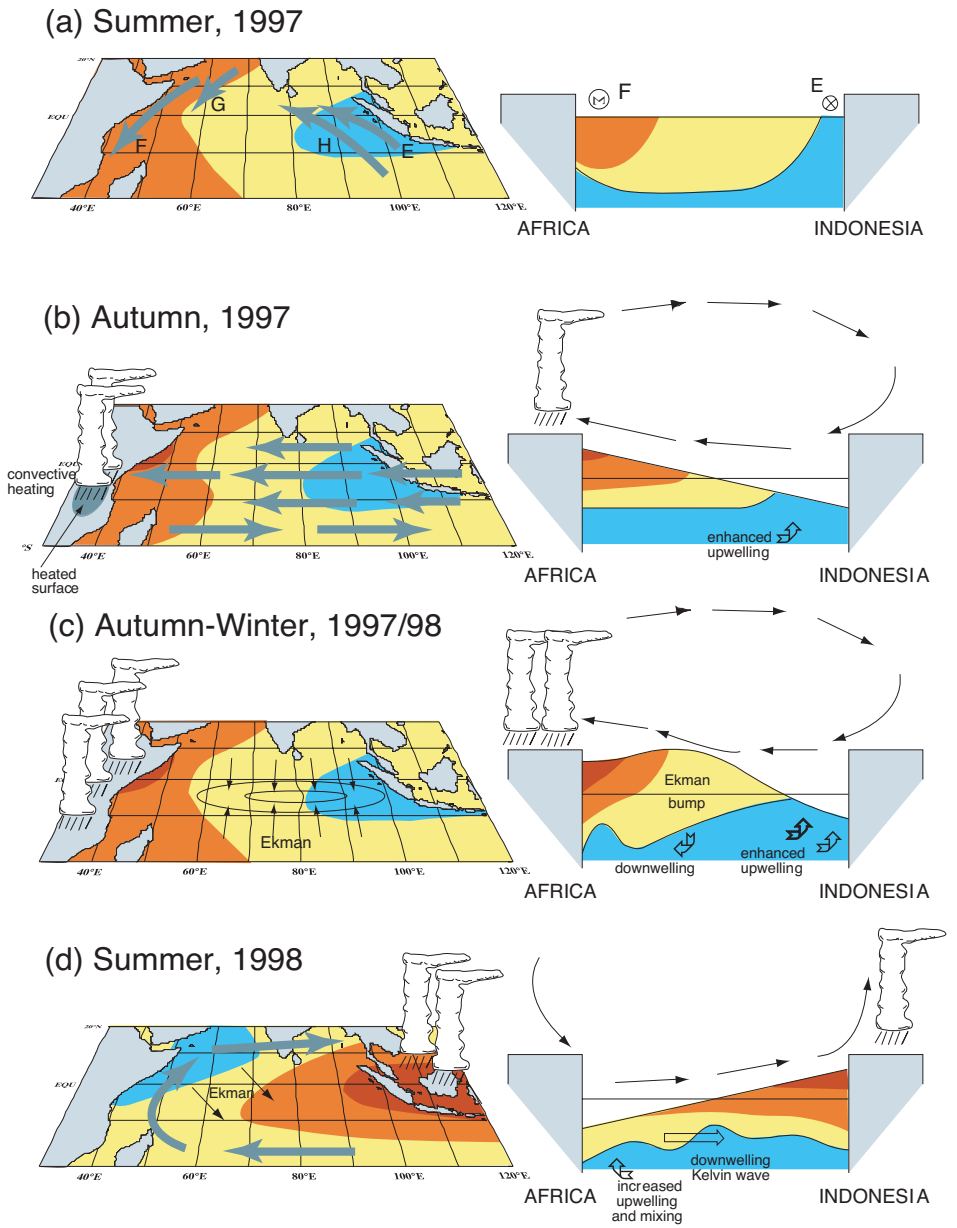

Figure 1.26. Diagram of the sequence of events in 1997–1998. (a) The climatological alongshore winds off Sumatra (E) and the east African coast (F). The winds observed in the late summer and early autumn are denoted by G and H, respectively. The right-hand panel shows the effect at the equator on the upper ocean induced by increased upwelling in the east and decreased upwelling in the west. Wind into and out of the plane of the paper are denoted by the bull's eye and cross-hair symbols, respectively. (b) Distribution of the winds resulting from the anomalous SST gradient along the equator and the changes in the SSH distribution. (c) Formation of the Ekman ridge in the central Indian Ocean and the forcing of westward-propagating downwelling equatorial Rossby waves to the west. The right-hand panel shows the effect on the upper ocean near 5°S. (d) Subsequent cooling of the western Indian Ocean through enhanced mixing and coastal Ekman transports from stronger than average monsoon winds and through circulation changes associated with the weakening of the 1997–1998 El Niño.

Adapted from Webster *et al.* (1999).

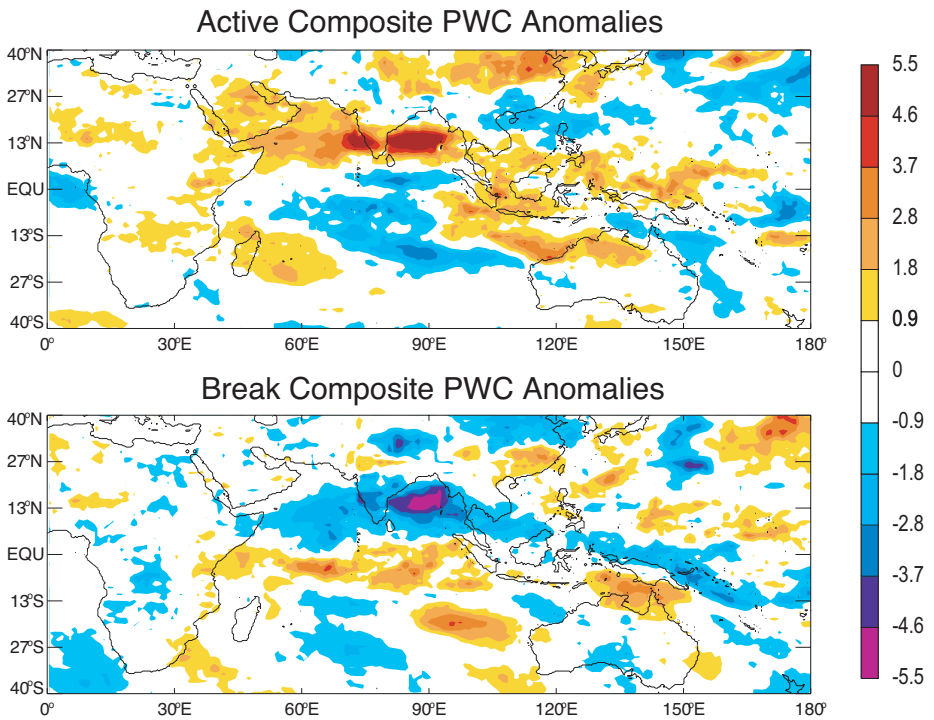

Figure 1.34. (a) Mean PWC (mm) composited for active and break periods of the monsoon over a 15-year period. The criterion used to determine an active and break period is described by Webster *et al.* (1998). (b) Intraseasonal variability of the monsoon depicted by the daily satellite microwave sounding unit (MSU) precipitation product along 90°E plotted against latitude as a function of time for the boreal summers of 1987 and 1988. Beginning in early summer, precipitation events begin near the equator and extend polewards in each hemisphere. The northward extension of the equatorial precipitation becomes the active period of the monsoon while the southward extension produces precipitation south of the equator and, eventually, enhances winter precipitation over southern Australia. Thirty-nine such events were identified in the 1984–1995 period. These events were used to create composites of monsoon intraseasonal events.
Data provided by T. Vonder Haar and D. Randel, Colorado State University.

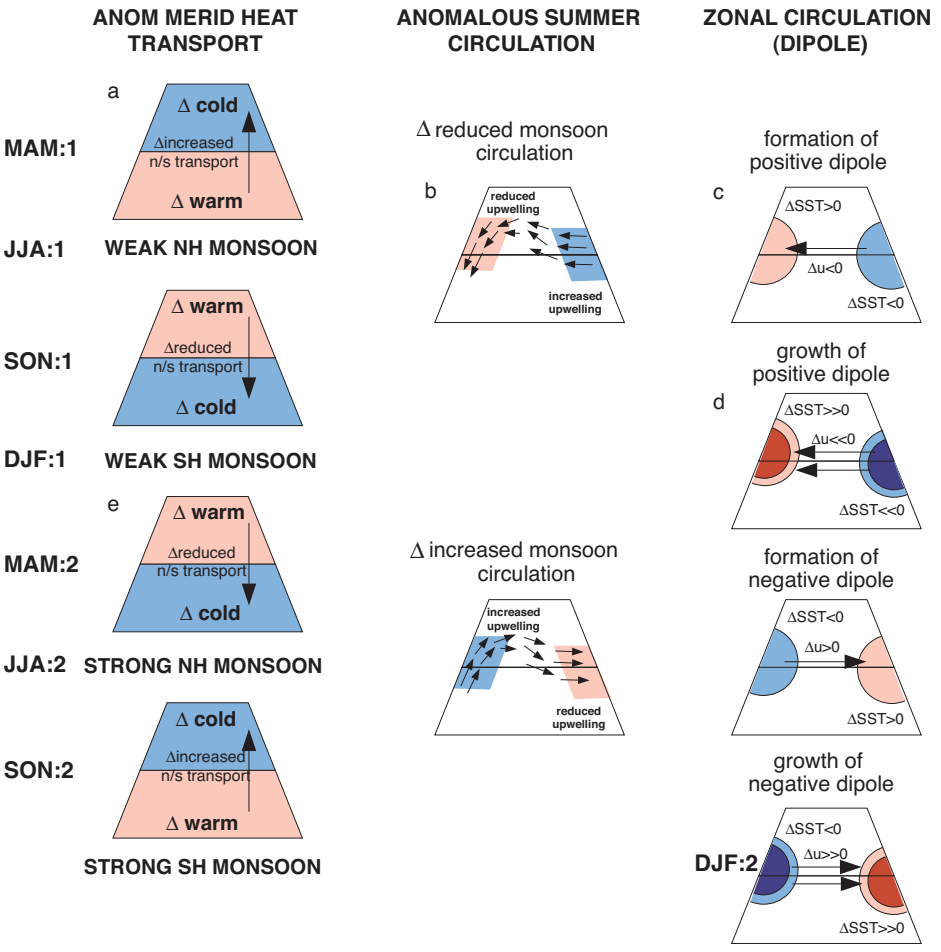

Figure 1.40. Schematic of a general theory of an ocean–atmosphere regulation system for the monsoon and the Indian Ocean. Each column indicates a set of processes. The first column shows modulation of the monsoon variability by changes in the heat transport induced by the monsoon winds. In essence this sequence represents the Meehl (1997) biennial oscillation mechanism but with ocean dynamics. The second column shows the impact of the strong and weak monsoons on the upwelling regions of the ocean basin. The third column represents the development of the Indian Ocean dipole relative to the upwelling patterns developed by the anomalous monsoon wind fields. Growth of the dipole anomaly is assumed to follow the coupled ocean–atmosphere instability described by Webster *et al.* (1999). Taken as a whole, the figure suggests that there are multiple components that regulate the monsoon with each component acting in corroboration. One important role of the dipole (either positive or negative) is to provide slow dynamics (or memory) to the SST anomalies induced by the strong or weak monsoons. For example, the sequence (a) to (e) helps perpetuate the northern hemisphere anomalously warm temperatures created by the weak monsoon during the previous summer.

Adapted from Webster *et al.* (2002) and Loschnigg *et al.* (2003).

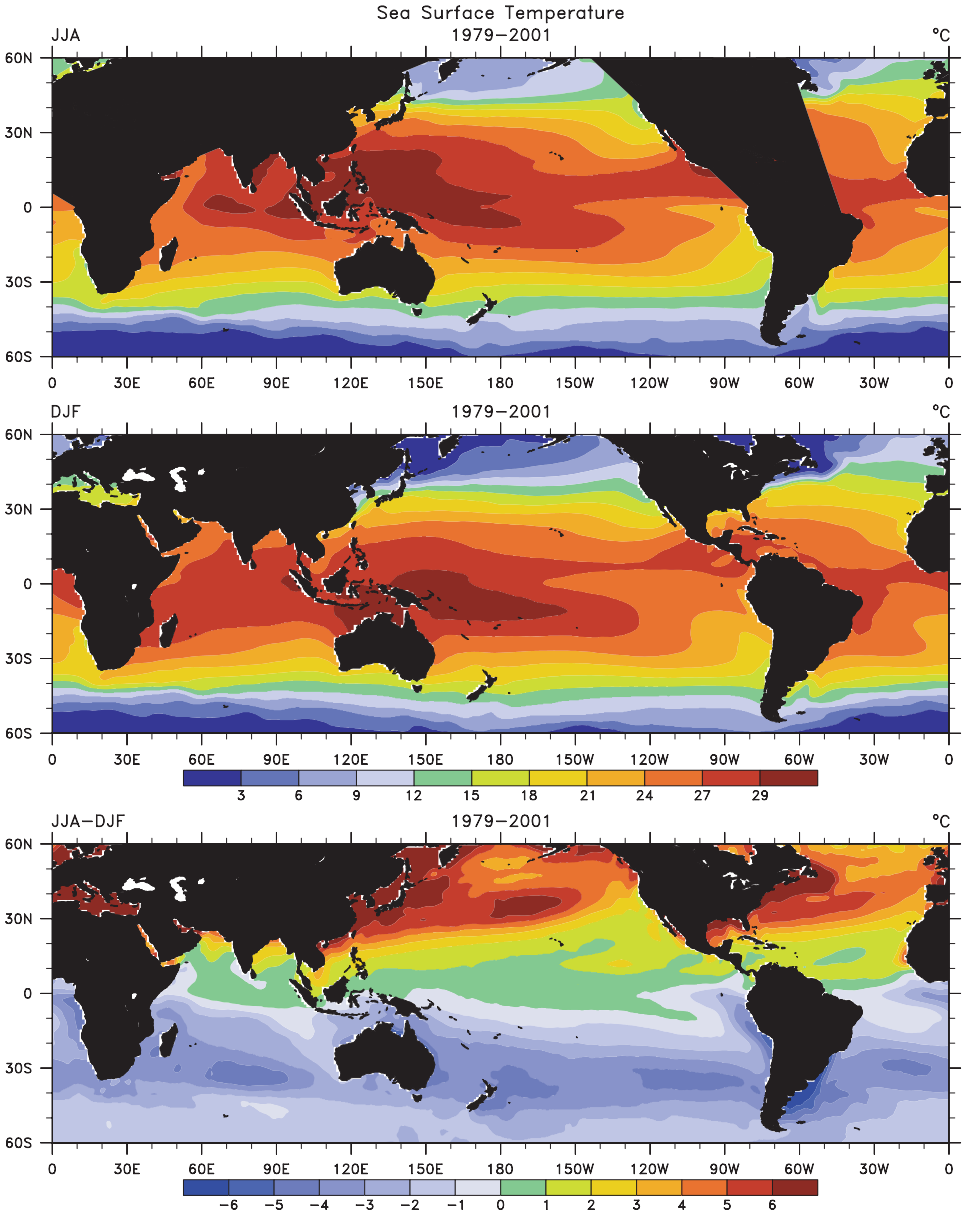

Figure 2.1. Sea surface temperatures for 1979–2001 averaged for JJA (*top*), DJF (*middle*), and their difference JJA – DJF (*bottom*). The contour interval in the top two panels is 3°C and is 1°C in the bottom panel.

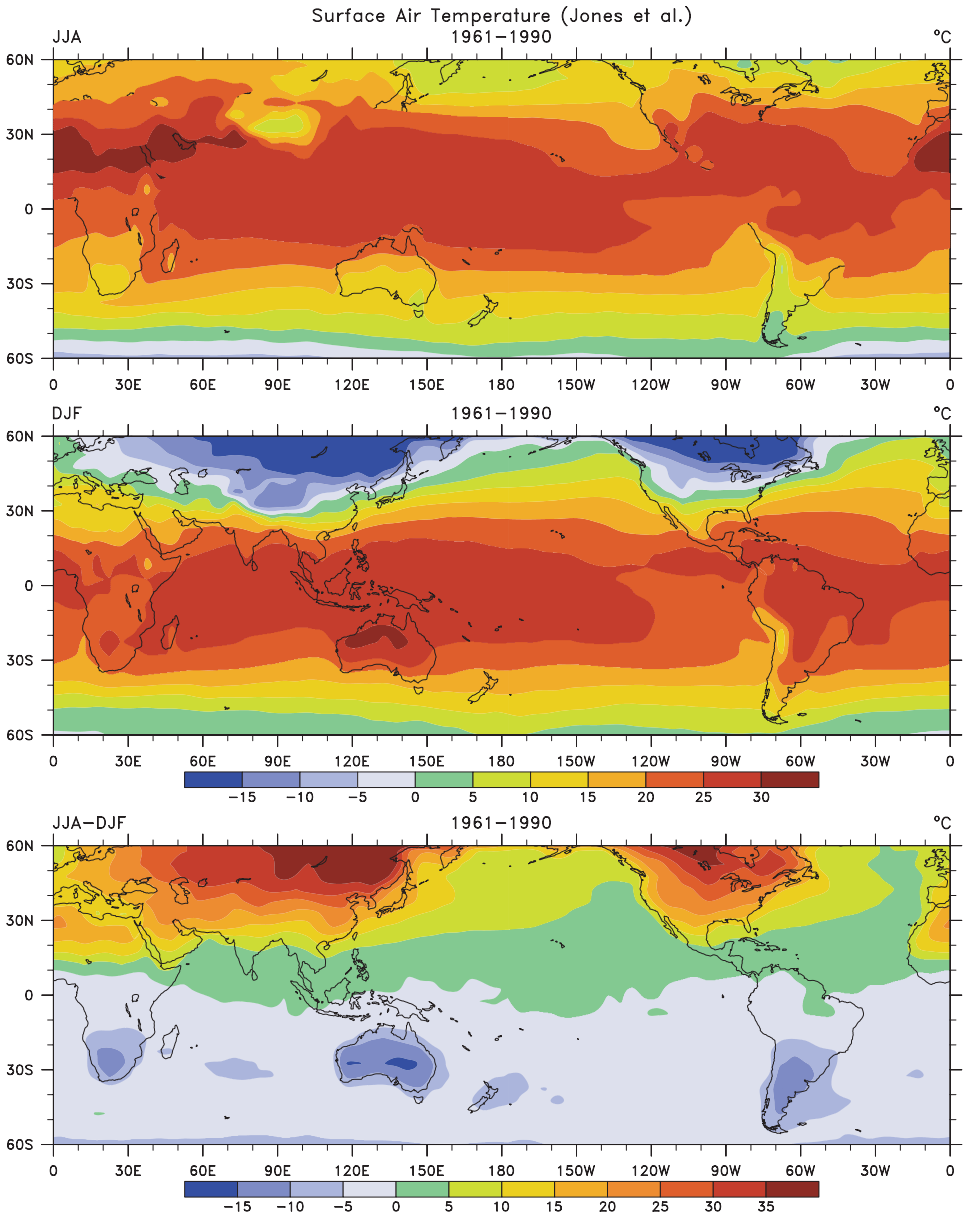

Figure 2.2. Surface air temperatures (from Jones *et al.*, 1999) for 1961–1990 averaged for JJA (*top*), DJF (*middle*), and their difference JJA – DJF (*bottom*). The contour interval is 5°C.

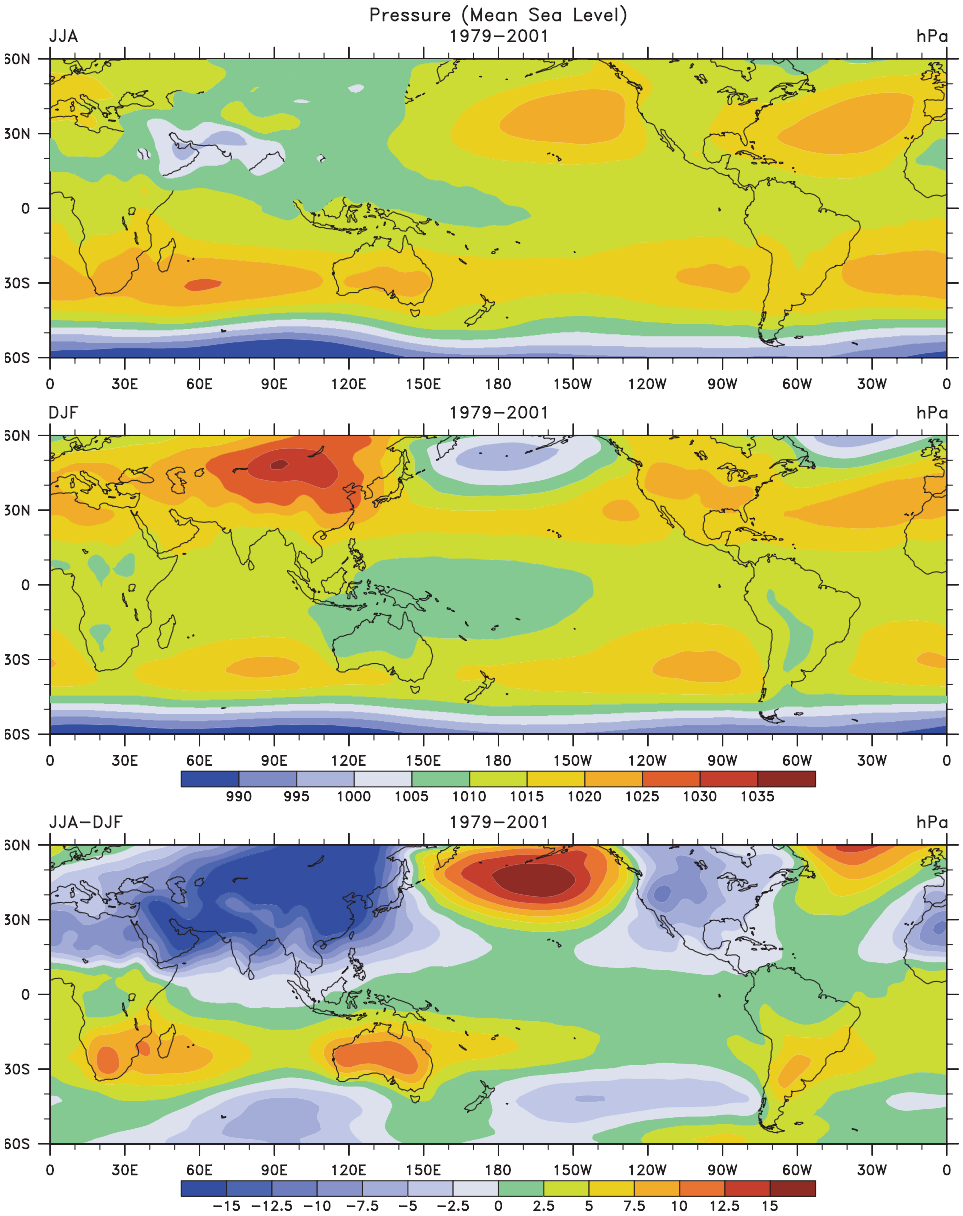

Figure 2.3. Sea level pressures for 1979–2001 averaged for JJA (*top*), DJF (*middle*), and their difference JJA – DJF (*bottom*). The contour interval in the top two panels is 5 hPa and in the bottom panel is 2.5 hPa.

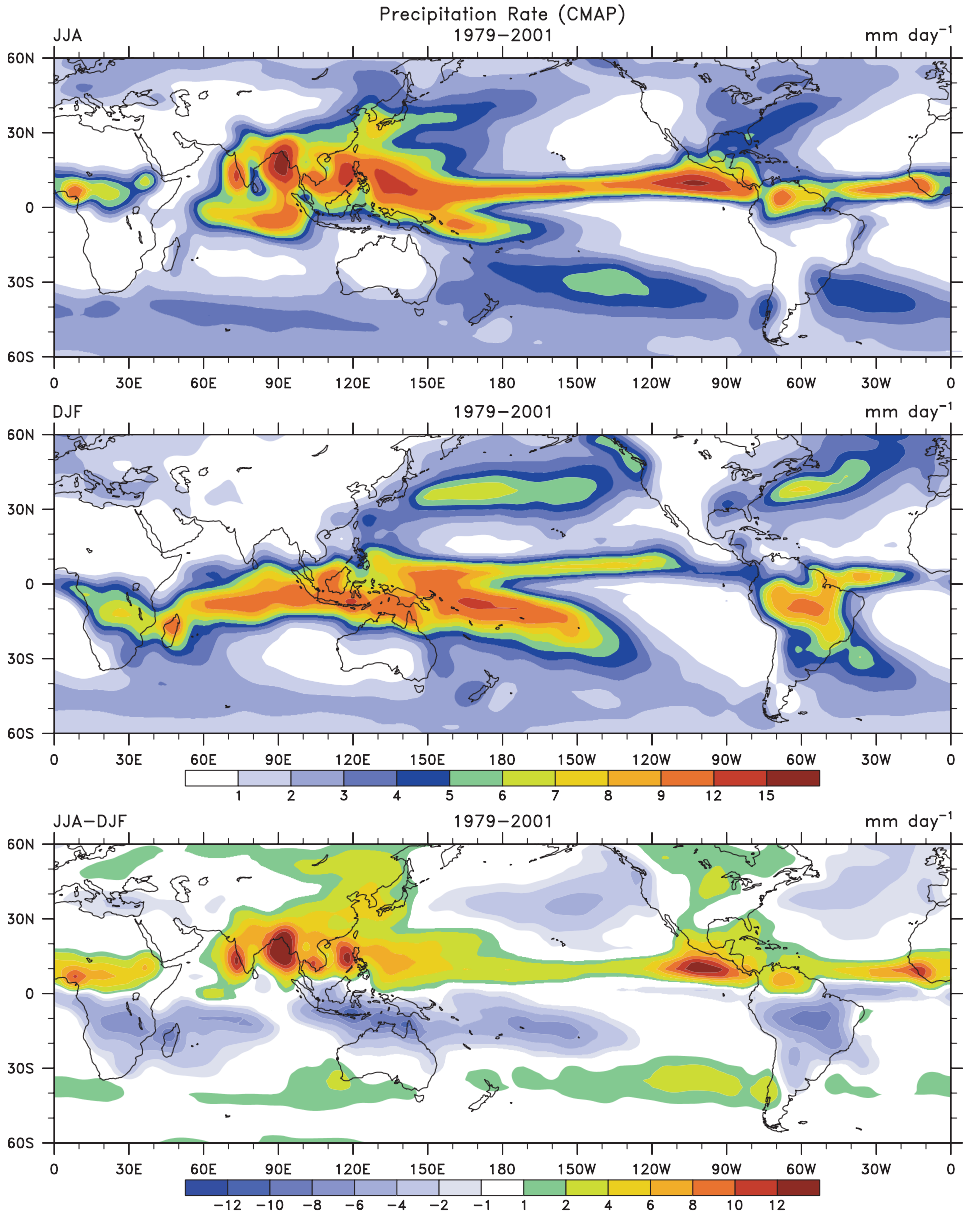

Figure 2.4. Precipitation rate (from CMAP) for 1979–2001 averaged for JJA (*top*), DJF (*middle*), and their difference JJA – DJF (*bottom*). The contour interval is in mm day^{-1}.

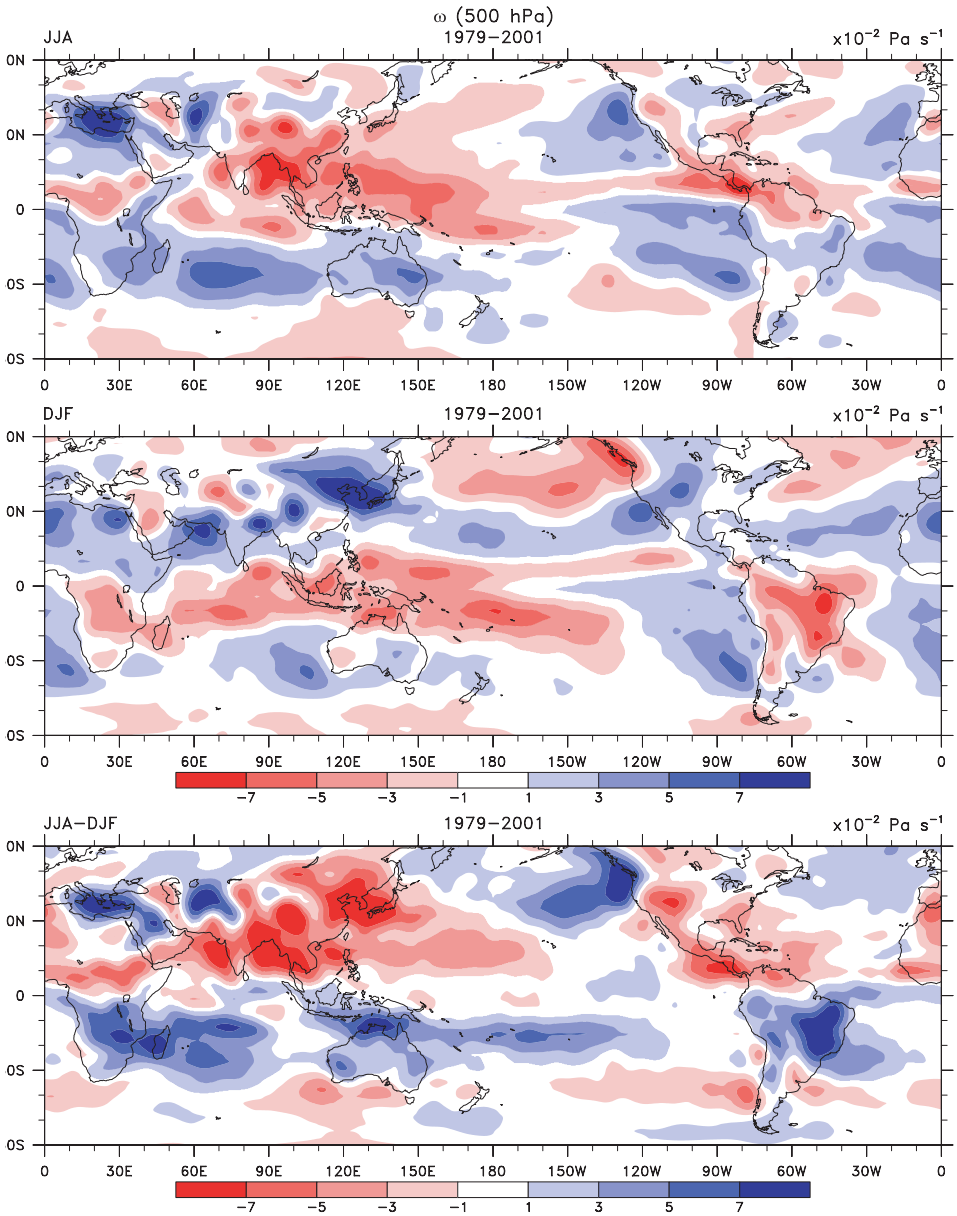

Figure 2.9. Vertical *p*-velocity (ω) at 500 hPa for 1979–2001 averaged for JJA (*top*), DJF (*middle*), and their difference JJA – DJF (*bottom*). The contour interval is 2×10^{-2} Pa s^{-1}.

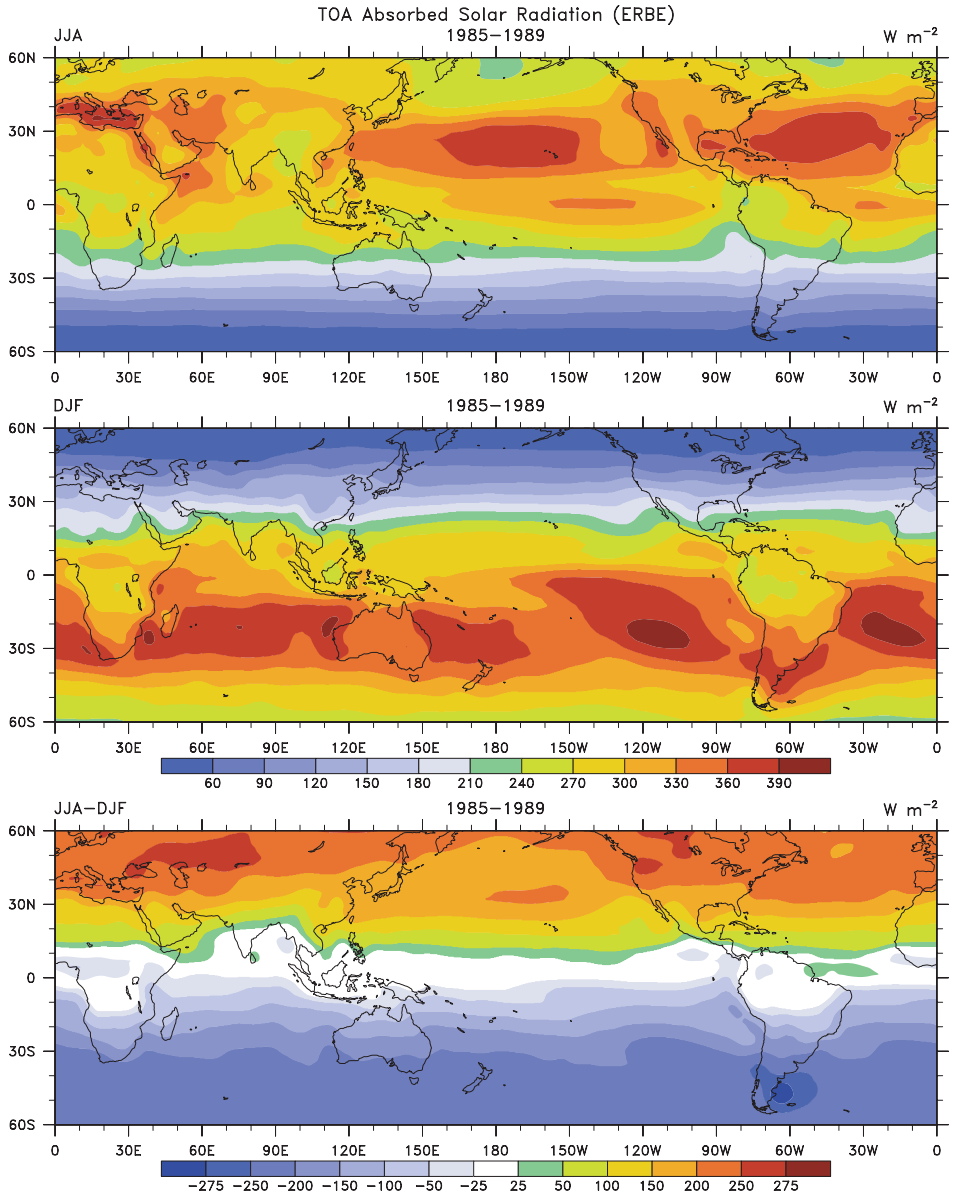

Figure 2.11. ASR for 1985–1989 averaged for JJA (*top*), DJF (*middle*), and their difference JJA – DJF (*bottom*). The contour interval in the top two panels is 30 W m^{-2} and 25 or 50 W m^{-2} in the bottom panel with the zero contour in black.
From Trenberth and Stepaniak (2004), copyright 2004 Royal Meteorological Society.

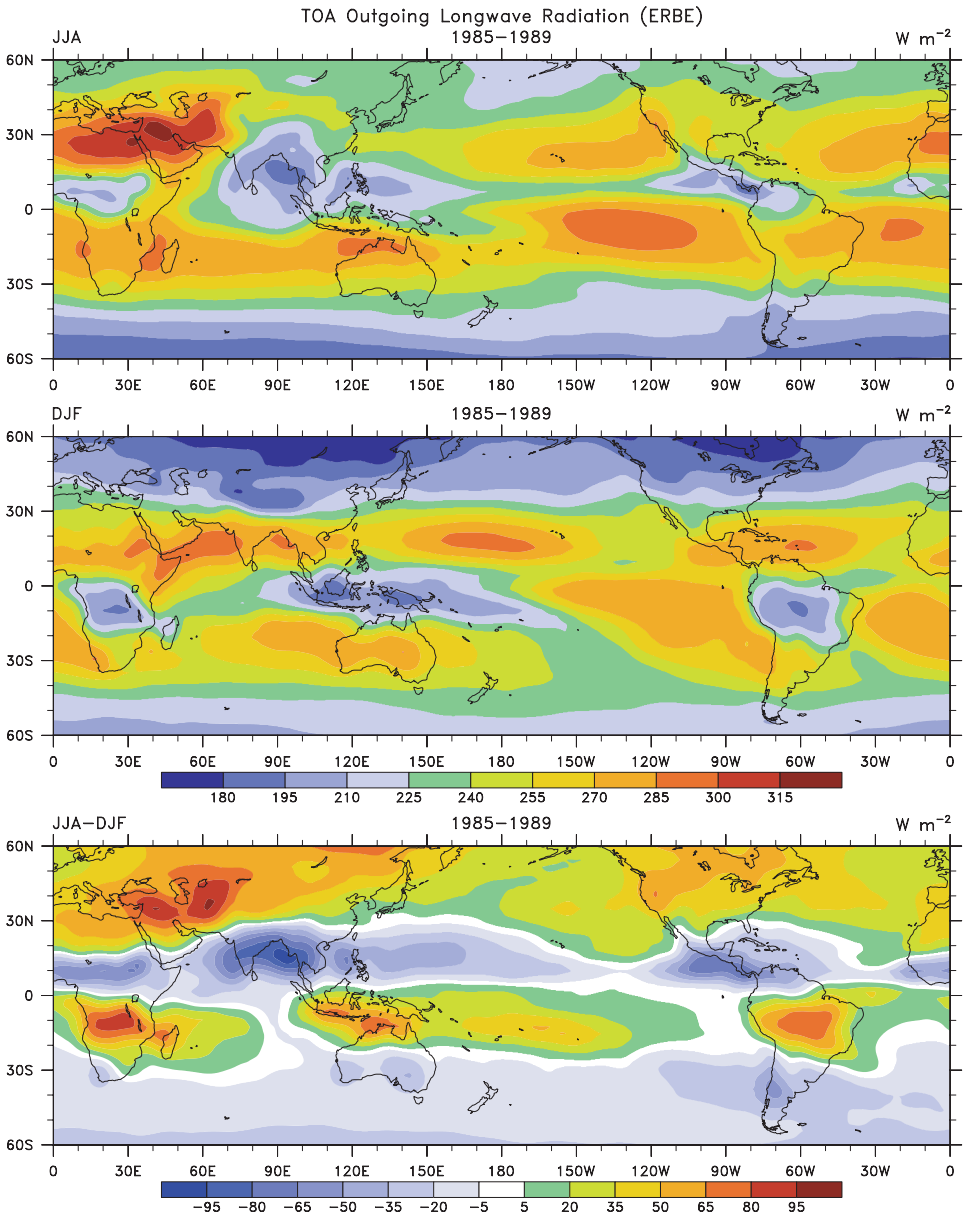

Figure 2.12. OLR for 1985–1989 averaged for JJA (*top*), DJF (*middle*), and their difference JJA – DJF (*bottom*). The contour interval is 15 W m^{-2}.

From Trenberth and Stepaniak (2004), copyright 2004 Royal Meteorological Society.

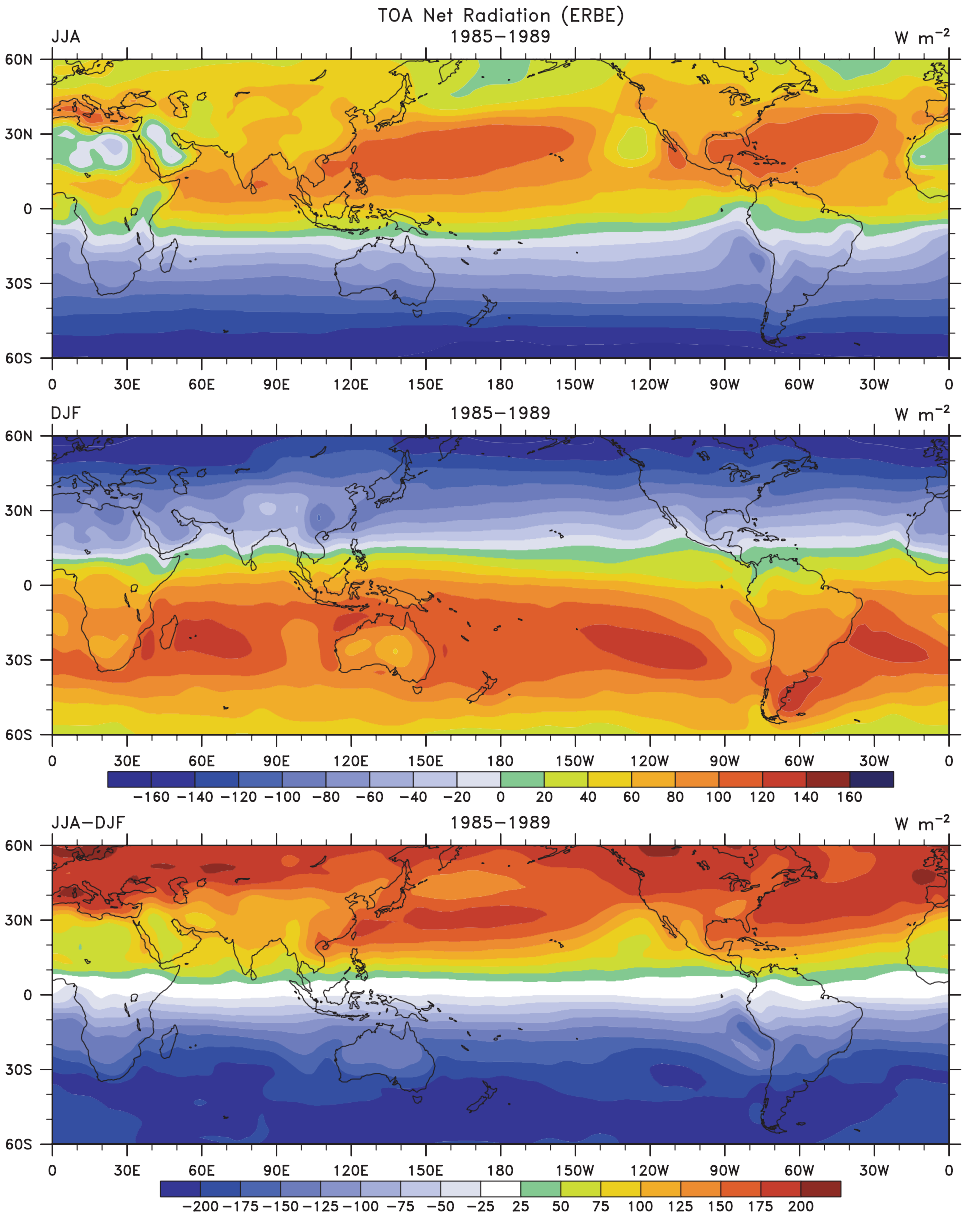

Figure 2.13. Net radiation for 1985–1989 averaged for JJA (*top*), DJF (*middle*), and their difference JJA – DJF (*bottom*). The contour interval in the top two panels is 20 W m^{-2} and is 25 W m^{-2} in the bottom panel, with the zero contour in black.
From Trenberth and Stepaniak (2004), copyright 2004 Royal Meteorological Society.

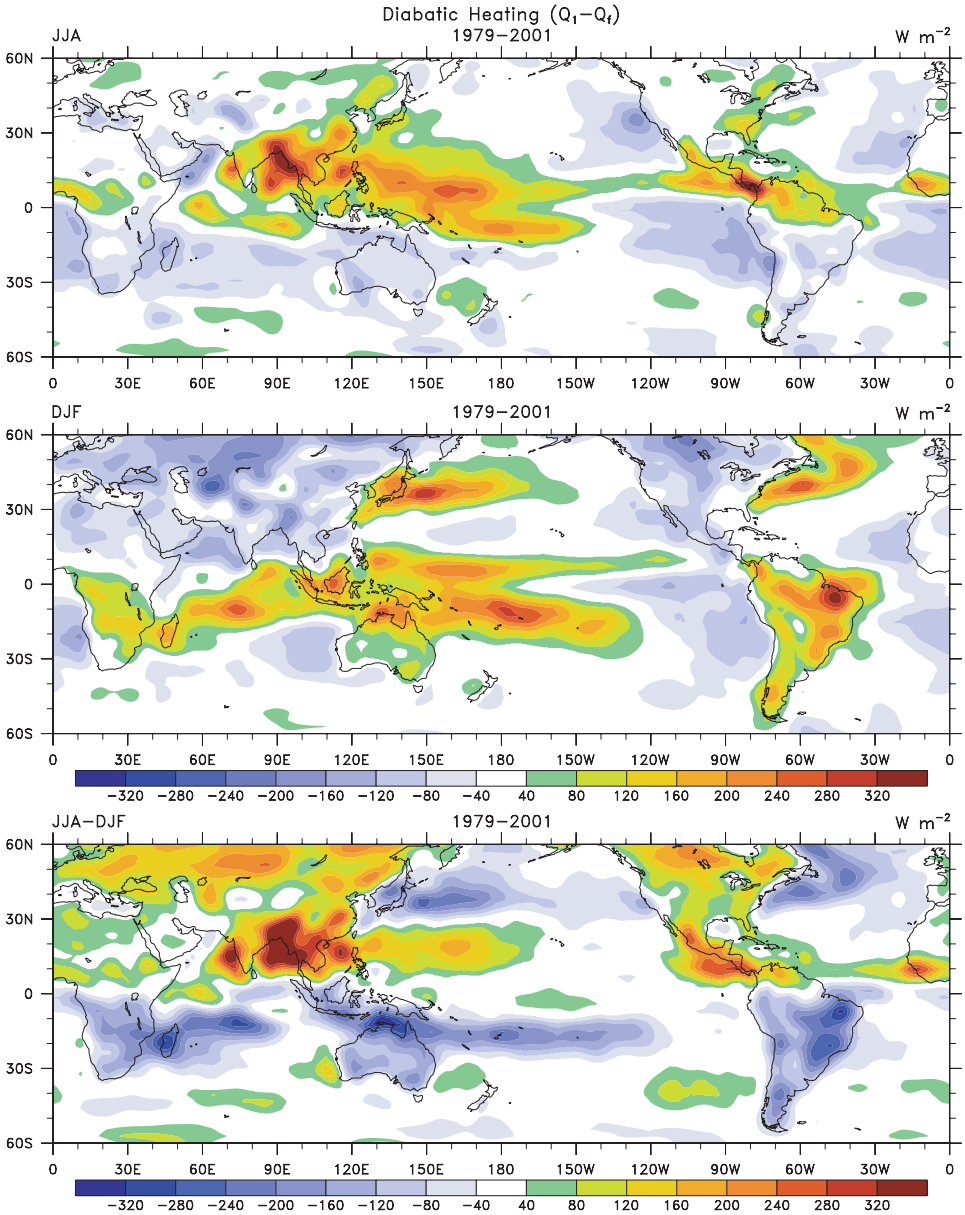

Figure 2.14. Vertically integrated atmospheric diabatic heating for 1979–2001 averaged for JJA (*top*), DJF (*middle*), and their difference JJA – DJF (*bottom*). The contour interval is 40 W m^{-2}.

From Trenberth and Stepaniak (2004), copyright 2004 Royal Meteorological Society.

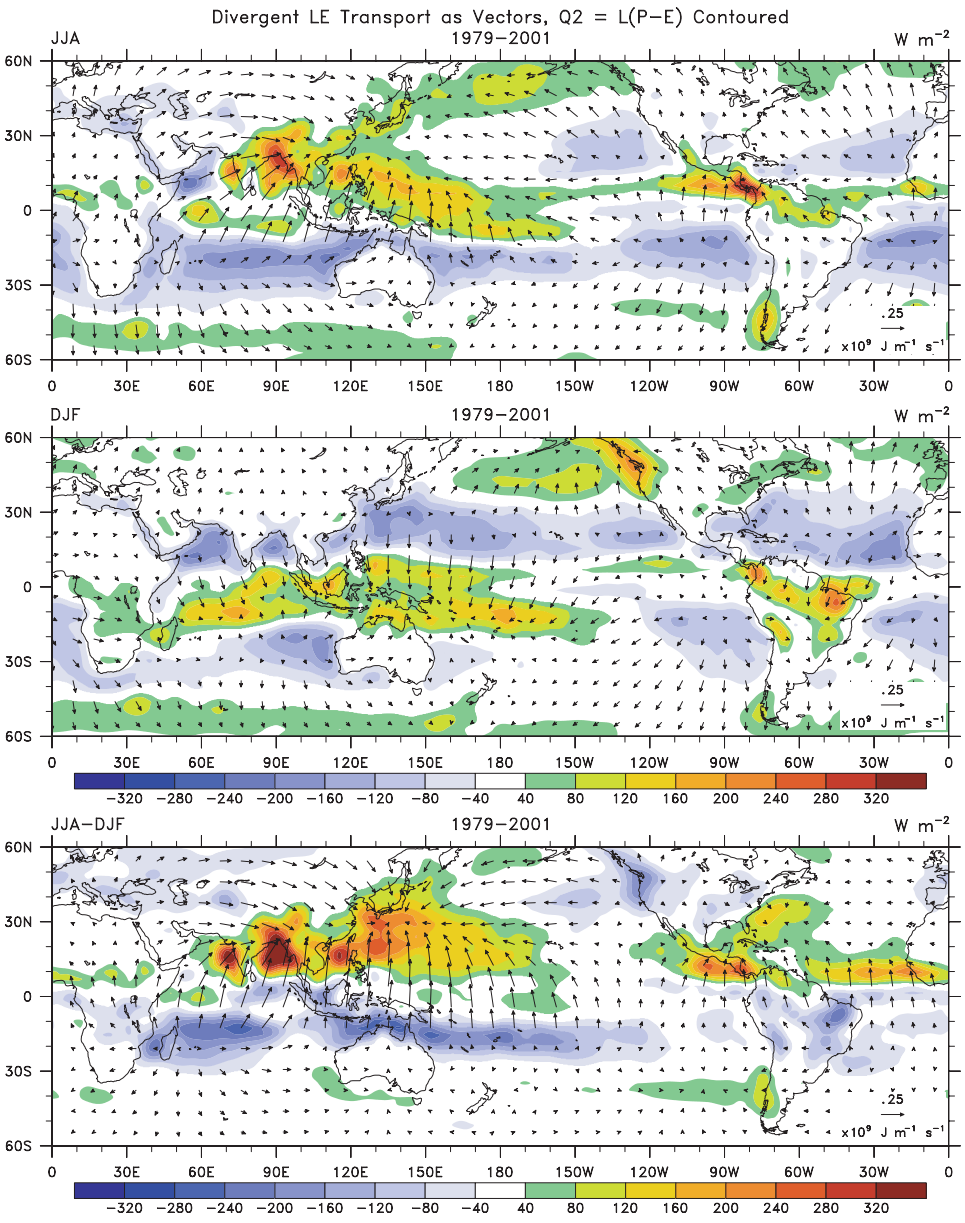

Figure 2.15. Vertically integrated atmospheric latent heating $L(P-E)$ for 1979–2001 averaged for JJA (*top*), DJF (*middle*), and their difference JJA – DJF (*bottom*). Also plotted is the divergent component of the latent energy transport as vectors, key at lower right of each panel, in $10^9\,\mathrm{W\,m^{-1}}$. The contour interval is $40\,\mathrm{W\,m^{-2}}$.

From Trenberth and Stepaniak (2004), copyright, 2004 Royal Meteorological Society.

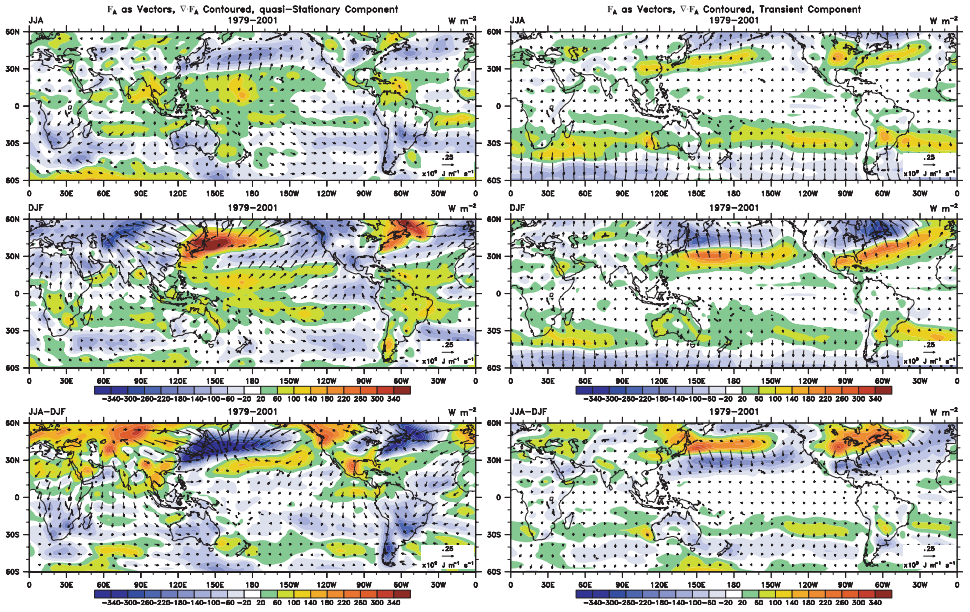

Figure 2.16. Divergence of and divergent component of vectors of the vertically integrated total atmospheric energy transports for 1979–2001 averaged for JJA (*top*), DJF (*middle*), and their difference JJA – DJF (*bottom*). The first set of panels show the component from the quasistationary flow (monthly means and longer) and second set of panels show the transient flow contributions. The contour interval is 40 W m^{-2}.

From Trenberth and Stepaniak (2004), copyright 2004 Royal Meteorological Society.

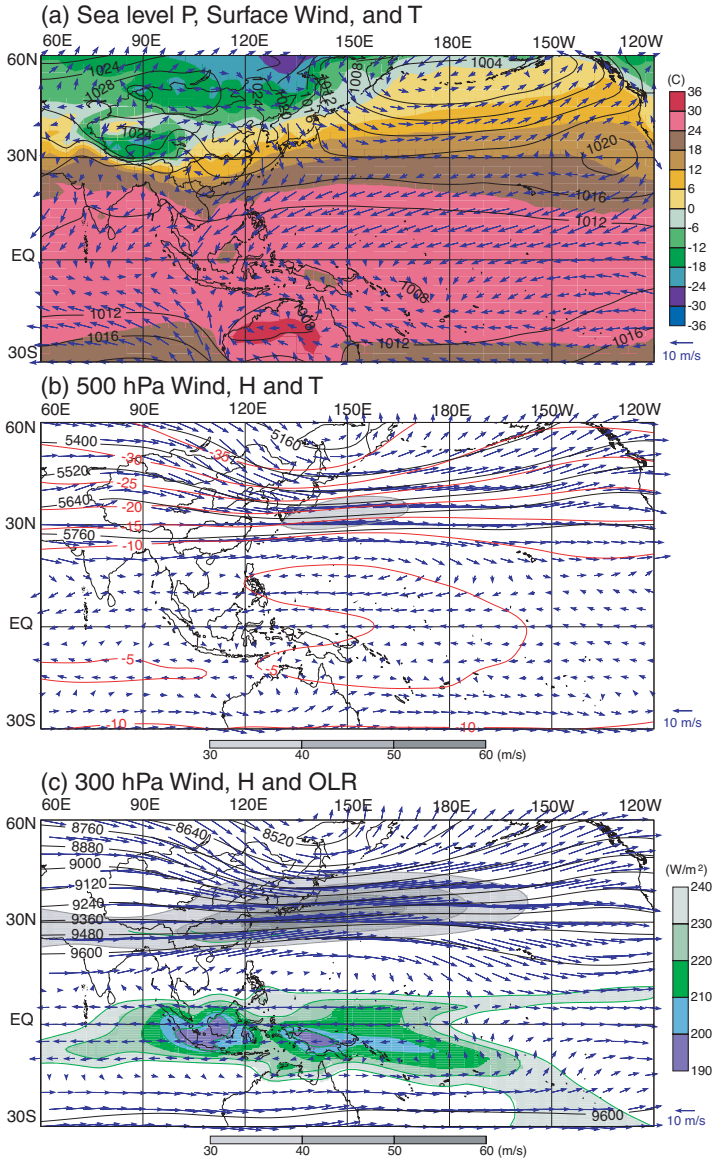

Figure 3.1. Climatological mean fields in northern winter (November–March): (a) Sea level pressure (isobars), surface air temperature (shading), and surface wind fields (vectors); (b) 500-hPa winds (vectors), geopotential height (black) and temperature (red); and (c) 300-hPa winds (vectors), geopotential height (black), and OLR in the tropics (values smaller than 240 W m^{-2} are color shaded). In (b–c) the zonal wind greater than 30 m s^{-1} is gray shaded to represent the jet stream. Wind vector scales are shown in the lower right corner of each panel. OLR data are the average during 1979–1995 and the other data are from NCEP/NCAR reanalysis during 1958–1996.

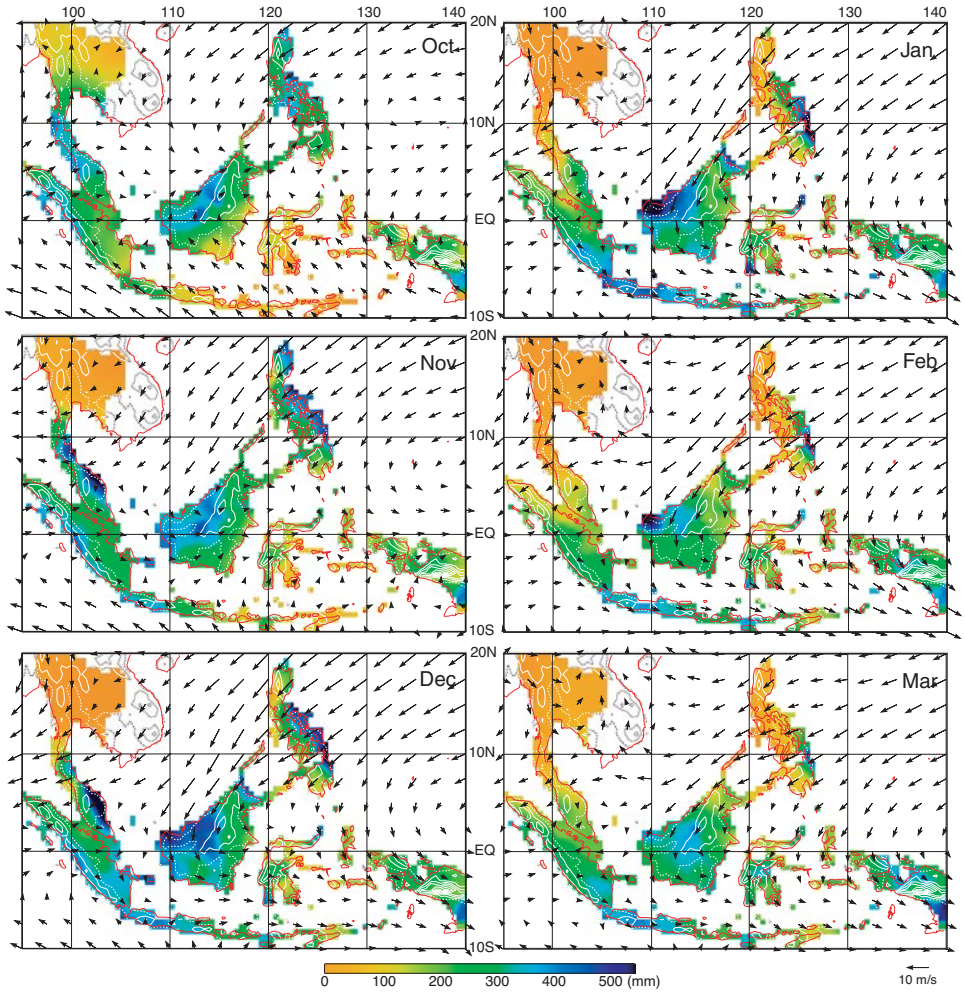

Figure 3.7. Monthly mean rainfall and topography for October–March. Data are analysed at $0.5^\circ \times 0.5^\circ$ grids from station rainfall reports of various periods with a minimum length of 48 years.

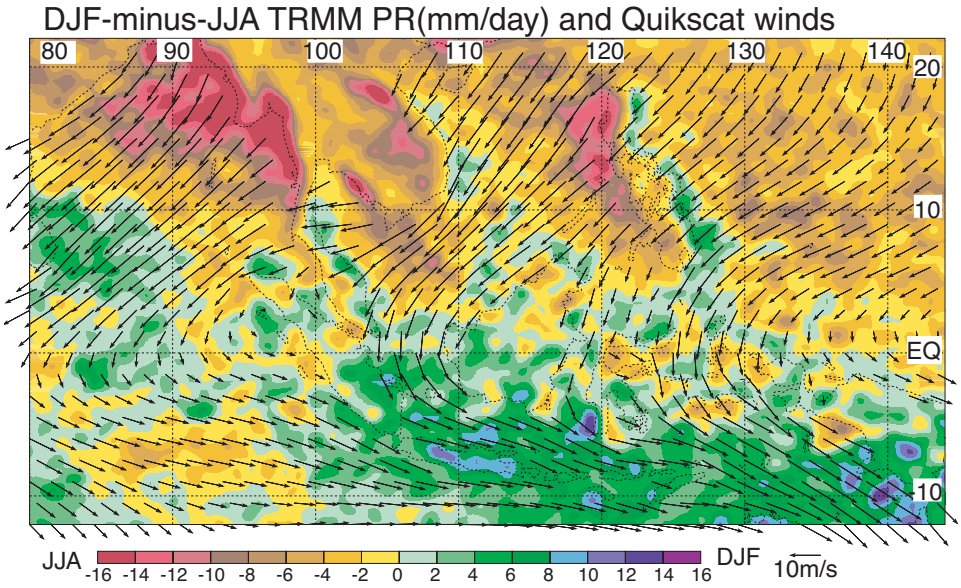

Figure 3.9. Differences of TRMM precipitation radar data and QuikSCAT winds between boreal winter and boreal summer (DJF – JJA). Warm colors are the boreal summer monsoon regime and cool colors are the boreal winter monsoon regime.
From Chang *et al.* (2005b).

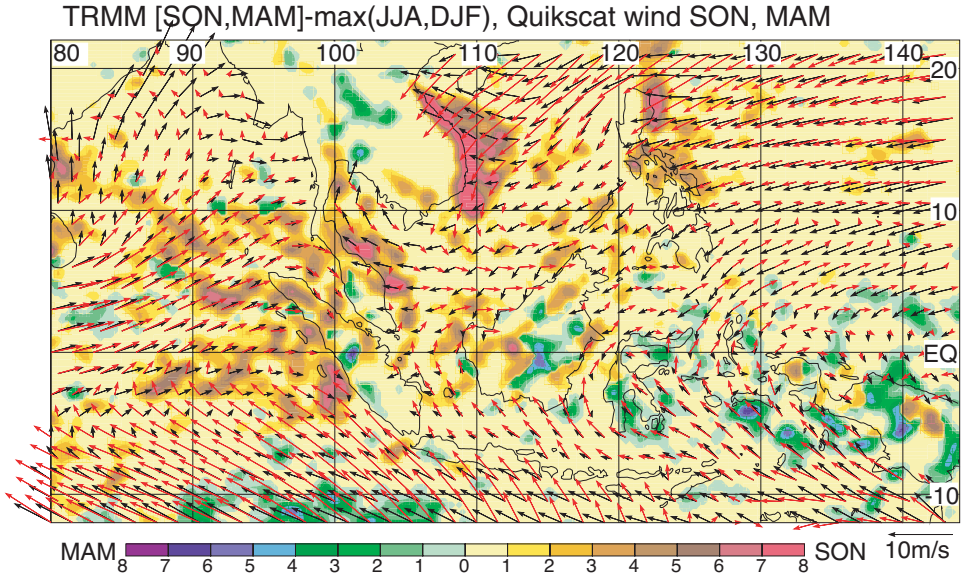

Figure 3.10. Monsoon regimes during transition seasons deduced from TRMM precipitation radar rainfall. A grid point is identified if the rainfall during one of the two transition seasons is the maximum in the annual cycle, and the value plotted is the difference between this transition season rainfall and the boreal winter or boreal summer whichever is highest. Warm colors are the boreal fall monsoon regime and cool colors are the boreal spring monsoon regime. The QuikSCAT winds are plotted with red for SON and black for MAM.
From Chang *et al.* (2005b).

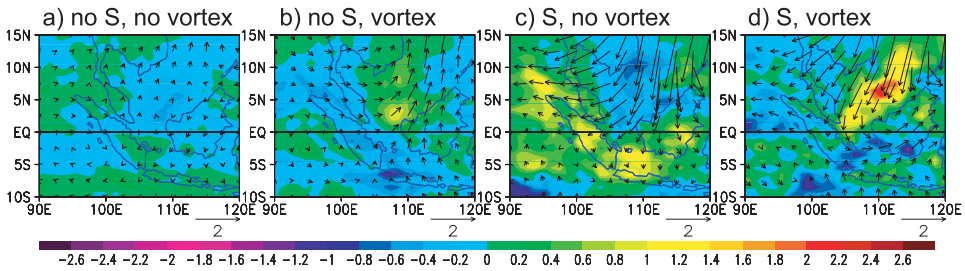

Figure 3.11. Composite maps of convective index and 925-hPa winds ($m\,s^{-1}$) for (a) no surge and no vortex cases, (b) no surge and vortex cases, (c) surge and no vortex cases, and (d) surge and vortex cases.
Adapted From Chang *et al.* (2005a).

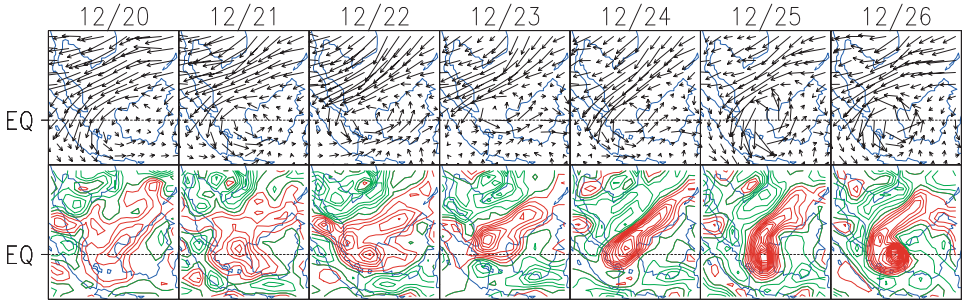

Figure 3.12. Evolution of 850-hPa wind (*upper panels*) and vorticity (*lower panels*; red positive, green negative) prior to the formation of Typhoon Vamei, 2001. Data based on Naval Operational Global Atmospheric Prediction System $1^\circ \times 1^\circ$ analysis at 00 UTC, 20–26 December 2001.
From Chang *et al.* (2003).

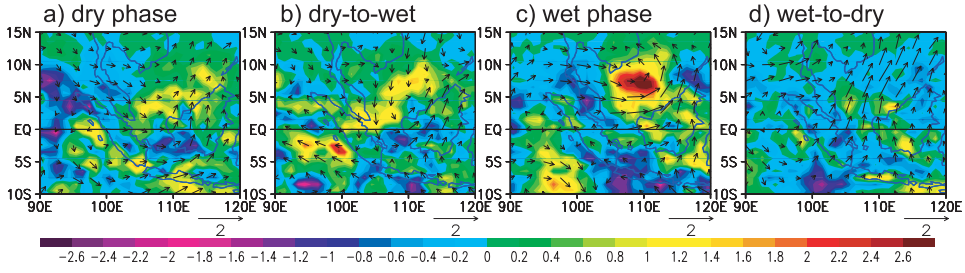

Figure 3.14. Composite maps of convective indices and 925-hPa winds ($m\,s^{-1}$) for MJO and vortex cases when the MJO is in (a) dry, (b) dry to wet, (c) wet, and (d) wet to dry phases.
Adapted from Chang *et al.* (2005a).

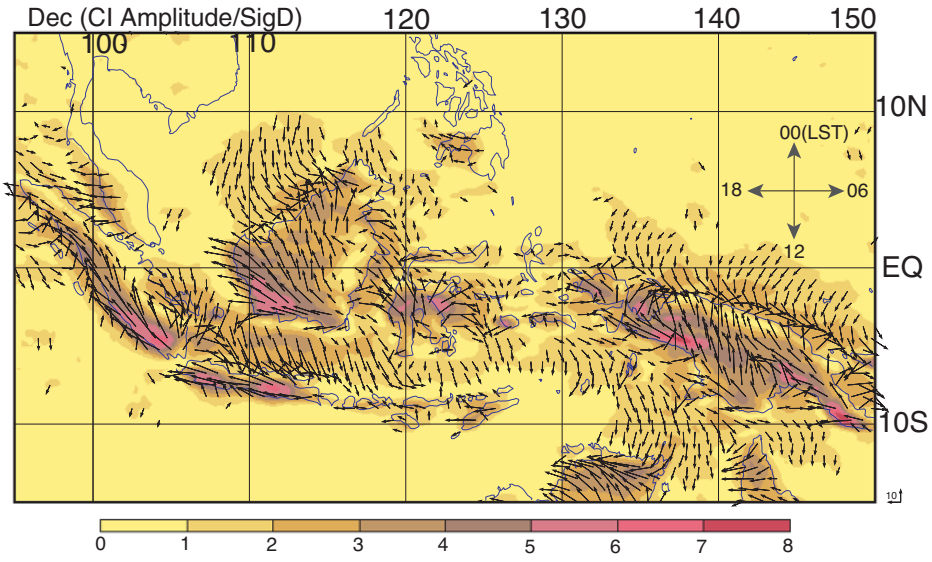

Figure 3.16. Vectors that represent the diurnal cycle are computed from hourly CI for December 1998–2001. The diurnal cycle phase is shown as a 24-hour clock with a northward arrow indicating maximum CI at 00:00 local standard time. The vectors are only plotted over areas where the ratio (scaled by color) of diurnal amplitude and the standard deviation, which are both illustrated in Figure 3.17, is ≤ 1.

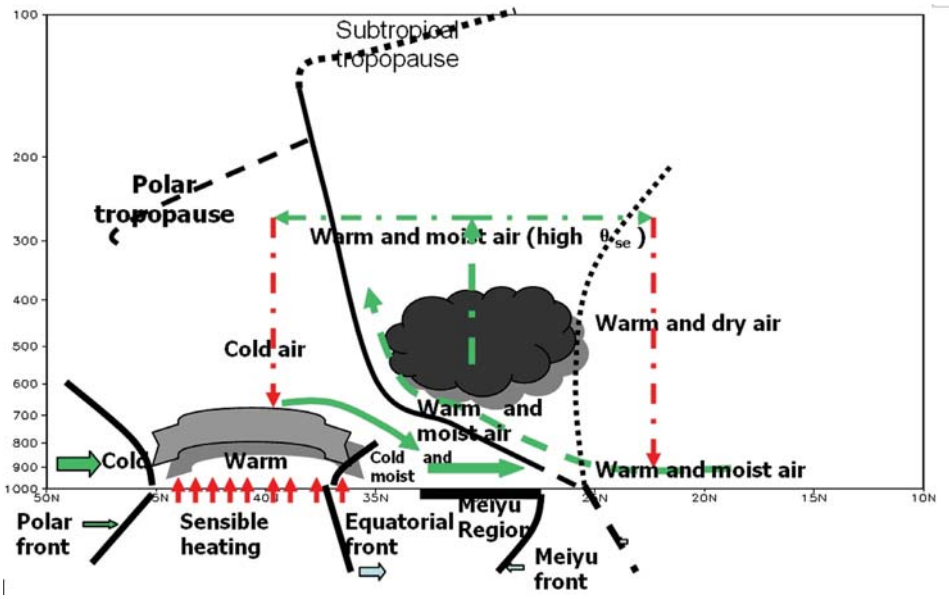

Figure 4.13. Synoptic model of the Meiyu season in east China.
From Liu *et al.* (2003).

Figure 4.20. Geographical distribution of locations and times of severe floods in China since 1931.
Shi (2003).

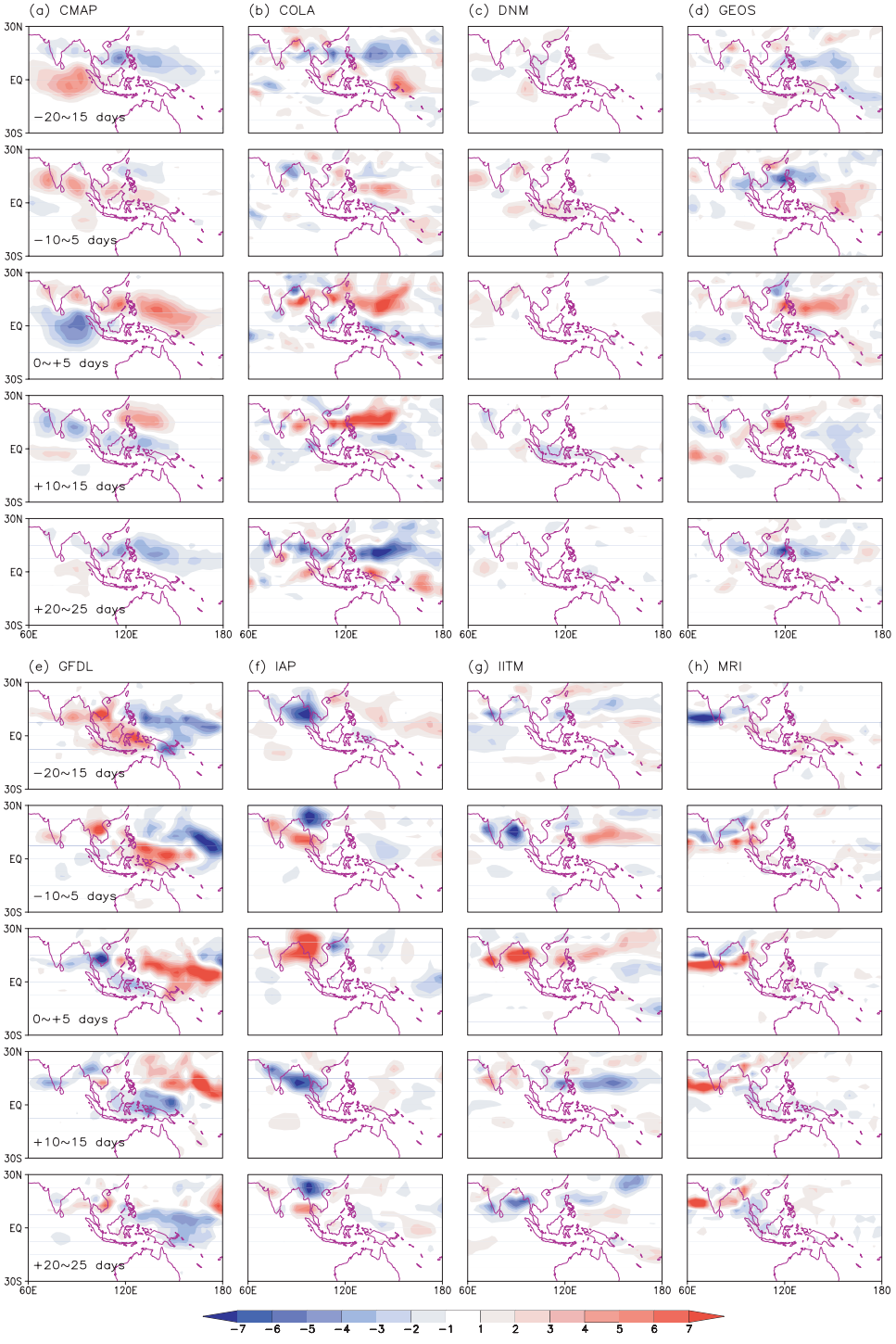

Figure 5.18. Composite ISO events in terms of rainfall (mm day^{-1}) from observations (a) and seven AGCMs (b–h) for the boreal summer.
From Waliser *et al.* (2003e).

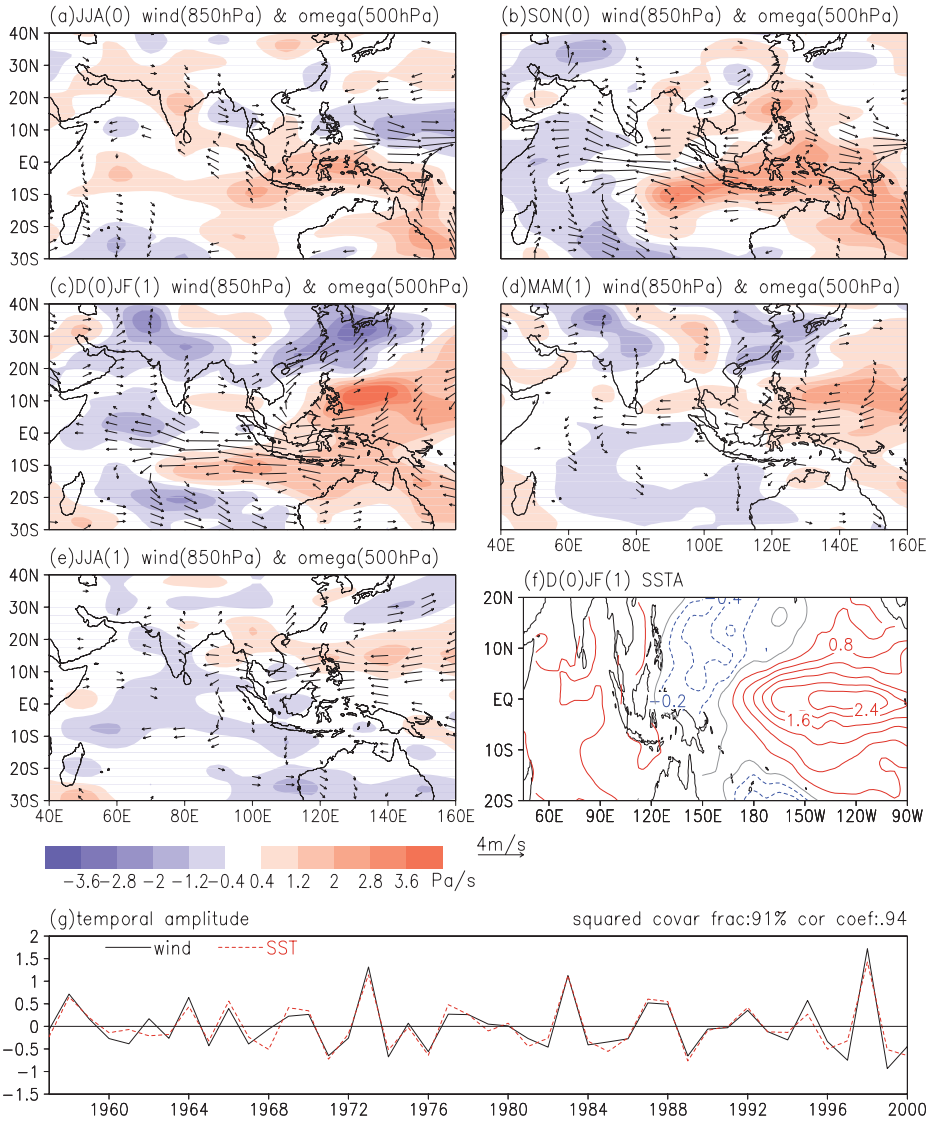

Figure 6.3. Spatial patterns (a–f) and corresponding time coefficients (g) of wind and SST anomalies. In panels (a–e), the vectors represent 850-mb horizontal winds (only those values significant at the 95% confidence level are shown) and the shadings show 500-mb vertical motions. Year 0 denotes the year when El Niño develops.
Modified from Wang *et al.* (2003b).

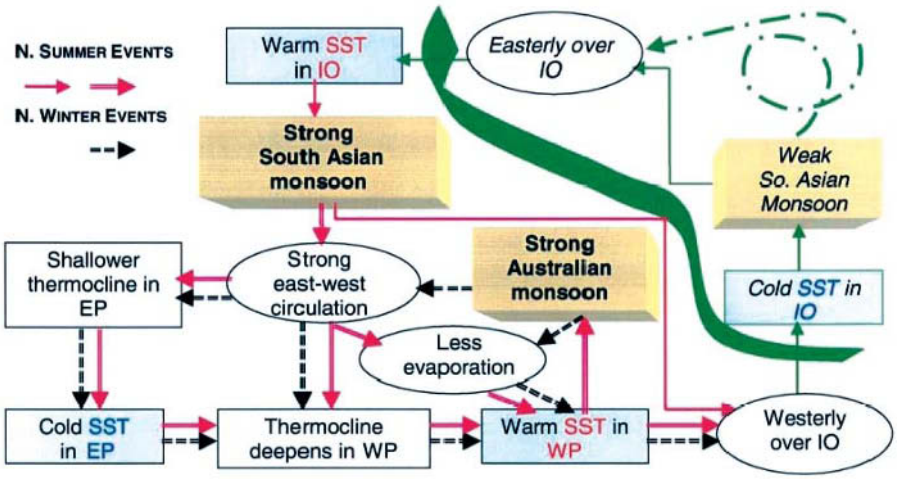

Figure 6.12. Schematic diagram illustrating the interactive processes leading to TBO with an emphasis on the remote SST effect. The scenario begins with warm SSTs in the Indian Ocean, which result in a strong south Asian monsoon in northern summer. Northern summer (winter) driven events follow solid (dashed) arrows. See text for more details.
From Chang and Li (2000).

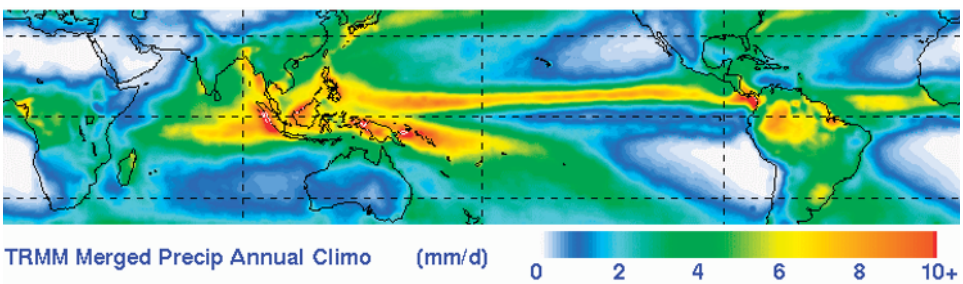

Figure 8.1. Six-year TRMM merged precipitation annual climatology (January 1998–December 2003).

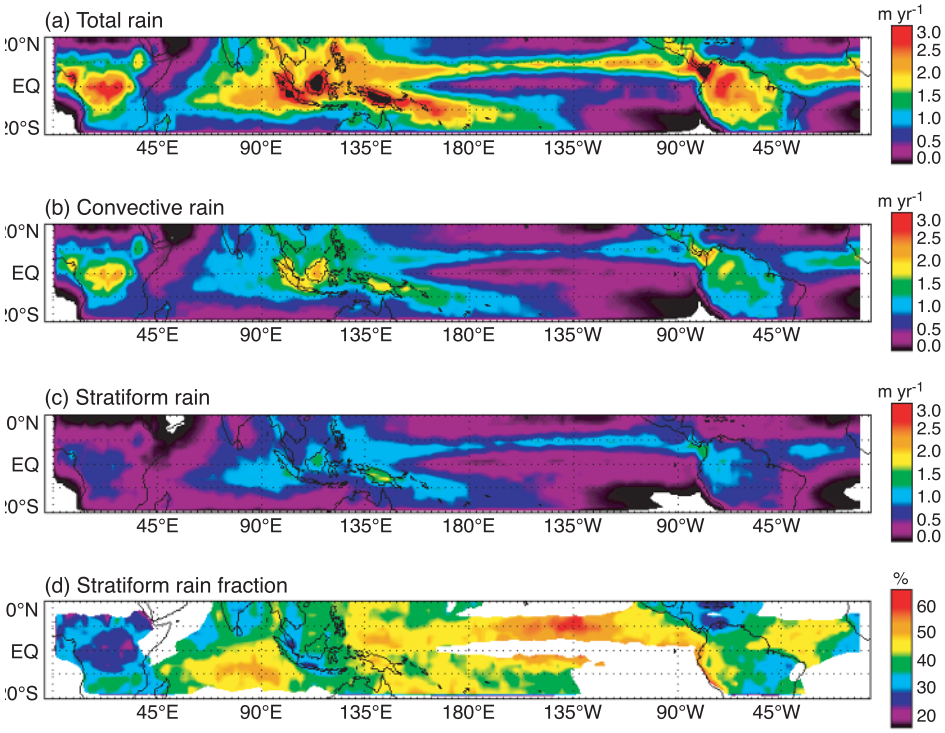

Figure 8.7. TRMM Precipitation Radar (PR) estimates of (a) total rain, (b) convective rain, (c) stratiform rain, and (d) stratiform rain fraction based on 2.5° grid averages for 1998–2000. From Schumacher and Houze (2003).

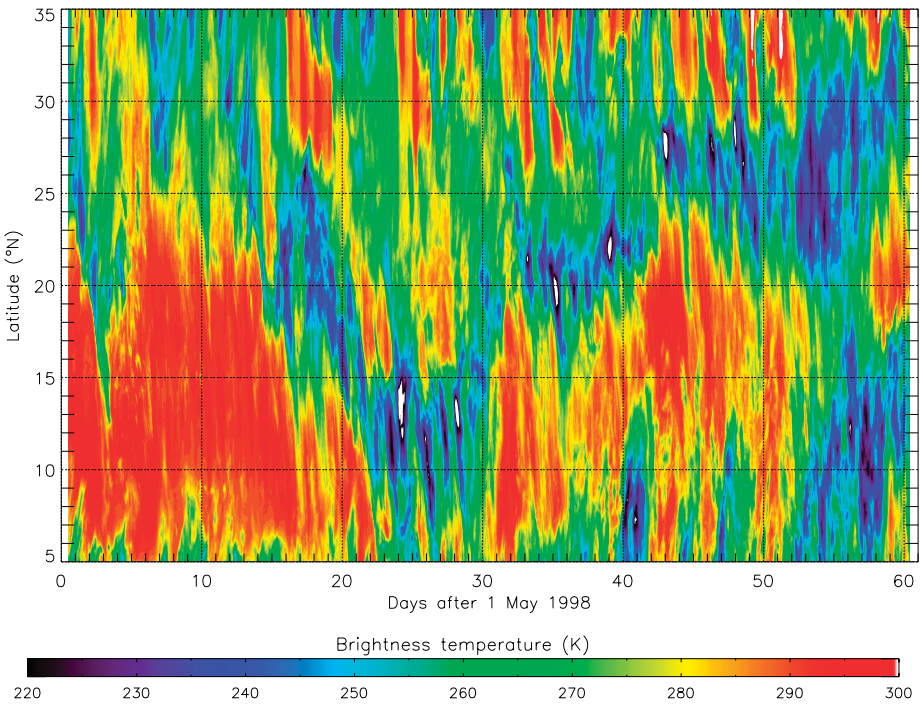

Figure 8.10. Time–latitude plot of IR brightness temperatures averaged over the South China Sea between 110°E and 120°E for 1 May to 30 June 1998.

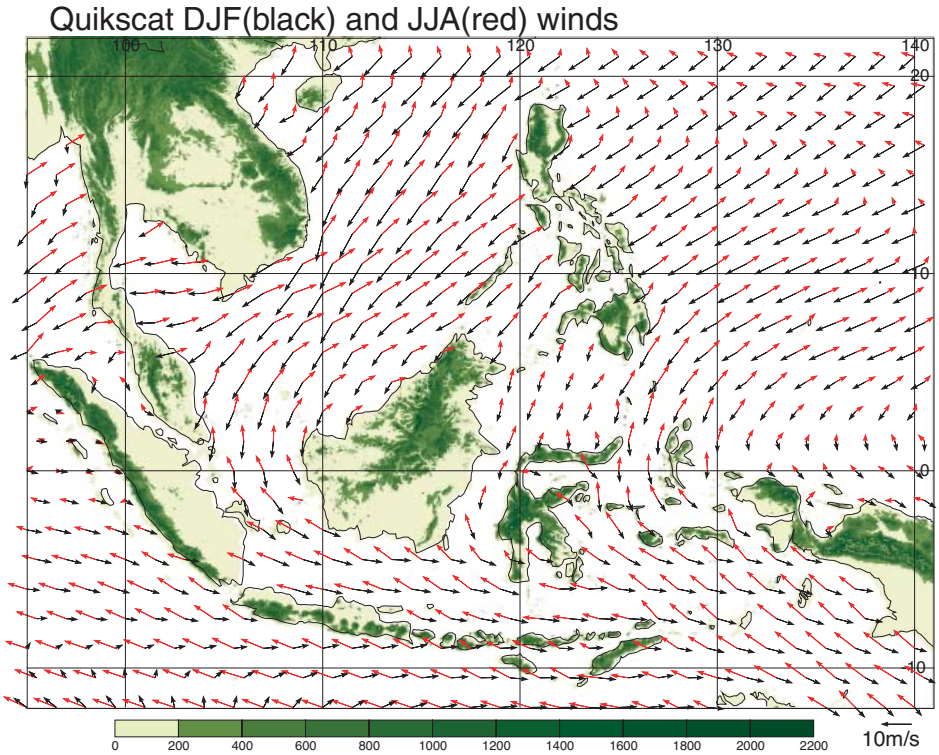

Figure 8.12. Mean QuikSCAT wind for DJF (black) and JJA (red). Topography in meters. From Chang *et al.* (2005).

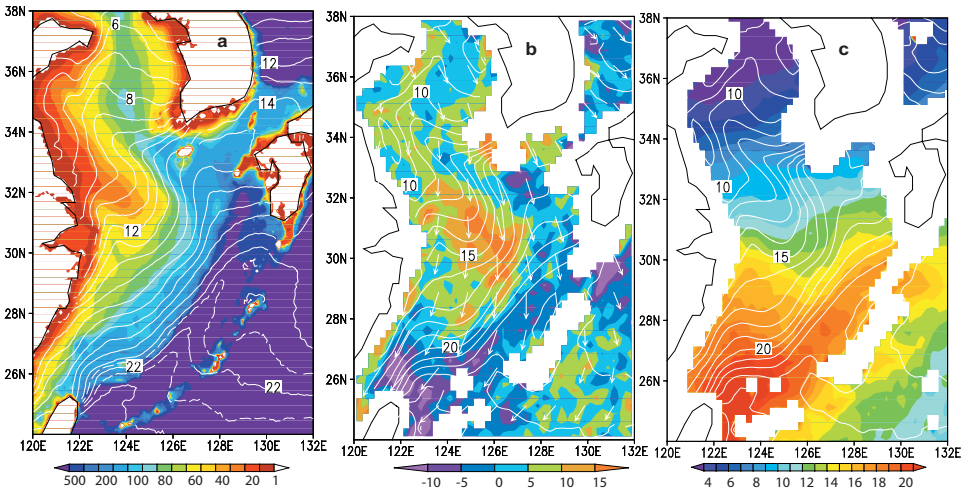

Figure 8.18. January–March SST climatology (contours in °C) over the Yellow and East China Seas, along with: (a) bottom depth (m); (b) velocity (vectors in $m\,s^{-1}$) and divergence (color in $10^{-6}\,s^{-1}$) of QuikSCAT wind; and (c) TMI cloud liquid water (10^{-2} mm). The QuikSCAT and TMI climatologies are January–March averages for 2000–2002. From Xie (2004).

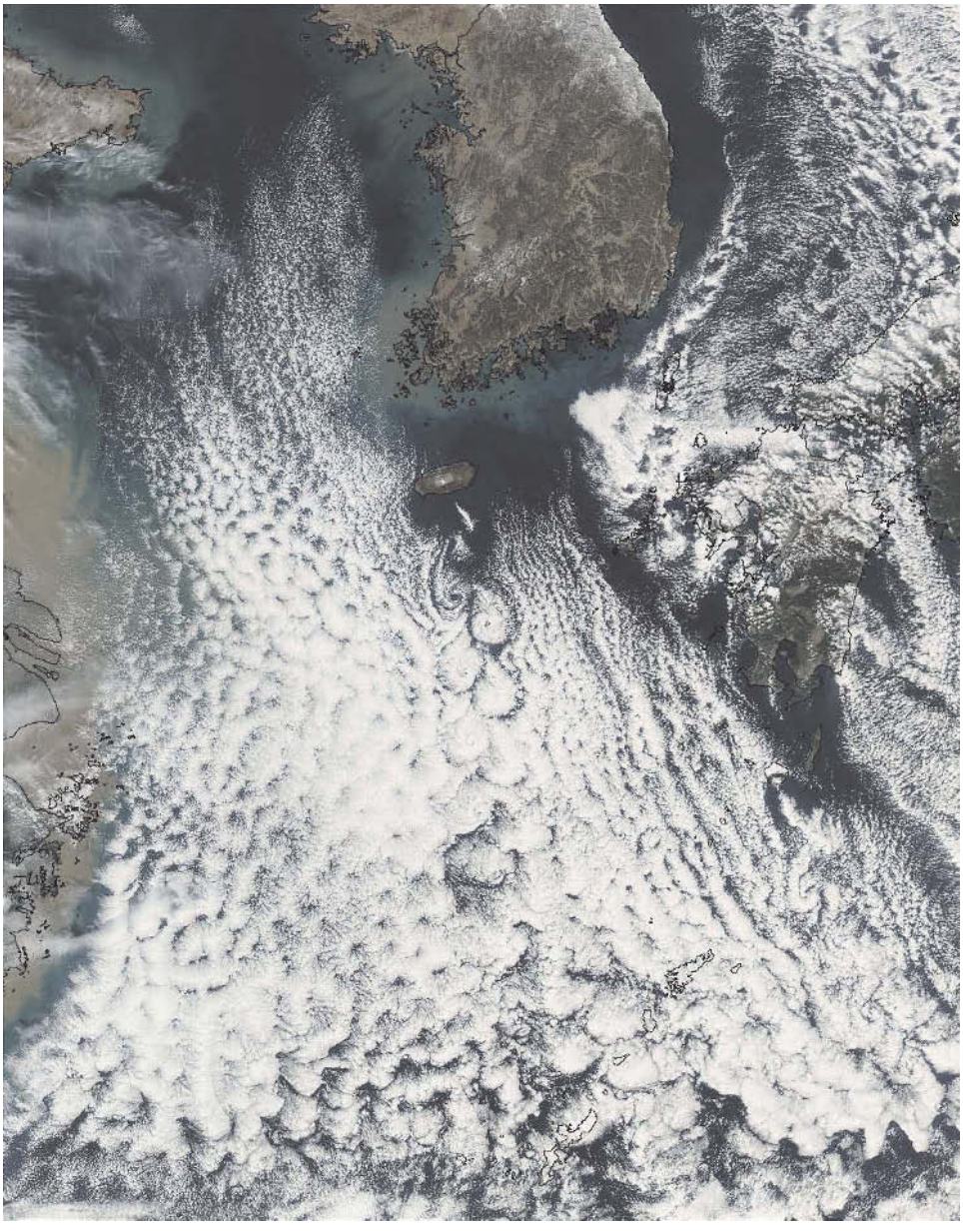

Figure 8.17. *Aqua* satellite image of cloud lines, closed cells, and vortex streets over the East China Sea on 15 January 2003 during a cold air outbreak.

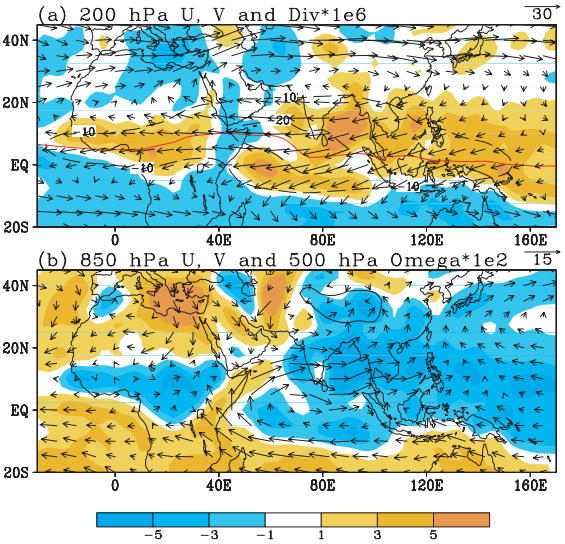

Figure 9.10. (a) The upper tropospheric Tibetan High and easterly jet at 200 hPa and associated divergence (units $10^{-6}\,s^{-1}$). Note the extent of the easterly jet that commences over the Philippine Sea and extends out across the Atlantic Ocean. (b) The lower tropospheric winds at 850 hPa and mid-tropospheric vertical pressure velocity. Note the strong cross equatorial Somalia jet and the confluence of the south-west monsoon and south-easterly trades.

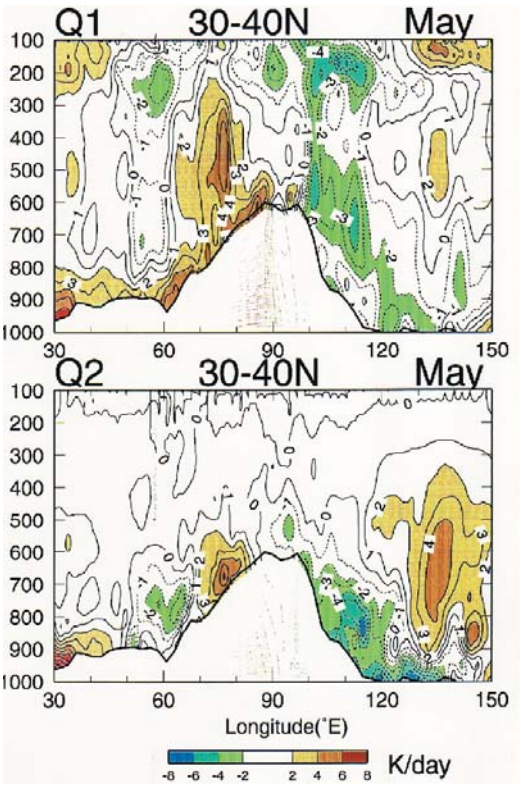

Figure 11.3. Longitude–vertical cross sections for May showing mean (a) heating rate Q_1/c_p (K day^{-1}) and (b) drying rate Q_2/c_p (K day^{-1}) for the 30°–40°N latitudinal band through the Tibetan Plateau. Dark (light) shaded regions indicate a heating rate greater (less) than +2 (−2) K day^{-1}.
Ueda *et al.* (2003).

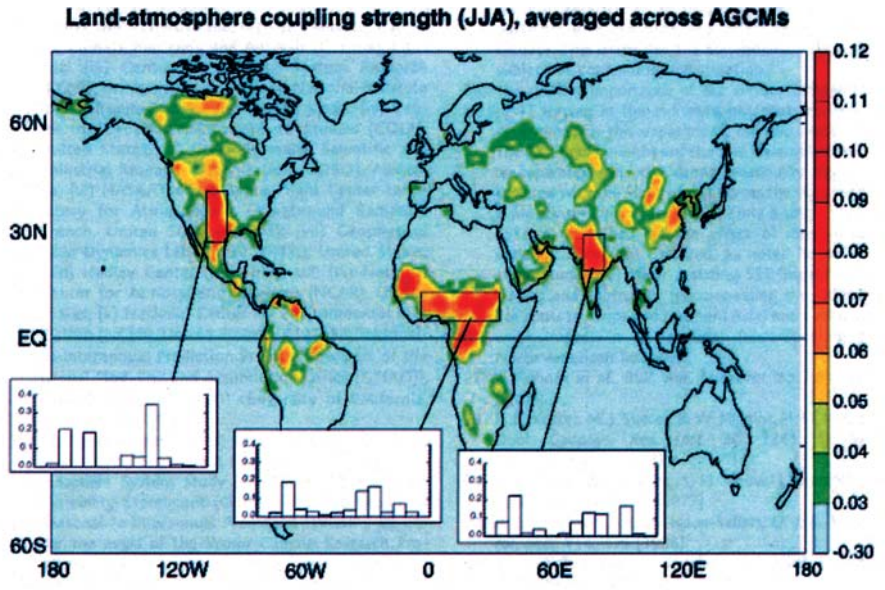

Figure 11.9. The land–atmosphere coupling strength diagnostic for boreal summer, averaged across the 12 models participating in GLACE. (Insets) Area-averaged coupling strengths for the 12 individual models over the outlined, representative hotspot region. No signal appears in southern South America or at the southern tip of Africa.
Koster *et al.* (2004).

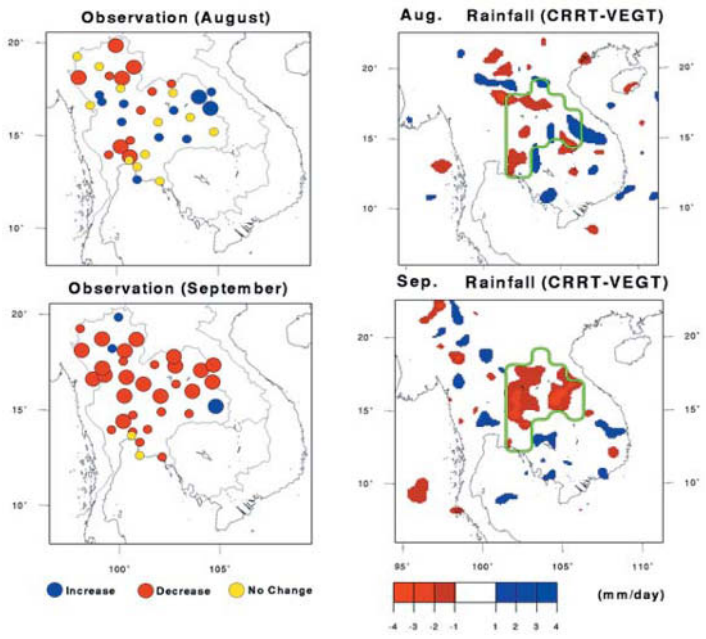

Figure 11.13. Observed rainfall trend during 1950–1990 in August (*left, upper*) and September (*left, lower*) and rainfall difference in August (*right, upper*) and September (*right, lower*) computed between vegetated condition and deforested condition. Blue (red) colour shows increasing trend or positive values, and size of circles in the left column shows the trend values.
Kanae *et al.* (2001).

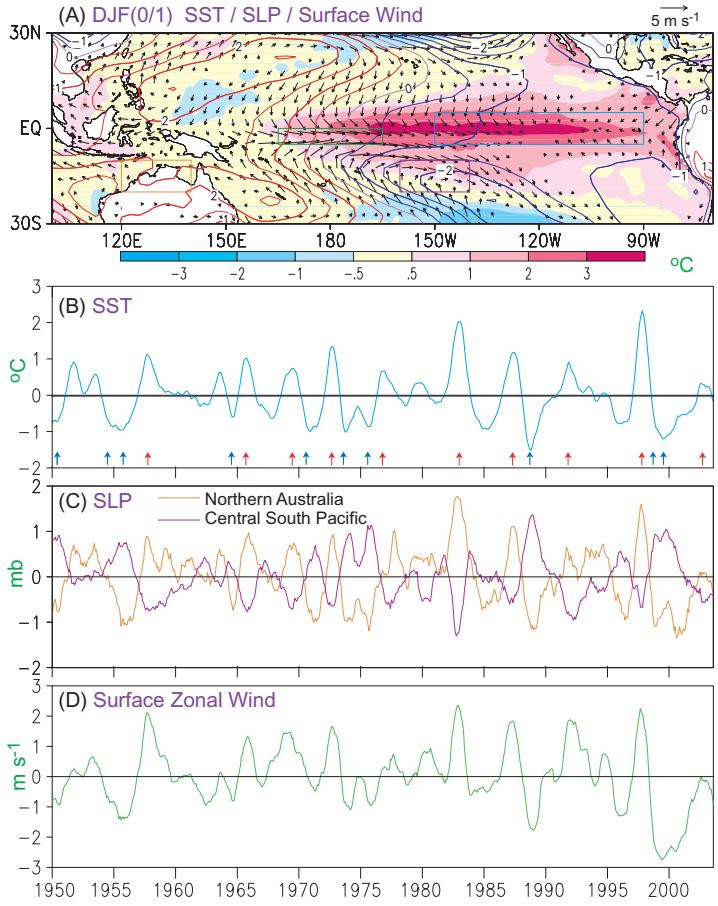

Figure 12.1. (a) Distribution of the warm-minus-cold composites of SST (shading), SLP (contour interval: 0.5 hPa), and surface wind vector (arrows) during DJF(0/1), as computed using observational data sets for ten warm and ten cold ENSO events (indicated by red and blue markers along the time axis in panel (b)). Time series of areal averages of anomalies of (b) SST in the central equatorial Pacific, (c) SLP in the vicinity of Tahiti and Darwin, and (d) surface zonal wind over the western equatorial Pacific. The rectangular sites used for computing the areal averages in (b–d) are indicated in (a), with colors matching those used in plotting the respective time series in the lower three panels.

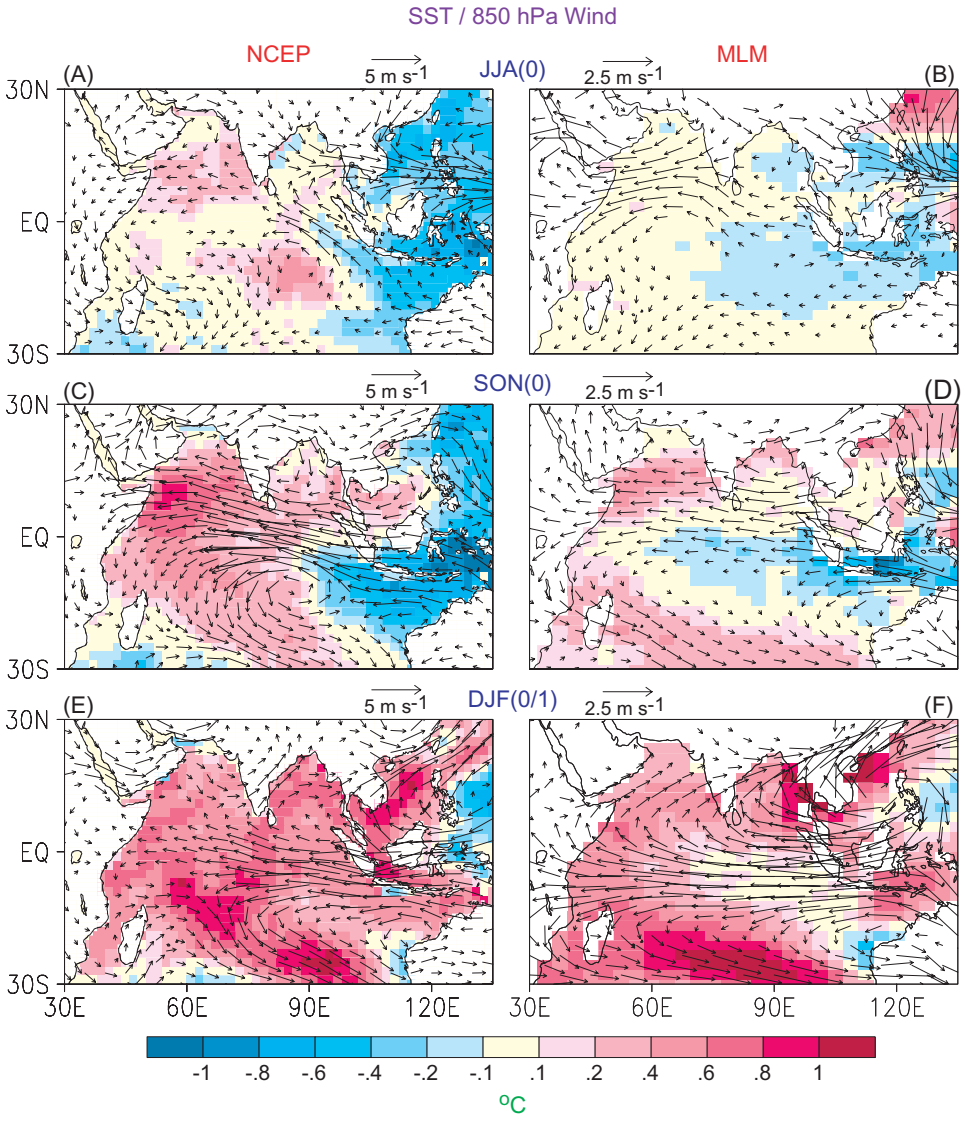

Figure 12.5. Distributions of the warm-minus-cold composites of 850-hPa vector wind (arrows; note different scales used in left and right panels) and SST (shading) fields, for (a, b) JJA(0), (c, d) SON(0), and (e, f) DJF(0/1). Results are based on NCEP data (left panels) and output from the MLM experiment (right panels) for six selected warm ENSO events and six cold events. The composite data shown in all following figures are based on the same set of ENSO events.

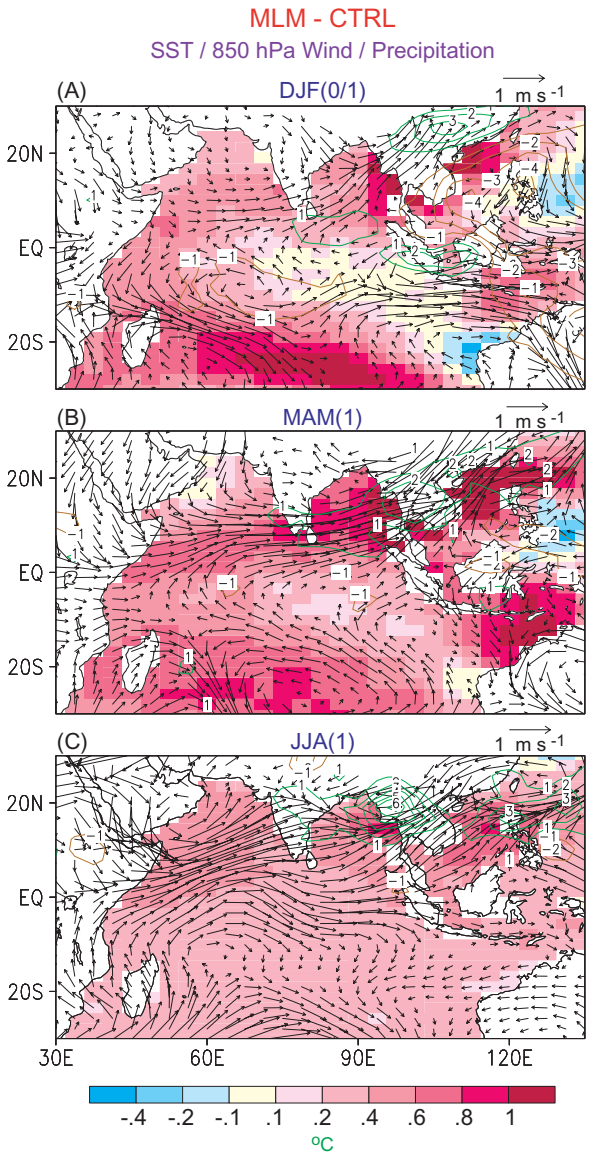

Figure 12.7. Distributions of the differences between the outputs from the MLM and CTRL experiments for the warm-minus-cold composites of SST (shading), 850-hPa vector wind (arrows), and precipitation (contour interval: 1 mm day^{-1}; zero contour omitted), for (a) DJF(0/1), (b) MAM(1), and (c) JJA(1).

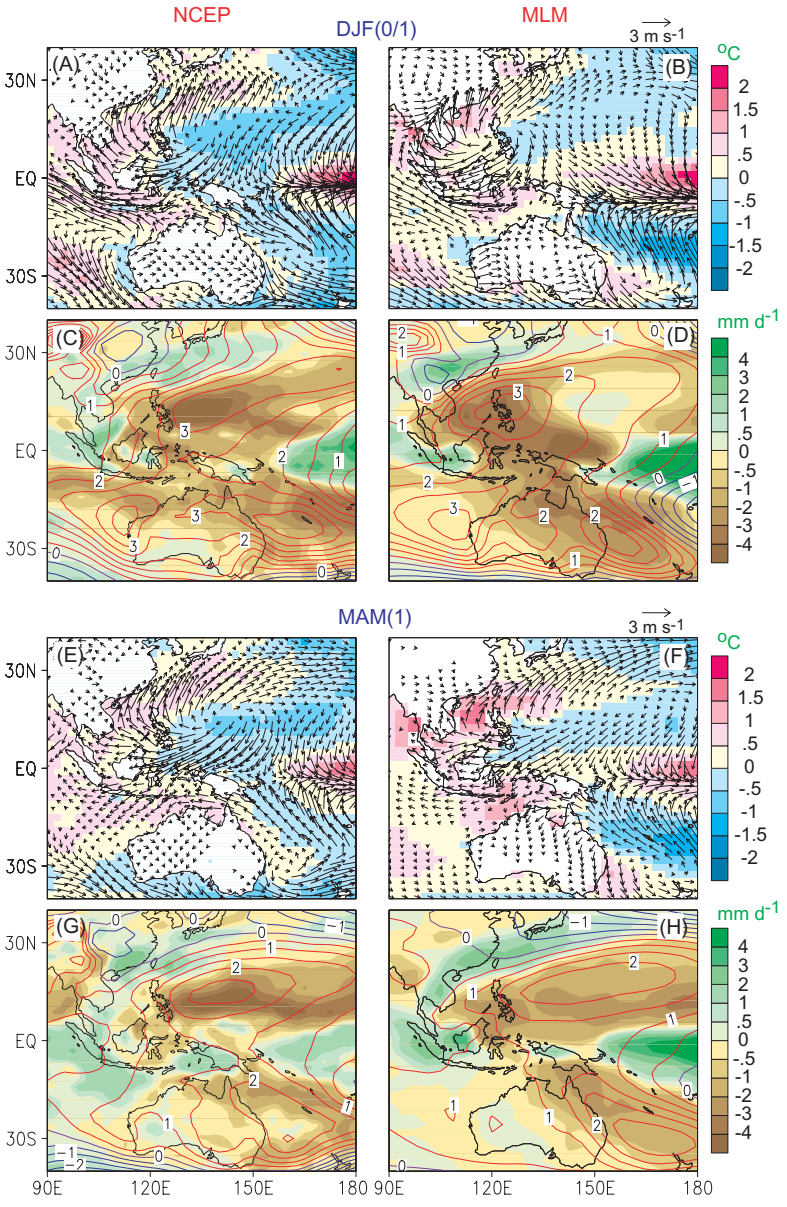

Figure 12.8. Distributions of the warm-minus-cold composites of (a, b, e, f) surface wind vector (arrows) and SST (shading), and (c, d, g, h) SLP (contour interval: 0.5 hPa) and precipitation (shading). Results are based on NCEP data (*left panels*) and output from the MLM experiment (*right panels*), for DJF(0/1) (*top four panels*) and MAM(1) (*bottom four panels*).

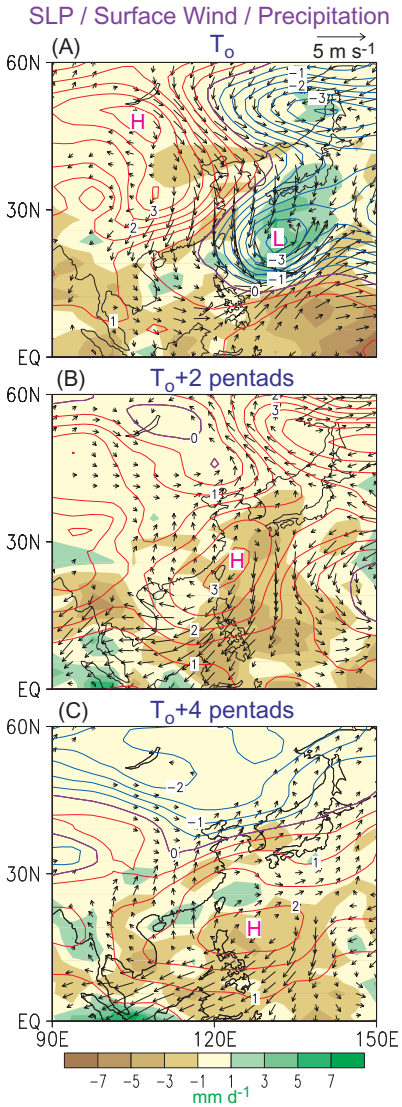

Figure 12.11. Distributions of the composite patterns of surface wind vector (arrows), SLP (contour interval: 0.5 hPa), and precipitation (shading), for the time periods of (a) T_o, (b) $T_o + 2$ pentads, and (c) $T_o + 4$ pentads, where T_o corresponds to the pentad when the SLP field over the South China and Philippine Seas makes a distinct transition to an anticyclonic pattern.

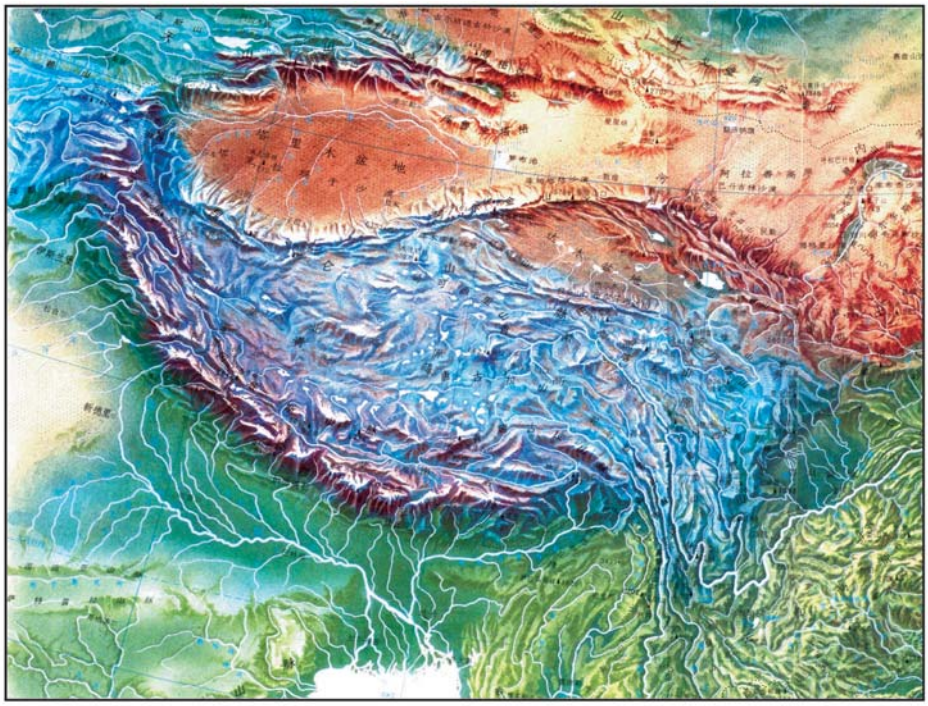

Figure 13.1. Orography of Tibetan Plateau.

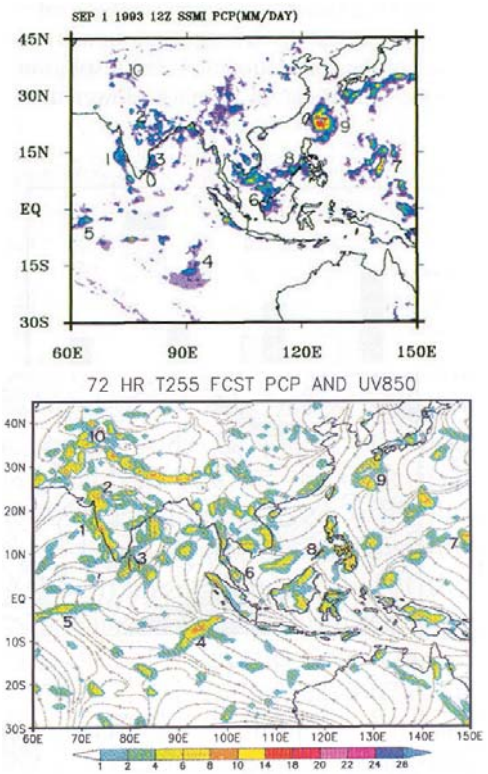

Figure 14.2. (a) Observed 24-hour rainfall (12 UTC , 1 September 1995; mm day^{-1}); (b) 72-hour forecast of 850-hPa flow field with superimposed accumulated rainfall (mm day^{-1}) using a global model at T255 resolution. Numbers (1–10) on each panel identify regions of heavy rainfall and a close match between the observed and forecast fields.

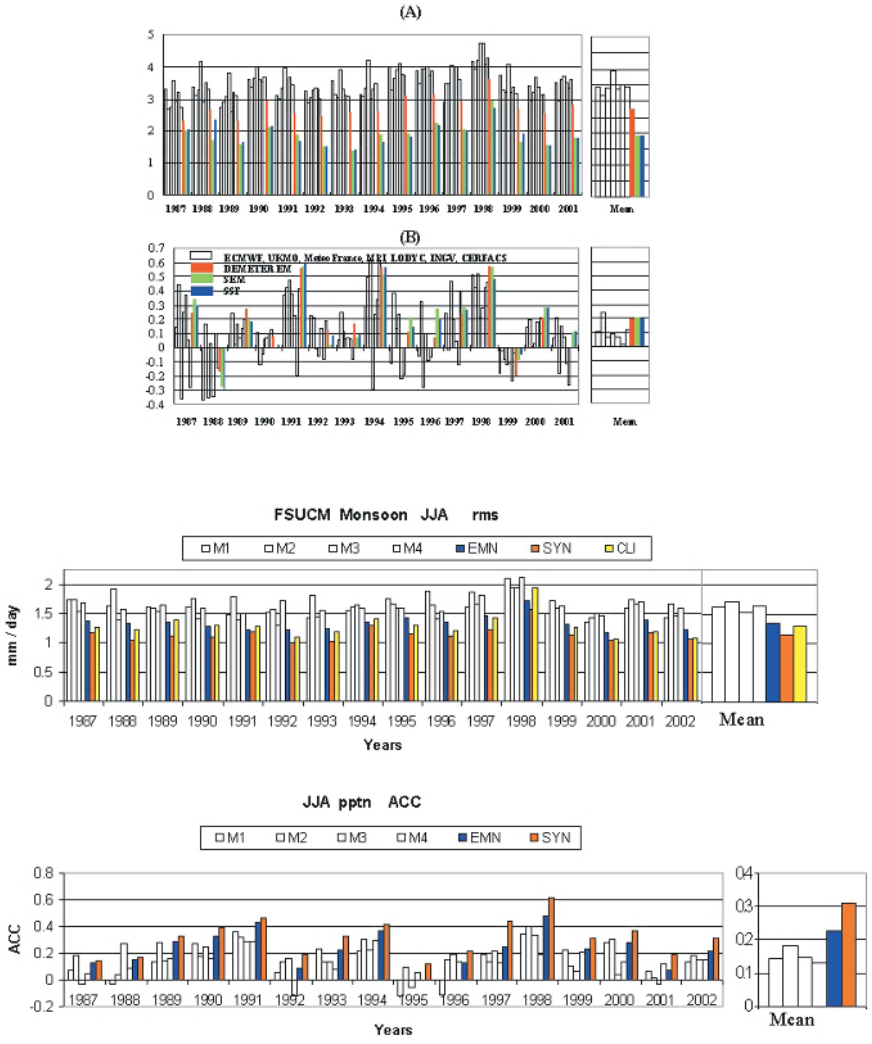

Figure 14.9. (a) r.m.s. errors and anomaly correlation of precipitation forecasts for different years for 7 DEMETER models, ensemble mean of the 7 DEMETER models, synthetic ensemble mean, and for the synthetic superensemble. Domain for the Asian summer monsoon is 50°E to 110°E, 10°S to 35°N. Units for r.m.s. are mm day^{-1}. (b) Same as (a) but for the suite of 4 FSU coupled models.

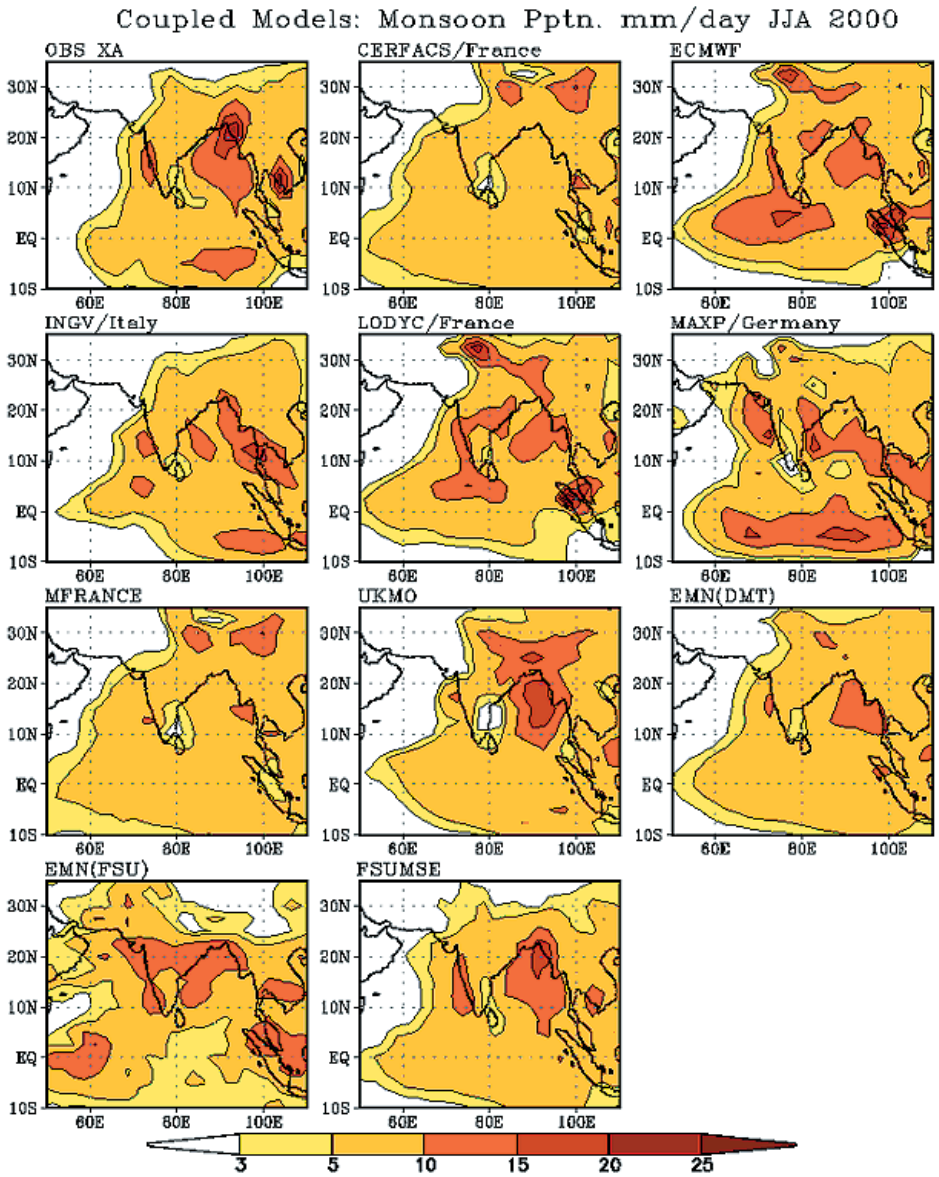

Figure 14.10. An example of the seasonal forecast of precipitation (mm day^{-1}) for a relatively wet monsoon year (2000 is shown). The observed estimates from Xie and Arkin (1997), from the member models of DEMETER, from the ensemble mean of the four FSU models, and from the FSU synthetic superensemble are all shown.

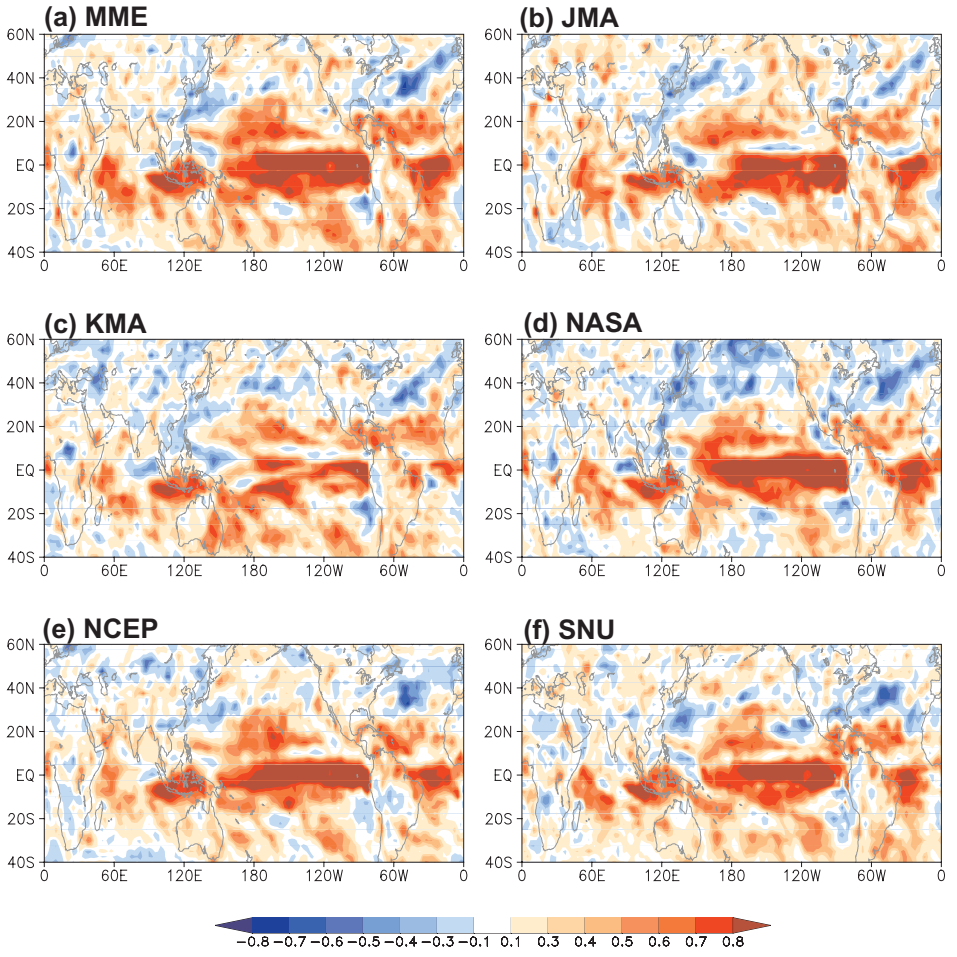

Figure 15.6. Distribution of the correlation coefficient between the observed and simulated ensemble mean precipitation at each grid point. Each model case is marked at the upper left corner of each panel, and the five model composite case is shown in (a).

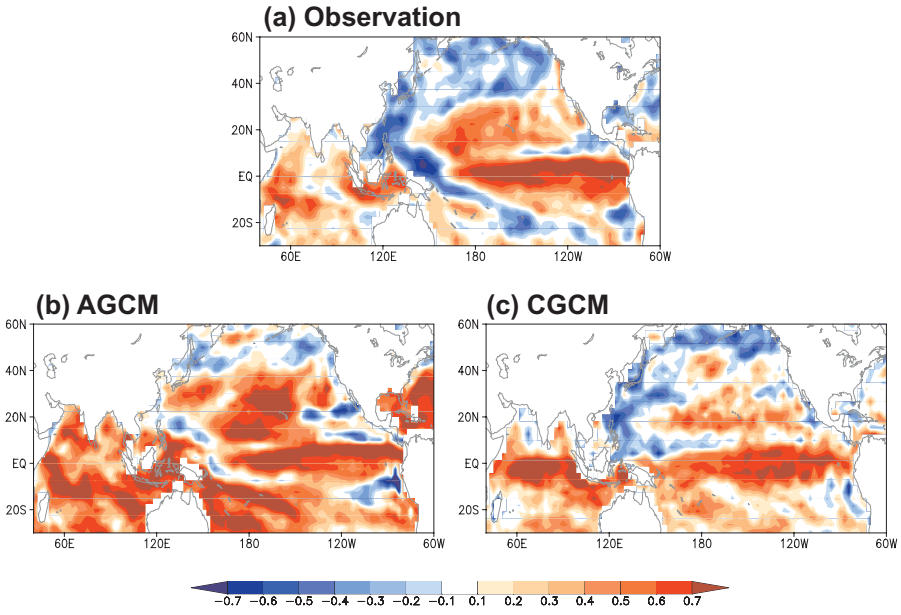

Figure 15.15. Local correlation coefficients between JJA rainfall and SST. (a) Observation calculated during 1979–1999, (b) AGCM for 1950–1999, and (c) CGCM for 25 years, respectively.

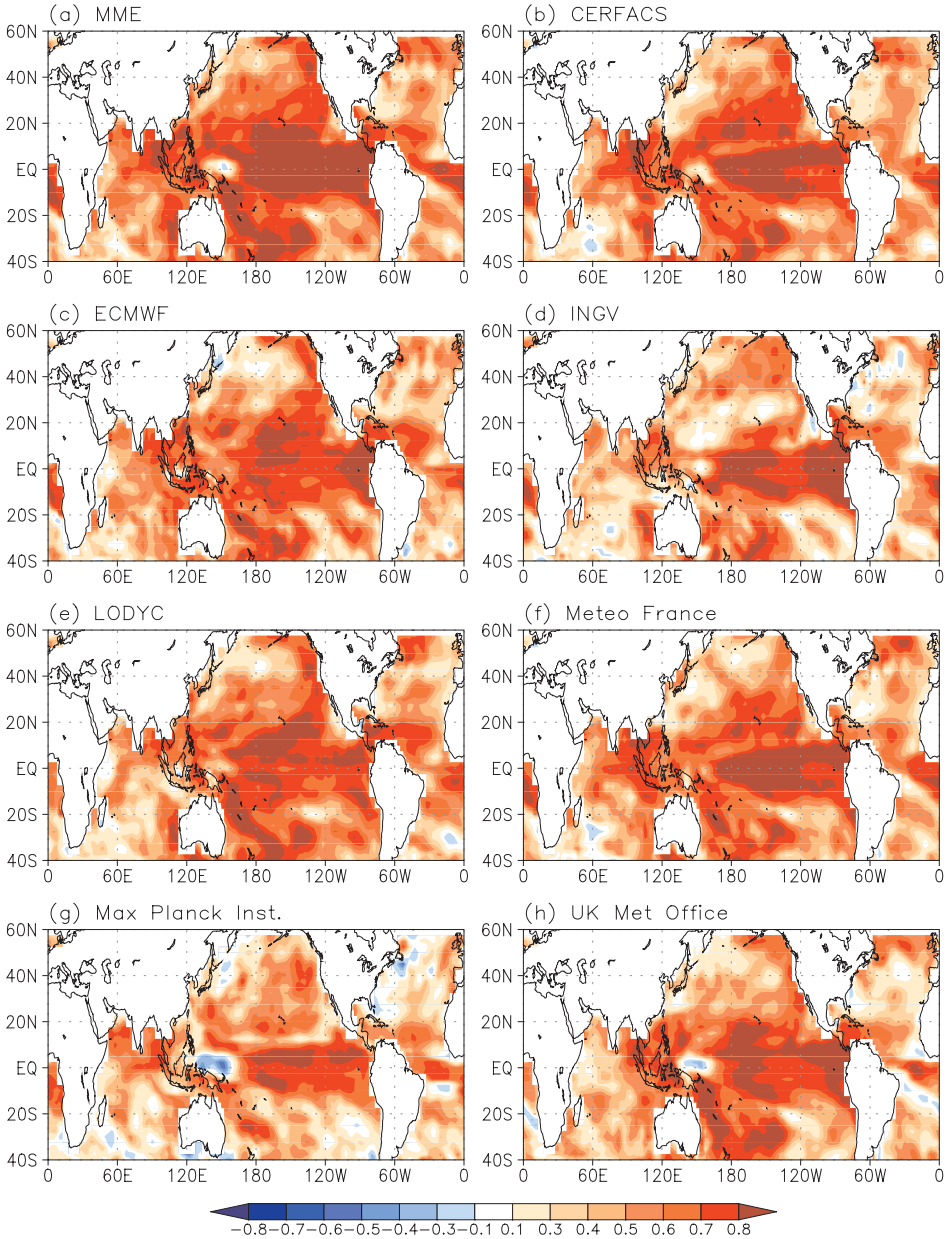

Figure 15.16. Correlation coefficient of summer mean SST for the multimodel composite (a) and the individual models (b–h) in a tier-one system of DEMETER over the globe during 1980–1999.

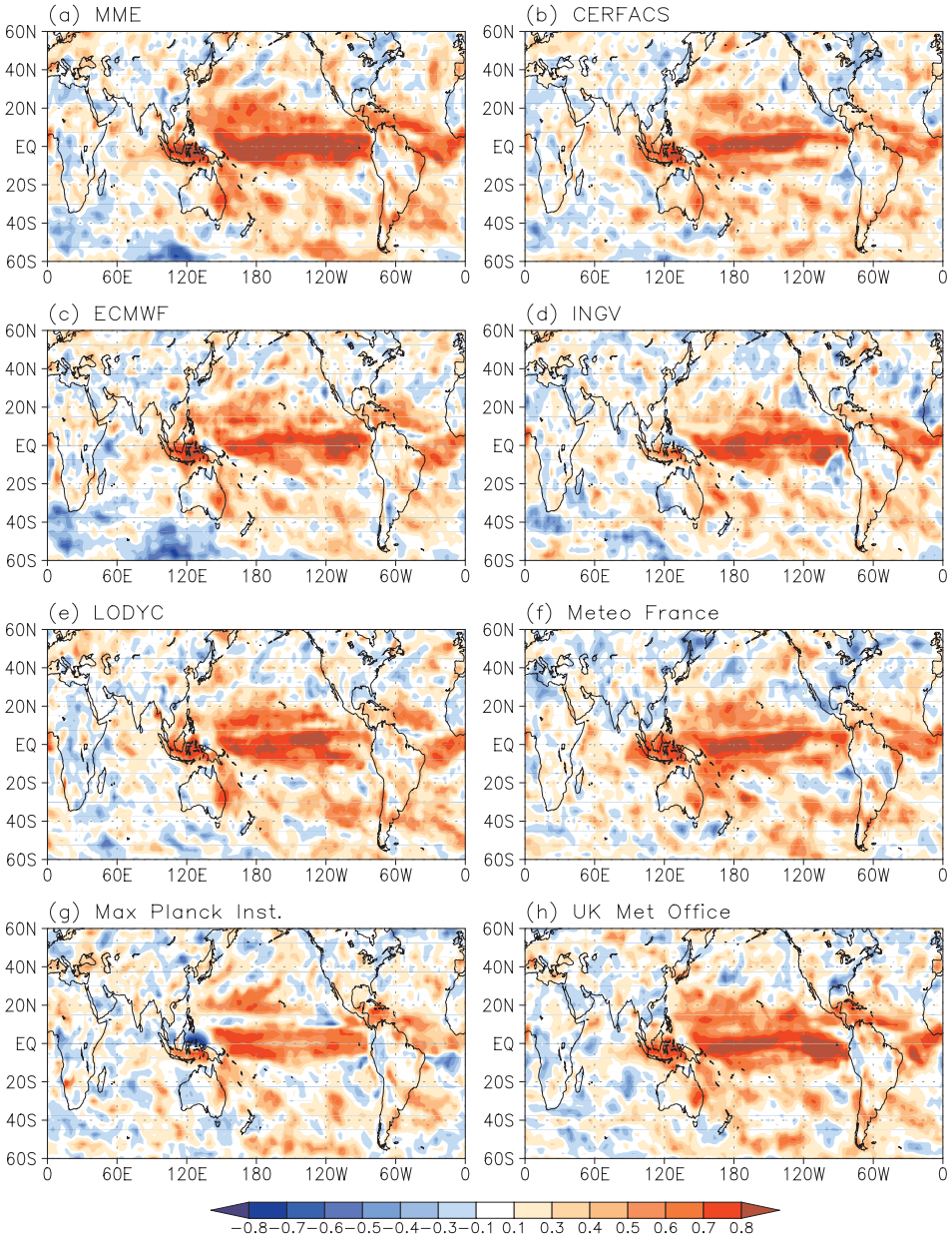

Figure 15.17. Correlation coefficient of summer mean precipitation for the multimodel ensemble (a) and the individual models (b–h) in a tier-one system of DEMETER over the globe.

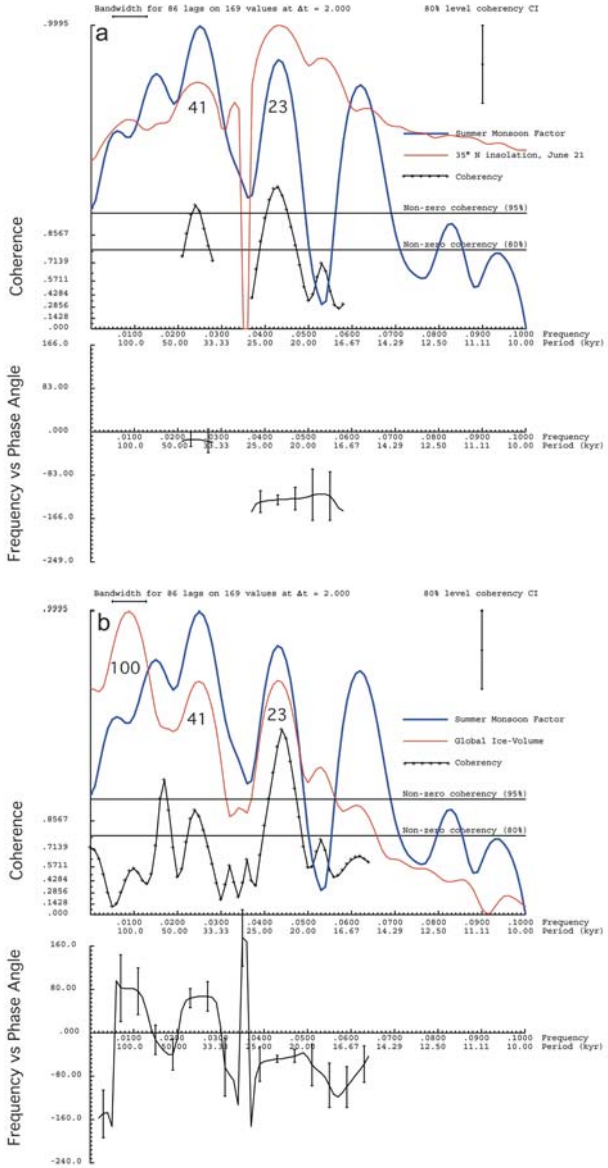

Figure 16.3. Coherence and phase relationships between the Indian summer monsoon, solar insolation, and global ice volume over the past 350,000 years. (a) Cross spectral analysis of the Indian summer monsoon (Clemens and Prell, 2003) and insolation for June 35°N. (b) Cross spectral analysis of the Indian summer monsoon and global ice volume. Coherence defines the extent to which two variables are linearly related at specific frequency bands while phase defines temporal lead–lag relationships at specific frequency bands. Spectral densities are normalized and plotted on log scales. The coherence spectra are plotted on a hyperbolic arctangent scale. The horizontal solid lines indicate confidence at the 80% and 95% levels. Positive phase angles indicate that summer monsoon maxima lead insolation or ice volume maxima whereas negative phase angles indicate that monsoon maxima lag maxima in these variables. For example, monsoon variability at the precession band (frequency = 0.043, period = 23 ky) is coherent with changes in summer insolation well above the 95% confidence interval. Phase indicates that the strongest summer monsoons occur 120° or 7.7 kyr after summer insolation maxima ($120°/360° \times 23$ kyr). These coherence and phase relationships are presented graphically in Figure 16.4.

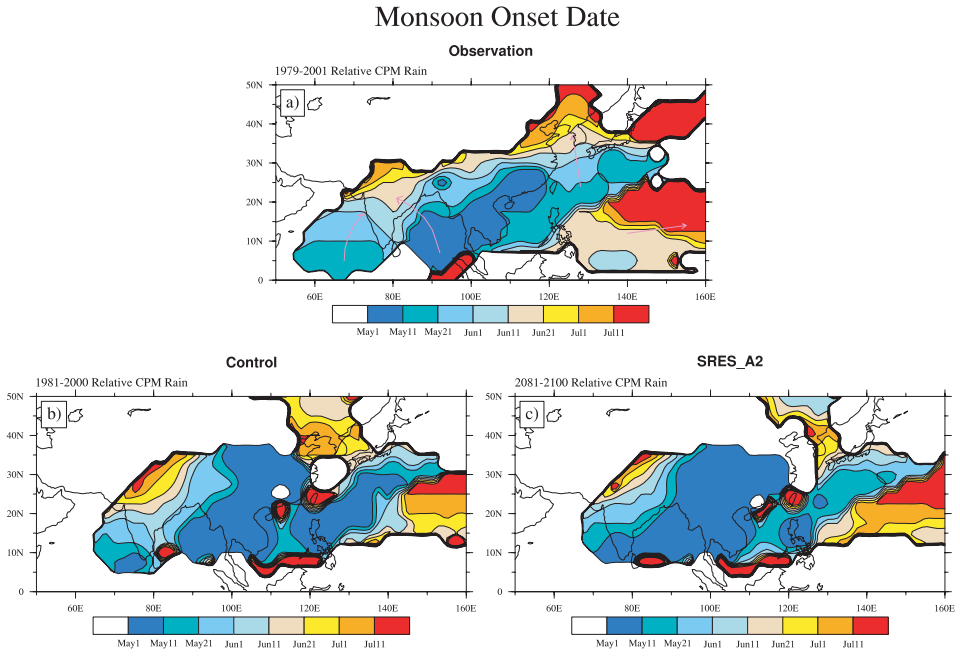

Figure 17.8. Onset dates of the rainy season. (a) Observation based on Xie and Arkin (1997) precipitation. (b) Present-day (1981–2000) simulation. (c) 2081–2100 in SRES-A2 scenario by the MRI-CGCM2.

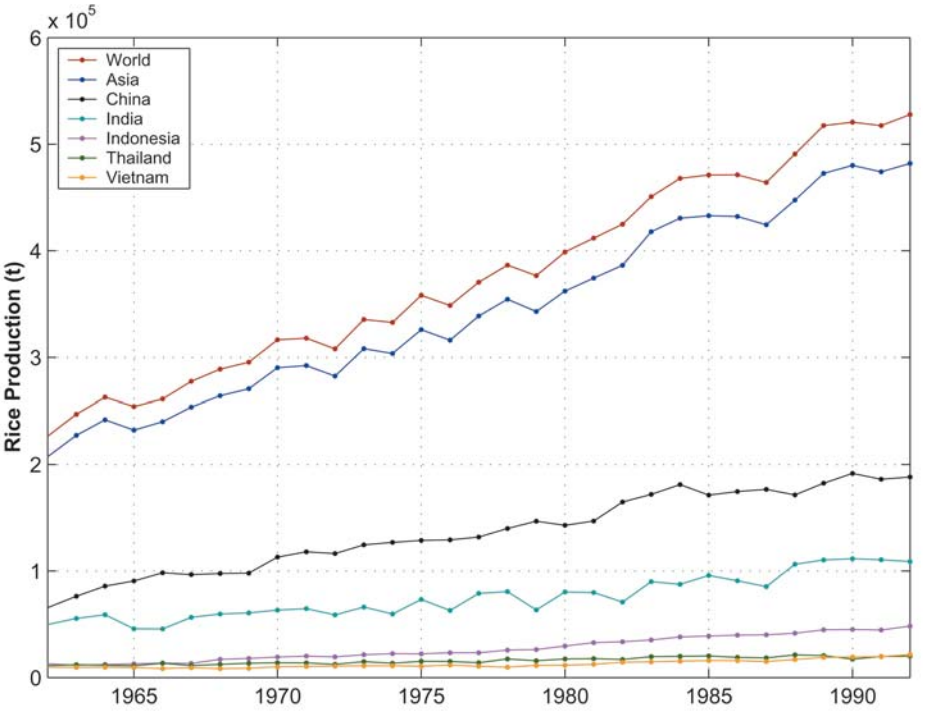

Figure 18.3. Annual rice production ($\times 10^5$ tonnes) in major rice-growing countries of the World during 1961–1993.

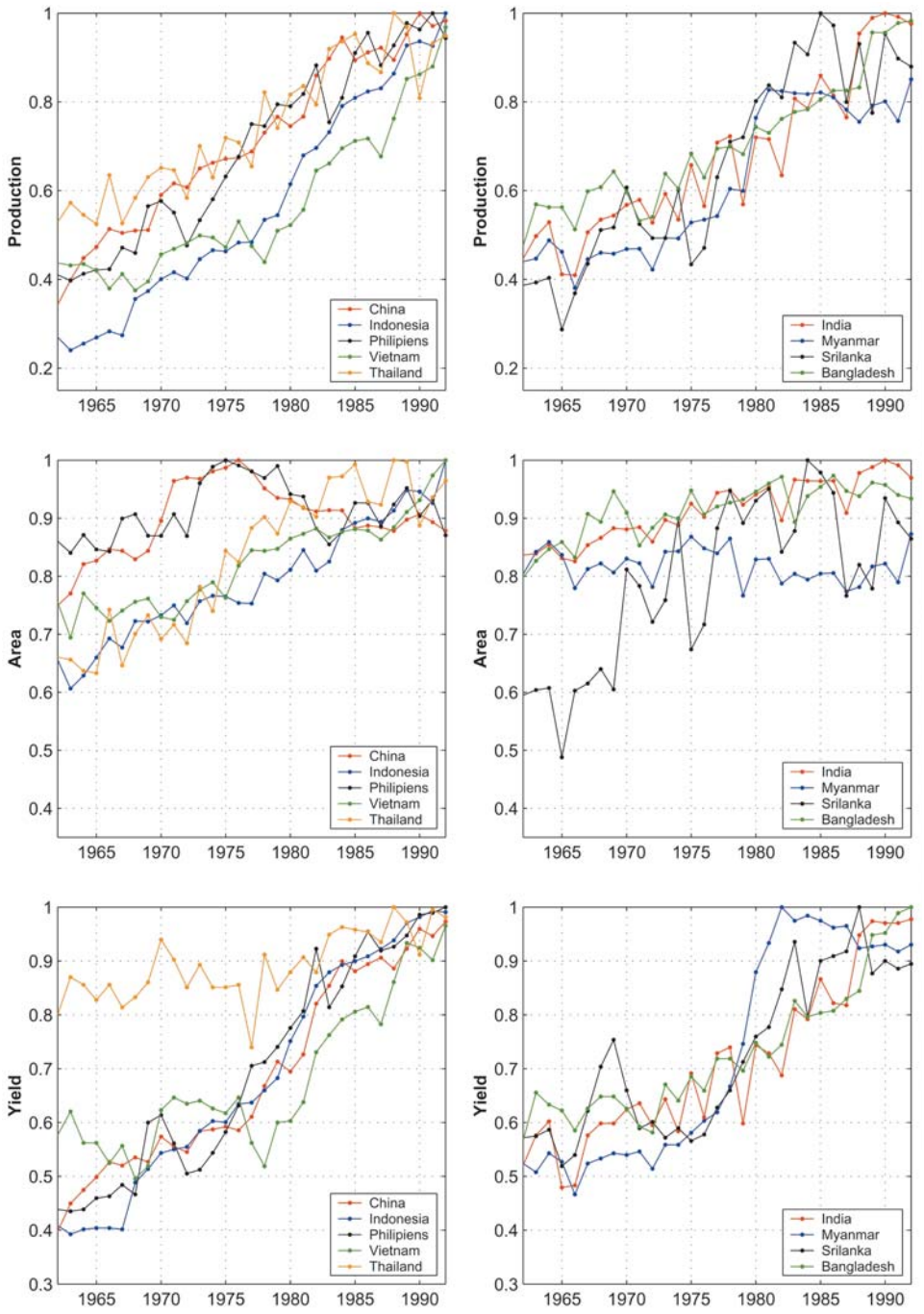

Figure 18.4. Variation of normalized annual rice production, area, and yield in the major rice-growing countries of Asia during 1961–1993.

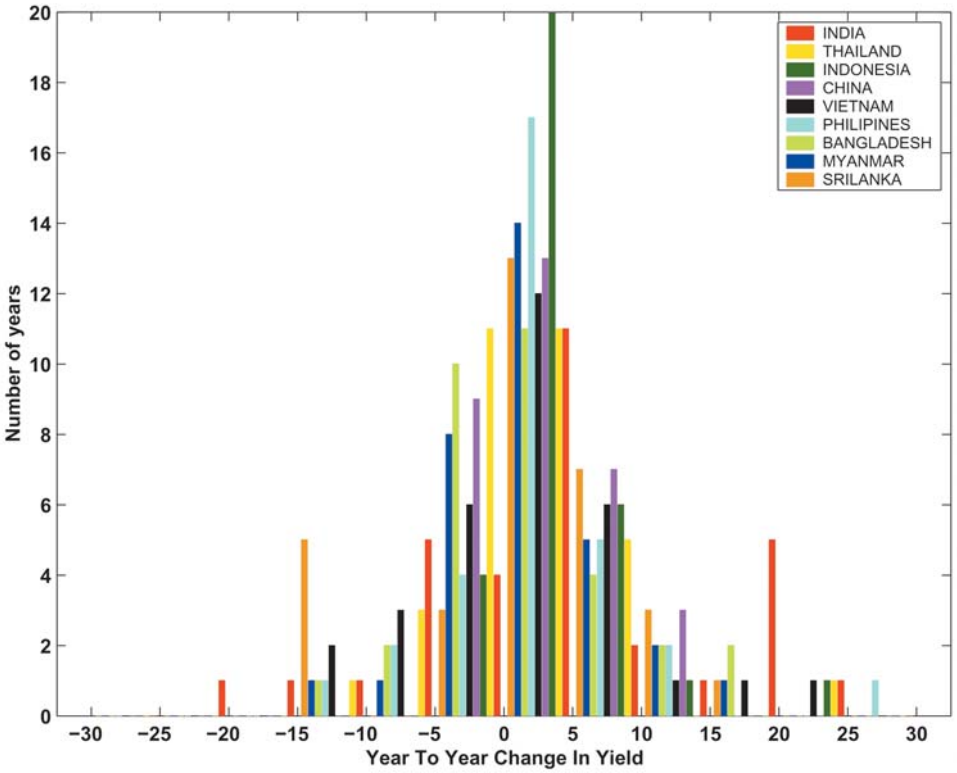

Figure 18.5. Frequency distribution of the change in yields from one year to the next (expressed as a percentage of the yield of the previous year) for different countries.

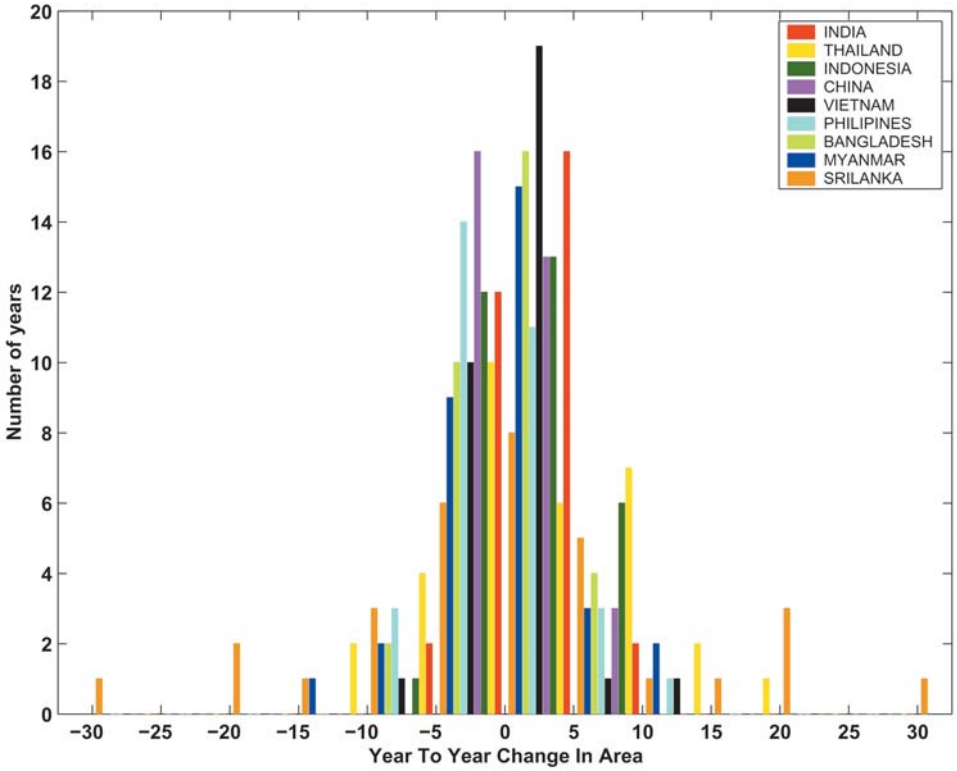

Figure 18.6. Frequency distribution of the change in area under rice cultivation from one year to the next (expressed as a percentage of the area of the previous year) for different countries.

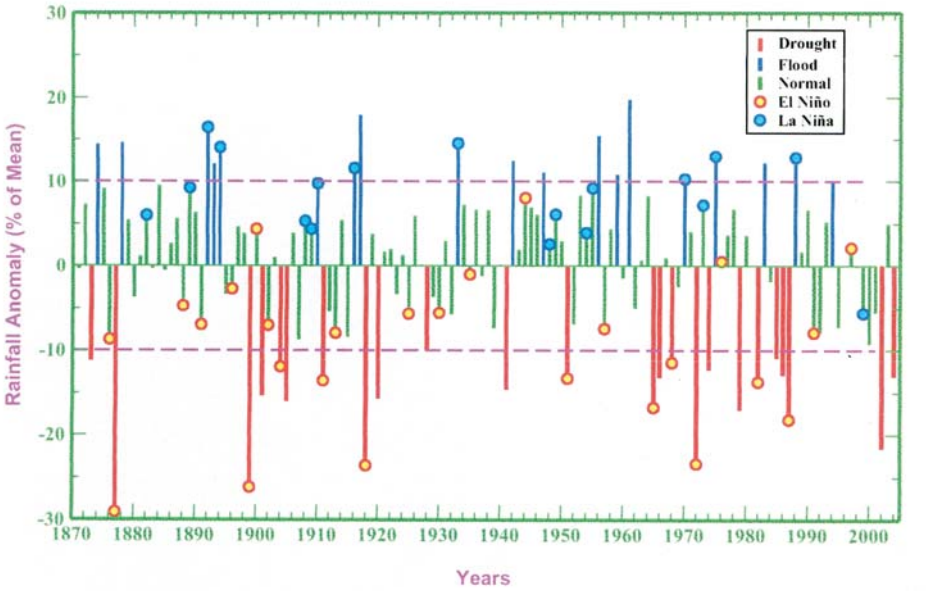

Figure 18.9. Variation of all-India summer monsoon rainfall anomalies during 1871–2004.

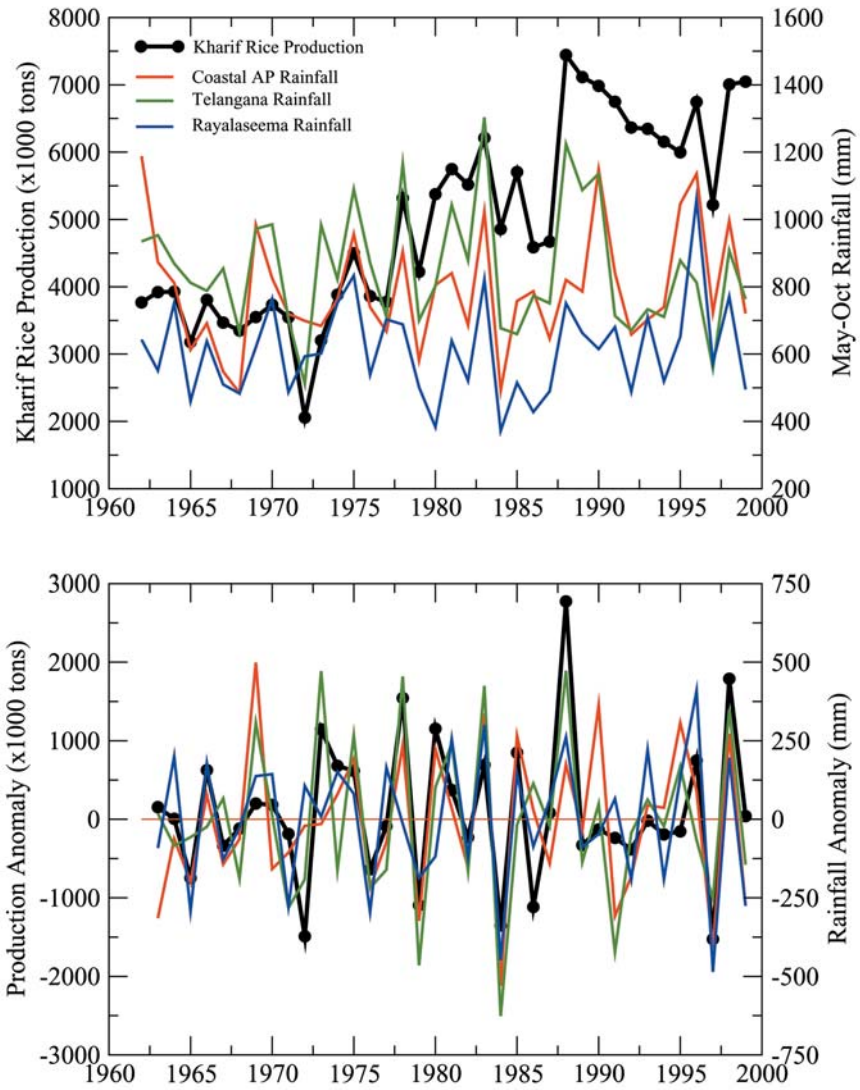

Figure 18.15. Interannual variation of the total kharif rice production in Andhra Pradesh and summer monsoon rainfall (May–October) in the three meteorological subdivisions of the state.

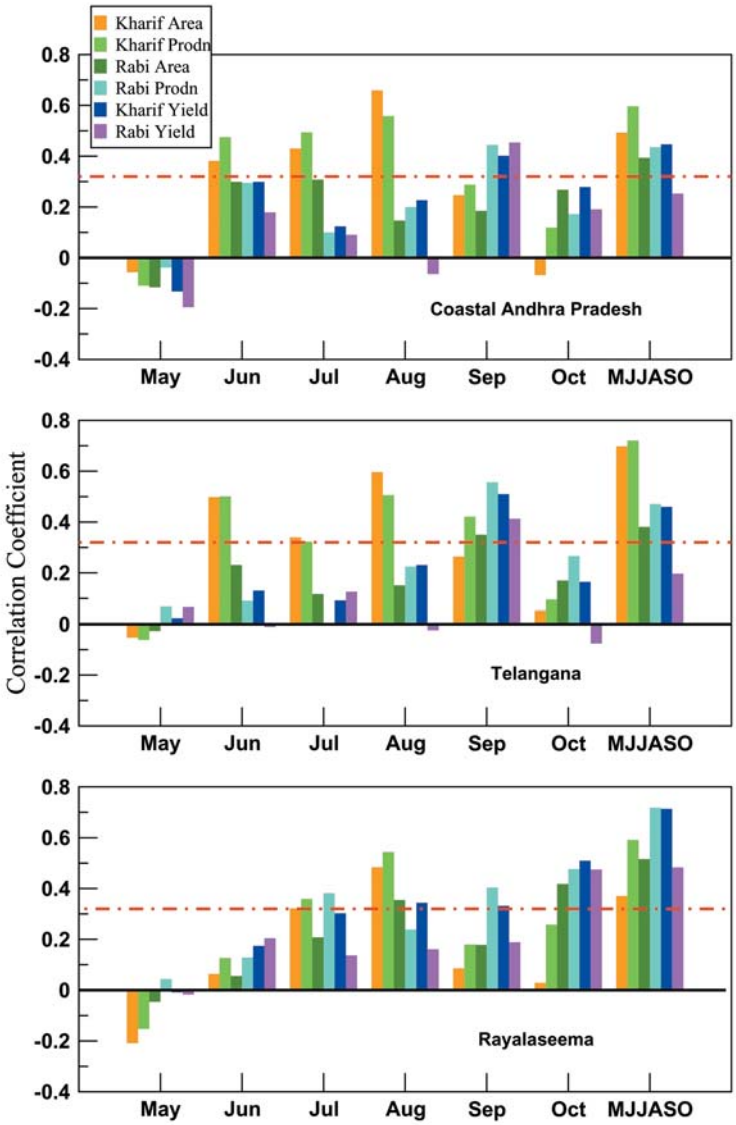

Figure 18.16. Correlation between various rice production parameters in Andhra Pradesh and the monthly/seasonal monsoon rainfall of the three meteorological subdivisions.

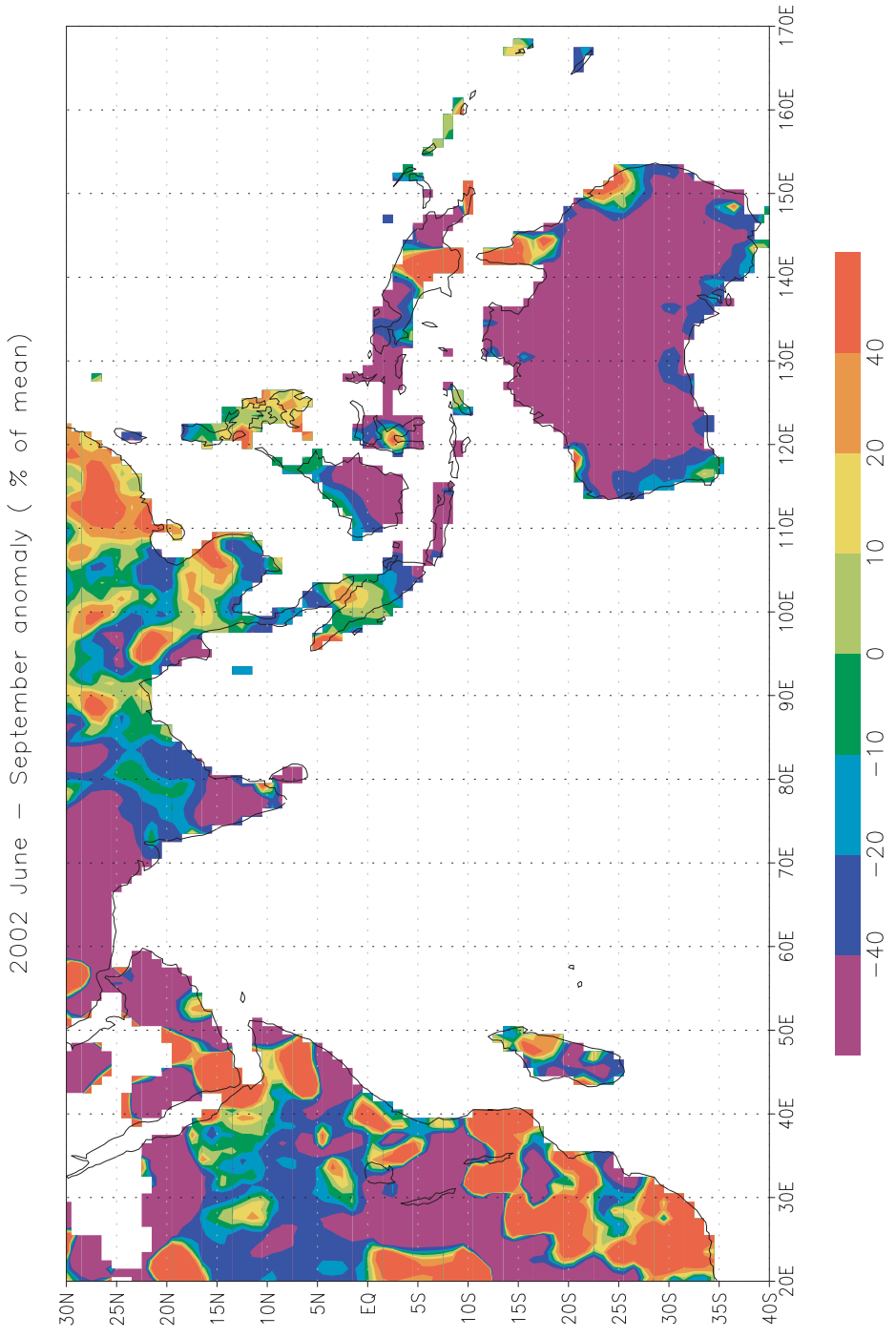

Figure 18.23. Summer monsoon (June–September) rainfall anomaly patterns during the two recent El Niño years of 1997 and 2002.

Printing: Mercedes-Druck, Berlin
Binding: Stein + Lehmann, Berlin